Ashish Chawla
Editor

Thoracic Imaging

Basic to Advanced

Springer

Ashish Chawla
Editor

Thoracic Imaging

Basic to Advanced

Springer

Editor
Ashish Chawla
Department of Diagnostic Radiology
Khoo Teck Puat Hospital
Singapore, Singapore

ISBN 978-981-13-2543-4 ISBN 978-981-13-2544-1 (eBook)
https://doi.org/10.1007/978-981-13-2544-1

Library of Congress Control Number: 2018961567

This Springer imprint is published by the registered company Springer Nature Singapore Pte Ltd.
The registered company address is: 152 Beach Road, #21-01/04 Gateway East, Singapore 189721, Singapore

I dedicate this book to my parents, wife, and my two lovely boys who inspired and continuously motivated me in this journey of writing this book. I am also grateful to the patients who unknowingly provided a great help in understanding the concepts of thoracic imaging.

Preface

Thoracic imaging is difficult and challenging due to the relatively low specificity of radiological findings in various diseases. Radiologists need active support from clinical colleagues to provide an accurate diagnosis in and reasonable differential diagnoses in most of the cases. The images are not just photographs but they tell a story of the patient that remains incomplete without the clinical and laboratory information. The description of the imaging features and the extent of abnormalities on imaging are as important as the diagnosis. One should be aware that the chest radiologist has a dual role of a diagnostic radiologist as well as a prognostic radiologist. The ability to prognosticate can be enhanced by staying updated with textbooks, research studies, routine work by registering the learning points from each case, along with attending multidisciplinary meetings.

I was fortunate to receive a two-year fellowship training in thoracic imaging at National Jewish Health, Denver. During the training and later as an educator, I tried to relate to the problems faced by residents and clinical radiologists in thoracic imaging. A common issue among radiologists is the difficulty in describing certain imaging findings to the refering physician, in order to generate an accurate virtual image. This book uses standard terms and lexicons to describe these imaging findings. There are 14 chapters in this book with the first chapter focusing on imaging patterns in lung diseases. I recommend a thorough review of the first chapter to have a better understanding of description of various pulmonary abnormalities. Chapter 13 includes description of the abnormalities that would be useful in the diagnostic pathway of these diseases. The book is curated to provide more emphasis on the imaging features and relevant clinical findings that may help in reaching an accurate diagnosis. Wherever possible, these imaging features are presented in tables for ease of memorizing. My coauthors have a special interest in chest imaging, and each one of them had given their best effort to bring this book to frution. We hope the book will be useful to both radiologists and pulmonologists in their clinical practice.

Singapore, Singapore — Ashish Chawla

Contents

About the Editor

Ashish Chawla is an American Board of Radiology certified radiologist. He completed his 2-year fellowship in cardiothoracic radiology at the University of Colorado Denver's School of Medicine and the National Jewish Health. He is Head of the Cardiopulmonary Imaging section, Senior Consultant, and Research Lead at the Department of Diagnostic Radiology in Khoo Teck Puat Hospital, Singapore. He is also an adviser to the CT Imaging section. His research interests include imaging of the chest in the emergency department and diffuse lung diseases. He has authored more than 60 peer-reviewed publications, presented numerous posters, and delivered lectures at international conferences. He is actively involved in radiology education and regularly organizes thoracic radiology educational courses.

List of Contributors

Ashish Chawla Department of Diagnostic Radiology, Khoo Teck Puat Hospital, Singapore, Singapore

Raymond Chung Department of Diagnostic Radiology, Khoo Teck Puat Hospital, Singapore, Singapore

Vijay Krishnan Department of Diagnostic Radiology, Khoo Teck Puat Hospital, Singapore, Singapore

Tze Chwan Lim Department of Diagnostic Radiology, Khoo Teck Puat Hospital, Singapore, Singapore

Rahul Lohan Department of Diagnostic Radiology, Khoo Teck Puat Hospital, Singapore, Singapore

Pratik Mukherjee Department of Diagnostic Radiology, Khoo Teck Puat Hospital, Singapore, Singapore

Sumer N. Shikhare Department of Diagnostic Radiology, Khoo Teck Puat Hospital, Singapore, Singapore

Dinesh Singh Department of Diagnostic Radiology, Khoo Teck Puat Hospital, Singapore, Singapore

Sivasubramanian Srinivasan Department of Diagnostic Radiology, Khoo Teck Puat Hospital, Singapore, Singapore

Chai Gin Tsen Department of Respiratory and Critical Care Medicine, Tan Tock Seng Hospital, Singapore, Singapore

Patterns and Signs in Thoracic Imaging

1

Sivasubramanian Srinivasan and Ashish Chawla

1.1 Introduction

The imaging appearances of pulmonary pathologies can be classified into various patterns for the ease of description and to narrow down the differential diagnoses. Imaging pattern refers to a finding or multiple findings suggesting one or more specific conditions [1, 2]. Many characteristic signs have also been described in computed tomography (CT) and radiographs. Along with the clinical features, these signs help in localizing the lesion or in arriving at a diagnosis.

1.2 Patterns

The general radiological patterns include airspace opacities, interstitial opacities, nodules or masses, and cystic lesions [1].The pattern recognition is important to conclude a diagnosis or formulate a list of differential diagnoses. The description of the abnormality is equally important to send a clear answer to the referring physician about the findings. Fleischner Society proposed a glossary of terms for thoracic imaging that is used in this book [2]. The definition of the terms used in thoracic imaging is substantially specific in describing the patterns. Further details about the specific pattern are available in the respective chapters. The common patterns of abnormalities are described below (Table 1.1).

Table 1.1 General patterns in chest radiology

Lines
Kerley lines
Curvilinear lines
Linear opacities
Linear atelectasis or scarring
Cystic pattern
Cystic lung diseases
Emphysema
Honeycombing
Others
Pneumatoceles
Cavities
Bulla, bleb
Cystic bronchiectasis
Nodule/mass
Diffuse nodular lung diseases
Solitary pulmonary nodule
Diffuse pattern
Reticular pattern
Reticulonodular pattern
Attenuation and density
Consolidation
Ground-glass opacity
Mosaic attenuation
Mediastinal contour abnormality
Mediastinal masses
Enlargement of normal structures
Air-fluid level
Pulmonary lesions
Esophageal abnormalities
Pleural/extrapleural abnormalities
Plaques
Effusions
Masses
Extrapulmonary air
Pneumothorax
Pneumomediastinum
Chest wall emphysema

1.2.1 Lines

Lines or linear bands are frequently seen on chest radiograph as well as CT. In the lung bases, it is common to see linear bands that represent subsegmental atelectasis or scarring from prior collapse, infection, or infarction (Fig. 1.1). Curvilinear bands parallel to the pleural surface are characteristically seen in early asbestosis. "Linear opacities" are considered the earliest hallmark of interstitial lung diseases and are described in detail in Chap. 13. Kerley lines are septal lines seen on a radiograph. Kerley A lines are deep septal lines radiating outward from hila and can be up to 4 cm in

S. Srinivasan · A. Chawla (✉)
Department of Diagnostic Radiology, Khoo Teck Puat Hospital, Singapore, Singapore

A. Chawla (ed.), *Thoracic Imaging*, https://doi.org/10.1007/978-981-13-2544-1_1

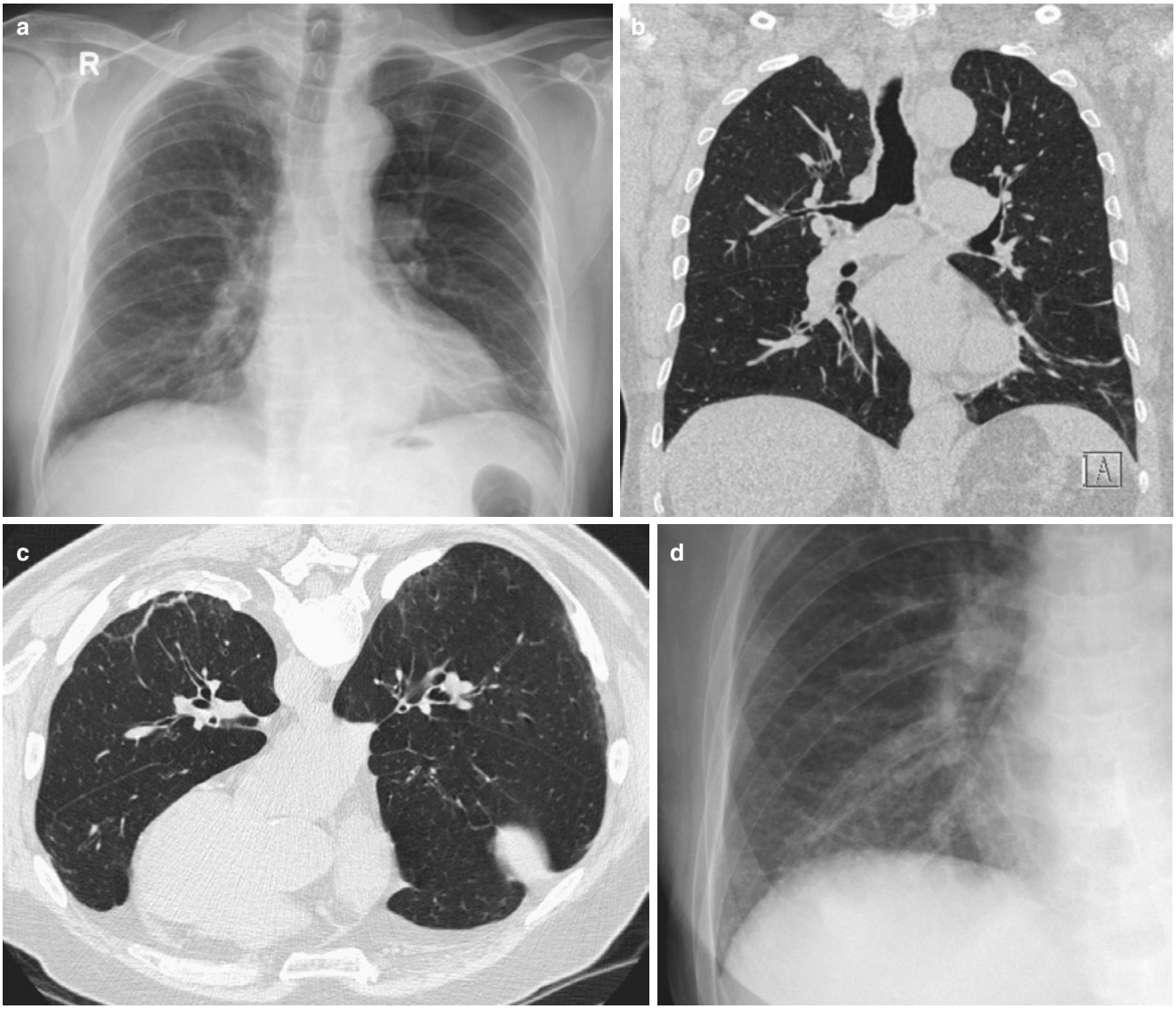

Fig. 1.1 Subsegmental atelectasis. (**a**, **b**) Frontal radiograph and CT image show linear bands in the left lung base. (**c**) Prone CT image shows curvilinear subpleural opacity with pleural plaque in a patient with asbestosis. (**d**) Kerley A lines in hilum and Kerley B lines in right costophrenic angle in a patient with chronic congestive heart failure

length. Kerley B lines are shorter horizontal lines located in the peripheral lung. These septal lines are limited to few conditions and most frequently observed in pulmonary edema.

1.2.2 Cystic Space Pattern

Cystic spaces are rounded sharply demarcated area of low attenuation and can be thin-walled (<2 mm) or thick-walled (Fig. 1.2). Cystic lung disease is a group of pulmonary disorders characterized by the presence of multiple cysts and includes lymphangioleiomyomatosis (LAM), pulmonary Langerhans cell histiocytosis (LCH), and Birt-Hogg-Dube syndrome. Multiple pulmonary cysts can also be seen in ILDs (desquamative interstitial pneumonia and lymphocytic interstitial pneumonia) and infections (*Pneumocystis jirovecii* pneumonia). Few clean thin-walled cysts incidentally seen on imaging are usually pneumatoceles from prior infection, trauma, or aspiration. The term "cavity" is used to describe a lucent space within a mass or consolidation (single or multiple). Cavities have thick wall and are seen in infections, tumors, and rarely vasculitis. Honeycombing cysts are clustered cystic airspaces, usually subpleural ranging in size from 3 mm to 2.5 cm, sharing their walls without intervening lung. Their significance is described in Chap. 13. Emphysema is another subtype of cystic spaces and is characterized by centrilobular or paraseptal lucencies usually without a true wall. However, the wall can be seen with long-standing emphysema due to associated fibrosis or due to superimposed consolidation in surrounding lung, outlining the lucencies.

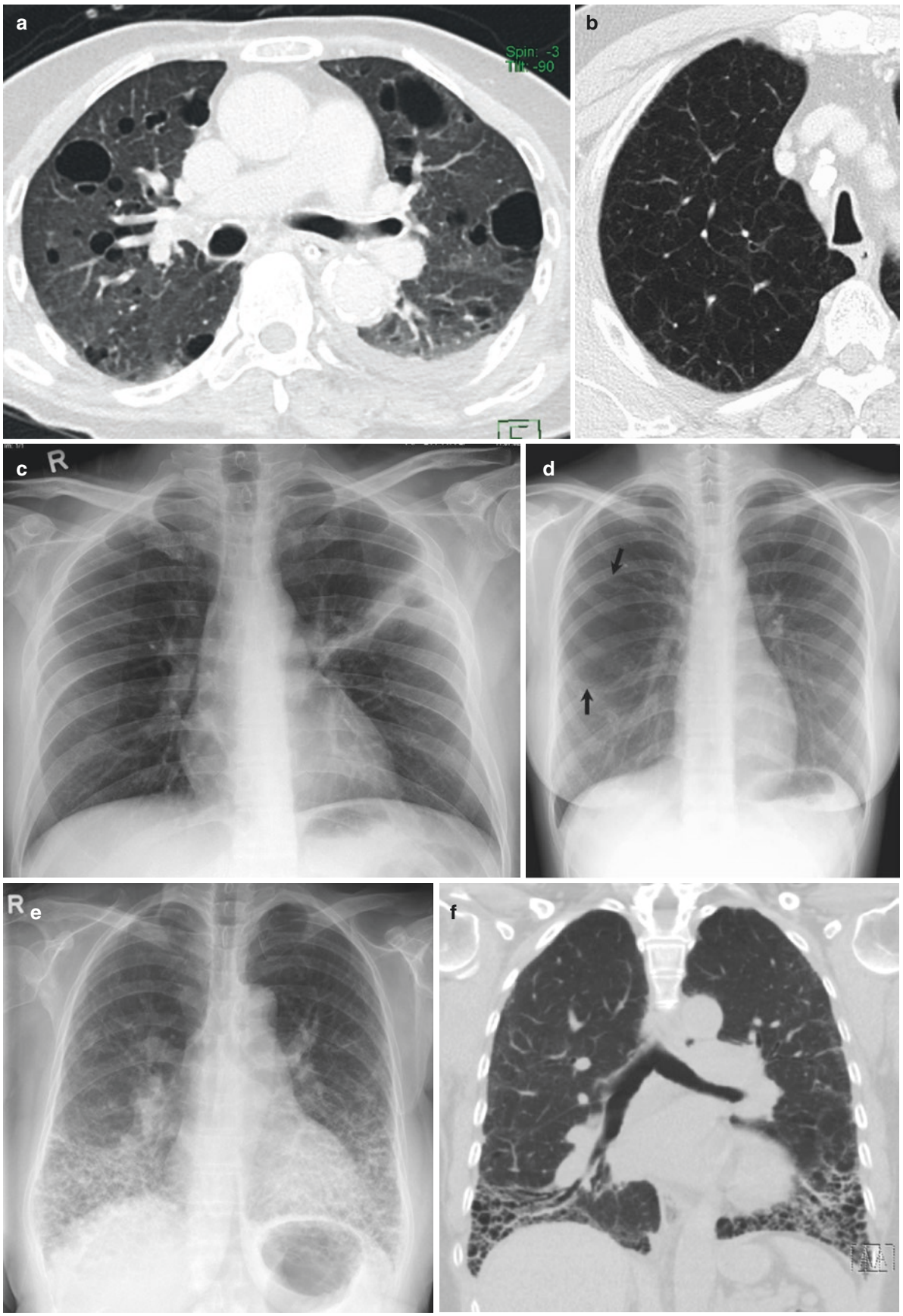

Fig. 1.2 Cystic space pattern. (**a**) Axial CT image showing cystic lung disease (LIP). (**b**) Confluent centrilobular emphysema. (**c**) Cavity in consolidation. (**d**) Pneumatocele. (**e**, **f**) Chest radiograph and CT image show honeycombing

1.2.3 Nodules and Masses

The nodule is a rounded opacity less than 3 cm in size, while a mass is larger than 3 cm. These can be single or multiple (Fig. 1.3). There are a large number of conditions that can present with nodules or masses on imaging, most important being lung cancer. These opacities are divided into subtypes like nodules with calcification/fat or nodules with cavitation, etc. These morphological features on imaging help in listing differential diagnoses and deciding management. Similarly a solitary pulmonary nodule requires radiological analysis and work-up. These are discussed in Chaps. 4 and 5. Multiple small (<5 mm) nodules are grouped in diffuse nodular diseases and described in Chap. 4 in detail. These nodules are categorized into three types based on their location with respect to secondary pulmonary nodules on HRCT (Table 1.2) (Fig. 1.4).

1.2.4 Diffuse Pattern

A diffuse pattern includes nodular pattern, reticular pattern, and reticulonodular pattern (Fig. 1.5). The reticular pattern consists of fine irregular netlike arrangement forming opaque rings with thin walls on chest radiograph. The reticulonodular pattern on chest radiograph results from a mixture of reticular and nodular pattern or extensive reticular shadows appearing nodular end on. The diffuse nodular pattern is seen in conditions discussed in Table 1.2. A wide variety of diseases can produce reticular pattern on radiograph including interstitial lung diseases, sarcoidosis, lymphangitis, airway disease, cystic lung diseases, interstitial edema, and viral pneumonia. The pulmonary involvement is usually diffuse but can be localized to the upper lungs (sarcoidosis and hypersensitivity pneumonitis) or lower lungs (idiopathic pulmonary fibrosis, connective tissue disorders) or focal in patients with bronchiectasis and infection.

1.2.5 Attenuation and Density

The pulmonary opacities can have two patterns of increased density on radiographs: consolidation and ground-glass opacity (Fig. 1.6). However, HRCT can demonstrate more variation in attenuation like the presence of fat, calcium, and air and mosaic attenuation. The mosaic attenuation can be produced by airway diseases, vascular diseases, and parenchymal diseases. The differentiation is discussed in detail in Chap. 13.

1.2.6 Mediastinal Contour Abnormality

The right mediastinal border is formed by the right brachiocephalic vein, superior vena cava, and right atrium, and the left heart border is formed by the neck vessels, aortic knob,

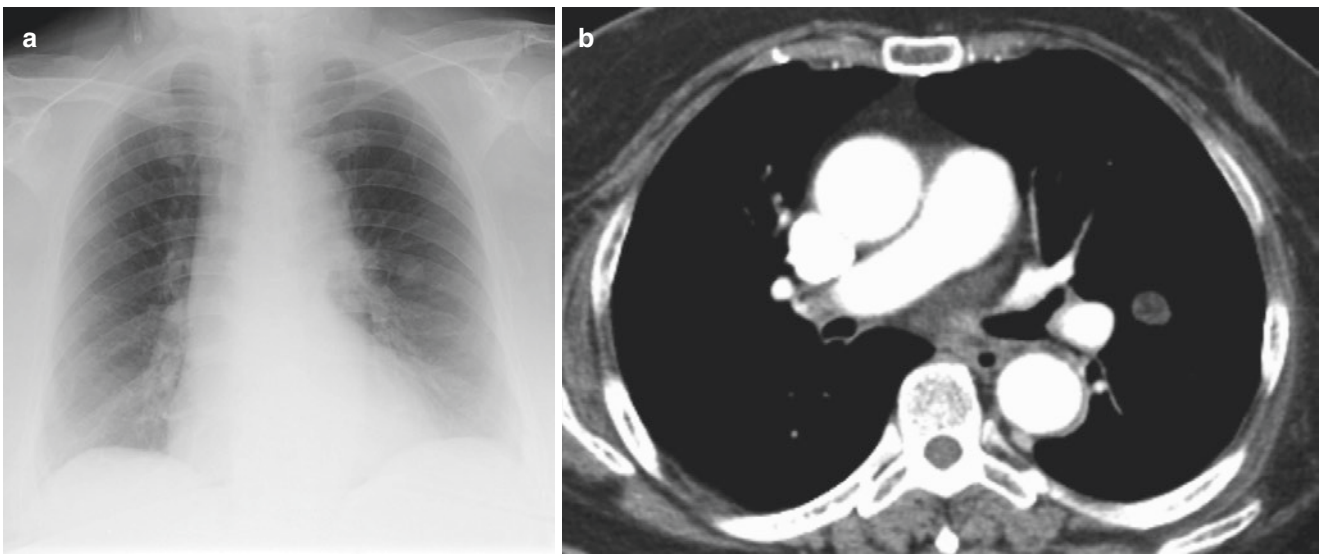

Fig. 1.3 Nodule. (**a**) Frontal radiograph shows a nodule in the left mid-zone. (**b**) Axial CT image shows fat in the nodule consistent with hamartoma

Table 1.2 Patterns of nodules on HRCT

Patterns	Features	Conditions
Centrilobular nodules (Fig. 1.6)	• Solid or ground-glass density nodules • Located in the center of a secondary pulmonary lobule • Peripheral but spare subpleural space • Spare fissures • Associated with abnormal airways	• Bronchiolitis • Endobronchial neoplasm • Hypersensitivity pneumonitis • Endobronchial infections
Perilymphatic nodules (Fig. 1.7)	• Perifissural • Centrilobular • Subpleural • Septa (along pulmonary veins)	• Sarcoidosis • Silicosis • Lymphangitis
Random nodules (Fig. 1.8)	• Distributed randomly	• Metastases • Infections

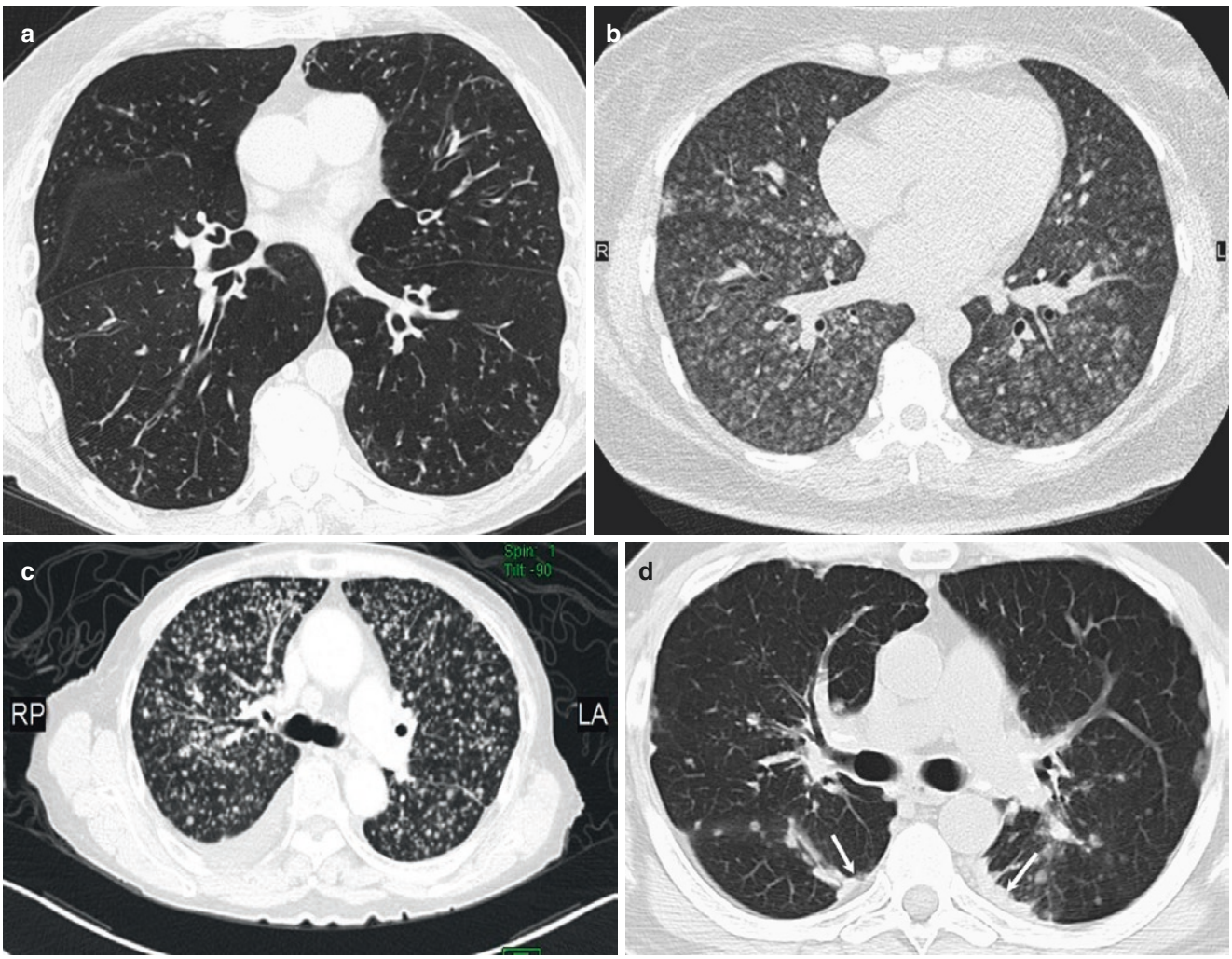

Fig. 1.4 Diffuse nodules. (**a**) Axial CT image shows centrilobular nodules and tree-in-bud opacities. (**b**) Axial CT images showing centrilobular nodules from subacute hypersensitivity pneumonitis. (**c**) Randomly scattered nodules due to metastases. (**d**) Perilymphatic nodules along fissures and subpleural region with pseudo-plaque (arrow) in sarcoidosis

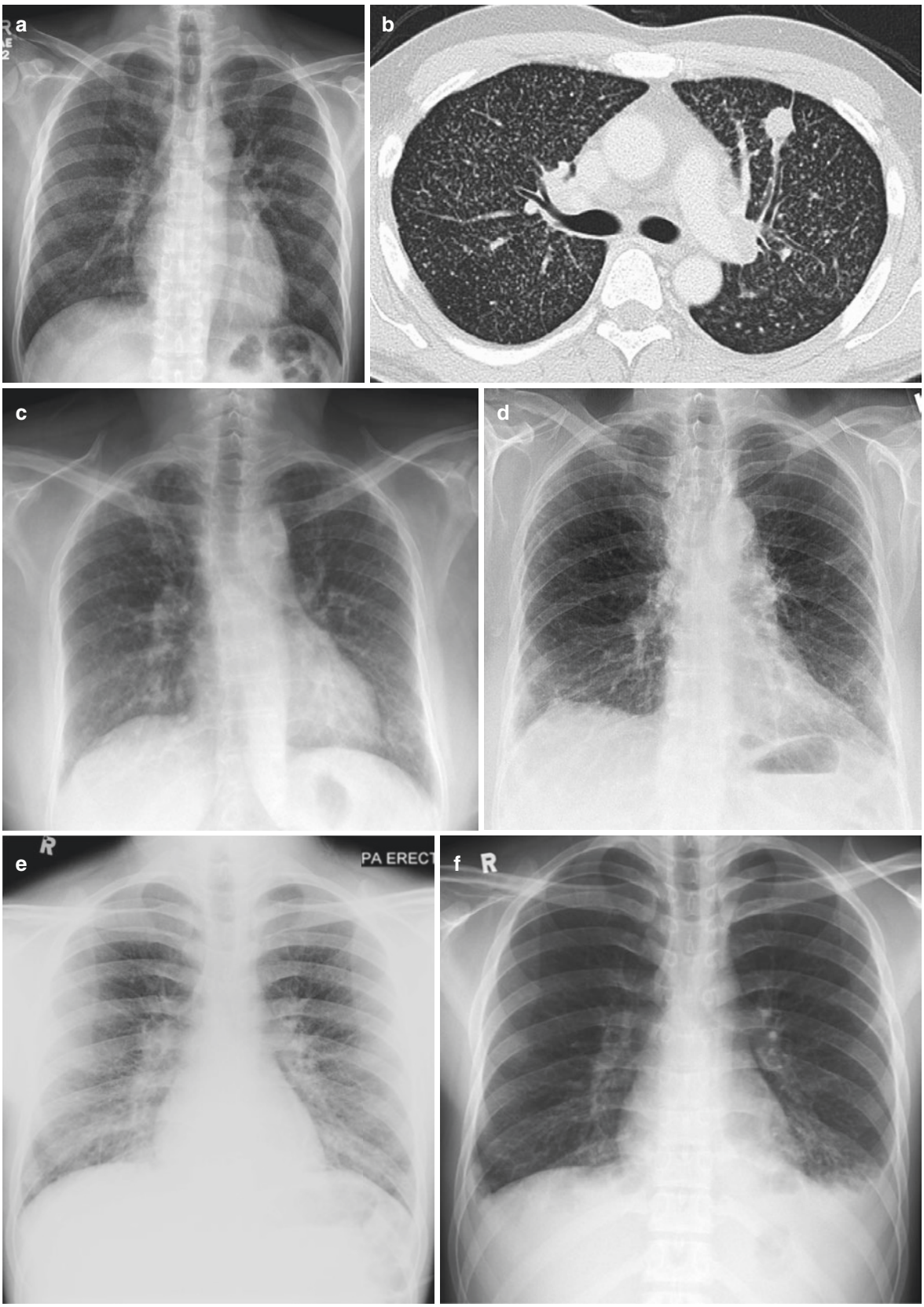

Fig. 1.5 Diffuse pattern. (**a**, **b**) Diffuse nodular pattern in a patient with miliary metastases from lung cancer. (**c**) Reticular pattern more severe in upper zone in a patient with sarcoidosis. (**d**) Reticular opacities in lower lungs due to early idiopathic pulmonary fibrosis. (**e**) Diffuse reticular opacities in a patient with acute interstitial edema with follow-up radiograph (**f**). (**g**) Upper lung predominant diffuse reticular pattern in a smoker. (**h**, **i**) Focal reticular opacities due to bronchiectasis

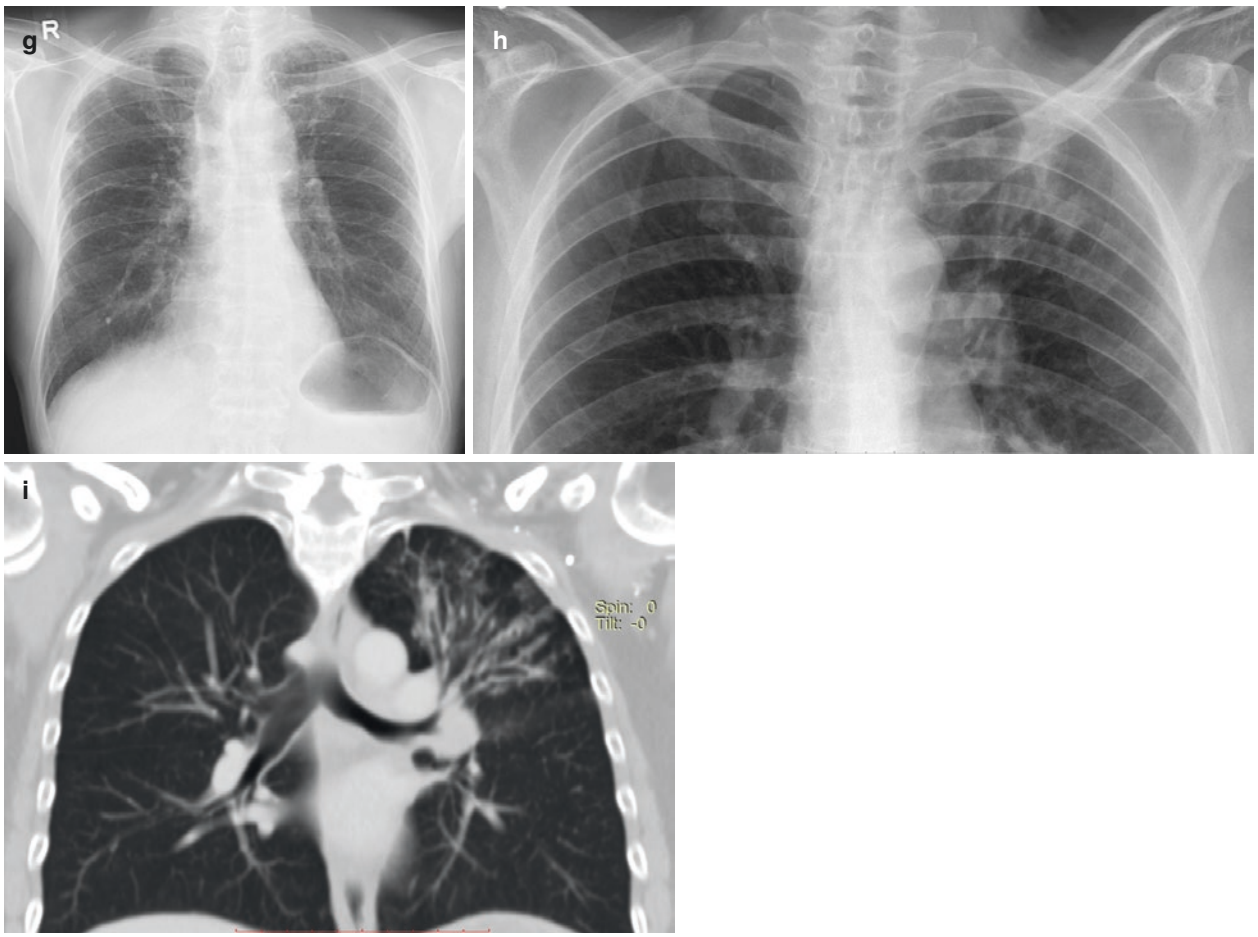

Fig. 1.5 (continued)

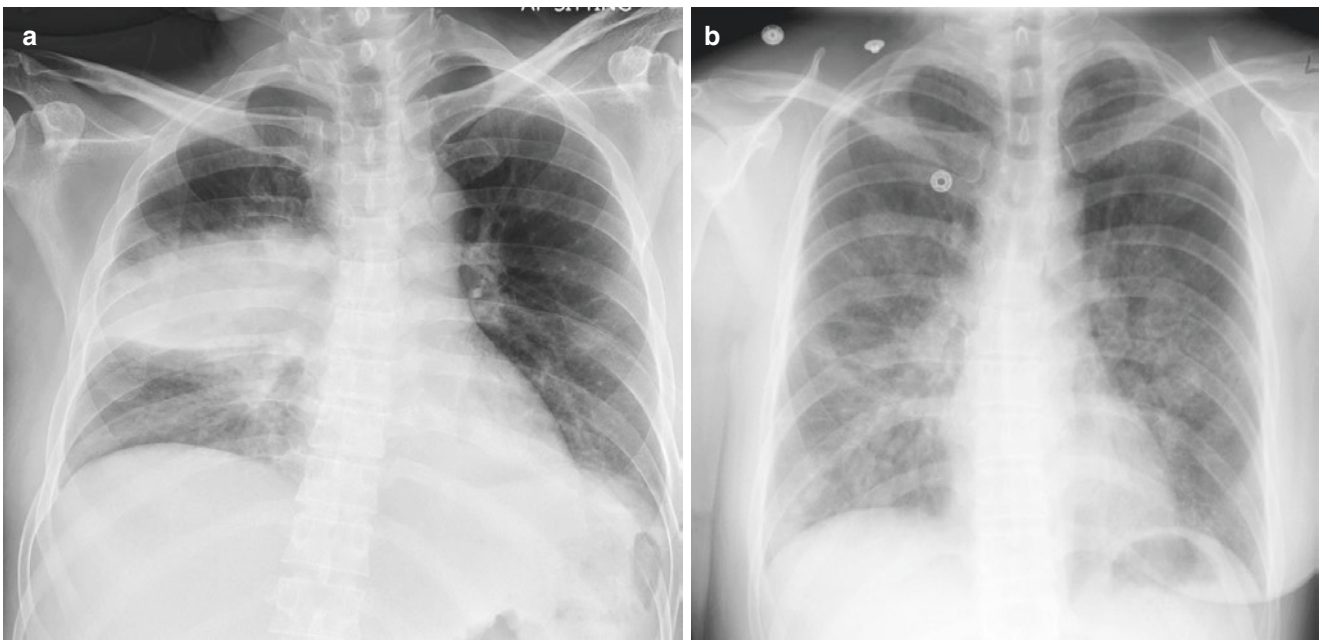

Fig. 1.6 Patterns of density. (**a**) Frontal radiograph shows dense consolidation in the right mid-zone due to pneumonia. (**b**) Radiograph shows perihilar ground-glass opacities due to *Pneumocystis jirovecii* pneumonia

main pulmonary trunk, and left ventricle. There are minor variations in contour from person to person on chest radiographs, but the overall picture remains the same. Abnormal enlargement of normal structures and mediastinal masses distort the mediastinal contour. Numerous signs described later in this chapter and Chap. 8 help in understanding the localization of masses.

1.2.7 Air-Fluid Level

The air-fluid levels on chest radiograph help in localizing the lesion (Fig. 1.7). In the central chest, an air-fluid level almost always indicates an esophageal lesion like a hiatal hernia, achalasia, or diverticulum. Rarely, a fistula from upper gastrointestinal tract can lead to air-fluid levels in the

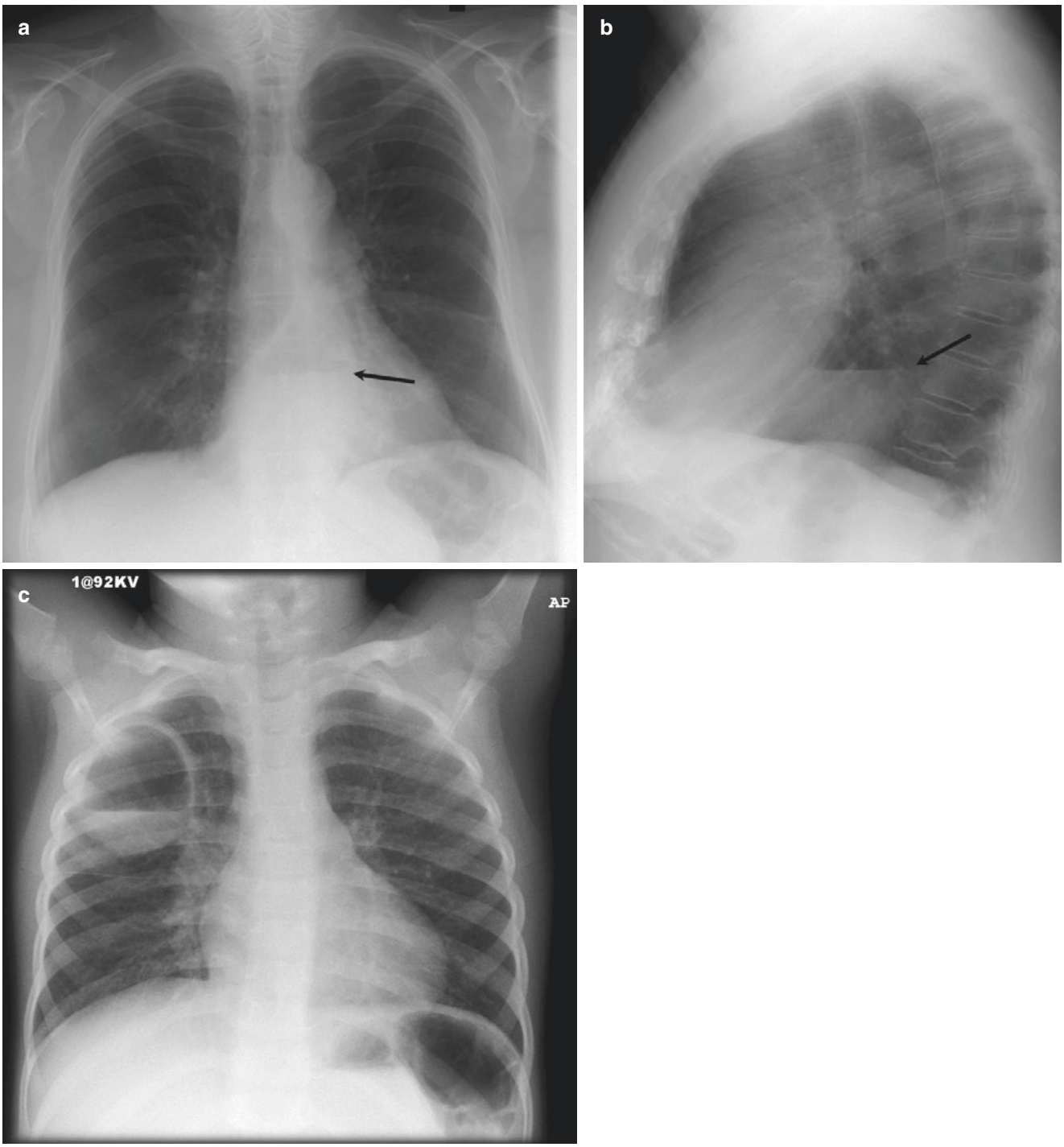

Fig. 1.7 Air-fluid level. (**a**, **b**) Frontal and lateral chest radiographs show retrocardiac opacity with air-fluid level (arrow), suggestive of a hiatal hernia. (**c**) Lung abscess

mediastinum. Lung abscess classically demonstrates air-fluid level in a pulmonary lesion.

1.2.8 Pleural/Extrapleural Abnormalities

Pleural and other extraparenchymal lesions produce characteristic shadows on chest radiograph (Fig. 1.8). Focal calcified plaques appear as high-density sharply demarcated masses. Extraparenchymal masses usually make an obtuse angle with the chest wall with an "incomplete border sign" (sharp inner border toward lung and an ill-defined outer margin merging with the chest wall). This topic is discussed in Chap. 12.

1.2.9 Extrapulmonary Air

The detection of extraparenchymal air particularly pneumomediastinum remains a challenging task on chest radio-

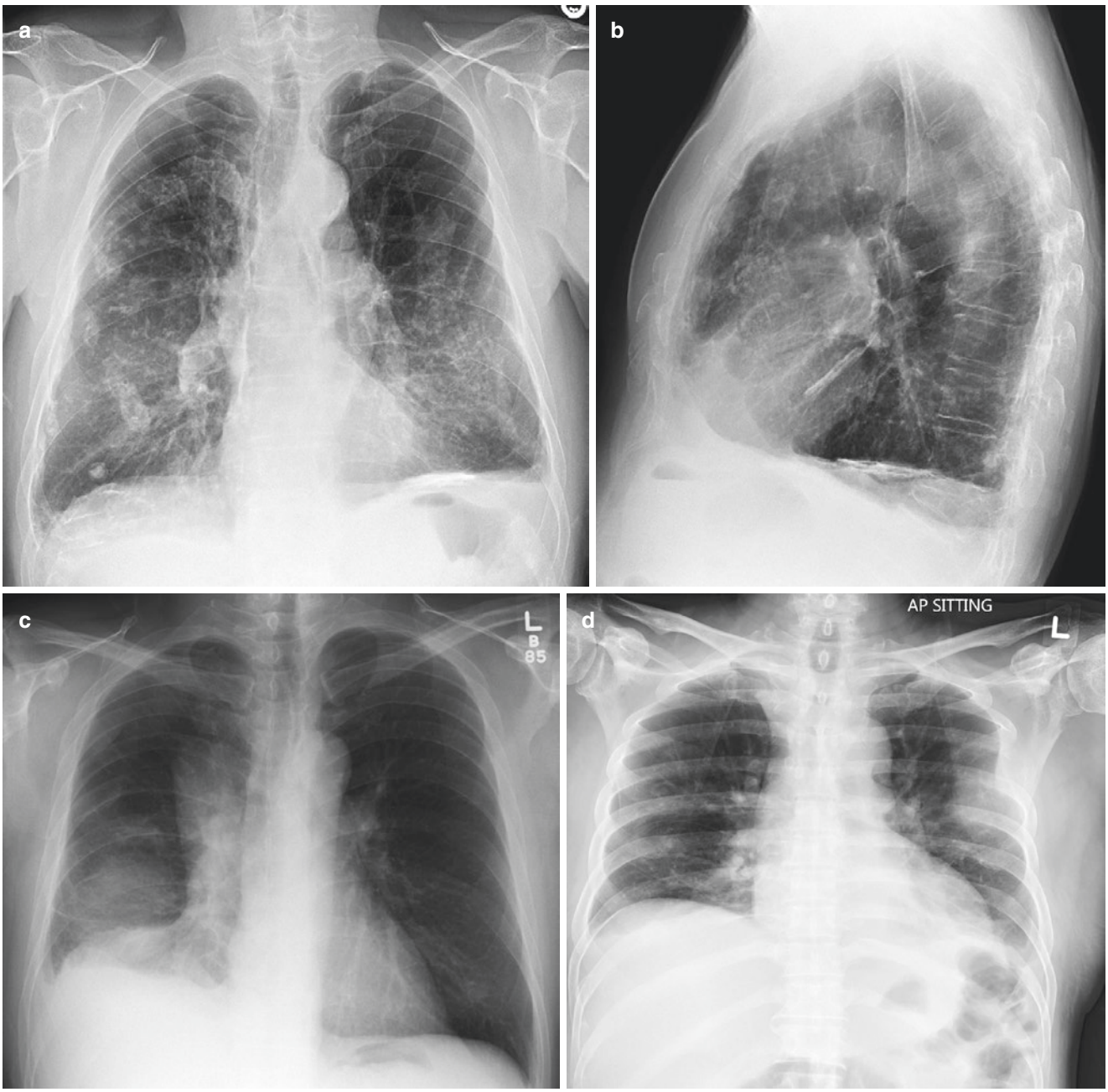

Fig. 1.8 Pleural lesions. (**a**, **b**) Frontal and lateral chest radiographs show sharply marginated opacities representing calcified pleural plaques. Note lateral radiograph reveals a fissural plaque. (**c**) Frontal radiograph shows a loculated pleural effusion with characteristics of extraparenchymal mass. (**d**) Chest radiograph shows rib metastases with extraparenchymal signs

graph. It is difficult to identify dark extrapulmonary air in the background of equally dark lung shadow. However, there are many signs that can help in picking up the presence of extrapulmonary air. These signs are discussed in Chap. 8.

1.3 Patterns of Lung Collapse

"Atelectasis" or "collapse" of the lung indicates volume loss of the lung parenchyma [3, 4]. It can be focal with the involvement of a subsegment, segment, lobe, or the entire lung. The types of atelectasis include obstructive atelectasis due to bronchial obstruction, passive atelectasis due to compression by fluid or air or mass, adhesive atelectasis (due to lack of surfactant), and cicatricial atelectasis due to lung scarring.

Direct signs of atelectasis are vague sharply marginated opacity, displacement of fissures, and crowding of vessels. Indirect signs include diaphragmatic elevation, mediastinal shift, compensatory hyperinflation of the normal lung, displacement of hilum, absent air bronchograms, and crowding of the ribs. The various radiographic appearances of lobar collapse and collapse of the entire lung are summarized in Tables 1.3 and 1.4 (Figs. 1.9, 1.10, 1.11, 1.12, 1.13, and 1.14).

Table 1.3 Lobar collapse and radiographic appearances

Lobe	Frontal radiograph	Lateral radiograph
Right upper lobe collapse (Fig. 1.9)	• Right paratracheal opacity • Tracheal shift to the right side • Upward shift of minor fissure • Elevation of right hilum • Juxtaphrenic peak	• Displacement of major and/or minor fissure toward the collapsed upper lobe
Right middle lobe collapse (Fig. 1.10)	• Opacity silhouetting the right cardiac margin	• Wedge-shaped opacity with apex at hilar region • Downward displacement of minor fissure • Anterior displacement of major fissure
Right lower lobe collapse (Fig. 1.11)	• Downward displacement of major fissure • Silhouetting of right diaphragmatic dome • Loss of visualization of right interlobar pulmonary artery • Displacement of the heart	• Loss of radiolucency along the lower spine • Obscuration of posterior aspect of the diaphragm • Posterior displacement of major fissure
Left upper lobe collapse (Fig. 1.12)	• Increased opacity in the upper thorax • Tracheal shift to left • Obscuration/silhouetting of left upper mediastinal margin • Luftsichel sign • Elevation of left hilum • Juxtaphrenic peak	• Anterior displacement of major fissure
Left lower lobe collapse (Fig. 1.13)	• Triangular retrocardiac opacity • Downward displacement of major fissure • Obscuration/silhouetting of left diaphragmatic dome • Loss of visualization of left interlobar pulmonary artery • Displacement of the heart	• Loss of radiolucency along the lower spine • Obscuration of posterior aspect of diaphragm • Posterior displacement of major fissure

Table 1.4 Complete collapse of the lung and radiographic appearances based on etiology

Cause	Radiographic appearance
Due to bronchial obstruction (Fig. 1.11c)	• Increased opacity of hemithorax • Absent air bronchograms (in central obstruction) • Elevated ipsilateral diaphragm • Ipsilateral mediastinal shift
Due to pneumothorax (Fig. 1.14)	• Collapsed lung is seen centrally adjacent to the hilum and mediastinum with mediastinal shift to the opposite side • In incomplete collapse, the lung may appear lucent
Due to pleural effusion	• Variable opacification of the hemithorax depending upon the aeration of the residual lung • Shift of mediastinum to the opposite site

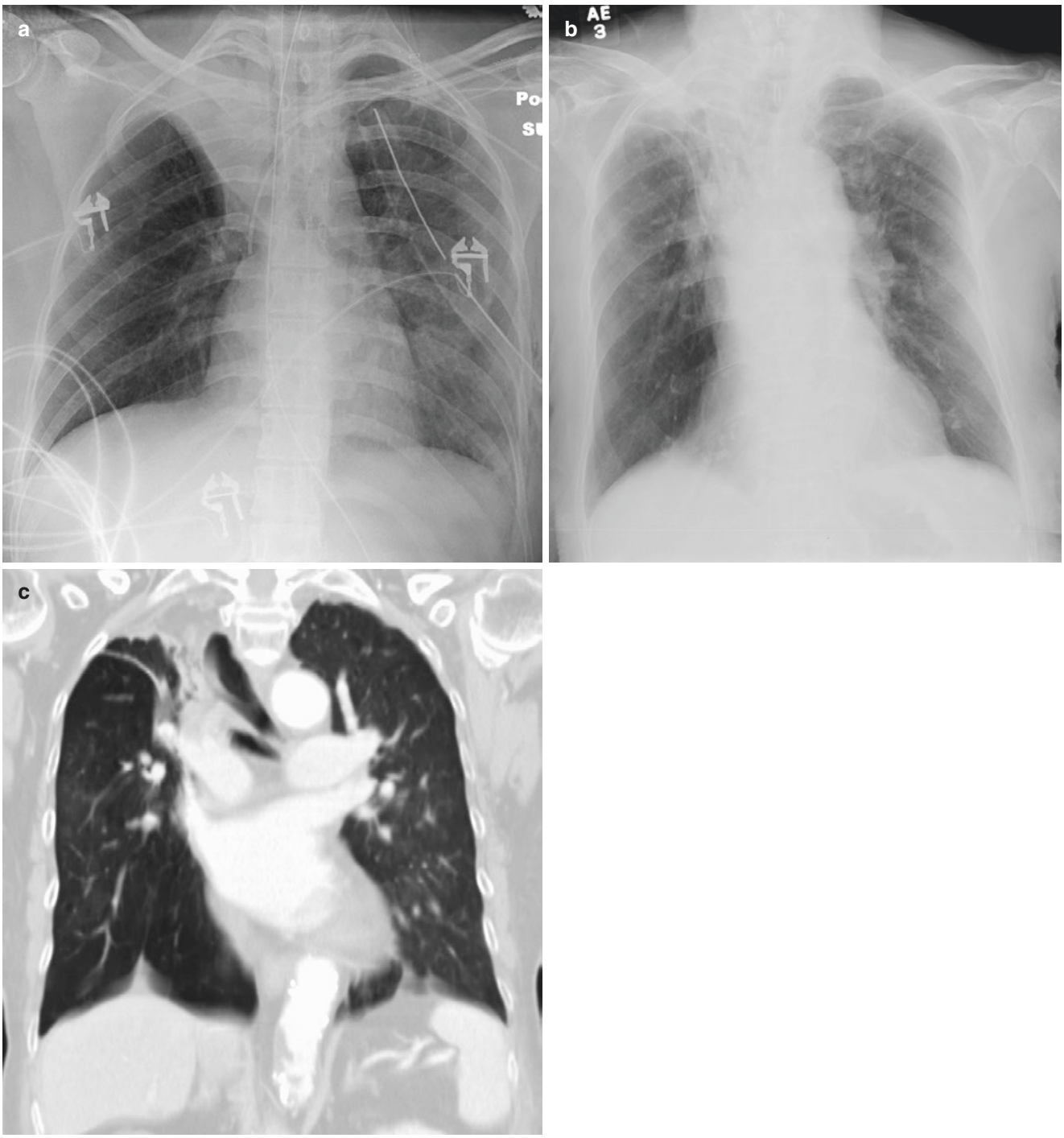

Fig. 1.9 Right upper lobe collapse. (**a**) Frontal chest radiograph shows triangular right paratracheal opacity, with an upward shift of minor fissure and tracheal shift to the right. (**b**, **c**) Chronic right upper lobe collapse with more extensive changes like pulled-up hilum and "juxtaphrenic peak"

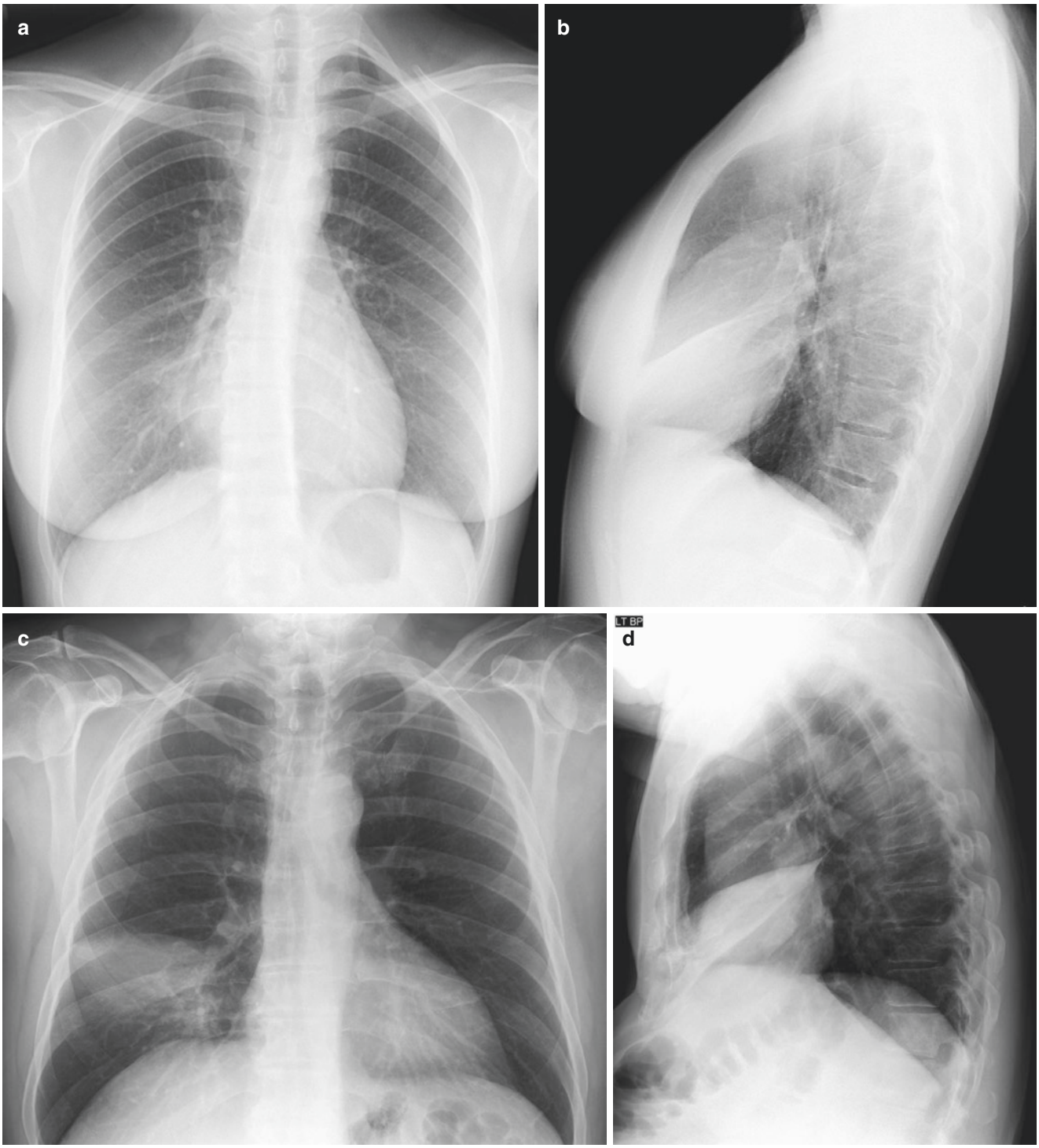

Fig. 1.10 Right middle lobe collapse. (**a**, **b**) Frontal and lateral radiographs of chest show blurring of the right heart border and a wedge-shaped opacity projected over the cardiac shadow. (**c**, **d**) Loculated effusion in the right major fissure. Notice the borders of opacity projected over the cardiac shadow are convex without any volume loss. (**e**–**g**) Consolidation with the collapse in a patient with lung cancer

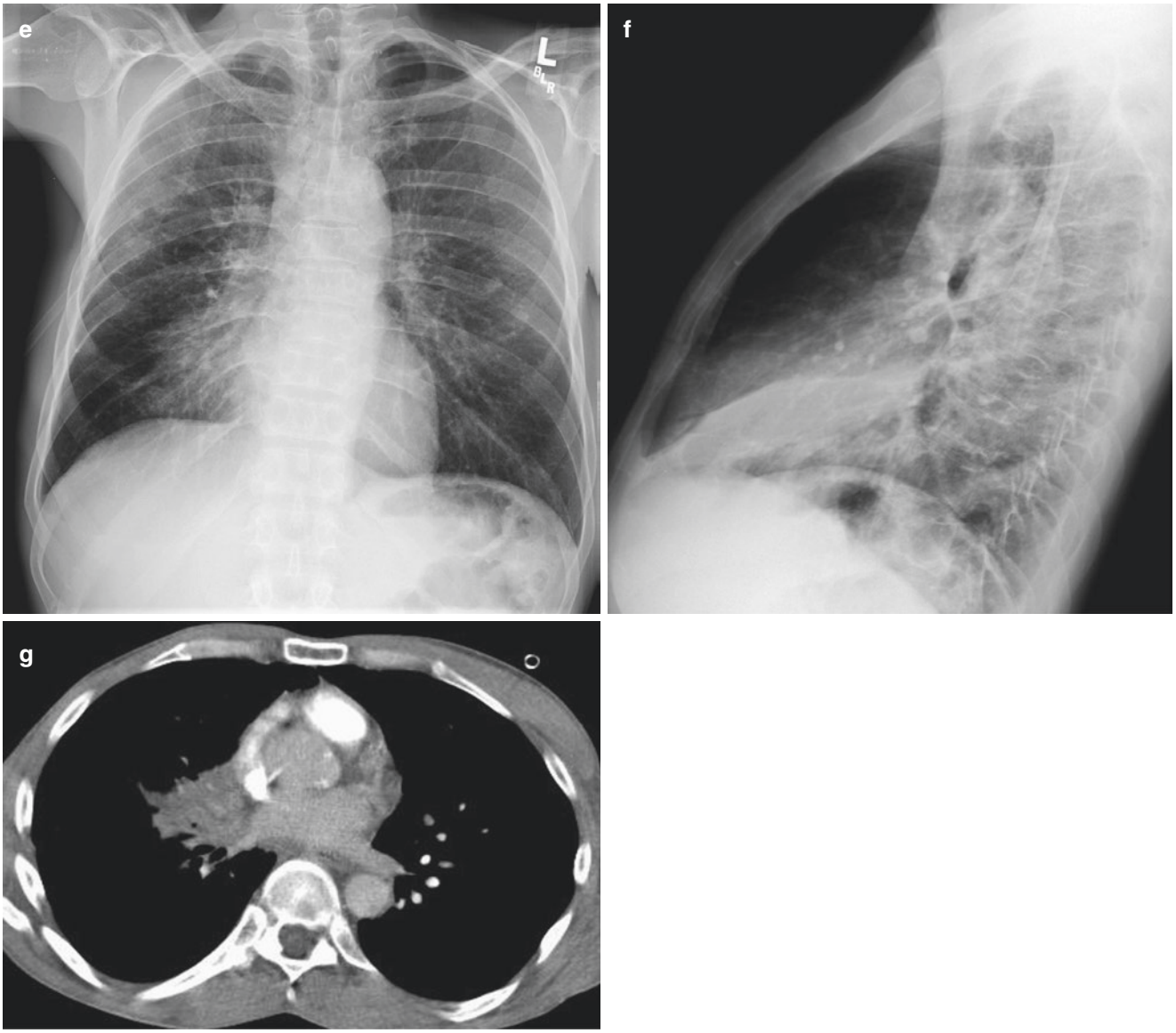

Fig. 1.10 (continued)

1.4 Signs in Thoracic Imaging

1.4.1 Radiographic Signs

1.4.1.1 Silhouette Sign

This is the most popular radiographic sign. This sign has been used to indicate obliteration of the border of an anatomical structure (the heart, aorta, or diaphragm) if the neighboring area is filled with tissue or material of similar density (Figs. 1.15 and 1.16). However, the border will not be obliterated if the lesion is not contiguous with one of these structures [5–7]. Other examples of silhouette sign on frontal radiograph include collapse/consolidation of middle lobe obliterating the right heart border, collapse/consolidation of lower lobe obliterating hemidiaphragm border, obliteration of ascending aorta by right upper lobe collapse/consolidation, obliteration of aortic knob by left upper lobe collapse/consolidation and cardiac margin, and obscuration of heart borders by mediastinal mass.

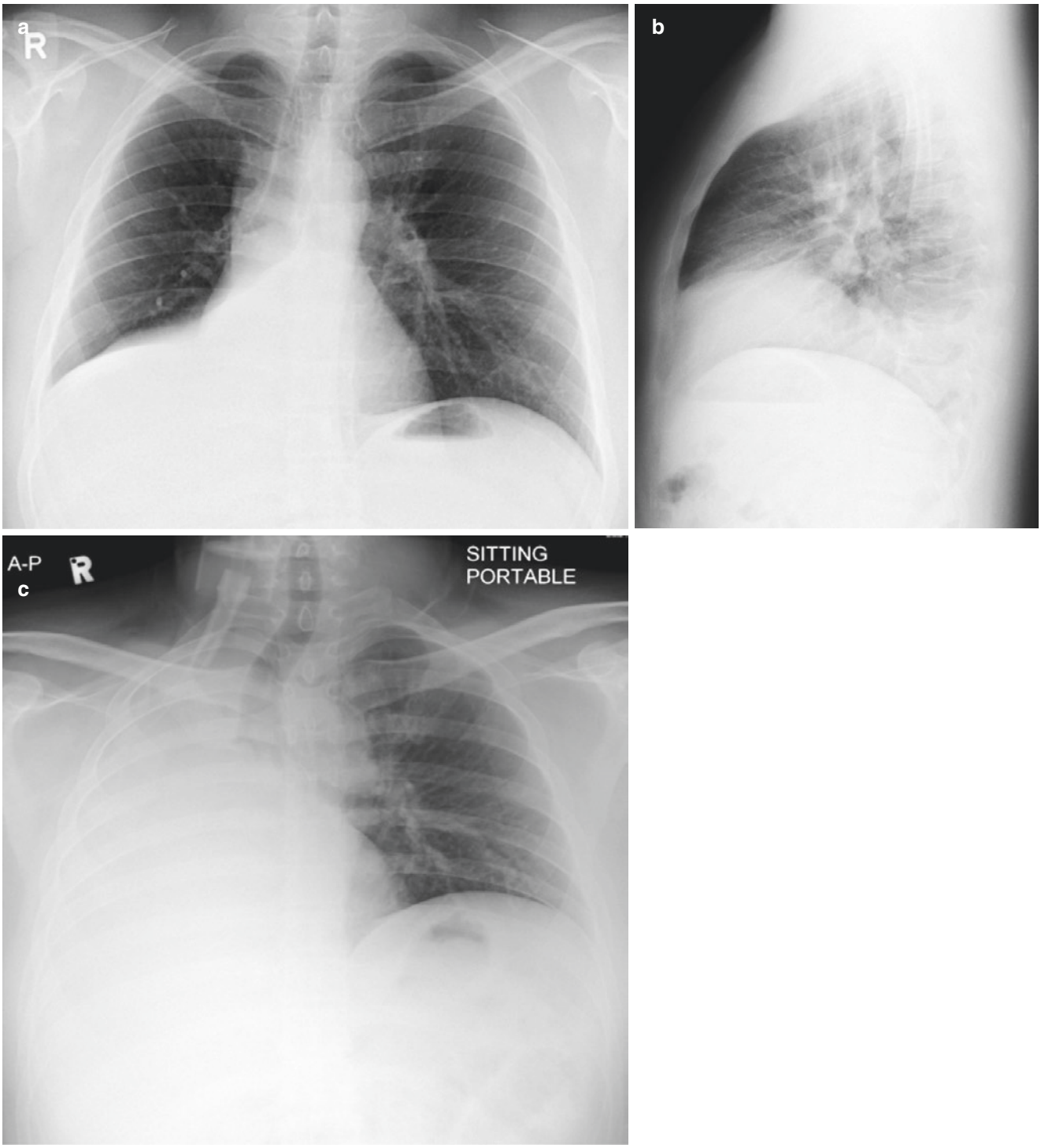

Fig. 1.11 Right lower lobe collapse in a young woman presenting to emergency department with dyspnea. (**a**, **b**) Frontal and lateral chest radiographs show signs of the collapse of the right lower lobe. (**c**) Frontal chest radiograph on the following day shows complete right lung collapse. (**d**, **e**) Axial CT images from the next day show collapsed right lung due to an endobronchial mass (arrow). Note acute collapse enhances (white asterisk), and chronic collapse doesn't enhance (black asterisk)

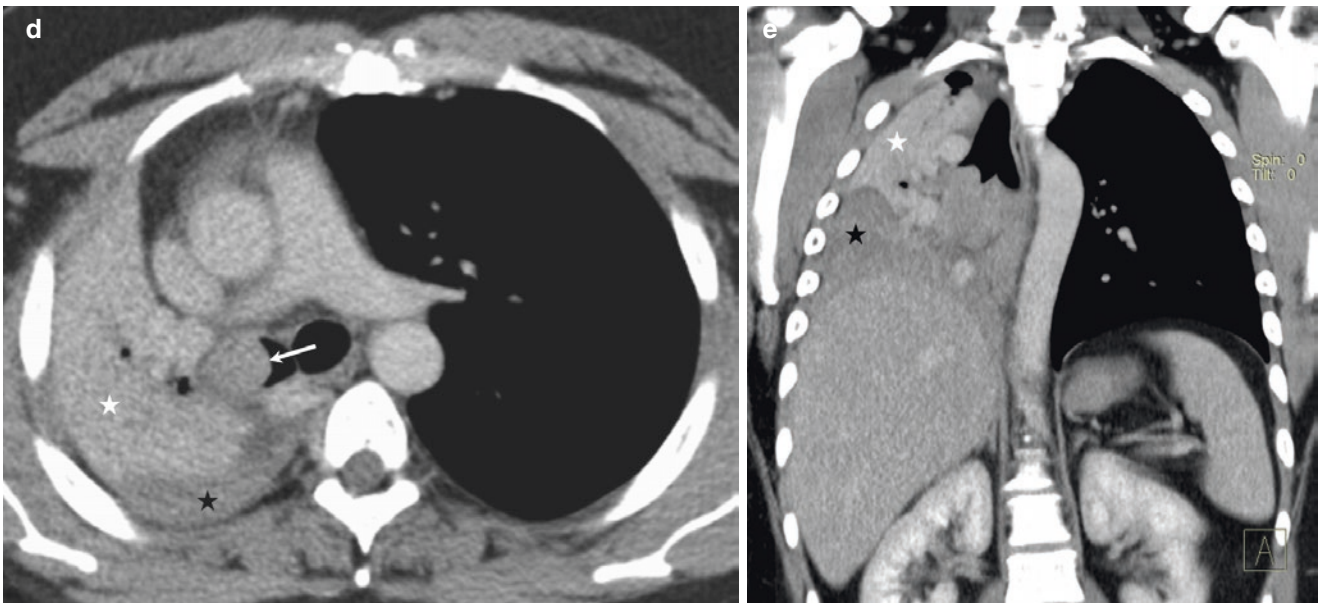

Fig. 1.11 (continued)

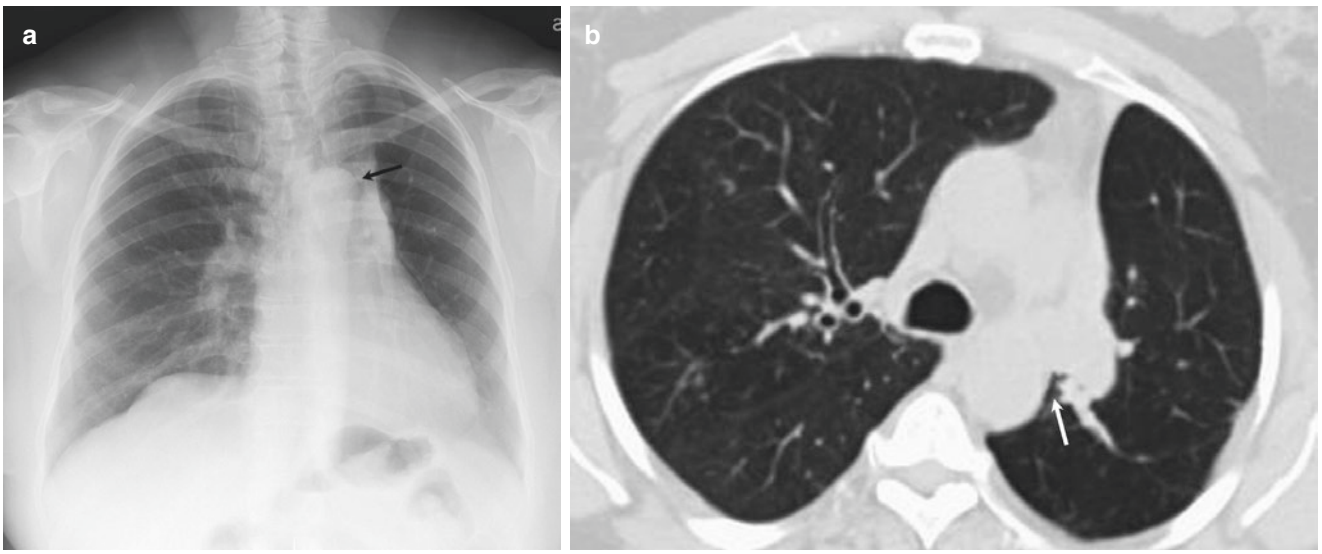

Fig. 1.12 Left upper lobe collapse. (**a**) Frontal radiograph reveals a left upper paramediastinal opacity, pulling trachea toward it. The hyperexpanded superior segment of the left lower lobe insinuates itself between the left upper lobe and the superior mediastinum, sharply silhouetting the aortic arch and resulting in "luftsichel" sign (black arrow). (**b**) Axial CT shows superior segment of left lower outlining aorta (white arrow). (**c**, **d**) Another case of left upper lobe collapse showing "luftsichel" sign (black arrow) and the left hilar mass (white arrow)

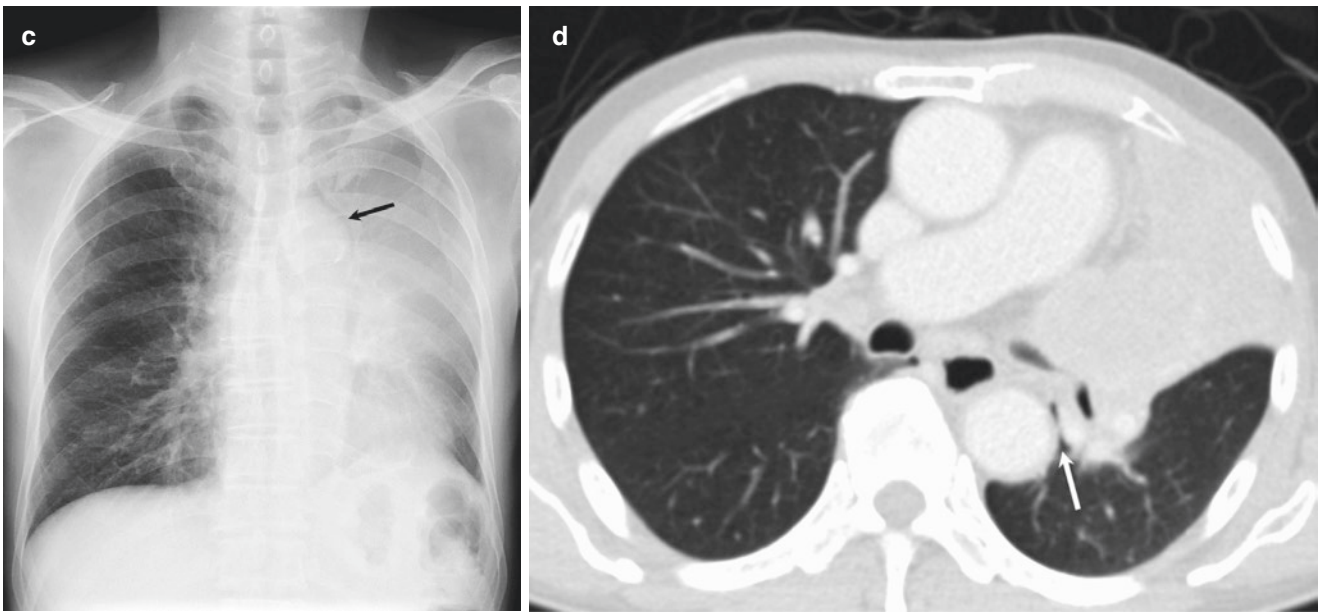

Fig. 1.12 (continued)

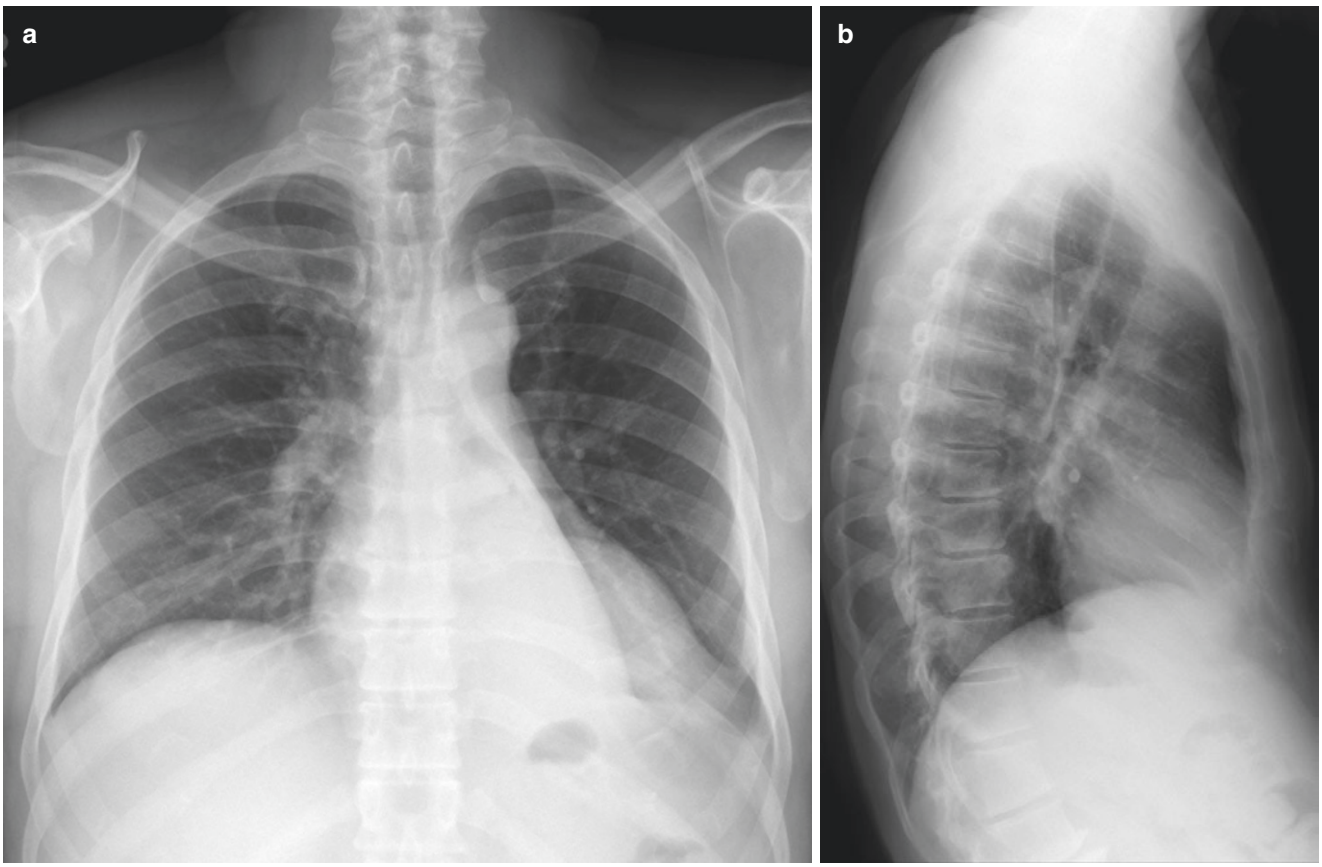

Fig. 1.13 Left lower lobe collapse. (**a**, **b**) Frontal and lateral chest radiographs show left lower lobe collapse which appears as a triangular retrocardiac opacity (arrow), paralleling the cardiac border

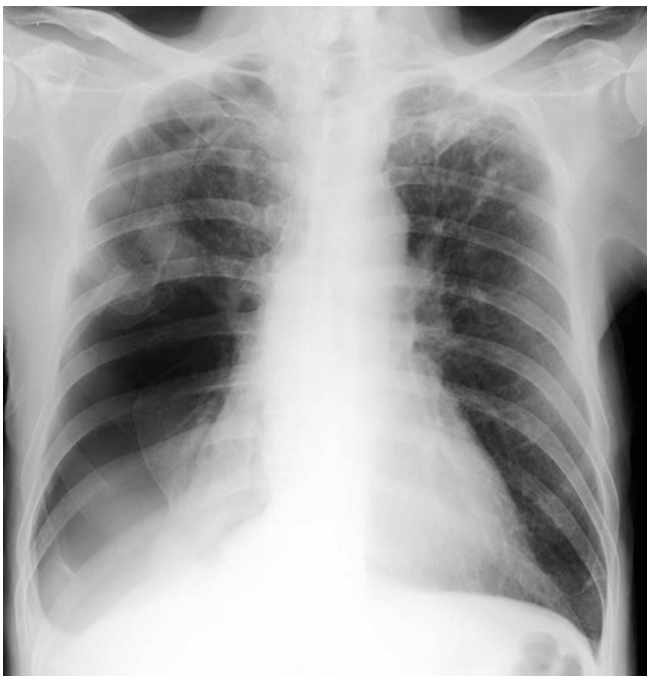

Fig. 1.14 Near-complete collapse of the right lung due to large pneumothorax

1.4.1.2 Hilum Overlay Sign

The hilum overlay sign is a helpful sign to distinguish between an anterior mediastinal mass and cardiac/pericardial sac enlargement [5, 7]. An anterior mediastinal mass may have a configuration closely resembling the enlarged cardiac contour; however the pulmonary artery can be seen well within the medial margin of the mediastinal mass (Fig. 1.16).

1.4.1.3 Hilum Convergence

The hilum convergence sign is a helpful sign to differentiate a bulky hilum due to pulmonary artery dilatation or a hilar mass [5]. If the pulmonary artery branches are seen converging toward the bulky hilum rather than toward the heart, the mass is likely due to an enlarged pulmonary artery (Fig. 1.17). The reverse indicates a hilar mass.

1.4.1.4 Cervicothoracic Sign

The cervicothoracic sign is used to describe the location of a lesion at the inlet of the thoracic cavity [5, 7]. The posterior portion of the lung apices is located more superiorly than the anterior portion. Therefore a lesion clearly visible above the

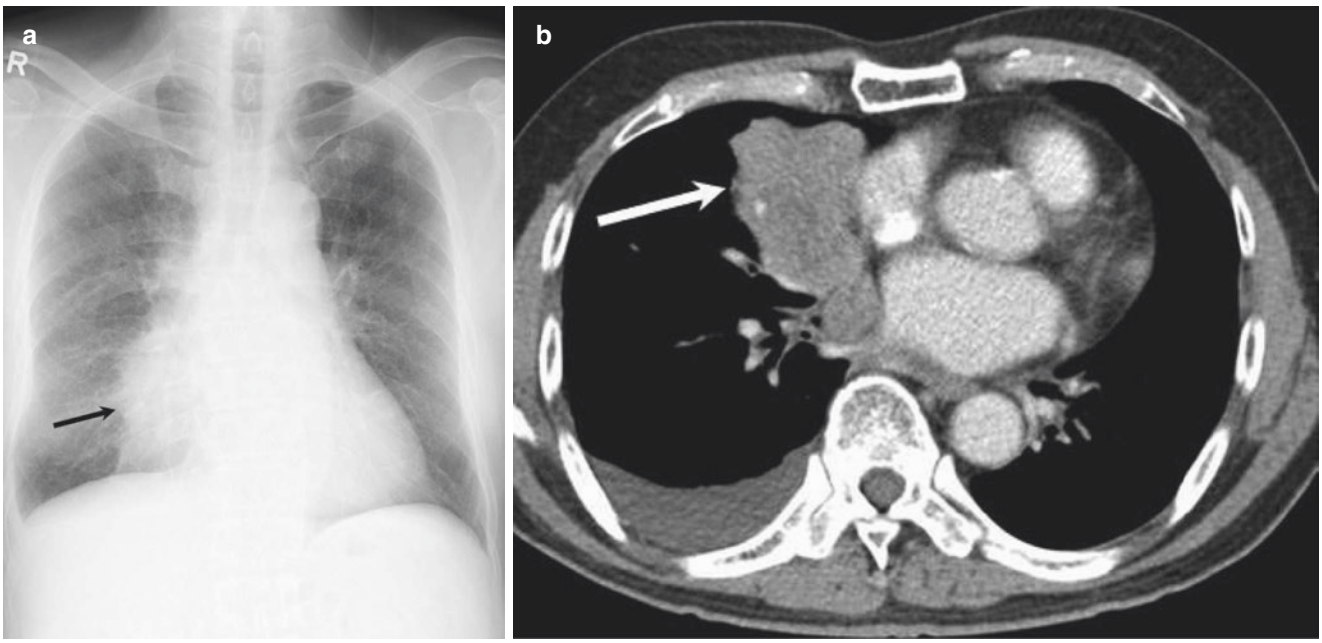

Fig. 1.15 Silhouette sign. (**a**) Chest radiograph of an adult patient shows soft tissue opacity in the right medial lower zone with obliteration of the right heart border, implying the mass is touching the heart, and probably located in the middle lobe. (**b**) Axial contrast-enhanced CT image confirms the location of the mass

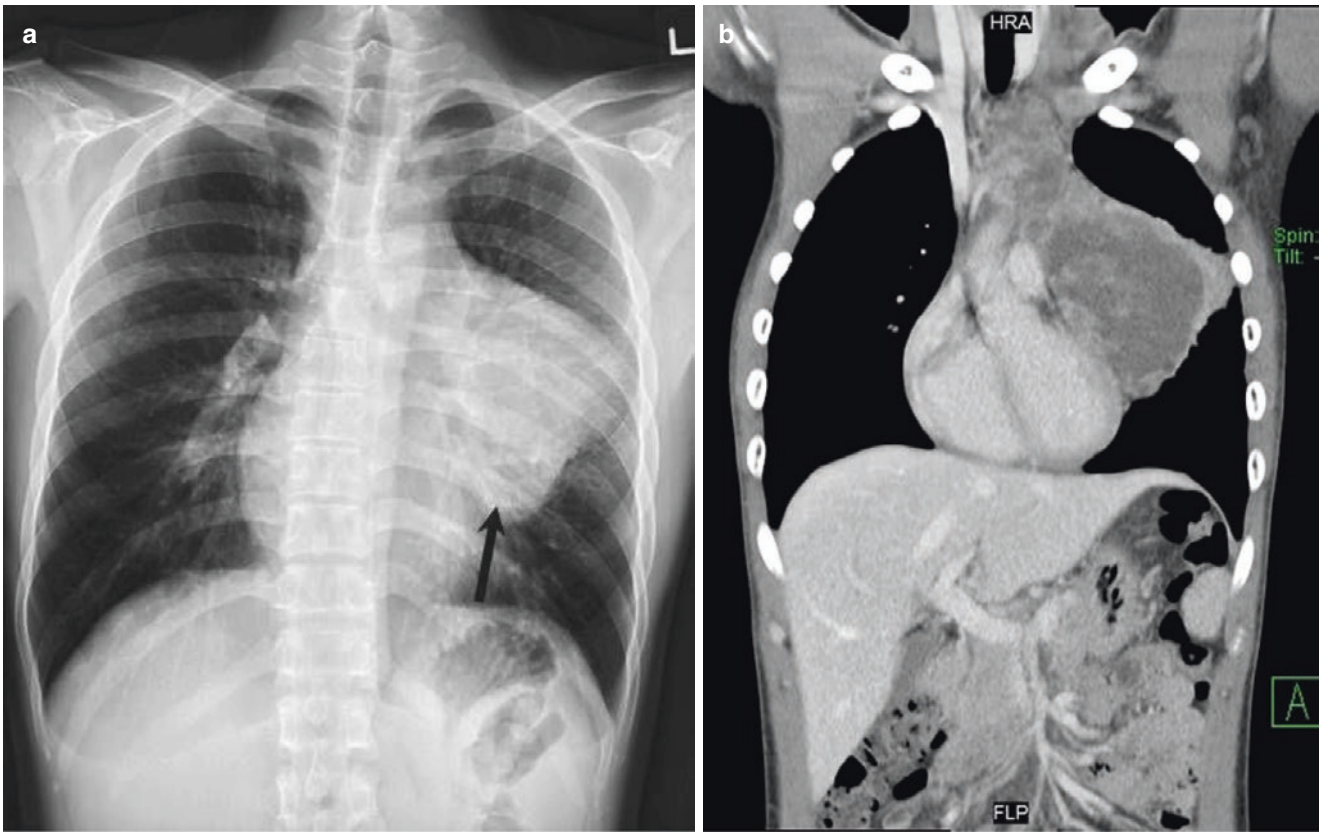

Fig. 1.16 Silhouette sign. (**a**) Frontal radiograph shows a large mass in the mediastinum, silhouetting the left heart border but without silhouetting the aortic knuckle and descending aorta that can be seen through it. Visualization of the left pulmonary artery through the mass represents "hilum overlay" sign. There is no bony involvement. The imaging features are consistent with anterior mediastinal mass. (**b**) Coronal CT image shows heterogeneously enhancing mass in the anterior mediastinum abutting the heart. Biopsy revealed germ cell tumor

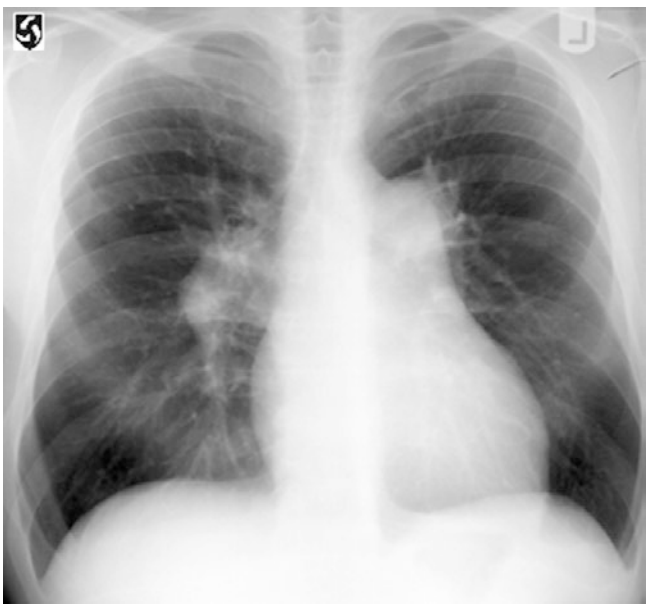

Fig. 1.17 Hilum convergence sign. Chest radiograph of a middle-aged woman with pulmonary artery hypertension shows bulky hila. The distal pulmonary arteries are seen to converge toward the enlarged hilum, and hence this represents a dilated pulmonary artery rather than a (non-vascular) mass lesion

clavicles on the frontal view must lie posteriorly (Fig. 1.18). If the cranial border of the lesion is obscured at or below the level of the clavicles, it is located in the anterior mediastinum.

1.4.1.5 Thoracoabdominal Sign

Posterior lung and costophrenic sulcus extends more caudally than anterior basilar lung. A lesion that terminates at the dome of the hemidiaphragm may be located anteriorly or may represent an iceberg configuration with a segment hidden below in the posterior lower thorax and abdomen (positive "thoracoabdominal" sign) [5] (Fig. 1.19). Positive "thoracoabdominal" sign can be seen in an aortic aneurysm, paraspinal mass, or azygos continuation of the inferior vena cava. In other words, a lesion that extends below the dome of the hemidiaphragm and appears well marginated is deemed located in the posterior chest and outlined by the surrounding aerated lung.

1.4.1.6 Extrapleural Sign

A lesion at an extrapleural location usually produces a sharp convex outline facing the lung with tapering margins [8]. If there is a sign of adjacent rib involvement,

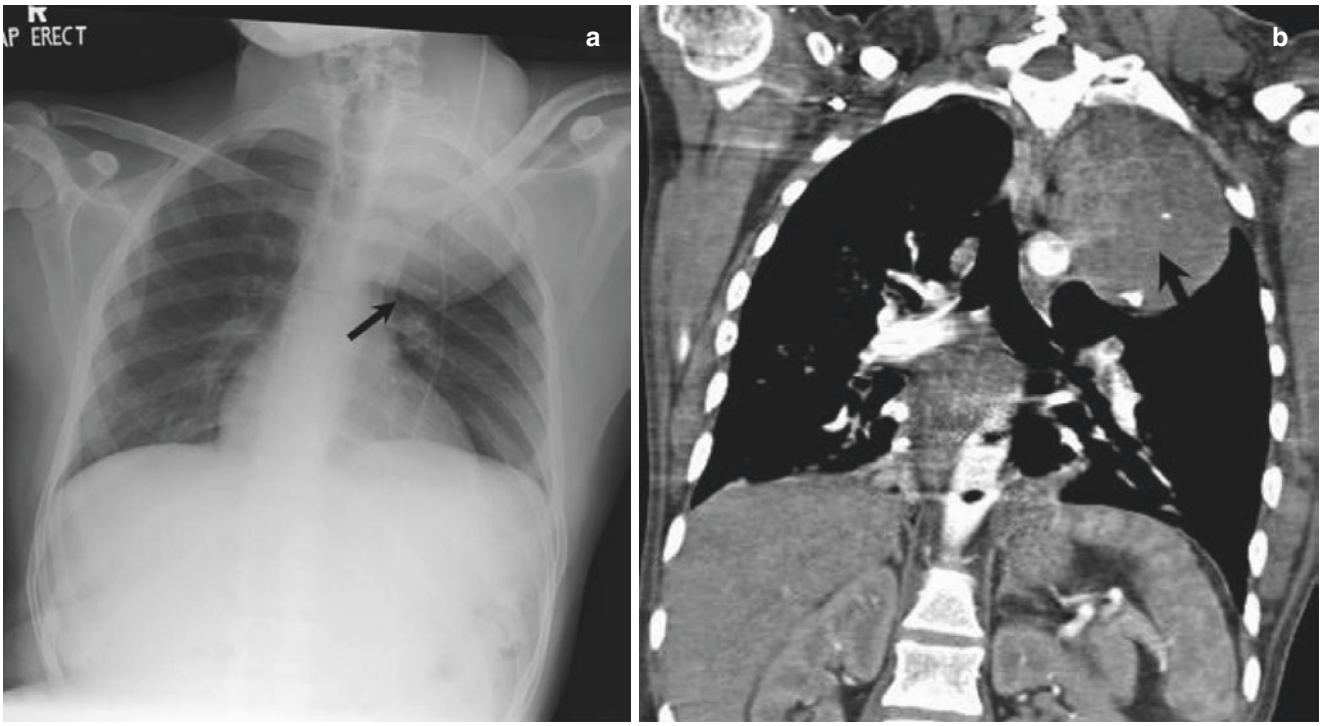

Fig. 1.18 Cervicothoracic sign. (**a**) Chest radiograph of a patient with neurofibromatosis showing a large mass in the left upper zone, extending well above the left clavicle up to the left neck, consistent with posterior mediastinal mass. (**b**) Coronal CT image shows the large posterior mediastinal mass with foci of internal calcification. Subsequent MRI study (not shown) demonstrated characteristic features of a plexiform neurofibroma

the lesion is even more likely to be in an extrapleural location (Fig. 1.20). Loculated pleural effusion may have similar appearances, but there are usually pleural changes elsewhere in the thorax, and rib involvement does not occur.

1.4.1.7 Double Lesion Sign

Felson suggested that if the collapse of two or more pulmonary segments cannot be explained by a single bronchial lesion, one has reasonable assurance that a neoplasm is not present [5] (Fig. 1.21). He also reminded the readers must keep in mind of a number of possible exceptions such as multicentric neoplasms, separate areas of collapse in which one is produced by neoplasm and one by a metastasis or concomitant inflammatory process, tumor extension through a fissure to involve another large bronchus, etc. However, these exceptions are rare.

1.4.1.8 Air Bronchogram Sign

Bronchi, which are not normally seen, become visible as a result of opacification of the adjacent lung parenchyma indicating that the pathology is in the lung parenchyma itself rather than in the mediastinum (Fig. 1.22). This was first observed by Fleischner, and Felson named it as air bronchogram sign [9].

1.4.1.9 Bulging Fissure Sign

The bulging fissure sign refers to lobar consolidation where the affected portion of the lung is expanded [10]. Felson was the first to observe this sign to be strongly associated with *Klebsiella pneumoniae* infection. This sign is also seen in other severe forms of pneumonia, tuberculosis, lung abscess, and even few cases of bronchogenic carcinoma. However, recognition of this sign may alert the clinician of the possible etiology of *Klebsiella* in the context of infection and may help in deciding appropriate antibiotics (Fig. 1.23).

1.4.1.10 Deep Sulcus Sign

Pneumothorax in supine radiographs may be appreciable only at the costophrenic sulci as the air tends to accumulate in the nondependent regions of basal zones [7, 11]. Hence the costophrenic sulci appear more lucent. This sign is very important in patients with blunt chest trauma in whom only supine radiographs are available (Fig. 1.24).

1.4.1.11 Continuous Diaphragm Sign

This sign is seen in pneumomediastinum and pneumopericardium as the diaphragm appears as a continuous shadow [7, 12]. This helps in differentiating from pneumothorax (where the air does not cross midline) and pneumoperitoneum (Fig. 1.25).

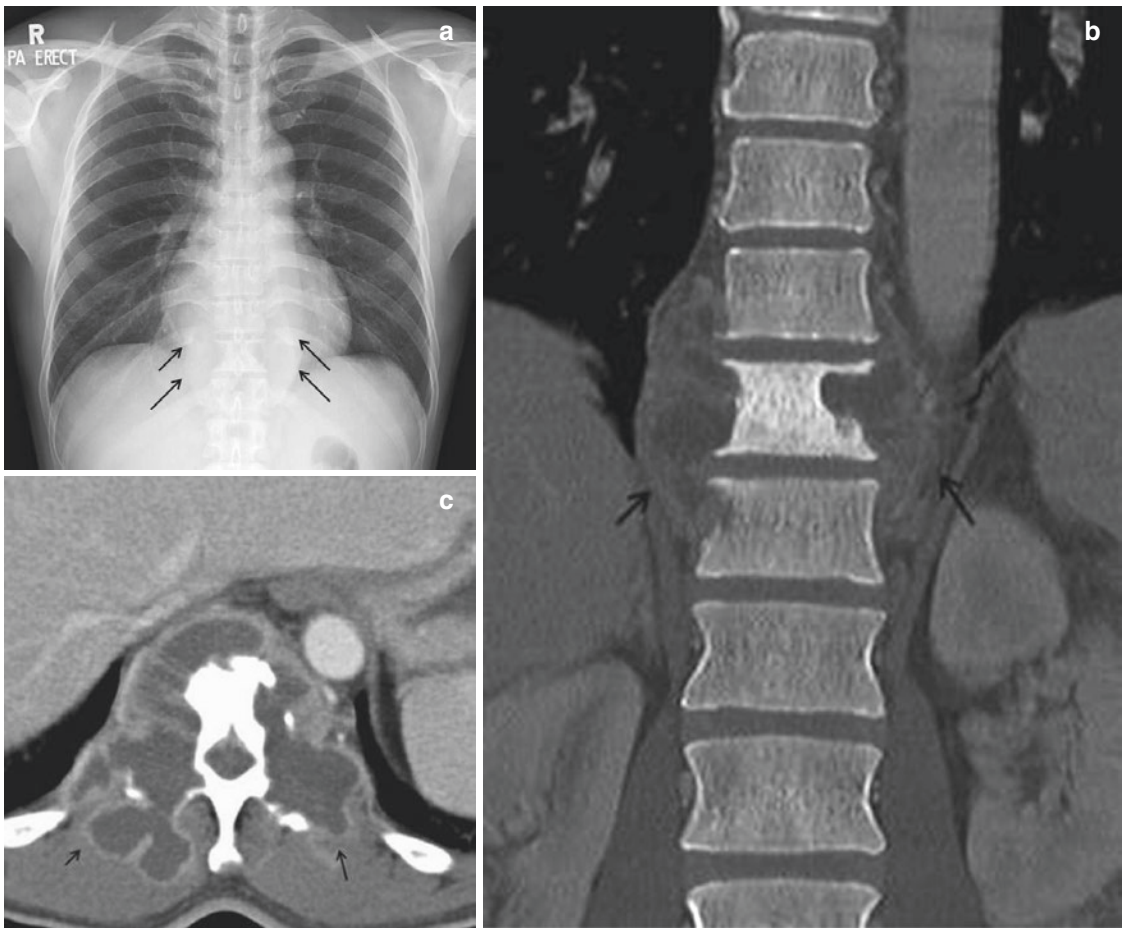

Fig. 1.19 Thoracoabdominal sign. (**a**) Chest radiograph of a young male patient who presented with back pain showing bilateral lower thoracic paraspinal mass (arrows), extending below the diaphragms with outer borders outlined by the adjacent posterior basilar lungs, indicating that the mass is entirely intrathoracic. Additionally, there is also the bony destruction of the adjacent T10 vertebra suggestive of infective spondylitis. (**b**, **c**) Coronal and axial images show bilateral extensive paraspinal abscesses (arrows) with the destruction of the anterior and posterior elements of the T10 vertebra. The abscesses are confined to the thorax

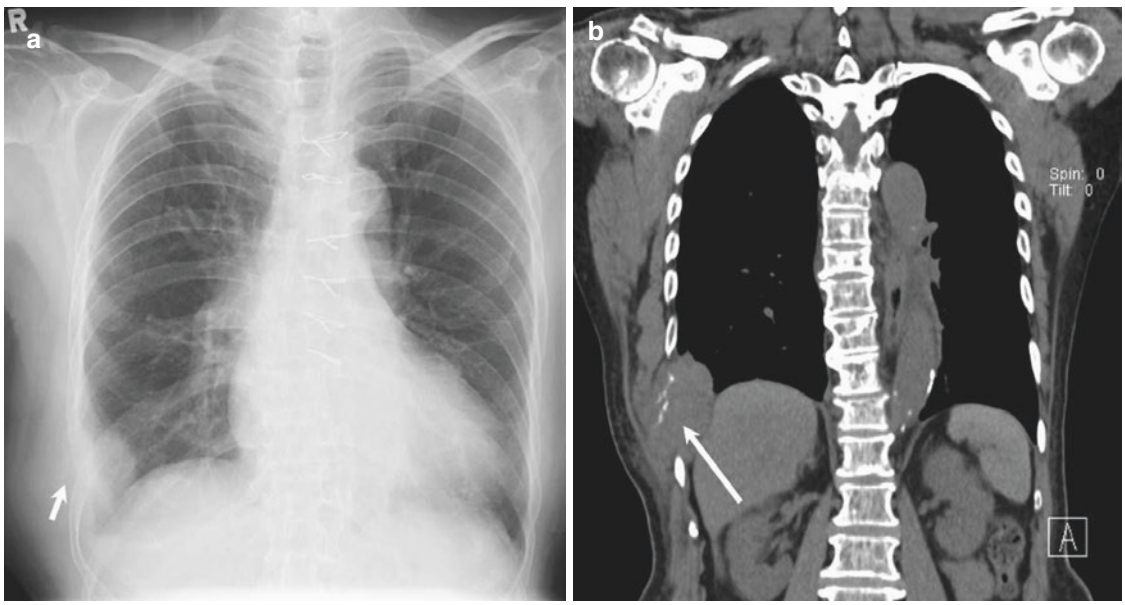

Fig. 1.20 Extrapleural sign in a plasmacytoma. (**a**) Chest radiograph of an elderly male showing a right lower zone peripheral-based opacity with sharp convex border and tapering superior edge. There is associated destruction of the adjacent right ninth rib (arrow) and hence indicative of an extrapleural mass lesion. (**b**) Coronal CT image confirms the extrapleural mass with the destruction of the adjacent rib (arrow)

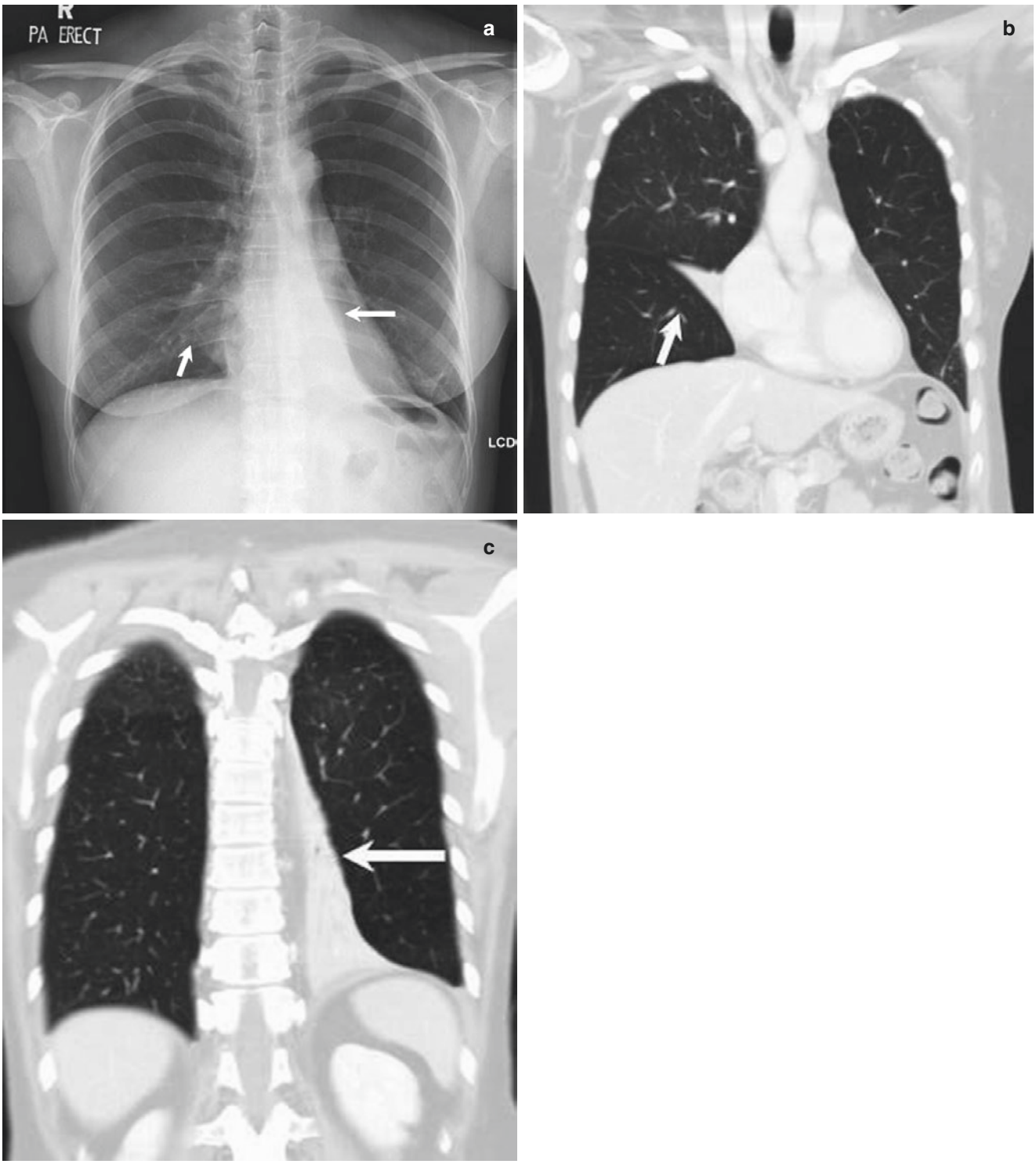

Fig. 1.21 Double lesion sign. (**a**) Chest radiograph of a patient with mucus impaction causing middle lobe and left lower lobe collapse. The right heart border and the outline of the left medial hemidiaphragm are obscured by the adjacent collapsed lung (silhouette sign). (**b**, **c**) Coronal CT images demonstrate the right middle and left lower lobe collapse

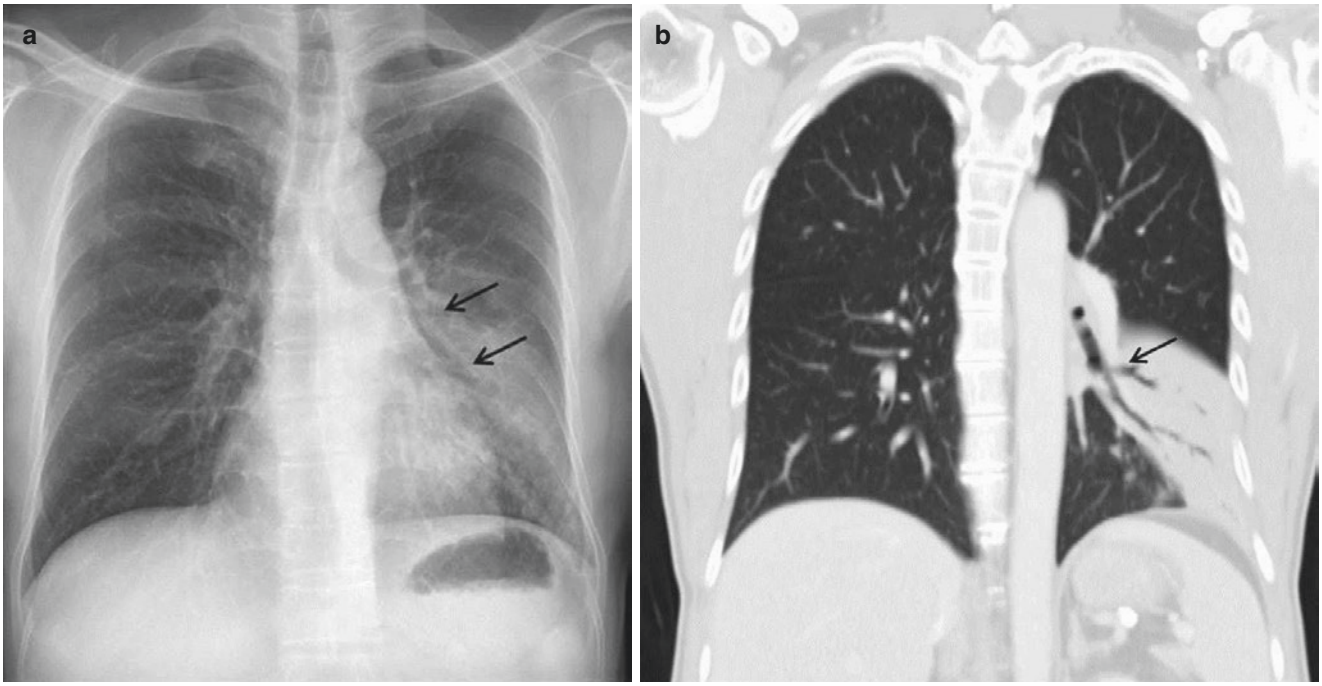

Fig. 1.22 Air bronchogram sign from tuberculosis. (**a**) Chest radiograph of an elderly patient demonstrating non-resolving opacities in the left mid-lower zone with air bronchogram (arrows), implying the location of the opacities is within the lung parenchyma. (**b**) Coronal CT image with lung window demonstrating consolidation with air bronchogram (arrow)

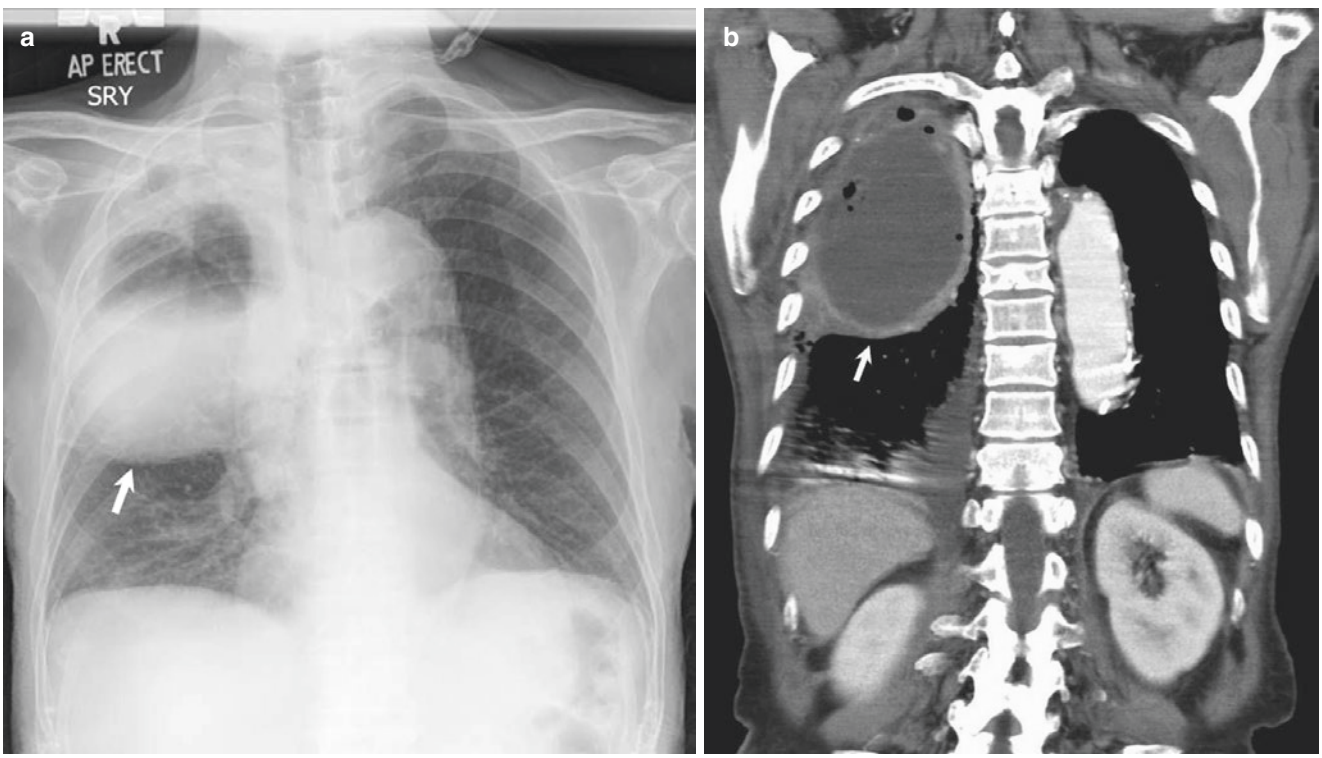

Fig. 1.23 Bulging fissure sign in necrotizing pneumonia from *Klebsiella pneumoniae*. (**a**) Chest radiograph and (**b**) coronal contrast-enhanced CT image of a middle-aged adult showing right upper lobe consolidation, bulging the minor fissure

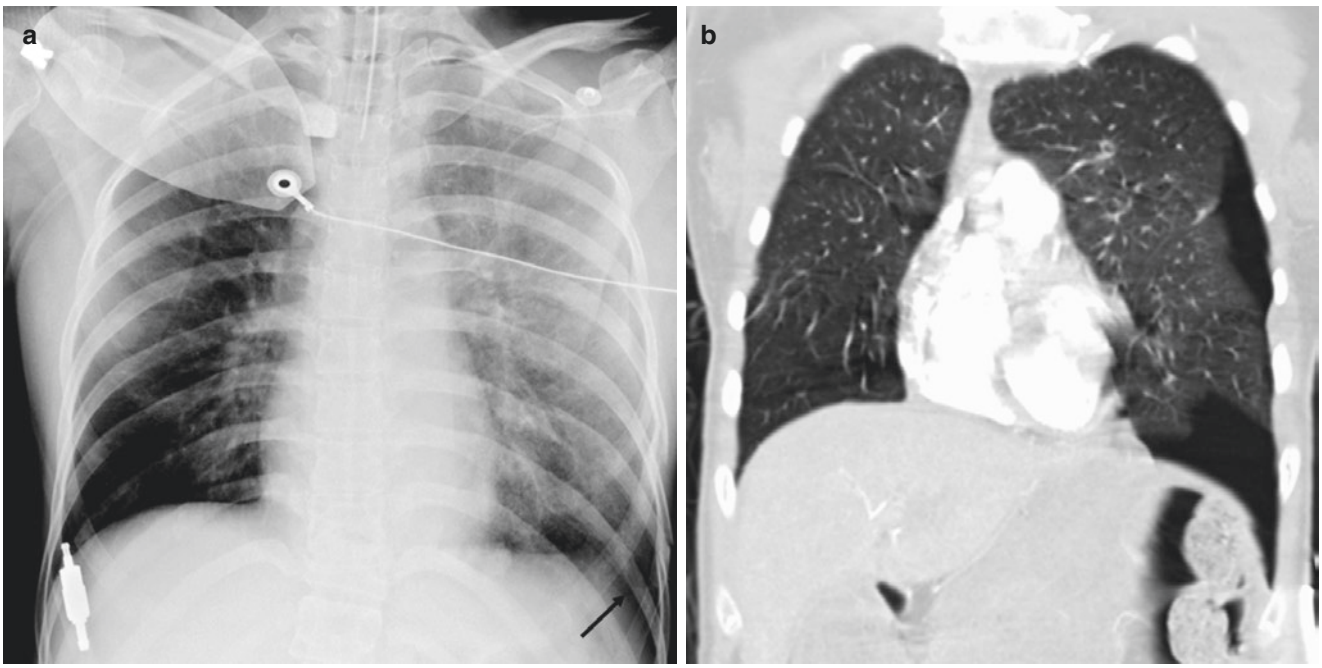

Fig. 1.24 Deep sulcus sign. (**a**, **b**) Radiograph and CT showing "deep sulcus" sign of pneumothorax in a supine patient due to trauma

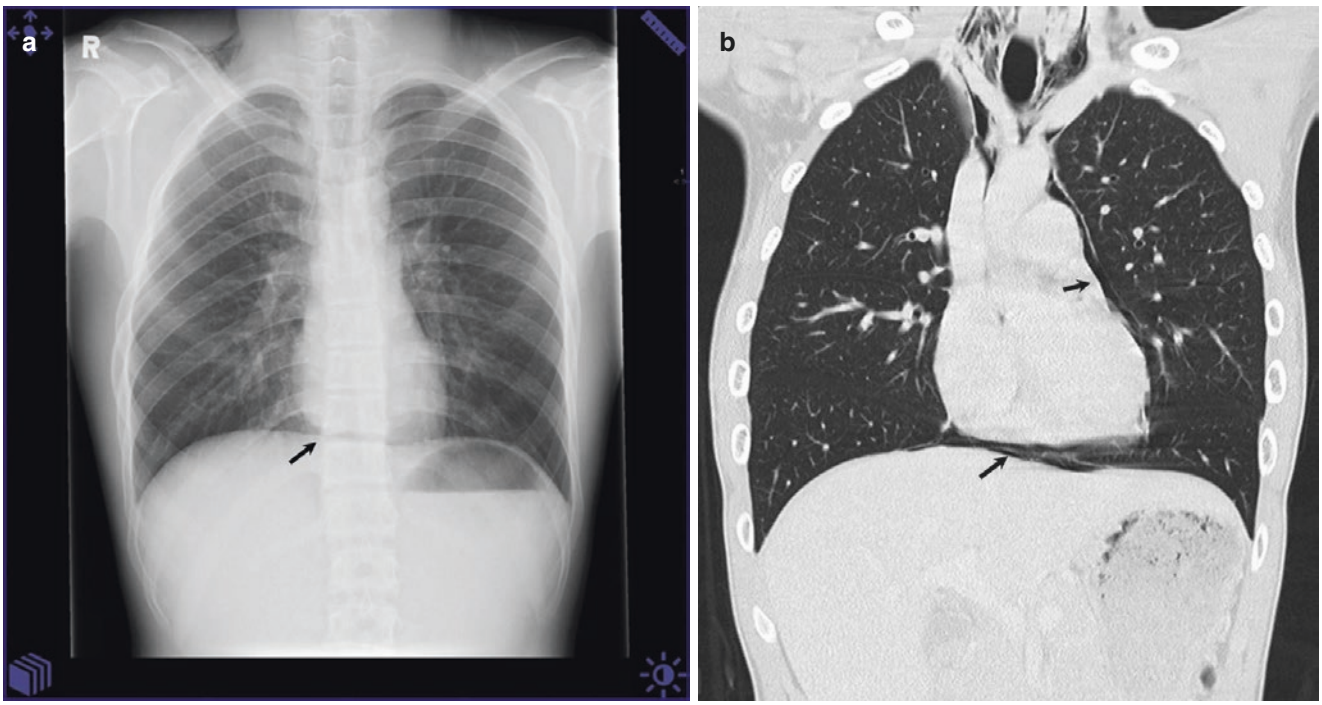

Fig. 1.25 Continuous diaphragm sign. Frontal radiograph (**a**) of the chest in a case of pneumomediastinum with continuous diaphragm sign (arrow). Findings confirmed on CT (**b**)

1.4.1.12 Golden S Sign

This is a radiographic sign seen in cases of collapsed right upper lobe due to a centrally located mass causing obstruction of the upper lobe bronchus [7, 13]. The mass causes bulge inferiorly, in the medial aspect, and forms the convex part of the S inferiorly, whereas the concave part laterally is formed by the collapsed upper lobe and the fissure (Fig. 1.26).

1.4.1.13 Scimitar Sign

This sign is seen in pulmonary hypoplasia with the partial anomalous pulmonary venous connection [14]. In one-third of cases, the anomalous draining vein may be seen as a tubular structure paralleling the right heart border in the shape of a Turkish sword (scimitar). The right heart border may be blurred (Fig. 1.27).

1.4.1.14 Hampton Hump Sign and Westermark Sign

These signs are described in Chap. 9 [15, 16].

1.4.1.15 Luftsichel Sign

"Luftsichel" means air crescent (German). In cases of complete left upper lobe collapse, a portion of the left lower lobe can migrate anterior-superiorly between the aortic arch and collapsed left upper lobe [7, 17]. This presents as a crescentic air lucency on the radiograph. This sign is useful in the diagnosis of left upper lobe collapse (Fig. 1.12).

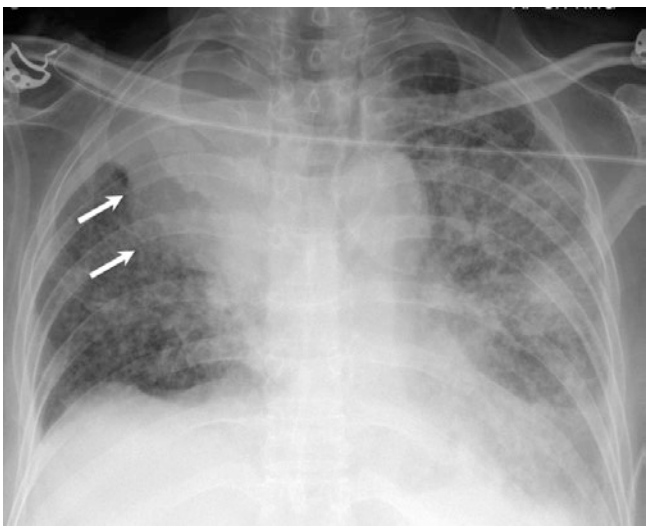

Fig. 1.26 Golden S sign. A 75-year-old man with right hilar mass. Frontal radiograph of the chest shows right upper lobe collapse with bulging of the right minor fissure (arrows)

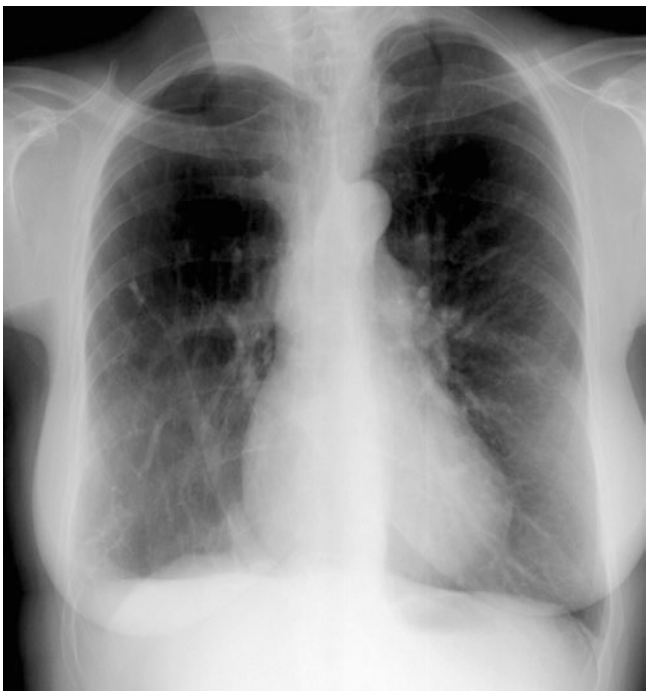

Fig. 1.27 Scimitar sign. Frontal chest radiograph in a 60-year-old woman shows a vertical linear opacity in right lower lung

1.4.1.16 Juxtaphrenic Peak Sign

This radiographic sign can be observed in cases of upper lobe collapse, due to elevation of the dome of the diaphragm with a peak at the center, likely due to inferior accessory fissure and upward retraction of visceral pleura upwards (Fig. 1.9) [18].

1.4.1.17 Black Pleura Sign

This sign is seen in pulmonary alveolar microlithiasis, which is a condition of idiopathic etiology characterized by deposition of calcium phosphate in the alveoli and reactive interstitial fibrosis [19, 20]. The apparent appearance of pleura as a dark linear strip is due to dense calcified nodules in the lungs and increased density of the ribs on either side.

1.5 CT Signs

The CT signs can be classified into parenchymal, vascular, and pleural signs (Figs. 1.28, 1.29, 1.30, 1.31, 1.32, 1.33, 1.34, 1.35, 1.36, 1.37, and 1.38) (Tables 1.5, 1.6, and 1.7) [7, 21–41].

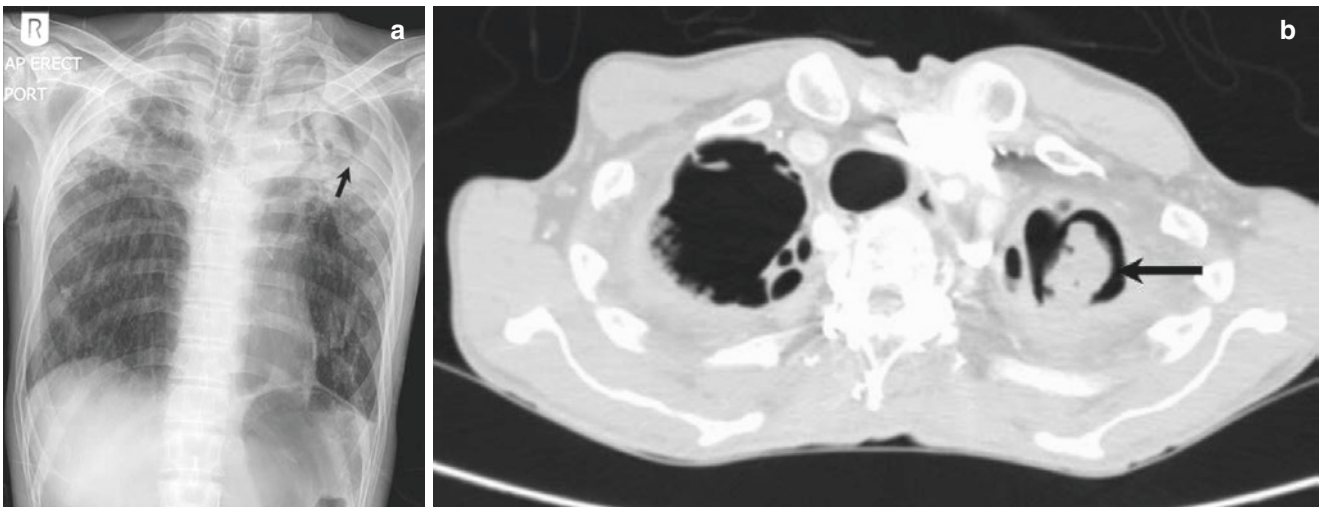

Fig. 1.28 Air crescent sign. (**a**) Chest radiograph of an elderly patient shows scarring with architecture distortion and cavities in bilateral upper zones. Additionally, crescent gas shadow is seen outlining a nodule in the left upper zone suggestive of a fungus ball (mycetoma). (**b**) CT image with lung window demonstrating the fungus ball surrounded by a rim of gas

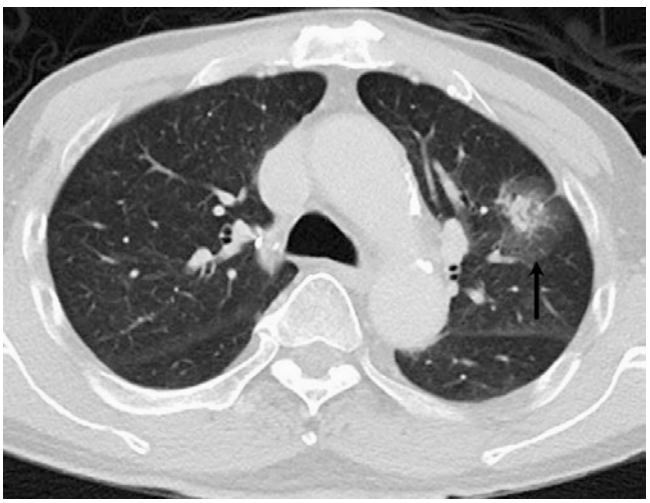

Fig. 1.29 Halo sign. Axial CT sections showing a halo around the solid nodule in the left upper lobe

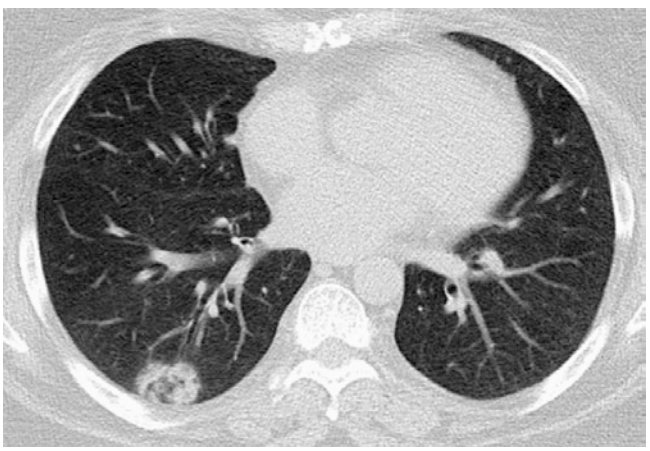

Fig. 1.30 Reverse halo sign in a case of cryptogenic organizing pneumonia. Center appears less dense compared to the periphery

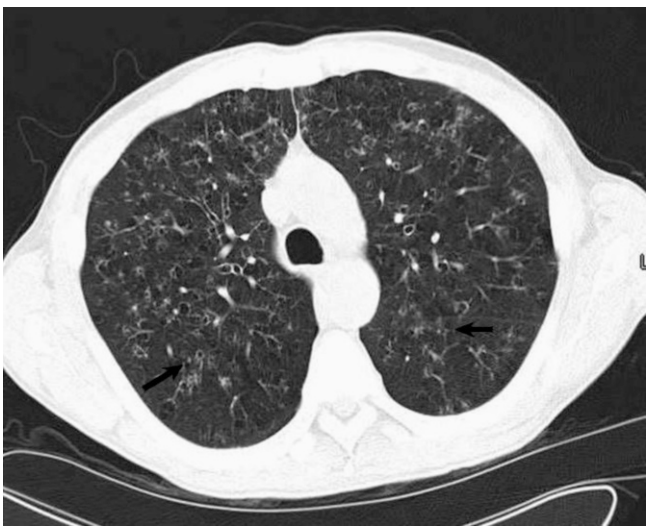

Fig. 1.31 Cheerios sign. Nodules with central lucency (arrow) in a case of Langerhans cell histiocytosis

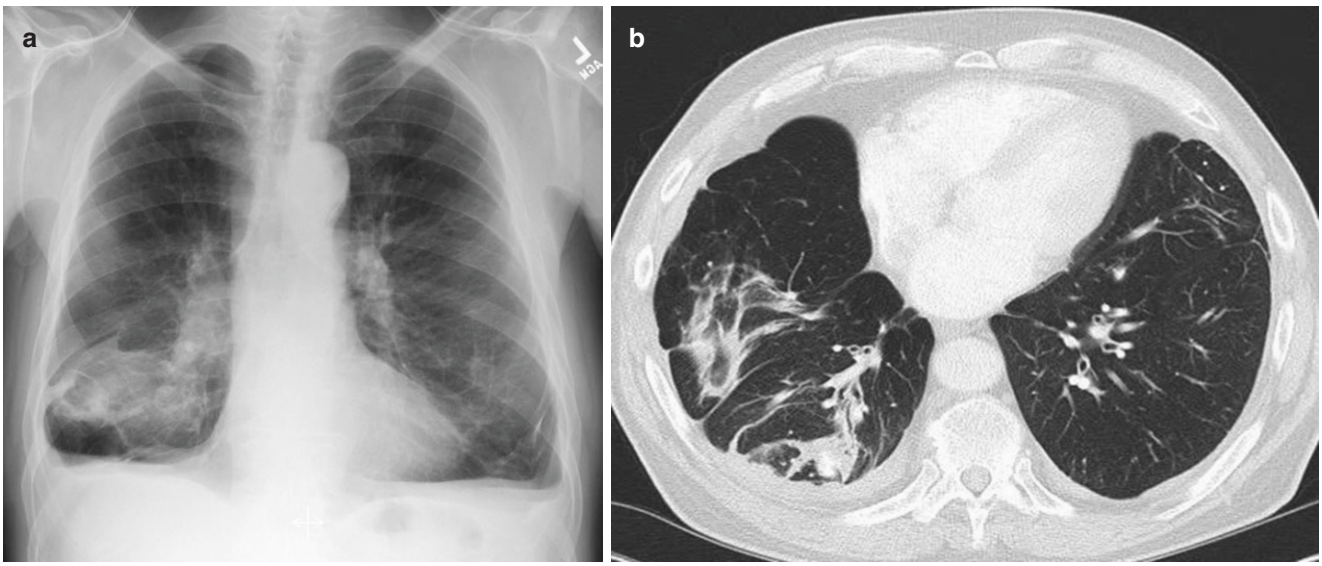

Fig. 1.32 Comet tail sign in round atelectasis. (**a**, **b**) Frontal radiograph and axial CT image show all criteria for rounded atelectasis (subpleural opacity, comet tail sign, volume loss, and pleural effusion)

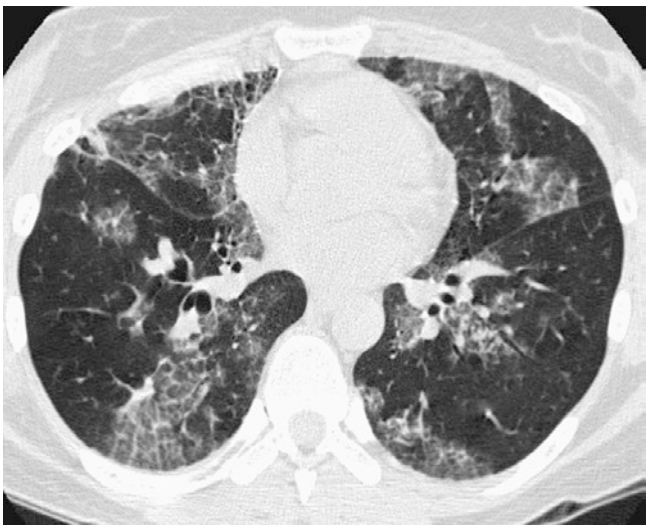

Fig. 1.33 Crazy paving pattern. Ground-glass opacities with thickened interlobular septa

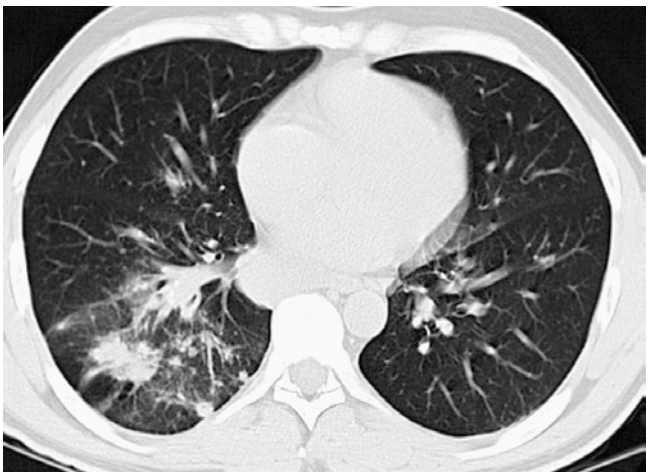

Fig. 1.34 Galaxy sign. Dense nodule with irregular margins with tiny surrounding nodules and perilymphatic nodules in a proven case of sarcoidosis

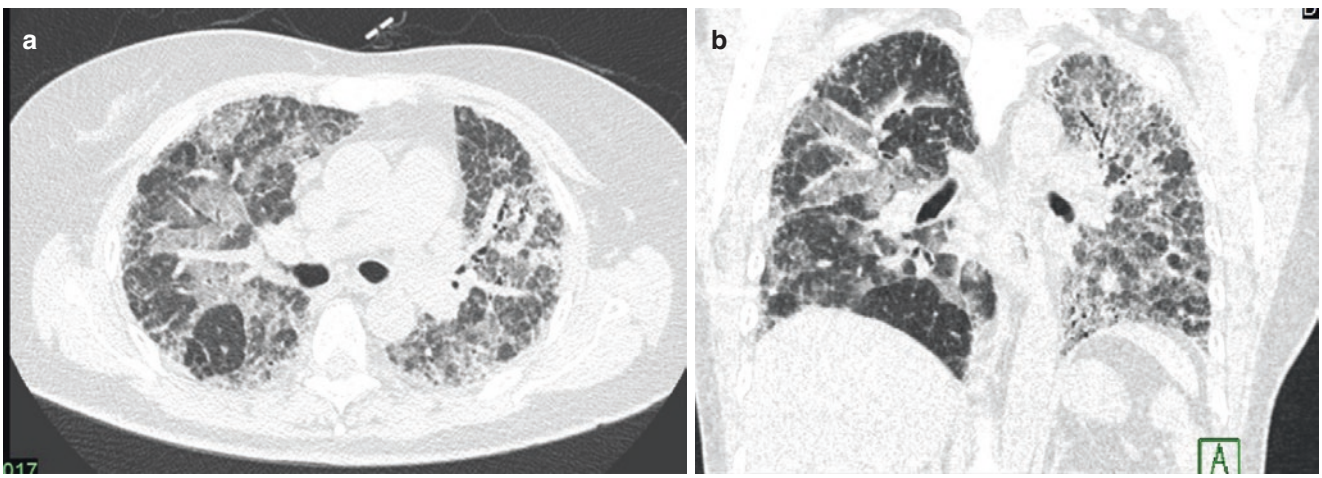

Fig. 1.35 Headcheese sign. (**a**, **b**) Axial and coronal CT images show areas of high attenuation interspersed with low attenuation areas in both lungs, in a case of subacute hypersensitivity pneumonitis

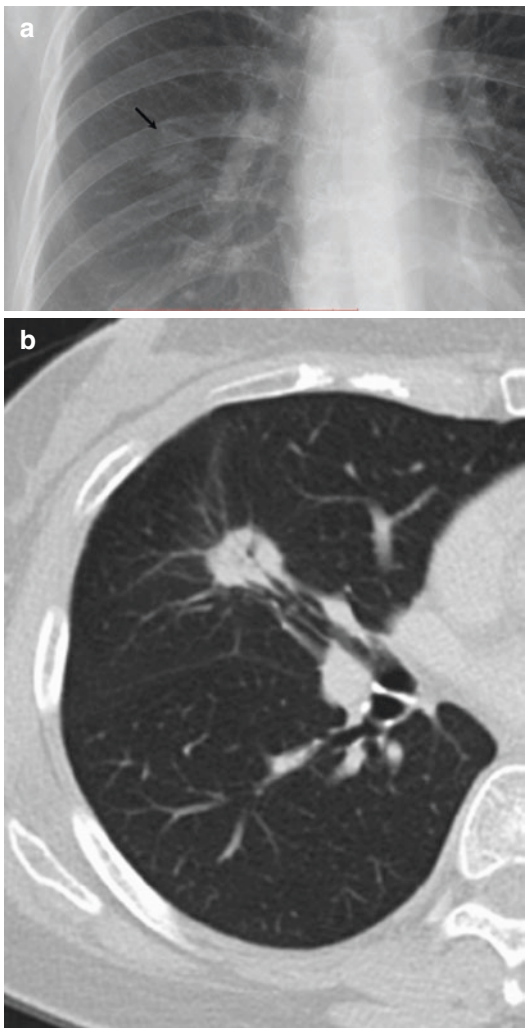

Fig. 1.36 Positive bronchus sign in a proven case of adenocarcinoma. (**a**) Frontal radiograph shows an ill-defined nodule with air bronchograms. (**b**) Axial CT image shows a nodule with dilated bronchi leading to it

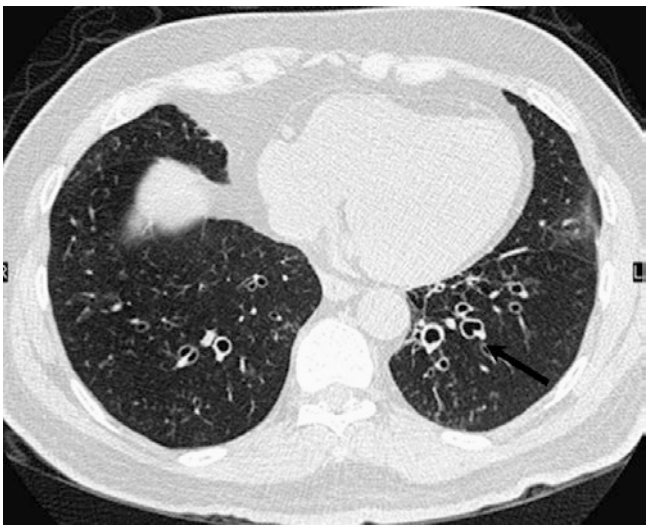

Fig. 1.37 Signet ring sign. Axial CT section showing signet ring sign due to dilated bronchus and normal-sized adjacent vessel (arrow)

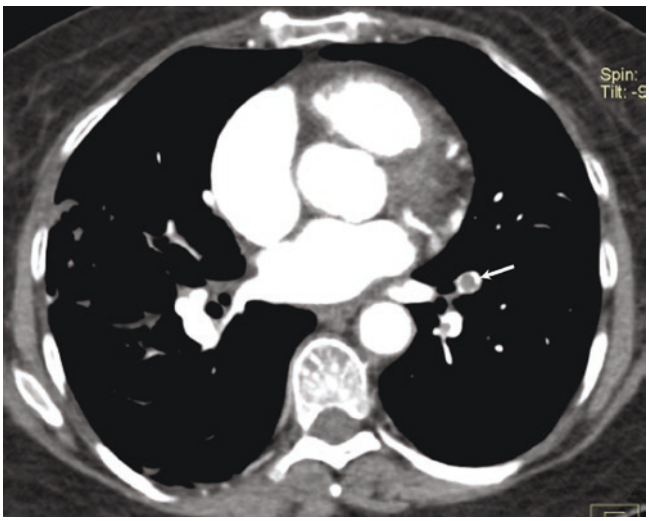

Fig. 1.38 Polo mint sign. Axial CTPA image shows a central filling defect (arrow) in a segmental branch of the left lower lobe pulmonary artery

Table 1.5 Parenchymal signs

Air crescent sign	• Rim of air around a focal consolidation or a nodule • Usually fungal ball in a preexisting cavity • Rarely cavitary malignancy with necrotic tissue
Halo sign	• Central consolidation with surrounding ground-glass opacities • Seen in invasive aspergillosis, adenocarcinoma in situ, invasive aspergillosis
Reverse halo sign or atoll sign	• Lesion with central ground-glass opacity with peripheral dense consolidation • Seen in organizing pneumonia, fungal infections, lymphomatoid granulomatosis, granulomatosis with polyangiitis, lipoid pneumonia, sarcoidosis
Cheerio sign	• Nodule with a relatively large central lucency and thin opaque rim • Seen in primary and metastatic mucinous adenocarcinomas, pulmonary Langerhans cell histiocytosis
Comet tail sign	• Refers to the vessels and airways which get pulled into mass-like atelectasis of lung • Classically seen in rounded atelectasis
Corona radiata sign	• Refers to spiculations along the margins of a lesion with distortion of blood vessels • Seen in primary malignancy and infection/inflammation in the background of emphysema
Crazy paving sign	• Refers to thickened interlobular septa with diffuse ground-glass opacity • Usually seen in alveolar proteinosis, pulmonary edema, mucinous adenocarcinoma, lipoid pneumonia, *Pneumocystis jirovecii* pneumonia, sarcoidosis, NSIP, etc.
Galaxy sign	• Central dense mass or nodule with surrounding tiny satellite nodules • Classically seen in sarcoidosis
Headcheese sign	• Refers to multiple densities seen in single CT image, i.e., normal lung interspersed with mosaic lung • Classically seen in hypersensitivity pneumonitis

NSIP nonspecific interstitial pneumonia

Table 1.6 Airways signs

Air bronchogram sign	• Refers to lucent airways surrounded by consolidated lung • Seen in pneumonia, malignancies, inflammatory conditions, etc.
Positive bronchus sign	• Refers to a prominent airway (bronchus) leading to a peripheral mass or nodule • Predictor of successful transbronchial lung biopsy
Signet ring sign	• Sign of bronchiectasis in CT images
Tree-in-bud sign	• Refers to small branching opacities within the center of the pulmonary lobules, similar to buds on a tree • Seen in endobronchial infections and rarely tumors
Gloved finger sign	• Refers to dilated bronchi filled with mucus or pus appearing as gloved fingers or linear tubular opacities in radiographs and CT • Seen in ABPM, congenital bronchial atresia

ABPM allergic bronchopulmonary mycosis

Table 1.7 Vascular signs

CT angiogram sign	• Refers to the appearance of dense vessel traversing through relatively hypodense lung • Initially was considered typical of (mucinous) adenocarcinoma • Can be seen in pneumonia, edema, and lymphoma
Feeding vessel sign	• Refers to a vessel leading to a mass or nodule • Usually seen in septic pulmonary emboli • Can also be seen in pulmonary infarction, AVM, and metastases
Polo mint sign	• Refers to a central filling defect inside a vessel with the rim of contrast opacification • Sign of acute pulmonary embolism

AVM arteriovenous malformation

References

1. Collins J. CT signs and patterns of lung disease. Radiol Clin N Am. 2001;39(6):1115–35.
2. Hansell DM, Bankier AA, MacMahon H, McLoud TC, Muller NL, Remy J. Fleischner society: glossary of terms for thoracic imaging. Radiology. 2008;246(3):697–722.
3. Proto AV, Tocino I. Radiographic manifestations of lobar collapse. Semin Roentgenol. 1980;15(2):117–73.
4. Woodring JH, Reed JC. Radiographic manifestations of lobar atelectasis. J Thorac Imaging. 1996;11(2):109–44.
5. Felson B, Felson H. Localization of intrathoracic lesions by means of the postero-anterior roentgenogram; the silhouette sign. Radiology. 1950;55(3):363–74.
6. Marshall GB, Farnquist BA, MacGregor JH, Burrowes PW. Signs in thoracic imaging. J Thorac Imaging. 2006;21(1):76–90.

7. Algın O, Gökalp G, Topal U. Signs in chest imaging. Diagn Interv Radiol. 2011;17(1):18–29.
8. Matsunaga K, Takanashi Y, Tajima S, Hayakawa T, Neyatani H. Solitary fibrous tumor originating from the visceral pleura presenting an extrapleural sign; report of a case. Kyobu Geka. 2017;70(6):474–6.
9. Kui M, Templeton PA, White CS, Cai ZL, Bai YX, Cai YQ. Evaluation of the air bronchogram sign on CT in solitary pulmonary lesions. J Comput Assist Tomogr. 1996;20(6):983–6.
10. Schmidt AJ, Stark P. Radiographic findings in Klebsiella (Friedlander's) pneumonia: the bulging fissure sign. Semin Respir Infect. 1998;13(1):80–2.
11. Gordon R. The deep sulcus sign. Radiology. 1980;136(1):25–7.
12. Schmitt ER, Burg MD. Continuous diaphragm sign. West J Emerg Med. 2011;12(4):526–7.
13. Gupta P. The golden S sign. Radiology. 2004;233(3):790–1.
14. Schramel FM, Westermann CJ, Knaepen PJ, van den Bosch JM. The scimitar syndrome: clinical spectrum and surgical treatment. Eur Respir J. 1995;8(2):196–201.
15. Frazier AA, Galvin JR, Franks TJ, Rosado-De-Christenson ML. From the archives of the AFIP: pulmonary vasculature: hypertension and infarction. Radiographics. 2000;20(2):491–524.
16. Sreenivasan S, Bennett S, Parfitt VJ. Images in cardiovascular medicine. Westermark's and Palla's signs in acute pulmonary embolism. Circulation. 2007;115(8):e211.
17. Blankenbaker DG. The luftsichel sign. Radiology. 1998;208(2):319–20.
18. Davis SD, Yankelevitz DF, Wand A, Chiarella DA. Juxtaphrenic peak in upper and middle lobe volume loss: assessment with CT. Radiology. 1996;198(1):143–9.
19. Marchiori E, Souza AS, Franquet T, Müller NL. Diffuse high-attenuation pulmonary abnormalities: a pattern-oriented diagnostic approach on high-resolution CT. AJR Am J Roentgenol. 2005;184(1):273–82.
20. Sosman MC, Dodd GD, Jones WD, Pillmore GU. The familial occurrence of pulmonary alveolar microlithiasis. Am J Roentgenol Radium Ther Nucl Med. 1957;77(6):947–1012.
21. Abramson S. The air crescent sign. Radiology. 2001;218(1):230–2.
22. Haber J, Cervenková J. Invasive pulmonary aspergillosis—imaging and invasive potential of diagnosis. Klin Mikrobiol Infekc Lek. 2007;13(5):190–4.
23. Pinto PS. The CT halo sign. Radiology. 2004;230(1):109–10.
24. Kim SJ, Lee KS, Ryu YH, Yoon YC, Choe KO, Kim TS, et al. Reversed halo sign on high-resolution CT of cryptogenic organizing pneumonia: diagnostic implications. AJR Am J Roentgenol. 2003;180(5):1251–4.
25. Chou S-HS, Kicska G, Kanne JP, Pipavath S. Cheerio sign. J Thorac Imaging. 2013;28(1):W4.
26. Partap VA. The comet tail sign. Radiology. 1999;213(2):553–4.
27. Wang Y-XJ, Gong J-S, Suzuki K, Morcos SK. Evidence based imaging strategies for solitary pulmonary nodule. J Thorac Dis. 2014;6(7):872–87.
28. Johkoh T, Itoh H, Müller NL, Ichikado K, Nakamura H, Ikezoe J, et al. Crazy-paving appearance at thin-section CT: spectrum of disease and pathologic findings. Radiology. 1999;211(1):155–60.
29. Aikins A, Kanne JP, Chung JH. Galaxy sign. J Thorac Imaging. 2012;27(6):W164.
30. Chong BJ, Kanne JP, Chung JH. Headcheese sign. J Thorac Imaging. 2014;29(1):W13.
31. Sherrick AD, Swensen SJ, Hartman TE. Mosaic pattern of lung attenuation on CT scans: frequency among patients with pulmonary artery hypertension of different causes. AJR Am J Roentgenol. 1997;169(1):79–82.
32. Ch'ng LS, Bux SI, Liam CK, Rahman NA, Ho CY. Sandstorm appearance of pulmonary alveolar microlithiasis incidentally detected in a young, asymptomatic male. Korean J Radiol. 2013;14(5):859–62.
33. Kerimoglu U, Kapicioglu S, Emlik D, Arazi M, Ural O. Case 161: hydatid disease with water lily sign manifesting as a soft-tissue mass in the calf of a child. Radiology. 2010;256(3):1007–10.
34. Zacharopoulos G, Adam A, Ind PW. The positive bronchus sign in patients with known lung cancer. Eur J Radiol. 1990;10(2):130–3.
35. Ouellette H. The signet ring sign. Radiology. 1999;212(1):67–8.
36. Cantin L, Bankier AA, Eisenberg RL. Bronchiectasis. AJR Am J Roentgenol. 2009;193(3):W158–71.
37. Gosset N, Bankier AA, Eisenberg RL. Tree-in-bud pattern. AJR Am J Roentgenol. 2009;193(6):W472–7.
38. Nguyen ET. The gloved finger sign. Radiology. 2003;227(2):453–4.
39. Shah RM, Friedman AC. CT angiogram sign: incidence and significance in lobar consolidations evaluated by contrast-enhanced CT. AJR Am J Roentgenol. 1998;170(3):719–21.
40. Dodd JD, Souza CA, Müller NL. High-resolution MDCT of pulmonary septic embolism: evaluation of the feeding vessel sign. AJR Am J Roentgenol. 2006;187(3):623–9.
41. Wittram C, Maher MM, Yoo AJ, Kalra MK, Shepard J-AO, McLoud TC. CT angiography of pulmonary embolism: diagnostic criteria and causes of misdiagnosis. Radiographics. 2004;24(5):1219–38.

Imaging of Large and Small Airways

2

Ashish Chawla

2.1 Large Airways

2.1.1 Anatomy of Airways, Lobes, and Bronchopulmonary Segments

Large airways or the central airways are composed of trachea and bronchi. The human tracheobronchial tree has 23 generations with the lobar bronchi being the first generation. The proximal, approximately, 16 generations of bronchi have conductive function, while the distal airways take part in gas exchange with a transition zone between the two where the bronchioles have both functions (Fig. 2.1). The respiratory bronchiole, alveolar duct, and alveolar sac have pure gas exchange function. The measurements of the trachea are described in Table 2.1 [1, 2]. The tracheal wall is composed of multiple rigid C-shaped hyaline cartilages covering the anterolateral wall and a collapsible membrane in posterior wall composed of muscle (trachealis) and connective tissue. CT plays an essential role in the identification of lobar and segmental bronchi as well as fissures. This is important in preoperative localization of the endobronchial and parenchymal lesion. The right bronchus is wider, shorter, and more vertical than the left lung. This leads to higher chances of right endobronchial intubation. The right bronchus, after giving rise to upper lobe bronchus, continues as bronchus intermedius and bifurcates into longer right middle lobe bronchus and shorter right lower lobe bronchus. The left bronchus divides into an upper lobe and lower lobe bronchus and subsequently to their segmental bronchi. Lingular bronchus arises from the left upper lobe bronchus. The segmental bronchi help in localizing the bronchopulmonary segments (Table 2.2).

The fissures are infolded reflection of the visceral pleura that completely or partially separate the lobes (Table 2.3). The major fissure appears like a thin line, and the minor fissure appears as an avascular zone on HRCT. These fissures can be complete or incomplete. The major fissures can be incomplete in up to 73% of the HRCT with right major fissure more common than the left [3, 4]. Accessory fissures are frequently seen in up to 32% of HRCT [5] (Fig. 2.2). These are inferior accessory (8.6%), azygos (1.2%), superior accessory (4.6%), and the left minor fissures (6.1%) [4]. The knowledge of the presence of accessory fissures is helpful in understanding some concepts of pulmonary imaging. Juxtaphrenic peak sign or "Katten sign" refers to tenting of the diaphragm in patients with upper lobe volume loss due to stretching of the inferior accessory fissure (Fig. 2.3).

Chest radiograph has a limited role in the evaluation of tracheobronchial tree. A good quality PA radiograph demonstrates the central tracheobronchial tree very well. The trachea is midline in position, with a focal indentation on its left lateral wall by a left aortic arch. A right aortic arch is often recognized on a radiograph by the indentation on the right lateral tracheal wall. Mediastinal masses and lymph nodes in relation to the trachea and proximal bronchi will also displace, indent, or narrow the lucent central airways. This sign is quite helpful but subtle and must be sought in the chest radiograph. CT due to its multiplanar capabilities has become a gold standard for noninvasive evaluation of tracheobronchial tree.

2.1.2 Tracheal Bronchus

Tracheal bronchus or "pig bronchus" is an example of a displaced bronchus where the entire upper lobe bronchus arises directly from the trachea. A common variant is a right apical segmental bronchus arising from the trachea. CT is diagnostic for this condition that is usually on the right side and is asymptomatic. A coronal CT reconstruction demonstrates

A. Chawla (✉)
Department of Diagnostic Radiology, Khoo Teck Puat Hospital, Singapore, Singapore

A. Chawla (ed.), *Thoracic Imaging*, https://doi.org/10.1007/978-981-13-2544-1_2

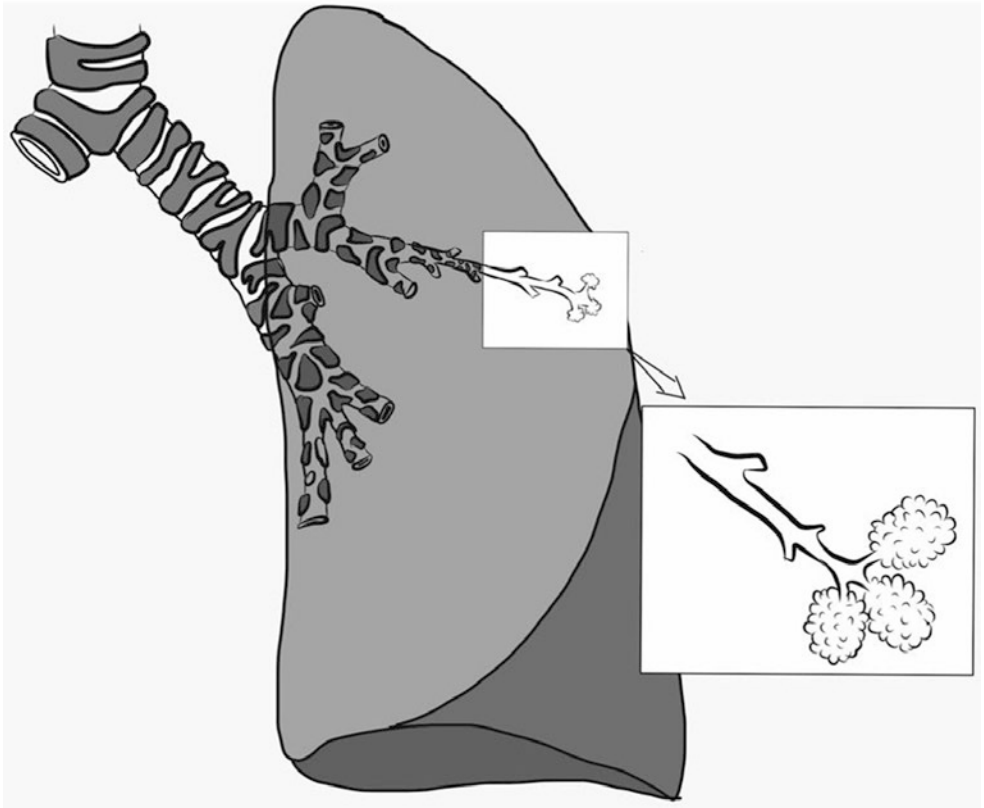

Fig. 2.1 Tracheobronchial tree

Table 2.1 Normal measurements of trachea

Total length: 10–12 cm Extrathoracic: 2–4 cm Intrathoracic: 6–9 cm
Diameter (coronal) Men: 13–25 mm Women: 10–21 mm
Wall thickness: 1–3 mm

Table 2.2 Bronchopulmonary segments

Right lung	Left lung
Upper lobe Apical segment Posterior segment Anterior segment	Upper lobe Apicoposterior segment Anterior segment
Middle lobe Lateral segment Medial segment	Lingula Superior segment Inferior segment
Lower lobe Superior segment Anterior basal segment Medial basal segment Posterior basal segment Lateral basal segment	Lower lobe Superior segment Anterior basal segment Medial basal segment Posterior basal segment Lateral basal segment

the separate bronchus arising from the trachea (Fig. 2.4). Nevertheless, it must be mentioned in the report as it can have implications, in case the patient requires intubation.

Table 2.3 Fissures of the lung

Major fissure Minor fissure	Separates the upper lobe from the lower lobe Separates the right middle lobe from the upper lobe
Accessory fissures	
Inferior accessory fissure	A thin curvilinear line extending from major fissure toward the inferior pulmonary ligament. The inferior accessory fissure surrounds the medial basal segment
Azygos fissure	Fissure from right upper paravertebral region to SVC anteriorly with the azygos vein located at the bottom
Superior accessory fissures	• Fissure between superior segment and basal segments of the lower lobe • Fissure between medial and lateral segments of the middle lobe • Fissure between superior and inferior segments of the lingula
Left minor fissure	Fissure between left the upper lobe and the lingula

2.1.3 Cardiac Bronchus

It's a supernumerary bronchus arising from the right main bronchus or bronchus intermedius and courses medially as a blind-ending structure. Usually asymptomatic, a cardiac bronchus can be a site of recurrent infection and hemoptysis. Coronal CT reconstruction shows the classical origin and course of the cardiac bronchus (Fig. 2.5).

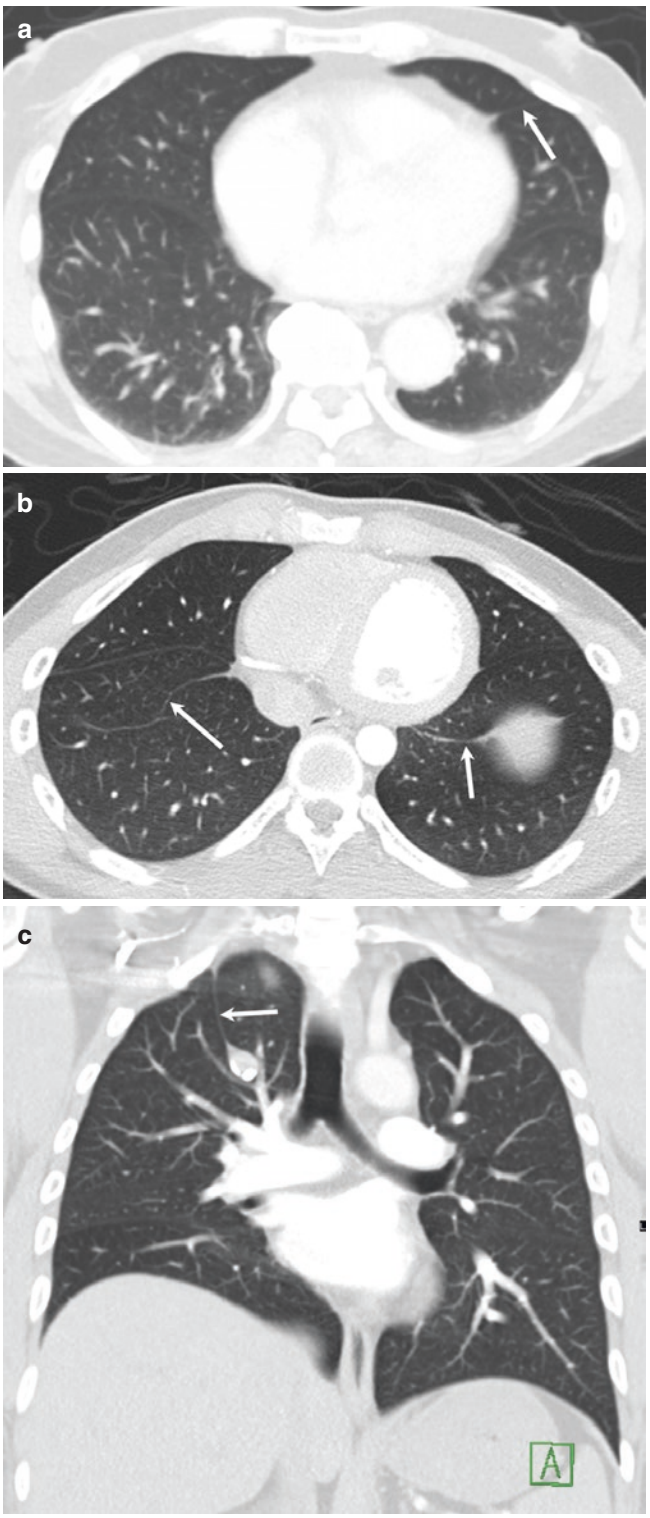

Fig. 2.2 Accessory fissures in three different patients. (**a**) Left minor fissure (arrow). (**b**) Bilateral inferior accessory fissures (arrows). (**c**) Azygos fissure (arrow)

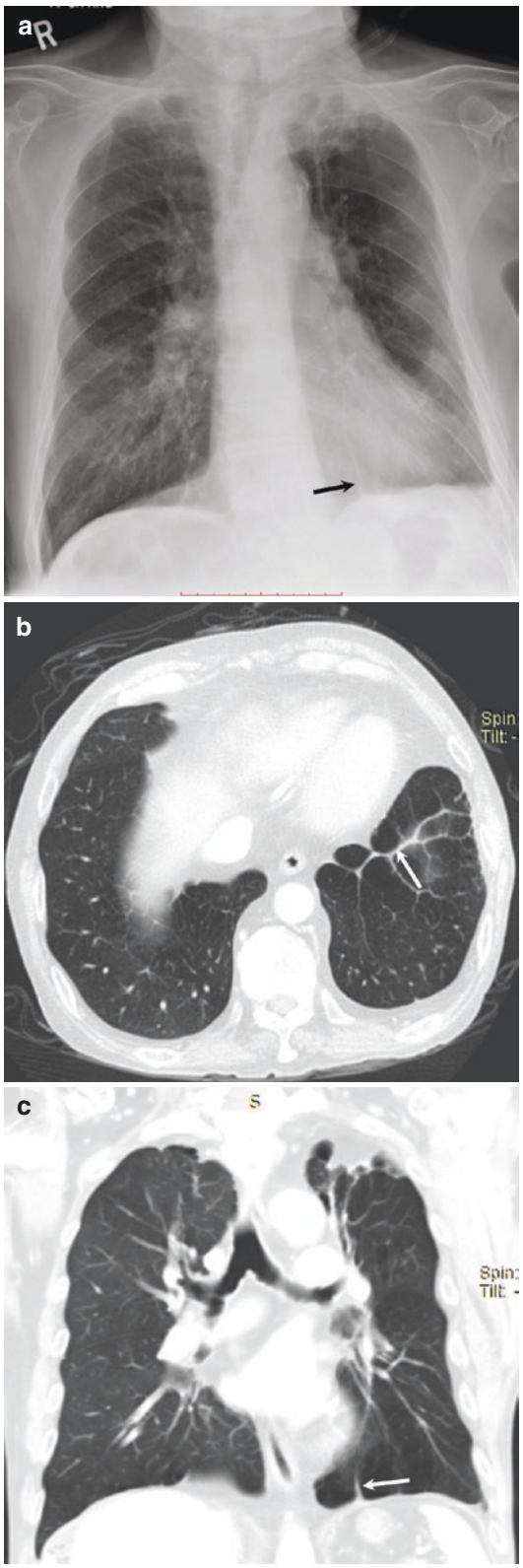

Fig. 2.3 Juxtaphrenic peak sign or "Katten sign" in a patient with upper lobe fibrosis. (**a**) Frontal chest radiograph shows scarring and volume loss in left upper lobe with tenting of the diaphragm. (**b**) Axial CT image from the lung base shows an inferior accessory fissure (arrow). (**c**) Coronal CT image shows volume loss in left upper lobe with stretching of the inferior accessory fissure (arrow)

2.1.4 Bridging Bronchus

This is an extremely rare airway malformation where the middle and right lower lobes are supplied by an aberrant bronchus originating from the left main stem bronchus that crosses the mediastinum. This variation is usually associated with congenital cardiac anomalies.

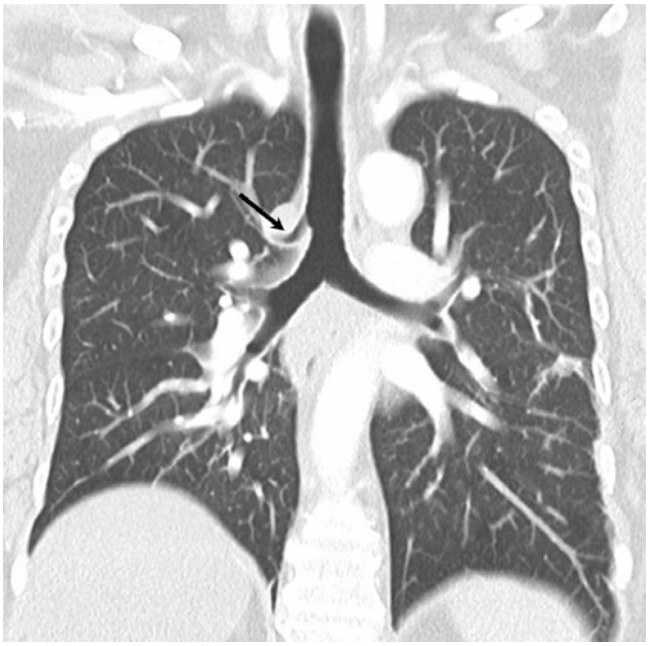

Fig. 2.4 Coronal CT MIP image showing a tracheal bronchus (arrow) supplying the entire right upper lobe, i.e., a "pig bronchus"

2.1.5 Congenital Tracheobronchomegaly or Mounier-Kuhn Syndrome

Congenital tracheobronchomegaly is a rare condition and is characterized by marked dilatation of central tracheobronchial tree. CT shows the coronal diameter of trachea more than 21 mm in women and 25 mm in men. The entire tracheobronchial tree is dilated with diverticula formation (Fig. 2.6).

2.1.6 Tracheal Diverticula

Small right posterolateral paratracheal diverticulum or cyst is a common finding on CT thorax or neck. These may be congenital or acquired, ranging in size from 1 mm to 15 mm, and are generally asymptomatic. CT does not show the communication between the cyst and trachea in the majority of the patients (Fig. 2.7). These must not be confused with pneumomediastinum or tracheal tear [6].

2.1.7 Bronchial Atresia

Bronchial atresia is a rare congenital condition that may remain undiagnosed till adulthood. It is characterized by non-development of lobar or one or more segmental/subsegmental bronchi with hyperinflation of the obstructed lung. The atretic bronchi are filled with mucus (bronchocele). Most bronchia atresias are recognized in left upper lobe with apicoposterior segment being most commonly involved. The distal hyperinflation results from trapped air in the affected lung that enters through intra-alveolar pores of Kohn and bronchoalveolar

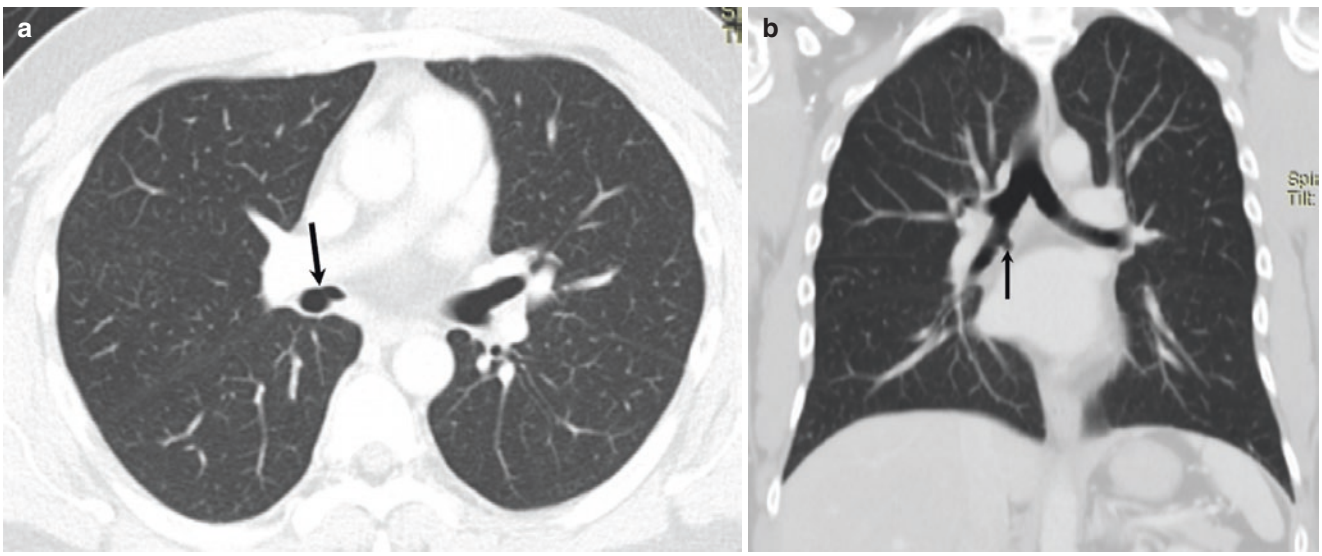

Fig. 2.5 (**a**, **b**) Axial and coronal CT images showing a cardiac bronchus (arrow)

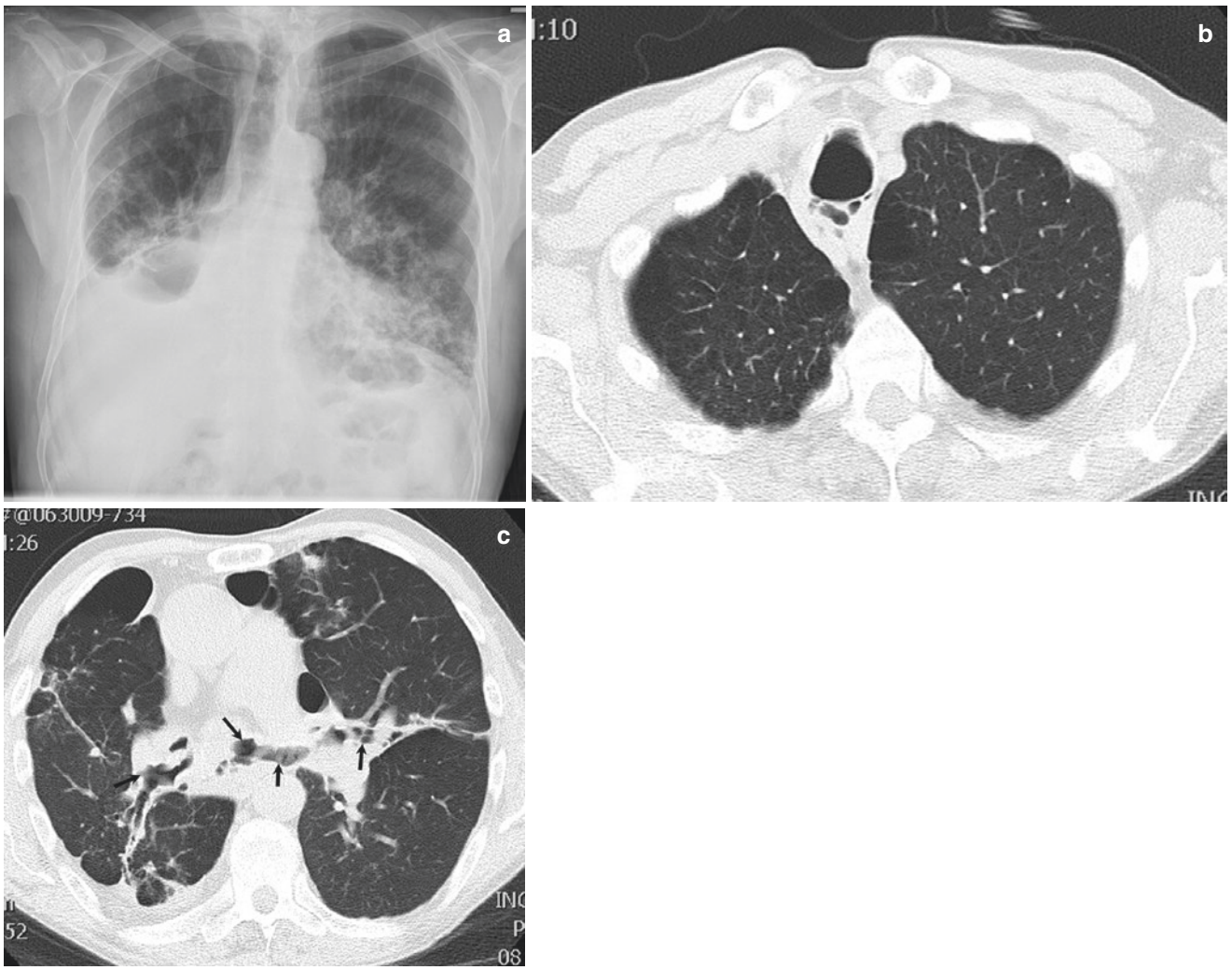

Fig. 2.6 A 63-year-old man with Mounier-Kuhn syndrome. (**a**) Frontal radiograph shows dilated trachea and bronchiectasis with air-space opacities in lower zones along with right pleural effusion. (**b**, **c**) Axial CT images show dilated trachea with multiple diverticula in the bronchi (arrows). Notice emphysema from smoking

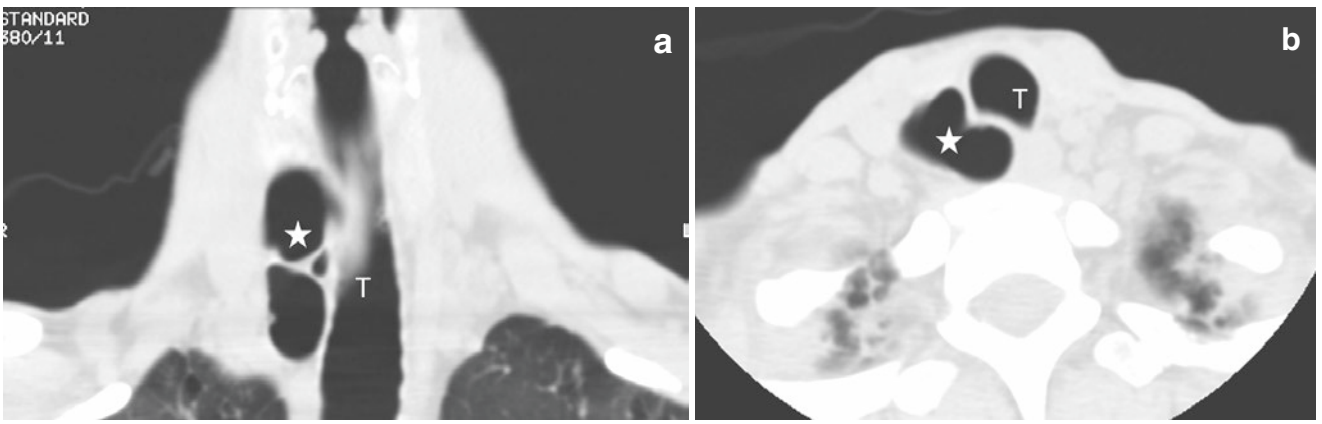

Fig. 2.7 (**a**, **b**) Coronal and axial CT images showing a large rare but asymptomatic right tracheal diverticulum (asterisk) with mass effect. T: trachea. (**c**) Small tracheal diverticulum (arrow) in another patient

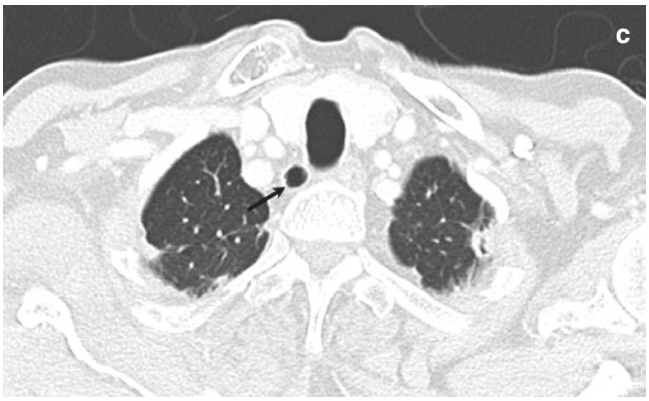

Fig. 2.7 (continued)

Table 2.4 Radiological features of bronchial atresia

Radiograph	Focal lucent area with a nodular or tubular area of increased opacity in the hilum
CT	Focal hyperinflated lobe, segment or subsegment Presence of central mucocele in the affected lung (may be calcified)
Differential diagnoses	
ABPM	Mucoid impaction but not striking hyperinflation
CLE	Lobar hyperinflation without any mucocele. There is focal emphysema (destruction of alveoli)
Swyer-James syndrome	Involves one or more lobes without mucocele

channels of Lambert that is further contributed by intrapulmonary vascular compression and hypoxic vasoconstriction [7]. Bronchial atresia in an adult is usually asymptomatic, but in the pediatric population, it presents with recurrent infection. The radiological features are mentioned in Table 2.4 (Figs. 2.8, 2.9, and 2.10). Chest radiograph shows a focal lucency in the lung with nodular or tubular opacity within it. CT shows focal hyperinflation of a distal anatomic area of the lung with tubular mucocele toward the hilum [7]. The mucocele may be calcified in some cases. Differential diagnoses of

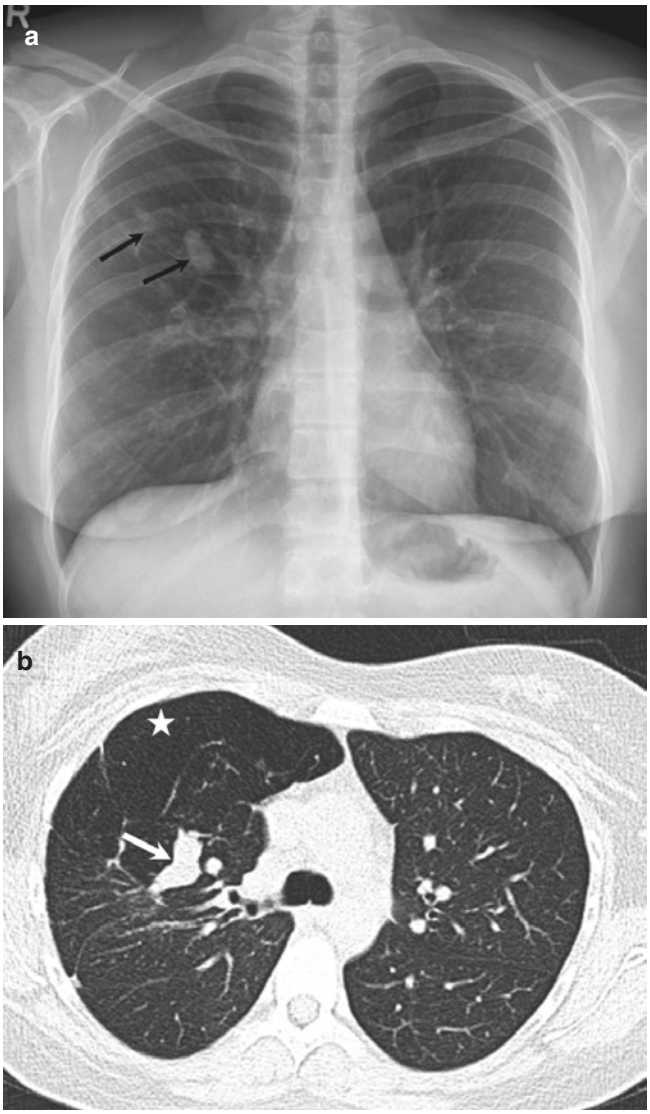

Fig. 2.8 A 57-year-old asymptomatic woman with congenital bronchial atresia of the anterior segment of the right upper lobe. (**a**) Frontal chest radiograph shows tubular opacities (arrows) in right upper lobe with "finger in glove" appearance. (**b**–**d**) Axial CT images show hyperlucent, hyperexpanded anterior segment of the right upper lobe (asterisk) with central bronchoceles (arrows)

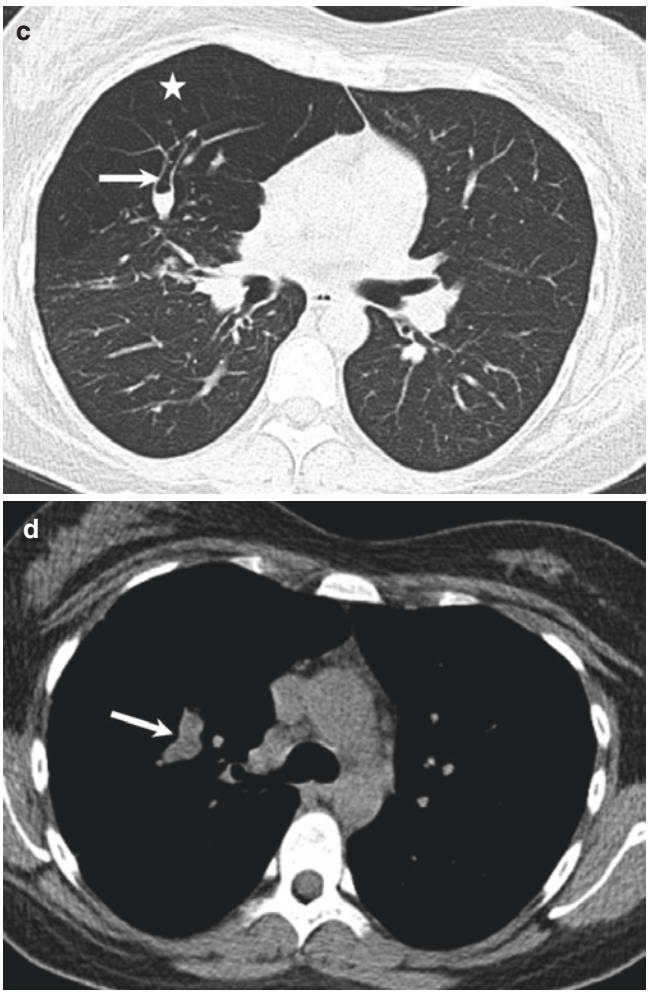

Fig. 2.8 (continued)

bronchial atresia include allergic bronchopulmonary mycosis (ABPM), congenital lobar emphysema (CLE), and Swyer-James syndrome.

2.1.8 Tracheal Narrowing

A wide spectrum of diseases can lead to large airways narrowing. These are described in Table 2.5.

2.1.8.1 Tracheobronchial Tumors

Tracheobronchial tumors are rare and include benign tumors, primary malignancy, and secondary malignant tumors (Table 2.6) [8, 9]. Benign tumors are less common than the malignant counterpart. CT scan is the investigation of choice

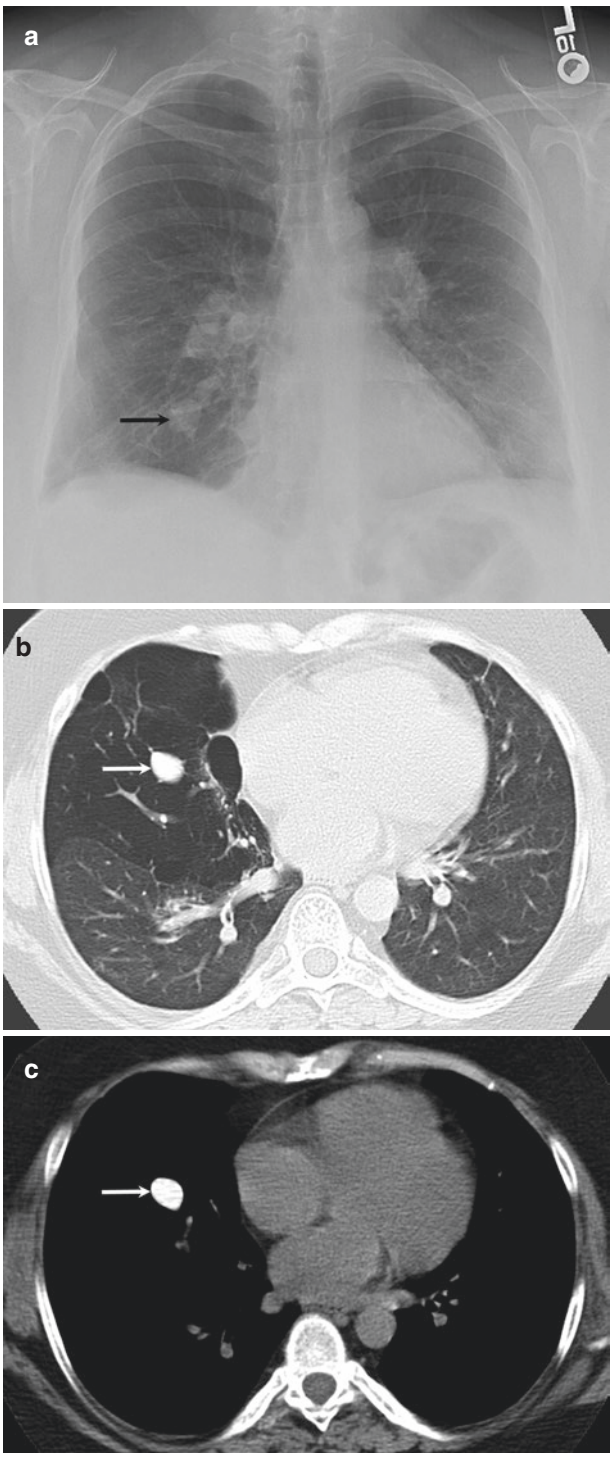

Fig. 2.9 A 56-year-old woman with congenital bronchial atresia. (**a**) Frontal radiograph shows a tubular opacity (arrow) in right lower zone. (**b**, **c**) Axial CT images reveal hyperlucent lung surrounding a calcified bronchocele (arrow)

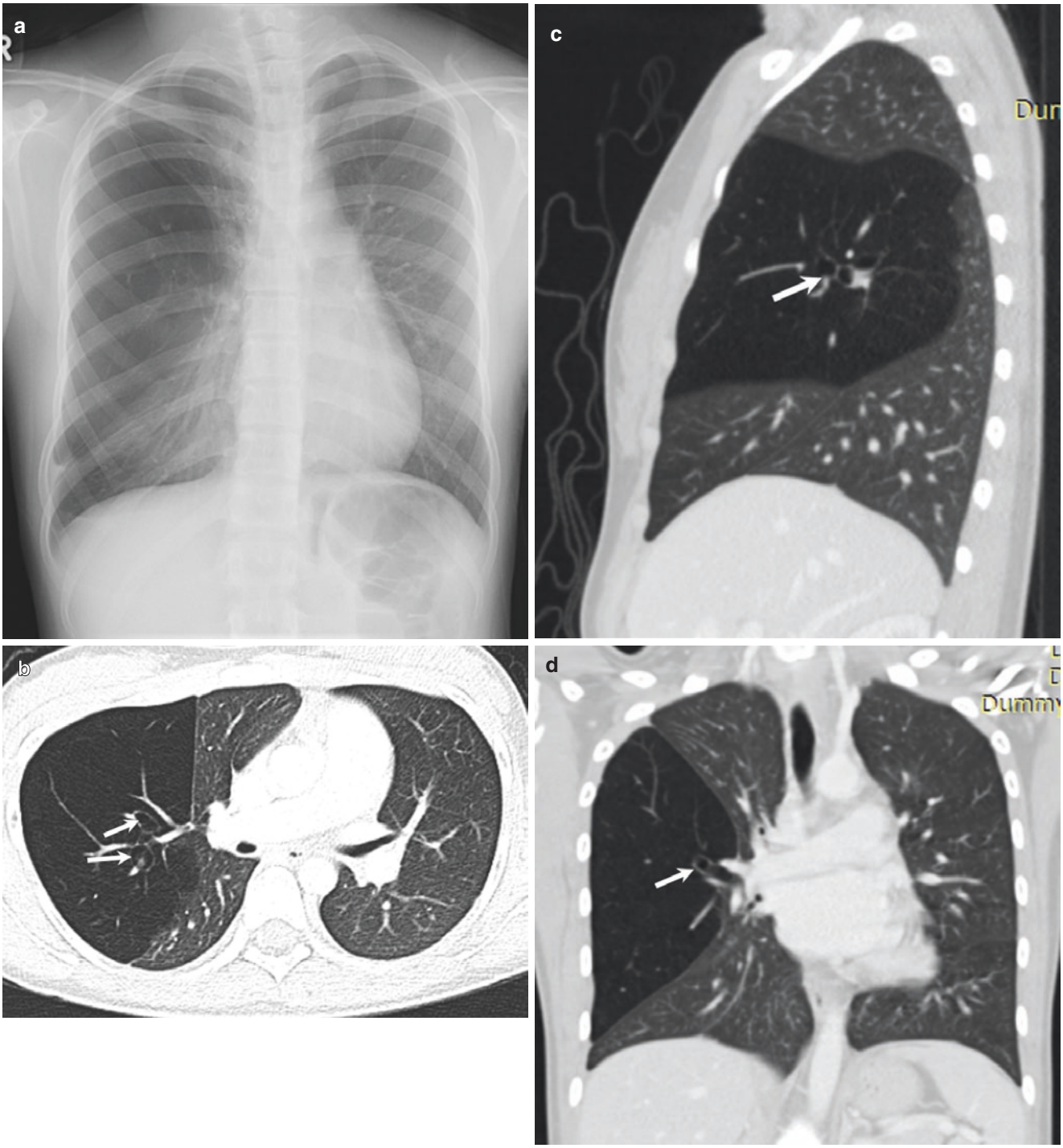

Fig. 2.10 A 23-year-old asymptomatic woman with congenital bronchial atresia. (**a**) Frontal chest radiograph shows a well-circumscribed wedge of hyperlucent lung in right mid zone. (**b**–**d**) Axial, sagittal, and coronal CT images show hyperlucent and a hyperexpanded segment of the right lung with central dilated airways (arrows) without any connection with the central tracheobronchial tree

in case of the suspected tracheobronchial tumor. The CT features of tracheobronchial tumors are nonspecific (Table 2.7) (Figs. 2.11, 2.12, 2.13, 2.14, and 2.15). Demonstration of fat or fat and calcification is diagnostic for lipoma and hamartoma, respectively [8, 9]. In other lesions, CT is useful in accurate localization of the tumor and helps in planning intervention. Squamous cell carcinoma is the most common malignancy of the trachea. Lung cancers, particularly the squamous cell cancer and small cell carcinoma, can be recognized in the early stage as an endobronchial nodule with or without atelectasis (Figs. 2.16 and 2.17).

Table 2.5 Tracheobronchial narrowing

• Tracheobronchial tumors
• Post-intubation stenosis
• Idiopathic subglottic stenosis
• Infection
• Broncholiths
• Anthracofibrosis
• Saber-sheath trachea
• Tracheobronchomalacia
• Foreign body aspiration
• Mural abnormalities

Table 2.6 Tracheobronchial tumors

Benign tumors
Hamartoma
Tracheobronchial papillomatosis
Hemangioma, leiomyoma, lipoma
Neurogenic tumor
Malignant tumors
Primary
Lung cancer
Squamous cell carcinoma
Mucoepidermoid carcinoma
Adenoid cystic carcinoma
Carcinoid
Secondary
Direct invasion
Lung, thyroid, esophagus malignancy
Endobronchial metastases
Breast and colon cancers

Table 2.7 Pearls on tracheobronchial tumors

• Perception is more important in identification of endobronchial lesion
• Radiological differentiation between benign and malignant tumor is difficult
• Malignant tumors are seen in elderly patients
• Malignant lesions are infiltrative or polypoidal or have both components
• Lymphadenopathy is a specific sign for malignant tumors
• Benign lesions usually have a dominant endobronchial component
• Endobronchial lesions may present with atelectasis
• Atelectasis limits the assessment of the exact size of the endobronchial tumor
• Isolated segmental or lobar collapse should raise alarm for endobronchial lesion
• Endobronchial lipoma is characterized by the presence of fat
• Hamartoma contains fat and frequently typical "popcorn" calcification
• Calcification can also be seen in bronchial carcinoid tumors
• Carcinoid tumors usually show enhancement
• Multiple tracheal nodules with lung cysts are seen in papillomatosis

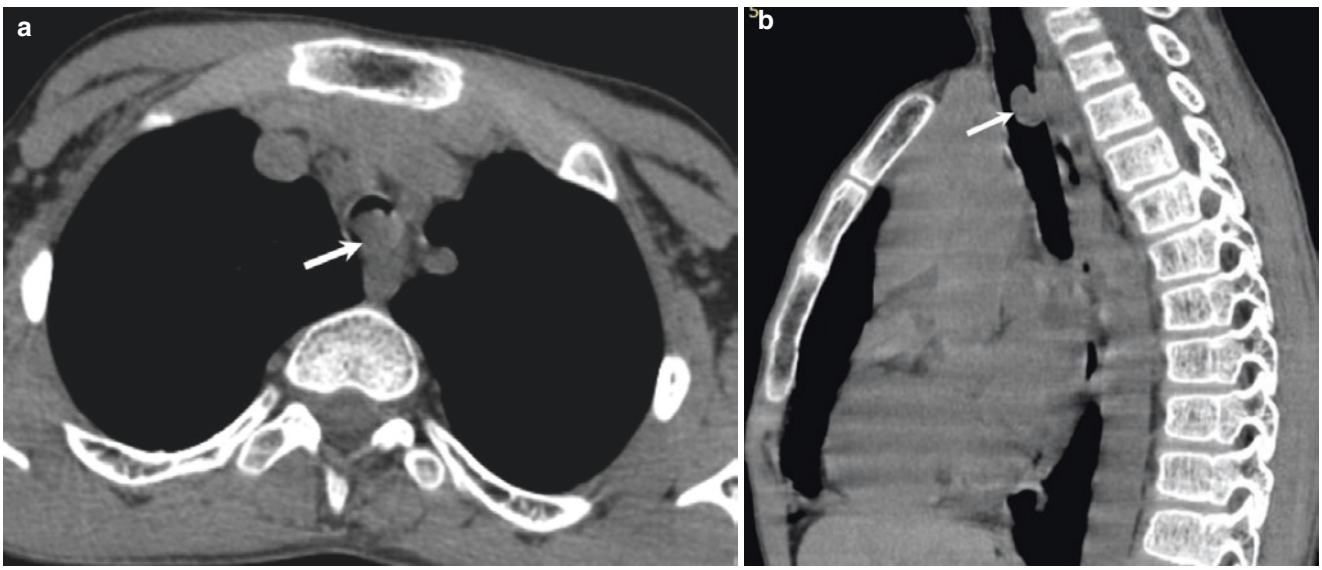

Fig. 2.11 A 71-year-old man with tracheal squamous cell carcinoma. (**a**, **b**) Axial and coronal unenhanced CT images show polypoidal soft-tissue mass arising from the posterior wall of the trachea, projecting in the lumen

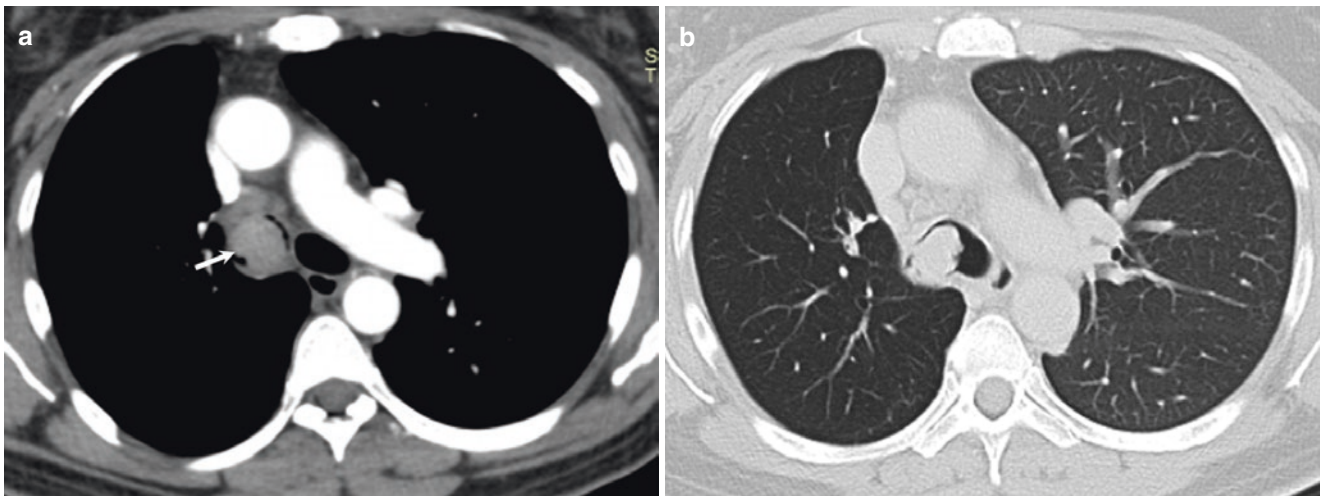

Fig. 2.12 A 49-year-old woman with endobronchial carcinoid with high vascularity and invasive features on histopathology. (**a**) Axial CTPA image shows enhancing mass (arrow) in the right main bronchus. (**b**) CT image with lung window settings shows hyperlucent right lung probably due to air trapping. Bronchoscopy biopsy was complicated by excessive bleeding and bronchospasm

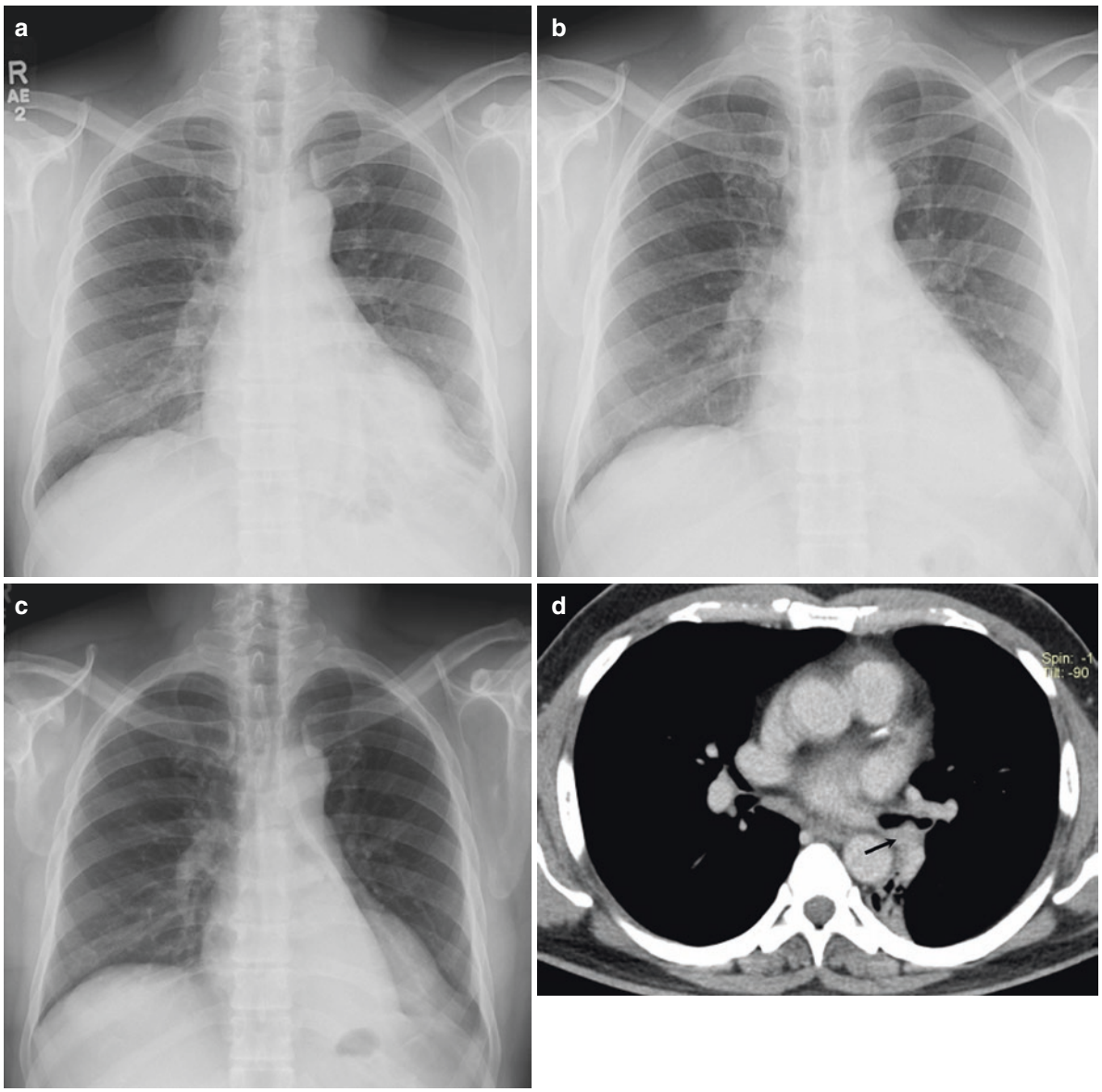

Fig. 2.13 A 50-year-old man with carcinoid tumor. (**a**) Baseline normal radiograph performed 1 year back. Progressive left lobar lobe collapse at the time of presentation (**b**) and 5 days later (**c**). (**d**) Axial CT image shows a small endobronchial nodule (arrow) with left lower lobe collapse

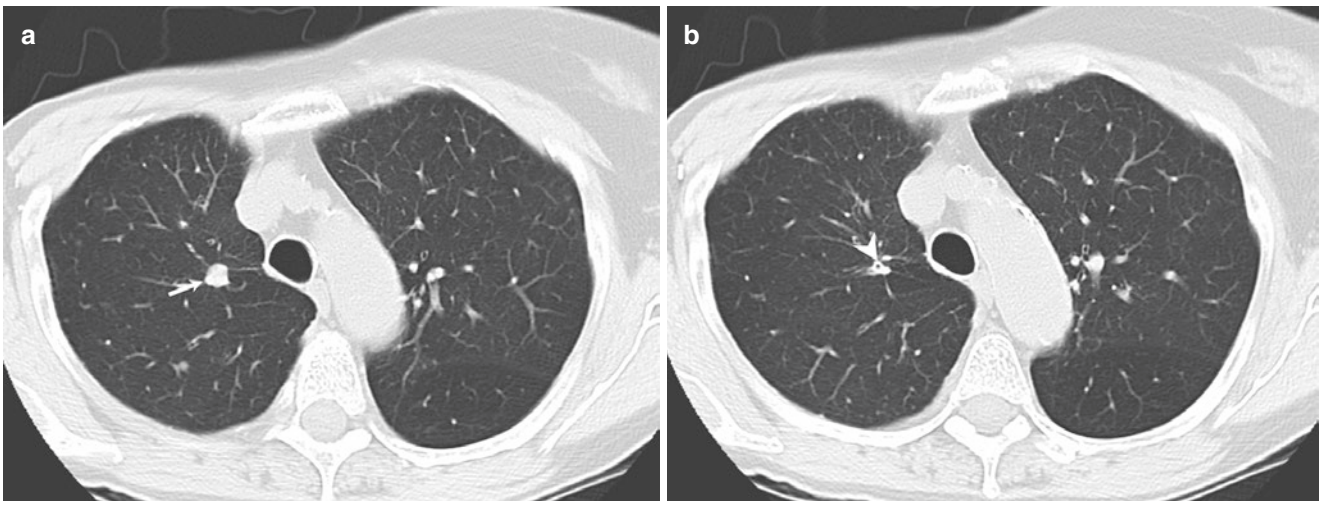

Fig. 2.14 A 61-year-old woman with endobronchial metastasis. (**a**, **b**) Axial CT images show a 7 mm nodule (arrow) in right upper lobe located in the path of a subsegmental bronchus (arrowhead). Note right mastectomy

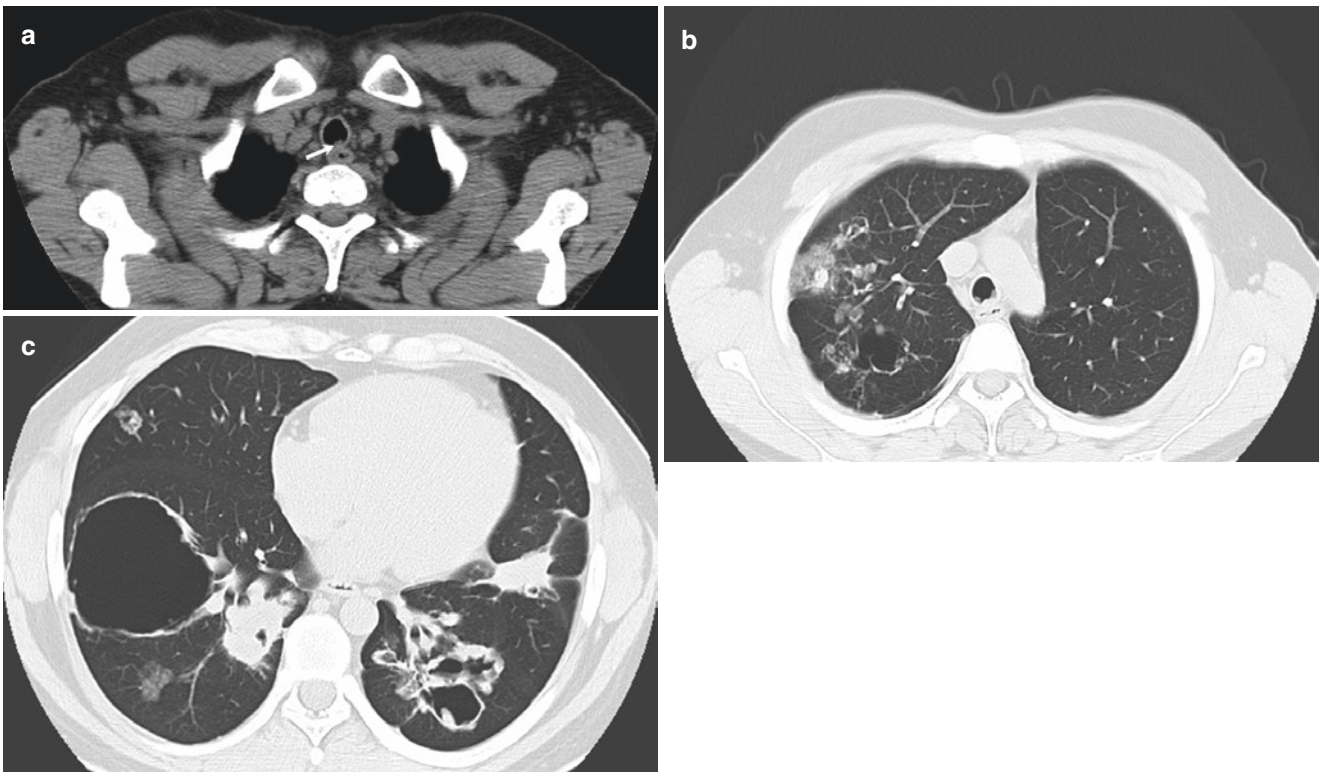

Fig. 2.15 25-year-old man with recurrent laryngeal and pulmonary papillomatosis. (**a**). Axial CT image shows small nodule (arrow) projecting in the lumen of the trachea. (**b**, **c**) Axial CT images with lung window settings show more nodules in lower trachea and cysts formation in the lungs along with areas of consolidations from infection

2.1.8.2 Post-intubation/Post-tracheostomy Stenosis

Post-intubation tracheal stenosis remains an important cause of acquired tracheal narrowing. The factors responsible for stenosis are cuff pressure, the size of the tube, duration of intubation, the age of the patient, material of the tube, and medication like steroids. Patient presents with weeks to months after extubation with symptoms of dyspnea, expectoration, and stridor from airway obstruction, often mistaken as asthma. Spirometry shows characteristic fixed extrathoracic airway obstruction. Tracheal stenosis is overlooked on chest radiograph as it's at the edge of the image. CT with

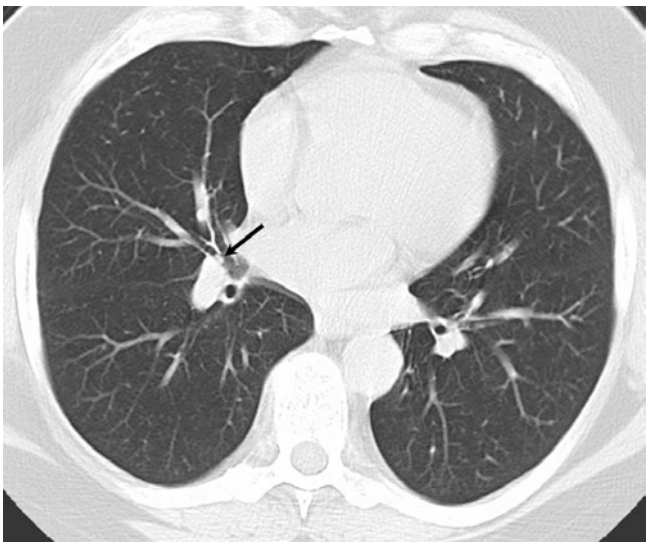

Fig. 2.16 Perception is important in CT of the endobronchial lesion. Axial CT image shows a tiny endobronchial nodule (arrow) in distal right middle lobe bronchus. Bronchoscopic biopsy showed a polyp with squamous metaplasia

coronal and sagittal reconstructions has high accuracy in assessment of location and severity of stenosis [10] (Fig. 2.18). Typical stenosis on the coronal image gives an "hour-glass" shape to trachea due to focal involvement. The length of the stenosis ranges from 0.2 to 3.5 cm. The distance of the stenotic site is 2.5–5 cm from the vocal cord. The severity of the stenosis should be measured in the sagittal and coronal plane and expressed as a percentage.

2.1.8.3 Idiopathic Subglottic Tracheal Stenosis

Idiopathic subglottic stenosis is a progressive fibroinflammatory condition that affects the lamina propria of the subglottis and upper cervical trachea [11]. This condition is almost exclusively seen in females and has been suggested as a localized presentation of granulomatosis with polyangiitis [11]. Patient, typically a middle-aged female without any history of trauma or intubation, presents with progressive shortness of breath, hoarseness, and stridor, commonly misdiagnosed as asthma. CT shows focal, concentric, or eccentric narrowing of the subglottic trachea, similar to

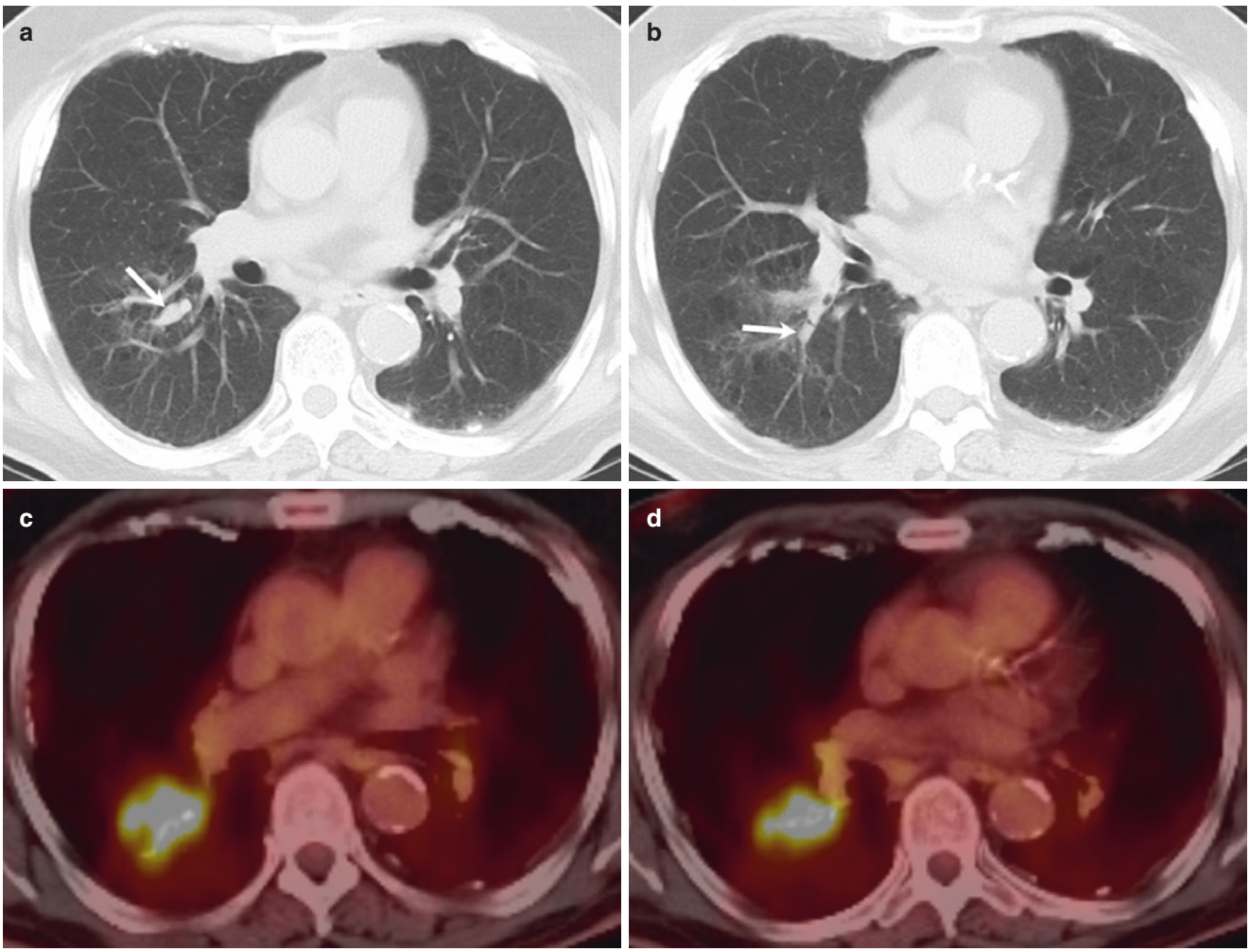

Fig. 2.17 A 69-year-old man with endobronchial squamous cell carcinoma. (**a**, **b**) Axial CT images show plugging of segmental bronchi (arrows). The plugging was persistent on yearly follow-up study, and hence PET CT (**c**, **d**) was performed that showed avid uptake in the affected bronchi. Bronchoscopic brushings revealed malignancy

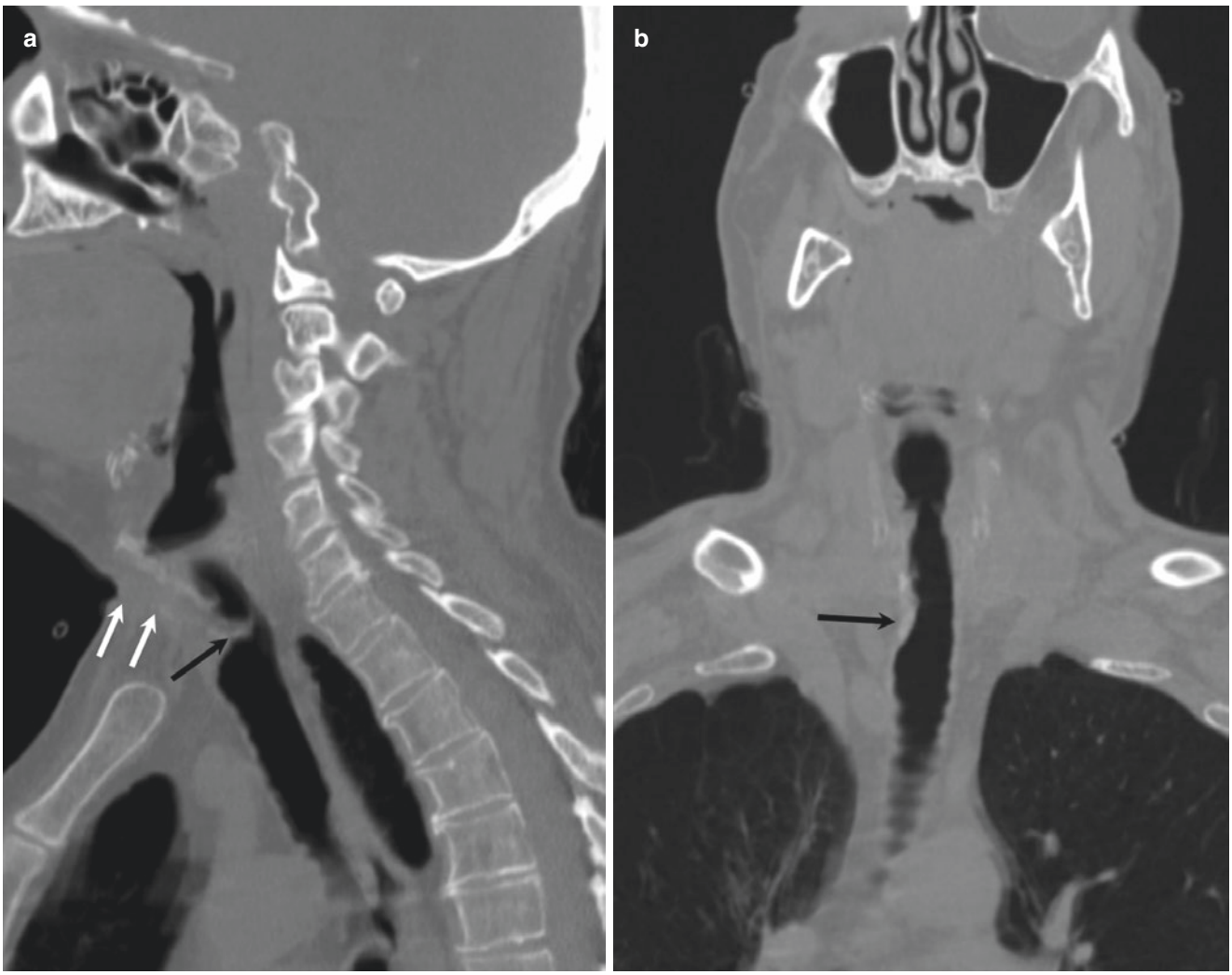

Fig. 2.18 Post-tracheostomy tracheal stenosis. (**a**) Sagittal CT image shows short segment narrowing (black arrow) in subglottic trachea caudal to internal opening of prior tracheostomy track (white arrows). (**b**) Coronal CT image also shows narrowing (black arrow)

post-intubation stenosis (Fig. 2.19). The stenotic segment is either smooth with tapered edges or irregular, lobulated, and eccentric involving a length of 2–4 cm of the subglottic trachea [12]. It's essential to evaluate the upper trachea in the first few axial CT images in every patient to avoid missing this entity in a patient with presumed asthma.

2.1.8.4 Tuberculosis (TB)

Viral and bacterial airway infections are common with imaging performed to assess the involvement of the lung parenchyma. Tuberculosis, primarily involving central tracheobronchial tree, is less common than parenchymal infection. TB of the tracheobronchial tree can result from infected sputum, nodal extension, parenchymal extension, or hematogenous route. Tracheobronchial TB can be active or fibrotic. The healing almost always is associated with some degree of narrowing of involved airways. CT shows the focal or multifocal involvement of central airways involving long segments (Figs. 2.20 and 2.21). The tracheobronchial involvement is usually contiguous, but there can be skip lesions. In active as well as fibrotic phase, there is eccentric or concentric wall thickening with a variable degree of stenosis [13]. In active disease, there can be mediastinal fat stranding representing mediastinitis. Mediastinal lymph nodes are not usually enlarged, but calcified lymph nodes are seen in the fibrotic disease.

2.1.8.5 Broncholiths

Broncholith implies calcific density within the lumen of the bronchi that may result in partial or complete obstruction. Broncholiths are usually calcified peribronchial lymph nodes eroding into bronchial lumen. These lymph nodes are almost always a sequel to prior granulomatous diseases like TB and histoplasmosis. The complications of broncholith are atelectasis, recurrent infection, bronchiectasis, and hemoptysis. CT demonstrates the broncholiths

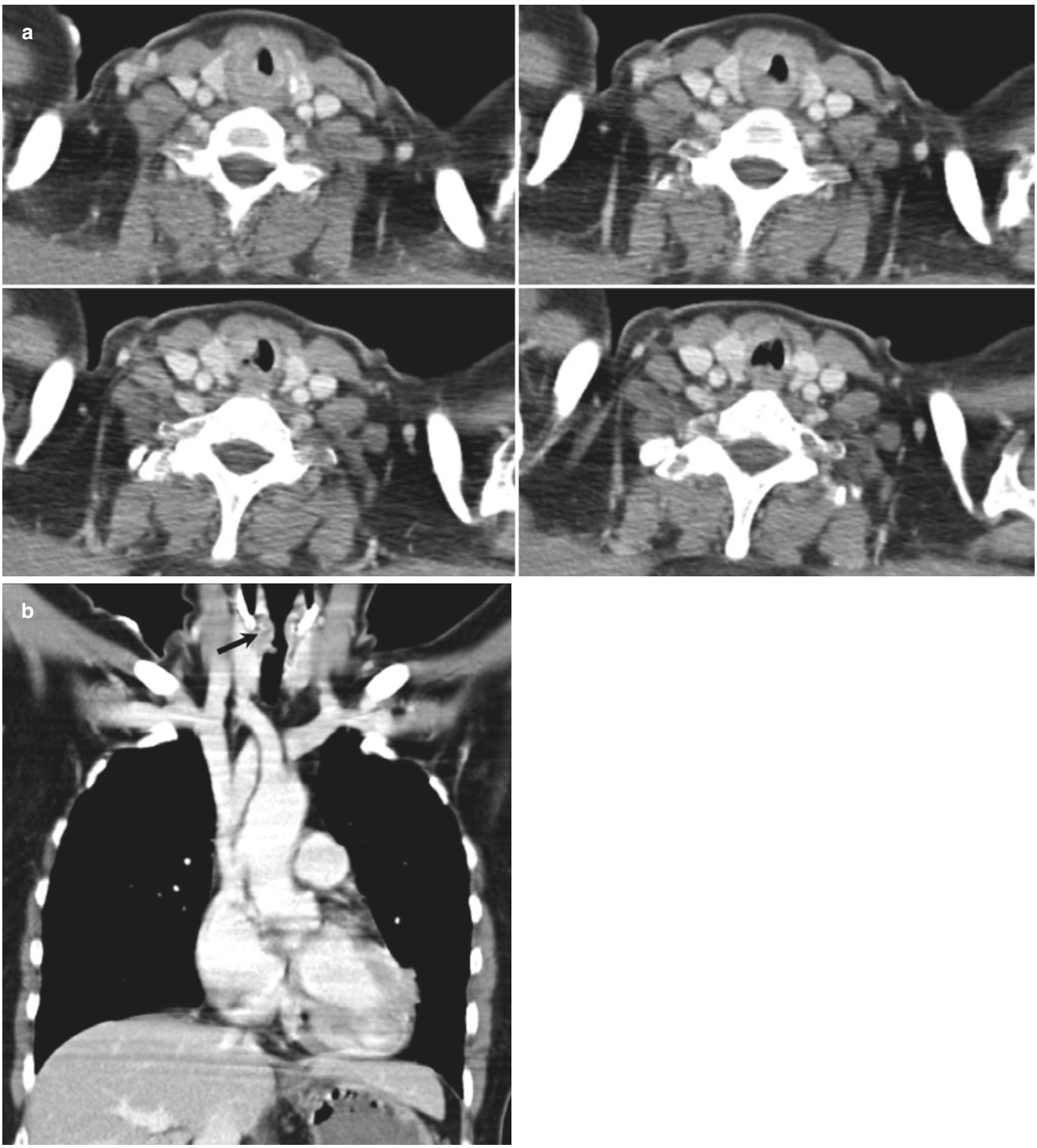

Fig. 2.19 A 51-year-old woman presenting with asthma-like symptoms. (**a**) 3 mm contiguous axial CT images of thoracic inlet show subglottic tracheal narrowing that can be easily overlooked. (**b**) Coronal CT image shows asymmetric thickening (arrow) leading to subglottic tracheal stenosis. Biopsy revealed granulation tissue

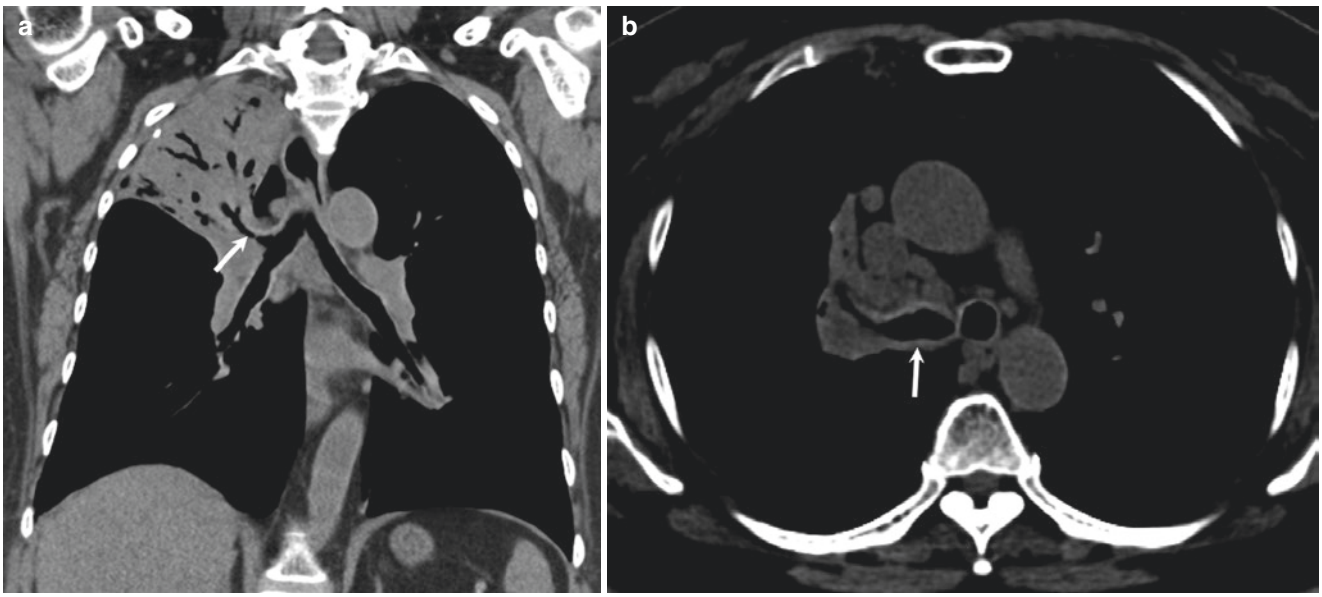

Fig. 2.20 Bronchostenosis from tuberculosis with anthracofibrosis on bronchoscopy. (**a**) Coronal unenhanced CT reconstruction shows a consolidation in right upper lobe with narrowing of right upper lobe bronchus (arrow). (**b**) Axial CT image with narrow soft-tissue window settings shows thickening of the right bronchus (arrow) with multiple mediastinal and right hilar lymph nodes

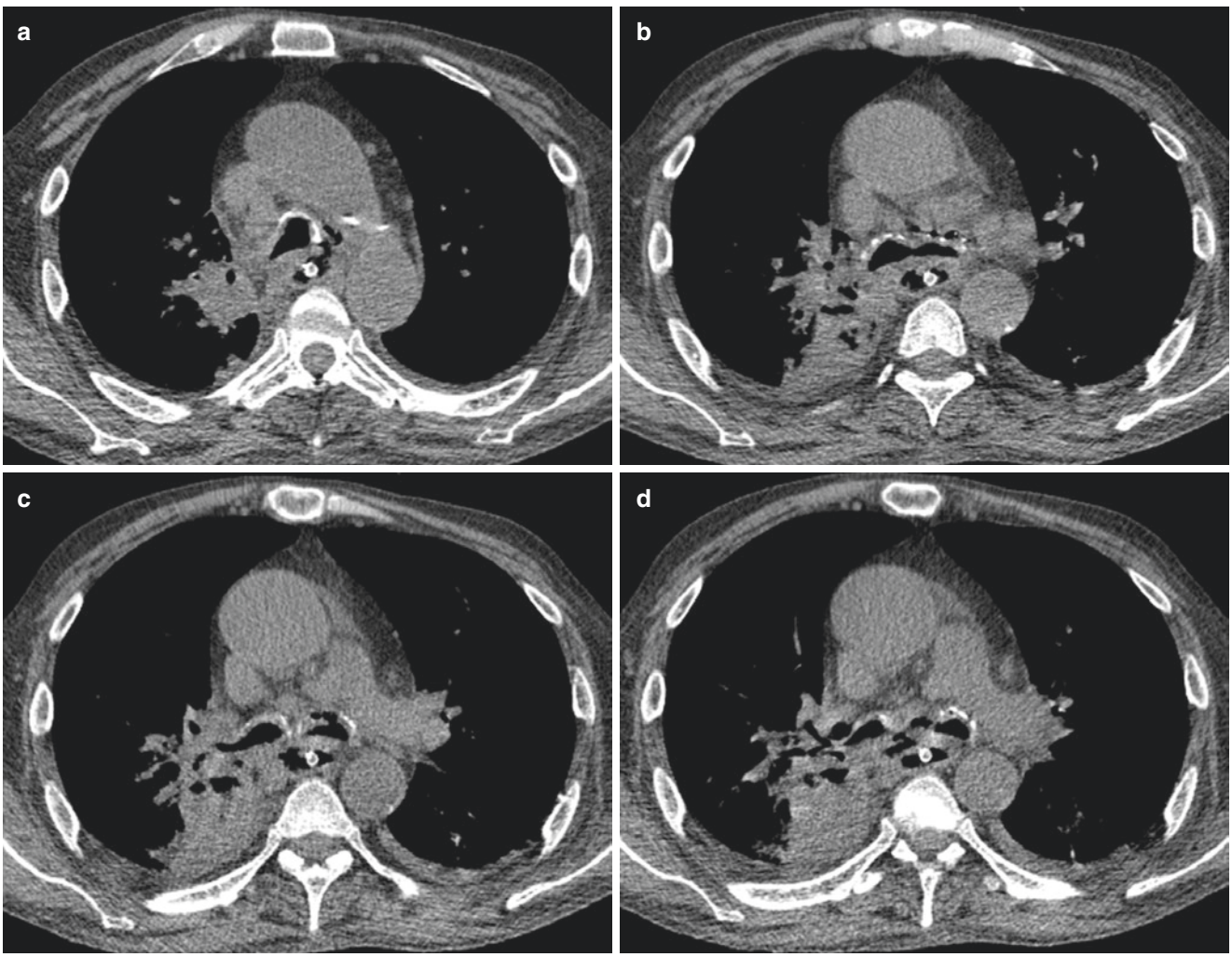

Fig. 2.21 Tracheobronchial and esophageal tuberculosis. (**a**–**d**) Axial unenhanced CT images show thickening of lower trachea and main bronchi with narrowing of these airways. There is contained pneumomediastinum and multiple tracheoesophageal fistulas (not shown)

and associated complications (Fig. 2.22). Sometimes it may be difficult to accurately localize the calcified lymph node in peribronchial or endobronchial location, especially in the presence of chronic atelectasis [14]. Nevertheless, peribronchial calcified lymph node causing extrinsic compression of bronchus has same clinical implications as a broncholith.

2.1.8.6 Anthracofibrosis

Anthracofibrosis is a rare cause of bronchostenosis that is characterized by the deposition of black (anthracotic) pigment in the affected bronchial mucosa in the absence of a history of smoking or pneumoconiosis. Anthracofibrosis is a bronchoscopy diagnosis. The typical patient is an elderly Asian woman with or without a history of tuberculosis who presents with a productive cough and dyspnea. CT demonstrates bronchostenosis and peribronchial noncalcified lymph nodes along with distal atelectasis (Fig. 2.20). TB has been implicated as a causative factor of anthracofibrosis, and it is challenging to differentiate the two entities on CT. Anthracofibrosis is multifocal, can be bilateral, and involves lobar and segmental bronchi, while TB involves central airways with contiguous spread [15].

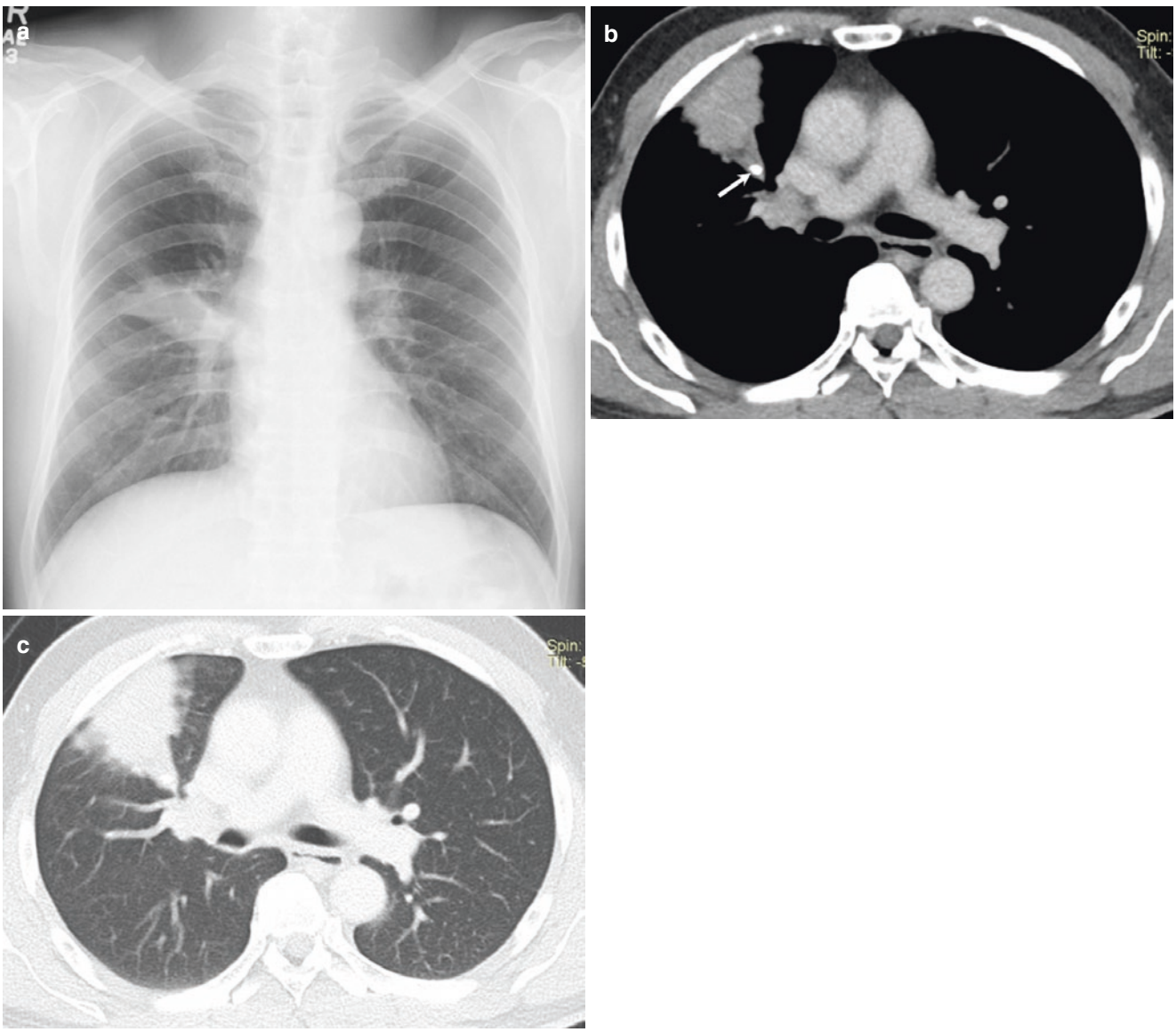

Fig. 2.22 A 56-year-old man with broncholith causing segmental collapse. (**a**) Frontal chest radiograph shows a small opacity in the right parahilar region. (**b**, **c**) Axial CT images show a segmental collapse in right upper lobe anteriorly, with a broncholith (arrow) at the tip of atelectasis. Bronchoscopy was performed to rule out any associated soft-tissue component or malignancy

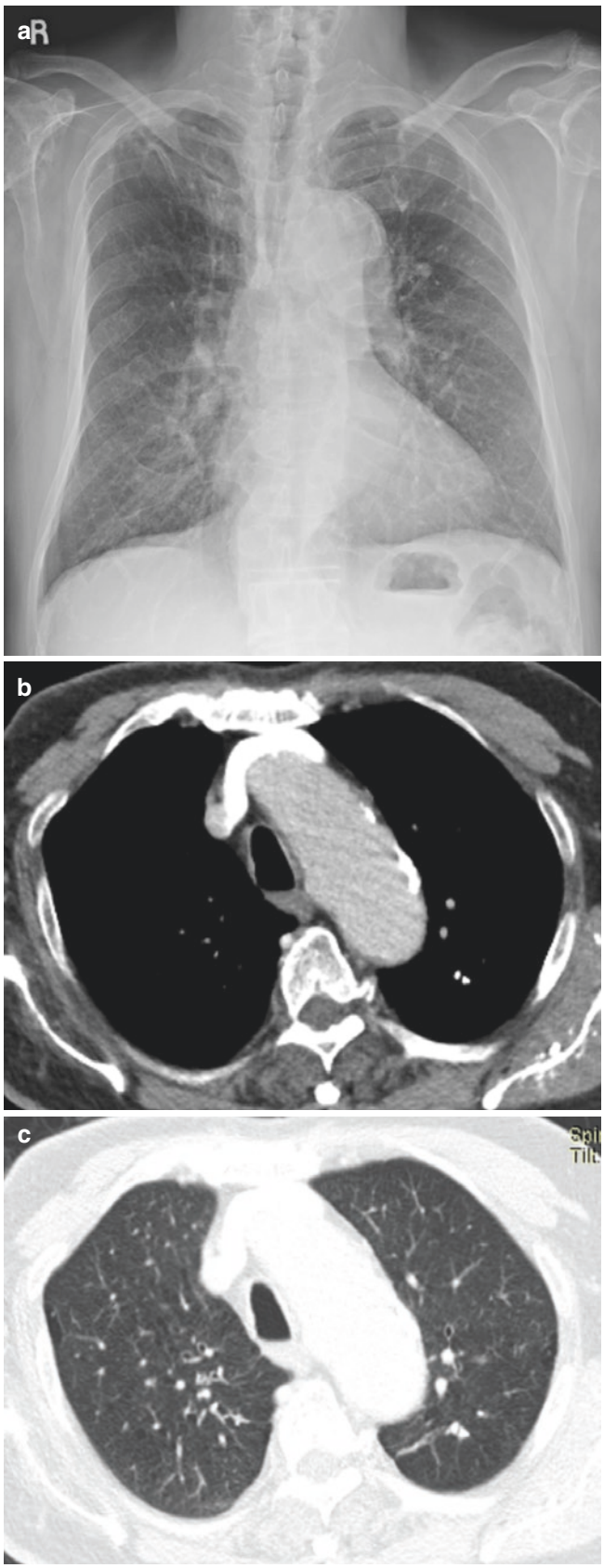

Fig. 2.23 63-year-old man with COPD. (**a**) Frontal chest radiograph shows narrowing of the thoracic trachea with thickened walls. (**b**, **c**) Axial CT images in end-inspiration show narrow trachea in the coronal plane with emphysema in the lungs. In expiratory images, the lateral tracheal walls tend to collapse further in such patients (not shown)

2.1.8.7 Saber-Sheath Trachea

The saber-sheath trachea is a fixed deformity of the intrathoracic trachea seen in elderly patients with chronic obstructive pulmonary disease (COPD). It is characterized by a coronal diameter one-half or less of the sagittal diameter, which abruptly changes to a rounded configuration at the thoracic outlet [16] (Fig. 2.23). Saber-sheath trachea has thickened lateral walls and frequently shows evidence of ossification of the cartilaginous rings. Saber-sheath trachea correlates very well with functional severity of airway obstruction.

2.1.8.8 Tracheobronchomalacia

Tracheobronchomalacia (TBM) is a condition characterized by excessive airway collapsibility, which is caused by weakness of the anterior tracheobronchial cartilage wall, as well as by increased flaccidity of the membranous portion of the central airways. Excessive dynamic airway collapse is another condition characterized by an inward bulging of posterior airway membrane during exhalation with narrowing of the tracheal lumen. TBM can be congenital or acquired from prolonged intubation, COPD, smoking, or inflammation. Symptoms are nonspecific that include cough, wheezing, and dyspnea and are often misinterpreted as asthma. Traditionally, bronchoscopy has been considered as a gold standard for evaluation of TBM with studies showing comparable results by CT [17]. A combination of inspiratory phase and dynamic expiratory phase (patient breathing out during the scan) CT images is required for the diagnosis of TBM. CT criterion for the diagnosis of TBM is ≥50% reduction in the anterior-posterior diameter or area of trachea on dynamic expiratory phase. A dynamic expiratory scan is more accurate than end-expiratory phase CT for eliciting tracheal collapse due to higher intrathoracic pressure generated in the dynamic scan [18]. "Frown sign" implies near complete collapse of the tracheal lumen with posterior membrane bowing anteriorly and paralleling the anterior wall, which is considered a specific sign of TBM. The tracheal collapse of 50% can be seen in healthy persons, and hence the cutoff of 70% has been suggested to avoid false positives [19] (Fig. 2.24). Assessing tracheal collapse by Cine CT during coughing is another maneuver that is more physiological for evaluation of TBM.

2.1.8.9 Foreign Body Aspiration

CT followed by chest radiograph is essential for preoperative localization of foreign body in the tracheobronchial tree. Identification of radiopaque foreign body is easy on CT. Radiolucent foreign bodies particularly the food material poses a diagnostic challenge. In the early presentation, CT shows an area of atelectasis while a CT performed later shows atelectasis and bronchostenosis in the area where the foreign body gets lodged (Fig. 2.25).

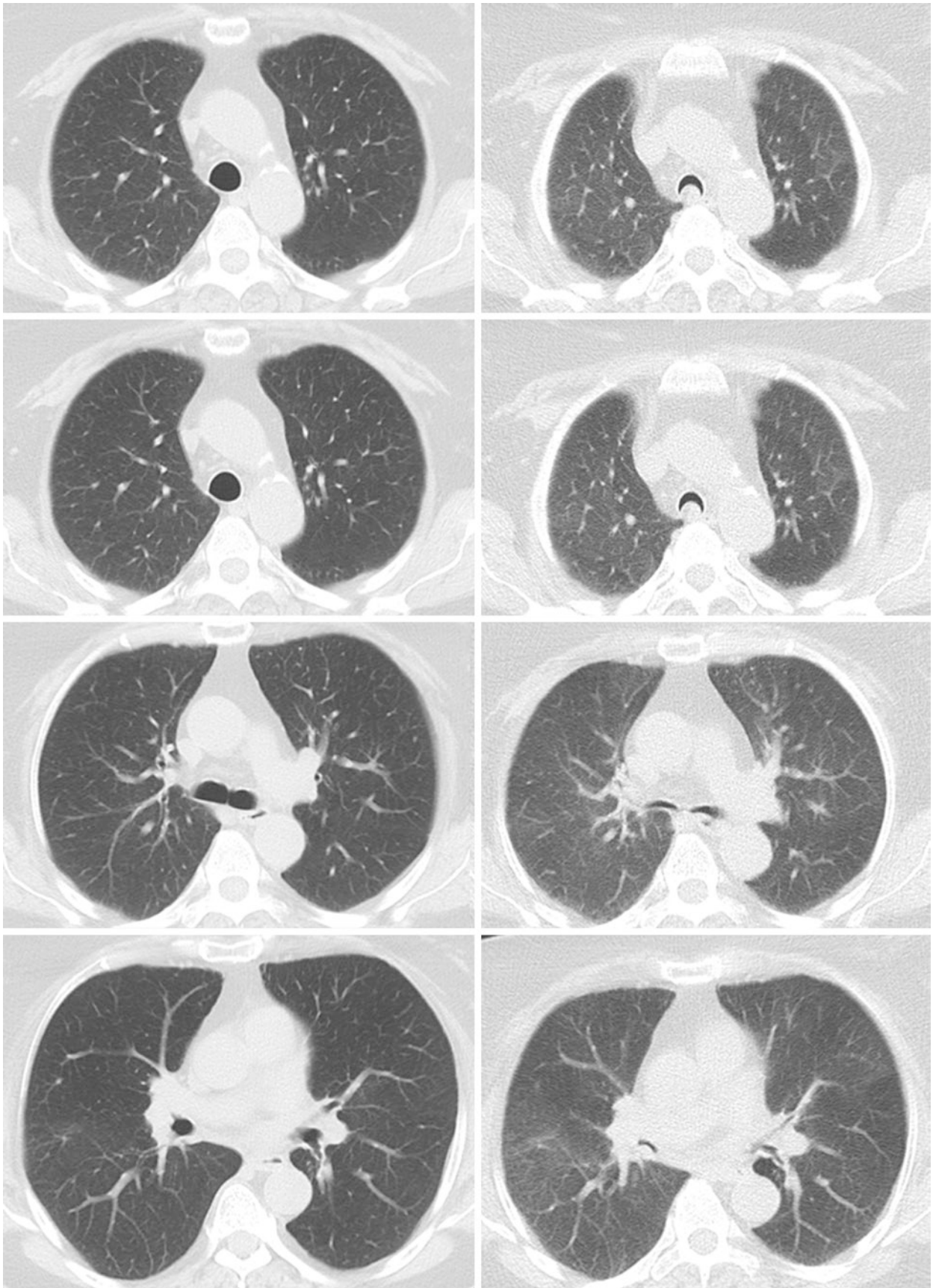

Fig. 2.24 Tracheobronchomalacia in a 49-year-old woman, who was being treated for steroid-resistant asthma. Inspiratory and expiratory phase CT images at same position show marked collapsibility of the tracheobronchial tree. Note the "Frown sign"

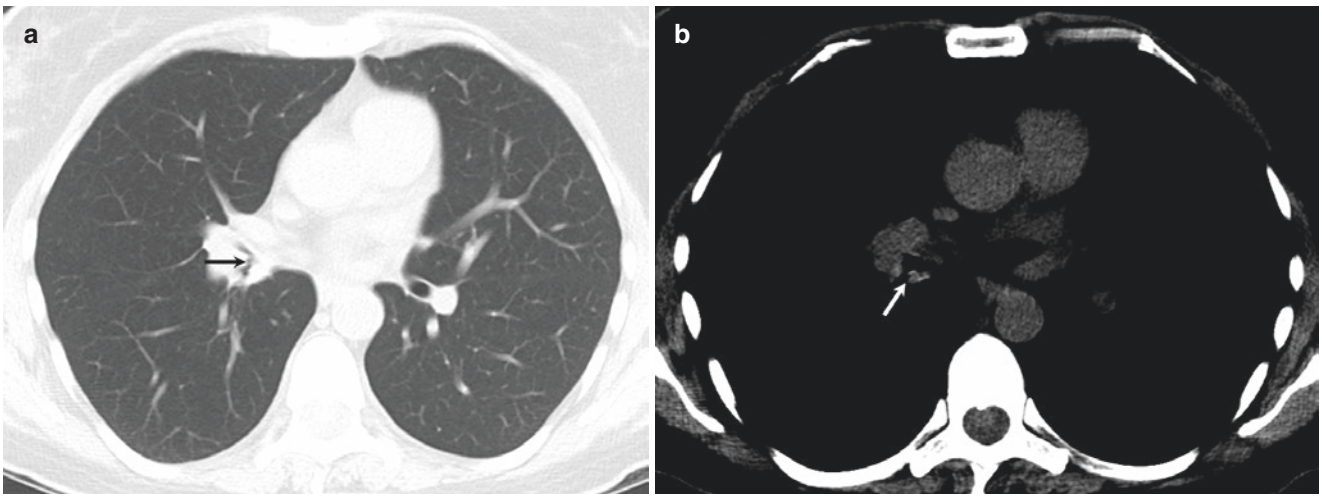

Fig. 2.25 A 79-year-old woman presenting with cough following few weeks of aspiration of iron tablets. (**a**) Axial CT image shows marked narrowing of bronchus intermedius at its bifurcation (arrow) and extending in lobar bronchi. (**b**) Axial CT image with narrow mediastinal window settings shows hyperdense walls (arrow) of involved bronchi. Bronchoscopic biopsy revealed granulation tissue in the walls

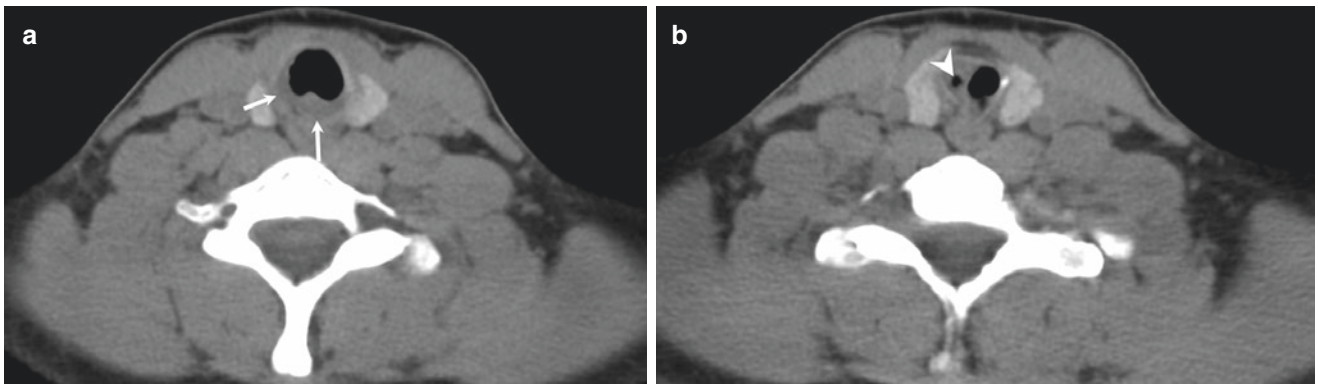

Fig. 2.26 A 21-year-old woman with widespread "granulomatosis with polyangiitis." (**a**, **b**) Axial CT images show focal semi-circumferential mucosal thickening (arrows) and ulceration (arrowhead) of the subglottic trachea

2.1.8.10 Mural Abnormalities

A large number of systemic or local diseases cause mural abnormalities in the tracheobronchial tree (Table 2.8) (Figs. 2.26, 2.27, 2.28, and 2.29). The radiological and other features of common diseases are described in Table 2.9 [20, 21]. Most of these diseases are associated with calcification of tracheobronchial tree in late stages. The differential diagnosis of tracheobronchial calcification is helpful in narrowing the diagnosis. The age-related calcification of tracheobronchial tree is smooth but can be patchy. However, unlike tracheobronchopathia osteochondroplastica (TO), there is no wall thickening, and there are no calcified nodules. Contiguous smooth calcification of anterior wall in relapsing polychondritis differs from nodular calcification of TO. Calcification in amyloidosis unlike relapsing polychondritis and TO doesn't spare the posterior membrane.

Table 2.8 Diseases causing mural changes in airways

Circumferential	Sparing posterior membrane
Granulomatosis with polyangiitis	Relapsing polychondritis
Amyloidosis	Tracheobronchopathia osteochondroplastica
Sarcoidosis	
Inflammatory bowel disease	

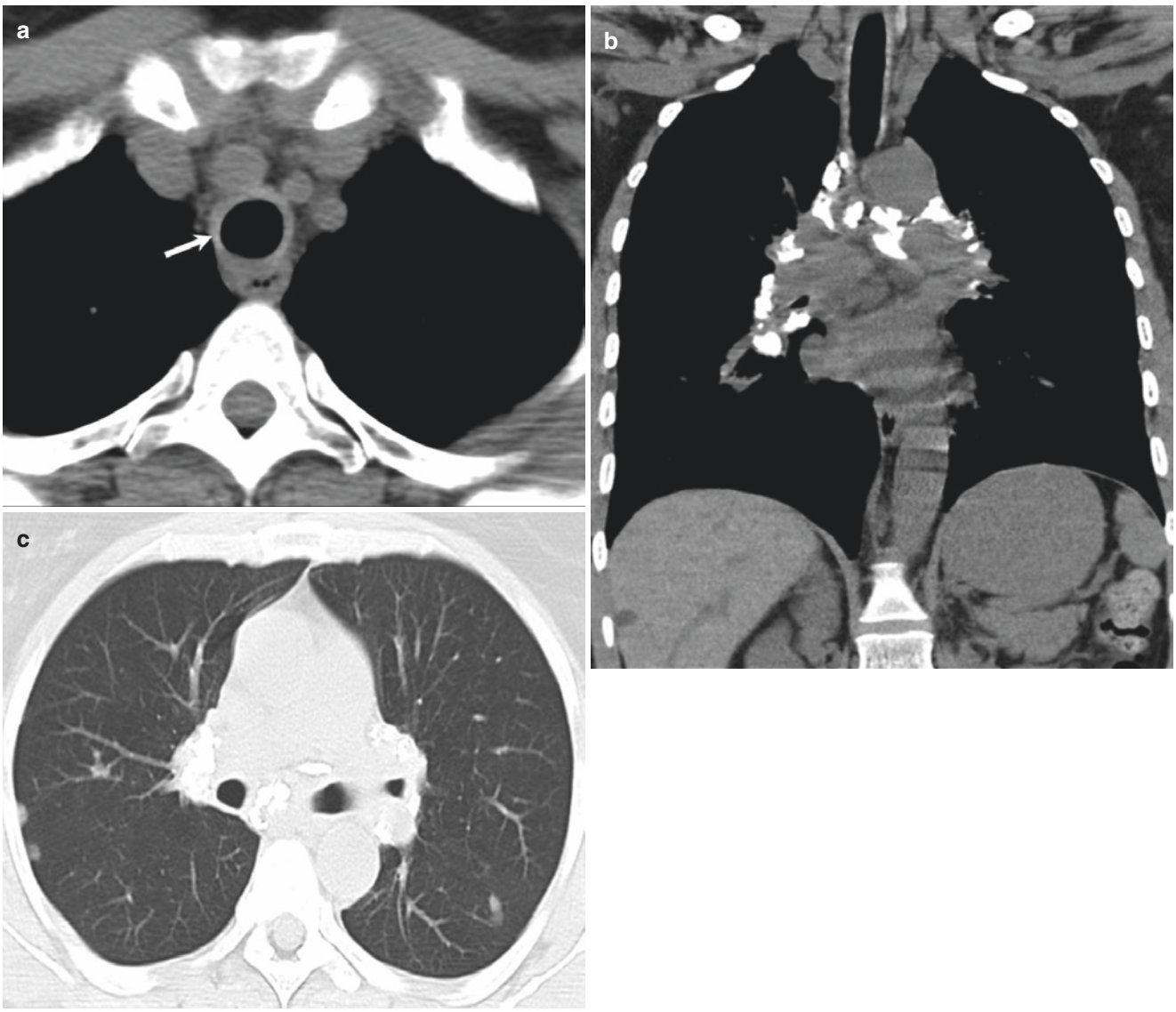

Fig. 2.27 A 58-year-old man with sarcoidosis. (**a**) Axial CT image shows circumferential thickening of the trachea. (**b**) Coronal CT image shows bulky hilar and mediastinal lymphadenopathy with calcification. (**c**) Axial CT image shows typical perilymphatic nodules of sarcoidosis

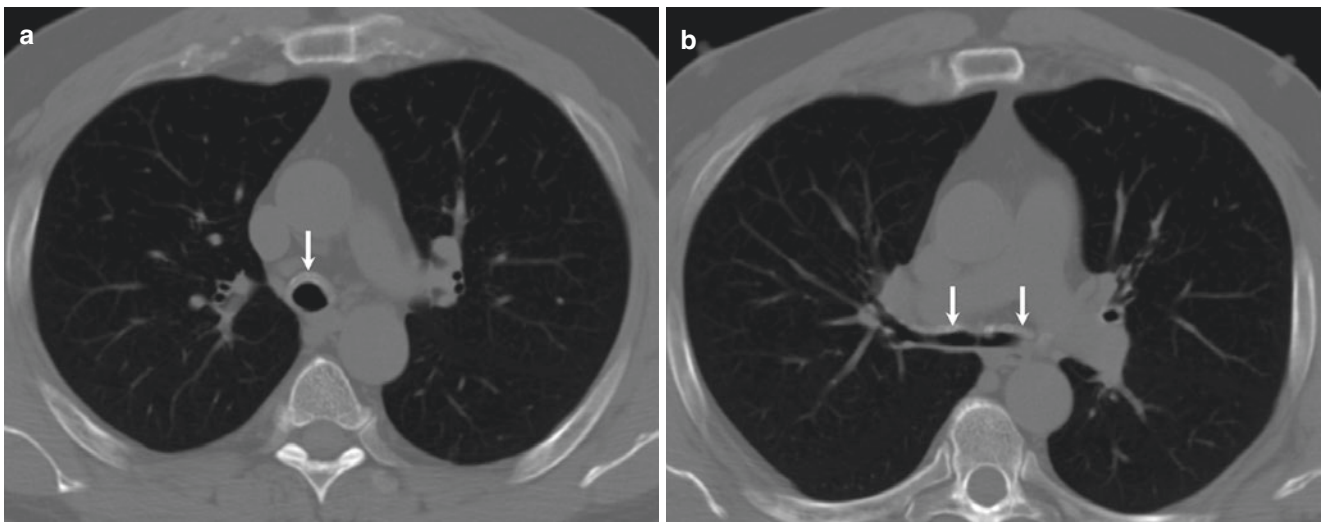

Fig. 2.28 A 55-year-old man with relapsing polychondritis. (**a**, **b**) Axial CT images show thickening and narrowing of the trachea and main bronchi with calcification involving the anterior cartilaginous portion of major airways

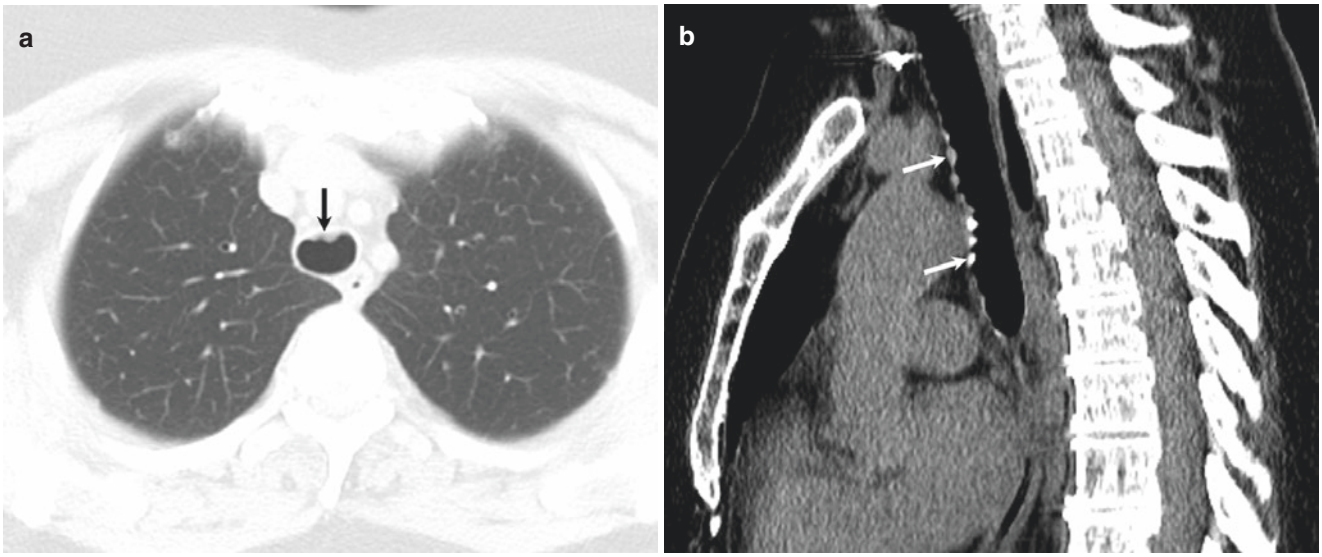

Fig. 2.29 Tracheobronchopathia osteochondroplastica. (**a**) Axial CT image shows luminal nodules (arrow) in the anterior wall of the trachea. (**b**) Sagittal CT image shows a chain of calcified and noncalcified nodules (arrows) in the anterior wall of the trachea

Table 2.9 Features of diseases causing mural changes in airways

Diseases	CT features	Other features
Granulomatosis with polyangiitis	• Focal or multifocal involvement • Nodular or smooth thickening of central airways • Mucus irregularity and ulcerations common • Subglottic trachea is commonly involved • Patchy calcification of tracheal rings • Tracheobronchomalacia • Pulmonary nodules with ground-glass halo	• Higher prevalence among young women • Systemic necrotizing granulomatous vasculitis affecting the sinuses, lungs, skin, and kidneys • Cytoplasmic antineutrophil cytoplasmic antibody (c-ANCA) and perinuclear-staining ANCA (p-ANCA) may be present
Amyloidosis	• Affects the trachea and proximal bronchi • Focal or multifocal nodules projecting in the lumen • Nodules may calcify • Involvement is circumferential (unlike TO)	• Disease of elderly patients • Younger patients with CVD (Sjogren syndrome being most common)
Sarcoidosis	• Affects the lobar and segmental bronchi more than trachea • Usually, involves long segments • Granuloma deposition lead to "beaded" appearance of bronchi • Other features of sarcoidosis: perilymphatic nodules, hilar lymphadenopathy	• Symptoms related to multiorgan involvement like the eyes, joints, lymph nodes, and skin
Inflammatory bowel disease	• Sclerosing tracheobronchitis: irregular narrowing of the trachea and main bronchi (similar to sclerosing cholangitis) • Bronchiectasis • Bronchiolitis	• History of bowel symptoms • History of colectomy for IBD
Relapsing polychondritis	• Early stage: larynx and subglottic trachea – Spares the posterior membrane • Late stage: lower trachea and bronchi – Involves posterior membrane • Diffuse wall thickening • No calcified nodules (unlike TO) • Increased attenuation of walls • Long stenosis • Tracheobronchomalacia	• An autoimmune disease characterized by destruction of cartilage • Usually, presents in fourth to fifth decade • Episodic involvement of cartilages of the ear (auricular chondritis), nose (nasal chondritis), and joints (non-erosive seronegative polyarthritis)
Tracheobronchopathia osteochondroplastica	• Typically affects distal two-third of trachea and proximal bronchi • Typically spares posterior membrane • Thickened cartilage with calcified and noncalcified (osteochondral) nodules projecting in the lumen	• Rare disease limited to airways • Most patients are asymptomatic • Minimal progression

2.2 Bronchiectasis

Bronchiectasis is defined as irreversible dilatation of bronchi and can be related to many causes (Table. 2.10). Morphologically, bronchiectasis can be described as cylindrical, varicose, or cystic variety. Traction bronchiectasis is a term used to describe bronchial dilatation in context of interstitial lung diseases. It is secondary to fibrosis in the adjacent interstitium, rather than due to an intrinsic abnormality of bronchi, and can be partly reversible. A chest radiograph is relatively insensitive for detecting mild to moderate bronchiectasis. In moderate and severe bronchiectasis, the radiograph shows "tram-track" parallel densities and ring shadows (Figs. 2.30 and 2.31). Historically, bronchography was considered as a gold standard for diagnosing earliest bronchiectasis. Multiplanar CT is now the standard investigation for diagnosing bronchiectasis. Thin contiguous CT slices (1–3 mm) from the volumetric acquisition are more sensitive than the traditional HRCT that skips a substantial portion of the lung [22, 23]. The CT signs of bronchiectasis are described in Table 2.11 [24, 25] (Figs. 2.30, 2.31, and 2.32).

Bronchiectasis is a finding on CT thorax and not a diagnosis. It is important to search for etiology of bronchiectasis. Bronchiectasis can be focal, multifocal, unilateral, bilaterally asymmetrical, or bilaterally symmetrical. Another useful way of describing the bronchiectasis is central (affecting the lobar and proximal central bronchi in the inner two-thirds of the chest) or peripheral (affecting distal airways). The constellation of findings on CT can help in suggesting a possible cause of bronchiectasis (Table 2.12). The disease-causing bronchiectasis can be recognized by their clinical and radiological features described in Table 2.13 [26–33] (Figs. 2.33, 2.34, 2.35, 2.36, 2.37, 2.38, 2.39, and 2.40).

Table 2.10 Common conditions with bronchiectasis

Post-infection
Recurrent aspiration and inhalation
Allergic bronchopulmonary mycosis (ABPM)
Smoking
Common variable immunodeficiency syndrome (CVID)
Sarcoidosis
Cystic fibrosis
Collagen vascular diseases
Inflammatory bowel disease
Miscellaneous
HIV-associated, radiation-induced, alpha-1 antitrypsin deficiency, Young syndrome, yellow nail syndrome

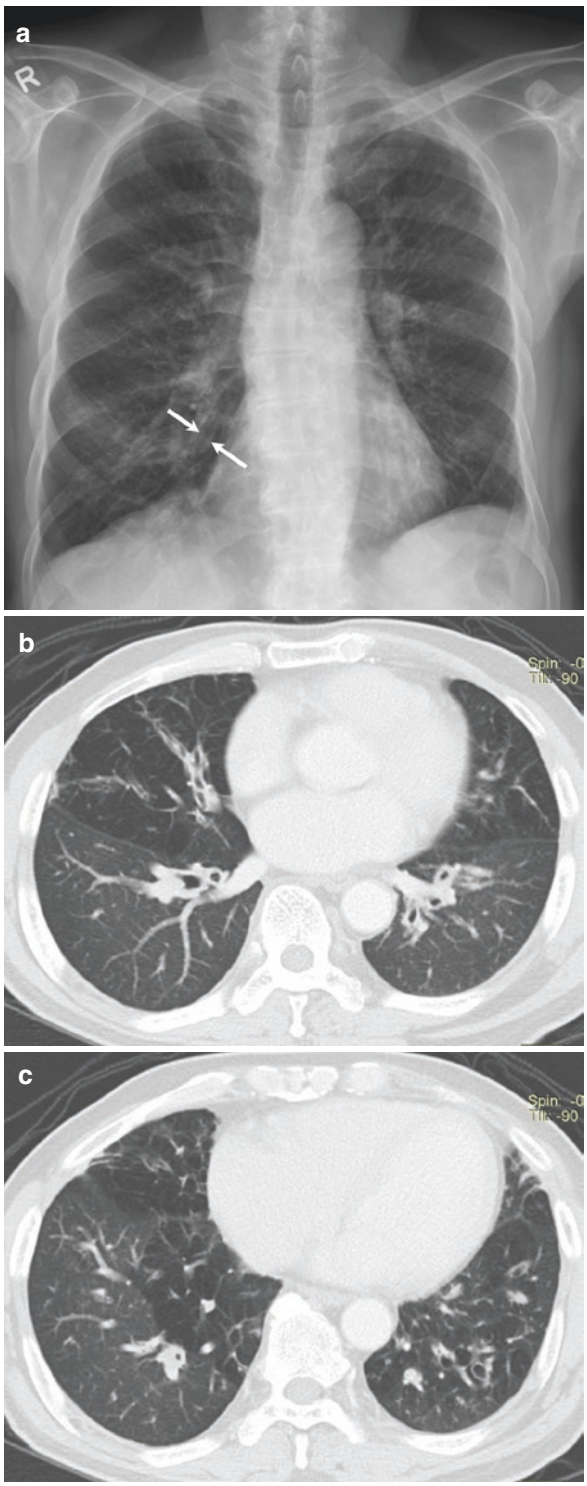

Fig. 2.30 A 59-year-old man with bronchiectasis in lower lungs. (**a**) Frontal chest radiograph shows linear streaky densities in right lower zone with "tram-track" appearance (arrows). (**b**, **c**) Axial CT images show bronchiectasis, bronchial wall thickening, and mucus plugging in bilateral lower lungs

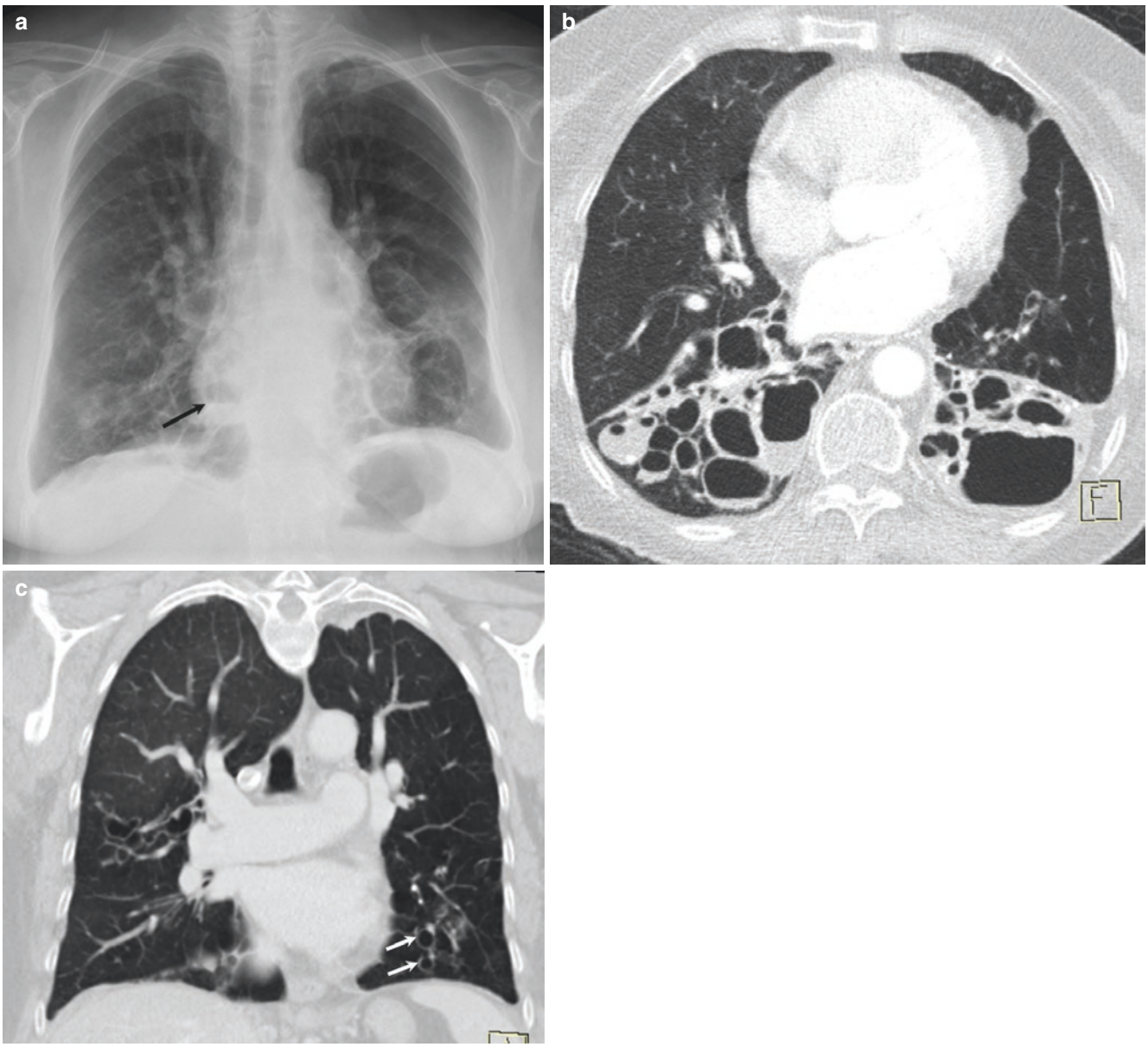

Fig. 2.31 A 75-year-old woman with cystic bronchiectasis. (**a**) Frontal chest radiograph shows multiple cystic spaces in lower lungs with few demonstrating air-fluid levels (arrow). (**b**) Axial and coronal CT images show cystic bronchiectasis with air-fluid levels in most of them. (**c**) Coronal CT image shows "signet ring" sign in the left lower lung (arrows)

Table 2.11 HRCT signs of bronchiectasis

Primary signs • Lack of progressive tapering of bronchi (earliest sign) • Bronchiole diameter more than accompanying artery ("signet ring" sign) • Identification of bronchi within 1 cm of pleura abutting the chest wall or mediastinal pleural surface
Secondary signs • Bronchial wall thickening • Mucus plugging • Small airways disease (centrilobular nodules, tree-in-bud opacities, mosaic attenuation) • Subsegmental atelectasis

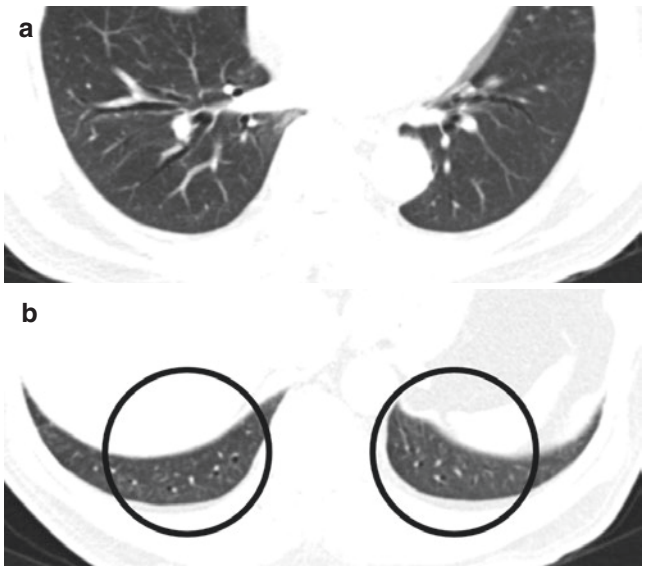

Fig. 2.32 CT signs of early bronchiectasis. (**a**) Lack of tapering of segmental bronchi in lower lobes and bronchial diameter more than accompanying pulmonary artery. (**b**) Bronchioles identification close to the pleural surface

Table 2.12 Clues for etiology of bronchiectasis

Central bronchiectasis	Allergic bronchopulmonary mycosis, asthma
Focal bronchiectasis	Congenital bronchial atresia, post-obstructive bronchiectasis, infective or post-infective, Swyer-James syndrome
Multifocal but asymmetric	Post-infective
Bronchiectasis communicating with the cavity Bronchiectasis with tree-in-bud opacities	Tuberculosis
Preferential involvement of RML and lingula	Nontuberculous mycobacterial disease
Asymmetric bronchiectasis in dependent lung Posterior segments of upper lobe Posterior and superior segments of lower lobe	Aspiration/recurrent aspiration
Upper lung bronchiectasis	Cystic fibrosis, sarcoidosis, tuberculosis
Beaded dilated bronchial wall	Sarcoidosis
Situs inversus	Kartagener's syndrome
Panlobular emphysema, cirrhosis	Alpha-1 antitrypsin deficiency

Table 2.13 Causes of bronchiectasis

Infective or post-infective	• History of chest infection that could be in childhood • Bronchiectasis is focal, multifocal, and if bilateral usually asymmetrical • Bronchiectasis is cystic or cylindrical or both • TB: dilated airways communicating with cyst/cavity • NTM: bronchiectasis with mucus plugging with preferential involvement of RML and lingula
Recurrent aspiration	• Predisposition factors for aspiration present • Dilated esophagus may be present • Multifocal bronchial dilatation usually in posterior segments • Features of proliferative bronchiolitis are frequently present • Atelectasis or consolidation may be present
ABPM	• Usually asthmatic • Blood eosinophilia • Immediate cutaneous reactivity to *Aspergillus* species • Elevated total serum IgE • Elevated serum IgE-A fumigatus and/or serum IgG-A fumigatus • Central bronchiectasis • High-attenuation mucus plugs in dilated bronchi • Tree-in-bud opacities
CVID	• Most frequent primary immunodeficiency syndrome in adults • Mild multifocal bronchiectasis • Mid and lower zone involvement • Features of proliferative bronchiolitis are common • Small patchy ground-glass opacities are frequent • Mediastinal lymphadenopathy
Kartagener's syndrome	• Classical triad of sinusitis, situs inversus, and bronchiectasis due to primary ciliary dyskinesia • Usually affects lower zone • Features of proliferative bronchiolitis are frequently present • Linear bands or scars from prior infections
CVD	• Usually seen in rheumatoid arthritis and Sjogren syndrome • Mild to advanced bronchiectasis usually in the lower lungs • Features of bronchiolitis are present in many cases
Inflammatory bowel disease	• History of ulcerative colitis or Crohn's disease present • Bronchiectasis more common than small airways disease • Symptoms of airways disease more frequent after colectomy
Cystic fibrosis	• Upper and mid lung involvement • Cylindrical bronchiectasis that progress to varicose and cystic type • Features of proliferative bronchiolitis are present
Alpha-1 antitrypsin deficiency	• Cystic bronchiectasis is more frequent than cylindrical • Multilobar bronchiectasis • Prevalence of the lower lung predominant panlobular emphysema depending upon the phenotype

TB tuberculosis, *NTM* nontuberculous mycobacterial disease, *ABPM* allergic bronchopulmonary mycosis, *CVID* common variable immunodeficiency syndrome, *CVD* collagen vascular disease

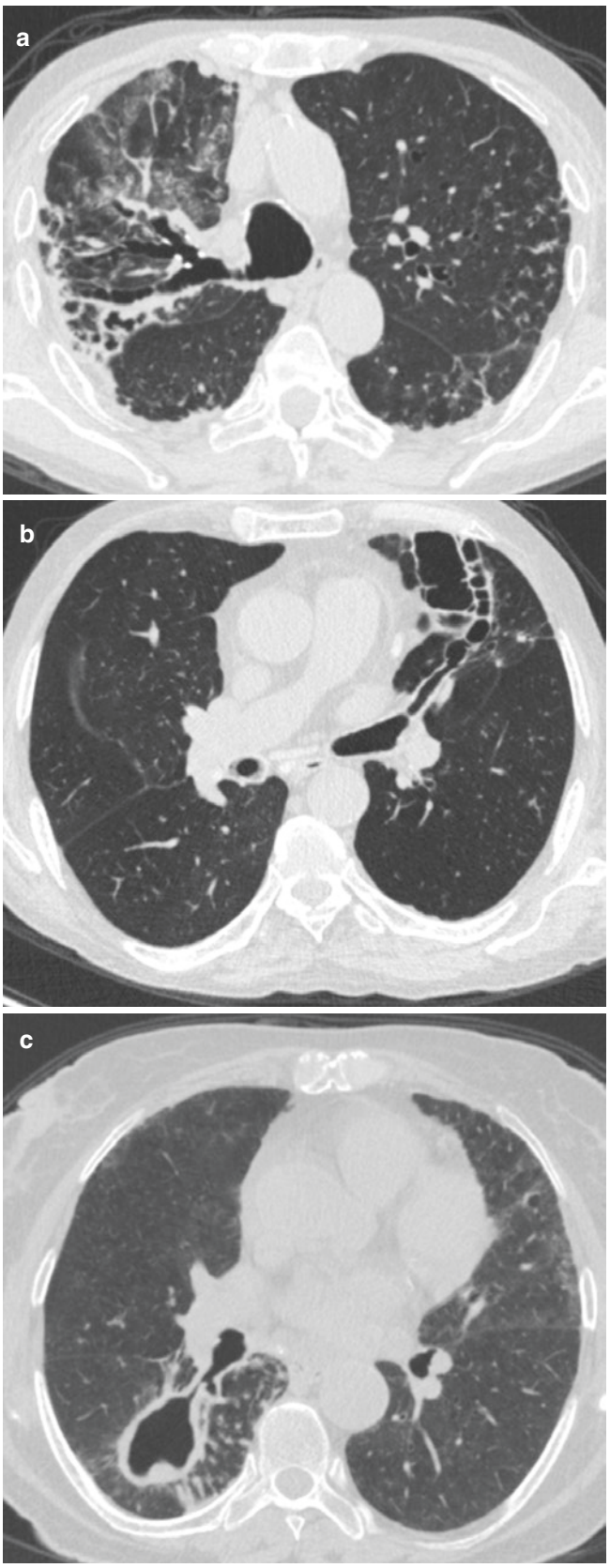

Fig. 2.33 (**a**–**c**) Focal infective/post-infective bronchiectasis in three different patients from tuberculosis. There is a cavity in the third patient, communicating with dilated airway, a characteristic feature of tuberculosis

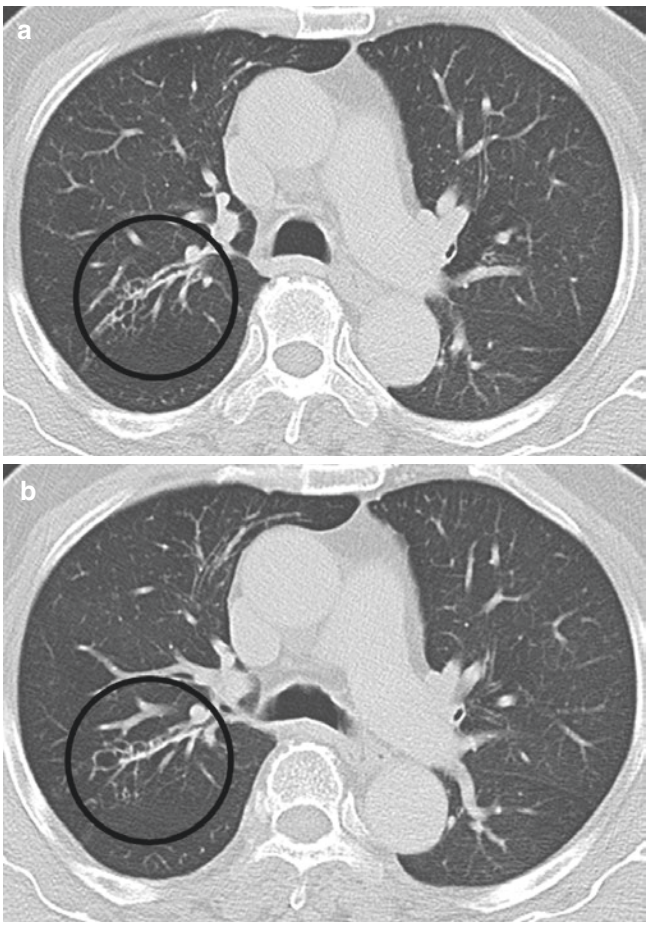

Fig. 2.34 Focal bronchiectasis in this patient with nasopharyngeal carcinoma, probably related to recurrent aspiration. (**a**, **b**) Axial CT image shows focal bronchiectasis in the posterior segment of the right upper lobe. Note early bronchiectasis in the anterior segment of the right upper lobe

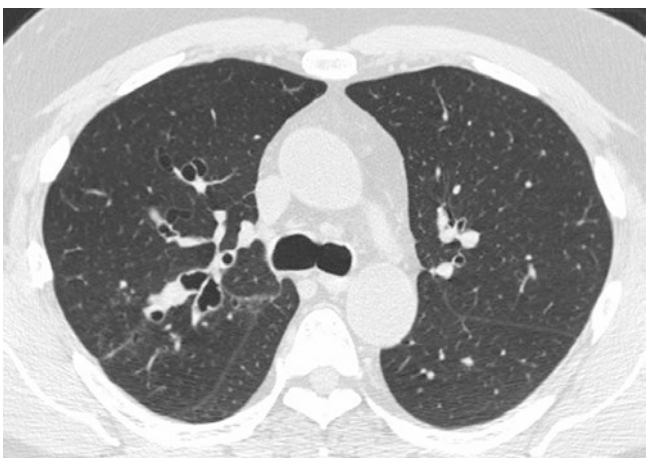

Fig. 2.35 Central focal bronchiectasis with mucus plugging in allergic bronchopulmonary pulmonary mycosis. Note diffuse centrilobular nodularity

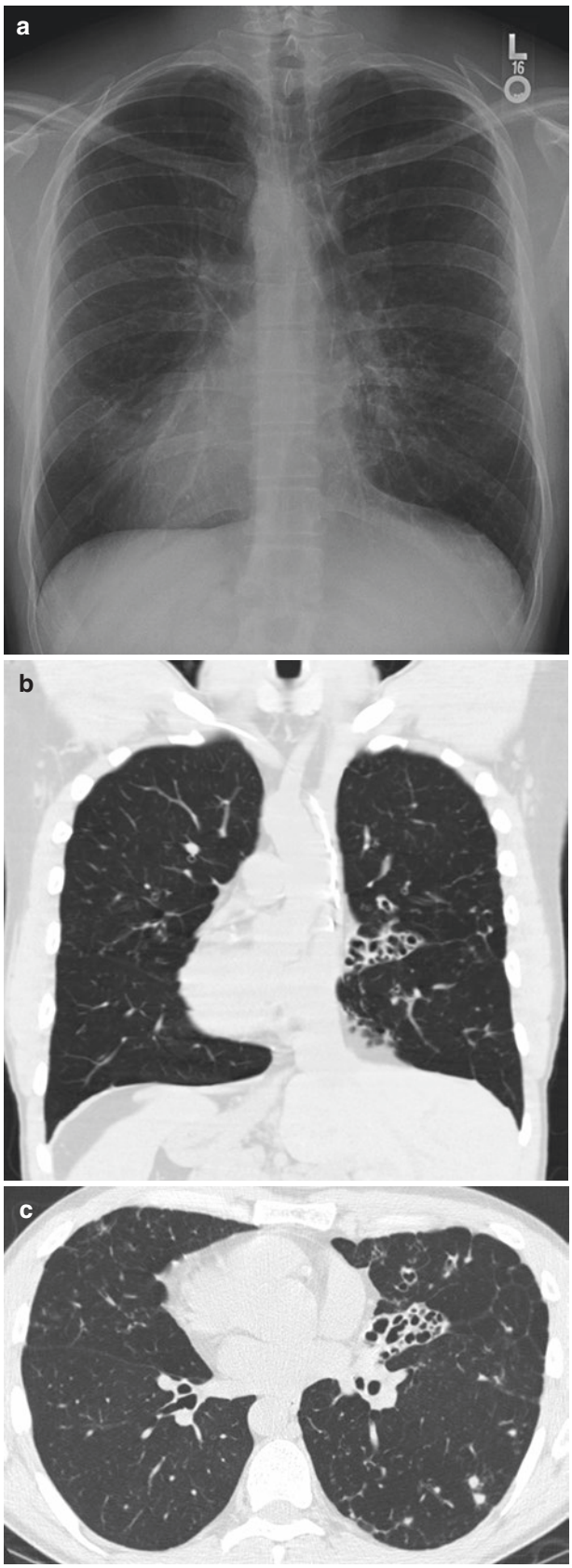

Fig. 2.36 Kartagener's syndrome. (**a**) Frontal chest radiograph shows situs inversus and bronchiectatic changes in the left parahilar lung. (**b**, **c**) Coronal and axial CT images confirm the radiographic findings

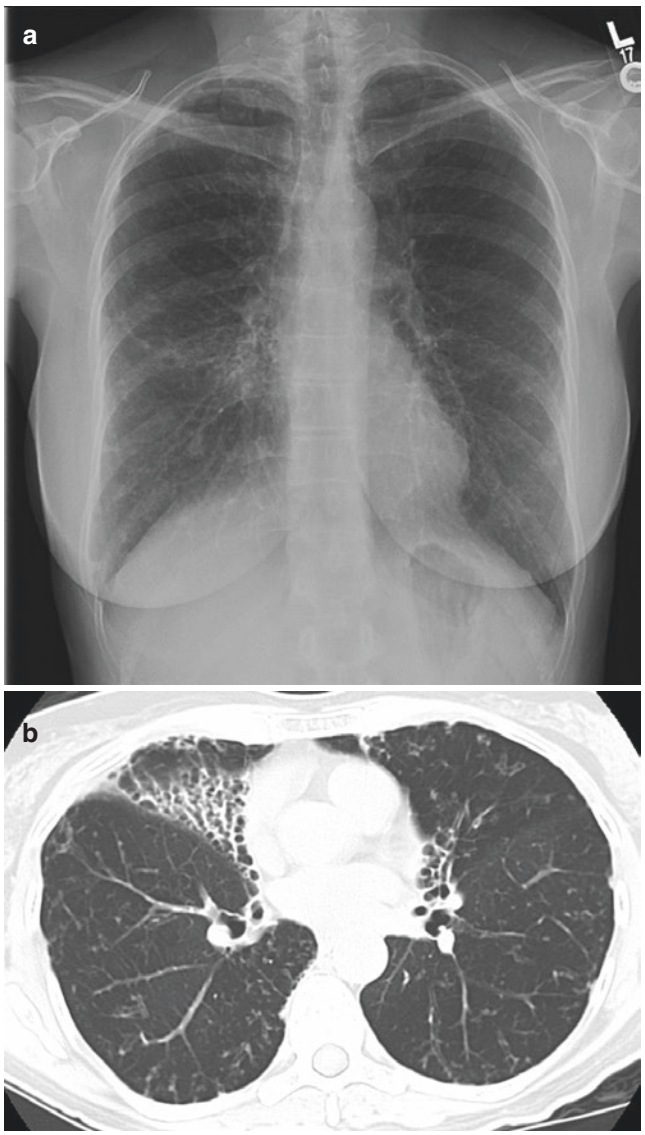

Fig. 2.37 A 55-year-old woman with nontuberculous mycobacterial disease. (**a**) Frontal chest radiograph shows bronchiectasis in the bilateral parahilar lung. (**b**) Axial CT image shows focal bronchiectasis with volume loss, predominantly involving right middle lobe and lingula. Note there is mild bronchiectasis in lower lobes with mucus plugging (proliferative bronchiolitis)

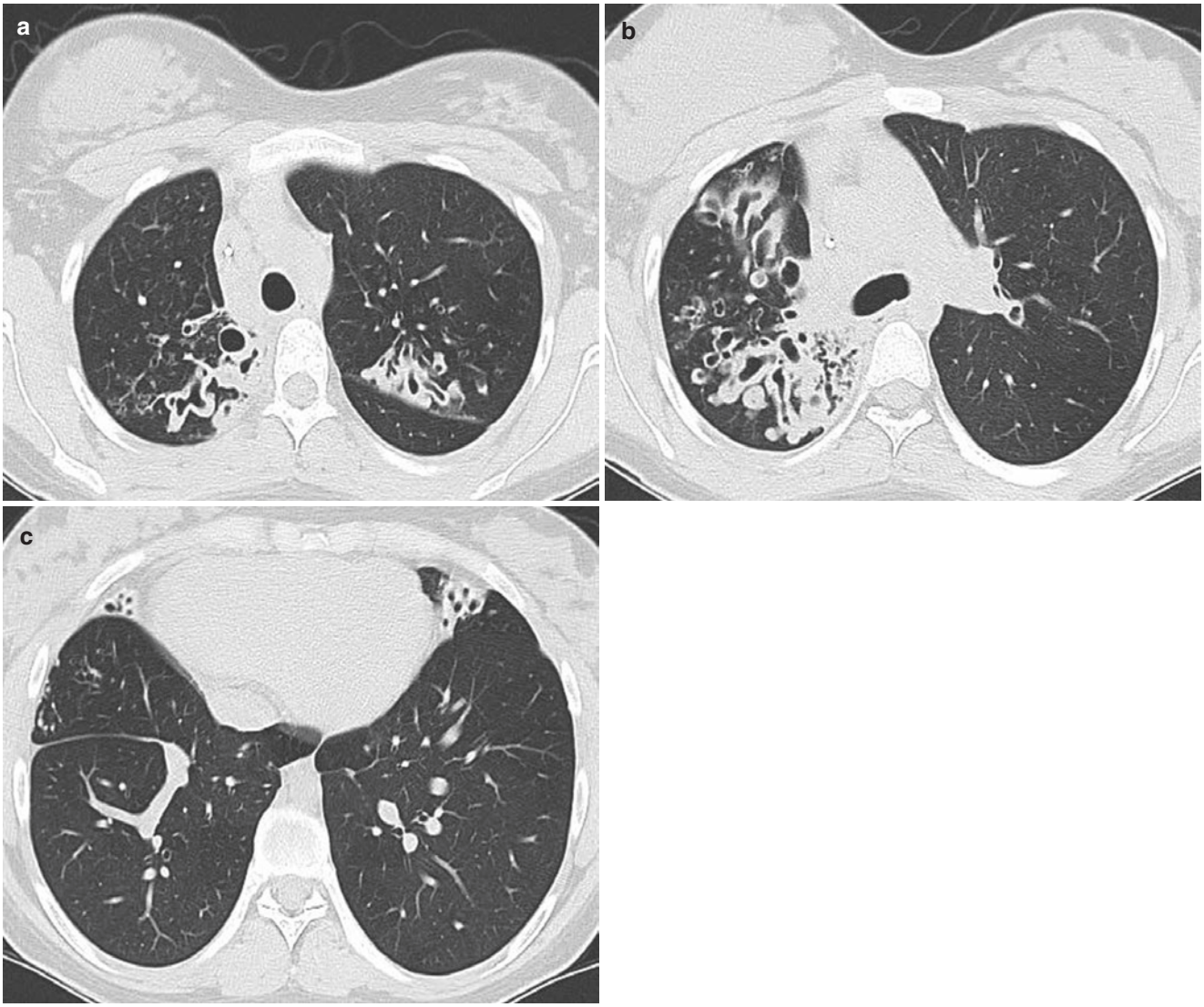

Fig. 2.38 (**a**–**c**) Upper lobe bronchiectasis in a patient with cystic fibrosis

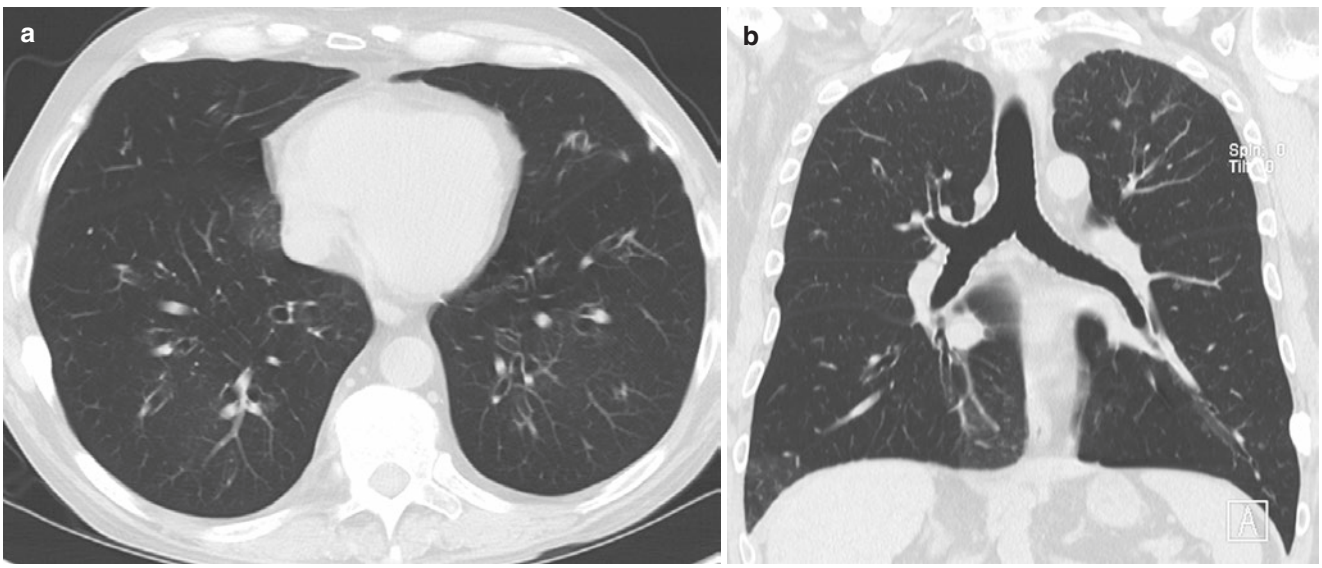

Fig. 2.39 A 46-year-old man with small and large airways disease from ulcerative colitis that flared after colectomy. (**a**, **b**) Axial and coronal CT images show bronchiectasis, mosaic attenuation, overinflated lungs, and the paucity of bronchovascular markings (obliterative bronchiolitis)

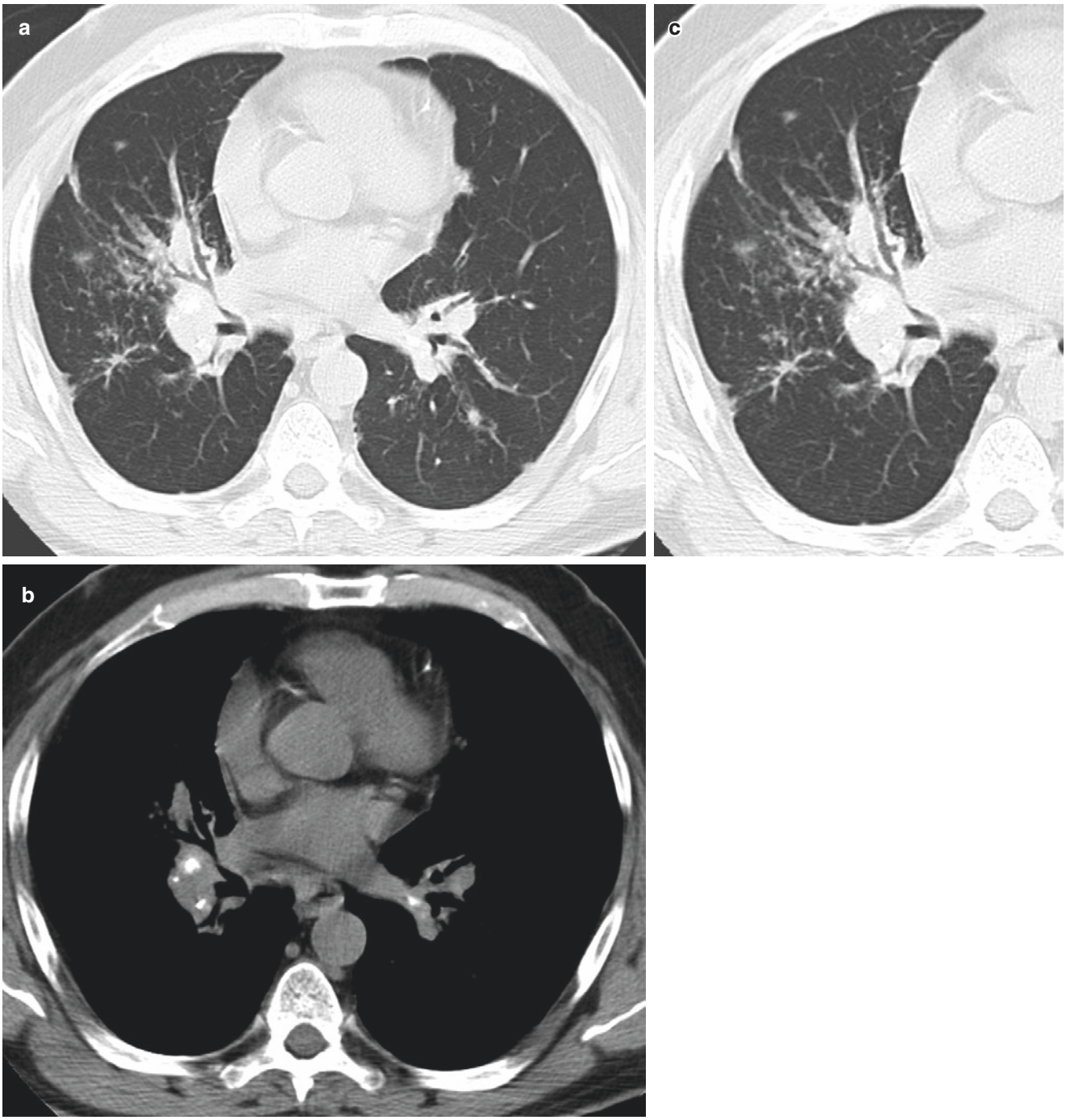

Fig. 2.40 Bronchial dilatation in sarcoidosis. (**a**, **b**) Axial CT images show mild bronchial dilatation in right middle lobe with calcified bilateral hilar lymph nodes. (**c**) HRCT image shows "beaded" appearance of dilated bronchi presumably due to granulomas

2.3 Small Airways Diseases

2.3.1 Anatomy of Small Airways

HRCT is extremely useful for the evaluation of small airways disease and along with clinical information frequently helps in specific diagnosis. Small airways refer to bronchioles in the secondary pulmonary lobules (SPL), and small airways disease implies bronchiolitis. The small bronchioles (<2 mm in diameter) are purely membranous; relatively proximal ones are conducting (till terminal bronchioles), and the distal bronchioles (respiratory bronchioles and beyond) are a part of the gas exchange mechanism. The terminal bronchioles branch into respiratory bronchioles that in turn

branch to alveolar ducts, followed by alveoli. The terminal bronchioles conduct air to acini, the smallest unit of the lung. Acini are usually described as ranging from 6 to 10 mm in size. There are 3–24 acini in each SPL [34]. Apart from terminal bronchiole, the acini also get collateral air from pores of Kohn (direct communication between adjacent alveoli) and canals of Lambert (accessory communication between terminal bronchi and alveoli). The centrilobular bronchiole supplying the SPL is technically preterminal bronchioles with a diameter of approximately 1 mm and a wall thickness of 0.15 mm [34]. These airways are not visualized in a normal scan as wall thickness is the limiting factor. However, the companion centrilobular artery of the diameter of 1 mm can be easily seen as a hyperdense linear branching structure.

2.3.2 CT Signs of Small Airways Disease

A combination of inspiratory and expiratory CT is essential for the evaluation of small airways disease. From an imaging perspective, the small airways diseases or bronchiolitis can be divided into two categories: (a) proliferative (cellular) bronchiolitis and (b) obliterative (constrictive) bronchiolitis. This division is helpful in constructing a list of differential diagnoses and along with clinical and lab data guides in making an accurate diagnosis in most of the cases. The common causes of bronchiolitis are mentioned in Table 2.14. The CT signs of proliferative versus obliterative bronchiolitis are described in Table 2.15 [35–38] (Fig. 2.41). Except in hypersensitivity pneumonitis, there is always a major component of large airways disease in proliferative bronchiolitis group. The differential diagnoses of proliferative bronchiolitis are discussed in Table 2.16 [35–38] (Figs. 2.42, 2.43, 2.44, and 2.45). Once the diagnosis of proliferative bronchiolitis is made on HRCT, bronchoscopy is the next investigation that provides useful and many times confirmatory information about the etiology.

The etiology of obliterative bronchiolitis is almost always related to a known disorder like collagen vascular disease, ulcerative colitis, and graft versus host reaction (Fig. 2.39). However, a surgical lung biopsy is required for confirmation in most of the cases. Swyer-James syndrome is a type of post-infective bronchiolitis affecting a lobe or more commonly an entire lung. This usually results from a viral infection in infancy or early childhood that damages the terminal and respiratory bronchioles and prevents the normal development of their alveolar buds. The affected lung is smaller in volume with resultant decrease pulmonary circulation. The entity can be seen in an asymptomatic adult. Chest radiograph shows a decrease in lung volume with focal hyperlucency that can also be seen in endobronchial lesions, CLE, and pulmonary artery aplasia. A combination of inspiratory and expiratory CT helps in accurate diagnosis by showing lucencies in the affected lung and dramatic air trapping on expiratory phase [39, 40] (Fig. 2.46). CT delineates the exact extent of bronchiolitis as in most of the cases, the involvement is multifocal. CT can also show associated bronchiectasis and atelectasis. Diffuse idiopathic pulmonary neuroendocrine cell hyperplasia (DIPNECH) is increasingly recognized entity due to enhanced awareness. DIPNECH, typically seen in a middle-aged woman, is characterized by diffuse hyperplasia and dysplasia of pulmonary neuroendocrine cells, multiple carcinoid tumorlets, and peribronchiolar fibrosis leading to obliterative bronchiolitis [41]. The proliferation of neuroendocrine cells in bronchial wall results in aggregates forming extraluminal nodules less than 5 mm (tumorlets) and more than 5 mm (carcinoid tumors). The obliterative bronchitis is possibly due to fibrogenic cytokines released by neuroendocrine cells the associated and inflammation. CT features of DIPNECH are scattered nodules with air trapping (Fig. 2.47). The larger nodules represent tumors, and small bronchiolocentric ground-glass density nodules represent tumorlets [41, 42]. Large airways disease is commonly present in these patients. A surgical lung biopsy is a gold standard for diagnosis.

Table 2.14 Bronchiolitis

Proliferative bronchiolitis	Obliterative bronchiolitis
• Infective bronchiolitis Tuberculosis, NTM Viral, bacterial	• Post-infective bronchiolitis
	• Lung transplant
	• Graft versus host reaction
	• Collagen vascular disease
• Aspiration bronchiolitis	• Ulcerative colitis
• Respiratory bronchiolitis	• Inhalational lung disease
• Follicular bronchiolitis	• DIPNECH
• Hypersensitivity pneumonitis	
• Diffuse panbronchiolitis	

NTM nontuberculous mycobacterial disease, *DIPNECH* diffuse idiopathic pulmonary neuroendocrine cell hyperplasia

Table 2.15 CT signs of bronchiolitis

Proliferative bronchiolitis	Obliterative bronchiolitis
Primary signs Centrilobular nodules Tree-in-bud opacities Air trapping	*Primary signs* Air trapping
Secondary signs Bronchial wall thickening Bronchiectasis Bronchioloectasis Subsegmental atelectasis	*Secondary signs* Increased lung volumes Bronchial wall thickening Absent centrilobular nodularity

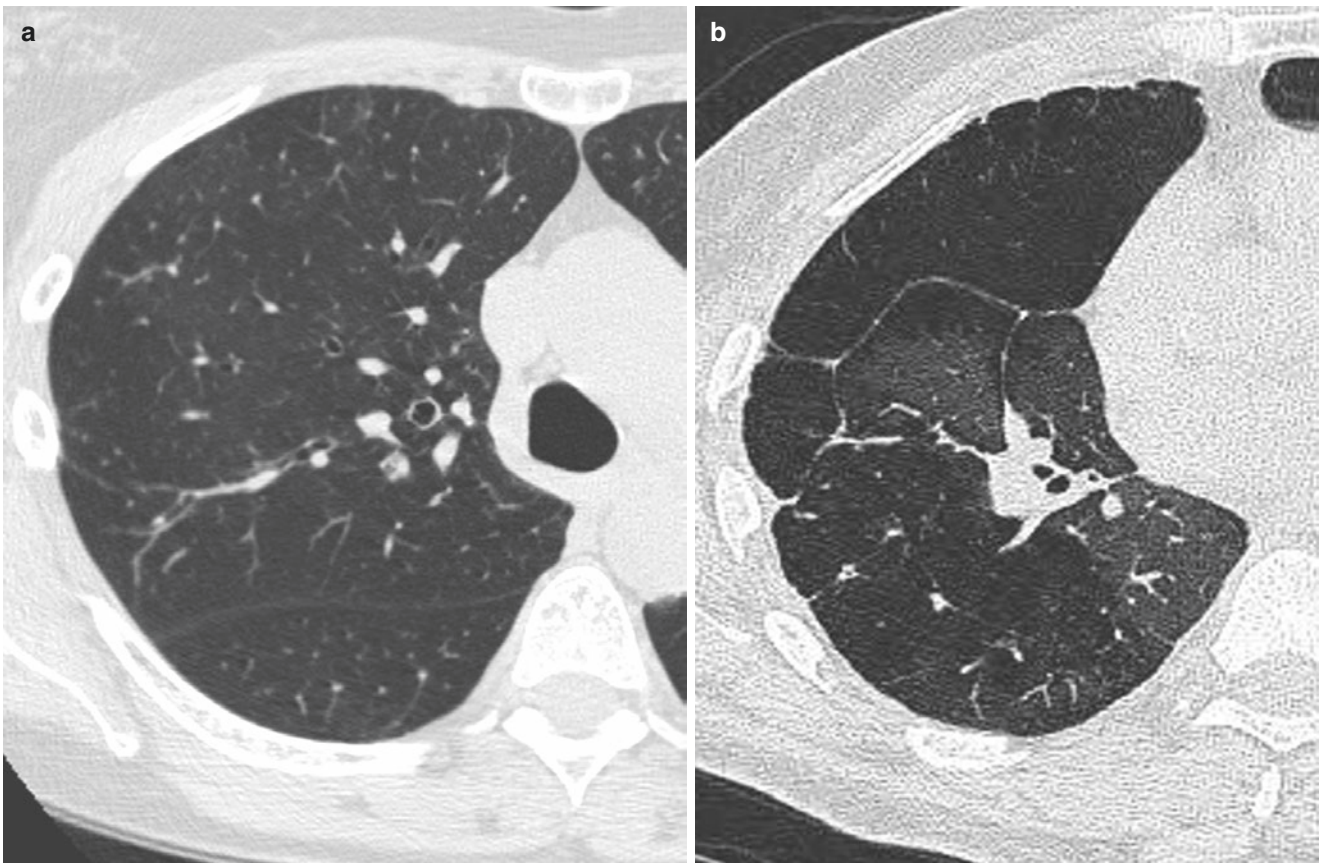

Fig. 2.41 Proliferative versus obliterative bronchiolitis. (**a**) HRCT image of proliferative bronchiolitis in an asthmatic patient shows centrilobular nodules, mosaic attenuation, bronchial dilatation, and bronchial wall thickening. (**b**) HRCT of obliterative bronchiolitis in a patient with rheumatoid arthritis showing mosaic attenuation as a dominant finding

Table 2.16 Radiological and clinical features of proliferative bronchiolitis

Infective bronchiolitis	• Clinical features of infection are present • Usually multifocal, if bilateral, the involvement is asymmetrical • TB: extensive signs of proliferative bronchiolitis, cavities communicating with large airways, pleural effusion, lymph nodes • NTM: preferential involvement of right middle lobe
Aspiration bronchiolitis	• Clinical features of aspiration • Predisposing factors for aspiration • Focal or multifocal involvement of dependent lower lungs • Abnormal esophagus
Respiratory bronchiolitis	• History of smoking (light to heavy) is always present • Upper lung involvement • Patchy small ground-glass densities may be present • Other smoking-related lung disease like emphysema
Follicular bronchiolitis	• History of HIV or collagen vascular disease like Sjogren syndrome and rheumatoid arthritis • Multifocal or diffuse involvement • CT features of proliferative bronchiolitis with or without ground-glass opacities
Hypersensitivity pneumonitis	• History of exposure may be present; usually, nonsmoker • Mid- to upper lung involvement • Acute phase: ground-glass density centrilobular nodules • Chronic phase: subtle nodularity with fibrotic changes
Diffuse panbronchiolitis	• Usually Asia-Pacific origin patient • Almost always mistaken as TB in the endemic zone • Sputum may grow *H. influenzae* or *P. aeruginosa* • Diffuse involvement mimicking endobronchial TB • Cavities are less common than TB

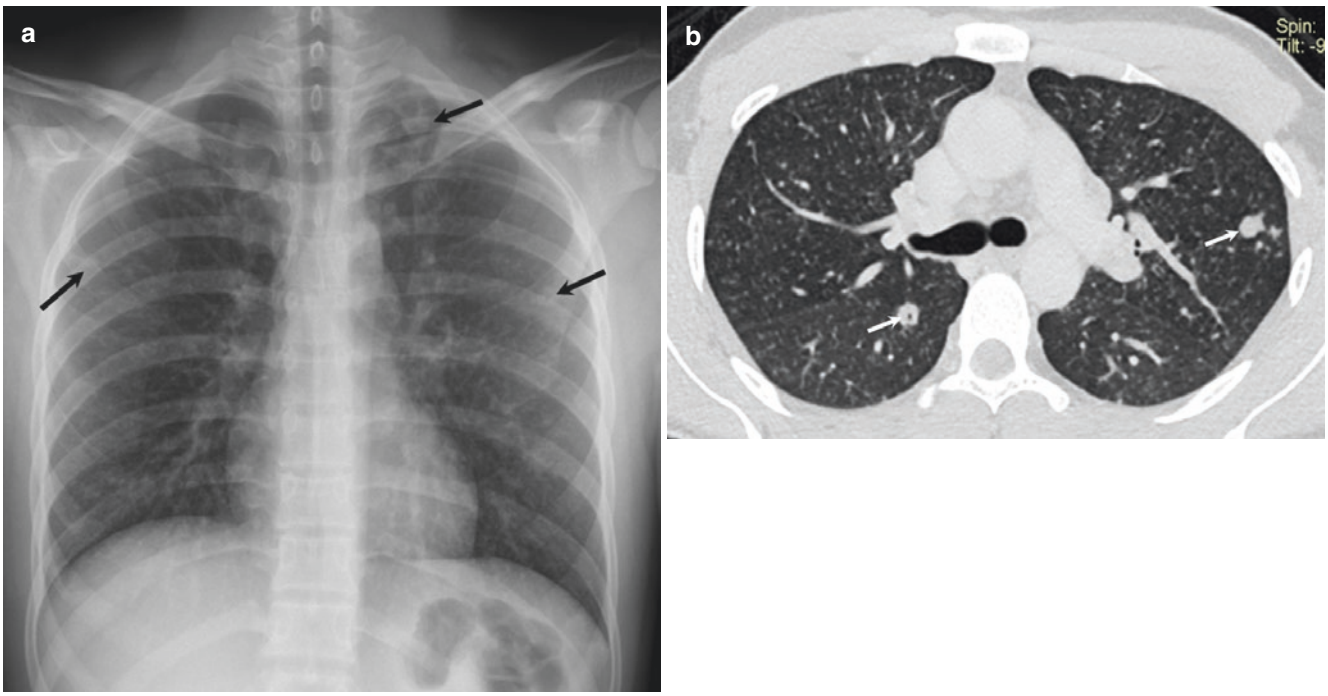

Fig. 2.42 A 21-year-old man with endobronchial tuberculosis. (**a**) Frontal chest radiograph shows a diffuse nodular pattern with few larger nodules (arrows). (**b**) Axial CT image shows diffuse centrilobular nodules with mild mosaic attenuation and granulomas (arrows). Right lung granuloma shows small cavity. Note the tiny nodules are sparing the subpleural space, a characteristic of centrilobular nodules

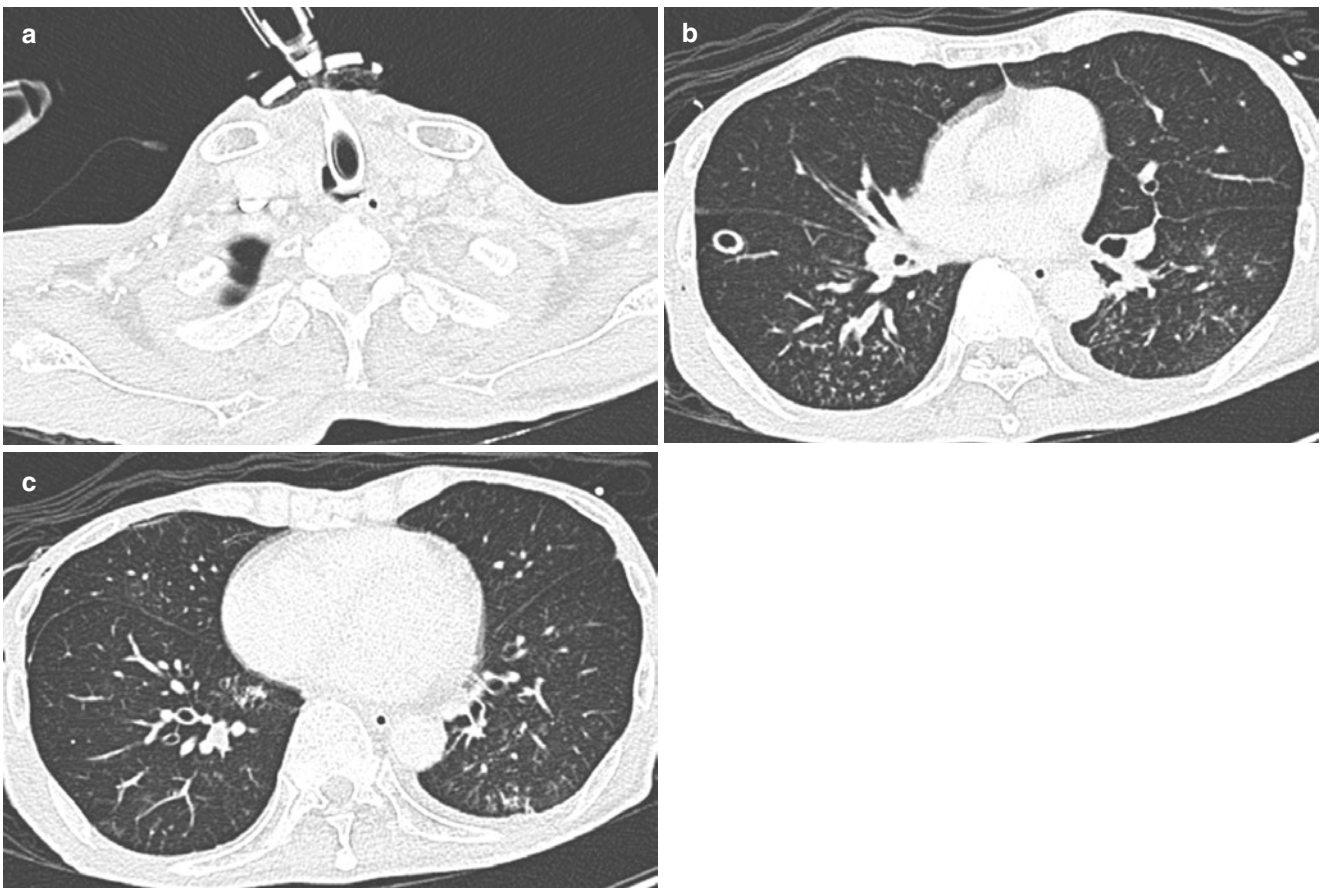

Fig. 2.43 Multifocal proliferative bronchiolitis from aspiration in an intubated patient. (**a**–**c**) Axial CT images show tree-in-bud opacities and mosaic attenuation in both lower lobes

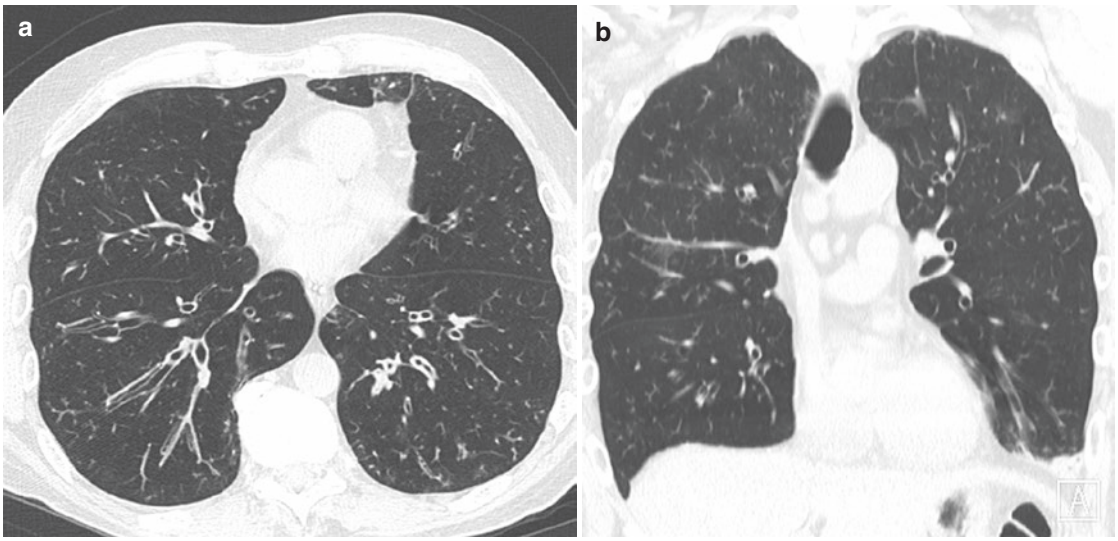

Fig. 2.44 A 61-year-old woman with rheumatoid arthritis and follicular bronchiolitis. (**a**, **b**) Axial and CT images show bronchiectasis, bronchial wall thickening, and changes of proliferative bronchiolitis (tree-in-bud opacities, mosaic attenuation, and increased lung volumes)

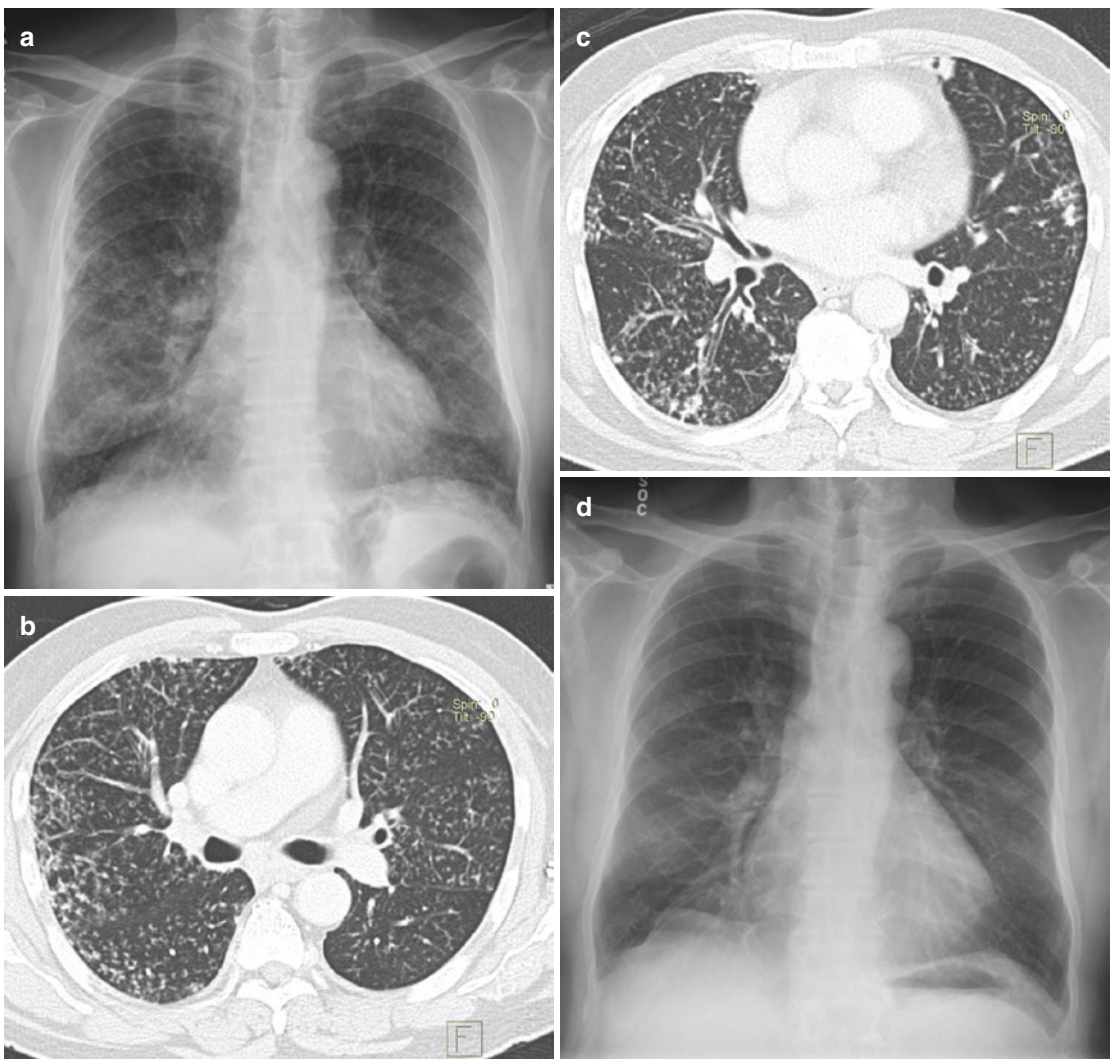

Fig. 2.45 A 69-year-old man with diffuse panbronchiolitis. (**a**) Frontal chest radiograph shows diffuse reticulonodular opacities in both lungs. (**b**, **c**) Axial CT images show diffuse centrilobular nodularity, tree-in-bud opacities, and bronchial wall thickening (small and large airways disease). (**d**) Follow-up radiograph after macrolide antibiotic shows clearing of lung opacities with complete clinical recovery

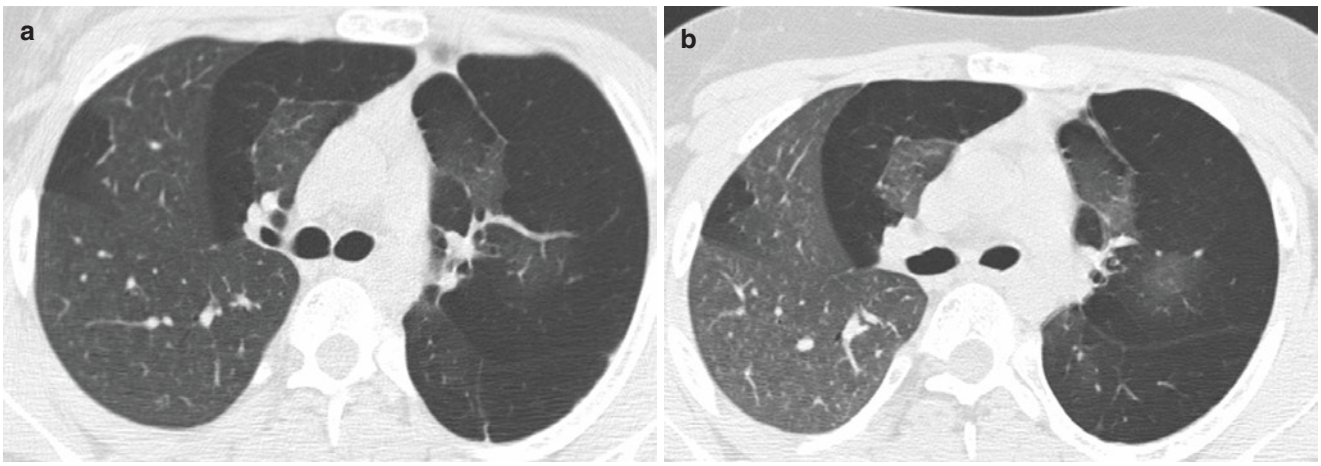

Fig. 2.46 A 9-year-old boy with post-infectious bronchiolitis obliterans (Swyer-James syndrome). (**a**) Inspiratory CT image shows extensive mosaic attenuation. (**b**) Expiratory CT image shows air trapping

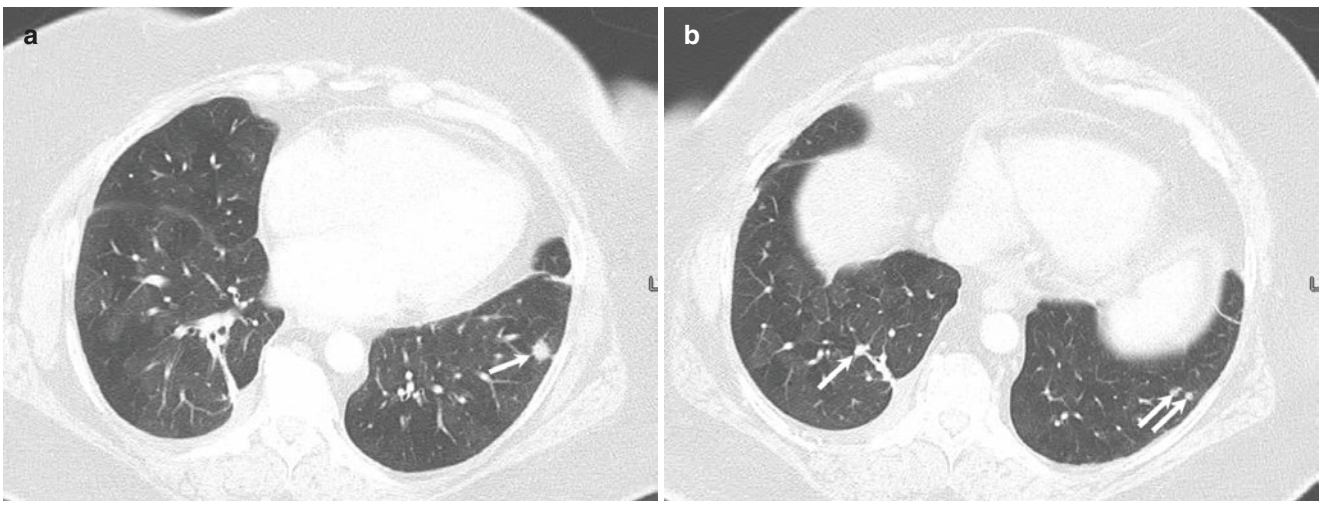

Fig. 2.47 A 32-year-old woman with DIPNECH. (**a**, **b**) Axial CT images show mosaic attenuation and scattered discrete nodules (arrows)

References

1. Gamsu G, Webb WR. Computed tomography of the trachea: normal and abnormal. Am J Roentgenol. 1982;139(2):321–6.
2. Boiselle PM. Imaging of the large airways. Clin Chest Med. 2008;29(1):181–93.
3. Glazer HS, Anderson DJ, DiCroce JJ, Solomon SL, Wilson BS, Molina PL, Sagel SS. Anatomy of the major fissure: evaluation with standard and thin-section CT. Radiology. 1991;180(3):839–44.
4. Aziz A, Ashizawa K, Nagaoki K, Hayashi K. High resolution CT anatomy of the pulmonary fissures. J Thorac Imaging. 2004;19(3):186–91.
5. Arıyürek MO, Gülsün M, Demirkazık F. Accessory fissures of the lung: evaluation by high-resolution computed tomography. Eur Radiol. 2001;11(12):2449–53.
6. Buterbaugh JE, Erly WK. Paratracheal air cysts: a common finding on routine CT examinations of the cervical spine and neck that may mimic pneumomediastinum in patients with traumatic injuries. Am J Neuroradiol. 2008;29(6):1218–21.
7. Gipson MG, Cummings KW, Hurth KM. Bronchial atresia. Radiographics. 2009;29(5):1531–5.
8. Park CM, Goo JM, Lee HJ, Kim MA, Lee CH, Kang MJ. Tumors in the tracheobronchial tree: CT and FDG PET features. Radiographics. 2009;29(1):55–71.
9. Ngo AV, Walker CM, Chung JH, Takasugi JE, Stern EJ, Kanne JP, Reddy GP, Godwin JD. Tumors and tumorlike conditions of the large airways. Am J Roentgenol. 2013;201(2):301–13.
10. Morshed K, Trojanowska A, Szymański M, Trojanowski P, Szymańska A, Smoleń A, Drop A. Evaluation of tracheal stenosis: comparison between computed tomography virtual tracheobronchoscopy with multiplanar reformatting, flexible tracheofiberoscopy and intra-operative findings. Eur Arch Otorhinolaryngol. 2011;268(4):591–7.
11. Zaghi S, Alonso J, Orestes M, Kadin N, Hsu W, Berke G. Idiopathic subglottic stenosis: a comparison of tracheal size. Ann Otol Rhinol Laryngol. 2016;125(8):622–6.
12. Bhalla M, Grillo HC, McLoud TC, Shepard JO, Weber AL, Mark EJ. Idiopathic laryngotracheal stenosis: radiologic findings. AJR Am J Roentgenol. 1993;161(3):515–7.

13. Kim Y, Lee KS, Yoon JH, Chung MP, Kim H, Kwon OJ, Rhee CH, Han YC. Tuberculosis of the trachea and main bronchi: CT findings in 17 patients. AJR Am J Roentgenol. 1997;168(4):1051–6.
14. Seo JB, Song KS, Lee JS, Goo JM, Kim HY, Song JW, Lee IS, Lim TH. Broncholithiasis: review of the causes with radiologic-pathologic correlation. Radiographics. 2002;22(suppl_1):S199–213.
15. Park HJ, Park SH, Im SA, Kim YK, Lee KY. CT differentiation of anthracofibrosis from endobronchial tuberculosis. Am J Roentgenol. 2008;191(1):247–51.
16. Greene R, Lechner GL. "Saber-sheath" trachea: a clinical and functional study of marked coronal narrowing of the intrathoracic trachea. Radiology. 1975;115(2):265–8.
17. Gilkeson RC, Ciancibello LM, Hejal RB, Montenegro HD, Lange P. Tracheobronchomalacia: dynamic airway evaluation with multidetector CT. Am J Roentgenol. 2001;176(1):205–10.
18. Baroni RH, Feller-Kopman D, Nishino M, Hatabu H, Loring SH, Ernst A, Boiselle PM. Tracheobronchomalacia: comparison between end-expiratory and dynamic expiratory CT for evaluation of central airway collapse. Radiology. 2005;235(2):635–41.
19. Stern EJ, Graham CM, Webb WR, Gamsu G. Normal trachea during forced expiration: dynamic CT measurements. Radiology. 1993;187(1):27–31.
20. Kang EY. Large airway diseases. J Thorac Imaging. 2011;26(4):249–62.
21. Heidinger BH, Occhipinti M, Eisenberg RL, Bankier AA. Imaging of large airways disorders. Am J Roentgenol. 2015;205(1):41–56.
22. Hill LE, Ritchie G, Wightman AJ, Hill AT, Murchison JT. Comparison between conventional interrupted high-resolution CT and volume multidetector CT acquisition in the assessment of bronchiectasis. Br J Radiol. 2010;83(985):67–70.
23. Dodd JD, Souza CA, Müller NL. Conventional high-resolution CT versus helical high-resolution MDCT in the detection of bronchiectasis. Am J Roentgenol. 2006;187(2):414–20.
24. Kim JS, Müller NL, Park CS, Grenier P, Herold CJ. Cylindrical bronchiectasis: diagnostic findings on thin-section CT. AJR Am J Roentgenol. 1997;168(3):751–4.
25. Perera PL, Screaton NJ. 5 Radiological features of bronchiectasis. Eur Respir Monogr. 2011;1(52):44.
26. Komiya K, Ishii H, Umeki K, Kawamura T, Okada F, Okabe E, Murakami J, Kato Y, Matsumoto B, Teramoto S, Johkoh T. Computed tomography findings of aspiration pneumonia in 53 patients. Geriatr Gerontol Int. 2013;13(3):580–5.
27. Shah A, Panjabi C. Allergic aspergillosis of the respiratory tract. Eur Respir Rev. 2014;23(131):8–29.
28. Tanaka N, Kim JS, Bates CA, Brown KK, Cool CD, Newell JD, Lynch DA. Lung diseases in patients with common variable immunodeficiency: chest radiographic, and computed tomographic findings. J Comput Assist Tomogr. 2006;30(5):828–38.
29. Mishra M, Kumar N, Jaiswal A, Verma AK, Kant S. Kartagener's syndrome: a case series. Lung India. 2012;29(4):366.
30. Perez T, Remy-Jardin M, Cortet B. Airways involvement in rheumatoid arthritis: clinical, functional, and HRCT findings. Am J Respir Crit Care Med. 1998;157(5):1658–65.
31. D'Andrea N, Vigliarolo R, Sanguinetti CM. Respiratory involvement in inflammatory bowel diseases. Multidiscip Respir Med. 2010;5(3):173.
32. Helbich TH, Heinz-Peer G, Fleischmann D, Wojnarowski C, Wunderbaldinger P, Huber S, Eichler I, Herold CJ. Evolution of CT findings in patients with cystic fibrosis. AJR Am J Roentgenol. 1999;173(1):81–8.
33. King MA, Stone JA, Diaz PT, Mueller CF, Becker WJ, Gadek JE. Alpha 1-antitrypsin deficiency: evaluation of bronchiectasis with CT. Radiology. 1996;199(1):137–41.
34. Webb WR. Thin-section CT of the secondary pulmonary lobule: anatomy and the image—the 2004 Fleischner lecture. Radiology. 2006;239(2):322–38.
35. Desai SR, Hansell DM. Small airways disease: expiratory computed tomography comes of age. Clin Radiol. 1997;52(5):332–7.
36. Abbott GF, Rosado-de-Christenson ML, Rossi SE, Suster S. Imaging of small airways disease. J Thorac Imaging. 2009;24(4):285–98.
37. Hansell DM. Small airways diseases: detection and insights with computed tomography. Eur Respir J. 2001;17(6):1294–313.
38. Berniker AV, Henry TS. Imaging of small airways diseases. Radiol Clin North Am. 2016;54(6):1165–81.
39. Moore AD, Godwin JD, Dietrich PA, Verschakelen JA, Henderson WR Jr. Swyer-James syndrome: CT findings in eight patients. AJR Am J Roentgenol. 1992;158(6):1211–5.
40. Marti-Bonmati L, Ruiz Perales F, Catala F, Mata JM, Calonge E. CT findings in Swyer-James syndrome. Radiology. 1989;172(2):477–80.
41. Davies SJ, Gosney JR, Hansell DM, Wells AU, du Bois RM, Burke MM, Sheppard MN, Nicholson AG. Diffuse idiopathic pulmonary neuroendocrine cell hyperplasia: an under-recognised spectrum of disease. Thorax. 2007;62(3):248–52.
42. Rossi G, Cavazza A, Spagnolo P, Sverzellati N, Longo L, Jukna A, Montanari G, Carbonelli C, Vincenzi G, Bogina G, Franco R. Diffuse idiopathic pulmonary neuroendocrine cell hyperplasia syndrome. Eur Respir J. 2016;47(6):1829–41.

Imaging of Cystic Lung Diseases

3

Ashish Chawla

3.1 Introduction

Cystic lung disease is a group of pulmonary disorders characterized by the presence of multiple cysts that are defined as low-attenuation areas with thin walls (wall thickness usually less than 2 mm). Cysts are increasingly being recognized on HRCT of the thorax and always present a diagnostic dilemma. The common cystic lung diseases are lymphangioleiomyomatosis (LAM), pulmonary Langerhans cell histiocytosis (LCH), and Birt-Hogg-Dubé syndrome. There are two interstitial lung diseases that can present with multiple cysts, namely, desquamative interstitial pneumonia (DIP) and lymphocytic interstitial pneumonia (LIP). Multiple pulmonary cysts (pneumatoceles) can also be seen during the course of *Pneumocystis carinii* pneumonia (PCP), now known as *Pneumocystis jirovecii* pneumonia (PJP). There are two challenges in reporting the HRCT with cystic lung diseases: first to differentiate the true cysts from their mimickers and second to provide an accurate diagnosis of cystic lung disease. In most cases, diagnosis can be made by the characterization of the cysts and ancillary radiological findings coupled with a careful review of clinical information.

3.2 Mimickers of Cysts

A variety of lucencies can be seen in lungs on HRCT. These can be mistaken for cysts resulting in misdiagnosis [1]. These are described in Table 3.1 (Figs. 3.1, 3.2, 3.3, 3.4, 3.5, and 3.6). A few scattered in cysts seen on HRCT can be ignored as pneumatoceles from the previous infection. Multiple small cysts (more than five to ten) or two or more large cysts must always be investigated to identify the underlying disease process.

Table 3.1 Mimickers of cysts and cystic lung diseases

Cysts	Cysts are parenchymal lucencies with a well-defined interface with normal lung. Cysts have a wall thickness less than 2 mm. Cysts can be rounded or may be bizarre shape
Emphysema	Emphysema is characterized by centrilobular or paraseptal lucencies usually without a true wall. However, the wall can be seen with long-standing emphysema due to associated fibrosis or due to superimposed consolidation in the surrounding lung, outlining the lucencies. There is always a history of smoking, at least more than 30 pack-years. Rare causes of emphysema are alpha one antitrypsin deficiency, pneumoconiosis, and intravenous drug abuse (Ritalin)
Honeycombing	Honeycombing cysts are clustered cystic airspaces, usually subpleural ranging in size from 3 mm to 2.5 cm. A well-defined wall is present with cystic airspaces sharing the walls. Other hallmarks of interstitial lung diseases like reticular bands, ground-glass opacities, and traction bronchiectasis are present
Cavities	Cavity is lucent space within a mass or consolidation and is usually solitary but may be multiple. Cavities characteristically have a thick wall or nodular wall. They are usually due to infection or neoplasm and rarely vasculitis
Pneumatoceles	Usually one or a few, pneumatocele is a transient thin-walled, gas-filled space in the lung. They are caused by infection, trauma, or aspiration of hydrocarbon

A. Chawla (✉)
Department of Diagnostic Radiology, Khoo Teck Puat Hospital, Singapore, Singapore

A. Chawla (ed.), *Thoracic Imaging*, https://doi.org/10.1007/978-981-13-2544-1_3

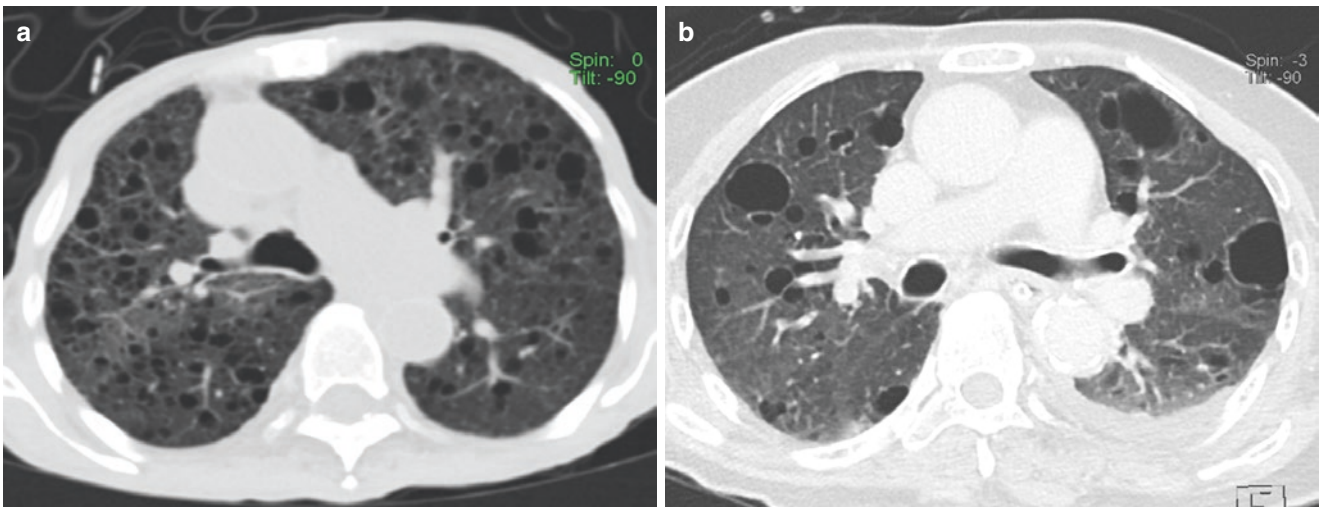

Fig. 3.1 True cysts from (**a**) LAM and (**b**) LIP showing well-circumscribed cysts

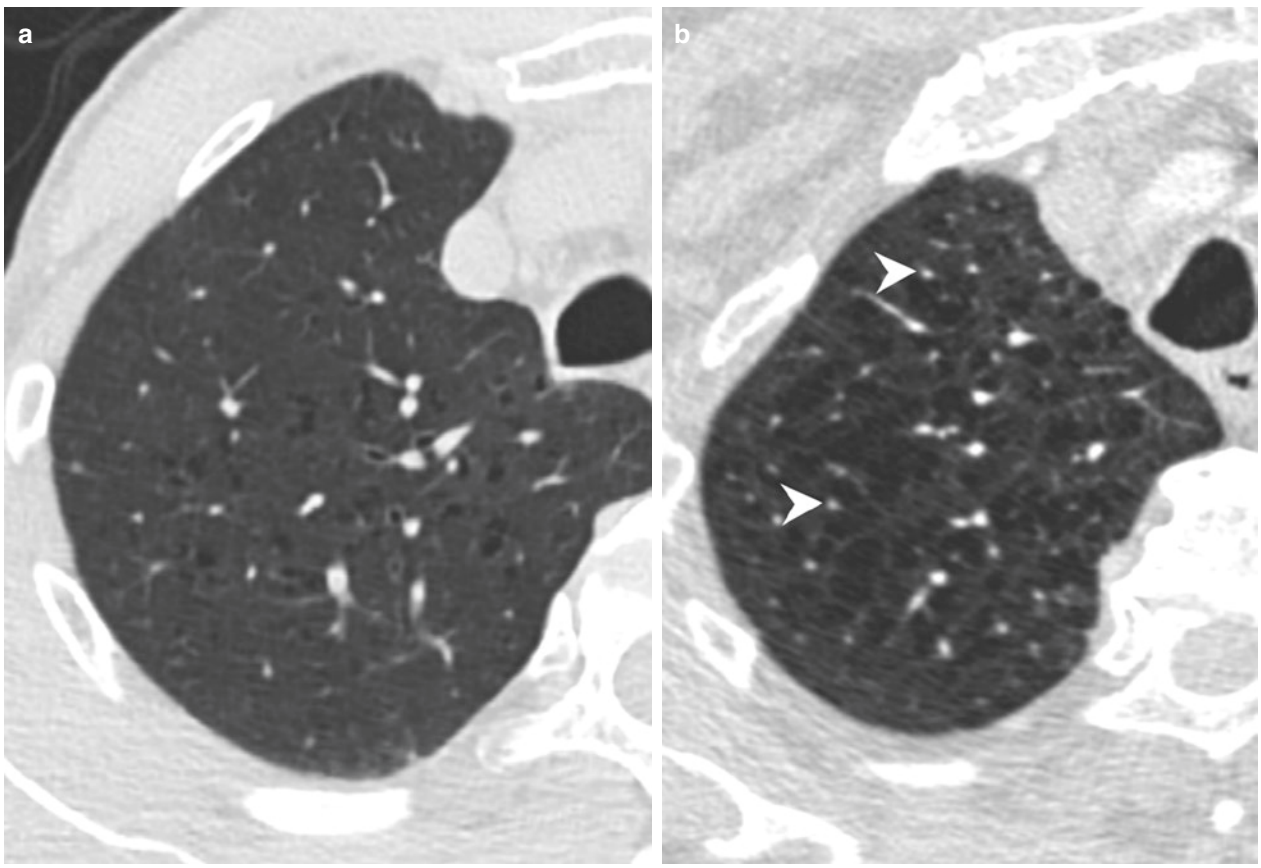

Fig. 3.2 Types of emphysema. (**a**) Early centriacinar emphysema involving acini with "moth-eaten" wall-less punch holes. (**b**) Moderate emphysema involving the lobules with eccentric dots (arrowheads). (**c**) Advanced confluent emphysema with false walls. (**d**) Paraseptal emphysema involving the subpleural lung

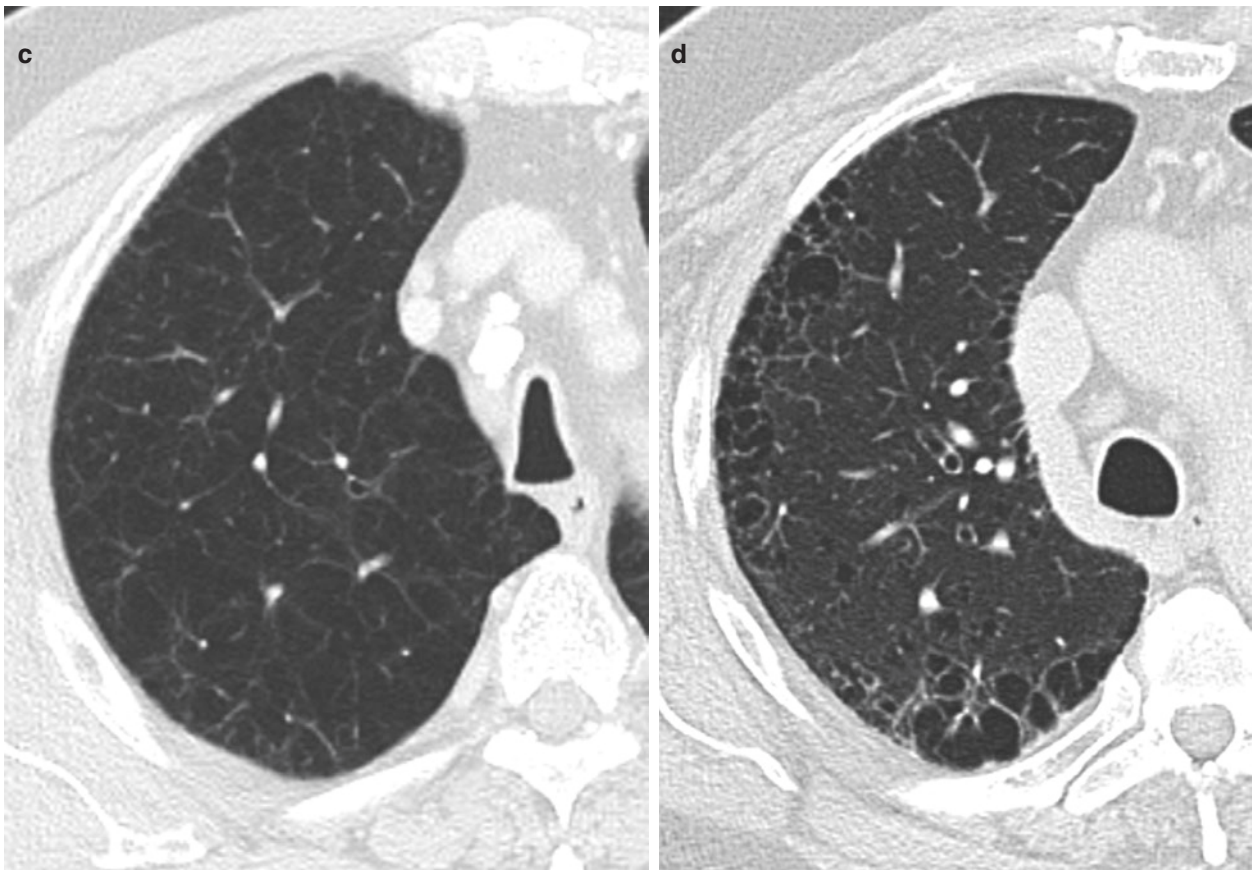

Fig. 3.2 (continued)

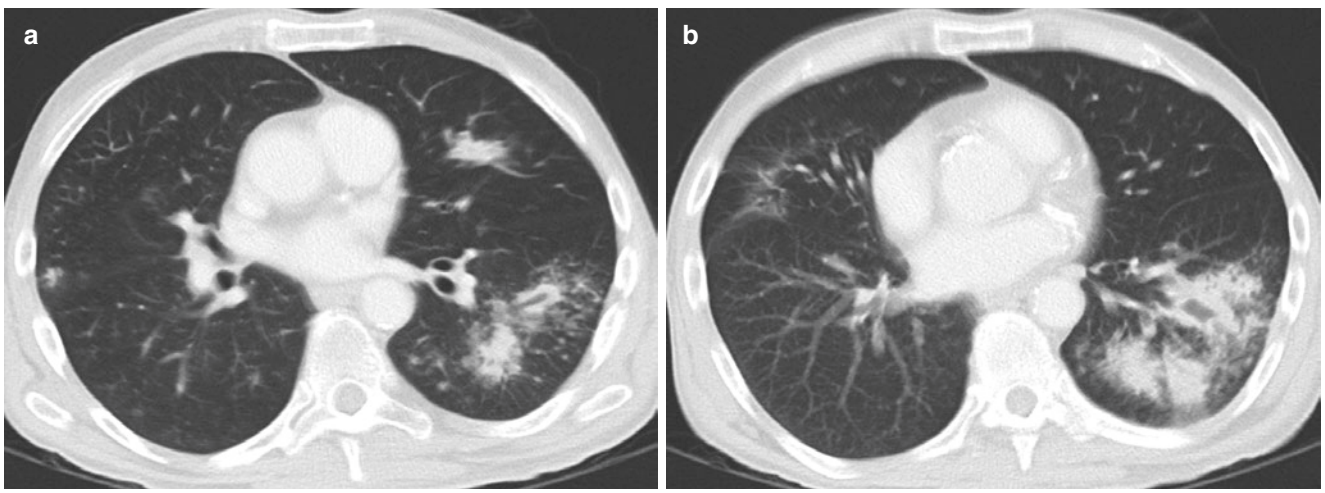

Fig. 3.3 Evolving pneumatoceles from aspiration pneumonia. (**a**, **b**) Axial CT images show consolidations in the left lower lobe and upper lobe. (**c**, **d**) Follow-up CT images after 6 months show cyst formation (arrows) at the site of prior pneumonia

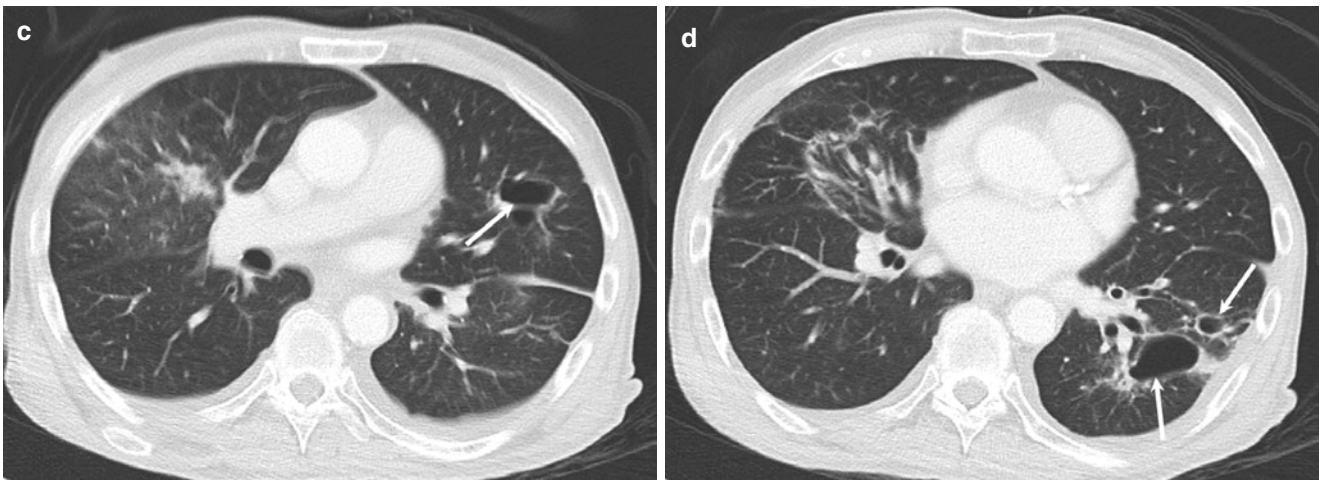

Fig. 3.3 (continued)

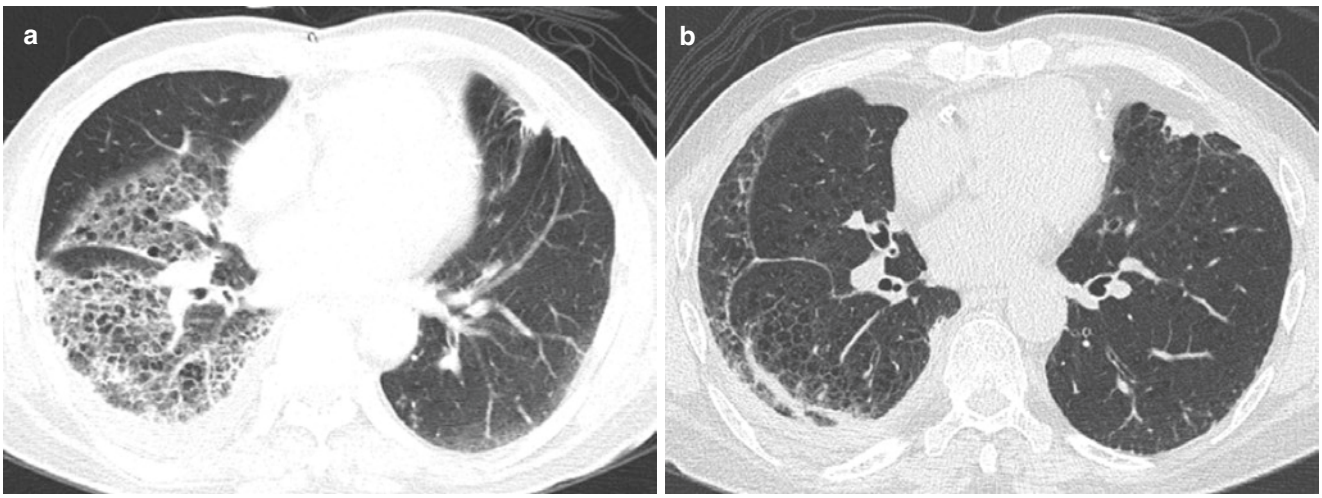

Fig. 3.4 Emphysema with pneumonia is often mistaken for cystic lung disease. (**a**) Initial CT image shows multiple small lucencies in the right lung with walls. Note mild emphysema in the left lung. (**b**) Follow-up CT after 2 months of antibiotics shows resolution of pneumonia but with emphysema more obvious bilaterally

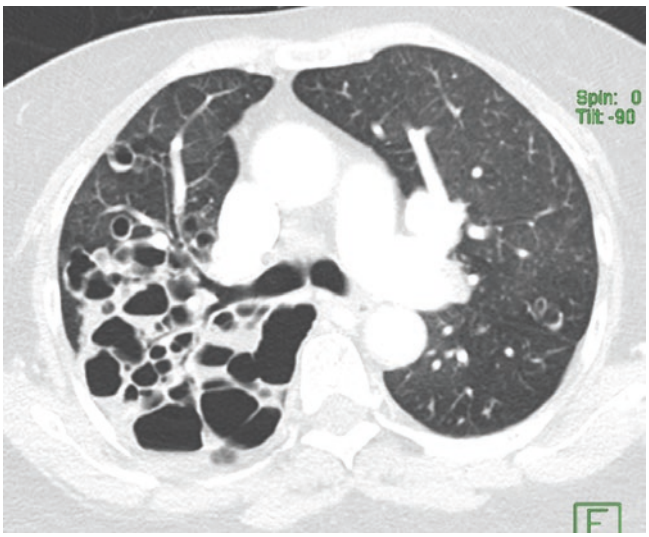

Fig. 3.5 Cystic bronchiectasis. Axial CT image shows multiple cysts in the right upper lung. These cysts are communicating with each other and bronchioles with an air-fluid level in them suggesting infection

3.3 Lymphangioleiomyomatosis

Lymphangioleiomyomatosis (LAM) is usually seen in young women with average age at diagnosis of about 35 years. Although progressive dyspnea is the most common presentation, spontaneous pneumothorax is also commonly seen in LAM [2]. LAM is a multisystem, progressive disorder characterized by proliferation and infiltration of smooth muscle cells in the interstitium along airways, blood vessels, and lymphatics. Peribronchial infiltration results in the formation of cysts due to air trapping. Chylous pleural effusion and chylous ascites result from obstruction of lymphatics. LAM occurs in two forms: in patients with tuberous sclerosis complex (TSC-LAM) and sporadically (S-LAM) with the former being much more common [3]. S-LAM is seen exclusively in women and carries poor prognosis compared to TSC-LAM. The risk of LAM in TSC patients is age-related. The prevalence of LAM in TSC patients by age 21 is 27% that increases to 81% in patients over 41 years old [4].

CT features of LAM are mentioned in Table 3.2 [2, 3] (Figs. 3.7, 3.8, 3.9, and 3.10). Diagnostic criteria for definite, probable, and possible LAM have been described in the literature [5]. A lung biopsy is the gold standard for the definite diagnosis of LAM but is required only in problematic cases.

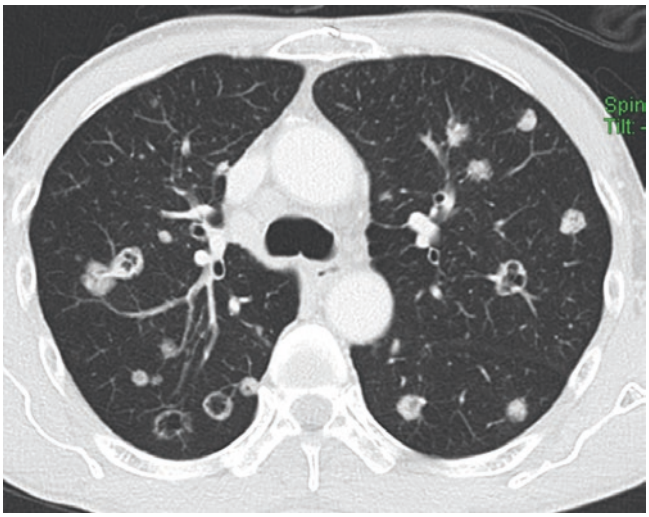

Fig. 3.6 Multifocal adenocarcinoma with some of the nodules showing cystic (pseudocavitation) changes and Cheerios sign

CT features and clinical information help in categorizing "probable" and "possible" LAM. The "probable" diagnosis requires the presence of more than ten characteristic cysts with relevant clinical history and/or altered pulmonary function tests, but if the cysts are less than ten in number, the "probable" diagnosis can be made only if there are additional findings like angiomyolipoma, chylous effusions, or ascites. It is recommended that all patients with LAM or suspected

Table 3.2 CT features of LAM

Lungs	• Numerous cysts (>10) ranging in size from 2 mm to 30 mm (usually 5 mm to 2 cm) • Cysts are rounded and are scattered diffusely in all planes • Cysts can be seen in costophrenic angles • Centrilobular nodules may be present • Fat-containing pulmonary angiomyolipoma is rare • Chylous pleural effusions may be present • Septal thickening can result from obstruction of lymphatics
Mediastinum	• Lymphangioma
Abdomen	• Angiomyolipoma in the kidney and liver • Dilated cisterna chyli • Chylous ascites • Lymphangioma/lymphadenopathy in retroperitoneum

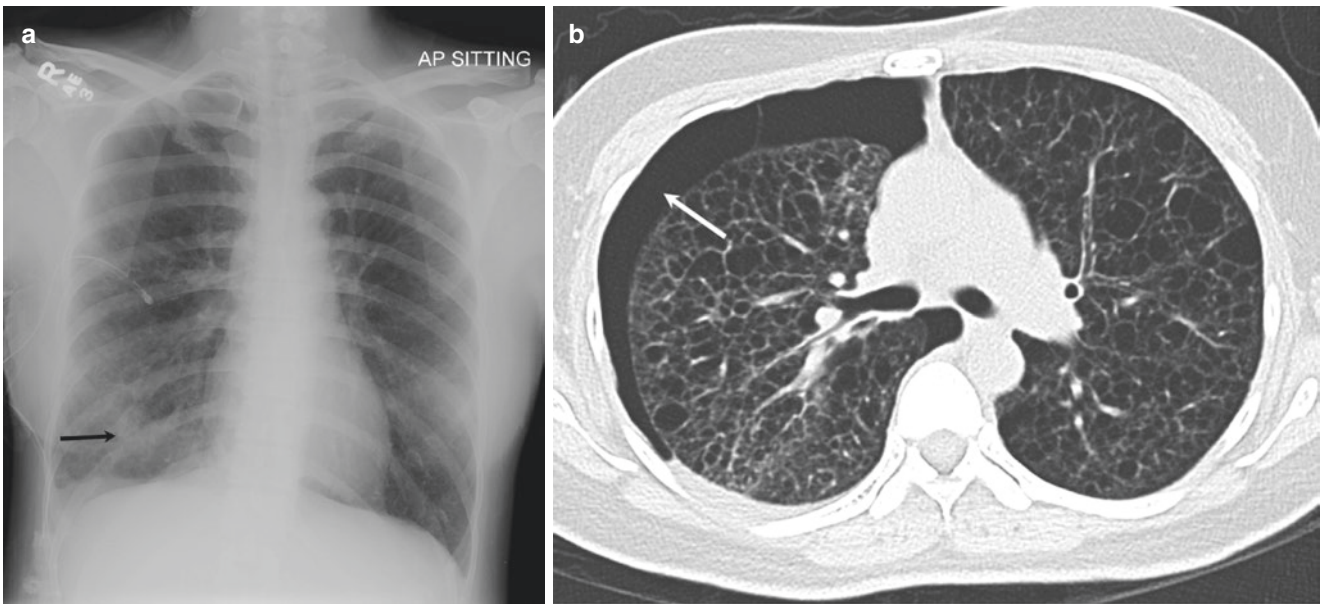

Fig. 3.7 Woman with tuberous sclerosis complex presenting to the emergency department with spontaneous pneumothorax. (**a**) Frontal chest radiograph shows a chest tube in the right hemithorax with subtle cystic changes in the lower lungs. Consolidation (white arrow) in the right lower zone is probably focal re-expansion edema. (**b**) Axial CT image demonstrates innumerable cysts in both lungs associated with pneumothorax (white arrow). (**c**) Axial CT brain image shows calcified subependymal nodules (white arrows). (**d**) Axial CT image of the abdomen shows giant angiomyolipomas (asterisks) distorting both kidneys

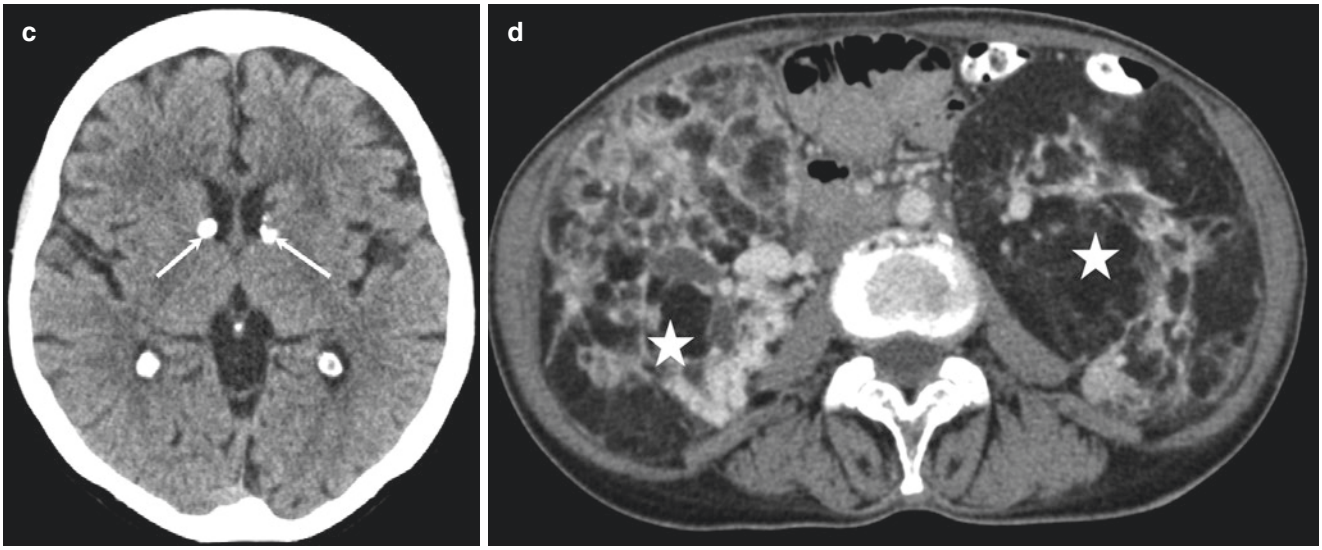

Fig. 3.7 (continued)

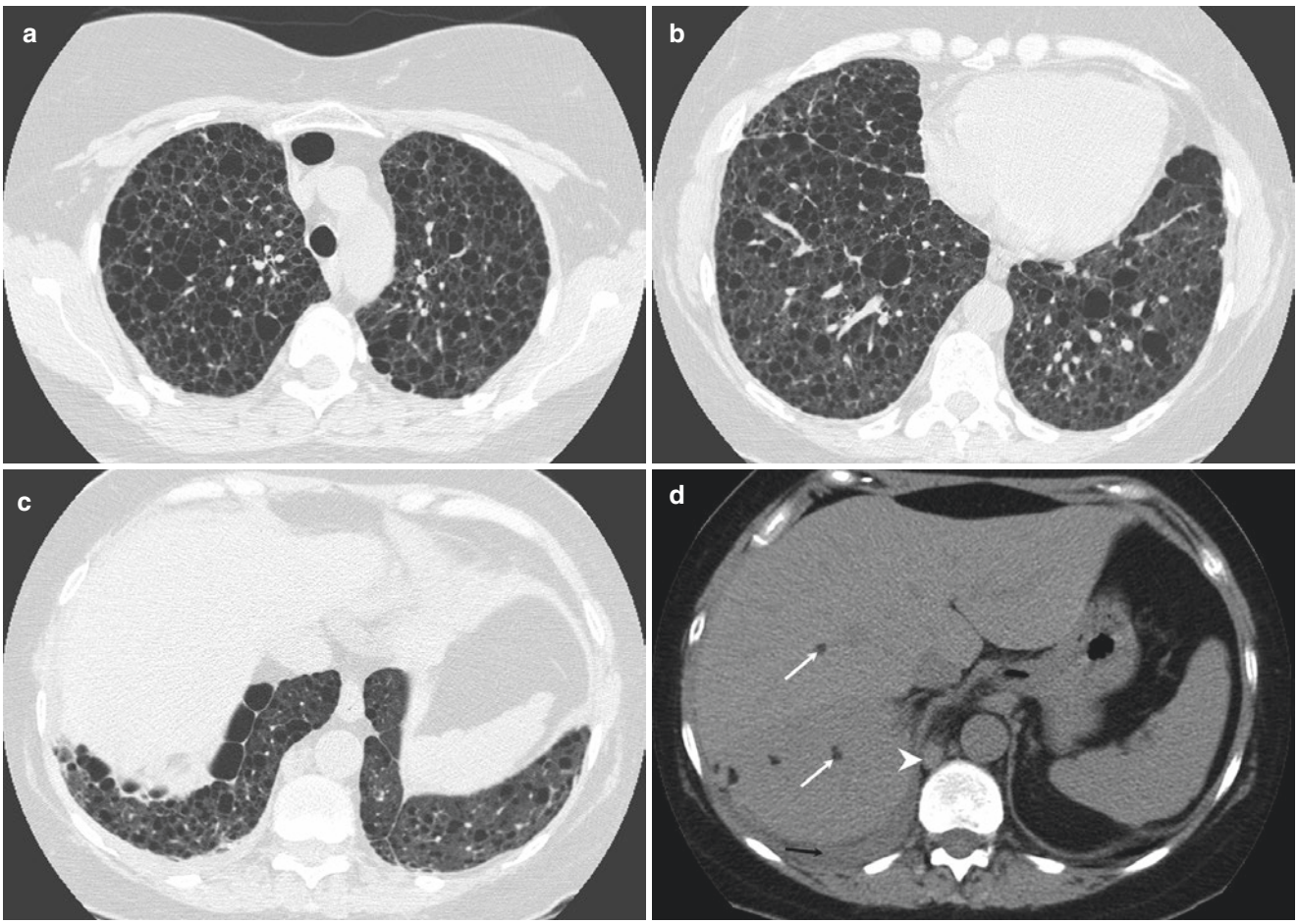

Fig. 3.8 A 55-year-old woman with LAM. (**a**–**c**) Axial CT images show innumerable variable sized rounded cysts in both lungs extending even to costophrenic angles. (**d**) Axial CT image in soft tissue window shows four small fat-containing angiomyolipomas (white arrows) in the liver, dilated cisterna chyli (arrowhead), and right pleural effusion (black arrow). The pleural effusion was chylous

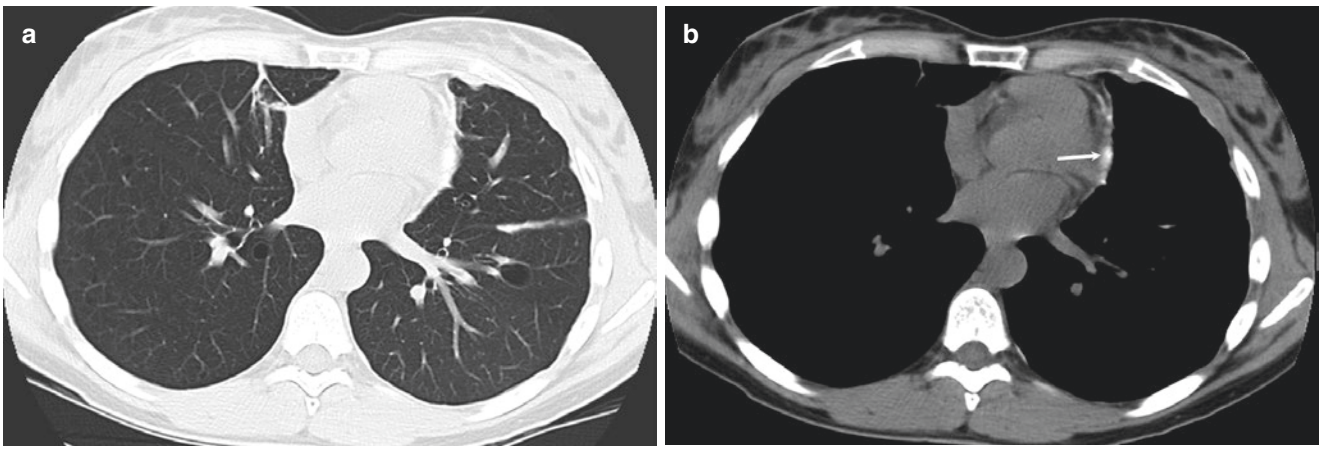

Fig. 3.9 A 37-year-old woman with recurrent pneumothorax from LAM with a history of talc pleurodesis. (**a**) Axial CT image shows a few scattered cysts in both lungs. (**b**) Axial CT image with soft tissue window settings shows hyperdensity (white arrow) along the mediastinal pleura representing talc used in pleurodesis

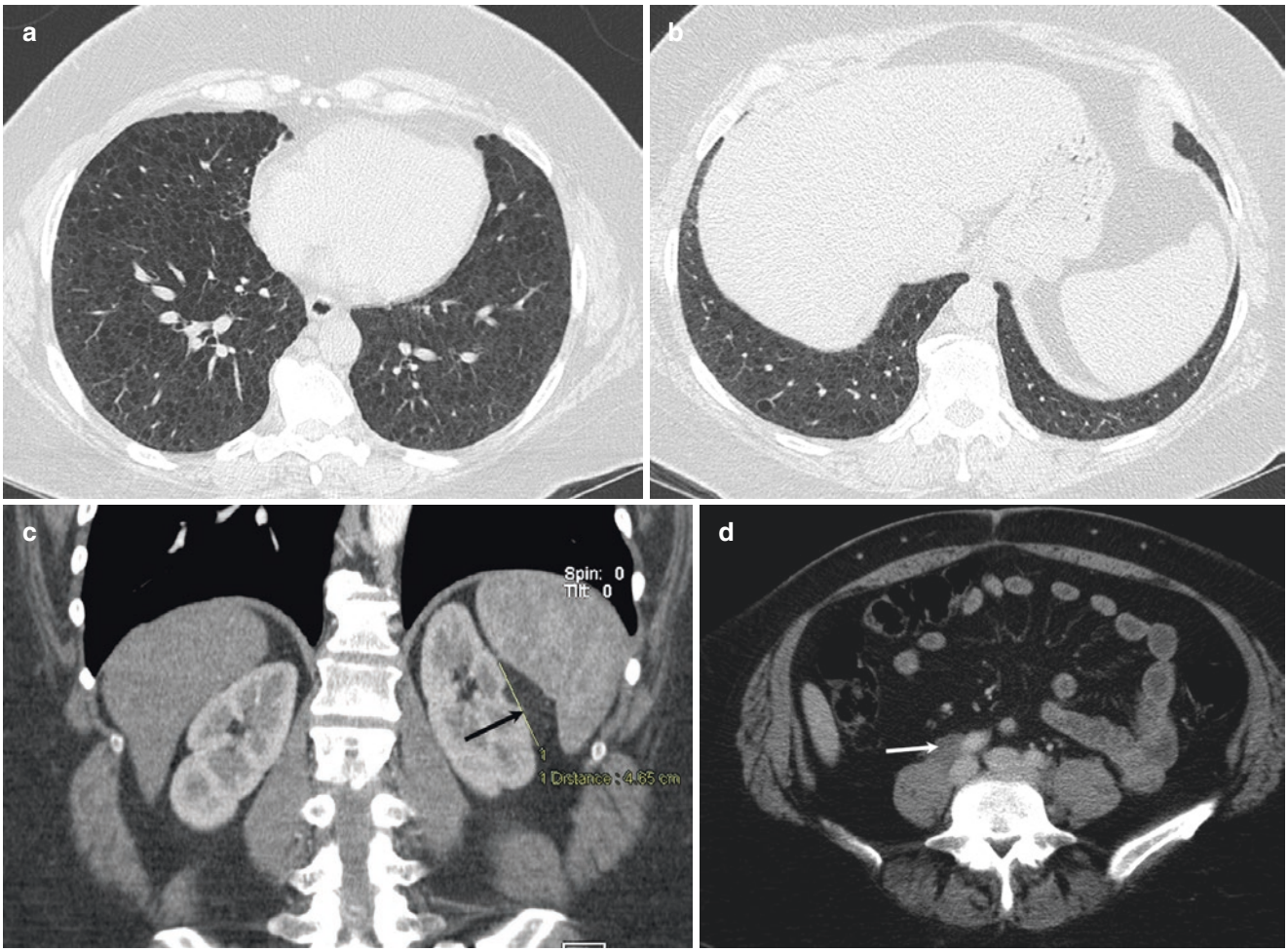

Fig. 3.10 A 38-year-old woman with LAM. (**a**, **b**) Axial CT images show innumerable small uniform round cysts in both lungs extending in costophrenic angles. (**c**) Coronal CT image of the abdomen shows a fat-containing angiomyolipoma in the left kidney (black arrow). (**d**) A small lymphangioma (white arrow) in the retroperitoneum

LAM should have an abdominal CT during work-up to identify angiomyolipoma and other abdominal lesions [5]. Apart from other neurological stigmata of TSC, women with LAM have a high prevalence of meningiomas; hence, the patients must be screened for it [6].

3.4 Pulmonary Langerhans Cell Histiocytosis

Langerhans cell histiocytosis (LCH) is a disease of young smokers between 20 and 40 years of age without any strong gender predilection. LCH is considered a disease related to smoking, and the affected individuals due to their age usually have an only modest cumulative smoking history [7, 8]. Most patients with LCH are symptomatic, and the most frequent presenting complaints include nonproductive cough and dyspnea [8]. Pneumothorax occurs frequently in patients over the course of their disease. Granulomatous infiltration of the distal bronchial walls with Langerhans cells results in the formation of bronchiolocentric pulmonary nodules that cavitate and result in the formation of bronchiolocentric cysts. HRCT features of LCH are described in Table 3.3 [7–10] (Figs. 3.11, 3.12, and 3.13).

A definite diagnosis of LCH requires histopathological confirmation of lung specimen obtained by video-assisted

Table 3.3 HRCT features of LCH

• Early stage shows multiple pulmonary nodules ranging in size from 1 to 10 mm in upper lungs
• Late stage shows cavitary nodules followed by thin-walled cysts in end stage
• Nodules that show cavitation in sequential scans are diagnostic of LCH
• Cysts are numerous and usually less than 1 cm in size but may be larger
• Cysts are irregularly shaped but always spare the costophrenic angles
• End-stage LCH is characterized by innumerable cysts with fibrosis in the upper and mid-lung

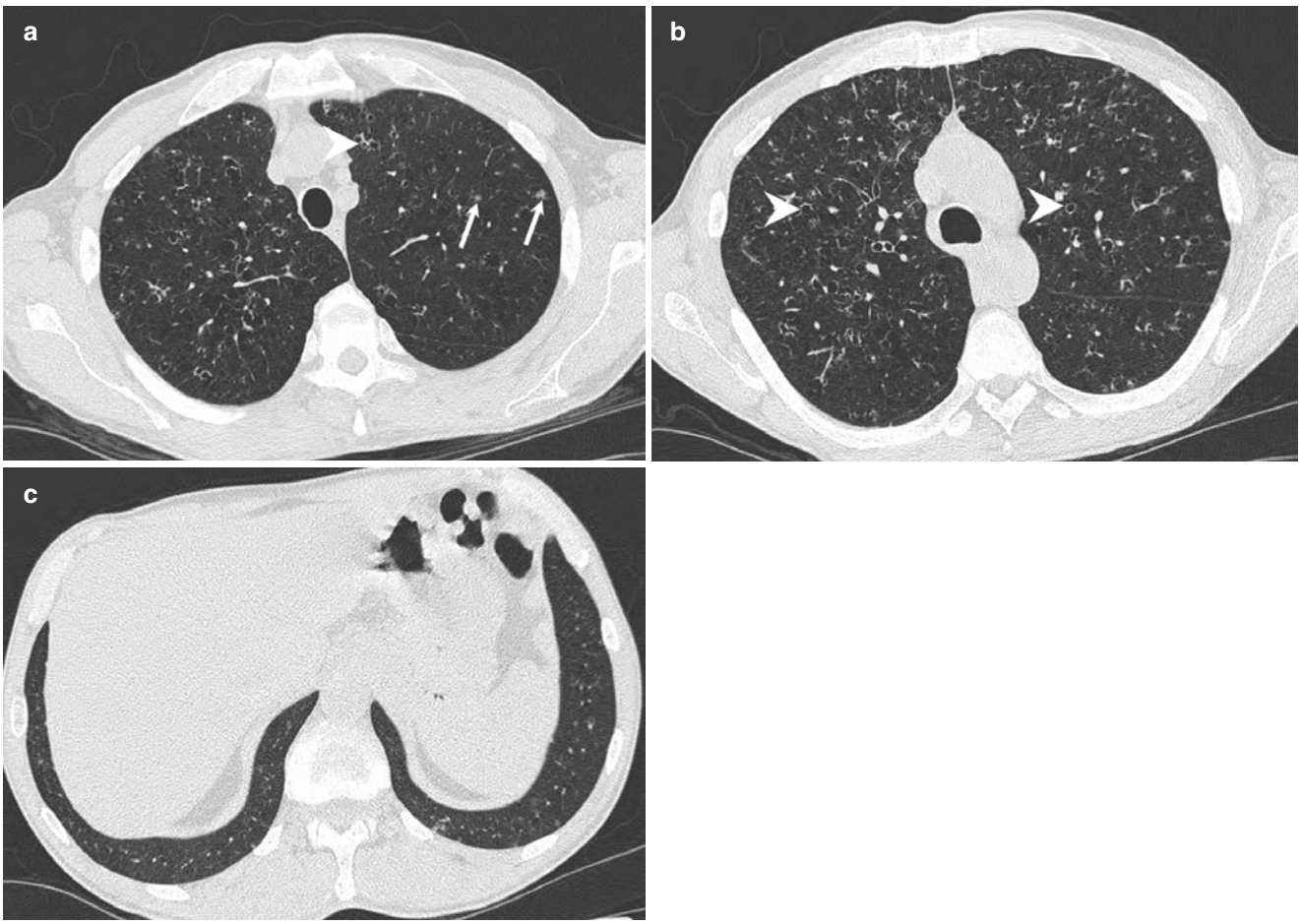

Fig. 3.11 A 59-year-old man with early LCH. (**a**, **b**) Axial CT images show nodules (white arrows) along with small cysts with a true wall suggesting that these cysts are cavities in preexisting nodules (arrowheads). (**c**) Axial image from lung bases shows sparing of costophrenic angles

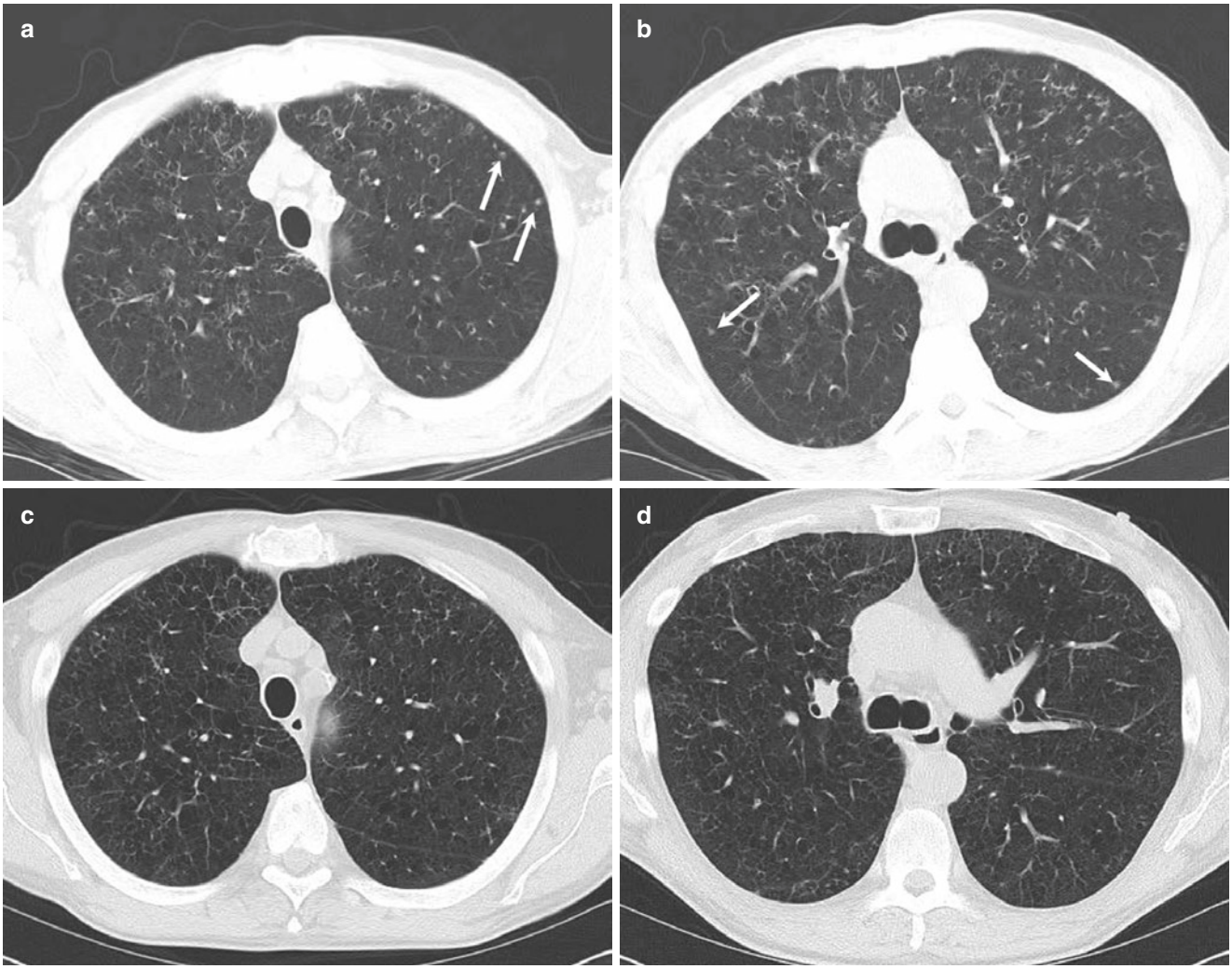

Fig. 3.12 A 55-year-old man with LCH on follow-up. (**a**, **b**) Axial images show bizarre-shaped cysts with definite walls and few scattered nodules (arrows). (**c**, **d**) CT scan images after 1 year show the disappearance of nodules. The cysts have increased in size and number, and they have lost their walls making it difficult to differentiate from emphysema

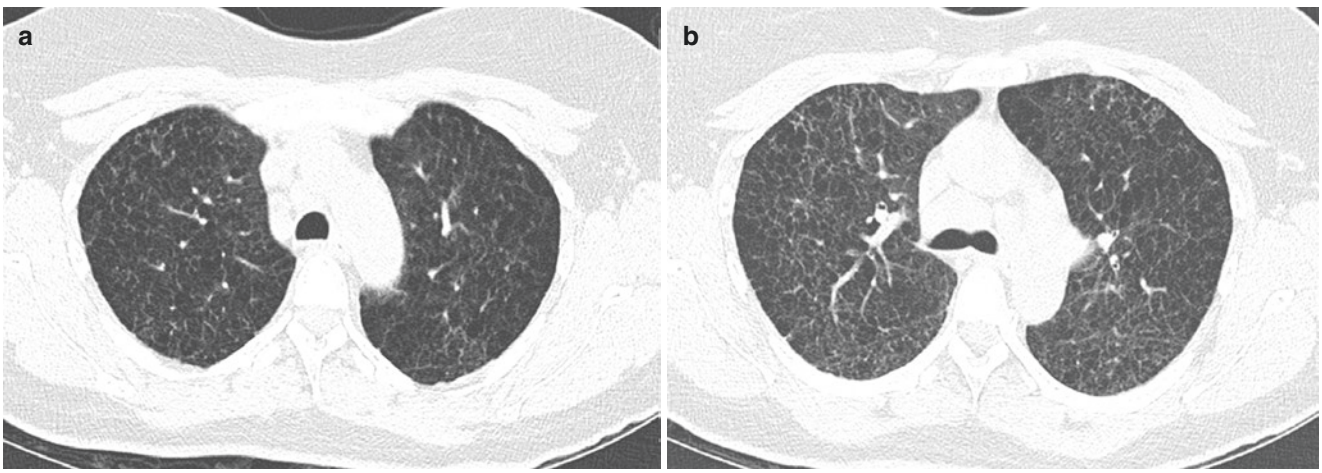

Fig. 3.13 LCH in a middle-age smoker with resolving pneumonia in the right lower lobe. (**a**–**d**) Axial CT images show bizarre-shaped cysts sparing the lung bases. Wall thickening in the cysts in the right lower lobe is due to resolving pneumonia

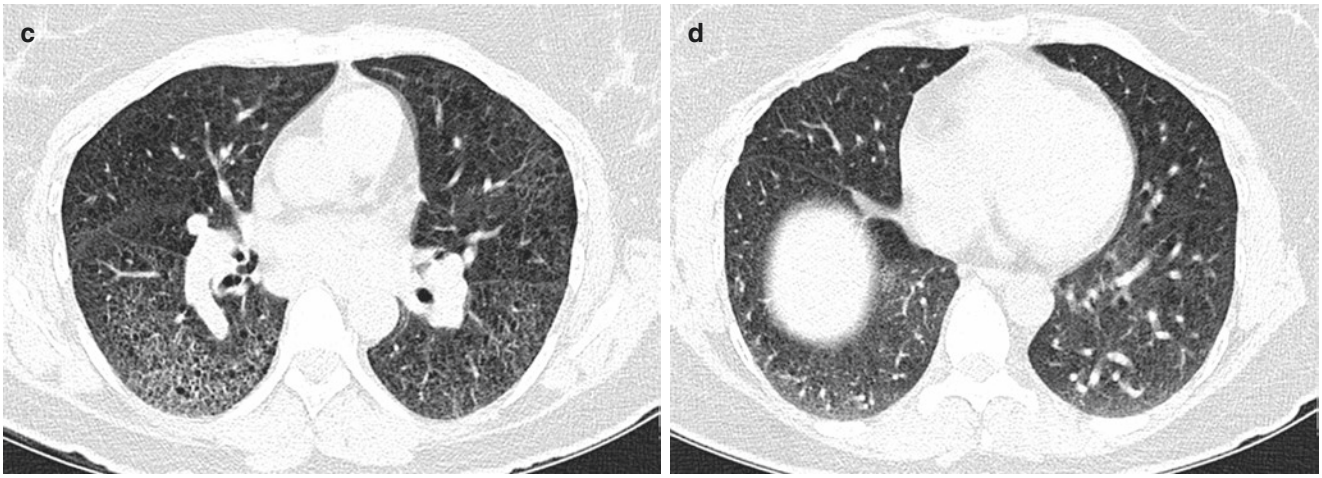

Fig. 3.13 (continued)

thoracoscopic surgery (VATS). On HRCT, the cysts of LCH can be differentiated from emphysema by the presence of well-defined walls. Moreover, lucent spaces of emphysema demonstrate an eccentric nodule representing displaced centrilobular artery. LCH is seen in young smokers, whereas emphysema is seen quite late in smokers. One should remember that often the lung tissue sample of a smoker shows the spectrum of smoking-related lung diseases including emphysema and LCH. LCH cysts can also be differentiated from LAM by their irregular shape and strong tendency of sparing the costophrenic angles even in end-stage disease.

3.5 Birt-Hogg-Dubé Syndrome

Birt-Hogg-Dubé syndrome is a rare autosomal dominant multisystem disorder affecting the skin, lungs, and kidneys [11]. Patients usually present in fourth and fifth decade or even later with pneumothorax or incidentally identified lung cysts. The diagnosis is suspected by a constellation of radiological and skin findings, but definite diagnosis requires genetic testing [10, 11]. The clinical and CT features are described in Table 3.4 [10–13] (Fig. 3.14). Diagnostic criteria for the diagnosis of Birt-Hogg-Dubé syndrome are detailed in Table 3.5. The cysts in this syndrome are less in number and larger in size compared to LAM and LCH. It is essential to request for clinical information in every patient with pulmonary cysts. Similar to LAM, a CT examination of the abdomen in suspected case of Birt-Hogg-Dubé syndrome provides useful information about the presence of renal neoplasms and lipomatas.

Table 3.4 Clinical and CT features of Birt-Hogg-Dubé syndrome

Lungs	• Less than 10 to more than 20 thin-walled cysts • Size of cysts ranges from 2 mm to 8 cm • Shape of cysts is variable: round, oval, and lentiform • Large cysts, particularly those in the lower lungs, have a lobulated multiseptated appearance • Lower lung predominant distribution in the craniocaudal plane • Cysts may predominate in paracardiac location
Abdomen	• Oncocytoma and renal cell carcinoma in kidneys • Multiple lipomata (mesentery, muscles, etc.)
Skin	• Fibrofolliculomas • Trichodiscomas • Acrochordons

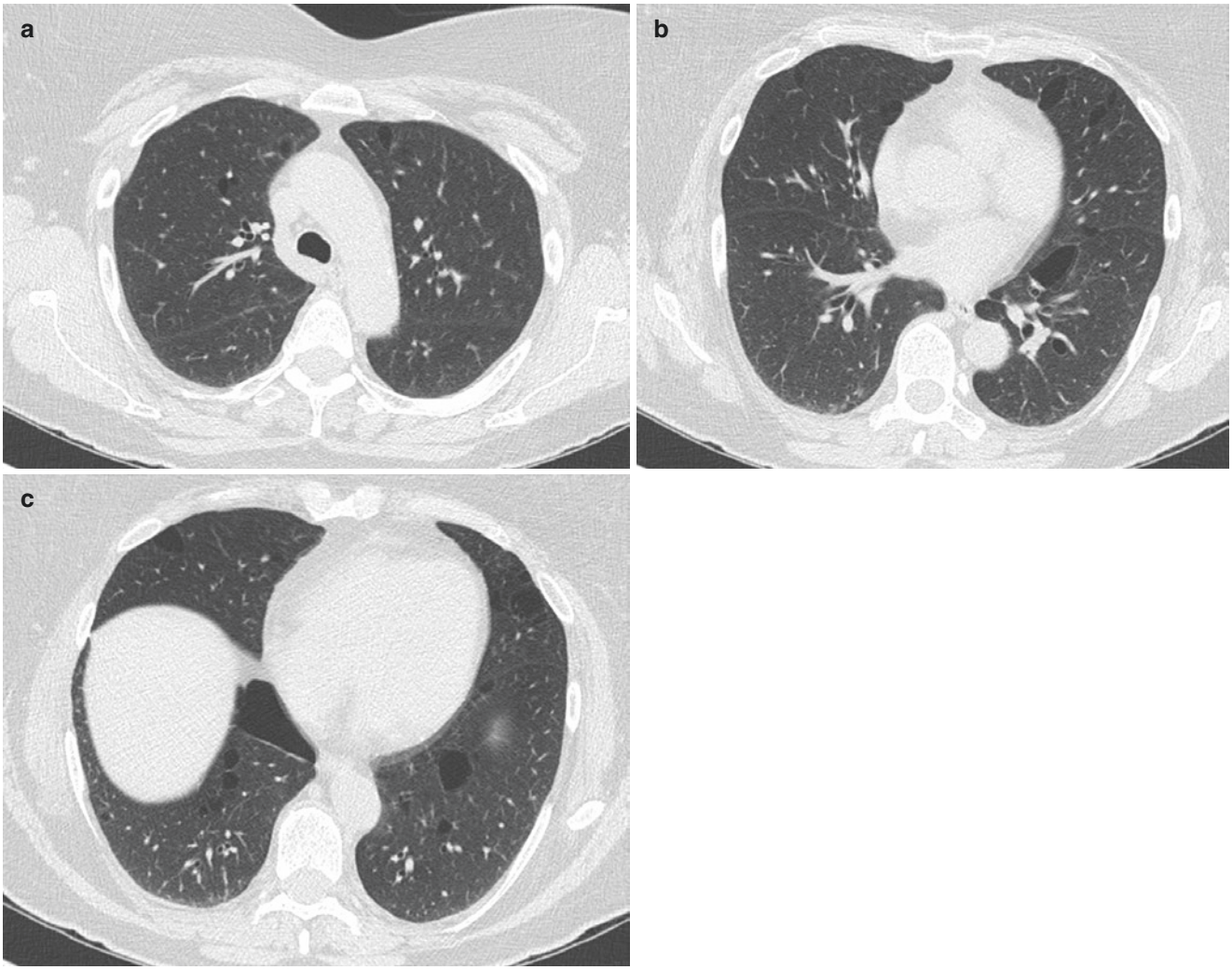

Fig. 3.14 Birt-Hogg-Dubé syndrome in a 43-year-old woman with renal cell carcinoma. (**a**–**c**) Axial CT images show variable-shaped cysts with few cysts in paracardiac location

Table 3.5 Diagnostic criteria for Birt-Hogg-Dubé syndrome[a]

Major criteria
• At least five fibrofolliculomas or trichodiscomas, at least one histologically confirmed, of adult onset
• Pathogenic FLCN germline mutation
Minor criteria
• Multiple lung cysts: bilateral basally located lung cysts with no other apparent cause, with or without spontaneous primary pneumothorax
• Renal cancer: early onset (<50 years) or multifocal or bilateral renal cancer or renal cancer of mixed chromophobe and oncocytic histology
• A first-degree relative with BHD

[a]Patients should fulfill one major or two minor criteria for diagnosis

3.6 Cystic Diseases Associated with Interstitial Lung Diseases

Two idiopathic interstitial diseases (DIP and LIP) with multiple pulmonary cysts can have similar HRCT appearance as above described cystic lung disorders. Hence, it is important to understand the imaging and clinical features of these two interstitial lung diseases.

3.6.1 Desquamative Interstitial Pneumonia (DIP)

Desquamative interstitial pneumonia (DIP) is an uncommon interstitial pneumonia that is strongly associated with cigarette smoking. Approximately 90% of patients with DIP are past or current smokers [14]. The DIP is occasionally observed to be associated with connective tissue diseases and drug-induced lung disease, while, infrequently, there may not be any association with any disease or exposure [14]. The HRCT features of the DIP are described in Table 3.6 [14, 15] (Figs. 3.15 and 3.16). The HRCT features are not specific and overlap with other interstitial lung diseases including respiratory bronchiolitis-associated interstitial lung disease (RBILD)

Table 3.6 HRCT features of DIP

• Bilateral patchy ground-glass opacities
• Ground-glass opacities are symmetrical in approximately 90% of cases
• Reticular opacities are not the dominant feature and are usually absent
• Subpleural and basal predominance of these opacities
• Presence of tiny cysts within the ground-glass opacities
• Emphysema may be present

in smokers as well as nonspecific interstitial pneumonia (NSIP) in nonsmokers. The presence of small cystic spaces within the ground-glass opacities is often helpful in the diagnosis of DIP. However, the final diagnosis requires a surgical lung biopsy. Smoking cessation is the primary treatment for DIP and may lead to disease regression.

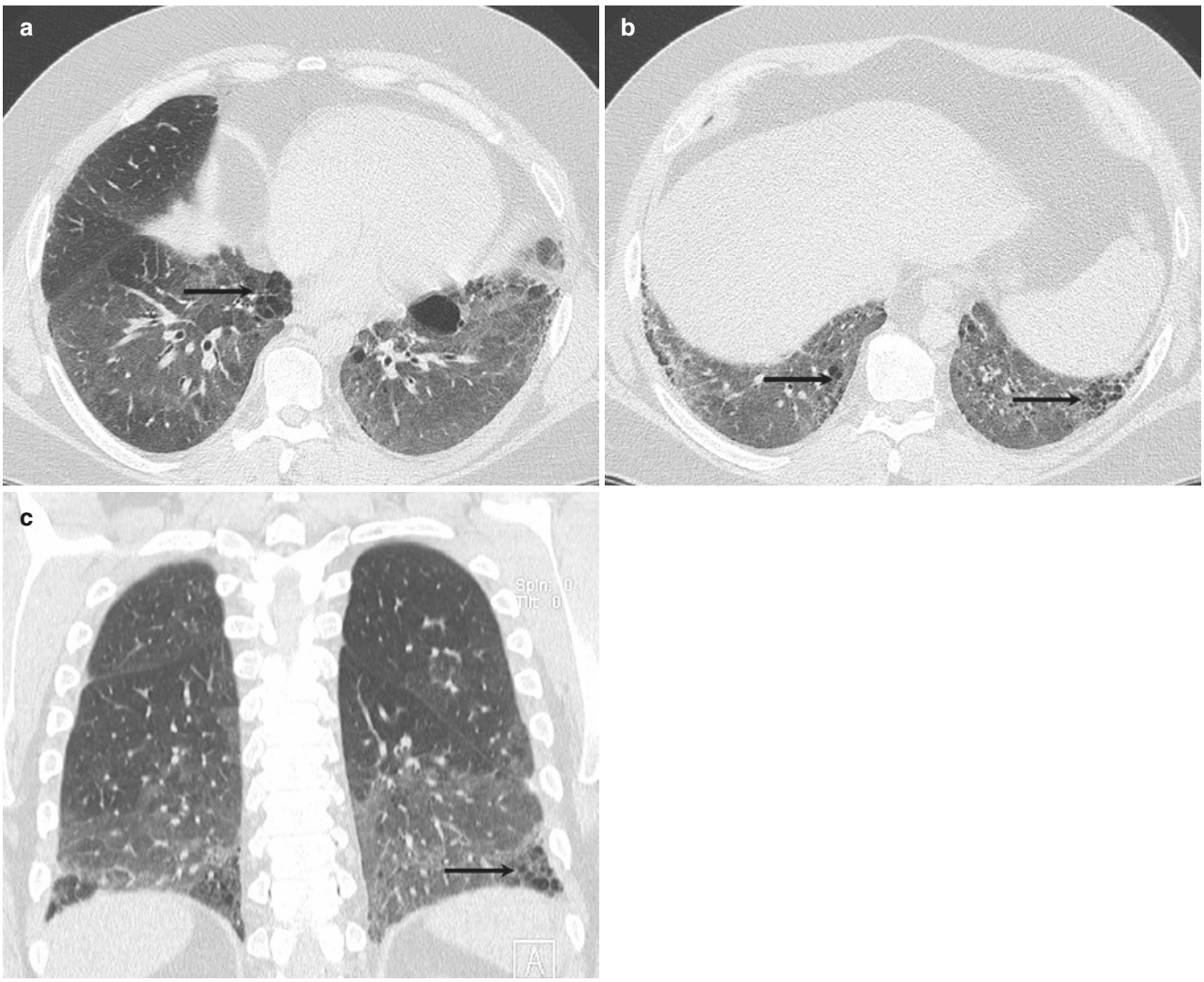

Fig. 3.15 A 34-year-old man with desquamative interstitial pneumonia on surgical lung biopsy. (**a**, **b**) Axial images and (**c**) coronal image show confluent ground-glass opacities in the lower lungs with small cyst formation (black arrows) within abnormal regions

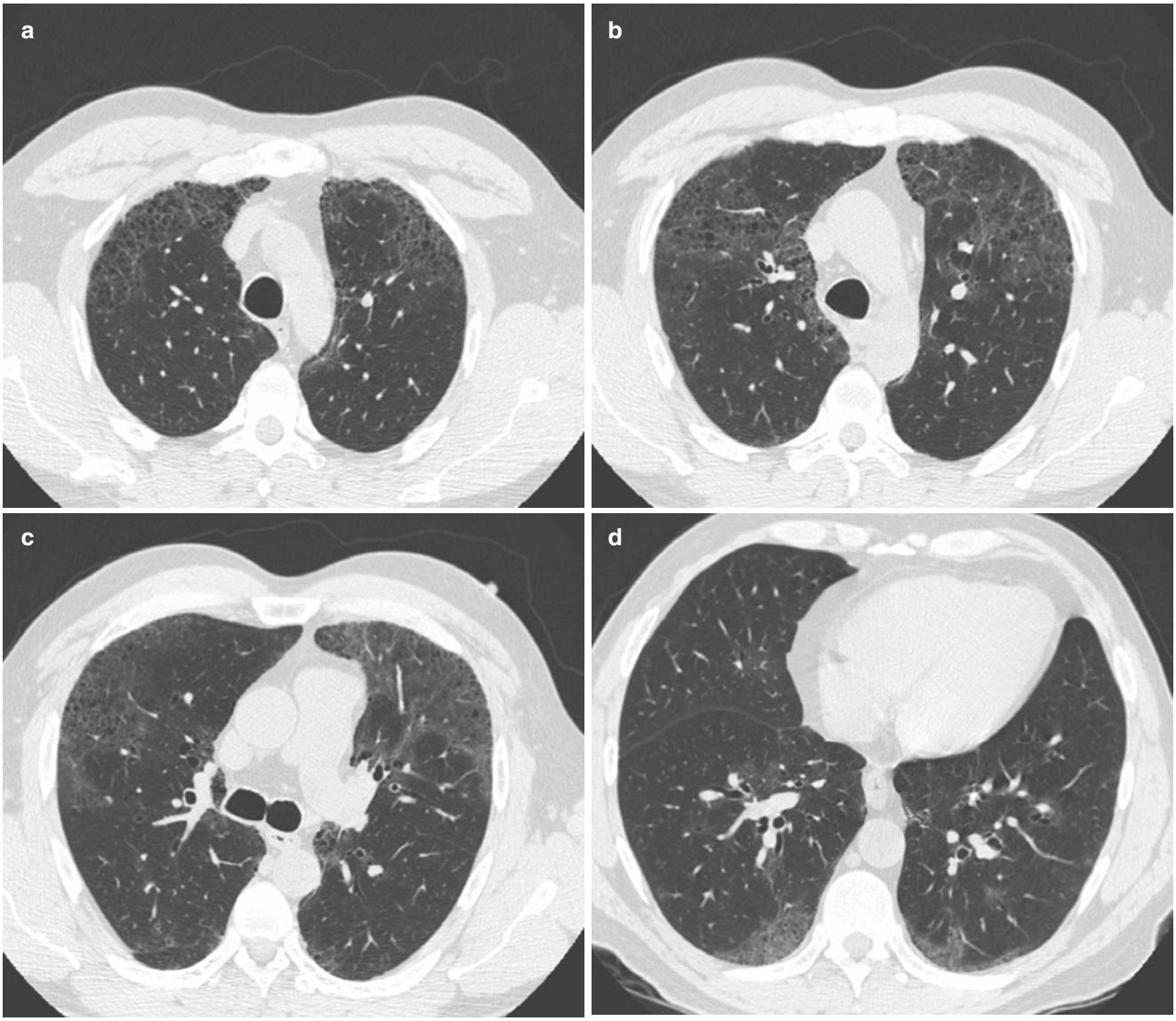

Fig. 3.16 A 50-year-old heavy smoker with desquamative interstitial pneumonia on histopathology. (**a**–**d**) Axial CT images show ground-glass opacities in both lungs with small cyst formation. Surgical lung biopsy was performed due to upper lung distribution of the lung abnormalities

3.6.2 Lymphocytic Interstitial Pneumonia (LIP)

Lymphocytic interstitial pneumonia (LIP) is a benign lymphoproliferative disorder characterized by interstitial infiltration by lymphocytes, plasma cells, and histiocytes. LIP is associated with systemic diseases like Sjogren syndrome, HIV infection, and multicentric Castleman's disease [10]. LIP has female predilection and is usually seen in the fifth decade. The HRCT features of LIP are described in Table 3.7 [10, 16, 17] (Figs. 3.17, 3.18, 3.19, and 3.20). Presence of cysts with ground-glass density in a patient with known systemic disease suggests the diagnosis of LIP. However, if there are larger nodules and consolidations, along with cysts, a malignant lymphoproliferative disorder, i.e., lymphoma, needs to be considered. Similar to other cystic diseases, the final diagnosis requires surgical lung biopsy.

Table 3.7 HRCT features of LIP

• Bilateral ground-glass opacities
• Mid- and basal predominance
• Poorly defined centrilobular nodules
• Interlobular septal thickening
• Larger and fewer cysts (contrast LAM) in peribronchial location

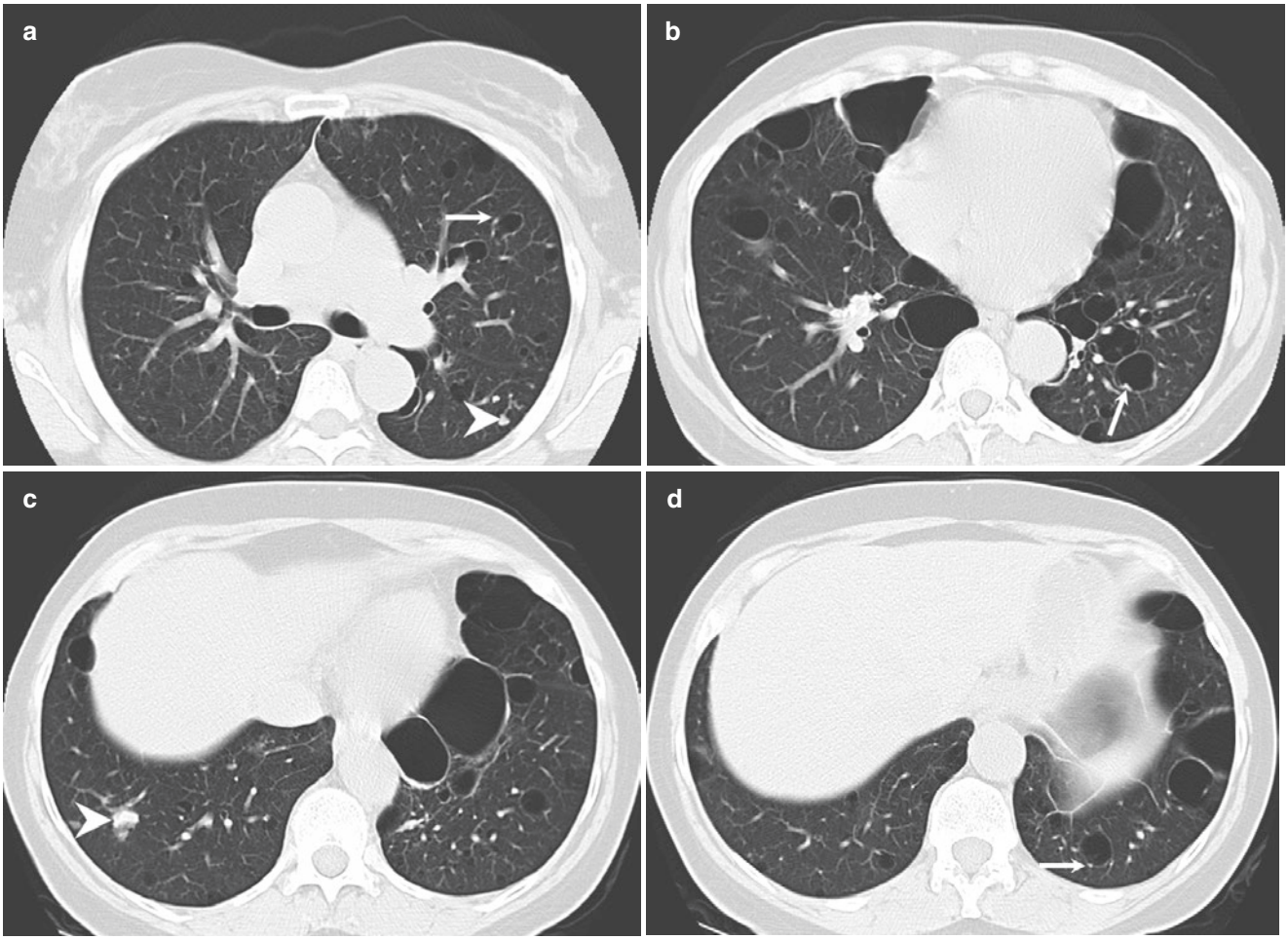

Fig. 3.17 A 60-year-old woman with Sjogren syndrome and LIP. (**a**–**d**) Axial CT images show multiple larger cysts with few nodules (arrowheads) in both lungs. The cysts tend to be distributed along bronchovascular bundles as suggested by an eccentric dot (white arrows) representing displaced vessel. Biopsy of the largest nodule revealed lymphoid hyperplasia

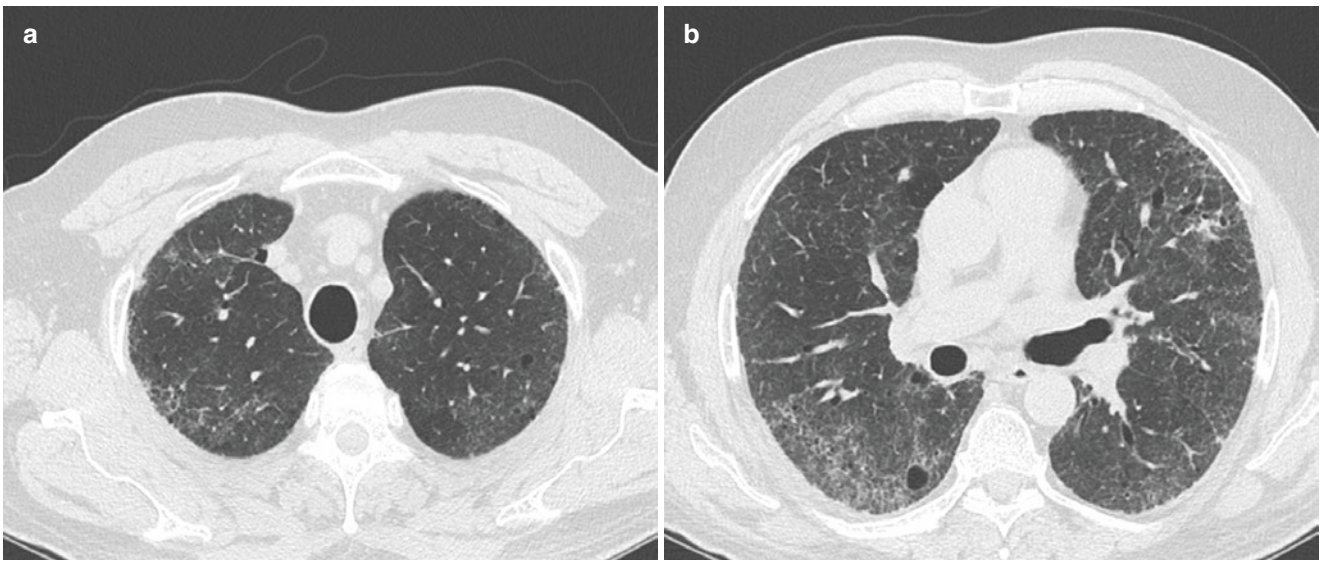

Fig. 3.18 A 65-year-old woman with Sjogren syndrome. (**a**–**d**) Axial images show multiple cysts scattered in both lungs with lower lung predominant reticular opacities, ground-glass opacities, and traction bronchiectasis

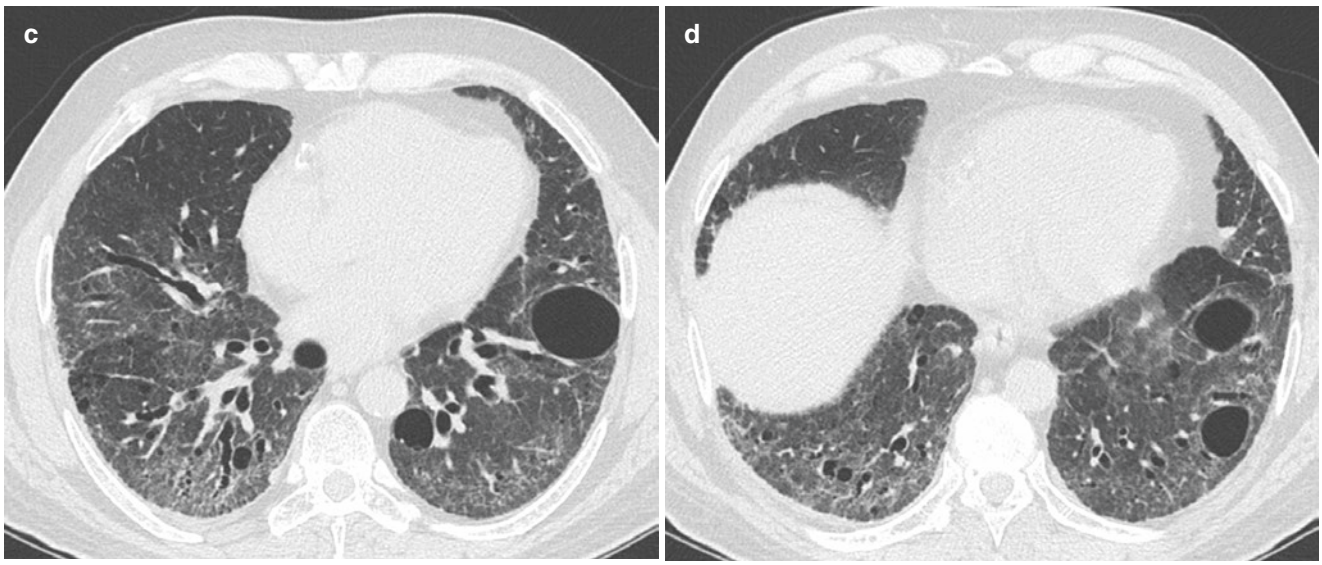

Fig. 3.18 (continued)

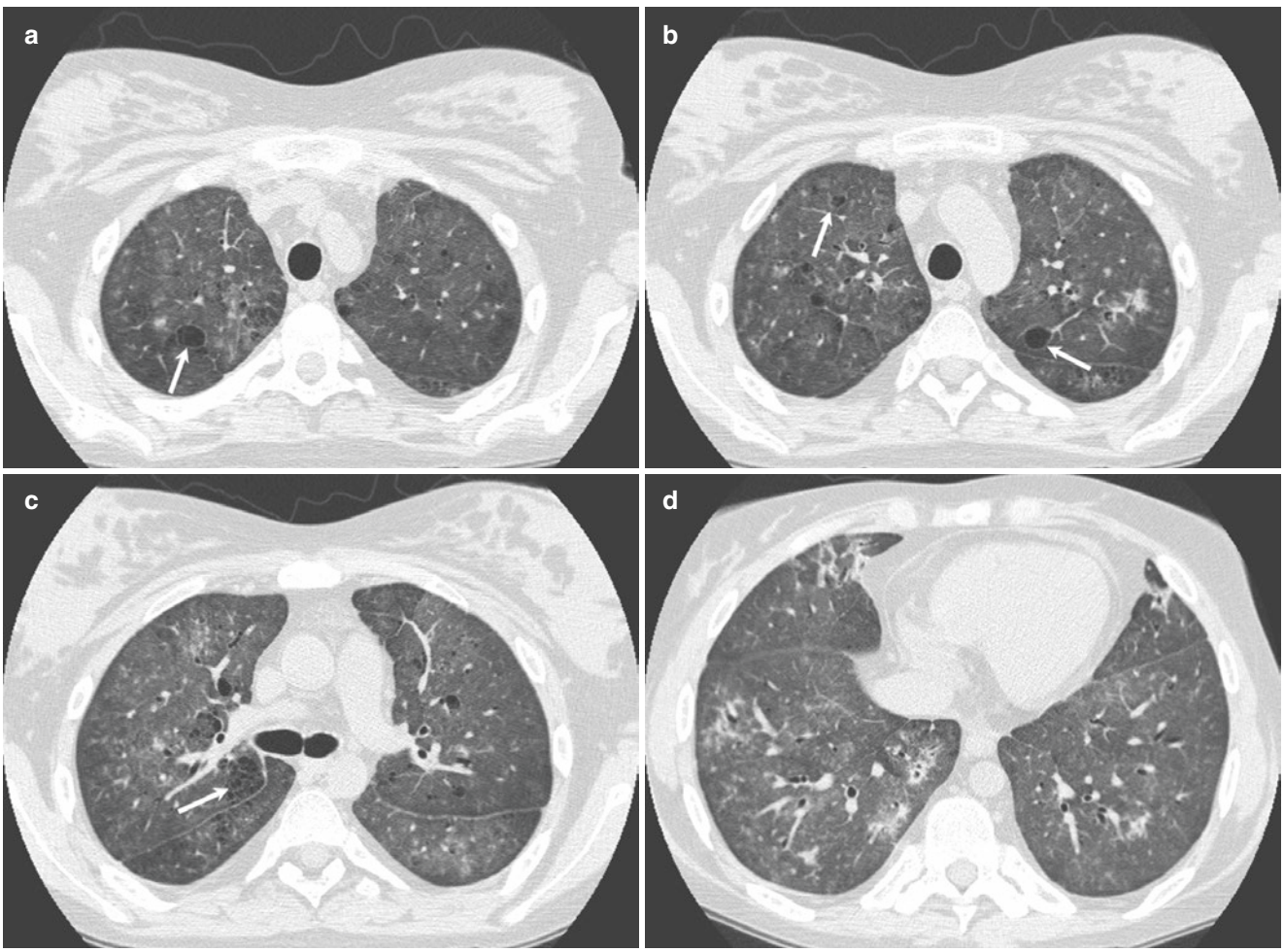

Fig. 3.19 A 55-year-old woman with biopsy-proven LIP in the background of immunosuppressive status from HIV infection. (**a**–**d**) Axial images show few cysts (arrows) scattered in lungs along with nodular as well as diffuse ground-glass opacities and peribronchial nodular opacities. Note that the cysts are located away from areas of ground-glass opacities (unlike DIP)

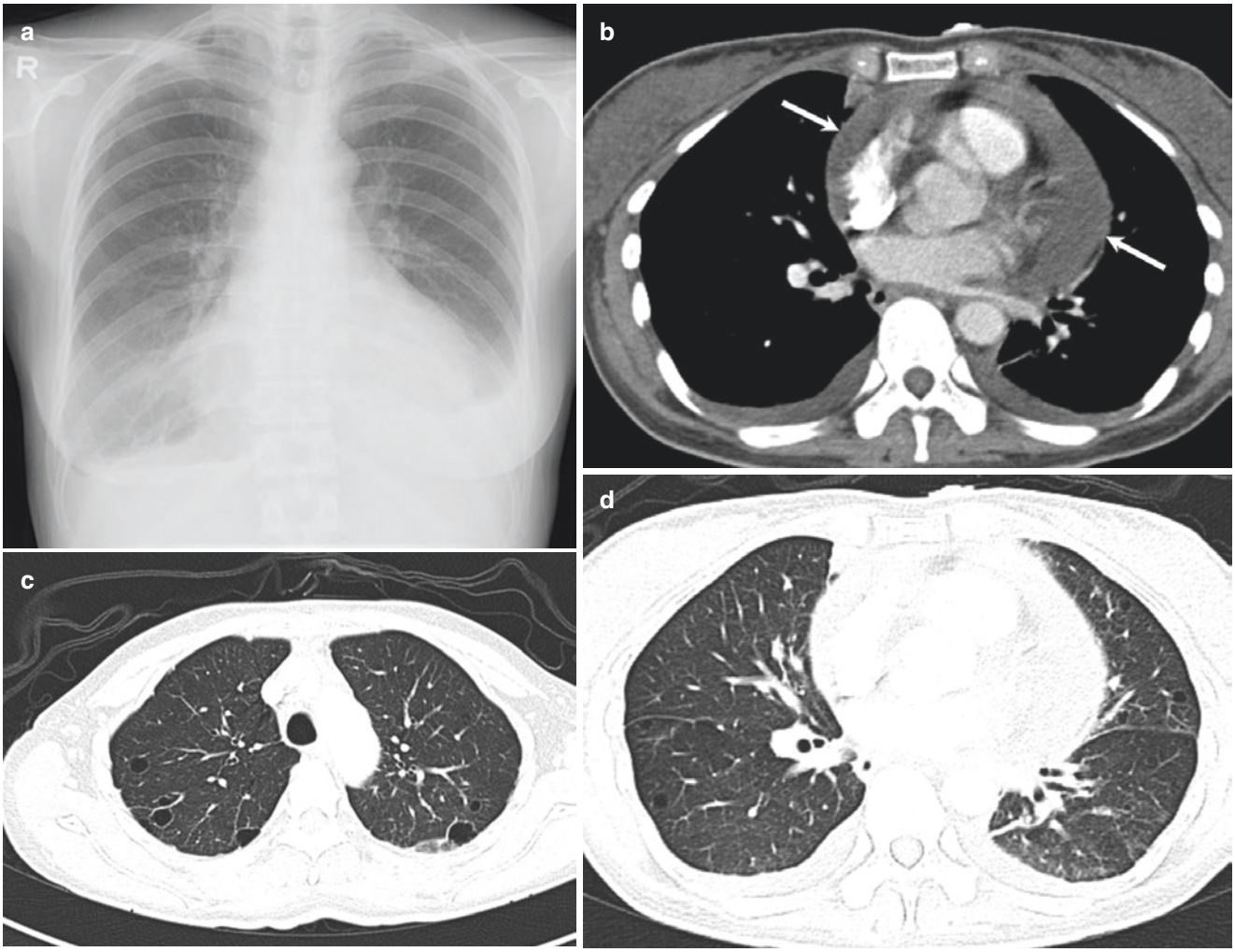

Fig. 3.20 A 58-year-old woman with mixed connective tissue disorder and LIP. (**a**) Frontal chest radiograph shows bilateral pleural effusions. (**b**) Axial CT image in soft tissue window shows bilateral pleural effusions and a pericardial effusion (white arrows). (**c**, **d**) Axial CT images show few scattered cysts in both lungs. Bilateral pleural effusions and pericardial effusion serve as a clue to the presence of underlying collagen vascular disease

3.7 Pneumocystis jirovecii Pneumonia (PJP)

Pneumocystis jirovecii pneumonia (PJP) is an atypical pulmonary infection caused by *Pneumocystis jirovecii* in an immunocompromised population with CD4 counts of less than 200 cells/mm^3. Rarely, it can also be seen in a patient with CD4 counts of more than 200. PJP is a dry infection characterized by extensive ground-glass opacities without mediastinal lymphadenopathy or pleural effusion [18, 19]. The ground-glass opacities are usually central with sparing of the subpleural region [18]. During the course of the disease, the HRCT may show multiple thin-walled pulmonary cysts of varying sizes (Fig. 3.21). These cysts are distributed within the ground-glass opacities and may lead to spontaneous pneumothorax. It is essential for the radiologist to obtain a proper history of the patient to avoid misinterpreting PJP infection as a pulmonary cystic disorder. The cysts related to PJP infection are pneumatoceles that resolve on the treatment of underlying fungal infection. Confirmation of the diagnosis requires identification of organisms in sputum or bronchoalveolar lavage. Monoclonal antibodies for detecting *P. jirovecii* in induced sputum are also available.

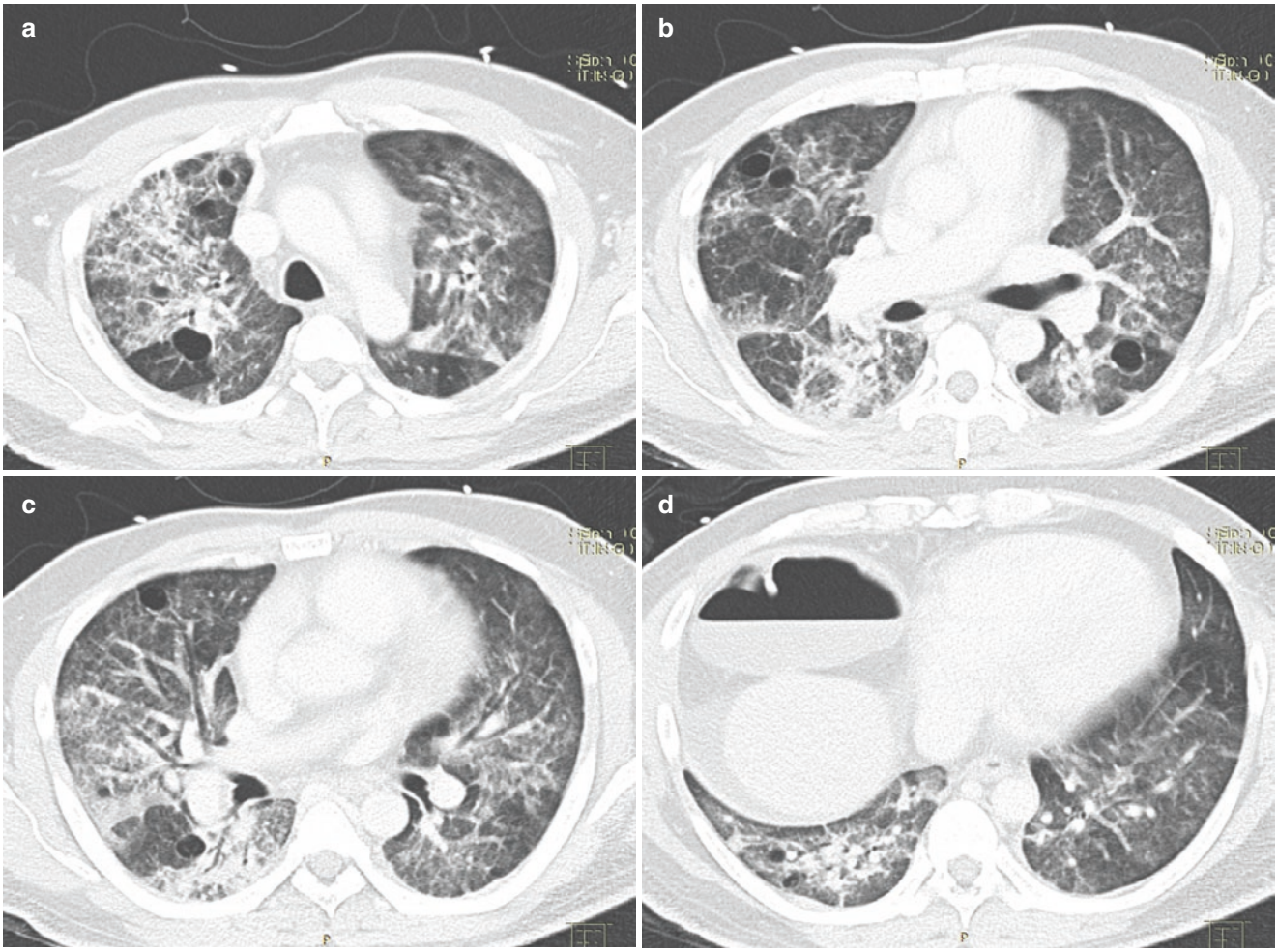

Fig. 3.21 *Pneumocystis jirovecii* pneumonia in a 50-year-old immunosuppressed man presenting to the emergency department with high fever. (**a**–**d**) Axial CT images show perihilar ground-glass opacities in both lungs with few scattered cysts. Note there is no pleural effusion or lymphadenopathy

3.8 Amyloidosis-Associated Cystic Lung Disease

Amyloid-associated cystic lung disease is extremely rare and can occur with or without underlying collagen vascular disease. The cysts are usually more than ten in number, thin-walled (<2 mm), and round or lobulated in shape [20]. The cysts may show internal septa and are located in subpleural region or along bronchovascular bundles (Figs. 3.22 and 3.23). Calcified and noncalcified nodules may be present. Pulmonary mucosa-associated lymphoid tissue (MALT) is present in up to one-third of cases; hence, all nodules must be carefully evaluated [20].

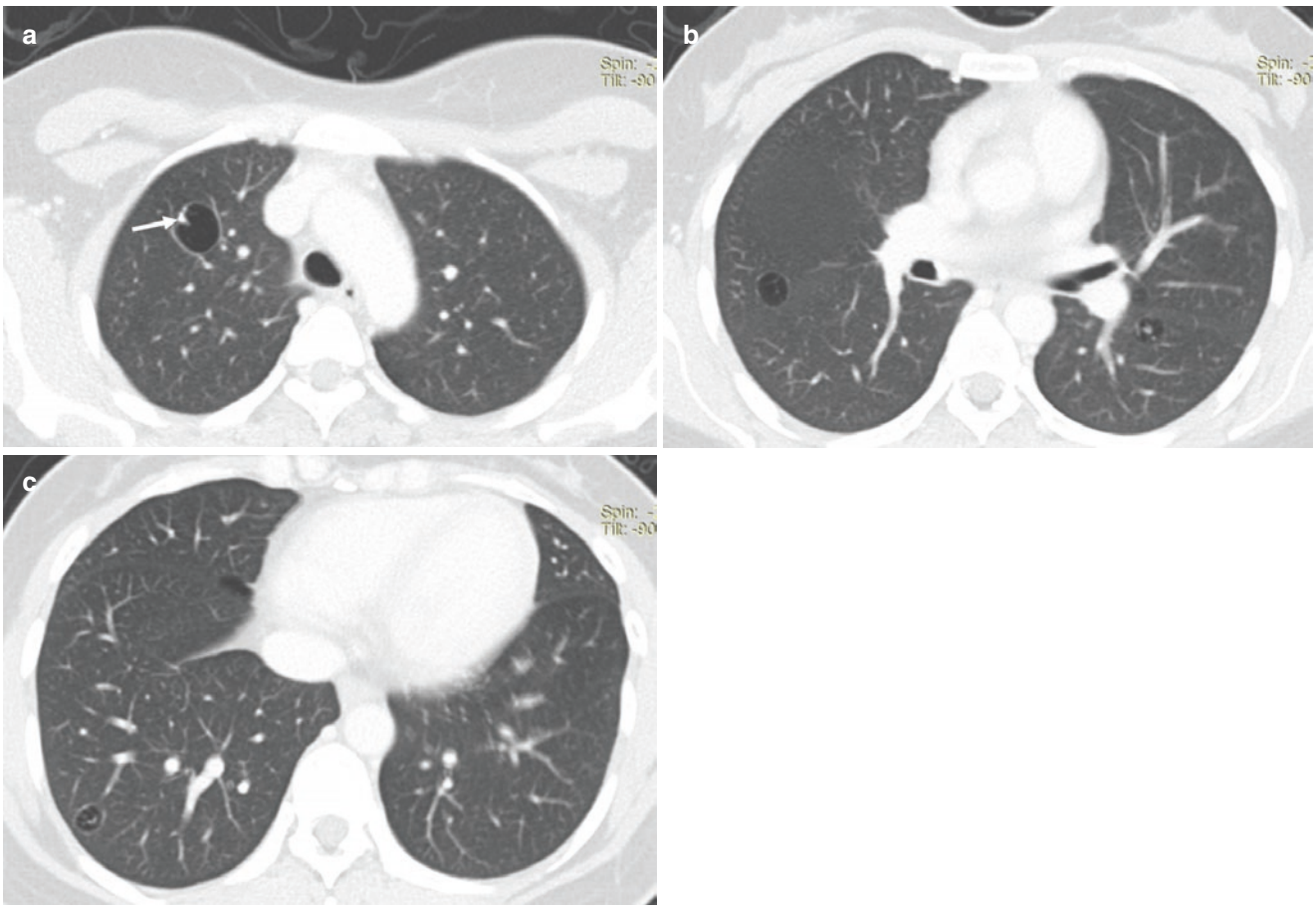

Fig. 3.22 Amyloid-associated cystic lung disease in a 34-year-old woman with biopsy-proven extensive pharyngeal and laryngeal amyloidosis. (**a**–**c**) Axial CT images show multiple cysts along the bronchovascular bundle and subpleural region. Few cysts show internal septa with an eccentric focus of calcification in the right upper lobe cyst (arrow)

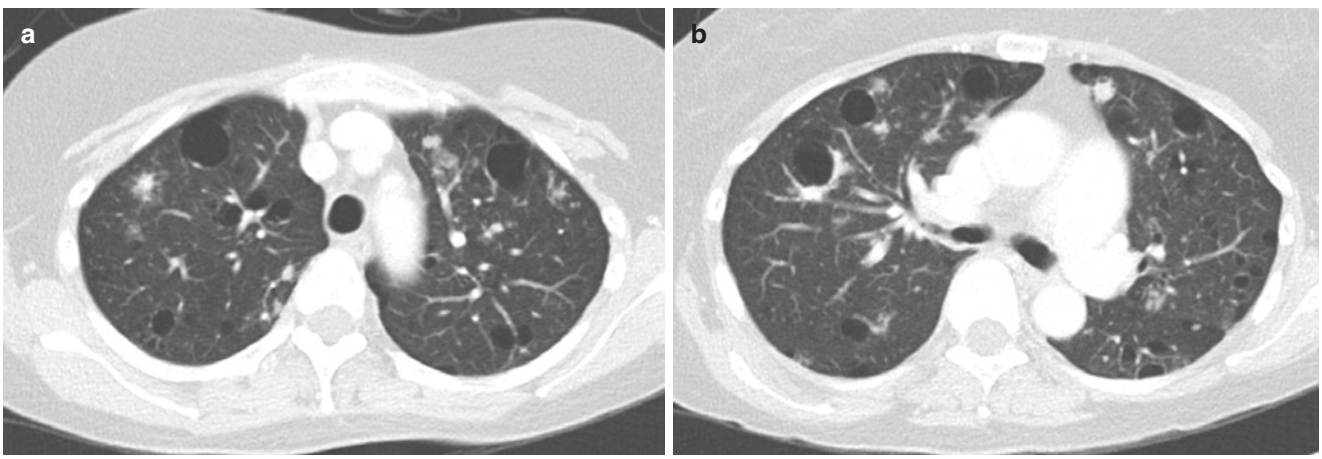

Fig. 3.23 A 49-year-old woman with cystic and nodular pulmonary amyloidosis. (**a**–**c**) Axial CT images show multiple nodular opacities and cysts of varying sizes. The cysts are subpleural and peribronchovascular in location. (**d**) Coronal CT reconstruction shows the same findings. The cyst in the right lower lobe shows internal septa

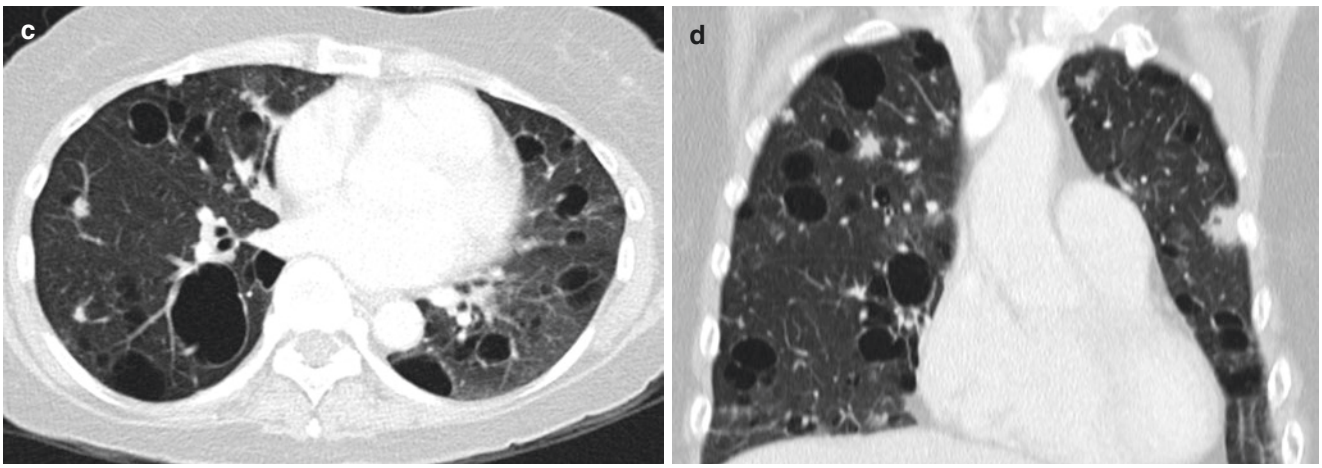

Fig. 3.23 (continued)

References

1. Hansell DM, Bankier AA, MacMahon H, McLoud TC, Muller NL, Remy J. Fleischner Society: glossary of terms for thoracic imaging. Radiology. 2008;246(3):697–722.
2. Seaman DM, Meyer CA, Gilman MD, McCormack FX. Diffuse cystic lung disease at high-resolution CT. Am J Roentgenol. 2011;196(6):1305–11.
3. Abbott GF, Rosado-de-Christenson ML, Frazier AA, Franks TJ, Pugatch RD, Galvin JR. Lymphangioleiomyomatosis: radiologic-pathologic correlation. Radiographics. 2005;25(3):803–28.
4. Cudzilo CJ, Szczesniak RD, Brody AS, Rattan MS, Krueger DA, Bissler JJ, Franz DN, McCormack FX, Young LR. Lymphangioleiomyomatosis screening in women with tuberous sclerosis. Chest J. 2013;144(2):578–85.
5. Johnson SR, Cordier JF, Lazor R, Cottin V, Costabel U, Harari S, Reynaud-Gaubert M, Boehler A, Brauner M, Popper H, Bonetti F. European Respiratory Society guidelines for the diagnosis and management of lymphangioleiomyomatosis. Eur Respir J. 2010;35(1):14–26.
6. Moss J, DeCastro R, Patronas NJ, Taveira-DaSilva A. Meningiomas in lymphangioleiomyomatosis. JAMA. 2001;286(15):1879–81.
7. Abbott GF, Rosado-de-Christenson ML, Franks TJ, Frazier AA, Galvin JR. From the archives of the AFIP: pulmonary Langerhans cell histiocytosis. Radiographics. 2004;24(3):821–41.
8. Vassallo R, Ryu JH, Schroeder DR, Decker PA, Limper AH. Clinical outcomes of pulmonary Langerhans'-cell histiocytosis in adults. N Engl J Med. 2002;346(7):484–90.
9. Castoldi MC, Verrioli A, De Juli E, Vanzulli A. Pulmonary Langerhans cell histiocytosis: the many faces of presentation at initial CT scan. Insights Imaging. 2014;5(4):483–92.
10. Raoof S, Bondalapati P, Vydyula R, Ryu JH, Gupta N, Raoof S, Galvin J, Rosen MJ, Lynch D, Travis W, Mehta S. Cystic lung diseases: algorithmic approach. Chest J. 2016;150(4):945–65.
11. Menko FH, Van Steensel MA, Giraud S, Friis-Hansen L, Richard S, Ungari S, Nordenskjöld M, vO Hansen T, Solly J, Maher ER, European BHD Consortium. Birt-Hogg-Dubé syndrome: diagnosis and management. Lancet Oncol. 2009;10(12):1199–206.
12. Agarwal PP, Gross BH, Holloway BJ, Seely J, Stark P, Kazerooni EA. Thoracic CT findings in Birt-Hogg-Dube syndrome. Am J Roentgenol. 2011;196(2):349–52.
13. Zamora CA, Rowe SP, Horton KM. Case 218: Birt-Hogg-Dubé syndrome. Radiology. 2015;275(3):923–7.
14. Ryu JH, Myers JL, Capizzi SA, Douglas WW, Vassallo R, Decker PA. Desquamative interstitial pneumonia and respiratory bronchiolitis-associated interstitial lung disease. Chest J. 2005;127(1):178–84.
15. Hartman TE, Primack SL, Swensen SJ, Hansell D, McGuinness G, Müller NL. Desquamative interstitial pneumonia: thin-section CT findings in 22 patients. Radiology. 1993;187(3):787–90.
16. Johkoh T, Müller NL, Pickford HA, Hartman TE, Ichikado K, Akira M, Honda O, Nakamura H. Lymphocytic interstitial pneumonia: thin-section CT findings in 22 patients. Radiology. 1999;212(2):567–72.
17. Cha SI, Fessler MB, Cool CD, Schwarz MI, Brown KK. Lymphoid interstitial pneumonia: clinical features, associations and prognosis. Eur Respir J. 2006;28(2):364–9.
18. Kanne JP, Yandow DR, Meyer CA. Pneumocystis jiroveci pneumonia: high-resolution CT findings in patients with and without HIV infection. Am J Roentgenol. 2012;198(6):W555–61.
19. Hidalgo A, Falco V, Mauleon S, Andreu J, Crespo M, Ribera E, Pahissa A, Caceres J. Accuracy of high-resolution CT in distinguishing between Pneumocystis carinii pneumonia and non-Pneumocystis carinii pneumonia in AIDS patients. Eur Radiol. 2003;13(5):1179–84.
20. Zamora AC, White DB, Sykes AM, Hoskote SS, Moua T, Eunhee SY, Ryu JH. Amyloid-associated cystic lung disease. Chest. 2016;149(5):1223–33.

Imaging of Pulmonary Nodules

4

Ashish Chawla

4.1 Introduction

Nodules by definition are lung opacities less than 3 cm in size [1]. Subcentimeter pulmonary nodules always pose a dilemma to reporting radiologist. Radiologist's role doesn't get over by just describing the number and size of the nodules. It is important to guide the referring physician and patient about the next course of action that may range from follow-up CT to percutaneous CT-guided intervention. In certain cases, CT can provide additional clues for the underlying diseases accounting for pulmonary nodules.

4.2 Differential Diagnosis of Pulmonary Nodules

CT appearance of subcentimeter pulmonary nodules is nonspecific with overlapping features. However, the larger-sized nodules may show some distinctive features that can help in narrowing the differential diagnosis (Table 4.1) (Figs. 4.1, 4.2, 4.3, 4.4, 4.5, 4.6, 4.7, 4.8, 4.9, 4.10, 4.11, 4.12, 4.13, 4.14, 4.15, 4.16, 4.17, 4.18, and 4.19). In many instances, accurate diagnosis can be made with the help of clinical information, other radiological investigations, and lab findings. In a patient with a known primary malignancy, every pulmonary nodule is considered as metastasis until proven otherwise. Moreover, the metastases display a spectrum of CT morphology depending on primary cancer. Septic pulmonary embolism is the working diagnosis in a patient with multiple characteristic pulmonary nodules (subpleural wedge-shaped nodules or nodules with cavities or air-fluid level) and clinical features of sepsis. The diagnosis is confirmed by rapid evolution or resolution on fol-

Table 4.1 Differential diagnoses of pulmonary nodules

Nodules with calcification	• Metastases (sarcomas, colonic, ovarian, breast, and papillary thyroid cancer) • Granulomas • Amyloidosis • Hamartoma • Malignancy engulfing granuloma
Nodules with cavitation	• Metastases (squamous cell carcinoma of the head and neck, transitional cell carcinoma of urinary bladder and angiosarcoma) • Septic pulmonary embolism • Granulomatosis with polyangiitis • Tuberculosis • Rheumatoid nodules
Nodules with halo sign	• Hemorrhagic metastases (angiosarcoma, thyroid cancer, renal cell carcinoma, choriocarcinoma, and melanoma) • Kaposi's sarcoma • Granulomatosis with polyangiitis • Invasive aspergillosis • Organizing pneumonia
Nodules with fat	• Hamartoma (may also show "popcorn" calcification) • Angiomyolipoma
Nodules with air-fluid level	• Septic pulmonary embolism • Abscess • Malignancy
Nodules with air-trapping	• Any nodular disease with background of constrictive bronchiolitis • DIPNECH
Nodules connected to vessels	• Arteriovenous malformation • Aneurysm
Multiple ground-glass density nodules	• Multifocal adenocarcinoma • Metastases • Multifocal micronodular pneumocyte hyperplasia
Isolated subpleural nodules	• Lymph nodes • Dependent atelectasis • Septic pulmonary embolism • Perilymphatic nodules

A. Chawla (✉)
Department of Diagnostic Radiology, Khoo Teck Puat Hospital, Singapore, Singapore

A. Chawla (ed.), *Thoracic Imaging*, https://doi.org/10.1007/978-981-13-2544-1_4

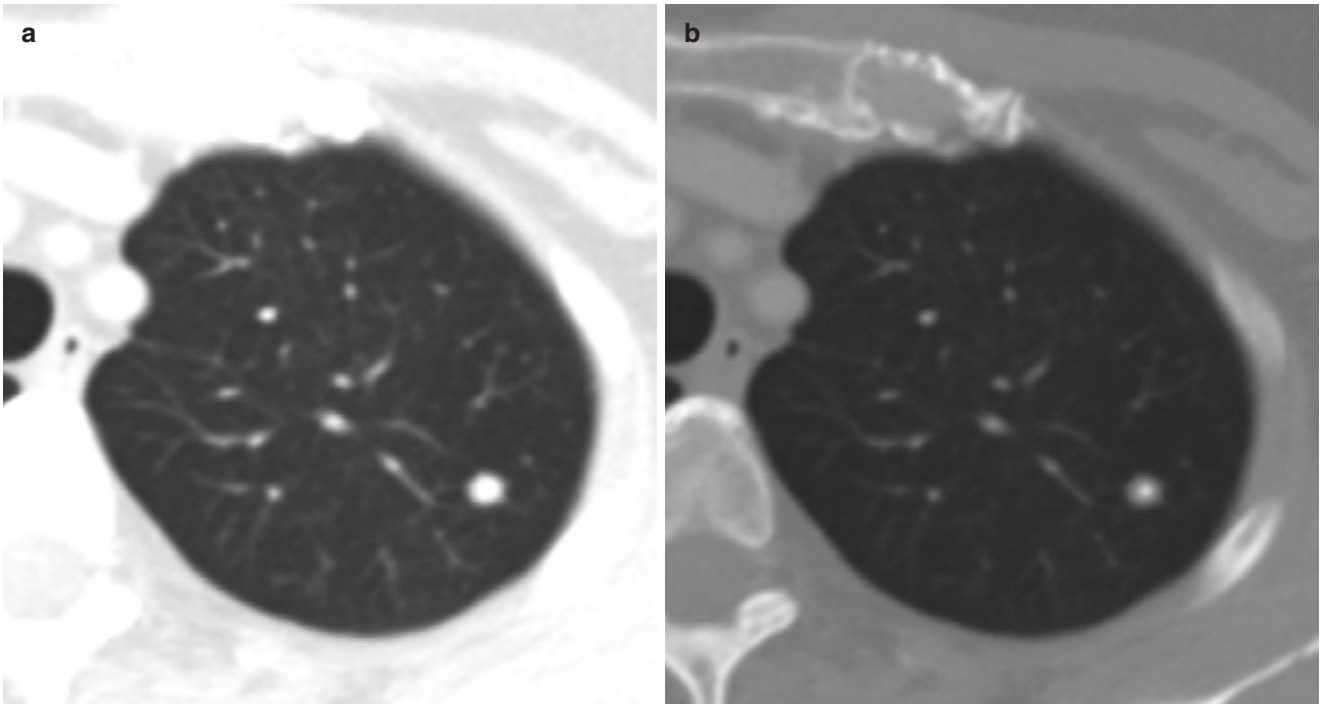

Fig. 4.1 Centrally calcified granuloma. (**a**, **b**) Axial CT images show a well-circumscribed solid nodule with central calcification, typical of a healed granuloma

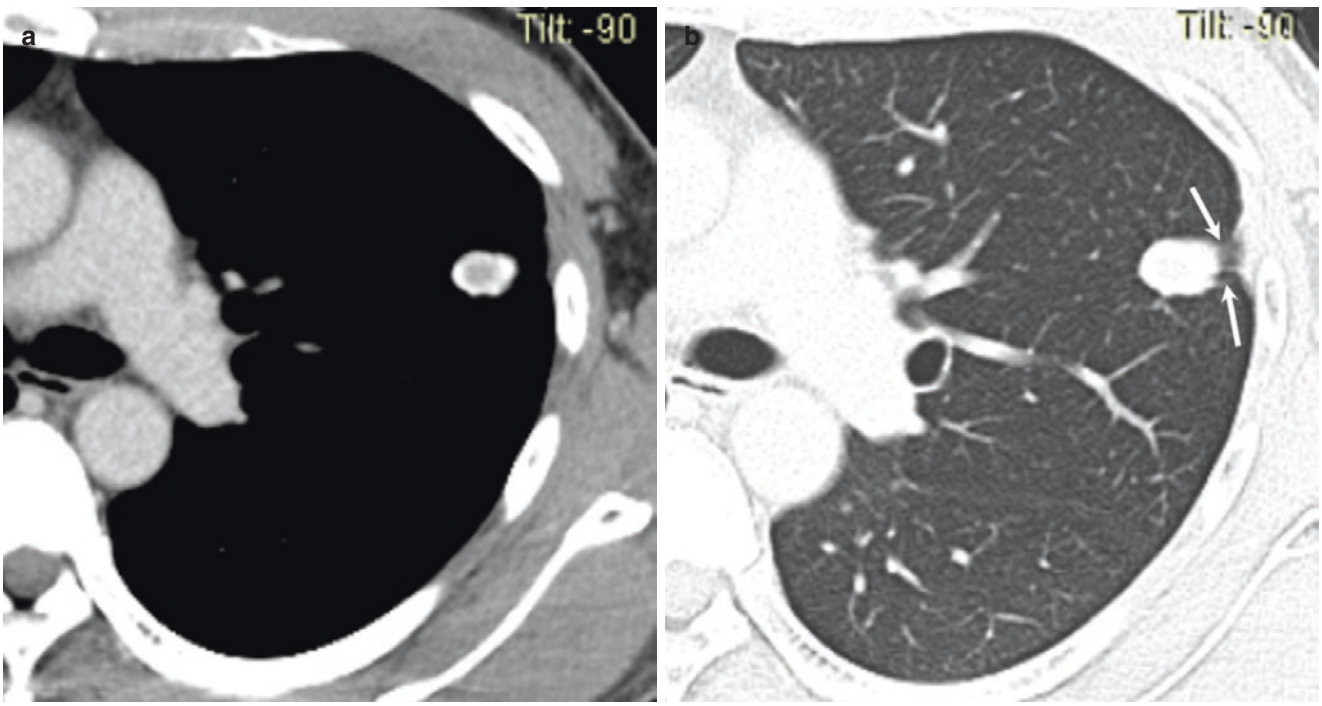

Fig. 4.2 Peripherally calcified granuloma in an asymptomatic patient. (**a**, **b**) Axial CT images show a well-marginated solid nodule with peripheral calcification. Note pleural tags (arrows) that can be seen in tuberculomas as well as adenocarcinomas. CT-guided percutaneous biopsy revealed *Mycobacterium bacilli* with caseation

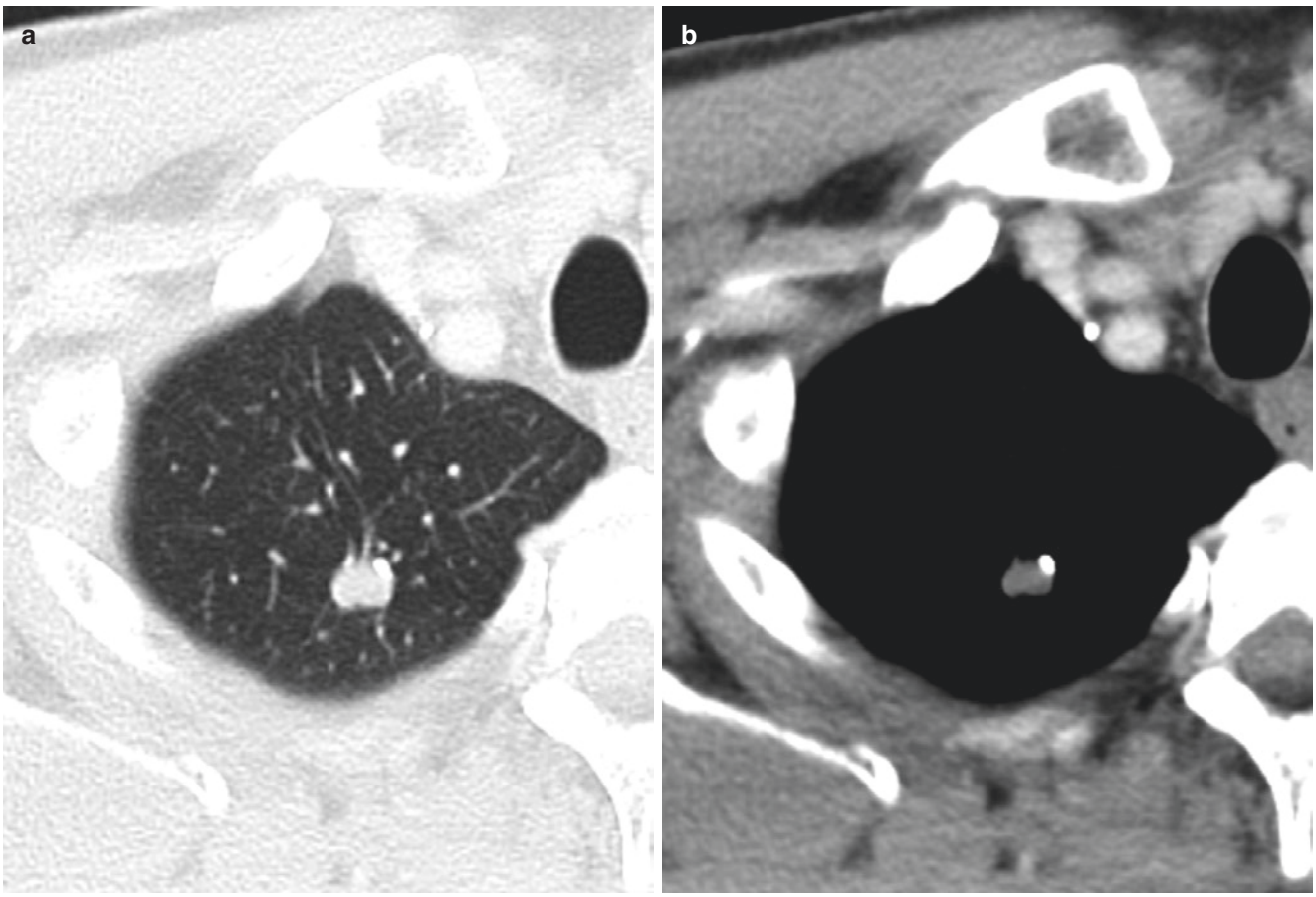

Fig. 4.3 Adenocarcinoma engulfing granuloma. (**a**, **b**) Axial CT images show a soft tissue nodule with focal eccentric calcification

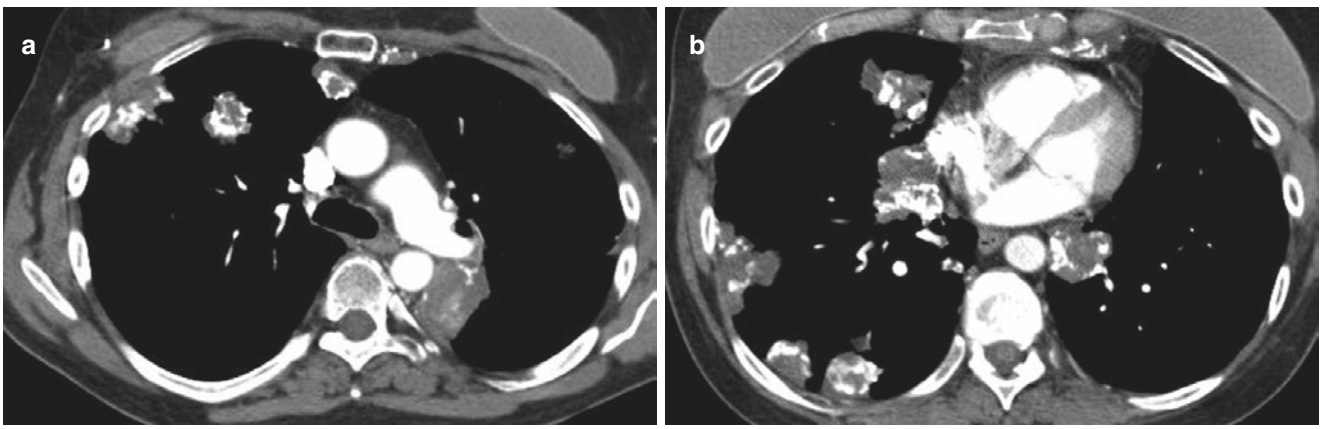

Fig. 4.4 A 49-year-old woman with calcified pulmonary metastases from breast cancer. (**a**, **b**) Axial CT images show partially calcified nodules in both lungs. Note postmastectomy breast implants

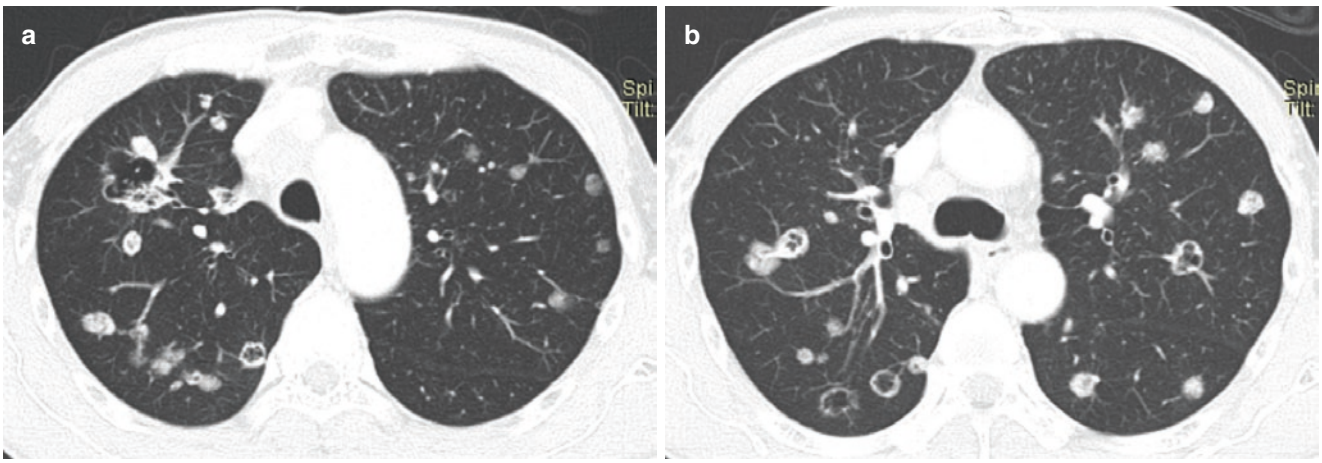

Fig. 4.5 A 60-year-old man with multifocal adenocarcinoma showing cavitations (pseudocavitations). (**a**, **b**) Axial CT images show multiple nodules. Biopsy of the largest nodule revealed adenocarcinoma

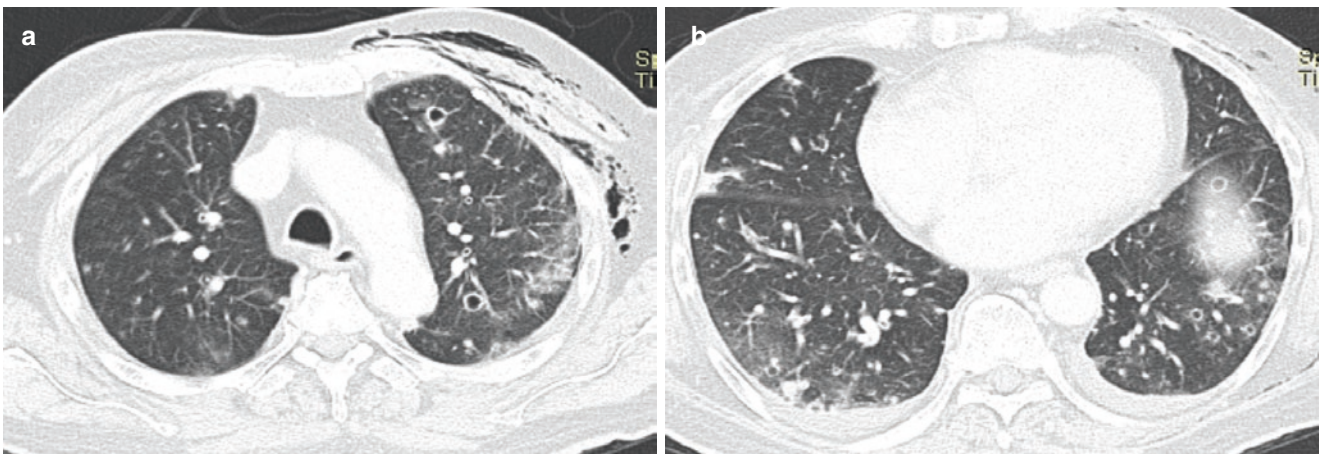

Fig. 4.6 Metastatic angiosarcoma presenting with spontaneous pneumothorax. (**a**, **b**) Axial CT images show multiple cystic nodules. Chest wall emphysema is related to chest tube insertion for pneumothorax

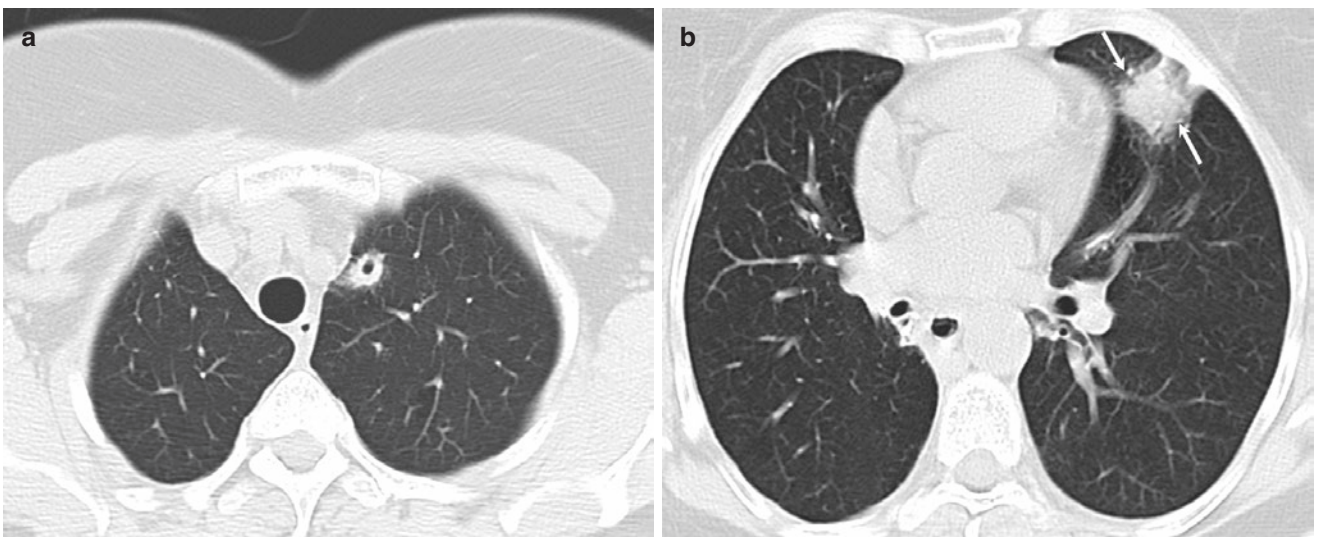

Fig. 4.7 A 57-year-old woman with granulomatosis with polyangiitis. (**a**–**c**) Axial CT images show cavitary nodules in the left upper and left lower lobe with a nodule with "halo" sign (arrows) in lingula

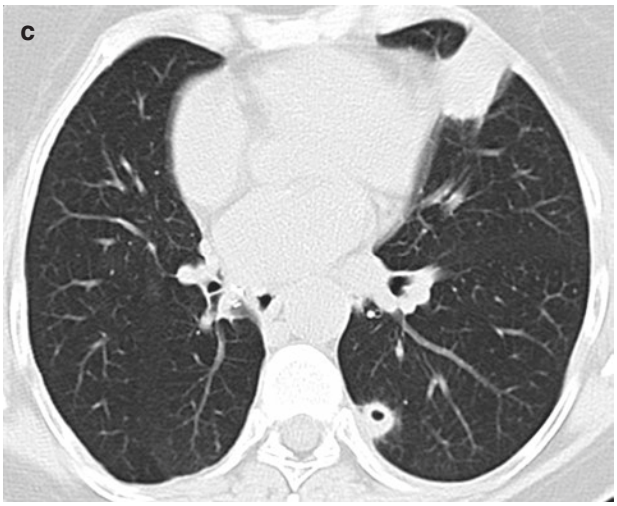

low-up examinations. A nodule containing macroscopic fat with or without calcification is diagnostic of a hamartoma. Similarly, a fat-containing nodule in a patient with tuberous sclerosis is diagnostic of angiomyolipoma. Rare conditions like amyloidosis, benign metastasizing leiomyoma, rheumatoid nodules, and DIPNECH can only be considered as a radiological differential diagnosis in the background of relevant history and require tissue sampling for confirmation. Benign metastasizing leiomyoma is a rare, usually asymptomatic entity characterized by nonspecific pulmonary nodules in a patient who has undergone hysterectomy for uterine fibroids. DIPNECH is suspected in a young to middle-aged woman who presents with asthma-like symptoms, and CT shows a combination of pulmonary nodules and extensive air-trapping.

Fig. 4.7 (continued)

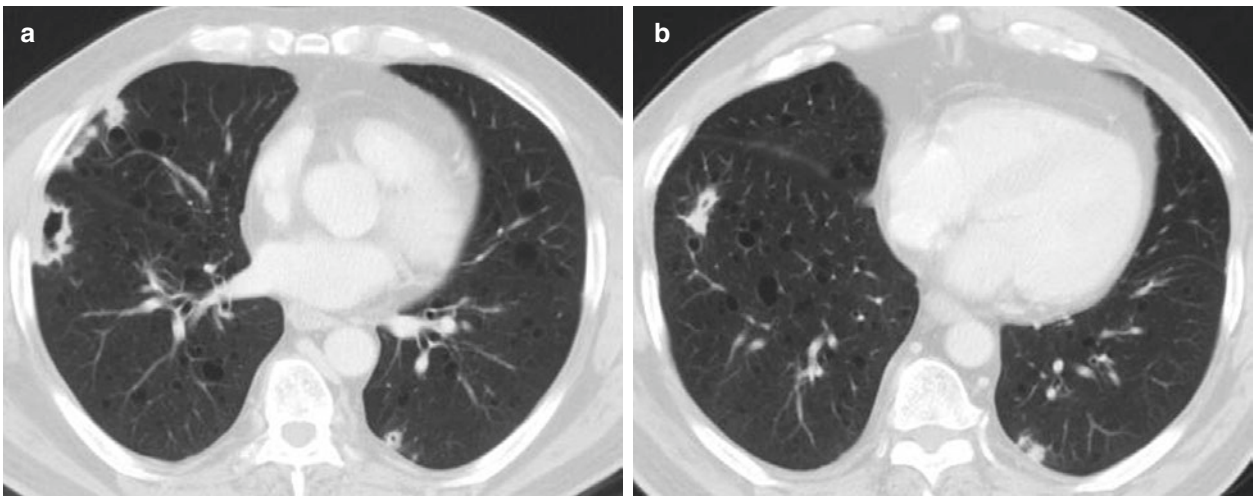

Fig. 4.8 (**a**, **b**) Rheumatoid cavitary nodules in a 60-year-old man

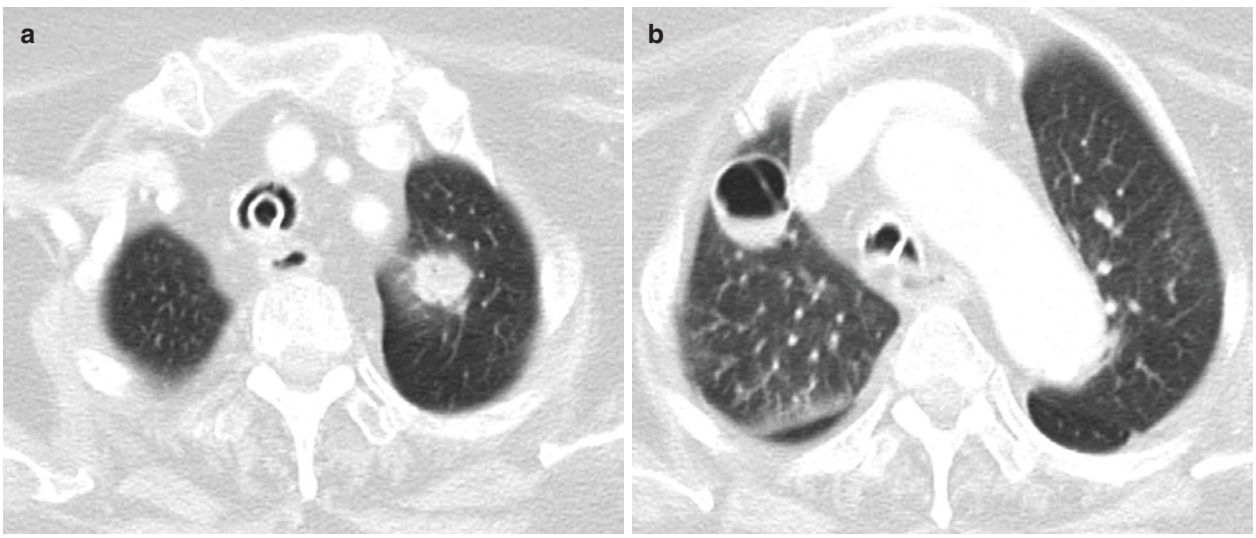

Fig. 4.9 A 73-year-old diabetic woman with septic pulmonary embolism and UTI. (**a**, **b**) Axial CT images show solid nodule with "halo" sign in the left upper lobe and a cavitary nodule with an air-fluid level in the right upper lobe

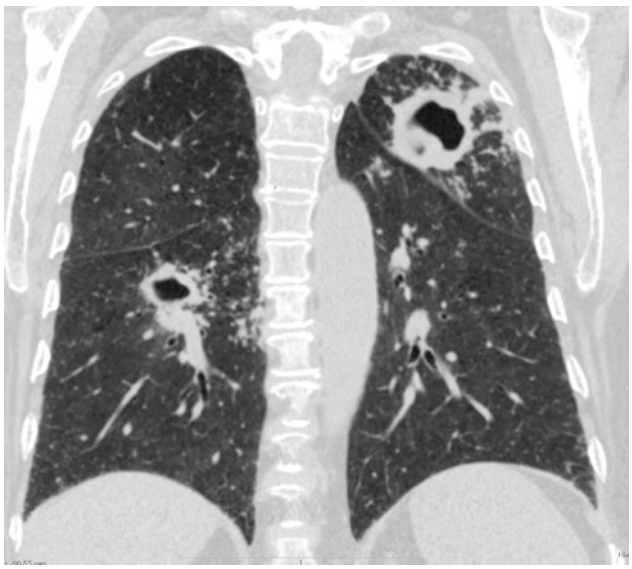

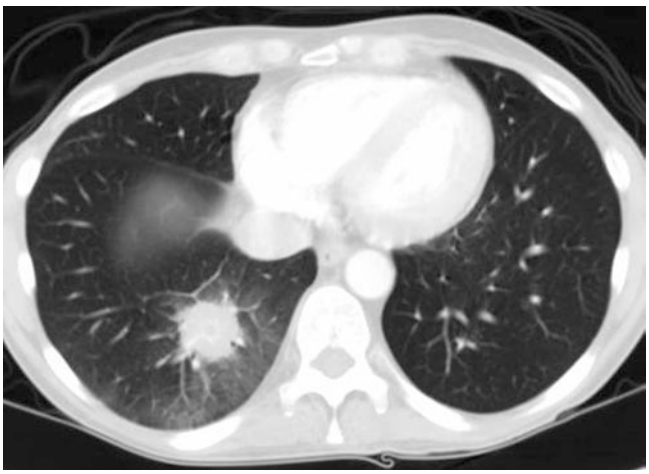

Fig. 4.11 Angioinvasive aspergillosis with "halo" sign

Fig. 4.10 Tubercular cavities with surround tree-in-bud opacities

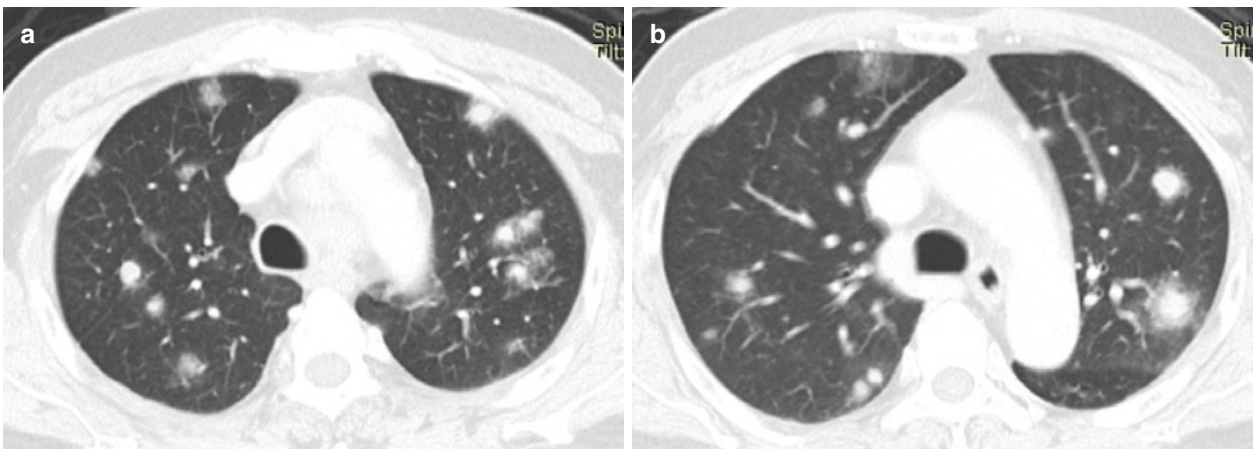

Fig. 4.12 A 72-year-old man with hemorrhagic metastases from papillary thyroid cancer. (**a**, **b**) Axial CT images show multiple nodules with a "halo" of ground-glass opacities

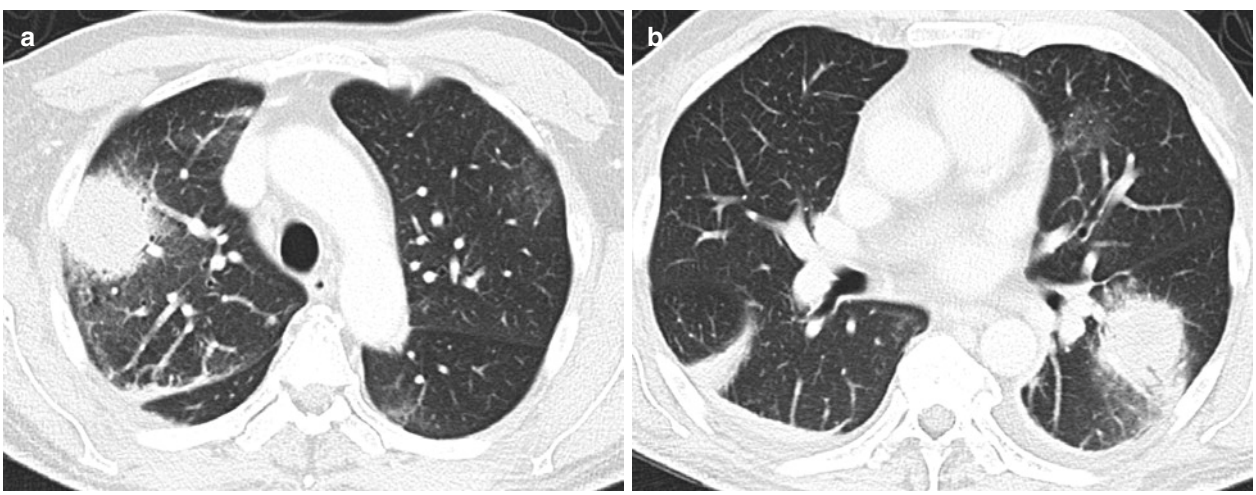

Fig. 4.13 A 55-year-old man with septic pulmonary embolism and UTI. (**a**, **b**) Axial CT images show large consolidations with surrounding "halo" of ground-glass opacities

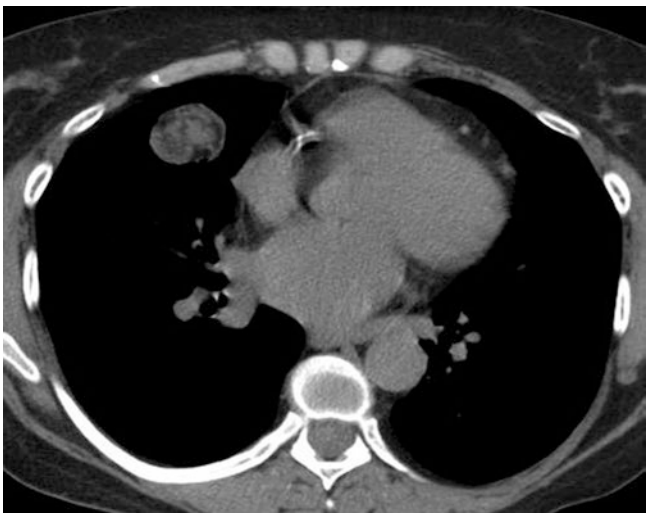

Fig. 4.14 A 57-year-old woman with fat-containing hamartoma

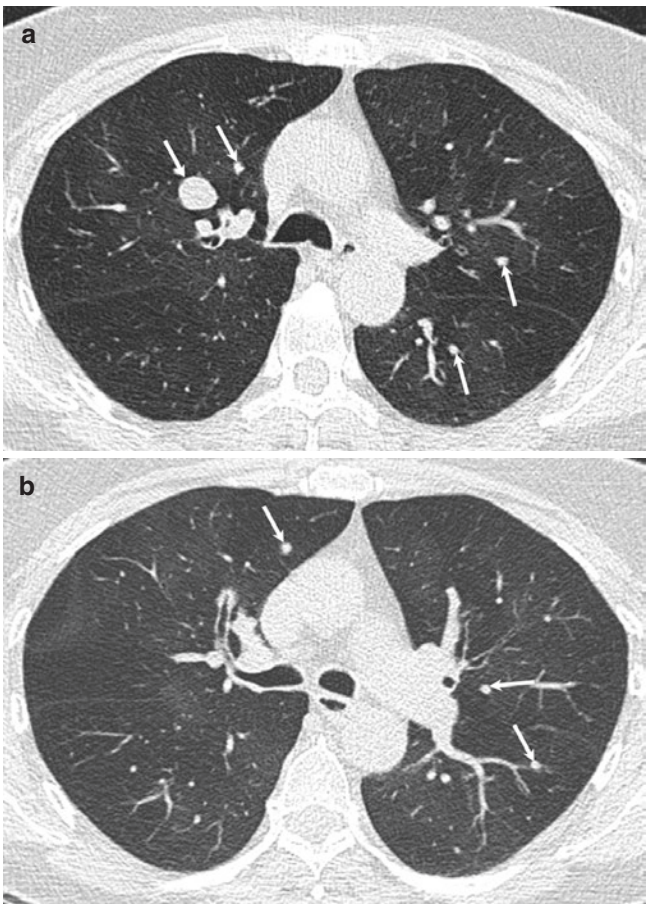

Fig. 4.15 DIPNECH in a middle-aged woman. (**a**, **b**) Axial CT images show multiple nodules (arrows) of varying sizes with mosaic attenuation

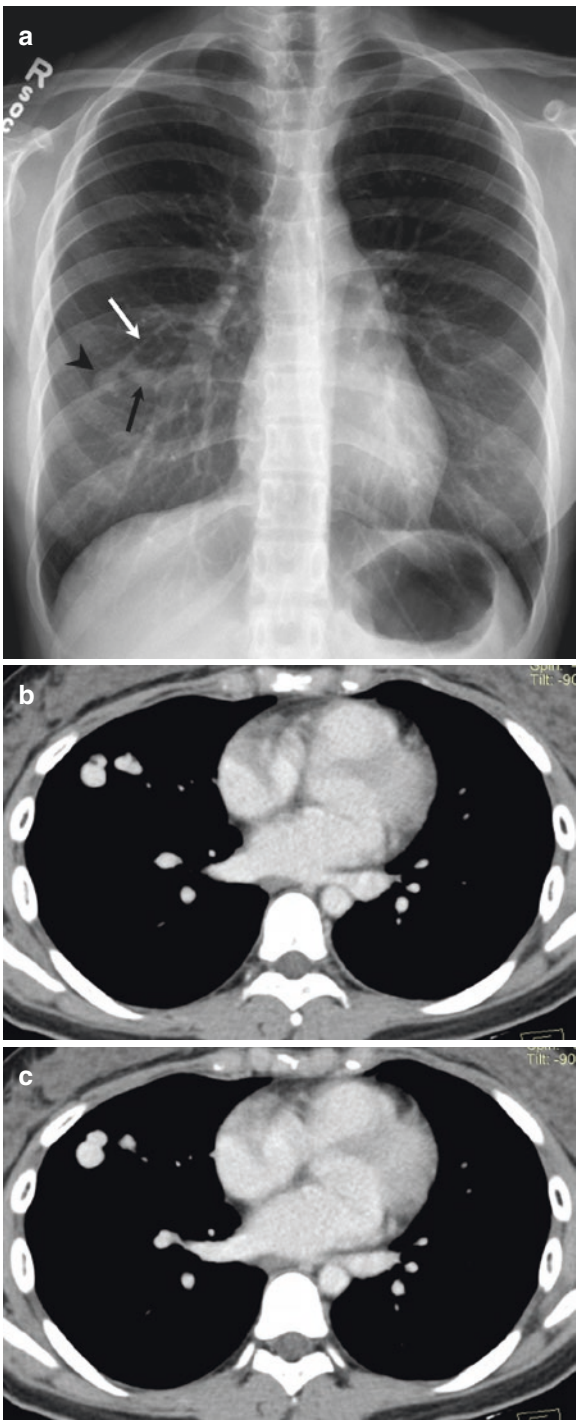

Fig. 4.16 A 23-year-old woman with right lung arteriovenous malformation (AVM). (**a**) Frontal chest radiograph shows a nodular opacity in the right mid-lower zone (arrowhead) with tubular vessels coursing toward it from the hilum (arrows). (**b**, **c**) Axial contrast-enhanced CT shows enhancing interconnected well-circumscribed nodular-tubular opacity in the right middle lobe. **(d)** Sequential coronal CT images of right hemithorax demonstrating the arterial and venous connections of the AVM

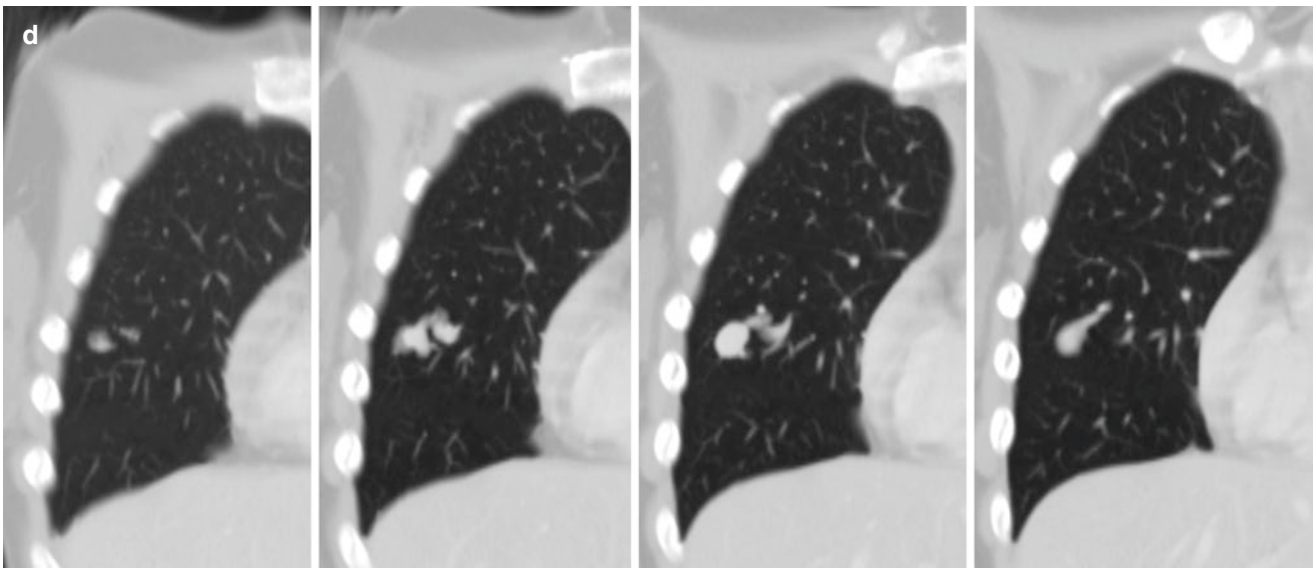

Fig. 4.16 (continued)

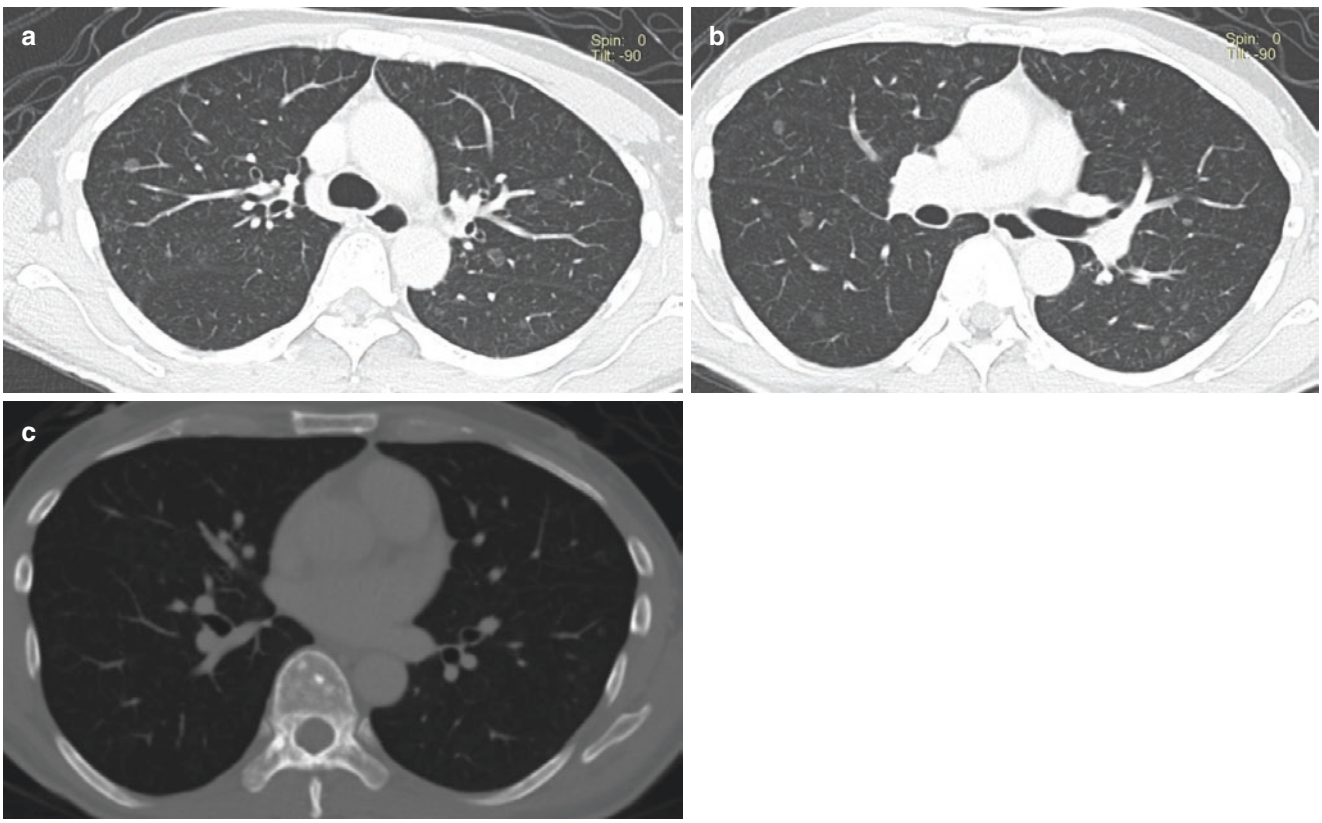

Fig. 4.17 Multifocal pneumocyte hyperplasia in a patient with tuberous sclerosis. (**a**, **b**) Axial CT images show innumerable ground-glass density nodules scattered in both lungs. (**c**) Axial CT with bone window settings shows ill-defined sclerotic foci in the vertebra: a finding commonly seen in tuberous sclerosis

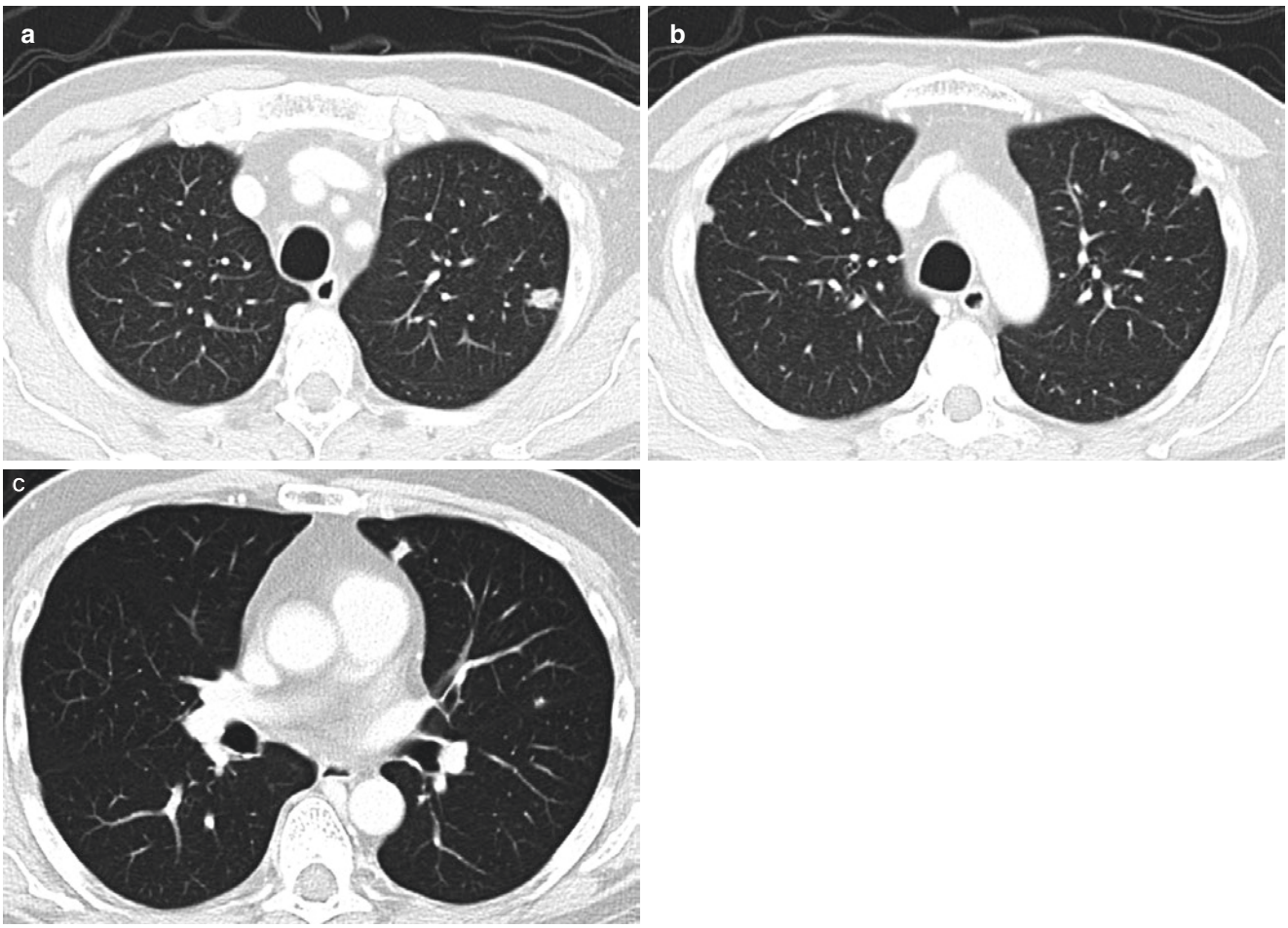

Fig. 4.18 (**a**–**c**) Scattered subpleural/peripheral septic pulmonary embolism in a patient with pyelonephritis that resolved on follow-up CT (not shown)

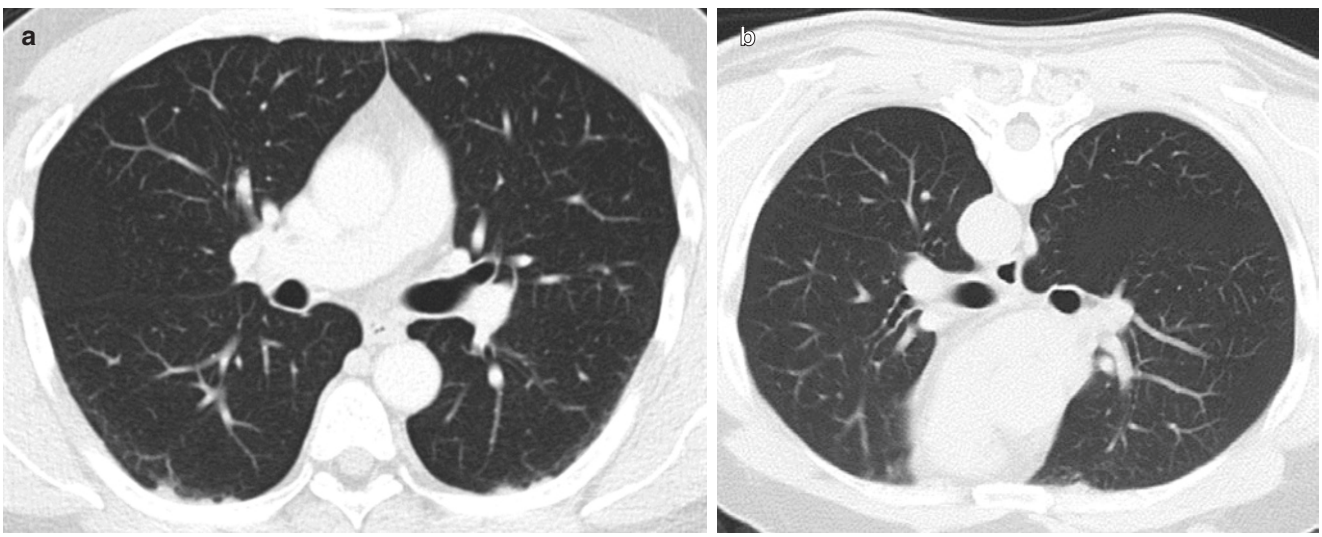

Fig. 4.19 Dependent nodular subpleural atelectasis. (**a**) Axial supine CT image shows nodular subpleural densities in this staging scan for breast cancer. (**b**) Prone CT image shows resolution of the dependent changes

4.3 Diffuse Pulmonary Nodules

Diffuse pulmonary nodules, ranging from few mm to 1 cm, are seen in various diseases. These nodules can be solid and ground-glass density or calcified on CT. Based on their distribution in relation to secondary pulmonary nodule (SPL), the nodules can be divided into three categories: centrilobular nodules, perilymphatic nodules, and random nodules. It is essential to understand the concepts of the distribution of nodules to reach a differential diagnosis that can guide appropriate workup of the patient for accurate diagnosis [2, 3].

4.3.1 Centrilobular Nodules

These are located in the center of the SPL along the centrilobular bronchovascular bundle. Because of their location in the centrilobular region of an SPL, they can be easily recognized on CT by characteristically sparing 5–10 mm of the subpleural and perifissural region. The detailed features of centrilobular nodules are described in Table 4.2 (Figs. 4.20, 4.21, 4.22, 4.23, 4.24, 4.25, and 4.26). "Tree-in-bud" pattern result due to plugging (by aspirated fluid, mucus, pus, or tumor) of centrilobular airways (trees) and filled alveolar duct/alveoli (buds) is always associated with centrilobular nodules. The diseases associated with centrilobular nodules are described in Table 4.3. The centrilobular nodules are seen in all patients with proliferative or cellular bronchiolitis. Silicosis can demonstrate subpleural nodules along with classic centrilobular nodules.

4.3.2 Perilymphatic Nodules

Perilymphatic nodules are located in the pulmonary interstitium, along the distribution of lymphatics in an SPL (Table 4.4) (Figs. 4.27, 4.28, and 4.29). These nodules are solid and may have triangular or bizarre shape. In contrast to centrilobular nodules, the perilymphatic nodules are identified by their location in the subpleural region. One should remember that lymphatics are also located in the interstitium along centrilobular bronchovascular bundles, and hence the sarcoid granulomas and silicotic nodules can be present in centrilobular location as well. The common causes of perilymphatic nodules are listed in Table 4.5.

Table 4.2 Characteristics of centrilobular nodules

• Solid or ground-glass density nodules
• Located in the center of a secondary pulmonary nodule
• Peripheral but spare subpleural space
• Spare fissures
• Associated with abnormal airways
Bronchiolectasis
Bronchiolectasis with mucus plugging (tree-in-bud opacities)
Bronchiolar wall thickening

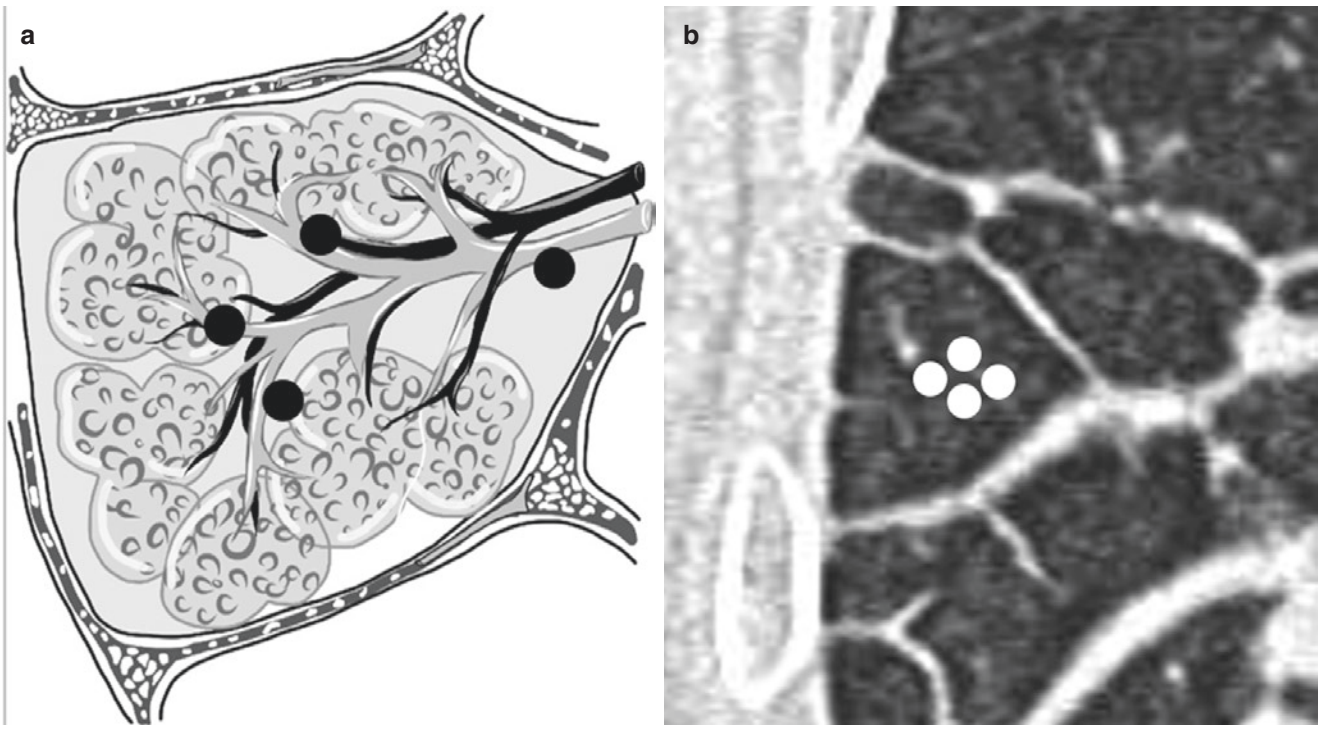

Fig. 4.20 (**a**, **b**) Illustration of SPL and magnified CT coronal image showing the location of centrilobular nodules in SPL

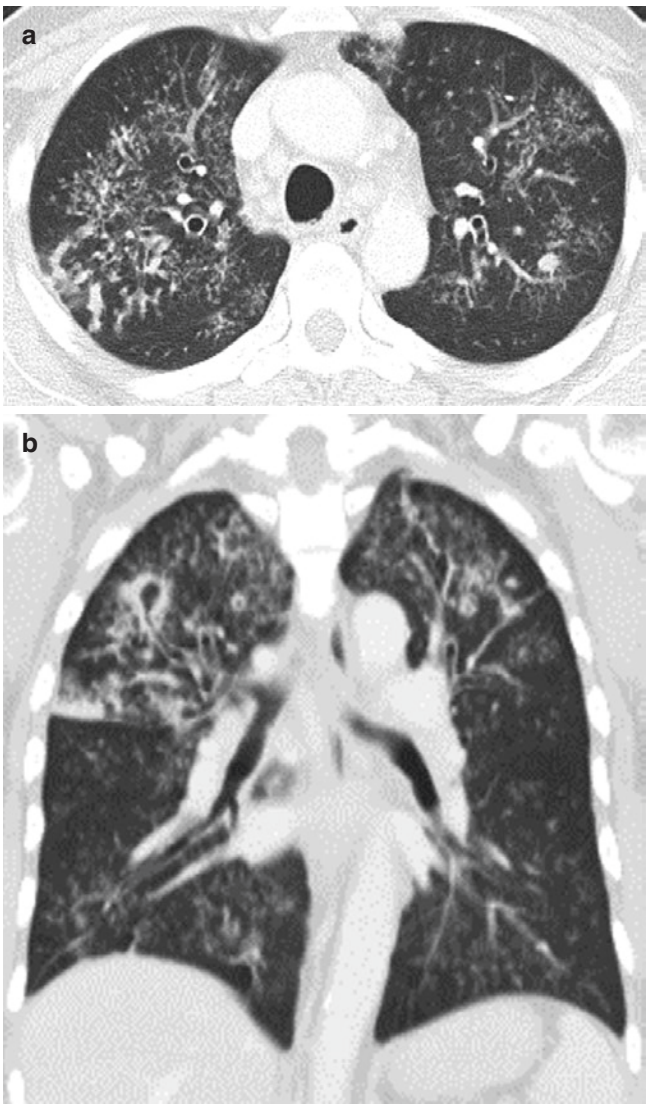

Fig. 4.21 (**a**, **b**) Axial CT images show endobronchial tuberculosis with centrilobular nodules and cavity

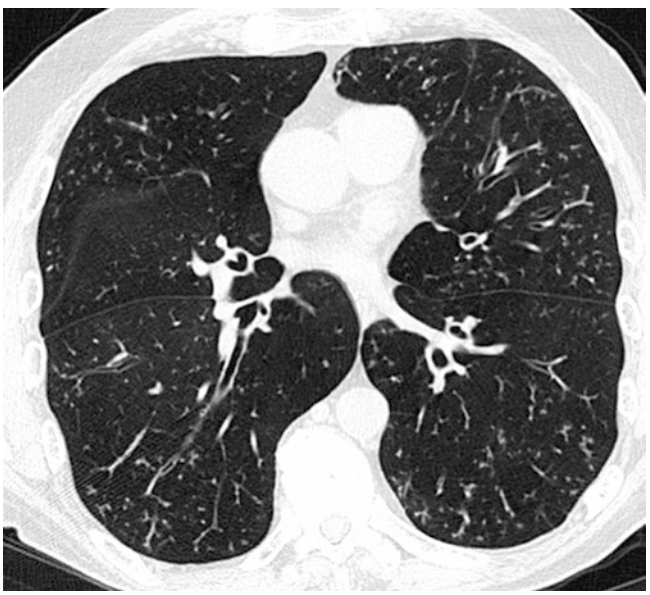

Fig. 4.22 Follicular bronchiolitis with centrilobular nodules representing proliferative bronchiolitis

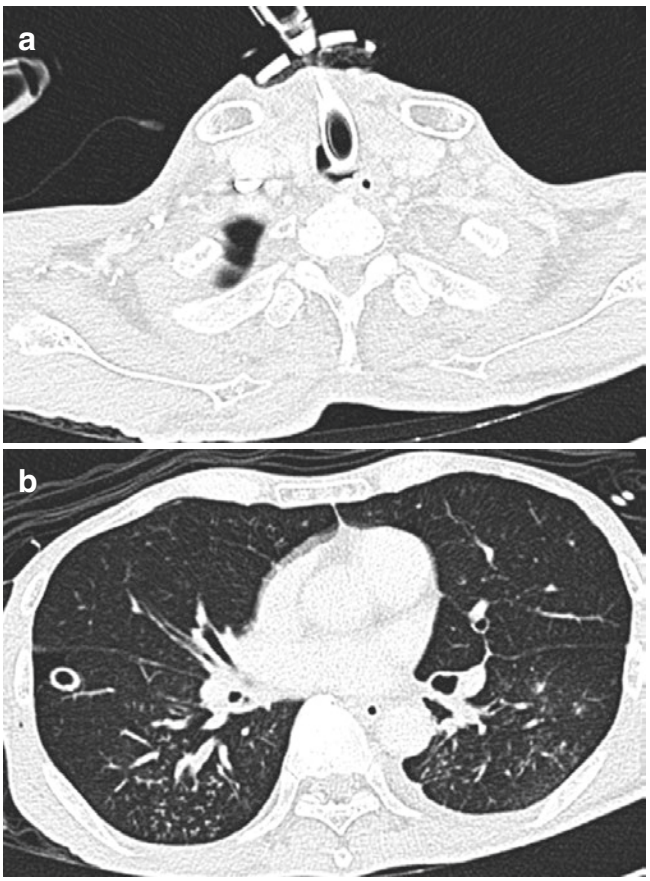

Fig. 4.23 (**a**, **b**) Centrilobular nodules due to aspiration in the lower lobes in an intubated patient

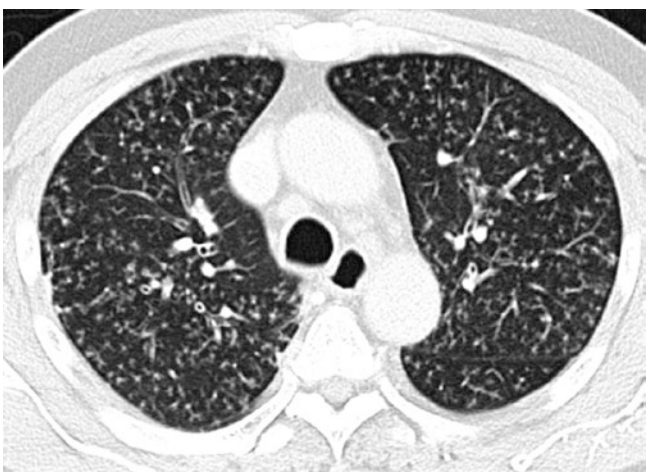

Fig. 4.24 Diffuse panbronchiolitis with extensive centrilobular nodules

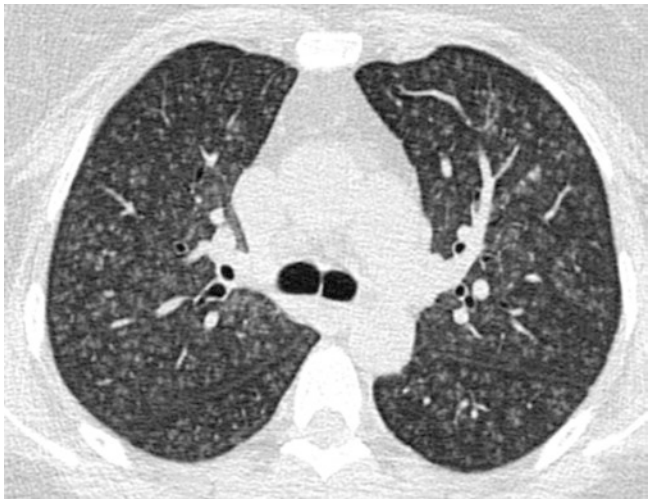

Fig. 4.25 Acute-subacute hypersensitivity pneumonitis with ground-glass density centrilobular nodules

Table 4.3 Diseases with centrilobular nodules

Focal	Diffuse
• Aspiration	• Hypersensitivity pneumonitis
• Tuberculosis	• Diffuse panbronchiolitis
• Infectious bronchiolitis	• Follicular bronchiolitis
• ABPM	• Respiratory bronchiolitis
• NTM	• Langerhans cell histiocytosis
• Malignancy	• Silicosis

ABPM allergic bronchopulmonary mycosis, *NTM* nontuberculous mycobacterial disease

Table 4.4 Characteristics of perilymphatic nodules

• Solid nodules
Perifissural
Centrilobular
Subpleural
• Associated findings
Septal thickening may be present
Architectural distortion may be present

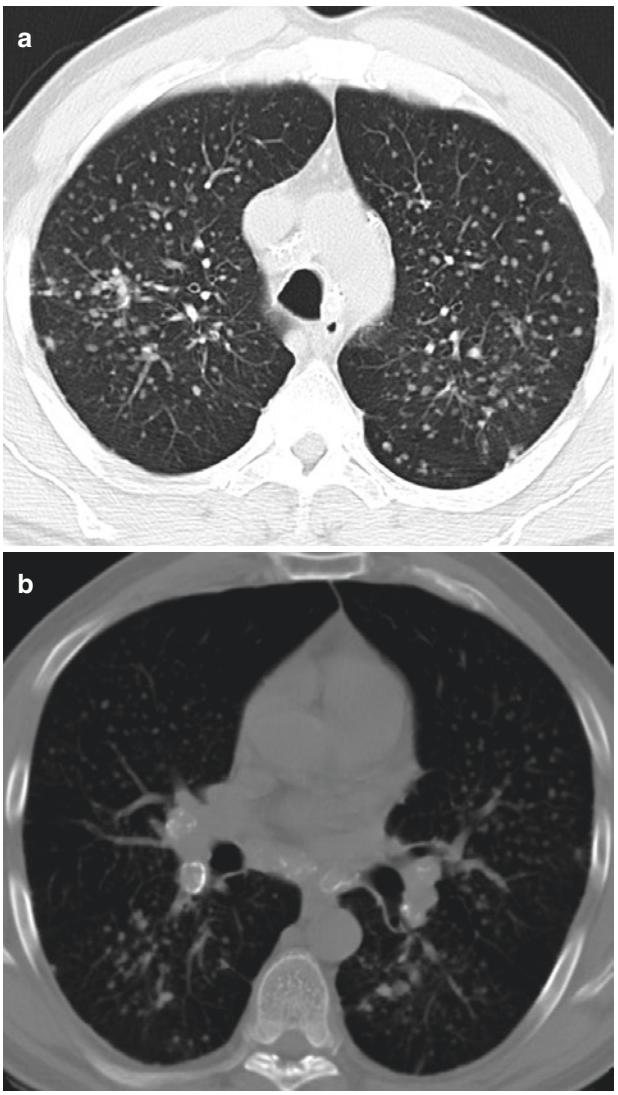

Fig. 4.26 Silicosis with centrilobular nodules. (**a**) Axial CT image shows innumerable nodules: majority away from the pleural surface. (**b**) Axial CT image shows "egg-shell" calcification in hilar and mediastinal lymph nodes

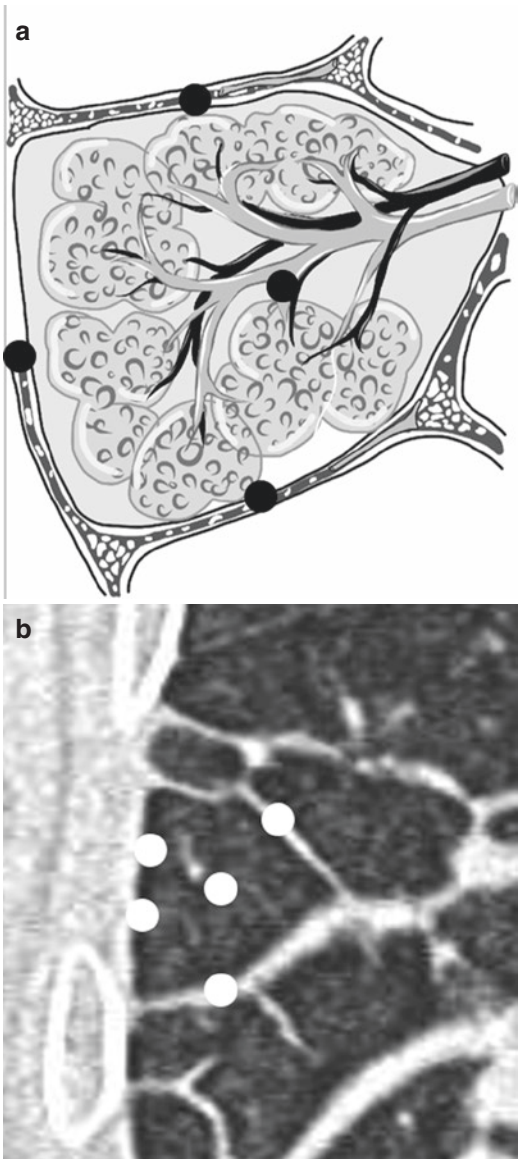

Fig. 4.27 (**a**, **b**) Illustration of SPL and magnified CT coronal image showing the location of perilymphatic nodules in SPL

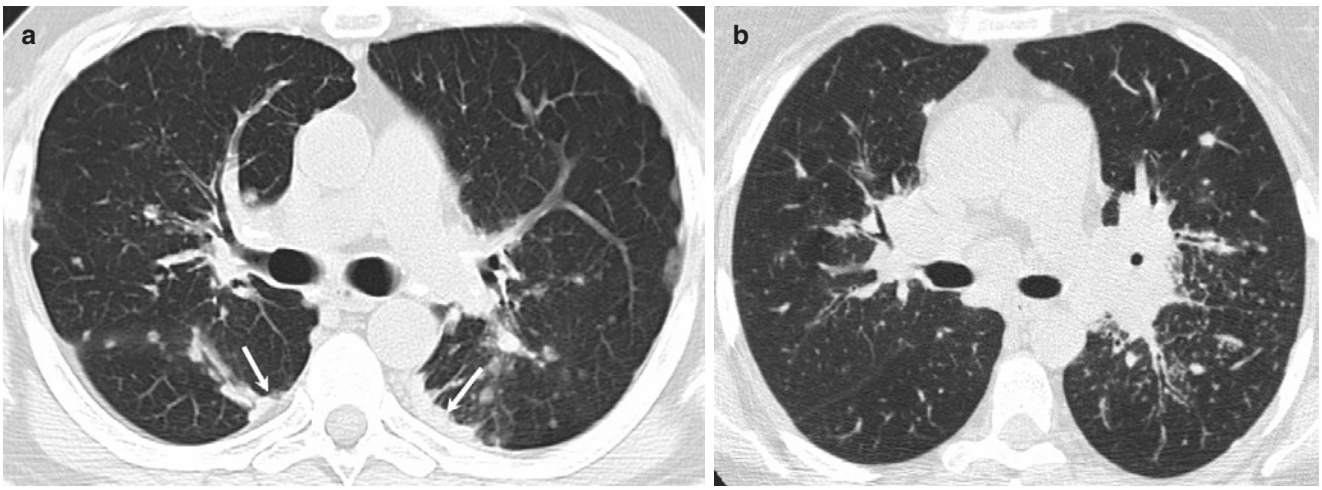

Fig. 4.28 Sarcoidosis with perilymphatic nodules. (**a**) Axial CT image in a patient shows perilymphatic nodules in subpleural region and fissures with subpleural "pseudoplaque" formation posteriorly (arrows). (**b**) Axial CT in another patient with sarcoidosis shows centrilobular nodules along segmental and subsegmental bronchioles in the left lung

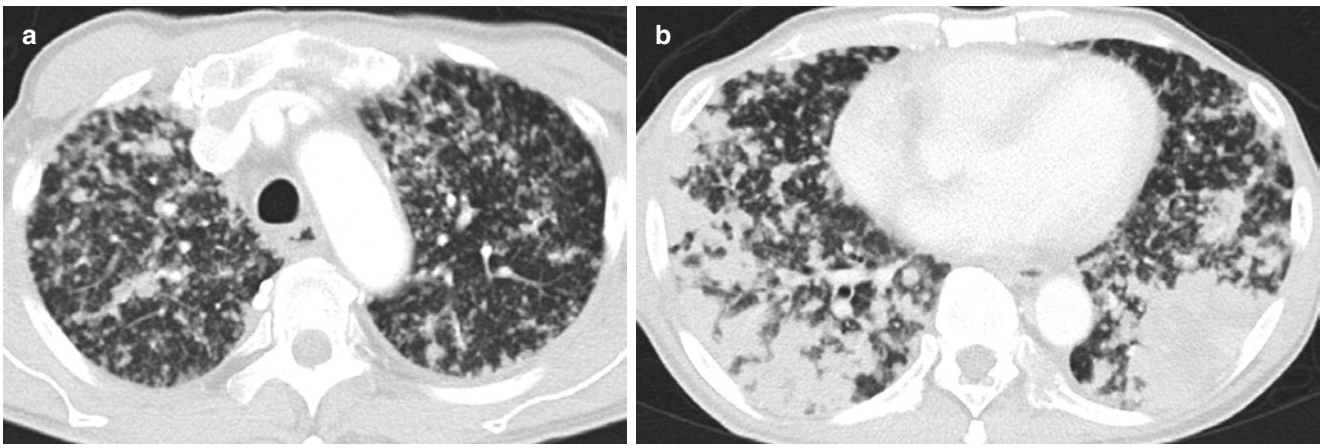

Fig. 4.29 Perilymphatic nodules and masses from lymphoma. (**a**, **b**) Axial CT images show innumerable nodules in both lungs with most of the nodules in the subpleural region and along the pulmonary venules. (**b**) CT image in lower thorax reveals multiple subpleural masses

4.3.3 Random Nodules or Angiocentric Nodules

Random nodules are those nodules that cannot be characterized as centrilobular or perilymphatic nodules. These are usually located along the vessels on close inspection. The two most common causes of random nodules are miliary tuberculosis and hematogenous metastases (Figs. 4.30 and 4.31).

Table 4.5 Diseases with perilymphatic nodules

• Sarcoidosis
• Lymph nodes
• Metastases
• Lymphoma
• Kaposi's sarcoma

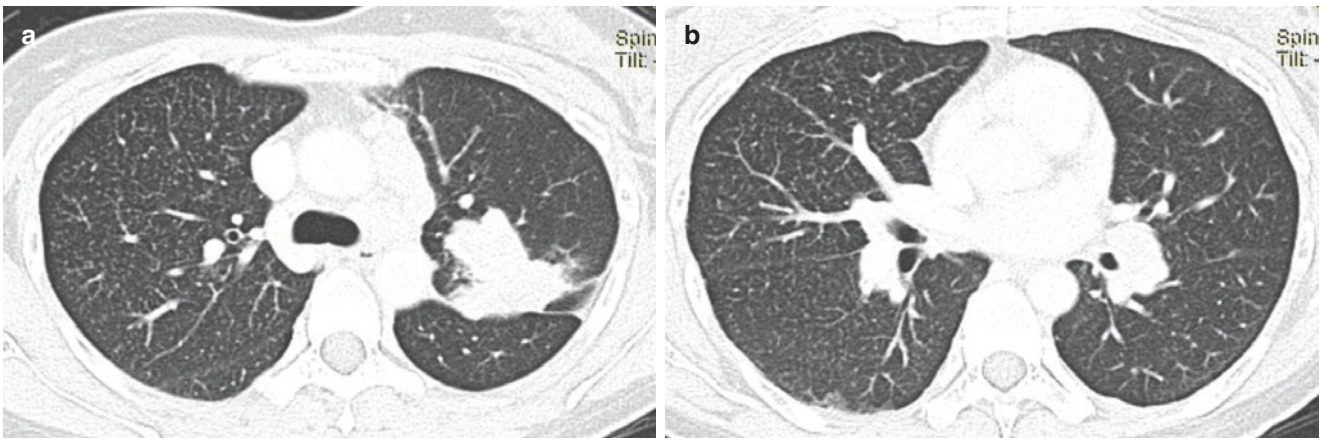

Fig. 4.30 Miliary metastases from left lung malignancy. (**a**, **b**) Axial CT images show innumerable 2 mm nodules with a mass in the left upper lobe. Note that the nodules are sparing the subpleural region similar to centrilobular nodules but are also present within the fissures similar to perilymphatic nodules

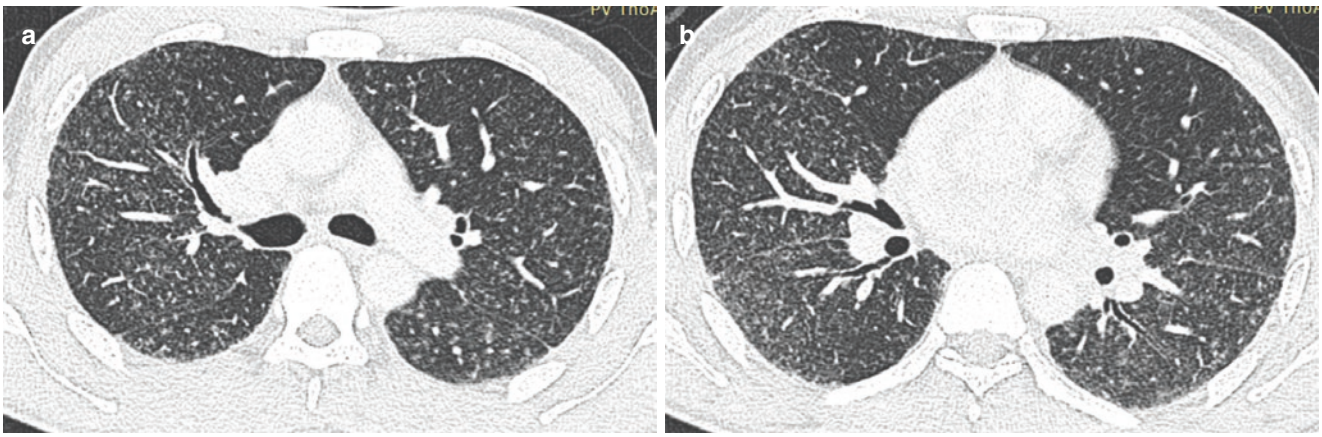

Fig. 4.31 Random nodules in miliary tuberculosis. (**a**, **b**) Axial CT images show innumerable miliary nodules without any definite pattern of localization

4.4 Incidental Pulmonary Nodules

Pulmonary nodules are frequently encountered incidentally on CT scan and can be due to various etiologies. Most of these are soft tissue nodules or solid nodules without any specific feature. In the absence of known malignancy, in the 35 years and above age group, the most helpful tool is the availability of any prior CT or else to follow the nodules in a recommended time. The Fleischner Society has updated its guidelines for the management of incidental pulmonary nodules in 2017 [4] (Tables 4.6 and 4.7). One should remember that the Fleischner Society guidelines are not meant for immunocompromised and for younger age group. The incidental nodules in younger patients require further assessment case-by-case basis. The time period for follow-up or intervention depends upon the size of the nodule, its morphology, location, as well as the patient profile: whether the patient is a high risk or low risk for malignancy (Table 4.8). In the revised guidelines, routine follow-up interval has been increased and is now given as a range rather than as a precise time period. The purpose is to reduce the number of unnecessary follow-up examinations. The time schedule is different for solid nodules and subsolid nodules. The solid nodules are completely solid (density as consolidation), while subsolid nodule includes ground-glass density nodules (hazy appearance) and part-solid nodules (contain a mixture of solid component and ground-glass component) (Fig. 4.32). The measurement is obtained manually in short and long axis in the plane and image where the nodule appears the largest (axial, coronal, or sagittal), and the mean is recorded. All

Table 4.6 Fleischner Society 2017 guidelines for management of *incidentally* detected solid pulmonary nodule in adults

Nodule type	Size			Comments
	<6 mm (<100 mm^3)	6–8 mm (100–250 mm^3)	>8 mm (>250 mm^3)	
Single				
Low risk	No routine follow-up	CT at 6–12 months, then consider CT at 18–24 months	Consider CT at 3 months, PET/CT, or tissue sampling	Nodules <6 mm do not require routine follow-up in low-risk patients
High risk	Optional CT at 12 months	CT at 6–12 months, then CT at 18–24 months	Consider CT at 3 months, PET/CT, or tissue sampling	Certain patients at high risk with suspicious nodule morphology, upper lobe location, or both may warrant 12-month follow-up
Multiple				
Low risk	No routine follow-up	CT at 3–6 months, then consider CT at 18–24 months	CT at 3–6 months, then consider CT at 18–24 months	Use the most suspicious nodule as guide to management. Follow-up intervals may vary according to size and risk
High risk	Optional CT at 12 months	CT at 3–6 months, then at 18–24 months	CT at 3–6 months, then at 18–24 months	Use the most suspicious nodule as guide to management. Follow-up intervals may vary according to size and risk

Published with permission from Ref. [4]

Table 4.7 Fleischner Society 2017 guidelines for management of *incidentally* detected subsolid nodule in adults

Nodule type	Size		Comments
	<6 mm (<100 mm^3)	>6 mm (>100 mm^3)	
Single			
Ground glass	No routine follow-up	CT at 6–12 months to confirm persistence, then CT every 2 years until 5 years	In certain suspicious nodules, <6 mm, consider follow-up at 2 and 4 years. If solid component(s) or growth develops, consider resection
Part solid	No routine follow-up	CT at 3–6 months to confirm persistence. If unchanged and solid component remains <6 mm, annual CT should be performed for 5 years	In practice, part-solid nodules cannot be defined as such until >6 mm, and nodules <6 mm do not usually require follow-up. Persistent part-solid nodules with solid components >6 mm should be considered highly suspicious
Multiple			
Multiple	CT at 3–6 months. If stable, consider CT at 2 and 4 years	CT at 3–6 months. Subsequent management based on the most suspicious nodule(s)	Multiple <6 mm pure ground-glass nodules are usually benign, but consider follow-up in selected patients at high risk at 2 and 4 years

Published with permission from Ref. [4]

measurements are recorded in lung window settings using a thin slice, typically of 1 mm thickness to avoid volume averaging artifact. *The size of the solid component of a part-solid nodule must always be recorded in such a nodule that is more than 6 mm in size*. In case of multiple nodules, the most suspicious nodule (e.g., one with speculated margins) that may not necessarily be the largest decides further management. Fleischner Society guidelines do not apply to low-dose lung cancer screening scans, which use Lung-RADS. The subsolid nodules require more attention as it has been revealed that the malignancy rate of subsolid nodules (34%) is higher than that of solid nodules (7%) [5].The malignancy rate for part-solid nodules is 63%, while the rate for pure ground-glass density nodules is 18% [5].

Table 4.8 High-risk vs low-risk patient population

Low risk	High risk
• Young age • Less smoking • Smaller nodule size • Regular margins • Location in an area other than the upper lobe	• Older age • Heavy smoking • Larger nodule size • Irregular or spiculated margins • Upper lobe location

4.4.1 Perifissural Nodules

Perifissural nodules are the nodules attached to the major fissure, minor fissure, or an accessory or rudimentary fissure (Fig. 4.33). A typical perifissural nodule is triangular-, rectangu-

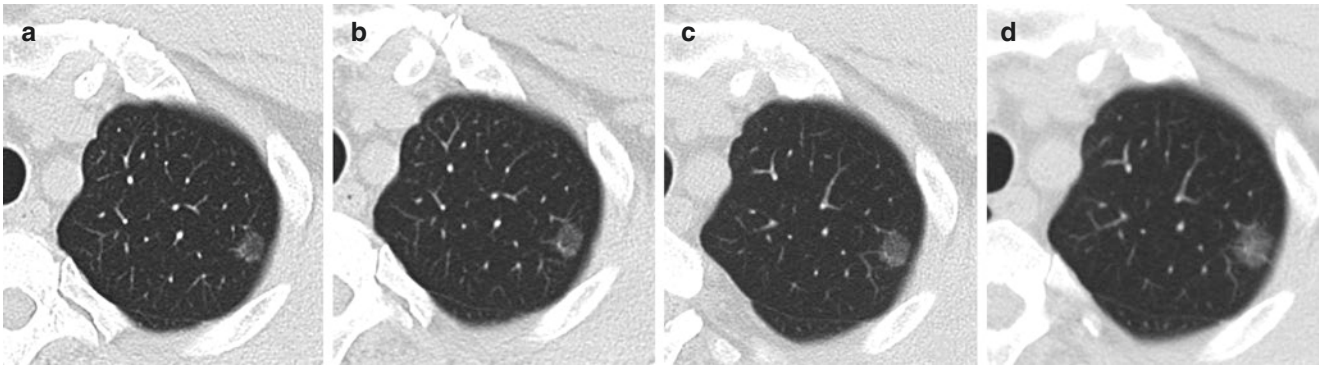

Fig. 4.32 Pure ground-glass density nodule developing small solid component on follow-up. (**a**–**c**) Yearly CT for evaluation of ground-glass density nodule in the left upper lobe shows minimal increase in the size of the nodule for 2 years. (**d**) Third follow-up scan shows a definite increase in size and some solid component. Histopathology revealed adenocarcinoma in situ

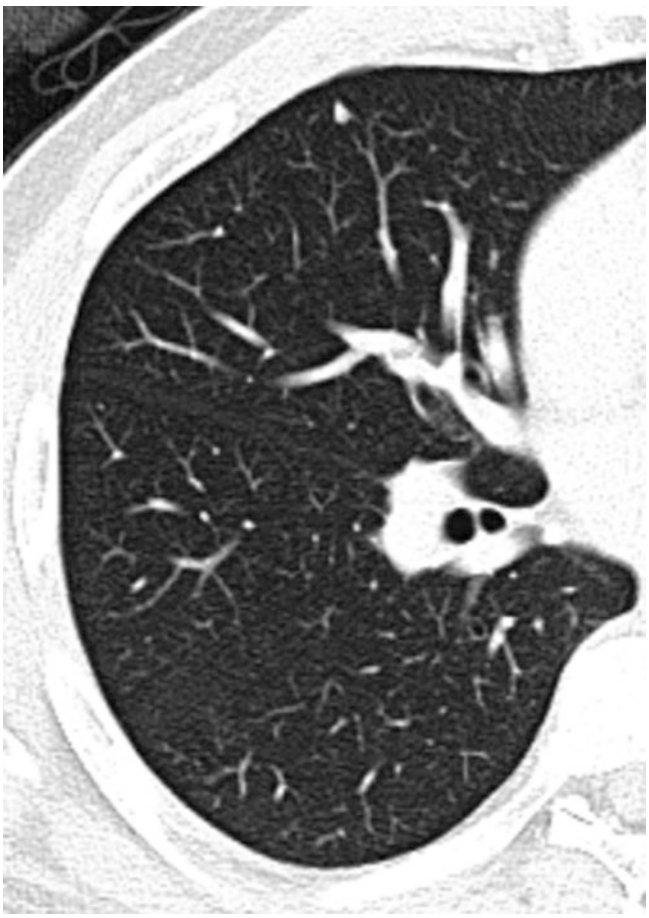

Fig. 4.33 Typical triangular perifissural nodule in right minor fissure

lar-, or biconvex-shaped sharply marginated homogeneous solid nodule, less than 6 mm in diameter [6, 7]. Most of the typical perifissural nodules correspond to intrapulmonary lymph nodes on histology. No follow-up is recommended for the nodules satisfying the criteria for perifissural nodes in a patient with no known primary malignancy. However, if there is doubt about any criteria, they can be followed up in 6–12 months [1].

References

1. Hansell DM, Bankier AA, MacMahon H, McLoud TC, Muller NL, Remy J. Fleischner Society: glossary of terms for thoracic imaging. Radiology. 2008;246(3):697–722.
2. Boitsios G, Bankier AA, Eisenberg RL. Diffuse pulmonary nodules. Am J Roentgenol. 2010;194(5):W354–66.
3. Raoof S, Amchentsev A, Vlahos I, Goud A, Naidich DP. Pictorial essay: multinodular disease. Chest. 2006;129(3):805–15.
4. MacMahon H, Naidich DP, Goo JM, Lee KS, Leung AN, Mayo JR, Mehta AC, Ohno Y, Powell CA, Prokop M, Rubin GD. Guidelines for management of incidental pulmonary nodules detected on CT images: from the Fleischner Society 2017. Radiology. 2017;284(1):228–43.
5. Henschke CI, Yankelevitz DF, Mirtcheva R, et al. CT screening for lung cancer: frequency and significance of part-solid and nonsolid nodules. Am J Roentgenol. 2002;178:1053–7.
6. de Hoop B, van Ginneken B, Gietema H, Prokop M. Pulmonary perifissural nodules on CT scans: rapid growth is not a predictor of malignancy. Radiology. 2012;265(2):611–6.
7. Ahn MI, Gleeson TG, Chan IH, McWilliams AM, MacDonald SL, Lam S, Atkar-Khattra S, Mayo JR. Perifissural nodules seen at CT screening for lung cancer. Radiology. 2010;254(3):949–56.

Imaging of Thoracic Malignancies

5

Sumer N. Shikhare

5.1 Introduction

Bronchogenic carcinoma remains the most common cause of cancer death worldwide with an estimated 155,870 deaths in 2017, which is approximately 26% of all cancer deaths in the United States. Lung cancer is also the most common non-skin cancer affecting both men and women, accounting for an estimated 222,500 new cases in 2017. Since a large proportion of cases with lung cancer get diagnosed at an advanced-stage, the overall 5-year relative survival rate is low—17% for men and 24% for women. The increased incidence of bronchogenic cancer is attributed to cigarette smoking [1, 2]. Cigarette smoking is a risk factor for all types of lung cancer.

5.2 Pathology

The most widely accepted histologic classification of lung cancer is that of the World Health Organization (WHO) [3]. The common cell types are adenocarcinoma, squamous cell carcinoma, small cell carcinoma, and large cell cancer [4].

Adenocarcinomas account for up to 35% of cases, and over the past three decades, their relative incidence is rising [5], and as a result, the frequency of adenocarcinomas over squamous cell carcinomas has increased with a current ratio of 1.4–1 [6].

Squamous cell carcinomas account for around 30–35% of cases and have the strongest association with cigarette smoking [7]. Over the past few decades, the relative incidence of squamous cell carcinomas appears to be decreasing, probably because the prevalence of smoking is declining [5].

Large cell carcinomas (LCCs) account for 10–15% of cases. LCCs are malignant epithelial neoplasms lacking glandular or squamous differentiation by light microscopy and lacking cytological features of squamous cell carcinoma [5].

Small cell carcinomas (SCCs) account for 20–30% of cases, which grow rapidly and metastasize early. They contain neurosecretory granules and are part of a spectrum of neuroendocrine tumors. SCCs show a strong correlation with cigarette smoking and are extremely rare in persons who never smoked [5].

5.3 Risk Factors

5.3.1 Age

The incidence of lung cancer increases with age and occurs most commonly in persons aged 55 years or older.

5.3.2 Smoking

There is 20- to 30-fold increase in the risk of lung cancer in smokers compared to non-smokers [8]. It is estimated that after quitting smoking for 15 years, the risk of lung cancer drops by 50% [9, 10].

5.3.3 Environmental Pollutants

General environmental pollutants have been suggested as a further risk factor for lung cancer development. Particles less than 2.5 μm in size are thought to be strongly associated with lung cancer, especially in non-smokers. These are commonly found in diesel engine exhaust [4].

5.3.4 Radon

It is the second common etiological cause of bronchogenic carcinoma after tobacco smoking. Certain geo-

S. N. Shikhare (✉)
Department of Diagnostic Radiology, Khoo Teck Puat Hospital, Singapore, Singapore

A. Chawla (ed.), *Thoracic Imaging*, https://doi.org/10.1007/978-981-13-2544-1_5

graphical areas have higher exposure levels. Radon risk is largely related to underground workers, where the levels are high [4].

5.3.5 Asbestos Exposure

Asbestos exposure is associated with increased risk of lung cancer as well as nonmalignant lung and pleural disease. Tobacco and asbestos exposure are synergistic and together have 15- to 50-fold increased risk of developing lung cancer [4, 11]. Occupational exposure to various other substances such as arsenic, nickel, chromium, beryllium, cadmium, pesticides, and uranium has been linked to lung cancer and may result in as many as 10% cases of lung cancer [8].

5.3.6 Genetic Factors

Although a major risk factor for lung cancer development is smoking, some genetic mutations have been identified to be associated with lung cancer development, particularly in non-smokers. These patients make up as much as 25% of the lung cancer patients in some populations [12].

5.3.6.1 Epidermal Growth Factor Receptor (EGFR)

Identifying genetic mutations associated with non-squamous cell carcinoma can help in guiding targeted therapy. Presently the most important oncogene, routinely searched for with genetic profiling assays, is epidermal growth factor receptor (EGFR). This protein is responsible for stimulating tyrosine kinase. Mutations in the tyrosine kinase domain of the EGFR gene can directly lead to tumor growth and progression. As a result, EGFR has itself become a target for chemotherapy. Specific agents have been developed that prevent activation, block the relevant signalling pathways, and improve response rates to therapy. The expression of epidermal growth factor receptor (EGFR) mutations is commonly seen in adenocarcinomas of non-smokers particularly women [4].

5.3.6.2 K-Ras

This protein is responsible for stimulating signalling pathways downstream from EGFR. Activated K-Ras proteins are produced due to specific mutations which continue to stimulate tumor growth. K-Ras mutations are more commonly identified in patients with adenocarcinoma who smoke, usually Caucasians. Lung cancer with K-Ras mutations has a poor prognosis [4].

5.3.6.3 ALK

Anaplastic lymphoma kinase (ALK) gene mutation is associated with NSCC (usually adenocarcinoma). Patients with ALK gene mutations may respond to the first approved ALK inhibitor, such as crizotinib.

Lung cancers have some other genetic mutations of potential importance which can only be identified by molecular testing, thus allowing targeted therapy or prediction of resistance [4]. Lastly, patients with diffuse pulmonary fibrosis have around a tenfold increase in the risk of lung cancer [8]. In one series, lung cancer was found in 32 out of 244 patients with idiopathic pulmonary fibrosis [5].

5.4 Clinical Features

The symptoms vary with the extent of disease (Table 5.1). Considering most patients are smokers, they have a history of a chronic cough [8].

Table 5.1 Clinical features

Local spread and intrathoracic growth
1. Cough
2. Hemoptysis
3. Wheezing
4. Dyspnea due to bronchial obstruction
5. Hoarseness of voice—recurrent laryngeal nerve involvement
6. Dysphagia—esophagus is involved
7. Superior vena cava (SVC) syndrome
• Mediastinal invasion
• Facial fullness, flushing, headache, edema of upper extremities
8. Diaphragmatic paralysis—phrenic nerve is involved
9. Chest pain—pleural or chest wall invasion
10. Horner's syndrome—Pancoast tumor
11. Brachial plexus neuropathy—Pancoast tumor
Paraneoplastic syndromes
1. Hypertrophic pulmonary osteoarthropathy (Fig. 5.1)
• 80% of cases are associated with lung cancer
• Common with SCC
• Characterized by clubbing of fingers
• Periosteal reaction involving the metadiaphysis and diaphysis of the long bones of distal extremities
2. Endocrine disorders
• Cushing's syndrome—commonly associated with a carcinoid tumor
• Hypercalcemia—commonly seen in SCC due to the production of a peptide similar to parathyroid hormone
• Inappropriate antidiuretic hormone secretion—commonly associated with small cell carcinoma
Neuromuscular syndrome—commonly associated with small cell carcinoma
1. Eaton-Lambert syndrome
• Proximal muscle weakness
• Due to the production of anti-calcium channel antibodies impairing release of acetylcholine
2. Peripheral neuropathy—due to anti-neuronal nuclear antibodies
3. Chronic intestinal pseudo-obstruction
4. Limbic encephalitis
5. Necrotizing myelopathy
6. Subacute cerebellar degeneration
7. Dementia

5.4.1 Paraneoplastic Syndromes

These are not directly related to the physical effects of the primary tumor and are seen in about 10% of cases of lung carcinoma, commonly with SCC. These syndromes result from the production of hormones or peptides by the tumor, antigen-antibody interactions, or neurovascular mechanisms. The symptoms may precede pulmonary findings by months or years [8].

5.5 Pulmonary Nodules

5.5.1 Incidental Pulmonary Nodules

The widely used Fleischner Society Guidelines for management of pulmonary nodules were updated in 2017 for non-screening CT in adult patients who are at least 35 years old [13]. This topic is discussed in Chap. 4.

5.5.2 Solitary Pulmonary Nodule

A solitary pulmonary nodule (SPN) is defined as a well or poorly defined, rounded opacity in the lung, measuring 3 cm or less in diameter (Fig. 5.2). While evaluating pulmonary nodules, it is important to bear in mind its various causes, both benign and malignant (Table 5.2). Identifying pulmonary nodules as potential lung cancers at an early stage is vital since the stage at diagnosis is crucial for prognosis [14].

While evaluating solid pulmonary nodules, it is important to assess nodule size, morphology, and other features (Table 5.3) (Figs. 5.3, 5.4, 5.5, 5.6, 5.7, 5.8, 5.9, 5.10, 5.11, 5.12, 5.13, and 5.14) [13, 15–35].

5.5.3 Perifissural Nodules

With multislice CT, perifissural nodules, a known entity, is now seen quite frequently. Perifissural nodules are small subpleural nodules usually representing an intraparenchymal lymph node and have characteristic findings on CT (Table 5.5) (Fig. 5.4).

In NELSON screening trial, none of these nodules developed into lung cancer on follow-up [20]. However, a nodule seen in perifissural or juxtapleural location does not rule out malignancy, and the specific nodule morphology must be considered [13, 20]. If the nodule shows spiculated border and displaces adjacent fissure or if the patient has a history of cancer, the possibility of malignancy increases, and a follow-up examination in 6–12 months should be considered [13].

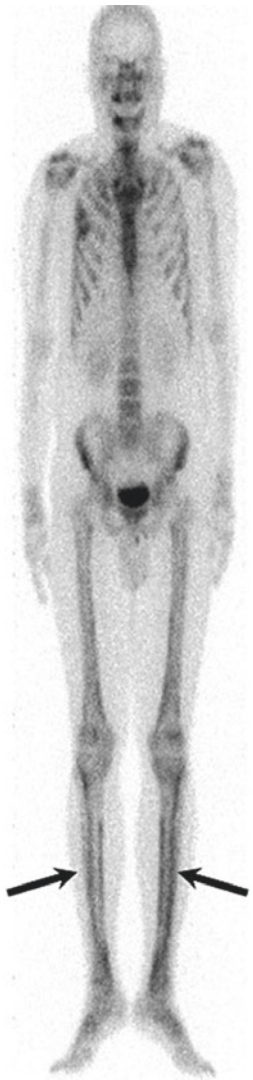

Fig. 5.1 Technetium-99m methylene diphosphonate bone scan (Tc-99m MDP) shows symmetrical periosteal reaction involving the metadiaphysis and diaphysis of the long bones of distal extremities (arrows)

5.5.4 Density of Nodules

Pure GGNs are defined as nodules of increased lung attenuation through which lung parenchymal structures, such as the pulmonary vessels or bronchial structures, are visible. Part-solid GGNs are nodules that present with both ground-glass and solid components. The term subsolid nodules (SSNs) includes both pure and part-solid GGNs. In the case of subsolid nodules, CT features such as nodule density and the presence and size of any solid component are useful in differentiating benign from malignant nodules. The central location of the solid component in subsolid nodule is more often associated with malignant lesions [31]. In a subsolid nodule, the internal solid component may signify an invasive constituent and/or

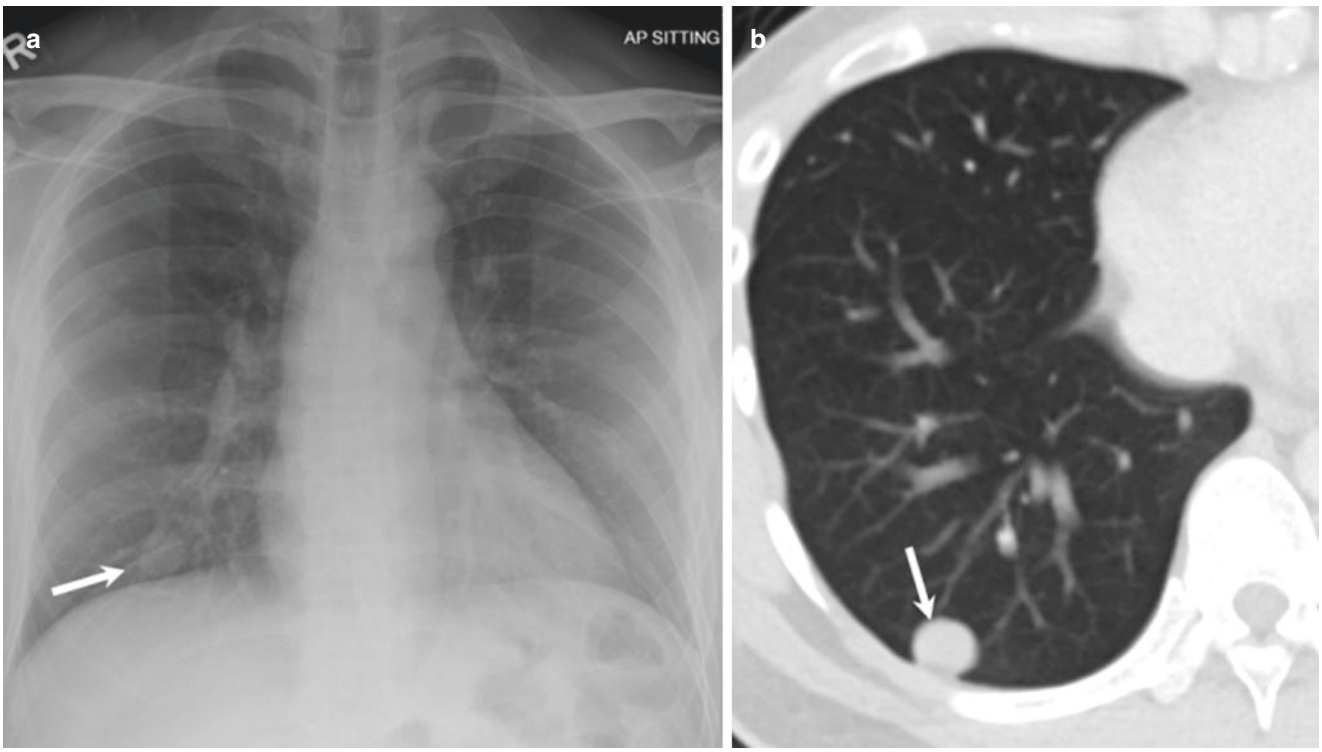

Fig. 5.2 A 28-year-old man with incidental solitary pulmonary nodule. (**a**) Frontal radiograph of chest shows a well-defined solitary pulmonary nodule in the right lower zone (arrow). (**b**) Axial CT thorax image in lung window confirms radiographic findings of well-circumscribed round nodule in the right lower lobe (arrow). Histopathology revealed a hamartoma

Table 5.2 Solitary pulmonary nodule

Malignant
• Primary lung cancer
• Metastasis
• Carcinoid
• Lymphoma
Benign
• Hamartoma
Infection
• Granuloma (TB, fungus, sarcoidosis)
• Round pneumonia
• Abscess
• Organizing pneumonia
Inflammatory
• Rheumatoid nodules
• Wegener's granulomatosis
Vascular
• AV malformation
• Pulmonary artery aneurysm
Airway
• Mucoid impaction (bronchiectasis)
Others
• Pulmonary infarction
• Sequestration
• Hematoma
• Bronchogenic cyst
• Rounded atelectasis

fibrosis with alveolar collapse. Based on current reports, the degree of invasion correlates directly with soft tissue component size on CT [22, 29] (Fig. 5.13). A new classification of adenocarcinoma was proposed by the International Association for the Study of Lung Cancer (IASLC), American Thoracic Society (ATS), and European Respiratory Society (ERS) based on pathologic and imaging findings and molecular biology information [29, 30] (Table 5.6).

In the new classification system, the term bronchoalveolar carcinoma has been replaced by invasive mucinous adenocarcinoma and classically manifests as a solid nodule or as an area of consolidation [22]. Patients with adenocarcinoma in situ or minimally invasive adenocarcinoma (categorized on CT as pure ground-glass lesions) have an excellent prognosis with almost 100% disease-free survival [32]. Prognosis of invasive adenocarcinoma is quite variable and depends on the histological subtype. It is recommended to evaluate the nodule in all three planes. The availability of multiplanar reconstructions helps in differentiating true nodule from focal pleural thickening or focal atelectasis as well as in assessing the three-dimensional shape of the nodule (Fig. 5.15).

5.5.5 Tissue Sampling/Biopsy

Suspicious lung nodules can be biopsied transbronchially, surgically, or percutaneously under imaging guidance.

Table 5.3 Pearls for evaluation of solitary pulmonary nodule

Nodule size	• As the nodule diameter increases, the risk of malignancy increases (Table 5.4)
Location and shape	• Lung cancers are commonly seen in upper lobes in approximately two-third of cases, particularly right upper lobe • 60% of cancers presenting as SPN are seen in the lung periphery (adenocarcinomas and metastases), and only 10% are seen in the medial third of the lung (squamous cell carcinoma) • Perifissural nodules are benign usually representing an intraparenchymal lymph node (Table 5.5)
Cavitation	• Cavitating nodules with thick and irregular walls usually favor malignant etiology • Benign cavitary nodules generally have a uniform thin wall • Bubbly lucencies or pseudocavitations are more frequent in malignant nodules (29%), particularly patients with adenocarcinoma due to the lepidic growth pattern
Nodule contour	• Benign nodules usually have smooth, well-defined margins, whereas malignant nodules generally have lobulated contours but there is considerable overlap • Metastatic nodules and 20% of primary lung malignancies may have smooth margins • Nodule with spiculated margins is more likely to be malignant
Nodule calcification	• Benign nodules: Solid, central, lamellated—granulomatous disease Popcorn-like pattern of calcification—hamartoma • Malignant nodules: Eccentric or stippled calcification within soft tissue density—seen in 10–15% malignant lesions
Halo and reverse halo sign	• Halo sign: Organizing pneumonia Adenocarcinoma in situ, Kaposi's sarcoma, hemorrhagic lung metastases • Reverse halo sign: Organizing pneumonia Post radiofrequency ablation of lung cancer
Density of nodules	• Differential diagnoses for GGO and subsolid nodule: infection, organizing pneumonia, vasculitis, and adenocarcinoma • Malignancy, specifically adenocarcinoma, should be suspected if a subsolid nodule persists, although it may be caused by benign conditions too such as focal interstitial fibrosis and organizing pneumonia • Central location of the solid component in subsolid nodule is more often associated with malignant lesions
Growth and doubling time	• Doubling time for a nodule is the time required for it to double in volume • Nodule which doubles in volume in less than 1 month and more than 200 days is more likely to be of benign etiology • Doubling times for solid cancers (one volume doubling corresponds to a 26% increase in diameter), ranges from 100 to 400 days • Adenocarcinomas which manifest as subsolid nodules have more indolent growth, with average doubling time ranging from 3 to 5 years
Contrast enhancement	• Malignancies have a greater tendency to enhance due to increased vascularity • Characteristically, benign nodules enhance less than 15 HU, and malignant nodules enhance more than 20 HU • If a nodule does not enhance, malignancy is virtually excluded

Bronchoscopic biopsy of central masses/perihilar nodules is possible; however, in the absence of an endoluminal component, bronchoscopic diagnosis may be quite challenging [36]. Peripheral lung masses are usually approached via image-guided techniques [4]. Histopathological diagnosis of malignancy using a percutaneous fine needle or cutting needle biopsy technique is quite accurate, but all the nodules are not suitable for this approach. This technique too is associated with false-positive results, the rate of which is quite low; however, more worrisome is its false-negative rate, particularly with nodules less than 1 cm in size [4, 8]. Newer transbronchial tissue sampling technique using endobronchial ultrasonography-guided transbronchial needle aspiration is a powerful tool for lung cancer diagnosis and staging and is now the first choice for staging mediastinal LNs, due to its high sensitivity (>90%) and specificity (almost 100%) [37].

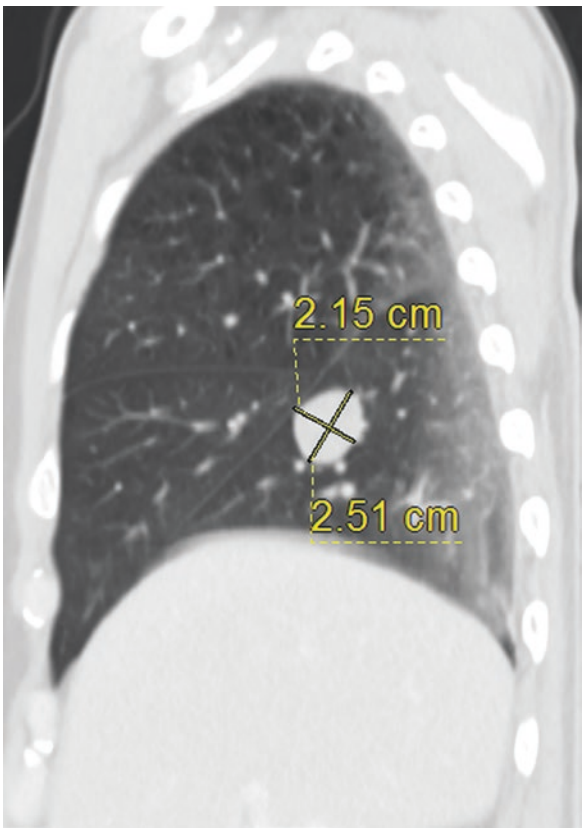

Fig. 5.3 Example of manual nodule measurements

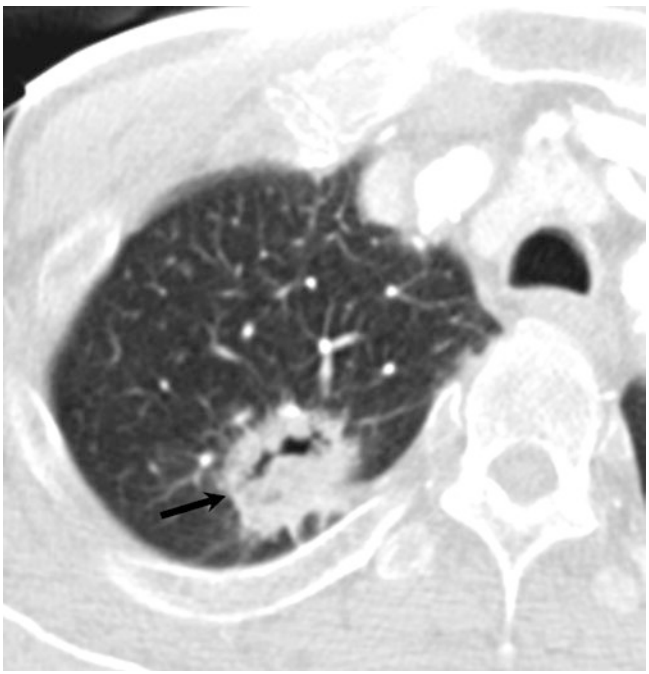

Fig. 5.5 Cavitary adenocarcinoma. Axial CT thorax image in lung window shows an irregular thick walled cavitary mass in the right upper lobe (arrow)

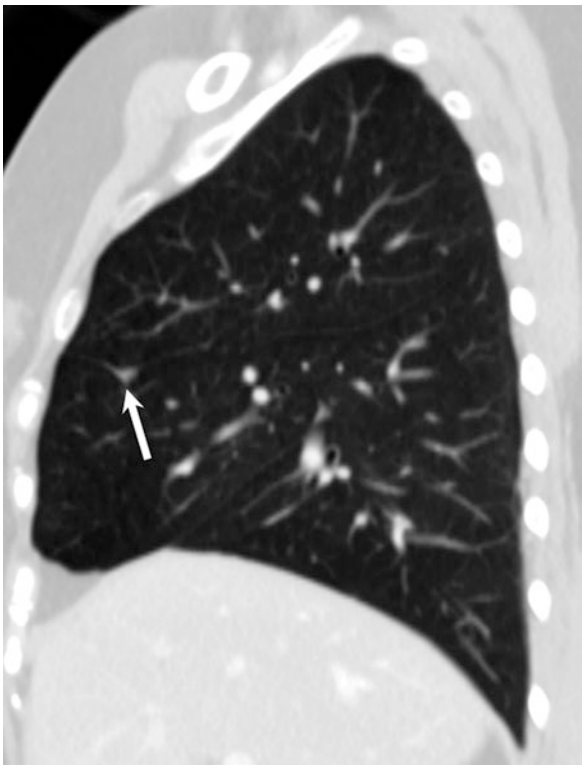

Fig. 5.4 A small triangular perifissural nodule with flat surfaces (arrow)

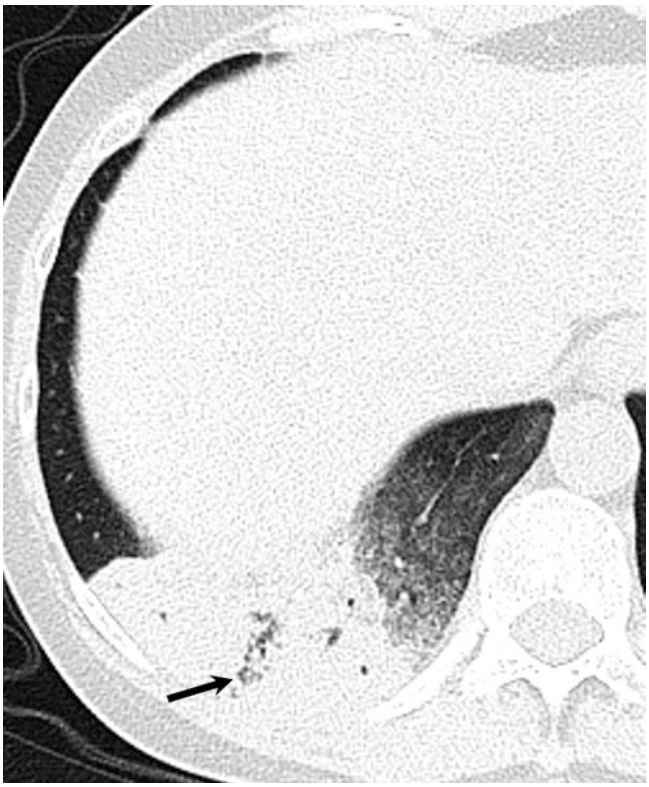

Fig. 5.6 A 57-year-old man with persistent consolidation. Transbronchial brushings revealed adenocarcinoma

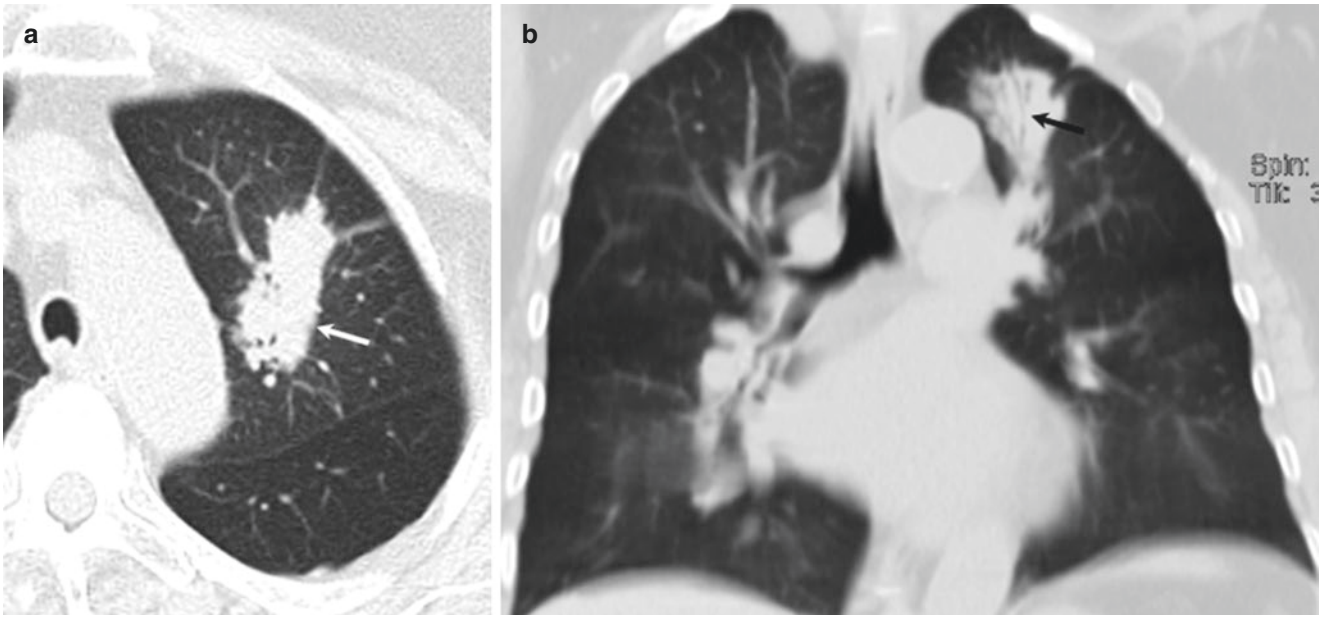

Fig. 5.7 A 65-year-old women with adenocarcinoma. (**a**) Axial and (**b**) coronal CT images show an area of consolidation with air-bronchograms that was persistent on serial radiographs (not shown) (arrow)

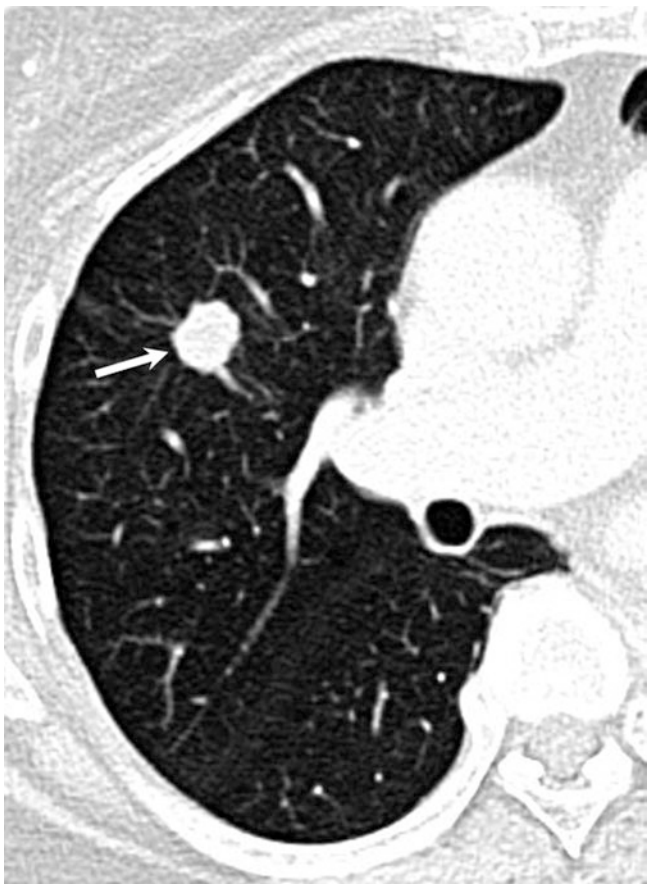

Fig. 5.8 Lobulated nodule favors malignancy (arrow). Histopathology confirmed it to be an adenocarcinoma

5.5.6 PET/CT

Currently PET/CT is considered the most accurate imaging modality for evaluating nodal and distant metastases in lung cancer and is considered an essential tool in the management and the work-up of patients with pulmonary malignancy. PET/CT is more precise than CT in its ability to assess locoregional lymph node spread. The commonest isotope used is 2-deoxy-2-[^{18}F] fluoro-D-glucose (FDG), which is a glucose analogue, containing positron-emitting radioactive isotope fluorine-18. The technique depends on the degree of FDG uptake depending on the rate of cellular glycolysis. As neoplastic nodules have higher rate of glucose metabolism, they show increased uptake of the radioisotope. However, this finding can be nonspecific, as increased radioisotope uptake can be seen with many infective or inflammatory processes too. Despite this, PET/CT has been shown to have sensitivity of 96% and specificity of 93% in detecting malignant nodules with a diameter of 10 mm or more. Likelihood of false-negative interpretation is high for nodules of less than 10 mm. Advocating PET/CT for evaluating nodules of less than 6 mm is currently not justified [4]. PET/CT has very high negative predictive value, and when the clinical suspicion for malignancy is low, a non-FDG-avid pulmonary nodule may be managed conservatively [38]. On the contrary, in high-risk patients an FDG-avid nodule warrants biopsy or intervention to obtain pathological confirmation [38–40]. Due to increased accuracy of PET/CT in nodal assessment and very high negative predictive value in normal-sized nodes, PET/CT is quite

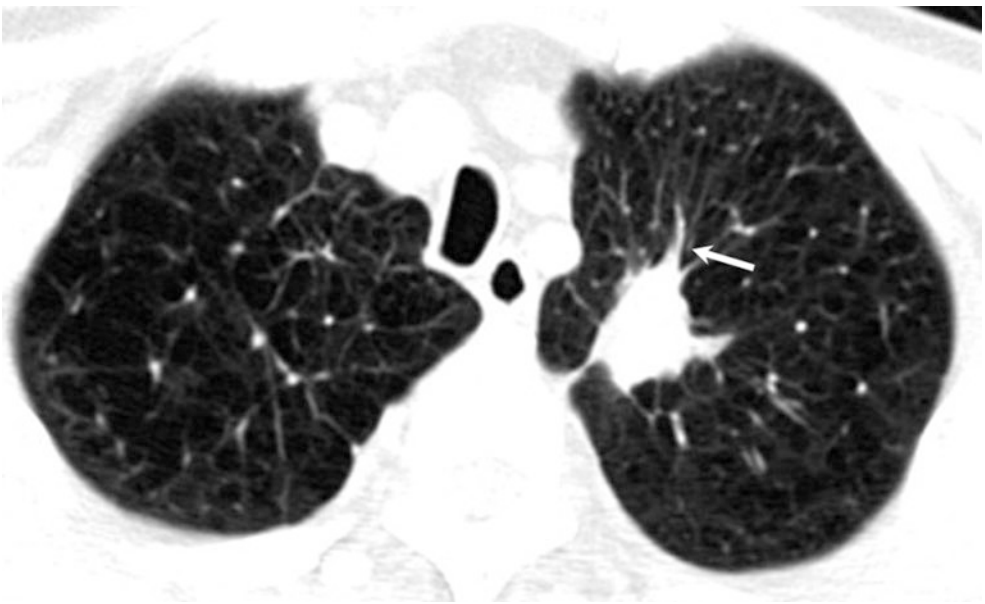

Fig. 5.9 Spiculated adenocarcinoma nodule (arrow), infiltrating into the adjacent lung. Note background centrilobular emphysema in upper lobes

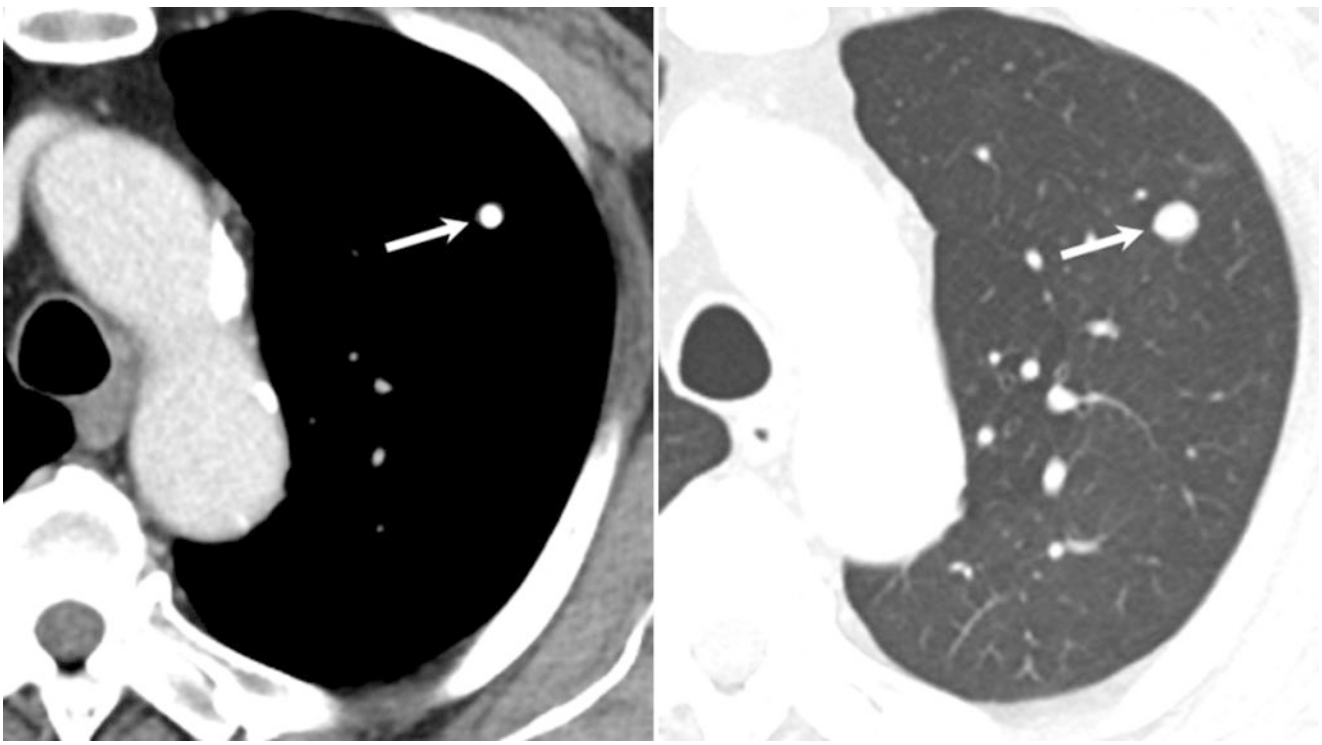

Fig. 5.10 A 53-year-old man with a calcified granuloma (tuberculoma). Contrast-enhanced axial CT thorax image in soft tissue and lung window shows a well-defined, round calcified nodule in the left upper lobe (arrow)

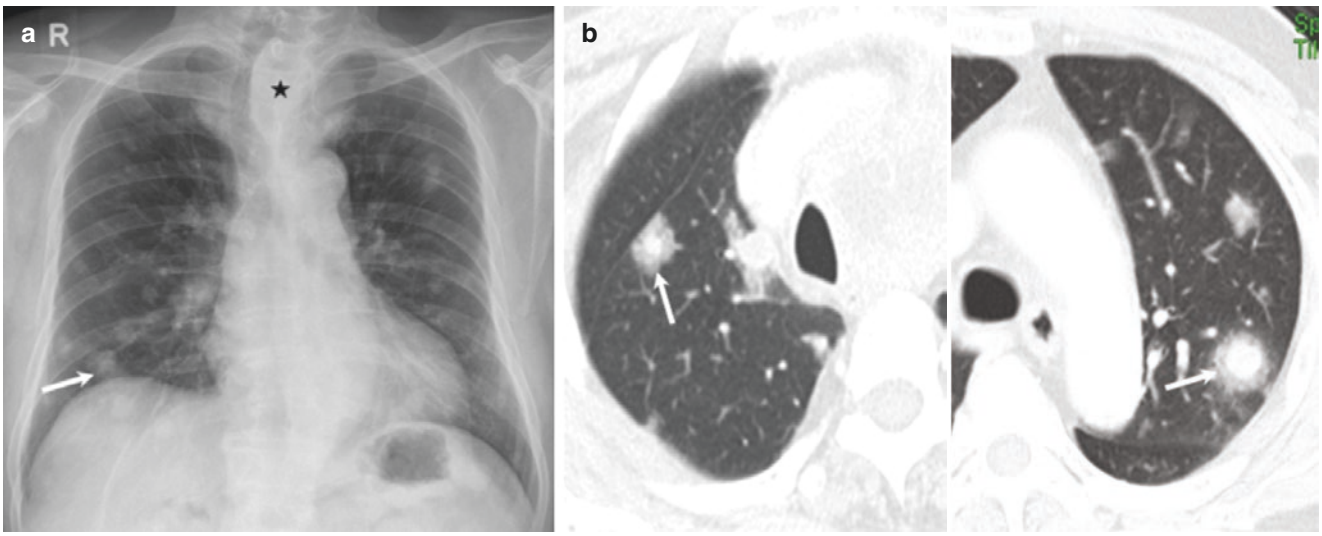

Fig. 5.11 Multiple hemorrhagic lung metastases from thyroid carcinoma. (**a**) Frontal radiograph of chest shows multiple nodules (arrow) in both lungs. A soft tissue mass is seen in the left paratracheal region displacing trachea to the right side (asterisk). (**b**) Axial CT thorax image in lung window shows multiple nodules in both lungs surrounded by an ill-defined rim of ground-glass attenuation (arrow) termed as "halo" sign

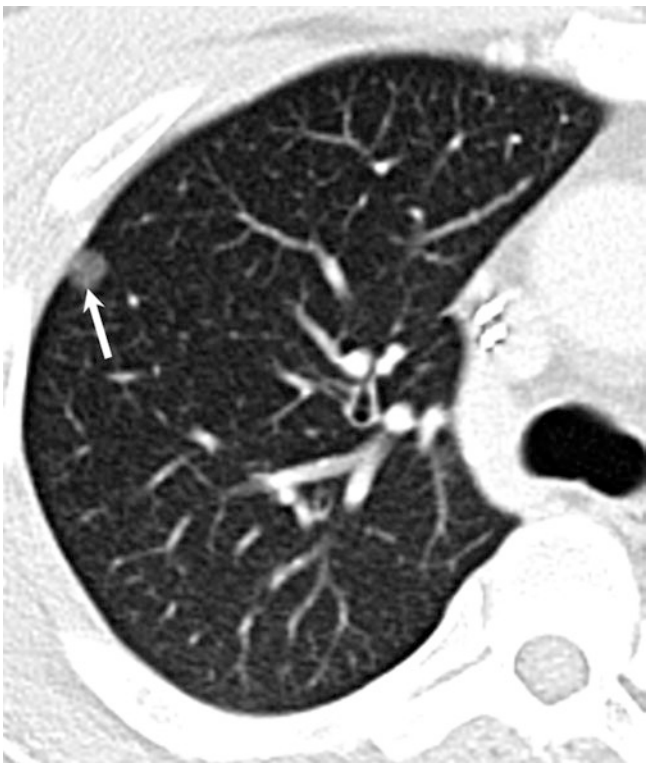

Fig. 5.12 Ground-glass density nodule. Axial CT thorax image in lung window shows a well-marginated lesion of increased lung attenuation in the right upper lobe (arrow) through which normal structures can be discerned

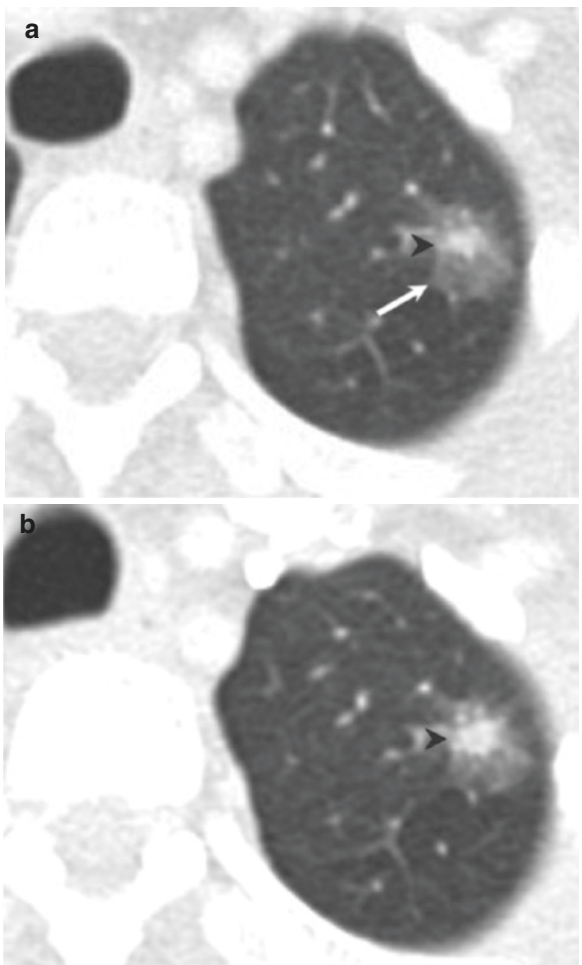

Fig. 5.13 Part-solid ground-glass nodule. (**a**) Axial CT thorax image in lung window shows a solitary part-solid ground-glass nodule in the left upper lobe (arrow) (**b**) On 3-month follow-up, there is increase in solid component (arrowhead). Histopathology confirmed it to be an adenocarcinoma

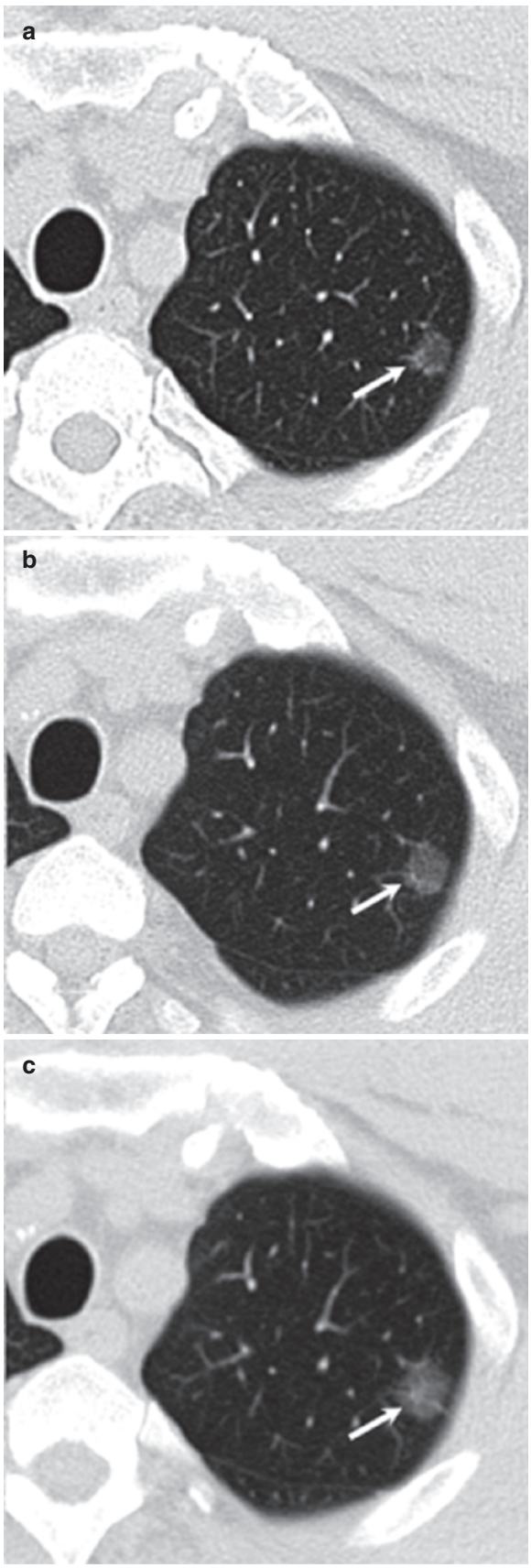

Fig. 5.14 A 49-year-old women with an enlarging pure ground-glass nodule. (**a**–**c**) Axial CT thorax images in lung nodule show interval increase in the size of a pure ground-glass nodule in the left upper lobe (arrow) at 12- and 24-month follow-up

Table 5.4 Likelihood of cancer, based on nodule diameter[a]

Diameter (cm)	Risk of malignancy (%)
0.5–1.0	35
1.0–2.0	50
>2.0	85

[a]Manual nodule measurements should be based on the average of short- and long-axis diameters

Table 5.5 Characteristic features of perifissural nodules

• Represent intrapulmonary nodes
• Commonly seen adjacent to pleural fissures and pleural surface
• Located less than 15 mm from the pleural surface
• Triangular or oval on transverse images and have a flat or lentiform configuration in sagittal or coronal reconstructions
• Straight surface of contact with the pleura or concave surfaces on all sides
• Connected to the pleural surface by a thin linear opacity
• If a nodule has characteristic features of perifissural nodule, follow-up CT is not recommended, even if the average dimension exceeds 6 mm

Table 5.6 Adenocarcinoma classification

Atypical adenomatous hyperplasia	• Lepidic growth • Measures less than ≤5 mm in diameter • Faint pure GGN • Single or multiple
Adenocarcinoma in situ	• Non-mucinous and mucinous variants • Pure lepidic growth without invasion • Measures <3 cm • Pure GGN but sometimes as a part-solid or occasionally a solid invasive lesion • Single or multiple
Minimally invasive adenocarcinoma	• Predominantly lepidic growth with no necrosis or invasion of blood vessels, lymphatics, or pleura • Usually measures <3 cm • Invasive component of no more than 5 mm • Part-solid nodule consisting of a predominant ground-glass component and a small central solid component measuring 5 mm or less
Invasive adenocarcinomas	• Lepidic predominant (formerly non-mucinous BAC pattern, with >5 mm invasion) • Acinar predominant • Papillary predominant • Micropapillary predominant • Solid predominant with mucin production • Usually, a solid nodule but may also be part solid and occasionally a GGN
Variants of invasive adenocarcinoma	• Invasive mucinous adenocarcinoma (formerly mucinous BAC) • Colloid fetal (low and high grade) • Enteric

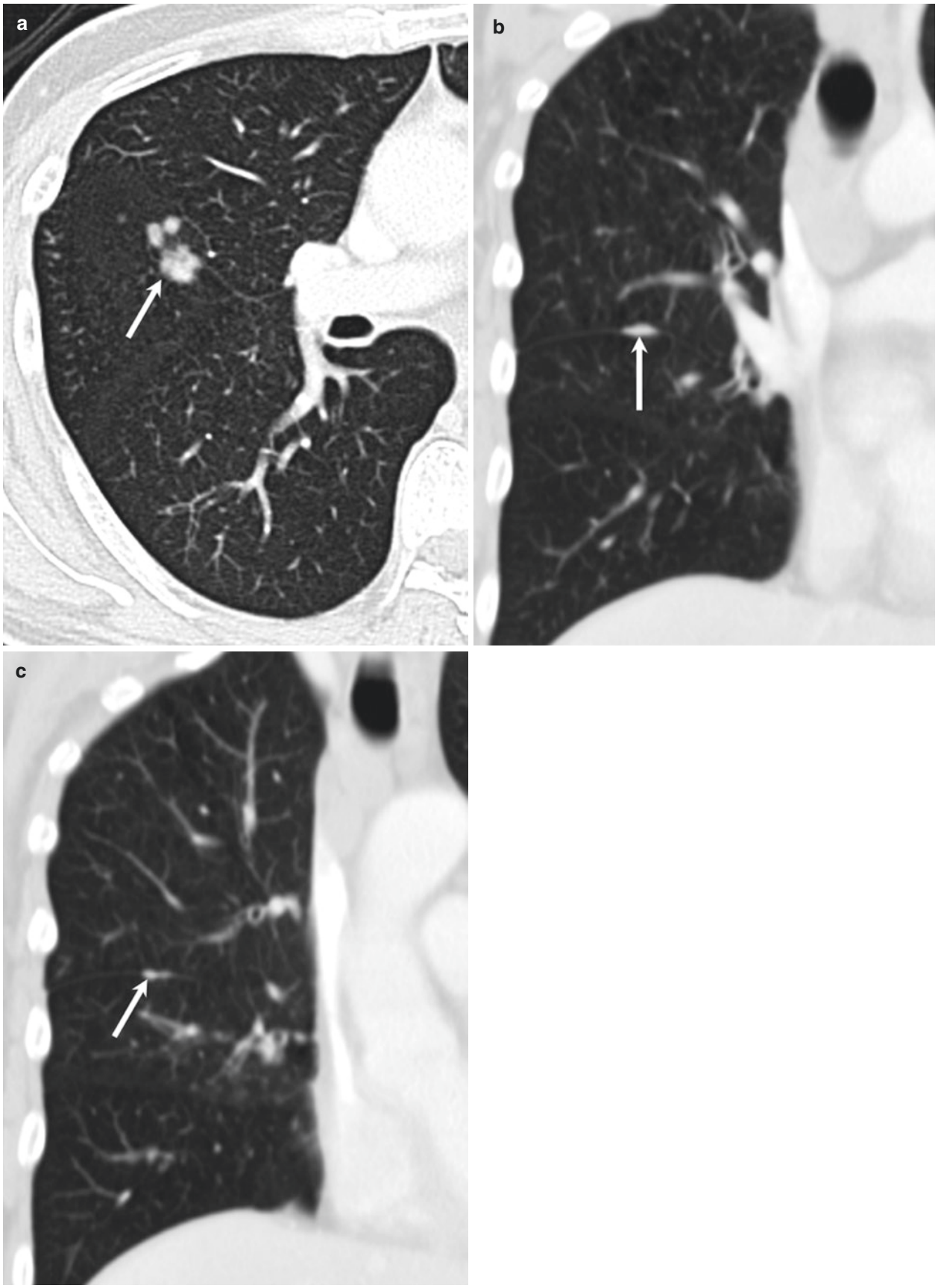

Fig. 5.15 Pseudonodules in a patient for staging cecal carcinoma. (**a**) Axial CT image shows cluster of nodules (arrow). (**b**, **c**) Coronal CT images show flat nodular thickening of the right minor fissure

useful in assessing early-stage lung malignancy [38]. However, for larger nodes measuring >10 mm, the false-positive rates remain significantly high and should be interpreted cautiously. PET/CT is also useful in detecting distant osseous and soft tissue metastases [38].

5.6 Bronchogenic Carcinoma

The imaging appearances of bronchogenic carcinomas are discussed under the following headings: (1) peripheral tumors (arising beyond the hilum/segmental bronchi), (2) central tumors (arising in large central bronchus at or close to the hilum), (3) intrathoracic spread, and (4) extrathoracic spread of bronchial carcinoma.

5.6.1 Peripheral Tumors

Approximately 40% of bronchial carcinomas arise beyond the segmental bronchi, and in 30% of the cases, a peripheral mass is the only radiographic finding [5]. Radiographic detection of non-calcified pulmonary nodule less than 1 cm is challenging and becomes difficult when they are located near hila. CT is better in detecting smaller lesions due to its better contrast resolution [5, 41, 42] (Fig. 5.16). CT helps in distinguishing mucus plugging from true nodules (Fig. 5.17).

5.6.1.1 Shape and Margin

Bronchial carcinomas located peripherally are generally spherical or oval in shape, except for tumors at the lung apex, such as Pancoast tumors which may present as apical pleural nodular thickening (Fig. 5.18). Some cases of bronchial carcinoma may present as a focal area of consolidation. Hence bronchogenic carcinoma must always be included in the differential of the solitary pulmonary nodule in an adult patient [5, 42, 43]. If a peripheral mass presents with hilar enlargement or bony metastases, it is considered as malignant (Fig. 5.19). However, frequently, a peripheral mass or nodule is the only visible abnormality on radiographs making a diagnosis of bronchial carcinoma more difficult [44]. A nodule with lobulated margins favors malignancy as it indicates uneven growth rates in different parts of the tumor. A notch within the nodule (umbilication) indicates relatively slow growth of a particular portion of the nodule, thus favoring malignant etiology [5].

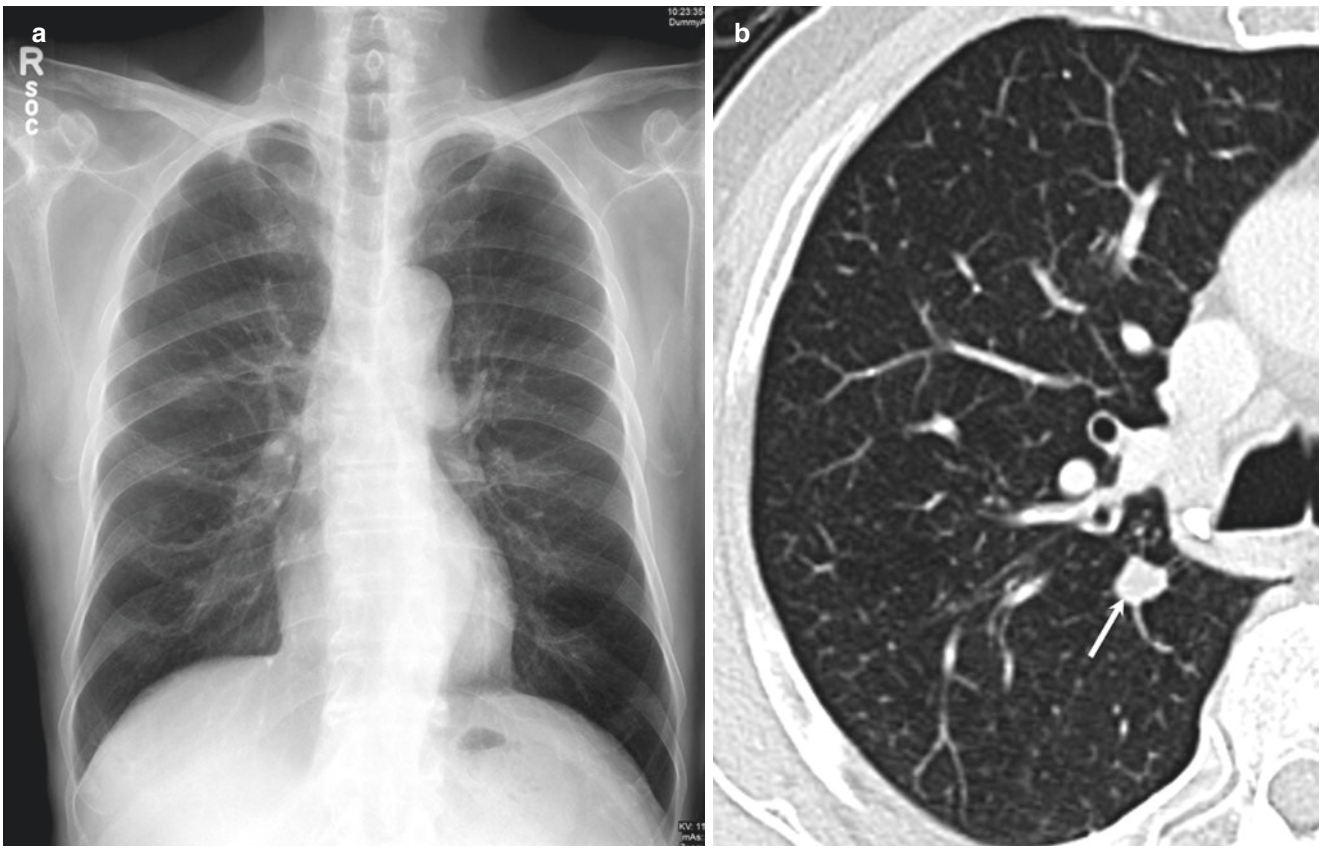

Fig. 5.16 Limitation of chest radiograph in detecting less than 1 cm size non-calcified nodule. (**a**) Frontal chest radiograph is unremarkable. (**b**) Axial CT image shows a 9 mm nodule in right lobe (arrow)

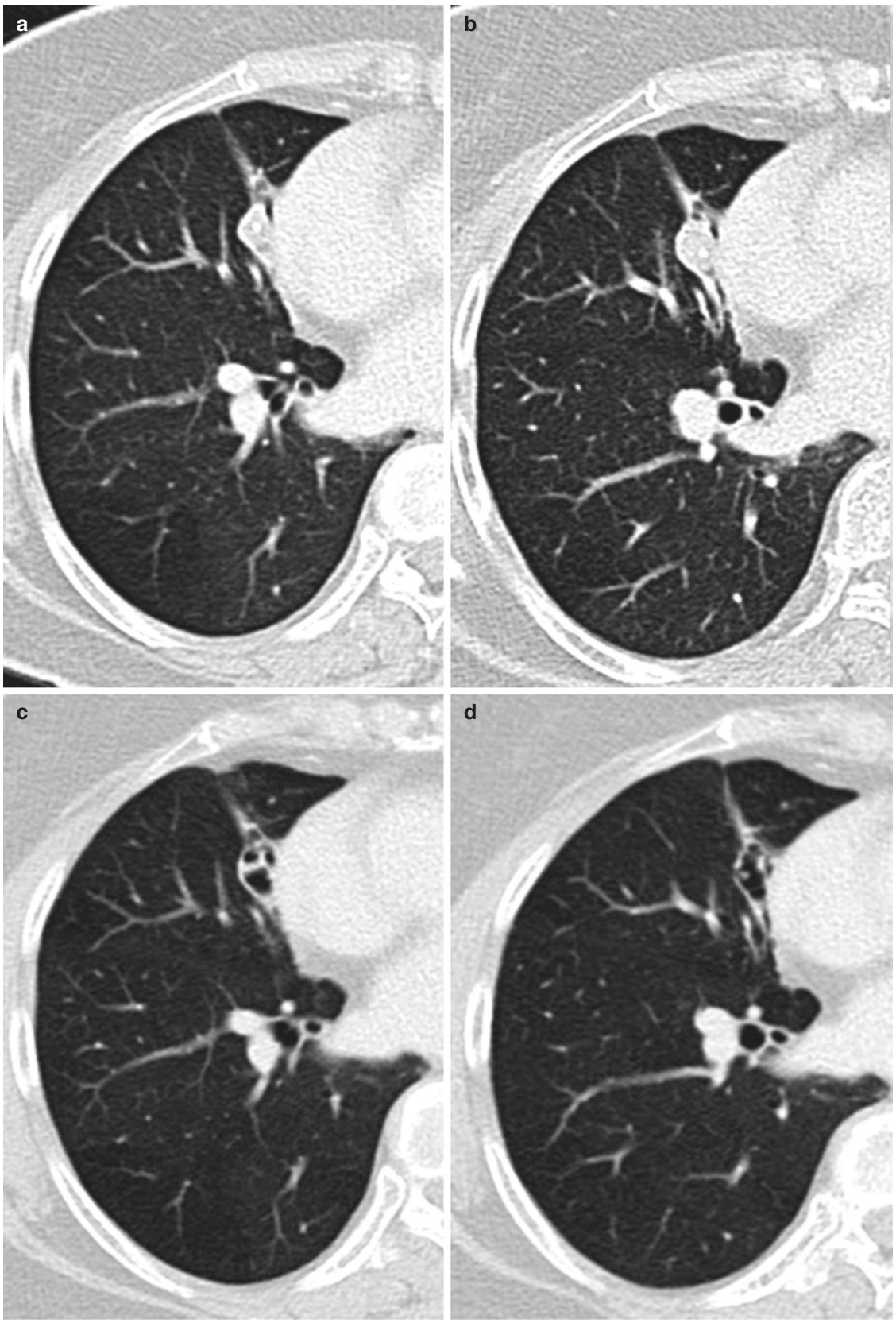

Fig. 5.17 Mucus plugging in the right middle lobe mimicking a nodule. (**a**) Baseline and (**b**) yearly follow-up axial CT images showed increase in size of the apparent nodule in medial right middle lobe containing foci of calcification. (**c**, **d**) Axial images on second and third year of follow-up showed clearing of mucus plug from dilated airways

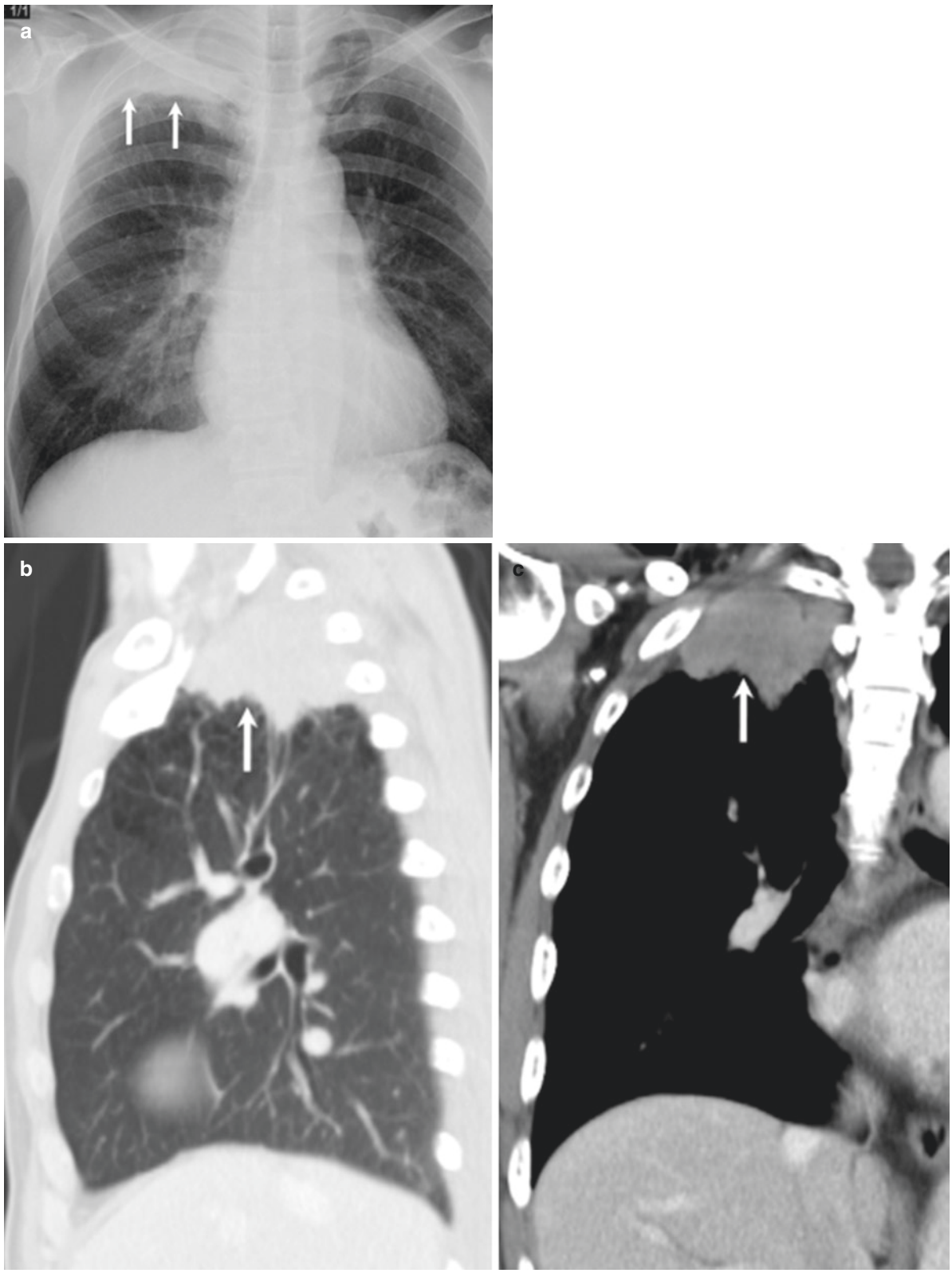

Fig. 5.18 A 71-year-old man with Pancoast tumor. (**a**) Frontal radiograph of chest shows asymmetric right apical pleural thickening (arrow). (**b**, **c**) Sagittal and contrast-enhanced coronal CT thorax image in lung and soft tissue window shows right apical lung mass in keeping with Pancoast tumor (arrow)

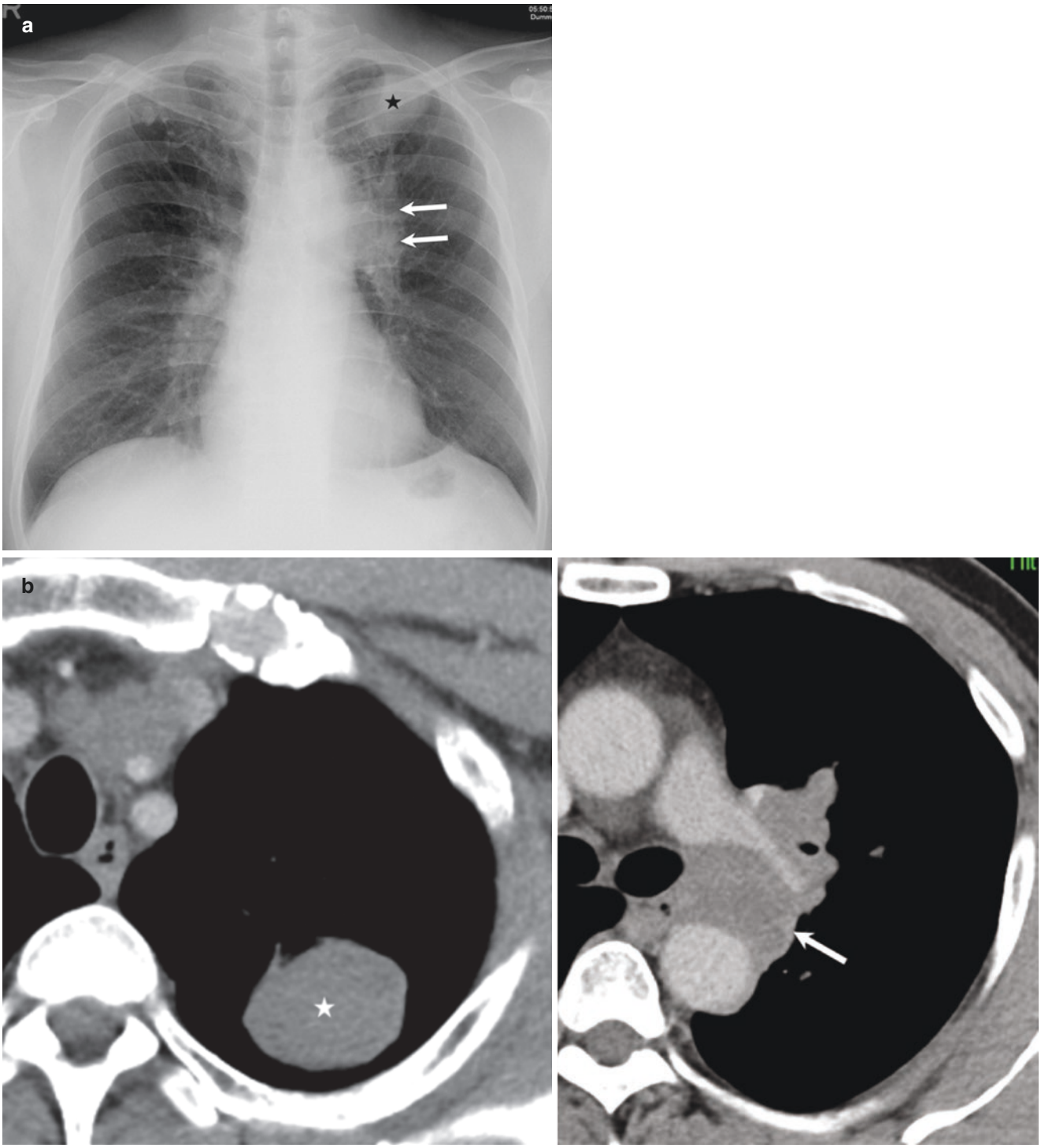

Fig. 5.19 A 68-year-old man with bronchial carcinoma. (**a**) Frontal radiograph of chest shows an ill-defined opacity projected over the left upper zone (asterisk) with dense left hilum (arrow). (**b**) Contrast-enhanced axial CT thorax image in soft tissue window confirms malignant left upper lobe mass (asterisk) with left hilar lymphadenopathy (arrow)

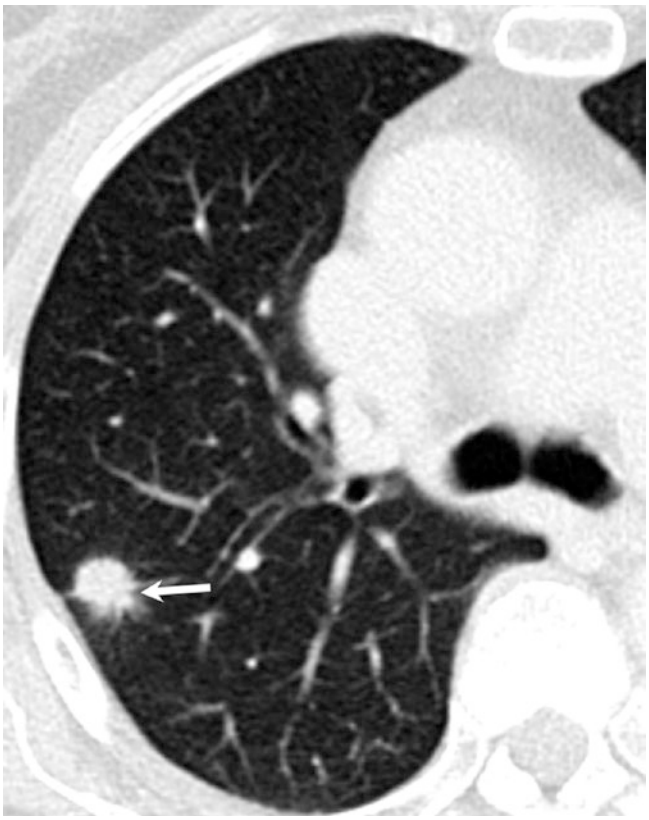

Fig. 5.20 A 54-year-old women with bronchial carcinoma. Axial CT image in lung window shows a nodular opacity in the right upper lobe with spiculated margins, infiltrating into the adjacent lung (arrow)

Peripheral bronchial carcinomas tend to have poorly defined, irregular, or spiculated margins attributed to the growth of malignant cells along the pulmonary interstitium (Fig. 5.20). Spiculated margin, often described as a "sunburst" or "corona radiata" sign, is best seen on CT and is highly predictive of malignancy, with a positive predictive value of 90%. Corona radiata sign is not specific but is very much suggestive of bronchial carcinoma. Rarely, other benign conditions, such as organizing pneumonia, focal atelectasis, tuberculoma, and progressive massive fibrosis, may also demonstrate irregular margins in the background of emphysema [22, 43].

"Pleural tail" or pleural tags are linear or band-like opacities between a peripherally located mass and adjacent pleura, where the tail probably represents either atelectasis secondary to bronchial obstruction or septal edema due to lymphatic obstruction [4] (Fig. 5.21). This sign was considered specific for adenocarcinoma but can be seen in tuberculomas in endemic areas [43].

Usually bronchial carcinomas have well-defined edges; however, some peripheral carcinomas such as adenocarcinomas may have poorly defined edge or may present as a focal area of consolidation, mimicking pneumonia [5] (Fig. 5.22a). Frequently, early lung cancers arising in segmental or subsegmental bronchi may appear as branching densities resembling mucoceles or bronchoceles and represent dilated bronchi filled with a tumor or inspissated secretions distal to the small endobronchial tumor (Fig. 5.22b, c) [5].

5.6.1.2 Cavitation and Pseudocavitation

Squamous cell carcinomas are more likely to cavitate reflecting central necrotic/hypoxic core (Fig. 5.23). Malignant cavitary nodules typically have thick, irregular walls and may show tumor nodules [22, 45]. It is suggested that 95% of cavitary nodules with a wall thickness of more than 15 mm are malignant [22, 45]. Nevertheless, cavity wall thickness may not be a reliable imaging feature to differentiate benign and malignant nodules (Fig. 5.24). The cavity may show air-fluid level, else may contain necrotic tumor fragments or debris [45].

Lung adenocarcinomas may demonstrate "pseudocavitation" and "Cheerio" sign. Pseudocavitation is a single or multiple bubble-like foci of low attenuation within a solid or ground-glass nodule (Figs. 5.25 and 5.26). Unlike true cavitation (due to central necrosis), pseudocavitation can be of any shape (round, oval, bizarre, or linear), eccentric and multiple. Histologically, pseudocavitation reflects airspaces or air bronchograms in a lesion, which may be accentuated by cicatricial contraction. Pseudocavitation corresponds to lepidic tumor, i.e., proliferating cells grow along alveolar walls without breaching the wall or vascular invasion and are associated with favorable prognosis. Cheerio sign is defined as a nodule with a relatively large central lucency and thin opaque rim seen on CT, resembling the ring-shape "Cheerios" and occurs due to the proliferation of neoplastic cells around a patent airway [46, 47]. Cheerios sign is seen in primary and metastatic mucinous adenocarcinomas as well as pulmonary Langerhans cell histiocytosis. A rare presentation of adenocarcinoma is of "crazy-paving" pattern with extensive ground-glass opacities and septal thickening (Fig. 5.27).

5.6.1.3 Calcification

Tumoral calcification may be seen on CT in 6–10% cases. Pathologically, these are dystrophic calcifications in areas of tumor necrosis or may be an intrinsic part of the tumor (Fig. 5.28). In most cases, calcification within the tumor represents pre-existing granulomatous calcifications engulfed by the tumor [5] (Fig. 5.29). However, amorphous, cloud-like, or punctate calcification representing dystrophic tumoral calcification may be seen in the small proportion of cases [22, 43]. Most tumors that show calcification are large with a diameter of 5 cm or more at initial imaging [48].

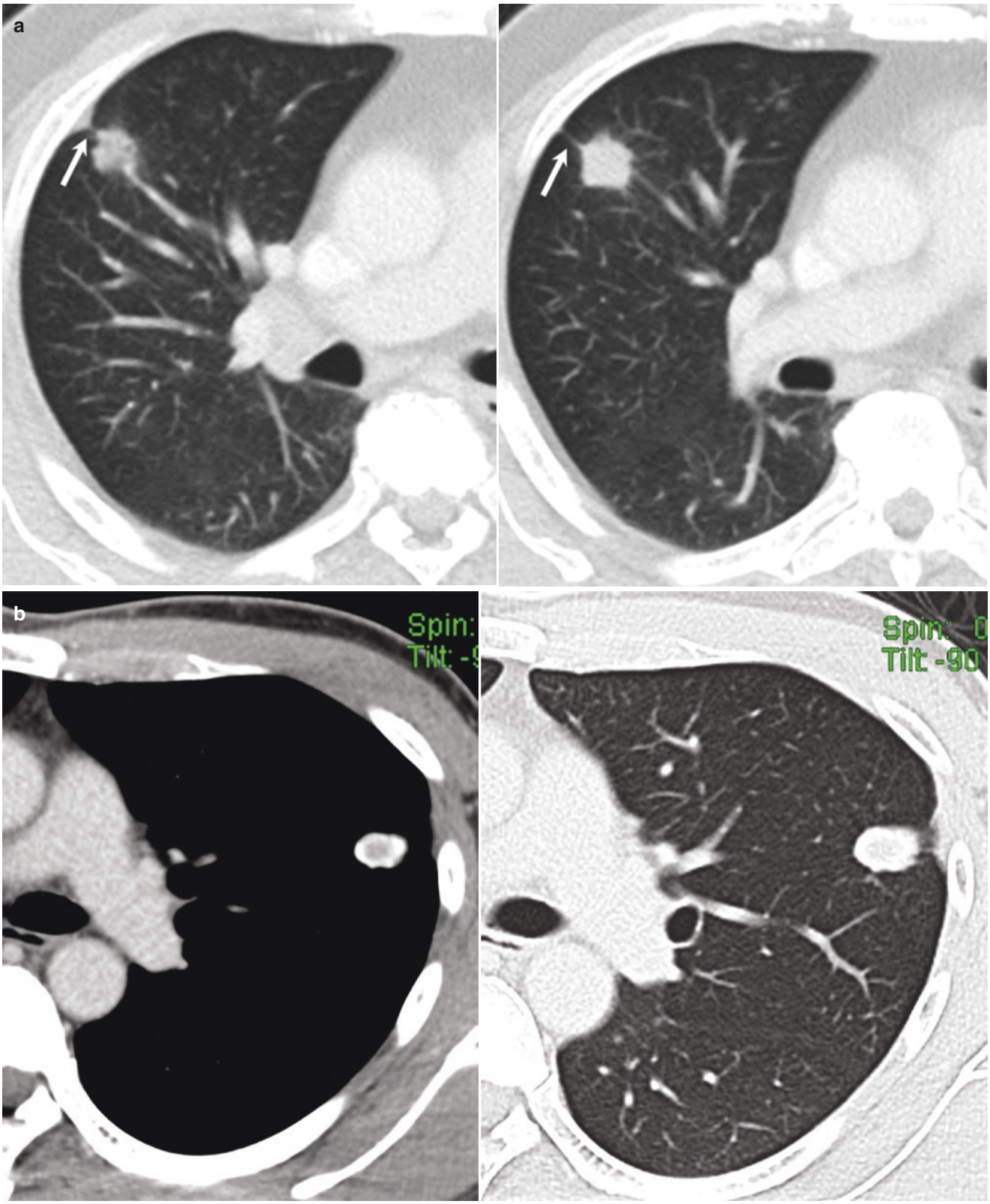

Fig. 5.21 Pleural tag. Adenocarcinoma. (**a**) Axial CT images show a linear or band-like opacity between a peripherally located mass and adjacent pleura (arrow). Tuberculoma. (**b**) Multiple pleural tags in peripherally calcified nodule

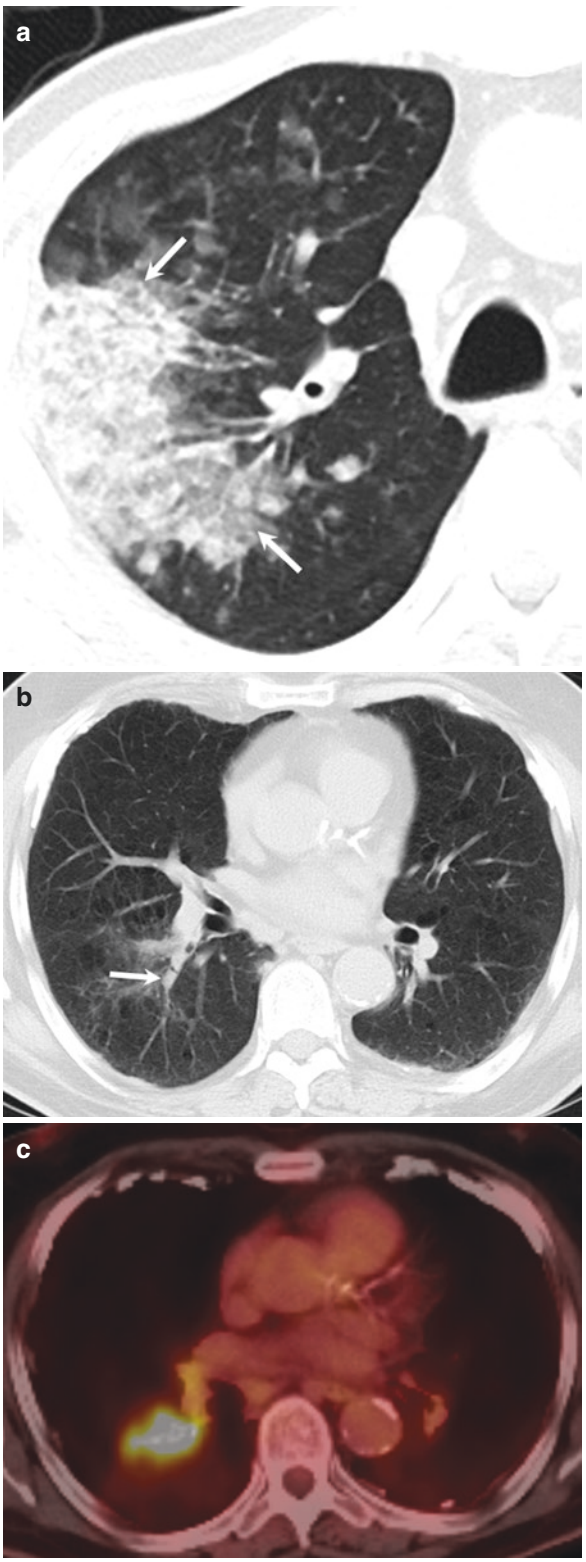

Fig. 5.22 Tumor as persistent consolidation. (**a**) Axial CT thorax image in lung window shows a large area of consolidation and ground-glass opacity with air bronchogram in the right upper lobe (arrows). Tumor in another patient presenting as persistent bronchocele. (**b**, **c**) Axial CT and PET images show a endobronchial tumor as bronchocele (arrow)

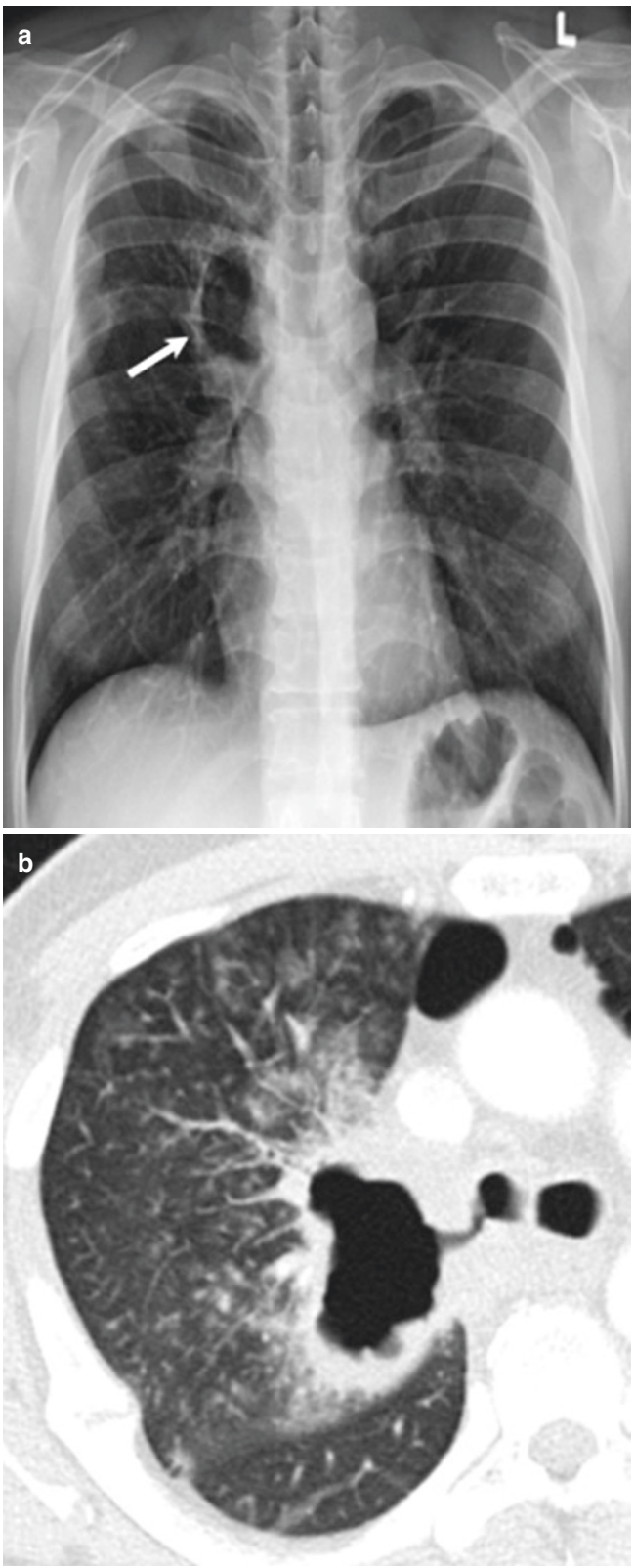

Fig. 5.23 A 59-year-old man with cavitary squamous cell carcinoma. (**a**) Frontal radiograph of chest shows a cavitary lesion in right perihilar region (arrow). (**b**, **c**) Contrast-enhanced axial CT images in lung and soft tissue window show a cavity with nodular walls in right perihilar region eroding into the right upper lobe bronchus

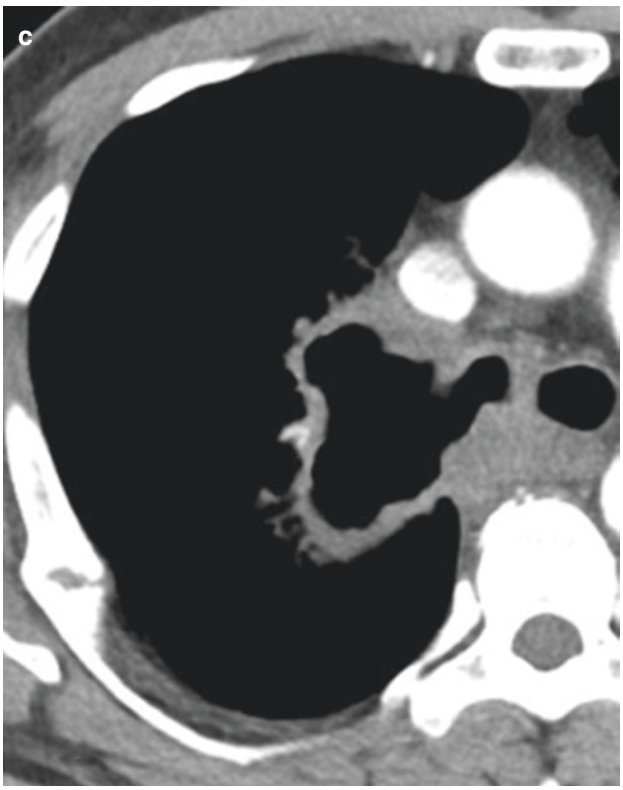

Fig. 5.23 (continued)

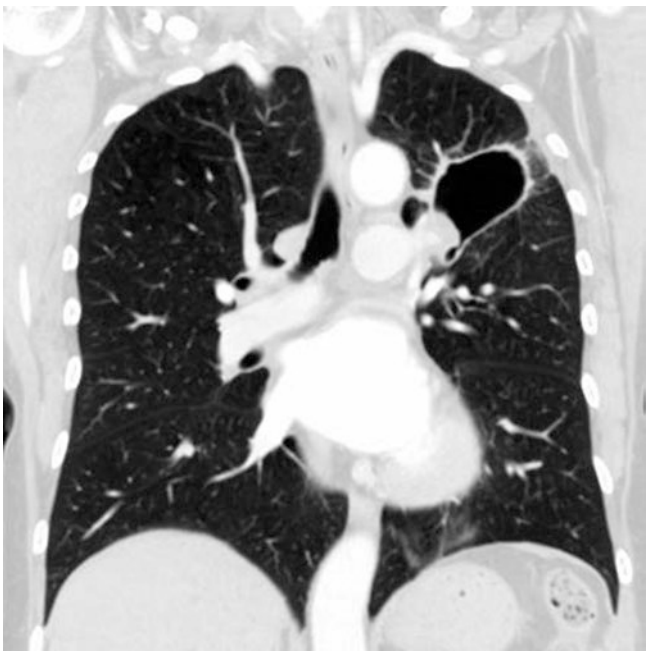

Fig. 5.24 A 57-year-old man with cavitary squamous cell carcinoma. Coronal CT image shows a thin-walled cavity in the left upper lobe with an eccentric nodule at hilum

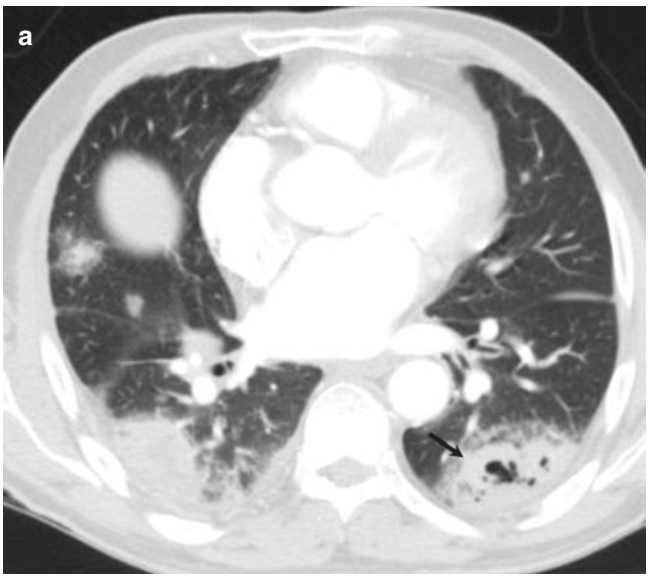

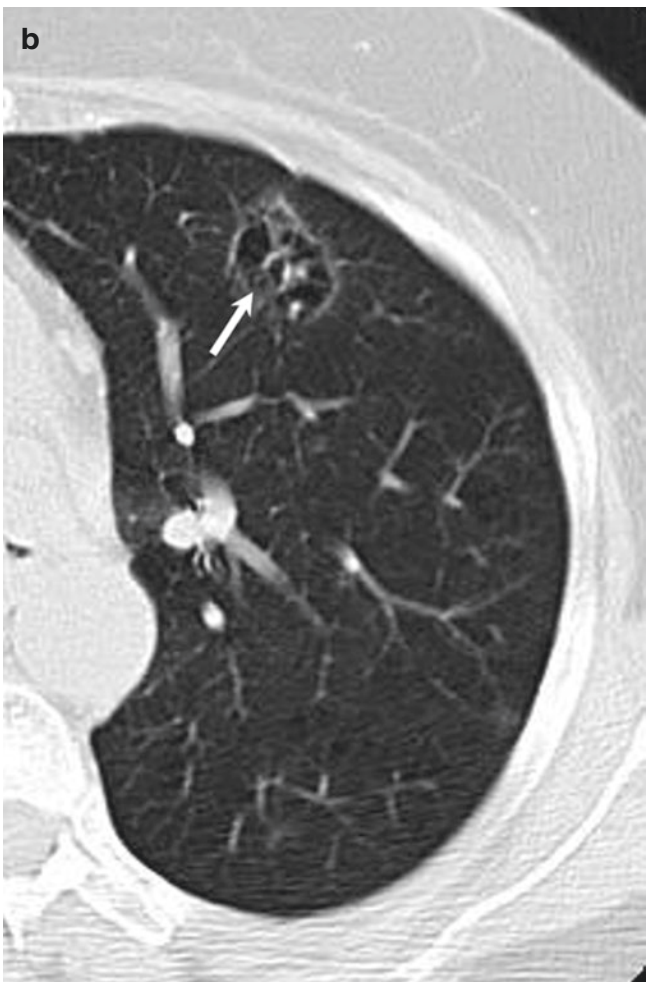

Fig. 5.25 Pseudocavitation or bubbly lucencies in two patients. (**a**) Axial CT image in a patient with mucinous colonic cancer with multiple pulmonary metastases with one in left lower lobe showing pseudocavitation (arrow). (**b**, **c**) Axial CT images in a 35-year-old woman with a cystic mass due to pseudocavitation (arrow) that was proven to be an adenocarcinoma

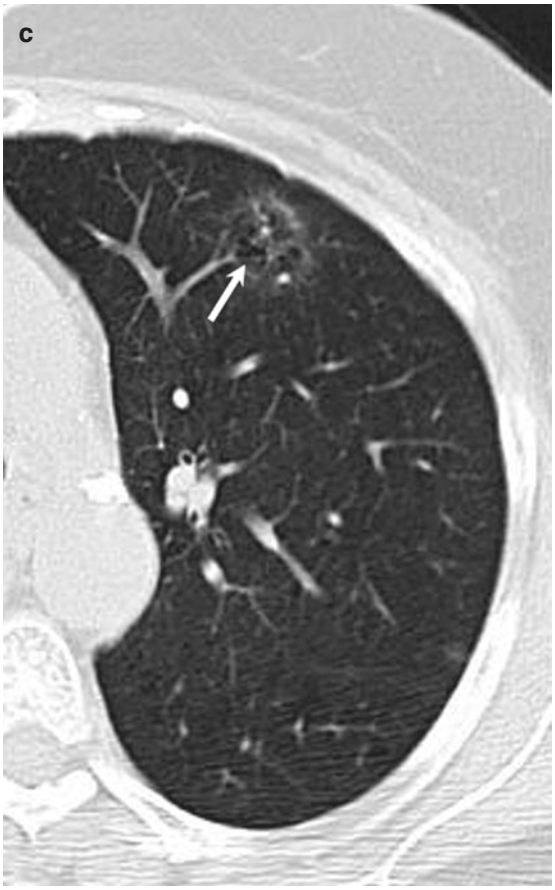

Fig. 5.25 (continued)

5.6.2 Central Tumors

Central tumors usually present with imaging features of collapse and consolidation of the lung beyond the tumor and hilar enlargement.

5.6.2.1 Collapse and Consolidation

Central tumors usually cause partial or complete bronchial obstruction resulting in the collapse of a single or multiple segments, lobes, or the entire lung. Post-obstructive atelectasis and consolidation are commonly associated with central tumors at initial imaging, particularly squamous cell carcinoma (Fig. 5.30). These changes may sometimes obscure an underlying primary tumor [44].

Imaging features that suggest collapse or consolidation are secondary to an obstructing neoplasm and require further evaluation by bronchoscopy are:

- Altered shape of the collapsed or consolidated lobe—as central mass results in lobar collapse, the fissure in the region of the mass may not move in the usual manner and may appear bulged ("Golden S" sign) (Fig. 5.31). This sign is quite specific and indicates that the collapse is the result of an underlying mass.
- Endobronchial malignancy should be suspected if consolidation or atelectasis is confined to a single segment or a lobe (or more lobes if there is a common bronchus) that remains unchanged for more than 4 weeks.
- In some cases, the consolidated lobe may appear larger due to the accumulation of secretions beyond the obstructing neoplasm, an appearance termed as drowned lobe [4, 5].
- CT showing convex soft tissue protruding in the main stem or lobar bronchus.

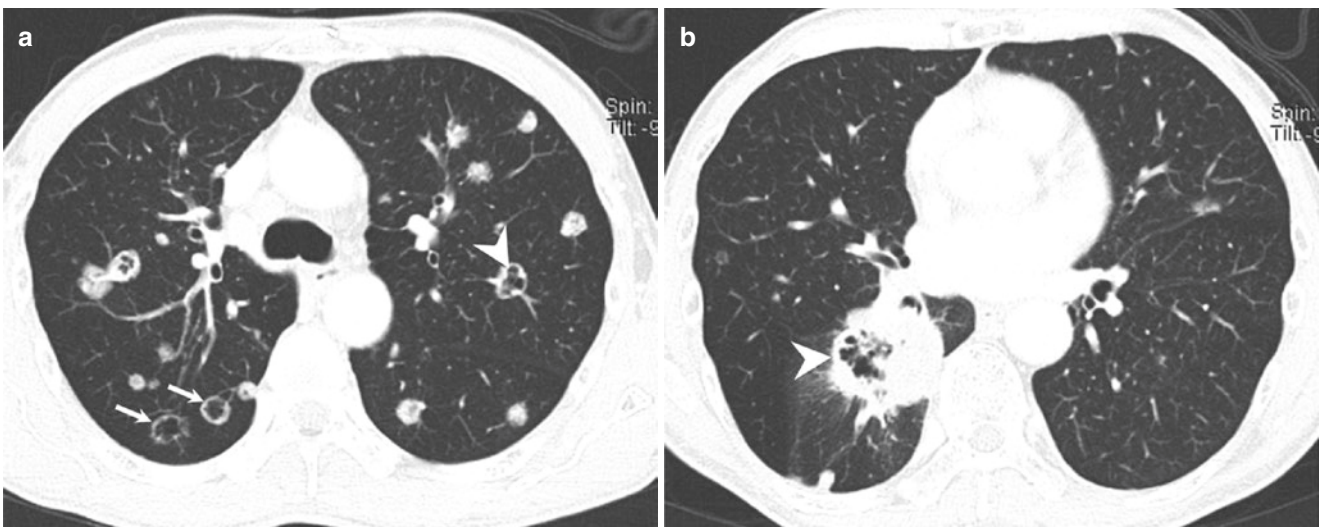

Fig. 5.26 Pseudocavitation and Cheerios sign in two patients with multifocal adenocarcinomas. (**a**, **b**) Axial CT images in one patient show Cheerios sign (arrows) and pseudocavitation (arrowhead). (**c**–**e**) Axial CT images in second patient show multiple ring-shape opacities and solid masses with pseudocavitation

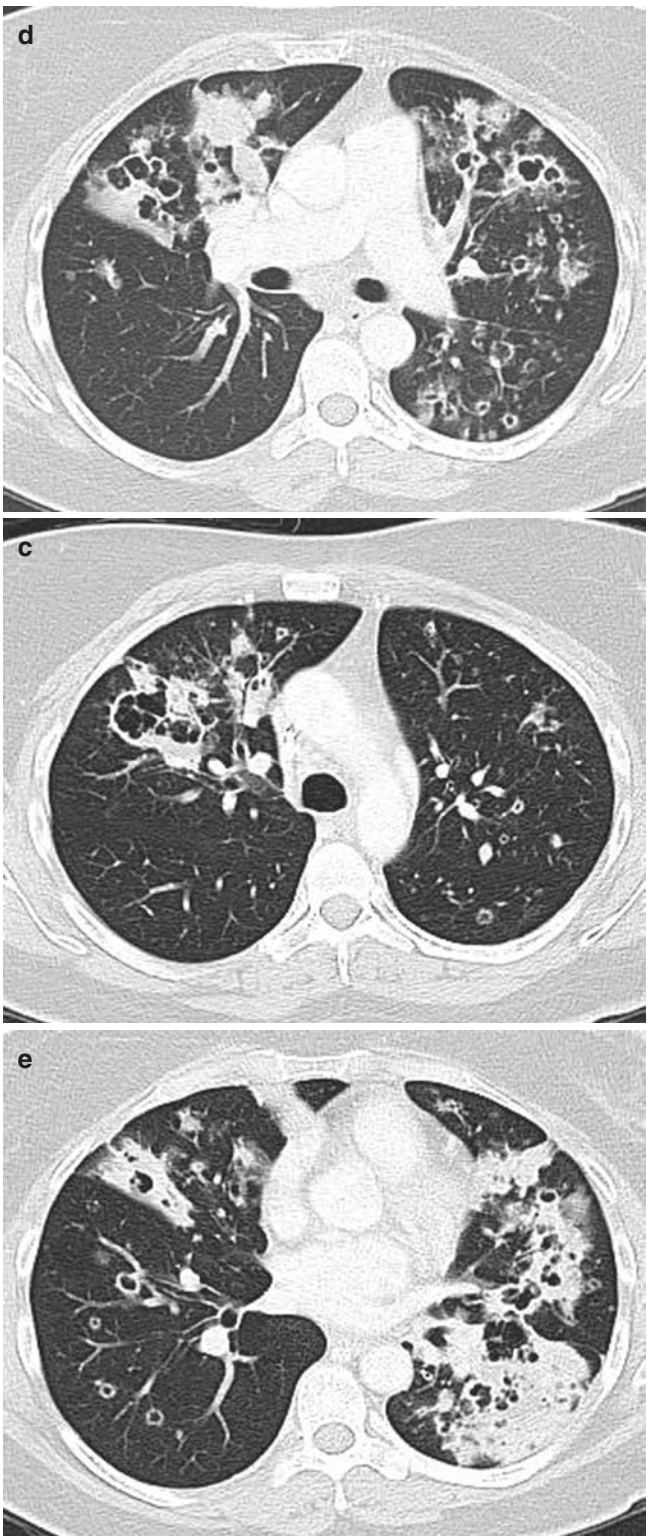

Fig. 5.26 (continued)

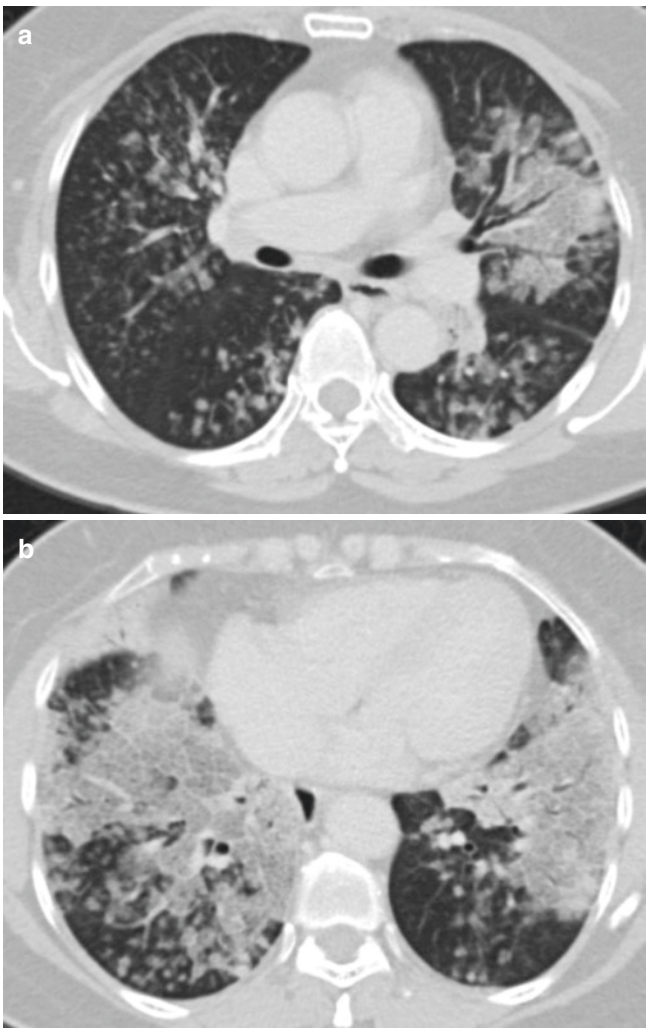

Fig. 5.27 Crazy-paving pattern of adenocarcinoma. (**a**, **b**) Axial CT images show numerous pulmonary nodules with multifocal ground-glass opacities associated with septal thickening. Transbronchial biopsy revealed adenocarcinoma. The ground-glass attenuation reflects the low-density intra-alveolar material (glycoprotein), whereas the superimposed lines are due to infiltration of the interstitium by tumor cells

- Simple pneumonia rarely results in enlarged lobulated hilar lymphadenopathy visible on chest radiographs, although enlarged nodes secondary to infection may be seen on CT or MRI.
- On contrast-enhanced CT or MRI, a collapsed lobe may demonstrate non-enhancing tubular low-density structures in keeping with mucus-filled dilated bronchi and should prompt a search for centrally obstructing neoplasm [4].

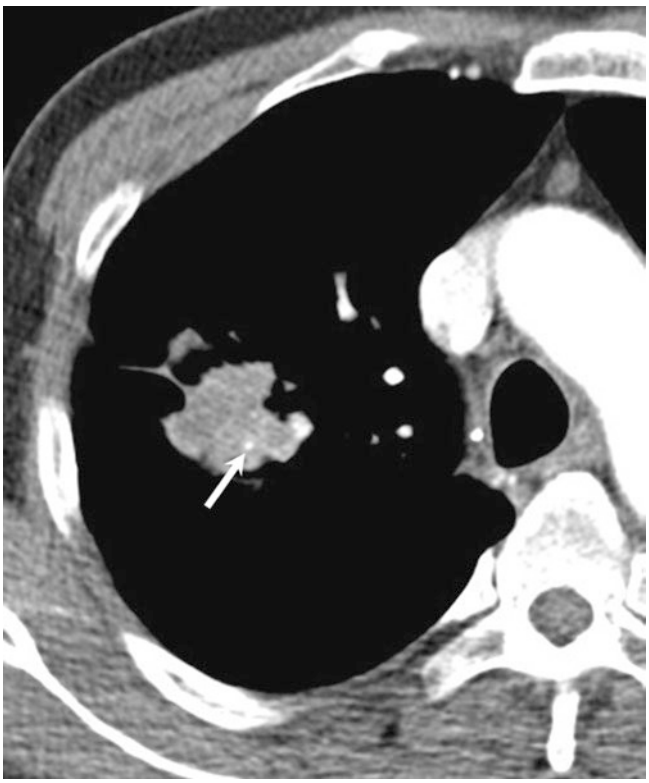

Fig. 5.28 A 62-year-old man with bronchial carcinoma. Contrast-enhanced axial CT image shows a soft tissue mass in right upper lobe with peripheral focus of calcification (arrow)

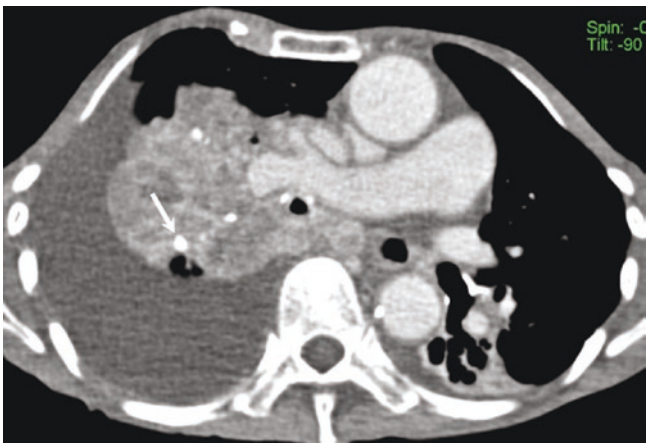

Fig. 5.29 A 74-year-old man with bronchial carcinoma. Contrast-enhanced axial CT thorax image shows a right upper lobe mass with few calcified granulomas (arrow). Patient had past history of tuberculosis

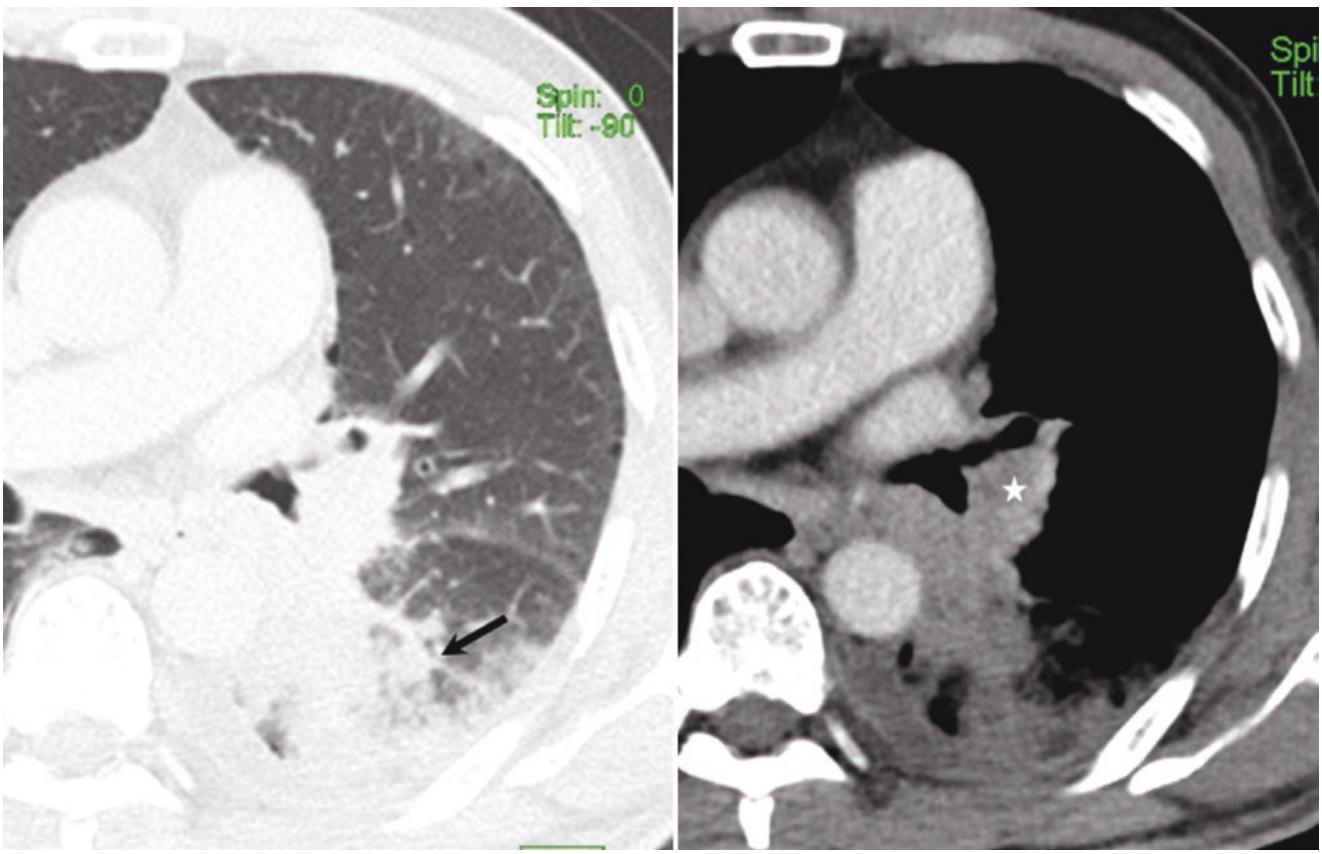

Fig. 5.30 A 65-year-old man with bronchial carcinoma. Contrast-enhanced axial CT image in lung and soft tissue window shows a focal area of post-obstructive atelectasis (arrow) secondary to a central mass (asterisk)

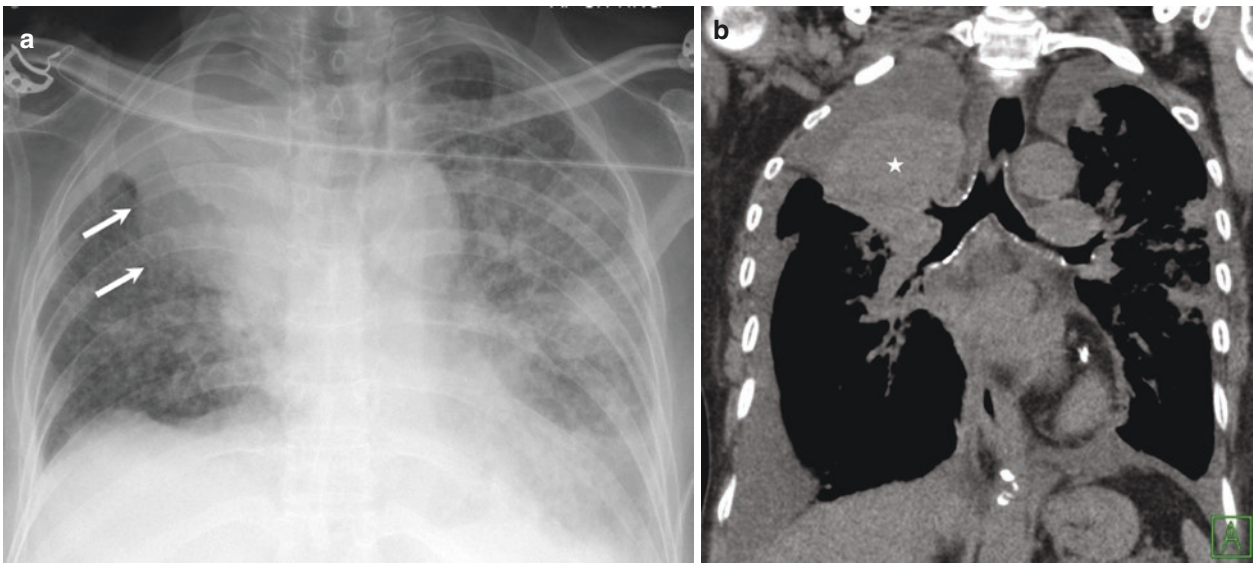

Fig. 5.31 A 75-year-old man with right hilar mass. (**a**) Frontal radiograph of chest shows right upper lobe collapse with bulging of the right minor fissure giving "Golden S sign" (arrows). (**b**) Non-contrast coronal CT image confirms right hilar mass (asterisk) causing right upper lobe collapse

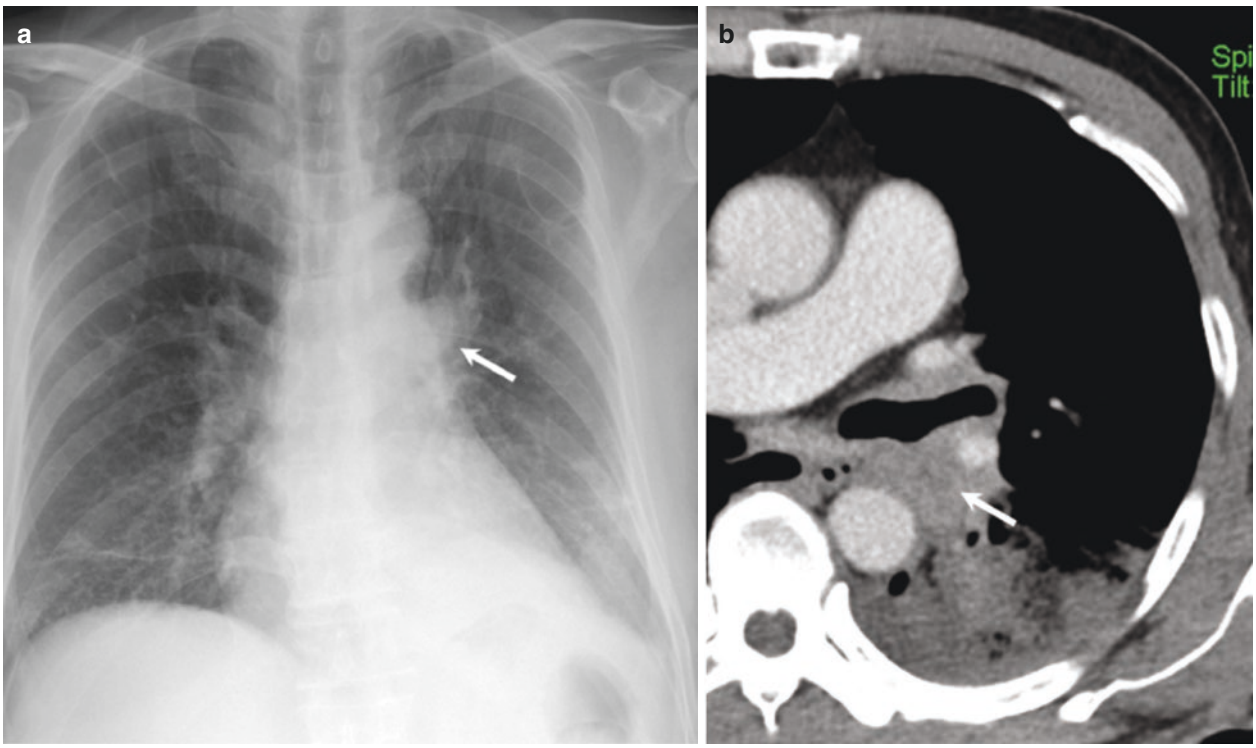

Fig. 5.32 A 66-year-old man with squamous cell carcinoma. (**a**) Frontal radiograph of chest shows dense left hilum (arrow) with opacity in left retrocardiac region. (**b**) Contrast-enhanced axial CT thorax in soft tissue window shows left perihilar mass (arrow) with post-obstructive atelectasis and consolidation

5.6.3 Intrathoracic Spread of Bronchial Carcinoma

5.6.3.1 Hilar Enlargement

Hilar enlargement is a common radiographic manifestation of bronchial carcinoma. It may represent a primary central tumor, metastatic lymphadenopathy, consolidation, or combination of these. In general, if the hilar mass appears lobulated, it is more likely due to an enlarged lymph node. On radiographs, the hilum usually appears dense in the case of a central hilar mass, due to summation shadows (Fig. 5.32). This sign on frontal chest radiograph may be the only indication of

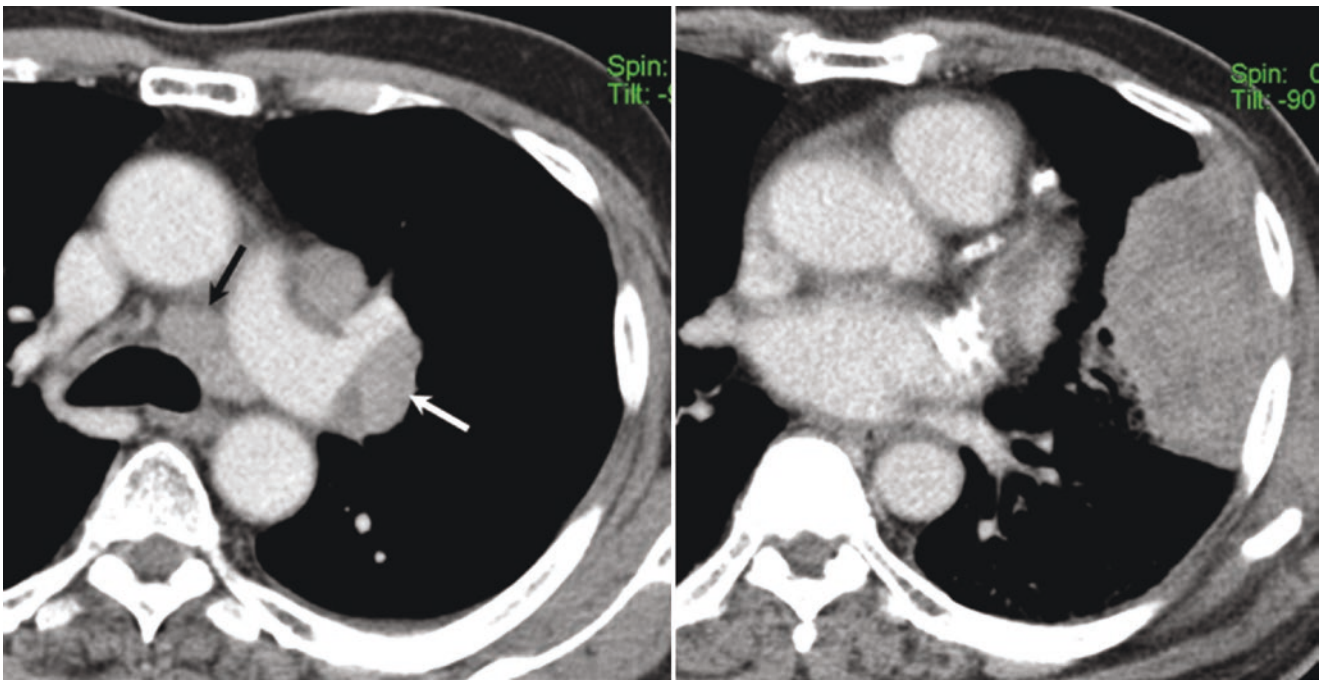

Fig. 5.33 A 69-year-old man with small cell lung cancer. Contrast-enhanced axial CT images show enlarged mediastinal (black arrow) and left hilar lymphadenopathy (white arrow) associated with left upper lobe lung mass

lung cancer and warrants a CT evaluation. Extensive hilar and mediastinal lymphadenopathy is frequently seen with small cell carcinomas (Fig. 5.33) [4].

5.6.3.2 Mediastinal Mass or Lymph Node Enlargement

Mediastinal lymph node metastasis in patients with lung carcinoma is quite common and is seen in up to 40% of patients and depends on the size, location, and histology of the primary tumor. CT is the initial modality of choice in assessing the mediastinal lymph nodes (Fig. 5.34). On CT and MRI, lymph node size is considered major criteria, which can predict metastatic involvement. As a general rule, the cutoff size for normal mediastinal lymph nodes is considered as the short-axis diameter of less than 10 mm. Nodes above this size should, therefore, be considered enlarged. Nevertheless, the problem with the size criteria is that there are other nonmalignant causes of lymph node enlargement such as previous tuberculosis, histoplasmosis, pneumoconiosis, sarcoidosis, and, most importantly, reactive hyperplasia to the tumor. On the other hand, normal-sized nodes may have microscopic involvement by tumor cells. Hence, there is no measurement below which all nodes can be considered to be benign and above which all can be assumed to be malignant.

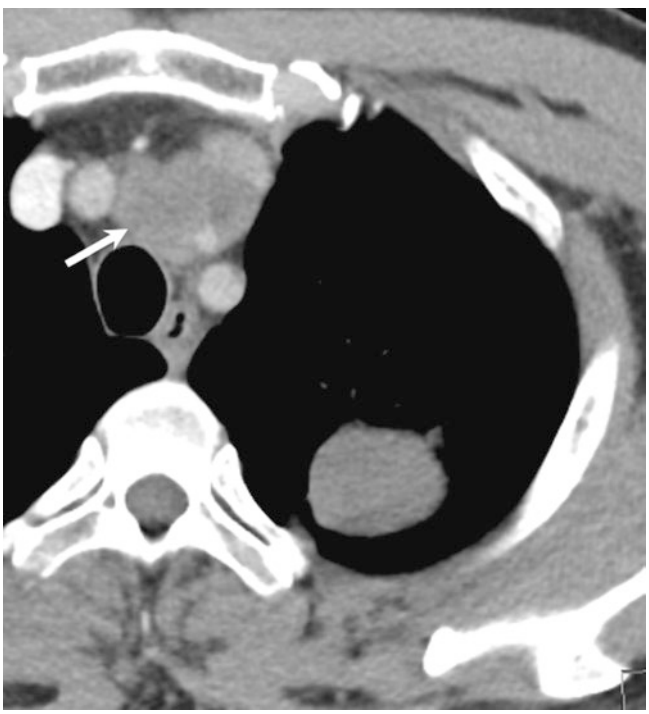

Fig. 5.34 A 61-year-old man with adenocarcinoma and mediastinal lymphadenopathy (arrow)

Endoscopic bronchial ultrasound can be used to assess the size and morphology of the mediastinal lymph nodes. Additionally, it can be used to guide fine needle aspiration (FNA) of subcarinal, aortopulmonary, and posterior mediastinal nodes [49].

Use of PET imaging for staging lung carcinoma is increasing and has shown greater accuracy in the detection of nodal disease compared to CT and MRI. However, similar to CT and MRI, PET is also associated with false-positive results, most commonly due to inflammation and reactive hyperplasia. Fused PET/CT imaging has an added advantage of anatomical detail of CT [50–52].

5.6.3.3 Mediastinal Involvement

Chest radiograph is not the modality to diagnose mediastinal invasion, although indirect radiographic evidence such as elevation of the ipsilateral hemidiaphragm may indicate phrenic nerve invasion (Fig. 5.35). However, other causes of the raised dome of the diaphragm such as underlying lobar collapse, subpulmonic effusion, and diaphragmatic eventration should be excluded, before considering phrenic nerve invasion. Mediastinal invasion is better demonstrated on CT and MRI, and the signs include tumor visible deep within the mediastinal fat; definite encasement of vital structures by tumor such as the mediastinal vessels, esophagus, and trachea; or deep penetration of tissue planes (Fig. 5.36). Mere tumor contact with the mediastinum is not sufficient for the diagnosis of invasion, and interdigitation of tumor with mediastinal fat can be a misleading sign on both CT and MRI [4].

The tumors that show less than 3 cm of contact with the mediastinum, demonstrated less than 90° of circumferential contact with the aorta or demonstrate a visible mediastinal fat plane between the mass and vital mediastinal structures are considered to have a very high likelihood of resectability, even if the tumor had crossed into the mediastinum [53]. However, tumors that obliterate fat planes or show greater contact than described above are not necessarily unresectable in all cases.

5.6.3.4 Chest Wall Invasion

A peripherally located lung carcinoma directly invading pleura and chest wall may or may not indicate that the tumor is unresectable, though it does adversely affect prognosis [54]. Such localized invasion of the chest wall need not be a contraindication but may require extensive surgery requiring en-bloc resection, and, in some instances, chest wall reconstruction which may be associated with increased morbidity and mortality, and it, therefore, helps the surgeon to know the extent of any chest wall invasion preoperatively [55]. Chest radiograph is not very useful in diagnosing chest wall invasion unless there is an extensive rib or spinal destruction [5] (Fig. 5.37). Even CT is not reliable in diagnosing chest wall invasion with accuracy ranging from 70–80% and sensitivity and specificity values ranging from 40–90% [8]. The definite CT findings indicating chest wall invasion are rib destruction or chest wall mass (Table 5.7) (Figs. 5.38 and 5.39). On CT, tumor touching the pleura and even associated with focal thickening of pleura does not necessarily indicate invasion. On the contrary, a clear

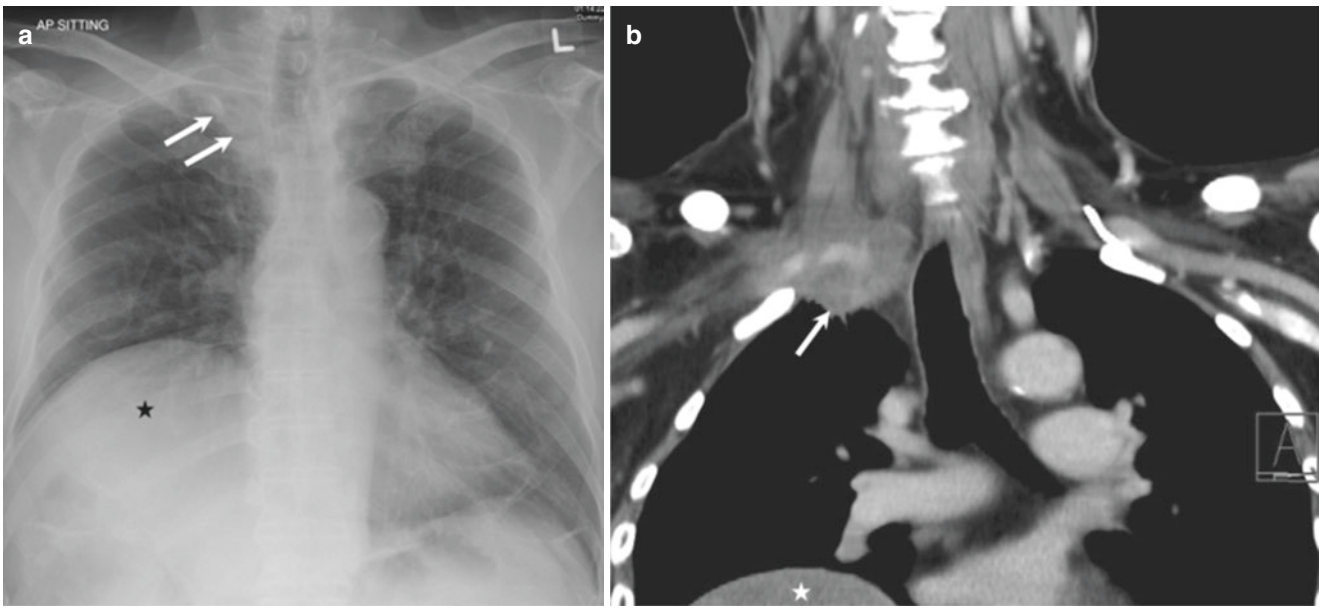

Fig. 5.35 A 74-year-old man with right Pancoast tumor. (**a**) Frontal radiograph of chest shows raised right dome of diaphragm (asterisk) and right apical pleural thickening (arrow). (**b**) Contrast-enhanced coronal CT image confirms right apical mass (arrow) with raised right dome of diaphragm (asterisk) as a result of phrenic nerve involvement

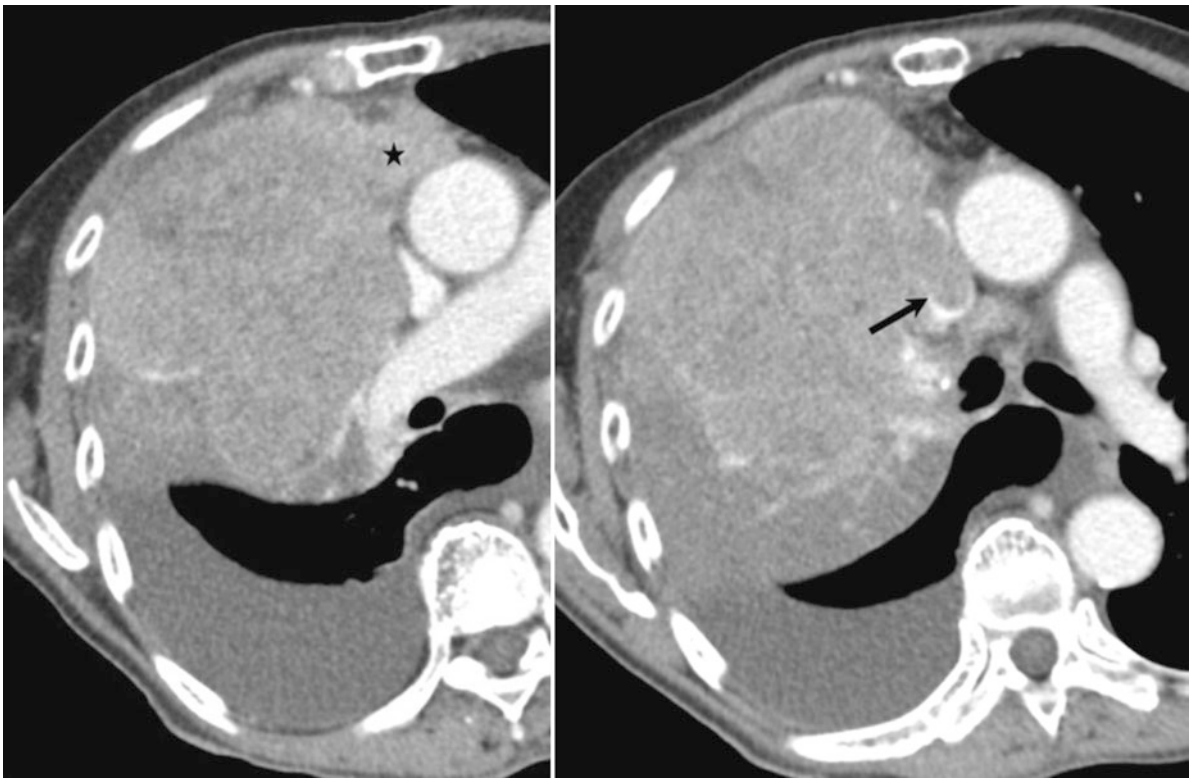

Fig. 5.36 A 70-year-old man with small cell cancer. Contrast-enhanced axial CT images show a large right upper lobe mass with mediastinal invasion (asterisk) and extension in the superior vena cava (arrow)

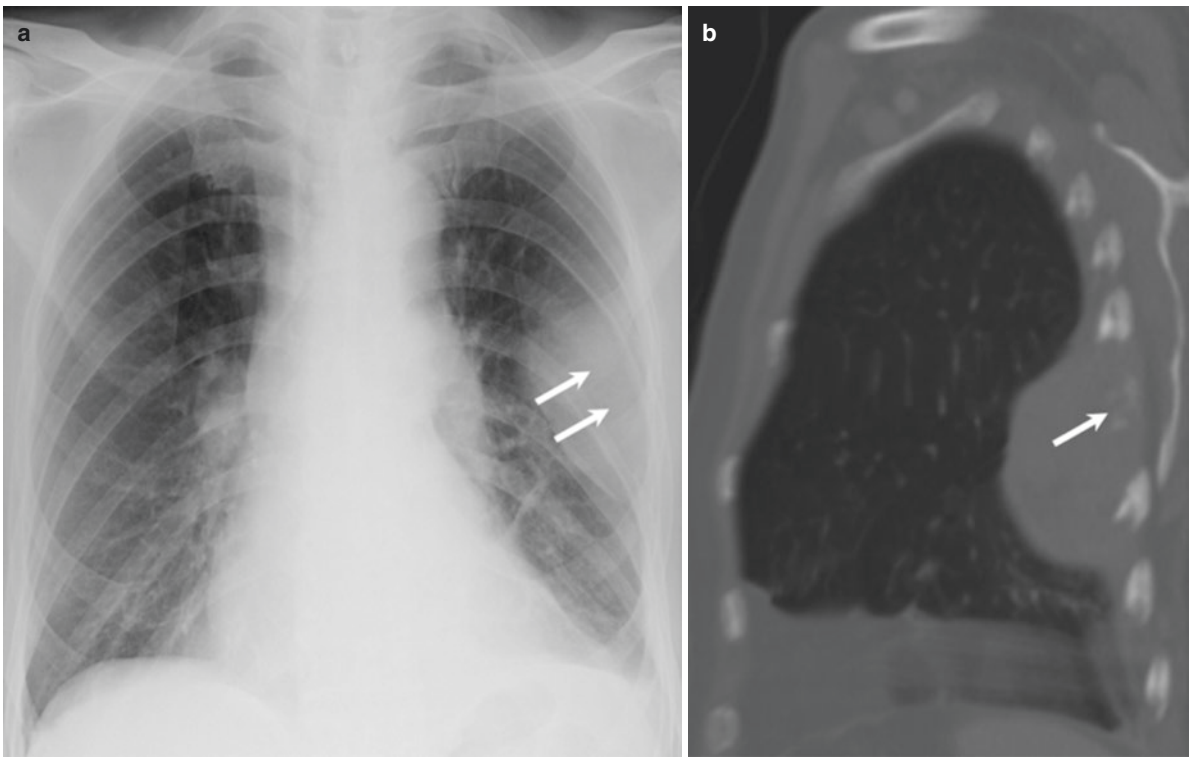

Fig. 5.37 A 69-year-old man with bronchial carcinoma invading the chest wall. (**a**) Frontal radiograph of chest shows a soft tissue mass projected over left mid zone with associated rib destruction (arrows). (**b**) Sagittal reformatted thorax image in bone window shows lung malignancy with underlying rib destruction (arrow)

Table 5.7 CT findings helpful in diagnosing chest wall invasion

• Obtuse angle at the point of contact between tumor and pleura
• Obliteration of extrapleural fat plane at the point of contact between tumor and the chest wall
• Extrapleural soft tissue
• More than 3 cm contact between tumor and the pleural surface
• Rib destruction

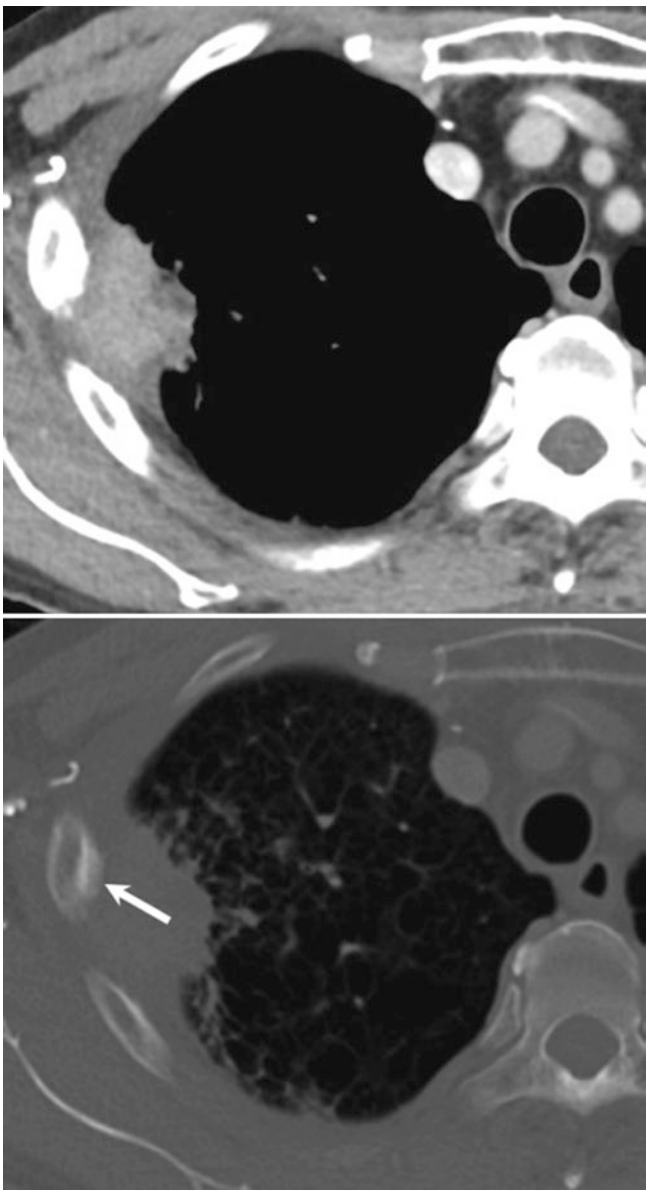

Fig. 5.38 A 65-year-old man with intractable right chest pain. Contrast-enhanced axial CT images show a peripherally located right upper lobe malignant mass touching the intercostal space and associated with focal pleural thickening, periosteal reaction (arrow) in the adjacent rib but without any destruction. CT findings were equivocal for chest wall invasion but the presence of pain helped in concluding the chest wall invasion

extrapleural fat plane adjacent to the mass does not exclude chest wall invasion [4]. Local chest wall pain remains the single most specific indicator of whether or not the tumor has spread to the parietal pleura or chest wall [56].

In selected cases, the extent of chest wall invasion or diaphragmatic invasion may be better shown using MRI due to its superior spatial resolution and soft tissue contrast [8]. For superior sulcus tumor (Pancoast tumor), MRI was regarded as the best modality for reliably diagnosing mediastinal invasion, root of the neck extension, and vascular and neural structure involvement. Now, with the advent of MDCT, providing multiplanar reformatted images, routine MRI for evaluating the extent of Pancoast tumor is usually not required [57] (Fig. 5.40).

5.6.3.5 Pleural Involvement

Lung carcinomas may involve pleura either directly, via lymphatics, or by tumor emboli. Pleural effusion can occur with lung carcinoma of all cell types, more frequently with adenocarcinoma. Presence of pleural effusion in a patient with lung carcinoma carries poor prognosis (Fig. 5.41). Moreover, the presence of tumor cells in the pleural effusion (malignant effusion) or on pleural biopsy rules out surgical management. Pleural effusion can be detected on chest radiograph, US, and CT. In some cases, CT may demonstrate pleural thickening or nodularity within or adjacent to pleural effusion and should be considered highly suspicious in the presence of lung malignancy [4, 5] (Fig. 5.41).

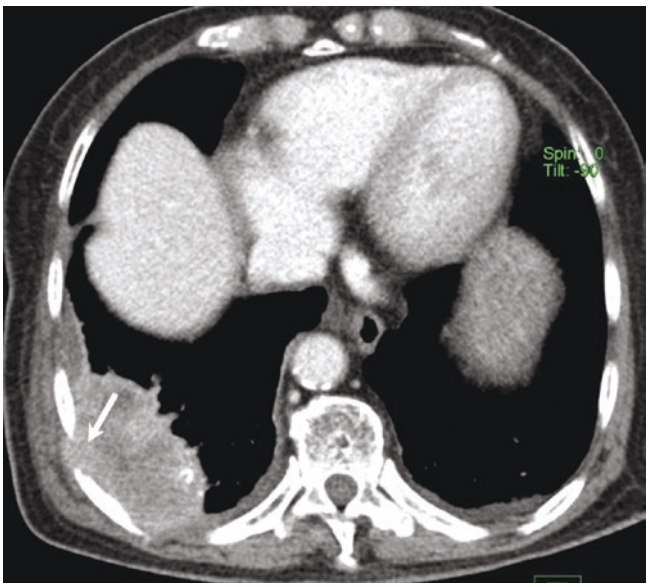

Fig. 5.39 Contrast-enhanced axial CT image shows a peripherally located right lower lobe mass extending across the adjacent chest wall (arrow) indicating chest wall invasion

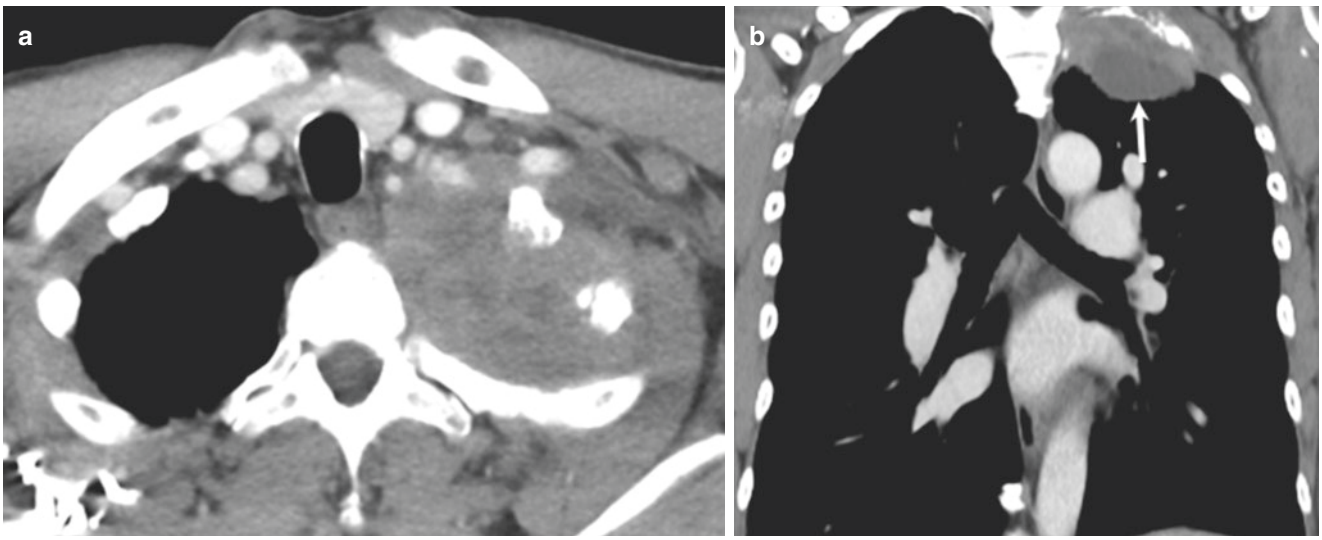

Fig. 5.40 A 62-year-old man with Pancoast tumor. (**a**, **b**) Contrast-enhanced axial and coronal CT images show left apical mass (arrow) with associated rib destruction

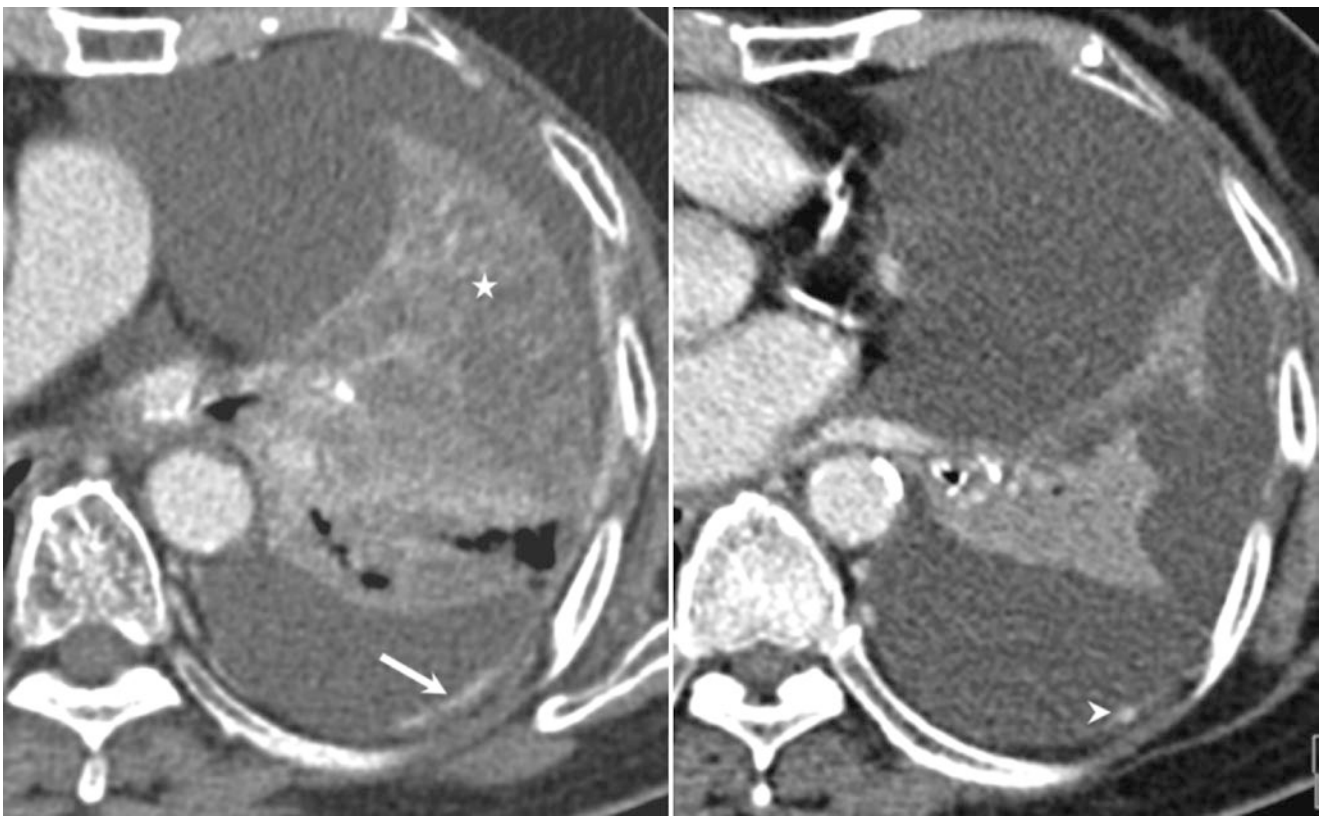

Fig. 5.41 A 67-year-old man with dense consolidation and pleural effusion. Contrast-enhanced axial CT image shows left heterogeneous consolidation (asterisk) with large pleural effusion showing focal pleural thickening (arrow) and nodularity (arrowhead). Biopsy revealed infiltrating adenocarcinoma in left lung

5.6.3.6 Metastases

Lung cancer is commonly associated with a widespread hematogenous dissemination at the time of presentation. Patients with distant metastasis have a poor prognosis and are treated with chemotherapy. Distant metastases preclude surgical resection of the primary tumor. Common sites of spread include the adrenal glands, bone, brain, liver, and more distant lymph nodes (Figs. 5.42 and 5.43).

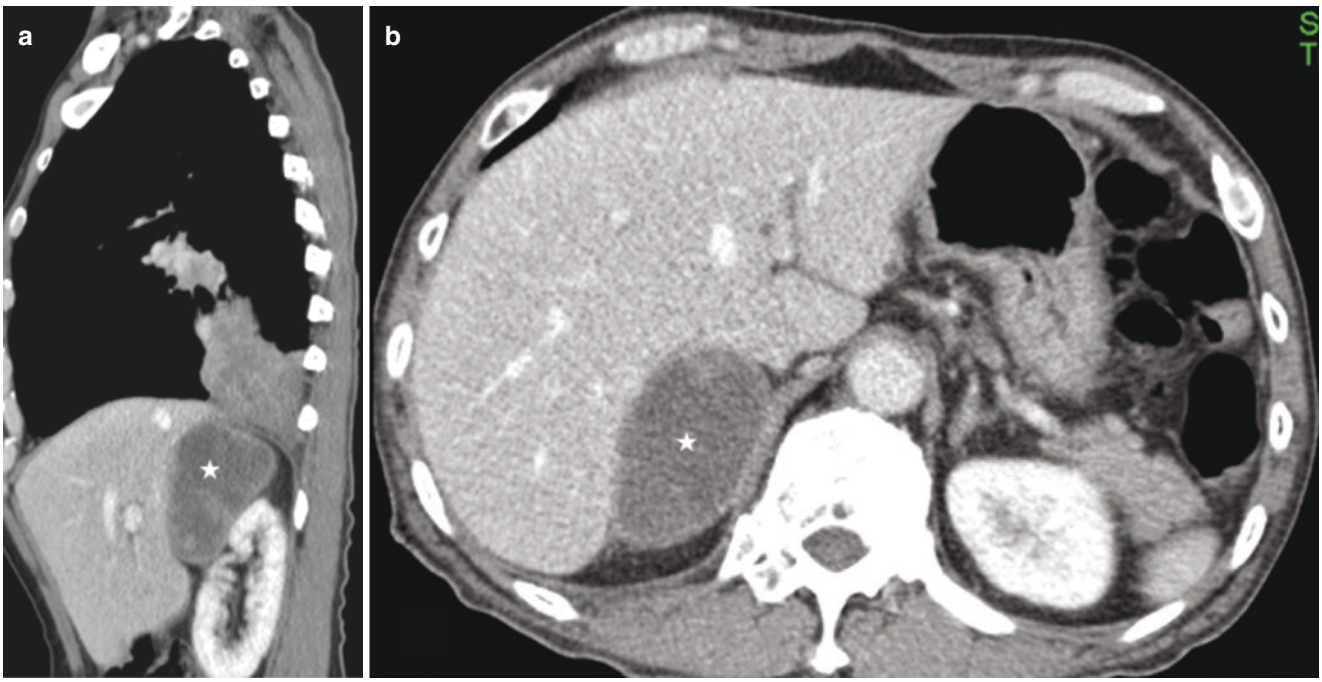

Fig. 5.42 Adrenal metastasis. (**a**, **b**) Contrast-enhanced sagittal and axial CT images show right lung mass with right adrenal metastasis (asterisk)

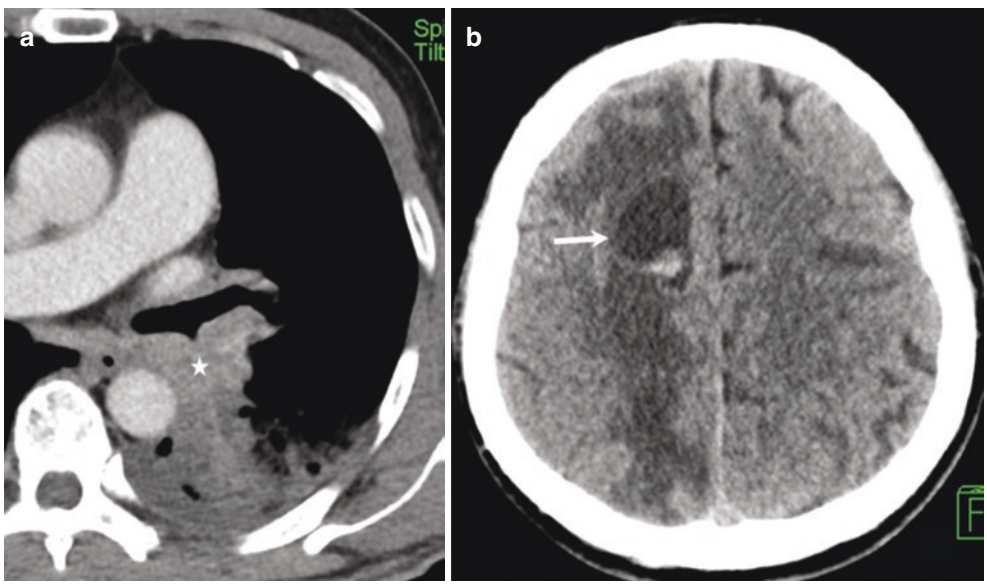

Fig. 5.43 Brain metastasis. (**a**) Contrast-enhanced axial CT image shows left lower lobe malignancy (asterisk). (**b**) Non-contrast axial CT brain shows hemorrhagic metastatic deposit in right frontal lobe (arrow)

5.7 Neuroendocrine Tumors

Neuroendocrine tumors (NETs) comprise a heterogeneous group of malignancies that arise from neuroendocrine cells throughout the body and most commonly originate from the lungs, small intestine, and rectum [58]. Neuroendocrine tumors of the lung arise from Kulchitsky cells that are normally present in the bronchial mucosa. These cells contain secretory granules and can produce active peptides. The World Health Organization (WHO) classifies neuroendocrine tumors of the lung into four subtypes: low-grade typical carcinoid, atypical carcinoid, high-grade small cell, and large cell neuroendocrine carcinoma. Neuroendocrine tumor of the lung accounts for 25% of the primary lung cancers. SCC of the lung is commonest with an incidence of 20%, followed by large cell neuroendocrine carcinoma (3%), typical carcinoid (2%), and atypical carcinoid (0.2%) [59].

5.7.1 Small Cell Lung Carcinoma

Small cell lung carcinomas (SCCs) are the most common primary pulmonary neuroendocrine tumors and account for 15–20% of all lung cancers. SCCs are more aggressive than non-small cell lung carcinomas and carry worst prognosis due to their propensity for rapid doubling time and a greater tendency for widespread metastases at an early stage [60, 61]. Approximately 60–70% of patients with SCC have metastatic disease at an early stage. Thus, early and accurate diagnosis is important. SCCs are strongly associated with smoking, which is responsible for approximately 95% of cases [61]. As many as 90–95% of SCCs arise from lobar or main bronchi; hence, the commonest manifestation is a large mass located centrally within the lung parenchyma or a mediastinal mass involving the hilum [60]. Due to a central location, they commonly present with the collapse of either a lobe or the entire lung. Although both the primary lung mass and mediastinal lymphadenopathy can sometimes be identified (Fig. 5.44), confluent mediastinal lymphadenopathy can be present without visualization of a primary lung tumor [60, 61]. Characteristically, these tumors are initially responsive to radiation and chemotherapeutic treatment but are also associated with early recurrence.

5.7.2 Bronchopulmonary Carcinoid Tumor

Carcinoid tumors are potentially malignant neuroendocrine tumors. They are now included in TNM staging system since seventh edition and are staged on the basis of the same criteria as those applied to non-small cell lung cancers [59]. There are two forms of bronchial carcinoids: typical (85–90%) and atypical (10–15%). Typical carcinoids are slow growing and locally invasive tumors, considered to be the most well-differentiated type of neuroendocrine carcinoma. In 5–15% cases, they metastasize to regional lymph nodes and rarely show distant metastases. Typical bronchial carcinoids commonly occur in the central airways, in the main, lobar (commonest), or segmental bronchi. Atypical carcinoids are considered more aggressive and have histological and clinical features intermediate between typical bronchial carcinoid and small cell carcinoma of the lung and have a

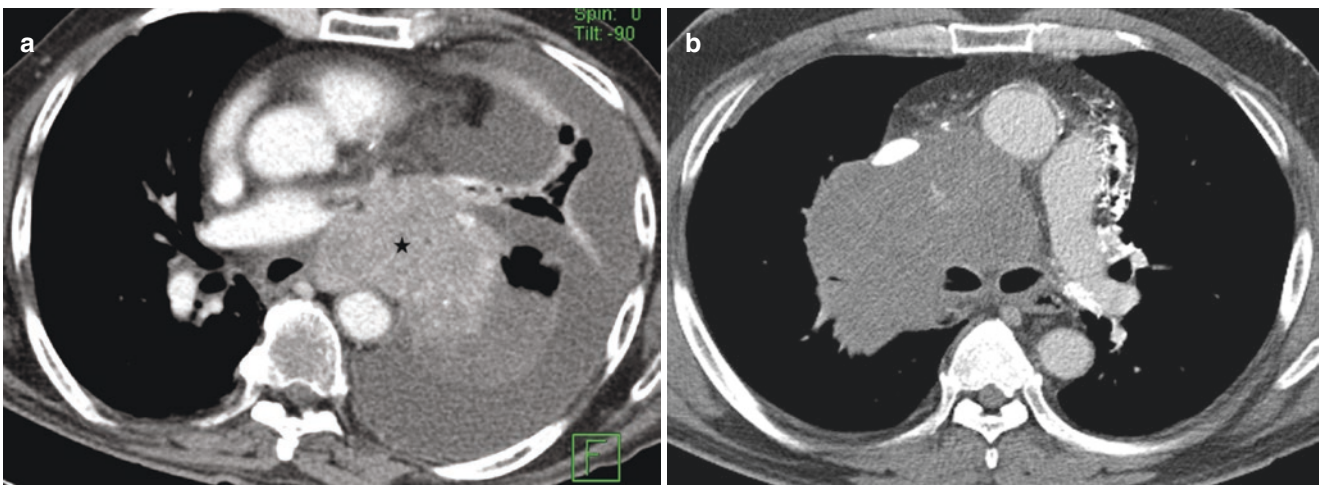

Fig. 5.44 Small cell carcinoma in three patients. Left hilar nodal mass in first patient (**a**) Contrast-enhanced axial CT thorax in soft tissue window shows a large left hilar mass (asterisk) with collapse of left lower lobe and large left pleural effusion. Confluent nodal mass in second patient. (**b**, **c**) Axial and coronal CT images show large confluent nodal mass in the right hila and paramediastinal region with encasement of vessels and airways. Contiguous nodes in a third patient with small cell lung cancer. (**d**–**g**) Axial CT images show enlarged contiguous nodes in right supraclavicular region, right paratracheal region, prevascular space and subcarinal region

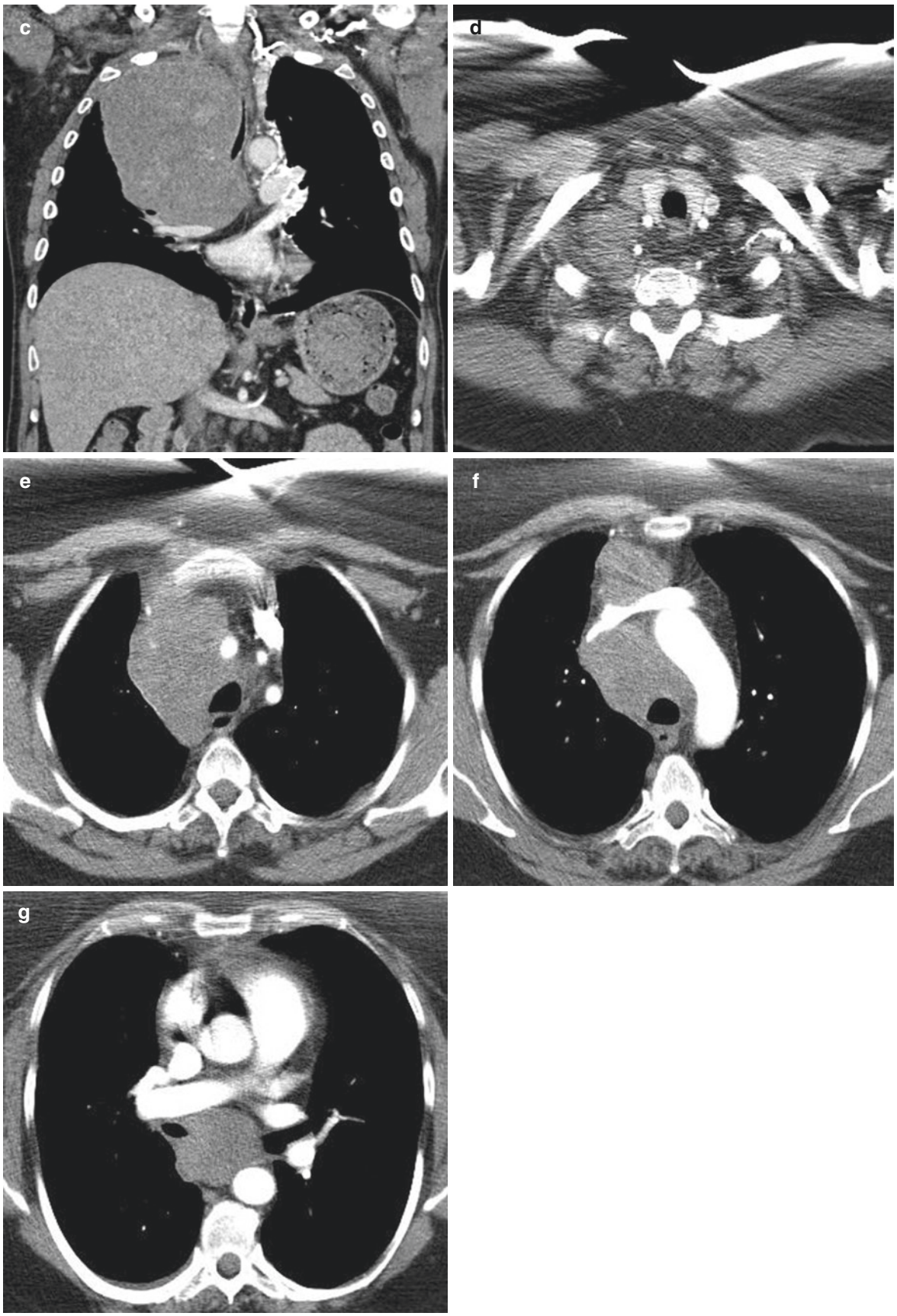

Fig. 5.44 (continued)

poorer prognosis. They usually arise in the lung periphery. Approximately 50% of patients with atypical carcinoid may show metastatic lymph nodes [8]. Bronchial carcinoids may metastasize to the brain, liver, and bones.

Bronchial carcinoids, particularly central ones, usually present with cough, wheeze, and pneumonia due to bronchial obstruction. Some patients may present with hemoptysis, as carcinoids are highly vascular tumors [59]. Bronchial carcinoids rarely cause carcinoid syndrome, unless there are liver metastases. Even small bronchial carcinoid tumors may secrete sufficient ACTH to cause Cushing's syndrome (ectopic ACTH syndrome) [5]. Other associations with bronchial carcinoid include Zollinger-Ellison syndrome, acromegaly, and hyperinsulinemia [8].

Imaging appearances of bronchial carcinoids vary with tumor location. Bronchial carcinoids show no lobar predilection and in approximately 1% cases may be intratracheal. Carcinoids arising in central bronchi (80–90% of cases) may be predominantly intraluminal having a polypoidal shape or more commonly present with a large extra-luminal mass ("iceberg" lesions). The extra-luminal component is seen as a hilar mass on imaging. Centrally located masses due to partial or complete bronchial obstruction result in atelectasis with or without "drowned lung" distally (Fig. 5.45) [4]. Peripheral lesions seen in 10–20% cases of carcinoids present as a spherical or lobular solitary pulmonary nodule. It is usually 2–4 cm in diameter, with a well-defined smooth edge. If non-calcified, peripheral bronchial carcinoid tumors are difficult to distinguish from bronchial carcinomas, both radiologically and cytologically. These are frequently surgically resected considering that they are carcinomas [4].

Bronchial carcinoids, particularly the central ones, may calcify and occasionally ossify. CT may show calcification in up to 30% of cases. In some cases, bronchial carcinoids due to their vascular nature may show marked contrast enhancement on CT and MRI [59].

The role of PET scan is not well defined for pulmonary carcinoids, with sensitivity ranging from 14 to 100%, as most carcinoid tumors except atypical ones do not show increased activity with FDG-PET scanning [59, 62]. However, as carcinoids contain somatostatin receptors, scintigraphy using somatostatin analogues (e.g., octreotide or pentetreotide) may be helpful to localize the tumor [59].

5.7.3 Diffuse Idiopathic Pulmonary Neuroendocrine Cell Hyperplasia (DIPNECH)

The neuroendocrine/carcinoid tumor spectrum may be further complicated by a preinvasive lesion of diffuse idiopathic pulmonary neuroendocrine cell hyperplasia (DIPNECH). DIPNECH is characterized by hyperplasia of single or multiple neuroendocrine cells that present either as small nodules (neuroendocrine bodies) or as linear proliferation in the walls of small airways. DIPNECH is typically seen in nonsmoking women, in the age range of 50–70 years. Characteristic imaging features of DIPNECH include the presence of multiple small nodules less than 5 mm in size, mosaic attenuation due to air-trapping, bronchial wall thickening, and bronchiectasis [4, 59] (Fig. 5.46).

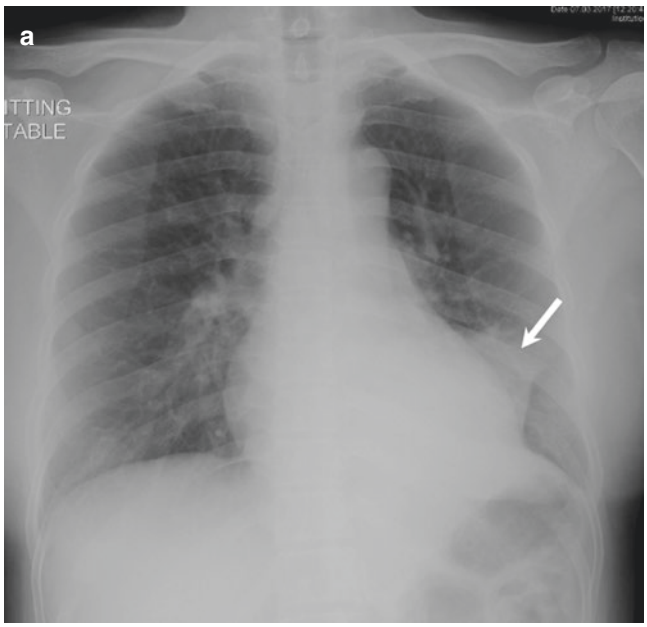

Fig. 5.45 A 55-year-old man with carcinoid tumor. (**a**) Frontal radiograph of chest shows left lower lobe collapse (arrow). (**b**, **c**) Contrast-enhanced axial CT image confirms left lower lobe collapse and a soft tissue nodule in left lower lobe bronchus (arrow). Fluid bronchograms in the left lower lobe are the marker of complete obstruction previously termed "drowned lung"

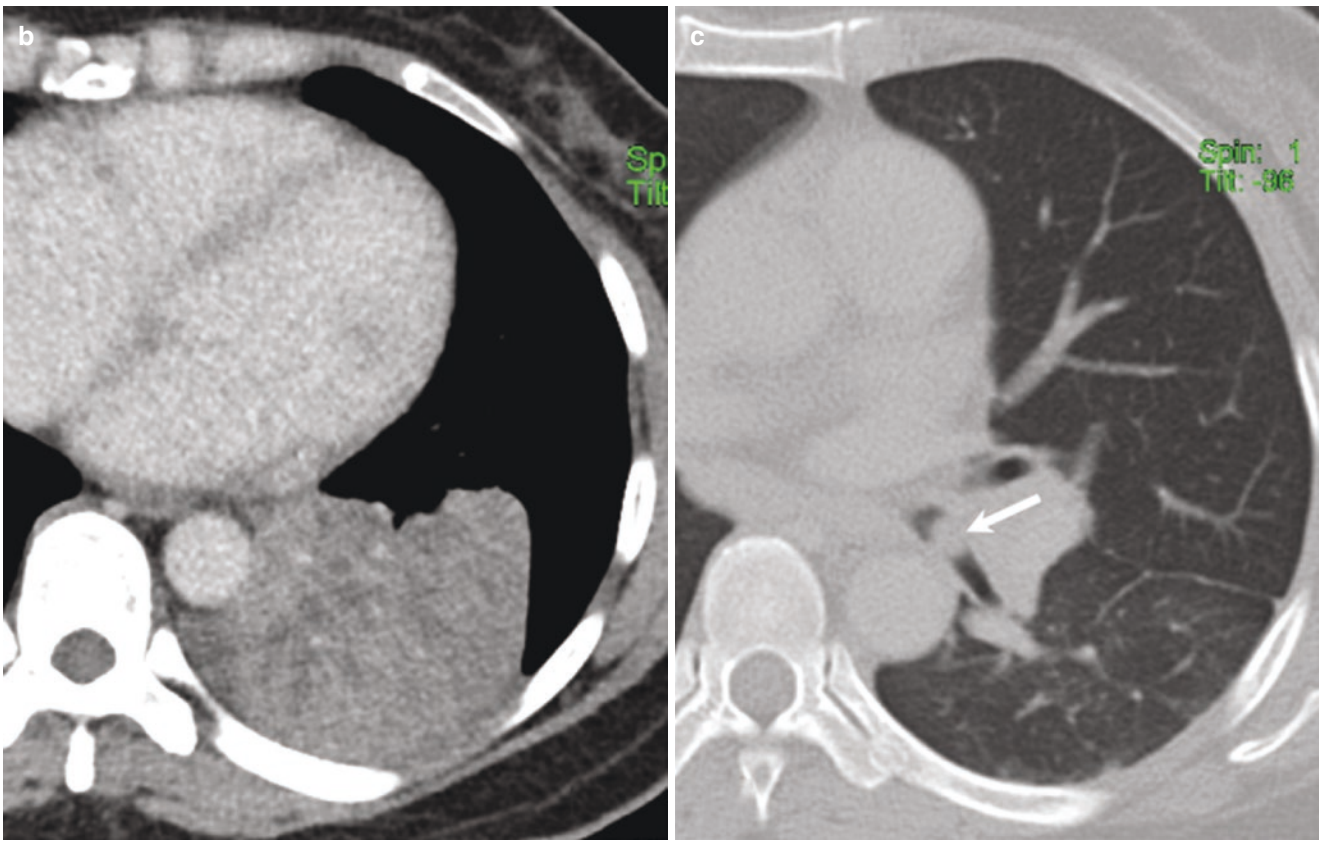

Fig. 5.45 (continued)

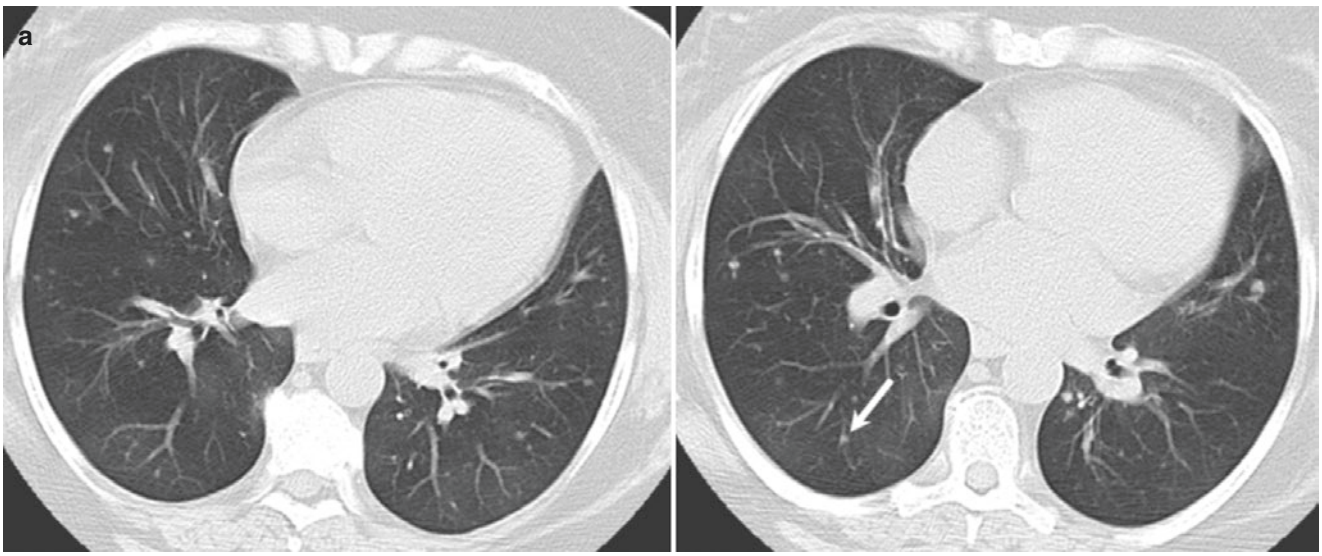

Fig. 5.46 A 53-year-old women with DIPNECH. Axial CT images (**a**) inspiratory phase shows multiple small nodules (arrows), and bronchial wall thickening, (**b**) expiratory phase shows air-trapping

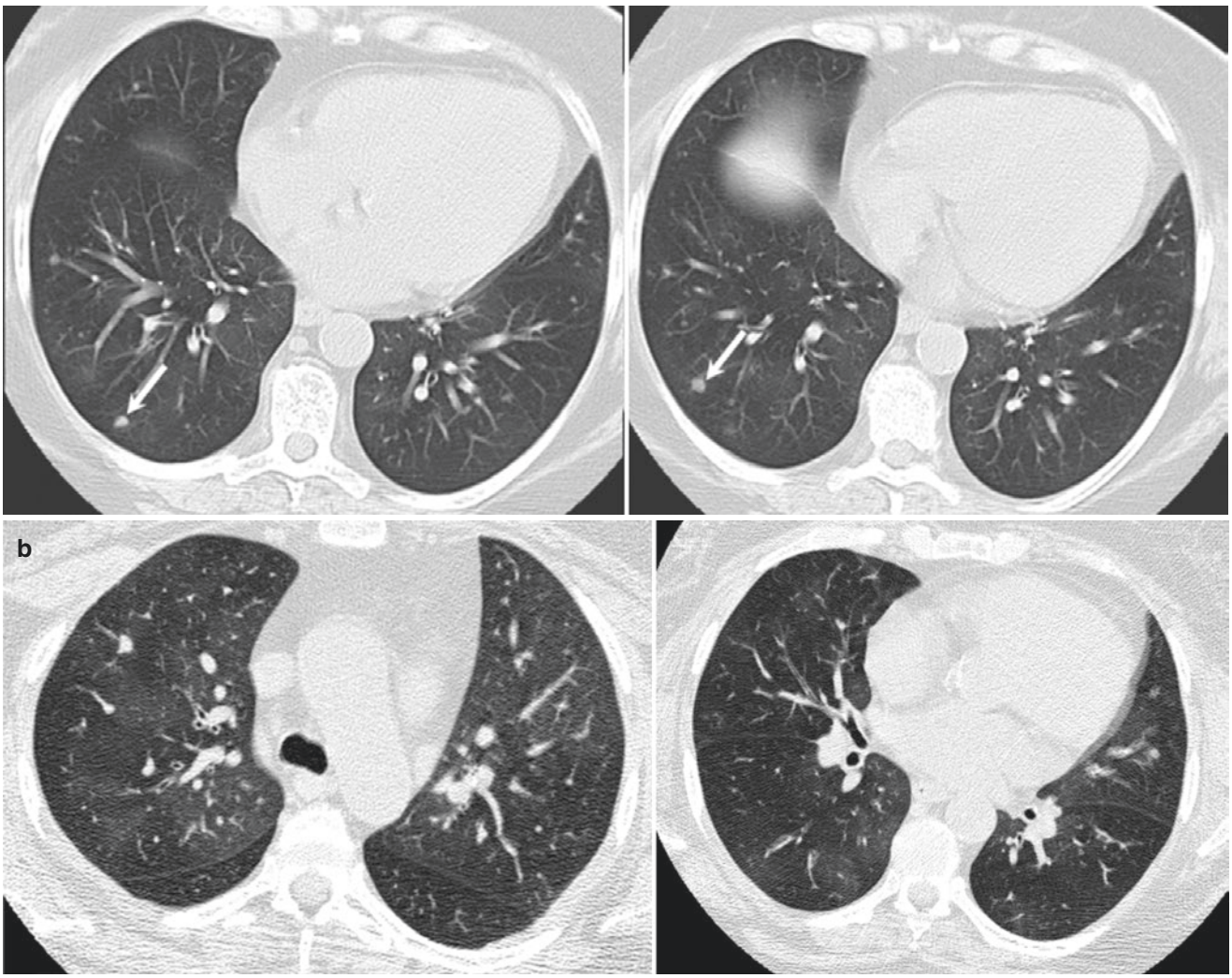

Fig. 5.46 (continued)

5.8 Staging

The new eighth edition of the TNM staging system is based on a database of 94,708 patients diagnosed between 1999 and 2010 from 35 sources and 16 countries and suggested considerable changes from previous editions [63, 64]. The eighth edition was published in 2016 and was enacted on January 1, 2017.

5.9 Lymphoma

Lung parenchymal involvement in lymphoma is usually secondary to hilar or mediastinal lymphadenopathy, rather than primary involvement. Parenchymal involvement becomes more frequent as the disease progresses and is commonly seen in patients who relapse after treatment [4, 5, 65]. Lung involvement is three times more common in Hodgkin than in non-Hodgkin lymphoma [4].

On imaging, lung parenchymal lymphomas usually demonstrate one or more, usually ill-defined pulmonary nodules which may rarely cavitate [5, 66]. Another common presentation is patchy consolidation resembling pneumonia, which may demonstrate air bronchogram. These patchy areas of consolidation often radiate from the hila or mediastinum, compatible with the theory that lung extension occurs by direct invasion from involved hilar or mediastinal nodes [4, 5] (Fig. 5.47). In some cases, CT may demonstrate peribronchial nodules or interstitial infiltrates extending into the parenchyma from the hila reflecting spread via interstitial lymphatics. Another uncommon presentation is reticulonodular opacities resembling interstitial lung disease, termed as "lymphangitic pattern" [5].

In Hodgkin lymphomas, the lung parenchymal involvement usually occurs secondary to intrathoracic lymphadenopathy (Fig. 5.48), while isolated pulmonary involvement is relatively more common in the non-Hodgkin lymphomas.

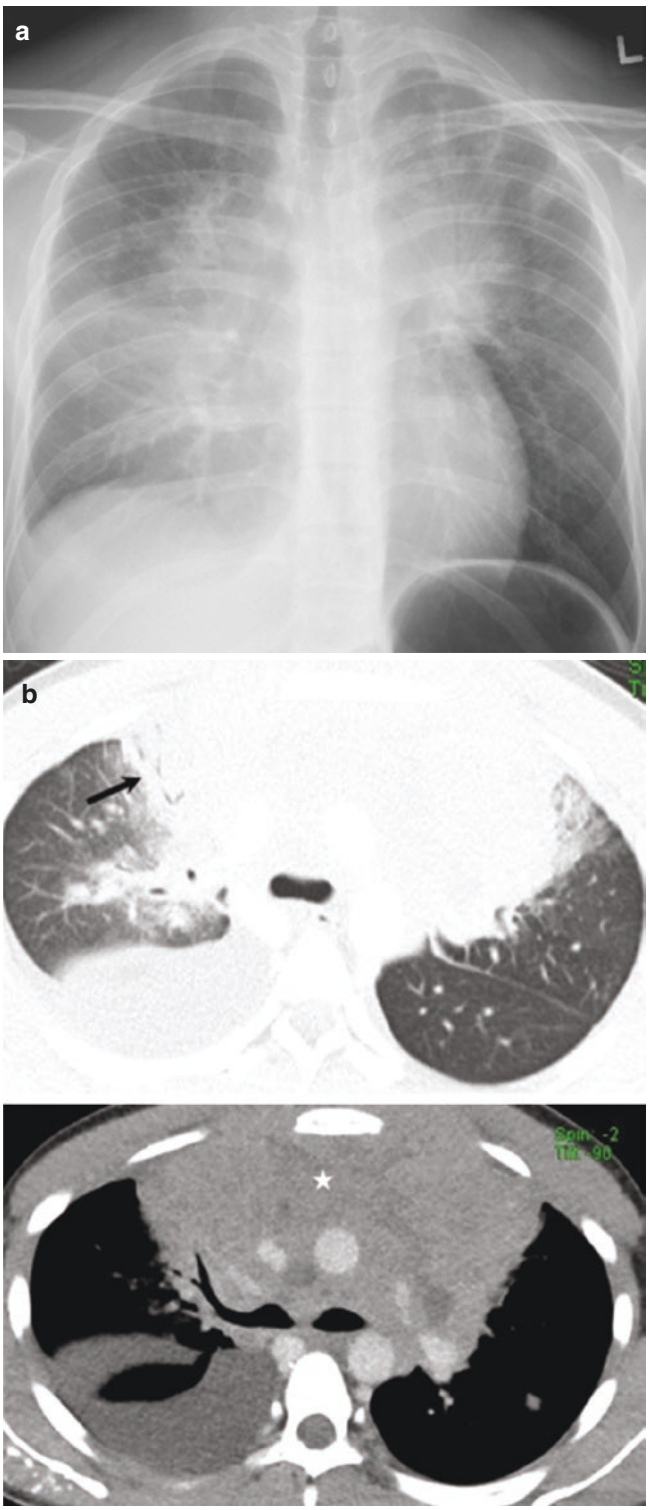

Fig. 5.47 A 59-year-old man with lymphoma. (**a**) Frontal radiograph of chest shows mediastinal widening with areas of consolidation in perihilar region. (**b**) Contrast-enhanced axial CT image in lung and soft tissue window shows areas of consolidation in upper lobes (arrow) with right pleural effusion and confluent mediastinal lymphadenopathy (asterisk) encasing mediastinal vessels

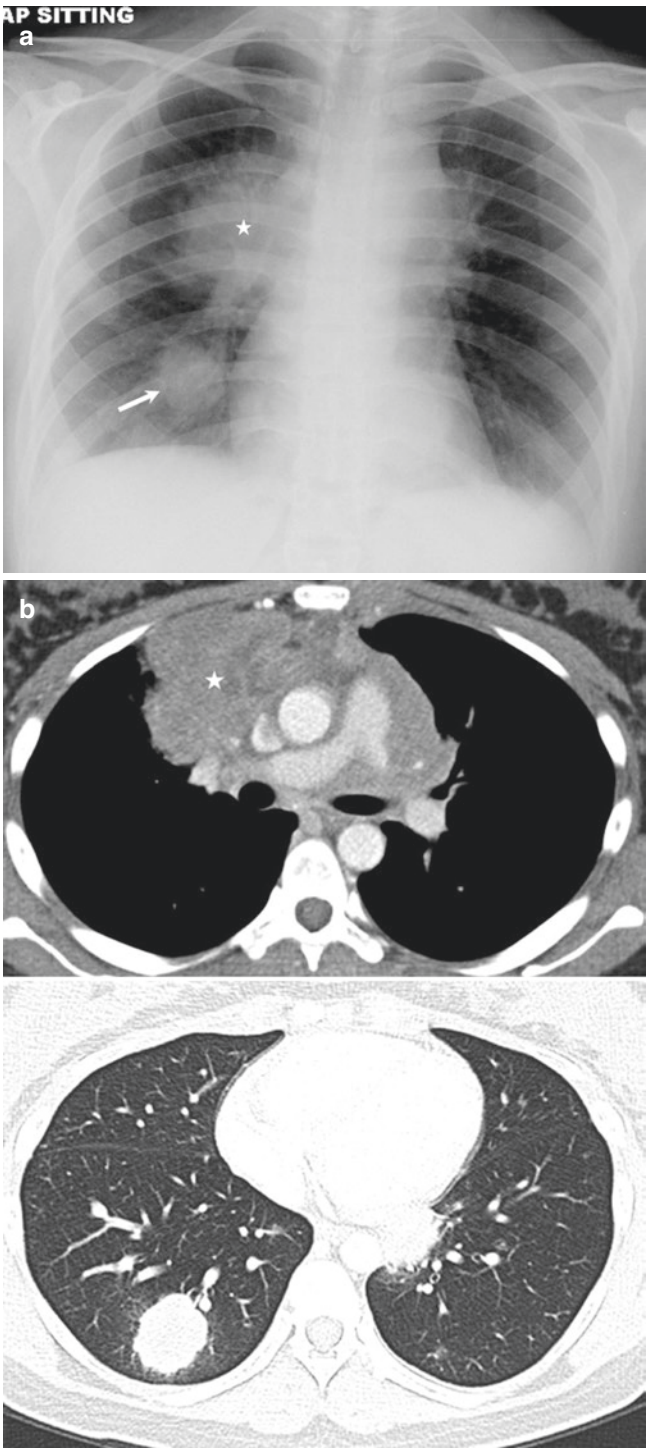

Fig. 5.48 A 52-year-old man with Hodgkin lymphoma. (**a**) Frontal radiograph of chest shows an opacity projected over the right lower zone (arrow) with right hilar mass (asterisk). (**b**) Contrast-enhanced CT thorax in soft tissue and lung window shows mediastinal lymphadenopathy (asterisk) with right lower lobe mass (arrow)

In both Hodgkin and non-Hodgkin lymphomas, peripheral consolidations or opacities with no visible communication with the enlarged mediastinal or hilar nodes may occasionally be seen. Patient with Sjogren syndrome are at high risk of developing lymphocytic interstitial pneumonia and parenchymal malignant lymphoma.

5.9.1 Primary Pulmonary Hodgkin Lymphomas

Primary pulmonary Hodgkin lymphoma is rare. The commonest imaging finding is single or multiple parenchymal nodules predominantly in upper lobes, some of which may be enlarged intrapulmonary lymph nodes. These lesions may cavitate. Endobronchial masses may also be present. Single or multiple focal areas of consolidation may be seen with or without pulmonary nodules [67].

5.9.2 Primary Pulmonary Non-Hodgkin Lymphomas

Most lymphomas arising primarily in the lung are MALT-type non-Hodgkin lymphomas [68]. These are "low-grade" B-cell lymphoma arising from MALT (also called bronchus-associated lymphoid tissue or BALT), composed of mucosal lymphoid follicles sited in distal bronchi and bronchioles, mainly at airway bifurcations [4].

On imaging, MALT lymphomas commonly present with an area of consolidation with or without air bronchograms, which may be located centrally or peripherally and show no lobar predilection. Other imaging findings include nodules, diffuse bilateral airspace consolidation, and segmental or lobar atelectasis. Pleural involvement is rare. Few lesions may show cavitation, and calcification is never seen [4, 67]. Additionally, CT may show centrilobular nodules and thickened interlobular septa, areas of ground-glass opacity, or diffuse interstitial shadowing resembling interstitial fibrosis [69, 70]. Enlarged hilar and/or mediastinal nodes may also be present. Primary pulmonary non-Hodgkin lymphomas other than MALT lymphoma are very rare and include lymphomatoid granulomatosis, intravascular large B-cell lymphomas, and unspecified peripheral T-cell lymphomas [5].

5.9.3 Other Findings in Pulmonary Lymphomas

Pleural effusion is usually unilateral and is accompanied by mediastinal or hilar lymphadenopathy. Pleural effusion may disappear once the mediastinal nodes have been irradiated; thus in such cases, pleural effusion probably occurred secondary to venous or lymphatic obstruction rather than neoplastic involvement of the pleura.

5.10 Sarcomas

Primary pulmonary sarcomas are quite rare, and most sarcomas affecting the lungs are metastases from extrathoracic primary tumors. The most frequently reported primary sarcomas in the lung are leiomyosarcoma, malignant fibrous histiocytoma, fibrosarcoma, chondrosarcoma, fibroleiomyosarcoma, rhabdomyosarcoma, carcinosarcoma, liposarcoma, and osteosarcoma. On imaging, primary pulmonary sarcomas have nonspecific findings and, in most cases, appear as a solitary pulmonary nodule or as a tracheal or endobronchial mass, radiologically indistinguishable from lung cancer, thus difficult to diagnose on the basis of imaging findings alone. The primary pulmonary sarcomas are usually diagnosed as an unexpected finding at histology. However, in the diagnostic work-up of these tumors, cross-sectional imaging plays an important role in helping delineate their extent and determine the most appropriate biopsy technique [71]. Nevertheless, angiosarcoma of the pulmonary artery may be diagnosed based on imaging findings of low attenuation filling defects in the pulmonary vasculature, heterogeneously enhancing mass in the lumen of the artery and extravascular spread of the mass. These findings are well demonstrated on contrast-enhanced CT and MRI [72].

Kaposi's sarcoma is primarily a tumor of the skin. However, cases involving the lung are increasingly diagnosed due to its association with acquired immunodeficiency syndrome (AIDS). In the absence of cutaneous involvement, Kaposi's sarcoma in the respiratory tract is rare. On imaging, the disease may show focal or widespread distribution [4, 73]. The localized form results in focal segmental or lobar opacities, while the endobronchial type may result in atelectasis or post-obstructive pneumonia. The more common, widespread pattern presents radiographically, as reticular, nodular, or reticulonodular shadowing, reflecting bronchocentric distribution of the lesions with bilateral perihilar predominance (Fig. 5.49). The pulmonary opacities of Kaposi's sarcoma, unlike its differentials such as pulmonary edema and opportunistic infections, remain stable in severity. Some series have reported hilar or mediastinal lymphadenopathy in 25–60% of cases of Kaposi's sarcoma. In addition, large bilateral pleural effusion is a common finding [4].

Other rare malignant pulmonary neoplasms include hemangiopericytoma, pulmonary blastoma, plasmacytoma, choriocarcinoma, teratoma, and Askin tumors.

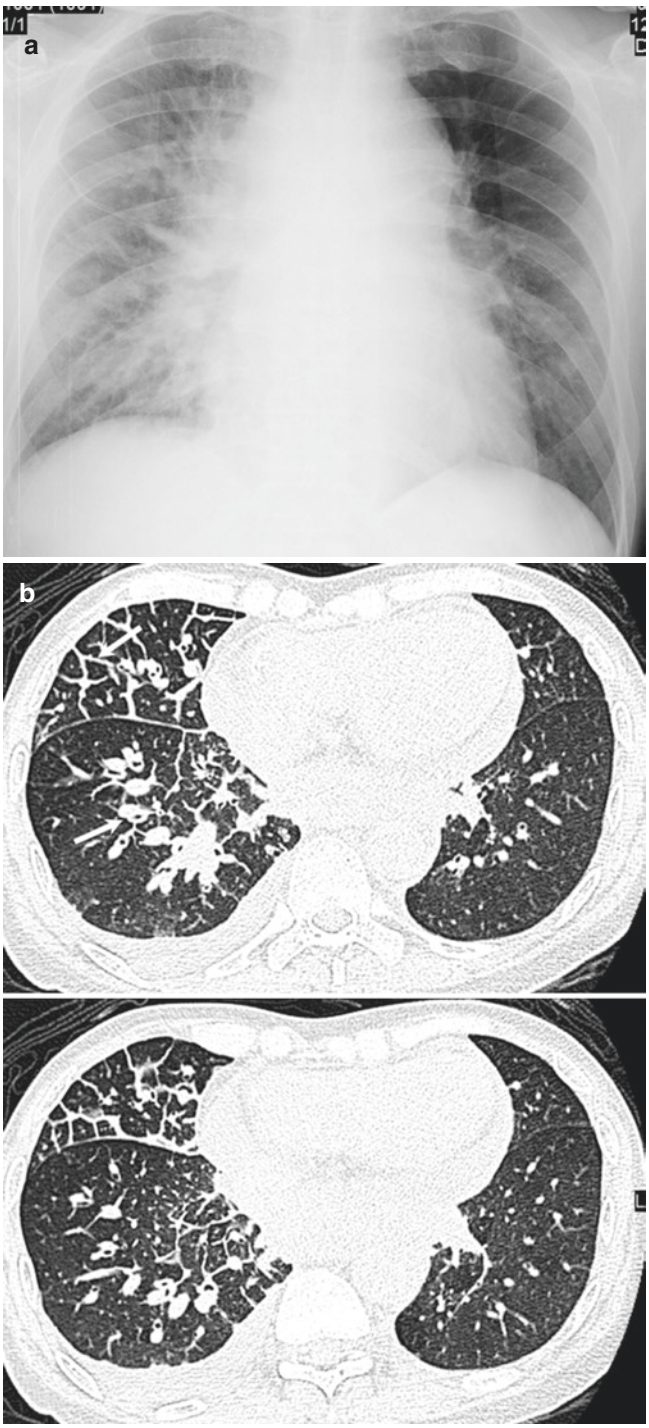

Fig. 5.49 A 57-year-old man with HIV-related Kaposi's sarcoma. (**a**) Frontal chest radiograph and (**b**) axial CT image shows septal thickening and peribronchial thickening in right lung (arrows)

5.11 Secondary Tumors of Lung

Common sources of hematogenous pulmonary metastases in adults are from the breast, gastrointestinal tract, kidney, uterus, prostate, testes, head, and neck tumors or from a variety of bone and soft tissue sarcomas [74, 75]. On imaging, hematogenous pulmonary metastasis present as one or more discrete pulmonary nodules of varying sizes, usually located in the lung periphery, with a basal predominance which receives more blood flow compared to upper lobes (Figs. 5.50 and 5.51). The nodules are usually oval or spherical in shape and have smooth, well-defined margins but may be of any shape and can infrequently demonstrate irregular edges in the presence of surrounding hemorrhage or due to local

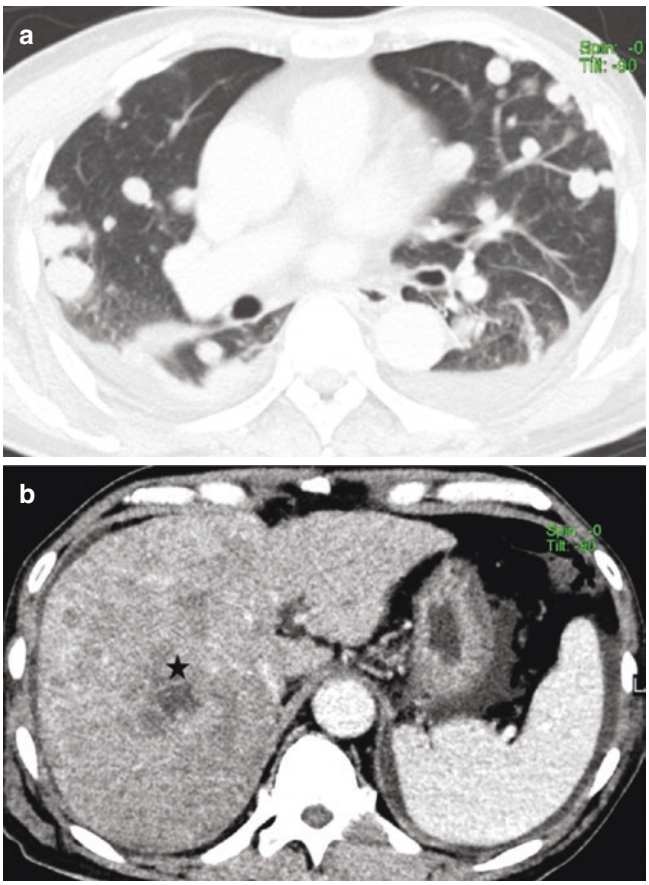

Fig. 5.50 A 62-year-old man with pulmonary metastases from hepatocellular carcinoma. (**a**) Axial CT image shows multiple well-defined nodules of varying sizes in both lungs. (**b**) Contrast-enhanced axial CT abdomen shows a large hepatocellular carcinoma (asterisk)

parenchymal invasion [4, 8]. Metastatic nodules are usually of soft tissue density but may show ground-glass opacity, if it is mucin-producing, as in gastric or colonic carcinoma metastases [5].

Pulmonary metastases may show cavitation on a radiograph in about 4% of cases. Cavitation is commonly associated with metastasis from squamous cell carcinoma of the head and neck, adenocarcinoma of the gastrointestinal tract, or breast sarcoma.

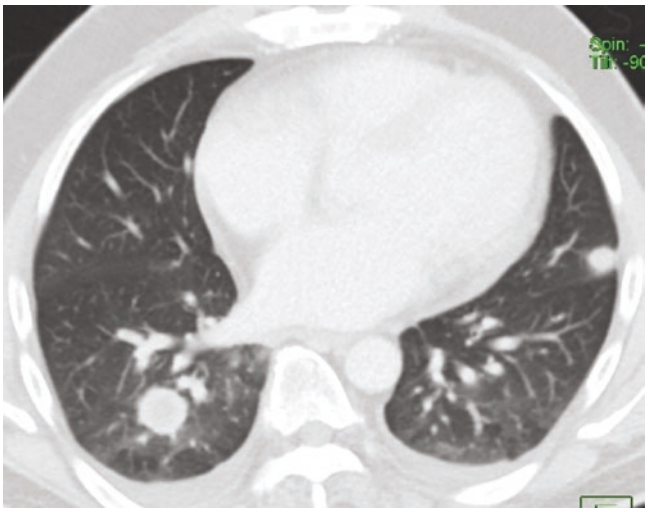

Fig. 5.51 A 68-year-old man with pulmonary metastases from renal cell carcinoma. Axial CT image shows well-defined nodules in lungs

Calcification or ossification within metastatic nodule is quite unusual, most commonly associated with metastasis from osteosarcoma or chondrosarcoma. Other primary tumors which may be associated with calcified lung metastasis include carcinoma of the thyroid, breast, and ovary, mucinous adenocarcinoma, and synovial sarcoma [4] (Fig. 5.52).

Highly vascular primary tumors, such as papillary thyroid cancer, choriocarcinoma, and angiosarcoma, may present with metastatic lung nodule surrounded by a halo of ground-glass opacity (CT halo sign) due to peritumoral hemorrhage [75] (Fig. 5.11).

5.12 Lymphangitic Carcinomatosis

Lymphangitic carcinomatosis results from the spread of tumor cells to the pulmonary lymphatics and the adjacent interstitial tissue. In the majority of cases, the tumor emboli spread by the hematogenous route to the lungs, lodging in smaller pulmonary arteries and secondarily penetrating the vessel wall and spreading into the surrounding interstitium and lymphatic vessels [76]. The most essential finding histologically is thicken-

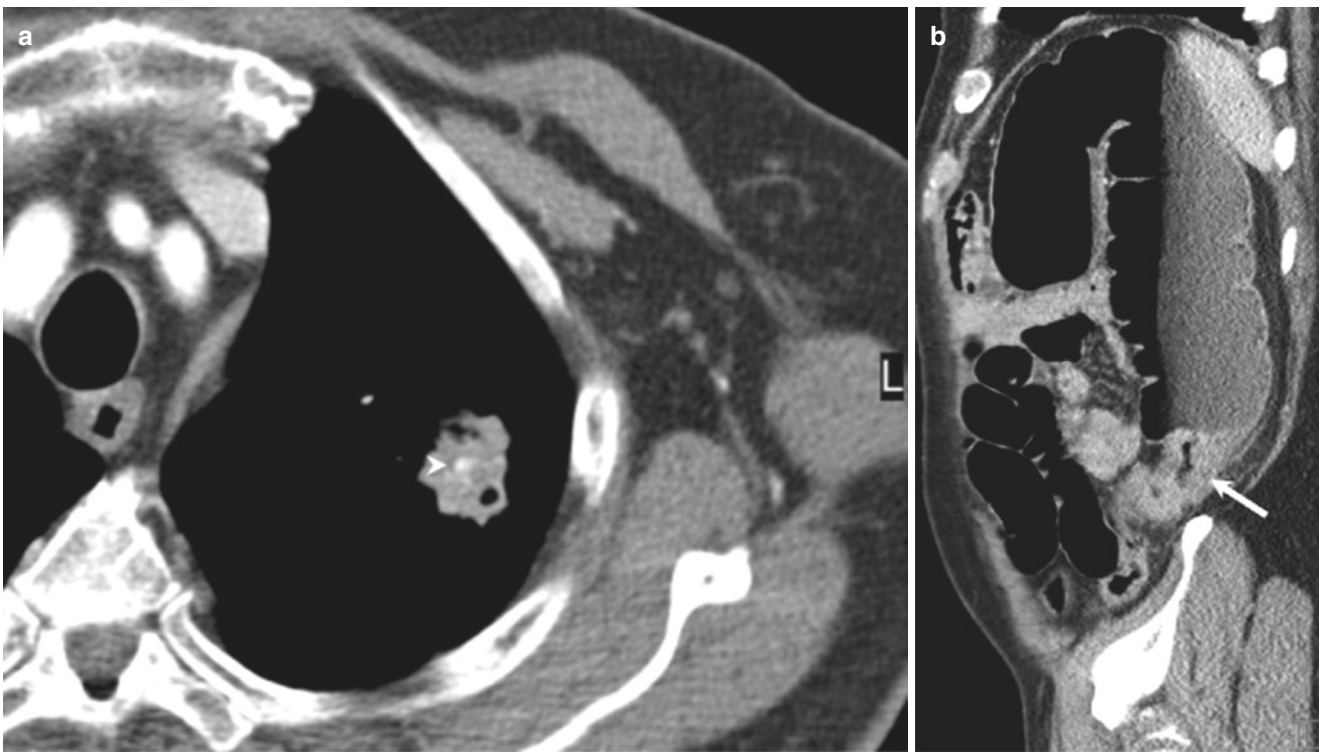

Fig. 5.52 Calcified lung metastasis from mucinous adenocarcinoma of colon. (**a**) Contrast-enhanced axial CT image shows a soft tissue mass in left upper lobe with a small focus of calcification (arrowhead). (**b**) Contrast-enhanced sagittal CT abdomen image shows an obstructing circumferential mass in the distal descending colon

ing of the interlobular septa and peribronchovascular interstitium caused by infiltration of tumor cells into the lymphatic vessels. The desmoplastic reaction, interstitial edema due to lymphatic obstruction or tumor secretion may contribute in interstitial thickening [77]. The commonest metastatic neoplasms that can cause pulmonary lymphangitic carcinomatosis are the breasts, stomach, lungs, pancreas, and prostate. Lymphangitic carcinomatosis may be bilaterally symmetrical (usually from non-pulmonary malignancies) or tends to be more localized if a primary carcinoma of the lung spreads directly into the adjacent peribronchovascular interstitium [4].

The characteristic radiographic finding in lymphangitic carcinomatosis is coarse and patchy reticulonodular opacities which may be diffuse and symmetric (Fig. 5.53). It is usually accompanied by asymmetric hilar or mediastinal lymphadenopathy and pleural effusion [78]. CT is more sensitive than plain radiographs in diagnosing lymphangitis carcinomatosis. CT findings include smooth and nodular interlobular septal and peribronchovascular bundle thickening (Fig. 5.54). This is in contrast to smooth septal thickening in pulmonary edema and Erdheim-Chester disease. Patchy airspace opacities are often seen. Lymphangitic carcinomatosis may affect all zones of both lungs, may show central or peripheral predominance, or may be confined to a lobe or one lung [4] (Fig. 5.55).

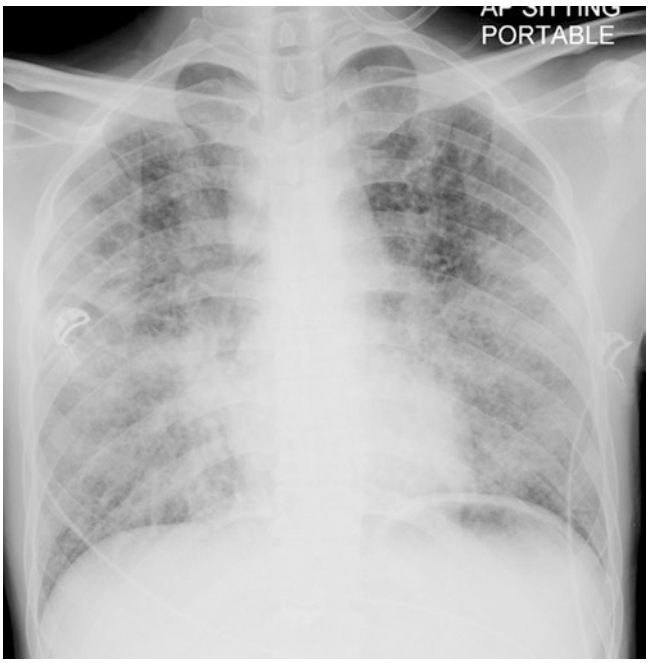

Fig. 5.53 A 58-year-old man with lymphangitis carcinomatosis secondary to gastric carcinoma. Frontal radiograph of chest shows diffuse, bilateral symmetrical reticular opacities. There is no pleural effusion or cardiomegaly

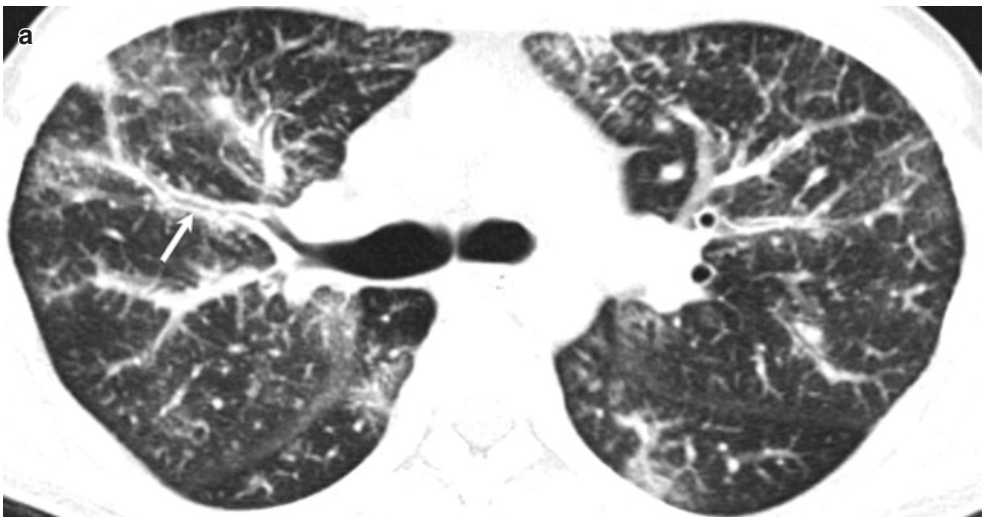

Fig. 5.54 A 58-year-old man with lymphangitis carcinomatosis secondary to gastric carcinoma. (**a**, **b**) Axial and coronal reformatted CT thorax in lung window shows diffuse smooth and nodular interlobular septal and peribronchovascular thickening with patchy areas of airspace opacities

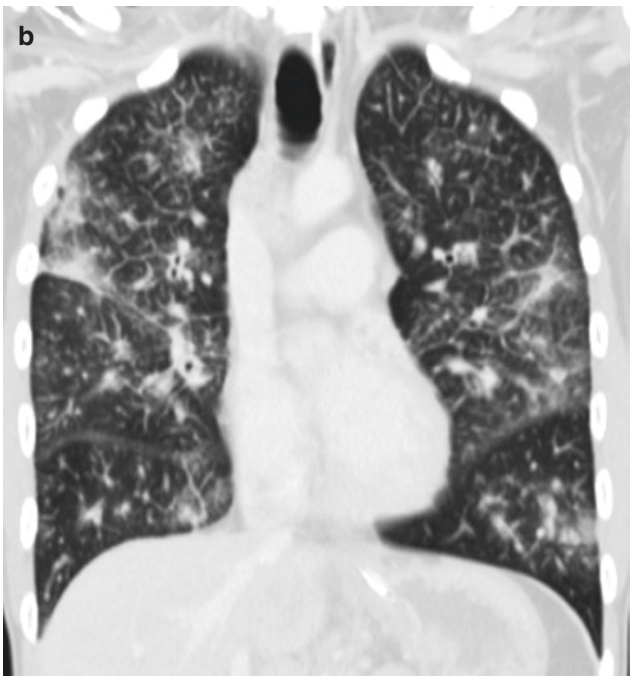

Fig. 5.54 (continued)

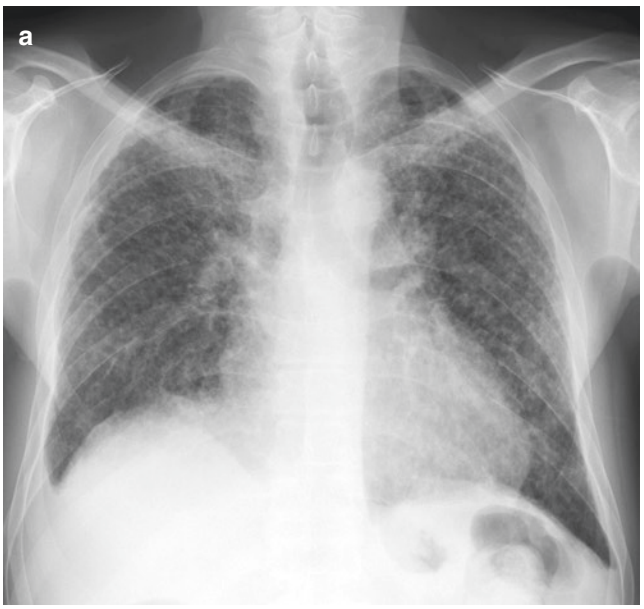

Fig. 5.55 54-year-old man with lymphangitis carcinomatosis secondary to right upper lobe bronchogenic cancer. (**a**) Frontal chest radiograph shows diffuse reticular opacities in both lungs with blunting of right costophrenic angle. (**b**, **c**) Axial CT images in lung window show a focal nodule in right upper lobe (arrow) with interlobular septal thickening in keeping with lymphangitis carcinomatosis. Note right pleural effusion

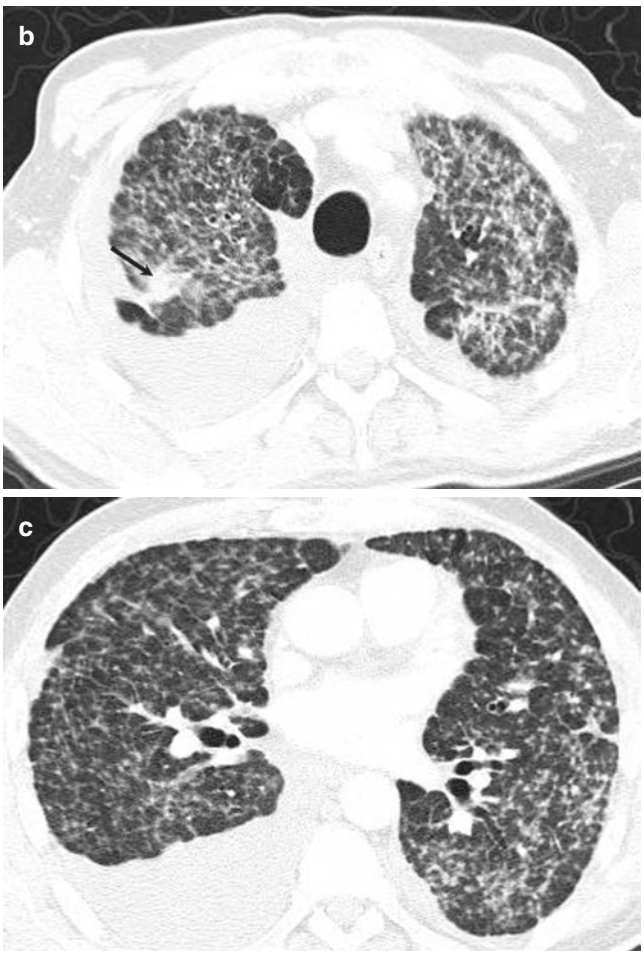

Fig. 5.55 (continued)

5.13 Endobronchial Metastases

Endobronchial metastases are quite rare and when present are few in number. The commonest primary tumors which can give rise to endobronchial metastases are kidney, breast, and colorectal cancers. The commonest radiologic feature is segmental or lobar collapse due to airway obstruction. CT may show a tiny, polypoidal endobronchial lesion in conjunction with atelectasis of the corresponding lobe (Fig. 5.56). In many cases, it is difficult to differentiate between a primary bronchogenic carcinoma and an endobronchial metastasis on imaging [75].

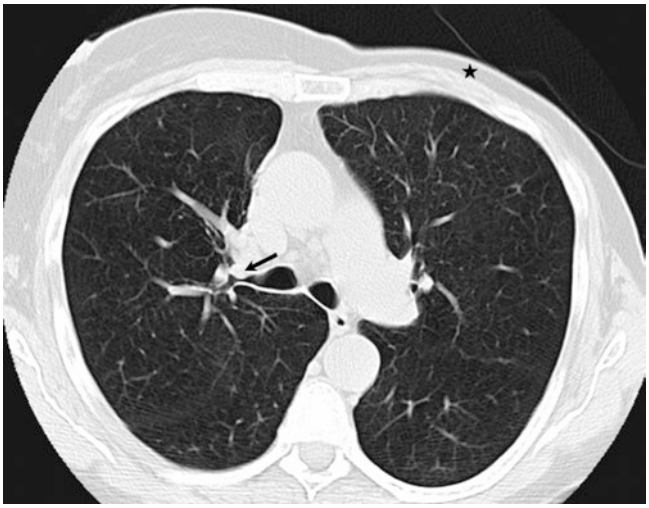

Fig. 5.56 A 59-year old women with endobronchial metastasis. Axial CT image shows a nodular filling defect within the right main bronchus (arrow) in a patient with history of operated left breast malignancy (asterisk)

5.14 Miliary Metastases

Infrequently, numerous small nodules may be seen throughout both lungs mimicking miliary tuberculosis, with no dominant masses and no evidence of lymphatic obstruction (Fig. 5.57). This pattern of metastatic presentation is quite rare and is most likely caused by thyroid and renal carcinomas, bone sarcomas, and choriocarcinoma [4].

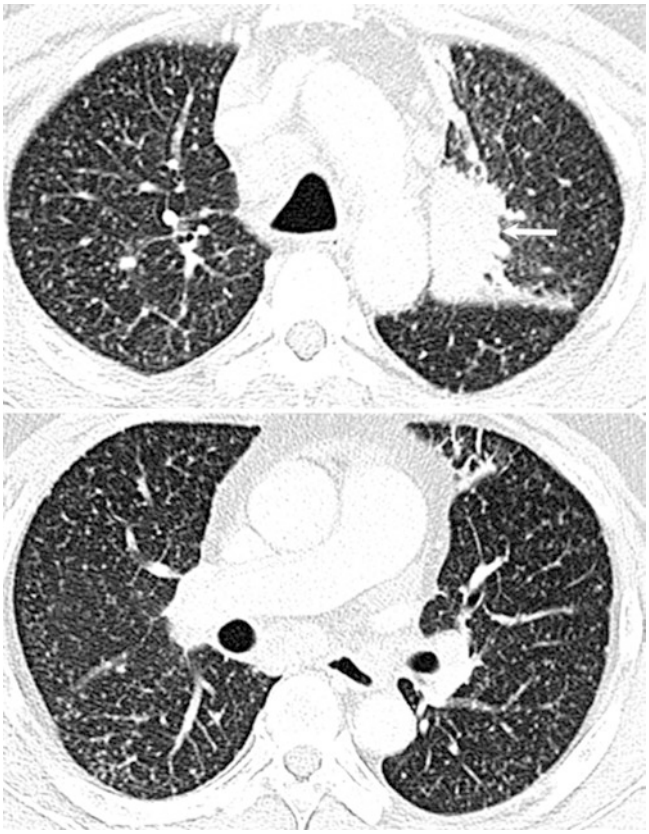

Fig. 5.57 A 51-year-old man with miliary metastasis from bronchial carcinoma. Axial CT images show multiple small pulmonary nodules (miliary opacities) scattered in both lungs with a left upper lobe lung malignancy (arrow)

5.15 Benign Tumors of Lung

5.15.1 Hamartoma

Pulmonary hamartomas are benign mesenchymal neoplasms composed of an abnormal mixture of epithelial and mesenchymal tissues, such as cartilage, fat, connective tissue, smooth muscle, and calcification. Hamartoma accounts for 77% of all benign lung tumors and 6–8% of solitary lung tumors [79]. It has a peak frequency in the fifth and sixth decades [80]. Pulmonary hamartomas are commonly seen in the lung periphery (approximately 90% of cases) and present as a solitary pulmonary nodule. The remaining 10% cases are located centrally, within a major bronchus. Central lesions may present with features of airway obstruction.

Table 5.8 Imaging features of hamartoma[a]

Chest radiograph	• Spherical or slightly lobulated, well-defined nodule, usually 1–4 cm in diameter
CT	• Smooth, well-defined, rounded, or lobulated nodule or mass • Central fat (60%)—diagnostic • Popcorn-like calcification or central calcification (25%)—diagnostic • Enhancement in the surrounding capsule or in septa separating unenhancing components on post-contrast images

[a]If a hamartoma contains no calcification or minimal fat, it may be difficult to distinguish it from a rounded or lobulated primary lung cancer on CT

Hamartomas have characteristic imaging features (Table 5.8) (Figs. 5.58 and 5.59).

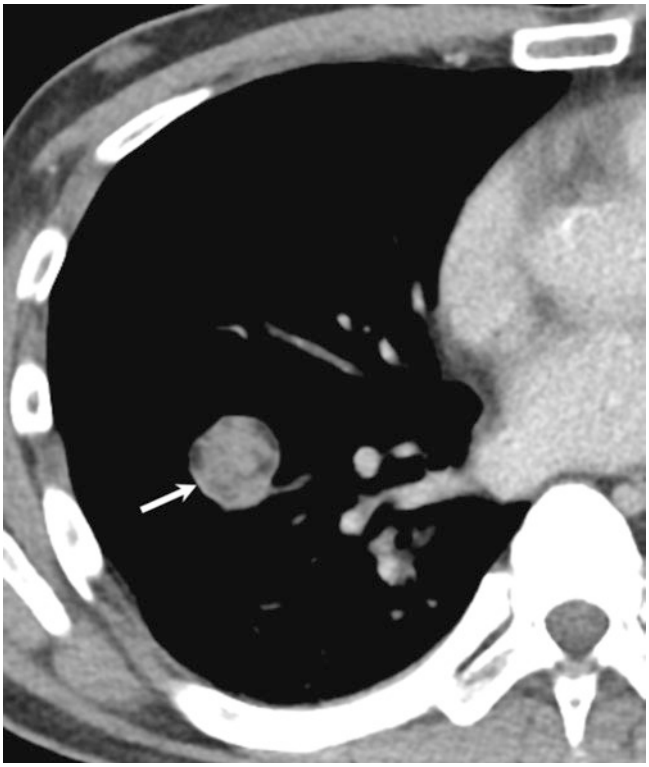

Fig. 5.58 A 30-year-old female with hamartoma. Contrast-enhanced axial CT thorax in soft tissue window shows a fat containing solitary pulmonary nodule in the right lung (arrow)

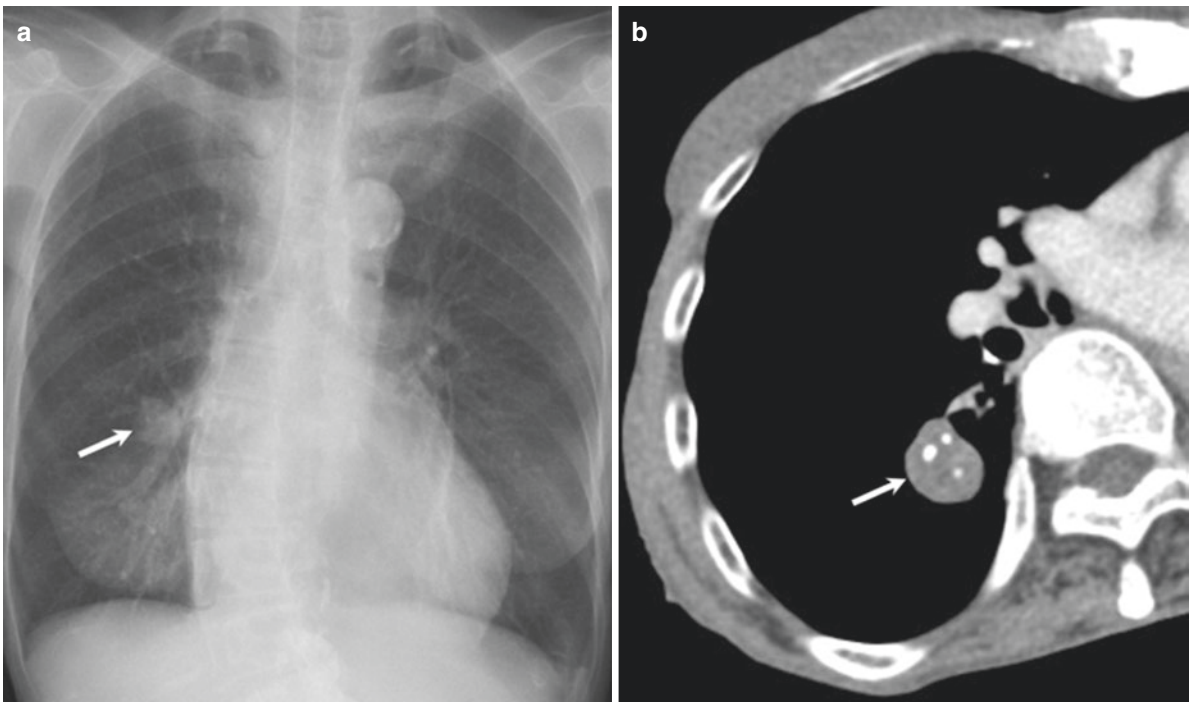

Fig. 5.59 A 64-year-old female with hamartoma. (**a**) Frontal radiograph of chest shows a well-defined solitary pulmonary nodule projected over right lower zone (arrow). (**b**) Contrast-enhanced axial CT image shows a well-defined pulmonary nodule in the right lower lobe (arrow) with internal fat (pixels with negative HU) and calcification

5.15.2 Other Benign Pulmonary Neoplasms

Inflammatory myofibroblastic tumor, pulmonary sclerosing hemangioma, pulmonary hyalinizing granuloma, neurogenic tumors, fibroma, hemangioma, benign clear cell tumors, chemodectoma, and granular cell myoblastoma are other benign neoplasms that are occasionally encountered in the trachea, bronchi, or lungs. These neoplasms cannot usually be distinguished from the more common primary and secondary lung malignancies on imaging; therefore, the specific diagnosis has to be made histologically (Figs. 5.60 and 5.61).

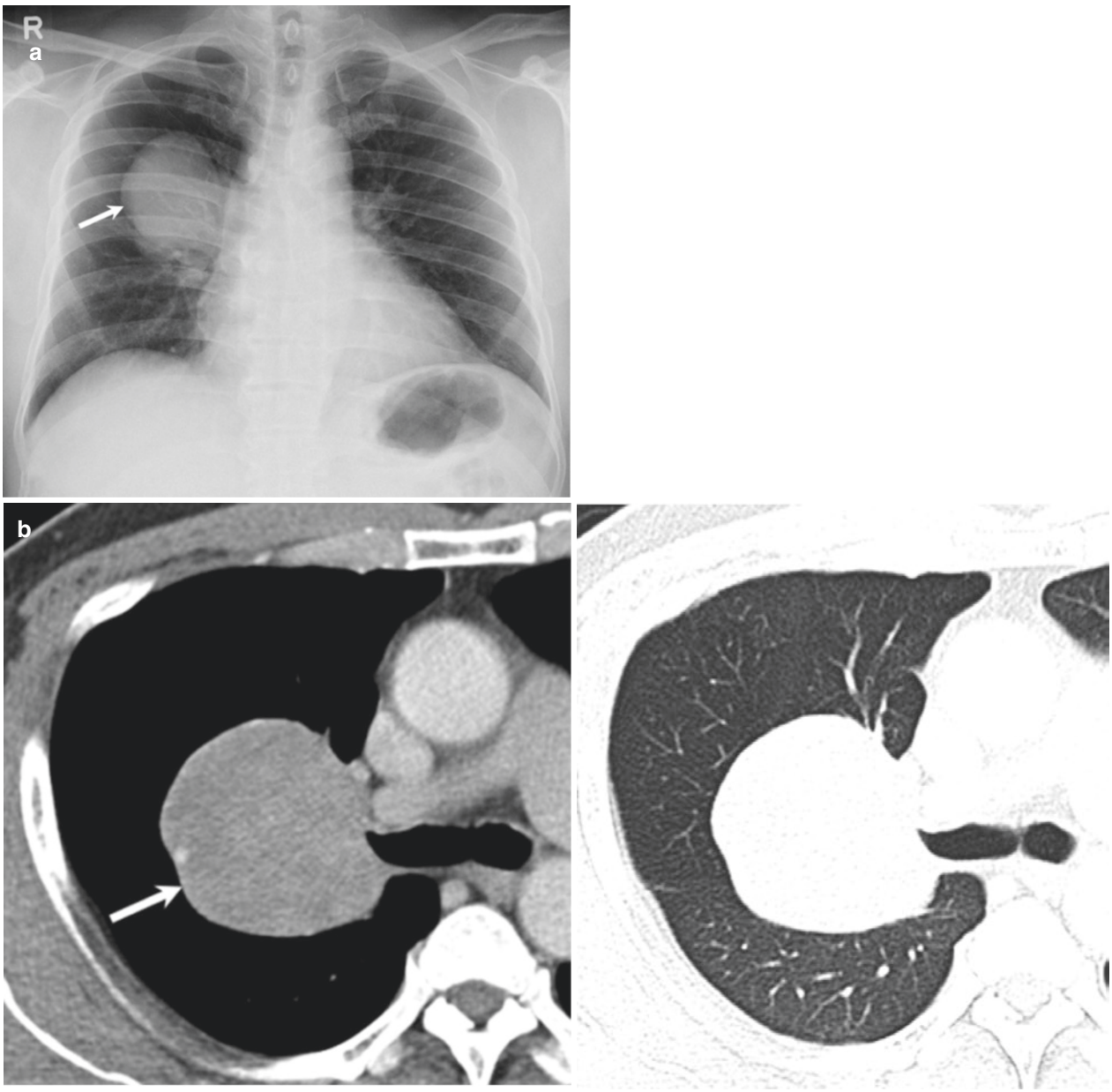

Fig. 5.60 A 49-year-old man with pulmonary hyalinizing granuloma. (**a**) Frontal radiograph of chest shows a large well-defined mass projected over right perihilar region (arrow). (**b**) Contrast-enhanced axial CT images show a large well-defined lobulated soft tissue mass in the right upper lobe (arrow). Histopathology confirmed it to be pulmonary hyalinizing granuloma

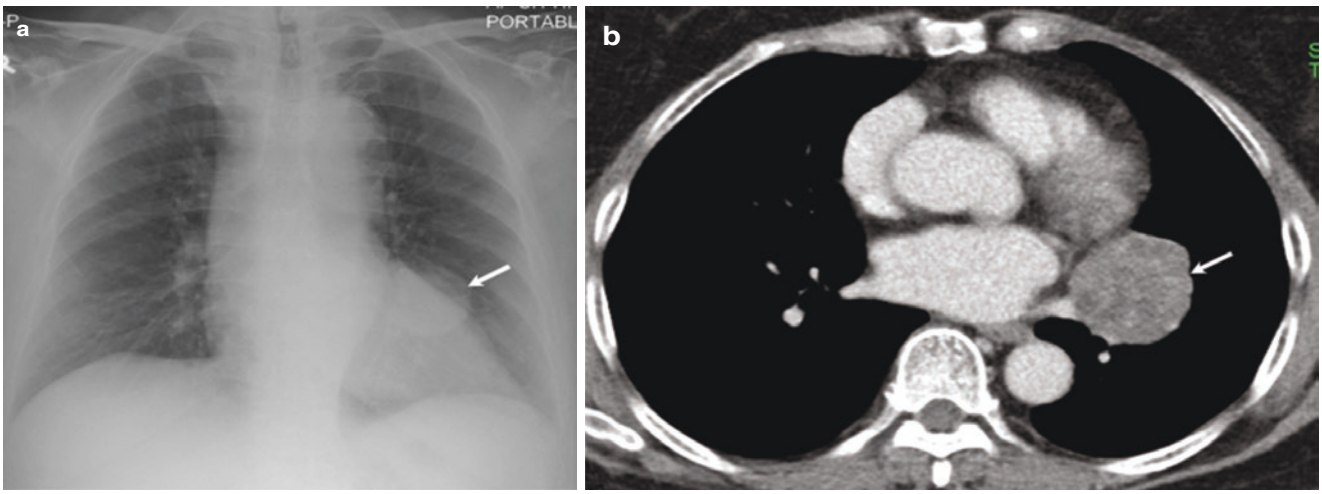

Fig. 5.61 A 44-year-old man with schwannoma in the left lung. (**a**) Frontal radiograph of chest shows a well-defined opacity in the left retrocardiac region (arrow). (**b**) Contrast-enhanced axial CT image shows a well-defined soft tissue mass in the left infrahilar region (arrow). Histopathology confirmed it to be a schwannoma

References

1. American Cancer Society. Cancer prevention & early detection facts & figures 2017–2018. Atlanta: American Cancer Society; 2017.
2. Smith RA, Andrews KS, Brooks D, Fedewa SA, Manassaram-Baptiste D, Saslow D, Brawley OW, Wender RC. Cancer screening in the United States, 2017: a review of current American Cancer Society guidelines and current issues in cancer screening. CA Cancer J Clin. 2017;67(2):100–21.
3. Travis WD, Brambilla E, Nicholson AG, Yatabe Y, Austin JHM, Beasley MB, Chirieac LR, Dacic S, Duhig E, Flieder DB, Geisinger K, Hirsch FR, Ishikawa Y, Kerr KM, Noguchi M, Pelosi G, Powell CA, Tsao MS, Wistuba I, WHO Panel. The 2015 World Health Organization classification of lung tumors: impact of genetic, clinical and radiologic advances since the 2004 classification. J Thorac Oncol. 2015;10(9):1243–60.
4. Padley SPG, Lazoura O. Pulmonary neoplasms. In: Adam A, Dixon AK, Gillard JH, Schaefer-Prokop CM, editors. Grainger & Allison's diagnostic radiology: a textbook of medical imaging. 6th ed. Philadelphia: Elsevier Churchill Livingstone; 2015.
5. Hansell D, et al. Neoplasms of the lungs. Airways, and pleura. In: Lynch D, editor. Imaging of diseases of the chest. 5th ed. New York: Elsivier; 2010. p. 787–879.
6. Yang P, Cerhan J, Vierkant R, et al. Adenocarcinoma of the lung is strongly associated with cigarette smoking: further evidence from a prospective study of women. Am J Epidemiol. 2002;156(12):1114–22.
7. Groot P, Munden RF. Lung cancer epidemiology, risk factors, and prevention. Radiol Clin N Am. 2012;50(5):863–76.
8. WR Webb. "Lung cancer and bronchopulmonary neoplasm." In: Thoracic imaging pulmonary and cardiovascular radiology, 2nd edn., Wolters Kluver, Alphen aan den Rijn, 2011, pp. 69–116.
9. Khuder SA, Mutgi AB. Effect of smoking cessation on major histologic types of lung cancer. Chest. 2001;120(5):1577–83.
10. Öberg M, Jaakkola MS, Woodward A, et al. Worldwide burden of disease from exposure to second-hand smoke: a retrospective analysis of data from 192 countries. Lancet. 2011;377(9760):139–46.
11. Cruz D, Tanoue LT, Matthay RA. Lung cancer: epidemiology, etiology, and prevention. Clin Chest Med. 2011;32(4):605–44.
12. Hoffmann D, Djordjevic MV, Hoffmann I. The changing cigarette. Prev Med. 1997;26(4):427–34.
13. MacMahon H, Naidich DP, Goo JM, Lee KS, Leung ANC, Mayo JR, Mehta AC, Ohno Y, Powell CA, Prokop M, Rubin GD, Schaefer-Prokop CM, Travis WD, Van Schil PE, Bankier AA. Guidelines for management of incidental pulmonary nodules detected on CT images: from the Fleischner Society 2017. Radiology. 2017;284(1):228–43.
14. Snoeckx A, Reyntiens P, Desbuquoit D, Spinhoven MJ, Van Schil PE, van Meerbeeck JP, Parizel PM. Evaluation of the solitary pulmonary nodule: size matters, but do not ignore the power of morphology. Insights Imaging. 2018;9(1):73–86.
15. McWilliams A, Tammemagi MC, Mayo JR, et al. Probability of cancer in pulmonary nodules detected on first screening CT. N Engl J Med. 2013;369(10):910–9.
16. Lindell RM, Hartman TE, Swensen SJ, et al. Five-year lung cancer screening experience: CT appearance, growth rate, location, and histologic features of 61 lung cancers. Radiology. 2007;242(2):555–62.
17. Horeweg N, van der Aalst CM, Thunnissen E, et al. Characteristics of lung cancers detected by computer tomography screening in the randomized NELSON trial. Am J Respir Crit Care Med. 2013;187(8):848–54.
18. Hyodo T, Kanazawa S, Dendo S, et al. Intrapulmonary lymph nodes: thin-section CT findings, pathological findings, and CT differential diagnosis from pulmonary metastatic nodules. Acta Med Okayama. 2004;58(5):235–40.
19. Edey AJ, Hansell DM. Incidentally detected small pulmonary nodules on CT. Clin Radiol. 2009;64(9):872–84.
20. Ahn MI, Gleeson TG, Chan IH, et al. Perifissural nodules seen at CT screening for lung cancer. Radiology. 2010;254:949–56.
21. Woodring JH, Fried AM. Significance of wall thickness in solitary cavities of the lung: a follow-up study. Am J Roentgenol. 1983;140(3):473–4.
22. Truong MT, Ko JP, Rossi SE, Rossi I, Viswanathan C, Bruzzi JF, Marom EM, Erasmus JJ. Update in the evaluation of the solitary pulmonary nodule. Radiographics. 2014;34(6):1658–79.
23. Winer-Muram HT. The solitary pulmonary nodule. Radiology. 2006;239(1):34–49.
24. Pinto PS. The CT halo sign. Radiology. 2004;230(1):109–10.

25. Kim SJ, Lee KS, Ryu YH, et al. Reversed halo sign on high-resolution CT of cryptogenic organizing pneumonia: diagnostic implications. AJR Am J Roentgenol. 2003;180(5):1251–4.
26. Naidich DP, Bankier AA, MacMahon H, et al. Recommendations for the management of subsolid pulmonary nodules detected at CT: a statement from the Fleischner Society. Radiology. 2013;266(1):304–17.
27. Lee HY, Lee KS. Ground-glass opacity nodules: histopathology, imaging evaluation, and clinical implications. J Thorac Imaging. 2011;26(2):106–18.
28. Kim HY, Shim YM, Lee KS, Han J, Yi CA, Kim YK. Persistent pulmonary nodular ground-glass opacity at thin-section CT: histopathologic comparisons. Radiology. 2007;245(1):267–75.
29. Travis WD, Brambilla E, Noguchi M, et al. International association for the study of lung cancer/American Thoracic Society/European Respiratory Society international multidisciplinary classification of lung adenocarcinoma. J Thorac Oncol. 2011;6(2):244–85.
30. Travis WD, Brambilla E, Noguchi M, et al. Diagnosis of lung adenocarcinoma in resected specimens: implications of the 2011 International Association for the Study of Lung Cancer/American Thoracic Society/European Respiratory Society classification. Arch Pathol Lab Med. 2013;137(5):685–705.
31. Li F, Sone S, Abe H, Macmahon H, Doi K. Malignant versus benign nodules at CT screening for lung cancer: comparison of thin-section CT findings. Radiology. 2004;233(3):793–8.
32. Travis WD, Brambilla E, Noguchi M, et al. International Association for the Study of Lung Cancer/American Thoracic Society/European Respiratory Society: international multidisciplinary classification of lung adenocarcinoma executive summary. Proc Am Thorac Soc. 2011;8(5):381–5.
33. Hasegawa M, Sone S, Takashima S, et al. Growth rate of small lung cancers detected on mass CT screening. Br J Radiol. 2000;73(876):1252–9.
34. Swensen SJ, Brown LR, Colby TV, et al. Pulmonary nodules: CT evaluation of enhancement with iodinated contrast material. Radiology. 1995;194:393–8.
35. Swensen SJ, Brown LR, Colby TV, et al. Lung nodule enhancement at CT: prospective findings. Radiology. 1996;201:447–55.
36. Saita S, Tanzillo A, Riscica C, et al. Bronchial brushing and biopsy: a comparative evaluation in diagnosing visible bronchial lesions. Eur J Cardiothorac Surg. 1990;4:270–2.
37. Ho CC, Lin CK, Yang CY, Chang LY, Lin SY, Yu CJ. Current advances of endobronchial ultrasonography in the diagnosis and staging of lung cancer. J Thorac Dis. 2016;8(Suppl 9):S690–6.
38. Patil SS, Godoy MC, Sorensen JI, Marom EM. Lung cancer imaging. Semin Diagn Pathol. 2014;31(4):293–305.
39. Hubner KF, Buonocore E, Gould HR, et al. Differentiating benign from malignant lung lesions using "quantitative" parameters of FDG PET images. Clin Nucl Med. 1996;21(12):941–9.
40. Gupta NC, Maloof J, Gunel E. Probability of malignancy in solitary pulmonary nodules using fluorine-18-FDG and PET. J Nucl Med. 1996;37(6):943–8.
41. MacMahon H, Austin JH, Gamsu G, et al. Guidelines for management of small pulmonary nodules detected on CT scans: a statement from the Fleischner Society. Radiology. 2005;237:395–400.
42. Takashima S, Sone S, Li F, et al. Small solitary pulmonary nodules (< or = 1 cm) detected at population-based CT screening for lung cancer: reliable high-resolution CT features of benign lesions. AJR Am J Roentgenol. 2003;180:955–64.
43. Klein JS, Braff S. Imaging evaluation of the solitary pulmonary nodule. Clin Chest Med. 2008;29:15–38.
44. Rubens MB, et al. Tumours of the lung. In: Textbook of radiology and imaging, vol. vol 1. 7th ed. London: Churchill Livingstone; 2003. p. 107–30.
45. Woodring JH, Fried AM, Chuang VP. Solitary cavities of the lung: diagnostic implications of cavity wall thickness. AJR Am J Roentgenol. 1980;135:1269–71.
46. Chou SH, Kicska G, Kanne JP, Pipavath S. Cheerio sign. J Thorac Imaging. 2013;28(1):W4.
47. Lee KS, Kim Y, Han J, et al. Bronchioloalveolar carcinoma: clinical, histopathologic, and radiologic findings. Radiographics. 1997;17(6):1345–57.
48. Grewal RG, Austin JH. CT demonstration of calcification in carcinoma of the lung. J Comput Assist Tomogr. 1994;18:867–71.
49. Gilbert C, Yarmus L, Feller-Kopman D. Use of endobronchial ultrasound and endoscopic ultrasound to stage the mediastinum in early-stage lung cancer. J Natl Compr Cancer Netw. 2012;10(10):1277–82.
50. Rohren EM, Turkington TG, Coleman RE. Clinical applications of PET in oncology. Radiology. 2004;231(2):305–32.
51. Dougherty B, Jersmann HP, Robinson PC, Nguyen P. Staging the mediastinum: what is current best practice? Lung Cancer Manag. 2013;2(2):153–62.
52. Caulo A, Mirsadraee S, Maggi F, et al. Integrated imaging of non-small cell lung cancer recurrence: CT and PET-CT findings, possible pitfalls and risk of recurrence criteria. Eur Radiol. 2012;22(3):588–606.
53. Glazer H, Kaiser L, Anderson D, et al. Indeterminate mediastinal invasion in bronchogenic carcinoma: CT evaluation. Radiology. 1989;173(1):37–42.
54. Allen MS, Mathisen DJ, Grillo HC, et al. Bronchogenic carcinoma with chest wall invasion. Ann Thorac Surg. 1991;51(6):948–51.
55. Cangemi V, Volpino P, D'Andrea N, et al. Results of surgical treatment of stage IIIA non-small cell lung cancer. Eur J Cardiothorac Surg. 1995;9:352–9.
56. Ratto G, Piacenza G, Frola C, et al. Chest wall involvement by lung cancer: computed tomographic detection and results of operation. Ann Thorac Surg. 1991;51(2):182–8.
57. Pauls S, Schmidt SA, Juchems MS, et al. Diffusion-weighted MR imaging in comparison to integrated [^{18}F]-FDG PET/CT for N-staging in patients with lung cancer. Eur J Radiol. 2012;81(1):178–82.
58. Hendifar AE, Marchevsky AM, Tuli R. Neuroendocrine tumors of the lung: current challenges and advances in the diagnosis and management of well-differentiated disease. J Thorac Oncol. 2017;12(3):425–36.
59. Dincer HE, Podgaetz E, Andrade RS. Pulmonary neuroendocrine tumors: part I. Spectrum and characteristics of tumors. J Bronchol Interv Pulmonol. 2015;22(3):267–73.
60. Lee D, Rho JY, Kang S, Yoo KJ, Choi HJ. CT findings of small cell lung carcinoma: can recognizable features be found? Medicine (Baltimore). 2016;95(47):e5426.
61. Carter BW, Glisson BS, Truong MT, Erasmus JJ. Small cell lung carcinoma: staging, imaging, and treatment considerations. Radiographics. 2014;34(6):1707–21.
62. Kruger S, Buck AK, Blumstein NM, et al. Use of integrated FDG PET/CT imaging in pulmonary carcinoid tumours. J Intern Med. 2006;260:545–50.
63. Detterbeck FC, Boffa DJ, Kim AW, Tanoue LT. The eighth edition lung cancer stage classification. Chest. 2017;151(1):193–203.
64. Rami-Porta R, Asamura H, Travis WD, Rusch VW. Lung cancer – major changes in the American Joint Committee on Cancer eighth edition cancer staging manual. CA Cancer J Clin. 2017;67(2):138–55.
65. Au V, Leung AN. Radiologic manifestations of lymphoma in the thorax. Am J Roentgenol. 1997;168(1):93–8.
66. Lewis ER, Caskey CI, Fishman EK. Lymphoma of the lung: CT findings in 31 patients. AJR Am J Roentgenol. 1991;156:711–4.
67. Lee KS, Kim Y, Primack SL. Imaging of pulmonary lymphomas. Am J Roentgenol. 1997;168(2):339–45.

68. Ferraro P, Trastek VF, Adlakha H, et al. Primary non-Hodgkin's lymphoma of the lung. Ann Thorac Surg. 2000;69:993–7.
69. King LJ, Padley SP, Wotherspoon AC, et al. Pulmonary MALT lymphoma: imaging findings in 24 cases. Eur Radiol. 2000;10:1932–8.
70. McCulloch GL, Sinnatamby R, Stewart S, et al. High-resolution computed tomographic appearance of MALToma of the lung. Eur Radiol. 1998;8:1669–73.
71. Foran P, Colleran G, Madewell J, O'Sullivan PJ. Imaging of thoracic sarcomas of the chest wall, pleura, and lung. Semin Ultrasound CT MR. 2011;32(5):365–76.
72. Desmarais P, Laskine M, Caporuscio C. Primary pulmonary artery angiosarcoma mimicking pulmonary embolism in a 66-year-old man with dyspnea. CMAJ. 2016;188(17–18):E509–12.
73. Naidich D, Tarras M, Garay S, et al. Kaposi's sarcoma. CT-radiographic correlation. Chest. 1989;96(4):723–8.
74. Coppage L, Shaw C, Curtis AM. Metastatic disease to the chest in patients with extrathoracic malignancy. J Thorac Imaging. 1987;2(4):24–37.
75. Seo JB, Im J-G, Goo JM, Chung MJ, Kim M-Y. Atypical pulmonary metastases: spectrum of radiologic findings. Radiographics. 2001;21(2):403–17.
76. Ikezoe J, Godwin JD, Hunt KJ, Marglin SI. Pulmonary lymphangitic carcinomatosis: chronicity of radiographic findings in long-term survivors. AJR Am J Roentgenol. 1995;165(1):49–52.
77. Johkoh T, Ikezoe J, Tomiyama N, Nagareda T, Kohno N, Takeuchi N, Yamagami H, Kido S, Takashima S, Arisawa J, et al. CT findings in lymphangitic carcinomatosis of the lung: correlation with histologic findings and pulmonary function tests. AJR Am J Roentgenol. 1992;158(6):1217–22.
78. Thomas A, Lenox R. Pulmonary lymphangitic carcinomatosis as a primary manifestation of colon cancer in a young adult. CMAJ. 2008;179(4):338–40.
79. Furuya K, Yasumori K, Takeo S, Sakino I, Uesugi N, Momosaki S, Muranaka T. Lung CT: part 1, Mimickers of lung cancer – spectrum of CT findings with pathologic correlation. AJR Am J Roentgenol. 2012;199(4):W454–63.
80. Siegelman S, Khouri N, Scott W, et al. Pulmonary hamartoma: CT findings. Radiology. 1986;160(2):313–7.

Imaging of Pulmonary Infections

6

Dinesh Singh

6.1 Introduction

Pulmonary infections have always been a cause of high morbidity and mortality, particularly in the pediatric and geriatric population and in immunocompromised hosts [1]. Pulmonary infections have various etiologies and have variegated patterns on radiographs and computed tomography (CT). Imaging plays an important role in the initial diagnosis and follow-up of various lung infections. Radiographs can be normal or non-specific during the initial evaluation, and CT findings may be more definitive. CT not only helps with the diagnosis but can also aid in management by guiding the diagnostic and therapeutic procedure. The pulmonary infections spread by direct or indirect contact with the infected host, droplet transmission, or an airborne spread. In rare cases, some infections can also be transmitted by vectors, namely, insect or animal hosts, and rarely by direct invasion from nearby infected organs. Pulmonary infections may have typical imaging patterns and distribution based on the mode of spread. There are a number of well-described imaging patterns of alveolar infections. The localization and morphological features on imaging may help in the diagnosis of infection and identification of mode of infection and, in certain cases, the microorganism responsible for the infection.

6.2 Patterns of Lung Infections

6.2.1 Consolidation

Consolidation is a typical pattern of a lung infection on a radiograph of the chest, usually initiating as a small focus close to the fissures. Pneumonia can be caused by a variety of organisms like bacteria, bacteria-like organisms like *Mycoplasma pneumonia*, fungi, or even a number of viruses.

D. Singh (✉)
Department of Diagnostic Radiology, Khoo Teck Puat Hospital, Singapore, Singapore

Lobar pneumonia and bronchopneumonia are two distinct patterns of pulmonary infections (Figs. 6.1 and 6.2). Lobar pneumonia results in a homogenous opacity, limited by the fissures and without any associated volume loss. There may be the presence of "air bronchograms" that result from relative sparing of the bronchi, appearing as dark air-filled linear spaces within the exudate-filled alveoli. Lobar pneumonia usually has surrounding ground-glass opacities, better seen on computed tomography (CT), and can have associated complications like an abscess, pleural effusion, or empyema. The opacification of an entire lobe is uncommon nowadays due to early antibiotic treatment, which stops the progress of the infective process. Some cases of lobar pneumonia have typical imaging patterns (Table 6.1) (Fig. 6.3) [2, 3]. However, one should remember that consolidation is not diagnostic of infection and can also be seen in other conditions like pulmonary edema, hemorrhage, organizing pneumonia, vasculitis, and even malignancies.

A unique pattern of lung infection, generally seen in children younger than 12 years of age, is called "round pneumonia" [4]. This pattern of infection is seen in children due to lack of development of interalveolar connections and collateral airways. Typically, occurring as a solitary lesion, these are usually due to bacterial infection, most commonly caused by *Streptococcus pneumonia*. Round pneumonia can be seen on a chest radiograph as rounded nodular opacity with ill-defined margins, commonly involving the superior segments of the lower lobes. Associated air bronchograms are usually confirmatory, thereby preventing delay in diagnosis.

Bronchopneumonia usually results from inhalation and rarely from hematogenous spread of microorganisms and is initially limited in and around the airways. The early airways and peribronchial ground-glass densities spread and become confluent resulting in consolidation (Fig. 6.2). The involvement eventually spread to larger areas, involving the segment or the entire lobe. The most common causes of bronchopneumonia include *Staphylococcus aureus*, *Pseudomonas aeruginosa*, *Haemophilus influenzae*, *Escherichia coli*, some fungi, and anaerobes. The appearance of bronchopneumonia

A. Chawla (ed.), *Thoracic Imaging*, https://doi.org/10.1007/978-981-13-2544-1_6

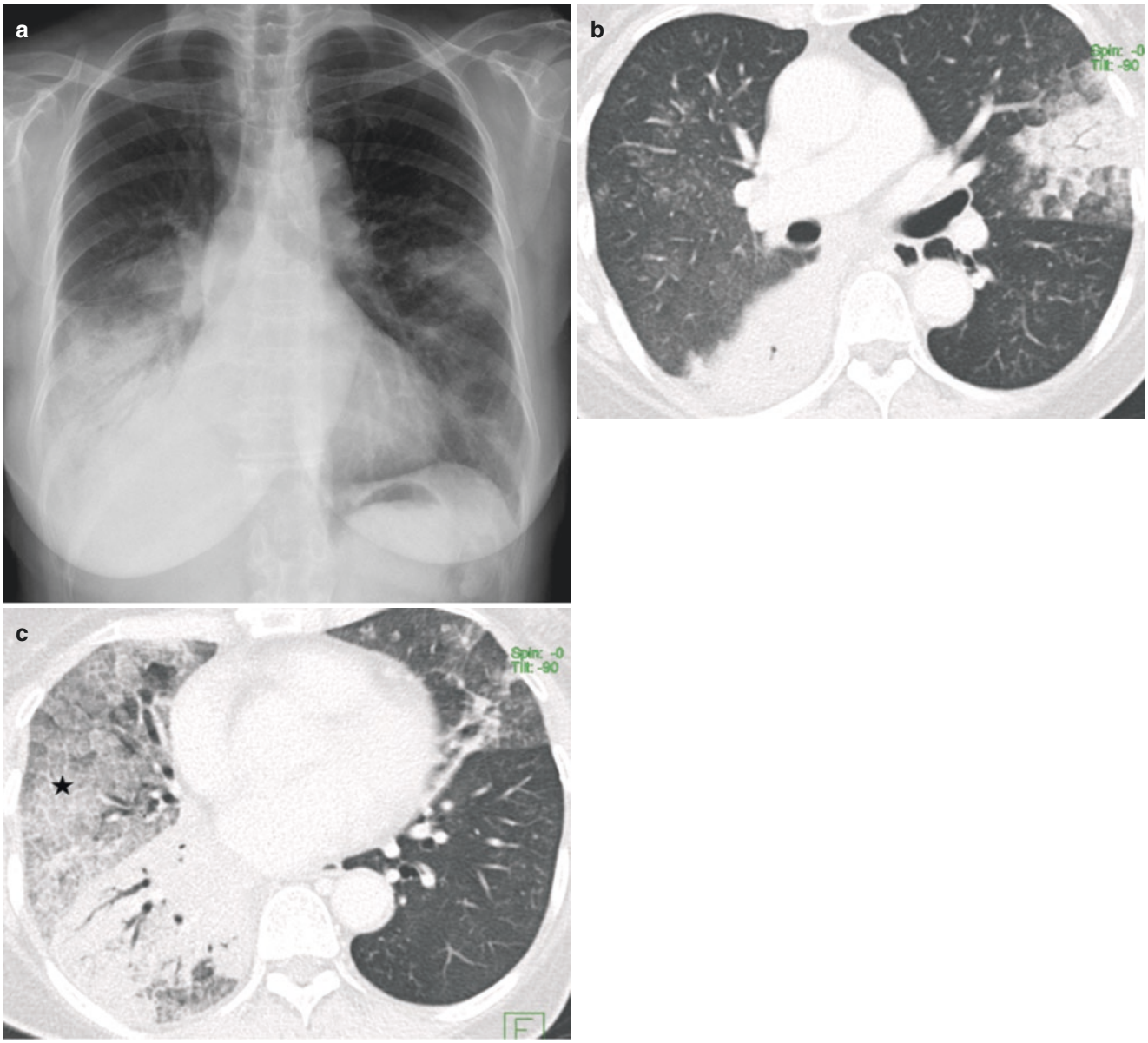

Fig. 6.1 Lobar pneumonia in a patient with Mendelson syndrome. (**a**) Frontal chest radiograph shows areas of consolidation in right mid- and lower zones and left midzone. (**b**, **c**) Axial CT images show consolidation with "air bronchograms" in the left upper lobe and right lower lobe along with "crazy-paving" pattern in the right middle lobe (asterisk)

on radiograph depends upon the stage and may range from multifocal ground-glass opacities to consolidations. The opacities are usually asymmetric in distribution and may predominantly involve the lung bases. The pattern is better appreciated on computed tomography (CT) scans. Usual CT features include focal bronchial wall thickening, centrilobular nodularity, and multifocal opacities around the bronchioles, which can also be associated with tree-in-bud appearance [5]. With the progression of infection, the ground-glass opacities lead to confluent areas of consolidation, and in most of the cases, CT shows scattered foci of the combination of two opacities.

6.2.2 Ground-Glass Opacities

The term "ground-glass opacification" describes lung opacity through which the bronchovascular markings are still visible. This is much better appreciated on CT scans and can be seen in a number of lung pathologies including interstitial

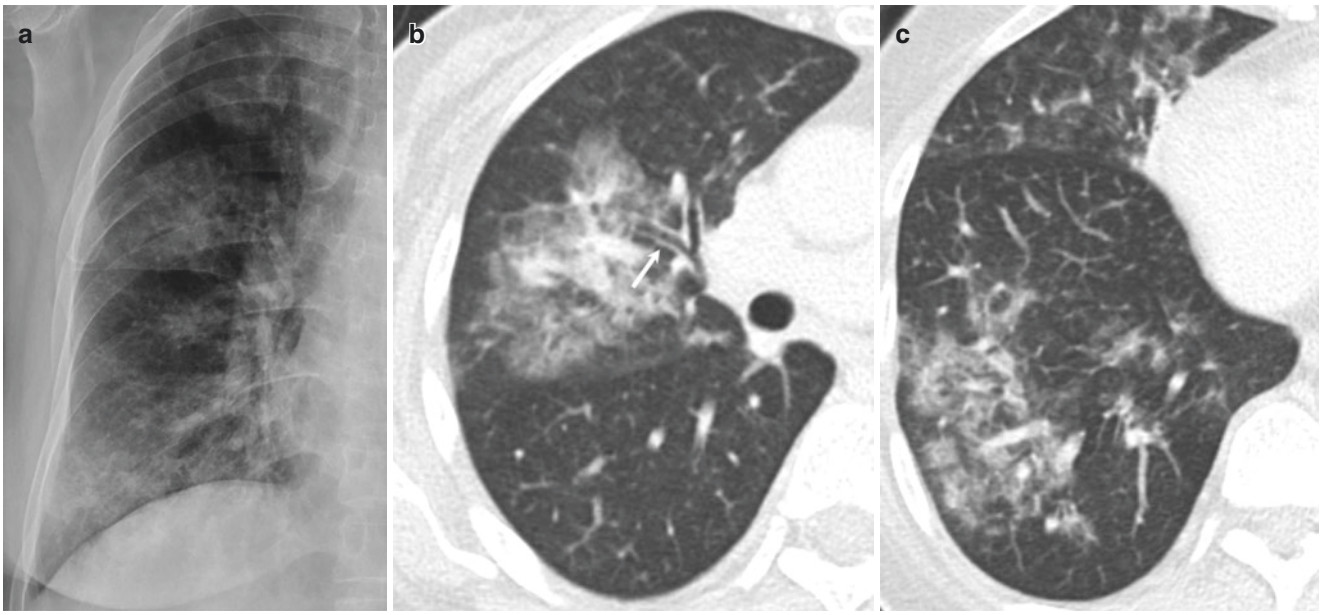

Fig. 6.2 Bronchopneumonia. (**a**) Chest radiograph shows patchy ground-glass opacities in the right lung. (**b**, **c**) Axial CT images show peribronchial ground-glass opacities with bronchial wall thickening (arrow)

Table 6.1 Lobar pneumonia patterns

Cause	Imaging findings
Streptococcus pneumonia	Unilobar with usually no collapse or cavitation, bulging fissures
Klebsiella pneumonia	Multilobar with lobar enlargement and often with areas of cavitation. Bulging fissures may be present
Staphylococcus aureus pneumonia	Consolidation with pleural effusion or even empyema, pneumatoceles, or even bronchopleural fistula. Commoner in children
Pseudomonas aeruginosa pneumonia	Bilateral basal involvement with abscess formation along with associated bronchial wall thickening
Primary tuberculosis	Consolidation with collapse, more common in the right lung particularly anterior segment of the upper lobe

pneumonia [6]. This is due to cellular infiltrate in the alveolar septa and the peribronchovascular interstitium with resultant peribronchial and interlobular septal thickening or due to partial filling of airspaces in the lungs by exudate or transudate [1]. Predominant ground-glass opacification is usually seen in atypical pneumonia caused by *Mycoplasma pneumonia* and viral infections, particularly the opportunistic infections in an immunocompromised host [7]. These include *Pneumocystis jiroveci pneumonia* (PJP), *cytomegalovirus* (CMV) *pneumonia*, and *herpes simplex virus* (HSV) *pneumonia*. There are many other causes for ground-glass opacities, in immunocompromised hosts (Table 6.2).

6.2.3 Nodules

Lung nodules are less than 3 cm, round to oval opacities that appear well-defined when surrounded by the normally aerated lung. They have a wide range of differentials ranging from infections, occupational lung diseases, malignancies, and immunological disorders. Solitary nodules can be seen in infections like tuberculosis, histoplasmosis, and hydatid disease. Multiple lung nodules can have centrilobular, perilymphatic (around fissures, peribronchovascular and subpleural), or random distribution [8]. These are discussed in the chapter of imaging of nodular lung diseases.

Nodules may demonstrate secondary changes like calcification and cavitation or can have surrounding ground-glass opacities. Cavitation is frequently seen in nosocomial infections and in immunocompromised hosts [9]. Some common causes of infective nodules include tuberculosis, nocardiosis, angioinvasive aspergillosis, cryptococcal infection, and atypical mycobacterial infection [1]. Miliary pattern, i.e., diffuse nodules less than 3 mm, can be seen in a number of infections. Septic pulmonary embolism should always be considered in cases of cavitary pulmonary nodules (Fig. 6.4). This condition results from embolization of infectious particles in the lungs, which block the peripheral pulmonary artery divisions, resulting in infarction and necrosis of the lung parenchyma. Common sources of septic emboli include infectious tricuspid endocarditis (especially in intravenous drug abusers), peripheral thrombophlebitis, infected central line, and cardiac pacemaker [10]. Although not a reliable

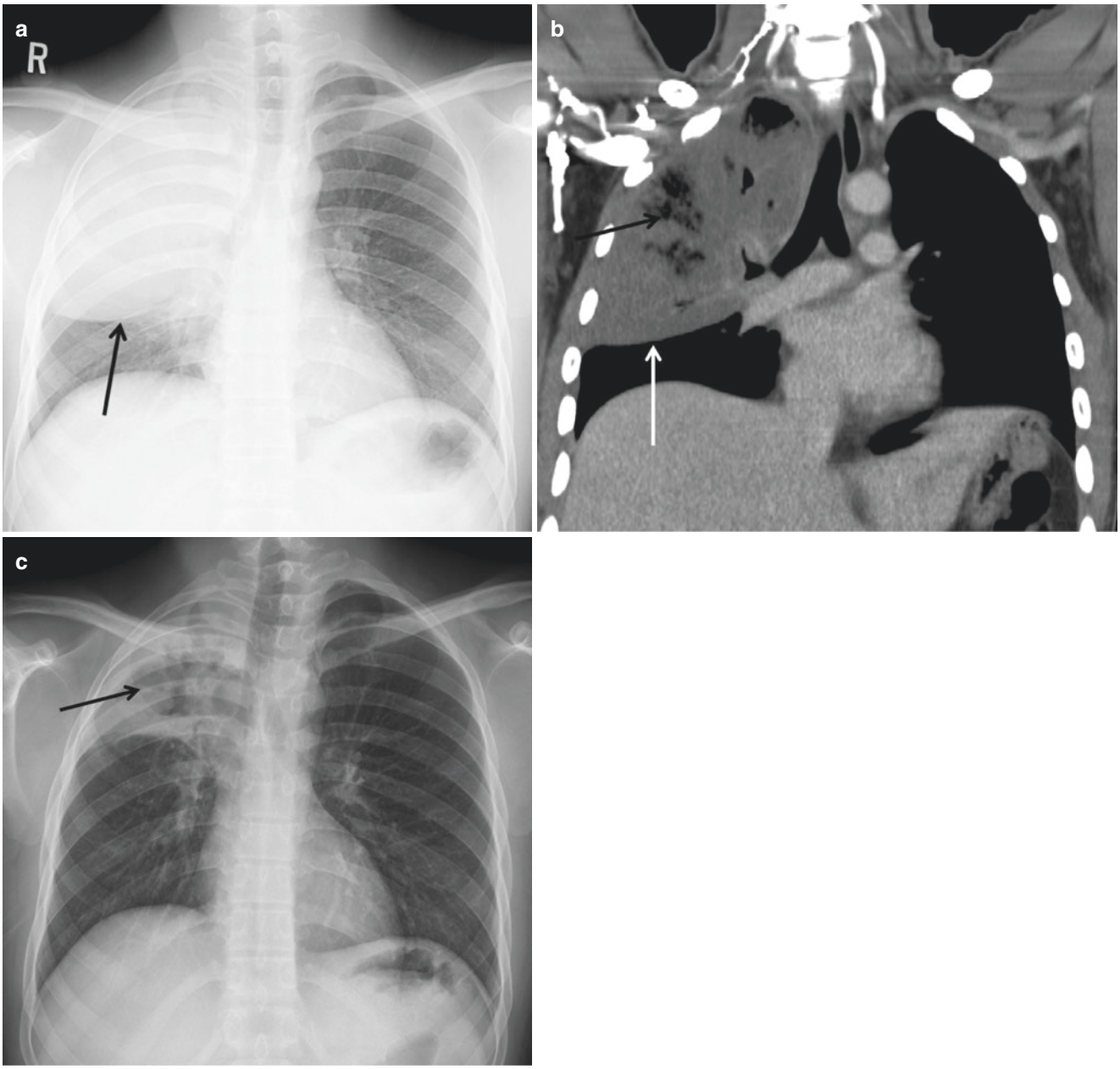

Fig. 6.3 *Klebsiella* pneumonia in a 35-year-old man, presenting with high-grade fever, rigors, cough, and high total white blood cell count. (**a**) Frontal chest radiograph shows a large homogeneous dense opacity in the right upper hemithorax with sagging inferior border (black arrow). (**b**) Corresponding coronal CT image demonstrates necrotizing consolidation (black arrow) in the right upper lobe with "bulging fissure" (white arrow). (**c**) Follow-up radiograph after treatment shows residual scarring in the right upper lung (black arrow). "Bulging fissure" is a characteristic but not specific sign of *Klebsiella* pneumonia

sign, feeding vessels leading to the cavitary nodule can be demonstrated on CT images [11]. Ground-glass changes surrounding lung nodules can also be due to surrounding hemorrhage and have been described in viral infections, atypical mycobacterial infection, and candida infection [12, 13, 14]. Nodules with surrounding ground-glass changes and subpleural wedge-shaped opacities are highly suggestive of angioinvasive aspergillosis, in a context of severe neutropenia.

6.2.4 Cavities

Lung cavities are thick-walled, gas-filled areas within the lung usually in a mass, area of consolidation, or even within a nodule. Bacterial infections can result in cavities as a complication of pneumonia, also termed as cavitating pneumonia. Lung abscess is a lesion within the lung with a collection of pus, usually seen in elderly, malnourished, or immunocompromised patients. Chest radiograph usually shows lung

Table 6.2 Infectious causes of ground-glass opacities in an immunocompromised host

Cause	CT findings
PJP (AIDS)	Ground-glass opacities in midzones and perihilar distribution, peripheral sparing, may be associated with reticular opacities, nodules, pneumatoceles, or even consolidation
HSV pneumonia (immunocompromised and mechanically ventilated patients)	Ground-glass opacities with mild bronchial dilatation and areas of consolidation
CMV pneumonia (especially following stem cell or solid organ transplant, AIDS)	Ground-glass opacities with lobar consolidation, miliary nodules, often with surrounding halo, irregular reticular opacities

opacity with or without an air-fluid level. CT with intravenous contrast is diagnostic, with a demonstration of thick-walled, rim-enhancing lesion, containing air-fluid level, within an area of consolidation (Fig. 6.5). Larger abscesses seldom respond to antibiotic treatment, usually need percutaneous or surgical drainage, and despite that have higher associated mortality rates.

6.2.5 Pneumatoceles

Pneumatoceles are air-filled cystic spaces within the lung sequel to pneumonia, trauma, or aspiration and are almost always asymptomatic. Pneumatoceles can be confused with abscesses; important differentiating features include smooth

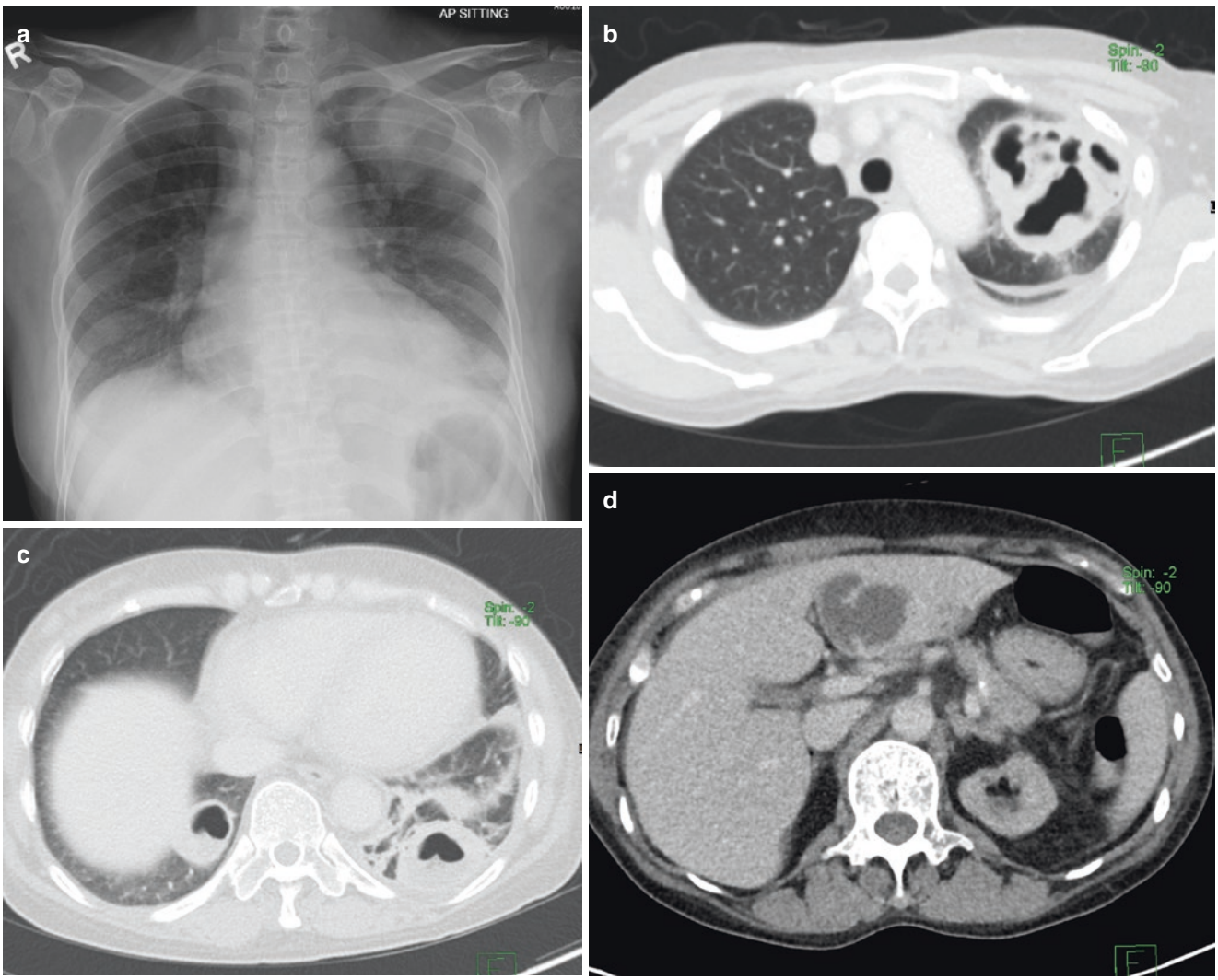

Fig. 6.4 Septic pulmonary emboli in an elderly female patient. (**a**) Frontal chest radiograph shows mass-like left upper zone opacity with left lower zone consolidation and effusion. (**b**, **c**) Axial CT lung window images show cavitary nodules and masses. (**d**, **e**) Axial and sagittal CT images of the liver show a left lobe liver abscess with thrombophlebitis of the hepatic vein branch (white arrow)

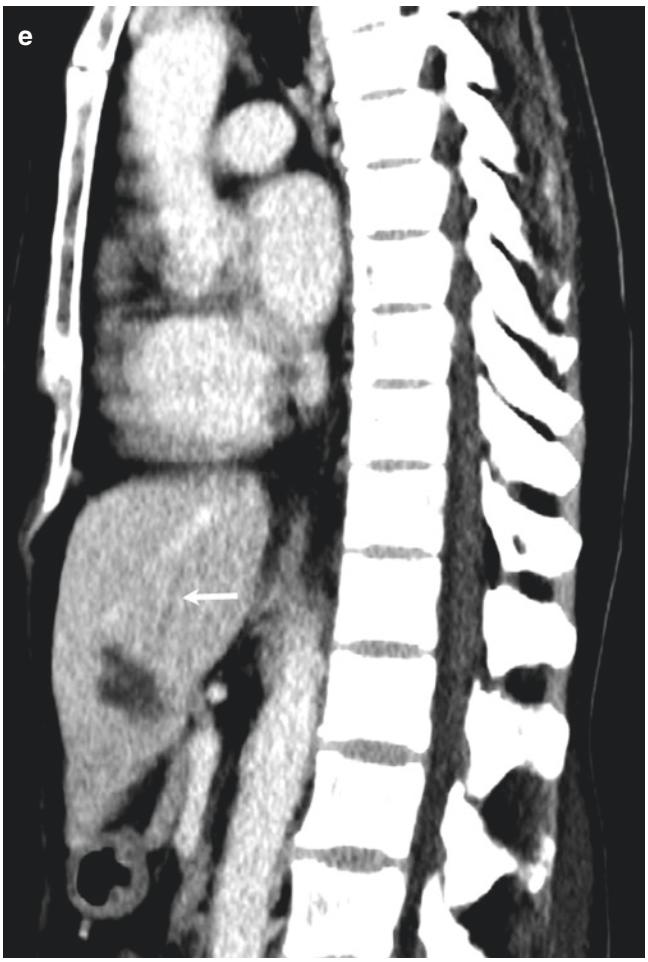

Fig. 6.4 (continued)

inner margins, thin wall, minimal fluid content, and usually asymptomatic course.

6.3 Associated Findings

Pulmonary infections are frequently associated with a number of ancillary findings like pleural effusion, pleural thickening, empyema, mediastinal lymphadenopathy, or even bone destruction. Simple parapneumonic effusions without associated pleural thickening usually respond to medical treatment; however loculated effusions and empyema typically need percutaneous drainage. Lung infections can present with enlargement of the hilar and the mediastinal nodes. Contrast-enhanced CT can not only identify enlarged nodes but can also characterize internal appearance and guide biopsy.

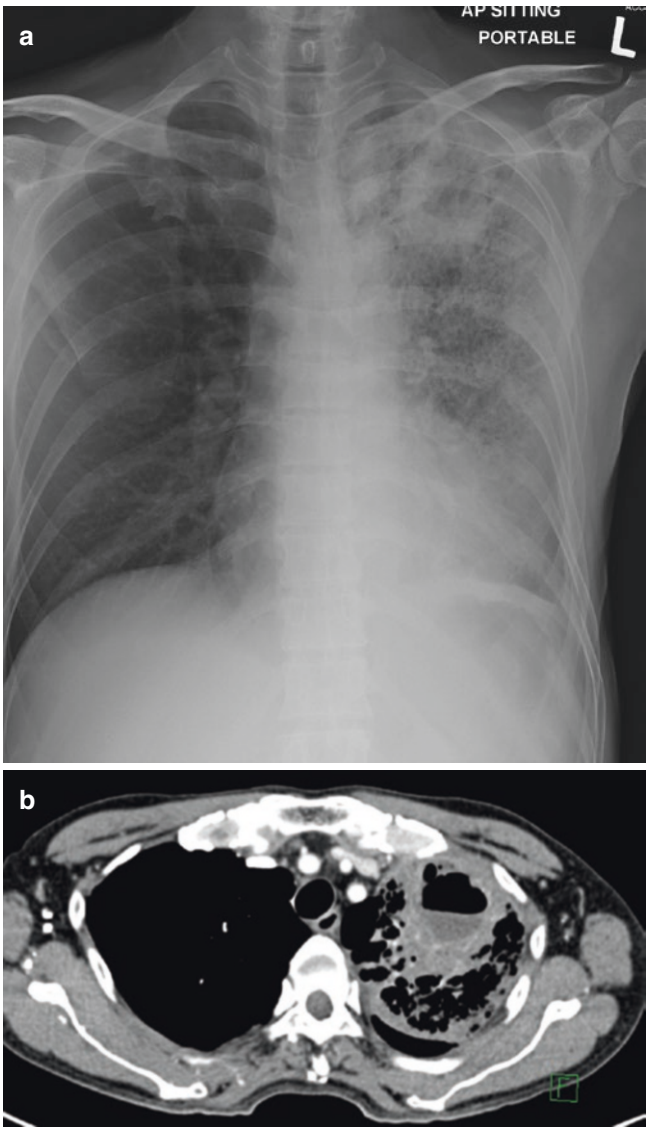

Fig. 6.5 Lung abscess in an elderly patient. (**a**) Frontal chest radiograph shows extensive left lung opacities with an air-fluid level in lesion. (**b**) Axial CT image demonstrates the thick-walled abscess with surrounding lung changes

6.4 Infections

6.4.1 Tuberculous

Tuberculosis is a granulomatous infection caused by *Mycobacterium tuberculosis*, a rod-shaped aerobic bacterium. It is a global health problem, common in developing Southeast Asian and African countries. Historically, pulmonary tuberculosis is classified into two subtypes: primary and

post-primary tuberculosis. Primary tuberculosis patients have no previous exposure and, usually, develop active disease within 2 years of infection. Post-primary tuberculosis is also known as reactivated tuberculosis, seen in patients who have had a previous infection. It is more commonly endogenous reactivation rather than due to superinfection (exogenous). Clinical presentation of tuberculosis varies with age and the immune status of the patient, with a cough, low-grade fever, anorexia, and loss of weight being the usual presenting complaints. There are no well-established criteria on imaging for the two subtypes of pulmonary tuberculosis. The role of imaging is to assess the disease burden, the presence of cavities, and complications of tuberculosis (Figs. 6.6, 6.7, 6.8, and 6.9).

6.4.1.1 Primary Tuberculosis

Primary tuberculosis occurs most commonly in children but is being seen with increasing frequency in adults. There are three main components of primary tuberculosis: parenchymal focus, lymphadenopathy, and pleural effusion (Table 6.3). The parenchymal focus is typically unilateral airspace consolidation due to bronchoalveolar caseous exudate. The parenchymal focus called "Ghon focus" usually resolves without any sequel on chest radiograph or less commonly heals by calcification or calcified granuloma [15, 16]. In a small number of cases, the infection progresses with enlargement of the parenchymal lesion and spread of infection along the lymphatics in the mediastinal lymph nodes. Majority of the cases of childhood primary tuberculosis in the endemic zones have dominant lymphadenopathy, a finding less commonly seen in adults. "Ranke complex" is suggestive of previous tuberculous infection and compromises of Ghon focus with calcification in the hilar node. Pleural involvement is seen in few cases, usually the same side as the parenchymal disease [17]. Historically, the cavities are considered as a hallmark of post-primary tuberculosis but are increasingly recognized in adults with primary tuberculosis.

6.4.1.2 Post-Primary or Reactivation Tuberculosis

Post-primary tuberculosis usually involves the apical and posterior segments of the upper lobe and the superior segment of the lower lobe, explained by relatively poor lymphatic drainage and higher oxygen tension [18] (Table 6.4). Most cases involve more than one segment, in many cases even showing bilateral disease. Cavitation may be present in almost up to 50% of cases of post-primary tuberculosis. The endobronchial spread of the disease occurs when the caseous necrosis liquefaction communicates with the bronchial tree, resulting in nodular lesions distant to the cavity. This results in classical "tree-in-bud" opacities on CT scan, compromising of tiny centrilobular nodules, and branching linear opacities [19]. Tuberculoma can be solitary or multiple, round, oval, or elongated nodules and appear hyperdense or demonstrate frank areas of peripheral calcification. Pleural disease and chest wall involvement are less common and seen only in a minority of the cases.

Lung cavities and bronchiectasis are late complications of pulmonary tuberculosis, usually seen in the apical and posterior segments of the upper lobes. A characteristic CT feature of the tubercular cavity is its communication with the tracheobronchial tree. Secondary colonization of a tuberculous cavity by *Aspergillus* can result in the formation of a fungal ball. CT imaging demonstrates air surrounding an intracavitary mass, also known as the "air crescent sign" [20]. Tuberculosis can also extend into the trachea and the bronchial tree, leading to scarring and bronchostenosis [21]. The infection can spread from the pleural space to the soft tissues of the chest wall, resulting in chest wall abscess also known as "empyema necessitans" [22]. Rasmussen aneurysm is a pseudoaneurysm that arises within or adjacent to a tuberculous cavity. It is a rare complication and results due to the weakening of the inflamed wall of a pulmonary artery branch (Fig. 6.10).

6.4.1.3 Miliary Tuberculosis

Miliary tuberculosis can be seen in both primary and post-primary tuberculosis and is due to hematogenous dissemination of the infection. Chest radiographs can be unremarkable until advanced disease, where it can show small nodules extensively involving the lung fields. CT is diagnostic with 1–3 mm nodules with or without associated interlobular septal thickening, identifiable on high-resolution computed tomography (HRCT) (Fig. 6.11).

6.4.2 Nontuberculous Mycobacterial Infection

Nontuberculous mycobacteria (NTM) infections were confirmed to be true human pathogens only by 1950 and were later shown to be very similar to post-primary tuberculosis by Christensen et al., in the 1970s [23]. The organisms causing most of the NTM infections include *M. avium-intracellulare* (MAC) (approx. 60%) and *M. kansasii* (about 25%) with other less common organisms being *M. xenopi*, *M. szulgai*, *M. fortuitum*, *M. abscessus*, and *M. gordonae* [23, 24]. "Lady Windermere" syndrome is a typical pattern

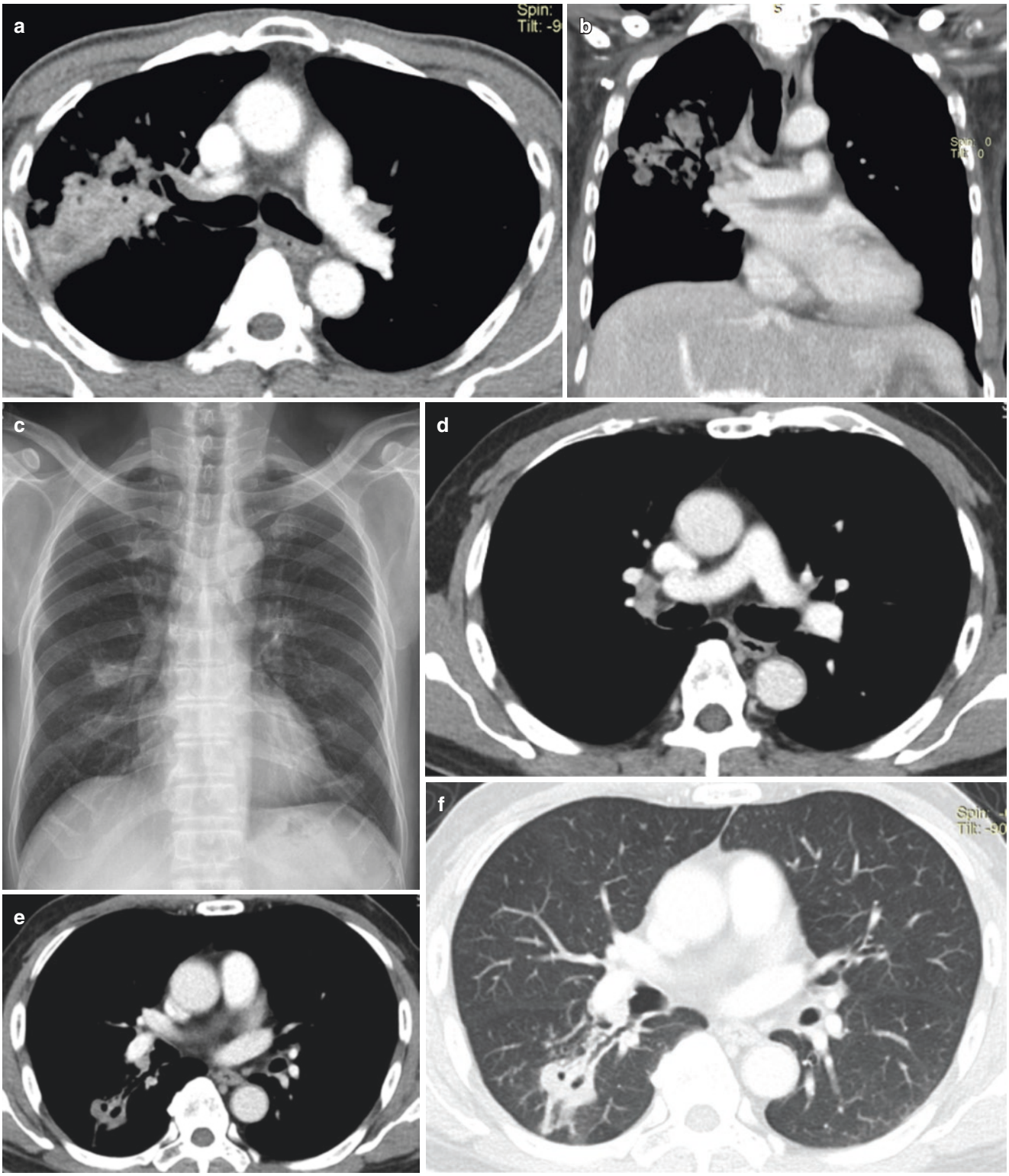

Fig. 6.6 Primary tuberculosis in an adult. (**a**, **b**) Axial and coronal CT images show heterogeneous consolidation in the right upper lobe with hilar lymph nodes. Post-primary tuberculosis in another patient. (**c**) Frontal chest radiograph shows a cavitary nodule in the right midzone. (**d**–**f**) Axial CT images show a thick-walled cavitary nodule in the superior segment of the right lower lobe communicating with the airway and right hilar node

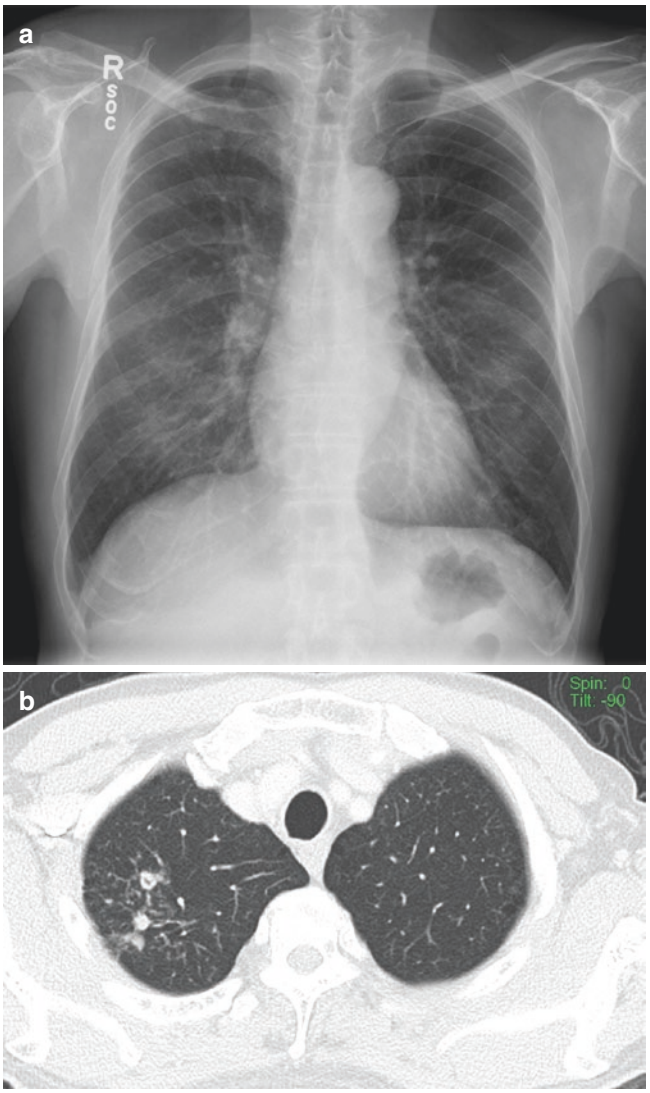

Fig. 6.7 A 30-year-old asymptomatic man for a pre-employment checkup. (**a**) Frontal chest radiograph shows small nodules in the right upper zone. (**b**) Axial CT image shows granulomas with tree-in-bud opacities in the right upper lobe. These were presumed to be sequel to primary tuberculosis

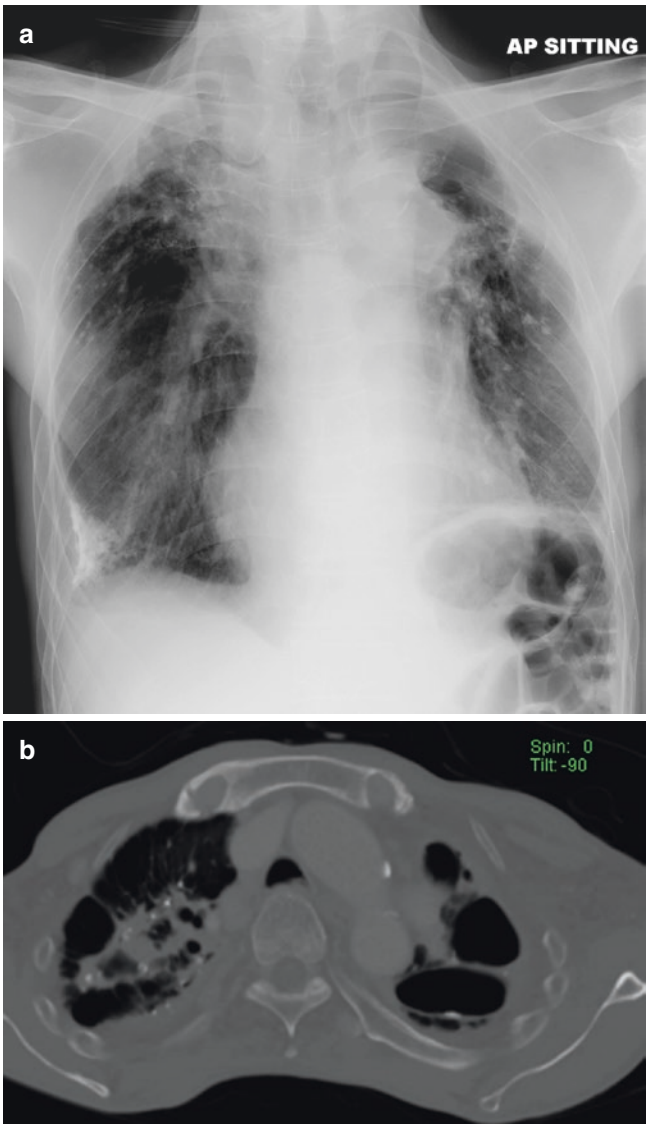

Fig. 6.8 Features of old tuberculosis. (**a**) Frontal chest radiograph shows extensive bilateral scarring, calcified nodules, volume loss, and pleural calcification (from previous empyema). (**b**) Axial CT image in the bone window shows calcified lung nodules, surrounding patchy consolidation and destruction of the left upper lobe lung parenchyma with cavity formation

of MAC infection in an elderly woman characterized by bronchiectasis, tree-in-bud opacities, centrilobular nodules, and eventual chronic atelectasis of the right middle lobe and lingula. The CT features of NTM are described in Table 6.5 (Figs. 6.12 and 6.13). Diagnosis of these infections is difficult as these organisms often colonize the airways and a positive culture is not diagnostic of an infection. Invasive measures like bronchoalveolar lavage and transbronchial biopsy are often needed for confirming the diagnosis.

There can be a disseminated pattern of nontuberculous mycobacterial infection in patients who are immunocompromised [25]. MAC is the most common organism for atypical mycobacterial infection in AIDS (acquired immune deficiency syndrome). These infections usually occur with low CD4 counts of below 100 cells/mm^3. The diagnosis is difficult on imaging as these infections coexist with a number of other opportunistic lung infections. The most common imaging feature is mediastinal lymphadenopathy, followed by airspace opacities, miliary lung nodules, and pleural effusion [26]. Nontuberculous mycobacterial infections can also be

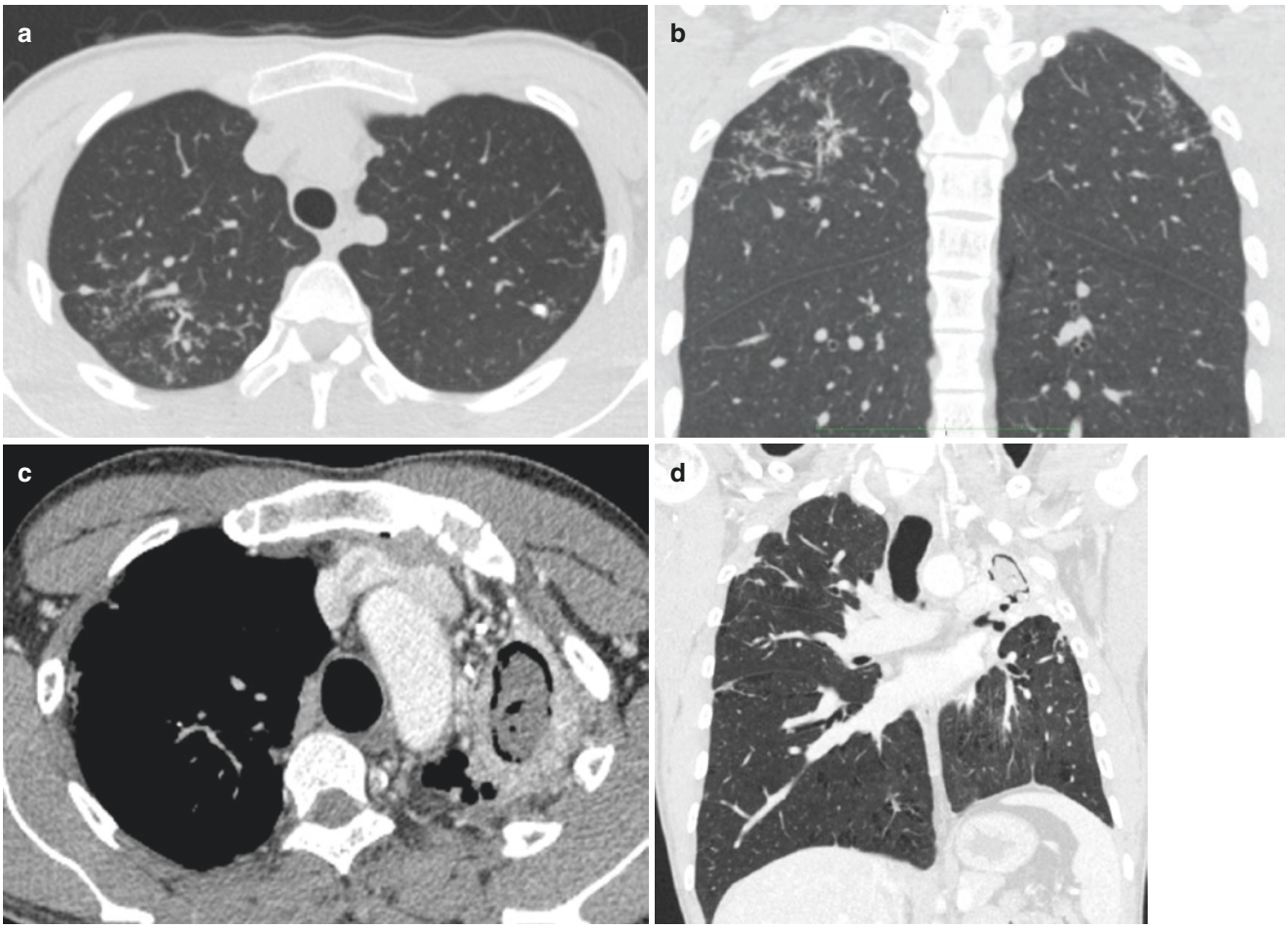

Fig. 6.9 Tree-in-bud opacities in a sputum-positive case of tuberculosis. (**a**, **b**) Axial and coronal CT images show tree-in-bud opacities in upper lobes. Fungal ball in another patient presenting with hemoptysis. (**c**, **d**) Axial and coronal CT images show a tubercular cavity with a soft-tissue mass surrounded by an air crescent. Note the increased vascularity around the cavity

Table 6.3 Imaging features of primary tuberculosis

Chest radiograph	CT findings
Dense airspace consolidation mainly middle and lower lobes	Homogeneous, dense consolidation, sometimes linear, nodular, patchy, or even like a mass Mass rarely show cavitation
Bulky hilum	Enlarged hilar and mediastinal nodes, showing central necrosis and peripheral rim enhancement
Pleural effusion with or without parenchymal disease	Pleural effusion with or without septa/nodularity, pleural thickening, air-fluid level (post-drainage or bronchopleural fistula)

Table 6.4 Imaging features of post-primary tuberculosis

Chest radiograph	CT findings
• Patchy airspace opacities, often in multiple areas, even bilateral in some cases	• Centrilobular nodules, mucoid impaction of branching contiguous bronchioles "tree-in-bud" pattern
• Cavity formation	• Area of cavitation, thick and irregular walls, sometimes small fluid level
• Hilar lymphadenopathy	• Thick wall cavity classically communicating with the bronchial tree
	• Round to oval nodule (tuberculoma) surrounded by satellite smaller nodules that may have calcification

seen in non-HIV immunocompromised cases, like patients on chemotherapy, post-organ transplantation, and long-term steroids and patients with lymphoma or leukemia [27, 28]. Radiographic findings are limited to reticulonodular opacities, cavities, and lymphadenopathy. There are reported cases of hypersensitivity pneumonitis caused by inhalation of MAC, most commonly from hot tub exposure [29].

6.4.3 Fungal Infections

Fungal lung infections can be seen in both immunocompromised and immunocompetent hosts. Infections in immunocompromised patients range from *Aspergillus*, cryptococci,

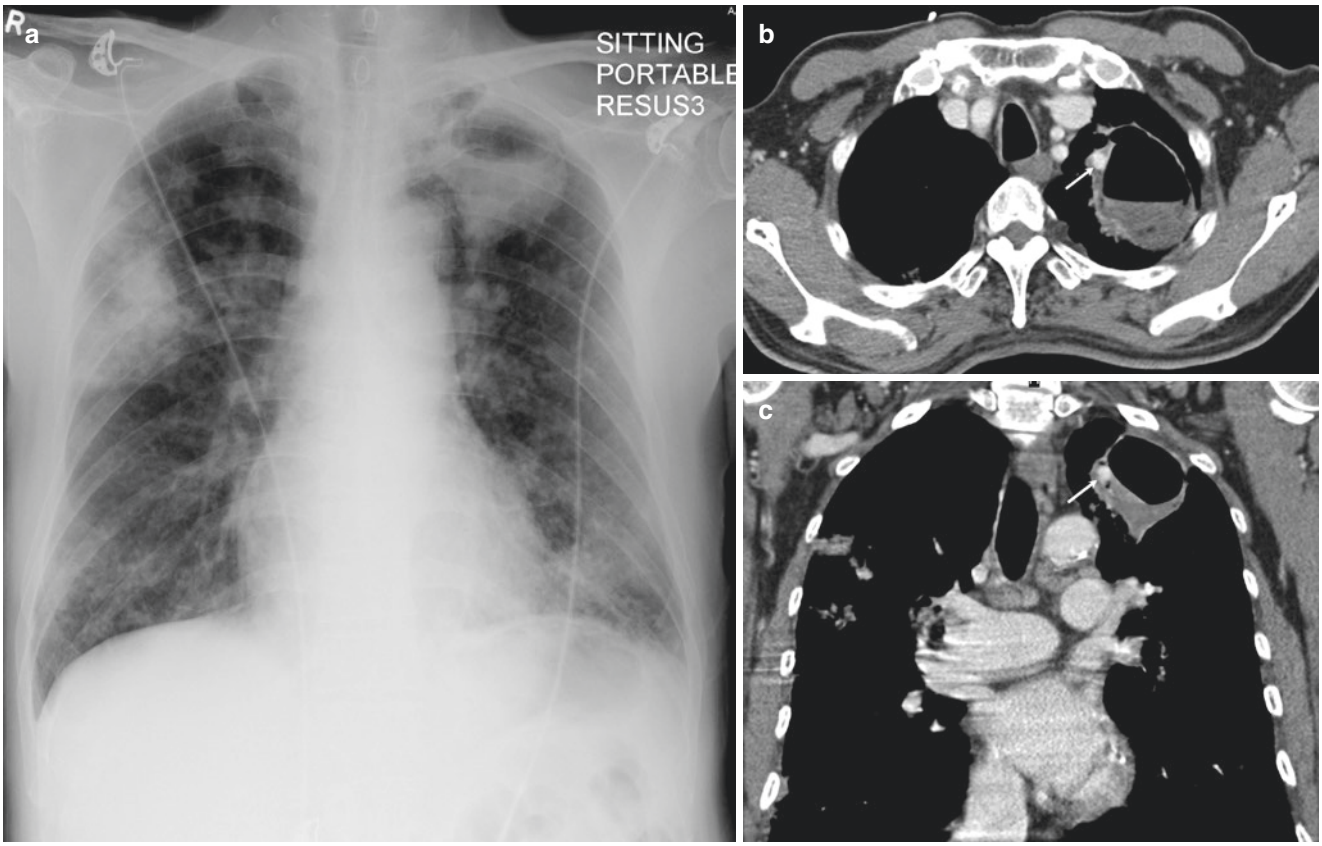

Fig. 6.10 Rasmussen aneurysm in an elderly patient with tuberculosis. (**a**) Frontal chest radiograph shows left upper zone opacity with an air-fluid level and areas of consolidation in both lungs. (**b**, **c**) Axial and coronal CT images show an enhancing aneurysm (white arrows) along the medial aspect of the cavity

Pneumocystis jiroveci, *Candida*, and mucormycosis, while those in the immunocompetent include histoplasmosis, coccidioidomycosis, blastomycosis, and *Paracoccidioides brasiliensis* [30]. Infection typically occurs due to inhalation of the fungal spores, conidia, or reactivation of a latent infection. The incidence of fungal infections is increasing due to increased numbers of immunocompromised and susceptible patients (hematological and stem cell transplant procedures, solid organ transplant, critical care setup). Diagnosing these infections is challenging and imaging can aid in early diagnosis.

6.4.3.1 Cryptococcosis

Cryptococcus neoformans, the causative organism for cryptococcosis, is found in soil with avian or pigeon droppings [31]. The infection can occur in both immunocompetent and immunocompromised hosts; the incidence is much more in the latter [32]. Pulmonary cryptococcosis in immunocompetent hosts is usually asymptomatic. Disseminated disease is not uncommon in AIDS, with the involvement of the central nervous system, bones, and skin. Imaging features of pulmonary cryptococcosis are described in Table. 6.6.

6.4.3.2 Candidiasis

Candidiasis is most commonly caused by *Candida albicans*, and lung infection is usually seen in immunocompromised patients, usually associated with widespread disease involving multiple organs. The imaging features of pulmonary candida infection are described in Table 6.7.

6.4.3.3 Coccidioidomycosis

This infection is caused by the dimorphic fungus *Coccidioides immitis* and is endemic in parts of southwestern America and Mexico. Chest radiographs in the acute stage are usually unremarkable, sometimes showing areas of consolidation and bulky hilum (node enlargement). Solitary or multiple nodules with cavities can be seen in the chronic stage of the infection, better assessed on CT scans, the nodules more commonly involving the lung bases [33] (Fig. 6.14). Cavities can be with thin ("grape-skin") or thick walls [34]. Disseminated disease in immunocompromised hosts usually shows diffuse reticulonodular or miliary pattern.

6.4.3.4 Blastomycosis

Pulmonary blastomycosis is caused by *Blastomyces dermatitidis*, usually seen as necrotizing granulomas, especially

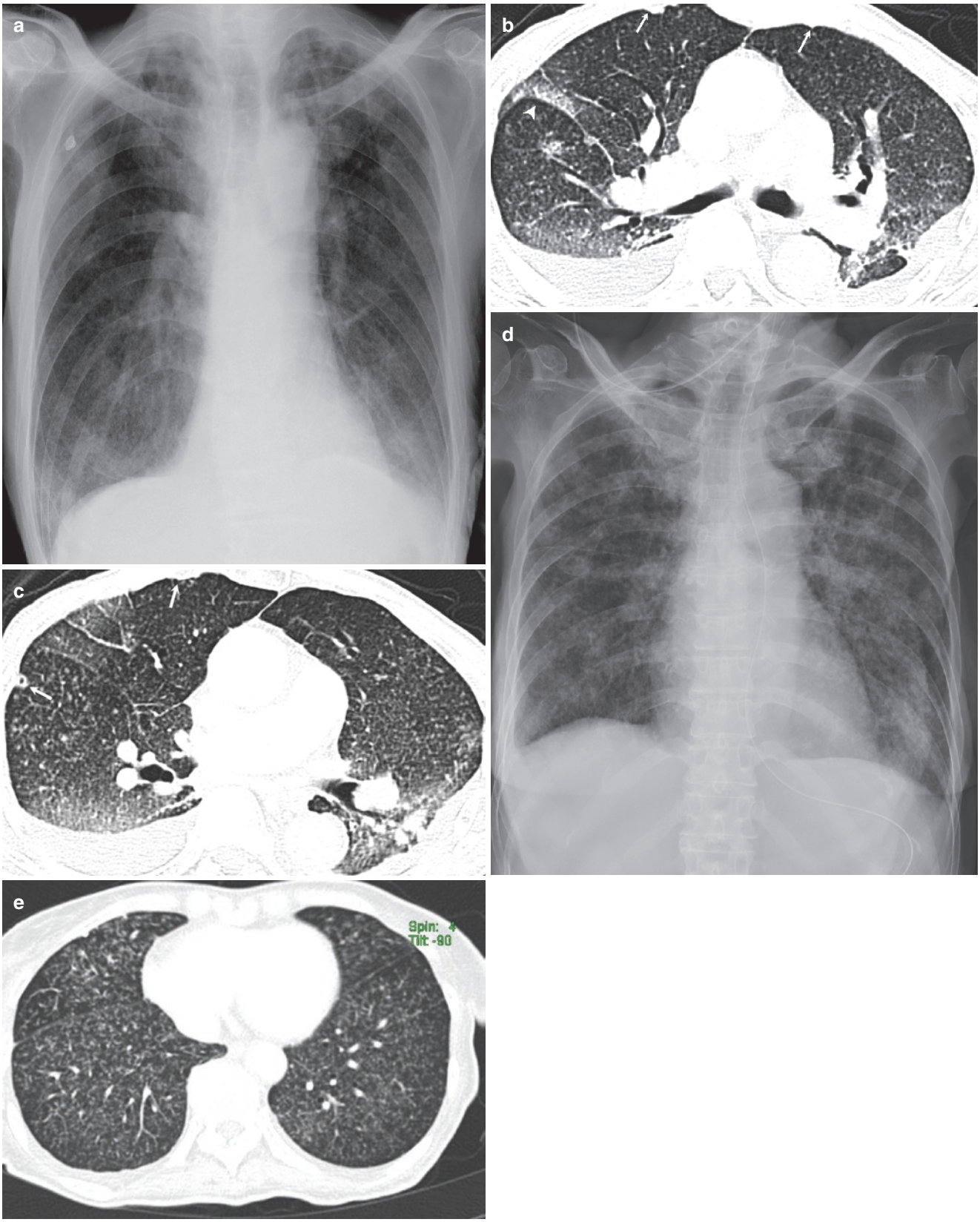

Fig. 6.11 Miliary tuberculosis. (**a**) Frontal chest radiograph shows numerous small nodules in both lungs. (**b**, **c**) Axial CT images in lung window show extensive randomly scattered miliary nodules including subpleural (white arrows) and fissural nodules (arrowhead). Another case of extensive endobronchial spread of tuberculosis with (**d**) frontal chest radiograph showing numerous small nodules in both lungs and (**e**) axial CT image in lung window showing innumerable tiny centrilobular nodules with subpleural and fissural sparing

suppurative type [30]. Imaging findings include patchy or confluent airspace consolidation, which may show associated cavitation. The other imaging feature is nodules or masses (Fig. 6.15). Disseminated infection results in a miliary pattern of involvement.

Table 6.5 Nontuberculous mycobacterial infection patterns

	Cavitary or classic form	Bronchiectatic form
Pattern	Similar to post-primary tuberculosis	Coexistence of mosaic pattern and bronchiectasis is highly suggestive
Organisms	Usually MAC	MAC or *M. kansasii*
Radiograph	Cavitary lesion with the endobronchial spread, atelectasis, pleural thickening	Randomly distributed nodular opacities
CT	Single cavity with ill-defined margins, bronchiectasis, pleural thickening	"Tree-in-bud" opacities, cylindrical bronchiectasis
Demographics	Elderly white patients with underlying chronic lung disease	Elderly white patients
Predominant involvement	Upper lobes	Right middle lobe and lingula Lower lobes are also involved

6.4.3.5 Aspergillosis

Aspergillosis is usually caused by *Aspergillus fumigatus*, a fungus of the *Aspergillus* species. The lung infection is only seen when there is hypersensitivity or in patients with reduced immunity. Pulmonary aspergillosis is a term collectively used for a number of recognized forms of lung disease (Table 6.8), each having distinct clinical and imaging features (Figs. 6.16, 6.17, 6.18, and 6.19). Aspergilloma and allergic bronchopulmonary aspergillosis (ABPA) are the noninvasive forms of the disease. Chronic necrotizing aspergillosis (CNA) is the locally invasive form, seen in immunocompromised patients and those with the chronic pulmonary disease. Invasive aspergillosis is a grave disease, affecting immunocompromised and critically ill patients or those with chronic obstructive pulmonary disease [35].

Aspergilloma is also known as "fungal ball" and is most commonly seen in a tuberculous cavity (Fig. 6.16). It can also be seen in other cavity-forming conditions or less commonly in cystic bronchiectasis [2]. ABPA is a type of eosinophilic lung disease, usually seen in patients with long-standing asthma, cystic fibrosis, or Kartagener's syndrome. The disease has various clinical stages from acute stage to end-stage fibrosis, patients usually presenting with asthma-like presentation with a recurrent lung infection. Imaging features are included in the major diagnostic criteria of ABPA. Invasive aspergillosis is the commonest fungal infection involving the lungs [30], typically seen in

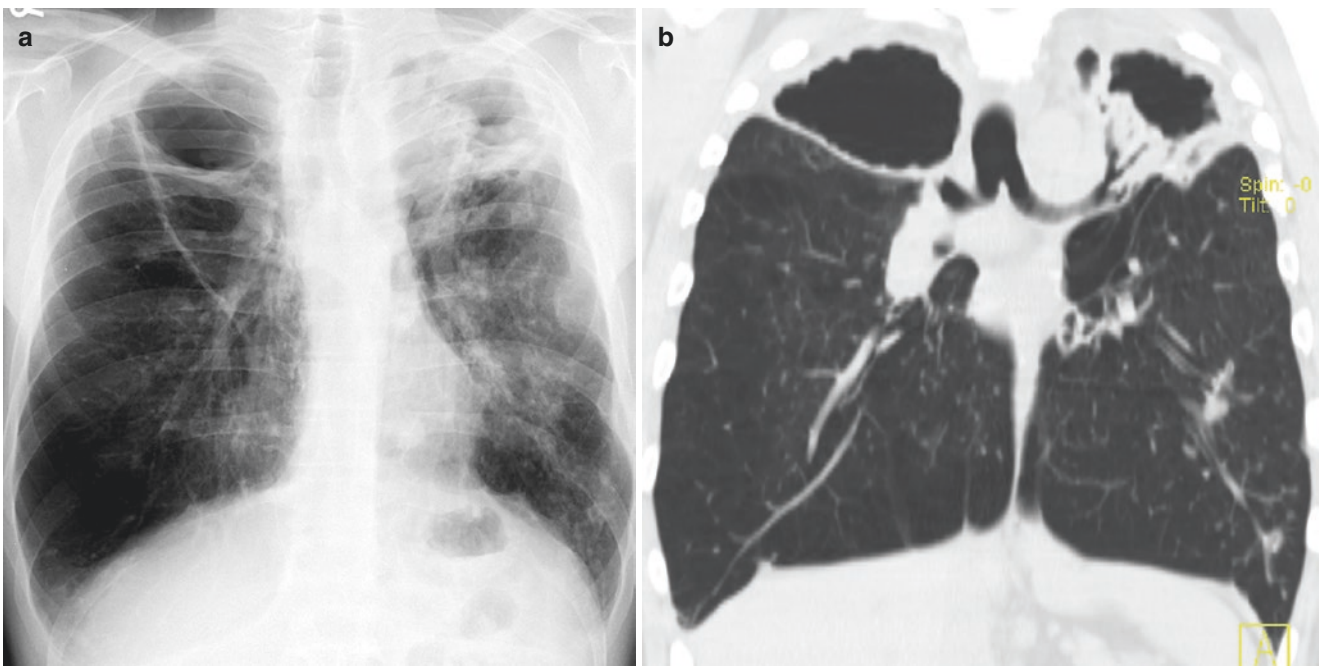

Fig. 6.12 Cavitary form of atypical mycobacterial infection in an elderly patient. (**a**) Frontal chest radiograph shows upper zone cavitary changes with background scarring and patchy opacities, more on the left side. (**b**) Coronal CT image in lung window demonstrates bilateral upper lobe cavitary lesions with scarring and atelectasis in the left lung

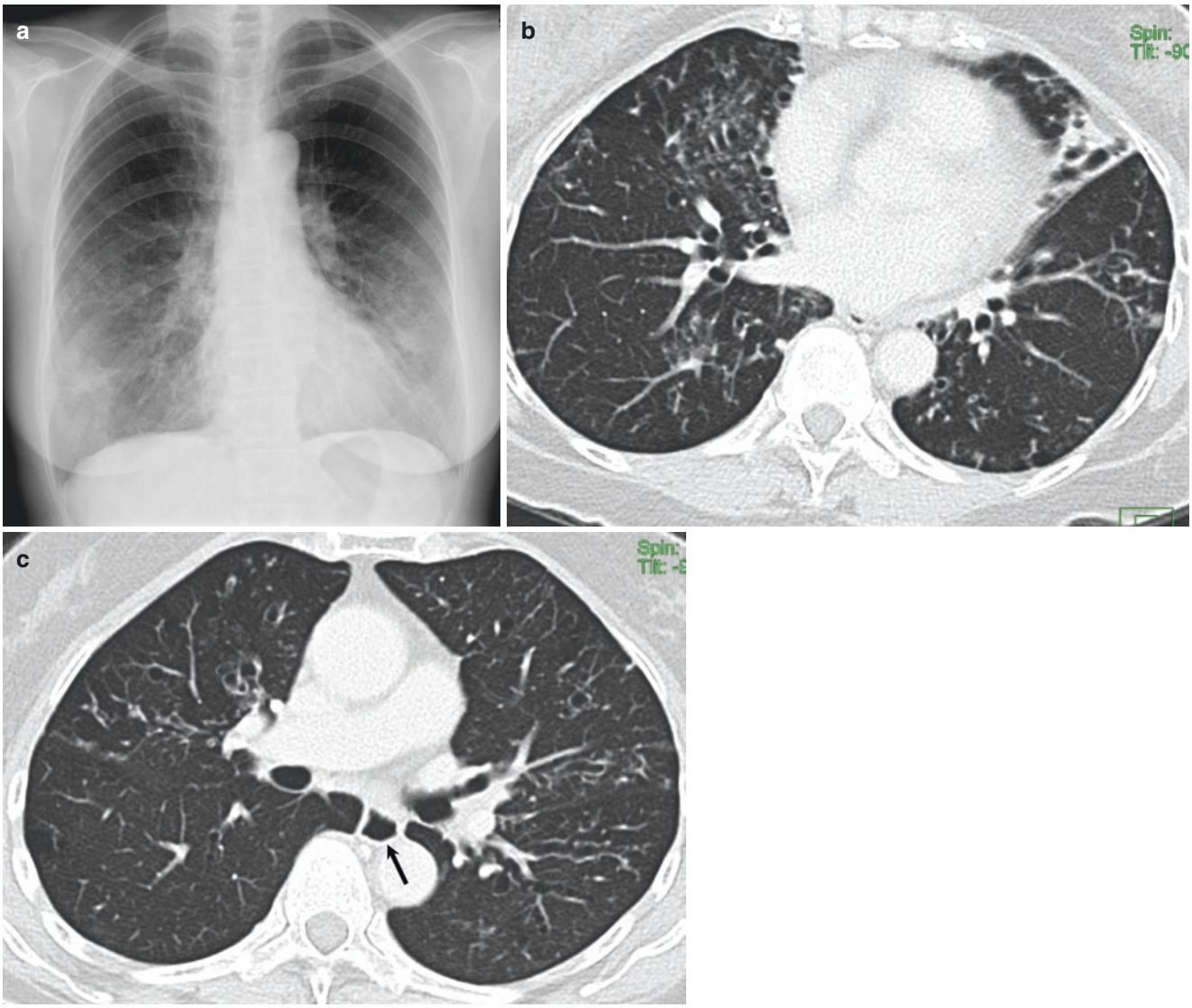

Fig. 6.13 Bronchiectatic form of atypical mycobacterial infection. (**a**) Frontal chest radiograph shows ill-defined opacities in the mid- and lower zones. (**b**, **c**) Axial CT images show bronchiectasis and centrilobular nodules, predominantly in the right middle lobe and lingula. There is dilatation of the esophagus (black arrow) commonly seen in these patients

Table 6.6 Imaging features of pulmonary cryptococcosis

Immunocompetent	Immunocompromised
• Small multiple nodules (upper and midzone predominance), patchy consolidation	• Nodules (may have cavitation in some cases), consolidation, enlarged hilar and mediastinal nodes (predominant finding in AIDS), pleural effusion

Table 6.7 Imaging features of pulmonary candida infection

Chest radiograph	CT
• Patchy airspace opacities and/or nodules	• Ground-glass opacities, nodules, patchy areas of consolidation

immunocompromised patients with neutropenia. Angioinvasive aspergillosis is seen in severely immunocompromised patients (graft-versus-host disease following bone marrow transplant, late stages of AIDS, long-term corticosteroids, prolonged severe neutropenia). Clinical features are not reliable and early imaging is the key to identifying the pulmonary lesions. The diagnosis is confirmed only by histopathology evaluation. Mortality rates due to invasive aspergillosis can be as high as up to 70% [30]. Chronic aspergillosis is seen in patients with background chronic lung disease or diabetes and can present in cavitary or fibrosing forms [36, 37].

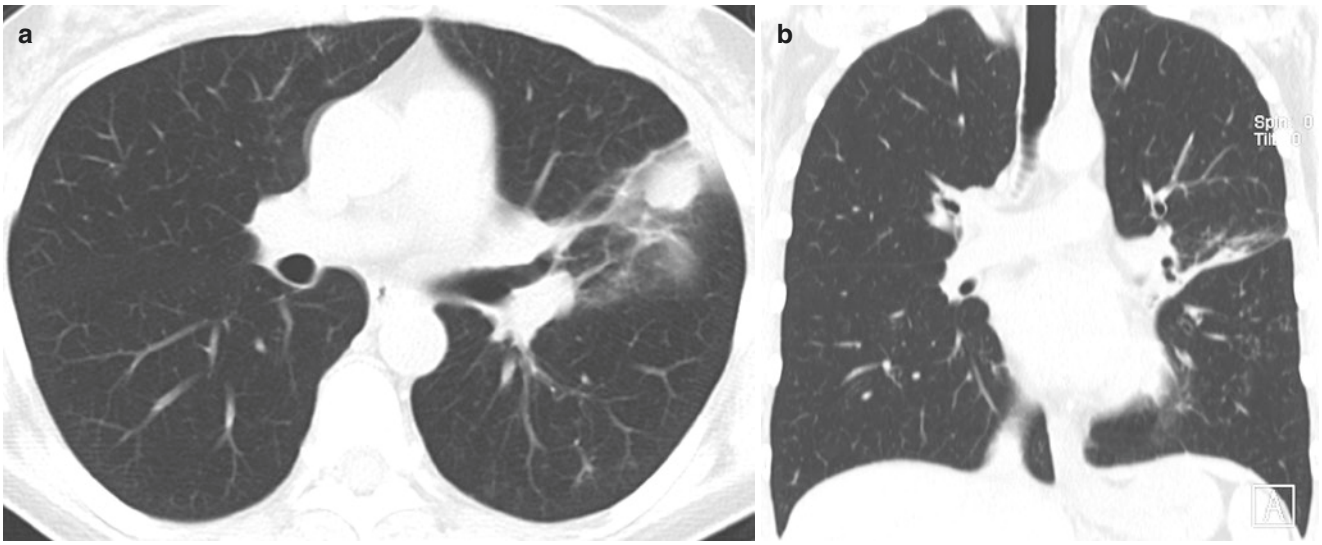

Fig. 6.14 A 59-year-old woman with coccidioidomycosis. (**a**, **b**) Axial and coronal CT images in lung window show a nodular lesion with surrounding ground-glass opacities and "tree-in-bud" opacities in the left lower lobe

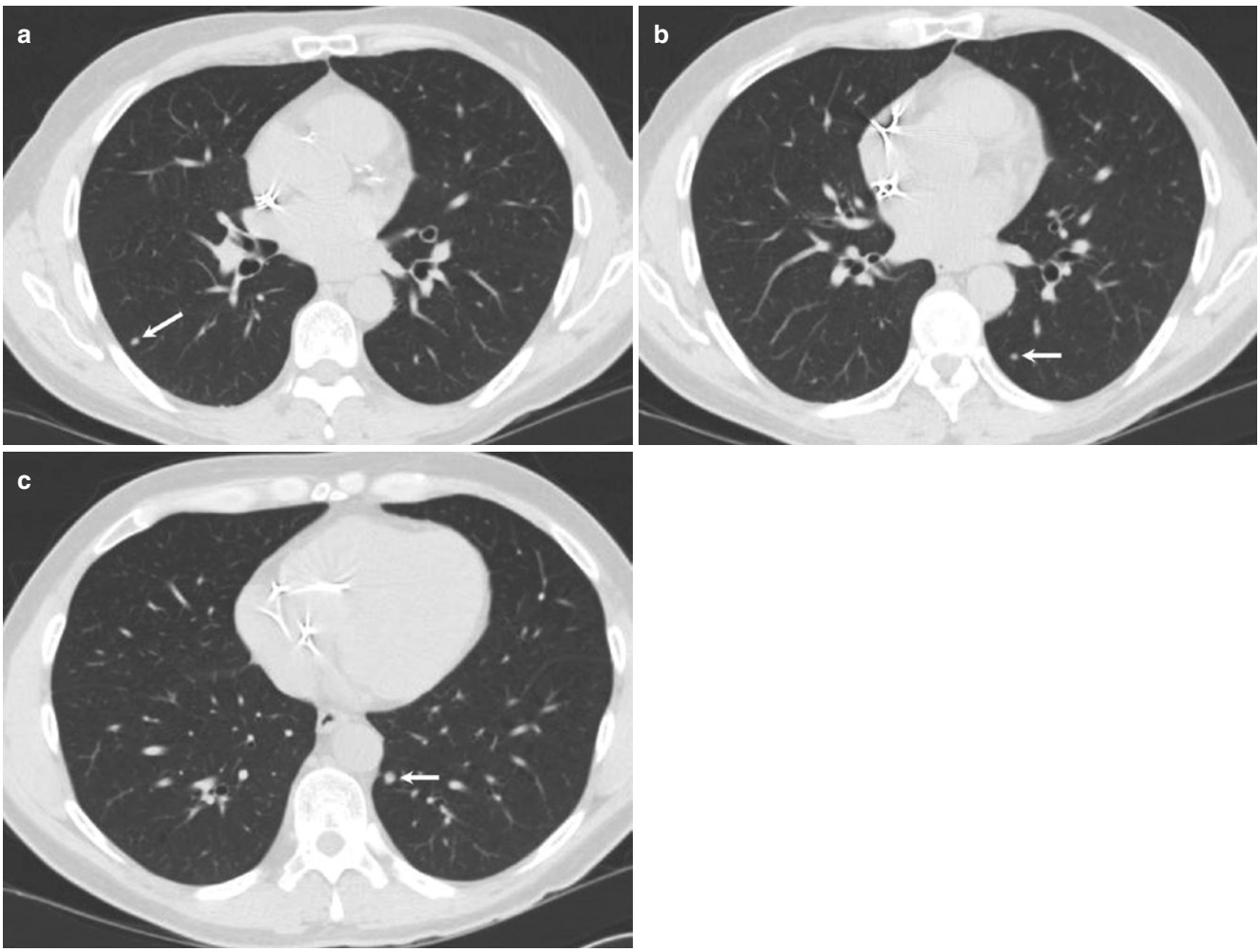

Fig. 6.15 Blastomycosis in a 55-year-old liver transplant recipient. (**a**–**c**) Axial CT images show small lung nodules (white arrows)

Table 6.8 Synopsis of imaging findings in different forms of pulmonary aspergillosis

Aspergilloma (most common form seen on imaging)	Intracavitary usually mobile soft-tissue mass with surrounding crescent of air. Rarely, soft tissue obliterates the surrounding air crescent. There may be reactive pleural thickening
Allergic bronchopulmonary aspergillosis (ABPA)	• Chest radiograph: Consolidation, atelectasis, mucoid impaction hyperinflated lungs, tubular or ring opacities, volume loss • HRCT: Fleeting ground-glass opacities or consolidation Bronchiectasis (central, upper lobe, cystic), mucous plugging (bronchocele formation: "finger in glove" sign), areas of atelectasis, bronchial wall thickening, mosaic attenuation, areas of air trapping
Semi-invasive or subacute invasive or chronic necrotizing aspergillosis (CNA)	• Early: Upper zone opacity • Late: Similar to aspergilloma (air crescent sign), multiple cavities, surrounding infiltrates, expanding cavity, adjacent pleural thickening
Airway invasive or bronchopneumonic aspergillosis (less common invasive form)	Tracheobronchial wall thickening Bronchiolitis: centrilobular nodules with "tree-in-bud" opacities Bronchopneumonia (peribronchial consolidation)
Angioinvasive aspergillosis (most aggressive form, life-threatening)	• Chest radiograph: Peripheral nodules or masses • CT: Nodules or masses with surrounding ground-glass opacities ("halo sign"), cavitation Certain cases show central ground-glass opacity with surrounding higher-density consolidation ("reverse halo" sign) Peripheral wedge-shaped consolidation (areas of infarction) "Air crescent" sign in the recovery phase
Chronic pulmonary aspergillosis	• Cavitary form (more common): single or multiple lung cavities, may contain the fungal ball • Fibrosing form (untreated cases): extensive scarring

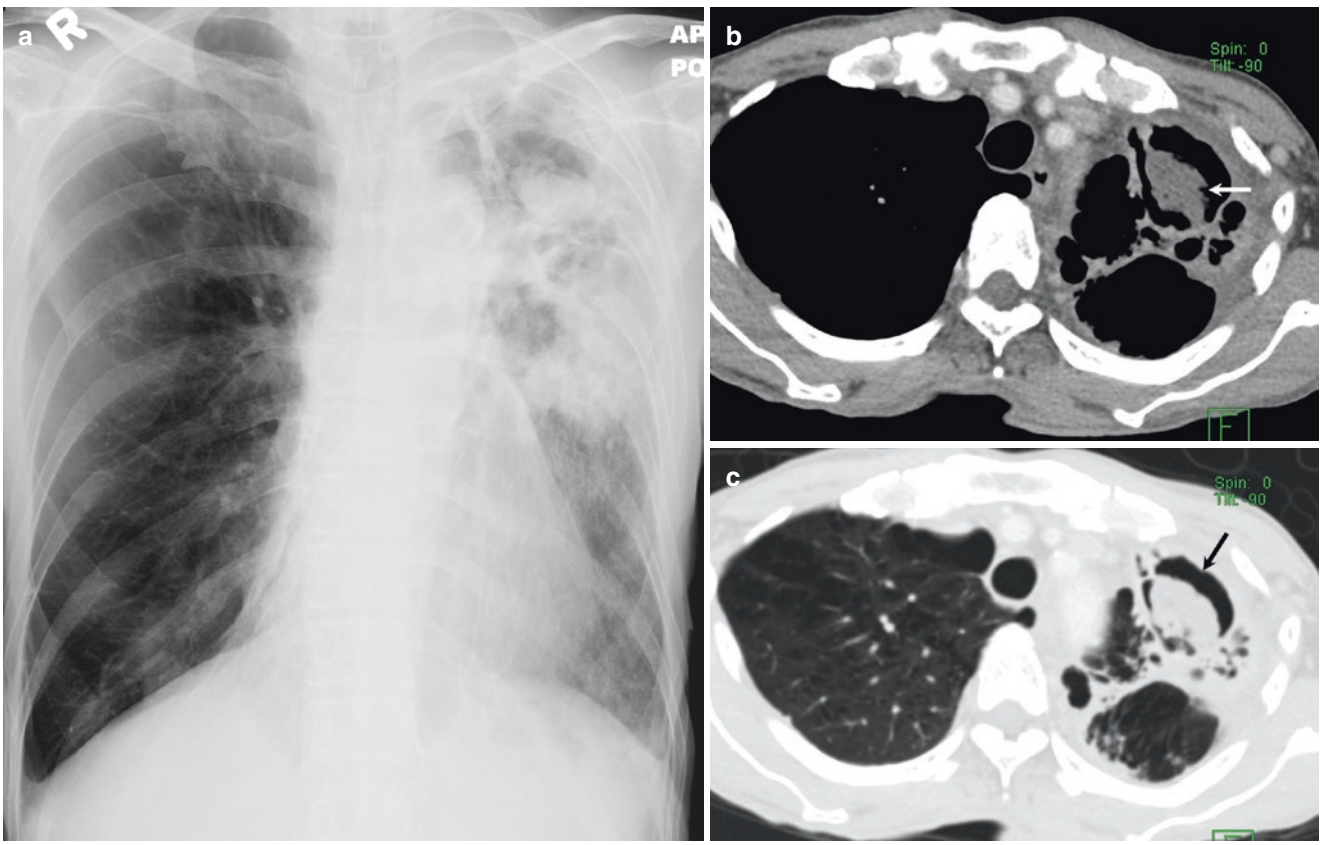

Fig. 6.16 A 69-year-old man with aspergilloma. (**a**) Frontal chest radiograph shows a lucent focus in the left upper zone with round opacity within, on the background of volume loss in the left hemithorax, extensive left lung opacities, and scarring. (**b**, **c**) Axial CT images show a left upper lobe cavity containing a soft-tissue density (white arrow) with surrounding air crescent (black arrow)

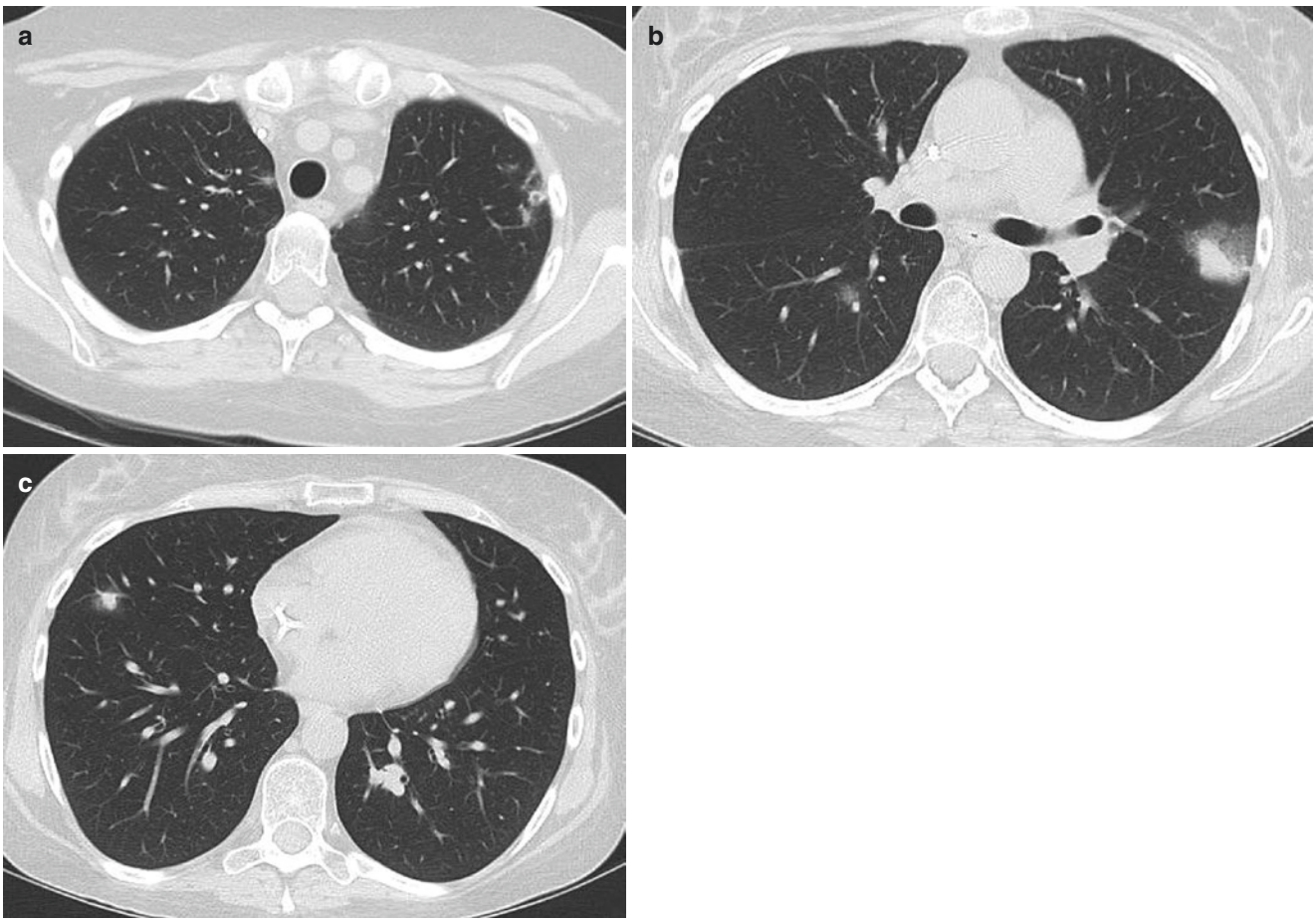

Fig. 6.17 Aspergillosis in a 28-year-old woman with acute lymphoid leukemia. (**a**–**c**) HRCT images show lung nodules with surrounding ground-glass attenuation and cavitation

6.4.3.6 Histoplasmosis

Histoplasmosis is caused by *Histoplasma capsulatum*, typically resulting in granulomatous inflammation, necrosis, and fibrosis, thereby resembling tuberculosis [30]. Acute histoplasmosis is often difficult to identify on chest radiograph, and CT evaluation is needed to identify the abnormalities. In some cases, the infection can extend to the mediastinal structures, resulting in fibrosing mediastinitis. Chronic histoplasmosis is a rare disease, typically seen in patients with background chronic obstructive pulmonary disease. Imaging findings in chronic histoplasmosis include patchy consolidation (upper lobe predominance), upper lobe cavitation, calcified hilar and mediastinal nodes, and rarely broncholithiasis (Table 6.9).

6.4.3.7 Nocardiosis

Nocardiosis is mostly commonly caused by *Nocardia asteroides* or *Nocardia brasiliensis* and can result in pulmonary or systemic infection. *Nocardia asteroides* is usually responsible for the pulmonary disease, causing severe opportunistic infection in immunocompromised patients with non-specific imaging findings (Fig. 6.20) (Table. 6.10).

6.4.3.8 *Pneumocystis jiroveci* Infection

Pneumocystis jiroveci pneumonia is caused by a yeast-like organism and was previously known as *Pneumocystis carinii* [38]. The infection is seen in AIDS (CD4 counts of below 100 cells/mm^3), patients with hematological cancers, solid organ transplant recipients, and bone marrow transplant patients. Dyspnea and nonproductive cough are the usual presenting symptoms. The typical radiological features are listed in Table 6.11 (Figs. 6.21, 6.22, and 6.23). Atypical imaging features can be seen in patients on prophylactic treatment. These features include consolidation, small nodules with tree-in-bud opacities, cavitating nodules, enlarged lymph nodes, and pleural effusion. Diagnosis is confirmed by identifying the organisms in bronchoalveolar lavage, in sputum, or by monoclonal antibody testing. Gallium-67 lung scintigraphy test has

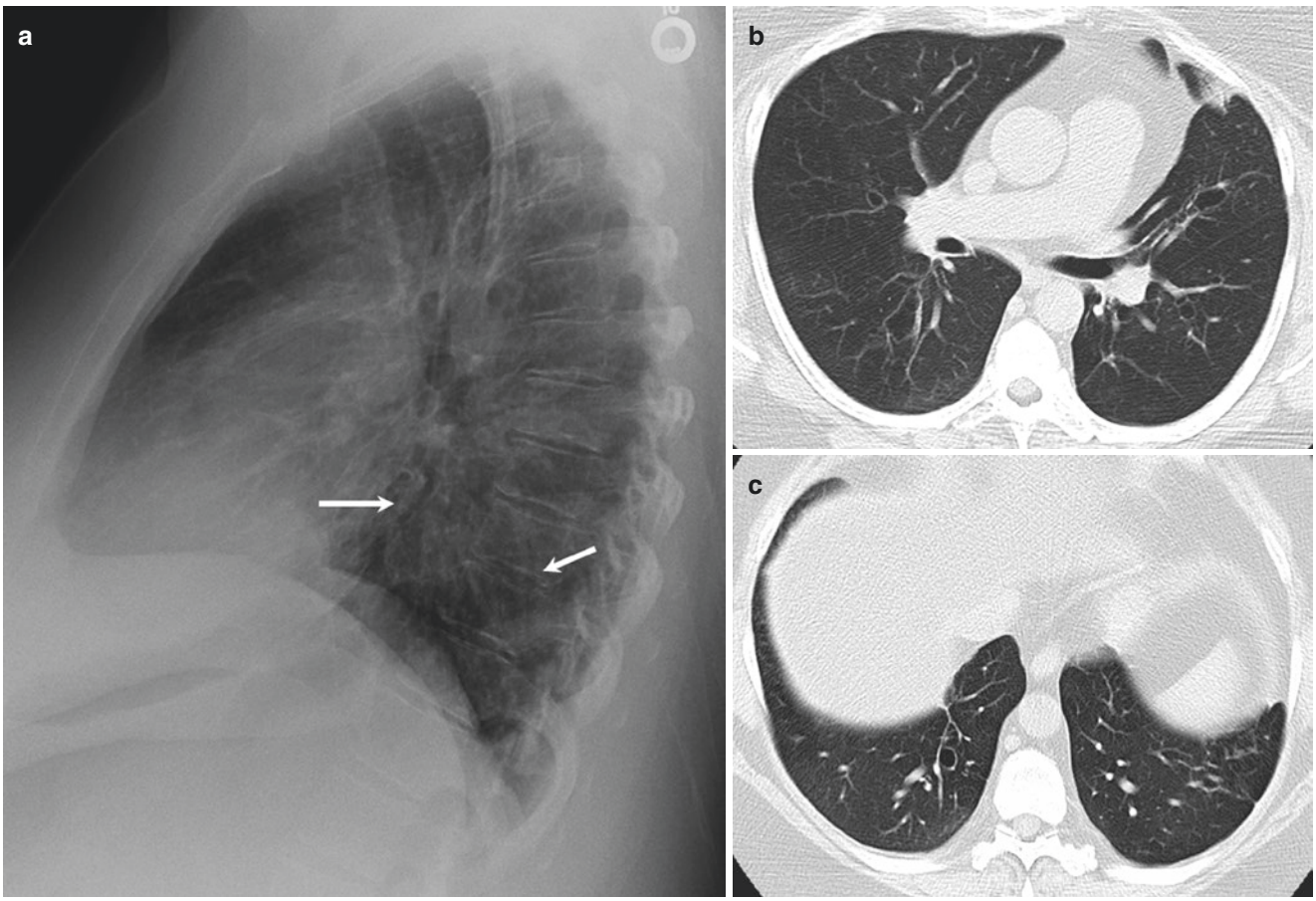

Fig. 6.18 Allergic bronchopulmonary aspergillosis (ABPA) in a 37-year-old woman with long-standing steroid-dependent asthma. (**a**) Lateral chest radiograph shows reduced lung volume, bronchial wall thickening, and bronchiectasis (white arrow). (**b**, **c**) HRCT images show areas of atelectasis, central cystic bronchiectasis, and bronchial wall thickening

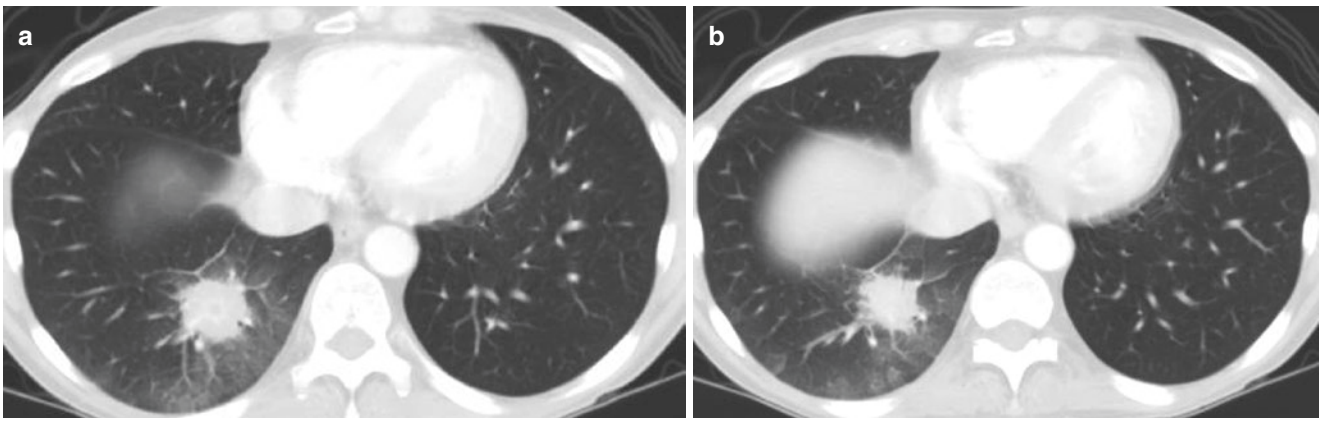

Fig. 6.19 Angioinvasive aspergillosis in a 42-year-old man presenting with neutropenic fever following chemotherapy for acute myeloid leukemia. (**a**, **b**) Axial CT images show right lower lobe nodule with "halo" sign

been shown to be highly sensitive for PCJ infection, and a negative test result virtually excludes this infection.

Table 6.9 Imaging features of pulmonary histoplasmosis

Chest radiograph	CT findings
• Usually normal • Ill-defined opacities, solitary nodule with calcification (healing stage)	• Patchy consolidation or solitary nodule with central or diffuse calcification • Disseminated disease in immunocompromised: reticulonodular or miliary opacities, enlarged mediastinal, hilar nodes, changes of fibrosing mediastinitis

6.4.4 Viral Infections

Various RNA and DNA viruses can cause clinically important pulmonary infections, in both immunocompetent and immunocompromised hosts. Clinical presentations of most of these infections are similar, and the diagnosis is heavily reliant on the background picture, risk factors, and exposures [7]. Imaging is useful in identifying the pattern and extent of the disease, assessing response on follow-up and for diagnostic procedures. Chest radiographs are unremarkable or may demonstrate non-specific changes, like patchy ground-glass opacities, consolidations, effusion, or nod-

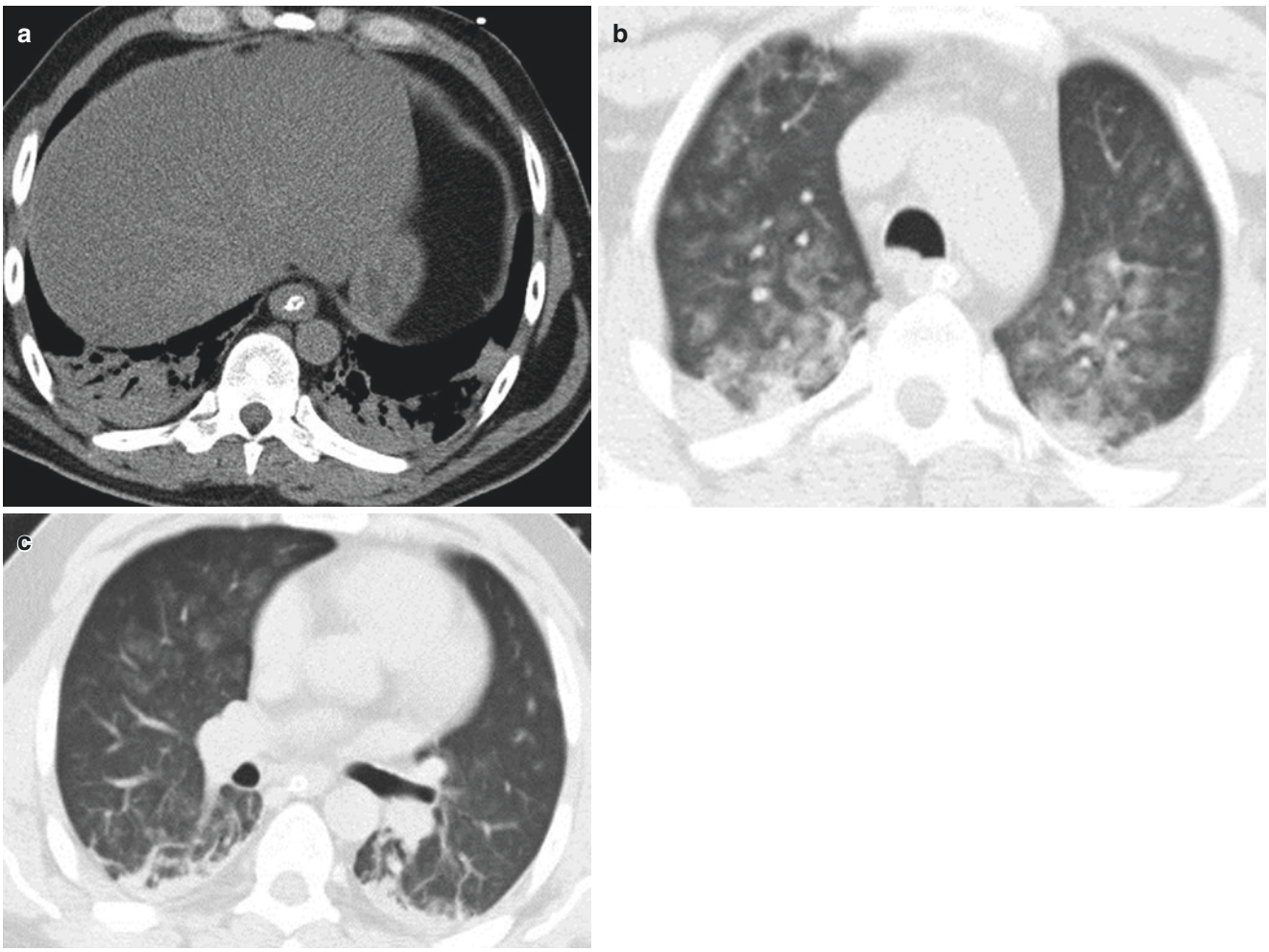

Fig. 6.20 Nocardiosis in a 58-year-old man. (**a**) CT thorax axial image shows lower lobe consolidation. Axial CT images (**b**, **c**) show multiple ground-glass density nodules

ules. Although imaging features in bacterial and viral pulmonary infections show considerable overlap, CT may be useful by demonstrating few main patterns of disease (Table 6.12) [39]. Some viral infections are more common

Table 6.10 Imaging features of pulmonary nocardiosis

Chest radiograph	CT findings
• Lobar consolidation	• Consolidation with areas of abscess formation, cavitation, solitary nodules, or mass
	• Pleural thickening, effusion, empyema necessitans
• Pleural effusion	• Disseminated disease in immunocompromised: multiple nodules and areas of cavitation

Table 6.11 Imaging features of PCJ infection

Chest radiograph	CT findings
• Usually non-specific	• Perihilar and midzone ground-glass opacities, peripheral sparing
• Fine reticular opacities which can progress to ground-glass opacities or consolidation	• "Crazy-paving pattern" with an overlap of reticular opacities and septal thickening, sometimes miliary pattern with small nodules
• Perihilar distribution, pneumatoceles	• Pneumatoceles in about one-third cases (improve after the acute stage). Upper zone predominance on patients on prophylactic aerosols increases the risk of pneumothorax
• Usually no effusion or lymphadenopathy	• Usually no effusion or lymphadenopathy

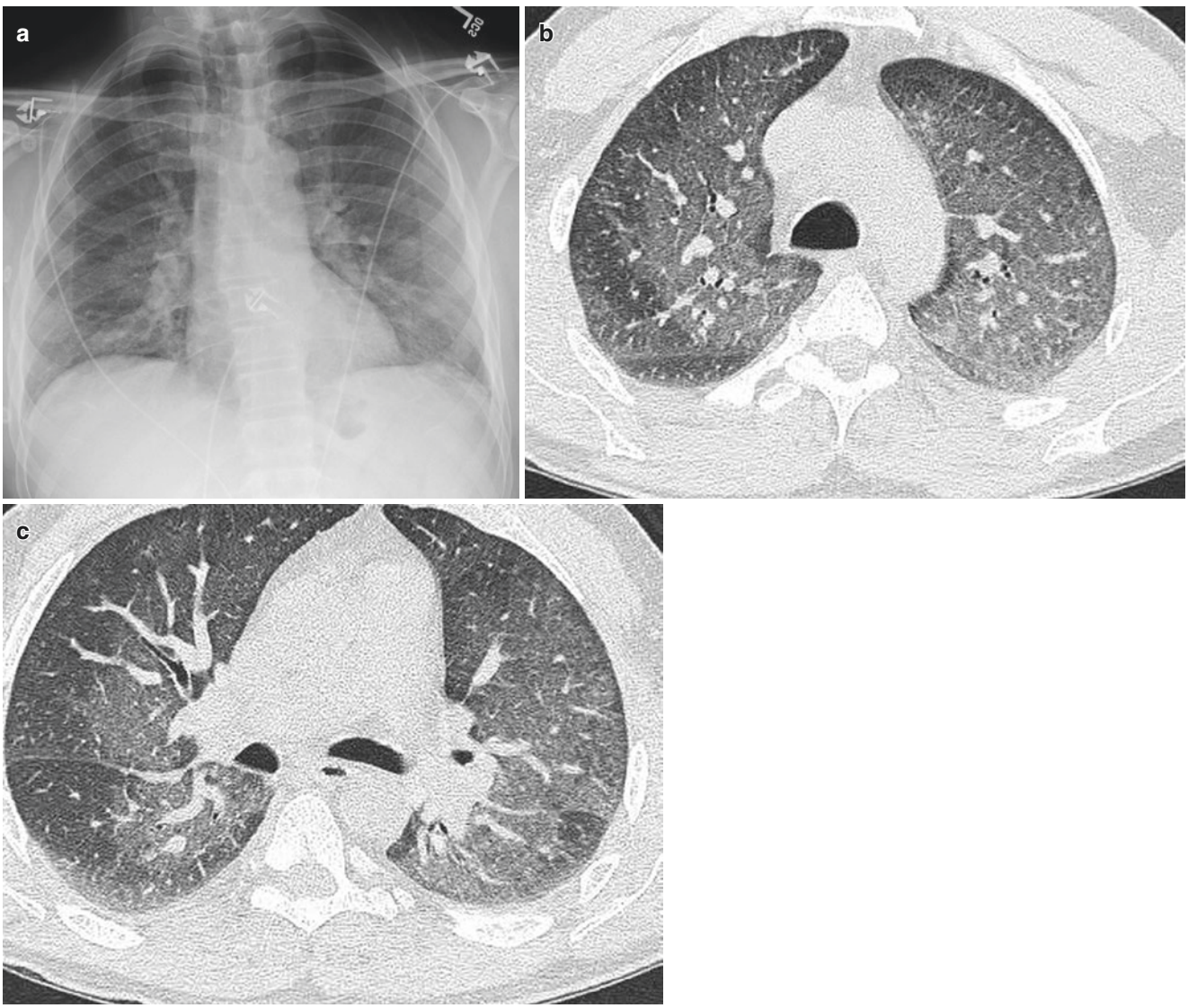

Fig. 6.21 PCJ infection in an immunocompromised male patient. (**a**) Frontal chest radiograph shows subtle diffuse haziness. (**b**, **c**) Axial CT images in lung window show extensive ground-glass pattern densities with midzone and hilar predominance. There is no pleural effusion or lymphadenopathy

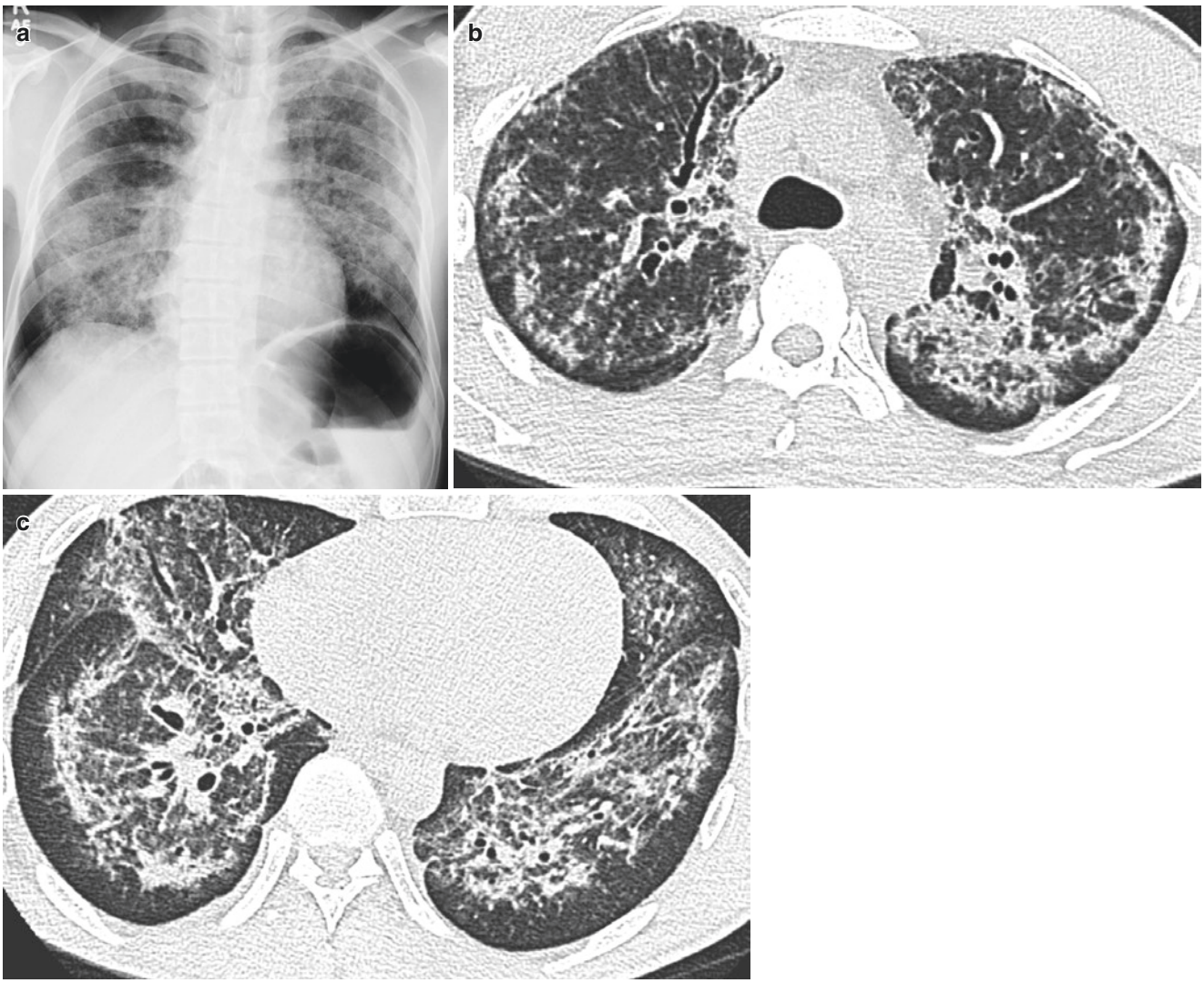

Fig. 6.22 PCJ infection with striking subpleural sparing. (**a**) Frontal chest radiograph shows extensive bilateral reticular opacities and ground-glass opacities. (**b**, **c**) Axial HRCT images show marked septal thickening, ground-glass changes, and peribronchial involvement sparing the subpleural lung. There is no pleural effusion or mediastinal lymphadenopathy

in specific scenarios with a particular imaging pattern. Ground-glass opacities, multiple nodules, or "interstitial pneumonia" pattern in a patient with hematopoietic stem cell transplant is most commonly seen in cytomegalovirus infection.

6.4.5 Aspiration Pneumonia

Aspiration pneumonia results from the passage of material from the oropharynx in the tracheobronchial tree instead of esophagus. Central nervous system diseases, drug overdose, alcohol intoxication, esophageal motility disorders, and anesthesia are some common predisposing risk factors for aspiration pneumonia [40]. It can be classified as acute and chronic aspiration pneumonitis, based on the time course. Mendelson syndrome is a form of acute chemical pneumonitis due to aspiration of acidic gastric content during general anesthesia usually for obstetric procedures. Imaging features are similar to noncardiogenic pulmonary edema. When aspiration occurs in a recumbent patient, the changes are seen involving the posterior segment of the upper lobes and the superior segment or posterior basal segments of lower lobes (Figs. 6.1, 6.24, 6.25, 6.26, and 6.27) (Table 6.13). Bilateral

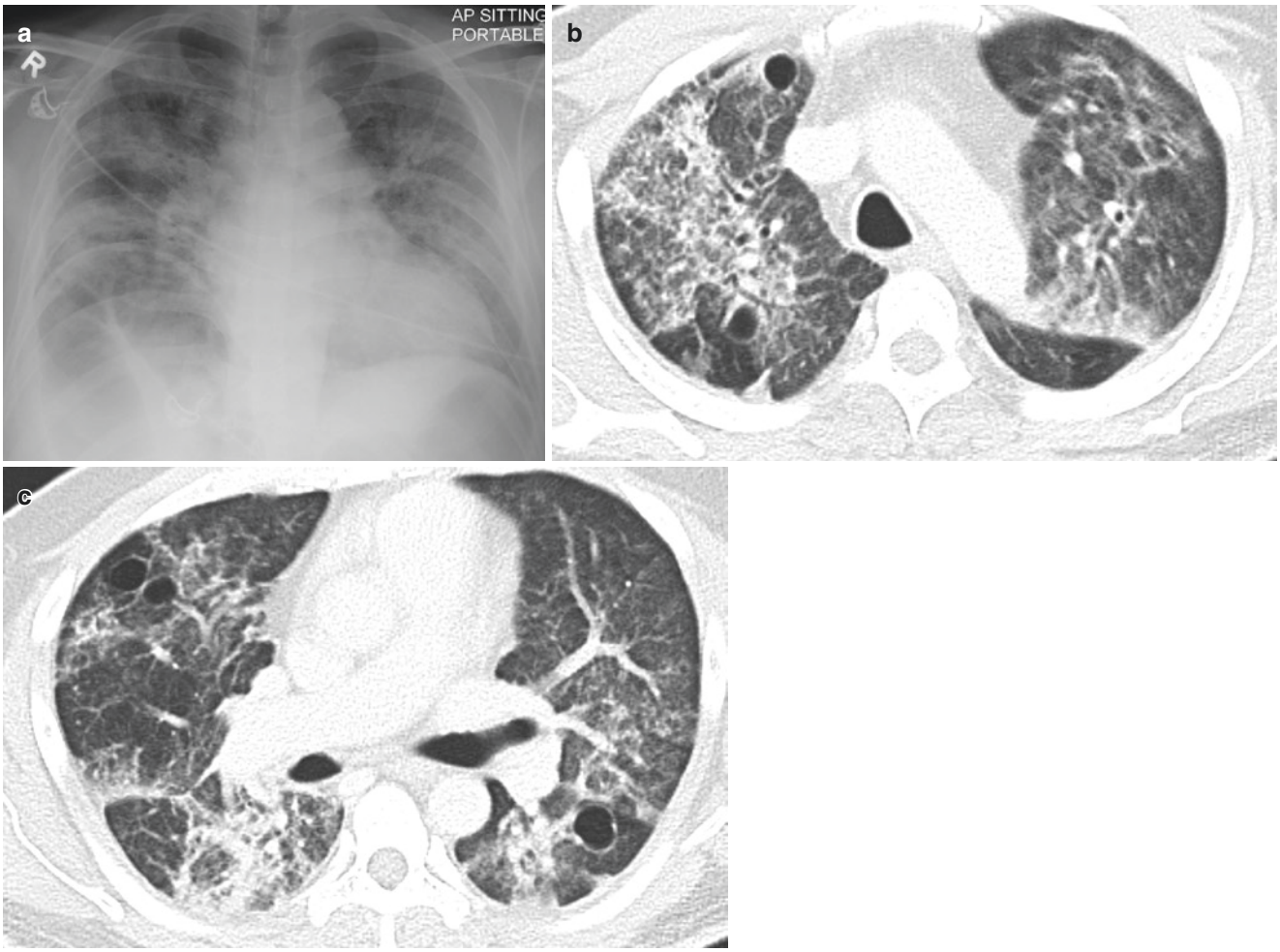

Fig. 6.23 PCJ infection with pneumatoceles. (**a**) Frontal chest radiograph shows bilateral lung opacities, predominantly in midzones. (**b**, **c**) Axial CT images in lung window show bilateral marked septal thickening, ground-glass pattern opacification, and thin-walled cysts

Table 6.12 CT findings in viral pulmonary infections

Cause	Predominant pattern
RNA viruses	Ground-glass opacities, consolidation, nodules, tree-in-bud opacities *Hantavirus infection*: interlobular septal thickening, acute respiratory distress syndrome *Coronavirus infection*: crazy-paving pattern
RSV	Airway-centric pattern with tree-in-bud opacities, prominent bronchial/bronchiolar wall thickening, and surrounding consolidation
Adenovirus	Multifocal ground-glass opacities, consolidation, bronchial wall thickening
HSV	Ground-glass opacities, consolidation, nodules with a surrounding halo
Varicella	Nodules with calcification or surrounding halo, ground-glass opacities, consolidation
CMV	Ground-glass opacities, consolidation, nodules with a surrounding halo

basal, lingula, and middle lobe involvement can be seen in otherwise ambulatory patients. Chronic/recurrent aspiration pneumonitis usually appears as small and large airways disease but may mimic fibrotic lung disease or even a lung mass. Lung abscess or empyema can be seen in complicated cases.

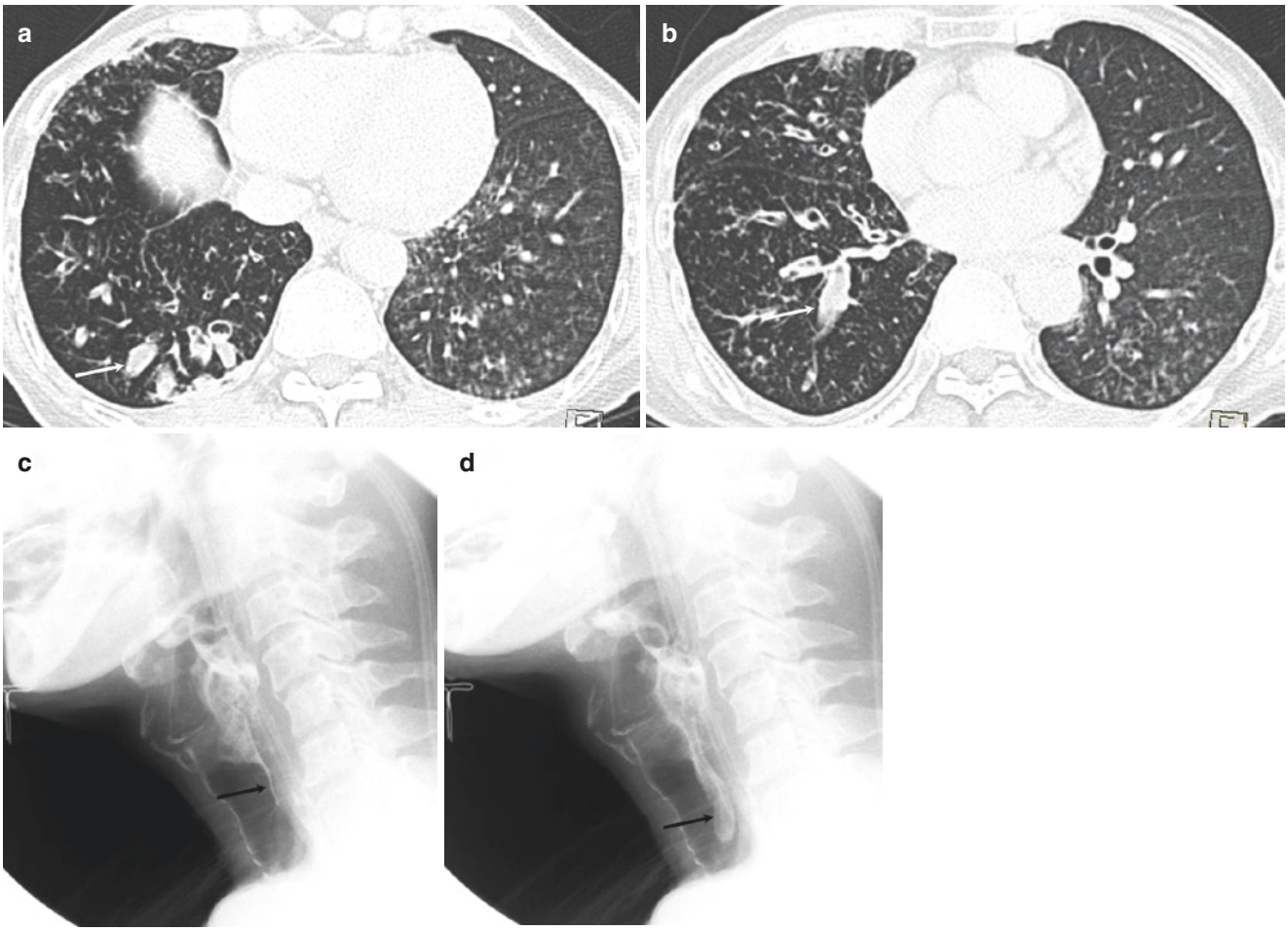

Fig. 6.24 A 76-year-old man with stroke and recurrent aspiration. (**a**, **b**) Axial CT images show bronchiectasis in bilateral lower lobes with mucus plugging (arrow), marked bronchial wall thickening, and extensive tree-in-bud opacities. (**c**, **d**) Serial video fluoroscopy images show aspiration of thin barium (arrow)

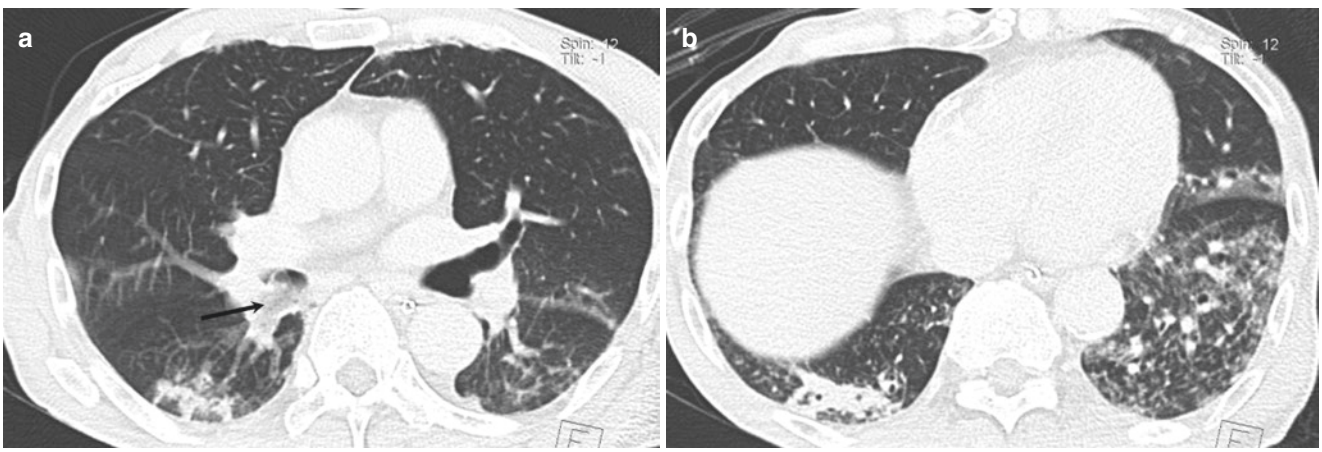

Fig. 6.25 Recurrent aspiration. (**a**, **b**) Axial CT images show consolidative opacity in the right posterior lung base, bronchiectasis, and tree-in-bud opacities in the left lung base. Note bubbly fluid in the right lower lobe bronchus (arrow)

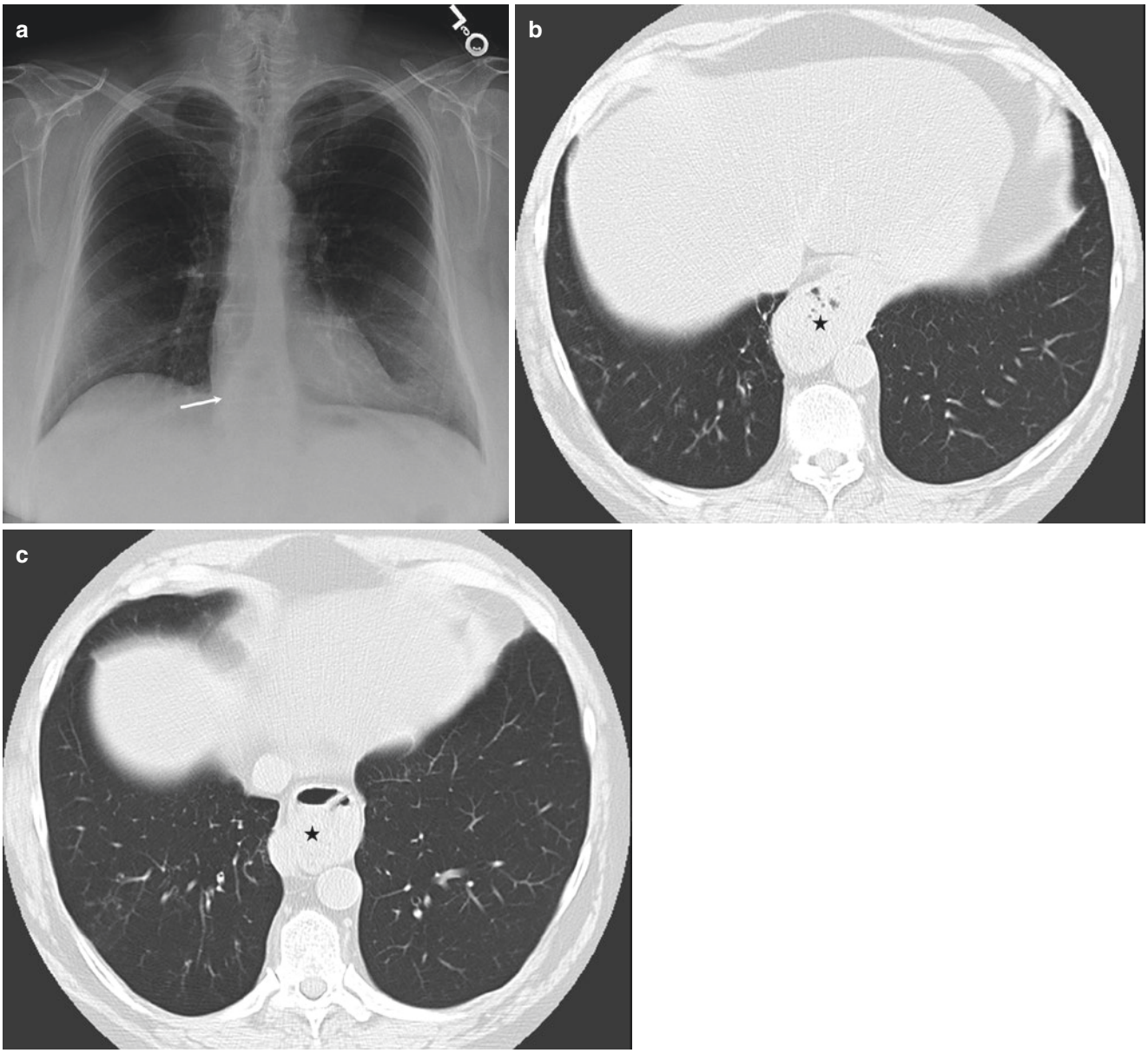

Fig. 6.26 Mild changes of recurrent aspiration. (**a**) Frontal chest radiograph shows a retrocardiac opacity displacing the azygo-esophageal recess (arrow). (**b**, **c**) Axial CT images show moderate size hiatal hernia (asterisk) with subtle ground-glass opacities, bronchial wall thickening, and bronchial dilatation in the right lower lobe

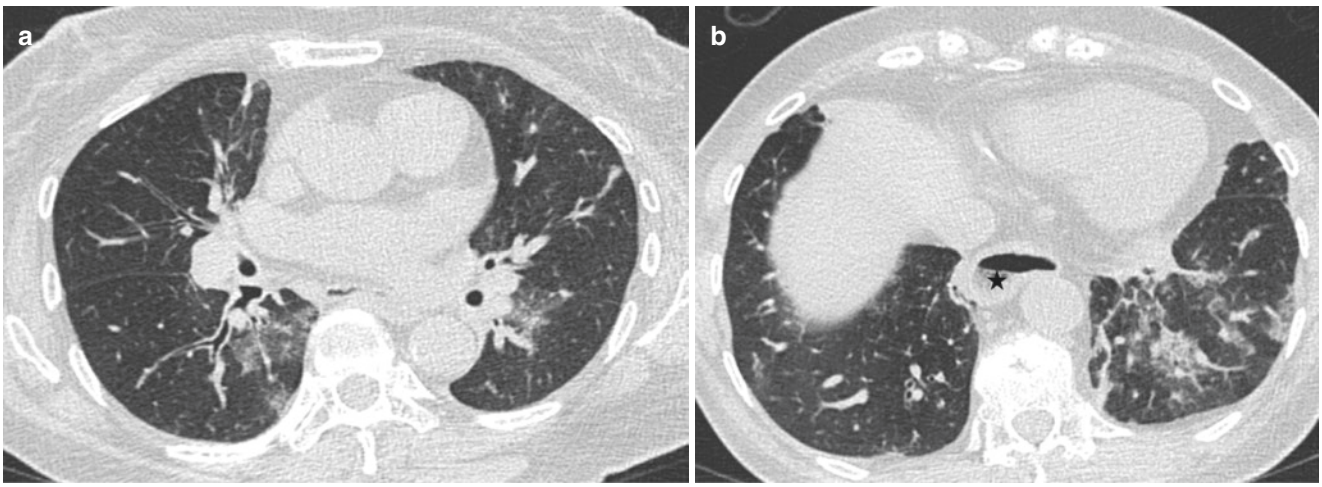

Fig. 6.27 Aspiration changes in a patient with scleroderma. (**a**, **b**) Axial CT images show dilated esophagus with air-fluid level (asterisk) with bilateral peribronchial ground-glass opacities. The opacities resolved on follow-up CT (not shown) excluding interstitial lung disease related to scleroderma

Table 6.13 Imaging findings in aspiration pneumonitis

Chest radiograph	CT findings
• Dilated esophagus or hiatal hernia	• Abnormal esophagus
• Lobar consolidation, if there is associated infection	• Aspirated material can be identified within the tracheobronchial tree
• Migratory opacities in recurrent aspiration	• Various patterns (bronchopneumonia, lobar pneumonia, bronchiolitis) involving posterior segment of upper lobes or superior and basal segment of lower lobes
	• Bronchiectasis with associated small airways disease in lower lungs (recurrent aspiration)

References

1. Beigelman-Aubry C, Godet C, Caumes E. Lung infections: the radiologist's perspective. Diagn Interv Imaging. 2012;93(6):431–40.
2. Walker CM, Abbott GF, Greene RE, Shepard JA, Vummidi D, Digumarthy SR. Imaging pulmonary infection: classic signs and patterns. Am J Roentgenol. 2014;202(3):479–92.
3. Okada F, Ono A, Ando Y, Nakayama T, Ishii R, Sato H, et al. Thin-section CT findings in Pseudomonas aeruginosa pulmonary infection. Br J Radiol. 2012;85(1020):1533–8.
4. Wagner AL, Szabunio M, Hazlett KS, Wagner SG. Radiologic manifestations of round pneumonia in adults. Am J Roentgenol. 1998;170(3):723–6.
5. Worsley DF, Nambu A, Ozawa K, Kobayashi N, Tago M. Imaging of community-acquired pneumonia: roles of imaging examinations, imaging diagnosis of specific pathogens and discrimination from noninfectious diseases. World J Radiol. 2014;6(10):779–93.
6. Elliott Ferguson EC, Berkowitz EA. Lung CT: part 2, The interstitial pneumonias – clinical, histologic, and CT manifestations. Am J Roentgenol. 2012;199(4):W464–76.
7. Franquet T. Imaging of pulmonary viral pneumonia. Radiology. 2011;260(1):18–39.
8. Lee KS, Kim TS, Han J, Hwang JH, Yoon JH, Kim Y, Yoo SY. Diffuse micronodular lung disease: HRCT and pathologic findings. J Comput Assist Tomogr. 1999;23(1):99–106.
9. Oh YW, Effmann EL, Godwin JD. Pulmonary infections in immunocompromised hosts: the importance of correlating the conventional radiologic appearance with the clinical setting. Radiology. 2000;217(3):647–56.
10. Ye R, Zhao L, Wang C, Wu X, Yan H. Clinical characteristics of septic pulmonary embolism in adults: a systematic review. Respir Med. 2014;108(1):1–8.
11. Dodd JD, Souza CA, Müller NL. High-resolution MDCT of pulmonary septic embolism: evaluation of the feeding vessel sign. Am J Roentgenol. 2006;187(3):623–9.
12. Franquet T, Müller NL, Giménez A, Martínez S, Madrid M, Domingo P. Infectious pulmonary nodules in immunocompromised patients: usefulness of computed tomography in predicting their etiology. J Comput Assist Tomogr. 2003;27(4):461–8.
13. Raju S, Ghosh S, Mehta AC. Chest CT signs in pulmonary disease: a pictorial review. Chest. 2017;151(6):1356–74.
14. Althoff Souza C, Müller NL, Marchiori E, Escuissato DL, Franquet T. Pulmonary invasive aspergillosis and candidiasis in immunocompromised patients: a comparative study of the high-resolution CT findings. J Thorac Imaging. 2006;21(3):184–9.
15. Cardinale L, Parlatano D, Boccuzzi F, Onoscuri M, Volpicelli G, Veltri A. The imaging spectrum of pulmonary tuberculosis. Acta Radiol. 2015;56(5):557–64.
16. Pombo F, Rodríguez E, Mato J, Pérez-Fontán J, Rivera E, Valvuena L. Patterns of contrast enhancement of tuberculous lymph nodes demonstrated by computed tomography. Clin Radiol. 1992;46(1):13–7.
17. Mathur M, Badhan RK, Kumari S, Kaur N, Gupta S. Radiological manifestations of pulmonary tuberculosis – a comparative study between immunocompromised and immunocompetent patients. J Clin Diagn Res. 2017;11(9):TC06–9.
18. Andreu J, Cáceres J, Pallisa E, Martinez-Rodriguez M. Radiological manifestations of pulmonary tuberculosis. Eur J Radiol. 2004;51(2):139–49.

19. Murata K, Itoh H, Todo G, Kanaoka M, Noma S, Itoh T, et al. Centrilobular lesions of the lung: demonstration by high-resolution CT and pathologic correlation. Radiology. 1986;161(3):641–5.
20. Ofori A, Steinmetz AR, Akaasi J, Asafu Adjaye Frimpong GA, Norman BR, Obeng-Baah J, Bedu-Addo G, Phillips RO. Pulmonary aspergilloma: an evasive disease. Int J Mycobacteriol. 2016;5(2):235–9.
21. Jeong YJ, Lee KS. Pulmonary tuberculosis: up-to-date imaging and management. Am J Roentgenol. 2008;191(3):834–44.
22. Boruah DK, Sanyal S, Sharma BK, Prakash A, Dhingani DD, Bora K. Role of cross sectional imaging in isolated chest wall tuberculosis. J Clin Diagn Res. 2017;11(1):TC01–6.
23. Martinez S, McAdams HP, Batchu CS. The many faces of pulmonary nontuberculous mycobacterial infection. AJR Am J Roentgenol. 2007;189(1):177–86.
24. Marchiori E, Müller NL, Soares Souza A Jr, Escuissato DL, Gasparetto EL, Franquet T. Pulmonary disease in patients with AIDS: high-resolution CT and pathologic findings. Am J Roentgenol. 2005;184(3):757–64.
25. Benson CA, Ellner JJ. Mycobacterium avium complex infection and AIDS: advances in theory and practice. Clin Infect Dis. 1993;17(1):7–20.
26. Levin DL. Radiology of pulmonary Mycobacterium avium-intracellulare complex. Clin Chest Med. 2002;23(3):603–12.
27. Phillips P, Bonner S, Gataric N, Bai T, Wilcox P, Hogg R, et al. Nontuberculous mycobacterial immune reconstitution syndrome in HIV-infected patients: spectrum of disease and long-term follow-up. Clin Infect Dis. 2005;41(10):1483–97.
28. Bennett C, Vardiman J, Golomb H. Disseminated atypical mycobacterial infection in patients with hairy cell leukemia. Am J Med. 1986;80(5):891–6.
29. Marras TK, Wallace RJ Jr, Koth LL, Stulbarg MS, Cowl CT, Daley CL. Hypersensitivity pneumonitis reaction to Mycobacterium avium in household water. Chest. 2005;127(2):664–71.
30. Chong S, Lee KS, Yi CA, Chung MJ, Kim TS, Han J. Pulmonary fungal infection: imaging findings in immunocompetent and immunocompromised patients. Eur J Radiol. 2006;59(3):371–83.
31. Fox DL, Müller NL. Pulmonary cryptococcosis in immunocompetent patients: CT findings in 12 patients. Am J Roentgenol. 2005;185(3):622–6.
32. Zinck SE, Leung AN, Frost M, Berry GJ, Müller NL. Pulmonary cryptococcosis: CT and pathologic findings. J Comput Assist Tomogr. 2002;26(3):330–4.
33. Capone D, Marchiori E, Wanke B, Dantas KE, Cavalcanti MA, Deus Filho A, Escuissato DL, Warszawiak D. Acute pulmonary coccidioidomycosis: CT findings from 15 patients. Br J Radiol. 2008;81(969):721–4.
34. Kim KI, Leung AN, Flint JD, Müller NL. Chronic pulmonary coccidioidomycosis: computed tomographic and pathologic findings in 18 patients. Can Assoc Radiol J. 1998;49(6):401–7.
35. Kousha M, Tadi R, Soubani AO. Pulmonary aspergillosis: a clinical review. Eur Respir Rev. 2011;20(121):156–74.
36. Denning DW, Cadranel J, Beigelman-Aubry C, Ader F, Chakrabarti A, Blot S, European Society for Clinical Microbiology and Infectious Diseases and European Respiratory Society, et al. Chronic pulmonary aspergillosis: rationale and clinical guidelines for diagnosis and management. Eur Respir J. 2016;47(1):45–68.
37. Desai SR, Hedayati V, Patel K, Hansell DM. Chronic aspergillosis of the lungs: unravelling the terminology and radiology. Eur Radiol. 2015;25(10):3100–7.
38. Feurestein IM, Archer A, Pluda JM, Francis PS, Falloon J, Masur H, et al. Thin-walled cavities, cysts, and pneumothorax in Pneumocystis carinii pneumonia: further observations with histopathologic correlation. Radiology. 1990;174(3 Pt 1):697–702.
39. Miller WT Jr, Mickus TJ, Barbosa E Jr, Mullin C, Van Deerlin VM, Shiley KT. CT of viral lower respiratory tract infections in adults: comparison among viral organisms and between viral and bacterial infections. Am J Roentgenol. 2011;197(5):1088–95.
40. Komiya K, Ishii H, Kushima H, Sato S, Kimura H, Yasuda T, Okabe E, Tokimatsu I, Yamamoto H, Kadota J. Physicians' attitudes toward the definition of "death from age-related physical debility" in deceased elderly with aspiration pneumonia. Geriatr Gerontol Int. 2013;13(3):586–90.

Imaging of ICU Patients

7

Rahul Lohan

7.1 Introduction

Imaging in intensive care unit (ICU) is integral to patient management. The portable chest radiograph is the most commonly requested imaging examination in ICU, and, despite its limitations, it significantly contributes to the decision-making process. Multidetector CT (MDCT) is reserved for relatively complex and challenging clinical scenarios. Bedside ultrasound is emerging as a promising imaging modality as it does not subject the patients to risks and resources involved in the transportation of these patients to the CT facility. Ultrasound is an effective modality to triage patients and is being increasingly incorporated into the emergency and intensive care management algorithms.

The commonly encountered disease states in ICU setting are pulmonary parenchymal diseases, pulmonary thromboembolism, barotrauma, and pleural fluid. Besides the evaluation of these conditions, imaging is routinely used for the assessment of various catheters and tubes commonly used in ICUs.

7.2 Pulmonary Parenchymal Diseases

The common pulmonary parenchymal disease processes in ICU patients include hydrostatic pulmonary edema, acute respiratory distress syndrome (ARDS), atelectasis, pneumonia, aspiration, and pulmonary hemorrhage.

R. Lohan (✉)
Department of Diagnostic Radiology, Khoo Teck Puat Hospital, Singapore, Singapore
e-mail: lohan.rahul@ktph.com.sg

7.2.1 Pulmonary Edema

Pulmonary edema is an abnormal accumulation of fluid in the extravascular compartment of the lungs. The fluid accumulation depends on the capillary permeability and the oncotic pressure, as described by the Starling equation, i.e., $Q = K\,(HPiv - Hpev) - T(OPiv - OPev)$, where Q represents the amount of fluid filtered and HP and OP denote the hydrostatic and oncotic pressures of the intravascular (iv) and extravascular (ev) compartments. K represents the conductance of the capillary wall, determined by the resistance offered to the water flow by the capillary endothelial cell junctions [1]. T represents the permeability of the capillary membranes to the macromolecules. Lymphatic drainage is another pathway for handling excess water in the lungs. However, the lymphatic drainage needs time to be effective, and in the acute situation, it often fails to eliminate the excess fluid [2]. Classically grouped into cardiogenic and non-cardiogenic variants, the pulmonary edema can be divided into the following four types based on the pathophysiology [3] (Fig. 7.1):

(a) Increased hydrostatic pressure edema
(b) Permeability edema with diffuse alveolar damage (DAD)
(c) Permeability edema without DAD
(d) Mixed edema

Almost all pulmonary edema presentations in critical care units are due to increased hydrostatic pressure or increased permeability with DAD. The two common pathophysiological forms are further discussed.

7.2.1.1 Hydrostatic Pulmonary Edema

The two most common causes of increased hydrostatic pressure edema (HPE) in critical care units are left heart failure and fluid overload. Besides renal and liver failure, overzealous hydration in settings of trauma and immediate postoperative care frequently contibutes to fluid overload. There are two distinct radiological phases of the

A. Chawla (ed.), *Thoracic Imaging*, https://doi.org/10.1007/978-981-13-2544-1_7

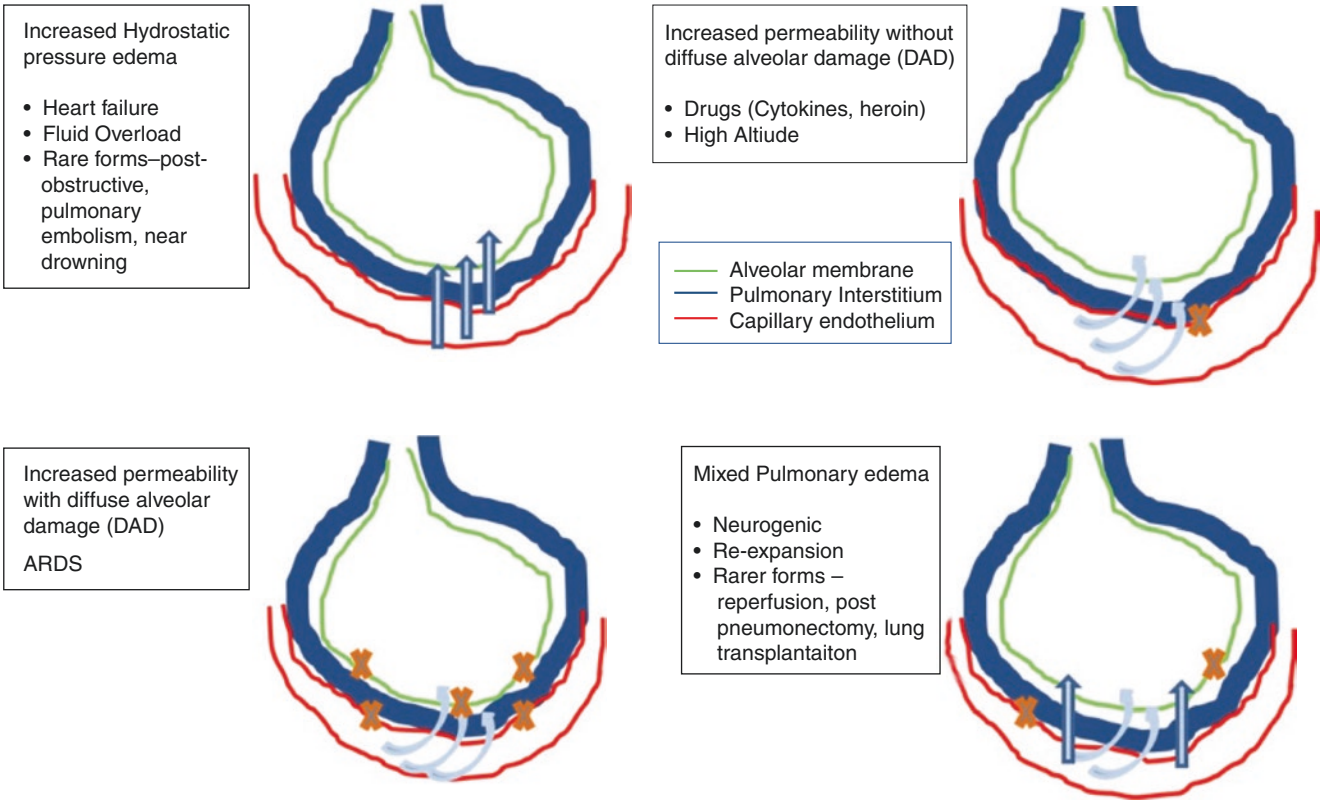

Fig. 7.1 Categories and underlying common etiologies of pulmonary edema on the basis of pathophysiology

pressure edema—the interstitial edema and the alveolar edema. The radiographic findings in the early interstitial phase include indistinctness of the intrapulmonary vasculature, peribronchial cuffing, and Kerley lines. Indistinctness of pulmonary vasculature is subtle but often the most useful radiographic sign of early interstitial edema in ICU patients. With increasing intensity and duration of pressure gradient, edema extends into the alveolar spaces, resulting in nodular or acinar areas of increased opacity that coalesce into frank consolidation (Fig. 7.2). There is a good correlation between the increased pressure in the intravascular compartment as measured by the pulmonary capillary wedge pressure (PCWP) and radiographic appearances (Table 7.1) [4].

The vascular pedicle width is measured from the SVC and azygos vein complex on the right to proximal descending thoracic aorta on the left. It can provide a reasonable estimate of intravascular volume status. Increased width of vascular pedicle (>7 cm) thus may help in differentiating hydrostatic pulmonary edema from non-cardiogenic edema (Fig. 7.3). The CT findings of hydrostatic pulmonary edema include smooth interlobular septal thickening, ground-glass opacities, consolidation, and pleural effusions (Fig. 7.4). The distribution of densities often demonstrates gravity-based gradient, with abnormalities being most notable at the lung bases. Atypical distribution or appearances similar to aspiration pneumonitis or pneumonia may be seen in presence of underlying chronic pulmonary disease, such as emphysema [5].

7.2.1.2 Permeability Edema with Diffuse Alveolar Damage

Acute respiratory distress syndrome (ARDS) represents the most severe form of permeability edema associated with DAD [2, 3]. In ICU settings, the common primary pulmonary pathologies causing ARDS are pneumonia, aspiration, and pulmonary contusions. The common extrathoracic causes include drug toxicity, systemic inflammatory response syndrome, sepsis, shock, and abdominal trauma [5]. Clinically, ARDS is defined by recently created "Berlin defi-

nition" (Table 7.2) [6]. ARDS involves three often overlapping and conflicting stages. The first or exudative stage is characterized by a rapidly progressing high protein content interstitial edema that quickly fills the alveoli and is associated with hemorrhage and hyaline membrane formation. The second or proliferative stage involves organization of the fibrinous exudate, regeneration of the alveolar lining, and thickening of the alveolar septa. The third or fibrotic stage manifests as varying degrees of scarring and formation of subpleural and intrapulmonary cysts.

The radiographic findings in exudative phase are that of interstitial edema pattern, rapidly progressing to perihilar opacities and subsequently widespread alveolar consolidation (Fig. 7.5). In comparison to hydrostatic edema,

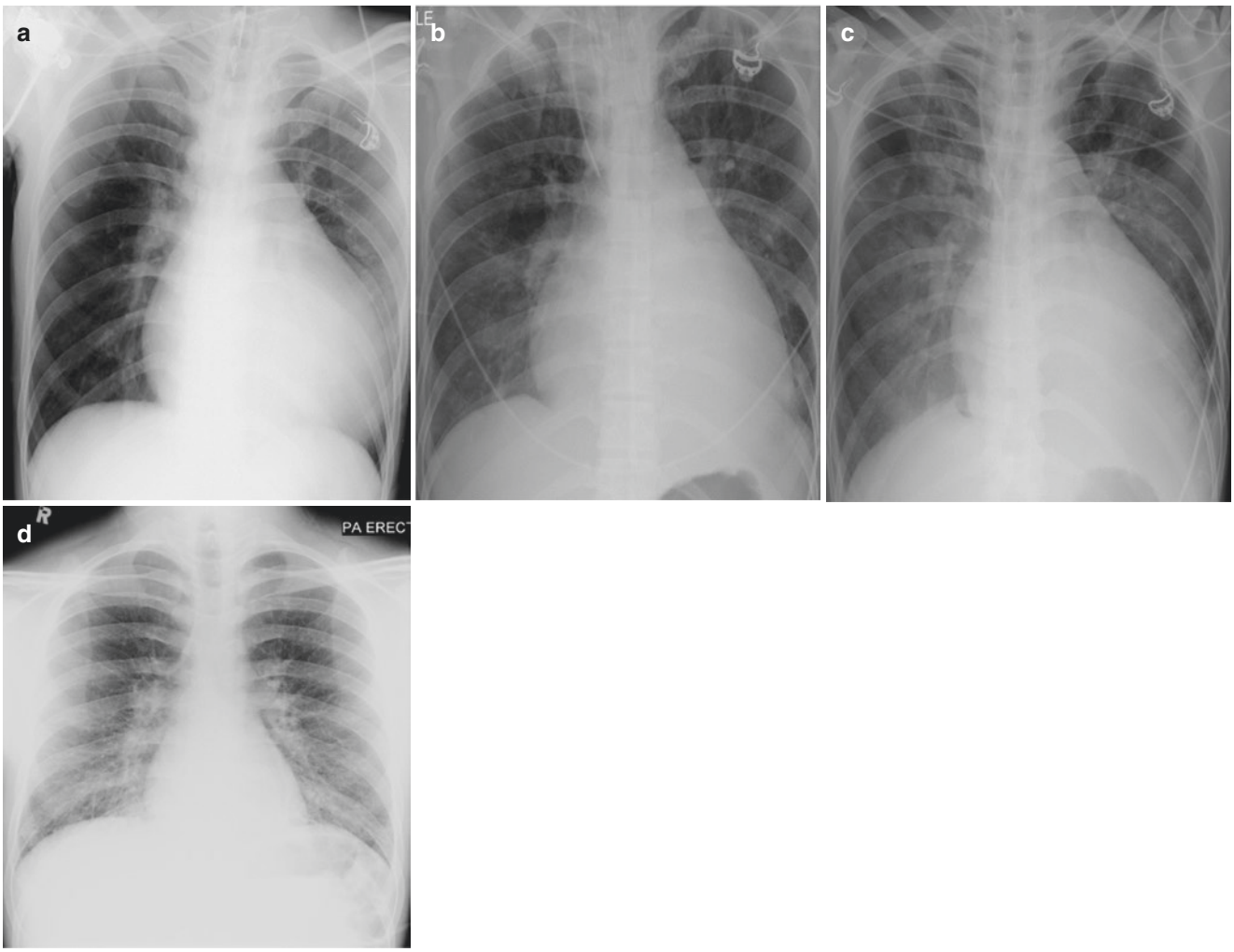

Fig. 7.2 Radiographic progression of hydrostatic pulmonary edema. (**a**) AP bedside chest radiograph obtained in a patient with acute myocardial infarction demonstrates redistribution of pulmonary vessels with upper lobe diversion upon admission to ICU. (**b**) Next day radiograph demonstrates features of interstitial edema in the form of indistinctness of pulmonary vessels and bilateral perihilar haziness. (**c**) Progression to bilateral central consolidation and small pleural effusions representing alveolar edema is seen on the radiograph obtained on the third day. Pulmonary edema in another patient. (**d**) Frontal radiograph at presentation shows interstitial thickening. (**e**–**g**) Axial CT images demonstrate peribronchial cuffing, septal thickening, gravity-dependent ground-glass opacities, and early alveolar opacities (arrows) and bilateral pleural effusions. (**h**) Follow-up radiograph after 2 days shows resolution of interstitial edema but persistent pleural effusions and bibasilar atelectasis

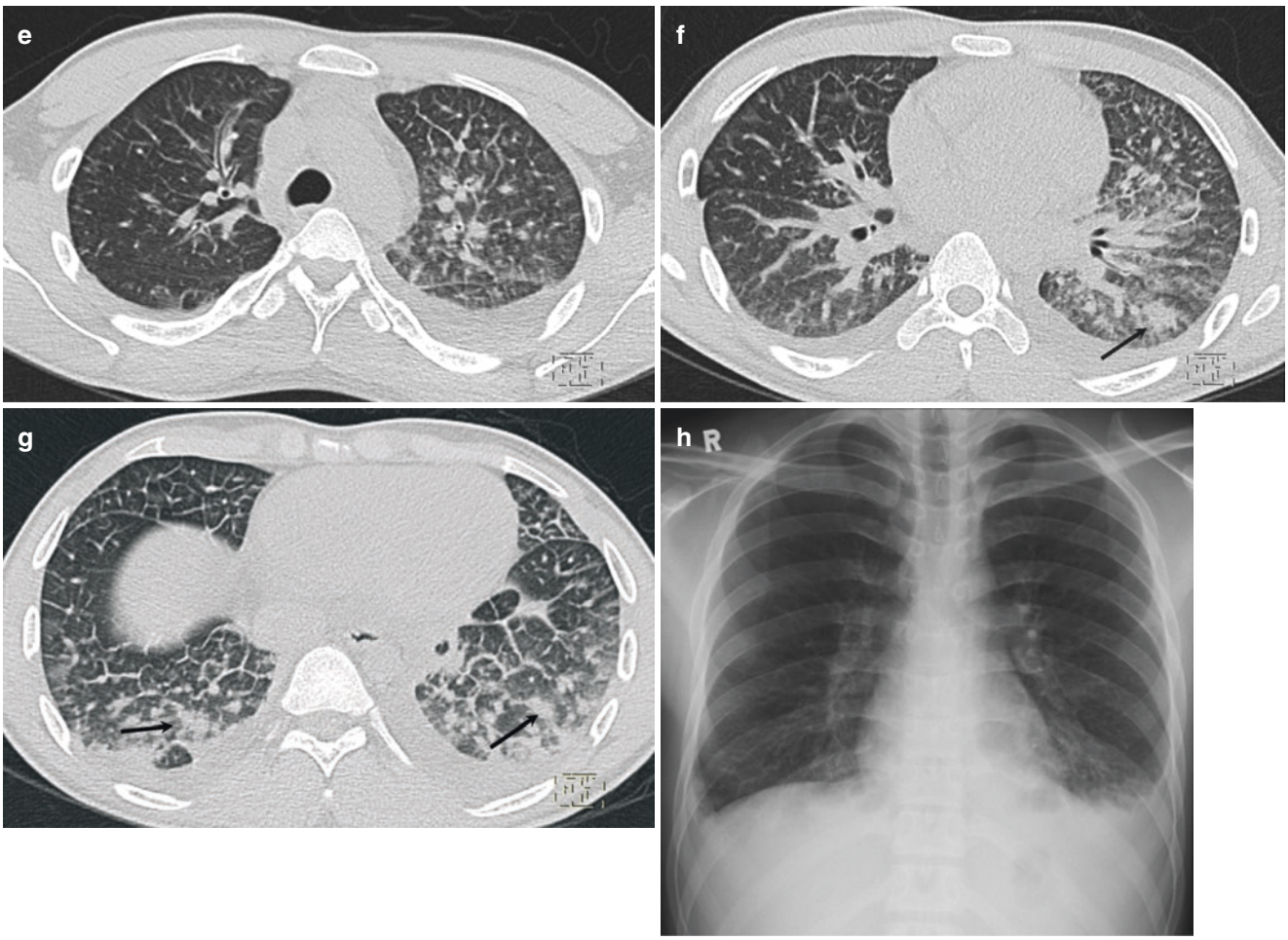

Fig. 7.2 (continued)

Table 7.1 Stages of hydrostatic pulmonary edema

	PCWP	Radiographic changes
Stage 1 Redistribution	13–18 mm Hg	• Redistribution of pulmonary vessels • Cardiomegaly • Increased vascular pedicle width
Stage 2 Interstitial edema	18–25 mm Hg	• Kerley lines • Peribronchial cuffing • Hazy contour of vessels
Stage 3 Alveolar edema	>25 mm HG	• Central consolidation • Bat wing appearance • Pleural effusion

the alveolar edema in ARDS usually has a more peripheral distribution (Fig. 7.6) [3]. The typical CT findings in this phase are dense consolidation in posterior dependent portions of the lung with ground-glass opacities in nondependent areas (Fig. 7.7). This gravitational distribution can be changed by patient's position (supine vs prone), suggesting a significant contribution from atelectasis [3]. The atypical pattern comprises of dense consolidation in anterior (in supine position) nondependent locations. This may be seen in up to 5% of ARDS patients and is more common in ARDS with underlying primary pulmonary cause [7]. "Crazy paving," i.e., ground-glass opacities with superimposed inter- and intralobular septal thickening, may be seen [8].

During the fibroproliferative stage, patchy heterogeneous areas of ground-glass opacification are seen with reticular changes. Traction bronchiectasis and bronchiolectasis may be seen on CT. These findings early in the course of ARDS are associated with a poorer clinical outcome [9]. Subpleural and intrapulmonary cystic lesions may be observed in the fibrotic stage which can directly result in pneumothoraces

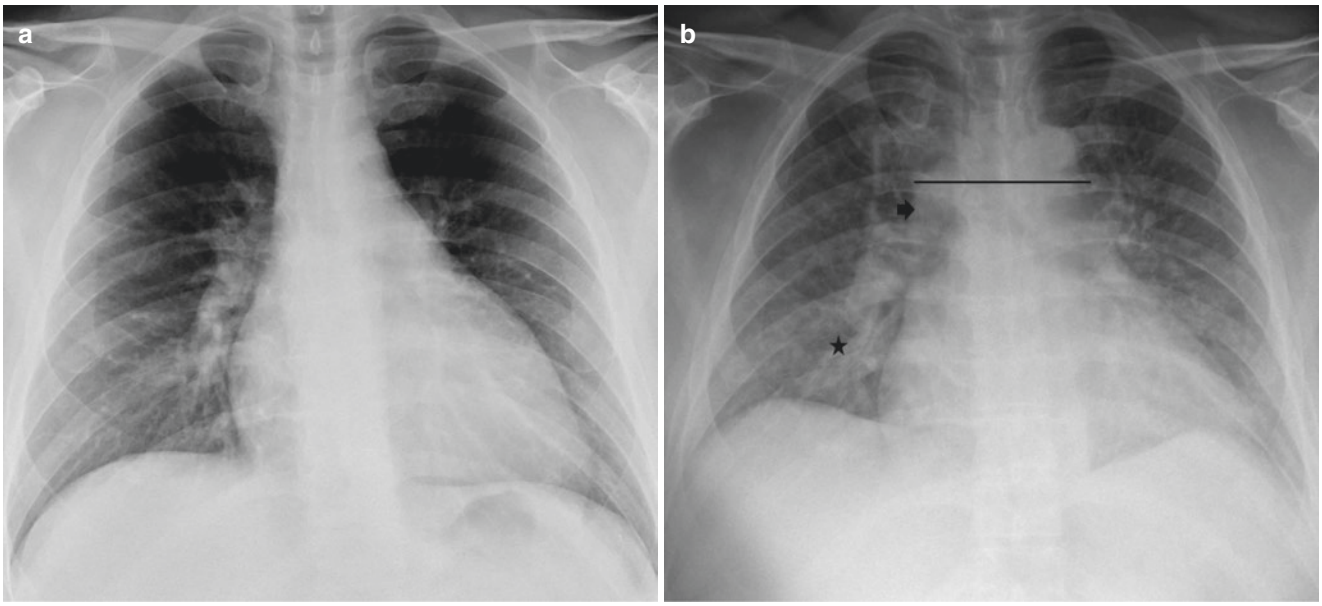

Fig. 7.3 Interstitial pulmonary edema from congestive cardiac failure. (**a**) Baseline AP chest radiograph and (**b**) early stage of pulmonary edema demonstrating progressively increasing width of vascular pedicle (as represented by the line), enlarged central vessels (arrow), and indistinctness of pulmonary vessels (asterisk)

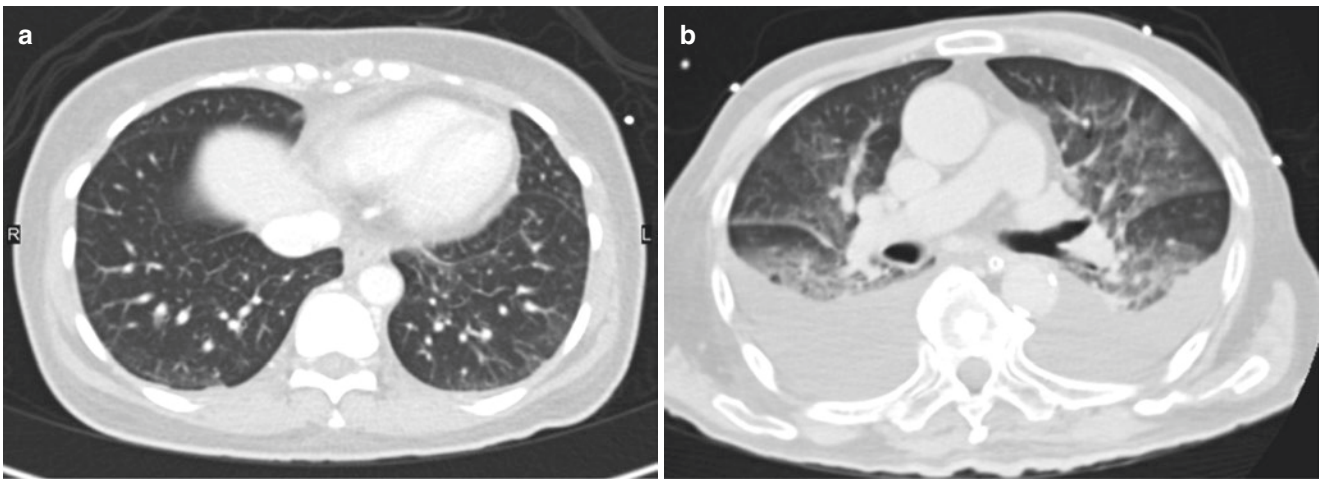

Fig. 7.4 CT findings of hydrostatic pulmonary edema. (**a**) Axial CT images in lung window show smooth interlobular septal thickening at lung bases during the early stage of pulmonary edema, (**b**) progressing to symmetrical central ground-glass opacities and bilateral pleural effusions at a later stage. Note there is a gravity-based gradient of increasing density in the lungs

[9]. Recurrent episodes of exudative phase in the proliferative and fibrotic stages often result in mixed radiologic findings. HRCT of the patients recovered from ARDS on subsequent follow-up shows characteristic anterior lung fibrotic bands with sparing of posterior lungs. Distinguishing imaging features between HPE and ARDS are described in Table 7.3.

7.2.2 Atelectasis

Atelectasis, defined as a decrease in lung volume, is the commonest cause of radiographic parenchymal opacities in ICU patients, particularly amongst the postoperative surgical ICU patients. The atelectasis most commonly involves the left lower lobe (66%), followed by the right lower lobe (22%) and right

Table 7.2 The Berlin definition of ARDS

Timing	Within 1 week of known insult or new or worsening respiratory symptoms
Origin of edema	Respiratory failure not explained by cardiac failure or fluid overload, objective evidence to exclude hydrostatic pulmonary edema (e.g., echocardiography) if no clinical risk factors
Chest imaging	Bilateral opacities—not fully explained by effusion, lobar/lung collapse, or nodules
Oxygenation	Mild, moderate, severe; PaO2/FiO2 ratio of 300–200, 200–100, and < 100, respectively

upper lobe (11%) [10]. Obstructive atelectasis from impaired mucociliary clearance, increased secretions, and altered consciousness is often encountered in the ICU patients. Distal obstruction manifests as crowding of air bronchograms, whereas the proximal mucus plugging leads to lobar or even complete lung collapse (Fig. 7.8). Compressive atelectasis from pleural effusion and cicatrization from fibrosis in later stages of ARDS are other forms of atelectasis seen in ICU setting. The imaging findings include linear, band-like, or wedge-shaped opacities with signs of volume loss.

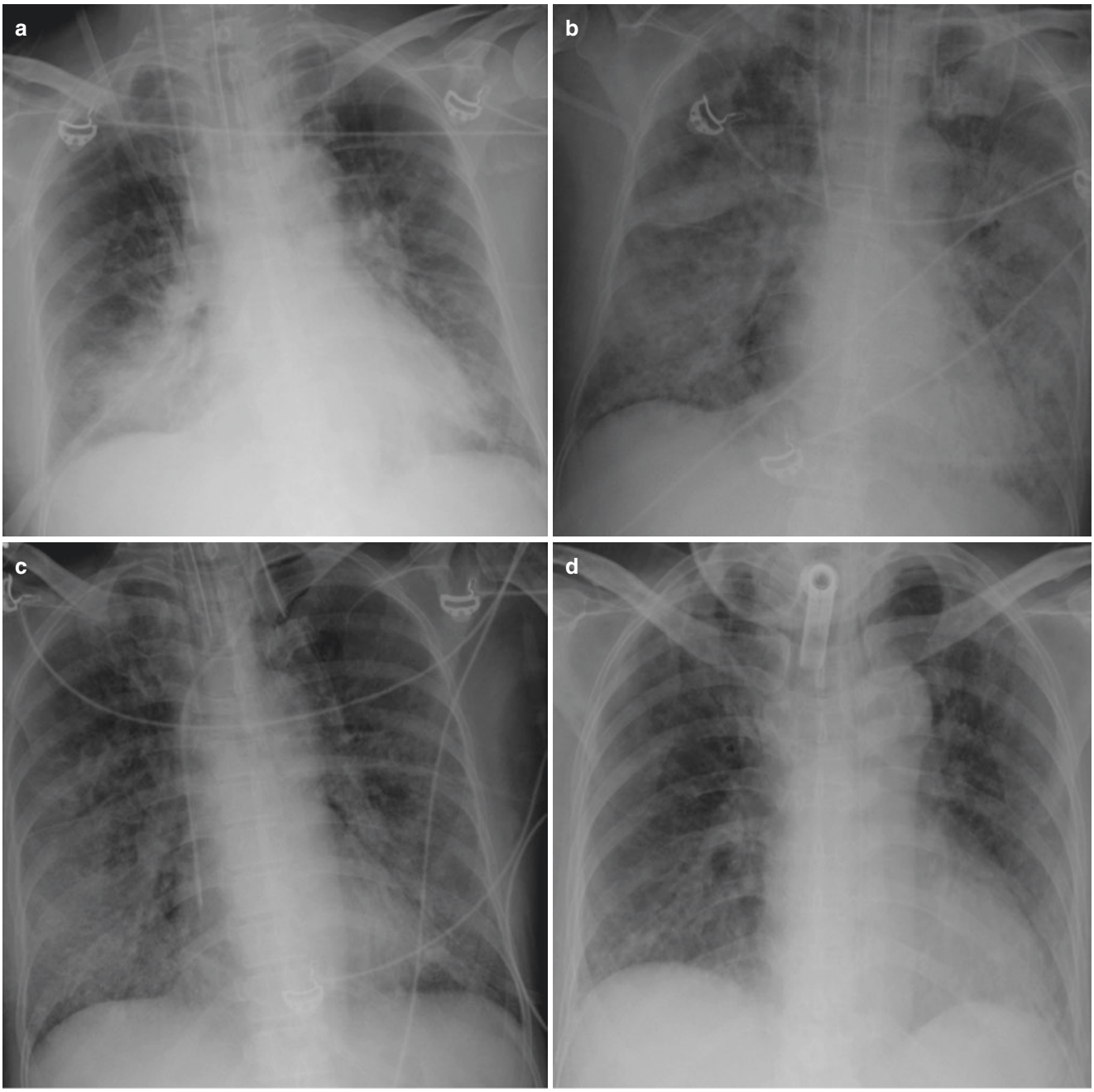

Fig. 7.5 Acute respiratory distress syndrome (ARDS). (**a**) AP bedside chest radiograph of a patient admitted to ICU with severe pneumonia demonstrates dense right lower zone consolidation from pneumonia, (**b**) rapidly progressing to extensive bilateral central consolidation representing the exudative phase of ARDS. (**c**) Follow-up radiographs during extended ICU stay show bilateral reticulonodular opacities and (**d**) patchy linear opacities with some volume loss in the fibrotic phases

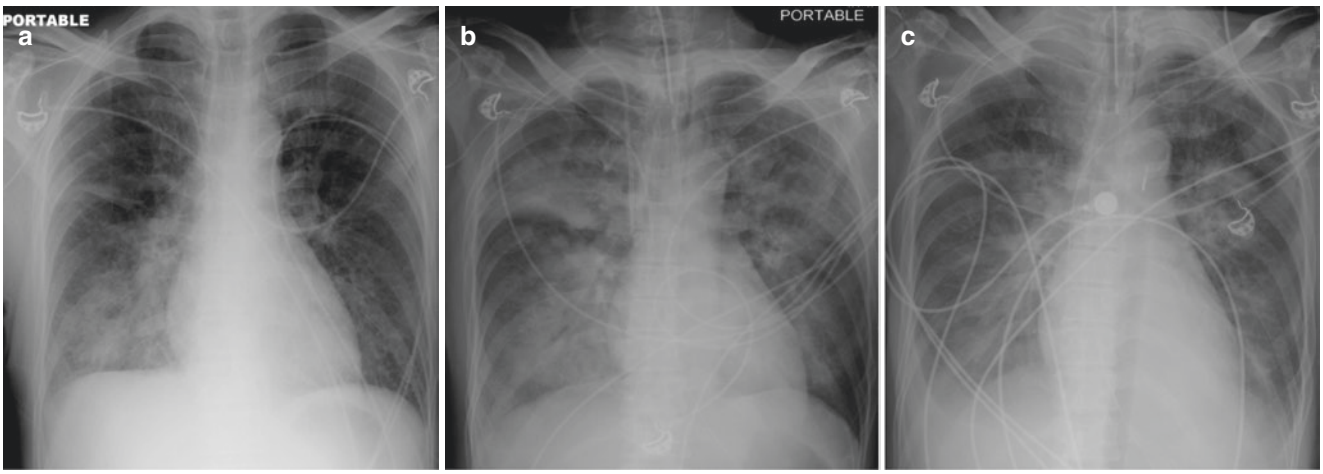

Fig. 7.6 ARDS vs hydrostatic pulmonary edema. (**a**) AP chest radiograph in a patient with pneumonia demonstrates right mid- and lower zone consolidation (**b**) rapidly progressing to bilateral extensive asymmetrical central consolidation with air bronchograms representing an exudative phase of ARDS. (**c**) AP chest radiograph of the same patient obtained 1 month later during ICU stay for acute myocardial infarction demonstrates bilateral symmetrical central consolidation with bilateral pleural effusions from alveolar phase of hydrostatic pulmonary edema. Note the intra-aortic balloon pump

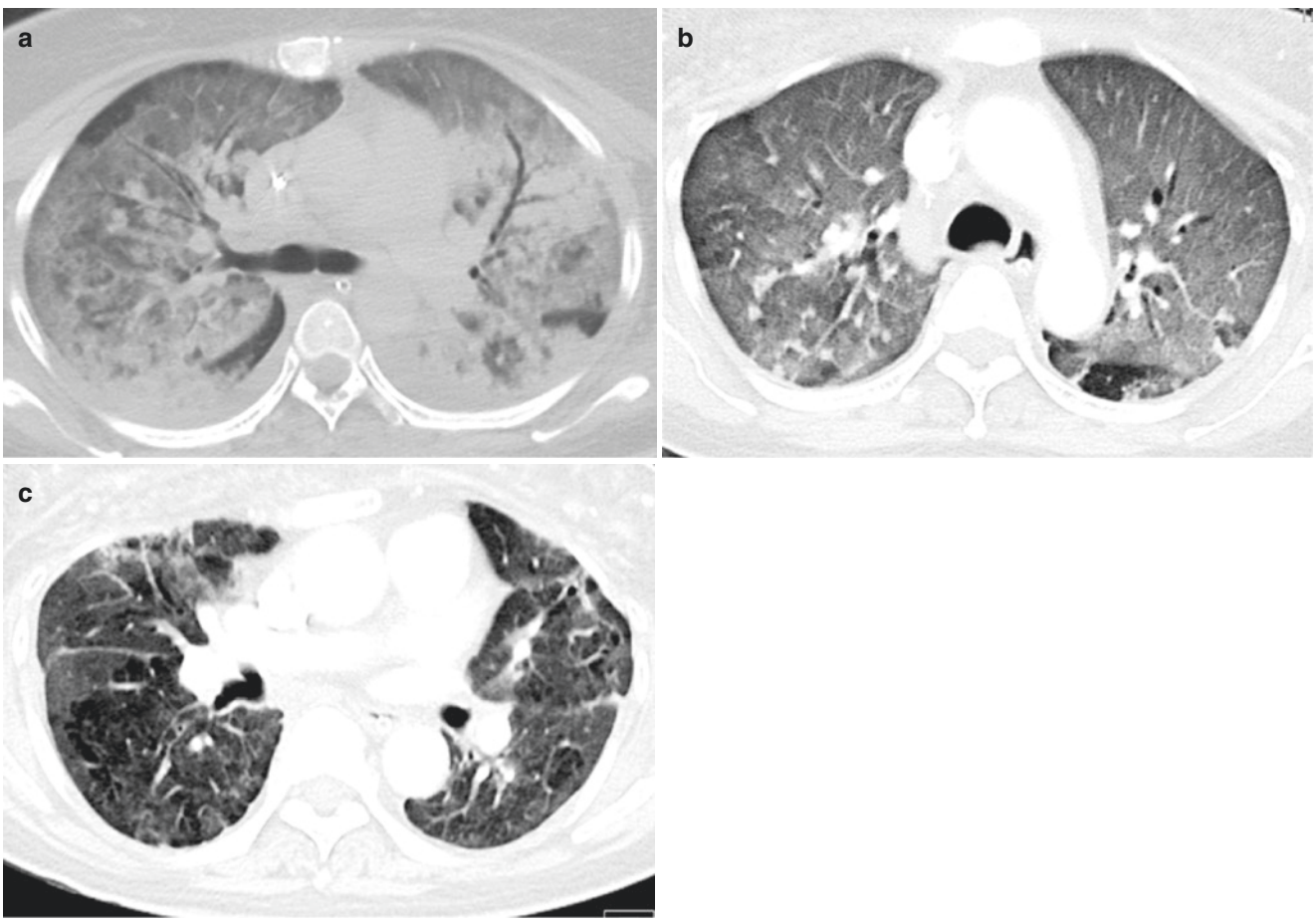

Fig. 7.7 CT features of ARDS. (**a**) Axial CT images in lung window demonstrating exudative phase of ARDS with bilateral dense consolidation in the dependent posterior parts of the lungs and ground-glass densities anteriorly. This gravitational gradient may change with prone position. (**b**) During later phase, reticular changes with ground-glass opacities are seen, (**c**) which progress to patchy areas of scarring

Table 7.3 Imaging clues: HPE vs ARDS

	HPE	ARDS
Heart size	Usually increased	Often normal
Vascular pedicle width	Increased or normal	Normal
Distribution of opacities	Central, even, often symmetric	Peripheral, patchy, often asymmetric
Air bronchograms	Usually absent	Common
Pleural effusion	Very common	Not common
Course	Opacities clear fast	Opacities last longer May progress to fibrotic phase

7.2.3 Pneumonia

Mechanical ventilation and aspiration are two main risk factors for pneumonia in ICU patients. Ventilator-associated pneumonia can occur in up to 24% of patients after 2 days of ventilation [11]. The diagnosis of pneumonia in ICU patients is often challenging as the airspace opacities seen on chest radiographs in these patients can be caused by atelectasis, aspiration, pulmonary hemorrhage, noninfectious lung inflammation (e.g., drug reaction), pulmonary edema, or

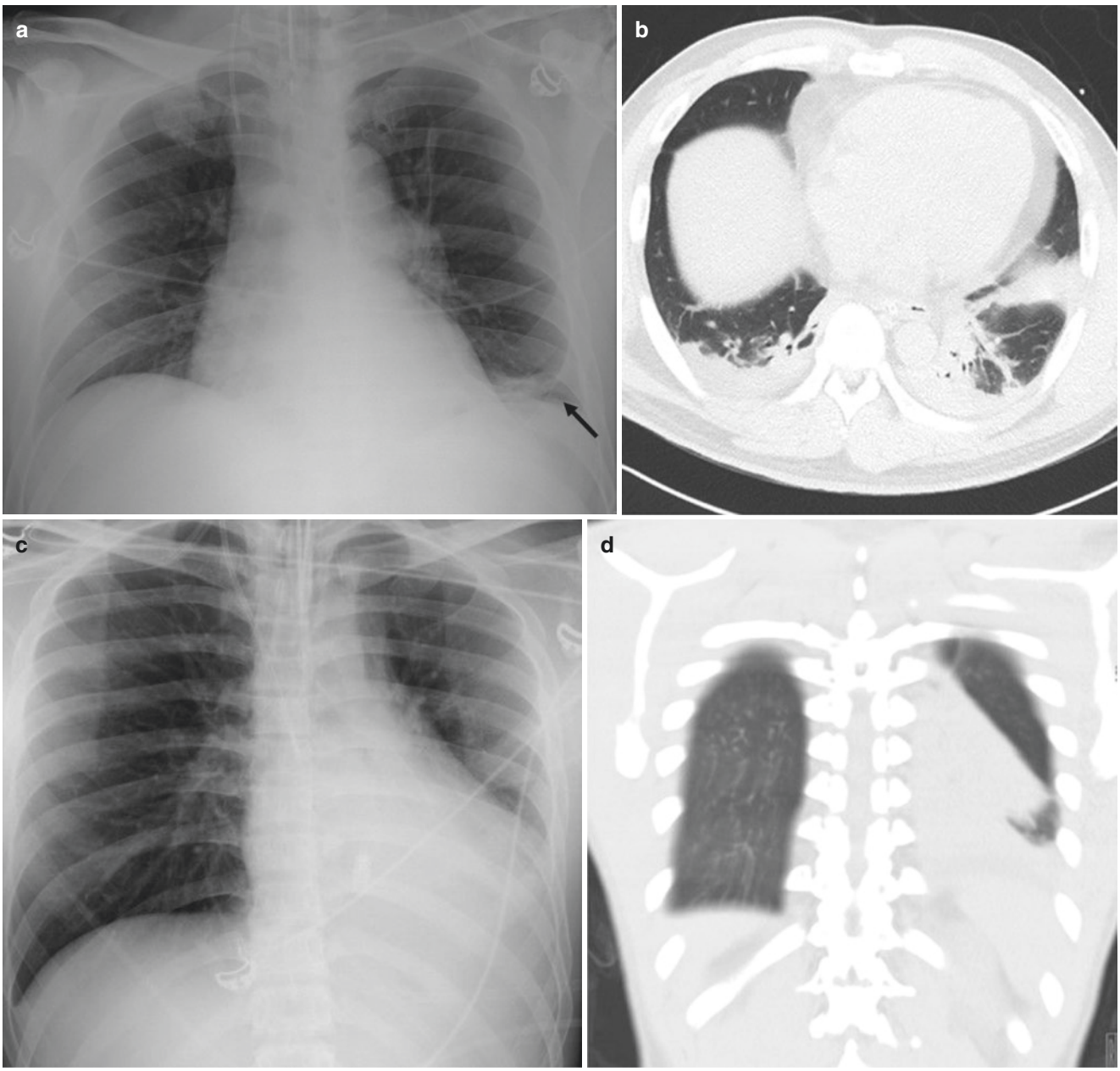

Fig. 7.8 Atelectasis. (**a**) AP chest radiograph of a postoperative patient demonstrates band-like opacity in the left lower zone. (**b**) Corresponding axial CT image in lung window demonstrates bilateral lower lobe densities with crowding of airways and wedge-shaped opacity in the lingula. (**c**) AP chest radiograph in another patient demonstrates left retrocardiac opacity with silhouetting of hemidiaphragm and signs of volume loss in the left lung. (**d**) Coronal CT image confirms the radiographic findings of left lower lobe collapse which often occurs from mucus plugging of the lobar bronchus in ICU patients

ARDS [12]. However, there are certain features that may favor pneumonia (Table 7.4). Air bronchograms typically associated with pneumonia result from the complete filling of the alveolar spaces around nonobstructed bronchi. However, when the airways get filled with mucus, air bronchograms are not seen on imaging which is often the case in critically ill patients (Fig. 7.9).

On CT, pneumonia can often be differentiated from atelectasis by lack of signs of volume loss. CT may provide additional clues to the possible causative agent of pneumonia. Cavities, upper lobe or superior segment of lower lobe airspace disease, endobronchial spread (tree-in-bud densities), and findings of prior granulomatous disease point toward reactivation tuberculosis (TB). Multiple peripheral lung nodules, solid as well as cavitary, in certain patients (long-term indwelling catheters, endocarditis, or history of IV drug abuse) suggest septic emboli [12]. Widespread bilateral predominantly central ground-glass opacities and cysts with or without spontaneous pneumothorax in immunocompromised patients are features of *Pneumocystis jiroveci* pneumonia (PCP), whereas focal areas of consolidation surrounded by a "halo" of ground-glass suggest angioinvasive aspergillosis [13].

Table 7.4 Imaging features of pneumonia and atelectasis

Pneumonia	Atelectasis
Confluent or nodular opacities	Opacities often linear, band-like, or wedge-shaped (lobar)
Opacities resolve slowly (except aspiration pneumonia)	Opacities appear and resolve rapidly
No signs of volume loss	Signs of volume loss: Crowding of air bronchograms Fissural deviation Mediastinal shift Diaphragmatic elevation
Barely enhances on contrast-enhanced CT as the exudates in alveoli are not vascularized	Acute atelectasis enhances but chronic atelectasis may not enhance

7.2.4 Aspiration

Intubation, diminished cough reflex, sedation, altered mental state, and enteric tube feeding predispose the ICU patients to increased risk of aspiration. The different manifestations of the aspiration include chemical pneumonitis, pneumonia, and airway obstruction. Aspiration of large amounts of severely acidic gastric contents can be fatal, resulting in a severe chemical pneumonitis and ARDS [14].

Aspiration is more common in the right lung, due to the vertical orientation of the right main bronchus. In the supine position, the frequently involved sites are the posterior segments of the upper lobes and superior segment of the lower lobe [12]. The radiographic abnormalities commonly seen with aspiration are patchy ill-defined ground-glass opacities, nodular opacities, or consolidation in the dependent regions of the lungs (Fig. 7.10). The opacities usually are seen over the first 1–2 days in aspiration pneumonitis demonstrating relatively rapid resolution on follow up radiographs. Persisting opacities indicate progression to infectious pneumonia, and this is one important reason for following up the patients on radiographs. The CT better demonstrates the ground-glass changes or consolidation. Areas of necrosis and cavitation can be seen when aspirates contain anaerobic organisms [12]. Tree-in-bud opacities present in the abovementioned dependent distribution are also frequently seen with aspiration [8].

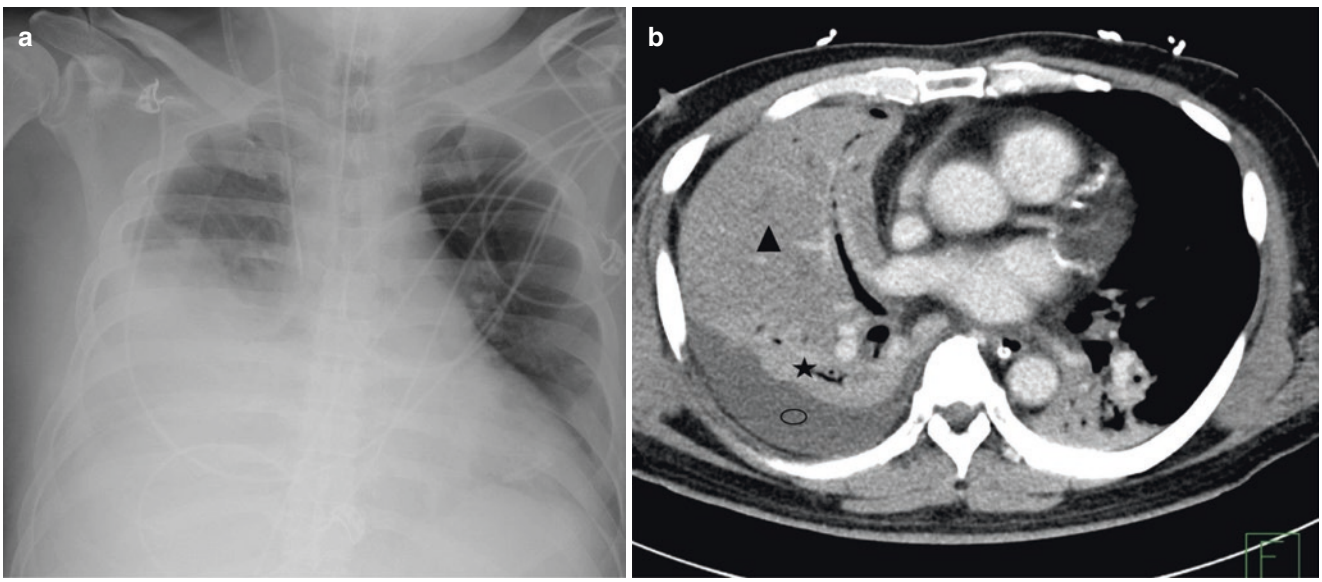

Fig. 7.9 Pneumonia. (**a**) AP chest radiograph of a patient admitted to ICU for severe community-acquired pneumonia demonstrates right mid- to lower zone dense opacity. (**b**) Axial CT image shows the radiographic opacity to be composed of a low attenuation anterior area of consolidation with no air bronchograms from pneumonia (black triangle), higher attenuation atelectasis in the middle (asterisk), and dependent fluid density pleural effusion posteriorly (open circle). A combination of atelectasis and pneumonia is present in the left lower lobe

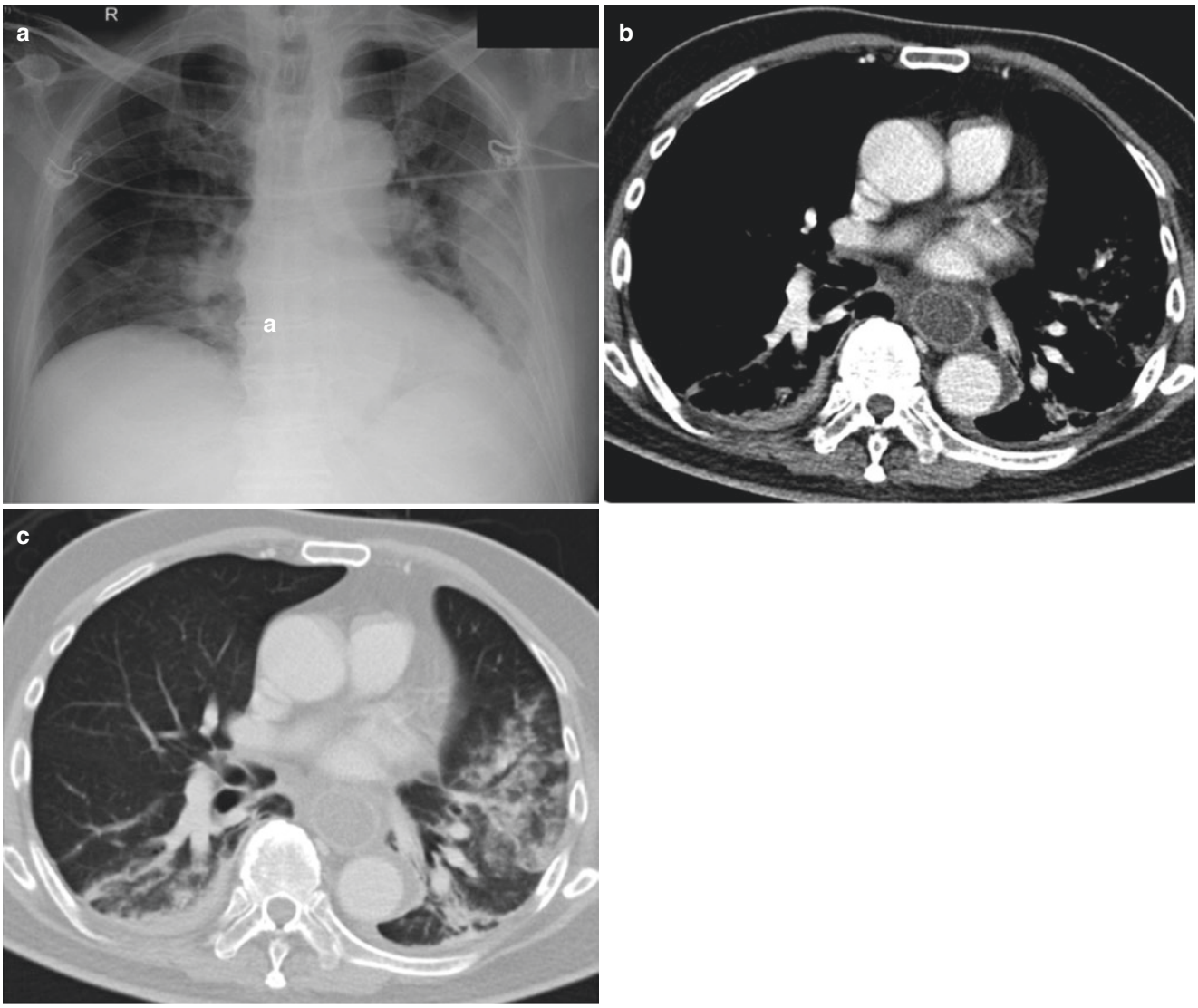

Fig. 7.10 Aspiration. (**a**) AP chest radiograph of a patient with gastric outlet obstruction shows consolidation in peripheral left lung and right central paracardiac region. (**b**) Axial CT image in the soft-tissue window reveals a fluid-filled distended esophagus and patchy opacities in both lower lobes. (**c**) Axial CT image in lung window demonstrates ill-defined ground-glass changes, nodular densities, and patchy consolidation in the dependent regions of both lungs

7.2.5 Pulmonary Hemorrhage

The pulmonary hemorrhage can be localized or diffuse. The localized form is often secondary to bronchiectasis, tumors, or some infections. The diffuse alveolar hemorrhage results from injury to the alveolar microcirculation leading to bleeding into the air spaces [15]. This form is encountered in various autoimmune diseases, bleeding diathesis, vasculitis, certain drugs, and infections (invasive aspergillosis, mucormycosis). In ICU patients, the culprit drugs often are systemic or catheter-directed thrombolytics (for myocardial infarction, PE, or stroke).

The differentiation of pulmonary hemorrhage from pneumonia or pulmonary edema may be difficult. Rapidly developing central and basilar predominant pulmonary parenchymal opacities sparing the costophrenic angles, along with drop in hemoglobin and hemoptysis (or blood in tracheal aspirate), should suggest the diagnosis of pulmonary hemorrhage. On CT scan, patchy ground-glass opacities, typically cloud-like opacities without significant interlobular septal thickening, are seen in the acute phase. In subacute phase, interlobular and intralobular interstitial thickening often develops [15]. Although the CT imaging features are nonspecific, the distribution of these findings, the temporal evolution of opacities, and the radiologic manifestations of predisposing disease (Table 7.5) can help in arriving at the diagnosis [15, 16] (Fig. 7.11).

Table 7.5 Imaging clues to the cause of diffuse alveolar hemorrhage

Wegener's granulomatosis	Cavities, tracheal involvement
Goodpasture's syndrome	Central (edema-like), no pleural effusion
SLE	Pleural and pericardial effusions
Churg-Strauss syndrome	Peripheral predominance, centrilobular nodules, pleural effusions
Long-standing pulmonary venous hypertension	Enlarged left atrium, mitral valve prosthesis/calcifications

7.3 Pulmonary Thromboembolism

The prevalence of pulmonary embolism (PE) in critically ill patients is as high as 27% with only one-third of these cases being suspected clinically [17]. Besides the general risk factors for PE such as obesity, past history of venous thromboembolism, cancer, immobilization, trauma, and recent surgery; the ICU patients are exposed to additional risk factors [18] like sepsis, vasopressor use, pharmacologic seda-

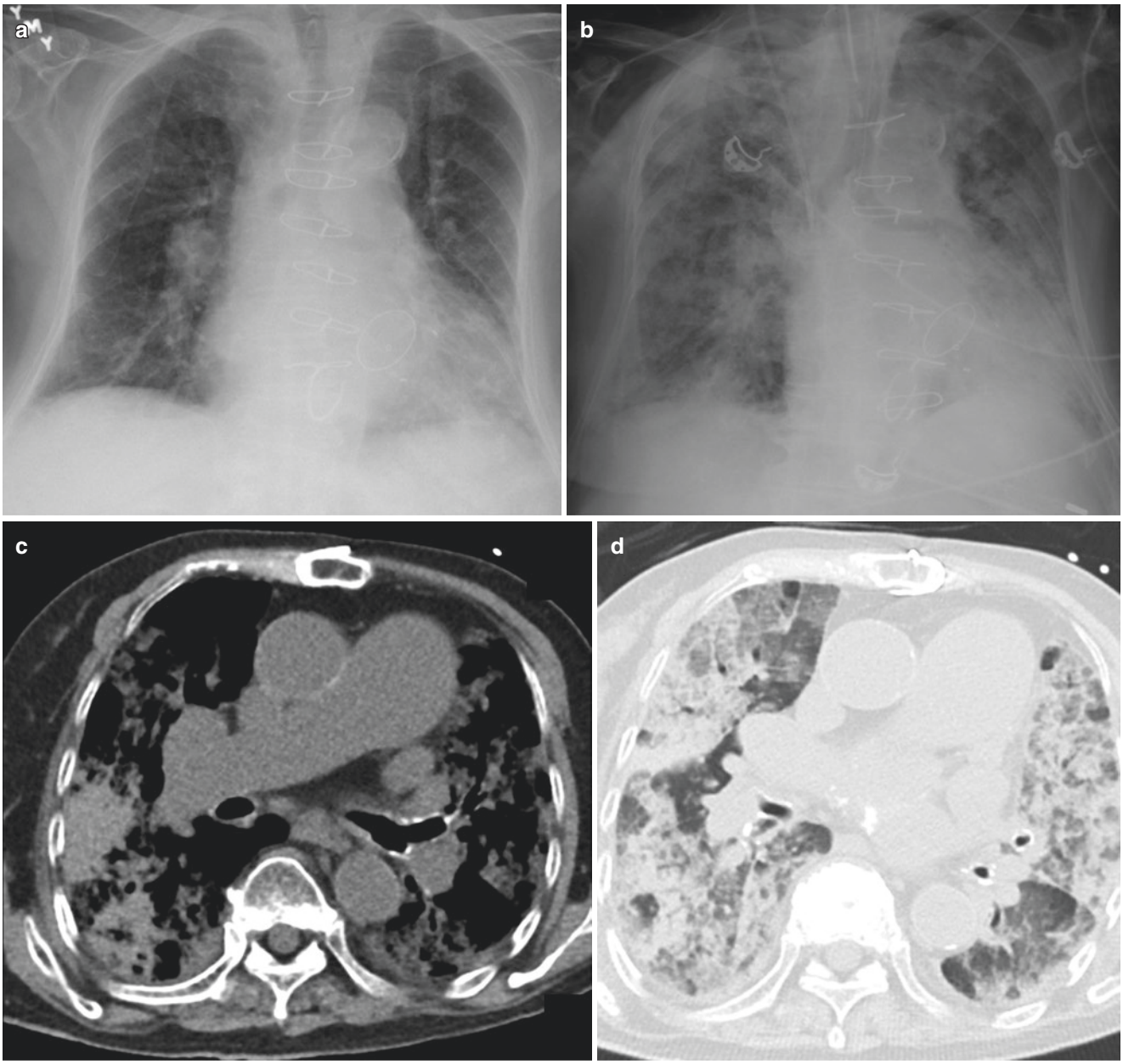

Fig. 7.11 Diffuse alveolar hemorrhage from parainfluenza virus infection. (**a**, **b**) AP chest radiographs taken a day apart, show rapidly progressing diffuse opacities in both lungs with no significant pleural effusion. (**c**) Axial non-contrast CT image shows widespread high attenuation (higher than muscle) patchy consolidation in both lungs. (**d**) On lung window, there are patchy diffuse ground-glass changes and areas of consolidation with no gradient

tion, mechanical ventilation, central venous catheters, and renal failure.

There are various radiographic signs (Table 7.6) described for PE [19–22]. Although these signs are difficult to interpret, their timely recognition might alert the physician to the possibility of PE before it is suspected clinically (Figs. 7.12 and 7.13).

Table 7.6 Radiographic signs of pulmonary embolism

Westermark sign: regional pulmonary oligemia
Fleischner sign: enlargement of the proximal pulmonary arteries
Knuckle sign: abrupt tapering of the occluded pulmonary artery
Hampton's hump: peripheral wedge-shaped opacity without air bronchograms

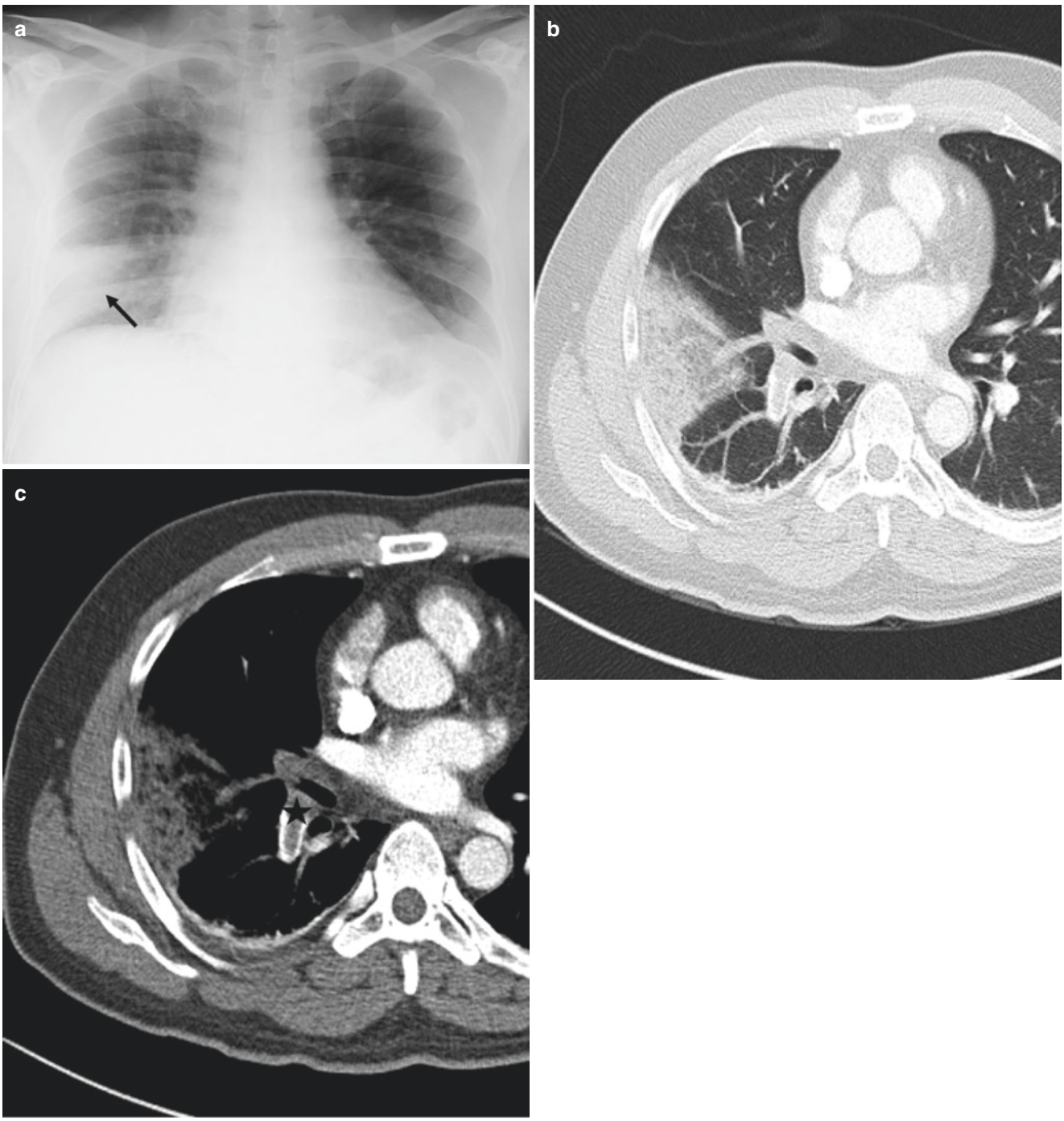

Fig. 7.12 Hampton's hump. (**a**) Peripheral wedge-shaped opacity (black arrow) in right lower zone on AP chest radiograph in a patient with suspected pulmonary thromboembolism. (**b**, **c**) Axial CT images in lung and soft-tissue windows show the typical wedge-shaped configuration of a pulmonary infarct with underlying occlusive thrombus in the right lower lobar artery (asterisk)

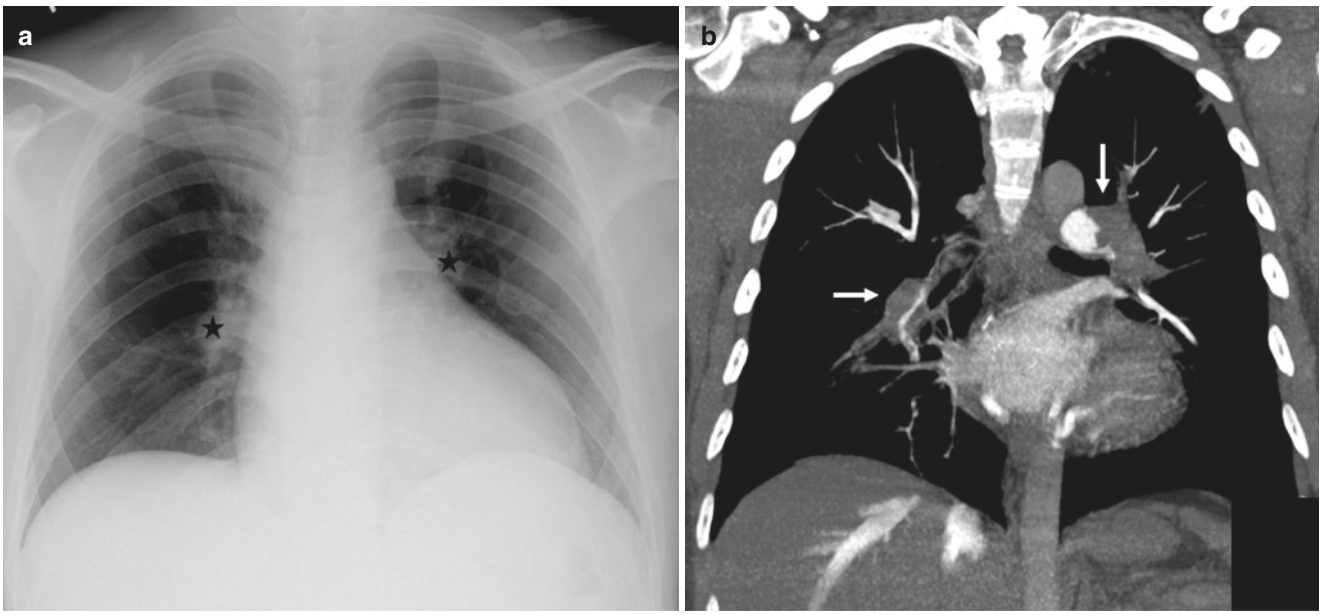

Fig. 7.13 Pulmonary embolism. (**a**) AP chest radiograph shows bilateral upper and mid-zone oligemic regions with increased lung parenchymal lucency (Westermark sign) along with abrupt truncation (arrows) of the right interlobar and left lower lobar arteries (Knuckle sign). (**b**) Coronal thick MIP CT image shows large thrombi in left main and right interlobar arteries (arrows)

CT pulmonary angiography (CTPA) is now the reference standard for diagnosing PE in ICU patients, with most ICUs moving away from the ventilation-perfusion scan and conventional invasive pulmonary angiography. CTPA not only detects PE by direct visualization of the thrombus in pulmonary arteries, it allows risk stratification by providing signs of right heart strain and quantification of thrombus burden. An RV/LV ratio > 0.9–1.5 has been shown to predict adverse outcomes similar to the echocardiographic measurements [23]. Newer CT techniques, such as dual-energy CT, can be used to assess functional lung perfusion [24] as well as reduce contrast burden in ICU patients who are prone to acute kidney injury [25].

7.4 Barotrauma

Barotrauma, particularly the pneumothorax, remains a common ICU complication despite continuously improving mechanical ventilation strategies of low tidal volumes and plateau pressures [26]. The other forms of barotrauma are pneumomediastinum, pneumopericardium, pneumoperitoneum, subcutaneous emphysema, and interstitial emphysema. Even a small pneumothorax can rapidly progress to tension pneumothorax in ventilated patients. The typical appearance of a thin curvilinear line, bordered by the lung on one side and pleural air space devoid of lung markings on the other, is often absent in the supine radiographs.

In the supine position, air collects to the least dependent anteromedial pleural space (Fig. 7.14) resulting in increased radiolucency at the bases and sharply elongated cardiophrenic and costophrenic sulci (the deep sulcus sign) [27]. CT is useful for evaluation of loculated air collections and guides the proper placement of chest tube when pneumothorax persists.

Pneumomediastinum (Fig. 7.15) in ventilated patients most commonly occurs from the rupture of the terminal airways. The pressure gradient between an alveolus and the interstitium directs the air from the ruptured alveolus to the perivascular and peribronchial fascial sheath. The fascial sheath at the lung root gives away letting the air escape into the mediastinum. With increasing severity, the air overflows into the subcutaneous tissues of the neck and into the retroperitoneum [28]. Pneumomediastinum can also be seen in tracheobronchial injury, following tracheostomy tube placement, asthma, and esophageal rupture.

7.5 Pleural Fluid

Pleural effusion in ICU patients is mostly transudative. Despite being a common occurrence, it is difficult to detect small to moderate pleural fluid on the supine radiograph. In addition, differentiating it from other causes of lower zone opacities such as consolidation and atelectasis is often not possible. The costophrenic angle is often not blunted on the

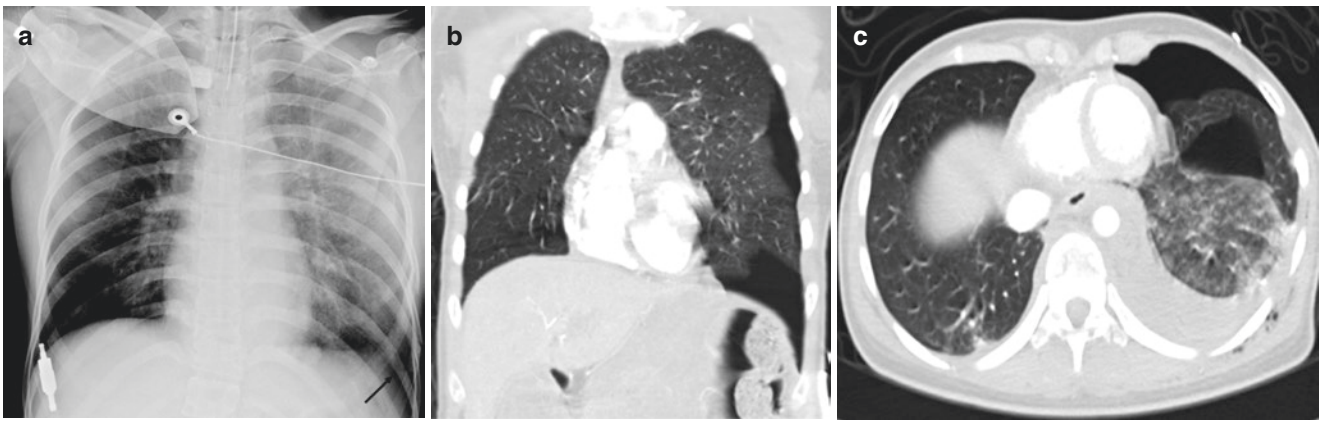

Fig. 7.14 Posttraumatic pneumothorax. (**a**) Supine chest radiograph shows increased lucency at the left lung base with an elongated left costophrenic sulcus (deep sulcus sign). (**b**) Coronal CT image confirms the presence of a pneumothorax. (**c**) Axial CT image demonstrates that the air collects at the most nondependent anteriormedial pleural space on supine position, leading to increased lucency at the lung bases and cardiophrenic angle on the radiograph. Also, note the presence of hemothorax resulting in diffuse haziness over the left lung on the radiograph despite the preserved costophrenic angle

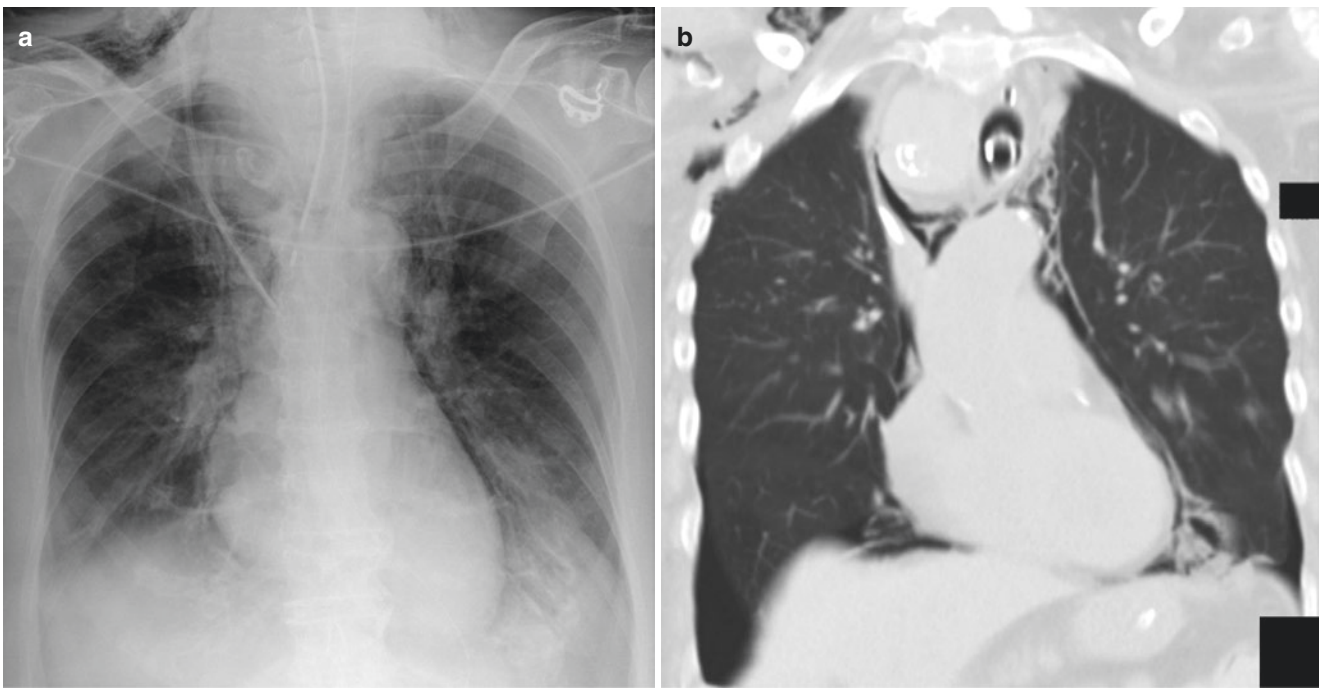

Fig. 7.15 Barotrauma. (**a**) AP chest radiograph in a ventilated patient demonstrates subcutaneous emphysema at the neck base and pneumomediastinum (thin lucencies outlining the arch of aorta, heart borders, and superior vena cava). (**b**) Coronal CT image demonstrates the extent of pneumomediastinum and also shows bilateral pneumothoraces from ventilator-related barotrauma

supine radiograph, and pleural fluid may only demonstrate diffuse hazy "veil-like" opacification from the layering of the pleural fluid (Fig. 7.16). The apex is the most dependent location in supine patients and fluid may manifest as an apical cap [29].

CT helps in differentiating pleural fluid from pulmonary parenchymal disease and better demonstrates the loculated pleural fluid collections. On CT, the thick enhancing visceral and parietal pleura suggests empyema often with a "split pleura" sign. Hemothorax is suggested by increased attenuation of the pleural fluid, commonly 35–70 HU [30]. Ultrasound, readily available as a bedside imaging modality in most ICUs, is very useful in demonstrating loculations and in guiding fluid sampling as well

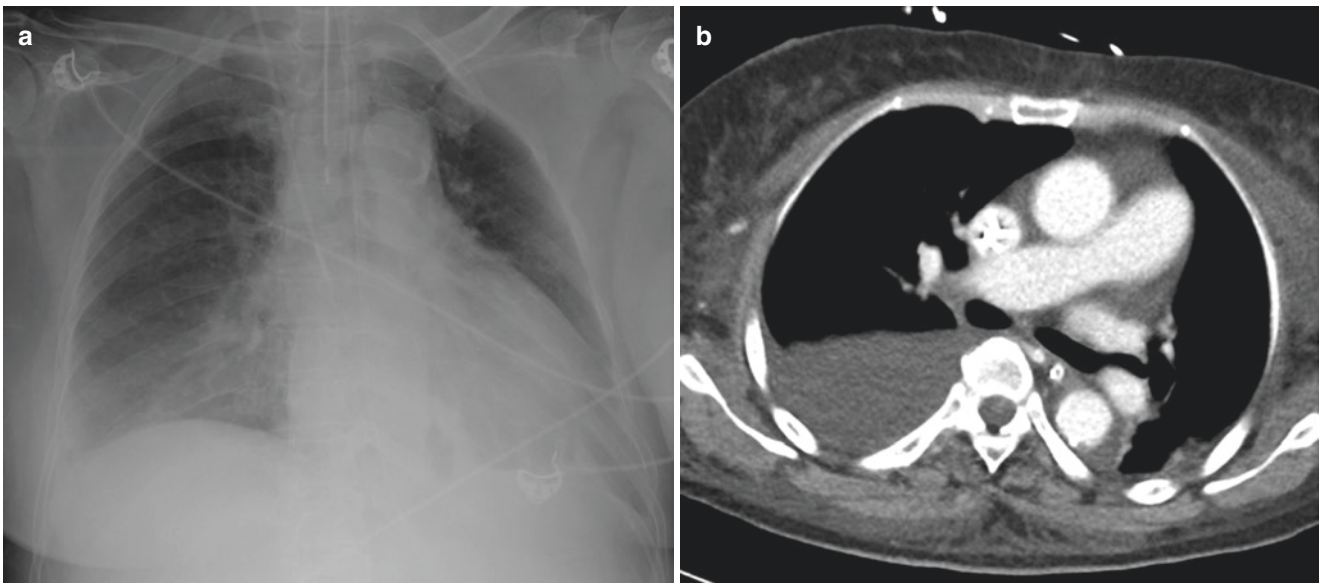

Fig. 7.16 Pleural effusion. (**a**) Supine AP chest radiograph demonstrates diffuse hazy "veil-like" opacification of the right mid- and lower zones, often the only radiographic sign of pleural effusion in ICU patients. (**b**) Axial CT image shows moderate right pleural effusion

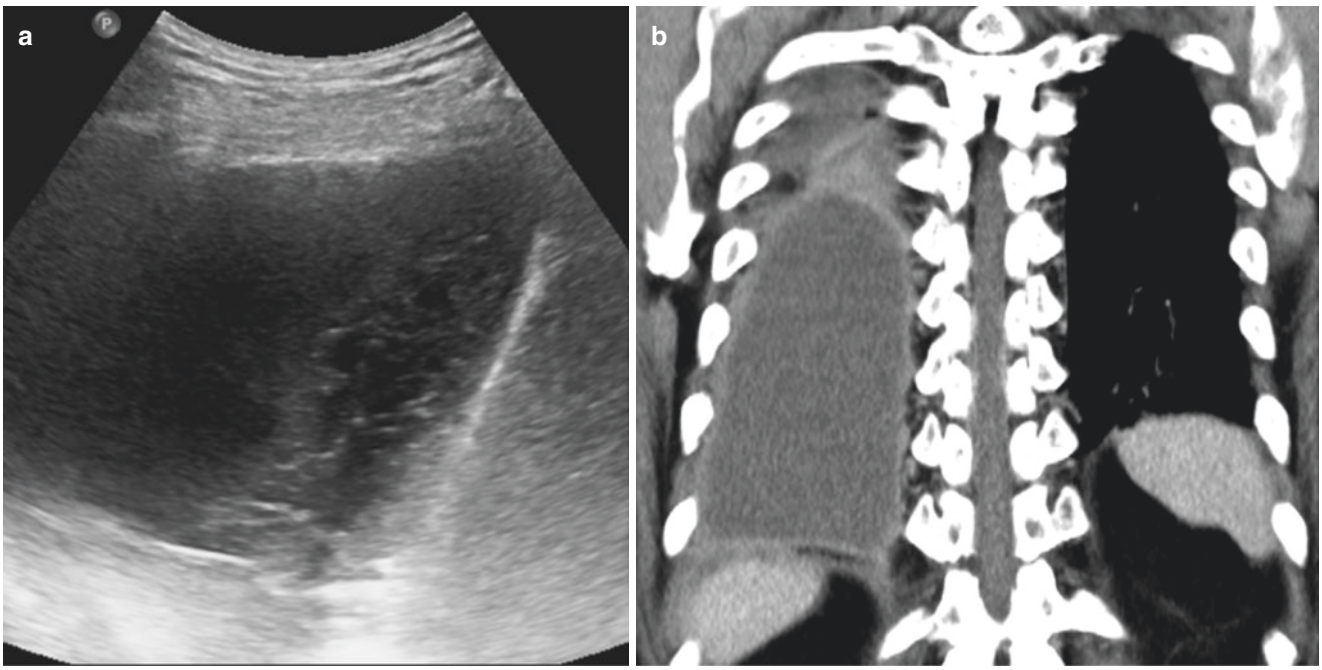

Fig. 7.17 Empyema. (**a**) Bedside ultrasound examination in a patient with pneumonia demonstrates moderate right pleural effusion with irregular echogenic strands (honeycomb appearance). (**b**) Coronal CT image shows diffuse thickening and enhancement of the parietal pleura suggestive of empyema

as therapeutic drainage. On ultrasound examination, complex exudative effusions (parapneumonic, hemothorax, malignant) often demonstrate septations with echogenic strands becoming thicker over time, eventually, thick enough to give a honeycomb-like appearance (Fig. 7.17) [31].

7.6 Tubes and Catheters

Tubes, lines, and catheters are always present in ICU radiographs. One major use of the radiographs in ICU is to check their position and to evaluate any complications related to their insertion (Table 7.7).

Table 7.7 Guidelines of lines/tubes in ICU chest radiographs

Lines/Tubes	Course	Tip	Complications during placement	Complications during daily use
Nasogastric tube	Midline course along the mediastinum, past the carina, past the diaphragm	10 cm past the gastroesophageal junction	Coiled in mouth Too distally past the stomach Pleural cavity Enteric perforation	Aspiration Tube migration Tube breakage
Endotracheal tube	Within tracheal lucency	2–6 cm proximal to the carina	Bronchus intubation Esophageal intubation Tracheal perforation Esophageal perforation	Barotrauma Stenosis
Central catheter	Via (R) internal jugular, into SVC—catheter should be vertically orientated Via (R)/(L) subclavian vein, into SVC—catheter should pass below level of the clavicle, then curves downward	Lower SVC above cavoatrial junction	Incorrect intravascular placement Into the right atrium/ventricle Azygos vein Incorrect extravascular placement Pleura Mediastinum Pericardium	Catheter migration
Dialysis catheter	Same as central catheters	Cavoatrial junction In (R) atrium	Same as above	Same as above
Chest tubes Pleural drains	Anterosuperiorly for pneumothorax Posteroinferiorly for pleural effusion/hemothorax	Variable	Malposition Lung parenchyma Interlobar fissure Subcutaneous tissue Mediastinum Pericardium/myocardium Diaphragm	Re-expansion pulmonary edema
Swan-Ganz catheter	From venous system into the (R) atrium, (R) ventricle, into pulmonary artery	(When not in use) the tip should be no more distal than the proximal interlobar pulmonary artery, ideally in main pulmonary artery—within mediastinal shadow. Must not be >1 cm lateral to mediastinal margin	Malposition IVC Intracardiac	Intracardiac knotting Pulmonary artery rupture Pulmonary infarct Cardiac rupture
Intra-aortic balloon pump	Passes retrograde from the femoral artery into the proximal descending thoracic aorta	Radiopaque marker at tip should align with the thoracic aorta and lie just below the aortic arch	Arterial dissection Malposition	Balloon migration
Pacing leads/ wires	Atrial pacing Ventricular pacing	Atrial appendage Apex	Puncture of the pleura Puncture of the mediastinum Puncture of the myocardium	Lead fracture Lead migration/ displacement

7.6.1 Endotracheal and Tracheostomy Tubes

Endotracheal tubes (ETT) are used for short-term respiratory support with mechanical ventilation. The tip of endotracheal tube should be located about 5 cm above the carina when the patient's head is in a neutral position [32]. The neck flexion moves the tube inferiorly by up to 2 cm, and the neck extension moves it superiorly by the same 2 cm, hence the saying "the hose goes with the nose" [5]. Intubation of the main bronchi (most frequently right sided) may result in subsegmental atelectasis (Fig. 7.18), segmental collapse, or complete collapse of the contralateral lung and puts the ipsilateral lung at risk of pneumothorax from overventilation. The too high a position of ETT can lead to inadvertent extubation or damage to the larynx. Overinflation of the endotracheal balloon cuff beyond the normal tracheal diameter chronically can lead to tracheal stenosis or may rarely result in acute rupture [33]. The tracheal rupture however mostly occurs in the peri-intubation period, through the membranous trachea within 7 cm of the carina [34]. Difficult intubation can occasionally result in hypopharyngeal injury (Fig. 7.19).

Tracheostomy tubes are placed when long-term intubation is necessary. The tracheostomy tube tip should be approximately at mid-T3 level. The tracheostomy tube maintains its position during neck movements. Pneumomediastinum can occur following an uncomplicated tracheostomy tube insertion.

7.6.2 Enteric Tubes

Nasogastric tubes are the most commonly used for feeding, medication administration, and suctioning of gastric contents.

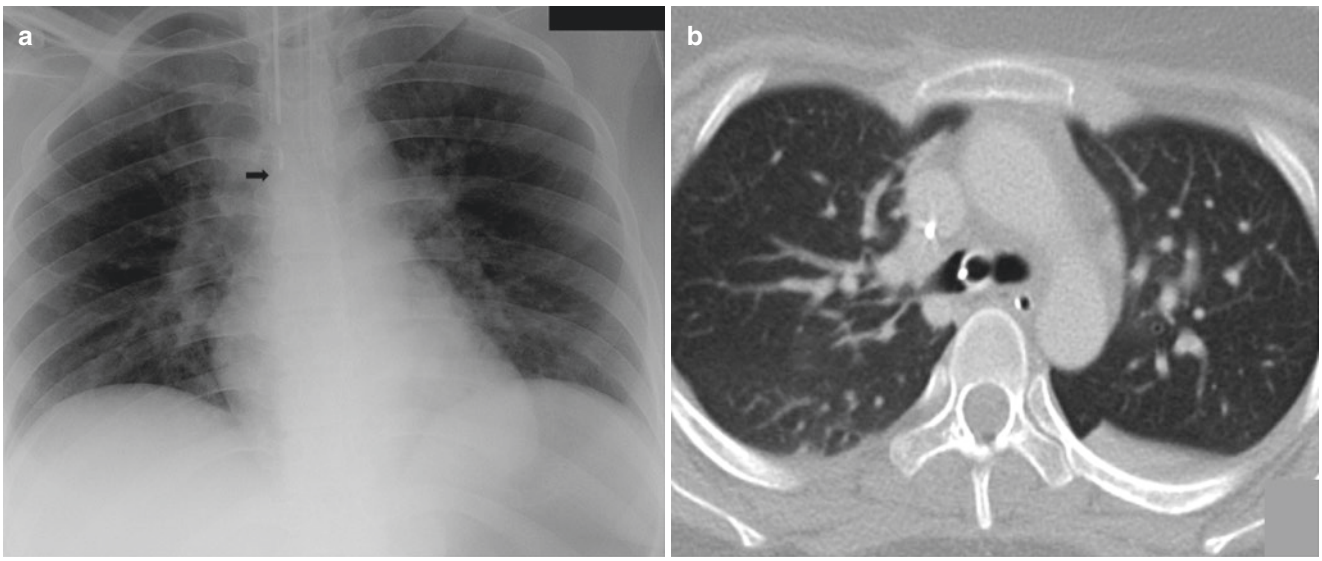

Fig. 7.18 Endotracheal tube malposition. (**a**) AP chest radiograph shows the tip of the endotracheal tube at the carina. (**b**) Axial CT image demonstrates the end of the endotracheal tube to be projected in the right main bronchus

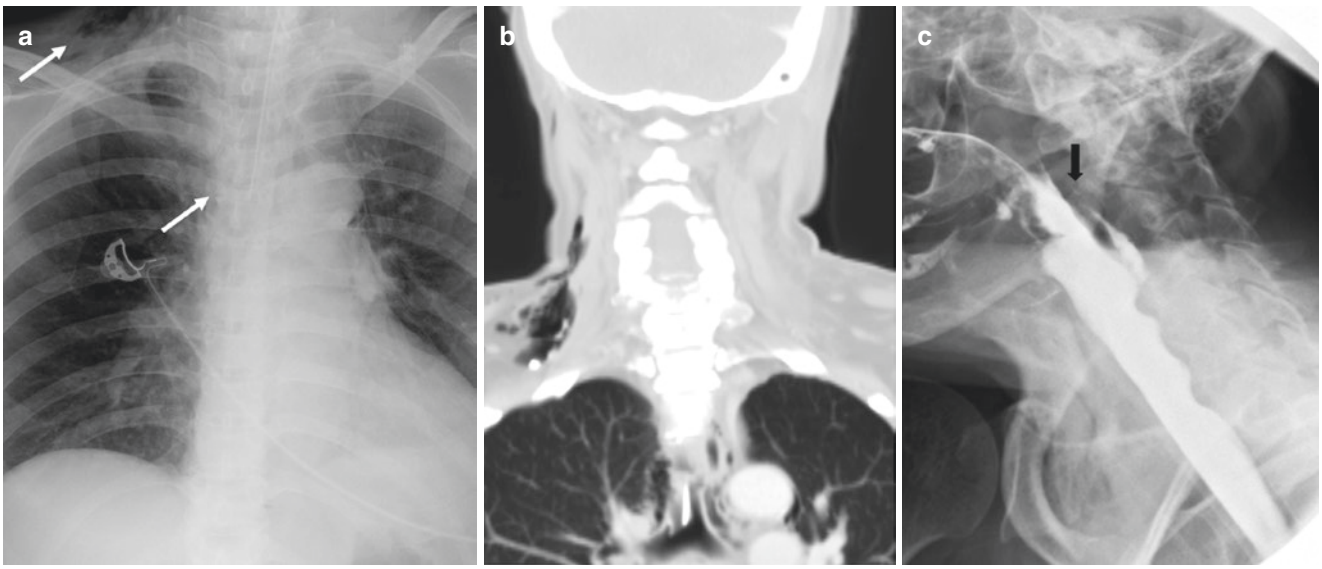

Fig. 7.19 Traumatic intubation. (**a**) AP chest radiograph demonstrates superior mediastinal and neck base linear and curvilinear lucencies. (**b**) Coronal CT image confirms pneumomediastinum and neck emphysema. (**c**) Water-soluble contrast study shows a defect in the posterior wall of the hypopharynx

The tip of a feeding tube should be ideally in the antrum of the stomach or distal to it (post-pyloric) to reduce the risk of aspiration. The proximal side hole of a nasogastric tube should extend beyond the gastroesophageal junction [35]. The bedside chest radiograph is the most important investigation to detect tube malposition. The enteric tubes can coil within the pharynx or esophagus, resulting in high risk of aspiration, or very rarely esophageal perforations. The nasogastric tubes occasionally may terminate in the large airways (Fig. 7.20) where ectopic feeding can result in direct bronchopulmonary injury, pneumonia, pneumothorax, pulmonary laceration, and pulmonary contusion [5].

The gastric feeding tubes are easier to insert than small bowel feeding tubes, allowing early initiation of enteral feeds, and are almost always placed at the time of ICU admission. Small bowel feeding tubes (nasojejunal or percutaneous jejunostomy) are reserved for patients who have high gastric residual volumes despite the use of prokinetics [36].

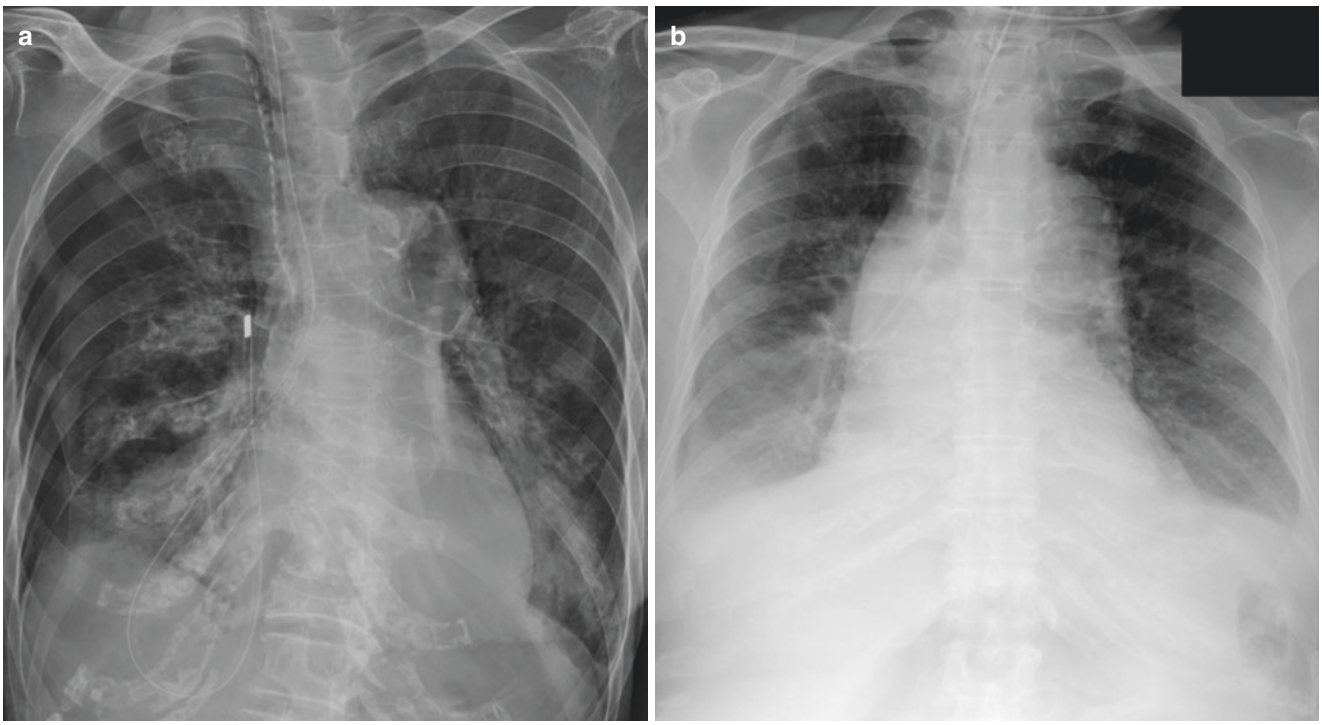

Fig. 7.20 Malpositioned nasogastric tube. (**a**) AP radiograph shows a nasogastric tube traversing the right main bronchus and coiling in the pleural space with a moderate pneumothorax. (**b**) AP radiograph in another patient shows feeding tube terminating in the bronchus intermedius

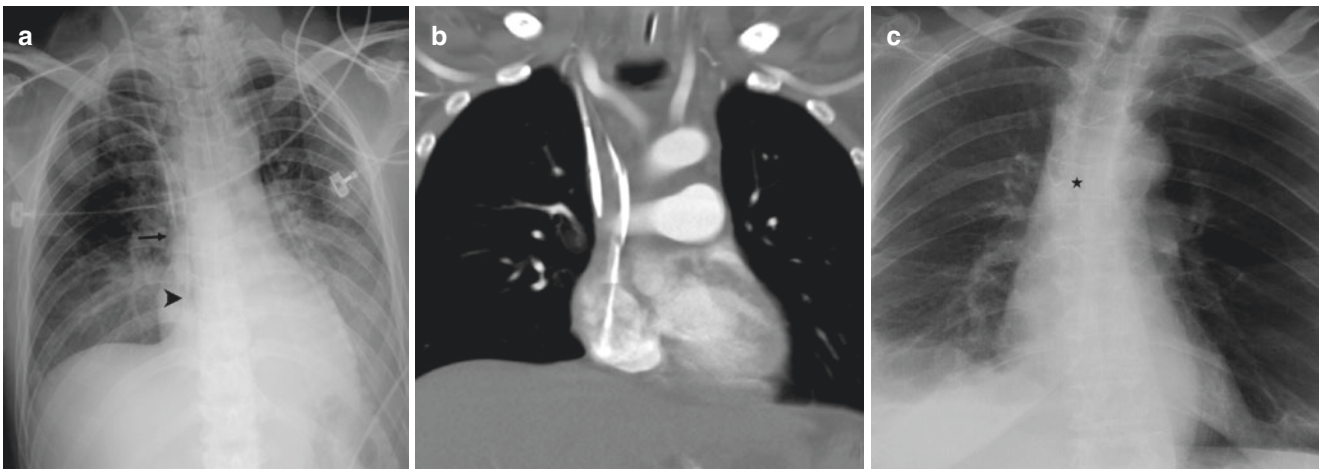

Fig. 7.21 Normal tip position of central venous catheters. (**a**) AP radiograph shows the tip of the right internal jugular central venous catheter at the level of the bronchus intermedius (arrow) and a right peripherally inserted central catheter (PICC) with its tip 2 cm caudal to the lower margin of the bronchus intermedius (arrowhead). (**b**) Coronal CT image confirms the tip of the internal jugular catheter to be in mid/distal superior vena cava and tip of PICC in the superior cavoatrial junction. Bronchus intermedius on AP chest radiographs serves as a good guide to distal SVC where the tip of central venous catheters should be positioned. (**c**) Malpositioned PICC in another patient with its tip in azygos vein, characteristically arching in right tracheobronchial angle (asterisk), the expected location of the azygos vein

7.6.3 Vascular Catheters

The tip of the central venous catheter should be distal to the last venous valve, which is located at the junction of the internal jugular and the subclavian veins. On the CXR, the position of the valve corresponds to the inner aspect of the anterior first rib [35]. A catheter is more likely to get blocked from thrombosis around it when its position is in proximal SVC or at the thoracic inlet than in the distal SVC or at the cavoatrial junction [37]. The inferior border of bronchus intermedius serves as a good guide to the distal SVC (Fig. 7.21). On the CXR, the cavoatrial junction corresponds to the lower border of the bronchus intermedius, while the arch of azygos is located at the right tracheobronchial angle

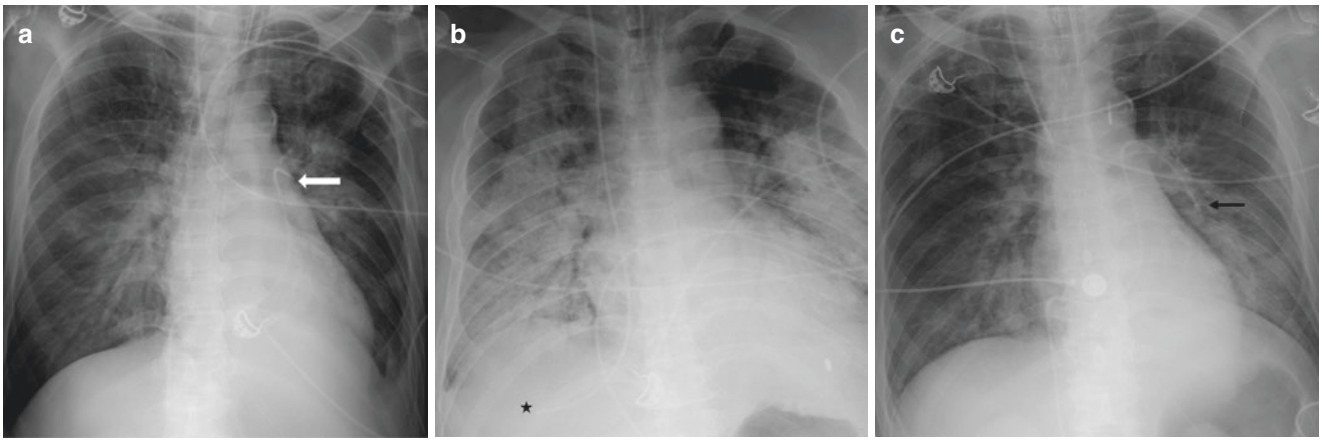

Fig. 7.22 Swan-Ganz catheter. (**a**) AP chest radiograph demonstrates a Swan-Ganz catheter inserted via the left subclavian vein with its tip at expected location in the left main pulmonary artery and the tip not extending beyond the pulmonary hilum. (**b**) Chest radiograph in another patient demonstrating an abnormal course of right internal jugular en route Swan-Ganz catheter terminating in the right hepatic vein (asterisk). (**c**) Distal catheter tip position in the left lower lobe pulmonary artery on a chest radiograph of another ICU patient. This position increases the risk of arterial injury or pulmonary infarct

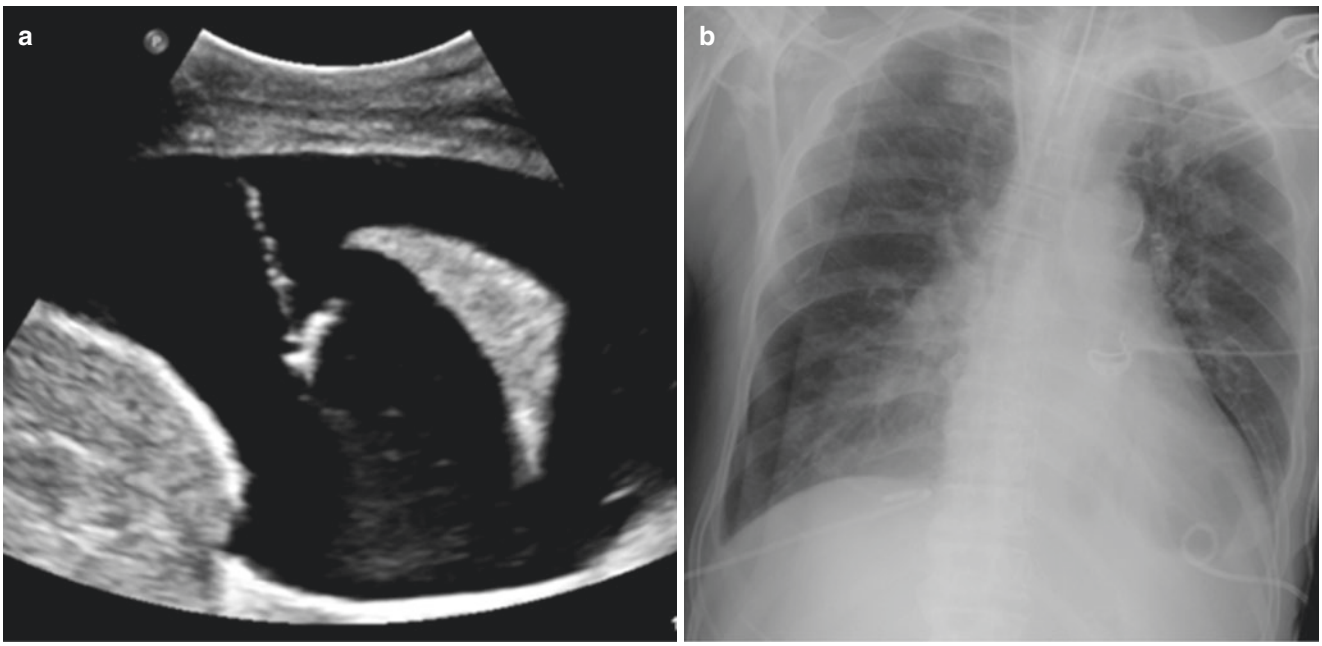

Fig. 7.23 Pleural drain for pleural effusion. (**a**) Ultrasound image after image-guided insertion of the pleural drainage catheter. A large anechoic pleural effusion is seen with collapsed lower lobe and an indwelling pigtail drainage catheter whose distal loop is directed toward the posteromedial pleural space, the most dependent portion of the thorax in the supine position. (**b**) AP chest radiograph shows bilateral pleural drainage catheters directed medially at the lung bases

(superior aspect of the origin of the right bronchus from the carina). Tip of any catheter near the right tracheobronchial angle can slip into azygos vein and result in complications. Azygos location of a catheter tip can be identified by its characteristic orientation and position (Fig. 7.21c). Too caudal a position in right atrium increases the risk of dysrhythmia for small caliber peripherally inserted central lines (PICC) and central venous catheters. The right atrial positioning, however, is desirable for large-caliber dialysis catheters. PICC lines may coil in the veins of the upper extremity, turn cranially into the internal jugular vein, cross to the contralateral brachiocephalic vein, or enter the azygos vein.

Pulmonary artery catheters or Swan-Ganz catheters are placed primarily to measure pulmonary capillary wedge pressure, which helps to differentiate cardiogenic pulmonary edema from non-cardiogenic pulmonary edema. The catheter tip should lie in the main pulmonary arteries or the proximal lobar pulmonary artery (Fig. 7.22). The catheter tip

should not extend beyond the pulmonary hilum on the chest radiograph [38]. A further distal catheter tip increases the risk of arterial injury and pulmonary infarction. Pulmonary infarcts may also occur secondary to persistent balloon occlusion or pericatheter thrombus.

7.6.4 Chest Tubes and Pleural Drains

The proper position of the chest tube depends on the contents to be removed from the pleural cavity. The tip of the tube is directed toward the apex for pneumothorax and toward the lung base for fluid drainage (Fig. 7.23). The side holes of the chest tube, identified on radiographs as interruptions of the tube's radiopaque line, should lie within the pleural space. An improper location of chest tube results in poor drainage and accumulation of air or fluid in the chest wall. The ineffective drainage may also result from tube kinking; blockage resulting from blood clots, pus, or debris in the tube; and apposition of the tip against the mediastinum [33].

An intrafissural location of the tube may or may not affect its function; however, rarely it may result in herniation of lung parenchyma into the holes of chest tube leading to infarction [39]. Inadvertent parenchymal insertion of a chest tube (Fig. 7.24) can lead to pulmonary laceration, hematoma, infarction, and bronchopleural fistula. Besides the lung parenchyma, an inappropriately positioned chest tube can injure the heart, great vessels, diaphragm, liver, and spleen [33].

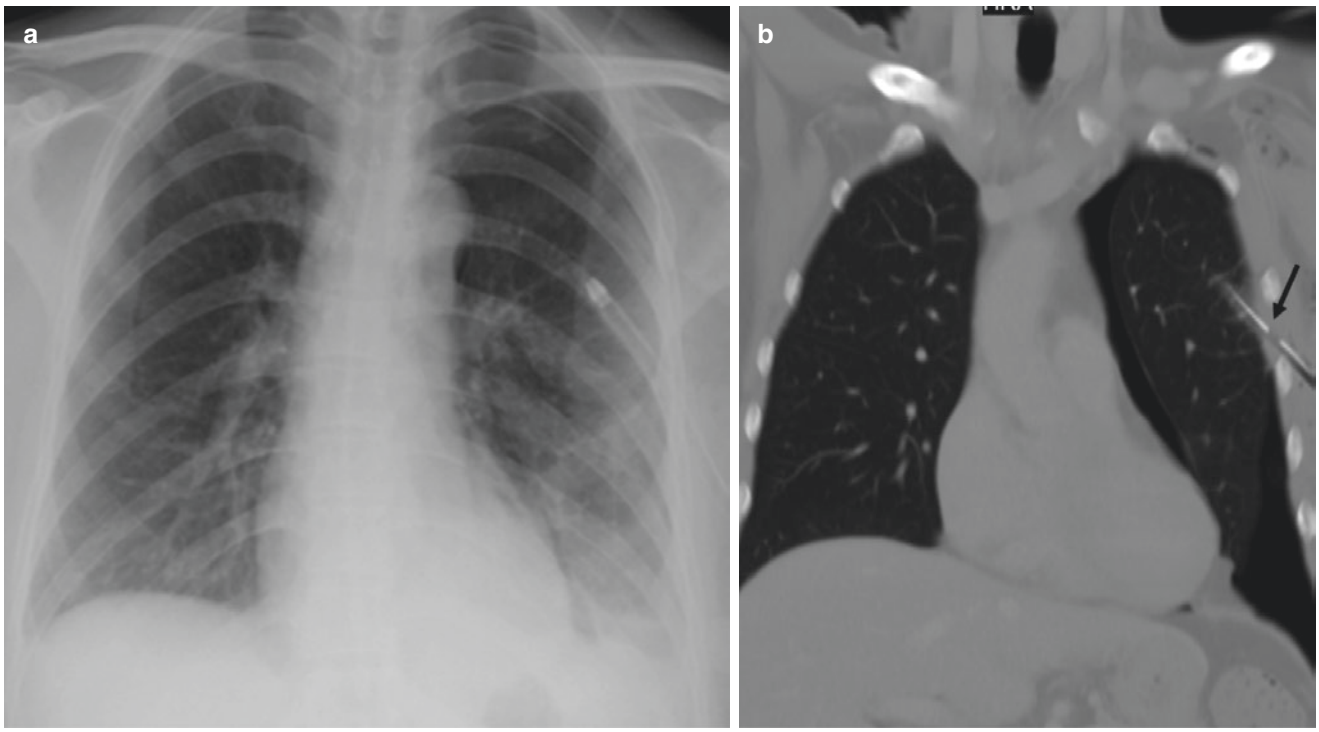

Fig. 7.24 Chest tube for pneumothorax. (**a**) AP chest radiograph shows a large-bore chest tube directed toward the lung apex for drainage of left pneumothorax. The marking for the side hole is not well seen. (**b**) Coronal CT image demonstrates the side hole to be outside the pleural cavity responsible for inadequate drainage. (**c**) AP chest radiograph in another patient after the insertion of chest tube for pneumothorax demonstrates a non-resolving right pneumothorax. (**d**) Axial CT images show the intraparenchymal course of chest tube

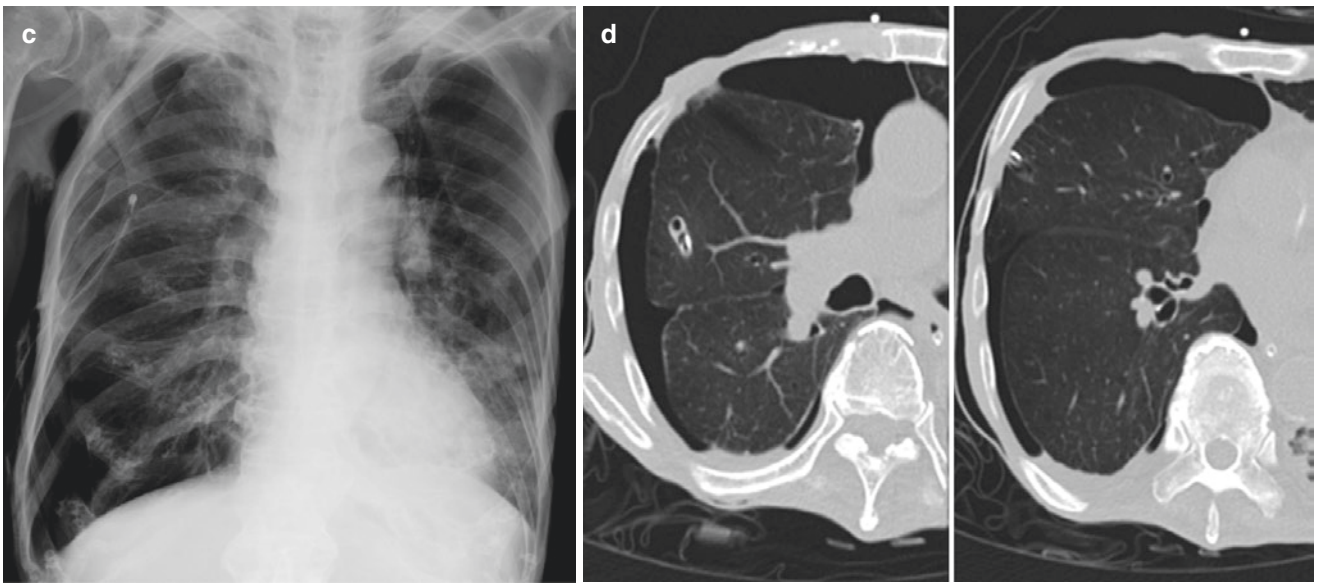

Fig. 7.24 (continued)

Table 7.8 Approach to reporting ICU radiographs

• Compare with as many previous radiographs as possible
• Note the differences in technique, patient position, rotation, and penetration
• Document every new opacity and lucency
• Register the migration of opacities, if any
• Monitor change in mediastinal contour that cannot be explained by the difference in technique and/or rotation
• Mention the site of insertion, course, and tip of all catheters, tubes, and lines
• Check for any prior CT thorax available for any preexisting COPD or fibrotic lung disease
• Wherever possible get the clinical information and answer the question asked in the request form

7.7 Conclusion

Interpretation of ICU radiographs is a challenging task. Important pearls for reporting ICU chest radiographs are summarized in Table 7.8.

References

1. Starling EH. On the absorption of fluids from the connective tissue spaces. J Physiol. 1896;19(4):312–26.
2. Ingram RH Jr, Braunwald E. Dyspnea and pulmonary edema. In: Fauci AS, Braunwald E, Isselbacher KJ, et al., editors. Harrison's principles of internal medicine. 14th ed. New York, NY: McGraw-Hill; 1998. p. 190–4.
3. Gluecker T, Capasso P, Schnyder P, Gudinchet F, Schaller MD, et al. Clinical and radiologic features of pulmonary edema. Radiographics. 1999;19(6):1507–31.
4. Cardinale L, Volpicelli G, Lamorte A, Martino J, Veltri A. Revisiting signs, strengths and weaknesses of standard chest radiography in patients of acute dyspnea in the emergency department. J Thorac Dis. 2012;4(4):398–407.
5. Bentz MR, Primack SL. Intensive care unit imaging. Clin Chest Med. 2015;36(2):219–34.
6. Definition Task Force ARDS. Acute respiratory distress syndrome: the Berlin definition. JAMA. 2012;307(23):2526–33.
7. Desai SR, Wells AU, Suntharalingam G, Rubens MB, Evans TW, Hansell DM. Acute respiratory distress syndrome caused by pulmonary and extrapulmonary injury: a comparative CT study. Radiology. 2001;218(3):689–93.
8. Rossi SE, Erasmus JJ, Volpacchio M. "Crazy-paving" pattern at thin-section CT of the lungs: radiologic-pathologic overview. Radiographics. 2003;23:1508–19.
9. Ichikado K, Suga M, Muranaka H, Gushima Y, Miyakawa H, Tsubamoto M, et al. Prediction of prognosis for acute respiratory distress syndrome with thin-section CT: validation in 44 cases. Radiology. 2006;238(1):321–9.
10. Shevland JE, Hirleman MT, Hoang KA, Kealey GP. Lobar collapse in the surgical intensive care unit. Br J Radiol. 1983; 56(668):531–4.
11. Morehead RS, Pinto SJ. Ventilator-associated pneumonia. Arch Intern Med. 2000;160:1926–36.

12. Rubinowitz AN, Siegel MD, Tocino I. Thoracic imaging in ICU. Crit Care Clin. 2007;23(3):539–73.
13. Diederich S. Chest CT for suspected pulmonary complications of oncologic therapies: how I review and report. Cancer Imaging. 2016;16:7.
14. Marom EM, McAdams HP, Erasmus JJ, Goodman PC. The many faces of pulmonary aspiration. AJR Am J Roentgenol. 1999;172(1):121–8.
15. Lichtenberger JP, Digumarthy SR, Abbott GF, Shepard JA, Sharma A. Diffuse pulmonary hemorrhage: clues to the diagnosis. Curr Probl Diagn Radiol. 2014;43(3):128–39.
16. Kang J, Litmanovich D, Bankier AA, Boiselle PM, Eisenberg RL. Manifestations of systemic diseases on thoracic imaging. Curr Probl Diagn Radiol. 2010;39(6):247–61.
17. McLeod AG, Geerts W. Venous thromboembolism prophylaxis in critically ill patients. Crit Care Clin. 2011;27:765–80.
18. Cook D, Attia J, Weaver B, McDonald E, Meade M, Crowther M. Venous thromboembolic disease: an observational study in medical-surgical intensive care unit patients. J Crit Care. 2000;15:127–32.
19. Westermark N. On the roentgen diagnosis of lung embolism. Acta Radiol. 1938;19:357–72.
20. Fleischner FG. Roentgen diagnosis of pulmonary embolism. Heart Bull. 1961;10:104–7.
21. Williams JR, Wilcox WC. Pulmonary embolism: roentgenographic and angiographic considerations. AJR Am J Roentgenol. 1963;89:333.
22. Hampton AO, Castleman B. Correlation of postmortem chest teleroentgenograms with autopsy findings with special reference to pulmonary embolism and infarction. AJR Am J Roentgenol. 1940;43:305–26.
23. Gibson N, Sohne M, Buller H. Prognostic value of echocardiography and spiral computed tomography in patients with pulmonary embolism. Curr Opin Pulm Med. 2005;11(5):380–4.
24. Nikolaou K, Thieme S, Sommer W, Johnson T, Reiser MF. Diagnosing pulmonary embolism: new computed tomography applications. J Thorac Imaging. 2010;25(2):151–60.
25. Yuan R, Shuman WP, Earls JP, Hague CJ, Mumtaz HA, et al. Reduced iodine load at CT pulmonary angiography with dual-energy monochromatic imaging: comparison with standard CT pulmonary angiography – a prospective randomized trial. Radiology. 2012;262(1):290–7.
26. Tocino I, Westcott JL. Barotrauma. Radiol Clin N Am. 1996;34:59–81.
27. Tocino IM, Miller MH, Fairfax WR. Distribution of pneumothorax in the supine and semirecumbent critically ill adult. AJR Am J Roentgenol. 1985;144(5):901–5.
28. Zylak CM, Standen JR, Barnes GR, Zylak CJ. Pneumomediastinum revisited. Radiographics. 2000;20:1043–57.
29. Muller N. Imaging of the pleura. Radiology. 1993;186:297–309.
30. Kuhlman JE, Sinha NK. Complex disease of the pleural space: radiographic and CT evaluation. Radiographics. 1997;17(1):63–79.
31. Hallifax RJ, Talwar A, Wrightson JM, Edey A, Gleeson FV. State-of-the-art: radiological investigation of pleural disease. Respir Med. 2017;124:88–99.
32. Goodman LR, Conrardy PA, Laing F, Singer MM. Radiographic evaluation of endotracheal tube position. AJR Am J Roentgenol. 1976;127(3):433–4.
33. Godoy MC, Leitman BS, de Groot PM, Vlahos I, Naidich DP. Chest radiography in the ICU: part 1, evaluation of airway, enteric, and pleural tubes. AJR Am J Roentgenol. 2012;198(3):563–71.
34. Rollins RJ, Tocino I. Early radiographic signs of tracheal rupture. AJR Am J Roentgenol. 1987;148:695–8.
35. Godoy MC, Leitman BS, de Groot PM, Vlahos I, Naidich DP. Chest radiography in the ICU: part 2, evaluation of cardiovascular lines and other devices. AJR Am J Roentgenol. 2012;198(3):572–81.
36. Marik PE, Zaloga GP. Gastric versus post-pyloric feeding: a systematic review. Crit Care. 2003;7(3):R46–51.
37. Cadman A, Lawrance JA, Fitzsimmons L, Spencer-Shaw A, Swindell R. To clot or not to clot? That is the question in central venous catheters. Clin Radiol. 2004;59:349–55.
38. Kazerooni EA, Gross BH. Lines, tubes, and devices. In: Kazerooni EA, Gross BH, editors. Cardiopulmonary imaging. Philadelphia: Lippincott Williams & Wilkins; 2004. p. 255–93.
39. Stahly TL, Tench WD. Lung entrapment and infarction by chest tube suction. Radiology. 1977;122:307–9.

Imaging of the Mediastinum

8

Ashish Chawla and Tze Chwan Lim

8.1 Introduction

Mediastinal abnormalities are generally uncommon—the most frequently encountered abnormality being mediastinal masses. Chest radiograph still remains the initial investigation of choice in patients with mediastinal abnormalities. Rarely, a mediastinal mass may be identified in an asymptomatic patient on routine screening chest radiograph. Hence, the radiologist must be aware of the signs of identifying and localizing mediastinal masses. The signs may not be specific; hence a sign in isolation is inadequate in diagnosis. However, a combination of imaging signs helps in accurate localization of a mediastinal mass on a chest radiograph. The absence of a sign is equally important in localization of an abnormality. CT is the investigation of choice for further characterization, assessing the extent of disease, and staging of mediastinal masses. Similarly, mediastinitis and pneumomediastinum are initially evaluated by chest radiographs and usually followed by a CT examination.

8.2 Radiological Anatomy of Mediastinum

There are no true anatomic compartments within the compact mediastinum, where various structures are placed close to each other, behind the sternum. Felson suggested an arbitrary division of the mediastinum from the radiography perspective [1]. In the Felson model, an arbitrary line traced upward from the diaphragm, along the back of the heart and front of the trachea, to the neck, separates the anterior mediastinum from the middle mediastinum. A second vertical line connecting points 1 cm behind the anterior margin of the thoracic vertebral bodies separates the middle mediastinum from the posterior mediastinum. In this model, the central airways, esophagus, lymph nodes (except prevascular nodes), aortic arch, and azygos vein are included in the narrow middle mediastinum. Anterior mediastinum includes the thyroid (if enlarged), heart, ascending aorta, and prevascular space, while contents of the paravertebral gutter, spine, posterior ribs, and overlying paraspinal musculature are within the posterior compartment.

Another commonly used division of the mediastinum with excellent correlation with CT is to consider pericardium and its contents, ascending aorta, and central airways as the middle mediastinum [2] (Fig. 8.1). Anterior mediastinum lies anterior to the pericardium, while posterior mediastinum is located posterior to the pericardium and trachea. The esophagus being behind the trachea is included in the posterior mediastinum in this model. An arbitrary line from the manubriosternal joint to the inferior surface of T4 vertebra divides superior mediastinum from the rest of the compartments. In tandem with the wider availability of CT, the role of radiography is limited to identification of mediastinal masses and follow-up of these patients. Nevertheless, radiologists are expected to comment on the probable location of the mediastinal mass when reporting chest radiographs.

8.3 Radiography of Mediastinal Masses

Despite advancement in imaging technology, the humble chest radiograph remains an important modality for initial detection of a mediastinal abnormality, especially in the screening of an asymptomatic individual. It is imperative for the radiologist to be aware of radiographic signs of mediastinal abnormalities as well as the limitations of these signs.

A. Chawla (✉) · T. C. Lim
Department of Diagnostic Radiology, Khoo Teck Puat Hospital, Singapore, Singapore
e-mail: tze_chwan_lim@whc.sg

A. Chawla (ed.), *Thoracic Imaging*, https://doi.org/10.1007/978-981-13-2544-1_8

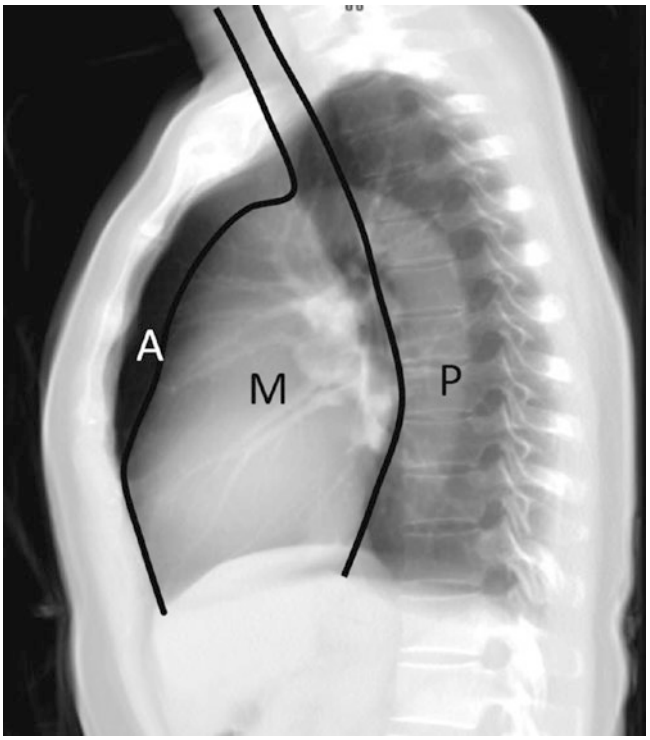

Fig. 8.1 Mediastinal compartments drawn on sagittal thick CT MPR image. *A* anterior, *M* middle, *P* posterior

8.4 General Signs of Mediastinal Mass: What Will Prompt a Radiologist to Suspect a Mediastinal Lesion?

8.4.1 Widening of Paratracheal Stripe

Tortuous vessels are the most common cause of widened paratracheal stripes. The widening is accentuated in an AP radiograph, further worsened if the projection is rotated (Fig. 8.2). Hence, it is always recommended to evaluate the mediastinum with an erect PA chest radiograph. The causes of paratracheal stripe widening are described in Table 8.1 (Figs. 8.3, 8.4, 8.5, 8.6, 8.7, 8.8, and 8.9). Focal bulge, lobulated, and irregular outline of the paratracheal stripe is more specific for the presence of paratracheal masses, while a smooth wavy margin suggests vascular causes. Mass effect on the trachea is more common in paratracheal mass and rarely caused by tortuous vessels. Tracheobronchial angle is a landmark for the azygos vein, appearing end-on as a less than 1 cm opacity. Frequently, the paratracheal mass extends and increases the size of opacity at the tracheobronchial angle.

8.4.2 Convexity of Aortopulmonary Window

The aortopulmonary window is in the middle mediastinum, and its convexity helps in localizing a mass in the middle mediastinum. The convexity is usually due to aortopulmonary lymph nodes (Fig. 8.10) and rarely aortic arch aneurysm. A pulmonary mass in the superior segment of the lower lobe can also be projected over this region.

8.4.3 Distortion of Mediastinal Contour

Mediastinal masses distort one or bilateral borders of the mediastinum. A large mediastinal mass projects beyond the border, forming an obtuse angle with it (Fig. 8.11).

8.4.4 Air-Fluid Level in Mediastinum

Air-fluid levels in the central chest are always abnormal and may represent an esophagus-related disease in the posterior mediastinum, less frequently a fistula or infection (Table 8.2) (Figs. 8.12, 8.13, 8.14, 8.15, and 8.16). The presence of two large air-fluid levels—one in the mediastinum (dilated herniated distal stomach) and one under the left hemidiaphragm (obstructed gastric fundus)—is highly suggestive of gastric volvulus in a patient with symptoms of gastric outlet obstruction [3]. A large air-fluid level in the mediastinum, in a patient with the classic triad of Borchardt (severe sudden epigastric pain, intractable retching without vomiting, and inability to pass a nasogastric tube), also suggests a gastric volvulus in the emergency settings.

8.4.5 Displacement of Mediastinal Lines

Visualization of the mediastinal lines is often subtle and may require changing of the window settings. Azygoesophageal recess is displaced and/or effaced by middle mediastinal masses (left atrial enlargement and enlarged subcarinal lymph nodes) as well as posterior mediastinal masses (foregut duplication cysts and esophageal masses) (Fig. 8.16). The displacement of paraspinal lines is seen in posterior mediastinal masses related to the vertebrae (extramedullary hematopoiesis), discs (infection), and paraspinal muscles (abscess, tumors) [4] (Fig. 8.17).

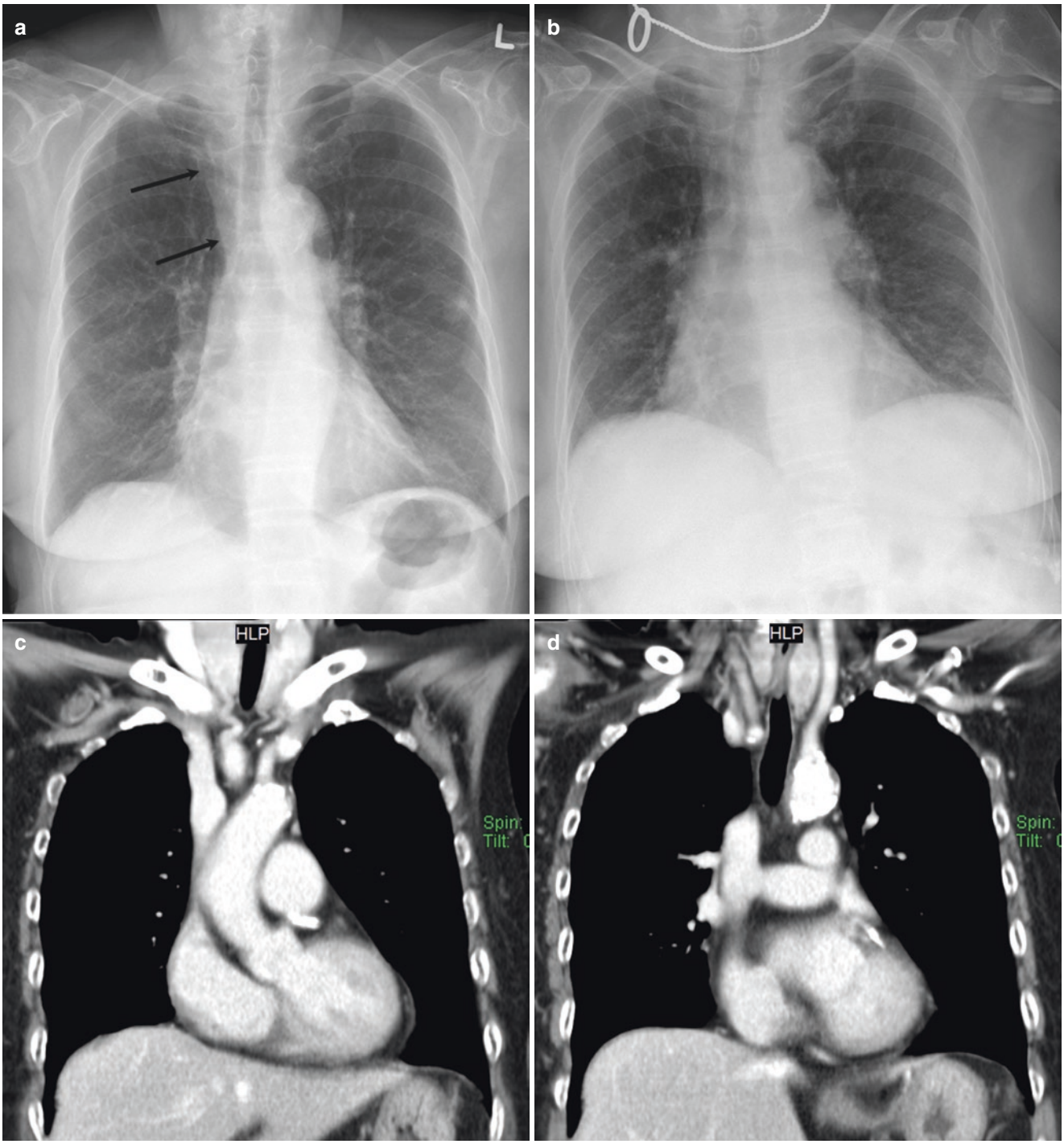

Fig. 8.2 81-year-old man with the widening of bilateral paratracheal stripes due to vascular shadows. (**a**) Frontal PA radiograph shows oblique wavy right paratracheal opacity (arrows), typical of vessels exiting the thoracic inlet. (**b**) AP radiograph of the same patient, a week apart, shows that the bilateral paratracheal stripes are more prominent. (**c**, **d**) Coronal CT images confirm paratracheal vessels accounting for paratracheal opacities on radiographs

8.5 Localizing Signs of Mediastinal Mass

8.5.1 Silhouette Sign

Historically, this has been the most useful sign for localization of the mediastinal masses. A mass involving the anterior mediastinum in the right hemithorax obliterates the right heart border and ascending aorta, while an anterior mediastinal mass projected over the left hemithorax obliterates the left heart border. A preserved outline of the aortic knuckle and descending aorta supports an anterior mediastinal mass, while a posterior mediastinal mass silhouettes the aortic knuckle and descending aorta, but will not obliterate the heart borders (Figs. 8.18, 8.19, 8.20, 8.21, 8.22, and 8.23).

Table 8.1 Causes of paratracheal stripe widening

Right paratracheal stripe	Left paratracheal stripe
• Tortuous neck vessels/ aneurysms • Retrosternal goiter/parathyroid mass • Lymph nodes • Bronchogenic cyst • Right upper lobe mass • Esophageal mass • Right aortic arch	• Tortuous neck vessels/ aneurysms • Retrosternal goiter • Left upper lobe mass • Persistent left SVC

8.5.2 Mass Effect on Tracheobronchial Tree

A good quality chest radiograph allows assessment of the entire thoracic trachea, right and left bronchi as well as their proximal branches. Mass effect on the tracheobronchial tree is a useful sign and often the only sign of an underlying middle mediastinal mass (Figs. 8.24, 8.25, and 8.26). Narrowing and deviation of the trachea indicate that the mass is in the vicinity of the trachea. However, a large anterior mediastinal mass can also exert mass effect on the trachea due to its bulk and limited space within the mediastinum. There is always an indentation on the left border of trachea caused by the aortic arch. If this indentation is seen on the right border of the trachea, it may be a sign of a right-sided aortic arch. Paratracheal masses, most commonly thyroid masses, usually cause some degree of mass effect on the trachea, while tortuous vessels rarely exert a mass effect.

8.5.3 Hilum Overlay Sign and Hilum Convergence Sign

Visualization of the pulmonary arteries through a mediastinal mass provides information that the mass is either anterior or far posterior to these vessels and is not likely to be in the middle mediastinum [1]. The overlapping pulmonary artery branches must be tracked and followed till the hilum to

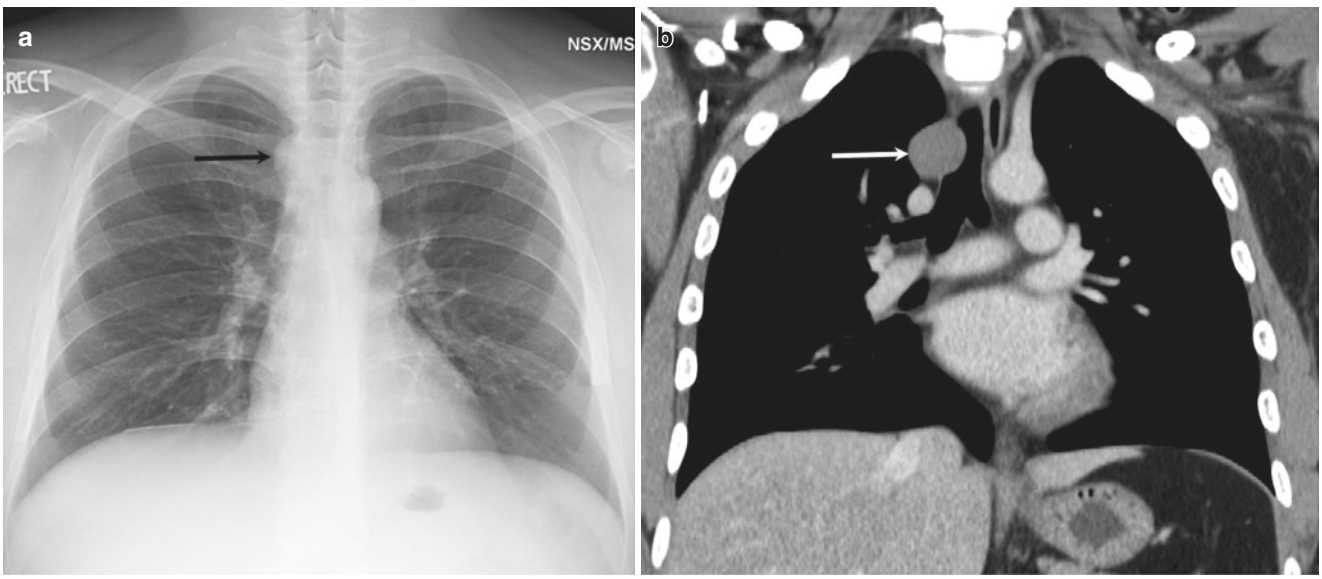

Fig. 8.3 22-year-old woman with an incidental bronchogenic cyst detected on pre-employment screening. (**a**) Frontal radiograph shows a focal bulge (black arrow) in the right paratracheal stripe. (**b**) Coronal CT shows a well-circumscribed cyst (white arrow) protruding into the trachea. Most of the bronchogenic cysts are located along the airways

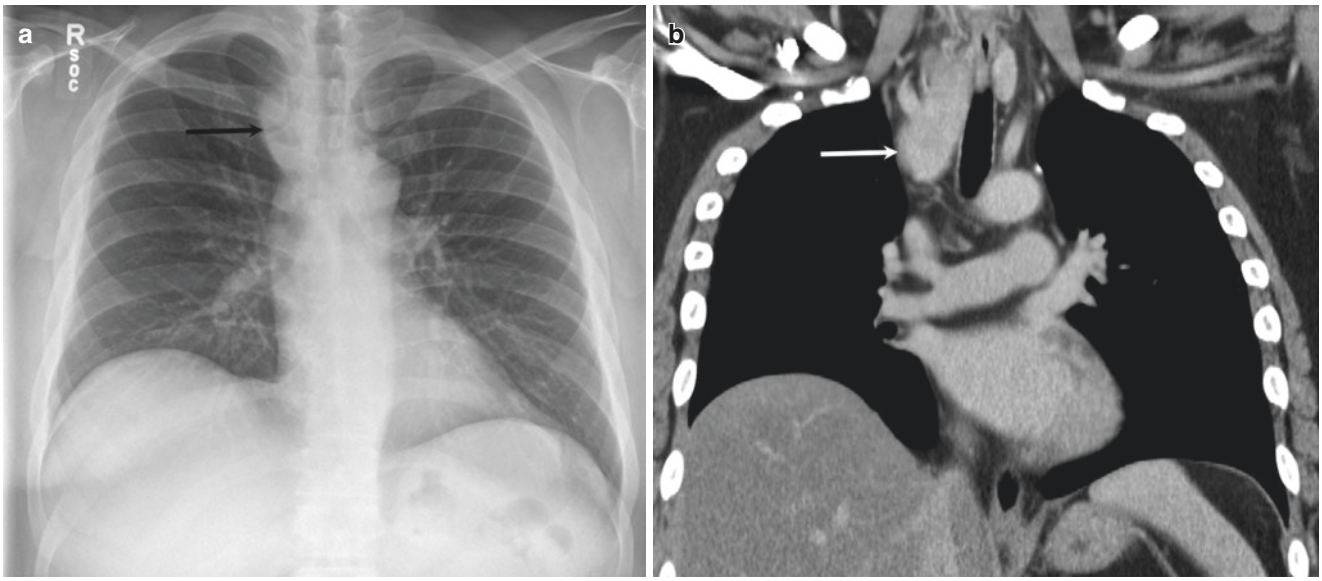

Fig. 8.4 33-year-old woman with parathyroid adenoma. (**a**) Frontal radiograph shows a convex paratracheal opacity (black arrow) widening the paratracheal stripe with subtle mass effect on the adjacent trachea. (**b**) Coronal CT shows retrosternal thyroid (white arrow) along the right paratracheal space. This extension of the thyroid was found to contain a parathyroid adenoma

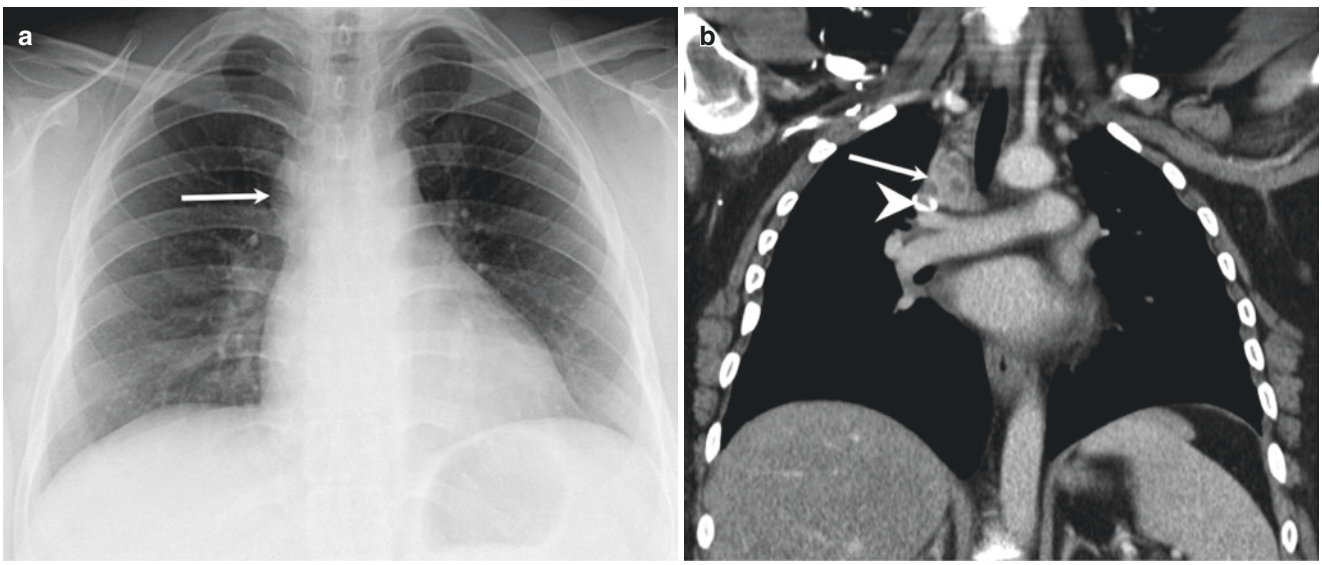

Fig. 8.5 32-year-old woman with right paratracheal lymphadenopathy from tuberculosis. (**a**) Frontal radiograph shows lobular widening of the right lower paratracheal stripe (arrow) extending to the tracheobronchial angle. (**b**) Coronal CT shows a nodal mass (arrow) with necrotic foci, with contrast in laterally displaced azygos vein valve (arrowhead)

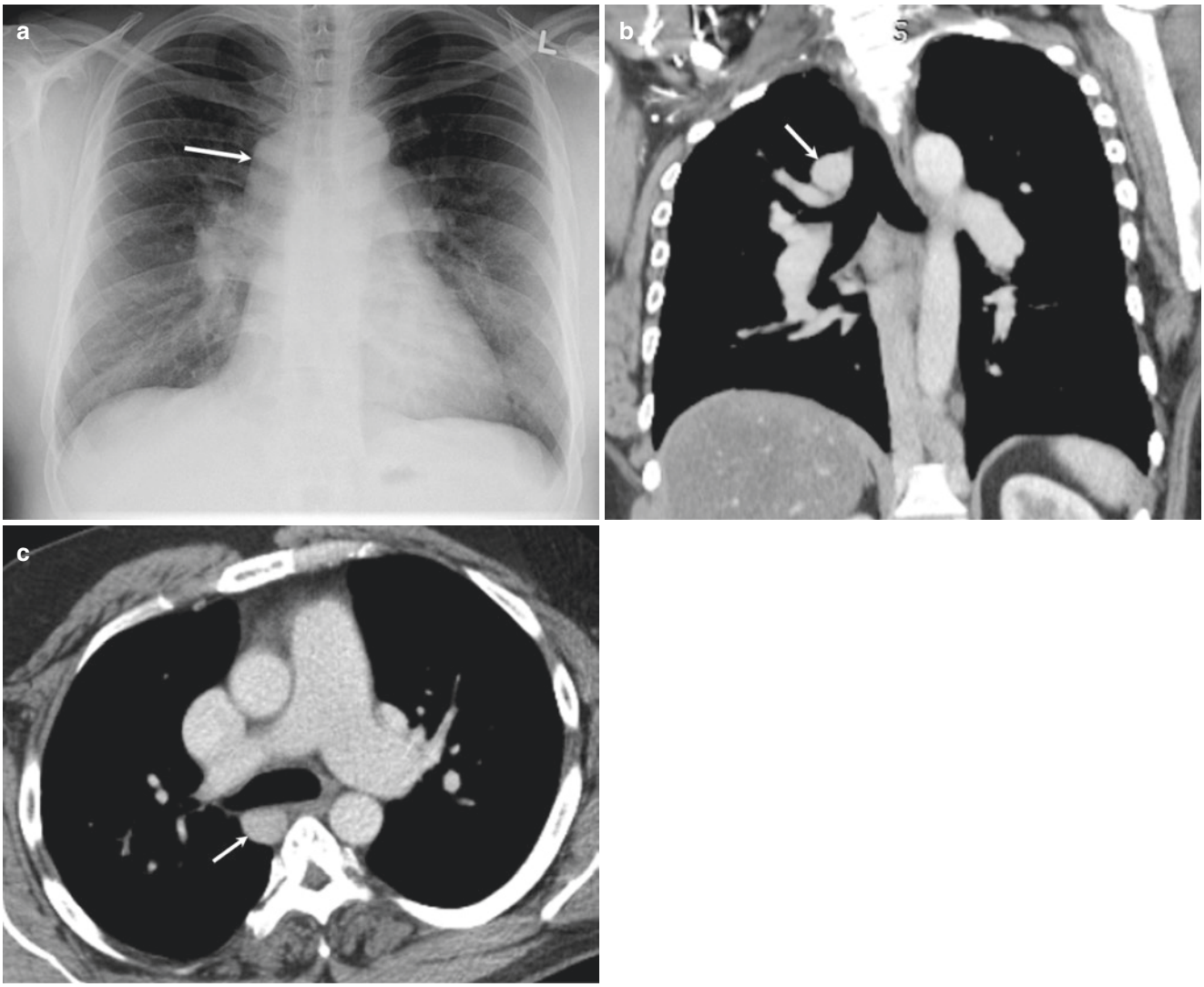

Fig. 8.6 56-year-old man with right lower paratracheal stripe widening due to enlarged azygos vein from azygos continuation. (**a**) Frontal radiograph shows a mass in the tracheobronchial angle and right lower paratracheal stripe. (**b**, **c**) Coronal and axial CT images show dilated azygos vein (arrow)

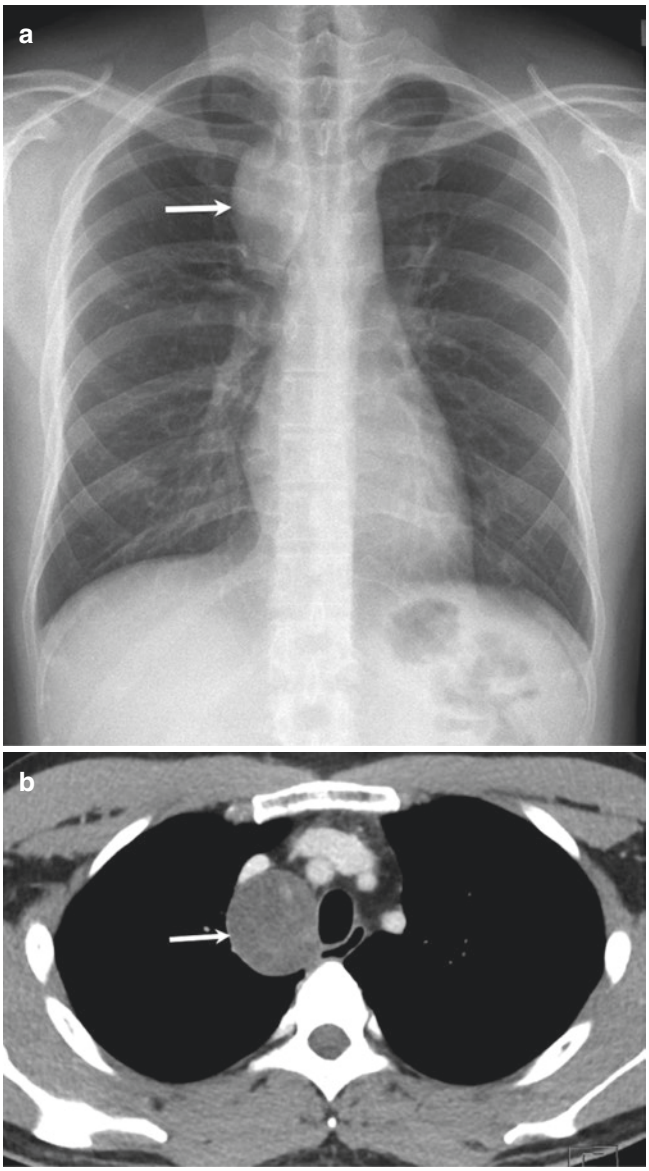

Fig. 8.7 33-year-old man with right paratracheal vagal schwannoma. (**a**) Frontal radiograph shows a smoothly marginated right paratracheal opacity (arrow) indenting the right lateral wall of the trachea. (**b**) Axial CT shows a well-circumscribed mass (arrow) in right paratracheal region with mass effect on the trachea

ensure that they are separate from the mass (Figs. 8.27 and 8.28). "Hilum overlay" sign is also useful in differentiating between cardiomegaly and an anterior mediastinal mass.

8.5.4 Bony Changes

The presence of scalloping, erosions, or destruction of vertebrae or posterior ribs is the most specific sign of a posterior mediastinal mass. Endplate narrowing with or without erosions associated with a paraspinal mass is suggestive of spondylodiscitis, and this finding will prompt further evaluation via MRI (instead of a thoracic CT) (Figs. 8.29 and 8.30).

8.5.5 Paracardiac Masses

Paracardiac masses usually arise from the middle mediastinum but may project into the anterior mediastinum and silhouette the cardiac borders in frontal chest radiographs (Table 8.3) (Figs. 8.31, 8.32, and 8.33). Morgagni hernia and lower esophageal mass can project over the paracardiac regions. The presence of bowel shadows in a paracardiac mass is suggestive of a Morgagni hernia.

8.5.6 Summary of Radiographic Features of Mediastinal Masses

The radiographic features of mediastinal masses, categorized based on their location, are summarized in the Tables 8.4, 8.5, and 8.6. For localization purposes, the absence of a sign is as important as its presence.

8.6 CT of Mediastinal Masses

CT is used for characterization, localization, and preoperative staging of patients with mediastinal masses. Proper correlation with the patient's age and relevant clinical

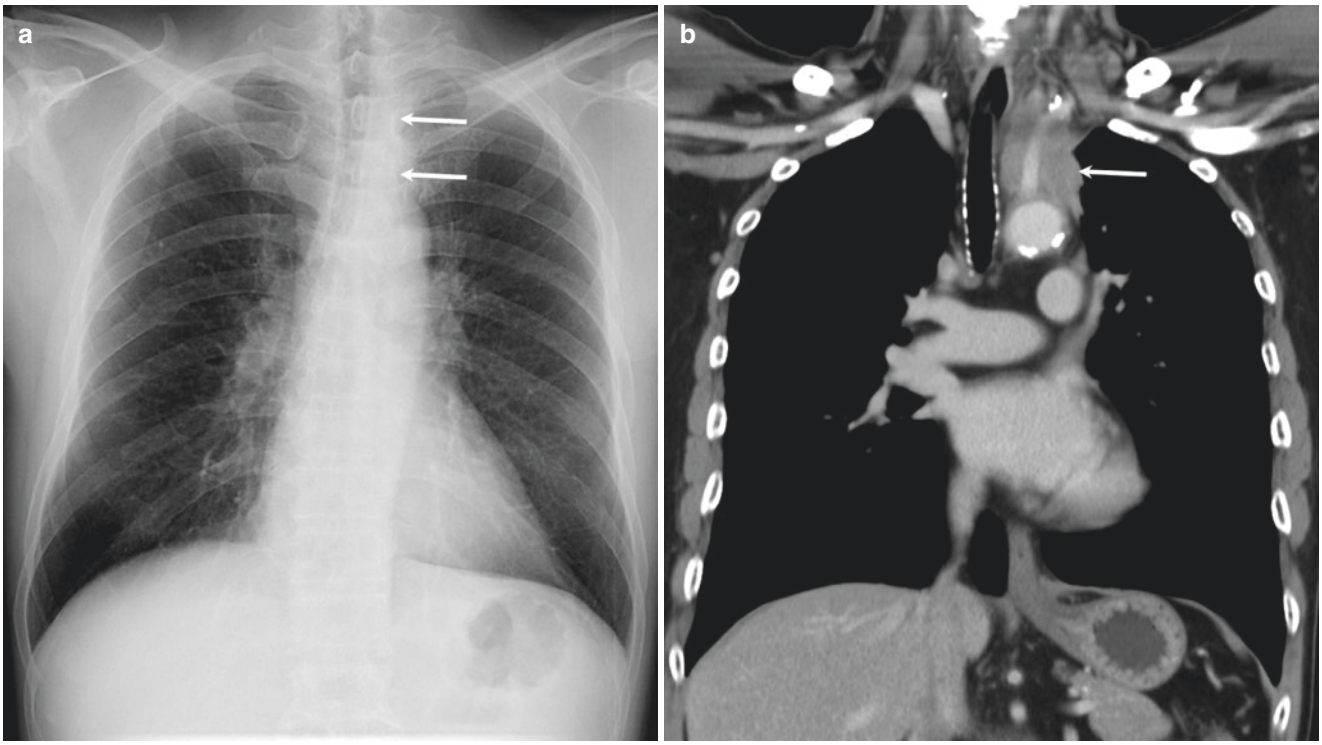

Fig. 8.8 61-year-old man with left upper lobe bronchogenic carcinoma. (**a**) Frontal radiograph shows thickening of the left paratracheal stripe (arrows) with fuzzy outlines and displacement of the trachea toward the right. (**b**) Coronal CT confirms the left paramediastinal upper lobe mass (arrow) encasing the vessels

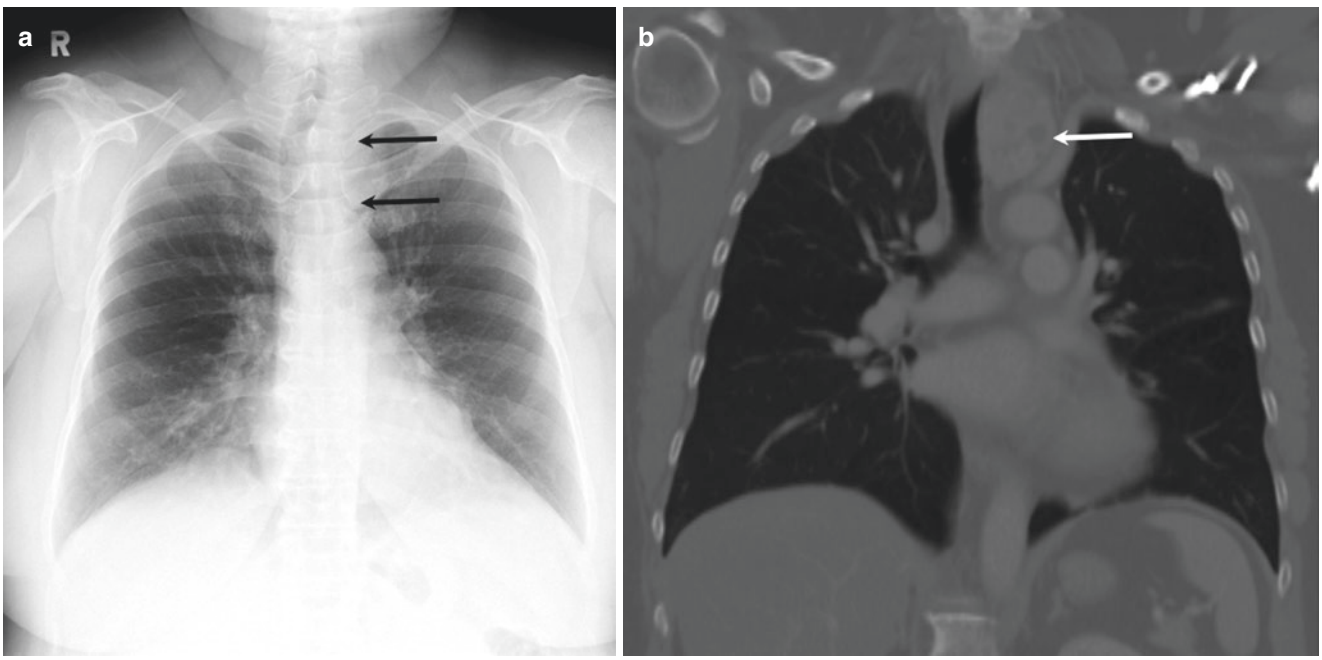

Fig. 8.9 51-year-old woman with goiter. (**a**) Frontal radiograph shows widening of the left paratracheal stripe (arrows) with displacement of the trachea toward the right. (**b**) Coronal CT confirms the retrosternal extension of the left lobe of thyroid (arrow)

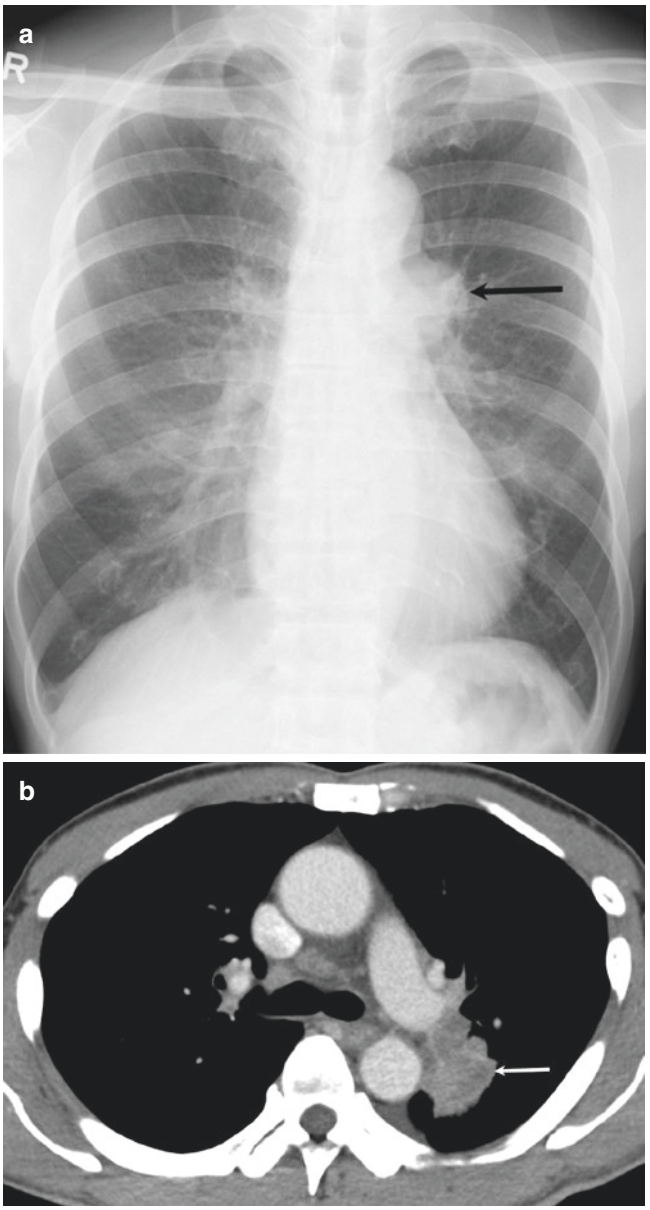

Fig. 8.10 61-year-old man with left hilar mass. (**a**) Frontal radiograph shows convexity of aortopulmonary window (arrow). (**b**) CT demonstrates left hilar mass that was biopsy-proven to be a bronchogenic carcinoma

information will enable an accurate radiological diagnosis in most of the cases.

Mediastinal masses in the various compartments are described in Table 8.7. CT is the investigation of choice for evaluation of a solid mass in the mediastinum. MRI is used in differentiation of thymic hyperplasia from thymoma as well as in differentiation of a cyst from the solid-cystic and solid mass.

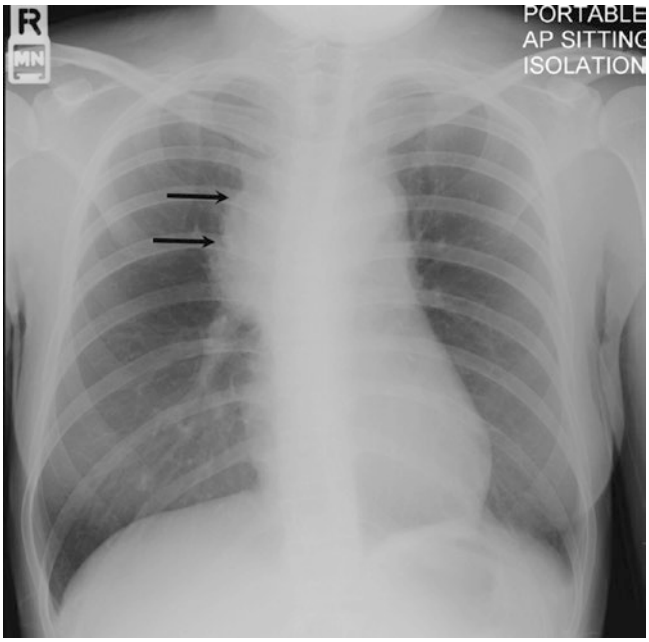

Fig. 8.11 Frontal radiograph shows a distorted contour of the right upper mediastinal border by an anterior mediastinal mass (arrows) that obliterates the normal upper mediastinum

Table 8.2 Causes of air-fluid level in mediastinum

• Large hiatal hernia
• Achalasia cardia
• Esophageal diverticula
• Volvulus of stomach
• Fistula/tear related to the trachea or esophagus
• Mediastinitis
• Morgagni hernia

8.6.1 Thymoma

Thymoma is the most common malignancy of the anterior mediastinum, accounting for half of the anterior mediastinal masses [5]. Rarely seen in children, the peak prevalence of thymoma is during the fifth and sixth decades of life. Thymoma is an indolent tumor with varying malignant potential—dependent on the histology type. Approximately half of the patients are asymptomatic, while the other half of the patients present with symptoms secondary to mass effect. A substantial proportion of patients with thymomas present with paraneoplastic syndromes. These syndromes include myasthenia gravis, pure red cell aplasia, hypogammaglobulinemia, endocrinopathy, and autoimmune disorders. About 30–40% of patients with thymoma have myasthenia gravis, and 10–15% of patients with myasthenia gravis have a

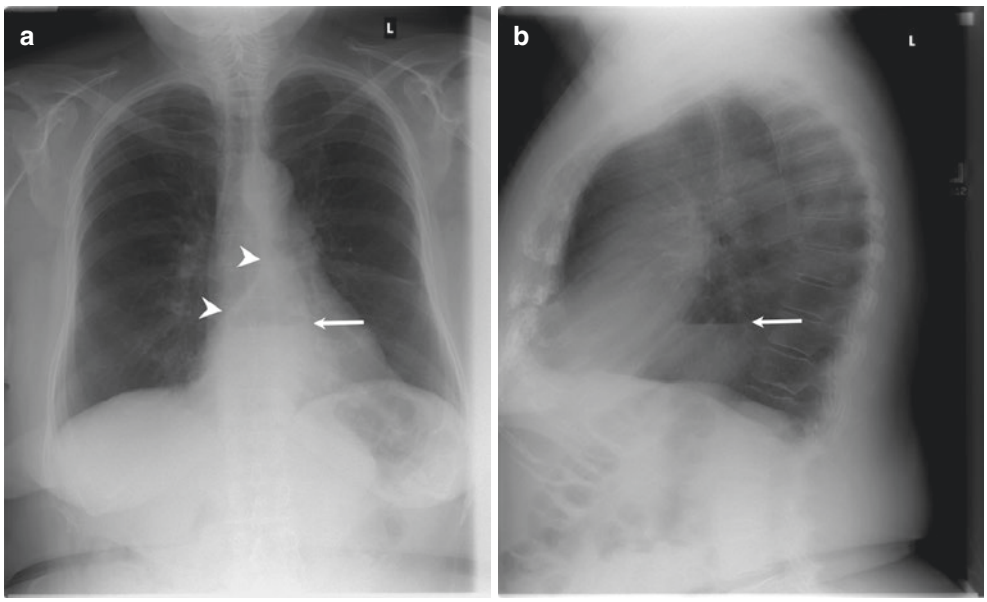

Fig. 8.12 67-year-old woman with a hiatal hernia. (**a**) Frontal radiograph shows central chest mass with air-fluid level (arrow). Displacement of azygoesophageal recess (arrowheads) is another sign of posterior mediastinal mass. (**b**) Lateral radiograph confirms a retrocardiac opacity with air-fluid level (arrow)

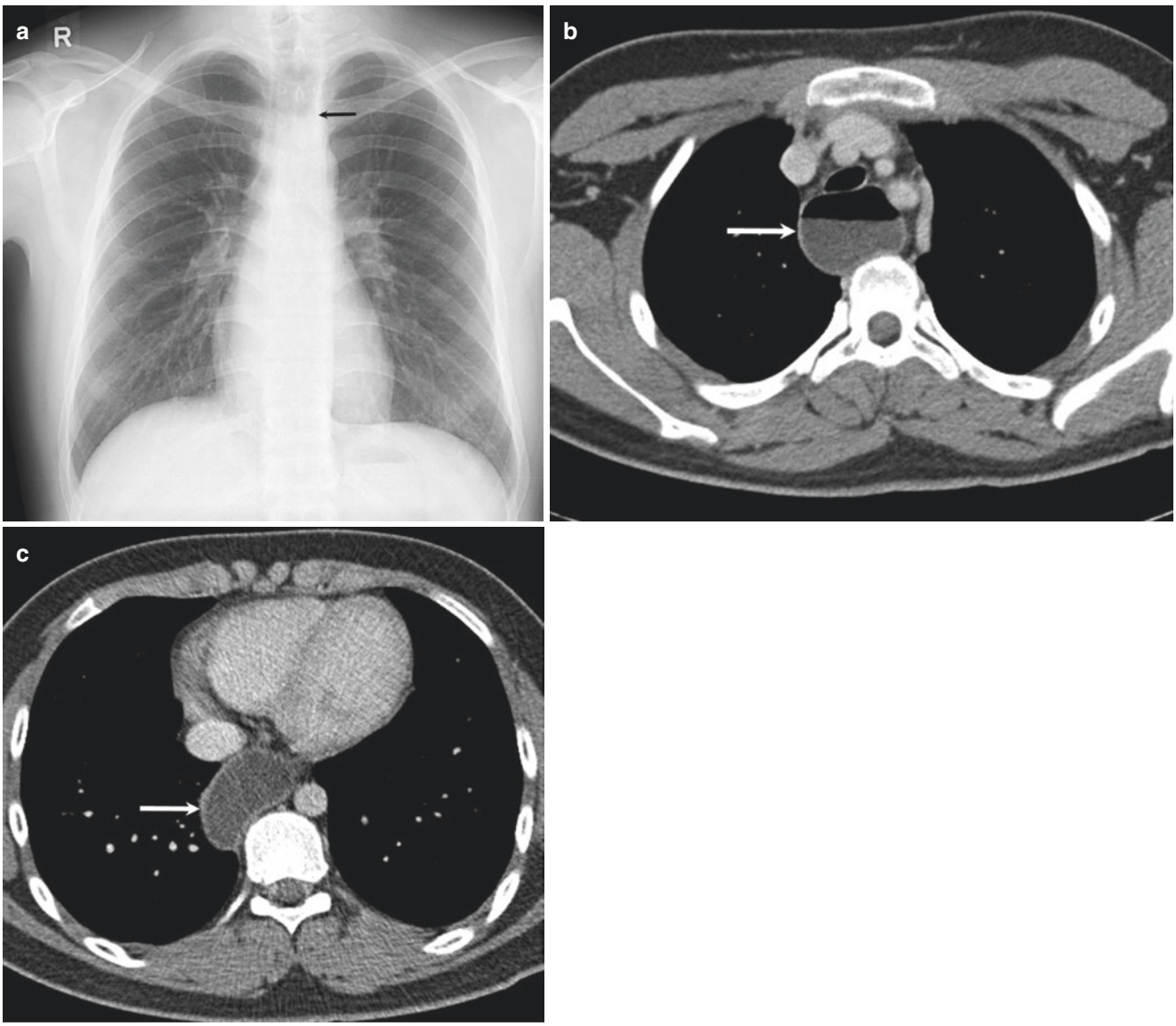

Fig. 8.13 21-year-old man with recurrent chest pain due to achalasia cardia. (**a**) Frontal radiograph shows an air-fluid level in the central upper mediastinum (arrow) superimposed on the tracheal lucency. (**b**, **c**) Axial CT images reveal a dilated esophagus (arrows) throughout its course

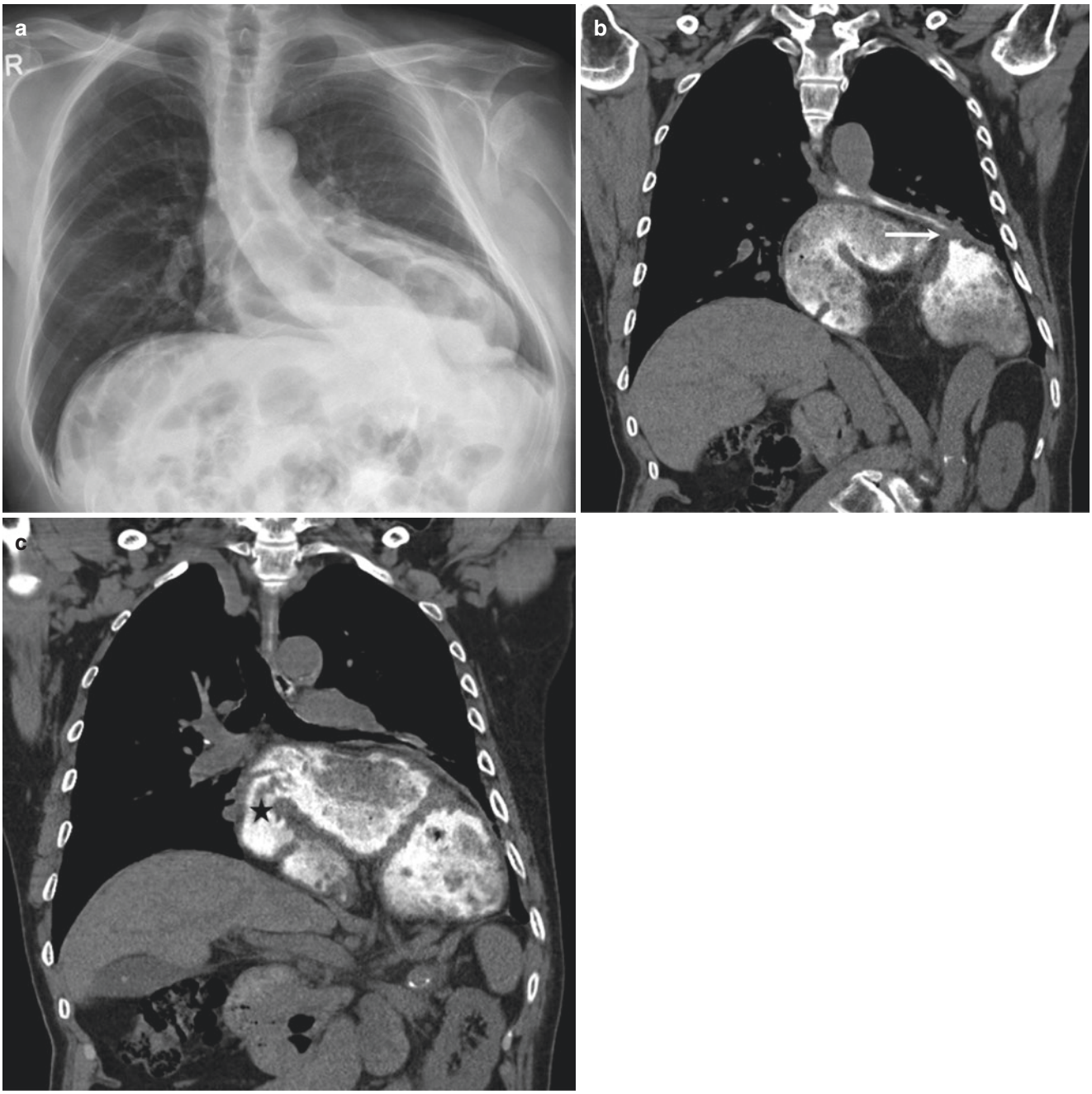

Fig. 8.14 79-year-old woman with volvulus. (**a**) Frontal radiograph shows a large air-fluid level in the central mediastinum. (**b**, **c**) Coronal CT images with diluted oral contrast show herniation of the stomach with approximation of gastroesophageal junction (white arrow) and gastroduodenal junction (asterisk)

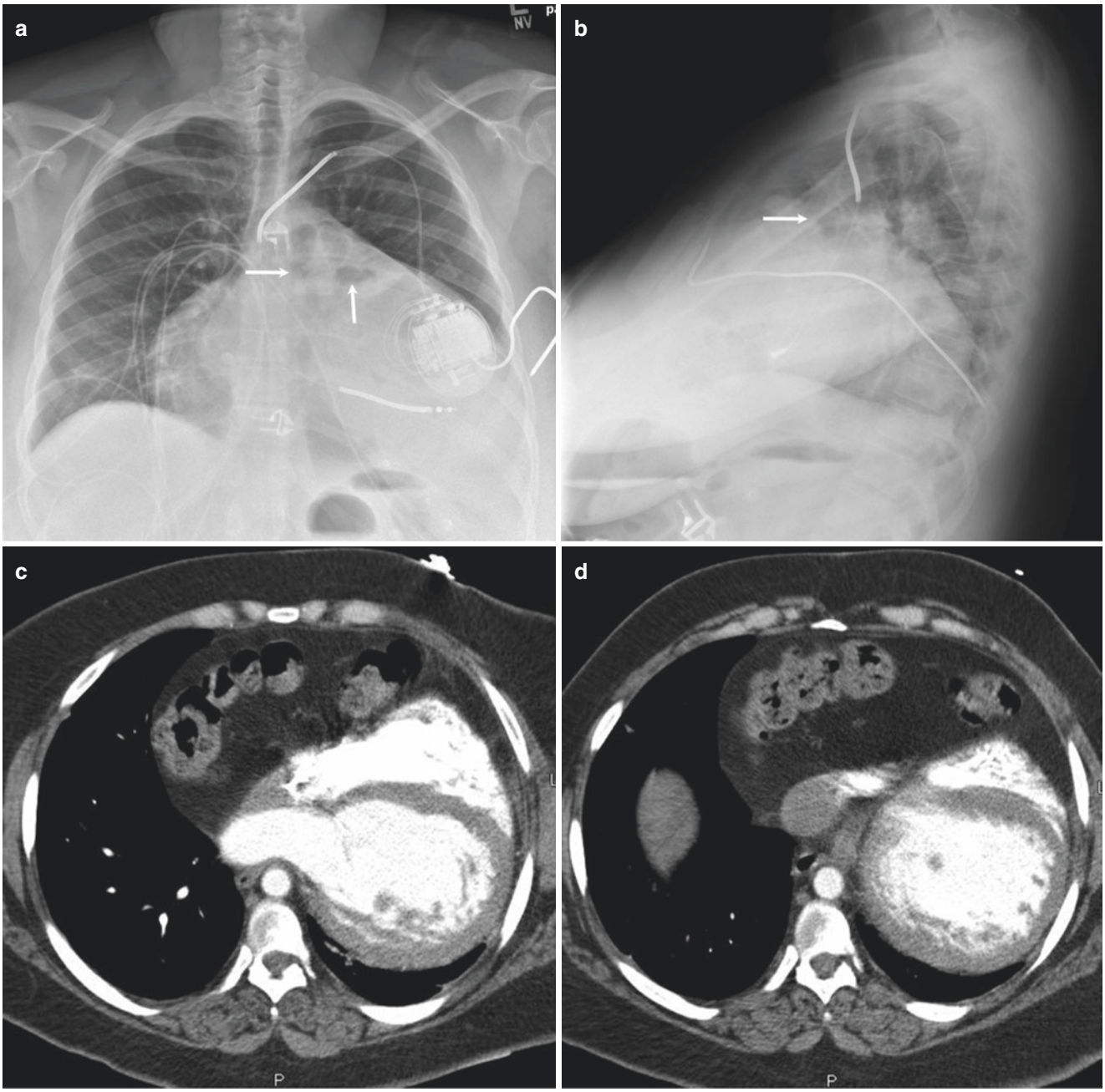

Fig. 8.15 64-year-old woman with Morgagni hernia containing transverse colon. (**a**, **b**) Frontal and lateral radiographs show large central mediastinal mass with bowels and air-fluid level (arrows). (**c**, **d**) Axial CT images reveal herniated transverse colon and fat displacing the heart

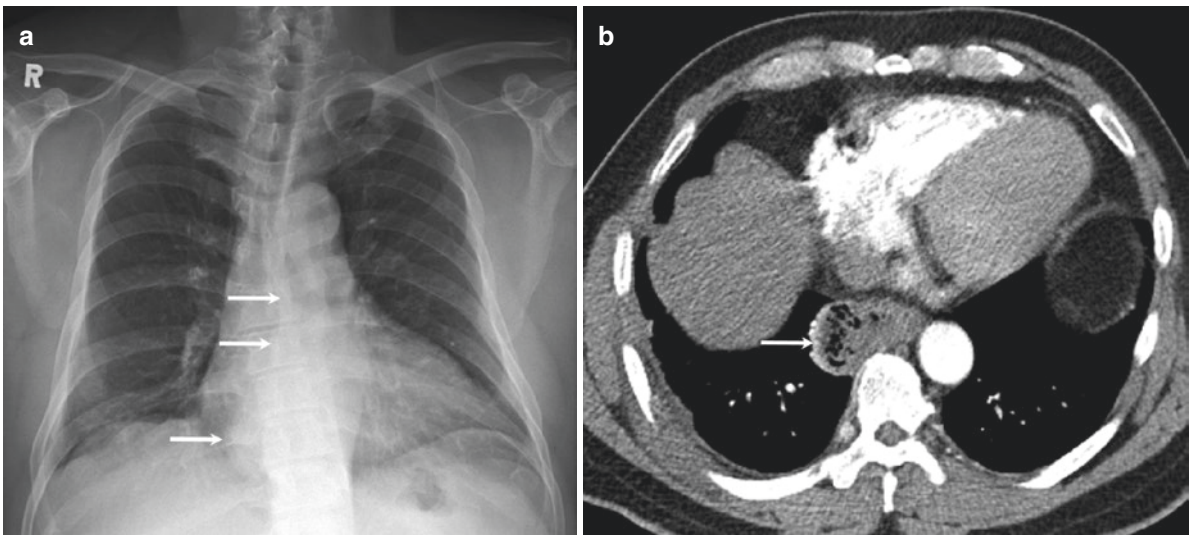

Fig. 8.16 53-year-old woman with an epiphrenic diverticulum. (**a**) Frontal radiograph shows displacement of azygoesophageal recess (arrows). (**b**) Axial CT image demonstrates the epiphrenic diverticulum (arrow)

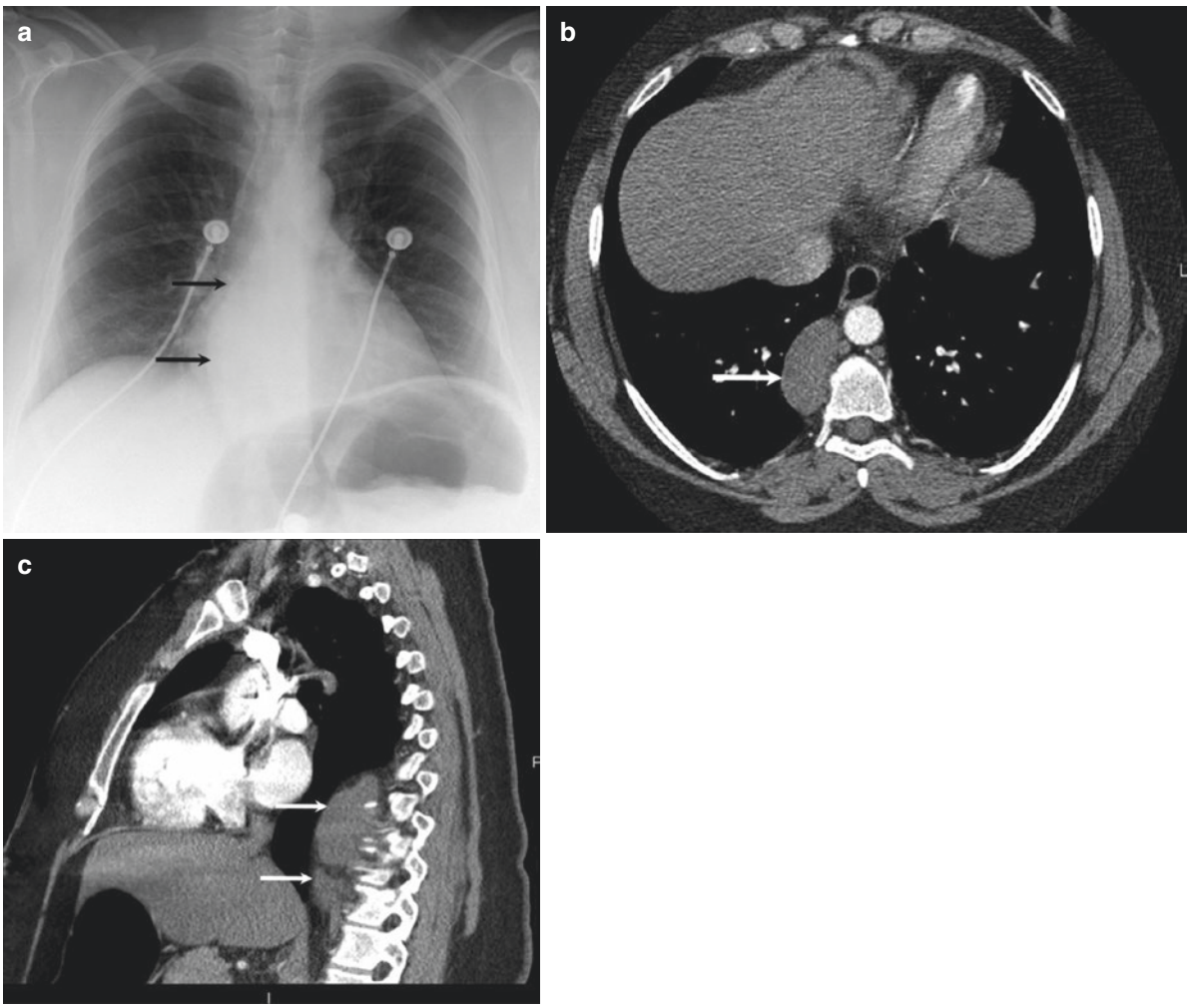

Fig. 8.17 35-year-old woman with ganglioneuroma in the posterior mediastinum. (**a**) Frontal radiograph shows retrocardiac opacity displacing the right paraspinal line (arrows), while the azygoesophageal recess is preserved. (**b**) Axial CT image shows a homogeneous well-circumscribed right paravertebral mass (arrow) without any extension in the spinal canal. (**c**) Sagittal image shows that mass (arrows) lies along multiple thoracic vertebrae

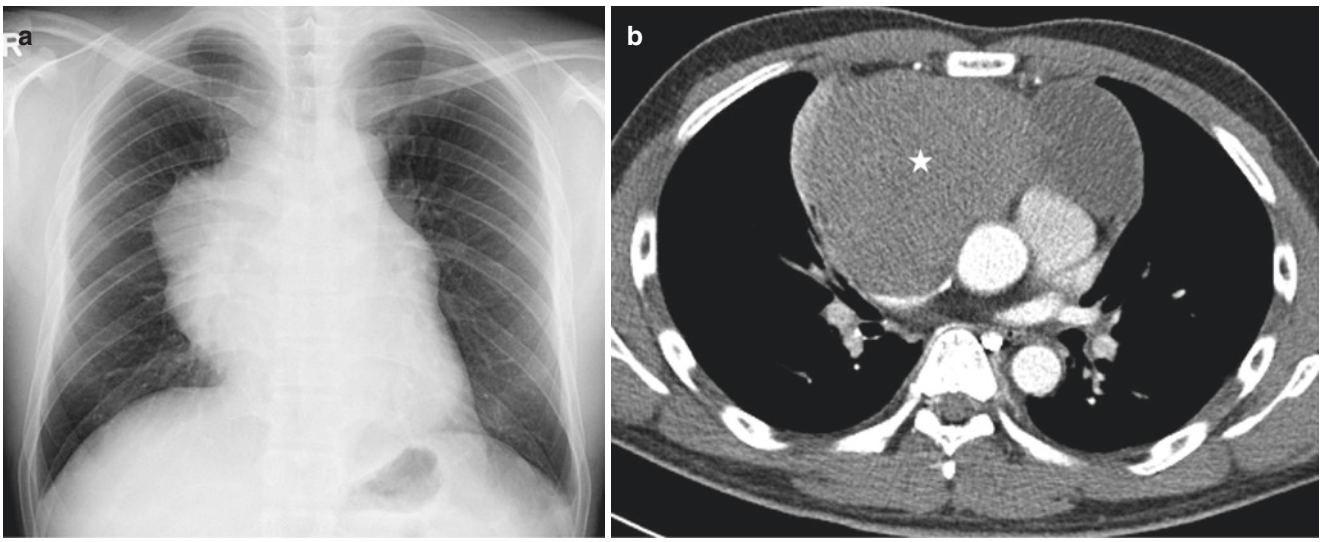

Fig. 8.18 41-year-old man with anterior mediastinal B-cell lymphoma. (**a**) Frontal radiograph shows a large mass in the mediastinum, silhouetting the right and left heart borders but without silhouetting the aortic knuckle. The descending aorta can be seen through it. Visualization of the right pulmonary artery represents "hilum overlay" sign. There is no bony involvement. The imaging features are consistent with anterior mediastinal mass. (**b**) Axial CT image confirms the anterior mediastinal mass (asterisk). Note that the mass is away from the lower lobe pulmonary arteries accounting for positive "hilum overlay" sign

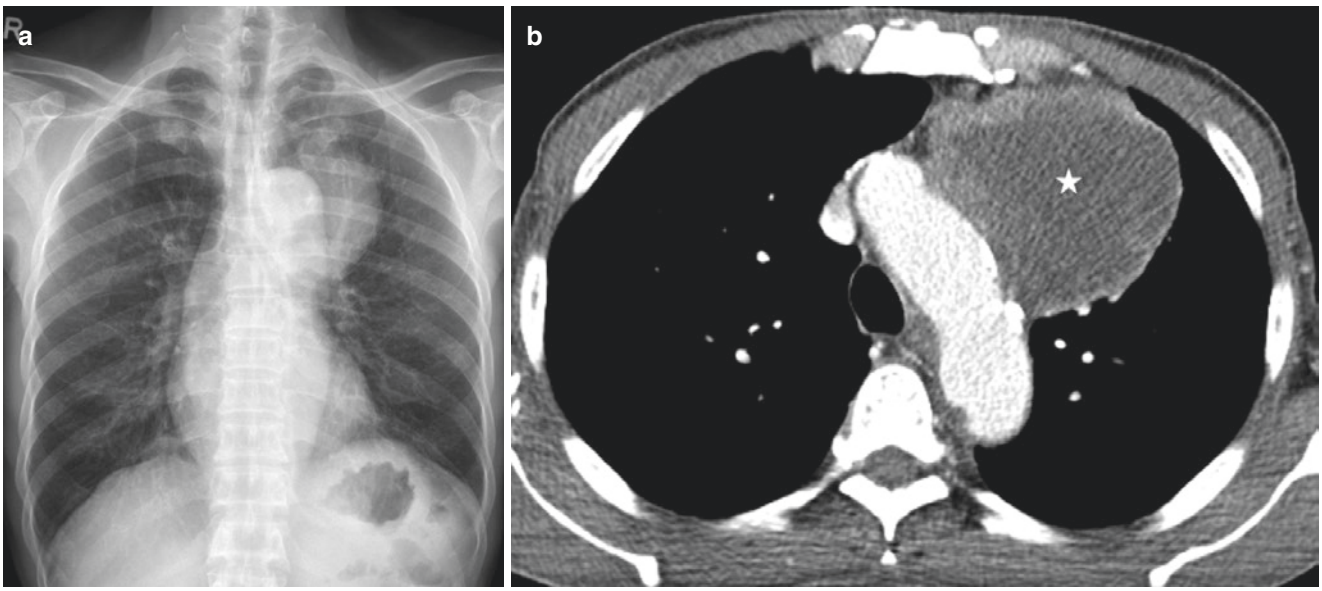

Fig. 8.19 59-year-old man with small-cell lung cancer in the anterior mediastinum. (**a**) Frontal radiograph shows a well-defined opacity in the left paramediastinal region not silhouetting the aortic knuckle or descending aorta and without any bony changes. Left upper lobe pulmonary artery can be seen through the mass, i.e., "hilum overlay" sign. (**b**) Axial CT image shows a heterogeneous mass (asterisk) in the anterior mediastinum, far away from the descending aorta and left upper lobe pulmonary vessels

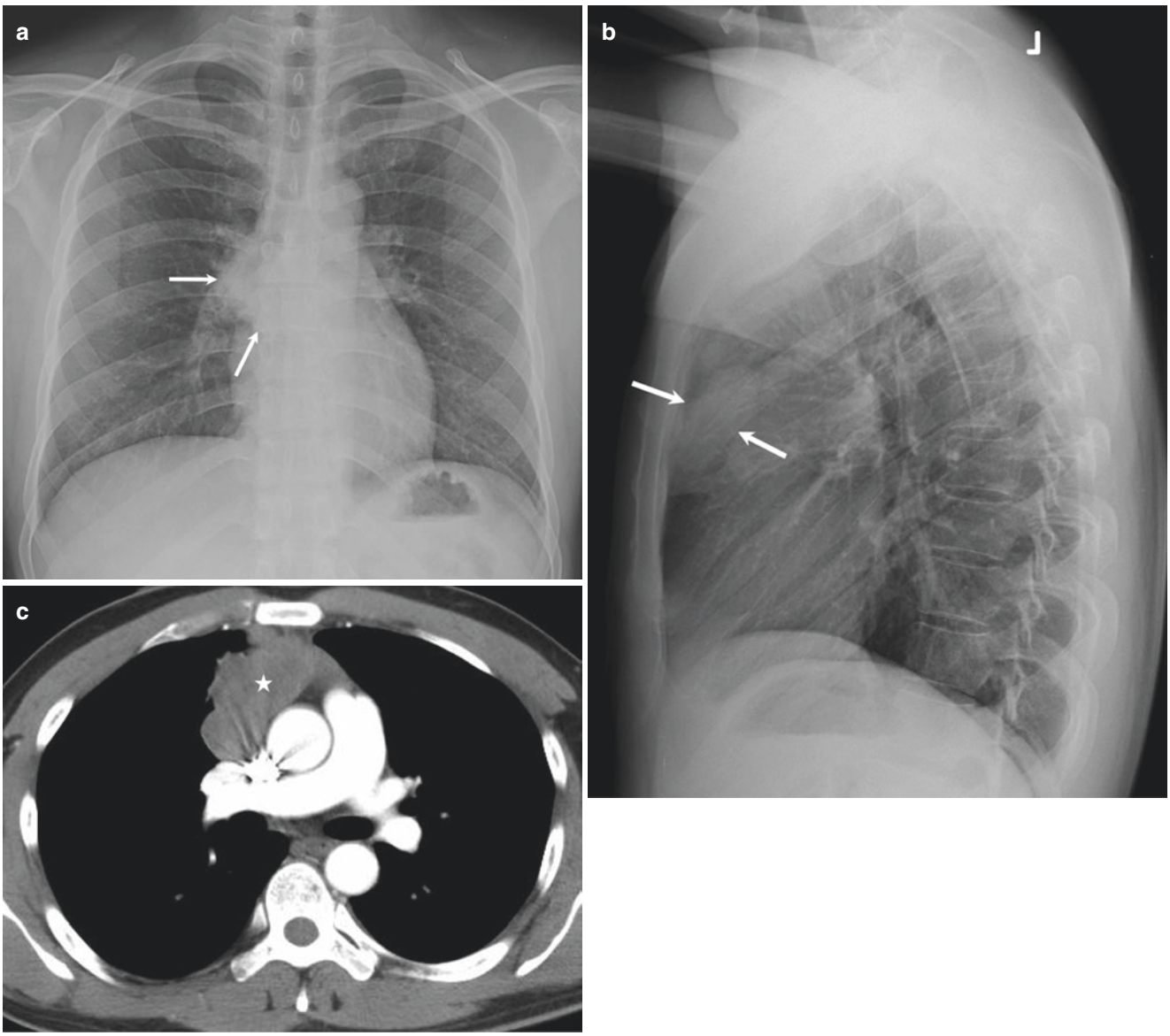

Fig. 8.20 49-year-old man with thymoma. (**a**) Frontal radiograph shows a right hilar opacity (arrows) silhouetting the adjacent right heart border with "hilum overlay" sign present. (**b**) Lateral radiograph shows a well-circumscribed mass (arrows) in the anterior mediastinum. (**c**) Axial CT image confirms the anterior mediastinal homogeneous mass (asterisk)

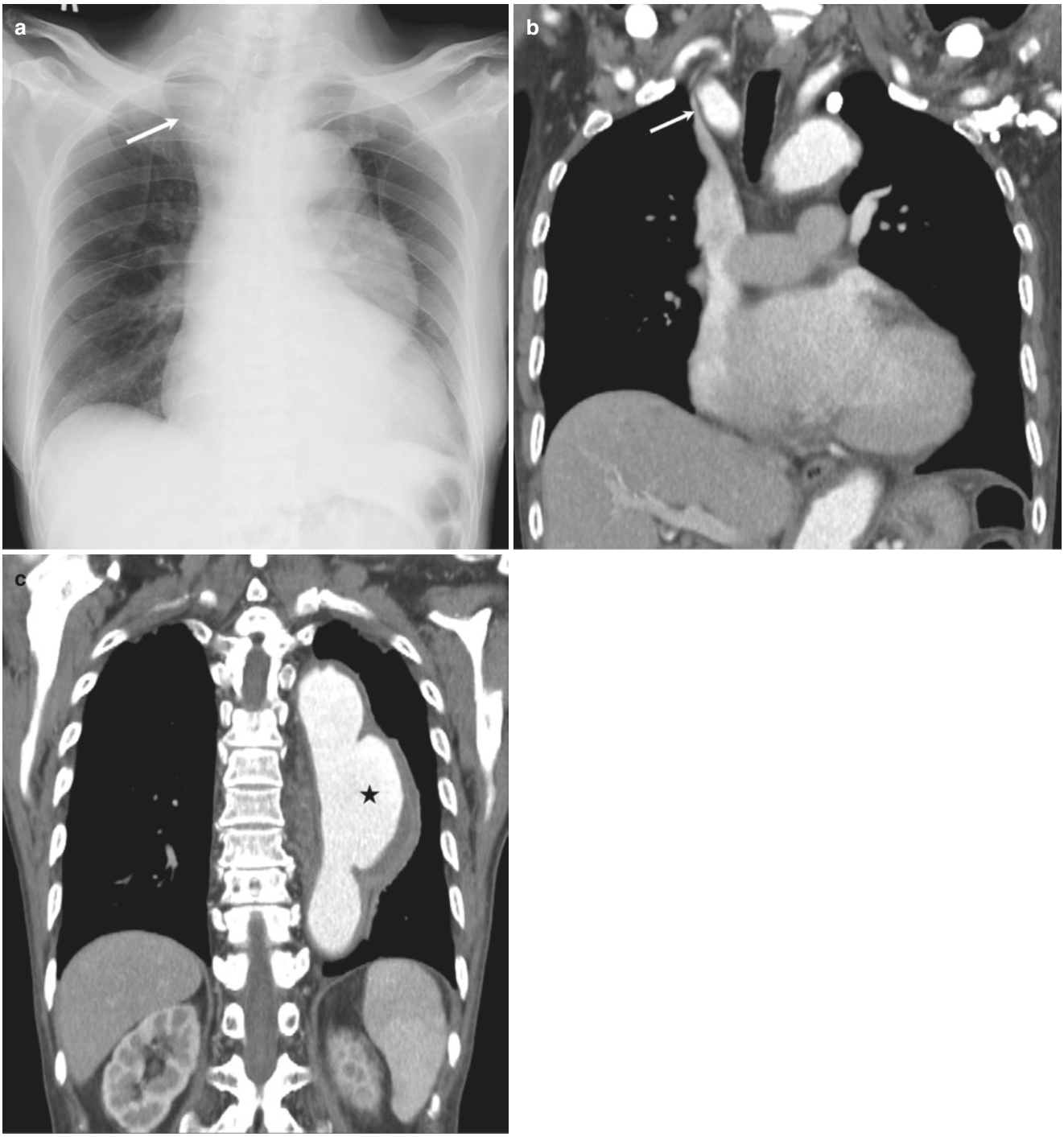

Fig. 8.21 74-year-old woman presented to the emergency department with acute chest pain from descending thoracic aortic aneurysm. (**a**) Frontal radiograph shows a left hilar mass not silhouetting the left heart border but obscuring the descending aorta. "Hilum overlay" sign is present. Imaging features are consistent with a posterior mediastinal mass. Note the wavy right paratracheal opacity (arrow) without any positive mass effect on the trachea. (**b**, **c**) Coronal CT images reveal a descending aortic aneurysm (asterisk). Right paratracheal opacity is caused by tortuous neck vessels (arrow)

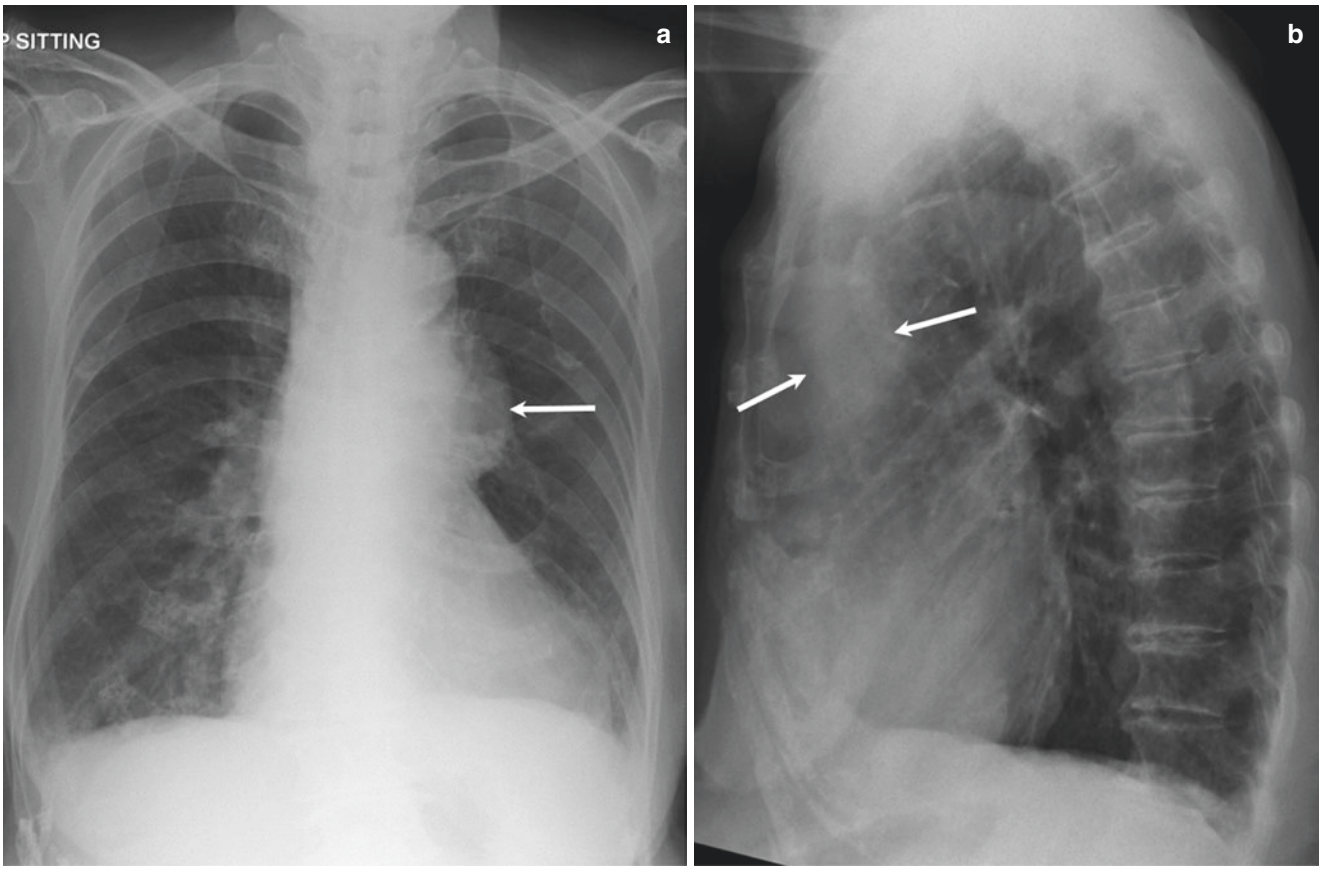

Fig. 8.22 61-year-old man with anterior mediastinal thymoma. (**a**) Frontal radiograph shows an opacity in the midline, silhouetting the left heart border but not silhouetting the descending aorta. Hilar vessels can be seen through the mass ("hilum overlay" sign). (**b**) Lateral radiograph shows a large anterior mediastinal mass (arrows)

thymoma [6]. On CT, thymoma appears as a smooth or lobulated mass, classically located in the prevascular space. Smaller lesions show homogeneous enhancement, but the larger masses may demonstrate areas of hemorrhage, necrosis, and cystic changes [7] (Figs. 8.34, 8.35, and 8.36). Coarse calcification is common and is not considered a hallmark of thymic carcinoma in the absence of other suspicious features. CT signs of invasive thymoma or thymic carcinoma include an irregular interface, loss of fat planes with the other mediastinal structures, pericardial or pleural thickening, encasement or invasion of mediastinal vessels, and mediastinal lymphadenopathy [8, 9]. Invasive thymoma and thymic carcinoma tend to invade the vessels and spread along the pleura without associated effusion. The pleura is also considered a common site for recurrence. Differentiation between invasive thymoma and thymic carcinoma is difficult by CT. However, in a large thymic tumor with invasion of the great vessels, lymph node enlargement, phrenic nerve palsy, or extra-thymic metastases on CT, thymic carcinoma is more likely than invasive thymoma [9].

Masaoka-Koga system is commonly used for staging of thymomas and is based on microscopic and macroscopic extent of disease [10]. Stage I tumors are the "non-invasive" thymomas that are completely encapsulated microscopically; stage II tumors demonstrate microscopic invasion through the capsule (IIa) or macroscopic invasion into the surrounding fat (IIb); stage III tumors are characterized by invasion into a neighboring organ such as the pericardium, great vessels, or lung; and stage IV disease shows pleural or pericardial dissemination (IVa) or lymphogenous/hematogenous metastasis (IVb). Prognosis depends on the surgical staging as well as histopathology type of the tumor.

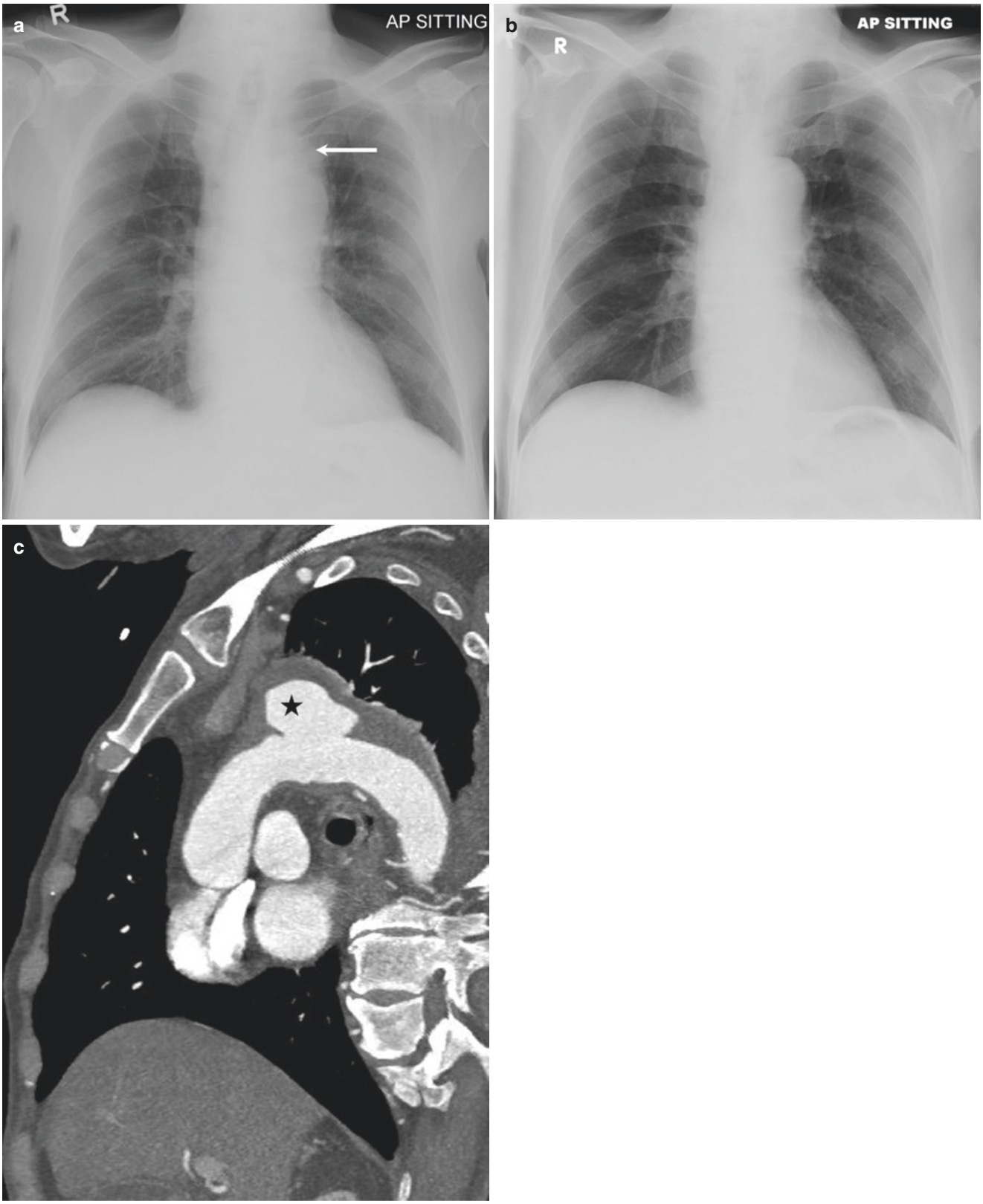

Fig. 8.23 80-year-old man presented with shortness of breath in the emergency department. (**a**) AP chest radiograph shows silhouetting of the superior border of aortic arch by an ill-defined opacity (arrow), a new finding since the radiograph acquired 2 months before (**b**). Note the increased mass effect on the adjacent trachea. (**c**) Reconstructed sagittal oblique CT aortogram image reveals an aneurysm (asterisk)

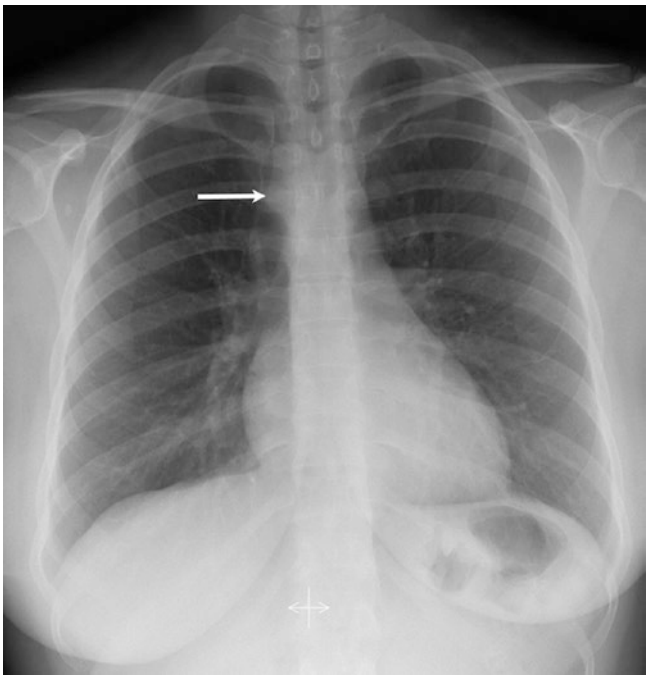

Fig. 8.24 Frontal radiograph of a 21-year-old woman with right-sided aortic arch (arrow). Indentation on the right lateral wall of the trachea is the only supporting evidence of right aortic arch

8.6.2 Thymic Cyst

Thymic cysts are rare usually asymptomatic, with acquired lesions more prevalent than congenital cysts. Congenital cysts are unilocular, whereas the acquired cysts are usually multilocular but can also be unilocular. Acquired thymic cysts may occur in patients before or after treatment of lymphoma, in association with thymomas, and after thoracotomy [11]. Multilocular thymic cysts may be idiopathic or seen rarely in adult patients with collagen vascular diseases and are considered to be of inflammatory etiology [12, 13]. Typical findings of a thymic cyst in a CT include a well-circumscribed, low-attenuation lesion without any contrast enhancement [11] (Fig. 8.37). The cyst can show high attenuation if there is hemorrhage or infection. In such cases, MRI helps in differentiating these cysts from cystic thymoma with thick enhancing walls or solid components (Fig. 8.37) [7]. Partial or complete cyst wall calcification may be seen in a few cases.

8.6.3 Thymolipoma

Thymolipomas are unusual benign anterior mediastinal tumors composed of thymic and adipose tissues. These are seen in patients of a wide age range, from 2 years old to 66 years old [14, 15], with a large proportion diagnosed incidentally due to an abnormal chest radiograph—frontal radiographs show features of a large anterior mediastinal mass, extending to both sides of the mediastinum, often mistaken for cardiomegaly. CT demonstrates admixture of fat and soft tissue with two patterns. The common pattern is of linear whorls of soft tissue intermixed with fat, and the second less common pattern is of an almost fatty mass with tiny internal linear foci of soft tissue attenuation [14] (Fig. 8.38). Thymolipomas are usually huge soft tumors that tend to adapt to the triangular shape of the mediastinal compartment and exert relatively less mass effect on the adjacent structures. The larger tumors are more frequent in the anterior inferior compartment reaching the diaphragm, probably due to their weight. There may be a pedicle extending from the inferiorly located mass to the normal location of the thymus in the superior component of the anterior mediastinum [14] (Fig. 8.39). Thymolipoma must be differentiated from other fat-containing anterior mediastinal masses, such as mature teratoma, lipoma, and liposarcoma. Mature teratomas tend to be round or lobulated, cystic masses. They are usually located in the superior mediastinum, do not conform to the shape of adjacent structures, and are frequently seen to contain calcifications in CT scans. Mediastinal liposarcomas are rare tumors that may be difficult to differentiate from thymolipoma, if located in the anterior mediastinum. Liposarcomas are usually symptomatic and show fat within them. However, in cases of pleomorphic and dedifferentiated liposarcomas, CT may not show fat [16].

8.6.4 Lymphoma

The majority (approximately 90%) of mediastinal lymphomas are part of a widespread systemic disease, while primary mediastinal lymphomas are less common (10%). Thoracic involvement is more common in Hodgkin lymphoma (HL) than in non-Hodgkin lymphoma (NHL). Eighty to eighty-five percent of patients with HL and 40–45% of patients with NHL have thoracic disease at the time of presentation [17, 18]. Lymphoma has a bimodal distribution of incidence—in young adults (third decade) and after 50 years old. Nodular sclerosing subtype is the most common HL affecting the mediastinum, while the B-cell lymphoma and lymphoblastic lymphoma are the most common subtypes of NHL found in the mediastinum [19].

On CT, mediastinal lymphomas appear as a large lobulated mass usually in the anterior mediastinum but may be found in the middle or posterior mediastinum (Fig. 8.40). They usually demonstrate homogeneous density, but the larger tumors may show necrosis, hemorrhage, or cystic

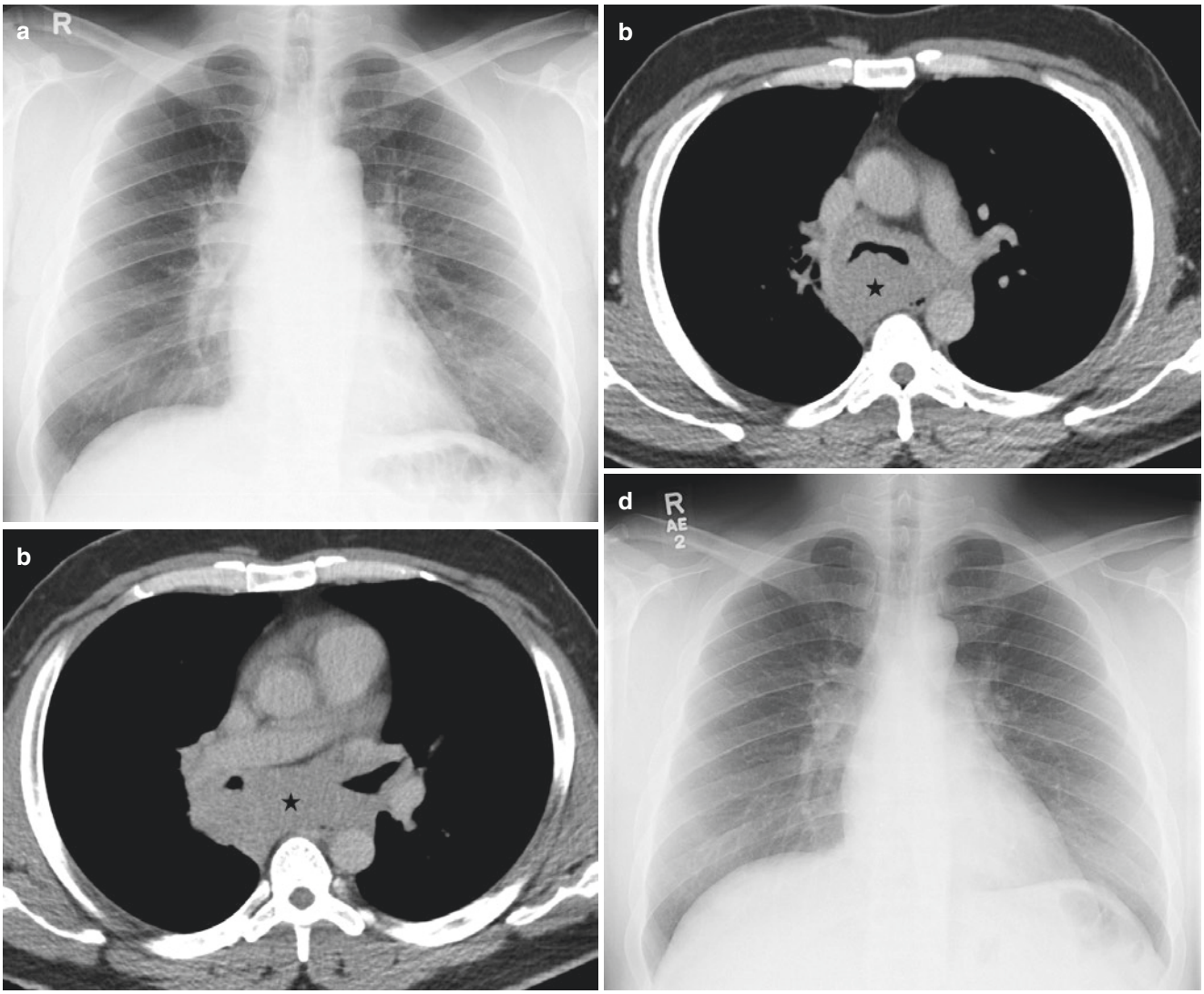

Fig. 8.25 51-year-old man with a large lymphoma involving the middle and posterior mediastinum. (**a**) Frontal radiograph shows an opacity in the central chest over the sternum with obscuration of the lower tracheobronchial tree. Carina and bronchi are barely visualized with non-visualization of the medial wall of lower lobe bronchi. (**b**, **c**) Axial CT images show a large homogeneous mass (asterisk) encasing and compressing the tracheobronchial tree. (**d**) Frontal radiograph after chemotherapy shows resolution of opacity and good visualization of the carina and major bronchi

degeneration [20, 21]. Calcification before treatment is rare but can be seen in aggressive lymphomas [21]. A characteristic feature of lymphomas is the encasement and compression of mediastinal vessels, without invasion. Lung cancer and mediastinal lymphomas are the common causes of superior vena cava syndrome. Large lymphomas displace the central airways [21]. It is uncommon for NHL and HL to be limited to the mediastinum at the time of diagnosis [20]. The diagnosis of lymphoma is suggested by the presence of enlarged lymph nodes in other compartments of the mediastinum, axilla, neck, retrocrural space, and upper abdomen. These are also areas included in a standard thoracic CT study. Pleural effusions are seen frequently, due to venous or lymphatic obstruction, and are associated with poor outcome [21]. Pericardial effusion is seen in up to one-third of the patients and is considered to be due to obstruction or lymphomatous invasion [21]. Hence, a diagnosis of lymphoma should be considered in young adults or patients above

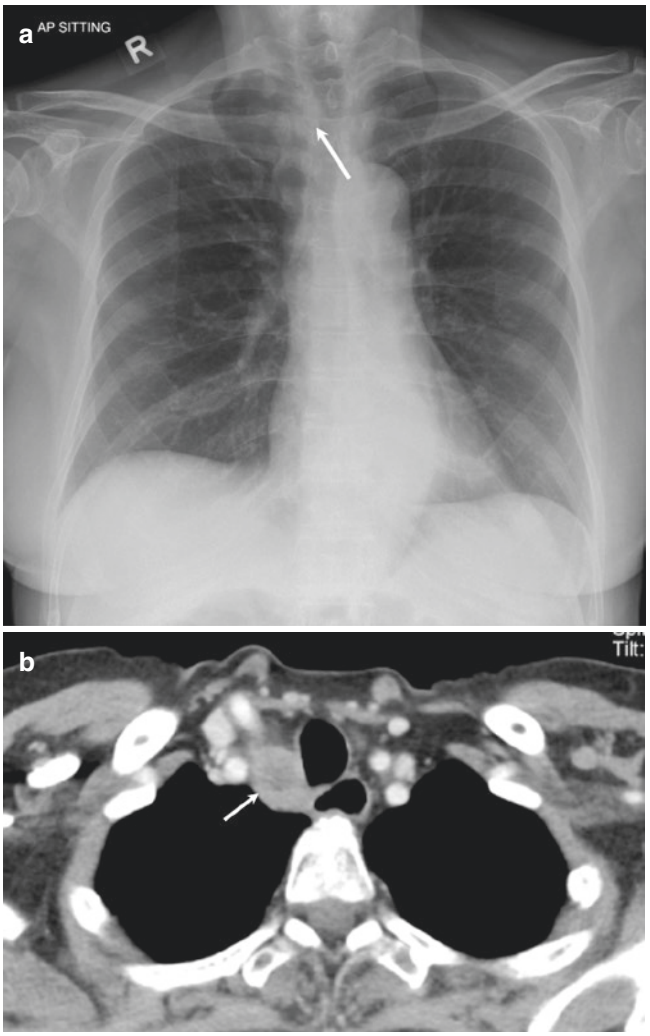

Fig. 8.26 51-year-old woman with stomach cancer. (**a**) Frontal radiograph shows indentation on the right lateral wall of the trachea with subtle focal thickening of the paratracheal stripe (arrow). (**b**) Axial CT image reveals a metastatic right paratracheal lymph node (arrow)

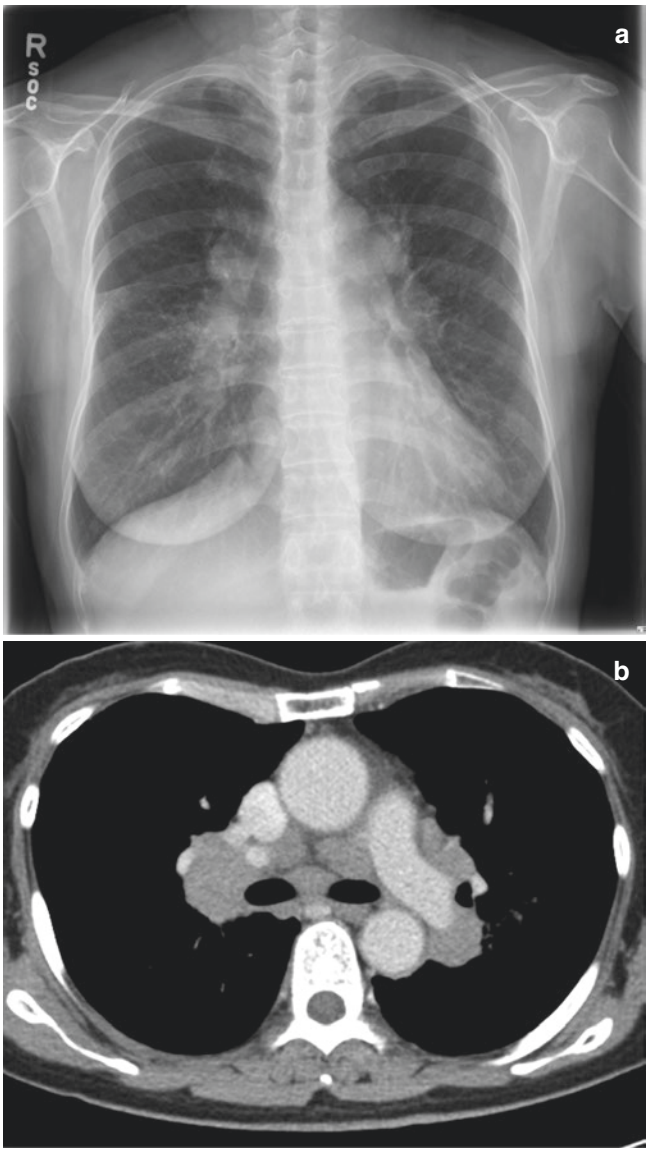

Fig. 8.27 Sarcoidosis with bilateral hilar lymphadenopathy. (**a**) Frontal radiograph shows lobular opacities in both hila while the pulmonary arteries can be seen through them (positive "hilum overlay" sign). The lower lobe pulmonary artery branches do not converge on the enlarged hilum ("hilum convergence" sign is absent) suggesting that the enlarged hilum is not due to dilated pulmonary arteries. (**b**) Axial CT image confirms the finding

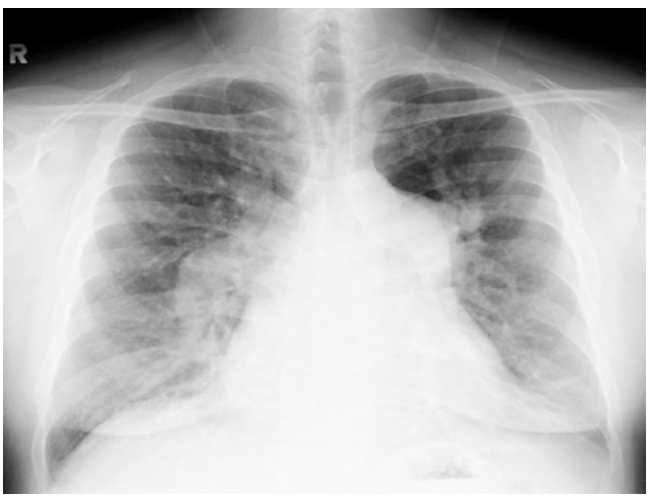

Fig. 8.28 Enlarged hilum due to dilated pulmonary arteries from pulmonary artery hypertension. The peripheral branches of pulmonary arteries are converging on the enlarged hila, in keeping with dilated pulmonary arteries ("hilum convergence" sign is positive)

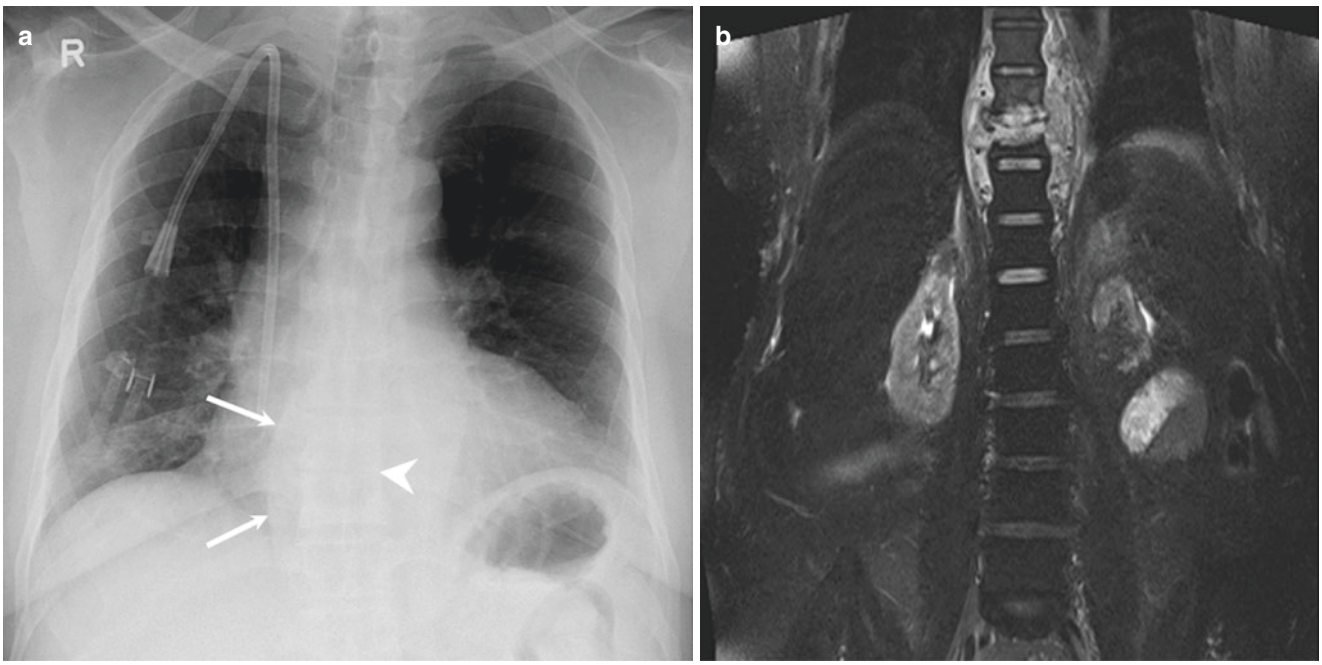

Fig. 8.29 62-year-old woman with spondylodiscitis. (**a**) Frontal radiograph shows paravertebral opacity in the lower dorsal region with a displacement of the right paraspinal line (arrows) and narrowing of the T10–11 intervertebral space (arrowhead). Bony changes are useful in localization of the mass adjacent to the spine. (**b**) Coronal MR image of dorsal-lumbar spine shows changes of spondylodiscitis with a paravertebral abscess

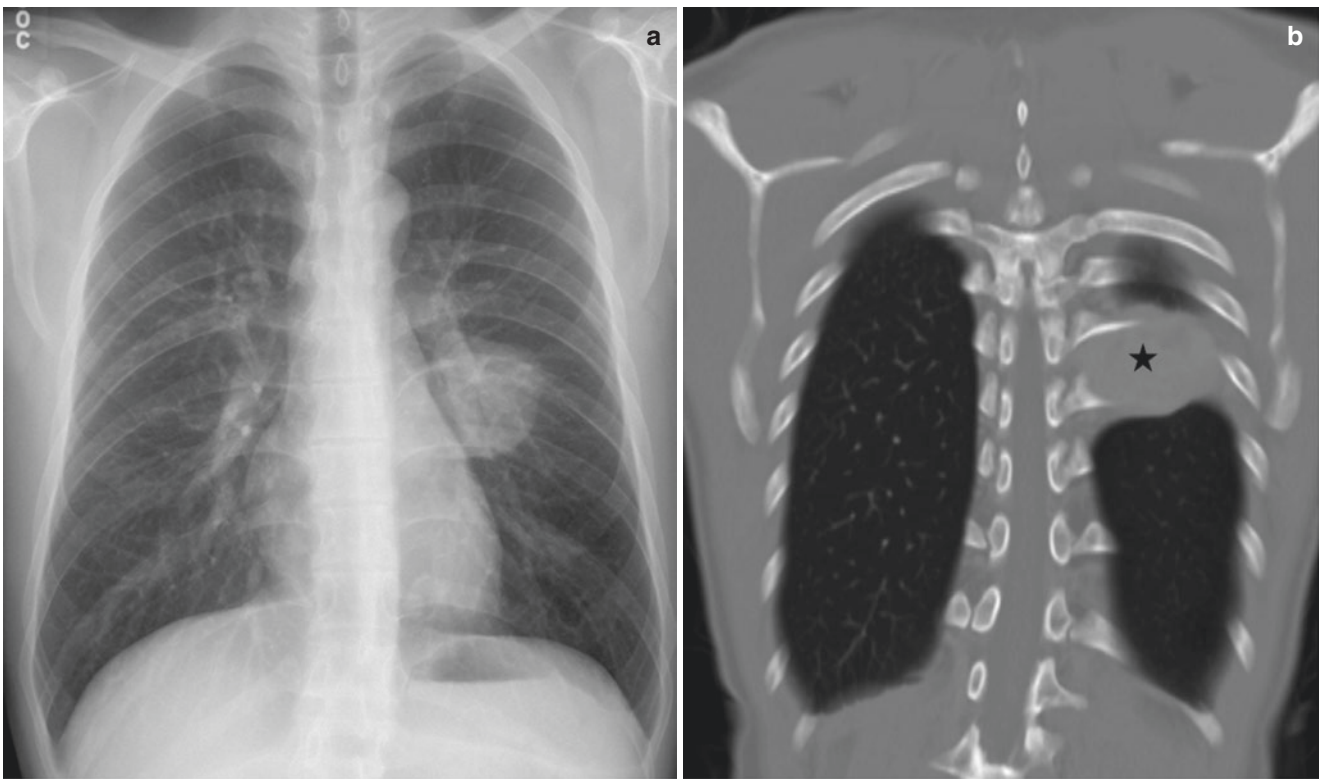

Fig. 8.30 Posterior mediastinal schwannoma. (**a**) Frontal radiograph shows a left parahilar opacity with scalloping of the adjacent posterior ribs confirming that the mass is in the posterior mediastinum. Note that the "hilum overlay" sign is present (left lower lobe pulmonary artery can be seen through the mass). (**b**) Coronal CT image demonstrates that the mass (asterisk) is located in the posterior intercostal space

Table 8.3 Paracardiac masses

• Paracardiac fat pad
• Pericardial cyst
• Thymolipoma
• Morgagni hernia
• Submucosal esophageal mass

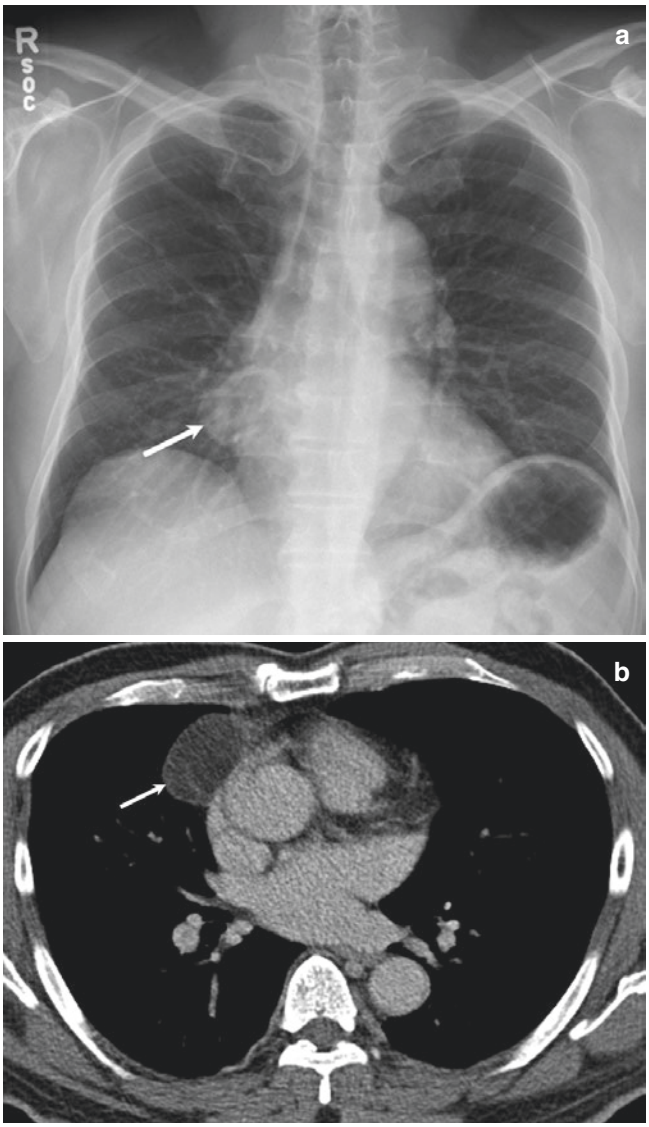

Fig. 8.31 Thymolipoma in the paracardiac location. (**a**) Frontal radiograph shows focal opacity (arrow) silhouetting and bulging out of the right heart border with "hilum overlay" sign present as pulmonary vessels can be seen through it. (**b**) Axial CT image shows a well-circumscribed, fatty soft tissue containing right paracardiac mass (arrow) in the anterior mediastinum

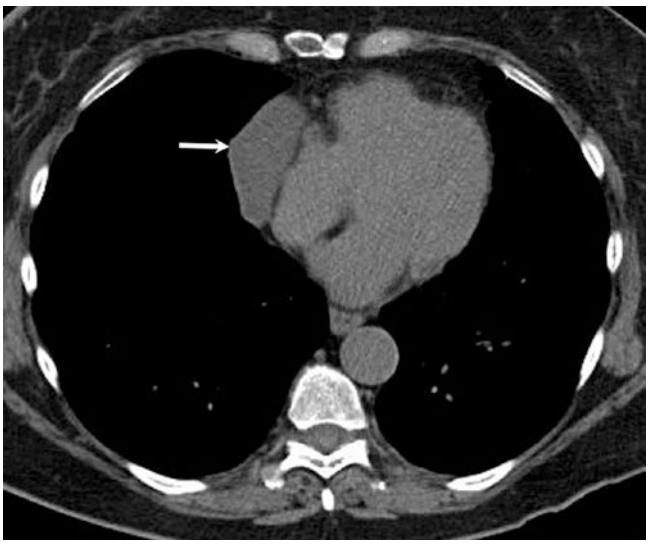

Fig. 8.32 Typical pericardial cyst (arrow) in paracardiac location

50 years old, with characteristic clinical and CT features. There is difficulty in differentiating the various types of lymphoma based on CT findings, as the lymphoma types show overlapping CT features. HL is characterized by large irregular lobulated anterior mediastinal mass with associated mediastinal lymphadenopathy. B-cell lymphoma is characterized by large anterior mediastinal mass with regular contour, necrotic areas, absence of mediastinal lymphadenopathy, and presence of vascular compression (Fig. 8.41). T-cell lymphoblastic lymphoma is characterized by regular contour, high prevalence of cervical and abdominal lymphadenopathy, and splenomegaly [22].

8.6.5 Thyroid Mass

Retrosternal extension of an enlarged thyroid gland can present as a mediastinal mass. The diagnosis is straightforward on CT—hyperdense paratracheal mass contiguous with the thyroid. Benign retrosternal goiter shows areas of cystic degeneration and calcification with mass effect on the trachea. Rarely, an "ectopic thyroid" mass may not reveal any communication with the thyroid gland. In such cases, CT attenuation and enhancement pattern of the mass similar to the thyroid help in making the diagnosis. If the "ectopic thyroid" contains functional thyroid tissue, then scintigraphy with a radioactive isotope of iodine is confirmatory. Thyroid malignancy extending to the mediastinum is less common.

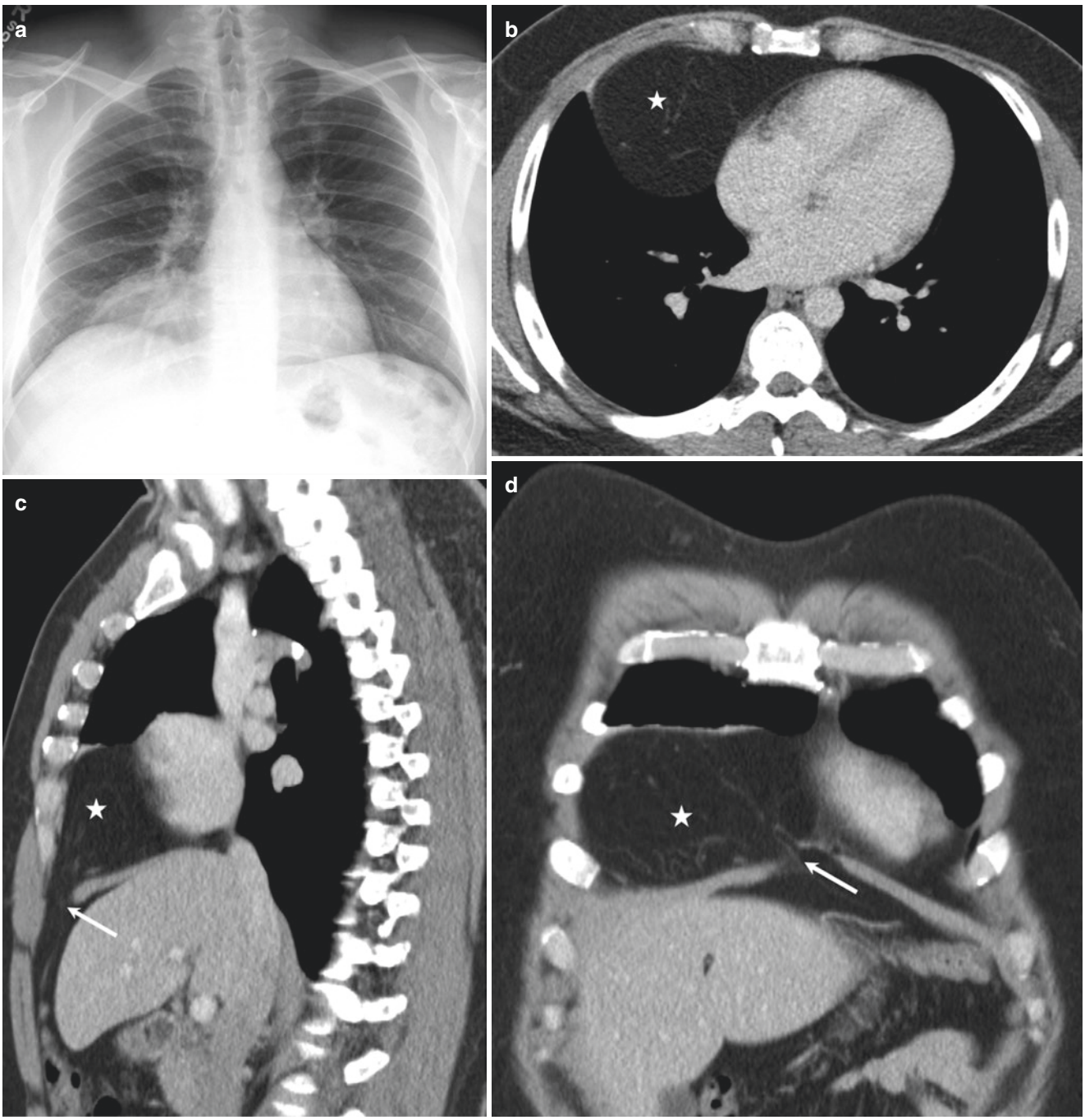

Fig. 8.33 Fat-containing Morgagni hernia as a paracardiac mass. (**a**) Frontal radiograph shows a low-density right paracardiac mass. (**b**). Axial CT image confirms it to be a paracardiac fat pad (asterisk). (**c**, **d**) Sagittal and coronal CT images show a defect (arrow) in the diaphragm with herniation of abdominal fat (asterisk) in the thorax

Table 8.4 Features of anterior mediastinal mass

• Mass may widen the paratracheal stripe with mass effect on the trachea
• Mass will silhouette the ascending aorta and right or left heart border
• Mass will *not* silhouette the aortic knuckle and descending aorta
• Pulmonary artery can be seen through the mass
• Posterior mediastinal lines, if identifiable, will be intact
• Air-fluid levels can be seen in Morgagni hernia

Table 8.5 Features of middle mediastinal mass

• Opacity in the central chest
• Mass effect on the central tracheobronchial tree
• Mass may not project from the mediastinal borders
• Displacement of the azygoesophageal recess (subcarinal mass or lymphadenopathy)
• *Non-visualization* of the outer surface of the medial wall of the right main stem bronchus and bronchus intermedius (subcarinal mass or lymphadenopathy)
• Convex aortopulmonary window
• *Absent* hilum overlay sign

Table 8.6 Features of posterior mediastinal mass

• Mass will silhouette the aortic knuckle and descending aorta
• Mass will *not* silhouette the ascending aorta and right or left heart border
• Pulmonary artery can be seen through the mass
• Azygoesophageal recess may be displaced
• Paraspinal lines, if identifiable, may be displaced
• Bony changes involving the vertebral column or ribs are the most specific sign
• Air-fluid levels may be present

Table 8.7 Common mediastinal masses

Anterior mediastinum	Middle mediastinum	Posterior mediastinum
Thymic tumor	Lymphoma	Lymphoma
Lymphoma	Arch of aorta aneurysm	Neurogenic tumor
Germ cell tumor	Pericardial cyst	Esophageal tumor
Metastases	Bronchogenic cyst	Extramedullary hematopoiesis
Thyroid goiter		Bochdalek hernia
Morgagni hernia		Descending aorta aneurysm
Ascending aorta aneurysm		Paravertebral abscess
		Duplication cyst
		Bronchogenic cyst

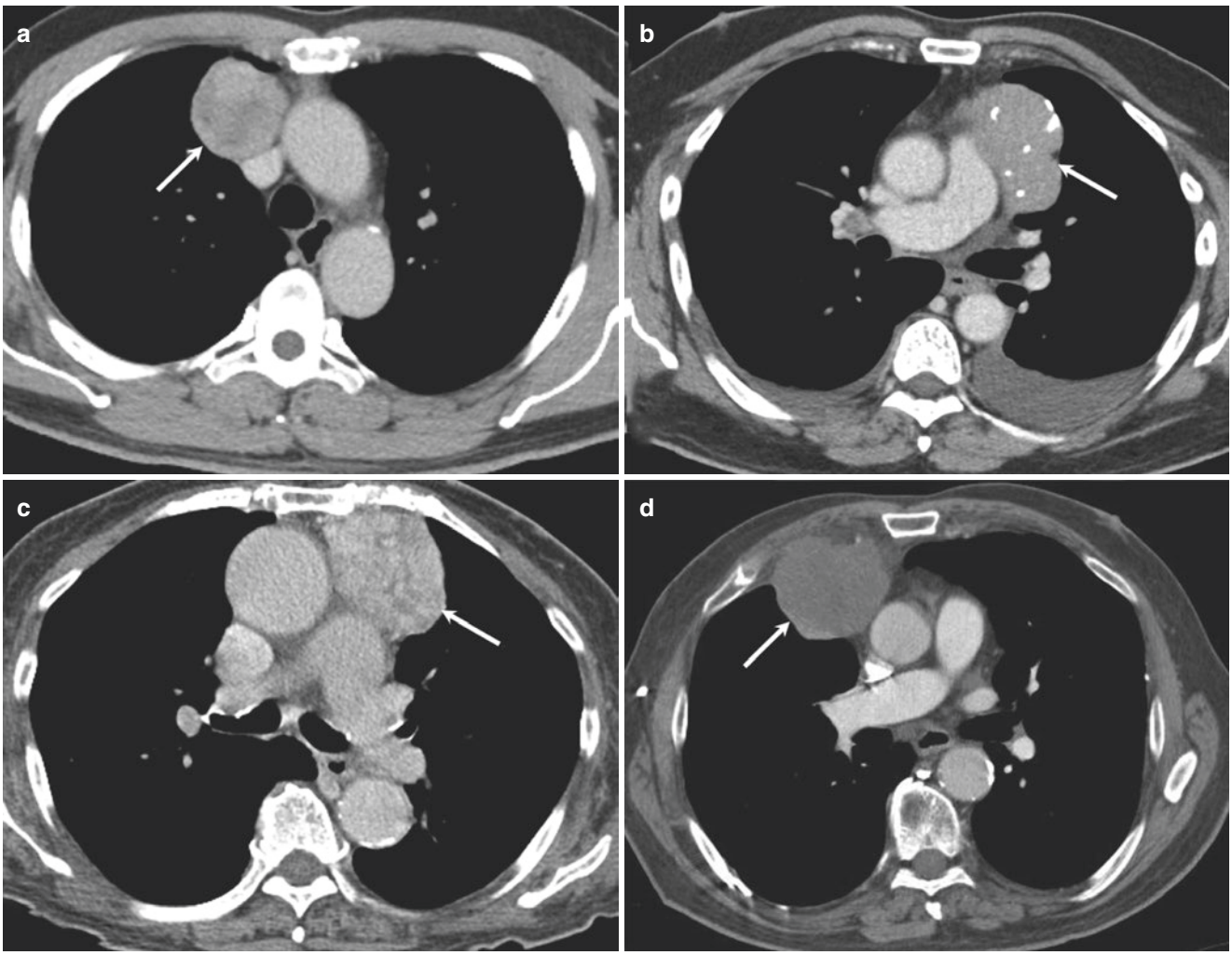

Fig. 8.34 Four different cases of thymoma. (**a**) Non-invasive well-circumscribed thymoma (arrow) with mild heterogeneous enhancement. (**b**) Non-invasive thymoma (arrow) with foci of calcification. (**c**) Non-invasive thymoma (arrow) with heterogeneous enhancement. (**d**) Poorly enhancing invasive thymoma (arrow) invading the chest wall

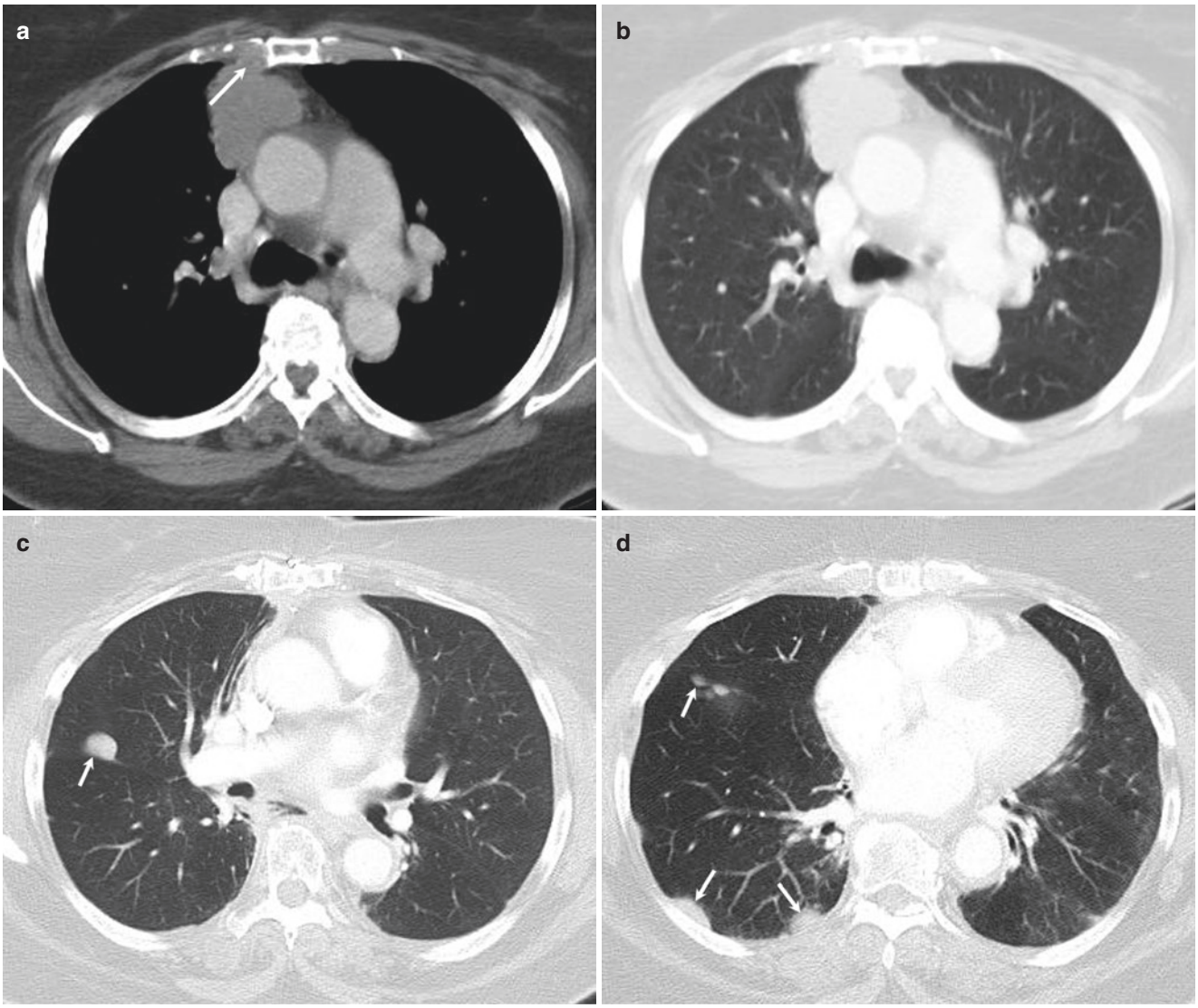

Fig. 8.35 Invasive thymoma with recurrence. (**a**, **b**) Axial CT images show a lobulated mass in the prevascular space with focal invasion of chest wall (arrow). (**c**, **d**) Post-operative follow-up after 6 years—axial CT images show multiple pleural-based nodules (arrows)

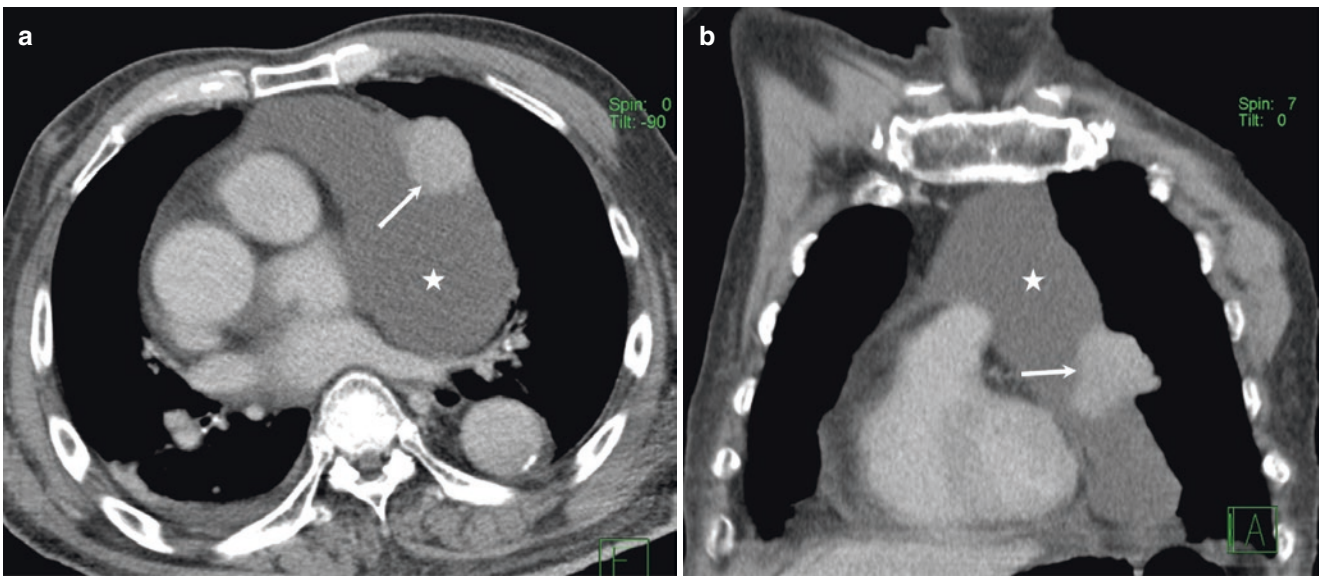

Fig. 8.36 Thymoma with a large thymic cyst. (**a**, **b**) Axial and coronal CT images show a mass (arrow) with a large cyst (asterisk). Surgery revealed an invasive thymoma

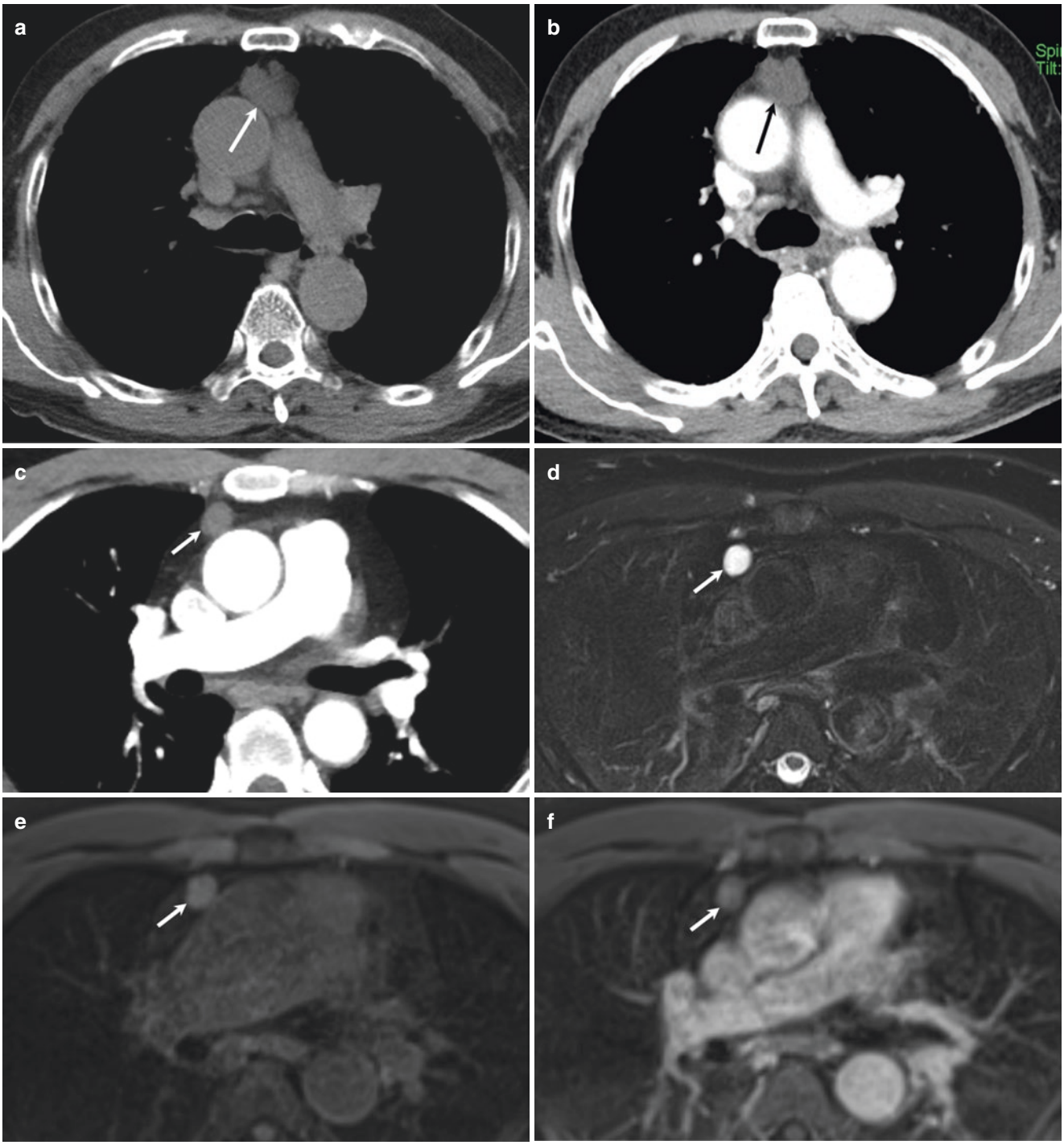

Fig. 8.37 (**a**, **b**) Unenhanced and contrast-enhanced CT images show a thymic cyst (arrow) in typical prevascular space location without any enhancement. High-density thymic cyst in another patient. (**c**) Axial CT image shows a small well-marginated nodule with CT density of 54HU. (**d**–**f**) Fat-supressed T2W, precontrast T1W, and postcontrast T1W images confirm a cystic lesion with no enhancing component. The high density on CT is likely due to thick proteinaceous content

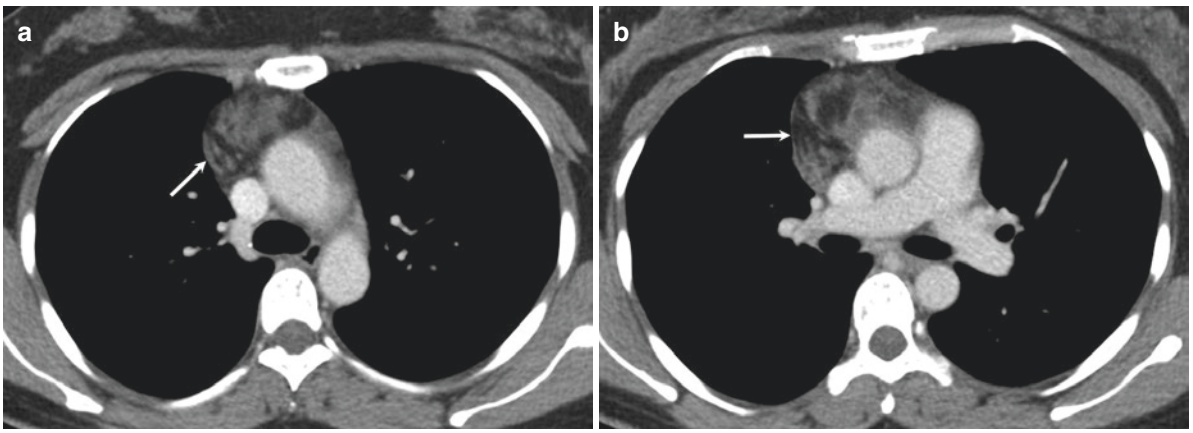

Fig. 8.38 31-year-old woman with thymolipoma. (**a**, **b**) Axial CT images show fat density mass (arrow) with whorls of the soft tissue component in the anterior mediastinum

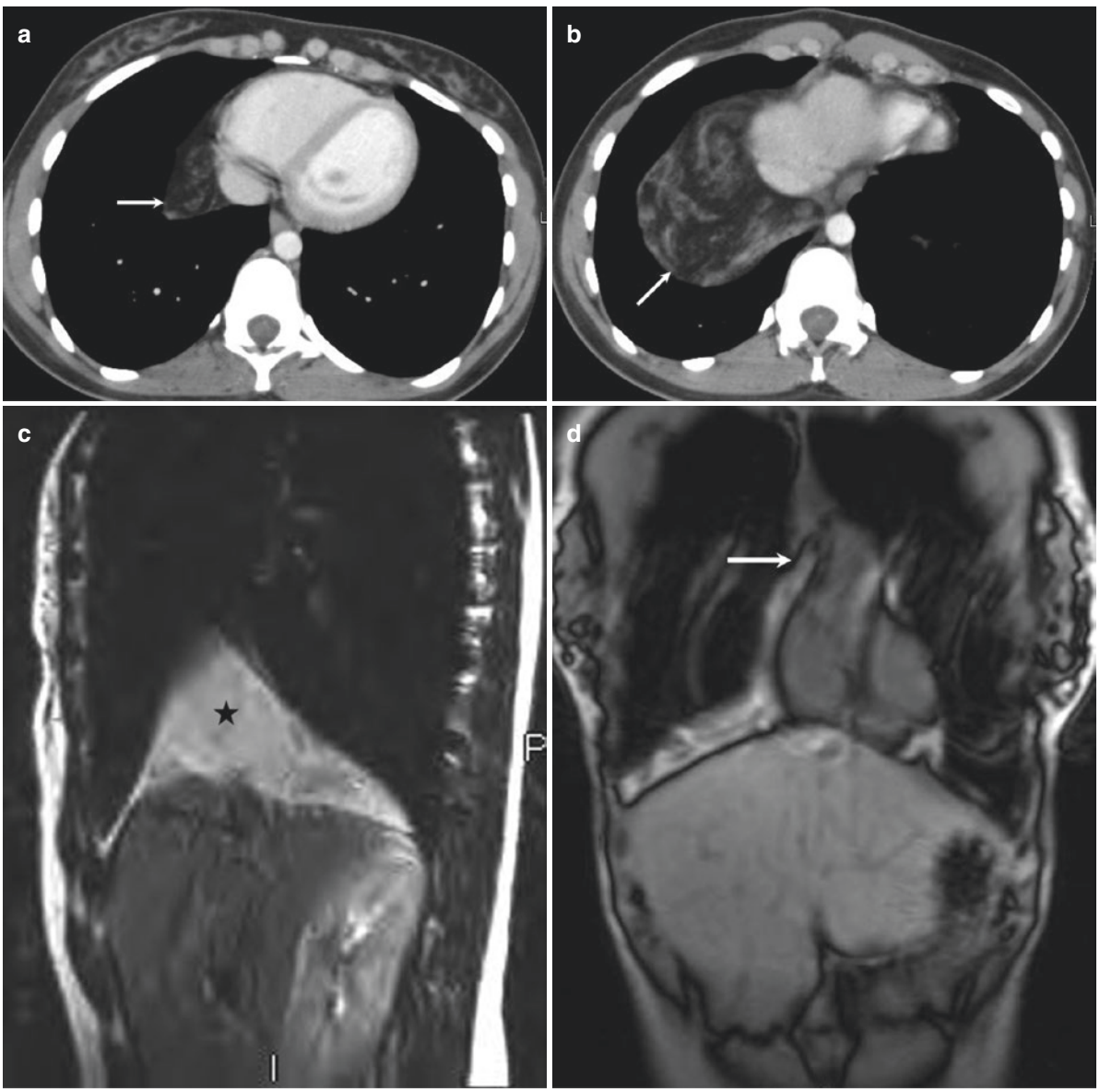

Fig. 8.39 Large thymolipoma in the inferior compartment of anterior mediastinum abutting the diaphragm. (**a**, **b**) Axial CT images show a well-circumscribed fat density mass (arrow) with whorls of soft tissue adjacent to the heart with larger component inferiorly. (**c**, **d**) Sagittal and coronal T1W MRI images show a triangular predominantly fat-containing mass (asterisk), based on the diaphragm but with a pedicle (arrow) extending toward the thymic region

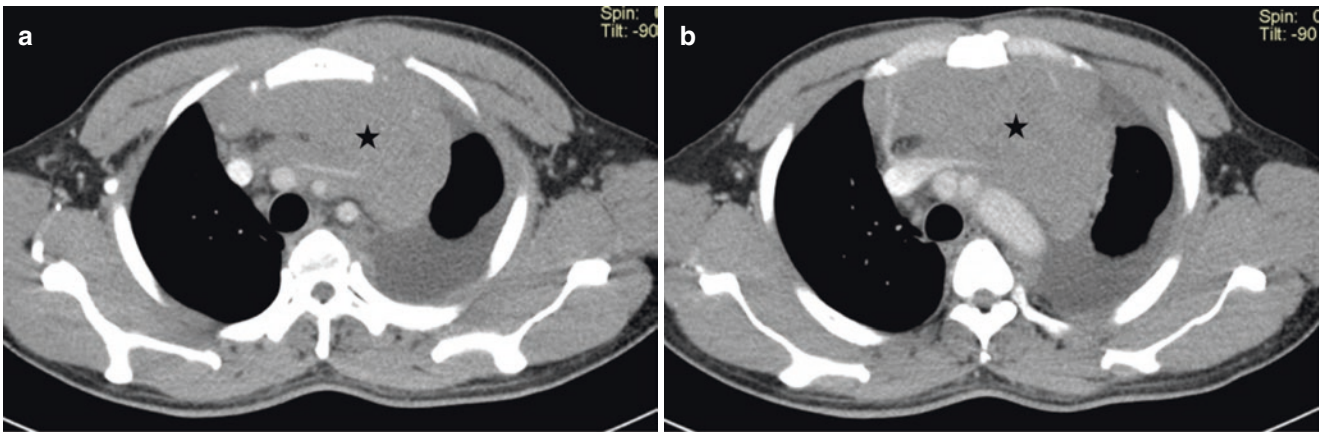

Fig. 8.40 Lymphoma in the anterior mediastinum. (**a**, **b**) Axial CT images show a homogeneous mass (asterisk) with mass effect on the vessels without invasion. There is left pleural effusion

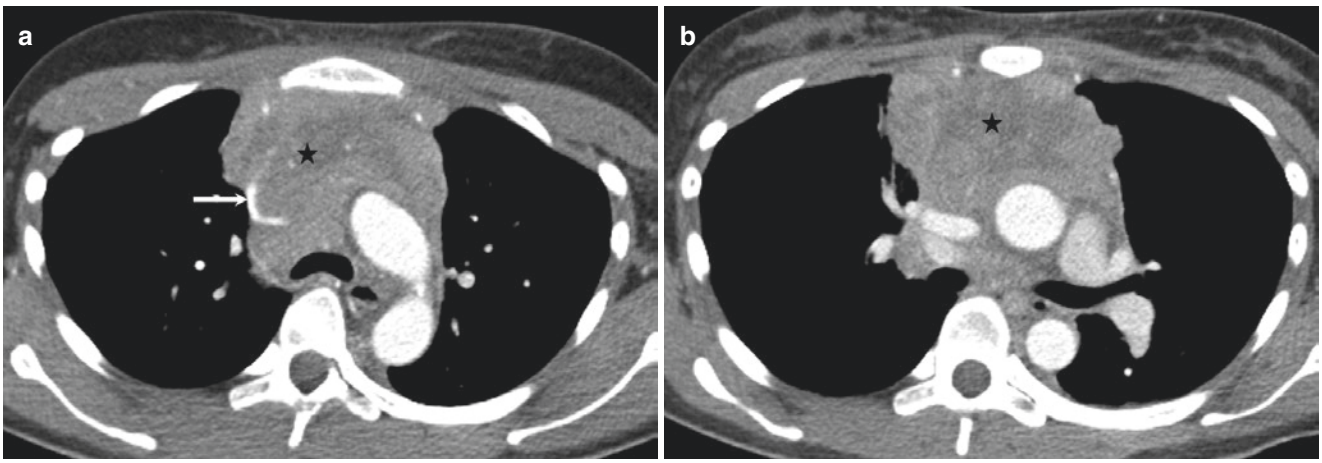

Fig. 8.41 51-year-old woman with superior vena cava syndrome from B-cell lymphoma. (**a**, **b**) Axial CT images show large lobulated mass with areas of necrosis compressing the superior vena cava (arrow) and encasing the great arteries

CT signs of thyroid malignancy include an invasive mass, lymphadenopathy, curvilinear calcification in the thyroid and/or lymph nodes, and low-density thyroid mass. A thyroid nodule with neck lymphadenopathy demonstrating spectrum of features like calcification, cystic degeneration/necrosis, and enhancement at various nodal levels is highly suspicious of a malignant thyroid lesion (Figs. 8.42 and 8.43).

8.6.6 Germ Cell Tumor

Germ cell tumors (GCTs) of the mediastinum are derived from primitive germ cells that fail to migrate completely during early embryonic development. These occur most commonly between the second and fourth decade of life. Generally, GCTs are divided into three groups: teratoma (dermoid cyst, mature teratoma, immature teratoma, and teratoma with malignant transformation), seminoma, and non-seminomatous malignant GCTs (embryonal carcinoma, endodermal sinus tumor, choriocarcinoma, and mixed type) [23]. Benign GCTs are more common in females, while malignant tumors are more common in males.

Teratomas are the most common GCTs and are commonly discovered in asymptomatic persons. On CT, benign teratomas appear as well-defined round or lobulated masses containing a variable amount of four densities: soft tissue, fluid, fat, and calcifications (central or rim calcifications), with the dominant component being fluid [24, 25]. All four components are seen in 39% of the teratomas, while 15% of the teratomas contain only fluid and soft tissue, without fat or calcium [24]. The calcification may represent ossification with tooth-like structures in some cases. A fat-fluid level, seen in 11% of the patients in a well-circumscribed anterior mediastinal mass, is diagnostic of a benign teratoma [24]. A malignant teratoma appears as a mass with irregular borders that infiltrates the mediastinal fat. Similar to the benign counterpart,

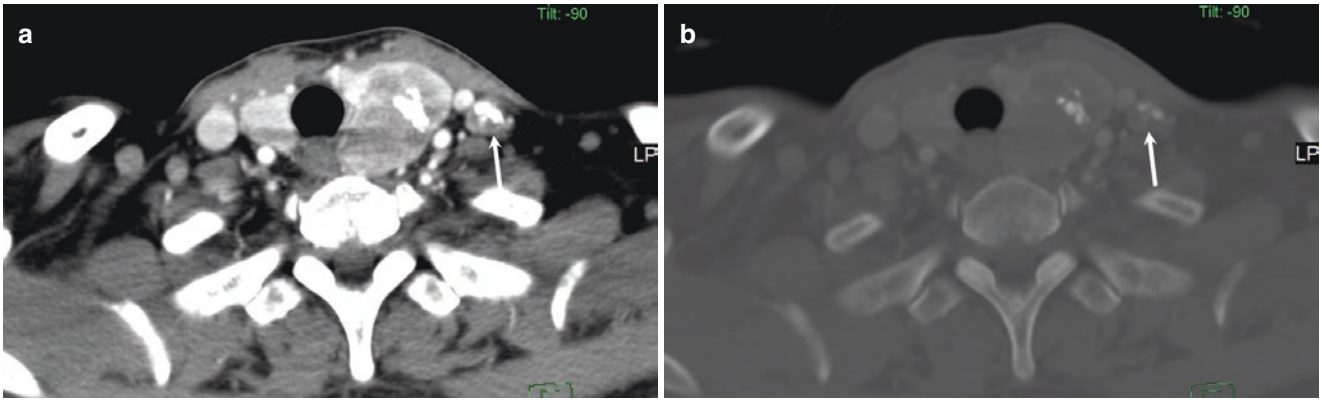

Fig. 8.42 Papillary thyroid cancer with nodal metastasis. (**a**, **b**) Axial CT images of thoracic inlet show hypodense mass in the left hemithyroid with a punctate and curvilinear pattern of calcification. The adjacent enlarged left supraclavicular lymph nodes also show similar calcifications (arrow)

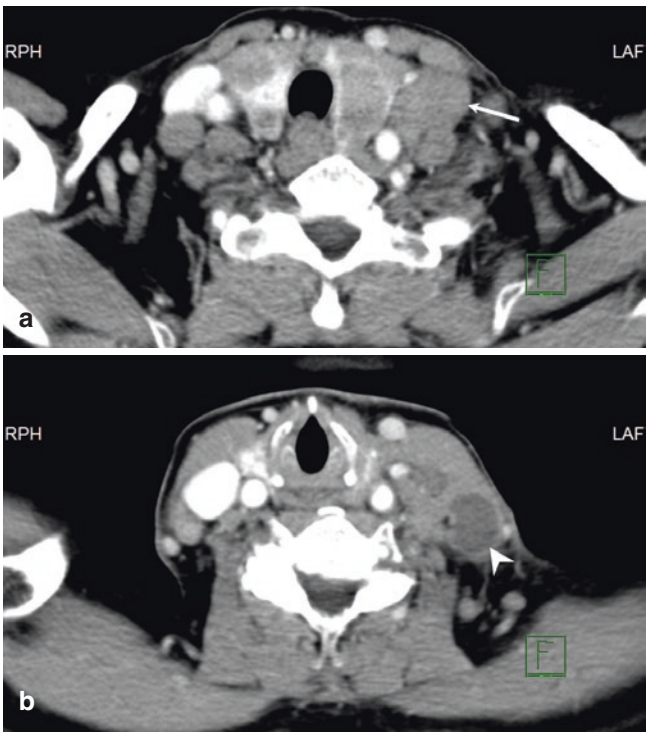

Fig. 8.43 Medullary thyroid carcinoma in a patient with multiple endocrine neoplasia type II (MEN2). (**a**) Axial CT image shows bilateral hypodense thyroid masses with enlarged, homogeneous density and bilateral lymph nodes (arrows). (**b**) Axial CT image slightly cranially shows cystic lymph nodes. A few lymph nodes showed dense calcifications (not shown)

malignant teratomas also contain a variable amount of fat, fluid, soft tissue, and calcification. Presence of large solid soft tissue, enhancement, or necrotic component, with elevated α-fetoprotein, should raise concern for a malignant teratoma [26]. Nevertheless, it is not always possible to differentiate mature from immature teratomas by CT. Teratomas can rupture with spillage of its contents into the bronchus with resultant obstructive pneumonitis and expectoration of sebum.

Seminomas are rare malignant GCTs with peak prevalence in the third and fourth decade of life. Patients are almost always symptomatic and present with substernal pain, respiratory symptoms, and weight loss, with some showing superior vena cava syndrome. CT shows a large lobulated mass with homogeneous or heterogeneous density, usually without any calcification [25, 27] (Fig. 8.44). A pattern of stippled or ring-like calcification has been described in a few cases [25]. The mass does not show local invasion but can have metastases to the lungs and bones. Thoracic lymph nodes may be present or can be the site of recurrence.

Non-seminomatous GCTs are rare tumors that affect young patients and are mostly symptomatic due to associated mass effect. On CT, a non-seminomatous GCT appears as a large heterogeneous mass with local invasion and metastases [25, 27] (Figs. 8.45 and 8.46). Pleural effusions, pericardial effusion, and chest wall invasion may be present with loss of fat planes at the interface of tumor and adjacent structures. A high α-fetoprotein or beta-human chorionic gonadotropin level in the presence of a large mediastinal mass helps in the diagnosis. Differentiation of seminomas and non-seminomatous GCTs from the other anterior mediastinal masses is not always possible, with a diagnostic accuracy of only 25% by CT [28].

8.6.7 Neurogenic Tumors

Neurogenic tumors account for 20% of all mediastinal masses in adults, with 95% located in the posterior mediastinum. Neurogenic tumors arise from the neural crest cells

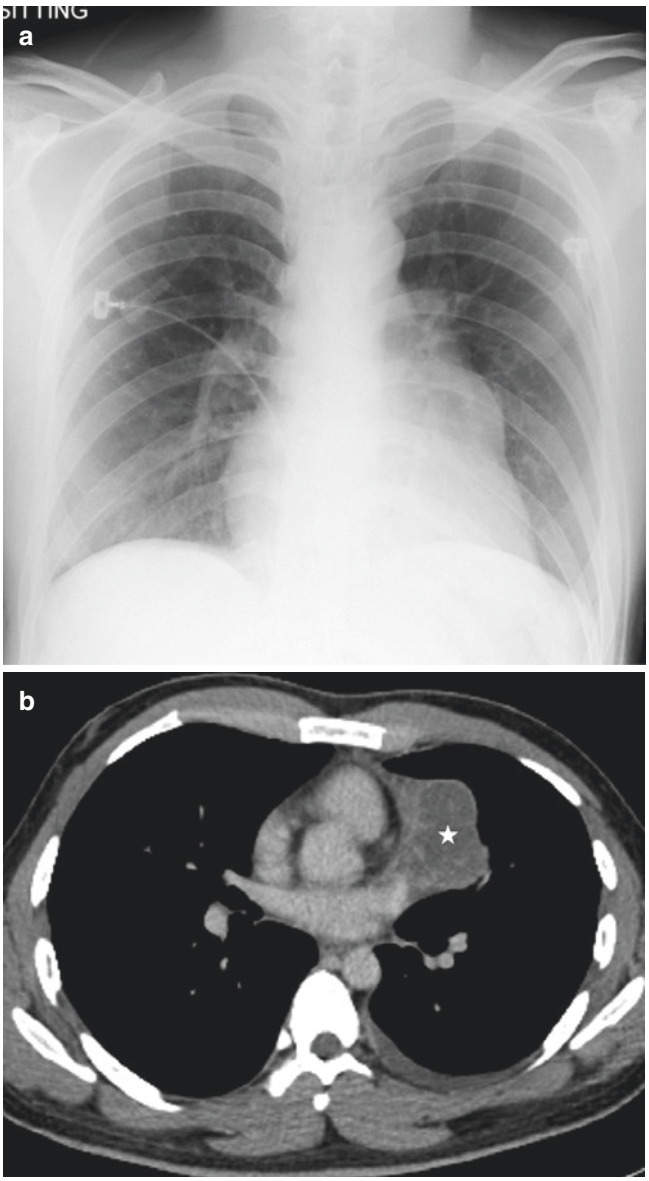

Fig. 8.44 28-year-old man with seminoma. (**a**) Frontal radiograph shows a left paramediastinal mass silhouetting the left heart border but preserving the descending aorta shadow. (**b**) Axial CT image shows a well-circumscribed lobulated mass in the anterior mediastinum with heterogeneous enhancement

located in three components of the nervous system: peripheral nerves, sympathetic ganglia, and paraganglia [29] (Table 8.8).

Nerve sheath tumors account for more than half of the neurogenic tumors in the mediastinum. These include benign schwannoma, neurofibroma, and malignant peripheral nerve sheath tumor. Most tumors originate from a spinal or proximal intercostal nerve and can have a component in the spinal canal as well. Benign tumors are slow growing, usually asymptomatic, and incidentally detected on routine chest radiographs, around the third decade of life. On CT, benign tumors appear as homogeneous, mildly enhancing mass associated with smooth scalloping or notching of the ribs or widening of the spinal foramen [30] (Fig. 8.47). Cystic degeneration, hemorrhage, hyalinization, and calcification are not uncommon in long-standing schwannoma termed as "ancient schwannoma." Malignant tumors can show invasive features and can be associated with metastases. MRI of the spine is more useful in the assessment of these neurogenic masses.

Neurogenic tumors of the autonomic nervous system arise in the sympathetic ganglia with approximately two-thirds occurring in patients less than 20 years old. These account for 25% of mediastinal neurogenic tumors and include ganglioneuroma, ganglioneuroblastoma, and neuroblastoma. Ganglioneuromas are benign, while neuroblastomas are malignant tumors [29]. Ganglioneuroblastomas are the least common malignant tumors among this group. These tumors may be biologically active, producing catecholamines, and are characteristically located in the paravertebral region alongside multiple vertebral bodies (Fig. 8.17). CT shows a large isodense or hypodense mass in a characteristic location, without any enhancement. Again, MRI is the investigation of choice for assessment of these masses [30].

Paragangliomas are extremely rare neurogenic tumors and include pheochromocytomas and chemodectomas. Pheochromocytomas arise from chromaffin cells, while chemodectomas originate from non-chromaffin cells. Paragangliomas are intensely enhancing masses located along the sympathetic chain in the paravertebral region (Fig. 8.48). Another characteristic location is in the aortopulmonary paraganglia, between the aorta and pulmonary artery [30].

8.6.8 Cystic Masses of the Mediastinum

Cystic masses are thin-walled structures containing fluid and are usually asymptomatic unless complicated by infection or hemorrhage (Table 8.9). Classically, CT demonstrates homogeneous low density in these masses (Figs. 8.49, 8.50, and 8.51). However, the CT attenuation in these cysts can be higher due to hemorrhage, infection, or thick mucoid content. MRI is useful in differentiating high-density cysts from solid masses (Fig. 8.37) [11]. Majority of the bronchogenic cysts are found along the central airways in the middle or posterior mediastinum and rarely in the lung parenchyma or diaphragm. Esophageal duplication cysts are located along the esophagus and may cause mass effect on the esophagus. Pericardial cysts most commonly occur near the cardiophrenic angle but can be seen anywhere along the pericardium including its superior recess. Lymphangiomas can be

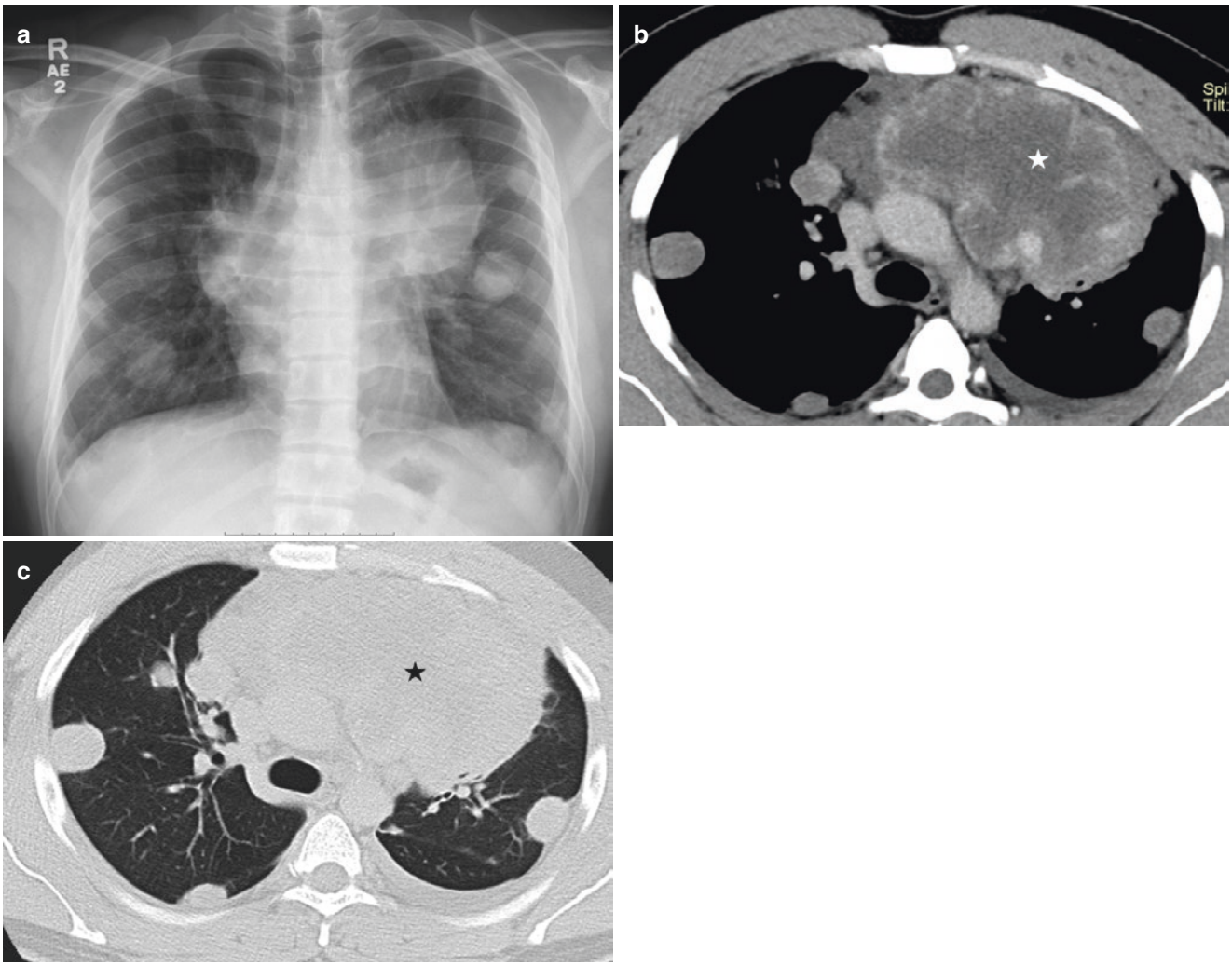

Fig. 8.45 25-year-old man with large anterior mediastinal non-seminomatous GCT (choriocarcinoma) with pulmonary metastases. (**a**) Frontal radiograph shows a left paramediastinal mass silhouetting the upper left heart border with positive "hilum overlay" sign. Multiple "cannonball" metastases are present. (**b**, **c**) Axial CT images show a heterogeneous invasive mass (asterisk) in the anterior mediastinum, inseparable from the great vessels and chest wall, with multiple pulmonary metastases and left pleural effusion. The non-seminomatous tumors, unlike seminoma, are often large in size at the time of presentation

uniloculated or multiloculated. They tend to mold themselves within the mediastinum, without any displacement of adjacent structures.

8.7 Pneumomediastinum

Pneumomediastinum or mediastinal emphysema can result from a breach in the wall of the esophagus, tracheobronchial tree, or lung. Pneumomediastinum can also result from tracking of air from the retroperitoneum and neck. The mediastinal emphysema can also track into the pleural cavity and present as pneumothorax; extend to the retroperitoneum through diaphragmatic hiatus; extend to the fascial planes of the superior mediastinum, neck, and chest wall; and extend to the spinal canal along the nerve roots as "pneumorrhachis". The radiographic signs of pneumomediastinum are described in Table 8.10 [31, 32] (Figs. 8.52, 8.53, and 8.54).

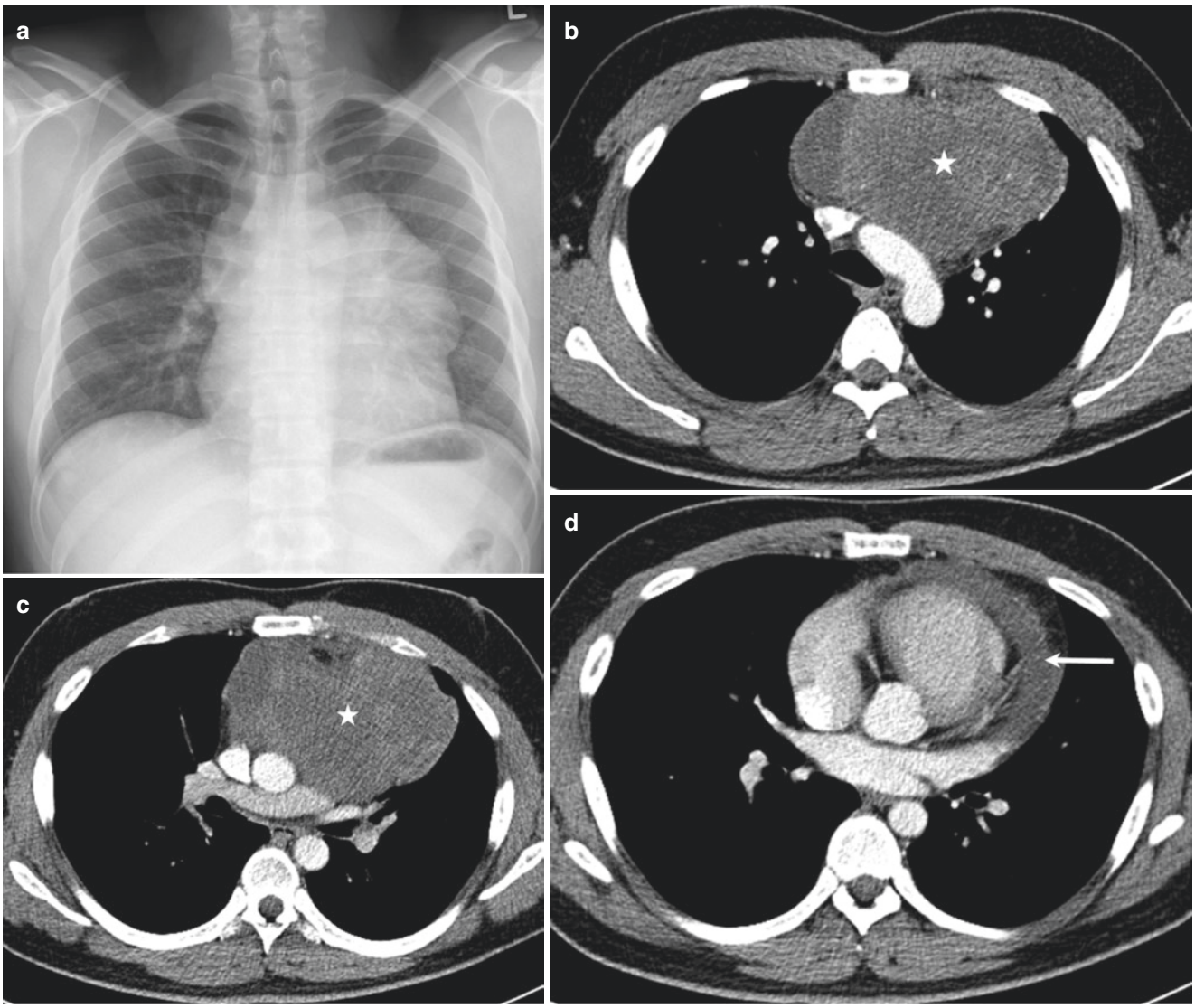

Fig. 8.46 28-year-old man with yolk sac tumor in the anterior mediastinum. (**a**) Frontal radiograph shows a large anterior mediastinal mass, silhouetting the right and left heart borders but not obscuring the descending aorta. "Hilum overlay" sign is present. (**b**–**d**) Axial CT images show large heterogeneous mass (asterisk) in the anterior mediastinum, inseparable from the chest wall and great vessels and causing mass effect. Note the pericardial effusion (arrow)

Table 8.8 Neurogenic tumors in the mediastinum

Types	Nerve sheath tumors	Neurogenic tumors of the autonomic nervous system	Paragangliomas
Tumors	Schwannoma Neurofibroma Neurilemmoma Malignant peripheral nerve sheath tumor	Ganglioneuroma Ganglioneuroblastoma Neuroblastoma	Pheochromocytomas Chemodectomas
Location	Paravertebral or "dumbbell" shape with two components	Paravertebral region alongside multiple vertebral bodies	Paravertebral region or aortopulmonary paraganglia

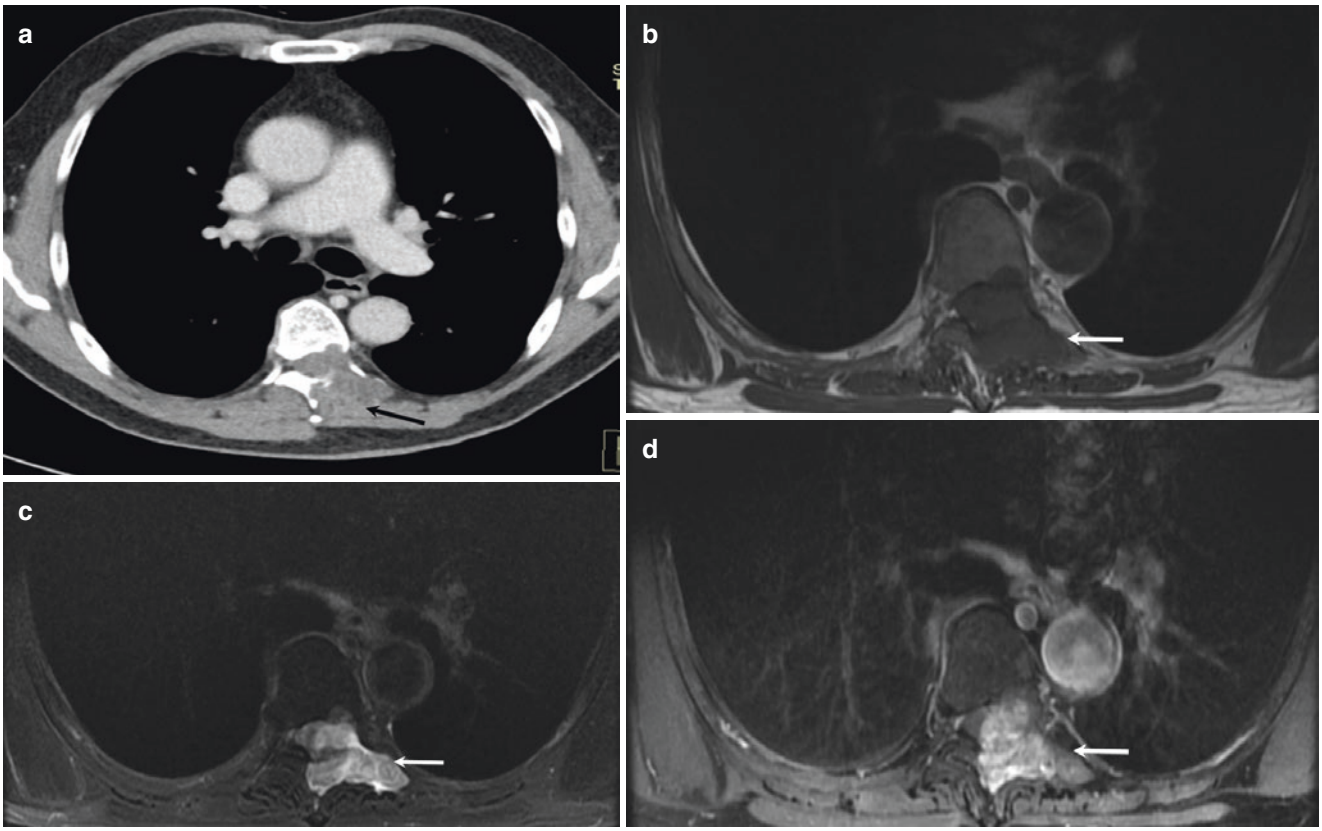

Fig. 8.47 Schwannoma in a 34-year-old man. (**a**) Axial CT shows a soft tissue mass in the left paravertebral region (arrow) with extradural spinal extension and smooth scalloping of the bones. (**b–d**) Axial T1W, fat-suppressed T2W, and postcontrast T1W images show typical features of a schwannoma (arrow)

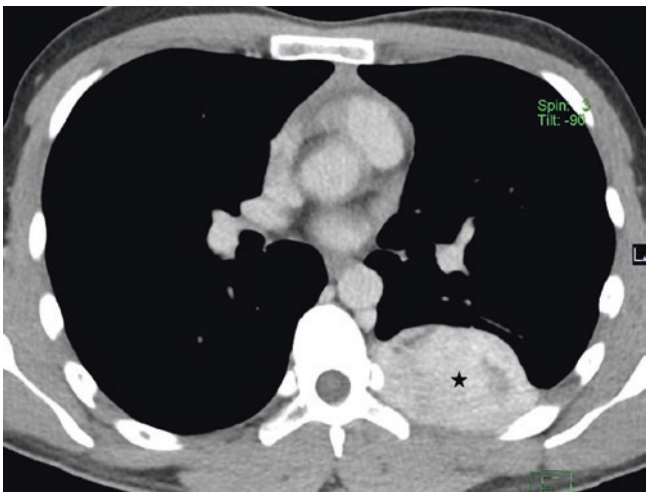

Fig. 8.48 31-year-old man with pheochromocytoma in the posterior mediastinum. Axial CT image shows an avidly enhancing well-circumscribed mass (asterisk) in the paravertebral region along the sympathetic chain

Table 8.9 Cystic masses in the mediastinum

• Thymic cyst
• Pericardial cyst
• Foregut duplication cysts
– Bronchogenic cyst
– Esophageal duplication cyst
• Lymphangioma
• High-riding pericardial recess

8.7.1 Spontaneous Pneumomediastinum

When no source of air in the mediastinum could be identified by endoscopy, CT scan, and barium examination, a diagnosis of spontaneous pneumomediastinum is considered. Spontaneous pneumomediastinum is usually seen in young adults presenting to emergency department with central chest pain. It is more common in asthmatic and smokers. A precipitating history of increased intrathoracic pressure like heavy exercise or screaming may be present [33]. The

patients with spontaneous pneumomediastinum usually have a benign course [33]. The pathophysiology is described by Macklin in 1939, based on a study of cat lung [34]. An increase in intra-alveolar pressure results in alveolar rupture, with air dissecting into the interstitium of the lung and subsequently extending to the mediastinum, near the root of the lung. With continuous leakage, the air enters the neck spaces, chest wall, and infrequently the retroperitoneum. The causes of the transient increase in intra-alveolar pressure are acute exacerbation of asthma, Valsalva maneuver (during coughing and sneezing), or intense physical exertion.

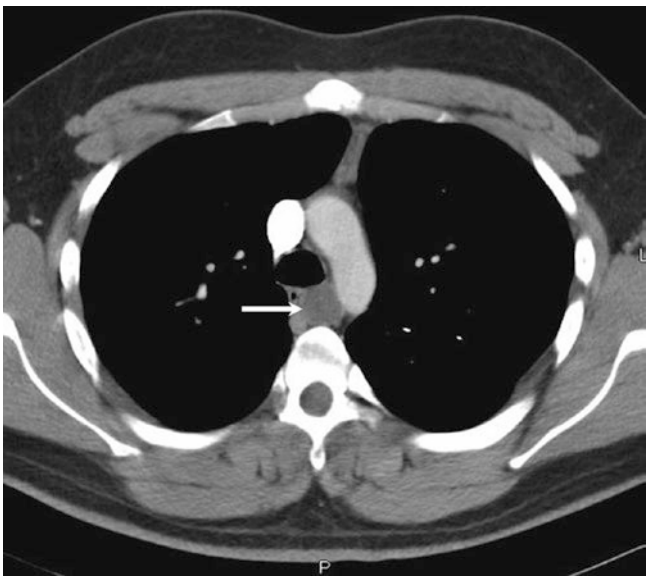

Fig. 8.49 Asymptomatic round esophageal duplication cyst (arrow) abutting the esophagus

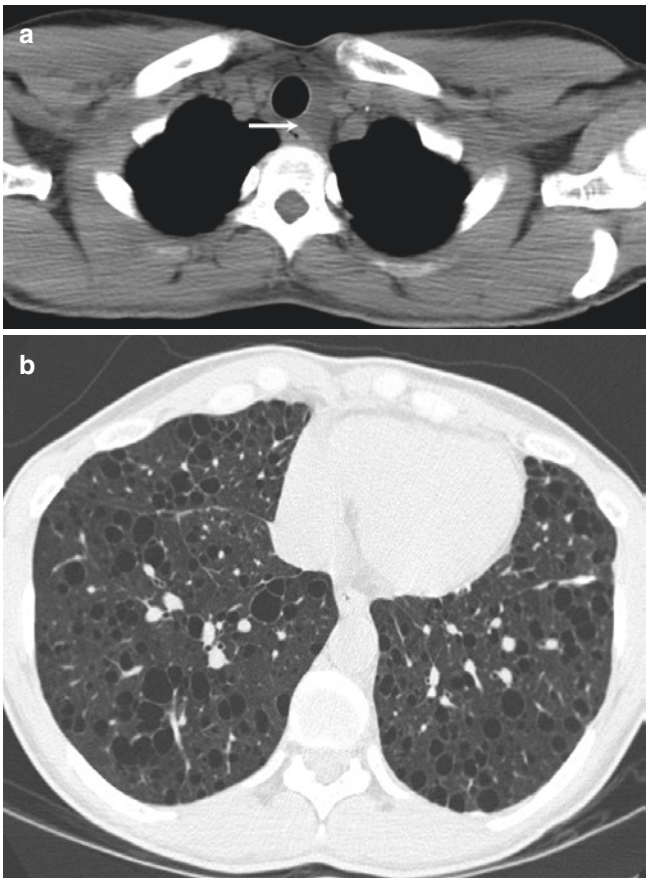

Fig. 8.50 Lymphangioma in a patient with lymphangioleiomyomatosis. (**a**) Axial unenhanced CT image shows a cystic lesion (arrow) molding itself in the superior mediastinum. (**b**) Axial CT image in lung window shows numerous well-defined round cysts in both lungs. The cyst is not round but molds itself in the space separating it from a duplication cyst

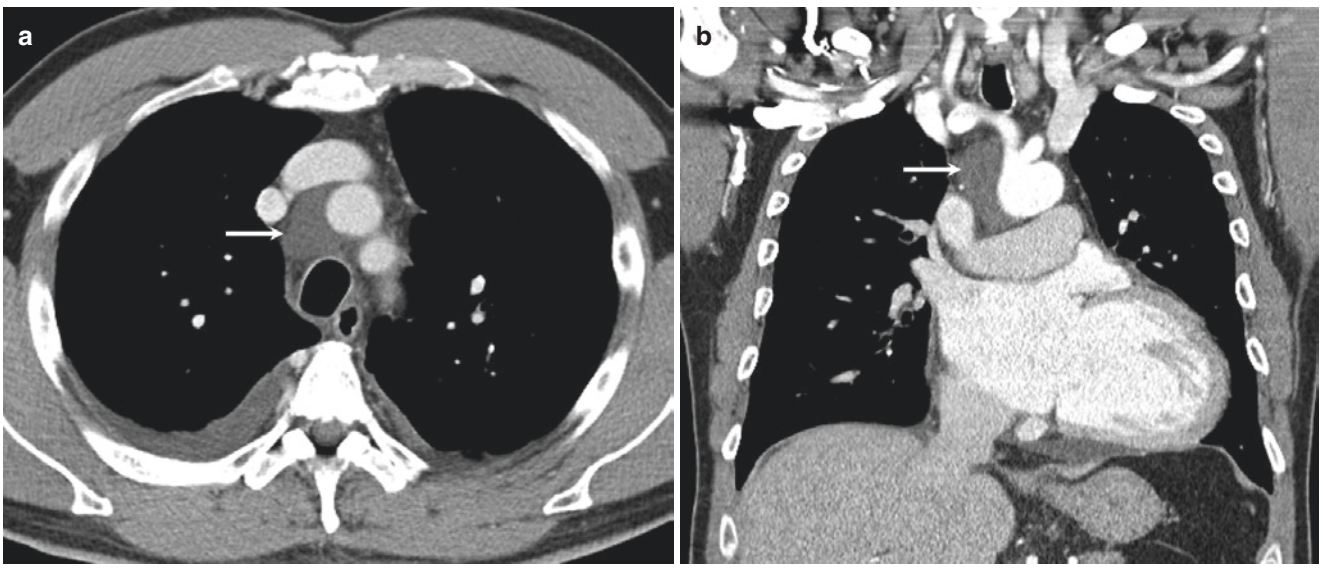

Fig. 8.51 High-riding superior pericardial recess. (**a**, **b**) Axial and coronal CT images show a structure of fluid density (arrow) in the right paratracheal location draping around the ascending aorta

Table 8.10 Radiographic signs of pneumomediastinum

Continuous diaphragm sign	Air extending between pericardium and diaphragm, depicting the superior surface of medial left hemidiaphragm. This can also be seen in pneumopericardium
Double bronchial wall sign	Mediastinal air wraps around the major bronchus, making its entire thickness visible
Tubular artery sign	Mediastinal air abutting the right border of descending aorta demarcating this normally concealed aortic interface
Left paracardiac air	Air in the mediastinum displaces the mediastinal pleura from the left heart border, resulting in a lucent line following the cardiac border. This sign is also seen in pneumopericardium
Naclerio's V sign	"V" formed by the crossing of a lucent line along the left border of the lower descending aorta and a lucent line over the left hemidiaphragm
Paratracheal air	Air in the superior mediastinum projects as multiple vertical streaky lines, paralleling the trachea
Chest wall emphysema	Presence of air pockets in the chest wall and supraclavicular region serves as an important clue for pneumomediastinum
Extrapleural air sign	Extension of mediastinal air between the parietal pleura and hemidiaphragm results in outlining of the pleura

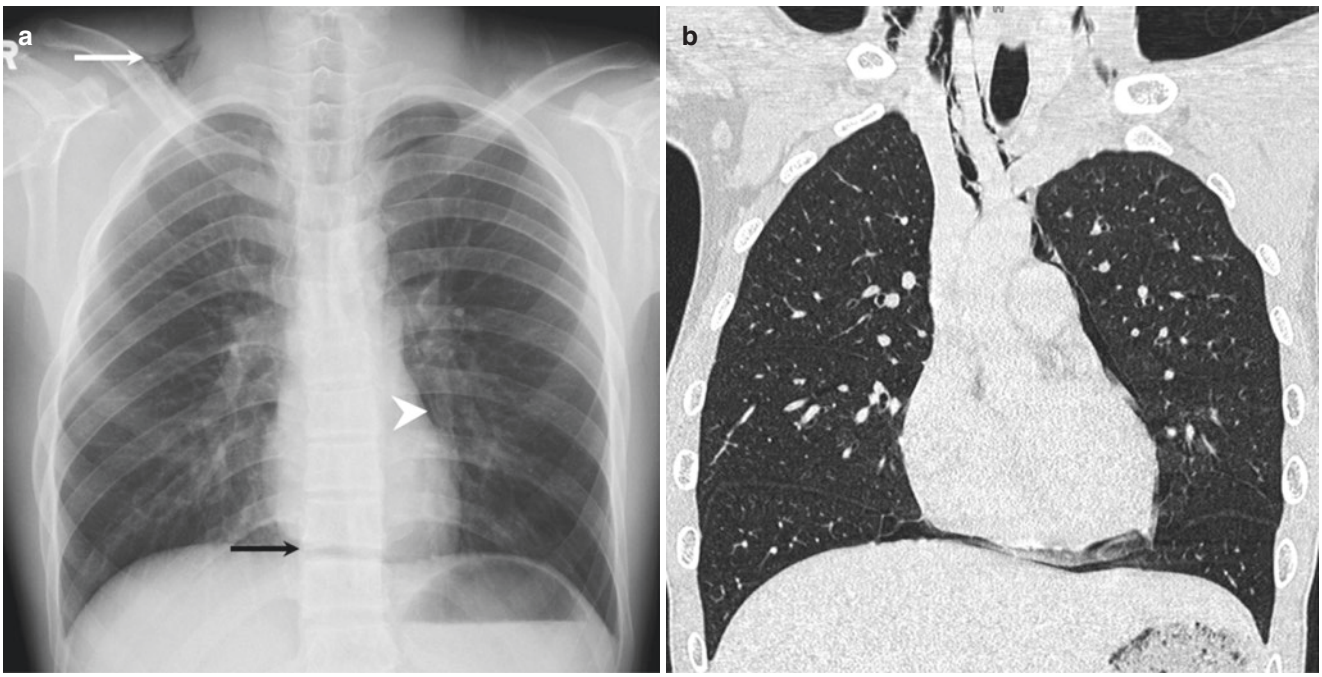

Fig. 8.52 Spontaneous pneumomediastinum in an 18-year-old man. (**a**) "Continuous diaphragm" sign (black arrow) with left paracardiac lucency (arrowheads), paratracheal streaky lucencies, and right supraclavicular emphysema (white arrow). (**b**) CT scan demonstrates air between pericardium and diaphragm (black arrow), explaining the appearance on the radiograph. Note the paratracheal emphysema and right supraclavicular emphysema

8.8 Fibrosing Mediastinitis

Fibrosing mediastinitis or sclerosing mediastinitis is a rare disorder characterized by fibrotic tissue proliferation in the mediastinum, causing mass effect on the mediastinal vessels, esophagus, and central airways. This entity has been associated with tuberculosis, histoplasmosis, and fungal infections. Sarcoidosis has also been implicated in some cases of fibrosing mediastinitis. Association with many other diseases has been described, including Behçet disease, rheumatic fever, radiation therapy, Hodgkin disease, retroperitoneal fibrosis, sclerosing cholangitis, Riedel thyroiditis, and pseudotumor of the orbit [35]. CT shows ill-defined, poorly enhancing soft tissue in the mediastinum, encasing the mediastinal struc-

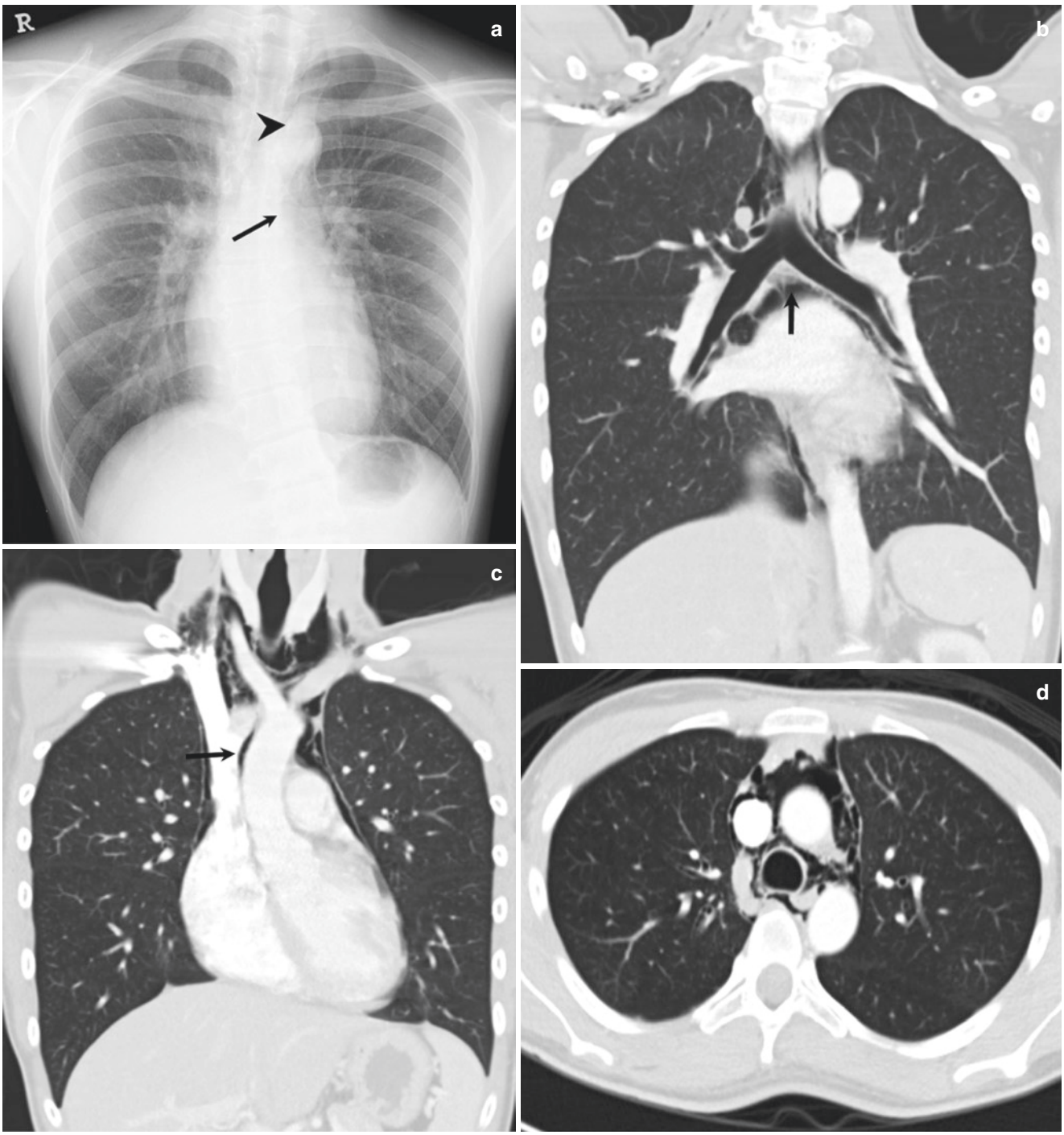

Fig. 8.53 20-year-old man with spontaneous pneumomediastinum. (**a**) Frontal radiograph shows "double bronchial wall" sign (black arrow) and "tubular artery" sign (black arrowheads). Note the paratracheal emphysema and right supraclavicular emphysema. (**b**) Coronal CT reconstruction reveals mediastinal air (black arrow) at the outer aspect of left bronchus, outlining the wall of bronchus, resulting in "double wall" sign. (**c**) More anterior coronal reconstruction and (**d**) axial CT images show air (black arrow) around the ascending aorta, explaining the "tubular artery" sign on the radiograph

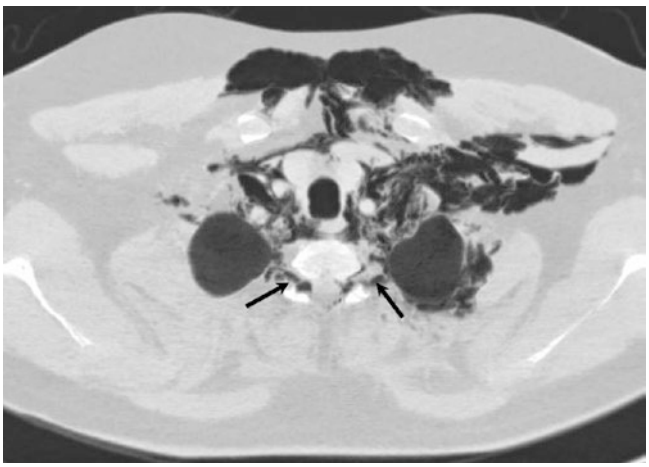

Fig. 8.54 Spontaneous pneumomediastinum in a 23-year-old man. MinIP axial image depicts extension of air along bilateral neural foramina (arrows)

tures (Figs. 8.55 and 8.56). There are dense scattered calcifications, except in cases associated with retroperitoneal fibrosis [35]. Depending on the location, the fibrotic tissue leads to mass effect and typical symptoms: compression of the superior vena cava (superior vena cava syndrome), pulmonary arteries (pulmonary artery hypertension), pulmonary veins (pulmonary venous hypertension), and airways (atelectasis). Narrowing of the pulmonary vein by fibrotic tissue results in dyspnea and hemoptysis termed as "pseudo-mitral stenosis syndrome" [35, 36].

8.9 Mediastinal Lymph Nodes

Morphology of the mediastinal lymph nodes may help in formulating a list of differential diagnoses (Table 8.11). Mediastinal lymph nodes are named according to their loca-

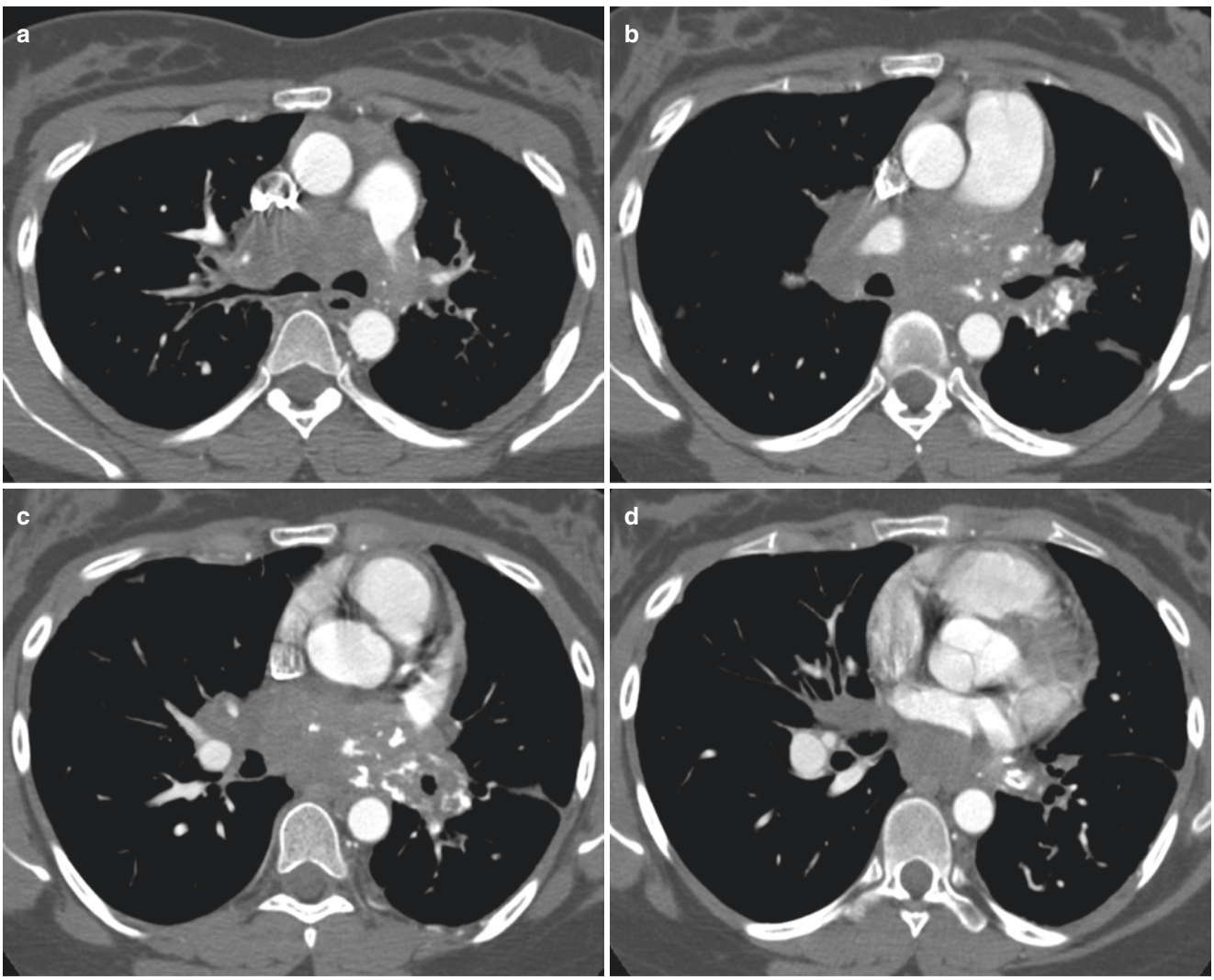

Fig. 8.55 A 28-year-old woman with fibrosing mediastinitis. (**a**–**d**) Axial CT images show hypodense non-enhancing soft tissue with scattered punctate calcific foci, causing narrowing of the bronchial tree and pulmonary arteries and obliteration of multiple pulmonary veins

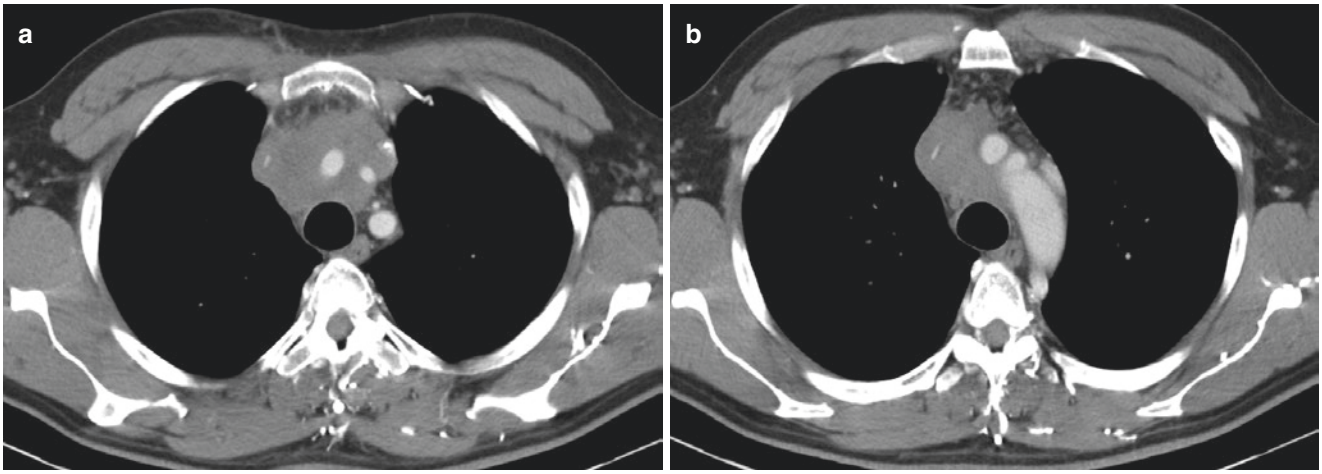

Fig. 8.56 A 48-year-old man with superior vena cava syndrome from fibrosing mediastinitis. (**a**, **b**) Axial CT images show non-enhancing ill-defined soft tissue encasing the origin of neck vessels from the aortic arch and compressing the superior vena cava. Biopsy revealed dense collagenous fibrosis with patchy lymphocytic inflammation, consistent with sclerosing mediastinitis. There was a history of histoplasmosis

Table 8.11 Morphology of lymph nodes for differential diagnoses

Eggshell calcification	Silicosis, coal worker's pneumoconiosis, sarcoidosis
Punctate calcification	Tuberculosis, histoplasmosis, sarcoidosis, treated lymphoma
Amorphous calcification	Sarcoidosis
Necrotic lymph node	Tuberculosis, metastasis, B-cell lymphoma, treated lymphoma
Homogeneous lymph node	Reactive, lymphoma, sarcoidosis, metastasis
Enhancing lymph node	Metastasis, Castleman disease

tion in the compact mediastinal space. It is essential for the radiologist to know the exact nomenclature of the lymph nodes, particularly in patients with lung cancer, for accurate disease staging. The International Association for the Study of Lung Cancer has designed a nodal "map" of intrathoracic lymph nodes that can be grouped in various zones to be used in the TNM lung cancer staging [37]. The nodal stations have been assigned a numeric value that may be used during the multidisciplinary discussion.

References

1. Felson B. The mediastinum. In: Seminars in roentgenology, vol. 4, no. 1. Philadelphia: WB Saunders; 1969. p. 41–58.
2. Whitten CR, Khan S, Munneke GJ, Grubnic S. A diagnostic approach to mediastinal abnormalities. Radiographics. 2007;27(3):657–71.
3. Menuck L. Plain film findings of gastric volvulus herniating into the chest. Am J Roentgenol. 1976;126(6):1169–74.
4. Gibbs JM, Chandrasekhar CA, Ferguson EC, Oldham SA. Lines and stripes: where did they go?—from conventional radiography to CT. Radiographics. 2007;27(1):33–48.
5. Morgenthaler TI, Brown LR, Colby TV. Thymoma. Mayo Clin Proc. 1993;68:1110–23.
6. Lara PN. Malignant thymoma: current status and future directions. Cancer Treat Rev. 2000;26(2):127–32.
7. Benveniste MF, Rosado-de-Christenson ML, Sabloff BS, Moran CA, Swisher SG, Marom EM. Role of imaging in the diagnosis, staging, and treatment of thymoma. Radiographics. 2011;31(7):1847–61.
8. Truong MT, Sabloff BS, Gladish GW, Whitman GJ, Munden RF. Invasive thymoma. Am J Roentgenol. 2003;181(6):1504.
9. Jung KJ, Lee KS, Han J, Kim J, Kim TS, Kim EA. Malignant thymic epithelial tumors: CT-pathologic correlation. Am J Roentgenol. 2001;176(2):433–9.
10. Masaoka A, Monden Y. Comparison of the results of transsternal imple, transcervical simple, and extended thymectomy. Ann N Y Acad Sci. 1981;377(1):755–65.
11. Jeung MY, Gasser B, Gangi A, Bogorin A, Charneau D, Wihlm JM, Dietemann JL, Roy C. Imaging of cystic masses of the mediastinum. Radiographics. 2002;22(suppl_1):S79–93.
12. Suster S, Rosai J. Multilocular thymic cyst: an acquired reactive process. Study of 18 cases. Am J Surg Pathol. 1991;15(4):388–98.
13. Choi YW, McAdams HP, Jeon SC, Hong EK, Kim YH, Im JG, Lee SR. Idiopathic multilocular thymic cyst: CT features with clinical and histopathologic correlation. Am J Roentgenol. 2001;177(4):881–5.
14. Rosado-de-Christenson ML, Pugatch RD, Moran CA, Galobardes J. Thymolipoma: analysis of 27 cases. Radiology. 1994;193(1):121–6.
15. Moran CA, Rosado-de-Christenson M, Suster S. Thymolipoma: clinicopathologic review of 33 cases. Mod Pathol. 1995;8(7):741–4.
16. Chen M, Yang J, Zhu L, Zhou C, Zhao H. Primary intrathoracic liposarcoma: a clinicopathologic study and prognostic analysis of 23 cases. J Cardiothorac Surg. 2014;9(1):119.
17. Castellino RA, Blank N, Hoppe RT, Cho C. Hodgkin disease: contributions of chest CT in the initial staging evaluation. Radiology. 1986;160(3):603–5.
18. Filly R, Blank N, Castellino RA. Radiographic distribution of intrathoracic disease in previously untreated patients with Hodgkin's disease and non-Hodgkin's lymphoma. Radiology. 1976;120(2):277–81.
19. Sutcliffe SB. Primary mediastinal malignant lymphoma. In: Seminars in thoracic and cardiovascular surgery, vol. 4, no. 1. New York: Elsevier; 1992. p. 55–67.

20. Bae YA, Lee KS. Cross-sectional evaluation of thoracic lymphoma. Radiol Clin North Am. 2008;46(2):253–64.
21. Shaffer K, Smith D, Kirn D, Kaplan W, Canellos G, Mauch P, Shulman LN. Primary mediastinal large-B-cell lymphoma: radiologic findings at presentation. AJR Am J Roentgenol. 1996;167(2):425–30.
22. Tateishi U, Müller NL, Johkoh T, Onishi Y, Arai Y, Satake M, Matsuno Y, Tobinai K. Primary mediastinal lymphoma: characteristic features of the various histological subtypes on CT. J Comput Assist Tomogr. 2004;28(6):782–9.
23. Takahashi K, Al-Janabi NJ. Computed tomography and magnetic resonance imaging of mediastinal tumors. J Magn Reson Imaging. 2010;32(6):1325–39.
24. Moeller KH, Rosado-de-Christenson ML, Templeton PA. Mediastinal mature teratoma: imaging features. AJR Am J Roentgenol. 1997;169(4):985–90.
25. Rosado-de-Christenson ML, Templeton PA, Moran CA. From the archives of the AFIP. Mediastinal germ cell tumors: radiologic and pathologic correlation. Radiographics. 1992;12(5):1013–30.
26. Ranganath SH, Lee EY, Restrepo R, Eisenberg RL. Mediastinal masses in children. Am J Roentgenol. 2012;198(3):W197–216.
27. Lee KS, Im JG, Han CH, Han MC, Kim CW, Kim WS. Malignant primary germ cell tumors of the mediastinum: CT features. Am J Roentgenol. 1989;153(5):947–51.
28. Tomiyama N, Honda O, Tsubamoto M, Inoue A, Sumikawa H, Kuriyama K, Kusumoto M, Johkoh T, Nakamura H. Anterior mediastinal tumors: diagnostic accuracy of CT and MRI. Eur J Radiol. 2009;69(2):280–8.
29. Reeder LB. Neurogenic tumors of the mediastinum. In: Seminars in thoracic and cardiovascular surgery, vol. 12, no. 4. Philadelphia: WB Saunders; 2000. p. 261–7.
30. Nakazono T, White CS, Yamasaki F, Yamaguchi K, Egashira R, Irie H, Kudo S. MRI findings of mediastinal neurogenic tumors. Am J Roentgenol. 2011;197(4):W643–52.
31. Zylak CM, Standen JR, Barnes GR, Zylak CJ. Pneumomediastinum revisited. Radiographics. 2000;20(4):1043–57.
32. Bejvan SM, Godwin JD. Pneumomediastinum: old signs and new signs. AJR Am J Roentgenol. 1996;166(5):1041–8.
33. Macia I, Moya J, Ramos R, Morera R, Escobar I, Saumench J, Perna V, Rivas F. Spontaneous pneumomediastinum: 41 cases. Eur J Cardiothorac Surg. 2007;31(6):1110–4.
34. Macklin CC. Transport of air along sheaths of pulmonic blood vessels from alveoli to mediastinum: clinical implications. Arch Intern Med. 1939;64(5):913–26.
35. Rossi SE, McAdams HP, Rosado-de-Christenson ML, Franks TJ, Galvin JR. Fibrosing mediastinitis. Radiographics. 2001;21(3):737–57.
36. McNeeley MF, Chung JH, Bhalla S, Godwin JD. Imaging of granulomatous fibrosing mediastinitis. Am J Roentgenol. 2012;199(2):319–27.
37. Rusch VW, Asamura H, Watanabe H, Giroux DJ, Rami-Porta R, Goldstraw P. The IASLC lung cancer staging project: a proposal for a new international lymph node map in the forthcoming seventh edition of the TNM classification for lung cancer. J Thorac Oncol. 2009;4(5):568–77.

Imaging of Pulmonary Artery

9

Ashish Chawla

9.1 Introduction

Radiology investigations play an important role in the assessment of pulmonary artery. Imaging is utilized in the diagnosis of pulmonary embolism (PE) and in the evaluation of a patient with pulmonary artery hypertension (PAH). PE is the third most common cardiovascular disease after coronary artery disease and stroke. The precise incidence of PE is not well known, but European guidelines estimated the incidence from 0.5 to 1 in 1000 [1]. Acute PE is associated with mortality rates as high as 30% [1, 2]. The clinical presentation of acute PE is variable accounting for its underdiagnoses. Most of the patients present with sudden onset of dyspnea, while a significant proportion may present with chest pain indistinguishable from more common coronary artery disease [3]. A small subset of patients may present with nonspecific symptoms like cough, hemoptysis, or syncope. Since the majority of the PEs are due to deep venous thrombosis (DVT) in the legs, one must be aware of predisposing conditions for DVT and PE that include advanced age, overweight, coagulation disorders, underlying malignancy, hormone replacement therapy, and oral contraception.

9.2 Acute Pulmonary Embolism

9.2.1 Chest Radiography Signs

The sensitivity of chest radiograph for the detection of acute PE is very low, while specificity is in the range of 80–85% [4]. Despite the limitations in accurately diagnosing or excluding PE, the chest radiograph is still a valuable tool to exclude other conditions. The findings on chest radiographs are cardiac enlargement, pleural effusion, dilated pulmonary arteries, atelectasis, elevated hemidiaphragm, pulmonary edema, and pulmonary infiltrates [4, 5]. These are nonspecific findings and can be seen in many other conditions. In addition, there are some relatively more specific radiographic signs of acute PE (Table 9.1) [4, 6, 7] (Figs. 9.1, 9.2, 9.3, and 9.4). These signs are subtle, subjective, and difficult to apply without the clinical information. However, the specificity of these signs increases in the appropriate clinical setting. The detectability of signs improves in a good quality posterior-anterior radiograph and if there are prior comparison radiographs to confirm that the changes are new.

9.2.2 CT Pulmonary Angiogram (CTPA)

9.2.2.1 Acute Pulmonary Embolism

CT pulmonary angiogram has become the gold standard for the evaluation of PE. A large meta-analysis has reported a sensitivity of CT ranging from 53% to 100% and specificity ranging from 81% to 100% [8]. The diagnostic criteria and CT features of acute pulmonary embolism are described in Table 9.2 [9] (Figs. 9.5 and 9.6).

The advances in CT technology have helped in improving the detection rate of subsegmental PEs [10]. The entire central and peripheral pulmonary artery vasculature must be evaluated segment by segment. Lack of enhancement or an abrupt cutoff of a small branch of the pulmonary artery with normal enhancement of the other branches must be interpreted as a peripheral embolism. The pulmonary arteries follow the bronchial tree perfusing the lung segments. Hence it is recommended to describe the involvement of pulmonary artery branches using the nomenclature of bronchopulmonary segments. It is also important to mention if the emboli are occlusive or nonocclusive as it is a component of CT severity indexes. The emboli description should provide the treating physician with an idea of clot burden. There are at least four scoring methods to calculate the clot burden, namely, Miller score, Walsh score, Qanadli score, and Mastora score [11]. The first two were adapted from catheter

A. Chawla (✉)
Department of Diagnostic Radiology, Khoo Teck Puat Hospital, Singapore, Singapore

A. Chawla (ed.), *Thoracic Imaging*, https://doi.org/10.1007/978-981-13-2544-1_9

Table 9.1 Chest radiography signs of acute pulmonary embolism

Fleischner sign and Knuckle sign	Fleischner sign refers to focal dilatation of the central pulmonary arteries due to distension by the embolus. Knuckle sign is often seen along with Fleischner sign and refers to the abrupt tapering or occlusion of the distal pulmonary artery beyond the embolus
Westermark sign	Westermark sign refers to focal oligemia in the lungs, corresponding to the area of hypoperfusion supplied by the occluded pulmonary artery. This is considered as the most specific sign but is difficult to interpret in a poor quality radiograph (rotated view or anterior-posterior view)
Hampton hump	Hampton hump is a wedge-shaped pleural-based opacity representing a pulmonary infarct. This is usually seen in lower lobes and frequently associated with elevated hemidiaphragm and/or pleural effusion
Fleischner lines	Fleischner lines represent focal linear subsegmental discoid atelectasis. Historically, these lines have been used to diagnose more peripheral emboli on chest radiograph. These lines measure 2–7 cm in length and 2–7 mm in thickness and always reach a pleural surface but never cross any fissure

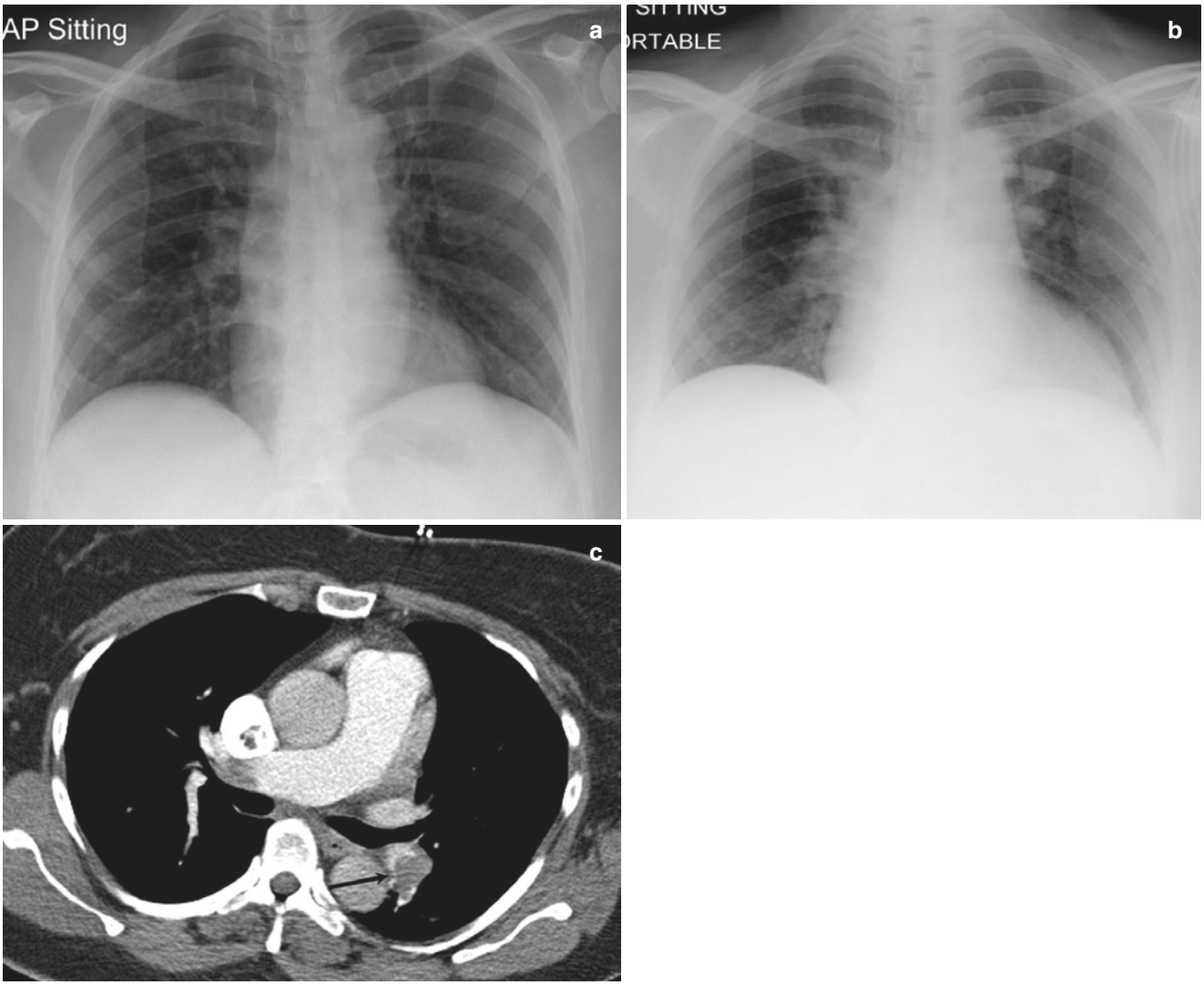

Fig. 9.1 A 50-year-old woman with acute PE. (**a**) Radiograph obtained 2 months before acute presentation. (**b**) Frontal radiograph on presentation with sudden-onset dyspnea after a long flight shows new focal oligemia (Westermark sign) in the left lower zone and dilatation of the right lower lobe pulmonary artery (Fleischner sign). (**c**) Axial CTPA shows a large expanding nonocclusive embolus (arrow) in lower lobe pulmonary arteries

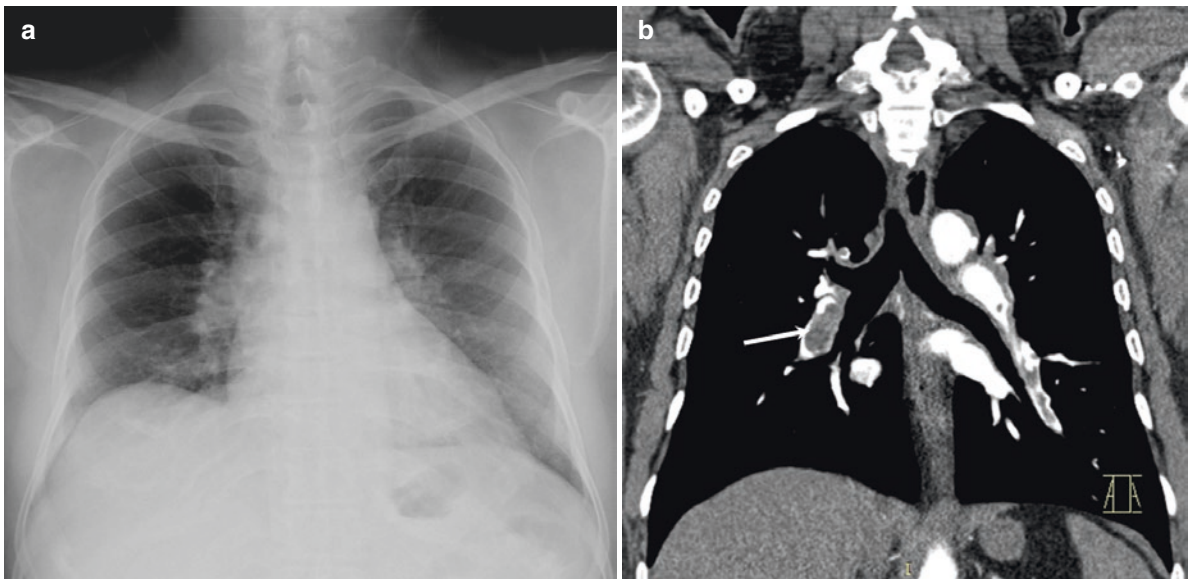

Fig. 9.2 A 65-year-old man with acute PE. (**a**) Frontal radiograph shows dilated right lower lobe pulmonary artery (Fleischner sign) with abrupt tapering (Knuckle sign). (**b**) Coronal CT image shows expanding nonocclusive embolus (arrow) in the right lower lobe artery. Note emboli in the left lower lobe artery as well

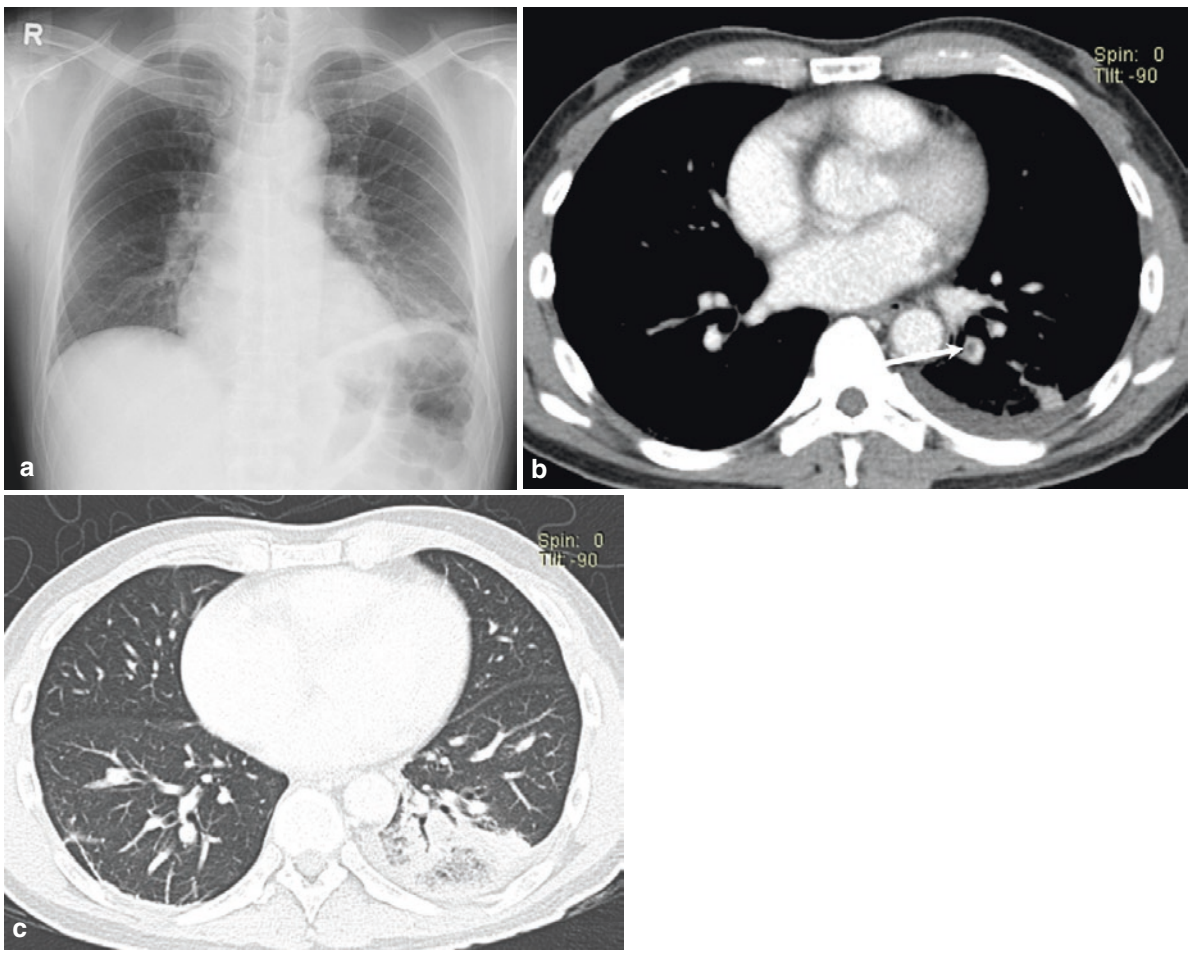

Fig. 9.3 A 57-year-old man with acute PE. (**a**) Frontal radiograph shows the elevation of the left hemidiaphragm and peripheral linear band-like opacity (Fleischner line) with surrounding haziness in the left costophrenic angle. (**b**) Axial CT image shows a central filling defect (arrow) in a subsegmental branch of the left lower lobe pulmonary artery. (**c**) Axial CT image shows a pulmonary infarct in the left lower lobe. Note small left pleural effusion

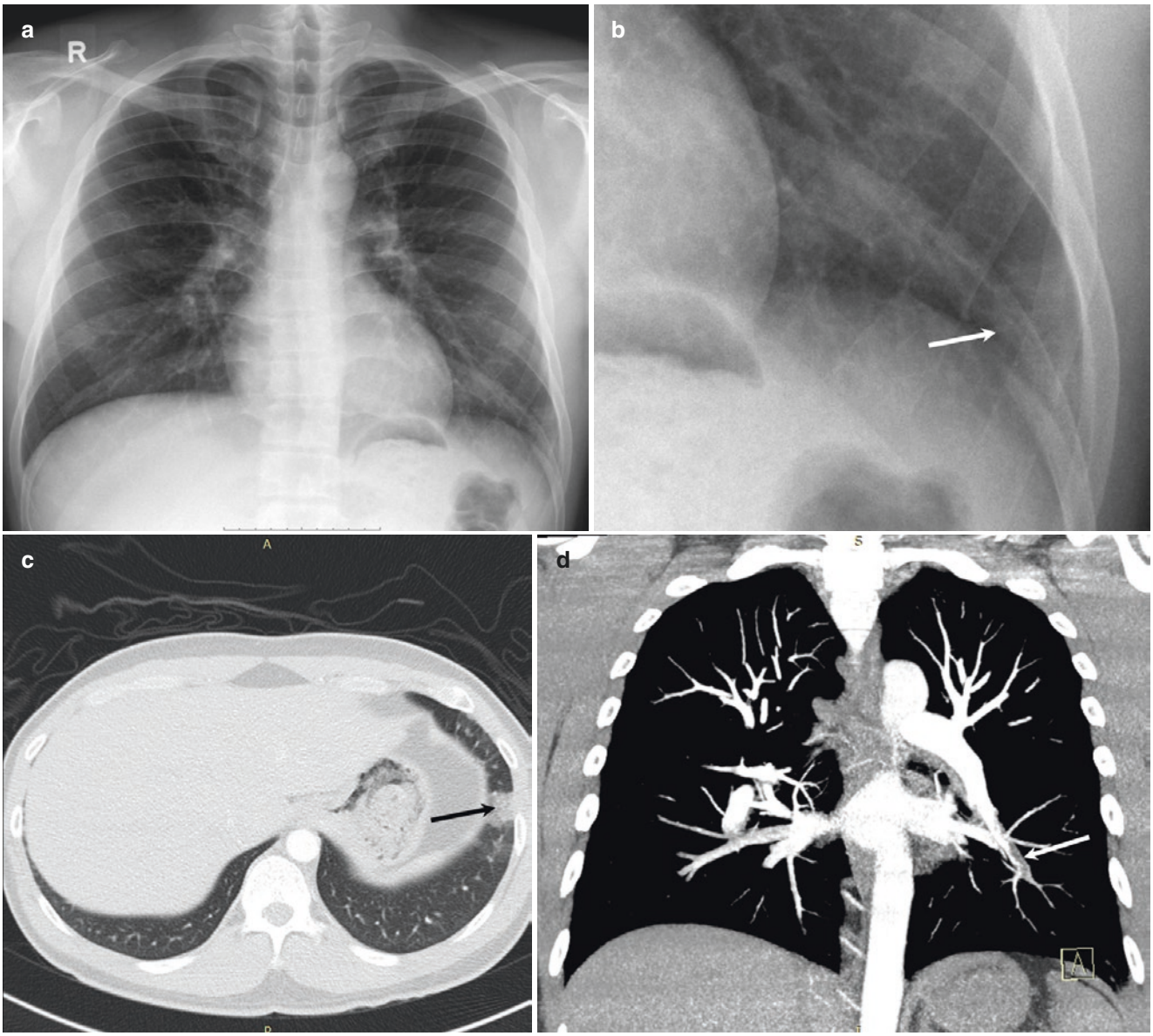

Fig. 9.4 A 27-year-old man with PE presented to the emergency department with chest pain and dyspnea. (**a**) Frontal radiograph shows a subtle peripheral wedge-shaped opacity (Hampton hump) in the left lower zone. (**b**) Magnified view shows the opacity better (arrow). (**c**) Axial CT image shows an infarct (arrow) in the left costophrenic angle. (**d**) Coronal MIP image shows a long segment nonocclusive embolism (arrow)

Table 9.2 CTPA features of acute pulmonary embolism

Criteria for acute PE	• Arterial occlusion with failure to enhance that may be associated with the expansion of the occluded vessel • A partial filling defect surrounded by contrast material representing a nonocclusive embolus
Signs of RV dysfunction	• RV/LV diameter more than 1–1.2 • RV/LV volume more than 1.2 • Bowing of interventricular septum • Dilatation of azygos vein • Reflux of contrast in IVC and hepatic veins
Parenchymal changes in acute PE	• No change or focal oligemia • Focal atelectasis • Focal hemorrhage • Pulmonary infarct • Diffuse mosaic attenuation

pulmonary angiography, and the last two were developed for CTPA and more commonly used currently. These CT severity scoring indexes allow quantifying the clot burden and risk stratification and help in deciding management and prognostication.

9.2.3 Signs of Right Ventricular Dysfunction and Prognosis

Right ventricular (RV) dysfunction is the major cause of mortality in patients with acute massive PE. Therefore, it is imperative to look for the CT signs of RV dysfunction for prognostication (Fig. 9.7). Sudden obstruction of pulmonary

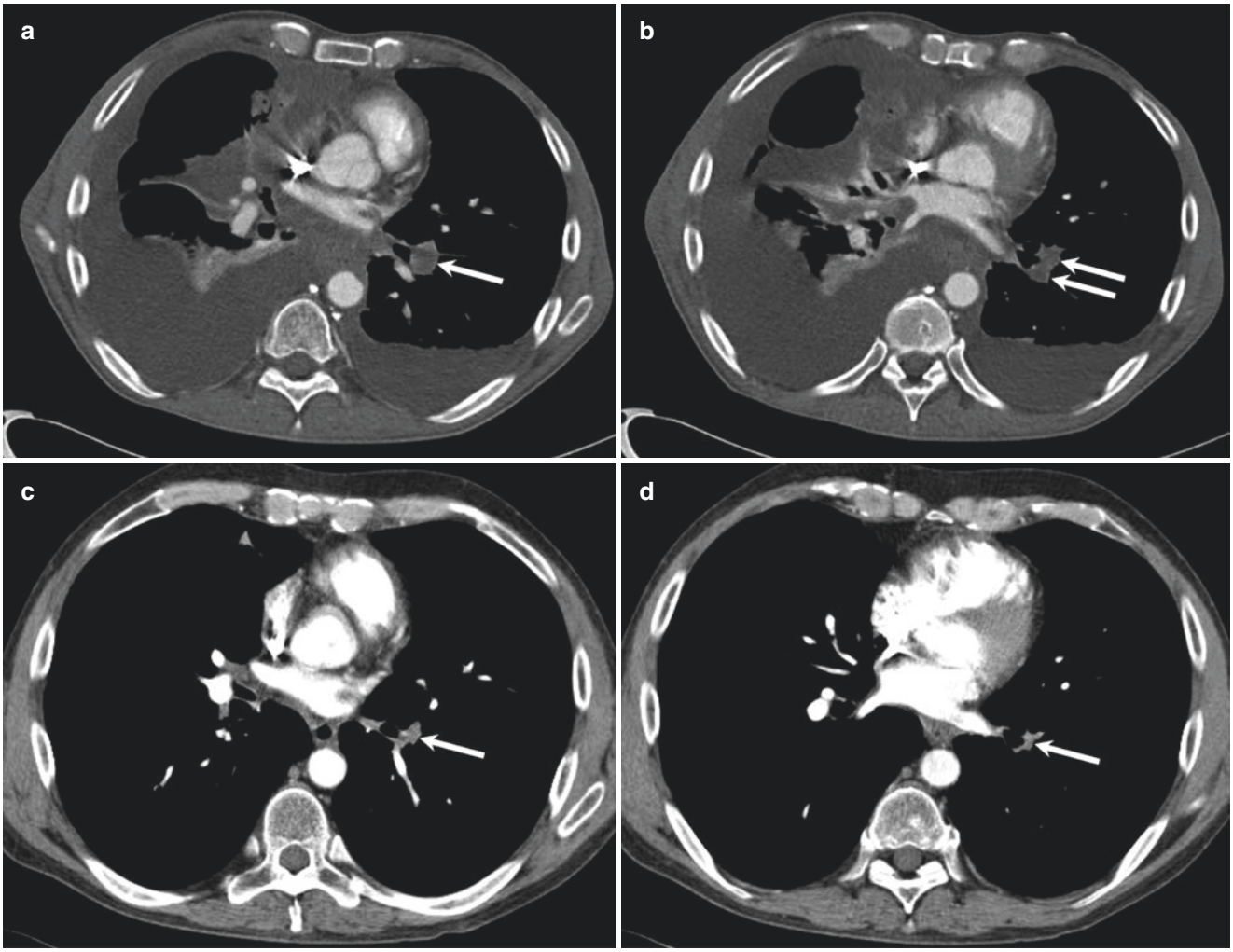

Fig. 9.5 Imaging difference between acute and chronic PE. (**a**, **b**) Axial CTPA images at presentation show complete occlusion of the left lower lobe pulmonary artery with the expansion of the involved vessels (arrows). (**c**, **d**) Axial CTPA images 6 months later show that occluded vessels are smaller than the vessels (arrows) on the contralateral side

arteries causes acute pulmonary hypertension and increases right ventricle afterload that is further worsened by the release of vasoactive agents from plasma, platelets, or tissue and reflex PA vasoconstriction. RV tries to compensate by increasing the contractile performance, increasing myocardial oxygen demand, and eventually resulting in right ventricular dilatation and dysfunction. The decline in RV function and bowing of the interventricular septum toward the left ventricle compromises the LV function as well. Echocardiography is an excellent modality to evaluate RV dilatation and dysfunction as it is quick, noninvasive, and reliable, but visualization of PE is limited. CTPA is a single reliable study that provides both diagnostic and prognostic information in PE.

On CTPA, RV/LV diameter more than 1 to 1.2 on axial images is considered as a sign of RV dysfunction. This dilatation of RV accompanying with bowing of septum shows excellent correlation with severity of PE and mortality [12–14]. The prognostic value of this sign increases if the measurements are obtained in reconstructed four-chamber view. A higher cutoff of 1.5 has better correlation with severity of PE [15]. A more accurate prognostic sign is the ratio of the volume of the right ventricle to left ventricle [16]. A ratio of more than 1.2 is a predictor of adverse outcome. The other signs of RV dysfunction are flattening or bowing of interventricular septum, dilatation of azygos vein (more than 1 cm), and reflux of contrast in IVC and hepatic veins (due to tricuspid regurgitation from RV dysfunction). Mild reflux in IVC can be seen in patients without PE that may be related to high injection rate or in the presence of other causes of raised RV pressure like constrictive cardiomyopathy. However, substantial reflux with at least some contrast in hepatic veins is a predictor of short-term mortality in patients with acute PE [17]. A dilated PA may reflect an increase in pulmonary pressure but has not been demonstrated to have any prognostic influence on survival of patients with acute PE.

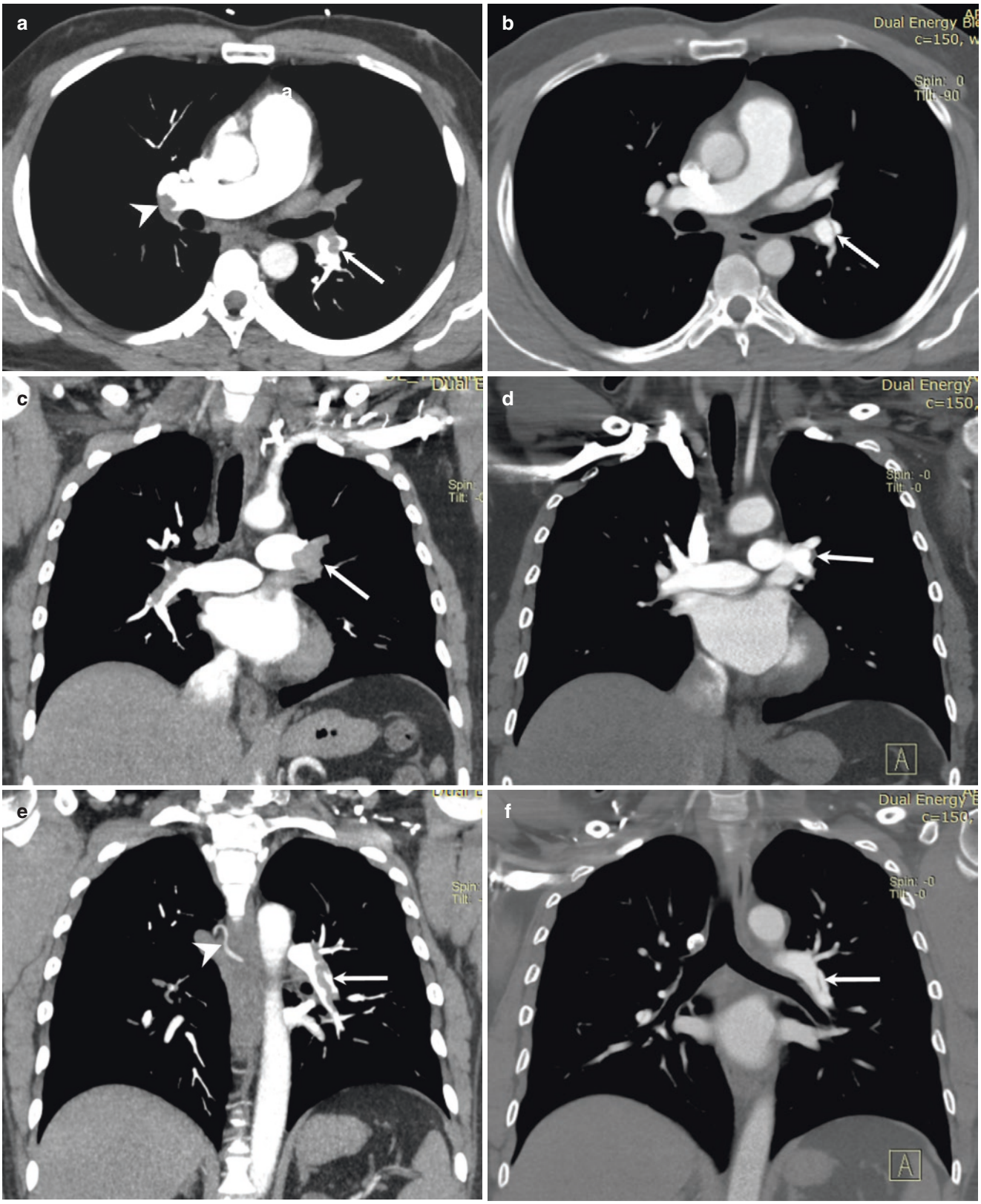

Fig. 9.6 Evolution of acute PE to chronic PE over 6 months. (**a**) Axial CT image shows an acute embolus in a distal right pulmonary artery (arrowhead) and an eccentric acute embolus in the left lower lobe pulmonary artery (arrow). (**b**) Axial CT image 6 months later shows resolution of the most of the embolus with a residual band (arrow). (**c**) Coronal CTPA image of the same patient during acute episode shows a saddle embolus (arrow) at the distal left pulmonary artery. (**d**) Coronal CTPA image, 6 months later, shows near-complete resolution of embolus with residual eccentric thickening of the vessel (arrow) representing chronic-organized embolus. (**e**) Initial coronal CTPA image shows nonocclusive linear filling defect (arrow) extending in the left lower lobe pulmonary artery. Note dilated right bronchial artery (arrowhead). (**f**) Coronal CT image 6 months apart shows a linear band (arrow) of the chronic embolus. Note that the chronic emboli are better seen on wider window settings

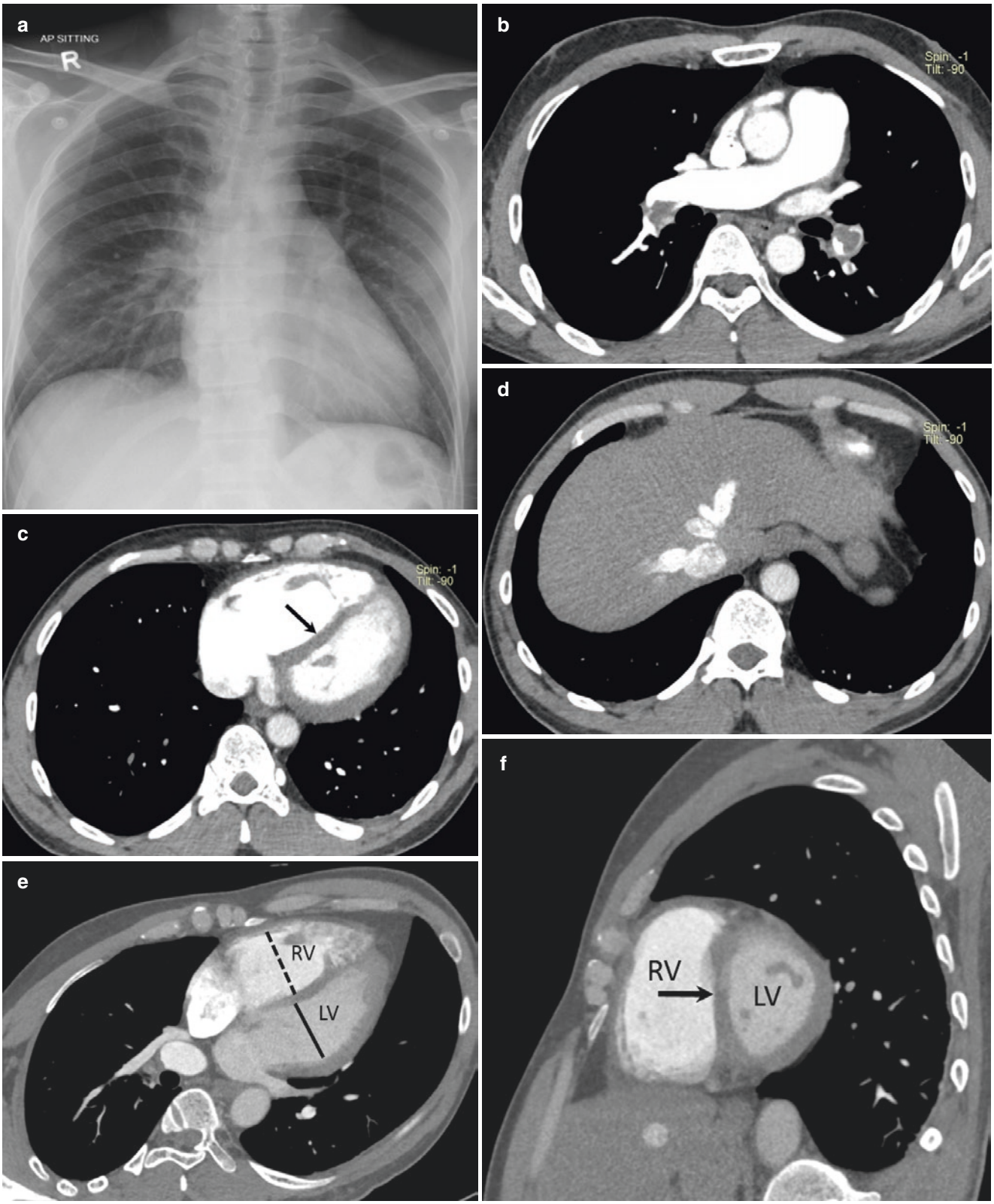

Fig. 9.7 A 42-year-old man with acute PE and right ventricular dysfunction. (**a**) Chest radiograph shows oligemia in the left lower zone (Westermark sign). (**b**–**d**) Axial CTPA images show bilateral acute PEs, septal deviation (arrow), and reflux of contrast in IVC. (**e**) Reconstructed four-chamber view shows more convincing septal deviation and is a preferred method for ratio calculation. (**f**) Two-chamber image shows flattening of the septum (arrow). *LV* left ventricle, *RV* right ventricle

9.2.4 Parenchymal Changes in Acute Pulmonary Embolism

Due to variability and dual blood supply to the lungs, the parenchymal changes in acute PE are also variable (Table 9.2). Focal oligemia is better appreciated on dual-energy CTPA perfusion images (Fig. 9.8). Focal hemorrhage results due to bleeding from the bronchial artery but resolves rapidly. A pulmonary infarct is seen in up to one-third of cases of acute PE and usually results from peripheral embolism [18]. Classically, an infarct is pleural-based consolidative opacity with truncated apex in the lower lobes [18] (Fig. 9.9). A characteristic feature of infarct is the presence of internal lucencies within a peripheral consolidation that has a specificity of 98% [19]. These lucencies are central round areas of low attenuation and should not be confused with linear air bronchograms (Fig. 9.10). In fact, the identification of internal lucencies in a peripheral consolidation on an unenhanced CT must prompt a radiologist to request for a CTPA in appropriate clinical context. The patients with underlying heart failure, malignancy, and higher emboli burden are at higher risk for developing infarct [18, 20]. These patients often complain of pleuritic chest pain. It's not uncommon to see diffuse mosaic attenuation in acute PE that results from a combination of arterial occlusions (emboli), vasoconstriction and bronchoconstriction (serotonin and prostaglandins released from platelet aggregations in embolus) (Fig. 9.11).

9.3 Chronic Pulmonary Embolism

The majority (up to 90%) of the acute PE resolves with total resolution and restoration of hemodynamics in 1 month of treatment [21]. The remaining 10% progress to chronic pulmonary thromboembolism. The CT diagnosis of chronic PE is challenging particularly in the absence of any previous CTPA study showing acute PE. The diagnostic criteria for chronic PE are described in Table 9.3 [9, 21] (Figs. 9.5, 9.12, 9.13, and 9.14). One should remember that the chronic emboli are better seen in wider window settings and can be missed in default narrow settings of CTPA.

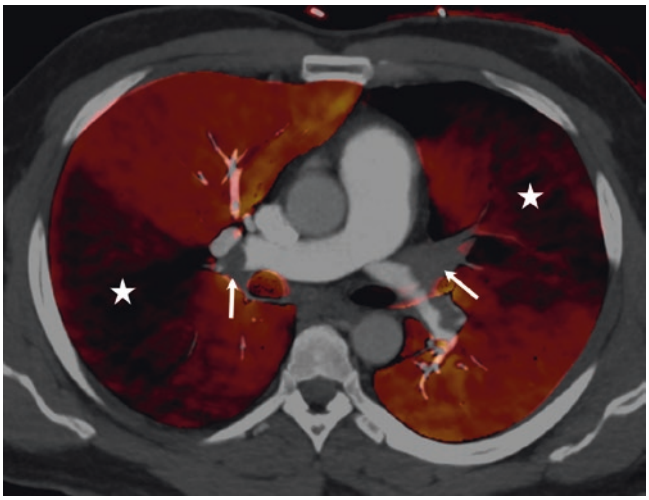

Fig. 9.8 Dual-energy perfusion maps in a patient with bilateral acute PE (arrows) show wedge-shaped perfusion defects (asterisks) in bilateral upper lobes

9.3.1 Secondary Signs of Chronic Pulmonary Embolism

The secondary signs are useful in the diagnosis of chronic PE [22]. Chronic PE sequel of a massive to submassive PE results in compensatory dilatation and tortuosity of bronchial arteries (Fig. 9.15). Rarely, the long-standing clot may undergo mural calcification (Fig. 9.16). The main pulmonary artery may be dilated due to development of pulmonary artery hypertension (PAH) with resultant inhomogeneous attenuation of lung parenchyma. The pulmonary infarct associated with an episode of acute PE undergoes fibrosis and may persist as a subpleural oblique or linear band of variable thickness on follow-up CT. Many patients with chronic PE, particularly those with recurrent episodes, develop thromboembolic PAH (Fig. 9.17).

9.4 Pitfalls in the Diagnosis of Pulmonary Embolism

Inter-observer variation in the diagnosis of PE, particularly the peripheral or segmental embolism, is well known [23, 24]. Good quality CTPA study is essential for the accurate

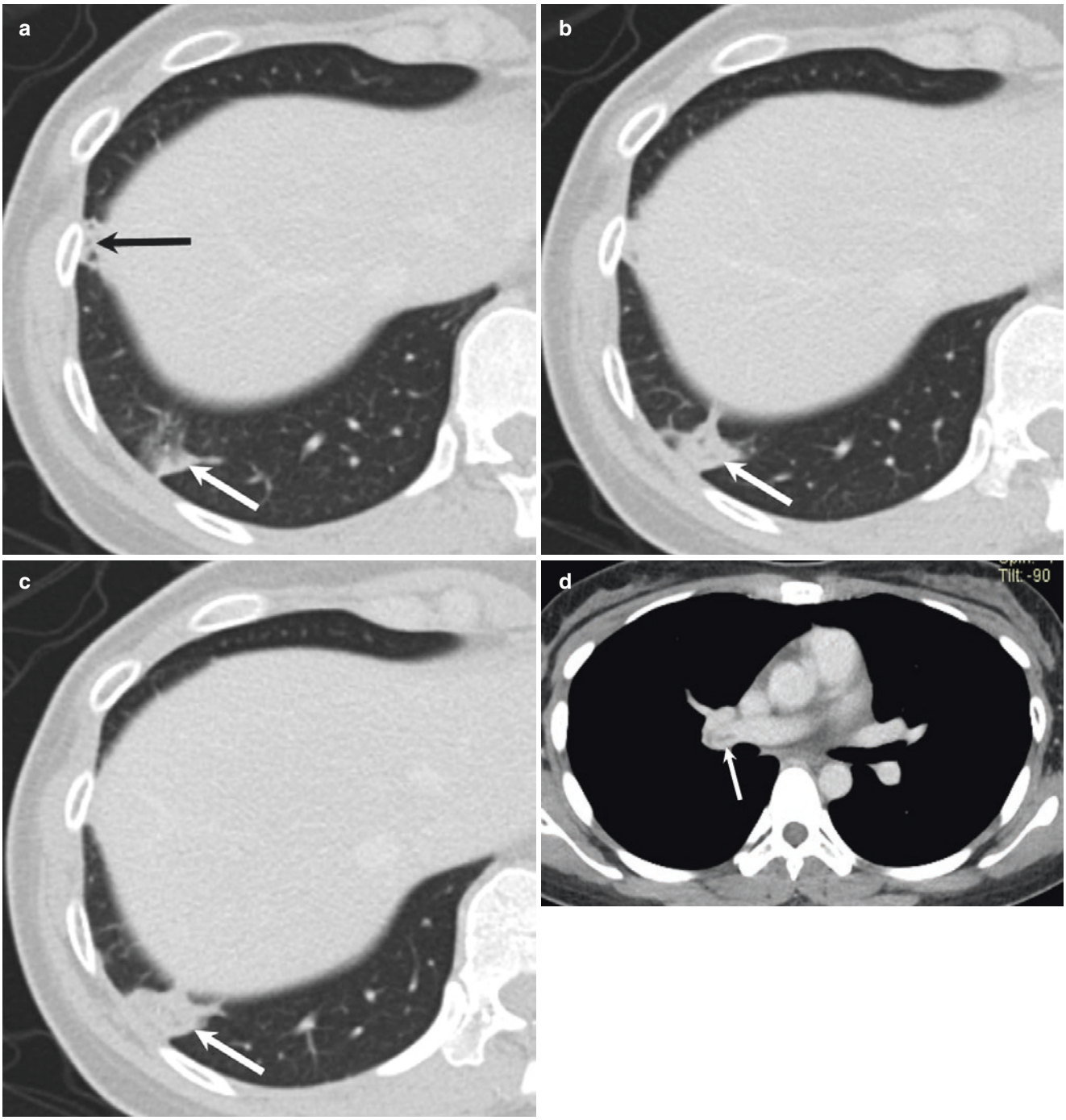

Fig. 9.9 Typical appearance of pulmonary infarct in a 37-year-old woman with nonspecific chest pain who underwent a regular contrast-enhanced CT thorax. (**a**–**c**) Axial CT images with lung window settings show two peripherally located wedge-shaped consolidations in the right lung base with subtle lucencies and absent air bronchograms. (**d**) A close look at contrast-enhanced mediastinal windows showed a linear filling defect in a right pulmonary artery, representing acute PE

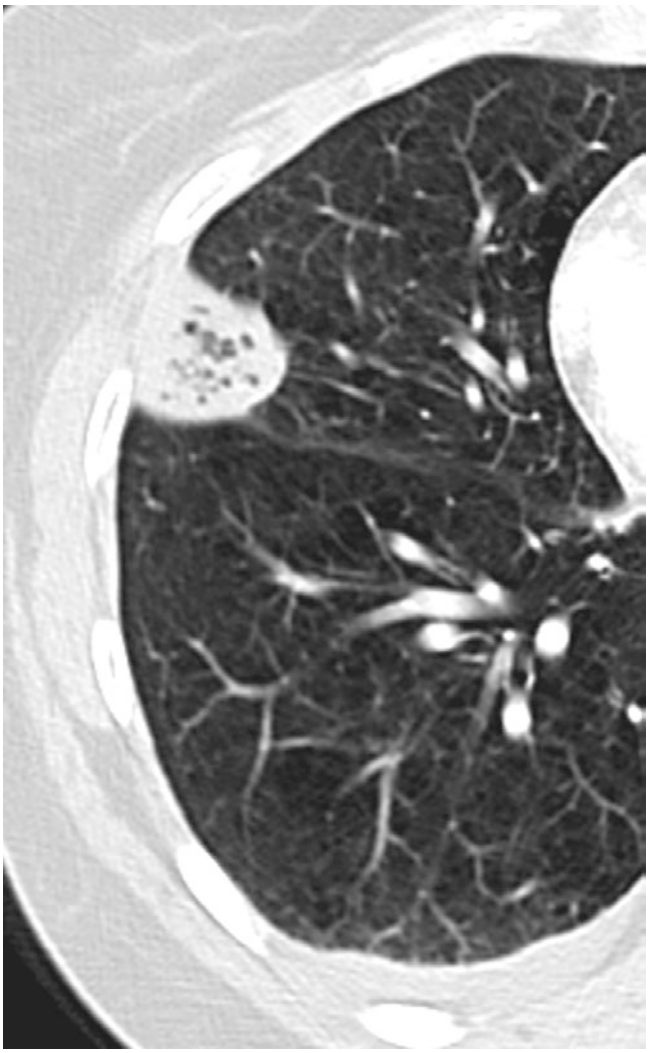

Fig. 9.10 Typical wedge-shaped pulmonary infarct in a subpleural location with central round lucencies. These lucencies are different from linear air bronchograms and are presumably due to necrosis. The specificity of these findings is reported to be 98% for pulmonary infarct

diagnosis of PE and in minimizing the pitfalls. A rule of thumb for a good quality CTPA is the density of contrast, which must be higher in pulmonary arteries in comparison to the aorta. Good enhancement of pulmonary arteries up to subsegmental branches (fourth generation) can be ensured by using the test-bolus technique, avoiding deep inspiration or expiration, using optimum quantity of contrast based on patient's weight, selecting larger vein for injection, and using higher and consistent injection rate. Readers must be aware of common artifacts in CTPA (Table 9.4) [9, 25, 26] (Figs. 9.11, 9.18, 9.19, and 9.20).

9.5 Non-thrombotic Pulmonary Embolism

A non-thrombotic pulmonary embolism is infrequent with various causes that can have no impact or can be life-threatening.

9.5.1 Air Embolism

Iatrogenic vascular air embolism is seen in 7% of CTPA studies [27]. The locations of air emboli can be the pulmonary artery, left brachiocephalic vein, right atrial appendage, and superior vena cava. A small air embolism usually does not require any intervention other than observation. Treatment for a large amount of air includes Durant's maneuver, i.e., left lateral decubitus, head-down positioning, to decrease air entry into the right ventricle outflow tract, hyperbaric therapy, 100% O_2, and supportive care.

9.5.2 Fat Embolism

Fat embolism occurs 1–3 days after major bone fractures. The diagnosis is clinically based on Gurd and Wilson criteria [28]. A classical triad of respiratory distress, cerebral abnormalities, and petechial hemorrhages in the skin is seen only in a small proportion of cases. High-resolution CT demonstrates focal or bilateral multiple subcentimeter nodules with or without ground-glass opacities in mild cases that can be subtle [29, 30] (Fig. 9.21). Clinically, severe cases are characterized by extensive bilateral consolidation [30]. An appropriate clinical history is essential for identifying radiological features of fat embolism that can be otherwise misinterpreted as aspiration or contusions. A filling defect in the pulmonary artery is rarely seen.

9.5.3 Glue Embolism

Glue (*n*-butyl-2-cyanoacrylate) embolism in the pulmonary artery is seen in 4% of the patients undergoing endoscopic injection sclerotherapy for bleeding gastric varices [31] (Fig. 9.22). The embolism is directly related to the volume of glue utilized for the procedure. Affected patients are either mildly symptomatic or asymptomatic.

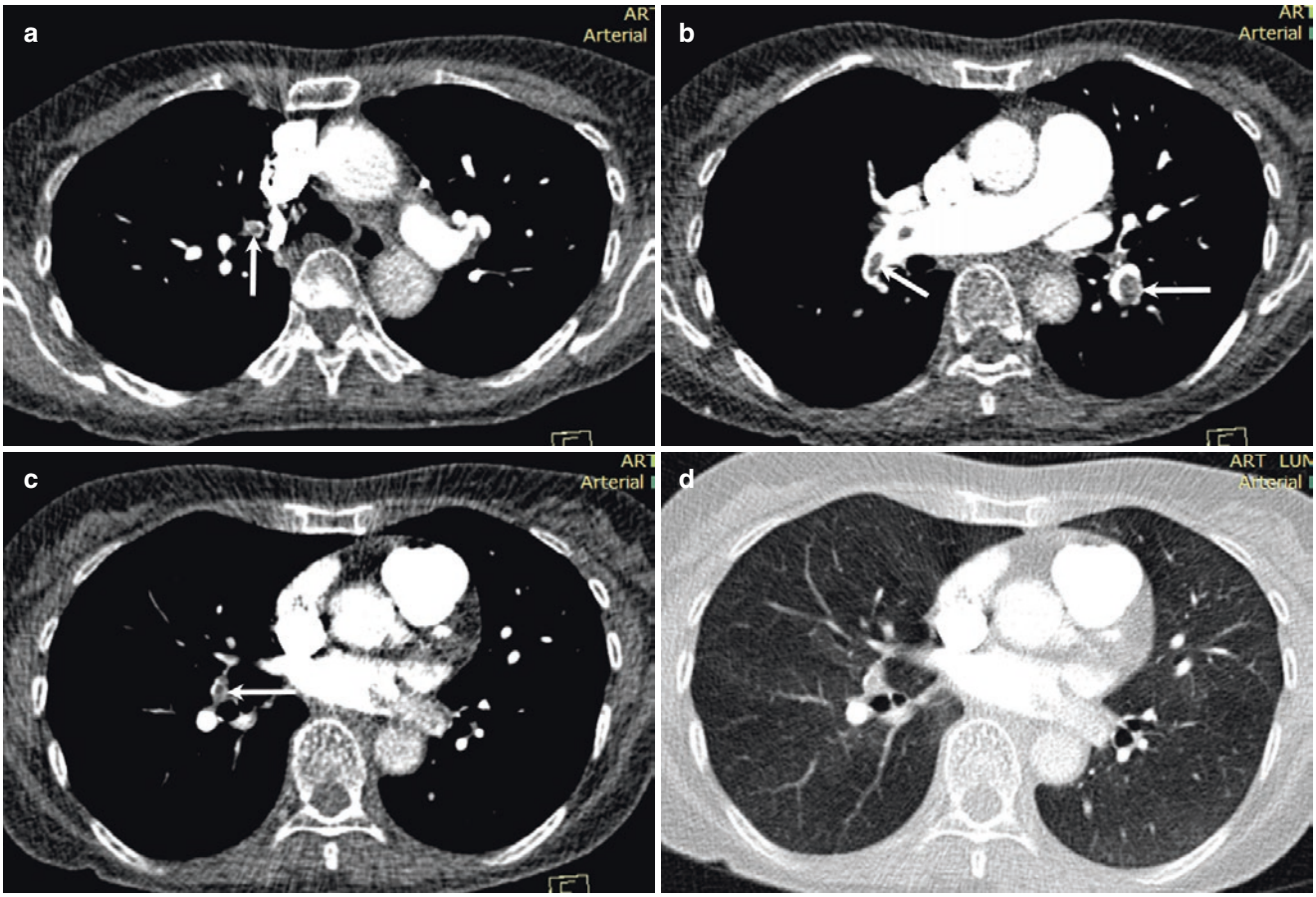

Fig. 9.11 A 60-year-old woman with acute PE and mosaic lung. (**a**) Axial CTPA image shows excessive streak artifact from the dense contrast in the left brachiocephalic vein and SVC limiting the evaluation of filling defect (arrow) in the subsegmental right upper lobe artery.(**b**, **c**) Lower axial CTPA images show emboli in pulmonary arteries (arrows). (**d**) Axial CTPA with lung window settings shows diffuse mosaicism in lungs

Table 9.3 CTPA features of chronic pulmonary embolism

Criteria for chronic PE	• Occluded vessels smaller than the diameter of surrounding enhancing branches • Peripheral eccentric wall thickening or crescentic partial filling defect • Web or a band, i.e., a hanging membrane crossing the contrast column in a branch of PA
Secondary signs of chronic PE	• Dilated bronchial artery • Dilated pulmonary artery • Mosaic attenuation of pulmonary parenchyma • Subpleural bands

9.5.4 Bone Cement Embolism

Bone cement (polymethyl methacrylate) embolism in pulmonary arteries can occur in 26% of patients undergoing vertebroplasty [32]. Most of the patients are asymptomatic. A few develop symptoms like chest pain and breathlessness, usually weeks or months after the procedure. High-density cement emboli are very well seen on CTPA or even on non-contrast CT (Fig. 9.23).

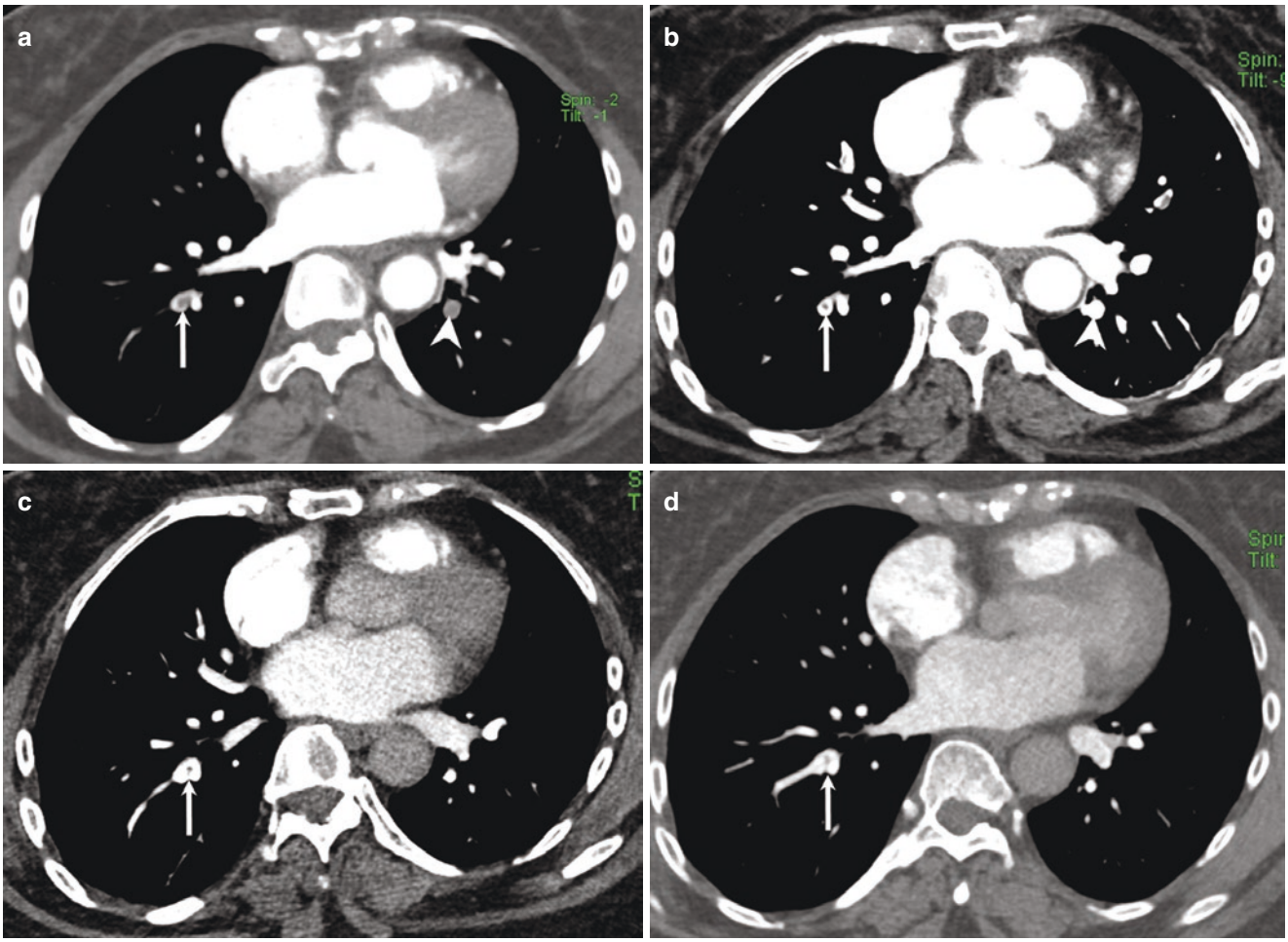

Fig. 9.12 Serial follow-up of acute PE showing its evolution to chronic PE on warfarin. (**a**) CTPA on the day of the presentation. (**b**) CTPA on the third day. (**c**) CTPA after 1 year. (**d**) CTPA after 2 years. Initial CT shows a nonocclusive filling defect in a segmental branch of the right lower lobe pulmonary artery (arrow) and occlusion of a segmental branch of the left lower lobe pulmonary artery (arrowhead). On the third day, there is complete recanalization of the left branch with gradual recanalization of embolus in the right branch, eventually forming a "web" or band

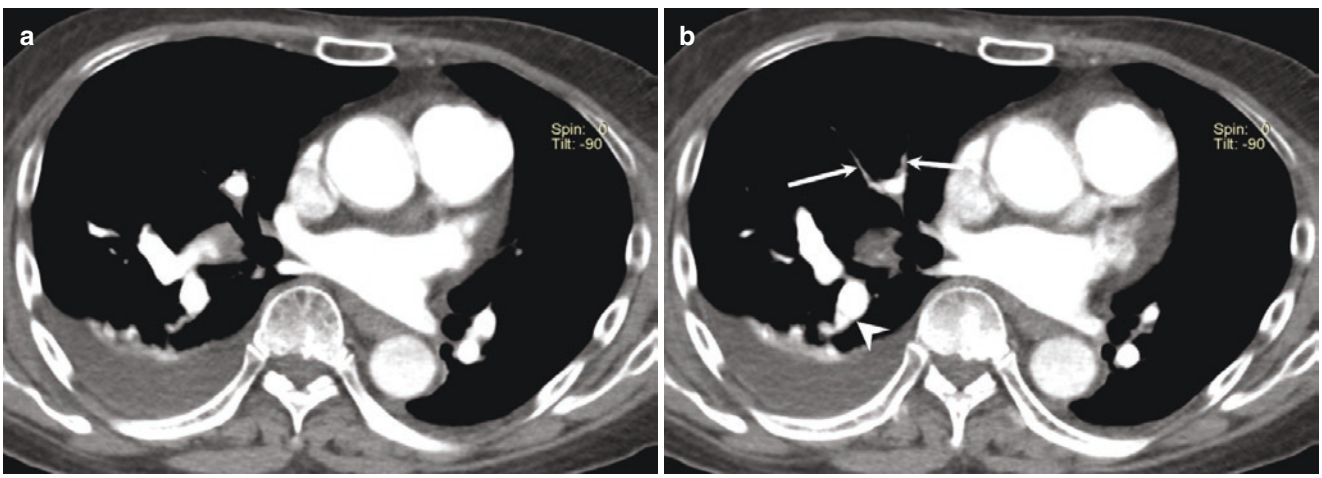

Fig. 9.13 Chronic PE in a patient with lung cancer. (**a**, **b**) Axial CTPA images reveal marked narrowing of segmental branches of the right middle lobe pulmonary artery (arrows) and a band in a segmental branch of the right lower lobe pulmonary artery (arrowhead)

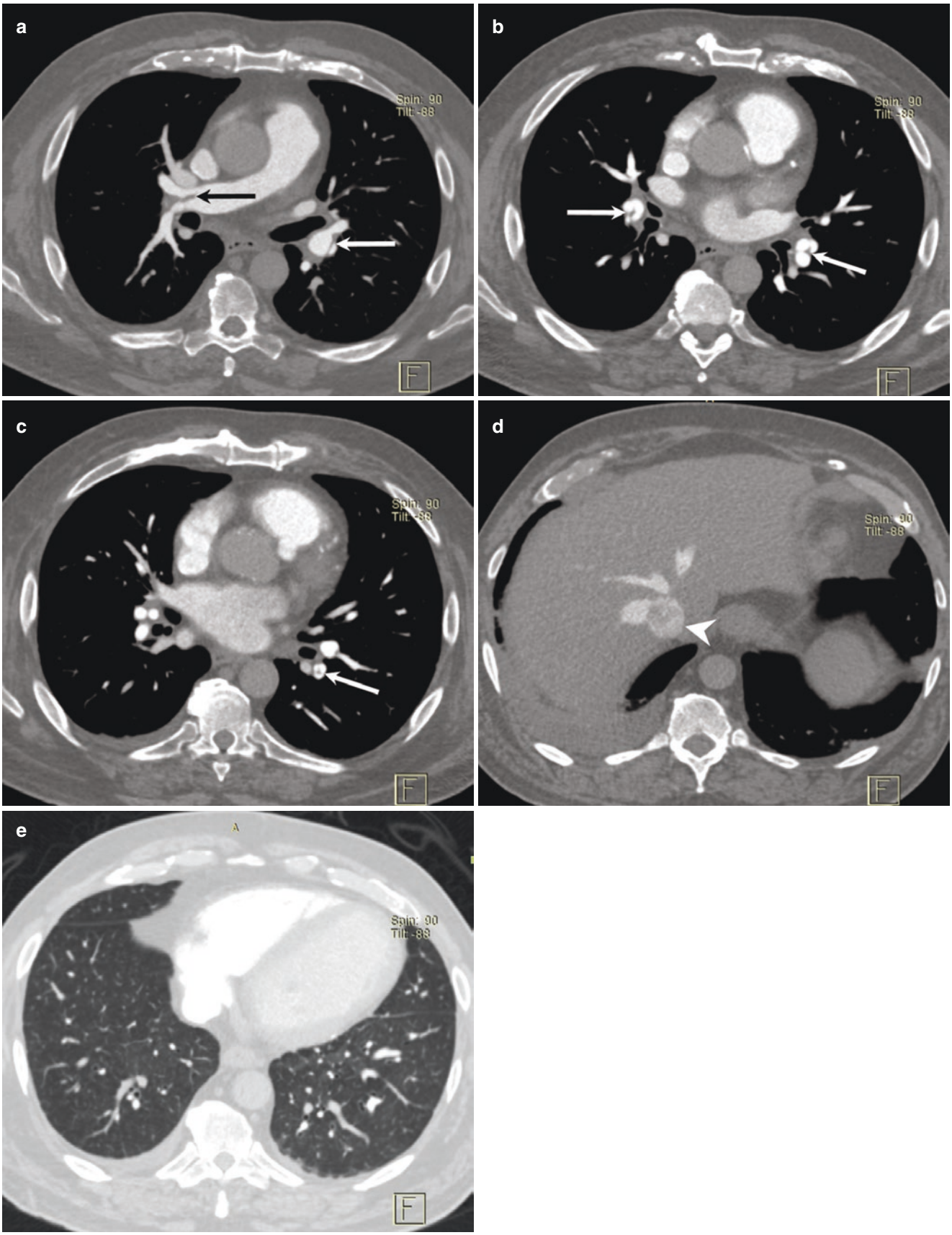

Fig. 9.14 A 59-year-old man with PAH from pulmonary thromboembolism. (**a**–**c**) Axial CTPA images show linear bands or "webs" in bilateral pulmonary arteries (arrows). (**d**) Axial CT image caudally shows reflux of contrast in IVC (arrowhead) and hepatic veins due to PAH. (**e**) Mosaic attenuation of the lungs

9.5.5 Prostate Seed Embolism

Radioactive seeds for prostatic brachytherapy can embolize to the right heart and pulmonary circulation depending upon the technique of placement. The seeds are small subcentimeter linear metallic (titanium or silver shell) with a distinctive appearance on chest radiograph and CT [33, 34] (Fig. 9.24). The effect of these seeds is not well known, but there is a possibility of radiation pneumonitis or myocardial infarction.

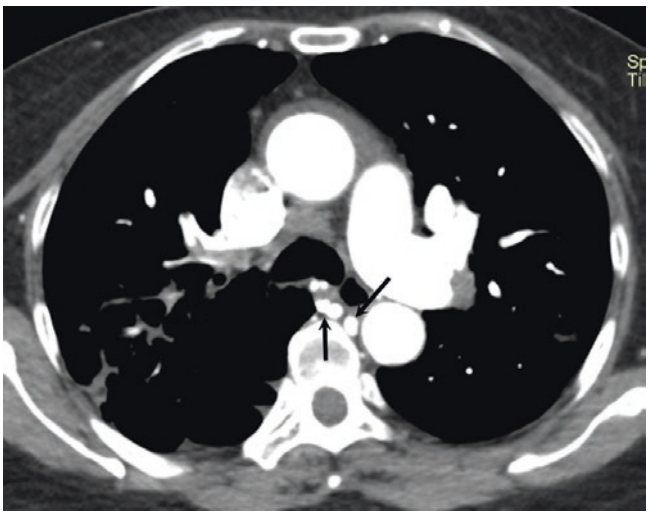

Fig. 9.15 A 67-year-old woman with recurrent PE. There are filling defects in distal right and left pulmonary arteries with dilated and tortuous bronchial artery (arrows)

9.5.6 Septic Pulmonary Embolism

Septic pulmonary emboli (SPE) comprise the triad of (a) multiple pulmonary opacities, (b) extrapulmonary infection, and (c) positive blood/fluid culture. A diagnosis can be suggested by the presence of typical peripheral pulmonary opacities and demonstration of a concomitant infection and/or thrombophlebitis by CT of the thorax, abdomen, and pelvis. Lemierre's syndrome is characterized by a triad of SPE, thrombophlebitis, and infection of the oropharynx (Fig. 9.25). The predominant pathogen is a gram-negative anaerobic bacillus, *Fusobacterium necrophorum*. CT features of SPE are described in Table 9.5 (Figs. 9.25, 9.26, and 9.27). Three patterns of peripheral opacities are described on CT, which can be upper or lower lung predominant. Clinical, laboratory, and other radiological investigations are helpful in accurate diagnosis by demonstrating metastatic sepsis.

9.5.7 Miscellaneous Embolism

Tumor emboli can lodge in the main, lobar, and segmental pulmonary arteries. Tumor embolism from hepatocellular carcinoma, gastric malignancy, choriocarcinoma, and renal cell carcinoma results from the invasion of systemic veins draining in the inferior vena cava (Fig. 9.28). Tumor embolism results in dilated and beaded appearance of multiple pulmonary artery branches associated with or without pulmonary infarcts on CTPA [34]. This appearance is useful to differentiate between bland emboli and tumor emboli. Rarely embolic/metastatic osteosarcoma can cause ossification of the branches. Fragments of the catheter and intravascular

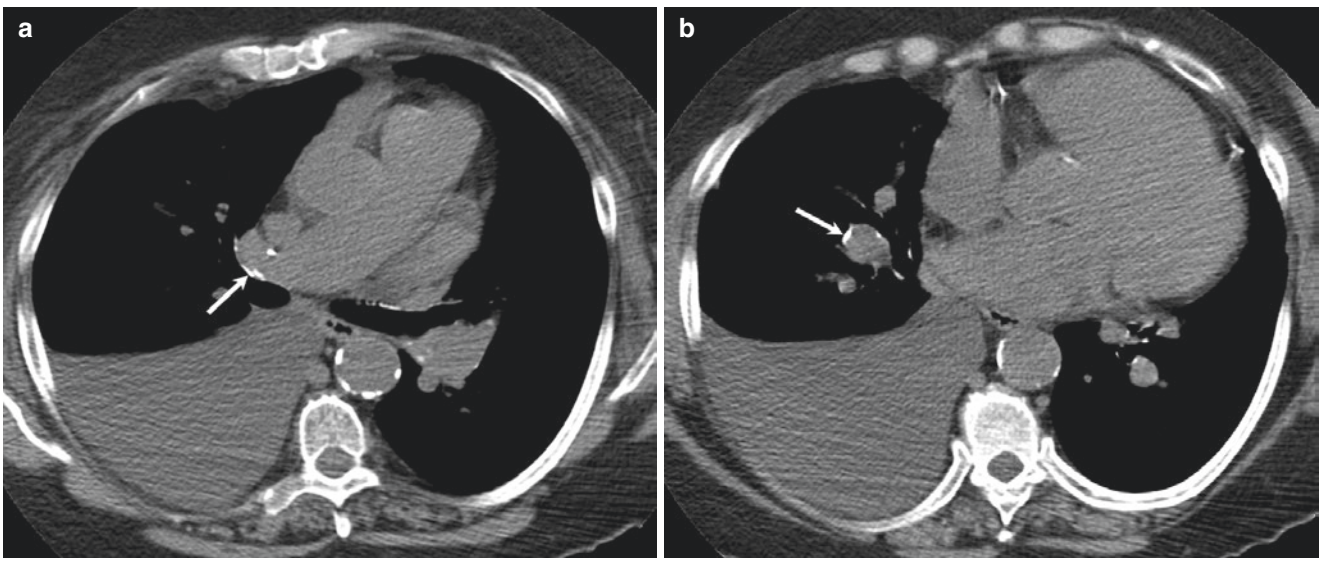

Fig. 9.16 (**a**, **b**) Calcification in the pulmonary artery (arrows) from long-standing PAH

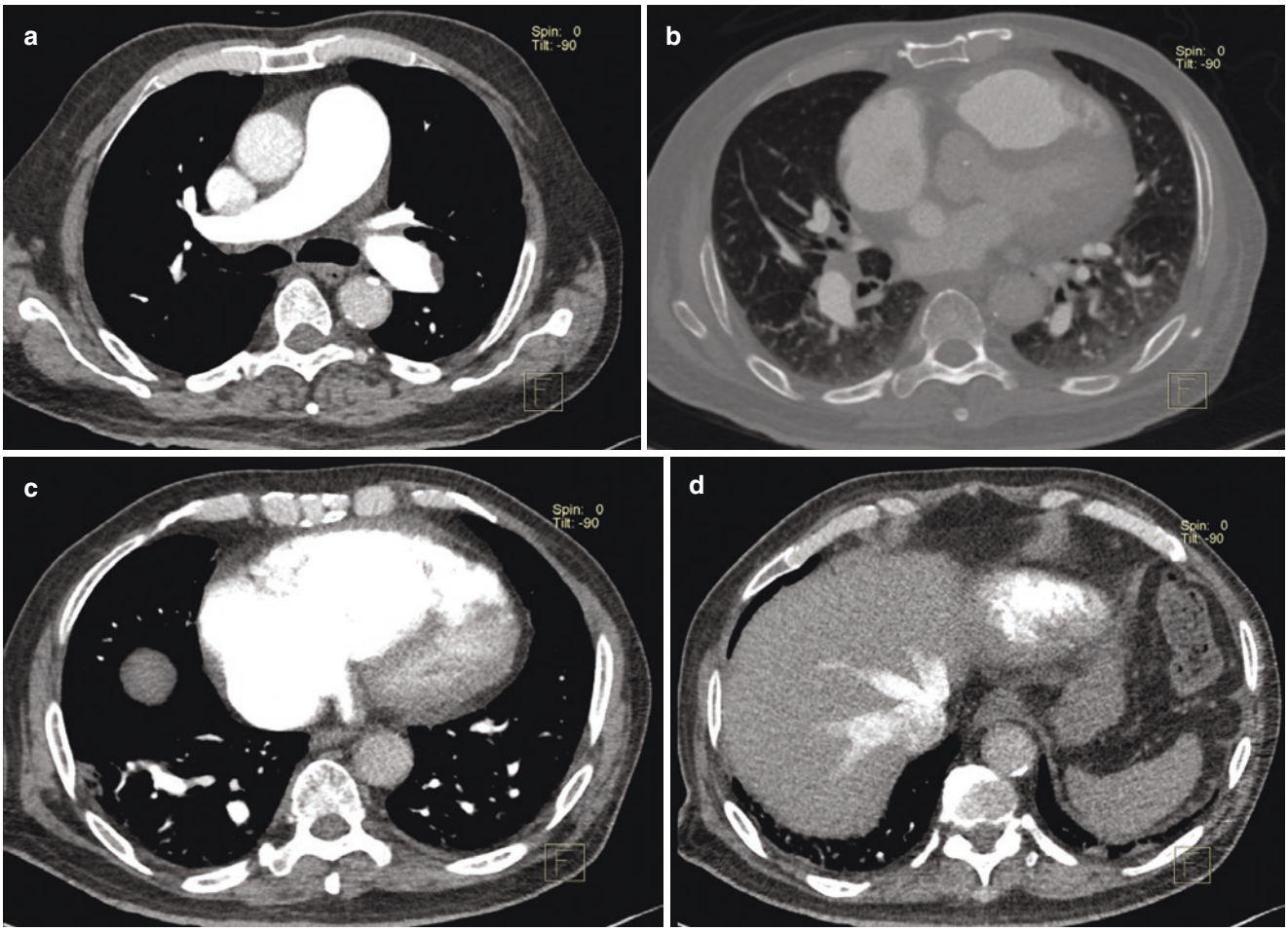

Fig. 9.17 Chronic PE with right ventricular dysfunction and PAH. (**a**–**d**) Axial CTPA images show dilated central pulmonary arteries with eccentric mural thrombus in a distal left pulmonary artery, dilated and tortuous segmental vessels in comparison to adjacent airways, and dilated right atrium and ventricle with reflux of contrast in IVC

Table 9.4 Pitfalls in the diagnosis of pulmonary embolism

Streak artifacts	Streaks are seen in the upper lung due to dense contrast in the superior vena cava and brachiocephalic vein. They limit the evaluation of vessels in the upper lung and can be avoided by using the saline-chasing technique of CTPA, while another option is to utilize a caudocranial scanning
Motion artifacts	They result from respiratory and cardiac motions. Respiratory motion can be easily recognized by changing to lung window that shows a band of blur images. Artifact due to cardiac motion is particularly annoying in the evaluation of pulmonary artery branches in the right middle lobe and lingula. An ECG-gating CTPA has been proposed to get rid of the artifacts related to cardiac motion, but it is associated with higher radiation dose
Mixing or flow artifact	This is a less common issue in the pulmonary arteries. Rarely in a patient with aortopulmonary fistula, the non-iodinated blood from high-pressure branches of the aorta to the lower pressure enhancing pulmonary artery resulting in false-positive interpretation
Volume averaging artifacts	These result when two structures of different densities are contained within a particular voxel and are assigned a single attenuation value that is an average of the two structures. These are further exaggerated by motion artifacts. Thin slices in modern scanners have cut down these artifacts. Multiplanar reconstructions also help in difficult cases
Misinterpretation artifacts	Intrapulmonary nodes, pulmonary veins, or mucus plug may be mistaken for PE. Multiplanar reconstruction helps in reducing these errors of interpretation

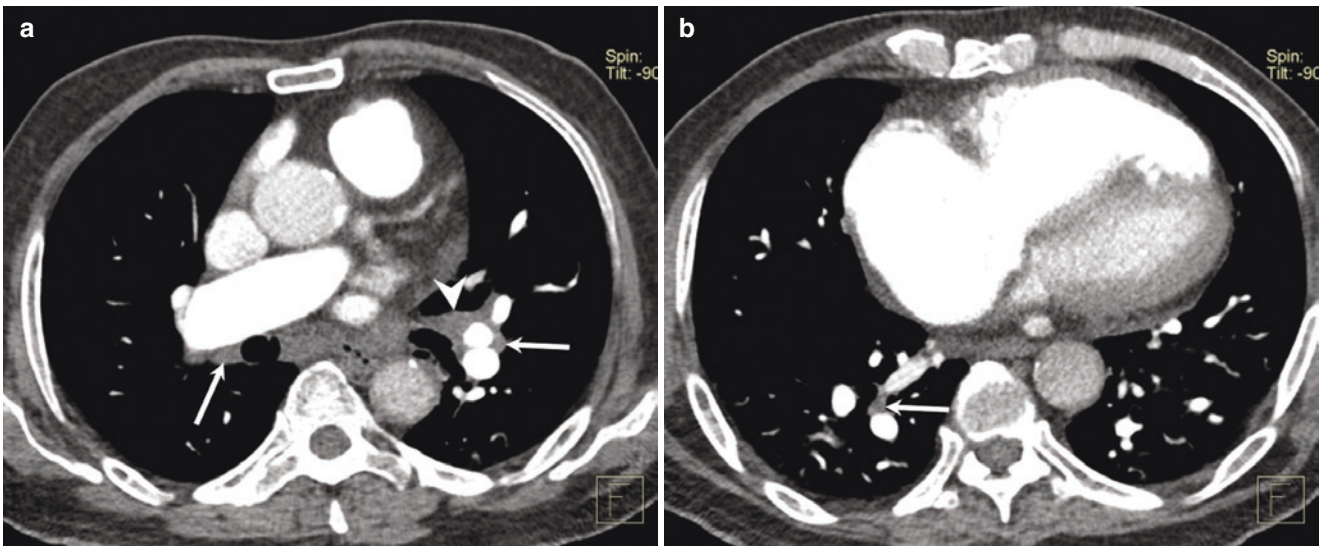

Fig. 9.18 Intraparenchymal nodes mimicking PE in a 69-year-old man with PAH. (**a**, **b**) Axial CTPA images show soft-tissue nodules (arrows) abutting the pulmonary artery branches. The nodal tissue in the left infrahilar region (arrowhead) is not discrete, unlike other nodes. Remember, the lymph nodes are located along bronchovascular bundles

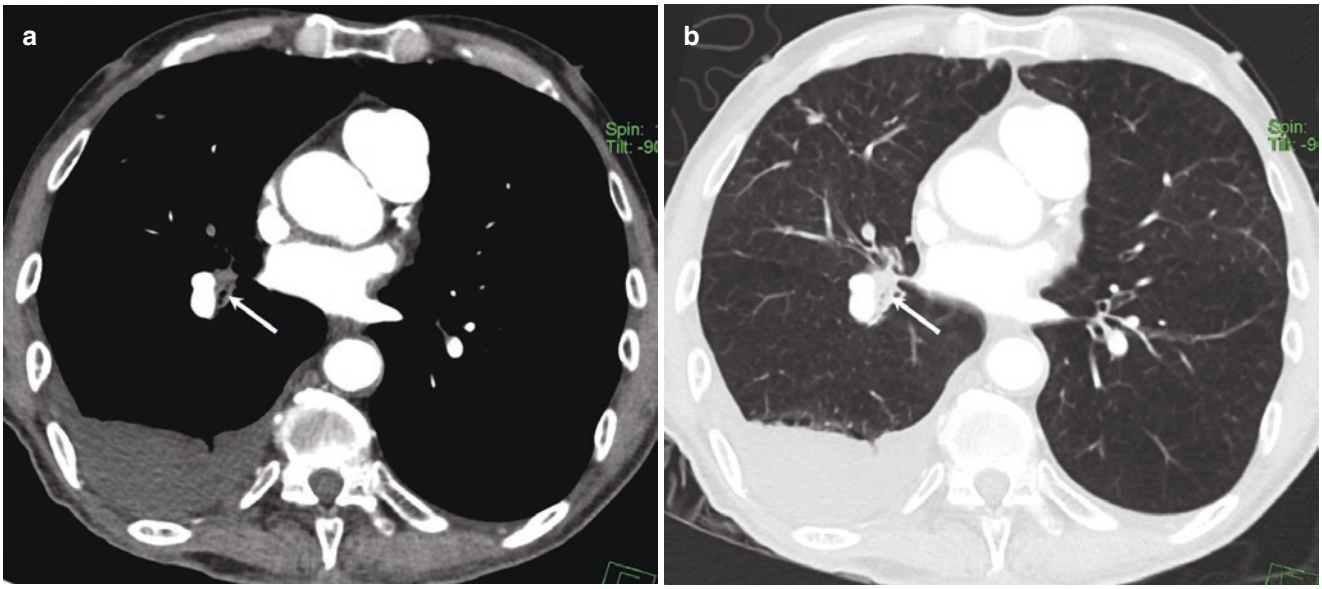

Fig. 9.19 Mucus plug mimicking PE. (**a**) Axial CTPA images show soft tissue (arrow) adjacent to pulmonary branches. (**b**) Axial image in lung window settings reveals bubbly fluid (arrow) in the bronchial tree

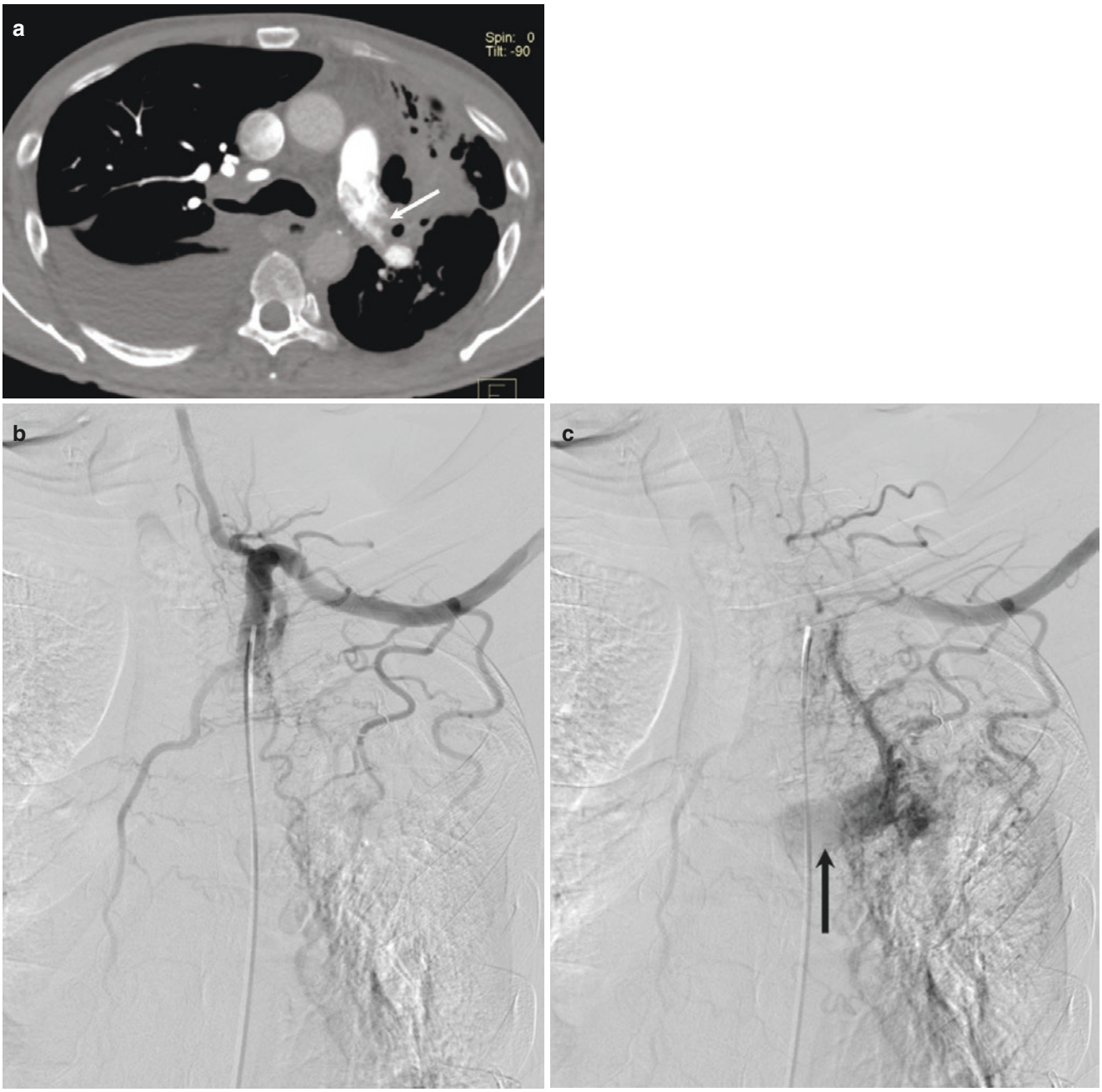

Fig. 9.20 Systemic artery-pulmonary artery fistula mimicking PE. (**a**) Axial CTPA image shows a heterogeneous density in the left pulmonary artery (arrow). Note post-tuberculosis fibrotic changes in the left upper lobe. (**b**, **c**) Digital subtraction angiography with left subclavian catheterization shows transpleural collaterals from branches of the subclavian artery opacifying the left pulmonary artery (arrow)

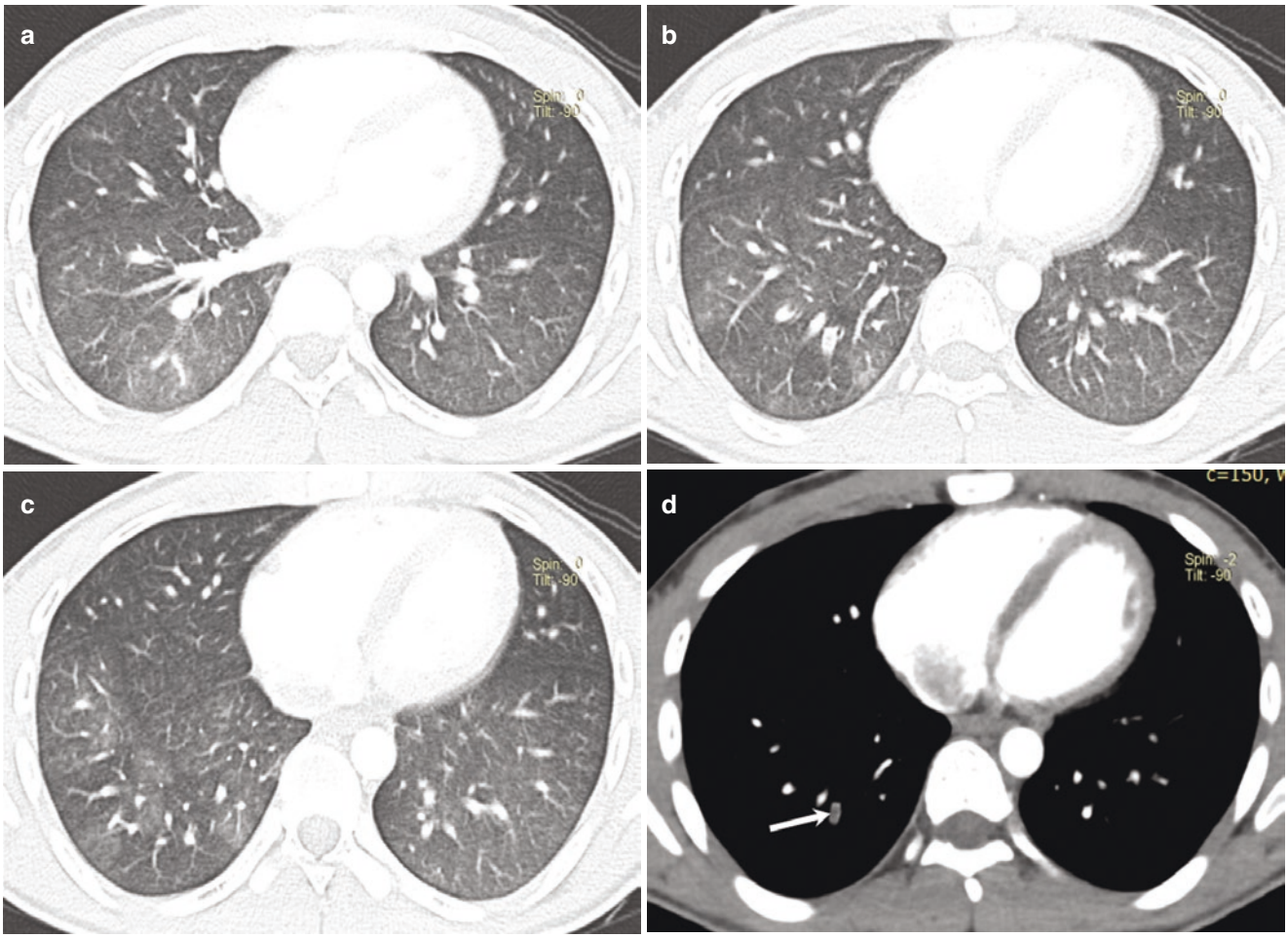

Fig. 9.21 A 27-year-old man with fat embolism immediately after internal fixation of the femoral fracture. The patient developed dyspnea, petechial skin rashes, and altered mental status. (**a**–**c**) Axial CT images show patchy ground-glass opacities, more on the right side with fine nodularity. (**d**) Axial CTPA image shows a low-density filling defect in a subsegmental branch of the right lower lobe pulmonary artery. A filling defect in the pulmonary artery with fat embolism is extremely rare

devices during or after an intervention can migrate, leading to non-thrombotic pulmonary embolism.

9.6 Pulmonary Artery Hypertension

PAH is defined as an increase in mean pulmonary artery (mPA) pressure ≥25 mm Hg at rest, as assessed by right heart catheterization. The normal mPA is 14 ± 3 mm Hg, with an upper limit of normal of approximately 20 mm Hg, while the clinical significance of an mPA 21–24 mm Hg is unclear. The elevated pulmonary pressure due to increased vascular resistance in pulmonary circulation results in increased RV afterload and failure. PAH may be caused by a wide variety of disease entities, and imaging plays a crucial role in their diagnosis. The WHO classification for the PAH divides it into five groups, but from an imaging perspective, it is more convenient to divide PAH into two categories: precapillary and postcapillary PAH (Table 9.6).

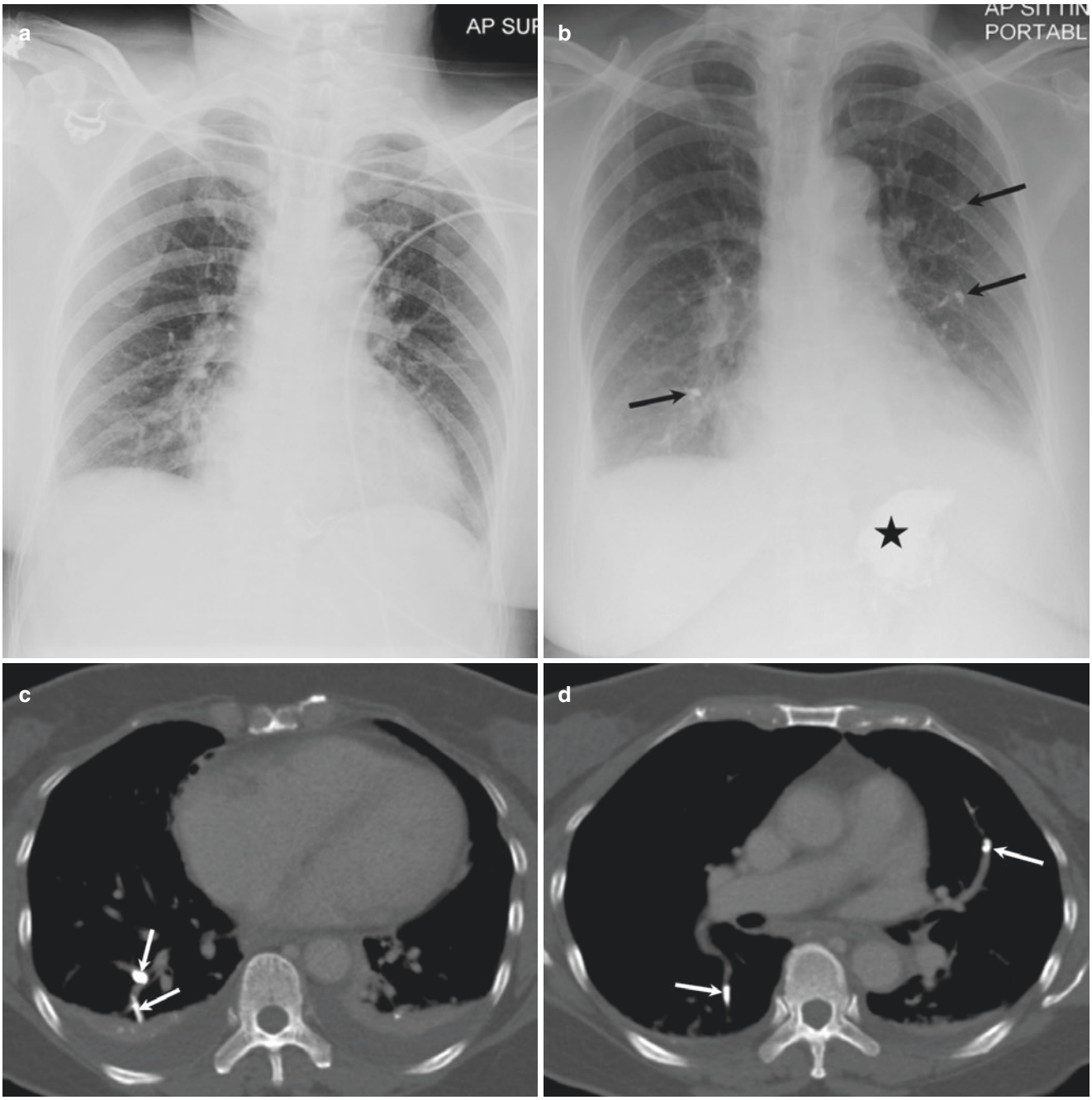

Fig. 9.22 A 67-year-old woman with hematemesis who underwent glue embolization for bleeding gastric varices. (**a**) Pre-op frontal radiograph. (**b**) Post-embolization frontal radiograph shows dense glue below the left hemidiaphragm in gastric varices (asterisk) with new hyperdense foci in both lungs (arrows). (**c**, **d**) Axial CTPA images with bone window settings reveal glue embolization in peripheral branches of pulmonary arteries (arrows)

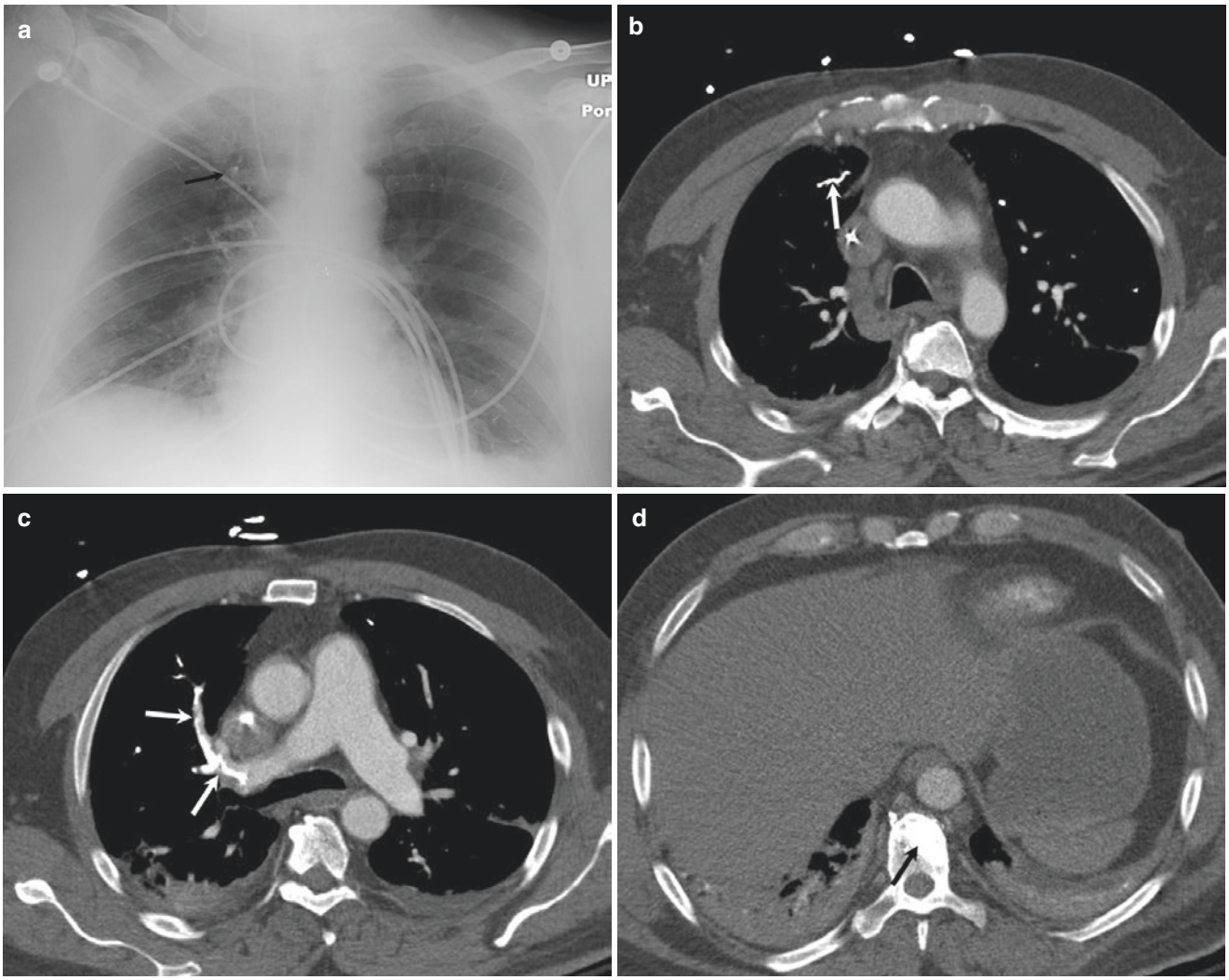

Fig. 9.23 A 60-year-old man with shortness of breath 2 days after elective kyphoplasty of T9 and T10 vertebra. (**a**) Chest radiograph shows faint calcific densities (arrow) in the right upper zone. (**b**, **c**) Axial CT images show linear embolized bone cement in the right upper lobe pulmonary artery and its branches (arrows). (**d**) Bone cement (arrow) in the vertebra

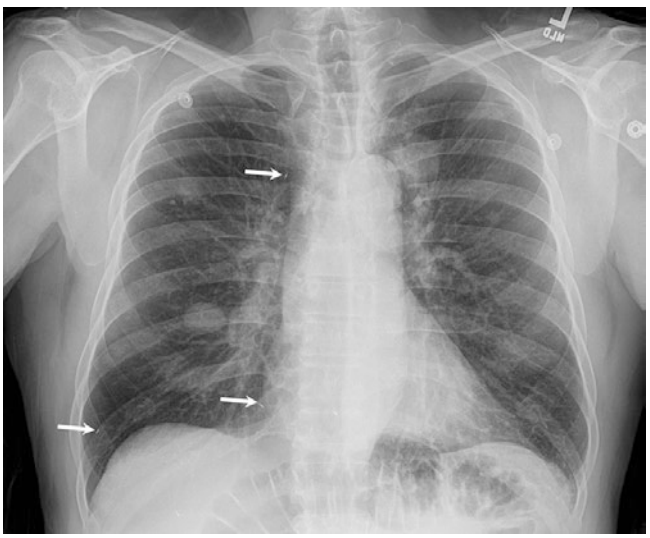

Fig. 9.24 A 67-year-old man with prostate cancer. Frontal radiograph shows embolized brachytherapy radiation seeds (arrows). Note pulmonary metastases

9.6.1 Chest Radiograph

A chest radiograph is not used for diagnostic purposes due to its low sensitivity and specificity. Nevertheless, a radiograph can demonstrate useful findings and has the following role when available (Table 9.7) [35].

9.6.2 CT Features of PAH

CT is an invaluable tool for the evaluation of a patient with PAH. CT has two major roles in PAH: (a) raise suspicion of PAH and (b) provide clues about the cause of PAH [35]. The CT features of PAH are listed in Table 9.8. CT diameter of pulmonary artery of more than 2.9 cm should raise the suspicion for PAH. A more useful and specific sign in elderly patients is the ratio of the pulmonary artery to ascending aorta of more than one (Fig. 9.29). A segmental artery to bronchus ratio more than one in three or four lobes has been

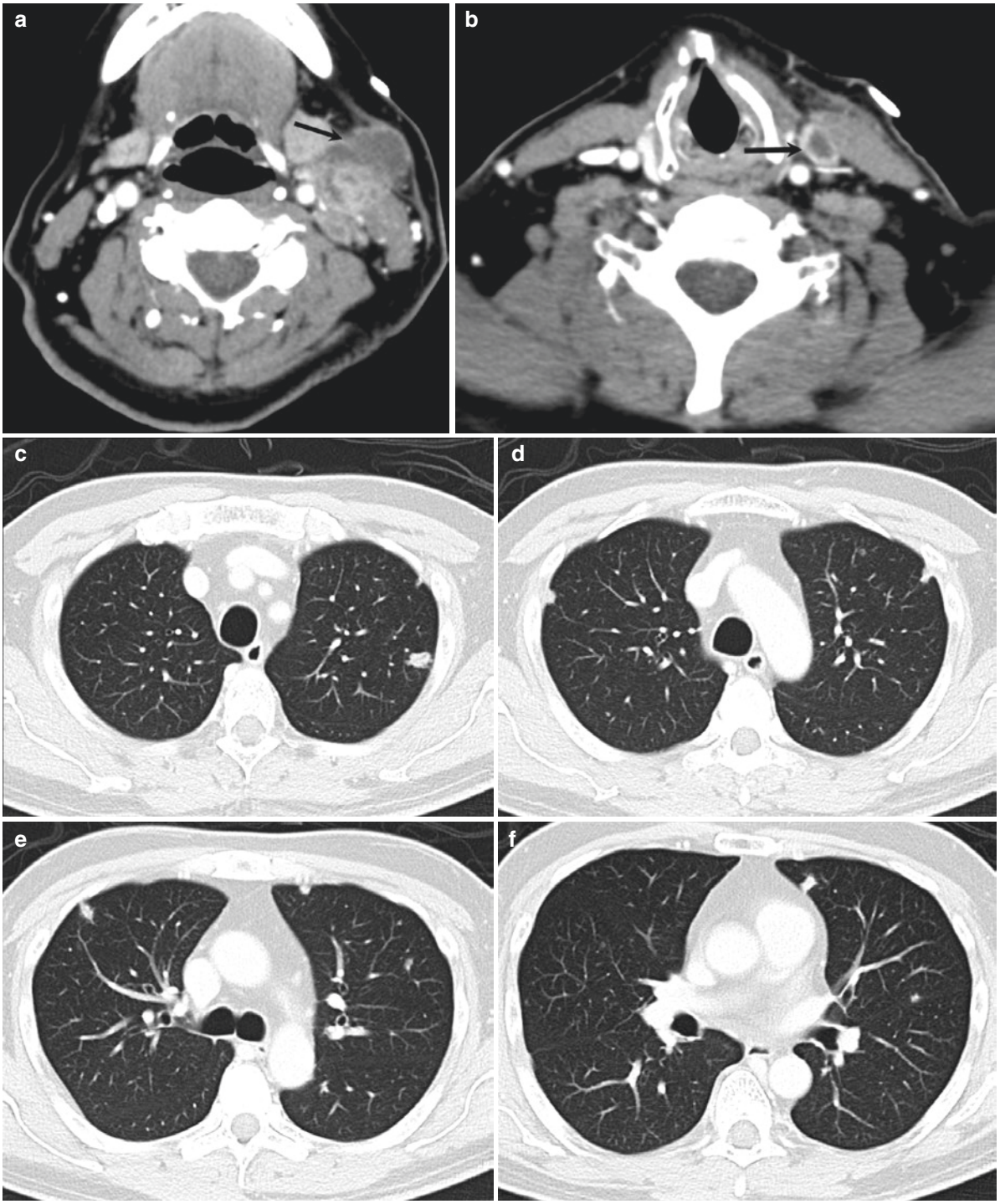

Fig. 9.25 Lemierre's syndrome in a 39-year-old man. (**a**) Axial CT neck image shows left large suppurative nodal mass (arrow). (**b**) CT image from the lower neck shows thrombophlebitis of the left internal jugular vein (arrow). (**c**–**f**) Axial CT images show multiple subpleural oblong opacities, suggestive of SPE

Table 9.5 Septic pulmonary emboli

Clinical lab-radiology	Concomitant extrapulmonary infection
CT features	• Peripherally located opacities • Wedge opacities with or without internal lucencies • Nodular opacities • Cavitary nodules • "Halo" sign around opacities • Thrombophlebitis in arteries or veins

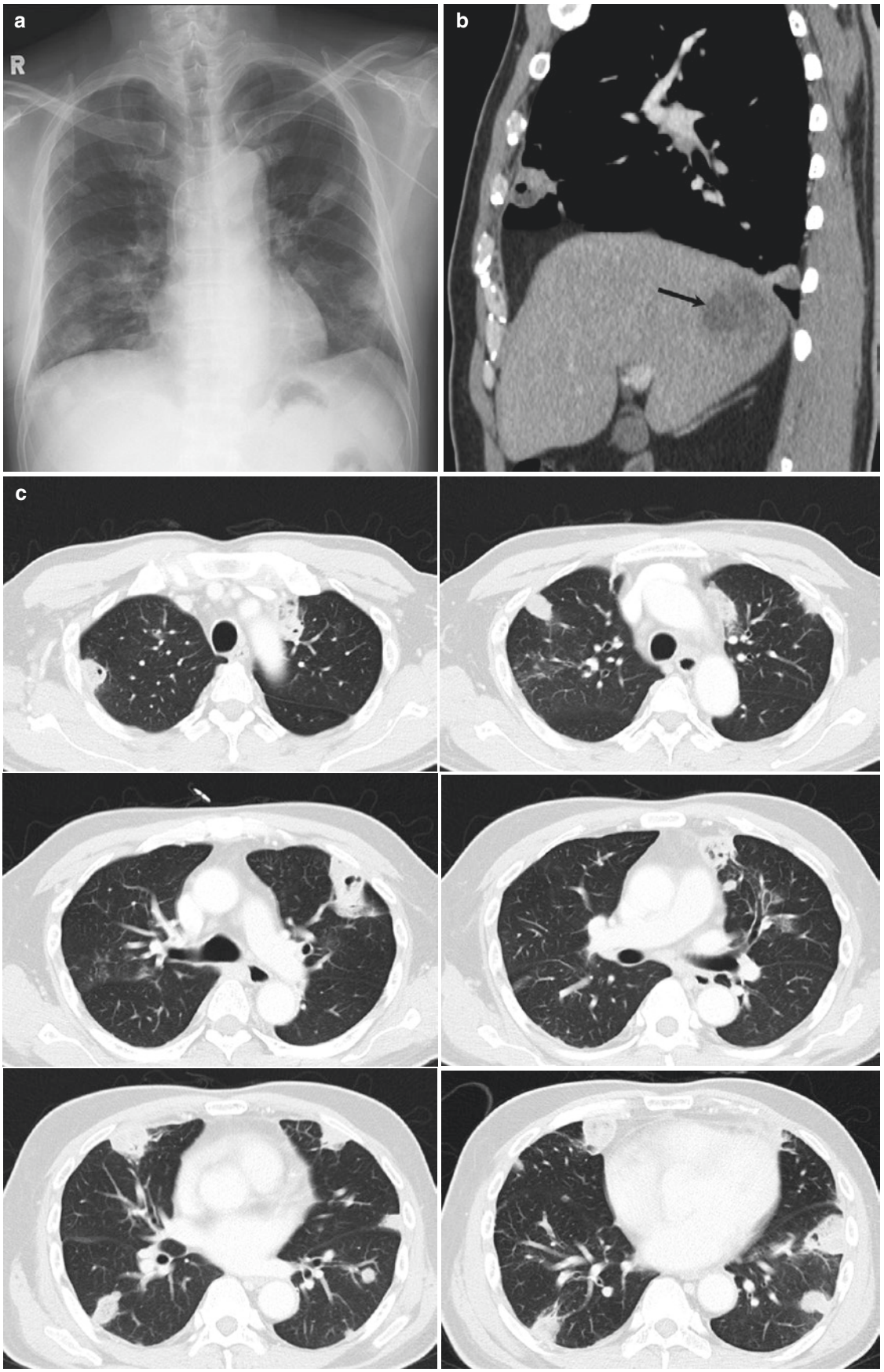

Fig. 9.26 Liver abscess with septic pulmonary emboli. (**a**) Frontal radiograph shows a multiple peripheral opacities in both lungs with few being wedge-shaped. (**b**) Sagittal CT image shows peripheral wedge-shaped opacities with a liver abscess (arrow). (**c**) Axial CT Images show multiple peripheral opacities with few showing central cavitations

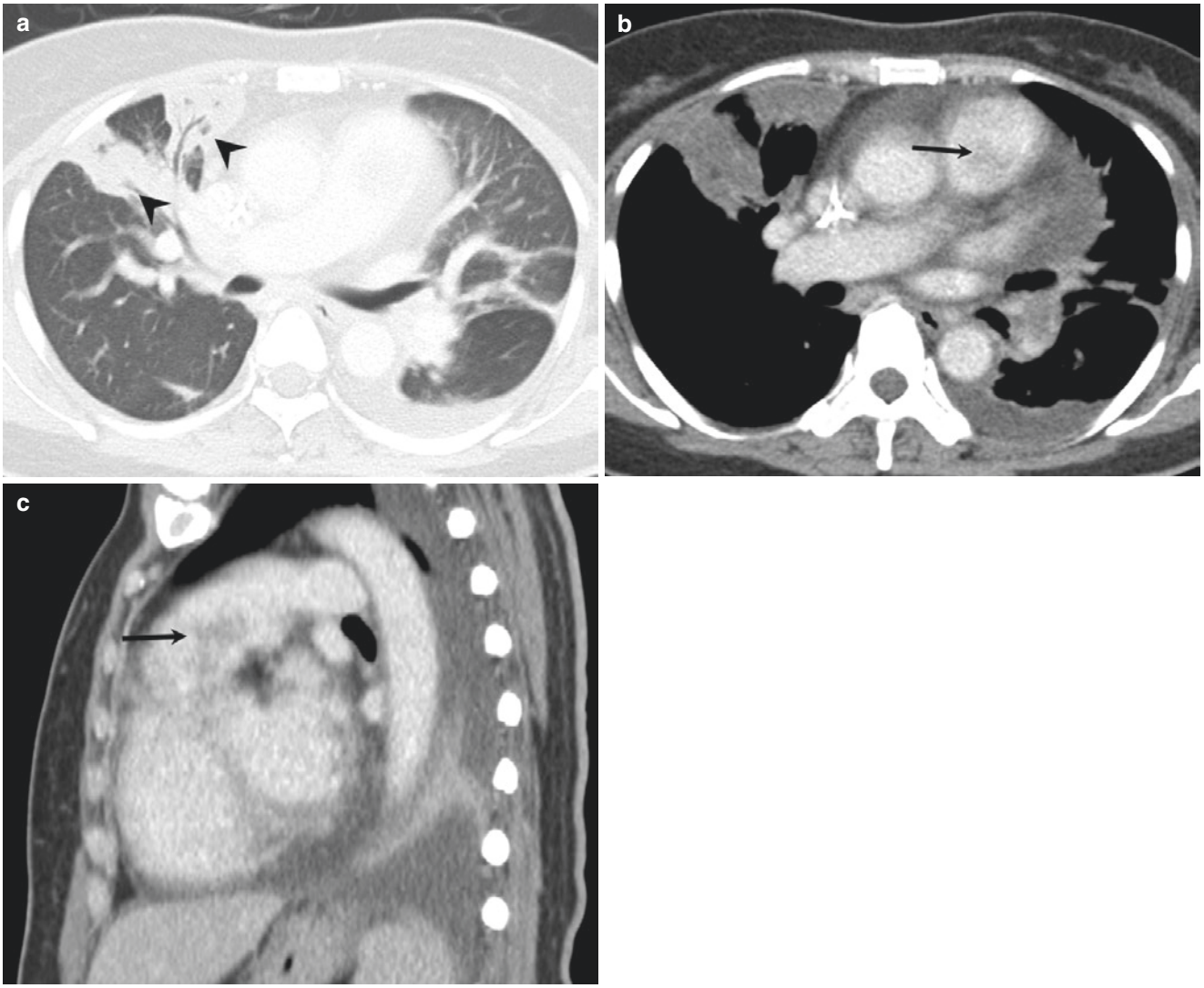

Fig. 9.27 Pulmonary valve infective endocarditis with septic pulmonary emboli. (**a**) Axial CT image shows peripheral peribronchial consolidations (arrowheads) in the anterior right upper lobe. (**b**, **c**) Axial and sagittal CT image shows filling defect (arrow) in the main pulmonary artery extending from the pulmonary valve representing vegetations

reported to have high specificity for PAH. The specificity can reach 100% if there is a combination of the dilated main pulmonary artery (>29 mm) and concomitant enlargement of three of four segmental arteries (arterial-to-bronchial diameter ratio, >1.25) [36]. In the presence of emphysema or fibrotic lung disease, the correlation between arterial dilatation and PAH is not significant. Pruning of peripheral branches similar to that in radiograph is also seen in chest CT.

Additionally, CT can show changes in RV dysfunction that include right chamber dilatation, straightening or bowing of interventricular septum toward the left, dilated IVC, and hepatic veins [37]. There is an increased prevalence of pericardial effusion in PAH. These changes are present irrespective of the cause of PAH. The lungs show mosaic attenuation due to perfusion variation in different segments. CT provides additional information and can help in diagnosing the cause of PAH. CT features are helpful in identifying the etiology of PAH in many patients as described in Table 9.9 (Figs. 9.14, 9.17, 9.30, 9.31, 9.32, 9.33, and 9.34).

9.7 Pulmonary Arteriovenous Malformation

Pulmonary arteriovenous malformation (PAVM) is an abnormal communication between the pulmonary artery and the pulmonary vein that may result in the extracardiac right-to-left shunt. These vascular malformations are usually congenital in origin but can be diagnosed at any age.

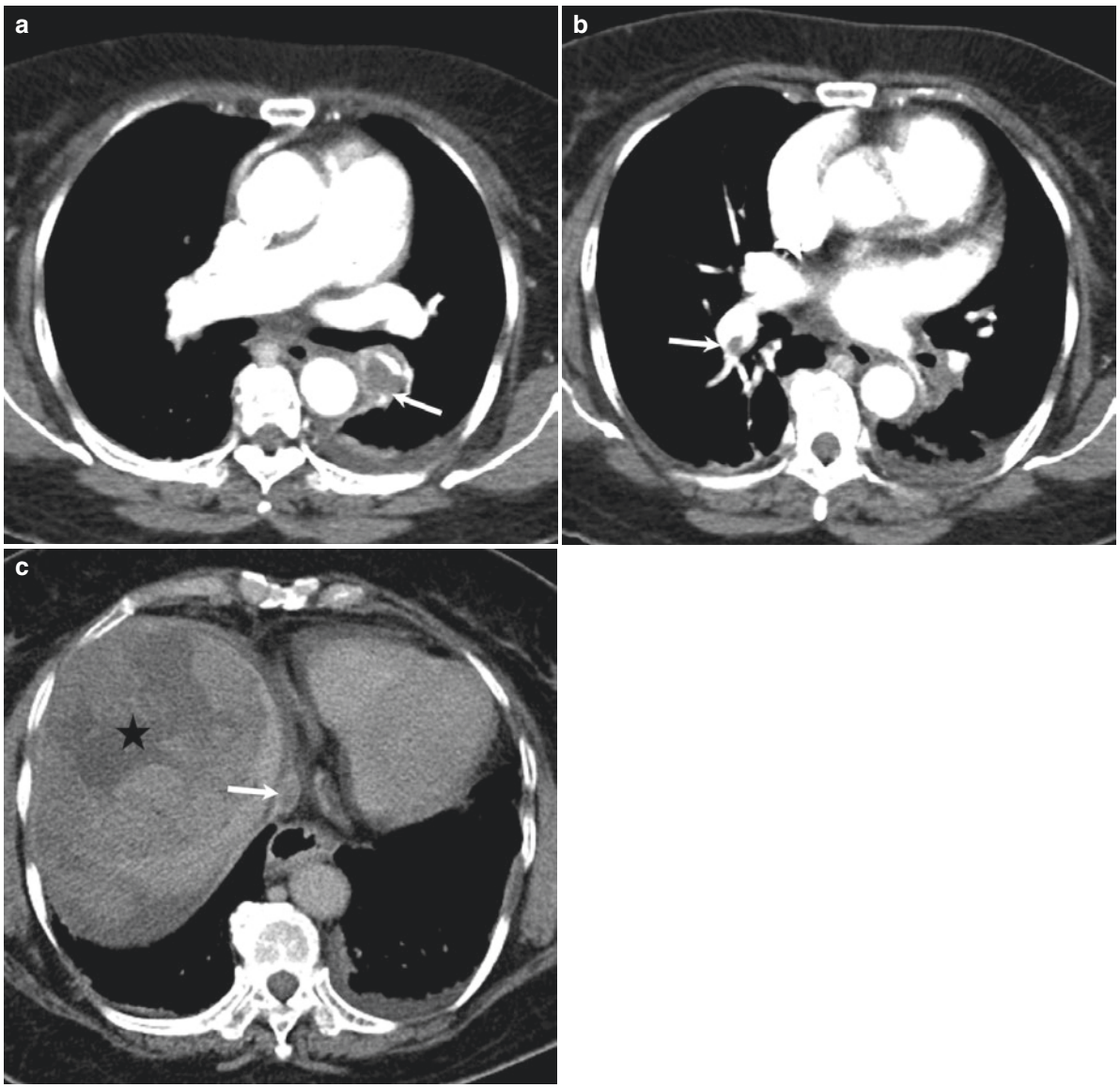

Fig. 9.28 Tumor embolism in a patient with hepatocellular carcinoma. (**a**, **b**) Axial CTPA images show thrombus in bilateral lower lobe pulmonary arteries (arrows). (**c**) Axial CT image in venous phase shows a large heterogeneous mass in the liver (asterisk) and tumor thrombus in IVC (arrow)

Table 9.6 Precapillary vs postcapillary PAH

Precapillary PAH	Postcapillary PAH
Mean pulmonary arterial pressure >25 mm Hg Pulmonary capillary wedge pressure ≤15 mm Hg	Mean pulmonary arterial pressure >25 mm Hg Pulmonary capillary wedge pressure >15 mm Hg
• Idiopathic PAH • Familial PAH • Chronic thromboembolic disease • Pulmonary parenchymal diseases • Obstructive sleep apnea • PAH associated with other diseases Collagen vascular diseases HIV Portal hypertension Drug toxicity • Venous diseases Pulmonary veno-occlusive diseases Pulmonary capillary hemangiomatosis	• Left heart diseases Atrial or ventricular diseases Valvular diseases

Table 9.7 Role of chest radiograph in PAH

• Radiograph can demonstrate changes of PAH, i.e., dilated central pulmonary arteries with pruning of peripheral branches, increased diameter (16 mm in men and 15 mm in women) of the right interlobar artery
• Radiograph can show right heart enlargement
• Radiograph may show moderate-to-severe lung disease associated with PAH
• Radiograph helps in differentiating between arterial and venous PAH

Table 9.8 CT features of PAH

Primary changes	• Dilated pulmonary artery >2.9 cm • Ratio of PA: Ascending aorta >1 • Segmental artery to bronchus ratio >1 in three or four lobes • Pruning of peripheral pulmonary artery branches
Secondary changes	• Right chamber dilatation • Leftward bowing of interventricular septum • Pericardial effusion • Mosaic attenuation of lungs

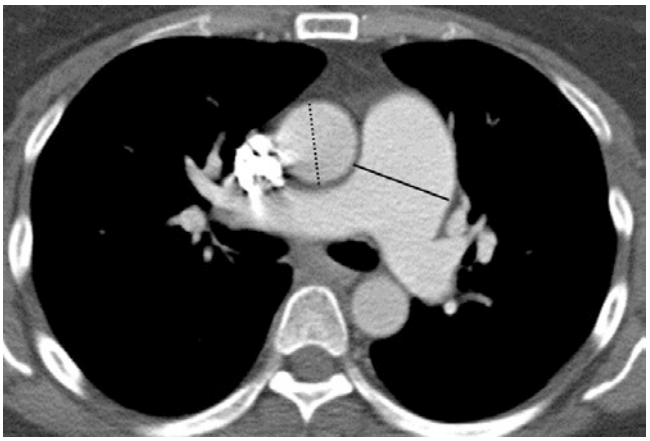

Fig. 9.29 PAH. Calculation of ratio of the main pulmonary artery to ascending aorta is more useful than dilatation of pulmonary artery alone

Table 9.9 CT findings in various causes of PAH

Cause of PAH	CT findings
Idiopathic	• Features of PAH • No filling defects in vessels • No dilatation of bronchial arteries • Mosaic attenuation in lungs • RV dilatation and pericardial effusion
Chronic thromboembolic disease	• Features of PAH • Imaging may show acute or chronic PE • Dilated bronchial arteries are common • Marked mosaic attenuation of lungs
Pulmonary thrombosis	• Markedly dilated pulmonary arteries with long continuous in situ thrombus along the pulmonary arteries • Thrombus may show calcification • Presence of Eisenmenger syndrome (usually ASD) • Features of PAH
Parenchymal lung disease	• Features of PAH • Background lung disease • Emphysema, pulmonary fibrosis, etc.
Collagen vascular disease (CVD)	• Features of PAH • Interstitial fibrosis may be present • Esophageal dilation, pericardial effusion
Cardiac diseases	• Features of PAH • Eisenmenger syndrome from PDA, ASD, or VSD
Pulmonary arteriovenous malformation	• Features of PAH • Pulmonary arteriovenous malformation • Vascular malformation in other organs
Hepatopulmonary syndrome	• Features of PAH • Dilated distal/subpleural pulmonary artery branches • Presence of cirrhosis • Stigmata of portal hypertension like varices
Portopulmonary hypertension	• Features of PAH • Presence of cirrhosis • Stigmata of portal hypertension (dilated portal vein, varices, ascites, etc.)
Pulmonary veno-occlusive disease	• Features of PAH • Interlobular septal thickening • Centrilobular ground-glass density nodules
Constrictive pericarditis	• Features of PAH • Thickening or calcification of the pericardium

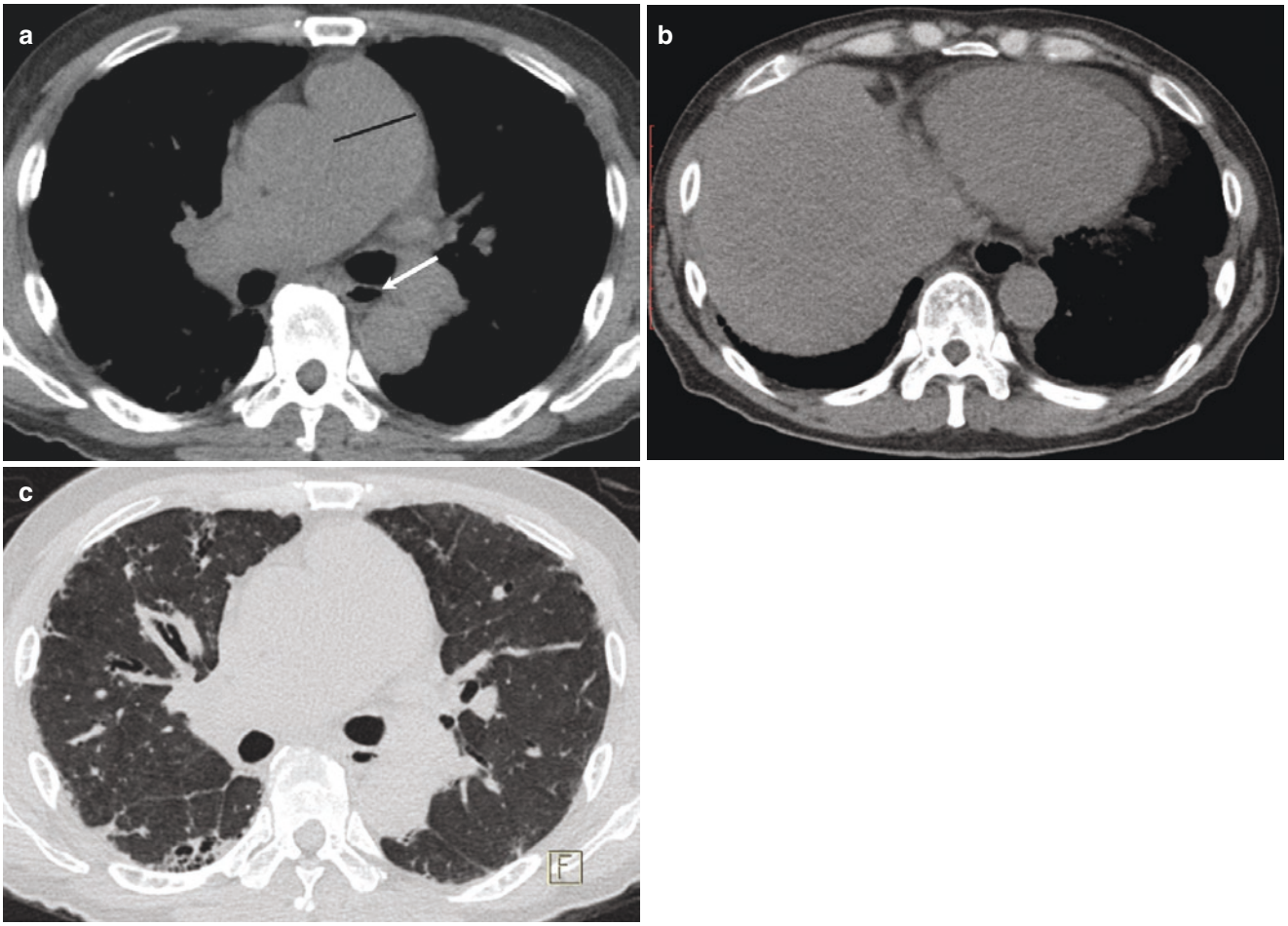

Fig. 9.30 PAH and esophageal dysmotility in a patient with mixed connective tissue disease. (**a**) Axial unenhanced CT shows dilated main pulmonary artery with respect to ascending aorta with an air-fluid level in the mid-esophagus. (**b**). Image from the lower thorax shows pericardial effusion and patulous lower esophagus. (**c**) HRCT image at the same level as figure a shows fibrotic lung disease

These are twice as common in women as in men. Approximately 70% of the cases of PAVM are associated with hereditary hemorrhagic telangiectasia (HHT). Conversely, approximately 15–35% of patients with HHT have PAVM. Acquired PAVM can be seen in hepatic cirrhosis, schistosomiasis, mitral stenosis, trauma, actinomycosis, mitral stenosis, and metastatic thyroid carcinoma. Left-to-right shunt can result from abnormal communication between the bronchial artery and pulmonary artery in patients with bronchiectasis or tuberculosis. Imaging features of PAVMs are described in Table 9.10 [38] (Figs. 9.35 and 9.36). The complications of PAVMs include hemoptysis, hemothorax, stroke, brain abscess, heart failure, polycythemia, and anemia [38].

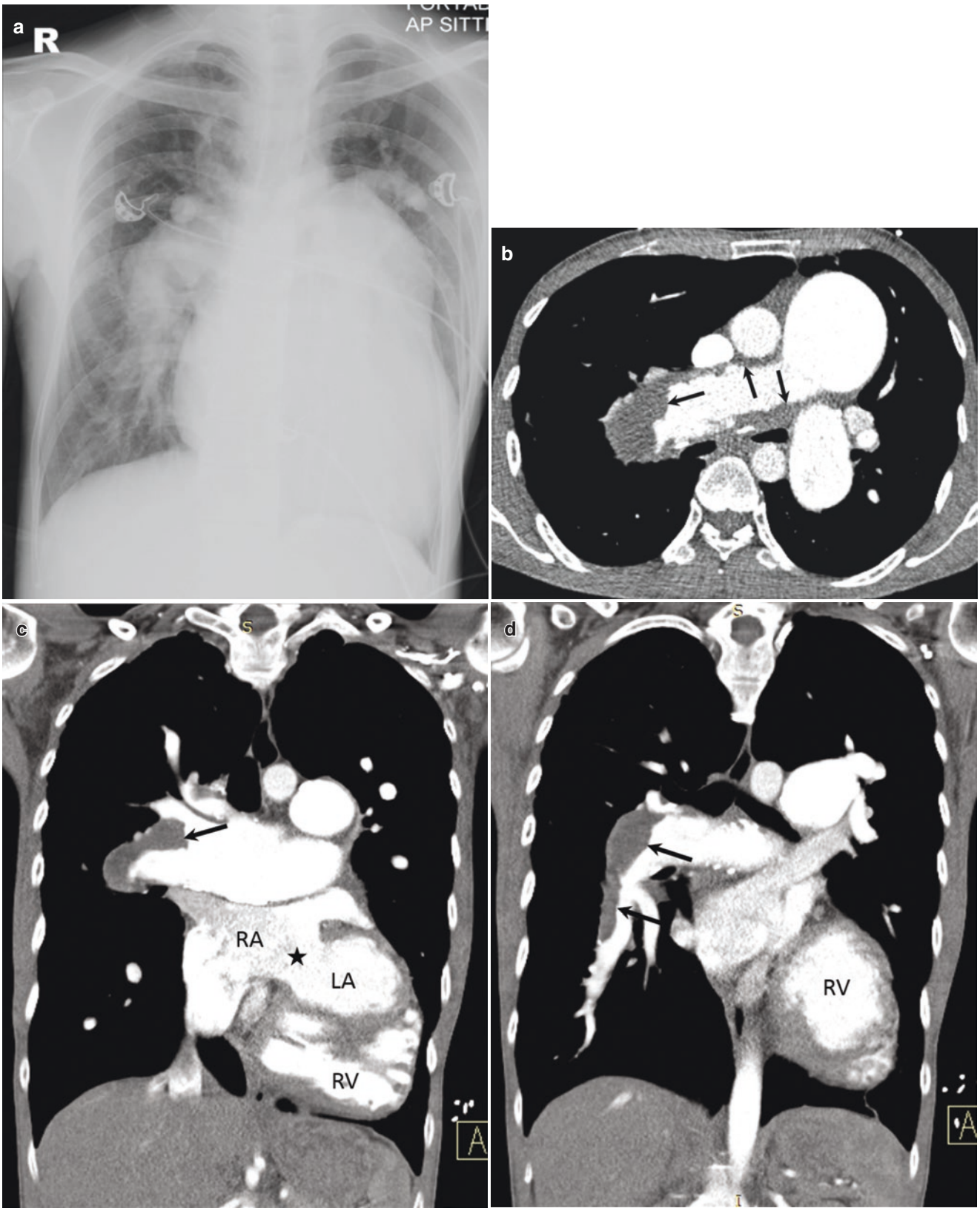

Fig. 9.31 Pulmonary artery thrombosis in a 46-year-old man with undiagnosed atrial septal defect (ASD), PAH, and Eisenmenger syndrome. (**a**) Chest radiograph shows markedly dilated pulmonary arteries and cardiomegaly. (**b–d**) Axial and coronal CTPA images show eccentric contiguous thrombus (arrows) along dilated right pulmonary artery and an ASD (asterisk) with the hypertrophied right ventricle. *RA* right atrium, *LA* left atrium, *RV* right ventricle

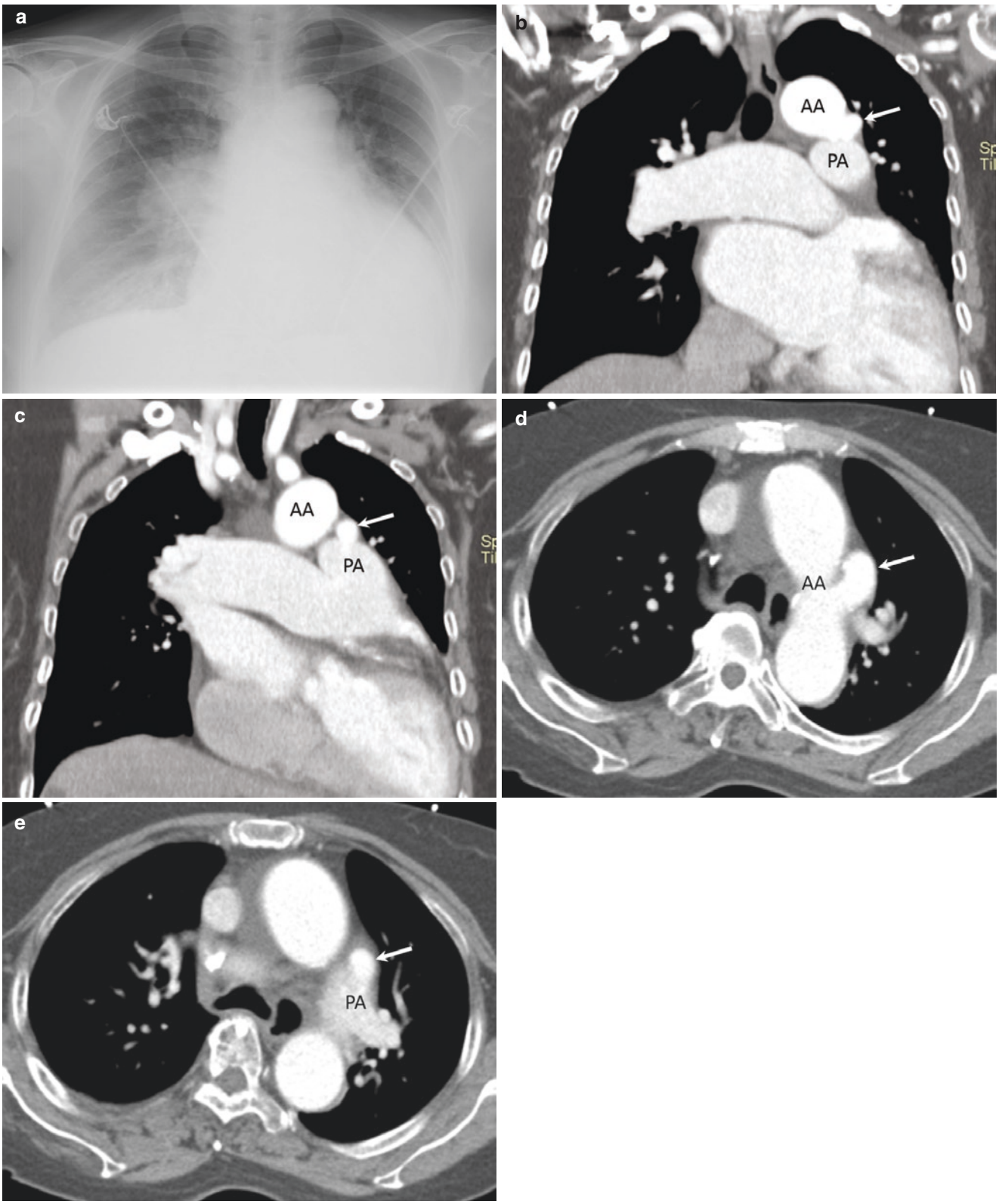

Fig. 9.32 A 68-year-old woman with PAH from patent ductus arteriosus (PDA). (**a**) Chest radiograph shows markedly dilated central pulmonary arteries. (**b**–**e**) Coronal and axial CT aortogram images show a PDA (arrows) arising from the undersurface of the aorta. *AA* arch of aorta, *PA* pulmonary artery. Note the pulmonary arteries are dilated

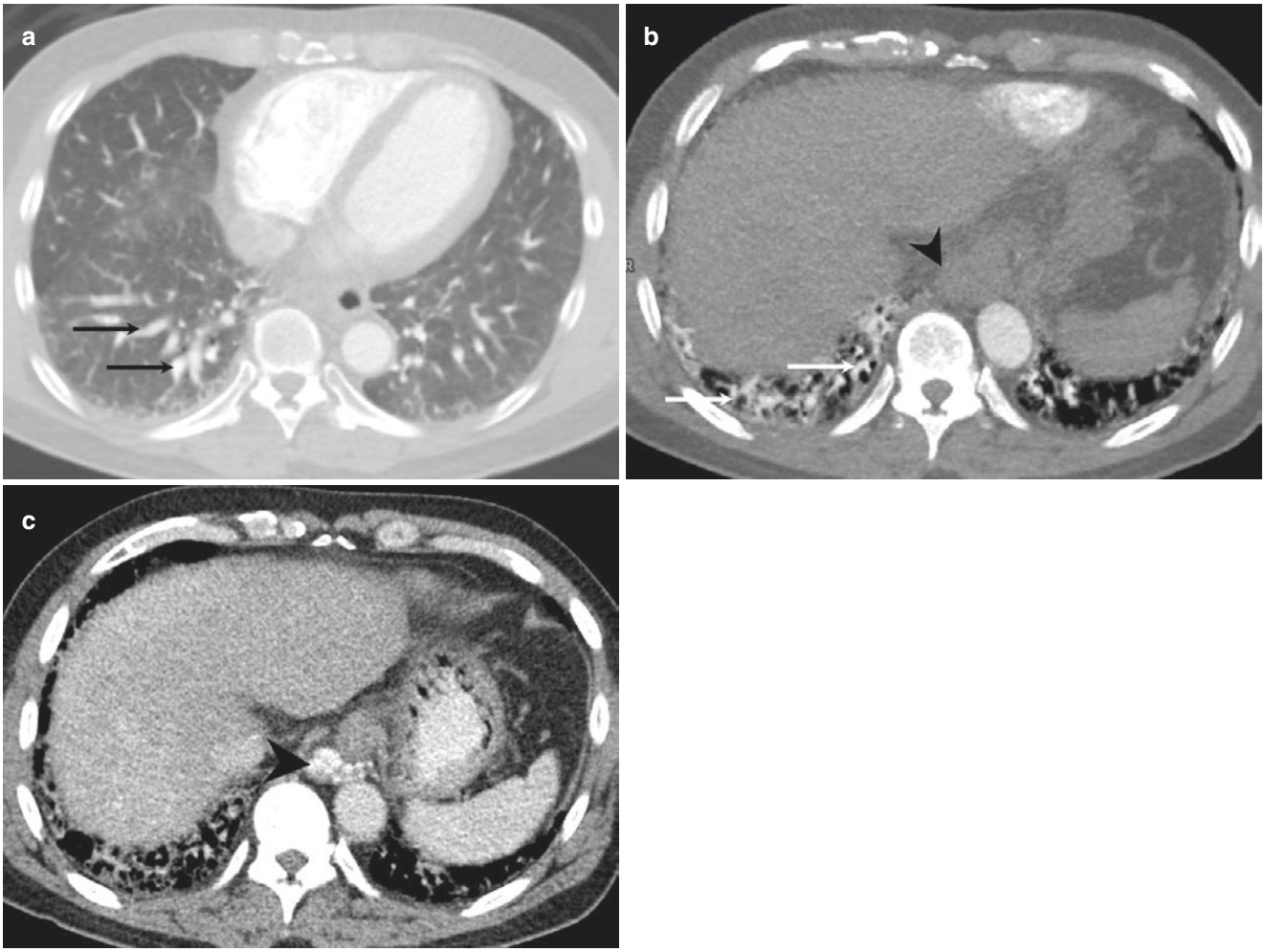

Fig. 9.33 A 57-year-old man with hepatopulmonary syndrome. (**a**, **b**) Axial CT images show dilatation of branches of the right lower lobe pulmonary artery (black arrows) as compared to adjacent bronchioles. (**c**) Caudal CT image shows aneurysmal dilatation (white arrows) of peripheral branches of the pulmonary artery. Note the non-enhancing varices (arrowhead) and surface nodularity of the liver suggesting cirrhosis

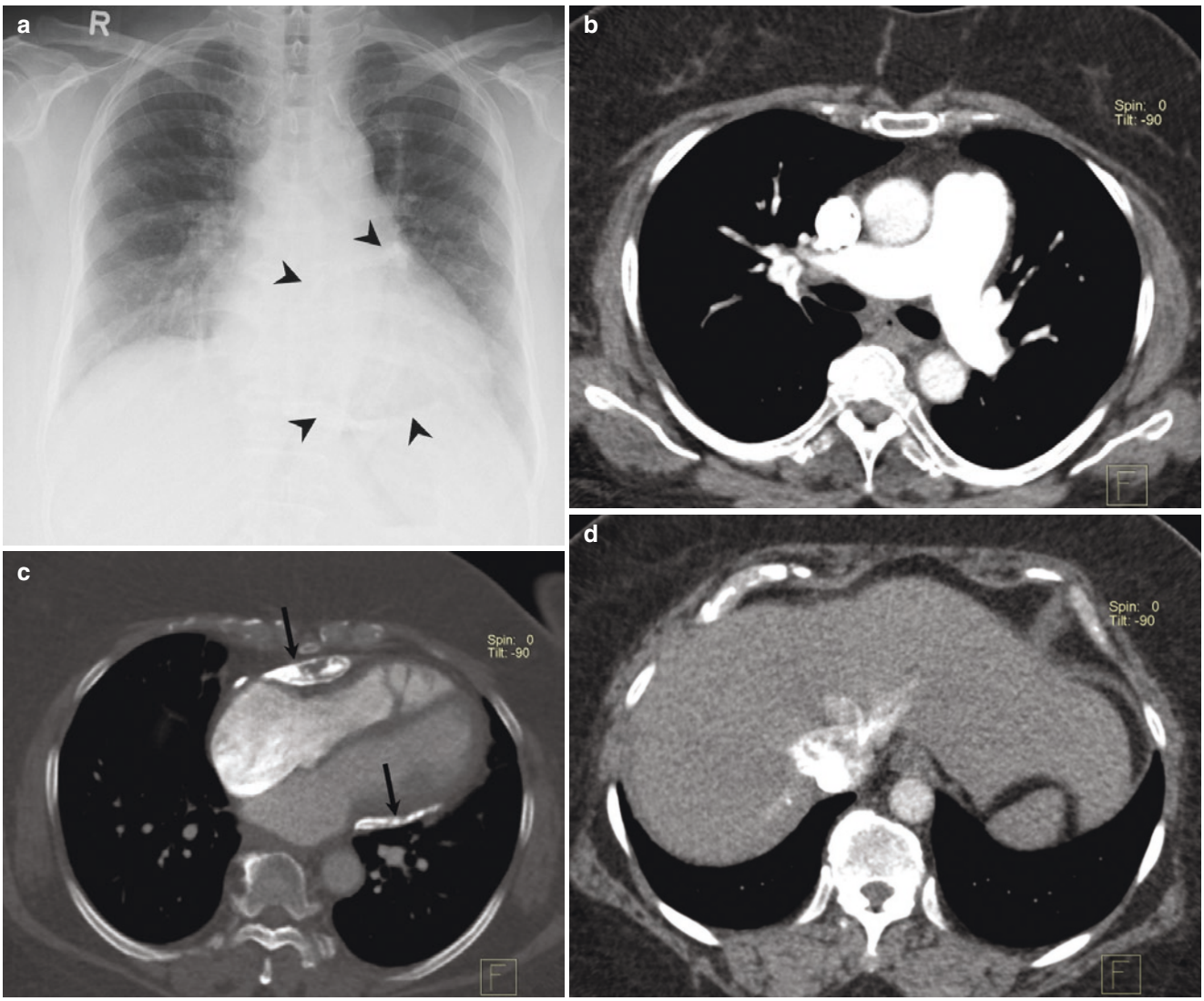

Fig. 9.34 A 49-year-old woman with PAH from calcific constrictive pericarditis. (**a**) Frontal chest radiograph shows curvilinear calcification along the pericardium (arrowheads). (**b**) Axial CTPA image shows dilated central pulmonary artery, compared to the ascending aorta. (**c**) Axial CTPA image in bone window settings shows dense calcification in the anterior and posterior pericardium (arrows). (**d**) Reflux of contrast in IVC

Table 9.10 Imaging features of PAVM

Radiograph	Round or ovoid opacity in the lower lobe Linear vessels from the opacity coursing toward the hilum
CT	Enhancing ovoid mass communicating with the pulmonary artery and vein 3D reconstructions are important for treatment planning
Contrast echocardiogram	Agitated saline appears in left heart chambers in three to eight cardiac cycles following its appearance in the right atrium confirming an extracardiac right-to-left shunt. In case of the intracardiac shunt, the saline bubbles will appear in one cardiac cycle

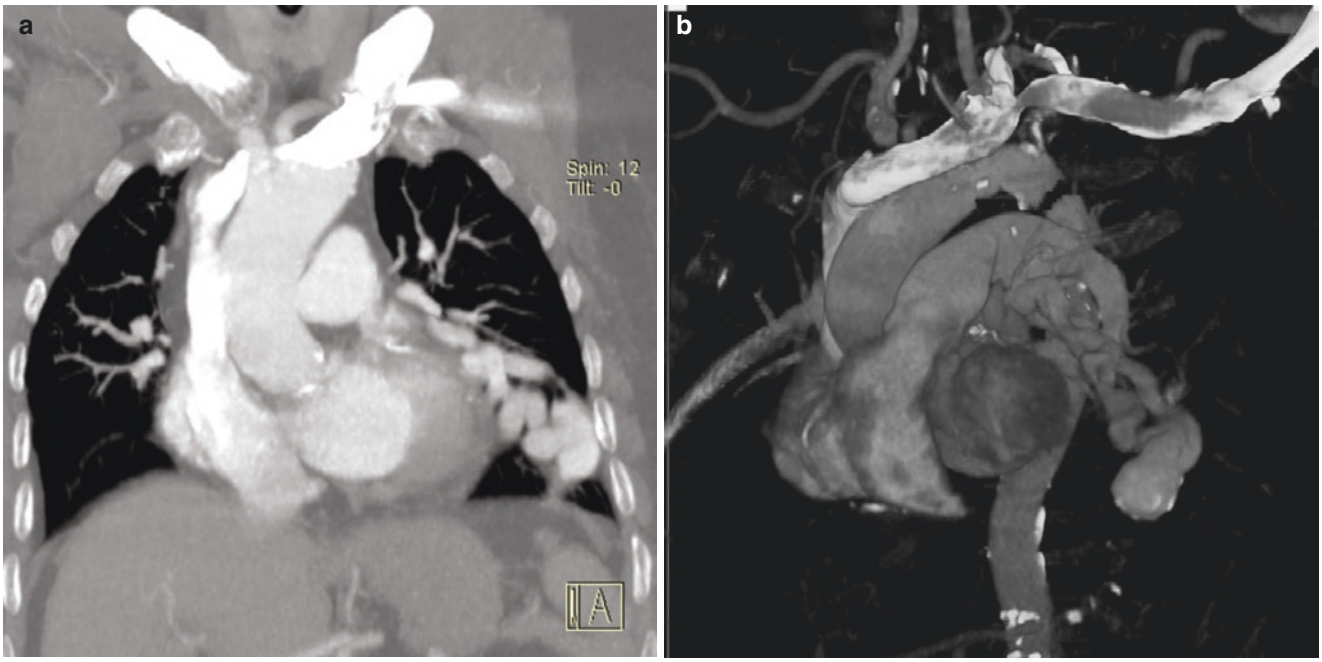

Fig. 9.35 A 78-year-old woman with PAH from a large left lower lung arteriovenous malformation associated with hereditary hemorrhagic telangiectasia. (**a**) Coronal thick MIP CTPA image and (**b**) volume-rendered reconstruction

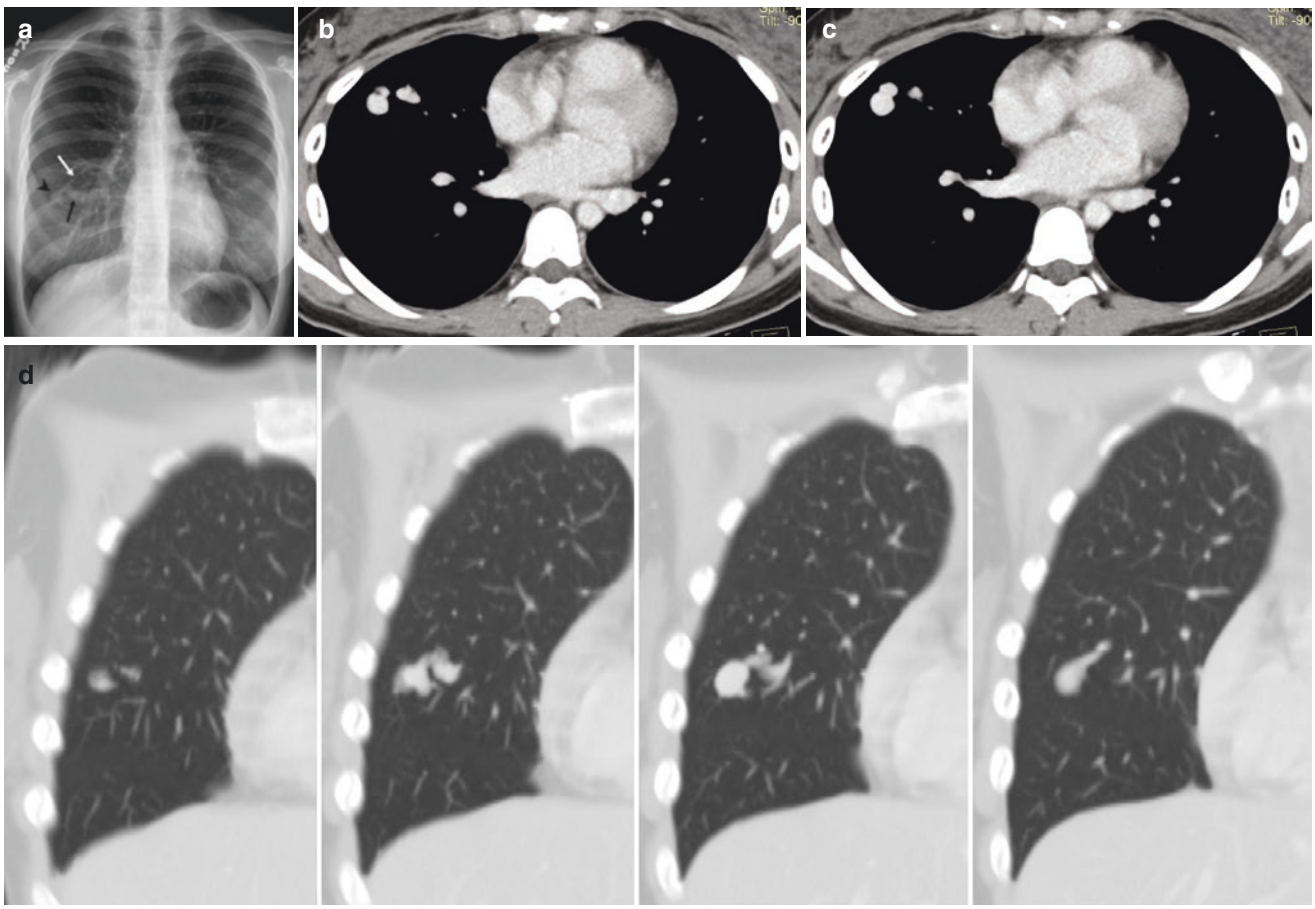

Fig. 9.36 A 23-year-old woman with right lung arteriovenous malformation (AVM). (**a**) Frontal chest radiograph shows a nodular opacity in the right mid-lower zone (arrowhead) with tubular vessels coursing toward it from the hilum (arrows). (**b**, **c**) Axial contrast-enhanced CT shows enhancing interconnected well-circumscribed nodular-tubular opacity in the right middle lobe. (**d**) Sequential coronal CT images of the right hemithorax demonstrating the arterial and venous connections of the AVM

References

1. Authors/Task Force Members, Torbicki A, Perrier A, Konstantinides S, Agnelli G, Galiè N, Pruszczyk P, Bengel F, Brady AJ, Ferreira D, Janssens U. Guidelines on the diagnosis and management of acute pulmonary embolism: the task force for the diagnosis and management of acute pulmonary embolism of the European Society of Cardiology (ESC). Eur Heart J. 2008;29(18):2276–315.
2. Goldhaber SZ, Visani L, De Rosa M. Acute pulmonary embolism: clinical outcomes in the International Cooperative Pulmonary Embolism Registry (ICOPER). Lancet. 1999;353(9162):1386–9.
3. Bělohlávek J, Dytrych V, Linhart A. Pulmonary embolism, part I: epidemiology, risk factors and risk stratification, pathophysiology, clinical presentation, diagnosis and nonthrombotic pulmonary embolism. Exp Clin Cardiol. 2013;18(2):129.
4. Worsley DF, Alavi A, Aronchick JM, Chen JT, Greenspan RH, Ravin CE. Chest radiographic findings in patients with acute pulmonary embolism: observations from the PIOPED study. Radiology. 1993;189(1):133–6.
5. Elliott CG, Goldhaber SZ, Visani L, DeRosa M. Chest radiographs in acute pulmonary embolism. Results from the International Cooperative Pulmonary Embolism Registry. Chest. 2000;118(1):33–8.
6. Baron MG. Fleischner lines and pulmonary emboli. Circulation. 1972;45(1):171–8.
7. Hampton AO, Castleman B. Correlation of postmortem chest teleroentgenograms with autopsy findings with special reference to pulmonary embolism and infarction. Am J Roentgenol Radium Ther. 1940;43:305–26.
8. Rathbun SW, Raskob GE, Whitsett TL. Sensitivity and specificity of helical computed tomography in the diagnosis of pulmonary embolism: a systematic review. Ann Intern Med. 2000;132:227–32.
9. Wittram C, Maher MM, Yoo AJ, Kalra MK, Shepard JA, McLoud TC. CT angiography of pulmonary embolism: diagnostic criteria and causes of misdiagnosis. Radiographics. 2004;24(5):1219–38.
10. Carrier M, Righini M, Wells PS, et al. Subsegmental pulmonary embolism diagnosed by computed tomography: incidence and clinical implications. A systematic review and meta-analysis of the management outcome studies. J Thromb Haemost. 2010;8:1716–22.
11. Ghaye B, Ghuysen A, Bruyere PJ, D'Orio V, Dondelinger RF. Can CT pulmonary angiography allow assessment of severity and prognosis in patients presenting with pulmonary embolism? What the radiologist needs to know. Radiographics. 2006;26(1):23–39.
12. Collomb D, Paramelle PJ, Calaque O, et al. Severity assessment of acute pulmonary embolism: evaluation using helical CT. Eur Radiol. 2003;13:1508–14.
13. Contractor S, Maldjian PD, Sharma VK, Gor DM. Role of helical CT in detecting right ventricular dysfunction secondary to acute pulmonary embolism. J Comput Assist Tomogr. 2002;26:587–91.
14. Lim KE, Chan CY, Chu PH, Hsu YY, Hsu WC. Right ventricular dysfunction secondary to acute massive pulmonary embolism detected by helical computed tomography pulmonary angiography. Clin Imaging. 2005;29:16–21.
15. Reid JH, Murchison JT. Acute right ventricular dilatation: a new helical CT sign of massive pulmonary embolism. Clin Radiol. 1998;53:694–8.
16. Kang DK, Thilo C, Schoepf UJ, Barraza JM Jr, Nance JW Jr, Bastarrika G, Abro JA, Ravenel JG, Costello P, Goldhaber SZ. CT signs of right ventricular dysfunction: prognostic role in acute pulmonary embolism. JACC Cardiovasc Imaging. 2011;4(8):841–9.
17. Aviram G, Cohen D, Steinvil A, Shmueli H, Keren G, Banai S, Berliner S, Rogowski O. Significance of reflux of contrast medium into the inferior vena cava on computerized tomographic pulmonary angiogram. Am J Cardiol. 2012;109(3):432–7.
18. He H, Stein MW, Zalta B, Haramati LB. Pulmonary infarction: spectrum of findings on multidetector helical CT. J Thorac Imaging. 2006;21(1):1–7.
19. Revel MP, Triki R, Chatellier G, Couchon S, Haddad N, Hernigou A, Danel C, Frija G. Is it possible to recognize pulmonary infarction on multisection CT images? Radiology. 2007;244(3):875–82.
20. Karabulut N, Kiroğlu Y. Relationship of parenchymal and pleural abnormalities with acute pulmonary embolism: CT findings in patients with and without embolism. Diagn Interv Radiol. 2008;14(4):189–96.
21. Castañer E, Gallardo X, Ballesteros E, Andreu M, Pallardó Y, Mata JM, Riera L. CT diagnosis of chronic pulmonary thromboembolism. Radiographics. 2009;29(1):31–50.
22. Wittram C, Kalra MK, Maher MM, Greenfield A, McLoud TC, Shepard JA. Acute and chronic pulmonary emboli: angiography–CT correlation. Am J Roentgenol. 2006;186(6_supplement_2):S421–9.
23. Ghanima W, Nielssen BE, Holmen LO, Witwit A, Al-Ashtari A, Sandset PM. Multidetector computed tomography (MDCT) in the diagnosis of pulmonary embolism: interobserver agreement among radiologists with varied levels of experience. Acta Radiol. 2007;48(2):165–70.
24. Hutchinson BD, Navin P, Marom EM, Truong MT, Bruzzi JF. Overdiagnosis of pulmonary embolism by pulmonary CT angiography. Am J Roentgenol. 2015;205(2):271–7.
25. Palacio D, Benveniste MF, Betancourt-Cuellar SL, Gladish GW. Multidetector computed tomography pulmonary angiography pitfalls in the evaluation of pulmonary embolism with emphasis in technique. Semin Roentgenol. 2015;50(3):217–25.
26. Chawla A, Bosco J, Lim TC, Gaikwad V, Chung R. Systemic-pulmonary artery shunt: a rare cause of false-positive filling defect in the pulmonary arteries. J Med Imaging Radiat Oncol. 2017;61(1):82–4.
27. Sodhi KS, Saxena AK, Chandrashekhar G, Bhatia A, Singhi S, Agarwal R, Khandelwal N. Vascular air embolism after contrast administration on 64 row multiple detector computed tomography: a prospective analysis. Lung India. 2015;32(3):216.
28. Gurd AR, Wilson RI. The fat embolism syndrome. Bone Joint J. 1974;56(3):408–16.
29. Malagari K, Economopoulos N, Stoupis C, Daniil Z, Papiris S, Muller NL, Kelekis D. High-resolution CT findings in mild pulmonary fat embolism. Chest J. 2003;123(4):1196–201.
30. Arakawa H, Kurihara Y, Nakajima Y. Pulmonary fat embolism syndrome: CT findings in six patients. J Comput Assist Tomogr. 2000;24(1):24–9.
31. Hwang SS, Kim HH, Park SH, Kim SE, Im Jung J, Ahn BY, Kim SH, Chung SK, Park YH, Choi KH. N-butyl-2-cyanoacrylate pulmonary embolism after endoscopic injection sclerotherapy for gastric variceal bleeding. J Comput Assist Tomogr. 2001;25(1):16–22.
32. Barbero S, Casorzo I, Durando M, Mattone G, Tappero C, Venturi C, Gandini G. Percutaneous vertebroplasty: the follow-up. Radiol Med. 2008;113(1):101–13.
33. Calvert AD, Dyer AW, Montgomery VA. Embolization of prostatic brachytherapy seeds to pulmonary arteries: a case study. Radiol Case Rep. 2017;12(1):34–8.
34. Shepard JA, Moore EH, Templeton PA, McLoud TC. Pulmonary intravascular tumor emboli: dilated and beaded peripheral pulmonary arteries at CT. Radiology. 1993;187(3):797–801.
35. Galiè N, Humbert M, Vachiery JL, Gibbs S, Lang I, Torbicki A, Simonneau G, Peacock A, Noordegraaf AV, Beghetti M, Ghofrani A. 2015 ESC/ERS guidelines for the diagnosis and treatment of pulmonary hypertension: the joint task force for the diagnosis and treatment of pulmonary hypertension of the European Society of Cardiology (ESC) and the European Respiratory Society (ERS): Endorsed by: Association for European Paediatric and Congenital Cardiology (AEPC), International Society for Heart and Lung Transplantation (ISHLT). Eur Heart J. 2016;37(1):67–119.

36. Tan RT, Kuzo R, Goodman LR, Siegel R, Haasler GR, Presberg KW. Utility of CT scan evaluation for predicting pulmonary hypertension in patients with parenchymal lung disease. Chest. 1998;113(5):1250–6.
37. Rajaram S, Swift AJ, Condliffe R, Johns C, Elliot CA, Hill C, Davies C, Hurdman J, Sabroe I, Wild JM, Kiely DG. CT features of pulmonary arterial hypertension and its major subtypes: a systematic CT evaluation of 292 patients from the ASPIRE registry. Thorax. 2015;70(4):382–7.
38. Gossage JR, Kanj G. Pulmonary arteriovenous malformations: a state of the art review. Am J Respir Crit Care Med. 1998;158(2):643–61.

Imaging of the Aorta

10

Raymond Chung

10.1 Introduction

Acute aortic pathologies often present with similar clinical symptoms, and thereby instigation of the appropriate management algorithm is heavily reliant on radiological findings. With the advent of multidetector CT (MDCT), rapid, replicable, noninvasive diagnostic imaging can be acquired. MRI and echocardiography can provide additional functional data without ionizing radiation but are hampered by their speed, availability, and operator dependence. In this chapter, imaging acquisition, potential pitfalls, and aortic imaging in the form of radiography and MDCT are discussed.

10.2 CXR in Aortic Diseases

A normal left aortic arch has a smooth contour with mild indentation on the left lateral wall of the lower trachea. An "aortic nipple" refers to a small projection or a pseudotumor adjacent to the projection of the transverse portion of the aortic arch due to a left superior intercostal vein (Fig. 10.1). The left superior intercostal vein drains second to fourth left posterior intercostal veins into the left brachiocephalic vein. The aortic nipple is visualized in 1.4% of normal erect posterior-anterior radiographs and can measure up to 4.5 mm in normal patients. An enlarged aortic nipple results from obstruction of the superior or inferior vena cava or rarely due to adjacent lymphadenopathy.

10.2.1 Thoracic Aortic Aneurysm and Dissection

The vast majority of aortic pathology requires cross-sectional imaging for definitive diagnosis, but chest radiographs are often the preliminary radiological investigation. While radiographic features between the dominant diagnoses of thoracic aortic aneurysm and dissection may overlap, chest radiographs offer a screening evaluation for alternative common differential diagnoses and a preliminary assessment of the aortic dimensions. Overall, chest radiography has a low sensitivity and specificity for acute aortic disease (overt dissection) at 64% and 86%, respectively, especially when pathology is isolated to the ascending aorta [1]. Furthermore, a normal radiograph does not exclude an aortic dissection. In assessing the aorta, preceding radiographs will often provide invaluable evidence of interim change and better highlight the radiographic signs of acute aortic pathology (Table 10.1) [2] (Figs. 10.2 and 10.3).

10.2.2 Intra-aortic Balloon Pump Catheter

There is a plethora of supportive medical devices regularly imaged and assessed on plain chest radiography. Of those relevant to aortic imaging, the most commonly encountered device in clinical practice is the intra-aortic balloon counterpulsation device, often referred to as an intra-aortic balloon pump (IABP). This is a temporary cardiac assist device used most commonly after acute myocardial infarction, cardiogenic shock, or following recent cardiac surgery.

IABP is inserted via the femoral artery and consists of an inflatable balloon mounted on a catheter. The optimal position is within the descending thoracic aorta, just distal to the left subclavian artery. The balloon is inflated with gas (carbon dioxide) during ventricular diastole to augment coronary artery perfusion and reduce left ventricular afterload. This aids cardiac function by increasing myocardial oxygen supply while decreasing the work requirement and thereby oxy-

R. Chung (✉)
Department of Diagnostic Radiology, Khoo Teck Puat Hospital, Singapore, Singapore
e-mail: rchung@doctors.org.uk

A. Chawla (ed.), *Thoracic Imaging*, https://doi.org/10.1007/978-981-13-2544-1_10

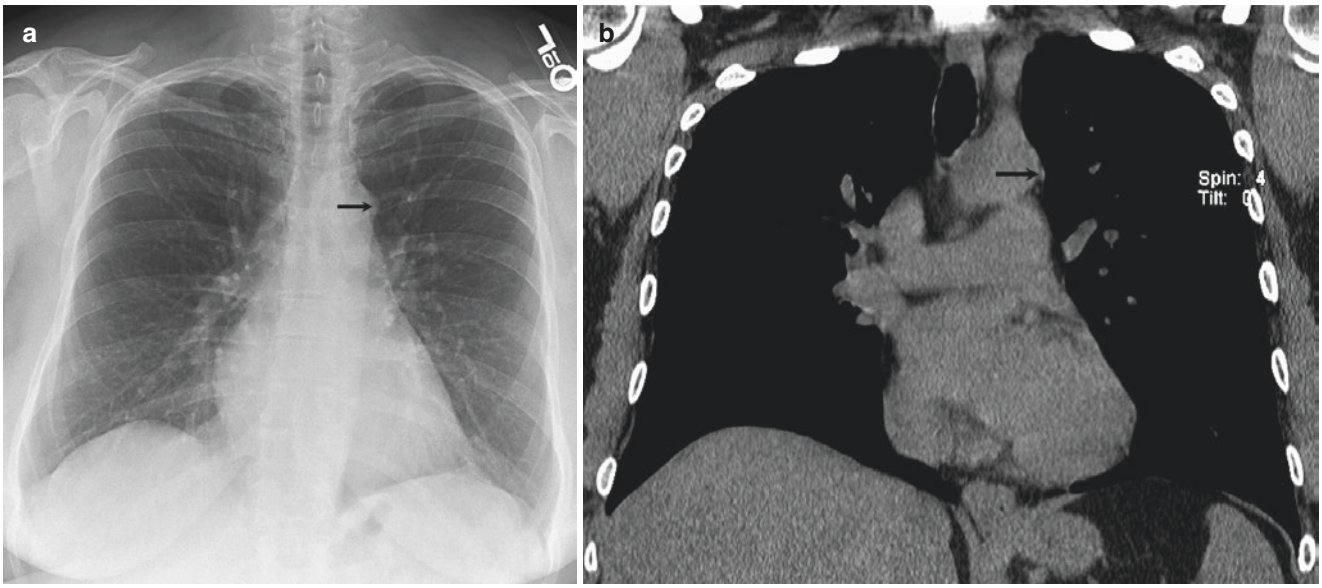

Fig. 10.1 Aortic nipple. (**a**) Frontal chest radiograph shows a nipple-like projection (arrow) from aortic knob. (**b**) Coronal unenhanced CT reconstruction shows a superior intercostal vein (arrow) accounting for the "aortic nipple"

Table 10.1 Radiographic signs of thoracic aortic pathology

Direct radiographic signs	
Calcium sign	(New) intimal calcification displacement, by the false lumen in aortic dissection or an intramural hematoma, from the outer margin of the aortic knuckle by >6 mm • Characteristically delineated at the junction of the aortic arch and descending aorta • False positive: those with excess mediastinal fat can create a false contour of the outer aortic wall
Widened/altered mediastinal contour	Mediastinal diameter of >8 cm at the level of the aortic knob on an anterior-posterior radiograph Ratio of mediastinum to chest width >0.25 • This may reflect aortic dilatation from either dissection or aneurysmal formation and is of limited specificity • Continuous or localized aortic changes may reflect fusiform or saccular aneurysmal morphology, respectively
Mediastinal mass	Enlargement of the ascending aorta, an anterior mediastinal structure, may alter the silhouette of the right cardiac contour, while aneurysmal enlargement of the descending thoracic aorta, a posterior mediastinal structure, will efface the outlines of posterior structures and preserve the left cardiac contour
Indirect radiographic signs	
Double density of the aortic knob	This reflects the distortion of the aortic contour from the aneurysmal change and secondary adjacent compressive lung atelectatic change
Pleural cap/pleural effusion	A non-specific finding of an apical opacity on a supine radiograph due to an underlying hemothorax as a complication of the acute aortic injury
Tracheal shift	A non-specific finding of mass effect from aortic enlargement

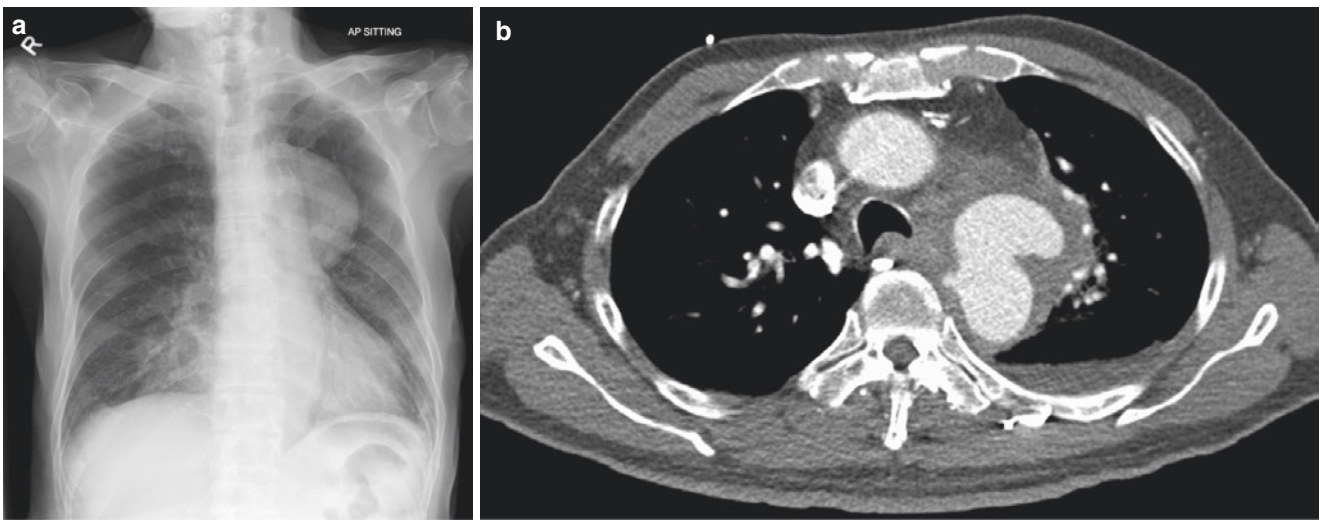

Fig. 10.2 76-year-old man with a thoracic aortic aneurysm. (**a**) Chest radiograph illustrating widened mediastinum. (**b**) Axial contrast-enhanced CT reveals an aortic arch aneurysm accounting for the widened mediastinum on chest radiograph

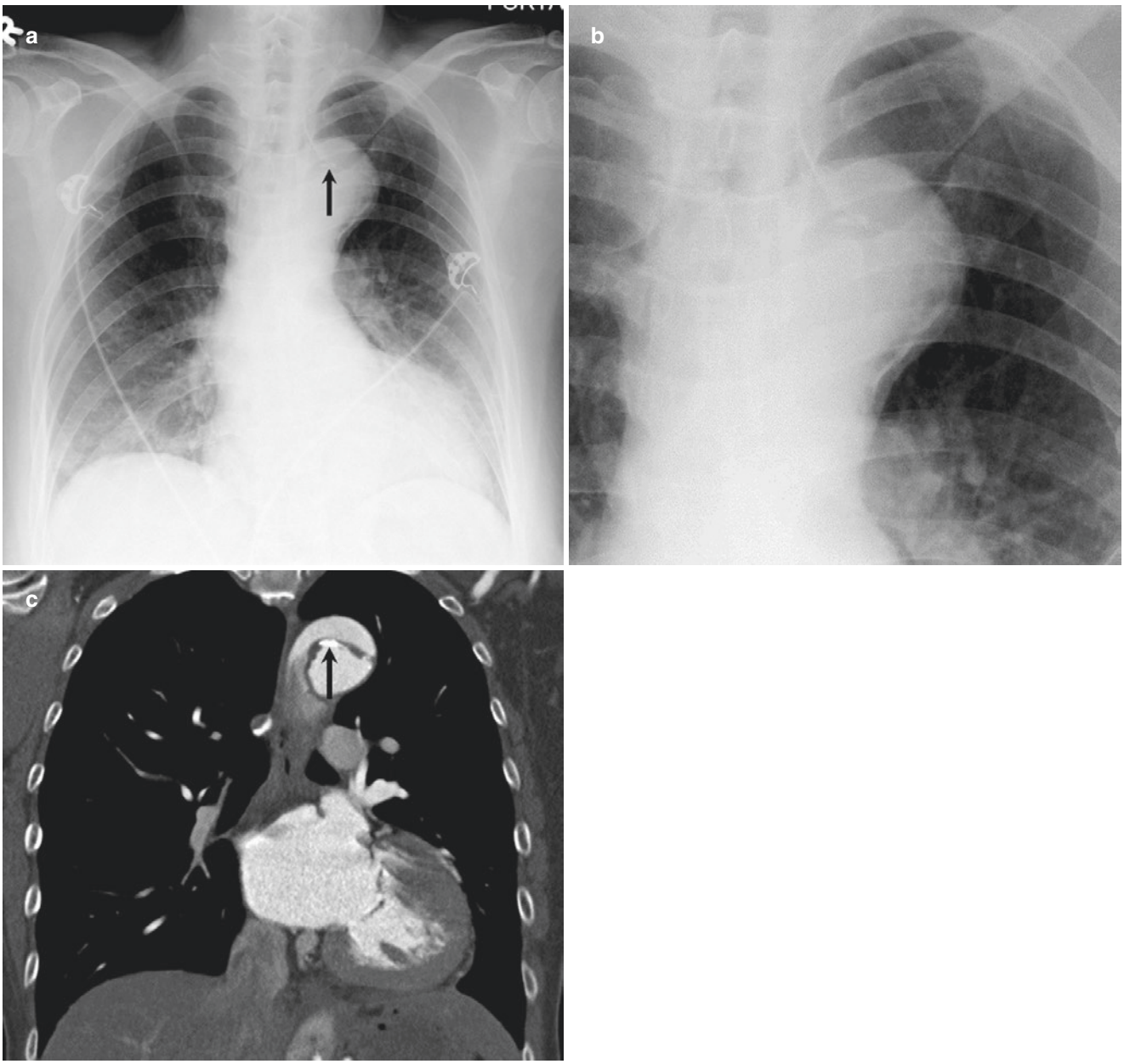

Fig. 10.3 78-year-old man with aortic dissection. (**a**) Frontal radiograph shows displacement of intimal calcification inferiorly (arrow). (**b**) Magnified view shows that the intimal calcification in the roof of aortic arch is displaced inferiorly, while the calcification in the lateral wall is not displaced. (**c**) Coronal CT shows intimal dissection flap with calcification (arrow)

gen demands of the myocardium [3]. Only the IABP tip is normally visible as a small rectangular radiodensity on chest radiography (Fig. 10.4). The balloon portion appears as a tubular radiolucency overlying the aorta if imaged during inflation.

10.2.3 Prosthetic Aortic Valve on CXR

There is a wide array of prosthetic mechanical and biological heart valves. Due to the diverse indications for use in both acquired and congenital conditions, identification of the replaced anatomical native valve can be difficult due to distortion of the cardiac shadow from pathological chamber enlargement. However, the distinction in clinical practice is more important and relevant between the mitral and aortic valves (Table 10.2) given their frequency of replacement compared to the tricuspid and rarely replaced pulmonary valves [4, 5].

While chest radiography is of limited value in the assessment of prosthetic cardiac valves, CT is playing an ever-increasing role with the advent of transcatheter aortic replacement techniques: both in the pre-procedural planning stages and in continuous assessment.

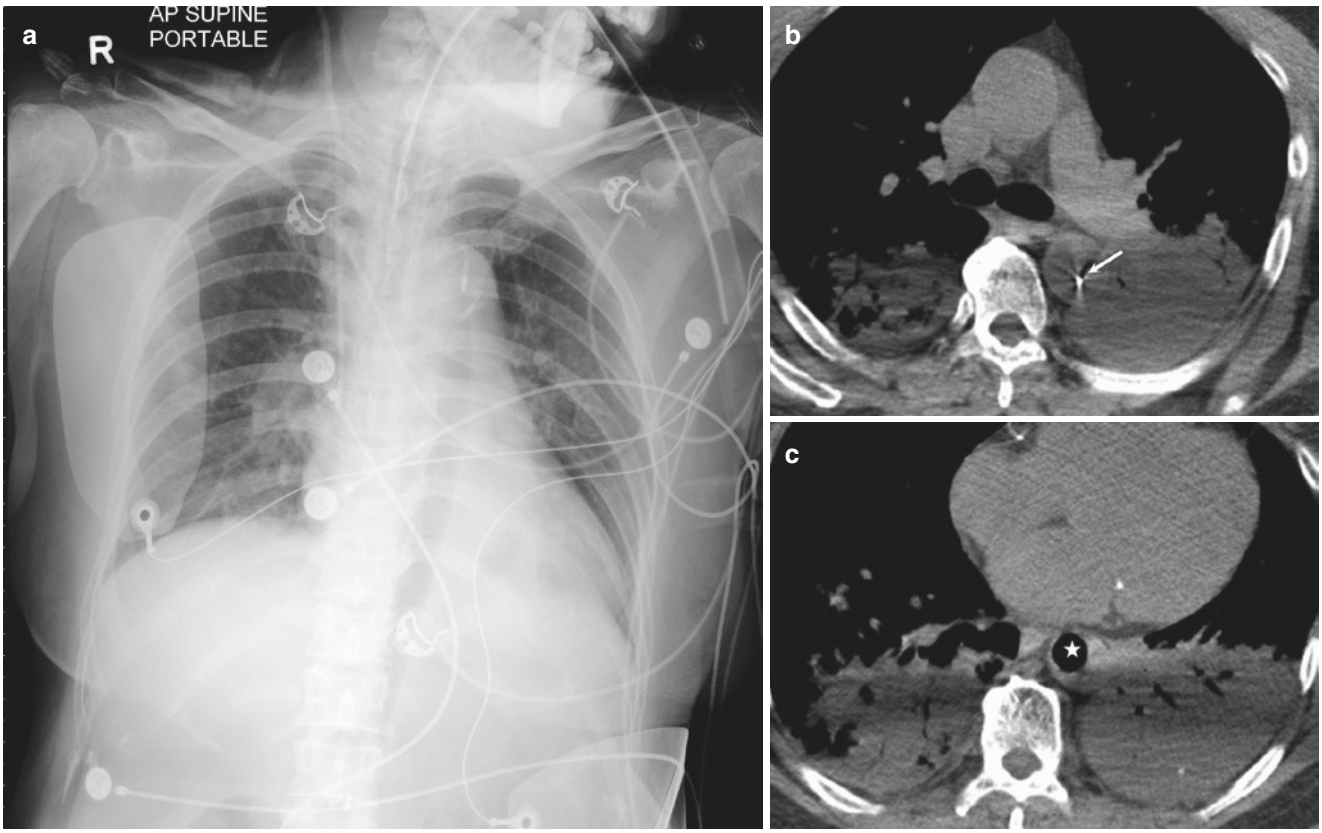

Fig. 10.4 (**a**) Chest radiograph with inflated intra-aortic balloon pump catheter visualised as a tubular lucency along the course of the descending thoracic aorta. (**b**, **c**) Axial unenhanced CT images show the tip of catheter (arrow) and inflated catheter (asterisk) in descending aorta

Table 10.2 Radiographic facilitation of prosthetic valvular identification

	Technique	Aortic	Mitral
Frontal chest radiograph—imaginary line (Fig. 10.5)	Line from the inferior margin of the left hilum to the right cardiophrenic recess	Lies above the line	Lies below the line
Valve orientation and blood flow direction (Fig. 10.6)		Orientated more horizontally, with side profile visible on a frontal chest radiograph with caudocranial flow toward the aortic outflow	Orientated more vertically with its orifice seen en face with the craniocaudal flow in the left chest, toward the cardiac apex

10.3 CT in Aortic Imaging

10.3.1 Imaging Technique

Echocardiography has historically been used as the main form of aortic root imaging. CT angiography, however, provides rapid acquisition of isotropic three-dimensional information allowing for multiplanar reformation, curved planar reformation, maximum intensity projection, and volume rendering of the whole thoracic aorta—affording a better understanding of complex aortic pathologies.

With greater relevance to the proximal thoracic aorta, image acquisition in non-cardiac gated CT scan techniques, especially during cardiac systole, results in considerable movement artifact propagated into the proximal thoracic aorta leading to potential misdiagnoses of aortic dissection (Fig. 10.7). ECG dictated cardiac gating allows relatively motionless imaging acquisition, reducing the chances of misdiagnoses and more precise measurements. Generally, techniques are divided into a retrospective and prospective gating. Retrospective gating involves image acquisition throughout the entire cardiac cycle, with image reconstruction subsequently from the best phase and least motion. Prospective gating involves image acquisition during a set

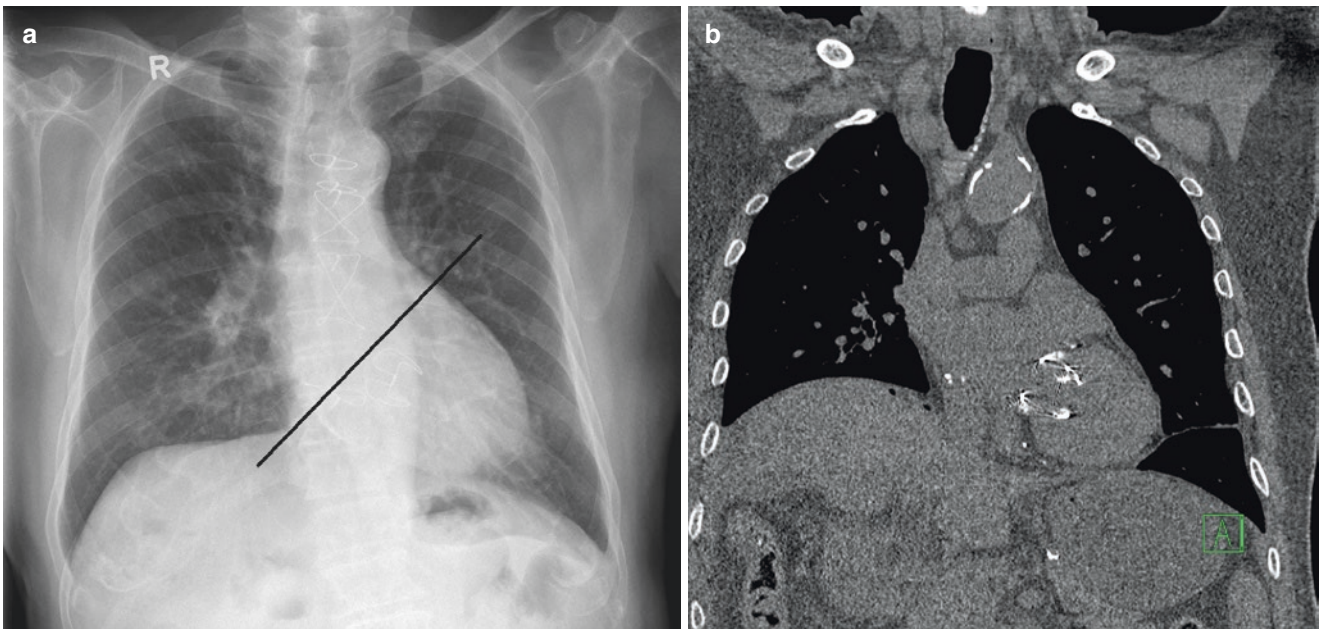

Fig. 10.5 (**a**) Chest radiograph with line aiding differentiation of an aortic and, in this case, a mitral valve. (**b**) Coronal unenhanced CT of a prosthetic mitral valve

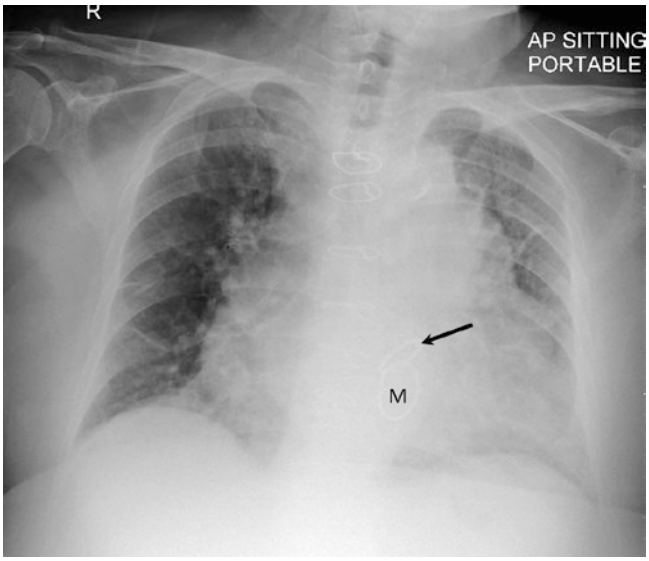

Fig. 10.6 Chest radiograph illustrating differences between aortic (arrow) and mitral valve replacement orientation. *M* mitral valve prosthesis

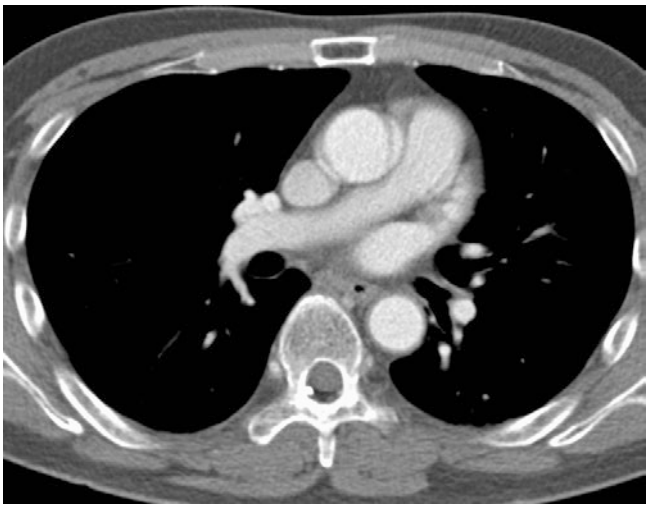

Fig. 10.7 Axial contrast-enhanced, non-cardiac gated CT with pitfall of aortic dissection appearance

phase of the cardiac cycle timed after a predetermined interval from the R wave, usually during diastole when the aortic root is relatively still. While there are varying protocols for imaging acquisition across institutes and product platforms, the protocol at our institute consists of triphasic CT angiography: (1) non-cardiac gated, unenhanced, (2) (gated, if concern for aortic root/ascending aortic pathology) arterial, and (3) non-gated portal venous phase (75-s delay to assess for malperfusion syndrome) imaging.

10.3.2 Anatomy of Aortic Root

The thoracic aorta can be subdivided into its root, ascending aorta, arch, and descending thoracic aortic segments. The aortic root is composed of the aortic valve annulus, sinuses of Valsalva, and the sinotubular junction (Fig. 10.8).

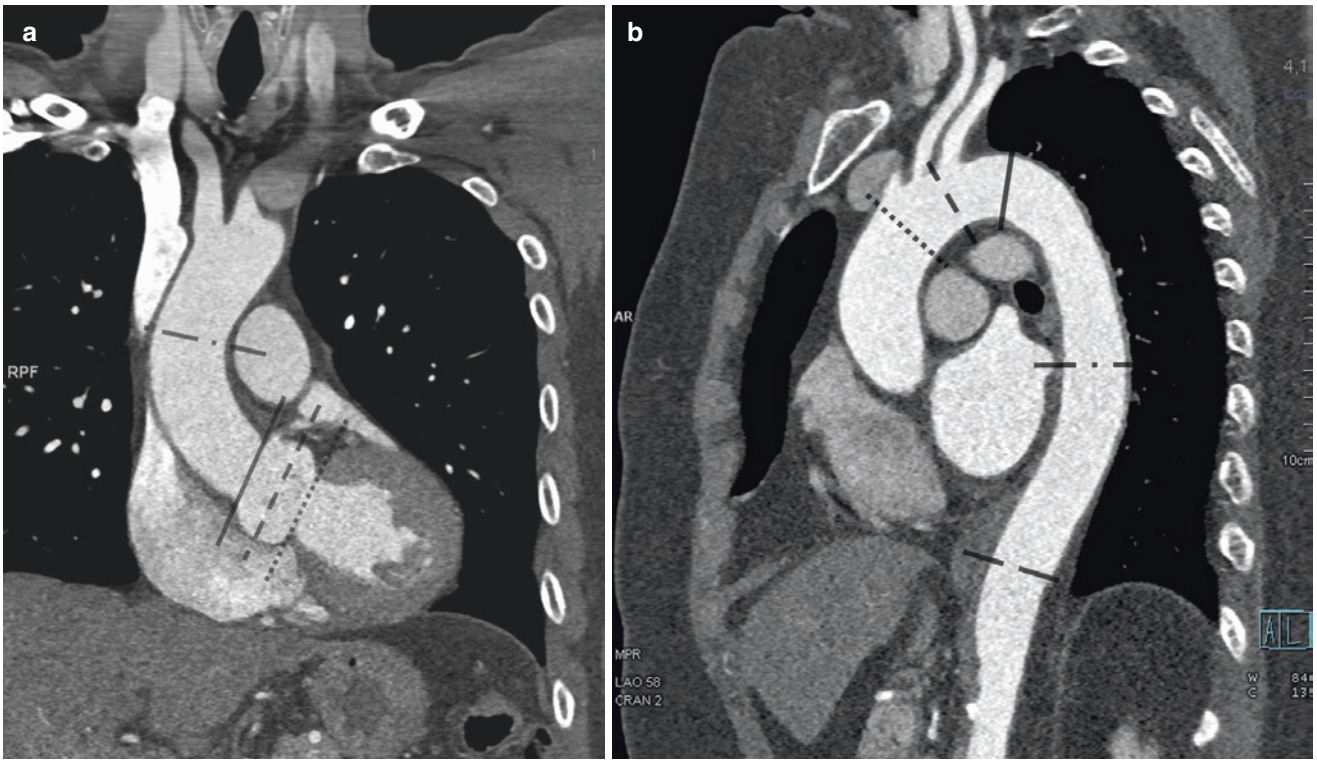

Fig. 10.8 Contrast CT illustrating (**a**) aortic valve annulus (……), sinuses of Valsalva (– – – –), sinotubular junction (———) and mid ascending aorta (— • —); (**b**) high ascending aorta (……), mid-aortic arch (– – – –), proximal (———), mid (— • —) and distal (— — -) descending aorta

The aortic valve is usually tricuspid, with its three leaflets attached to the annulus at the junction of the left ventricle and aorta. The sinuses of Valsalva, alternatively known as aortic sinuses, lie immediately beyond the aortic valve. As with the standard aortic trivalvular cusp configuration, there are three sinuses namely, right, left, and noncoronary, conventionally corresponding to the origins of the coronary arteries. The aortic sinuses bulge outward before narrowing at the sinotubular junction, demarcating its junction with the ascending aorta.

10.3.3 Anatomy of Thoracic Aorta: Variations

The proximal thoracic aorta continues cranially from the sinotubular junction as the ascending aorta and becomes the aortic arch at the origin of the brachiocephalic (innominate) artery. The level of the ligamentum arteriosum subsequently delineates the transition to the descending thoracic aortic segment until it passes the diaphragmatic hiatus.

The classical aortic arch, crossing the left main bronchus at the level of the fifth thoracic body, with a left descending thoracic aorta is present in approximately 70% of the population [6], with the most common three supra-aortic vessel configuration comprising of the brachiocephalic, left common carotid, and left subclavian arteries (Fig. 10.8).

Variations from this standard configuration include differences in its supra-aortic branching pattern and its side of aortic arch: left, right, or double. The side the aortic arch is named is according to which bronchus it crosses.

The commonest branching variant accounting for more than two-thirds of arch vessel variations is the common brachiocephalic trunk, historically termed "bovine" arch, in which the brachiocephalic trunk and left common carotid artery share a common stem. Its inaccuracies in reflecting the true bovine configuration is one of the reasons the term is not encouraged [7].

Another common variation with a prevalence of 6% is a left vertebral artery arising directly from the aortic arch between the left common and left subclavian arteries [7]. Other vertebral arterial variations including duplication or a single left vertebral artery arising after the left subclavian artery are less common [8]. While these variations may have implications for those looking to perform invasive procedures, these are otherwise asymptomatic variations with no isolated clinical sequelae.

Table 10.3 "Normal" values of aortic diameter[a]

Level	Mean diameter ± standard deviation	General maximum normal diameters	Aneurysmal	Cutoff for treatment
Aortic root	29.8 ± 4.6 mm	<30 mm	>40 mm	≥55 mm with no aortopathy or biscuspid aortic valve ≥50 mm with bicuspid aortic valve/risk factors ≥45 mm with Marfan syndrome/risk factors
Ascending aorta	33.2 ± 4.1 mm	<40 mm	>50 mm	
Aortic arch	25.4 ± 3.5 mm	<30 mm	>40 mm	≥55 mm if isolated
Descending thoracic aorta	24.6 ± 3.0 mm	<30 mm	>40 mm	≥55 mm if suitable for TEVAR ≥60 mm if necessitates open

[a]Demographic characteristics such as age, sex, body surface area ought to be considered

10.3.4 Aortic Measurements

Accurate and consistent aortic measurements are pivotal in the management pathway of aortic disease, directing both timing and potential therapeutic options, i.e. endovascular repair (Table 10.3) [9–12]. Multiplanar reformats (MPR) with image manipulation allow appreciation of vascular dimensions according to the true short axis acquired in double oblique views [9]—in a plane directly perpendicular to the direction of blood flow (Fig. 10.9). Measurements obtained in less than a direct orthogonal plane to the aortic lumen may overestimate the true aortic diameter. MPR also allows easier identification of anatomic landmarks and thereby more standardized levels of aortic measurement. At our institute, authors typically report two perpendicular outer luminal diameters in cross-section orthogonal to the center line of the aorta at levels of the aortic annulus, sinuses of Valsalva, sinotubular junction, mid-/high ascending aorta, mid-aortic arch (just after the left common carotid artery), and proximal (2 cm from the left subclavian artery origin)/mid-/distal descending aorta (Fig. 10.8). Additional values will be given at sites of involved aortic disease with special reference to maximal aortic diameter, length of the involved segment, the volume of thrombus/calcification, the degree of stenosis if any, and presence of intervening normal aortic segments with the supra-aortic vessels.

10.4 Aortic Conditions

10.4.1 Coarctation

Coarctation is a relatively common anomaly with a prevalence of up to 8% of congenital heart defects, in which there is a discrete constricted aortic segment, most commonly in a juxtaductal location. Age of presentation varies depending upon the degree of obstruction, with hemodynamic effects evident by the hypertrophied collateral vessel formation in the intercostal and internal mammary vascular territories [8]. Chest radiography findings include a prominent aortic arch, scalloping/notching of the inferior margins of the ribs due to hypertrophied collateral intercostal arteries and pulmonary venous congestion.

Pseudocoarctation is a rare anomaly in which there is kinking of the descending aorta at the level of the ligamentum arteriosum with higher than usual location of the aortic arch in the mediastinum (Fig. 10.10). As there is no hemodynamically significant gradient across this lesion, no collaterals are formed and therefore are usually a clinically silent finding. However, those with the aneurysmal formation, presumed due to the turbulent flow immediately after the kinked segment, are candidates for early treatment due to the risk of rupture or dissection [13].

10.4.2 Annuloaortic Ectasia

Annuloaortic ectasia describes symmetrical dilatation of the aortic root and the ascending aorta with effacement of the sinotubular junction secondary to cystic medial necrosis, while the aortic arch remains normal in caliber (Fig. 10.11) [14]. It is associated with Marfan syndrome, Ehlers-Danlos syndrome, homocystinuria or may be idiopathic.

10.4.3 Acute Aortic Syndrome

Acute aortic syndrome encompasses a spectrum of life-threatening acute aortic conditions including aortic dissection (AD), penetrating atherosclerotic ulcer (PAU), and aortic intramural hematoma (AIH). These conditions are considered as a continuum often with similar symptomatology. CT is the most commonly used technique for investigation given its availability and rapid acquisition (Table 10.4).

10.4.3.1 Penetrating Atherosclerotic Ulcer

Penetrating atherosclerotic ulcer most commonly presents in the elderly affecting the mid-/lower descending aorta or

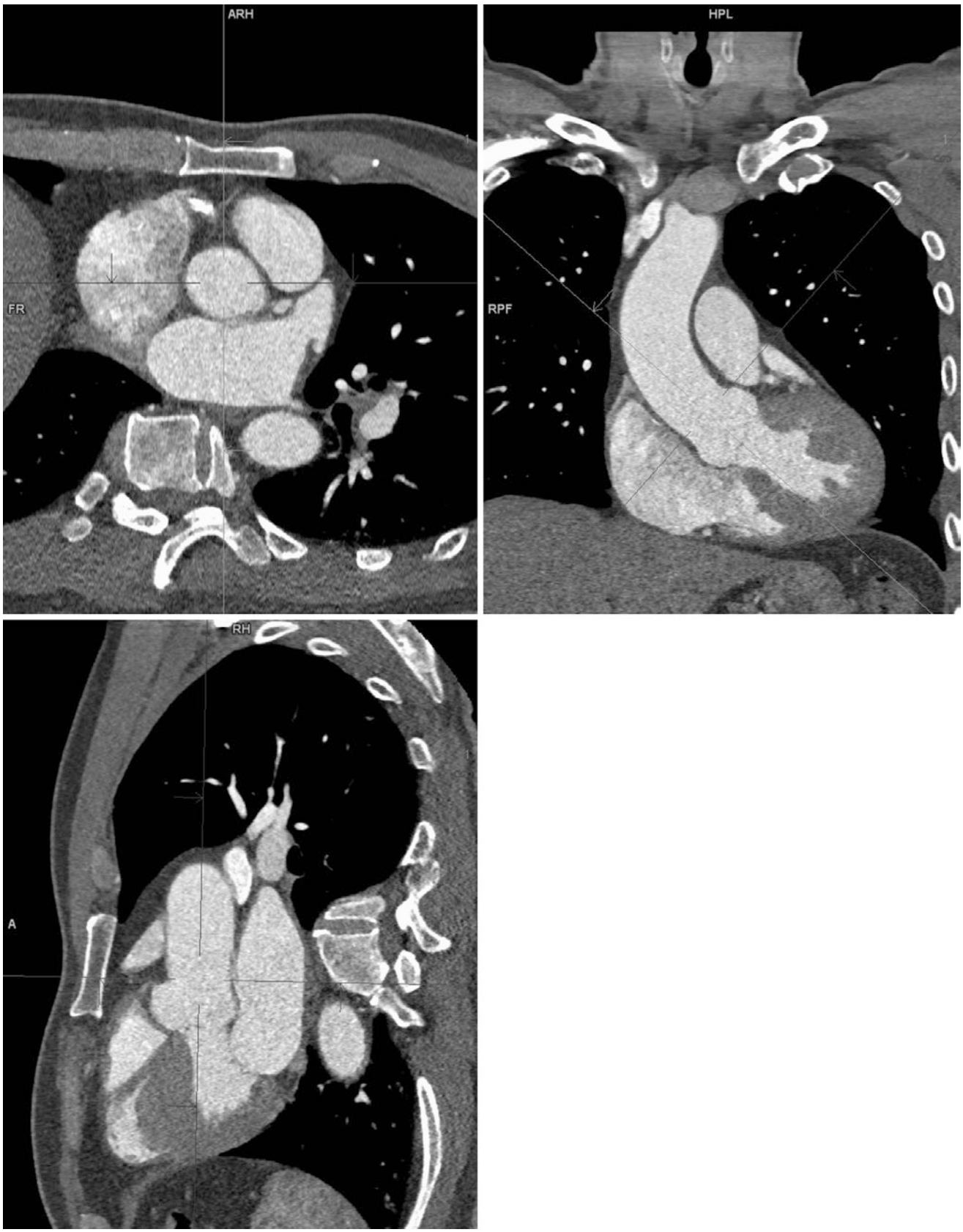

Fig. 10.9 Multiplanar reformats to allow double oblique view for accurate aortic measurements

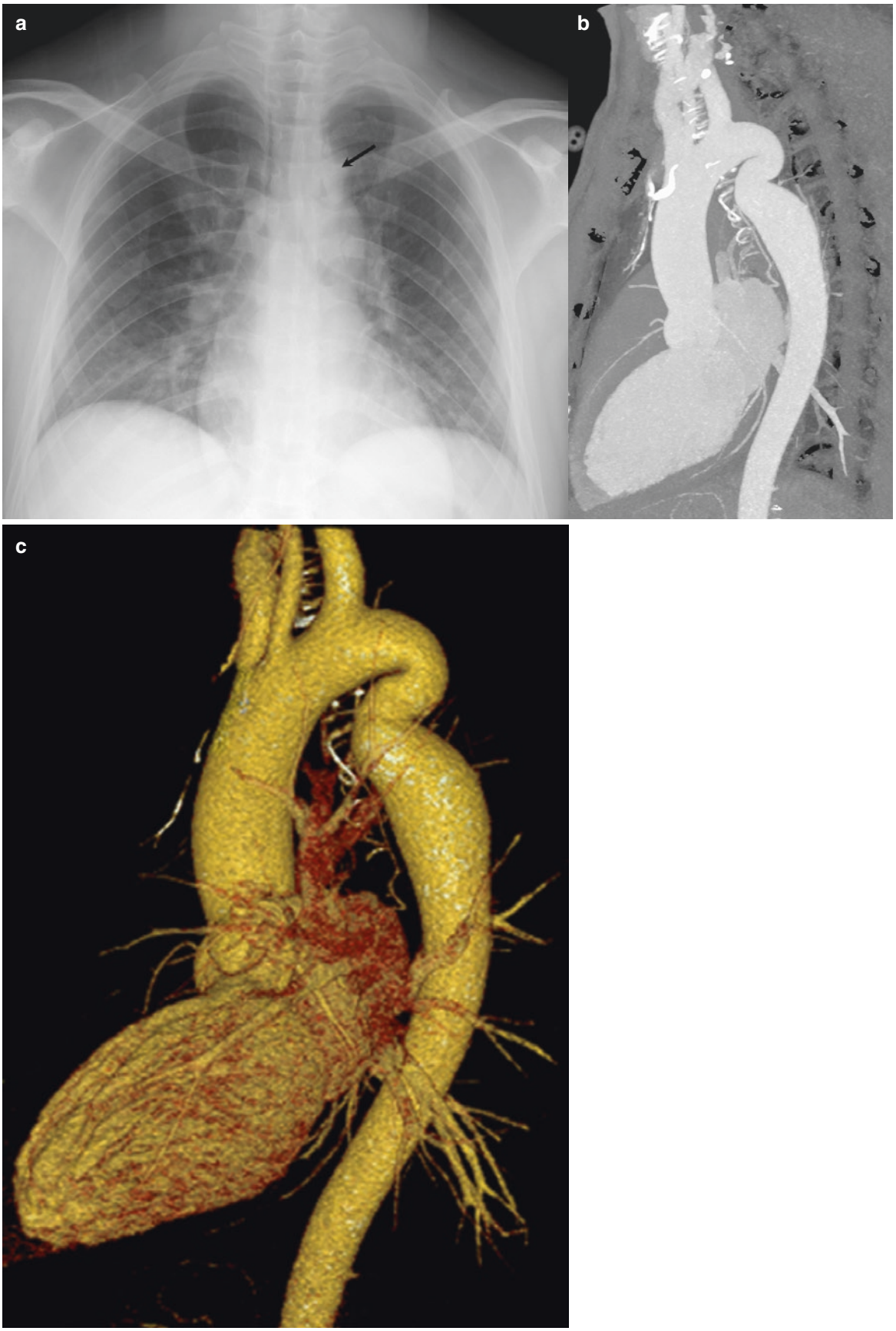

Fig. 10.10 Pseudocoarctation. (**a**) Anterior-posterior chest radiograph demonstrates left superior mediastinal widening (arrow) indenting the trachea without any rib notching. (**b**, **c**) CT MIP and volumetric reconstruction of pseudocoarctation

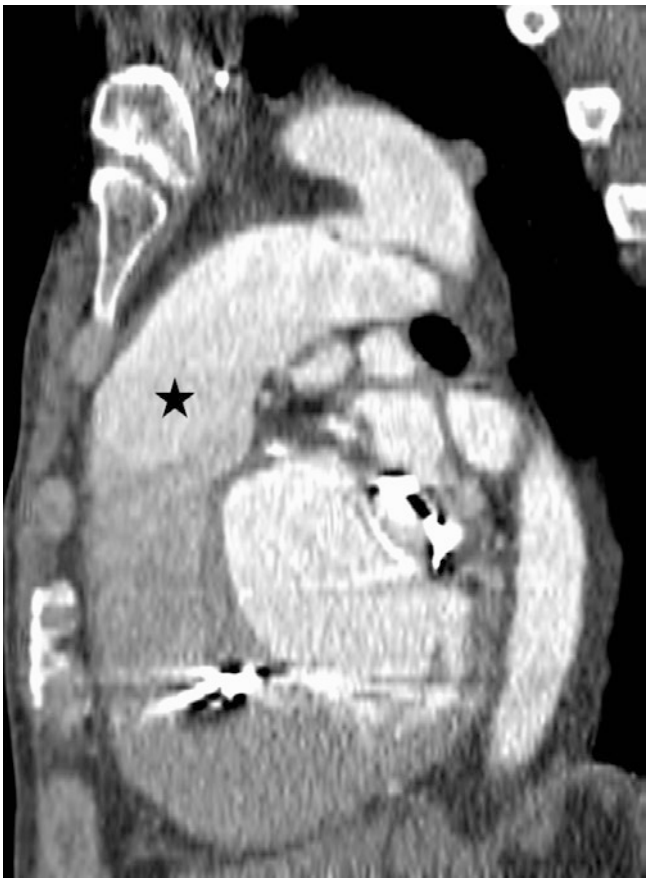

Fig. 10.11 Annuloaortic ectasia (asterisk) (diffuse dilatation of aortic root) in a patient with Marfan syndrome

Table 10.4 Signs on CT indicative of aortic pathology

• Irregular luminal outline
• Thrombus
• Intimal flap
• Intramural hematoma
• Perivascular stranding
• Aortic contour deformity
• Pseudoaneurysm: unlike a true aneurysm when all three layers of the aortic wall (intima, media, and adventitia) are involved, pseudoaneurysms more commonly involve the intima and media with the adventitial layer solely responsible for containment. These are usually saccular in appearance and commonly due to infection and trauma
• Aortic transection
• Indirect signs include hemomediastinum and hemothorax

arch. It is characterized by ulceration of the aorta secondary to an atherosclerotic plaque disrupting the internal elastic lamina [15].

Evaluation is best performed on postcontrast images demonstrating focal contrast enhancement beyond the aortic lumen with communicating flow (Fig. 10.12). These may occur singularly or as multiple lesions. The aortic wall is commonly thickened with overhanging edges and may enhance post contrast. On unenhanced images, there are extensive background atherosclerosis and potential central intimal displacement [16].

There is currently no clear size cutoff at which the PAU diameter (depth) or neck requires treatment. However, an ulcer diameter >2 cm or neck >1 cm has been associated with a more aggressive natural history and requires earlier intervention [17]. Complications of this entity include aneurysmal degradation, thrombus with distal embolization, dissection, and rupture.

10.4.3.2 Aortic Intramural Hematoma

While AIH and AD share similar clinical features, their pathophysiological process is initially distinct. AIH is secondary to rupture of the vasa vasorum with hemorrhage into the aortic media, without an intimal tear. Those that progress with intimal rupture and formation of the so-called entry tear are then considered AD.

Unenhanced images are pivotal in establishing the presence of a circular- or crescent-shaped, non-spiral, hyperattenuating (60 ± 15 HU) wall thickening of ≥5 mm [18] (Fig. 10.13). Normal aortic wall thickness is <3 mm. There may be central displacement of intimal calcification and a degree of vascular luminal narrowing, but the luminal-wall interface remains smooth. Postcontrast images alone are prone to false-negative interpretation due to masking from adjacent vascular luminal high-attenuation contrast. Otherwise, the hematoma remains similar in appearance on contrast CT, with no propagation of density beyond the hematoma. Other than the lack of an intimal flap and intimal tear, an AIH can be differentiated from an AD by its relative constant circumferential relationship with the wall rather than the spiral configuration commonly seen in AD [19].

In identifying high-risk features of AIH (Table 10.5), two separate entities need to be distinguished, intramural blood pool and ulcer-like projection [20, 21]. Intramural blood pool is focal contrast pooling within the hematoma communicating with and seen at the base of an aortic side branch such as an intercostal artery—this is a benign feature. An ulcer-like projection is an intimal disruption with a >3 mm communicating neck with the AIH which is associated with a poorer prognosis [20] (Fig. 10.14).

10.4.3.3 Thoracic Aortic Dissection

Acute aortic dissection accounts for up to 95% of acute aortic syndromes [22], and most occur spontaneously secondary to systemic hypertension. Symptomatically, the AD is classified as acute if symptoms/signs are within 2 weeks or chronic if beyond that.

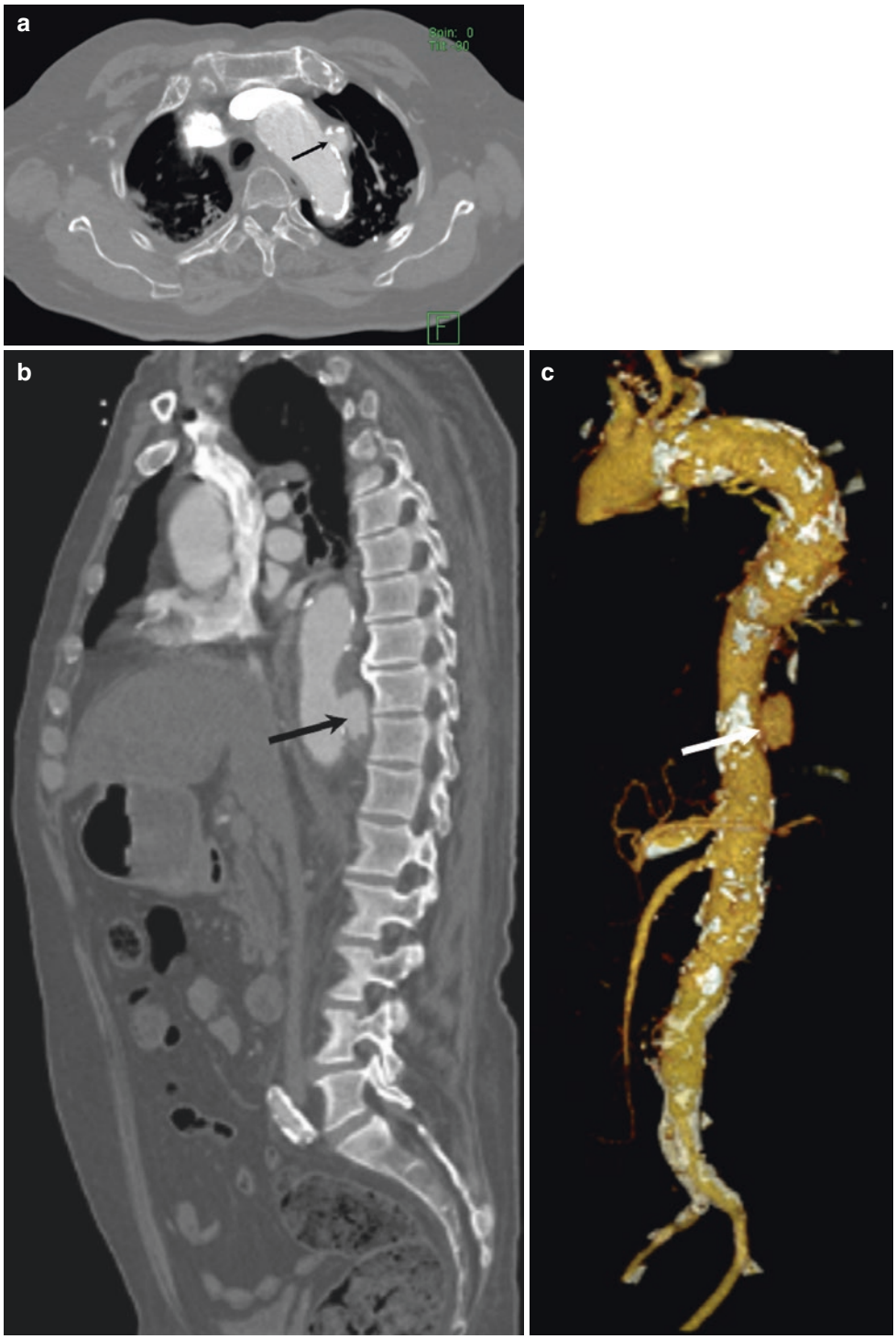

Fig. 10.12 Penetrating aortic ulcers. (**a**) Axial contrast-enhanced CT illustrating a penetrating aortic ulcer of the arch (arrow). (**b**) Sagittal contrast-enhanced CT and (**c**) volumetric reformats demonstrating a penetrating aortic ulcer in descending thoracic aorta

The two recognized classifications are Stanford [23] and DeBakey systems [24] (Table 10.6), the former preferred due to its relevant dictation of management. Application of this classification to AIH and PAU is also widely adopted.

CT has been shown to reach sensitivities and specificities of up to 100%, while MRI is slightly lower at 95–100% and 94–98%, respectively [22]. Unenhanced image acquisition facilitates identification of displaced intimal calcification, which needs to be distinguished from calcified mural thrombus. Postcontrast images depict the presence of an entry intimal tear which is the pathognomonic imaging characteristic of acute aortic dissection, with the formation of a false lumen

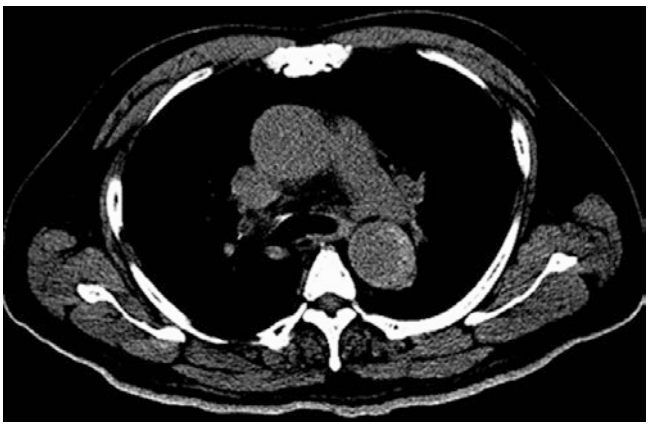

Fig. 10.13 Unenhanced CT with hyperdense appearing acute intramural hematoma

in the tunica media (Fig. 10.15). Differentiation between the two lumens is critical in management (Table 10.7) [25, 26]. Certain signs on CT aortogram are helpful in this regard (Figs. 10.16 and 10.17).

Aortic dissection with a thrombosed false lumen may be difficult to differentiate from an aortic aneurysm with non-circumferential mural thrombus. Imaging features such as a

Table 10.5 Radiological markers of a higher probability of progression/poorer prognosis

• Localized within ascending aortic segment
• Aortic dimension >5 cm
• Aortic wall thickness >1.1 cm
• Increasing aortic dimension
• Ulcer-like projection

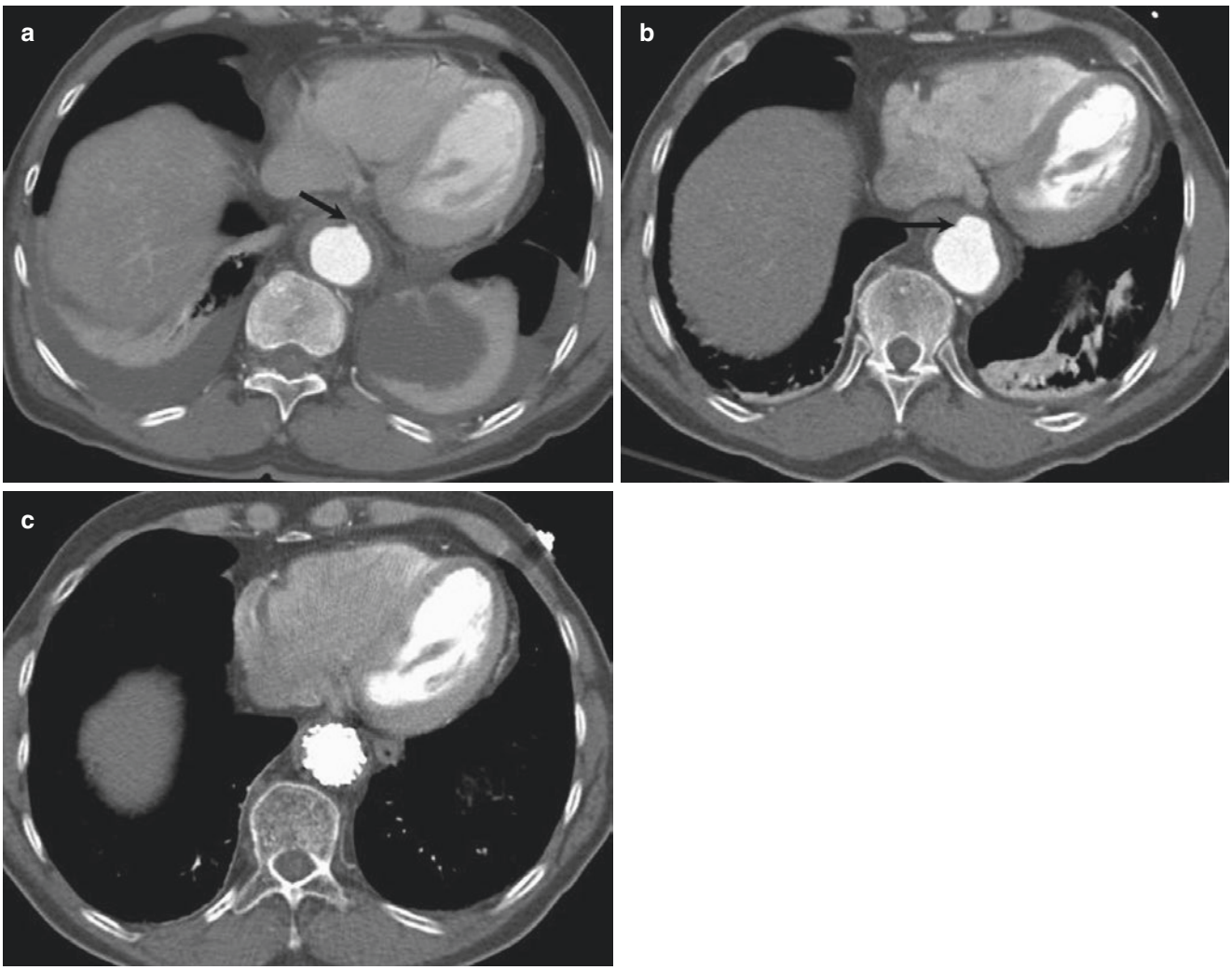

Fig. 10.14 Complication of intramural hematoma. (**a**) Axial image of initial CT aortogram shows a near circumferential intramural hematoma with focal penetrating "ulcer-like" projection anteriorly (arrow). (**b**) Follow-up CT aortogram after 3 days of medical management due to persistent backache shows an enlarging ulcer (arrow). (**c**) Post endograft CT aortogram confirms resolution of the ulcer

Table 10.6 Stanford and DeBakey classification of the AD

		Treatment
Stanford classification		
A	All dissections involving the ascending aorta ± arch	Prompt surgical intervention due to the risk of cardiac involvement
B	Only involve the descending aorta beyond the left subclavian arterial origin	Historically treated medically in uncomplicated cases Growing endovascular treatment option for select patients with uncomplicated type B dissection to improve aortic remodeling with an aim to reduce aortic-related mortality
DeBakey classification		
I	Dissections propagating from the ascending aorta, extending to the aortic arch and distally	
II	Confined to ascending aorta only	
III	Confined to descending aorta only	

spiral configuration, smooth inner margin, and central displacement of intimal calcification [27] are more indicative of AD.

In addition to diagnosis and procedural planning (Table 10.8), cross-sectional imaging is invaluable in the detection of its major complications of rupture, aneurysmal dilatation, and ischemic malperfusion injury. The latter can be attributed to four mechanisms [28]:

1. "Static" extension of the aortic dissection flap into the branch vessel resulting in vascular stenosis—treated by target organ vessel stenting
2. "Dynamic" direct compression of the artery by the expanding false lumen with the intima occluding the vessel origin—treated by penetrating the intimal flap to reduce the false lumen pressure
3. Combined mechanism with the extension of the dissection into the target vessel and subsequent compression of the true lumen by the pressurized false lumen
4. Ostial disconnection by the dissection

10.4.3.4 Thoracic Aortic Aneurysm

An aneurysm is defined as the permanent dilatation of a vascular segment greater than 50% or two standard deviations the expected normal diameter and may either be saccular or fusiform in its configuration. Saccular describes a localized dilatation of one part of the aortic wall vs fusiform in which there is circumferential involvement of the vessel wall (Fig. 10.18). While atherosclerosis remains overall the most common etiology for aneurysm formation, medial degeneration is the most common cause in the ascending aortic segment.

As in AD, CT is ideal in delineating aneurysmal characteristics (Table 10.9). While a single cutoff is not wholly accurate given the variation according to age, gender, and body mass index, the thoracic aortic diameter is considered aneurysmal when >40 mm. Generally, aneurysms are repaired when the aorta >55 mm or if there is documented growth of more than 5 mm in 6 months.

10.4.3.5 High-Risk Features and Rupture

In newly diagnosed patients and/or those exhibiting new/worsening symptoms, cross-sectional imaging is pivotal in identifying high-risk features of impending rupture (Table 10.10) [18, 29–31]. While not limited solely to aneurysmal disease, contained or uncontained rupture may occur in any of the described acute aortic entities into the adjacent compartments.

In uncontained rupture, unenhanced CT will demonstrate periaortic hyperdense hematoma often extending further into the mediastinum, pericardium, and pleural cavities. The site of rupture may be obscured due to the volume of hemorrhage although displaced aortic mural calcification can aid delineation of the site of the vascular breach. Postcontrast images will demonstrate the characteristic contrast-enriched blood extravasating into extraluminal spaces and the irregular aortic vascular wall. In a contained rupture (Fig. 10.19), there may be conformation of the posterior aortic wall to the adjacent vertebral body with indiscernible margins—"draped aorta" sign [29].

Additional fistulation into neighboring organ systems such as aorto-esophageal (Fig. 10.20) and aorto-bronchial fistulas have both been imaged with blood in the respective aerodigestive lumina. Secondary features of air within the aorta can also help the imaging diagnosis, but these complications are often fatal.

10.5 Endoleaks

Thoracic endovascular aortic repair, TEVAR, has revolutionized the management of aortic disorders, in which multiphasic (unenhanced, arterial, and delayed phase) MDCT is the imaging workhorse in the evaluation and follow-up post-TEVAR. Accurate sizing of endografts is critical for endovascular treatment and one of the dominant factors in avoiding complication. As aortic diameters may vary depending on cardiac phase at the time of acquisition, being smaller during end diastole compared to peak systole, care

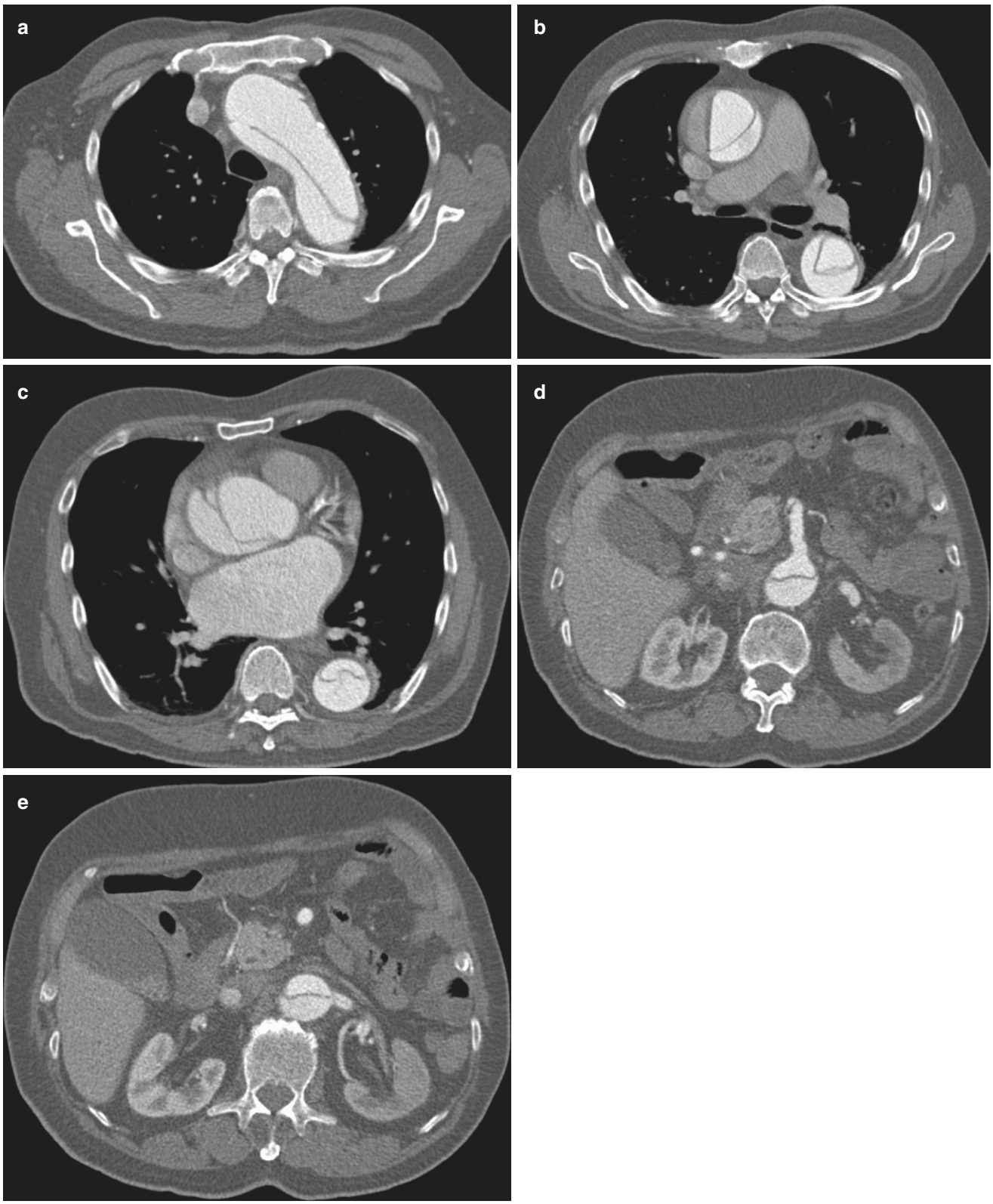

Fig. 10.15 Type A aortic dissection. (**a**–**e**) Axial contrast-enhanced CT aortogram images show extensive dissection extending from ascending aorta to abdominal aorta and even into the left renal artery

Table 10.7 Differentiation between the true and false lumens in aortic dissection on CT

Imaging features	True lumen	False lumen
Size	Smaller with a crescentic shape	Larger than true lumen
Lumen	Maintains direct continuity with the native uninvolved vascular lumen	Intraluminal thrombus
Enhancement characteristics	Higher attenuation on the arterial phase study	High attenuation on the unenhanced scan Delayed/prolonged enhancement due to sluggish blood flow
Signs		"Cobweb" sign: faint low-attenuation linear strands representing residual intact media in the false lumen are highly specific but may not be present in all cases
		"Intimomedial rupture" sign: refers to the ends of the intimal tear that point toward the false lumen due to the antegrade flow of blood from true to the false lumen. However, its mobility and orientation are dependent upon hemodynamic pressures of the two lumina and phase of the cardiac cycle
		"Beak" sign: acute angle between the dissection flap and the outer wall is always seen in false lumen of acute and chronic dissection

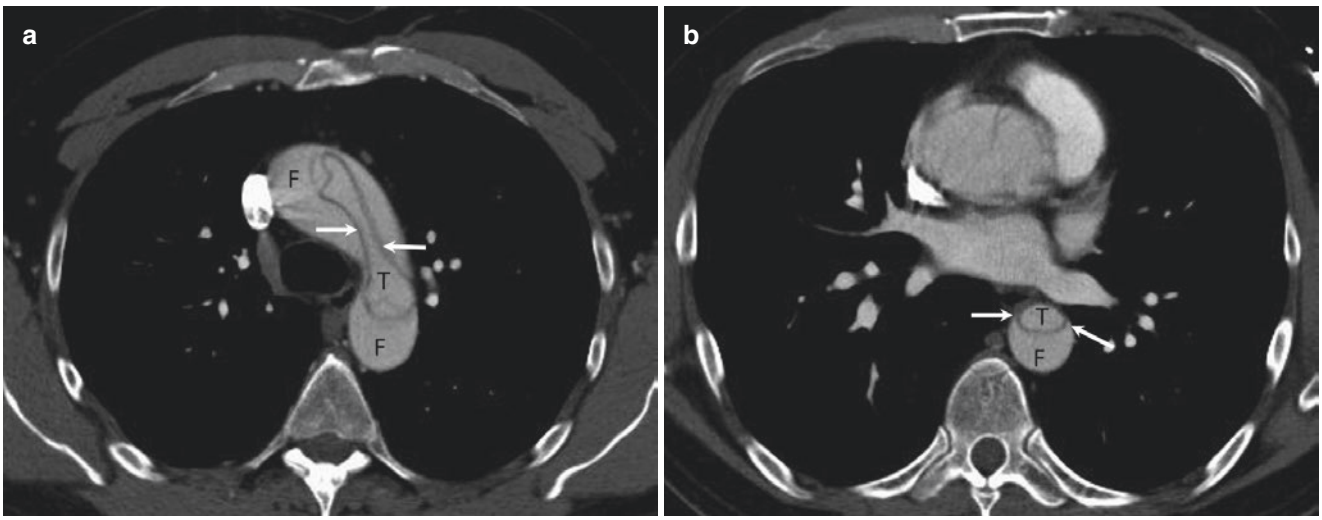

Fig. 10.16 Circumferential dissection and "beak" sign. (**a**) Axial CT aortogram image shows circumferential dissection flap (arrows). (**b**) CT image from midthorax shows a "beak" sign (arrows) in false lumen. *T* true lumen, *F* false lumen

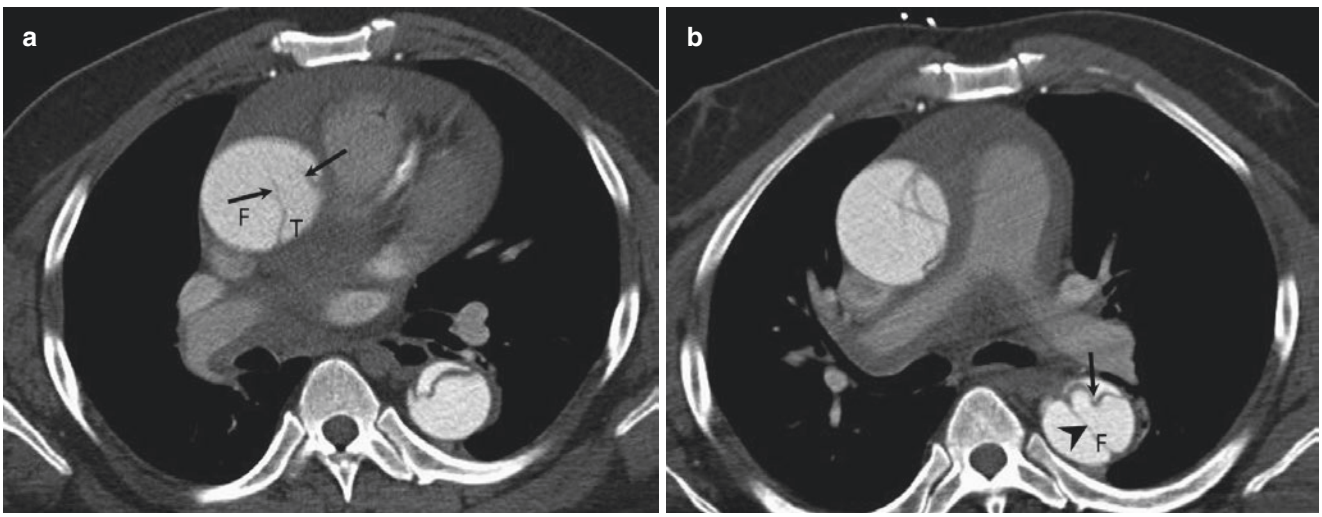

Fig. 10.17 "Intimomedial rupture" sign, "cobweb" sign, and pericardial effusion in type A dissection. (**a**) Axial CT aortogram shows intimomedial entrance tear (arrows) opening toward the false lumen. (**b**, **c**) Axial CT aortogram images show a dissection flap (arrow) with linear bands or webs (arrowhead) in false lumen and a haemopericardium. *T* true lumen, *F* false lumen

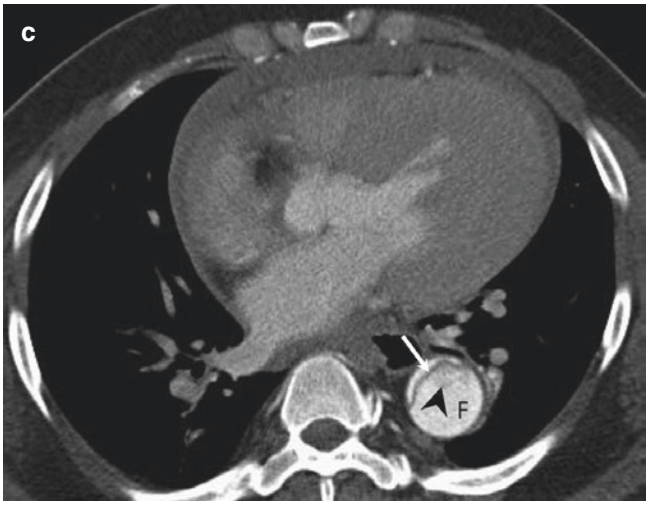

Fig. 10.17 (continued)

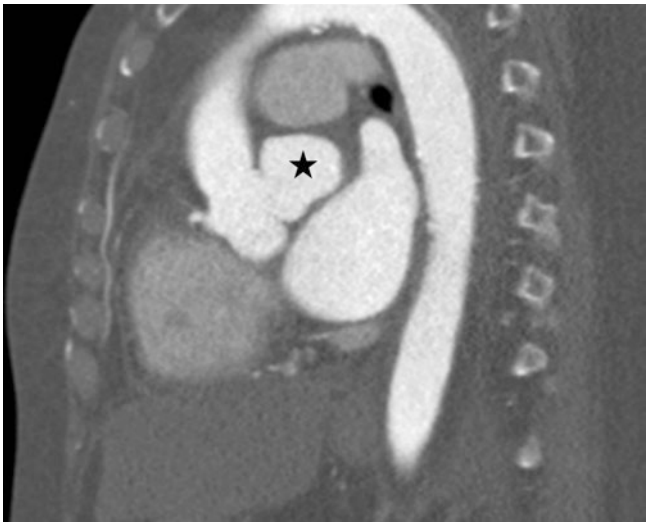

Fig. 10.18 Sagittal contrast-enhanced CT of a saccular (left) sinus of Valsalva aneurysm

Table 10.8 Radiological reporting in AD

• Site of the "entry" and "reentry" intimal tears
• Extent of aortic dissection and involvement of major aortic branches
• Identification of the true and false lumen
• Degree of compression of true lumen/size of false lumen
• Degree of false lumen perfusion/thrombosis
• Size of aorta of dissected portion/evidence of aneurysmal change
• Size/length of aorta in native uninvolved aorta, proximal and distal to the dissection sites: "landing zones" for TEVAR
• Presence of complication: proximal propagation causing aortic valve regurgitation, cardiac tamponade, aortic rupture, malperfusion syndrome with end-organ ischemia, and distal emboli
• Aberrant supra-aortic branch anatomy
• Patency, size, and morphology of iliofemoral arteries for TEVAR vascular access

Table 10.9 Radiological reporting in an aortic aneurysm

• Dimensions: measured in true short axis projection acquired in double oblique views on multiplanar reformats
• Qualities: angulation, tortuosity, mural calcification
• Thrombus: volume and distribution/thrombus to lumen ratio
• Mass effect of an aneurysm
• Compression of coronary arteries, SVC, esophagus, recurrent laryngeal nerve
Landing zone properties (for TEVAR evaluation):
• Aortic diameters of the proximal and distal landing zones—ideal <40 mm
• Quality of the landing zones with respect to atheroma/thrombus/calcification
• Distance from the last aortic branch vessel/left subclavian artery (proximal)—ideal >20 mm on the lesser curvature of the aortic arch
• Distance to the coeliac artery (distal)—ideal >15 mm
• Patency, size, and morphology of iliofemoral arteries for TEVAR access

must be taken to avoid graft undersizing and subsequent endoleaks [32].

The described Achilles heel of endograft treatment, endoleaks (EL), is the persistent perfusion of the aortic aneurysm sac outside of the endograft. The location of the dominant contrast nidus and its source of perfusion will aid characterization of the EL (Table 10.11).

Due to the potential for delayed EL formation, continued surveillance is required. An example follow-up imaging regime involves a post-TEVAR CTA prior to discharge, at 1 month and 6 months and yearly thereafter. In those with symptoms or high-risk concerns, a more intensive patient-centric protocol may be required.

Table 10.10 CT features of impending thoracic aneurysmal rupture

• Rapid enlarging size
• Focal discontinuity of the intimal wall calcification (missing calcium sign), especially if the lumen tapers toward the focal discontinuity ("tangential calcium" sign)
• Eccentric aortic luminal shape
• "Crescent sign"—delineated on non-contrast CT as localized high attenuation within aortic mural thrombus depicting fresh blood dissecting into mural thrombus with a subsequent preponderance to penetration of the aortic wall
• Thrombus fissuration: delineated on enhanced CT as communications between the aortic lumen and fissures within the low-attenuation thrombus
• Periaortic stranding

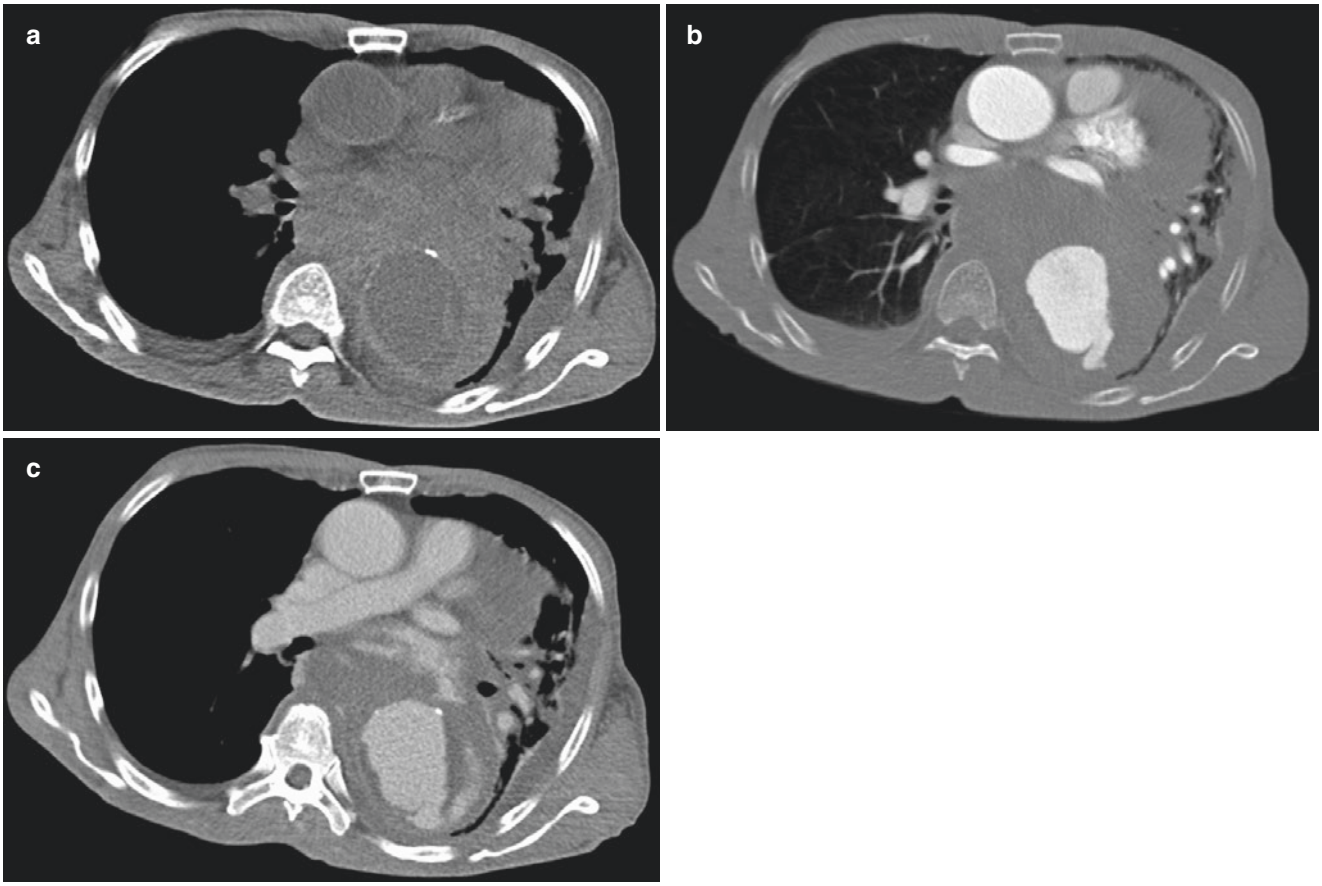

Fig. 10.19 Rupture of descending thoracic aortic aneurysm with active bleeding. (**a**) Axial unenhanced, (**b**) arterial phase and (**c**) delayed phase CT. Note the aortic lumen shows low attenuation compared to extravascular hematoma

10.6 Aortitis

Aortic vasculitis (aortitis) refers to a wide group of disorders with an underlying common vascular inflammatory process of which Takayasu arteritis and giant cell arteritis are the most common.

Takayasu arteritis is a necrotizing, obliterative segmental, large-vessel arteritis commonly affecting young women in their third decade of life. This is typically named "pulseless disease" due to its frequent involvement of the subclavian arteries with resulting reduced peripheral pulses. Aortic involvement is common, affecting the abdominal, descending thoracic, and aortic arch segments, in decreasing order of frequency [33]. Radiological appearances are of concentric vascular mural thickening, stenosis, occlusion, ectatic/aneurysmal change, and ulceration [34] (Fig. 10.22). On contrast-enhanced CT, the "double-ring" sign depicted by poorly enhancing central intima and enhancing inflamed outer media/adventitia is a marker of acute disease [35]. In the chronic stages, vascular wall calcification may occur and appears linear.

Giant cell arteritis, also termed "temporal arteritis," is a systemic granulomatous vasculitis usually involving people >50 years old. While the vascular radiological findings are similar to Takayasu arteritis, the distribution of disease differs, classically involving the branches of the external carotid vessels such as the superior temporal and vertebral arteries. Up to a third of patients experience aortic/main branch involvement, more commonly resulting in annuloaortic ectasia or aneurysmal change of the ascending aorta [34].

IgG4-related aortitis is a recently recognized disease entity and can have concurrent involvement of other organs like the pancreas and bile ducts. This entity is more common in adult males and characterized by high serum IgG4 concentrations and prompts response to steroids. Multiphasic CT angiogram shows eccentric or concentric soft-tissue thickening around the aortic wall. The soft tissue characteristically shows enhancement in the delayed phase signifying

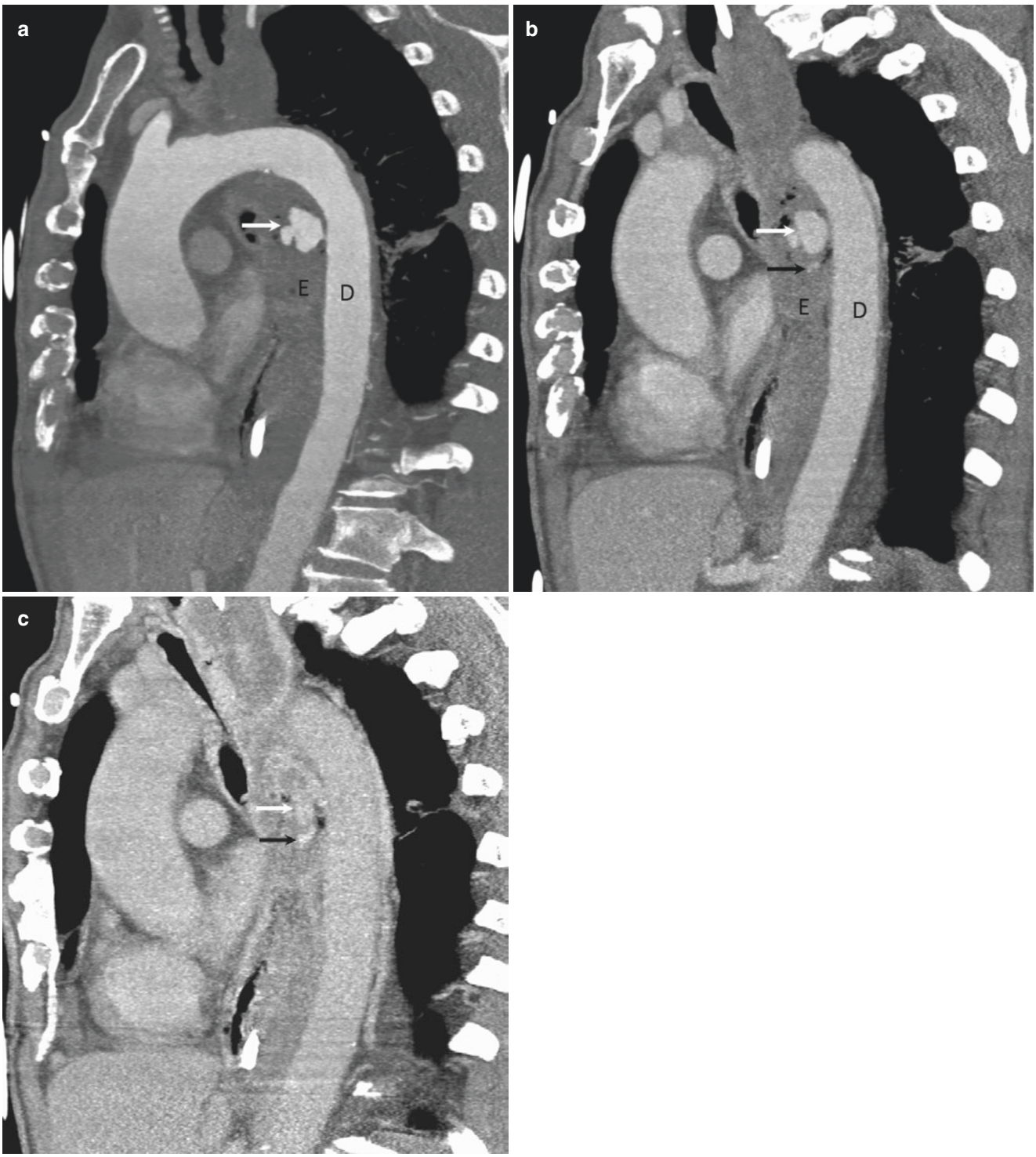

Fig. 10.20 Aorto-esophageal fistula due to esophageal cancer eroding the descending aorta. (**a**) Oblique sagittal CT image in arterial phase shows a pseudoaneurysm (white arrow) from aorta extending into the esophagus. (**b**) Venous phase and (**c**) delayed phase images demonstrate progressive pooling of contrast (black arrow) in the esophagus. *D* descending aorta, *E* esophagus

Table 10.11 Endoleak classification and management strategy

Endoleak	Description	Management
1	(1a) Proximal or (1b) distal attachment site leak between the endograft and the vessel	Type 1 and 3 EL are considered "high pressure," with systemic perfusion of the aneurysm sac and warrant intervention irrespective of sac size measurements
2	Retrograde flow from aortic branch vessels perfusing the aneurysm sac	Type 2 EL is the most common, usually from either a covered left subclavian artery (Fig. 10.21), bronchial or intercostal vessel. These are usually treated in the presence of continued/new symptomatology or documented evidence of aneurysm sac expansion
3	Intrinsic endograft structural failures, including fractures, fabric holes, and modular disconnection	See type 1 endoleak (above)
4	Endograft porosity	Usually identified at the time of endograft implantation and commonly resolve with the reversal of anticoagulation
5	Endotension—defined as persistent high intrasac pressure with documented aneurysm sac enlargement despite the absence of a visible endoleak	May require endograft reinforcement or open conversion

the presence of sclerosing inflammation in the vessel wall, particularly the adventitial layer (Fig. 10.23) [36].

10.7 Dual-Energy CT: Vascular Applications in the Aorta

Dual-energy CT (DECT) imaging hinges on the differential interaction of materials with X-ray photons of varying energies. While both dual- and single-source MDCT scanners are available, the former is more commonly used.

The dual-source configuration employs two tubes, characteristically comprising of a high kVp (140) and a lower kVp (80–100) energy, and two detectors mounted opposite each tube on the gantry. The tubes rotate simultaneously during image acquisition with the X-ray beams orientated 90° perpendicular to each other.

With the raw imaging data, images may be interrogated separately (monoenergetic) or as a combined data set with mixed image reconstruction of approximately 120 kVp.

DECT is well suited to vascular imaging secondary to the higher attenuation of iodine at lower kVp due to a higher proportion of photons that undergo photoelectric absorption interaction as a result of its proximity to the K-edge of iodine (33 keV). While there is increased image noise at low kVp imaging, the overall gain in contrast to noise ratio permits better vascular luminal interrogation especially when there is suboptimal contrast opacification or in assessing small vessels [37]. Clinical utilization in aortic imaging includes detection of subtle endoleaks. While endoleak imaging protocol is varied, DECT acquisition with a single delayed venous phase, reconstructing virtual unenhanced data set and monoenergetic low kVp assessment, has been shown to be equitable to the standard triple-phase imaging (unenhanced, arterial, and delayed), resulting in a significant radiation dose reduction [38]. Secondarily, the increased contrast vascular attenuation permits reduced contrast volume usage while maintaining diagnostic accuracy. Conversely, high-peak-kilovoltage monoenergetic data sets reduce the degree of metal artifact caused by beam hardening which lends itself to improved stent assessment [37].

Using the dual-energy data sets, vascular post-processing protocols allow virtual non-contrast image production and bone-mask imaging. VNC images use the two monochromatic data sets to create an imaging series with the iodine removed (Fig. 10.24) allowing further interrogation in cases such as questionable dissection and confirming the presence of hyperdense intramural hematoma or intimal calcification [39]. Calcium and plaque subtraction techniques also allow better assessment of true luminal diameter.

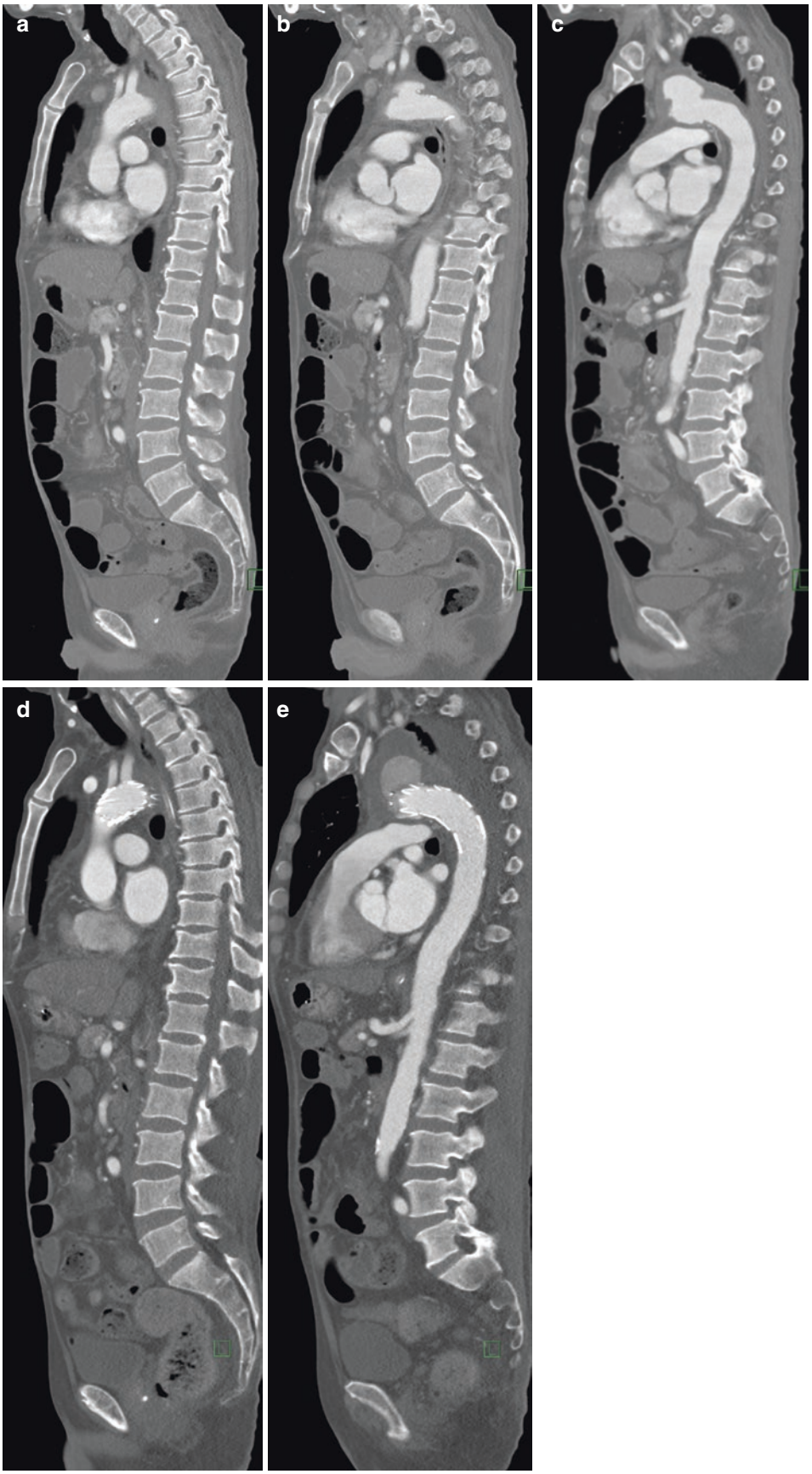

Fig. 10.21 Type 2 endoleak. (**a**–**c**) Sagittal contrast-enhanced CT pre-TEVAR. (**d**, **e**) Sagittal contrast-enhanced CT post-TEVAR with endoleak. (**f**, **g**) Digital subtraction angiogram from the left subclavian artery demonstrating type 2 endoleak. (**h**) Sagittal contrast-enhanced CT post left subclavian and endoleak nidus embolization for the type 2 endoleak reveals no further filling of endoleak

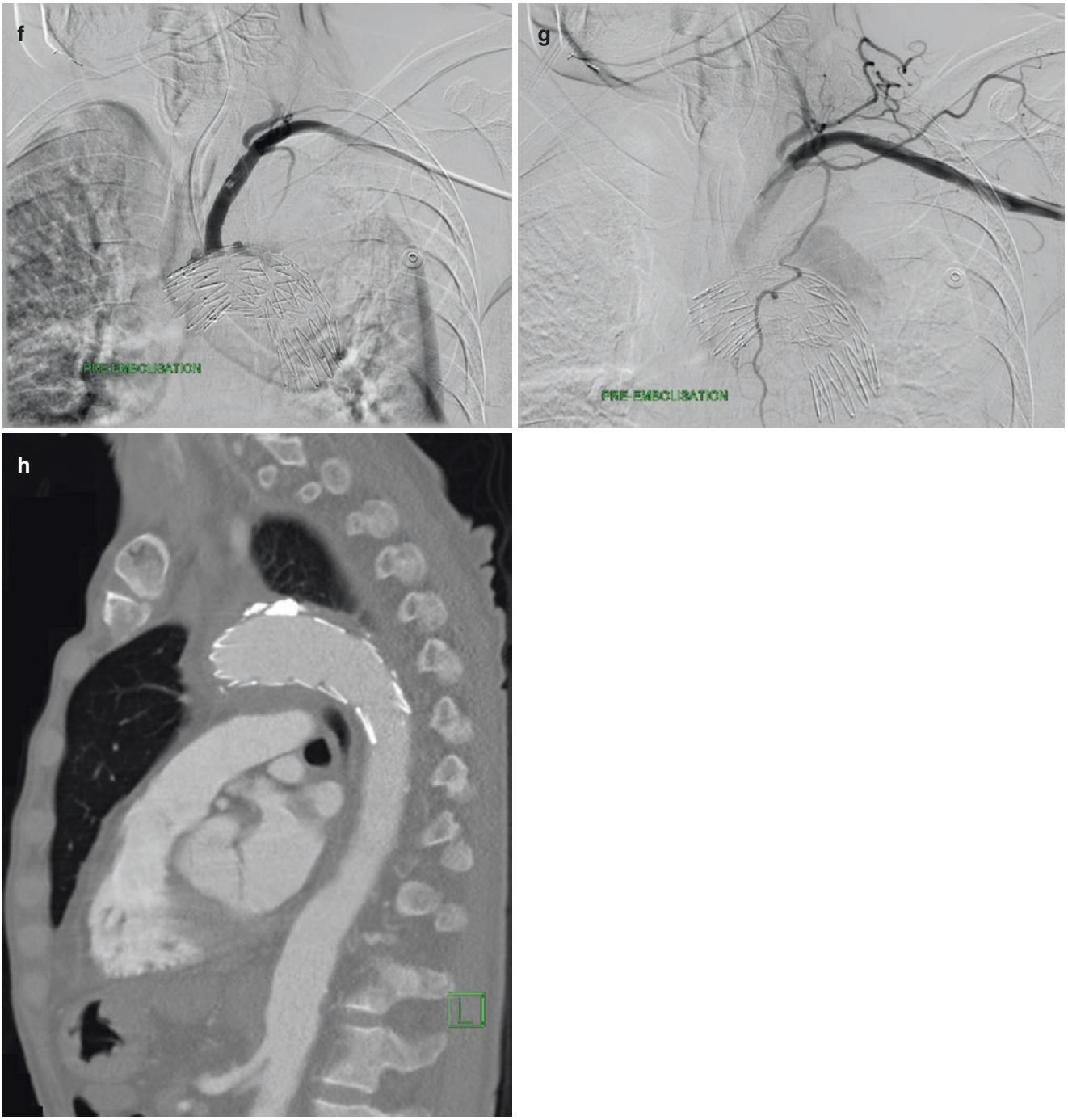

Fig. 10.21 (continued)

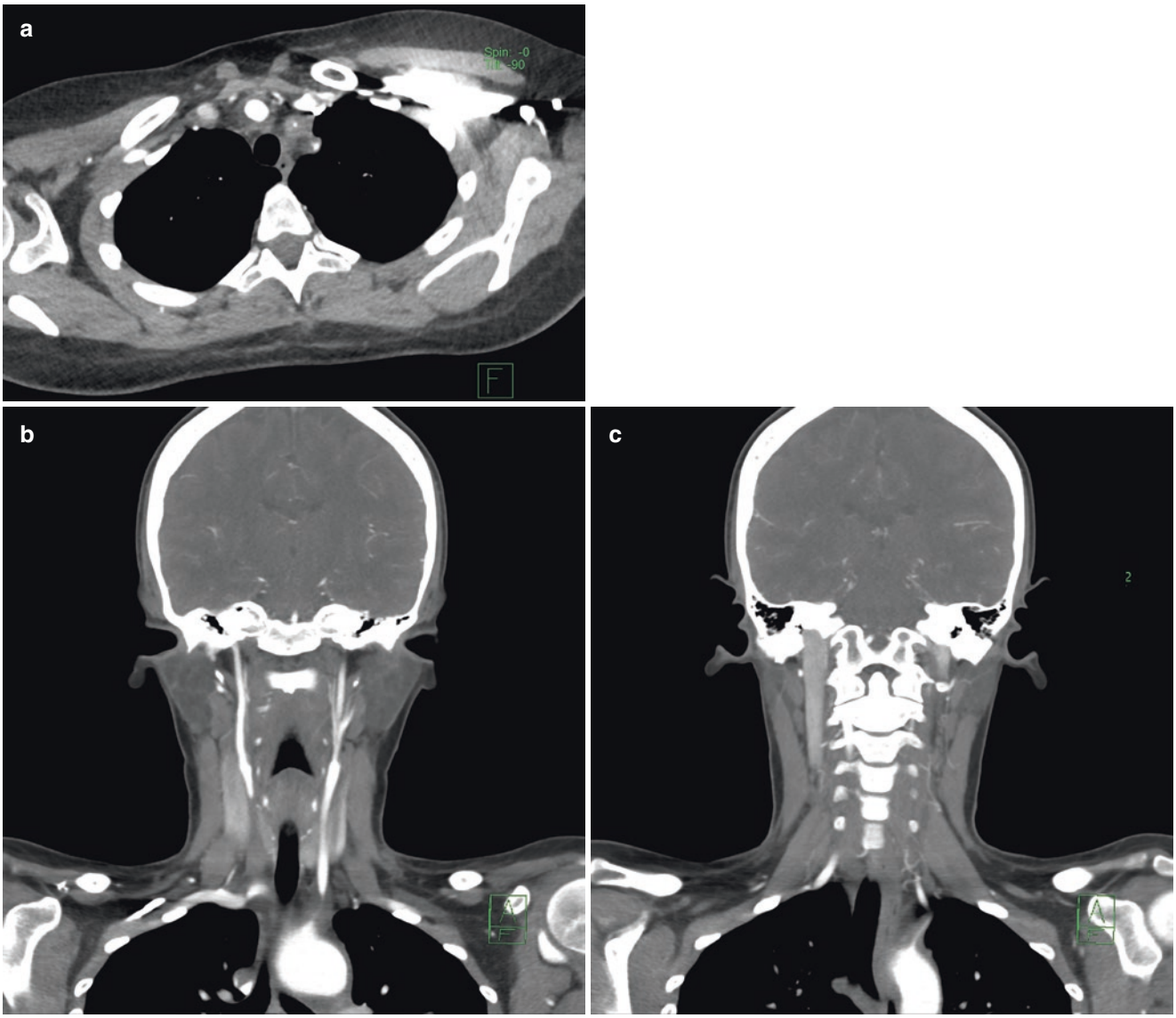

Fig. 10.22 Takayasu arteritis. (**a**) Axial contrast-enhanced CT of vasculitis—circumferential soft tissue thickening of the supra-aortic vessels with luminal narrowing. (**b**) Coronal contrast-enhanced CT shows severe stenosis of left common carotid arterial and complete right common carotid occlusion. (**c**) Coronal contrast-enhanced CT shows soft tissue thickening with luminal narrowing of the left subclavian artery

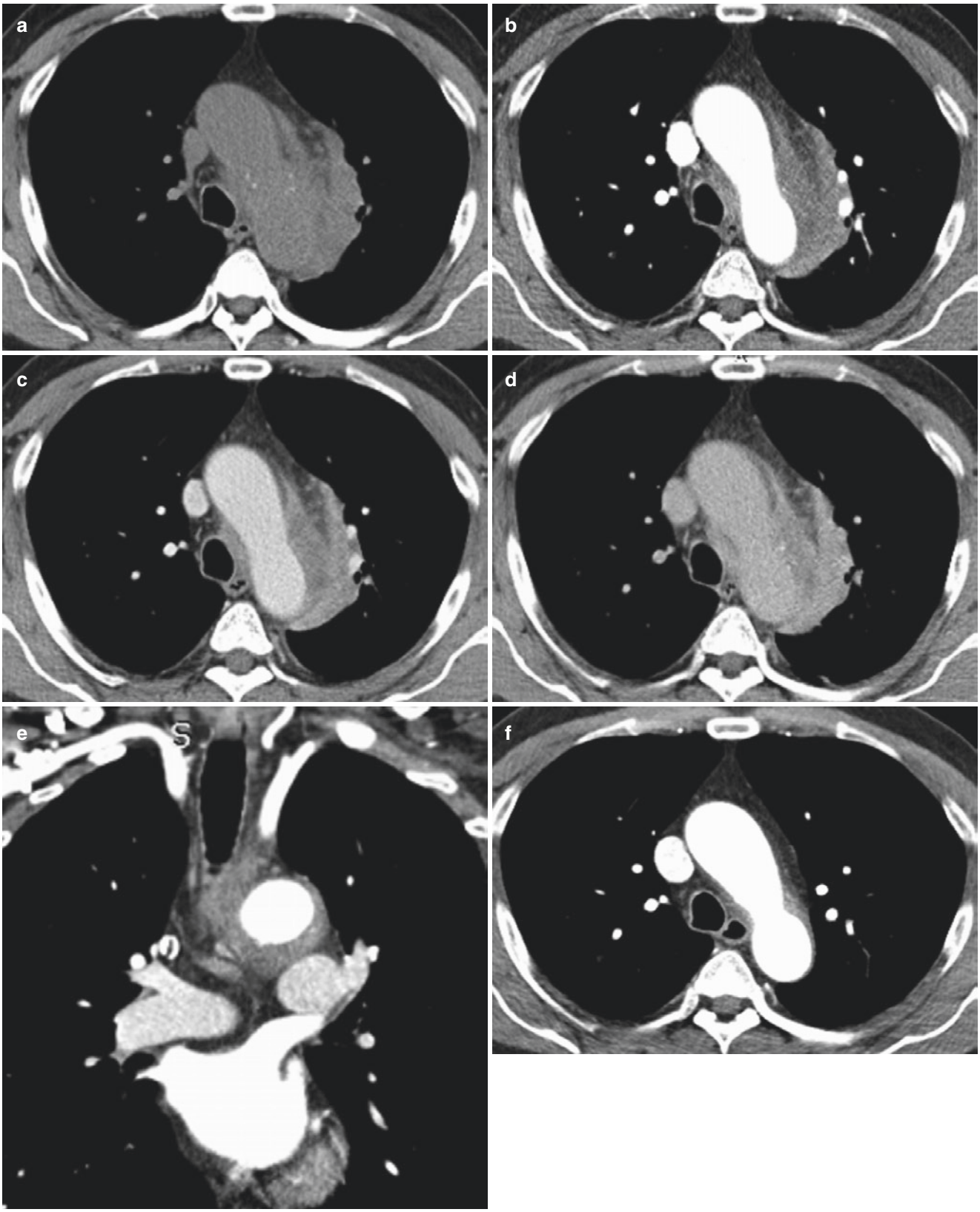

Fig. 10.23 IgG4 periaortitis in a 52-year-old man presenting to emergency department with chest discomfort. Axial CT aortogram in unenhanced phase (**a**), arterial phase (**b**), venous phase (**c**), delayed phase (**d**), and coronal CT aortogram image (**e**) shows an ill-defined soft tissue around the aorta that shows progressive enhancement in delayed phase. Note linear atelectasis of the left upper paramediastinal lung. Follow-up CT aortogram after 6 months of steroid treatment (**f**, **g**) shows near-complete resolution of periaortic soft tissue

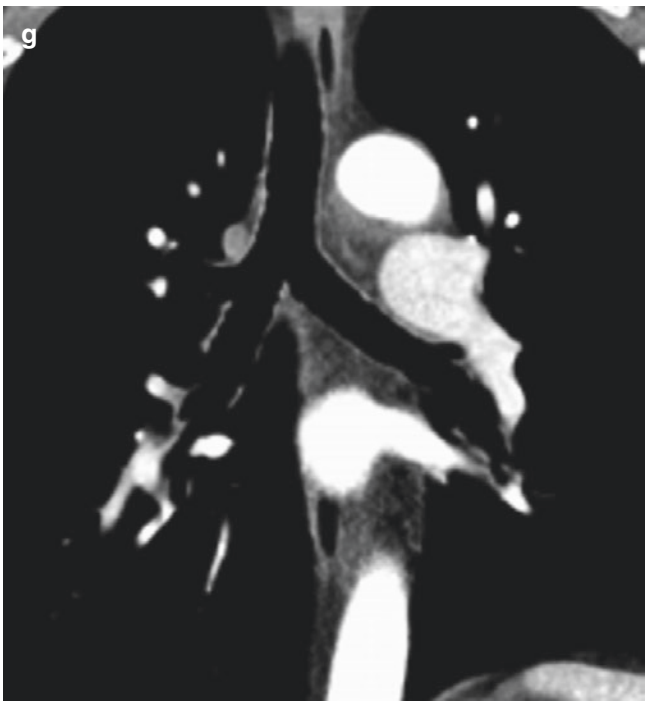

Fig. 10.23 (continued)

10.8 Conclusion

While the diverse acute aortic pathologies may have similar clinical presentations, contrast-enhanced MDCT provides rapid assessment of disease status, progress, and complications. Accurate aortic evaluation requires an appreciation of acquisition techniques to optimize imaging, reduce patient radiation exposure, and reduce artifact to avoid misdiagnoses. Furthermore, the imaging characteristics of each entity, with their high-risk features, are pivotal in guiding appropriate clinical management and must be succinctly identified in radiological interpretation.

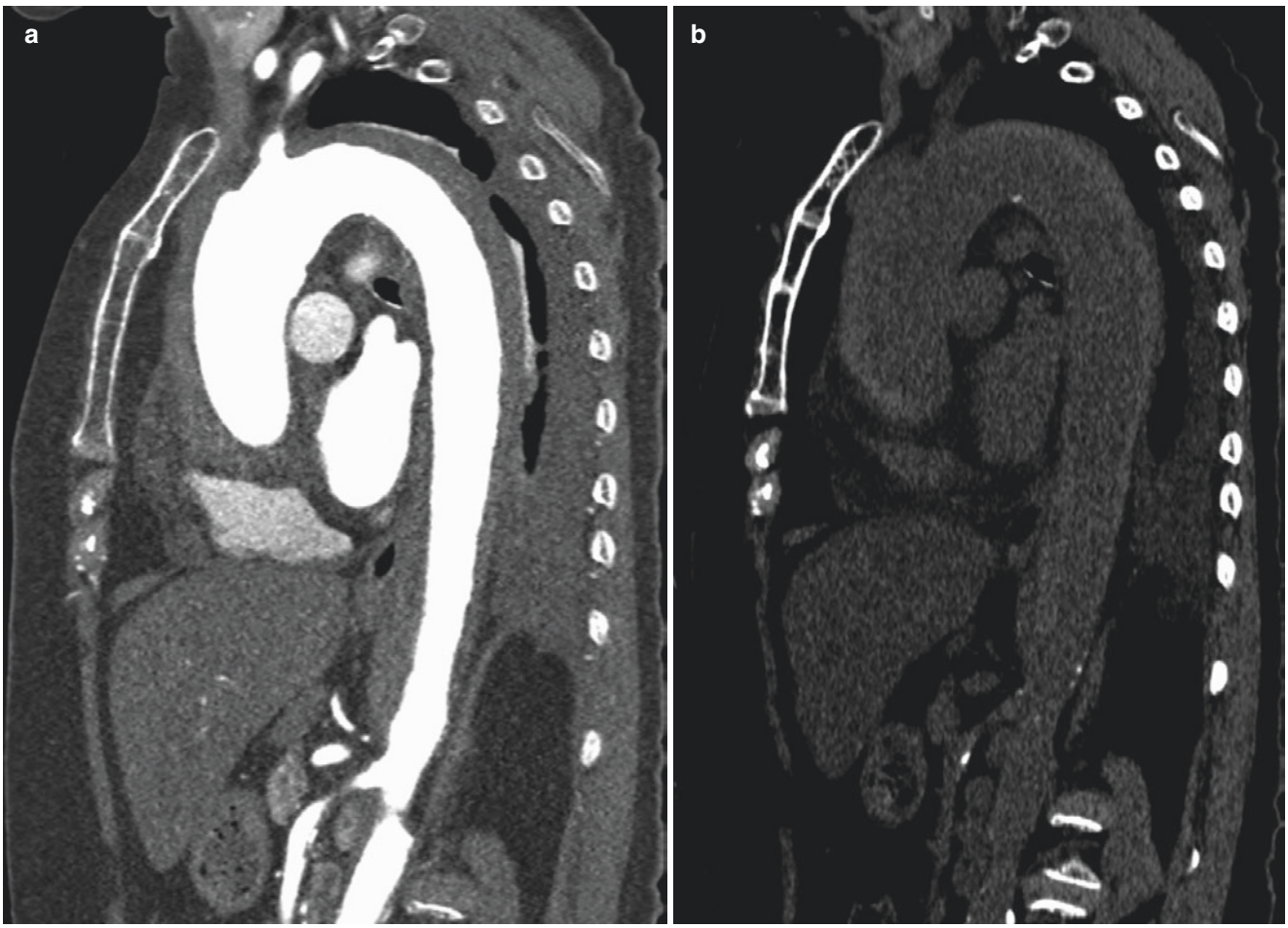

Fig. 10.24 Utility of dual-energy CT in intramural hematoma. (**a**) Sagittal contrast-enhanced dual-energy CT—underlying acute intramural hematoma masked by the contrast. (**b**) Sagittal virtual non-contrast reconstruction from dual-energy CT shows underlying high-attenuation acute intramural hematoma

References

1. von Kodolitsch Y, Nienaber CA, Dieckmann C, Schwartz AG, Hofmann T, Brekenfeld C, Nicolas V, Berger J, Meinertz T. Chest radiography for the diagnosis of acute aortic syndrome. Am J Med. 2004;116(2):73–7.
2. Chawla A, Rajendran S, Yung WH, Babu SB, Peh WC. Chest radiography in acute aortic syndrome: pearls and pitfalls. Emerg Radiol. 2016;23(4):405–12.
3. Hunter TB, Taljanovic MS, Tsau PH, Berger WG, Standen JR. Medical devices of the chest. Radiographics. 2004;24(6):1725–46.
4. Mundy J, Stickley M, Venkatesh B, Coucher J, Foot CL. The imaginary line method is not reliable for identification of prosthetic heart valves on AP chest radiographs. Crit Care Resusc. 2006;8(1):15.
5. Gross BH, Shirazi KK, Slater AD. Differentiation of aortic and mitral valve prostheses based on postoperative frontal chest radiographs. Radiology. 1983;149(2):389–91.
6. Jakanani GC, Adair W. Frequency of variations in aortic arch anatomy depicted on multidetector CT. Clin Radiol. 2010;65(6):481–7.
7. Layton KF, Kallmes DF, Cloft HJ, Lindell EP, Cox VS. Bovine aortic arch variant in humans: clarification of a common misnomer. Am J Neuroradiol. 2006;27(7):1541–2.
8. Kau T, Sinzig M, Gasser J, Lesnik G, Rabitsch E, Celedin S, Eicher W, Illiasch H, Hausegger KA. Aortic development and anomalies. Semin Interv Radiol. 2007;24(2):141.
9. Erbel R, Aboyans V, Boileau C, Bossone E, Bartolomeo RD, Eggebrecht H, Evangelista A, Falk V, Frank H, Gaemperli O, Grabenwöger M, Haverich A, Iung B, Manolis AJ, Meijboom F, Nienaber CA, Roffi M, Rousseau H, Sechtem U, Sirnes PA, Allmen RS, Vrints CJ, ESC Committee for Practice Guidelines. 2014 ESC guidelines on the diagnosis and treatment of aortic diseases: document covering acute and chronic aortic diseases of the thoracic and abdominal aorta of the adult. The task force for the diagnosis and treatment of aortic diseases of the European Society of Cardiology (ESC). Eur Heart J. 2014;35(41):2873–926.
10. Hager A, Kaemmerer H, Rapp-Bernhardt U, Blücher S, Rapp K, Bernhardt TM, Galanski M, Hess J. Diameters of the thoracic aorta throughout life as measured with helical computed tomography. J Thorac Cardiovasc Surg. 2002;123(6):1060–6.
11. Wolak A, Gransar H, Thomson LE, Friedman JD, Hachamovitch R, Gutstein A, Shaw LJ, Polk D, Wong ND, Saouaf R, Hayes SW. Aortic size assessment by noncontrast cardiac computed tomography: normal limits by age, gender, and body surface area. J Am Coll Cardiol Cardiovasc Imaging. 2008;1(2):200–9.
12. Lee SH, Lee W, Choi HJ, Kim DJ, Park EA, Chung JW, Park JH. Measurement of the aortic diameter in the asymptomatic Korean population: assessment with multidetector CT. J Korean Soc Radiol. 2013;69(2):105–12.
13. Hanneman K, Newman B, Chan F. Congenital variants and anomalies of the aortic arch. Radiographics. 2016;37(1):32–51.
14. Cotrufo M, Agozzino L, De MF, Della AC, Santo De LS, Di GB, Esposito S, Nappi G. Aortic valve dysfunction and dilated ascending aorta. A complex and controversial association. Ital Heart J. 2003;4(9):589–95.
15. Bolger AF. Aortic intramural haematoma. Heart. 2008;94(12):1670–4.
16. Castañer E, Andreu M, Gallardo X, Mata JM, Cabezuelo MÁ, Pallardó Y. CT in nontraumatic acute thoracic aortic disease: typical and atypical features and complications. Radiographics. 2003;23(Suppl 1):S93–110.
17. Ganaha F, Miller DC, Sugimoto K, Do YS, Minamiguchi H, Saito H, Mitchell RS, Dake MD. Prognosis of aortic intramural hematoma with and without penetrating atherosclerotic ulcer: a clinical and radiological analysis. Circulation. 2002;106(3):342–8.
18. Valente T, Rossi G, Lassandro F, Rea G, Marino M, Muto M, Molino A, Scaglione M. MDCT evaluation of acute aortic syndrome (AAS). Br J Radiol. 2016;89(1061):20150825.
19. Rubin GD. Helical CT angiography of the thoracic aorta. J Thorac Imaging. 1997;12(2):128–49.
20. Kitai T, Kaji S, Yamamuro A, Tani T, Kinoshita M, Ehara N, Kobori A, Kita T, Furukawa Y. Impact of new development of ulcer-like projection on clinical outcomes in patients with type B aortic dissection with closed and thrombosed false lumen. Circulation. 2010;122(11 suppl 1):S74–80.
21. Nagpal P, Khandelwal A, Saboo SS, Bathla G, Steigner ML, Rybicki FJ. Modern imaging techniques: applications in the management of acute aortic pathologies. Postgrad Med J. 2015;91:449–62.
22. Mussa FF, Horton JD, Moridzadeh R, Nicholson J, Trimarchi S, Eagle KA. Acute aortic dissection and intramural hematoma: a systematic review. JAMA. 2016;316(7):754–63.
23. Daily PO, Trueblood HW, Stinson EB, Wuerflein RD, Shumway NE. Management of acute aortic dissections. Ann Thorac Surg. 1970;10(3):237–47.
24. Debakey ME. Surgical management of dissecting aneurysms of the aorta. J Thorac Cardiovasc Surg. 1965;49:130–49.
25. Jones MR, Reid JH. Emergency chest radiology: thoracic aortic disease and pulmonary embolism. Imaging. 2006;18(3):122–38.
26. Kapoor V, Ferris JV, Fuhrman CR. Intimomedial rupture: a new CT finding to distinguish true from false lumen in aortic dissection. Am J Roentgenol. 2004;183(1):109–12.
27. McMahon MA, Squirrell CA. Multidetector CT of aortic dissection: a pictorial review. Radiographics. 2010;30(2):445–60.
28. Willoteaux S, Lions C, Gaxotte V, Negaiwi Z, Beregi JP. Imaging of aortic dissection by helical computed tomography (CT). Eur Radiol. 2004;14(11):1999–2008.
29. Agarwal PP, Chughtai A, Matzinger FR, Kazerooni EA. Multidetector CT of thoracic aortic aneurysms. Radiographics. 2009;29(2):537–52.
30. Ahmed MZ, Ling L, Ettles DF. Common and uncommon CT findings in rupture and impending rupture of abdominal aortic aneurysms. Clin Radiol. 2013;68(9):962–71.
31. Schwartz SA, Taljanovic MS, Smyth S, O'Brien MJ, Rogers LF. CT findings of rupture, impending rupture, and contained rupture of abdominal aortic aneurysms. Am J Roentgenol. 2007;188(1):W57–62.
32. Parodi J, Berguer R, Carrascosa P, Khanafer K, Capunay C, Wizauer E. Sources of error in the measurement of aortic diameter in computed tomography scans. J Vasc Surg. 2014;59(1):74–9.
33. Sueyoshi E, Sakamoto I, Hayashi K. Aortic aneurysms in patients with Takayasu's arteritis: CT evaluation. Am J Roentgenol. 2000;175(6):1727–33.
34. Restrepo CS, Ocazionez D, Suri R, Vargas D. Aortitis: imaging spectrum of the infectious and inflammatory conditions of the aorta. Radiographics. 2011;31(2):435–51.
35. Hayashi H, Katayama N, Takagi R, Matsuoka Y, Matsunaga N. CT analysis of vascular wall during the active phase of Takayasu's aortitis [abstr]. Eur Radiol. 1991;1:S239.
36. Inoue D, Zen Y, Abo H, Gabata T, Demachi H, Yoshikawa J, Miyayama S, Nakanuma Y, Matsui O. Immunoglobulin G4–related periaortitis and periarteritis: CT findings in 17 patients. Radiology. 2011;261(2):625–33.
37. Vlahos I, Godoy MC, Naidich DP. Dual-energy computed tomography imaging of the aorta. J Thorac Imaging. 2010;25(4):289–300.
38. Maturen KE, Kleaveland PA, Kaza RK, Liu PS, Quint LE, Khalatbari SH, Platt JF. Aortic endograft surveillance: use of fast-switch kVp dual-energy computed tomography with virtual non-contrast imaging. J Comput Assist Tomogr. 2011;35(6):742–6.
39. Vlahos I, Chung R, Nair A, Morgan R. Dual-energy CT: vascular applications. Am J Roentgenol. 2012;199(5 Supplement):S87–97.

Imaging of the Esophagus

11

Pratik Mukherjee, Tze Chwan Lim, and Ashish Chawla

11.1 Introduction

The esophagus is a tubular structure measuring approximately 25 cm in length, connecting the pharynx and the stomach. Most of the esophagus lies in the thorax, with small cervical and intra-abdominal segments. The longest thoracic segment lies posterior to the trachea in the midline, until the tracheal bifurcation, after which it courses slightly left of the midline to cross the diaphragm via the diaphragmatic hiatus and forms the gastroesophageal junction. The abdominal esophagus lies posterior to the left lobe of the liver. The esophagus is therefore composed of a short cervical segment, a long thoracic segment, and a short abdominal segment [1, 2]. The esophageal wall consists of four layers: mucosa, submucosa, muscular layer, and external fibrous layer [3]. The upper third of the esophagus consists of striated muscles, gradually transitioning into completely unstriated muscles in the distal third. Columnar epithelium lines the distal third and gastroesophageal junction, with squamous epithelium lining the rest of the esophagus.

There is no clear definition of a normal esophageal wall thickness. However, in a well-distended esophagus, wall thickness exceeding 3 mm can be considered abnormal. Any eccentric thickening in the esophagus is also deemed abnormal and warrants endoscopic correlation. An anterior-posterior diameter of more than 16 mm and a transverse diameter of more than 24 mm are considered abnormal as well [1].

The role of the esophagus is to move ingested material from the pharynx to the stomach and to prevent reflux of the gastric contents.

The regulation of food passage is done by the upper esophageal sphincter and lower esophageal sphincter. The upper esophageal sphincter is a high-pressure zone at the pharyngoesophageal junction and comprises of cricopharyngeus, thyropharyngeus, and the superior part of the cervical esophagus [4]. The lower esophageal sphincter is a 2–3 cm high-pressure zone at the gastroesophageal junction and is composed of the lower esophageal muscle fibers and the diaphragmatic hiatus. The gastroesophageal junction is anchored by several ligaments, most important being the phreno-esophageal ligament (or membrane) that allows the esophagus to slide longitudinally through the diaphragmatic hiatus while acting as a seal between the thoracic and abdominal cavities [5].

Swallowing reflex induces a cascade of primary peristaltic waves that propel the residual material in the esophagus to stimulate the esophageal sensory receptors activating secondary peristalsis. Non-propulsive tertiary contractions are seen in a variety of motility disorders [6].

11.2 Imaging

The initial imaging investigation for assessment of the esophagus is usually a chest radiograph. Contrast (usually barium) fluoroscopic studies allow us to observe motility functions of the esophagus in real time and can be complementary to direct internal visualization provided by endoscopy. Fluoroscopic studies are indicated for frail patients, patients with suspected motility disorders, and postsurgical evaluation. In many centers, CT is often the first-line investigation in the context of trauma and is also essential for malignancy work-up.

11.2.1 Radiography

Radiographs have a limited role in the assessment of esophageal disease barring evaluating for suspected perforation or ingested foreign bodies, where a radiograph is the preliminary study performed. Some esophageal pathologies can be incidentally detected on chest or lateral neck radiographs. For example, an air-fluid level or air-containing dilated esophagus seen in a chest radiograph will alert the discerning radiologist to an underlying esophageal abnormality (Figs. 11.1 and 11.2).

P. Mukherjee (✉) · T. C. Lim · A. Chawla
Department of Diagnostic Radiology, Khoo Teck Puat Hospital, Singapore, Singapore
e-mail: pratik_mukherjee@whc.sg; tze_chwan_lim@whc.sg

A. Chawla (ed.), *Thoracic Imaging*, https://doi.org/10.1007/978-981-13-2544-1_11

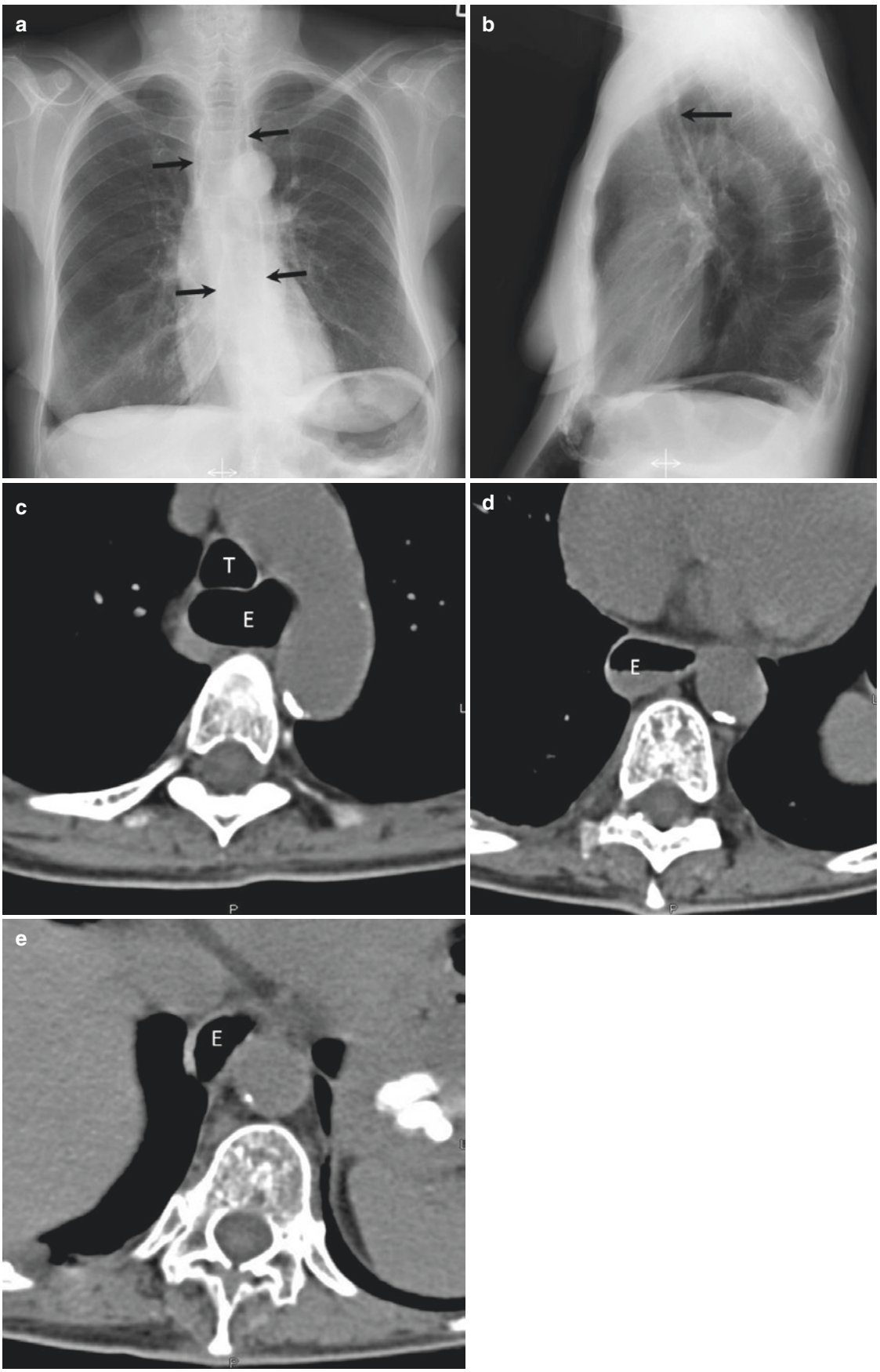

Fig. 11.1 Split esophagus in achalasia. (**a**) A tubular structure in the posterior mediastinum with displacement of azygo-esophageal line representing dilated esophagus (arrows). (**b**) Lateral radiograph shows thickening of the posterior tracheal wall (arrow) as the only evidence of dilated esophagus. (**c–e**) Axial CT images show dilated esophagus. *T* trachea, *E* esophagus

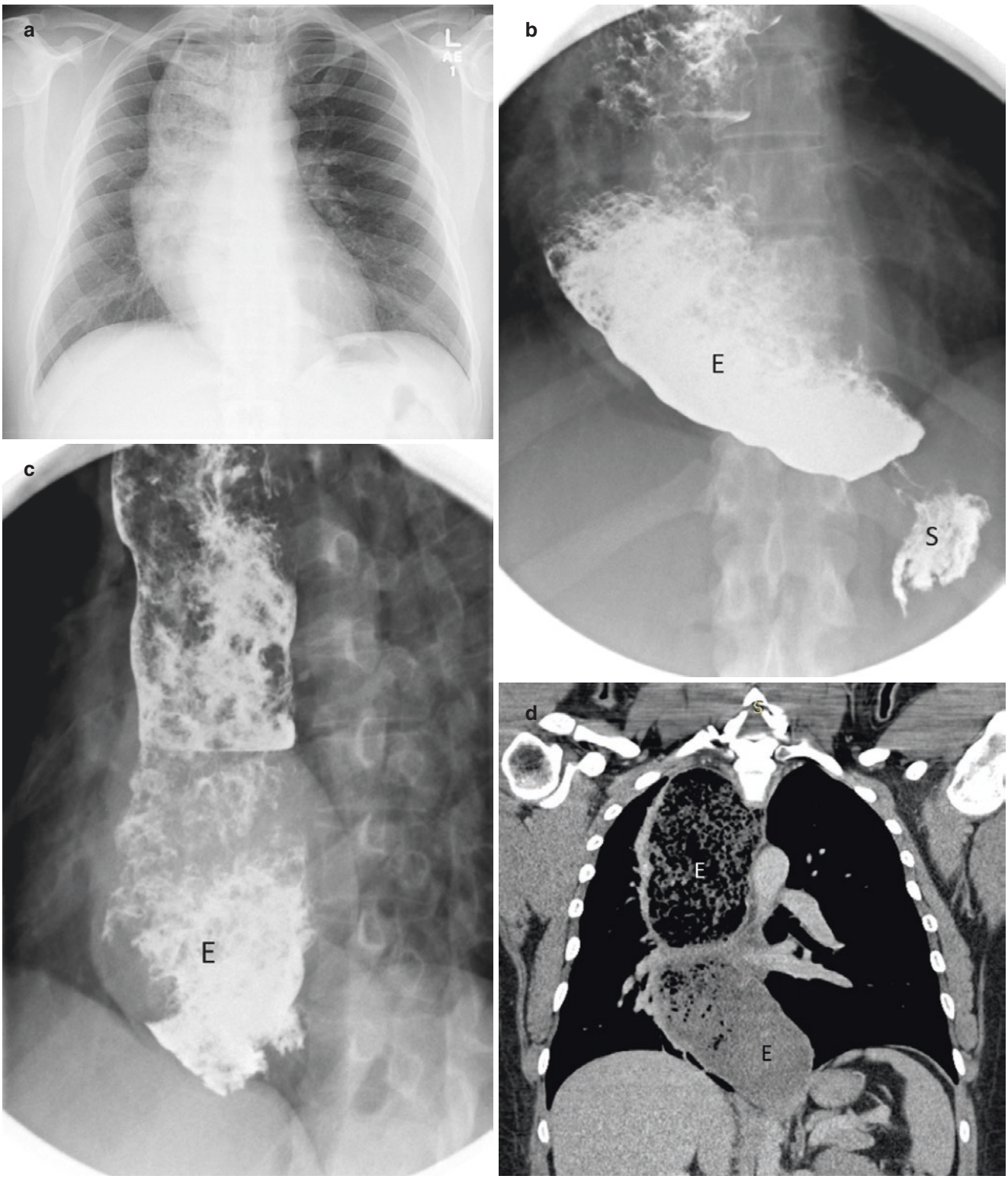

Fig. 11.2 A 25-year-old man with recurrent chest pain due to achalasia cardia. (**a**) Frontal radiograph shows a large mediastinal mass with mottled densities in keeping with a dilated esophagus. (**b**, **c**) Esophagogram images show dilated esophagus with food residue. (**d**) Coronal CT image reveals a dilated esophagus with relatively thin walls. *E* esophagus

11.2.2 Fluoroscopy

Contrast fluoroscopy used to be the main investigation for diagnosing esophageal diseases, prior to the advent and continuous improvement in advanced cross-sectional imaging. Such studies remain relatively affordable and are still performed as an initial assessment of the alimentary tract. However, the diagnostic yield is dependent on the performing procedurist.

One has to strike a balance between good mucosal coating and optimal contrast density. If possible, double-contrast images should be obtained using an effervescent agent, usually in the erect position. These are complementary to prone, single-contrast images [3].

Water-soluble contrast medium is used for postsurgical patients to detect anastomotic leakage in the esophagus (Fig. 11.3). For patients with pulmonary edema, low-osmolar agents are used in place of high-osmolar agents.

11.2.3 CT

CT has a key role in the imaging of esophageal diseases, particularly in the staging of esophageal cancer. A dedicated CT study of the thorax, abdomen, and pelvis is usually performed after ensuring adequate esophageal and gastric distension. Ideally, the patient should be imaged after administration of 1–1.5 L of water and, if possible, effervescent granules. Unless contraindicated, intravenous contrast agent is routinely used and the upper abdomen imaged in both the arterial and portal venous phases. Prone images are acquired in patients with esophageal cancer and suspicion of aortic invasion, as it is considered more accurate.

In the context of suspected esophageal trauma (including Boerhaave syndrome) and in the postoperative setting, positive water-soluble oral contrast medium is recommended. In cases of suspected tracheoesophageal fistula, an initial acquisition without the use of oral contrast medium is usually diagnostic. These topics are discussed in detail in the subsequent sections.

11.2.4 MRI

To date, MRI is not routinely used for evaluation of the esophagus, and its application may be limited to only some academic institutions.

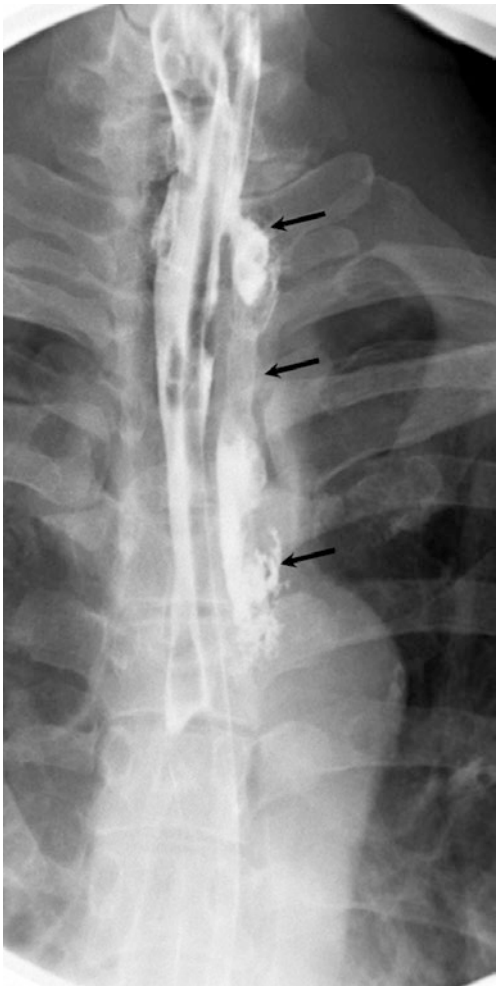

Fig. 11.3 A 41-year-old man with esophageal perforation after endoscopic retrieval of ingested fishbone. Water-soluble contrast swallow study shows a linear blind-ending track on the left lateral aspect of the upper thoracic esophagus (black arrows). The contrast study reveals the site and extent of perforation

11.2.5 Endoscopic Ultrasound (EUS)

EUS is used to further characterize abnormalities identified with other imaging techniques, especially in the staging of esophageal cancer. Less frequently, EUS is used for assessment of submucosal lesions of the esophagus. The high frequency and close proximity of the ultrasound probe allow delineation of the five layers of the esophageal wall. EUS achieves the highest spatial resolution and is performed by using a high-frequency (7–12 MHz) ultrasound probe mounted at the end of an endoscope. Images produced by the radial echoendoscope are perpendicular to the axis of the

scope. A linear echoendoscope produces images parallel to its axis and is used for EUS-guided fine needle aspiration [7].

11.2.6 ^{18}F-Fluorodeoxyglucose Positron-Electron Tomography-CT (PET-CT)

A large proportion of patients with esophageal carcinoma has unsuspected metastatic disease at presentation, and PET-CT is the investigation of choice for disease staging of such patients, who will require radical treatment [8]. The improved anatomic localization of integrated PET-CT makes it superior to other modalities in detecting metastasis (Fig. 11.4) [9].

Technetium-based radionuclide imaging of the esophagus is used for the assessment of esophageal motility disorders and gastroesophageal reflux disease (GERD). Patients are imaged while swallowing both liquid and solid material (usually ^{99m}Tc-labeled sulfur colloid and scrambled egg, respectively).

11.3 Esophageal Motility Disorders

There are many classifications of motility disorders related to smooth muscle, and no single classification system is complete in itself. Motility disorders may be classified based on the major symptom, clinical syndrome, esophageal motility study findings, esophageal bolus transport, pathophysiology, or the anatomic site of major involvement [4]. Figure 11.5 demonstrates the radiologic appearances of some of the common motility disorders involving the smooth

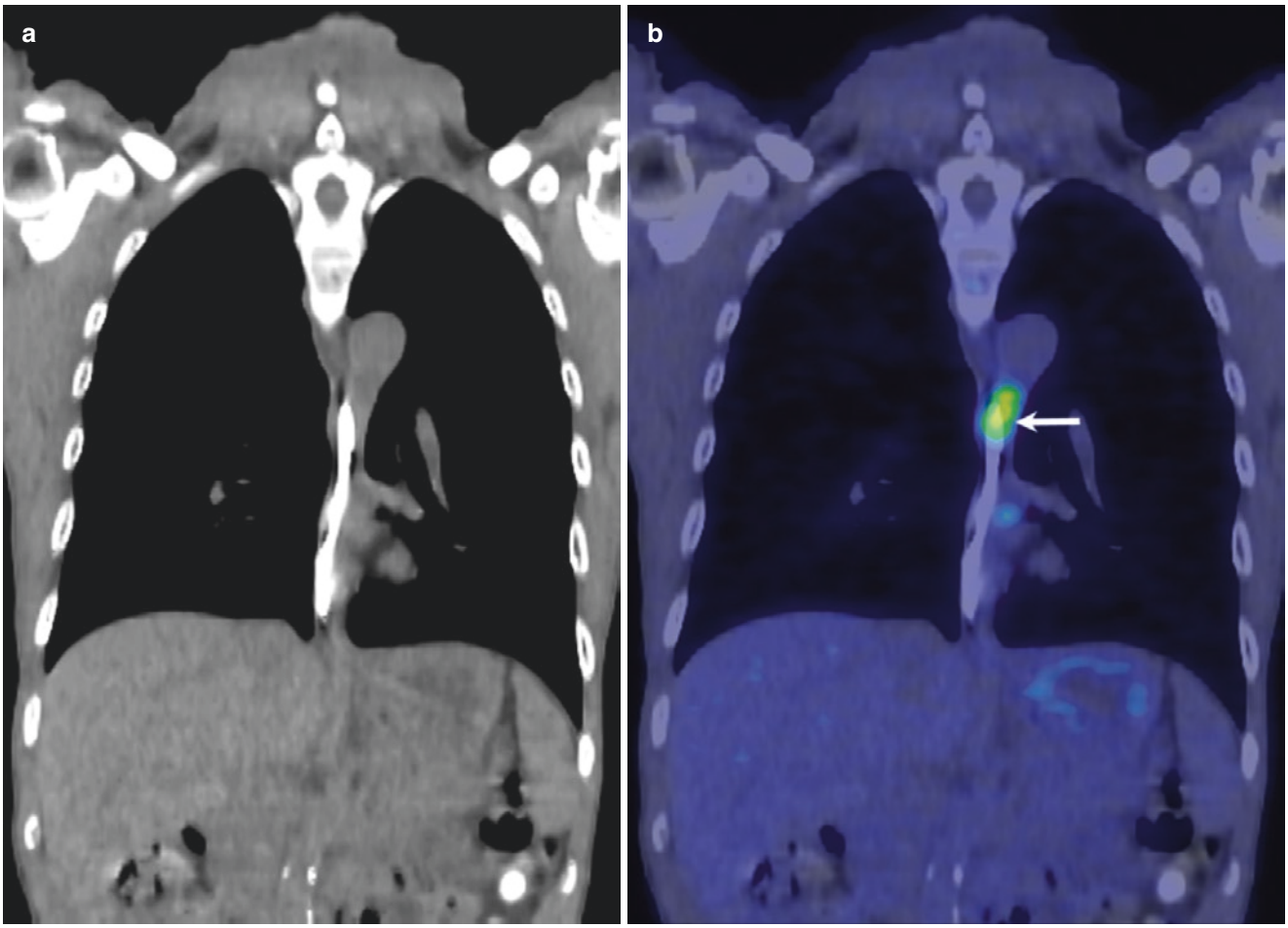

Fig. 11.4 (**a**) Coronal CT and (**b**) fused PET-CT image shows primary mid-esophageal malignancy (arrow). (**c**) MIP images shows primary mid-esophageal malignancy with multiple distant lymph node metastases

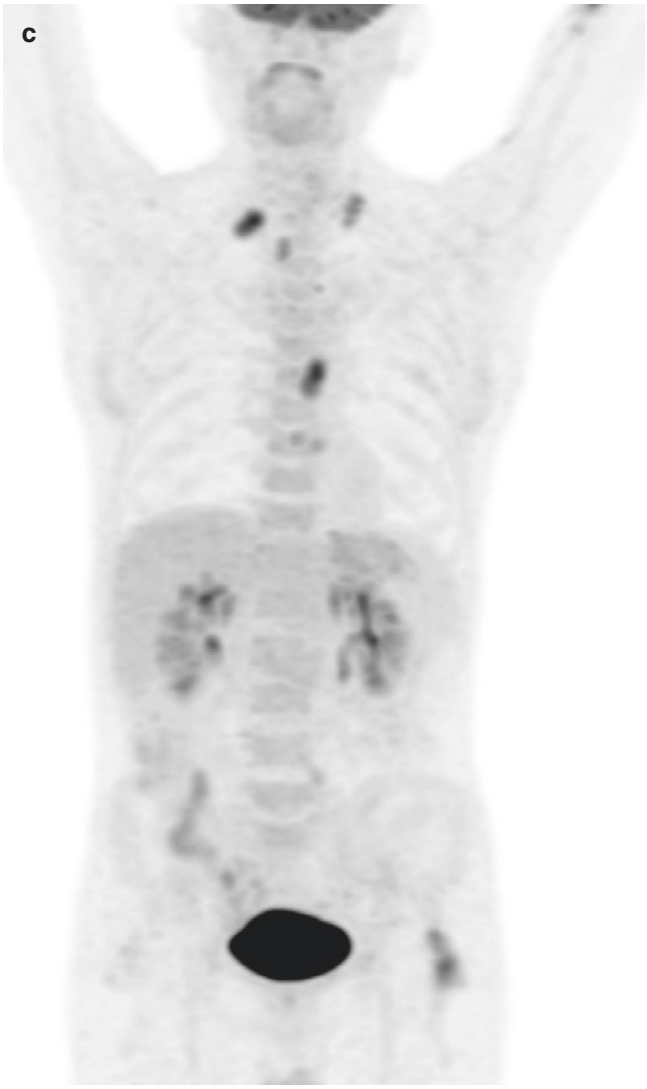

Fig. 11.4 (continued)

muscles of the esophagus. Achalasia is the most important motility disorder and is described below.

11.3.1 Achalasia

This is an uncommon disease of the esophagus affecting 0.2–0.6 per 100,000 people per year [10]. The causes of achalasia are described in Table 11.1 [11, 12]. Table 11.2 summarizes the clinical and radiological features of achalasia (Figs. 11.1, 11.2, 11.6, and 11.7) [2].

It is imperative to differentiate between idiopathic achalasia and secondary achalasia caused by malignancies, as the management and prognosis of the two conditions are different. Table 11.3 lists the differences between the two conditions [12].

11.3.2 Gastroesophageal Reflux Disease (GERD)

The term encompasses a spectrum of disorders including columnar-lined esophagus (Barrett's esophagus), reflux esophagitis, and non-erosive reflux disease. In non-erosive reflux disease, the patient is symptomatic but the esophagus is normal on endoscopy [3, 13]. GERD is the commonest cause of esophageal symptoms. Dysfunction of the lower esophageal sphincter, hiatus hernia, reduced resistance of the esophageal mucosa to ulceration, reduced esophageal and gastric emptying rates, as well as lifestyle choices such as drinking and smoking have all been established as causative factors.

Fluoroscopy has an important role in the identification of gastroesophageal reflux if performed with the correct maneuvers, and can be used as a safe as well as inexpensive test (Fig. 11.5) [14]. McCauley et al. have devised a grading of GERD based on barium esophagography (Table 11.4) [15]. In addition to reflux, fluoroscopy may also show impaired and abnormal peristalsis, slow clearance, esophagitis with scarring, lower esophageal strictures, and Barrett's esophagus.

The standard test for establishing the presence of GERD is 24-hour pH monitoring. However, in clinical practice a therapeutic trial of a proton pump inhibitor is usually the initial step [3, 13]. An endoscopy is the most accurate method for identifying the complications of gastroesophageal reflux, such as reflux esophagitis and Barrett's esophagus.

11.3.3 Hiatus Hernia

Hiatus hernia is caused by a weakness or tear of the phrenoesophageal membrane [5]. A large lower esophageal diverticulum arising from the right lateral wall of the esophagus can mimic a hiatus hernia and vice versa. There are two main types of hiatus hernia: sliding hernia and rolling/paraesophageal hernia (Figs. 11.8 and 11.9) [3] (Table 11.5).

Occasionally, there is herniation of omental fat into the thoracic cavity with the stomach in its anatomical position. This mimics a fat-containing mass in the mediastinum and is referred as a paraesophageal omental hernia.

There is a close relationship between a hiatus hernia and GERD. It is widely agreed that a hiatus hernia has major pathophysiological effects favoring gastroesophageal reflux and is contributory to esophageal mucosal injury [16].

11.3.4 Diverticulum

Diverticulum is a focal outpouching of the gastrointestinal tract wall. A diverticulum can be classified either based on its

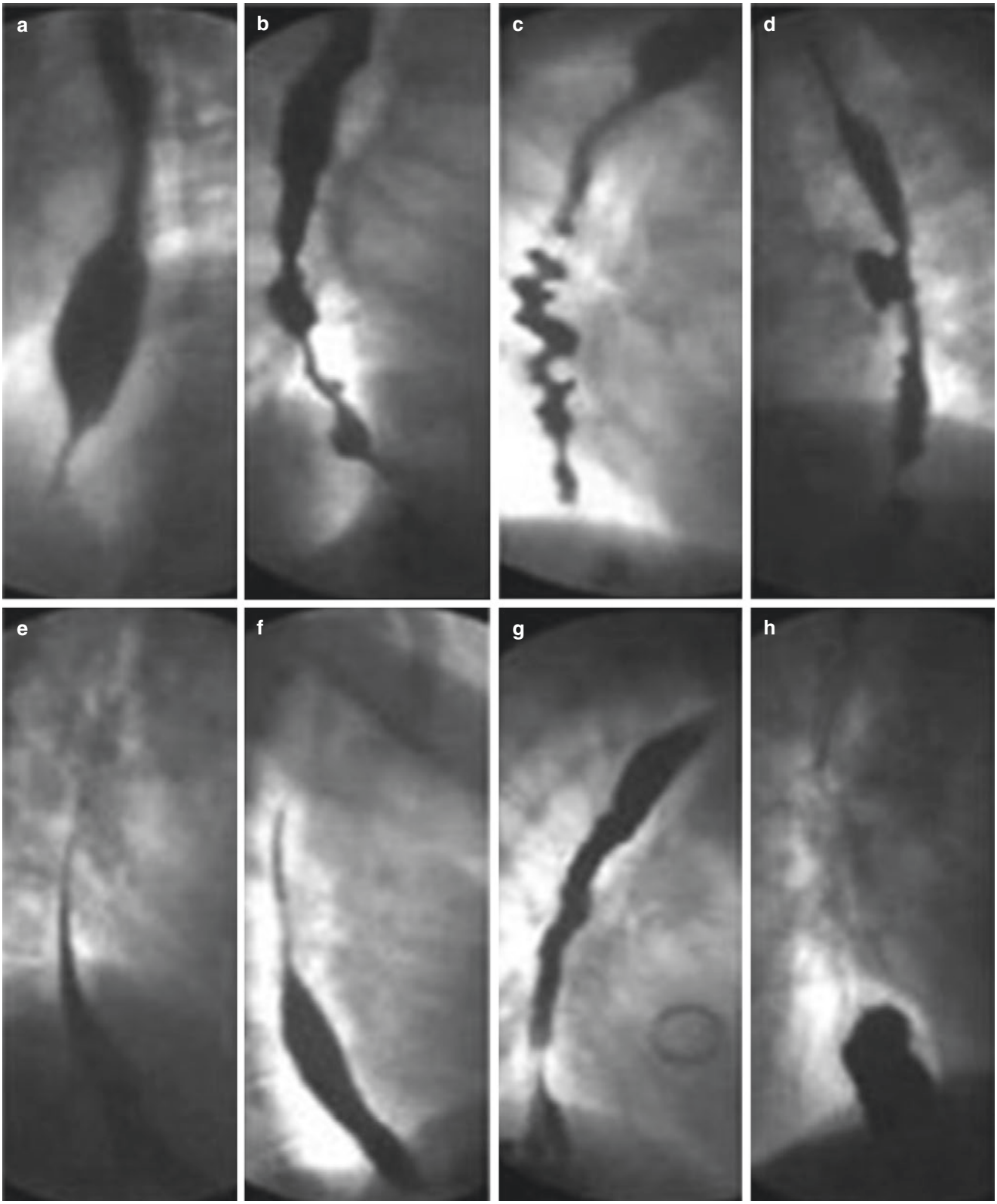

Fig. 11.5 Radiologic appearance of some motility disorders of smooth muscle portion of the esophagus. (**a**) Classical achalasia, showing a dilated esophagus and "bird beak" narrowing of the lower esophageal sphincter. (**b**) Vigorous achalasia showing diffuse spasm-like contractions in the esophageal body with closed lower esophageal sphincter. (**c**) Diffuse esophageal spasm shows typical corkscrew appearance of the lower part of the esophagus. (**d**) Mid-esophageal propulsion diverticulum with esophageal motility disorder. (**e**) Normal peristaltic sequence for comparison with slow esophageal transit. (**f**) Hypotensive (incompetent) esophageal peristalsis with slow esophageal transit through the esophagus. (**g**) Gastroesophageal reflux. (**h**) A sliding hiatal hernia. Courtesy: GI Motility online (May 2006). doi:https://doi.org/10.1038/gimo20

Table 11.1 Causes of achalasia

Idiopathic		
Secondary achalasia	Benign	Chagas disease Eosinophilic gastroenteritis Amyloidosis AAA syndrome: achalasia associated with alacrima (juvenile Sjögren's syndrome) and achlorhydria Neuropathic chronic intestinal pseudo-obstruction
	Malignant	Carcinoma of the stomach, esophagus, lung, pancreas, liver, colon, lymphoma, or mesothelioma

Table 11.2 Clinical and radiological features of achalasia

Cause	Aperistalsis of the lower esophageal segment and inadequate relaxation of LES
Demographic	No gender predilection; common in middle-aged population
Clinical symptoms	Dysphagia; worse with liquids Occasional heartburn
Diagnosis	Combination of findings on barium esophagography, manometry, nuclear examination, and endoscopy
Chest radiograph	Air-fluid level in dilated esophagus on frontal chest radiograph
Barium findings	Characteristic "bird beak" appearance of the lower end of esophagus/gastroesophageal junction Generally a proximal dilated esophagus with barium column. Whole column of barium contrast passes into the stomach when the patient is asked to subsequently drink hot or carbonated water in an erect position. This is due to immediate pronounced relaxation of the gastroesophageal junction
CT	Moderate dilatation of the esophagus not associated with wall thickening in the distal segment of the esophagus Normal wall thickness is an important feature that distinguishes idiopathic achalasia from secondary achalasia CT is also helpful in excluding squamous cell carcinoma in long-standing cases of achalasia (>20 years)
MR fluoroscopy	Advantage over barium fluoroscopy: MR can depict morphological and functional alterations of the esophagus as well as abnormalities in the wall and extraluminal structures at the same time Ultrafast sequences: steady-state precession or T1-weighted turbo fast low-angle shot to assess peristalsis

anatomical origin or the mechanism of formation. Anatomically, the "true" diverticulum contains all layers of the esophageal wall, while a "false" diverticulum does not have a muscular layer. The "pulsion" diverticulum is a false diverticulum and results from increased intraluminal pressure, while the "traction" diverticulum is a true diverticulum, usually seen in the mid-esophagus, and often results from mediastinal tuberculosis or histoplasmosis. "Pulsion" diverticulum can be of three types based on location along the esophagus: Zenker diverticulum, mid-esophageal diverticulum, and epiphrenic diverticulum. These are described in Table 11.6 (Figs. 11.10, 11.11, 11.12, and 11.13) [17].

11.3.5 Diffuse Esophageal Spasm

This is a condition caused by intermittent contraction of the mid and distal esophageal smooth muscles and is usually associated with chest pain. Patients with diffuse esophageal spasm tend to be elderly, and they present with chest pain and/or dysphagia. Diagnosis of this condition is based on manometry, and imaging in the context of appropriate symptoms. Barium swallow shows marked contractions resulting in the appearance of "curling" or "corkscrew" esophagus (Fig. 11.5c). On CT, there is circumferential marked esophageal wall thickening, more severe in the lower esophagus than in the upper esophagus [18] (Fig. 11.14).

11.4 Varices

Varices are commonly encountered in imaging due to increasing prevalence of liver diseases and consequent portal hypertension. The clinical and radiological features of varices are described in Table 11.7 (Fig. 11.15) [3].

11.5 Dysphagia Lusoria

This condition arises when the esophagus is compressed by a congenital aberrant right subclavian artery. Diagnosis of this condition is considered in a symptomatic patient after excluding other causes such as malignancy. Contrast-enhanced CT and MRI can identify the aberrant artery and its associated mass effect. On fluoroscopy, there is an oblique tubular extrinsic impression seen in the upper esophagus. Treatment is symptomatic unless the symptoms are refractory and severe [8].

11.6 Esophageal Strictures

Strictures of the esophagus can be broadly classified into benign and malignant etiologies. The causes and imaging features are described in Table 11.8 [19, 20]. The common

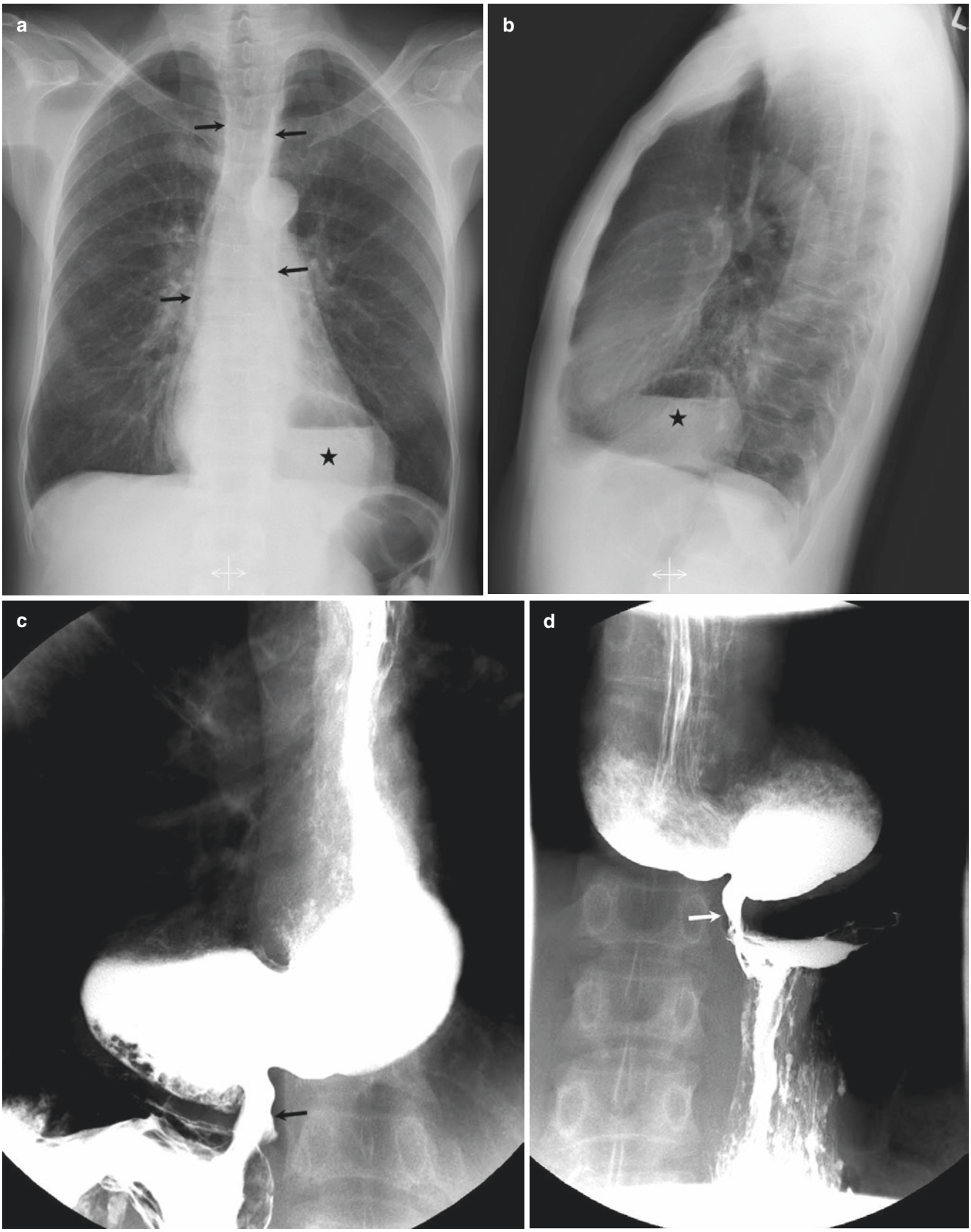

Fig. 11.6 (**a**) Frontal radiograph shows dilated esophagus as outlined by the interface (arrows) between air in the esophagus and adjacent lung, with an air-fluid level (asterisk). (**b**) Lateral radiograph shows thickening of posterior tracheal wall and an air-fluid level (asterisk). (**c**, **d**) Esophagogram images with thin barium show dilated tortuous distal esophagus with a smooth narrowing of the gastroesophageal junction (arrow)

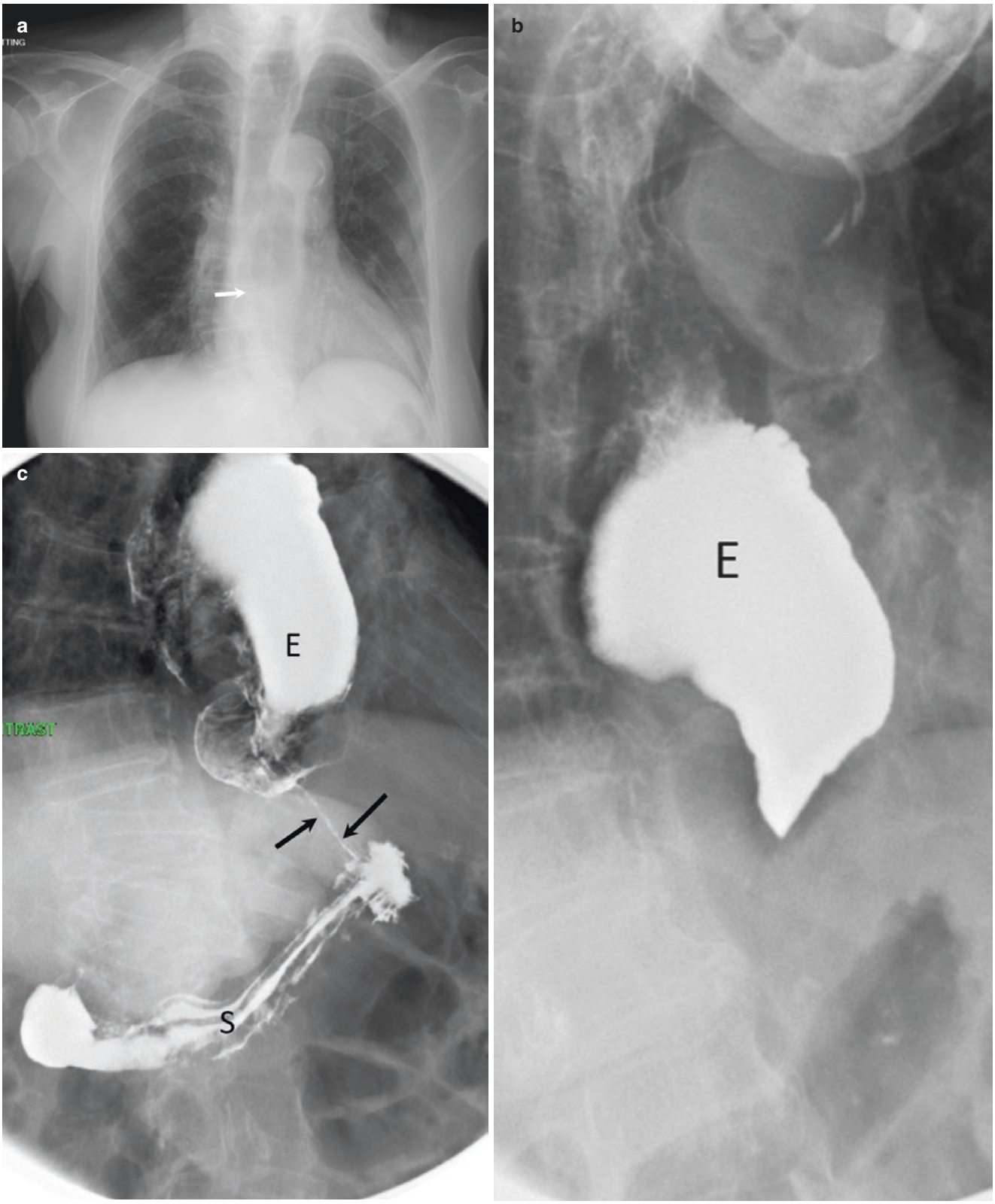

Fig. 11.7 Secondary achalasia in a 78-year-old woman. (**a**) Frontal chest radiograph shows a dilated esophagus with an air-fluid level (arrow). (**b**, **c**) Esophagogram images with thin barium show dilated tortuous distal esophagus with long stricture of gastroesophageal junction (arrows) and proximal shouldering. (**d**–**f**) CT images show dilated esophagus with a small enhancing mass at gastroesophageal junction (arrow). *E* esophagus

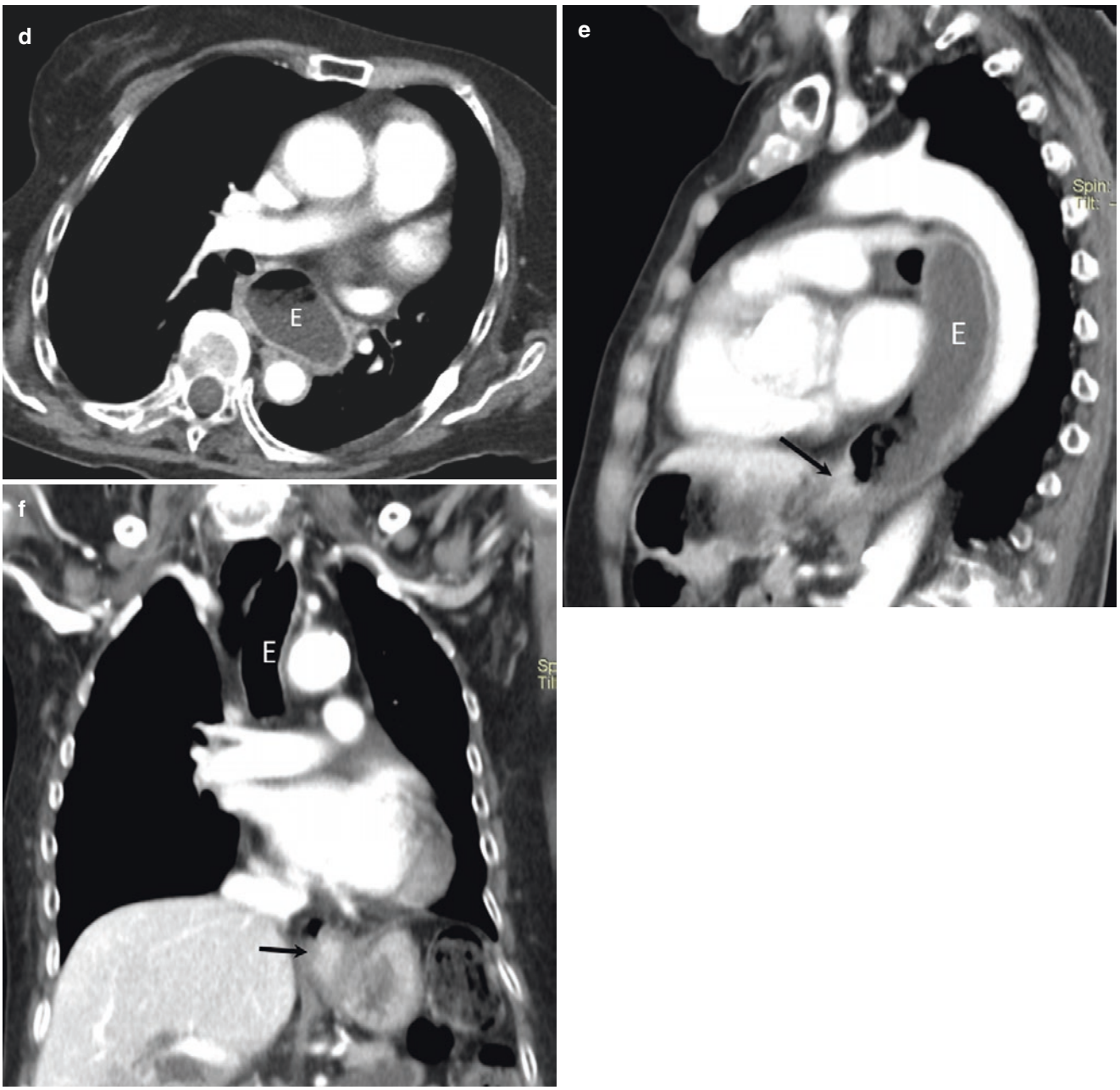

Fig. 11.7 (continued)

Table 11.3 Differences between achalasia and secondary achalasia

Pseudo-achalasia	Achalasia
Elderly patient	Young to middle age
Short-duration symptoms	Long-standing symptoms
Mild to moderate esophageal dilatation	Moderate to severe esophageal dilatation
Asymmetric thickening or mass causing narrowing of the gastroesophageal junction	Mild but symmetric thickening
Usually >10 mm wall thickening	<10 mm wall thickening

Table 11.4 Grading of GERD

Grade	Description
I	Reflux into distal esophagus only
II	Reflux extending above the carina
III	Reflux into the cervical esophagus
IV	Free persistent reflux into the cervical esophagus with a wide open cardia (chalasia)
V	Reflux of barium with aspiration into the trachea or lungs
D	Delayed reflux—barium is seen in the esophagus on delayed films

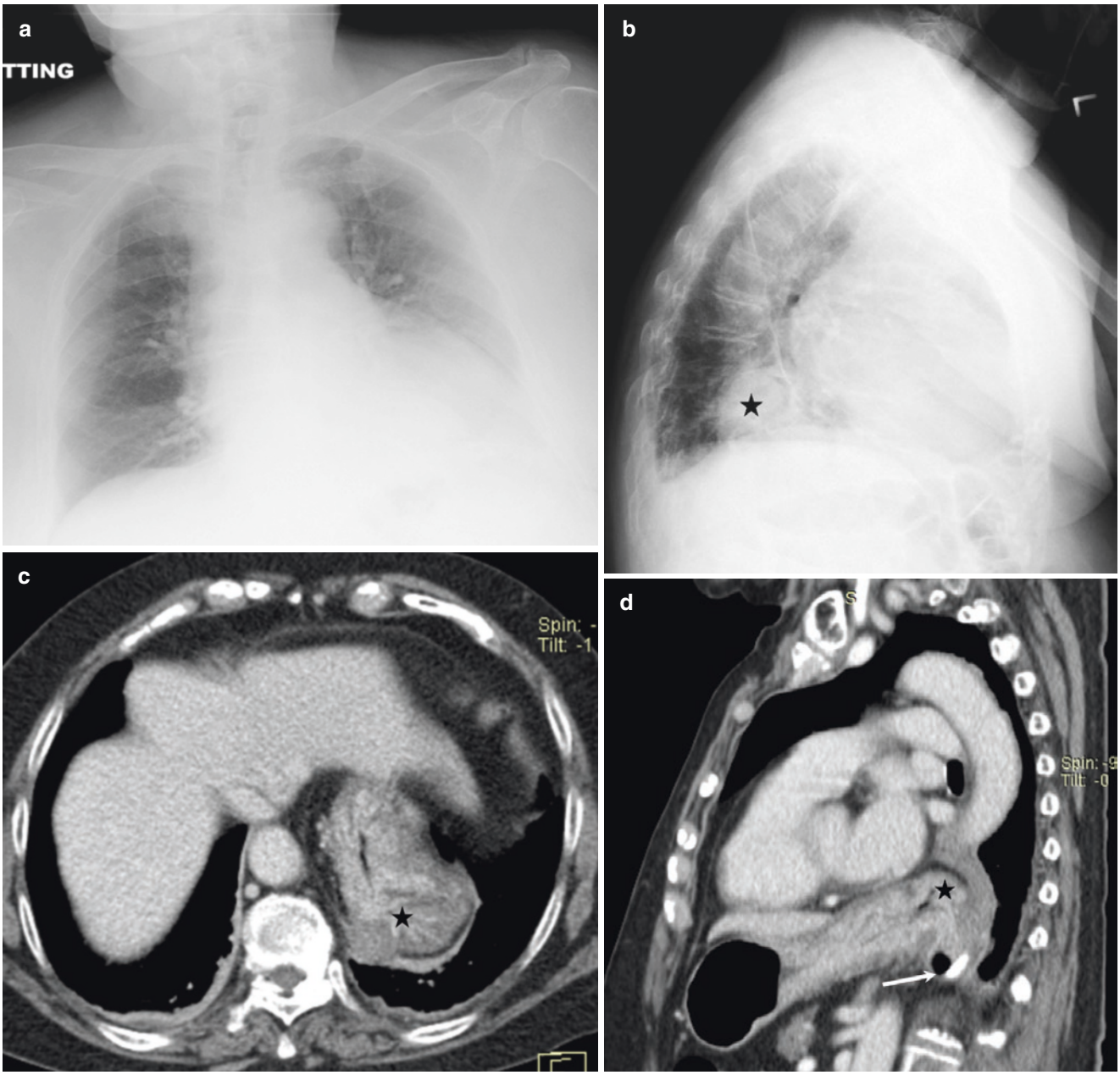

Fig. 11.8 Rolling hiatal hernia. (**a**, **b**) Frontal and lateral chest radiographs show a retrocardiac opacity (asterisk) with curvilinear lucency around it. (**c**, **d**) Axial and sagittal CT images show herniated segment of the stomach (asterisk) along the lower esophagus. A tablet is lodged at the gastroesophageal junction (arrow)

causes of a benign stricture are long-standing reflux, radiation, long-standing gastric tube placement, chronic medication-induced esophagitis, epidermolysis bullosa, and eosinophilic esophagitis.

11.7 Barrett's Esophagus

Metaplasia into specialized non-secretory columnar epithelium from normal esophageal squamous epithelium is the primary feature of a Barrett's esophagus. The condition arises as a complication of long-term severe GERD and is a risk factor for adenocarcinoma. These patients may have a hiatal hernia, severe lower esophageal sphincter hypotension, and esophageal contraction abnormality.

Typical appearance in a barium swallow in majority of Barrett's esophagus is a peptic stricture in the distal esophagus (Fig. 11.16). However, a small percentage of patients with Barrett's esophagus develop strictures in the upper or mid-esophagus. Double-contrast esophagography may occasionally reveal a reticular pattern of the mucosa. Endoscopy and biopsy are essential for diagnosis. The junction between the two mucosa manifests as a ring and is also the point where most complications, such as ulceration and secondary stricture formation, occur.

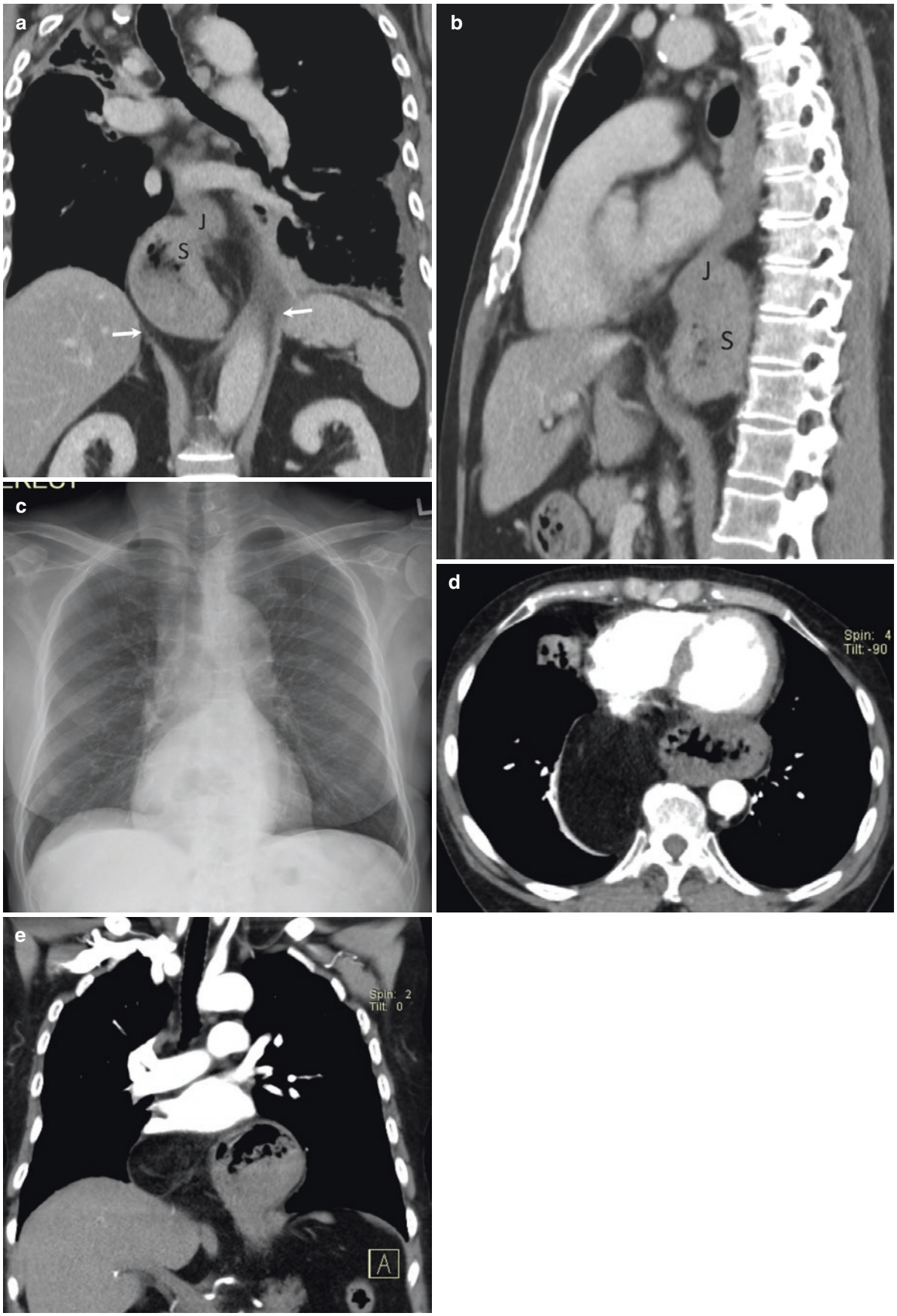

Fig. 11.9 Sliding hiatal hernia. (**a**, **b**) Coronal and sagittal CT images show herniated segment of the stomach (S) across the wide hiatus (arrows). The gastroesophageal junction (J) is located above the hiatus differentiating sliding hernia from rolling hernia. Sliding hernia with fat in another patient. (**c**) Frontal chest radiograph shows a large retrocardiac opacity. (**d**, **e**) Axial and coronal CT images show herniation of the stomach along with peritoneal fat

Table 11.5 Types of hiatus hernia

Type	Sliding	Rolling/paraesophageal
Anatomy	Gastroesophageal junction is above the esophageal hiatus of the diaphragm	Variable part of the stomach herniates into the chest, but gastroesophageal junction is below the diaphragm
Frequency	90–99%	1–10%
Complications	Reflux esophagitis, Barrett's esophagus	Higher chances of volvulus, incarceration, or strangulation of herniated segment
Diagnosis	On endoscopy: Z line is visible at approximately 40 cm from incisors. Identification at 38 cm or less indicates sliding hernia	On barium swallow: prolapsed fundal portion is seen above the diaphragm

Table 11.6 Three types of esophageal diverticulum

	Zenker	Mid-esophageal	Epiphrenic
Location	Posteriorly at site of Killian's dehiscence: superior boundary is thyropharyngeal muscle, and inferior boundary is cricopharyngeal muscle	Found in the mid-esophagus	Lower esophagus (within 10 cm of gastroesophageal junction), along the lateral wall; right more than left
Demographics	Older women	Young population	No age predilection
Imaging	Appears as triangular contrast-filled pouch posteriorly at the site of Killian's dehiscence between horizontal and oblique components of the cricopharyngeal muscle	Secondary to fibrosis from infected lymph nodes. Associated with calcified/ inflamed lymph nodes	CT shows a thin-walled, air-filled, or air-fluid-filled structure arising from the esophagus Common association with a hiatus hernia and should be differentiated from the latter as well as mediastinal abscess and tumors

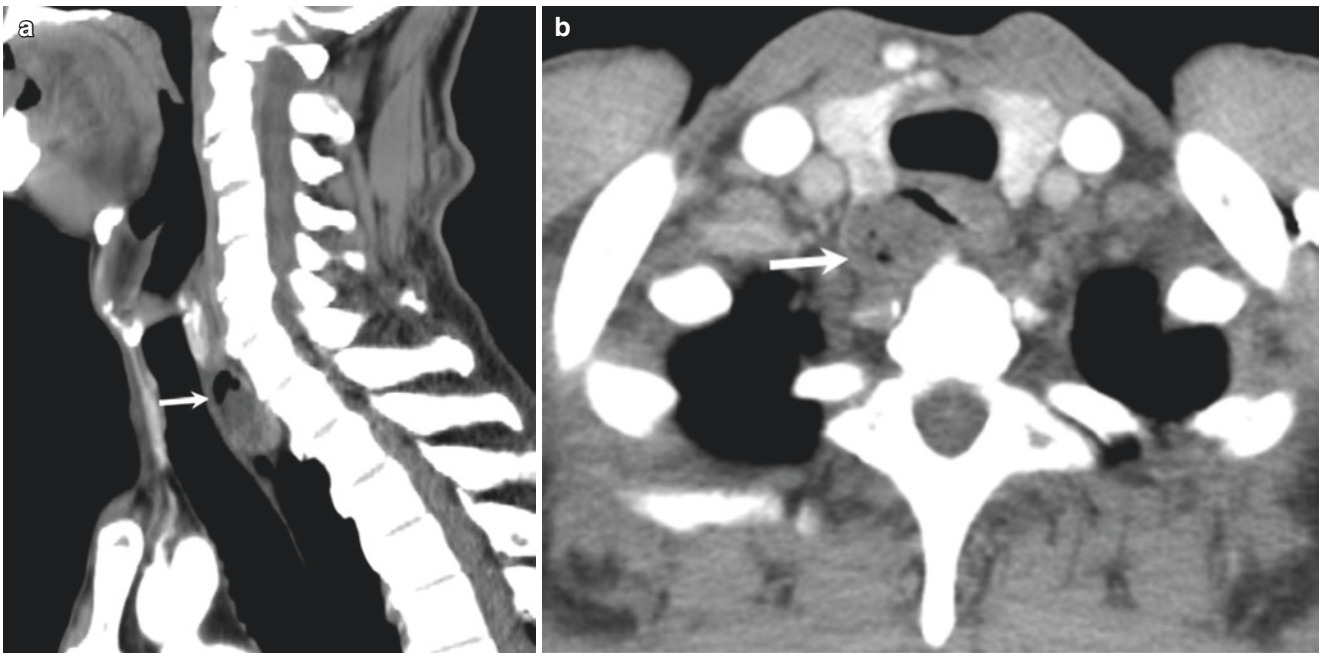

Fig. 11.10 Zenker diverticulum. (**a**, **b**) Sagittal and axial CT images demonstrate a diverticulum (arrow) arising from the midline of the posterior wall of the distal pharynx near the pharyngoesophageal junction

Long-segment (>3 cm) and short-segment (<3 cm) Barrett's esophagus is found in 5% and 15% of patients, respectively, undergoing endoscopy for GERD [21]. A major concern for this condition is its association with adenocarcinoma, as approximately 0.5% of patients with Barrett's esophagus may develop adenocarcinoma per year. The progression occurs through increasingly worse grades of histologic dysplasia [22].

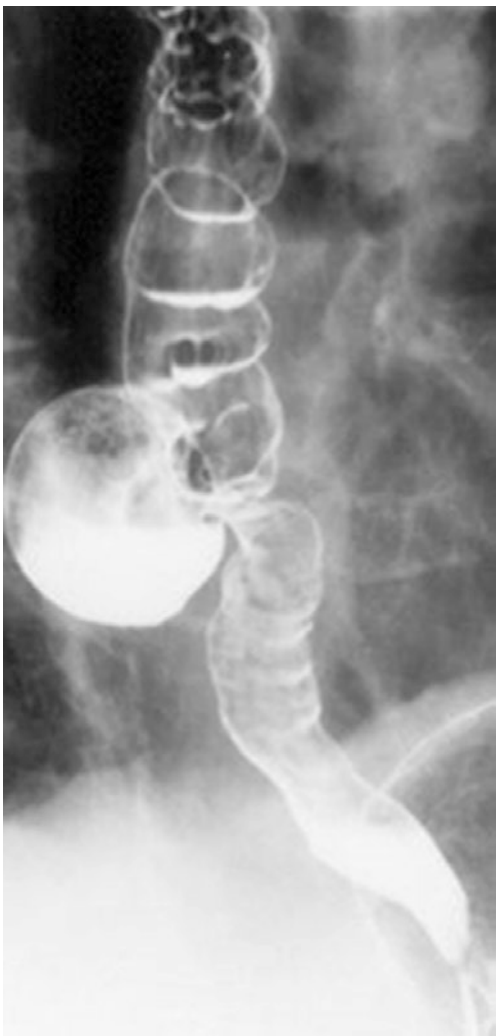

Fig. 11.11 Pulsion diverticulum. Barium swallow frontal spot image shows a large mid-esophageal pulsion diverticulum. Courtesy: GI Motility online (May 2006). doi:https://doi.org/10.1038/gimo29

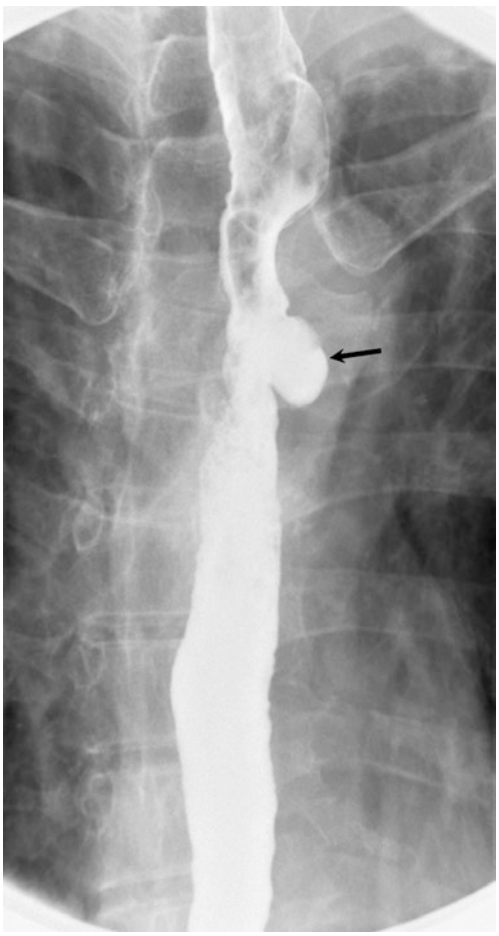

Fig. 11.12 Traction diverticulum in the mid-esophagus. A frontal barium-filled spot image shows a contrast-filled outpouching from the lateral wall of the esophagus (black arrow)

11.8 Benign Esophageal Tumors

11.8.1 Leiomyoma

This is the most common benign esophageal tumor and accounts for more than 50% of all benign esophageal tumors. This is in contrast to the rest of the gastrointestinal tract, where gastrointestinal stromal tumors predominate. Leiomyomas are usually solitary lesions, with 3–4% of the patients having multiple lesions. In children, these are usually associated with Alport syndrome [23].

Patients are usually asymptomatic but may present with dysphagia. On CT, an intraluminal well-defined and homogeneous mass of soft-tissue attenuation is the most common appearance. A few punctate calcifications can also be seen (Fig. 11.17). The surrounding mediastinal fat planes are preserved. Confirmation is usually with EUS, which shows the mass arising from the muscularis mucosa or less commonly the muscularis propria [2].

11.8.2 Fibrovascular Polyp

Fibrovascular polyp is a rare benign intramural tumor covered by normal squamous epithelium. It usually develops in the upper third of the esophagus, near the level of the cricopharyngeus, and is commonly seen in older men presenting with symptoms of long-standing dysphagia, vomiting, and weight loss. On CT, there is a wide range of attenuation depending on the ratio of adipose tissue and fibrovascular tissue. If the former predominates, intraluminal esophageal mass with fat attenuation is considered diagnostic. MRI typically demonstrates high T1 signal depicting fat and mucoid

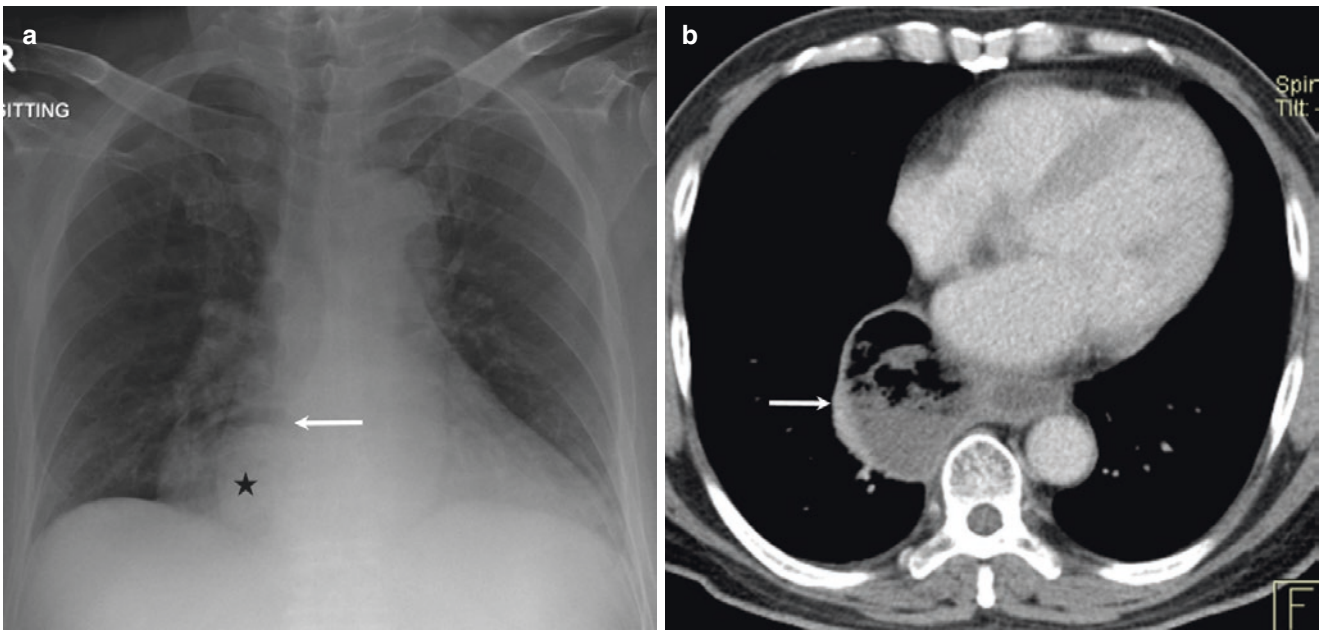

Fig. 11.13 A 53-year-old woman with an epiphrenic diverticulum. (**a**) Frontal radiograph shows displacement of azygo-esophageal line (arrows). (**b**) Axial CT image demonstrates the epiphrenic diverticulum (arrow)

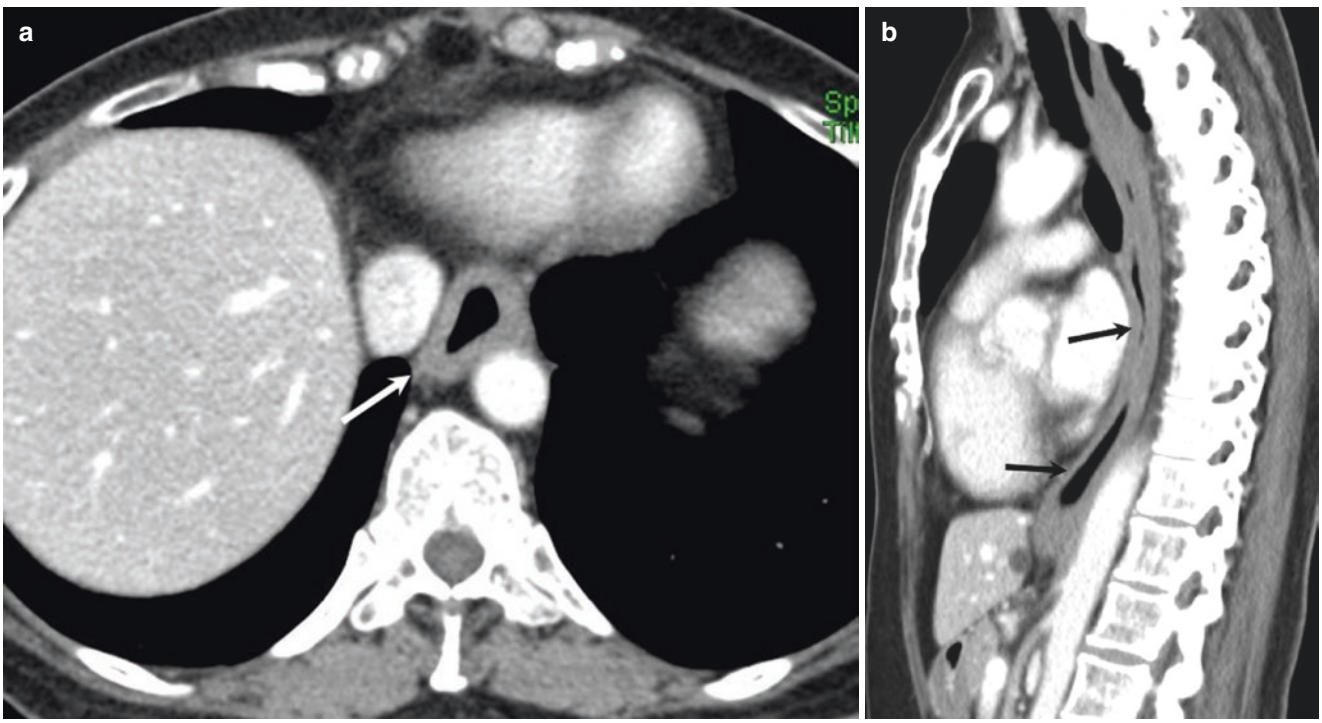

Fig. 11.14 Diffuse esophageal spasm. (**a**, **b**) Axial and sagittal CT images show long-segment diffuse circumferential esophageal thickening (arrows) involving the mid and lower esophagus with more severe thickening of the lower esophagus. Endoscopy did not reveal any mass or stricture

Table 11.7 Clinical and radiological features of esophageal varices

Definition	Dilatation of submucosal veins which act as collaterals in the presence of obstruction elsewhere	
Types	Uphill, common	Downhill, rare
Location	Lower esophagus	Upper or mid-esophagus
Pathology	Blood flows in superior direction from the left gastric veins of the portal system to systemic venous tributaries; usually of the azygos system in the context of portal hypertension and underlying cirrhosis	Superior vena cava obstruction, blood from the head and neck is redirected via the esophagus to the azygos vein
Imaging	Characteristic serpiginous filling defects best seen on prone barium swallow images Large varices can present as a posterior mediastinal mass on chest radiographs CT is diagnostic	

secretion, while T2-weighted images show intermediate signal intensity in the soft tissue and muscle within the lesion [2, 3].

11.8.3 Other Rarer Benign Conditions

Although not a true neoplasm, glycogenic acanthosis is worth mentioning as this is seen in a substantial proportion of symptomatic patients undergoing upper gastrointestinal endoscopy. This manifests as multiple mural nodules, usually measuring 2–5 mm. This condition is of no clinical consequence although it may be associated with GERD, celiac disease, and rarely Cowden syndrome. Multiplicity of lesions in this condition is helpful in fluoroscopic diagnosis [3, 24].

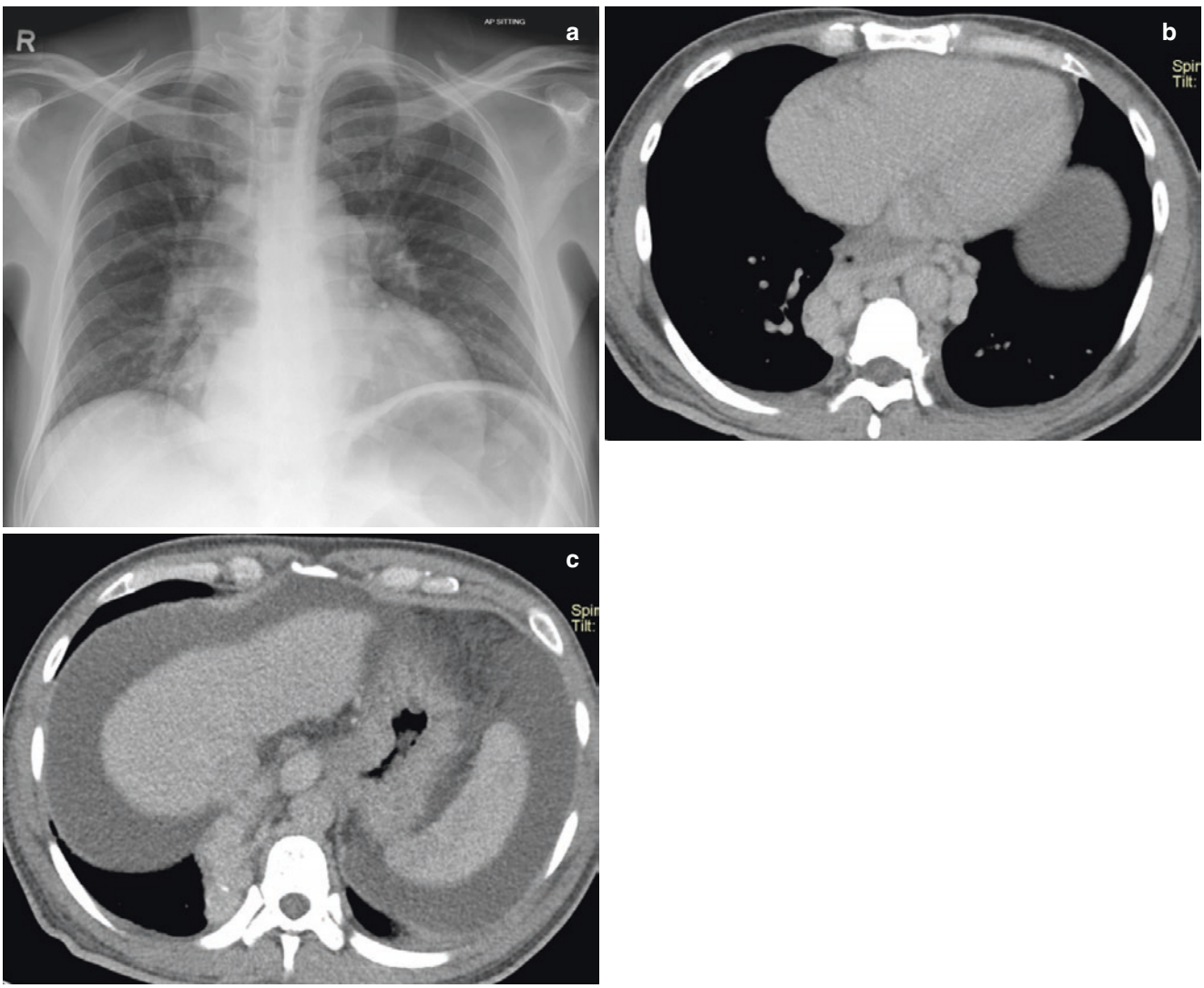

Fig. 11.15 Uphill varices. (**a**) Frontal radiograph shows a large right paraspinal opacity. (**b**, **c**) Axial CT images in venous phase show dilated tortuous varices with liver diseases and ascites

Papilloma is another uncommon benign tumor of the esophagus, usually appearing as a solitary sessile polyp and rarely measuring more than 1 cm. Due to its non-specific appearance, biopsy is required to distinguish a papilloma from an early adenocarcinoma or squamous cell carcinoma [3].

11.8.4 Foregut Duplication Cyst

These are uncommon and constitute about 0.5–2.5% of all esophageal tumors [25]. Majority of duplication cysts are located in the lower esophagus with the rest distributed equally between the upper and middle thirds of the esophagus (Figs. 11.18 and 11.19) [25]. These cysts are of congenital origin and may be attached to the esophagus in a

Table 11.8 Radiological features of benign and malignant stricture

Type	Barium	CT
Benign	• Long-segment involvement • Outpouching of ulcer crater beyond the contour (exoluminal) • Smooth rounded and deep ulcer crater • Smooth ulcer mound	• Smooth long-segment mucosal thickening • Usually no lymphadenopathy
Malignant	• Short-segment involvement • Ulcer does not protrude beyond the esophageal contour (endoluminal) • Irregular and shallow ulcer crater • Nodular and angular ulcer mound	• Short-segment eccentric or circumferential thickening • Advanced stage tumors with invasion of adjacent structures • Lymphadenopathy

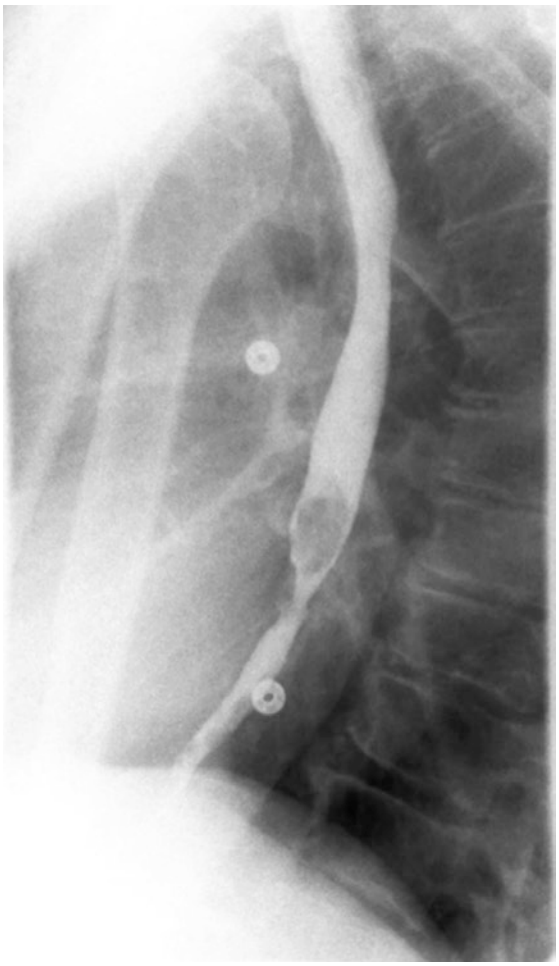

Fig. 11.16 Barrett's esophagus. Spot image of barium swallow shows a long-segment inflammatory stricture of distal esophagus due to reflux disease. Endoscopy revealed Barrett's esophagus

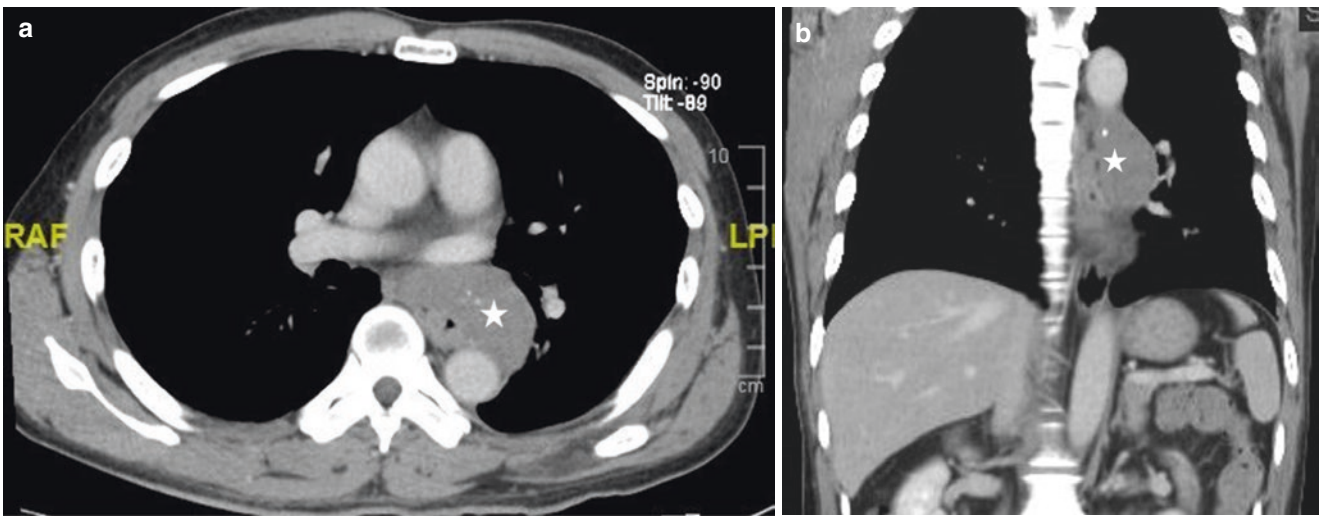

Fig. 11.17 Leiomyoma. (**a**, **b**) Axial and sagittal CT images reveal a homogenous well-defined soft-tissue mass (asterisk) arising from the outer wall of the esophagus, with foci of calcification

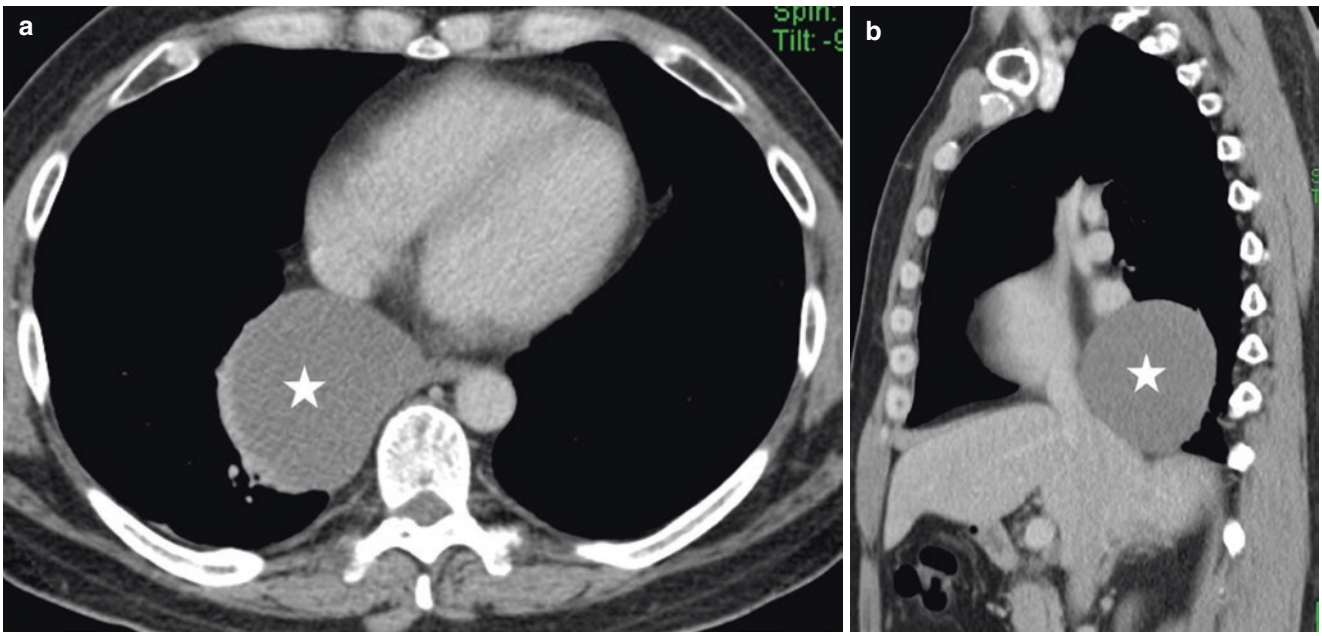

Fig. 11.18 Foregut duplication cyst. (**a**, **b**) Axial and sagittal CT images reveal a homogenous well-defined cystic posterior mediastinal mass in close proximity to the lower esophagus (asterisk)

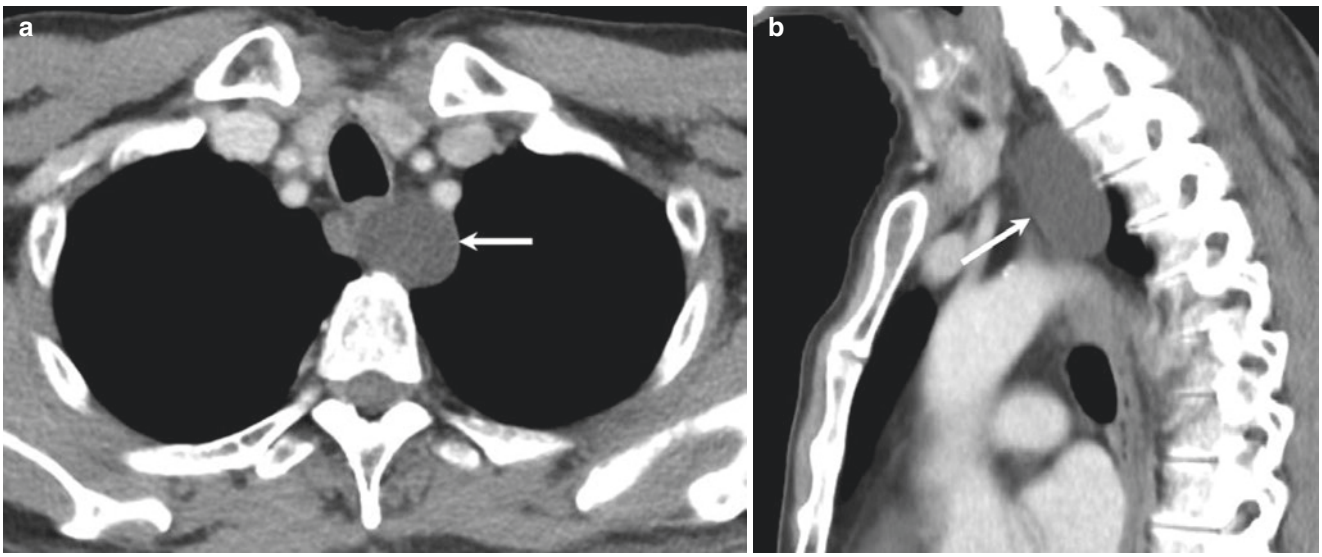

Fig. 11.19 Foregut duplication cyst. (**a**, **b**) Axial and sagittal CT images reveal a homogenous elongated well-defined cystic mass (arrow) in close proximity to the esophagus

paraesophageal location or located within the esophageal wall [26]. Table 11.9 describes the radiological features of foregut duplication cyst [26–28]. Dysphagia is secondary to the mass effect exerted by the cyst on adjacent structures. Although CT cannot definitely differentiate an esophageal duplication cyst from other benign paraesophageal lesions such as abscess, chronic hematoma, neurofibroma, lipoma, leiomyoma, or other foregut duplications, it can often suggest a presumptive diagnosis [29]. Esophageal duplication cyst usually has a thicker wall as compared to the bronchogenic cyst, which has an imperceptible wall [30].

Table 11.9 Imaging features of foregut duplication cyst

Modality	Findings
Chest radiograph	Middle or posterior mediastinal mass
Barium swallow	Smooth, rounded impression on the esophagus
Tc99m sodium pertechnetate radionuclide scan	Helpful in children, in whom 50% of thoracic duplication cysts contain ectopic gastric mucosa
CT	Homogeneous, low-attenuation mass with smooth borders

11.9 Malignant Esophageal Tumors

11.9.1 Esophageal Carcinoma

It is the sixth most common cause of death in the world, with increasing incidence [31–33]. Majority of esophageal malignancies are squamous cell carcinoma or adenocarcinoma. As discussed earlier, Barrett's esophagus is a well-recognized premalignant condition, and patients with Barrett's esophagus have a 30- to 50-fold increased risk of developing adenocarcinoma.

Age, male gender, GERD symptoms, Caucasian, obesity, family history, and use of lower esophageal sphincter-relaxing medications are the known risk factors. Potential factors with negative association include dietary patterns and use of aspirin or nonsteroidal anti-inflammatory drugs.

A barium study can detect the tumor as a stricture or ulcerative mass, but further endoscopy and biopsy are required for direct visual as well as histological confirmation. Once a stricture is identified and appears unequivocally benign, with symmetrical, smooth narrowing, and a gradual tapering to normal caliber, malignancy can be confidently excluded [20]. When an esophageal stricture shows an ulcerated, irregular mucosa and shouldered shelf-like margins or "shouldering", malignancy is suspected (Fig. 11.20).

Table 11.10 lists the various modalities used in diagnosis and staging of esophageal cancer with the respective benefits and limitations of each modality.

The eighth edition of the American Joint Committee on Cancer (AJCC) staging of epithelial cancers of the esophagus and esophagogastric junction presents separate classifications for clinical (cTNM), pathologic (pTNM), and postneoadjuvant (ypTNM) stage groups [34–37]. CT and PET-CT serve important roles in evaluating the mediastinal invasion by esophageal cancer (Table 11.11) (Figs. 11.21, 11.22, and 11.23) [37, 38].

Endoscopic ultrasound has an important role in evaluating patients without nodal or metastatic disease. A healthy patient with T2N0M0 tumor can opt for surgery, whereas a patient with more advanced tumor will require neoadjuvant chemotherapy to reduce disease burden prior to surgery [37].

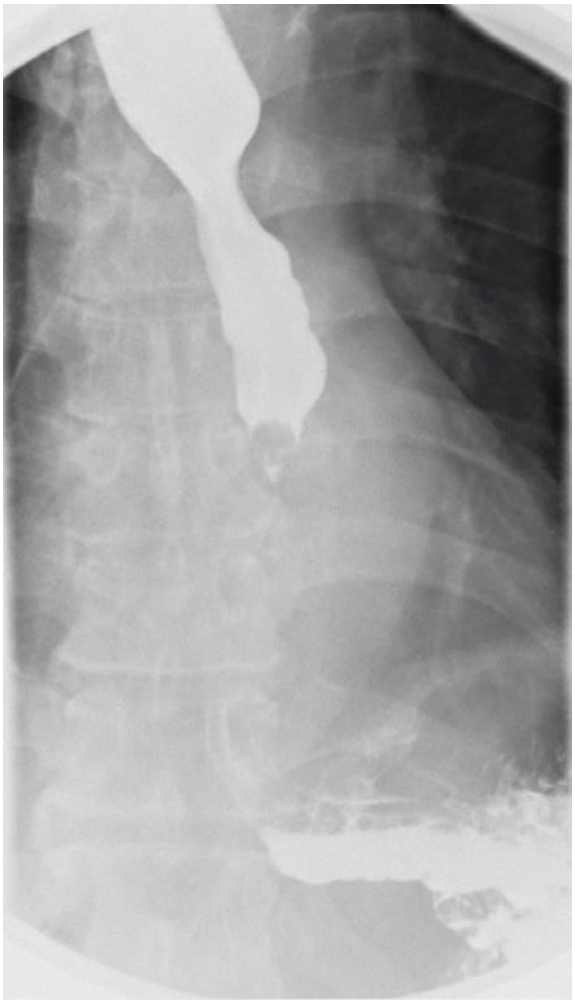

Fig. 11.20 Esophageal cancer. Spot images of a barium swallow study reveal a long-segment irregular ulcer and shouldering, involving the mid to distal esophagus with proximal esophageal dilatation

Nodal Disease

- Nodes with short-axis diameter of more than 1 cm on CT are considered malignant.
- Common sites: periesophageal, subcarinal, left gastric, and celiac stations.
- Most frequent sites of metastasis are non-regional nodal stations: supraclavicular and retroperitoneal. The left supraclavicular nodal involvement is more commonly seen in gastric cancer.
- The size criterion for lymph node metastasis is generally not applicable to esophageal cancers because of microscopic involvement of normal size lymph nodes.
- In rare instances, small periesophageal duplication cysts can mimic a necrotic node, and caution must be exercised before labeling it as such because it may upstage the disease.

Table 11.10 Diagnostic tools to evaluate esophageal cancer

Modality	Benefits	Disadvantages	Inference
Barium study	Can detect early tumor	Operator dependent Factors like inadequate distension can limit diagnosis Still requires endoscopy for histology	Can be used as a screening and early diagnostic tool but would still require other cross-sectional modalities and endoscopy for confirmation and staging
Endoscopy	Can get tissue for histology in the same sitting	Operator dependent	If T1 disease is diagnosed, patient can undergo endoscopic mucosal resection
CT	Easily available Better at detecting lymph nodes and other organ involvement	Less sensitive than EUS/PET-CT Unable to delineate layers of esophageal wall	Useful in distinguishing T1 vs. T3/T4 disease (invasion of structures)
EUS	Superior to CT and PET-CT for T staging (T1/T2/T3 tumors) Superior for nodal disease	Less specific than CT/PET-CT Peritumoral edema leads to over staging	If tumor not traversable by standard echo endoscope, T stage is almost always T3 or T4
PET-CT	Better at detecting metastatic disease to nodes and other organs Higher sensitivity for nodal disease, less specificity	T1 disease usually not detected False-positive result in esophagitis or GERD Same limitation as CT in terms of mural invasion	If tumor is not detected—in 70% of such cases—it is T2 or less

Table 11.11 CT signs of mediastinal organ invasion

Pericardium	• Loss of fat plane at the level of the tumor with the pericardium; the fat plane above and below the tumor is preserved • Pericardial thickening • Pericardial effusion • Indentation on the heart
Aorta	• Tumor abutting more than 90° of the aortic circumference • Obliteration of fat at the junction of the esophagus, aorta, and spine
Airways	• Indentation or protrusion into airways • Loss of fat planes at the level of tumor, while the fat planes above and below are preserved • Displacement of airways

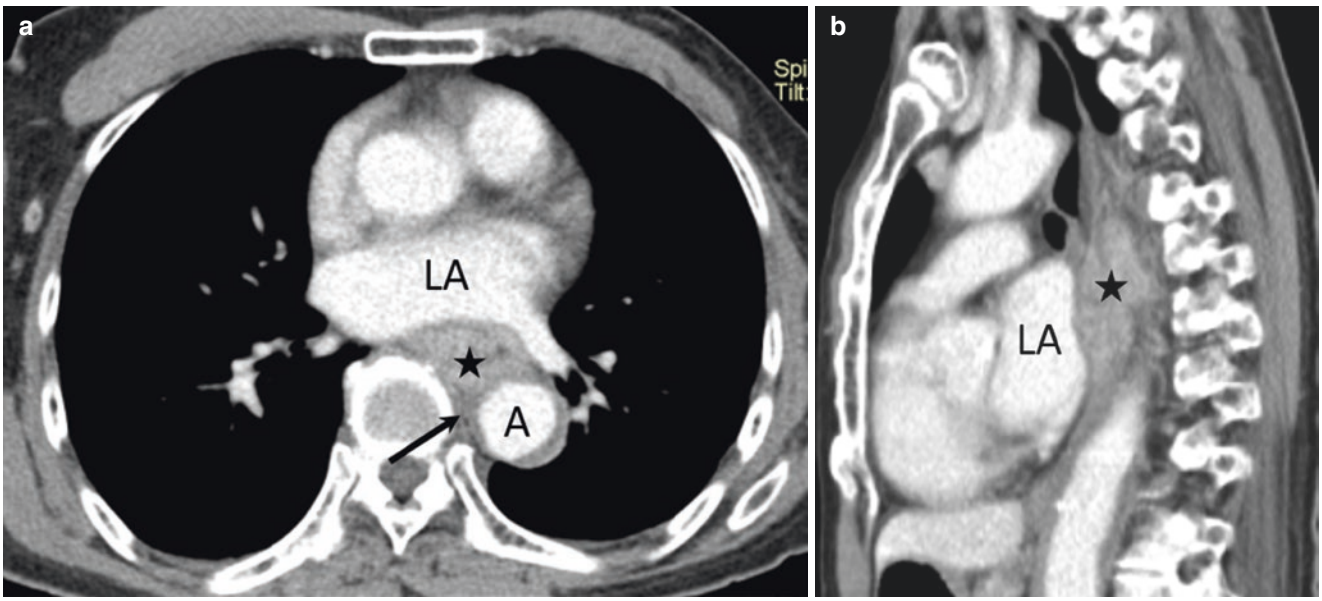

Fig. 11.21 Pericardium and aortic involvement by esophageal cancer. (**a**, **b**) Axial and sagittal CT images show mid-esophageal mass (asterisk) indenting the left atrium. Although the mass is in contact with less than half of the aortic circumference, there is loss of triangular fat (arrow) between the spine, mass, and aorta suggesting a high likelihood of aortic involvement. *LA* left atrium, *A* aorta

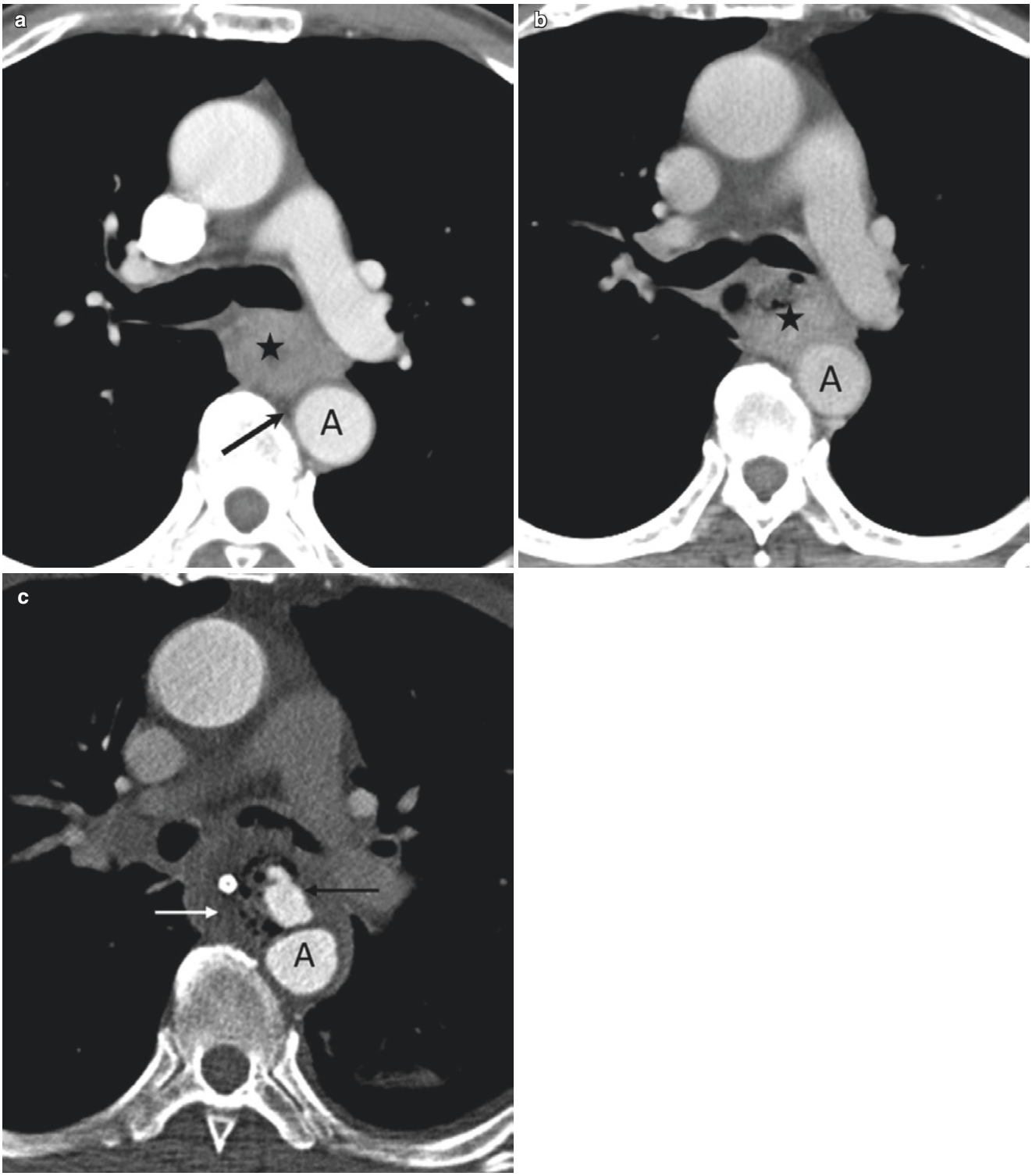

Fig. 11.22 Progressive involvement of aorta and formation of aorto-esophageal fistula. (**a**) Staging axial CT image shows circumferential thickening of the mid-esophagus (asterisk) with anterior bowing of the left bronchus suggesting airway involvement but preservation of triangular fat (arrow). (**b**) Axial CT images 6 months later show ulcerative mass (asterisk) with involvement of the aorta as suggested by loss of triangular fat. (**c**) Follow-up CT aortogram when patient presented with hematemesis shows an aorto-esophageal fistula (black arrow). *A* aorta

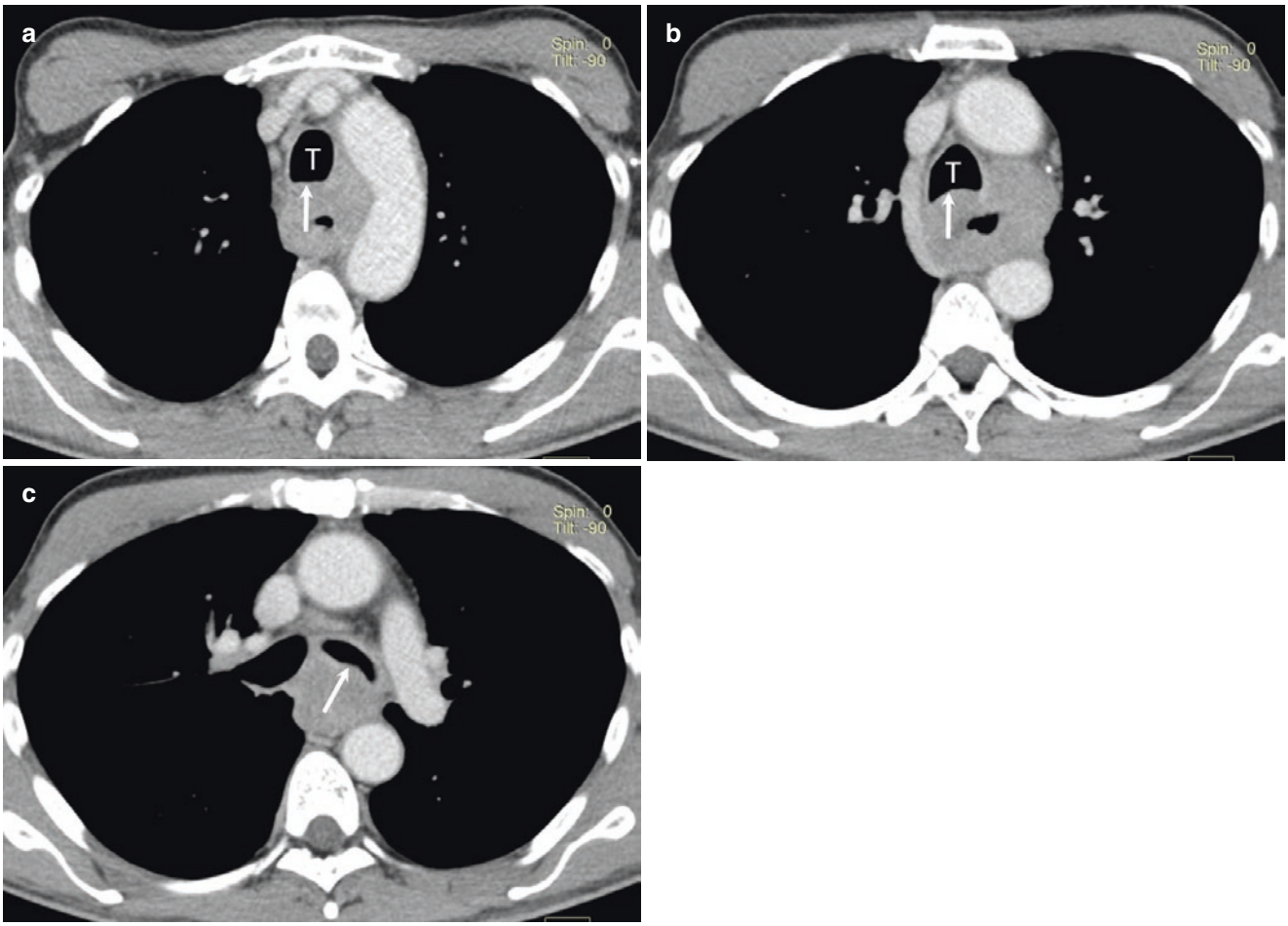

Fig. 11.23 Airway involvement but sparing of the aorta. (**a**–**c**) Axial CT images show an upper-mid-esophageal mass with bowing of the posterior tracheal wall and projecting in the left main bronchus suggesting airway involvement (arrow). Aorta is not involved. *T* trachea

11.10 Other Esophageal Malignancies

11.10.1 Small-Cell Carcinoma

This is a rare and highly aggressive type of esophageal cancer. It tends to occur in elderly males and manifests clinically as rapidly progressive dysphagia, odynophagia, weight loss, and rarely symptoms related to ectopic hormone production. It metastasizes early and has a poor prognosis [39]. Most patients receive palliative treatments such as esophageal stenting. CT shows irregular eccentric wall thickening and extensive nodal metastasis to the mediastinum, supraclavicular region, and upper abdomen [40].

11.10.2 Leiomyosarcoma

This is a rare lesion accounting for less than 1% of all esophageal cancers and is usually seen in middle-aged or older individuals. It carries a better prognosis than squamous cell carcinoma as it is slow growing with late metastasis. The growth pattern is either polypoidal or infiltrative (Table 11.12) [41].

Table 11.12 Imaging features of leiomyosarcoma

Location	Mid and distal third
CT	Thickening of the esophageal wall Soft-tissue mass containing areas of low attenuation associated with necrosis, exophytic components, and extraluminal gas or orally administered contrast agent within the tumor Two types: • Polypoidal: bulky nonobstructing intraluminal mass with large exophytic component should be considered leiomyosarcoma • Infiltrative: indistinguishable from other infiltrating tumors
MR	Mass with similar signal intensity to skeletal muscle on T1w and higher T2w signal. Signal voids within mass can be seen due to extraluminal gas

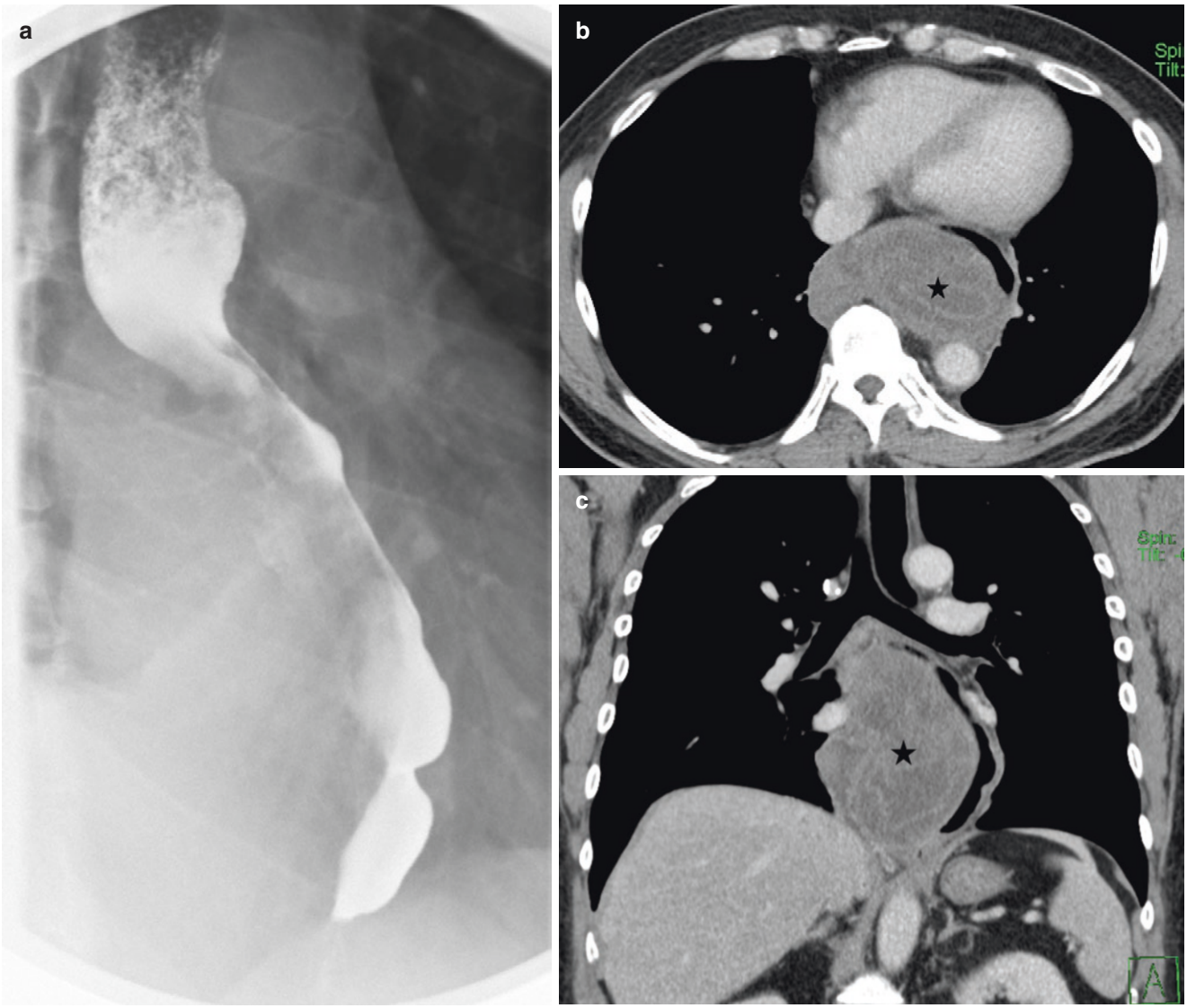

Fig. 11.24 Gastrointestinal stroma tumor. (**a**) Barium spot view shows a submucosal eccentric mass in the mid-esophagus causing luminal narrowing and proximal intraluminal stasis. (**b**, **c**) Contrast-enhanced axial and coronal CT images demonstrate a heterogeneous enhancing lower esophageal eccentric mass (asterisk) causing displacement and distortion of the esophageal lumen

11.10.3 Gastrointestinal Stromal Tumor (GIST)

These are rare mesenchymal tumors, which are considered to arise from a precursor of interstitial cells of Cajal, normally seen in the myenteric plexus [42]. On CT, these appear as well-defined hypervascular enhancing, either extraluminal or intraluminal, masses [43]. The smaller tumors are homogeneous, but the larger lesions may demonstrate heterogeneity with areas of necrosis, hemorrhage, and cystic degeneration (Fig. 11.24). GISTs may also develop punctate calcifications on follow-up CT examination (Fig. 11.25).

Other malignancies like lymphoma, primary malignant melanoma, and malignant spindle cell tumor are extremely rare without specific imaging features.

11.10.4 Metastasis to the Esophagus

Metastases to the esophagus are rare and usually arise from primary malignancies of the bronchus, pancreas, and breast (Fig. 11.26).

11.11 Inflammatory/Infective Esophagitis

CT has a limited role in the assessment of the esophagitis due to limited ability to assess the mucosa. Regardless of the underlying cause, CT findings of esophagitis include long-segment circumferential wall thickening with or without the "target sign". "Target sign" refers to enhancement of the mucosa with a hypodense submucosa

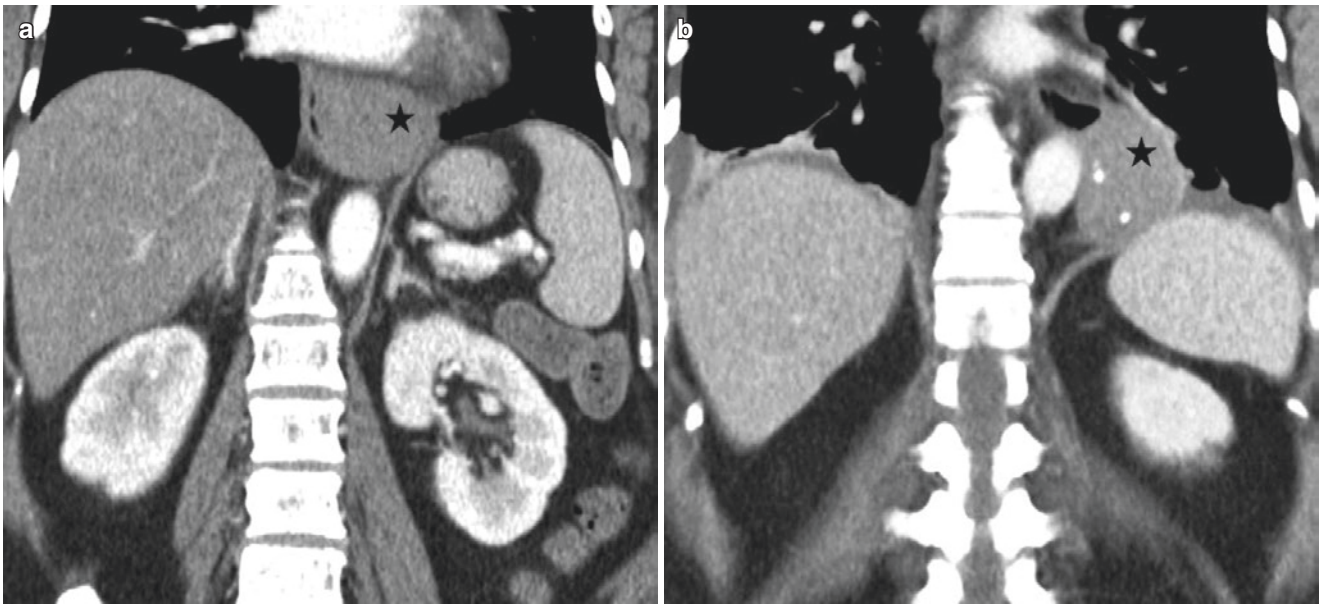

Fig. 11.25 Gastrointestinal stroma tumor. (**a**) Coronal image of contrast-enhanced CT reveals a well-defined homogenous enhancing soft-tissue eccentric mass in the distal esophagus causing mass effect on the esophageal lumen. (**b**) Follow-up CT image after 4 year shows interval development of punctate calcifications within the mass. No increase in size or invasive features

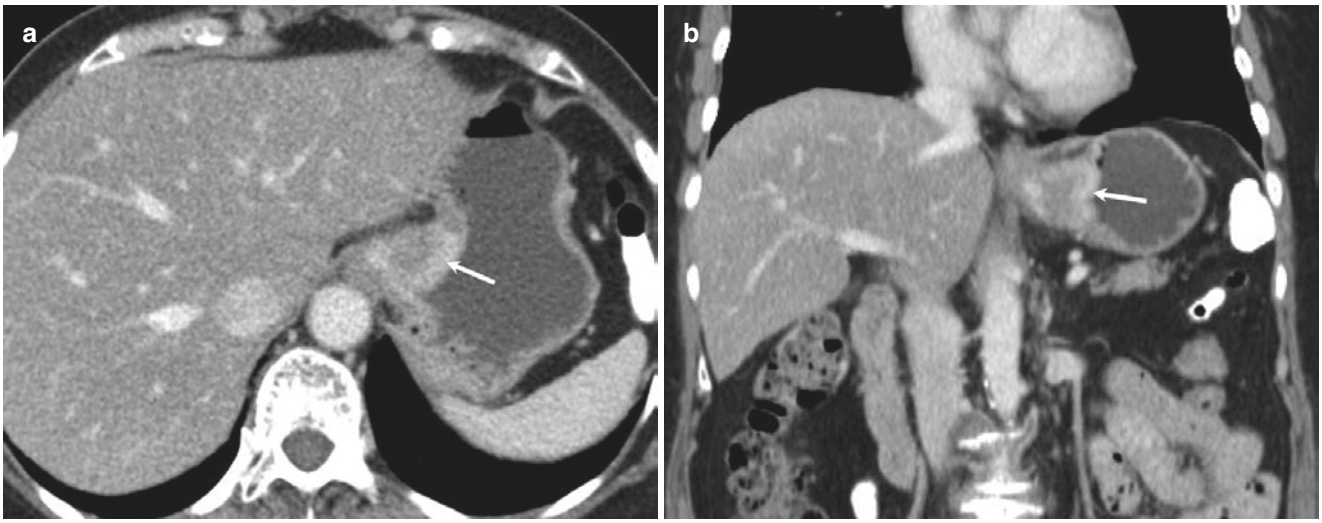

Fig. 11.26 Metastasis from breast cancer. (**a**, **b**) Axial and coronal contrast-enhanced CT images show a heterogeneously enhancing ill-defined submucosal mass (arrow) in the gastroesophageal junction

(Fig. 11.27). Even when the "target sign" is seen, in the absence of additional clues or history, it is not possible to differentiate between infectious and non-infectious esophagitis on CT [44]. Barium fluoroscopic studies, on the other hand, have a higher specificity and sensitivity in the evaluation of mucosal irregularities [45]. CT is useful for detection of the associated complications, if any (such as perforation, obstruction, or aspiration) (Table 11.13).

11.12 Mallory-Weiss Syndrome

Mallory-Weiss syndrome is a life-threatening condition characterized by massive gastric hemorrhage with hematemesis that may result in circulatory collapse. The tear termed as "Mallory-Weiss tear" is classically located at cardio-esophageal junction and involves mucosa and submucosa [44, 46]. This condition is seen in alcoholics who indulged in long and heavy drinking sessions but also rarely seen in young women

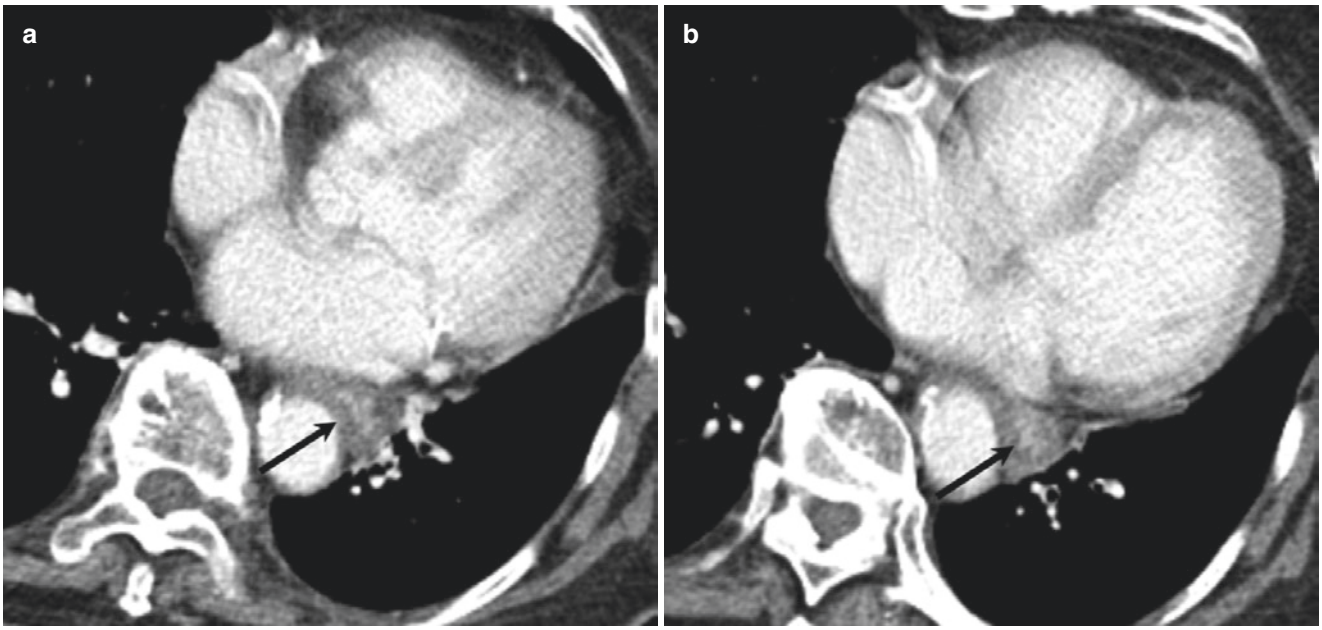

Fig. 11.27 "Target sign" in viral esophagitis. (**a**, **b**) Axial CT images show enhancement of esophageal mucosa with hypodense submucosa

Table 11.13 Barium findings of common infective/inflammatory esophagitis

Candida esophagitis	Barium trapped between raised mucosal plaques
Herpes esophagitis	Barium pools in multiple small ulcers
Cytomegalovirus and HIV esophagitis	Larger ulcers in the esophagus
Reflux esophagitis and Barrett's esophagitis	Reticular appearing mucosa in the distal esophagus
Recent mediastinal radiation	Long-segment mid-esophageal esophagitis

with hyperemesis gravidarum, emotional disorders, and migraine. Vomiting is the precipitating factors in majority of the patients but may not be always present. Endoscopy is diagnostic, and a multiphasic CT angiogram can demonstrate active contrast extravasation in some patients (Fig. 11.28) (Table 11.14).

11.13 Boerhaave Syndrome

Boerhaave syndrome is another rare potentially fatal condition characterized by a spontaneous perforation of the distal esophagus. A delay in diagnosis and treatment can lead to potentially lethal complications such as mediastinitis, pleural empyema, septic shock, and multiple organ failure [47, 48]. The perforation occurs due to increase in esophageal intraluminal pressure with failure of relaxation of the upper esophagus. Similar to Mallory-Weiss syndrome, there may be a history of retching and vomiting after ingestion of a heavy meal combined with large volume of alcohol consumption. Although it is a clinical diagnosis, imaging plays an important role in unsuspected cases that may mimic more common acute thoracic emergencies like myocardial infarction, pulmonary embolism, and aortic dissection. Imaging is also utilized to detect the complications of Boerhaave syndrome (Table 11.15). CT helps in preoperative localization of the esophageal tear by demonstrating the wall discontinuity and presence of periesophageal air pockets/fluid or intramural hematoma (Figs. 11.29 and 11.30) [47].

11.14 Aorto-esophageal Fistula (AEF)

AEF is a rare life-threatening condition that usually results in fatal hematemesis. The patients may present with the Chiari triad of chest pain and sentinel bleeding, followed by exsanguination after an asymptomatic interval [48]. A review of

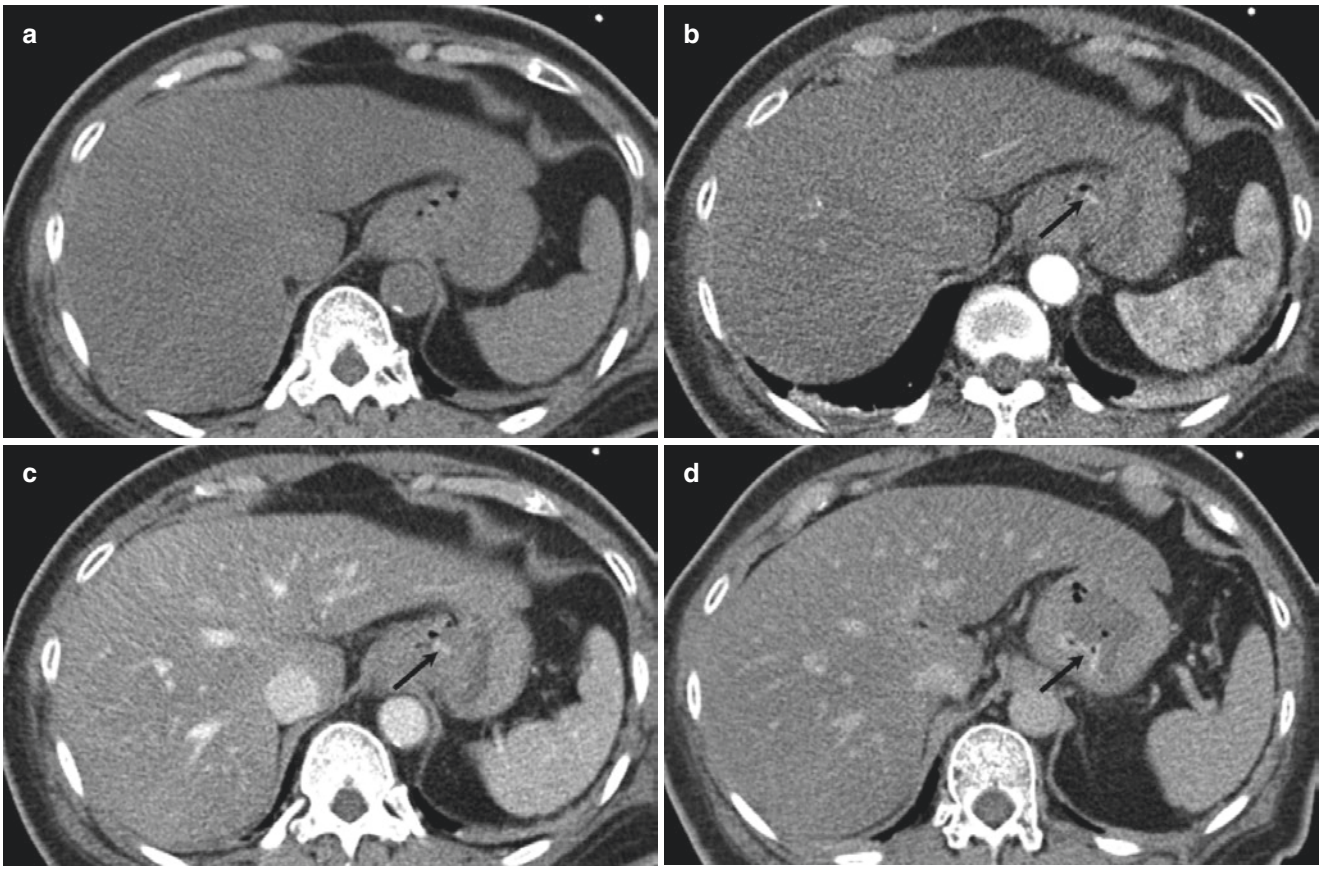

Fig. 11.28 Mallory-Weiss syndrome. (**a**–**c**) Unenhanced, arterial phase, and venous phase CT images show extravasation of contrast at gastro-esophageal junction (arrow). (**d**) Delayed image shows accumulation of extravasated contrast in gastric mucosal folds

Table 11.14 Clinical and radiological features of Mallory-Weiss syndrome

Definition	Mucosal and submucosal laceration with massive hemorrhage
Pathophysiology	Increased intraluminal pressure in setting of emesis
Location	Cardio-esophageal junction
Precipitating factor	Usually vomiting
Clinical presentation	Hematemesis/"coffee-ground" vomitus following forceful vomiting. Endoscopy is the most reliable method of diagnosis
Barium	Contrast will form linear collection in the mucosal lacerations
CT	Usually normal CT angiogram may reveal active extravasation Occasionally small foci of gas or punctate hemorrhage may be present in the distal esophagus to suggest a contained tear
Management	Spontaneous cessation of bleeding in most cases Transcatheter embolization of bleeder Rarely partial gastrectomy may be required

Table 11.15 Clinical and radiological features of Boerhaave syndrome

Definition	Spontaneous transmural tear in supradiaphragmatic esophagus
Pathophysiology	Increased intraluminal pressure in the setting of emesis
Location	Left posterior aspect of the lower esophagus, 3–6 cm proximally to the gastroesophageal junction
Precipitating factor	Vomiting preceded by heavy meal and alcohol consumption
Clinical presentation	Mackler's triad: vomiting, sudden severe chest pain, and subcutaneous emphysema Sepsis, hypotension, and shock may be present
Water-soluble contrast esophagography	Esophageal pleural fistula Esophageal contrast extravasation in mediastinum
Chest radiograph and CT	Pleural effusion Atelectasis and consolidations Pneumothorax Pneumomediastinum Periesophageal air or esophageal tear Mediastinal fluid or abscess Subcutaneous emphysema
Management	Surgery with open thoracotomy or laparoscopic approach

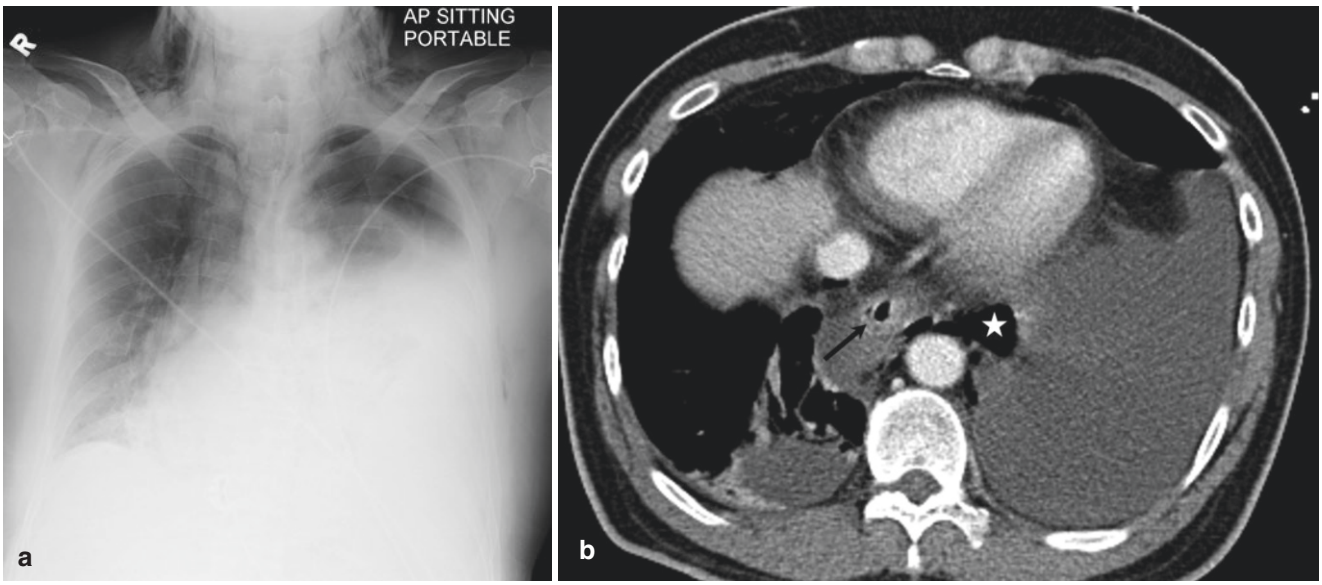

Fig. 11.29 Boerhaave syndrome. (**a**) Frontal chest radiograph shows bilateral pleural effusions, left pneumothorax, and subcutaneous emphysema. (**b**) Axial CT image shows a large air pocket (asterisk) along the left lateral wall of the lower esophagus (arrow) suggesting the site of tear in the esophagus

500 cases of AEF revealed that the most common (accounting for 54.2%) cause of AEF was primary aortic disease with rupture of the descending thoracic aortic aneurysm into the esophagus. The other causes of AEF were identified as foreign body ingestion (19.2%), advanced esophageal cancer (17%), and postoperative (4.8%) [48]. There are recent case reports attributing AEF to concurrent chemoradiotherapy [49–51].

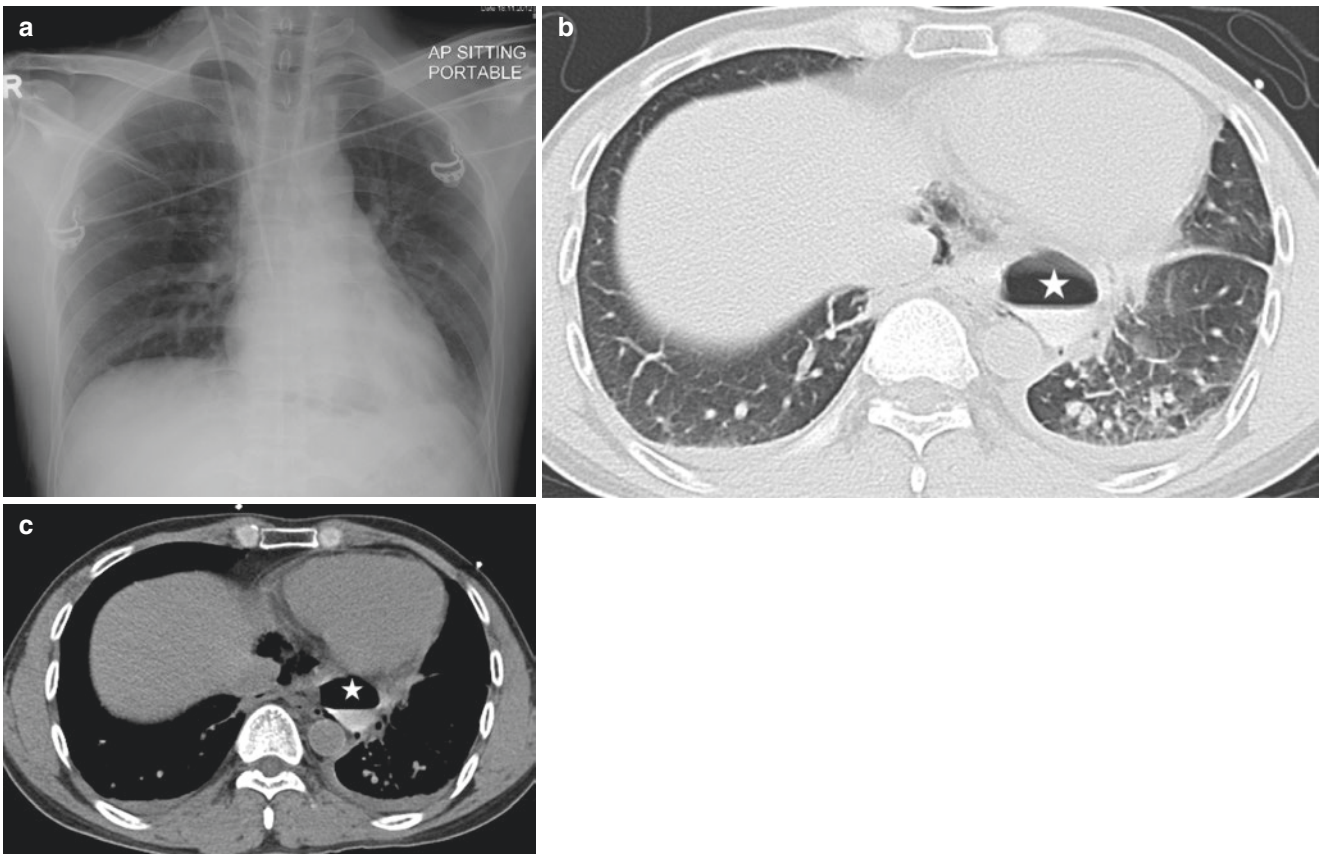

Fig. 11.30 Boerhaave syndrome. (**a**) Frontal radiograph shows subtle lucencies beneath the cardiac shadow. (**b**, **c**) Axial CT images after swallowing a small cup of water-soluble contrast show air pockets around the lower esophagus. There is extraluminal air and contrast (asterisk) along the left lateral wall of the lower esophagus indicating the area of tear

References

1. Oezcelik A, DeMeester SR. General anatomy of the esophagus. Thorac Surg Clin. 2011;21(2):289–97.
2. Ha HK, Park SH, Lee S. Gastrointestinal tract. In: Haaga JR, Dogra VS, Forsting M, Gilkeson RC, editors. CT and MRI of the whole body. 5th ed. Philadelphia: Mosby Elsevier; 2009. p. 1213–35.
3. Godfrey EM, Freeman AH. The oesophagus. In: Adam A, Dixon AK, Gillard JH, Schaefer-Prokop CM, editors. Grainger & Allison's diagnostic radiology a textbook of medical imaging. 6th ed. Edinburgh: Churchill Livingstone Elsevier Limited; 2015. p. 610–26.
4. Sivarao DV, Goyal RK. Functional anatomy and physiology of the upper esophageal sphincter. Am J Med. 2000;108:27S–37S.
5. Kwok H, Marriz Y, Al-Ali S, Windsor JA. Phrenoesophageal ligament re-visited. Clin Anat. 1999;12(3):164–70.
6. Patti MG, Gantert W, Way LW. Surgery of the esophagus. Anatomy and physiology. Surg Clin North Am. 1997;77(5):959–70.
7. Godfrey EM, Rushbrook SM, Carroll NR. Endoscopic ultrasound: a review of current diagnostic and therapeutic applications. Postgrad Med J. 2010;86(1016):346–53.
8. Allum WH, Blazeby JM, Griffin SM, Cunningham D, Jankowski JA, Wong R. Guidelines for the management of oesophageal and gastric cancer. Gut. 2011;60(11):1449–72.
9. Chowdhury FU, Bradley KM, Gleeson FV. The role of 18F-FDG PET/CT in the evaluation of oesophageal carcinoma. Clin Radiol. 2008;63(12):1297–309.
10. Rabushka L, Fishman E, Kuhlman J. CT evaluation of achalasia. J Comput Assist Tomogr. 1991;15:434–9.
11. Abubakar U, Bashir MB, Kesieme EB. Pseudoachalasia: a review. Niger J Clin Pract. 2016;19(3):303–7.
12. Carter M, Deckmann RC, Smith RC, Burrell MI, Traube M. Differentiation of achalasia from pseudoachalasia by computed tomography. Am J Gastroenterol. 1997;92(4):624–8.
13. Levine MS, Carucci LR, DiSantis DJ, Einstein DM, Hawn MT, Martin-Harris B, et al. Consensus statement of society of abdominal radiology disease-focused panel on barium esophagography in gastroesophageal reflux disease. Am J Roentgenol. 2016;207(5):1009–15.
14. Levine MS, Carucci LR. Esophageal abnormalities in gastroesophageal reflux disease. Abdom Radiol. 2017;43(6):1284–93.
15. McCauley RG, Darling DB, Leonidas JC, Schwartz AM. Gastroesophageal reflux in infants and children: a useful classification and reliable physiologic technique for its demonstration. Am J Roentgenol. 1978;130(1):47–50.

16. Gordon C, Kang J, Neild P, Maxwell J. The role of the hiatus hernia in gastro-oesophageal reflux disease. Aliment Pharmacol Ther. 2004;20(7):719–32.
17. Marini T, Desai A, Kaproth-Joslin K, Wandtke J, Hobbs SK. Imaging of the oesophagus: beyond cancer. Insights Imaging. 2017;8(3):365–76.
18. Grubel C, Borovicka J, Schwizer W, Fox M, Hebbard G. Diffuse esophageal spasm. Am J Gastroenterol. 2008;103(2):450–7.
19. Ba-Ssalamah A, Zacherl J, Noebauer-Huhmann IM, Uffmann M, Matzek WK, Pinker K, et al. Dedicated multi-detector CT of the esophagus: spectrum of diseases. Abdom Imaging. 2009;34(1):3–18.
20. Gupta S, Levine MS, Rubesin SE, Katzka DA, Laufer I. Usefulness of barium studies for differentiating benign and malignant strictures of the esophagus. AJR Am J Roentgenol. 2003;180(3):737–44.
21. Spechler SJ. Part 1. Oral cavity, pharynx and esophagus. GI Motil online. 2006. https://doi.org/10.1038/gimo44.
22. Cossentino MJ, Wong RKH. Barrett's esophagus and risk of esophageal adenocarcinoma. Semin Gastrointest Dis. 2003;14(3):128–35.
23. Rabushka LS, Fishman EK, Kuhlman JE, Hruban RH. Diffuse esophageal leiomyomatosis in a patient with Alport syndrome: CT demonstration. Radiology. 1991;179(1):176–8.
24. Berliner L, Redmond P, Horowitz L, Ruoff M. Glycogen plaques (glycogenic acanthosis) of the esophagus. Radiology. 1981;141(3):607–10.
25. Whitaker JA, Deffenbaugh LDCA. Esophageal duplication cyst. Am J Gastroenterol. 1980;73:329–32.
26. Feguson CC, Young LN, Sutherland JBMR. Intrathoracic gastrogenic cyst-preoperative diagnosis by technetium scan. J Pediatr Surg. 1973;8:827–8.
27. Fitch SJ, Tonkin IL, Tonkin AK. Imaging of foregut duplication cysts. Radiographics. 1986;6(2):189–201.
28. Weiss L, Fragelman DWJ. CT demonstration of an esophageal duplication cyst. J Comput Assist Tomogr. 1983;7:716–8.
29. Kuhlman JE, Fishman EK, Wang KP, Siegelman SS. Esophageal duplication cyst: CT and transesophageal needle aspiration. Am J Roentgenol. 1985;145(3):531–2.
30. Jeung M-Y, Gasser B, Gangi A, Bogorin A, Charneau D, Wihlm JM, et al. Imaging of cystic masses of the mediastinum. Radiographics. 2002;22(suppl_1):S79–93.
31. Siegel RL, Miller KD, Jemal A. Cancer statistics, 2016. CA Cancer J Clin. 2016;66(1):7–30.
32. Pisani P, Parkin DM, Bray F, Ferlay J. Estimates of the worldwide mortality from 25 cancers in 1990. Int J Cancer. 1999;83(1):18–29.
33. Jemal A, Tiwari RC, Murray T, Ghafoor A, Samuels A, Ward E, et al. Cancer statistics, 2004. CA Cancer J Clin. 2004;54(1):8–29.
34. Hong SJ, Kim TJ, Lee IS, Yang HC, Kim K. New TNM staging system for esophageal cancer: what chest radiologists need to know. Radiographics. 2014;34(6):1722–41.
35. Rice TW, Patil DT, Blackstone EH. 8th edition AJCC/UICC staging of cancers of the esophagus and esophagogastric junction: application to clinical practice. Ann Cardiothorac Surg. 2017;6:119–30.
36. Rice TW, Ishwaran H, Ferguson MK, Blackstone EH, Goldstraw P. Cancer of the esophagus and esophagogastric junction: an eighth edition staging primer. J Thorac Oncol. 2018;12(1):36–42.
37. Ajani JAB. Esophageal and esophagogastric junction cancers. J Natl Compr Cancer Netw. 2015;9(8):830–87.
38. Picus D, Balfe DM, Koehler RE, Roper CL, Owen JW. Computed tomography in the staging of esophageal carcinoma. Radiology. 1983;146(2):433–8.
39. Mori M, Matsukama A, Adachi Y, Al E. Small cell carcinoma of the oesophagus. Cancer. 1989;63:564–73.
40. Levine MS, Pantongrag-Brown L, Buck JL, Buetow PC, Lowry MA, Sobin LH. Small-cell carcinoma of the esophagus: radiographic findings. Radiology. 1996;199(3):703–5.
41. Levine MS, Buck JL, Pantongrag-Brown L, Buetow PC, Hallman JR, Sobin LH. Leiomyosarcoma of the esophagus: radiographic findings in 10 patients. AJR Am J Roentgenol. 1996;167(1):27–32.
42. Nishida T, Hirota S. Biological and clinical review of stromal tumours in the gastrointestinal tract. Histol Histopathol. 2000;15:1293–301.
43. Sandrasegaran K, Rajesh A, Rushing D, Et A. Gastrointestinal stromal tumours: CT and MRI findings. Eur Radiol. 2005;15:1407–14.
44. Young CA, Menias CO, Bhalla S, Prasad SR. CT features of esophageal emergencies. Radiographics. 2008;28(6):1541–53.
45. Currie S, Menias CO, Mellnick V. Imaging of esophageal emergencies. Appl Radiol. 2016;45(10):16–21.
46. Sparberg M. Roentgenographic documentation of the Mallory-Weiss syndrome. JAMA. 1968;203(2):151–2.
47. Ghanem N, Altehoefer C, Springer O, Et A. Radiological findings in Boerhaave's syndrome. Emerg Radiol Emerg Radiol. 2003;10(1):8–13.
48. Khawaja FI, Varindani MK. Aortoesophageal fistula. Review of clinical, radiographic, and endoscopic features. J Clin Gastroenterol. 1987;9:342–4.
49. Hollander JE, Quick G. Aortoesophageal fistula: a comprehensive review of the literature. Am J Med. 1991;91:279–87.
50. Hou PY, Teng CJ, Chung CS, Liu CY, Huang CC, Chang MH, Shueng PW, Hsieh CH. Aortic pseudoaneurysm formation following concurrent chemoradiotherapy and metallic stent insertion in a patient with esophageal cancer. Medicine (Baltimore). 2015;94(20):862.
51. Sivaraman SK, Drummond R. Radiation-induced aortoesophageal fistula: an unusual case of massive upper gastrointestinal bleeding. J Emerg Med. 2002;23:175–8.

Imaging of Chest Wall and Pleura

12

Dinesh Singh

12.1 Introduction

Chest wall and pleural pathologies have always been a diagnostic challenge for the clinicians and the radiologists. These pathologies range from various congenital chest wall deformities, inflammatory or infectious lesions, as well as benign and malignant tumors. Radiographs are often the first-line imaging modality and are useful in the follow-up assessment. Ultrasound is helpful in the assessment of soft-tissue lumps involving the chest wall and pleural pathologies. Its role is much more important in guiding drainage procedures. Cross-sectional imaging techniques, namely, computed tomography (CT) and magnetic resonance imaging (MRI), are used in the localization and extent assessment of the chest wall and pleural abnormalities.

12.2 Chest Wall

Chest wall pathologies can arise from the superficial soft tissues, the muscles, the bony wall, the nerves, or even the blood vessels.

12.3 Congenital and Developmental Abnormalities

Congenital and developmental chest wall abnormalities include pectus excavatum, pectus carinatum, rib agenesis or hypoplasia, supernumerary ribs, Poland syndrome, Sprengel's deformity, and cleidocranial dysplasia [1]. The anterior chest wall abnormalities are usually related to the rib cage and sternum and often present as palpable chest wall masses in children and adults [2].

D. Singh (✉)
Department of Diagnostic Radiology, Khoo Teck Puat Hospital, Singapore, Singapore

12.3.1 Pectus Excavatum

Pectus excavatum, also known as "funnel chest," is the commonest congenital abnormality involving the sternum [3]. Most of the cases of pectus excavatum are congenital; however, a few become conspicuous later in life, often associated with conditions like Marfan syndrome, Ehler-Danlos syndrome, Noonan syndrome, etc. [4]. The main clinical problem is the cosmetic deformity; however, pectus excavatum can be associated with mitral valve prolapse and other cardiac abnormalities. There is a narrowing of the anterior-posterior diameter of the thorax with a shift of the heart to the left [5]. Diagnosis can be made on frontal and lateral projections of the chest radiograph, while CT is used to assess the severity (Tables 12.1 and 12.2) (Fig. 12.1). MR imaging is usually limited to dynamic assessments of the chest wall and the diaphragm [6].

12.3.2 Pectus Carinatum

Pectus carinatum also known as "pigeon chest" is much less common in comparison to pectus excavatum. The deformity is usually cosmetic due to the anterior protrusion of the sternum and can be associated with cyanotic heart diseases or scoliosis (Table 12.3) (Fig. 12.2). Corrective surgical procedures are recommended only in severe symptomatic cases [4]. Compressive bracing is a noninvasive alternative, especially in children.

12.3.3 Poland Syndrome

Poland syndrome is a rare congenital condition due to the partial or complete absence of the pectoralis major and minor muscles, associated with limb abnormalities including syndactyly or brachydactyly, on the affected side (Fig. 12.3). The etiology is unknown, popularly believed to be related to compromise of blood supply during embryonic development

A. Chawla (ed.), *Thoracic Imaging*, https://doi.org/10.1007/978-981-13-2544-1_12

Table 12.1 Imaging features of pectus excavatum

• Indistinct right heart border with a leftward shift
• Horizontal orientation of posterior ribs and more vertical orientation of anterior ribs
• Reduced density of cardiac silhouette
• Deep sternal depression on the lateral view
• Ribs protruding anteriorly compared to sternum on the lateral view
• Obliteration of descending aortic interface

Table 12.2 CT in pectus excavatum

• Haller index: ratio of maximum internal transverse chest diameter to minimum anterior-posterior diameter. Values of >3.25 usually require surgical correction
• Haller index can be affected by the phase of the respiratory cycle, values significantly lower in inspiratory phase
• Haller index can be higher in females, compared to males of the same age

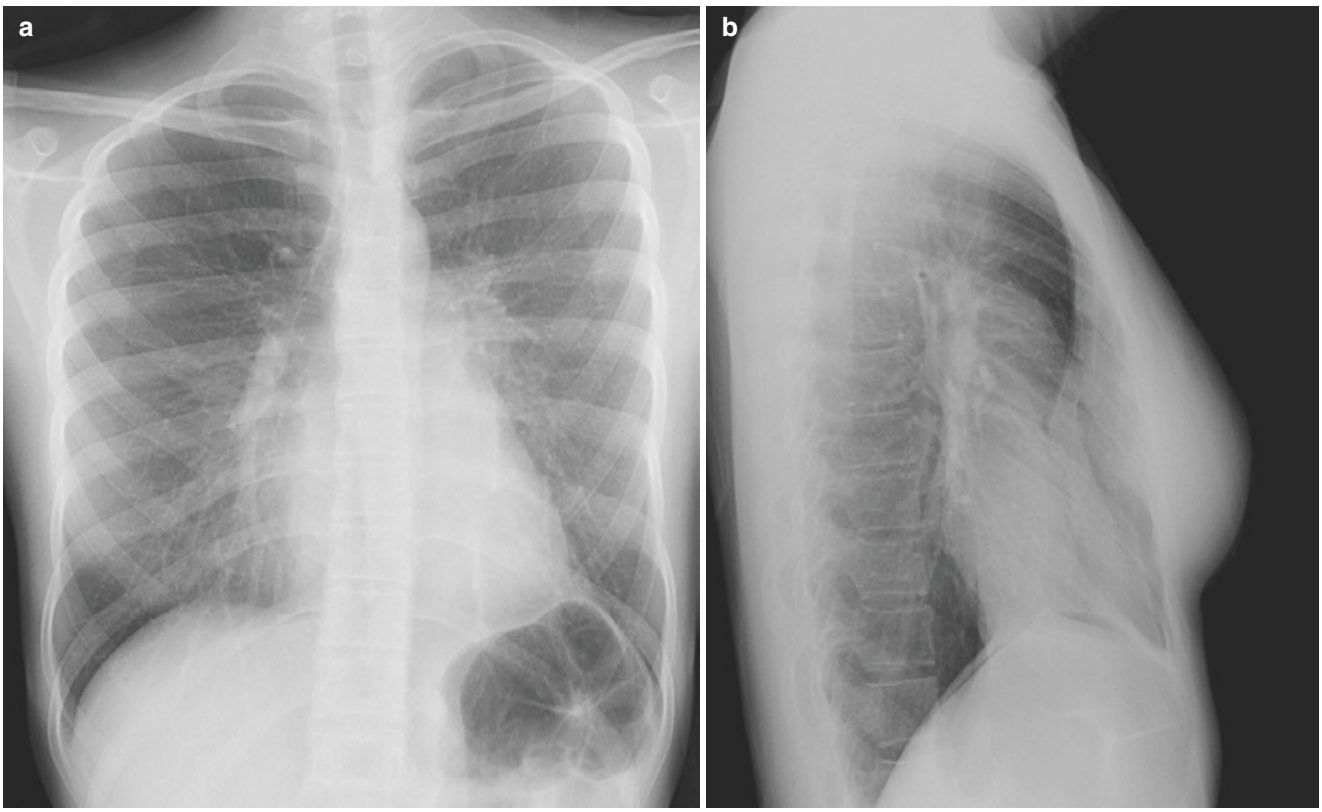

Fig. 12.1 Pectus excavatum. (**a**, **b**) Frontal radiograph showing blurring of the right heart border mimicking the right middle lobe pathology, horizontal posterior ribs, and vertical anterior ribs. (**b**) Lateral radiograph reveals depressed sternum

Table 12.3 Imaging features of pectus carinatum

• Convex anterior protrusion of the sternum and costochondral joints
• Chondrogladiolar subtype: protrusion of sternal body, can be asymmetric
• Chondromanubrial subtype: protrusion of manubrium
• CT Haller index can be used for assessing the severity

[4]. It can be associated with varying degrees of breast and nipple involvement. Poland syndrome is a cause of unilateral translucent lung (Tables 12.4 and 12.5).

12.3.4 Cervical Rib

It is also known as accessory rib or "Eve's rib" and usually arises from the seventh cervical vertebra [3] (Fig. 12.4). More than 90% of the cervical ribs are asymptomatic, while few cases may result in cervical rib syndrome, where the extra bone leads to compression on the thoracic outlet structures, resulting in swelling and weakness of the affected arm, pain, or even reduced pulse intensity on certain arm positions. Radiographs are often diagnostic demonstrating an accessory rib arising from the seventh cervical

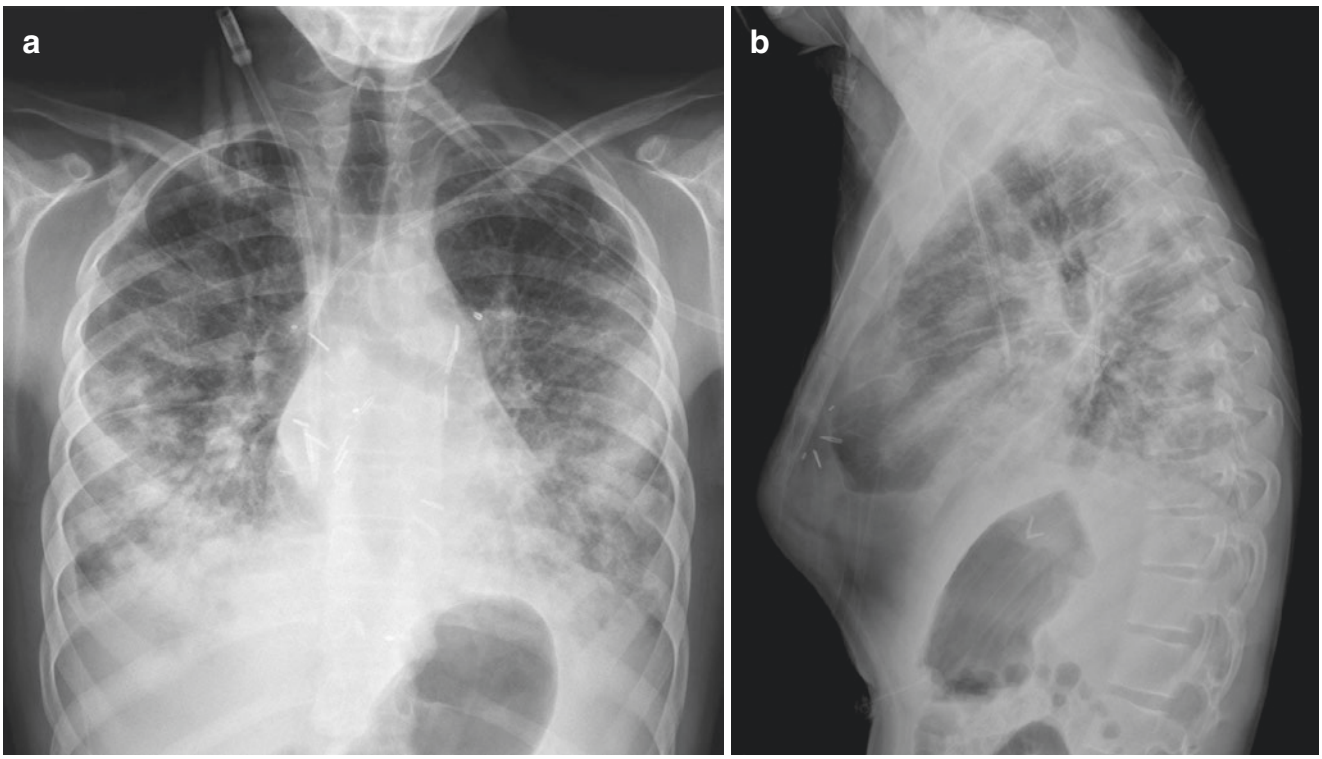

Fig. 12.2 Pectus carinatum in a patient with cystic fibrosis. (**a**) Frontal radiograph shows multifocal opacities representing infection. (**b**) Lateral chest radiographs demonstrate protruding sternum

vertebra, while CT angiography and multiplanar reconstructions are reserved for the evaluation of symptomatic cases.

12.4 Infections

Various pyogenic, fungal, and tuberculous infections can involve the chest wall, particularly in immunocompromised patients causing life-threatening complications [7]. Pyogenic infections usually present with chest wall swelling, chest discomfort, pain, and fever (Fig. 12.5). However, the signs and symptoms of infection may be absent in tuberculosis "cold abscess." Imaging features of infections of the chest wall are described in Table 12.6.

Pyogenic infections are commonly caused by *Staphylococcus aureus* (general population) and *Pseudomonas aeruginosa* (more frequent in drug addicts) and can present as osteomyelitis involving the ribs or the sternum [3]. Tuberculous involvement of the chest wall is due to hematogenous seeding without active lung disease or due to direct extension from pleural or pulmonary disease (Fig. 12.6). The hematogenous tubercular infection may involve the sternoclavicular joint, ribs, and rarely sternum. Thoracic actinomycosis is an uncommon granulomatous infection caused by bacteria from *actinomycetes* species. These bacteria are present in natural human cavities but become saprophytes in immunocompromised patients. Actinomycosis may spread directly from the lung to the pleura and chest wall (Fig. 12.7) [7]. *Aspergillus* infection is predominantly seen in immunocompromised hosts, *Aspergillus fumigatus*, accounting for the majority of the cases. Invasive disease results in involvement of the chest wall with fistula formation [8].

12.5 Chest Wall Tumors

Chest wall tumors can arise from bone, muscle, adipose tissue, blood vessels, or even the nerves. Primary chest wall neoplasms only account for a small percentage of all thoracic tumors, almost half of these being benign [9]. Majority of the malignant chest wall masses are metastatic deposits or result of direct invasion of lung cancer

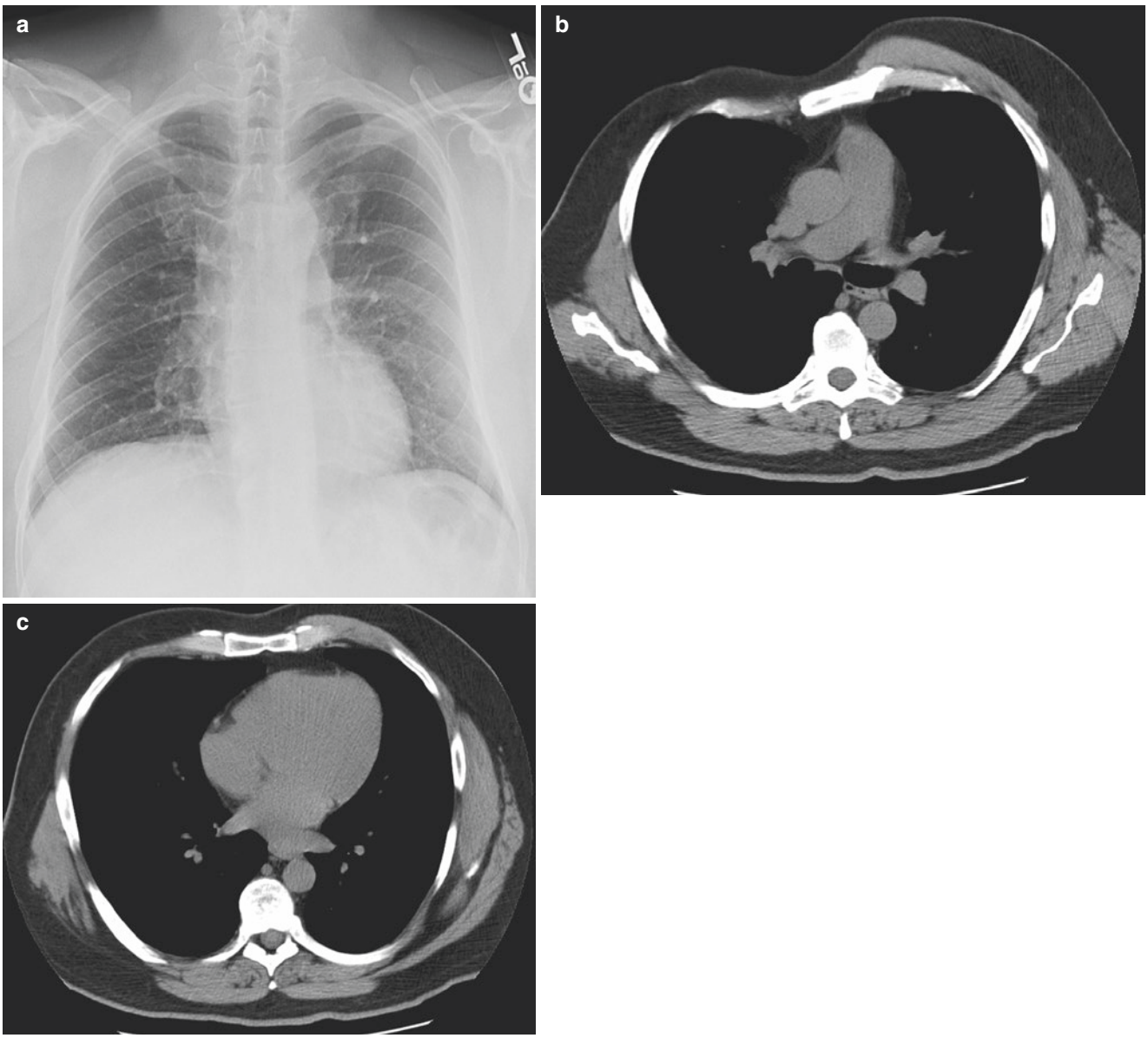

Fig. 12.3 Poland syndrome. (**a**) Frontal radiograph shows asymmetric translucency on the right hemithorax. (**b**, **c**) Axial CT images reveal the absence of multiple right-sided chest wall muscles

Table 12.4 Imaging features of Poland syndrome

• Hyperlucent hemithorax, most commonly unilateral
• Chest wall, rib cage, and breast deformities
• Absence of pectoralis major and minor muscles (MRI preferred over CT to avoid radiation)
• Ipsilateral syndactyly, shortening of phalanges, dextrocardia in some cases

Table 12.5 Differential diagnoses of unilateral translucent lung

• Positional (rotation)
• Endobronchial foreign body
• Pneumothorax
• Mastectomy
• Emphysema, with overlying disease
• Pulmonary embolism
• Macleod's syndrome

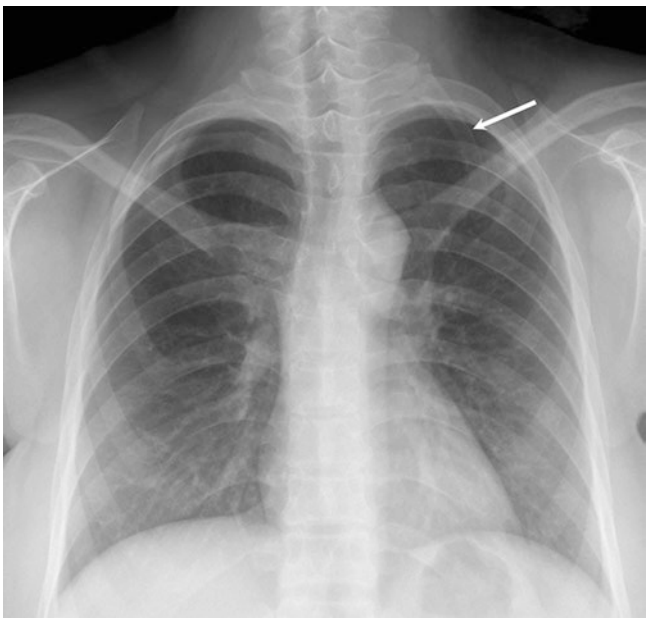

Fig. 12.4 Cervical rib. Frontal chest radiograph shows a left-sided cervical rib (arrow) arising from C7 vertebra

Table 12.6 Synopsis of imaging findings in infections of the chest wall

Pyogenic infections	• Destruction of the ribs/sternum with or without periosteal reaction, adjacent soft-tissue mass • Involvement of adjacent pleura, lung, or mediastinum Postmedian sternotomy: • Radiographs: air in retrosternal soft tissue with mass-like opacity • CT: retrosternal abscess, mediastinal involvement
Tuberculosis	• Bone destruction with soft-tissue masses and abscess • Joints are commonly involved • Calcification may be present in abscess • Absence of new bone formation • Bony sequestra in the areas of bone destruction • Empyema necessitans
Actinomycosis infection	• Lytic rib lesions, wavy periosteal reaction, underlying pleural or lung disease, fistula formation

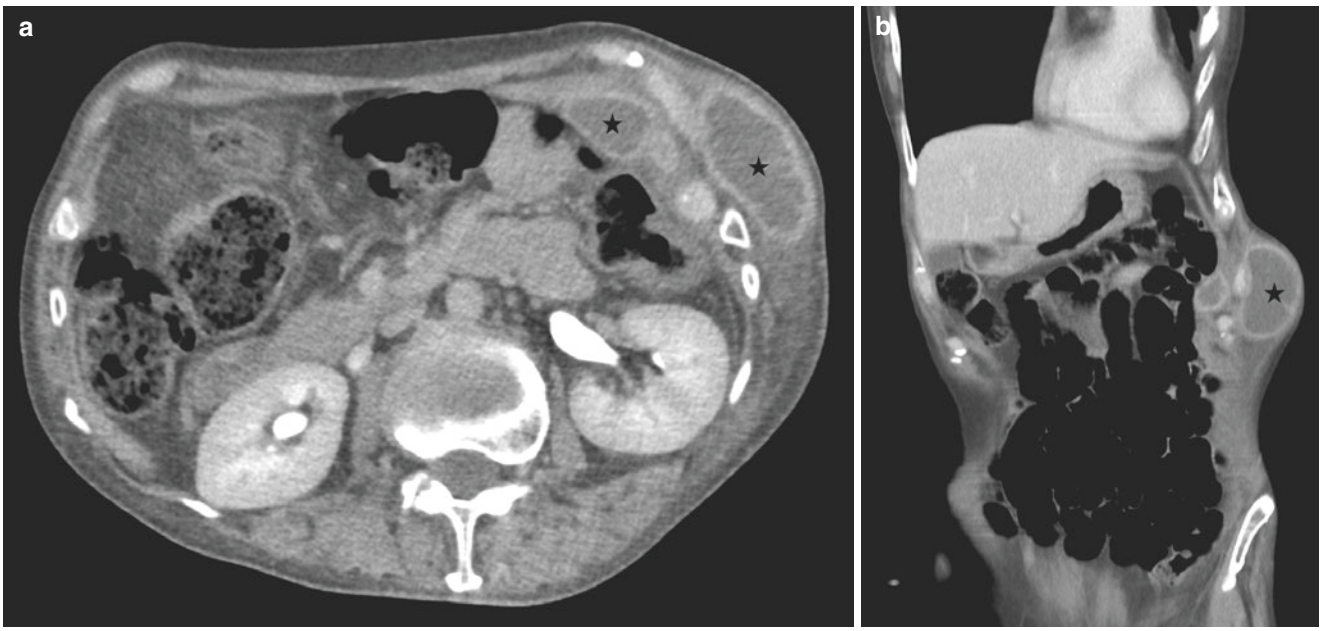

Fig. 12.5 A 70-year-old man presenting with fever and a left lower chest wall lump. (**a**, **b**) Axial and coronal CT images show left lower chest wall abscess with deep extension (asterisks)

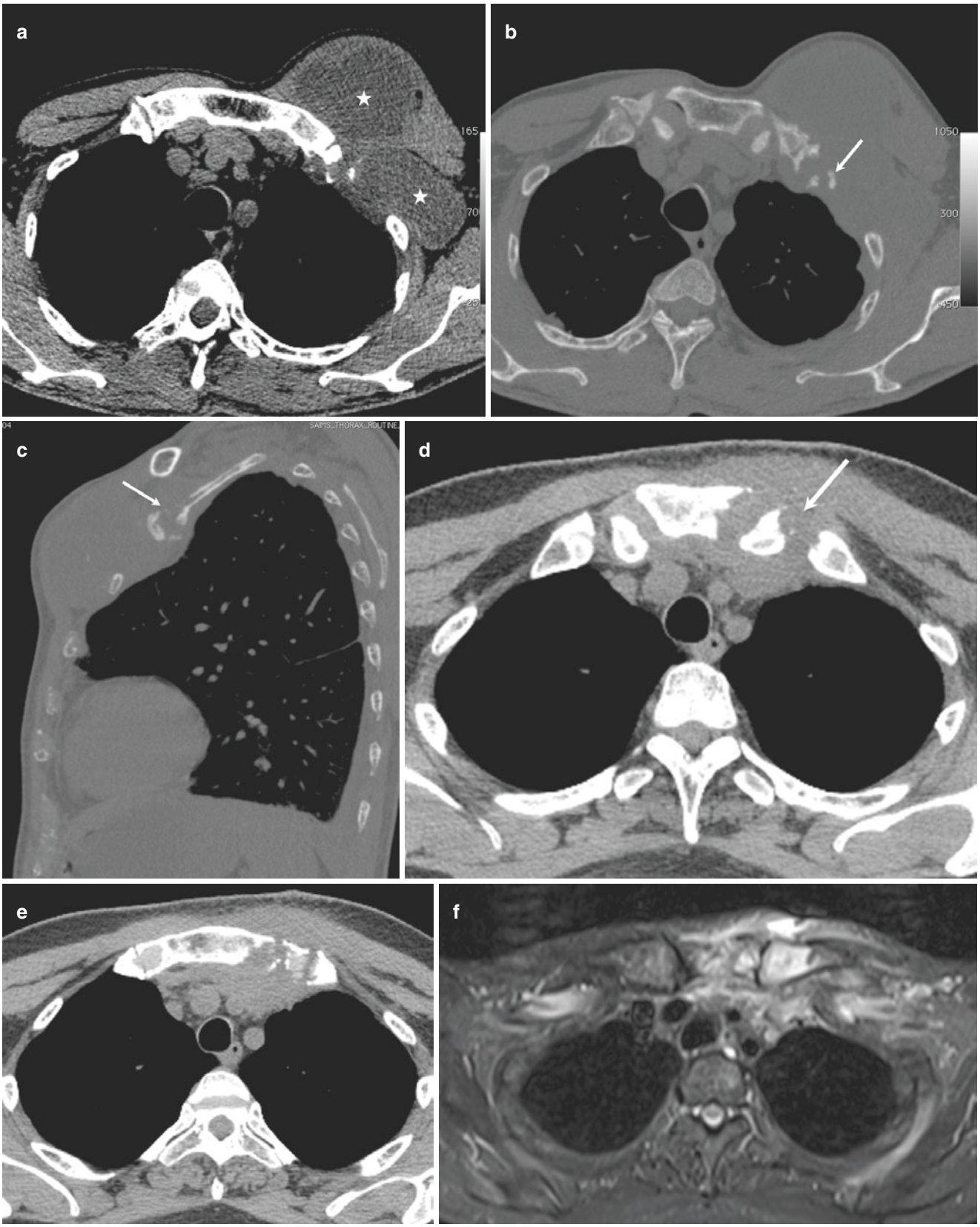

Fig. 12.6 Chest wall tuberculosis in three different patients. (**a**, **b**) Axial and (**c**) coronal CT images show two large abscesses (asterisks) in the left upper anterior chest wall with the destruction of the underlying rib (arrow). Sternoclavicular joint tuberculosis. (**d**, **e**) Axial CT images show soft-tissue thickening centered around the left sternoclavicular joint (arrow). (**f**, **g**) Axial STIR images show edema and involvement of the sternum and adjacent left clavicle. Cold abscess. (**h**, **i**) Axial CT images show thick-walled cold abscess with calcification. Note tree-in-bud opacities in the right upper lobe from pulmonary tuberculosis

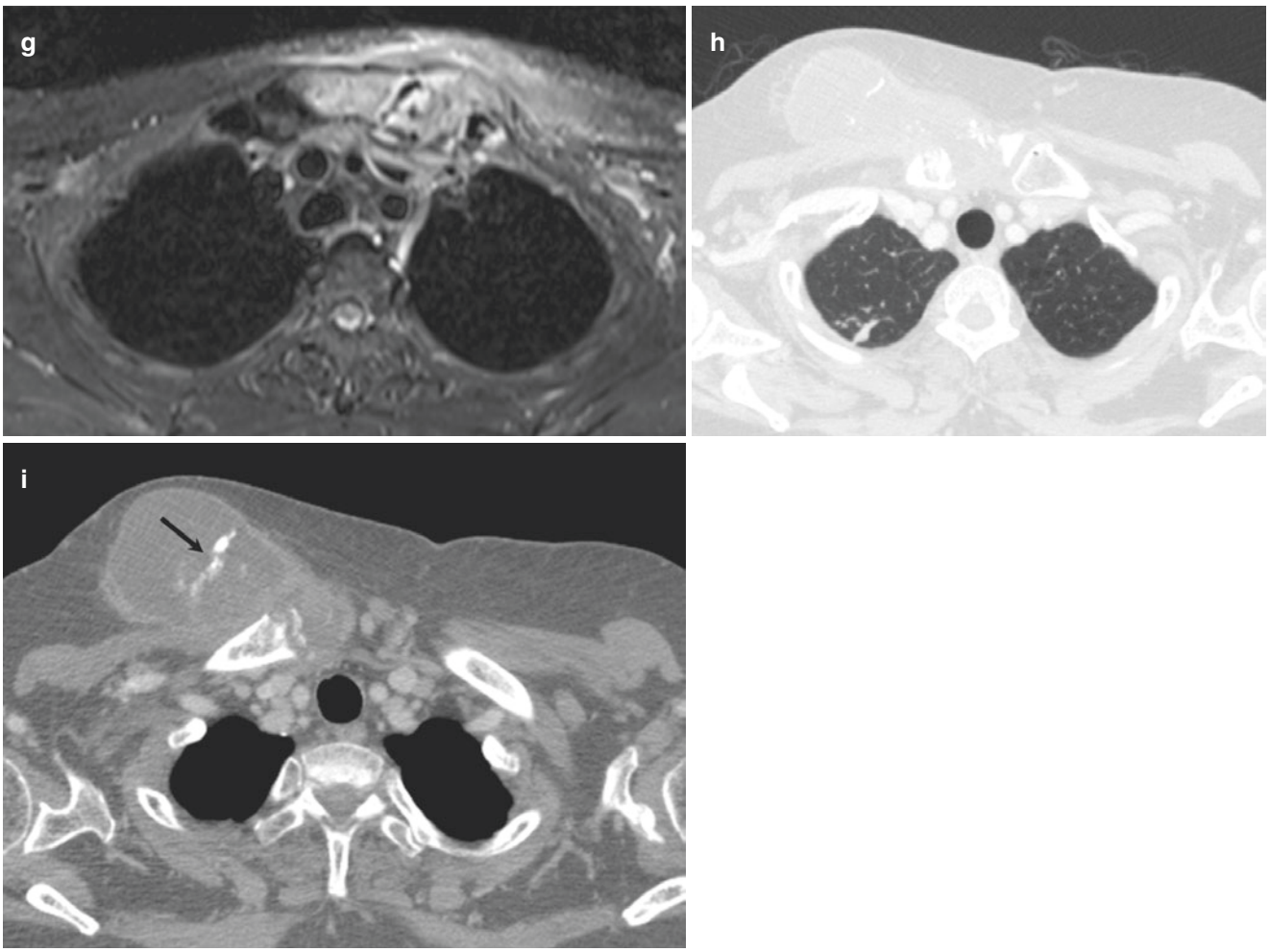

Fig. 12.6 (continued)

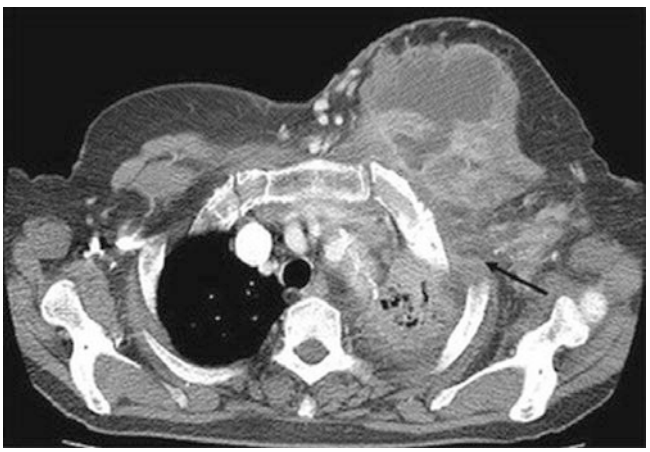

Fig. 12.7 Actinomycosis involving the chest wall in a 75-year-old woman, manifesting as a palpable mass on the left chest wall. Axial CT image shows a heterogeneous mass with central low attenuation and peripheral enhancement on the left chest wall, contiguous with consolidation (arrow) in lung parenchyma, and pleural effusion (Courtsey Han et al., reference [7])

[10]. Assessment of a chest wall lesion needs a systematic problem-based approach, choosing the most appropriate imaging modality, and the use of percutaneous biopsy procedures in indeterminate cases [11].

12.6 Benign Tumors

Benign chest wall tumors are usually asymptomatic, presenting as slow-growing lesions. Although radiographs and CT evaluation are useful, MRI is the modality of choice in the assessment of chest wall neoplasms [12]. The benign lesions can be broadly subclassified as lipomatous, vascular, neurogenic, fibroblastic-myofibroblastic, osseous, and cartilaginous lesions. These extrapleural chest wall masses usually cause displacement of the parietal and visceral pleura and present on radiographs, as masses forming an obtuse angle with the chest wall with sharp margin facing toward the lungs [13].

12.6.1 Peripheral Nerve Tumors

These tumors arise from the intercostal nerves, spinal nerve roots, and branches of the brachial plexus [14]. Imaging features of the peripheral nerve tumors are described in Table 12.7. Schwannomas are usually slow-growing mass lesions usually seen in patients between 20 and 50 years of age. They present typically as painless masses, seldom over 5 cm in size. Larger tumors may show cystic degeneration (ancient change), hemorrhage, or calcification (Fig. 12.8). Neurofibromas are usually seen in younger patients (second and third decade) and can be localized, diffuse, or plexiform. These tumors are inseparable from the involved nerve roots and have to be excised along with the nerve root [15]. Ganglioneuromas arise from the chest wall sympathetic ganglia and often present as large encapsulated masses. Malignant peripheral nerve sheath tumors (MPNST) are rare malignant neoplasms that usually occur sporadically but can also be seen in a patient with neurofibromatosis type 1 (NF 1).

12.6.2 Lymphovascular Tumors

These include hemangiomas, lymphangiomas, and glomus tumors usually seen in the pediatric population. Hemangiomas typically are cutaneous in location and present at birth or by third decade [12]. Lymphangiomas are congenital tumors consisting of dilated lymphatic channels. These lesions almost always present by 2 years of age [14]. Apart from long-standing history, the presence of phlebitis, T2 brightness, and variable enhancement helps in making a diagnosis of these tumors.

12.6.3 Osseous and Cartilaginous Tumors

Many osseous and cartilaginous neoplasms can involve the bones (particularly ribs) of the chest wall. The commoner lesions include osteochondroma, fibrous dysplasia, and enchondroma, while the rarer lesions include aneurysmal bone cyst (ABC), giant cell tumor (GCT), and chondroblastoma. Imaging findings in benign osseous and cartilaginous chest wall tumors are described in Table 12.8 (Figs. 12.9, 12.10, 12.11, and 12.12) [12, 14].

12.6.4 Adipose Tissue Tumors

Chest wall lipomas are often incidentally visualized deep-seated fat-containing masses involving the muscles and intervening planes. On contrast-enhanced CT and MRI, the lipoma is a non-enhancing fat-containing lesion. However, mild enhancement can be seen involving the thin septa. Hibernoma also termed "pseudolipoma" is a benign adipose tissue tumor arising from the vestiges of fetal brown fat. Hibernoma presents as a slow-growing painless lump with duration of symptoms ranging up to 12 years and has no malignant potential. CT shows a well-defined fat-density lesion with a prominent feeding vessel. MRI features of hibernoma are characteristic, and T1 features are helpful in differentiating it from lipoma and well-differentiated liposarcoma. On T1W images, hibernoma appears as a well-defined, heterogeneous mass, mildly or clearly hypo-intense to subcutaneous fat on T1W images, with prominent thin low-signal bands in the tumor. On the other hand, the signal intensity of the lipoma and the fatty elements in well-differentiated liposarcoma is isointense with subcutaneous fat. Hibernoma

Table 12.7 Synopsis of imaging findings in benign peripheral nerve tumors

Schwannoma	• Radiograph: may show secondary changes like bony scalloping or erosion • CT: homogeneous well-defined mass (attenuation similar to or slightly lesser than muscle). Postcontrast attenuation similar to or slightly higher than the muscle • MRI: T1 signal intensity similar to or slightly higher than muscle, markedly bright appearance on T2WI. Nerve leading to the tumor may be visible • Homogeneous enhancement in small tumors, heterogeneous enhancement in larger tumors • "Fascicular sign": heterogeneous low signal intensity with the ringlike pattern on T2WI (more common than neurofibroma)
Neurofibroma	• Widening of the neural foramina on the radiograph • CT: hypodense lesions with heterogeneous contrast enhancement • MRI: target-like appearance (rim of high signal on T2WI with central lower signal intensity). Target appearance may also be present on postcontrast images with marked enhancement of the central part. This sign is less common in schwannoma • Localized, plexiform (bag of worms appearance), and diffuse forms
Ganglioneuroma	• CT: Ovoid, sharply marginated paravertebral tumor. May contain calcification • MRI: "whorled appearance" on T1WI and T2WI (curvilinear bands of the low signal)

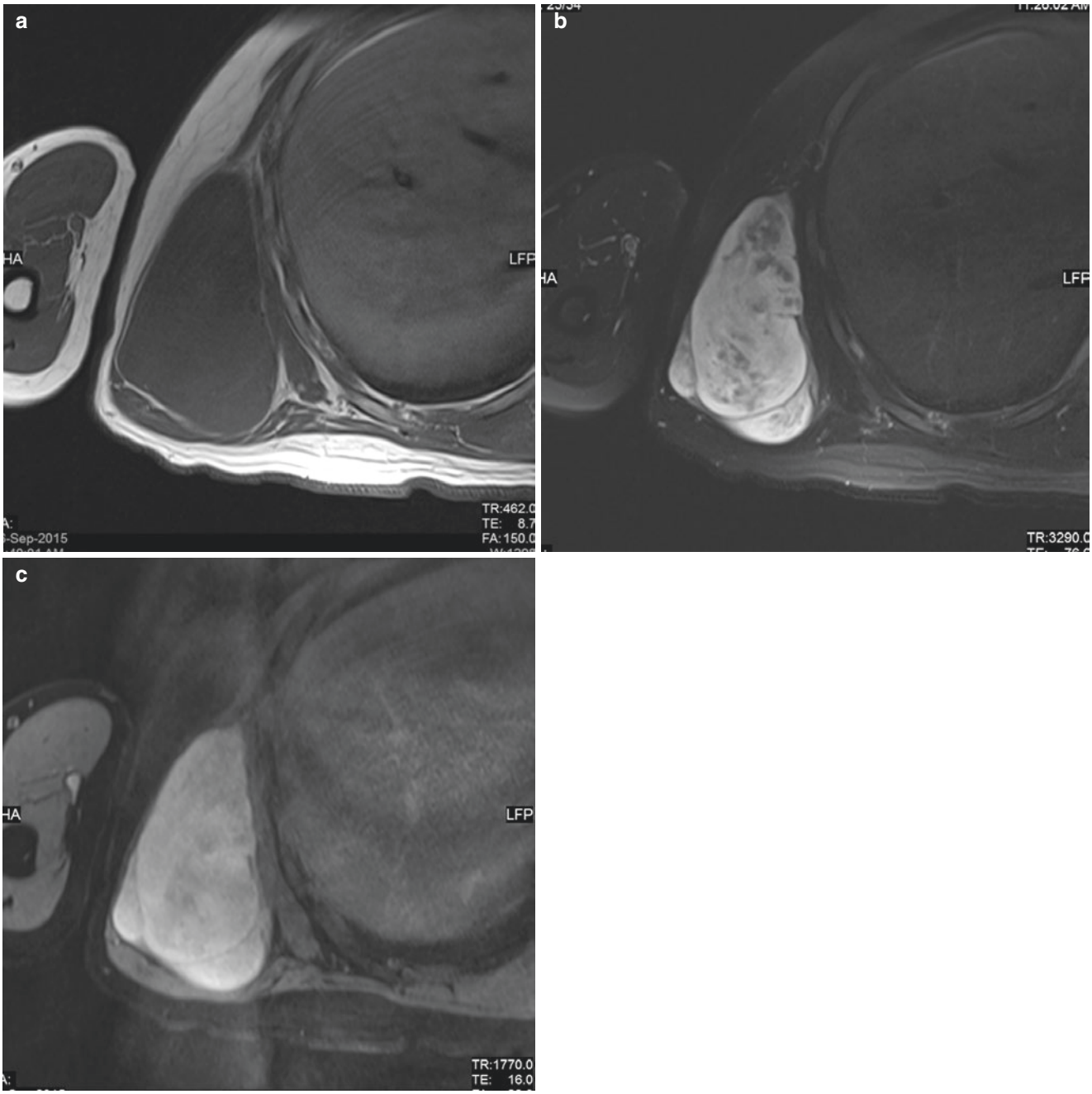

Fig. 12.8 Ancient schwannoma. (**a**) T1W, (**b**) T2W, and (**c**) postcontrast T1W MR images in a patient with long-standing right chest wall lump

Table 12.8 Imaging findings in benign osseous and cartilaginous chest wall tumors

Osteochondroma	• Young adults, usually less than 30 years of age • Pedunculated bony outgrowths • Ribs (predilection for costochondral junction), scapula, or clavicle • Complications: fracture, nerve compression, vascular injury, and malignant transformation • Radiograph: cartilage cap can be seen if calcified • CT and MRI: tumor is contiguous with bony marrow cavity • Cartilage cap is better assessed on MRI • Cartilage cap high signal on T2WI, thickness >2 cm in adults or >3 cm in children, suspicious of malignant transformation

(continued)

Table 12.8 (continued)

Fibrous dysplasia	• Young adults, usually less than 30 years of age • Radiograph and CT: fusiform expansile lytic lesion, usually from lateral or posterior rib with bony deformity, ground-glass matrix, and may show peripheral trabeculation • MRI: variable signal intensity depending on the amount of fibrous tissue, cellularity, collagen, trabeculation, and cystic or hemorrhagic degeneration, usually high signal on T2WI, a variable pattern of enhancement
Enchondroma	• Young adults usually less than 30 years of age • Radiograph: lytic expansile lesion, "rings and arcs" calcifications • CT: lesion characteristics much better visualized, lesion arising from the central medullary cavity • Increasing size, cortical break, soft-tissue component, and permeative pattern are concerning for malignant transformation • MRI: hyperintense signal on T2WI, low signal in areas of calcification, a variable pattern of enhancement
Giant cell tumor	• Age group: 20–50 years of age • Usually lytic expansile lesions, more commonly involving the posterior aspects of the ribs • May also have aggressive features or fluid-fluid levels
Aneurysmal bone cyst	• Age group: 15–30 years of age • Radiograph: well-defined expansile lesion • CT: delineates osseous and extra-osseous components • MRI: septated or lobulated mass with thin, low-signal rim, may show fluid-fluid levels (internal hemorrhages)
Langerhans cell histiocytosis	• Multisystem disorder, commonly involving skull and long bones • Rib involvement is more commonly seen in young adults and presents as a lytic lesion

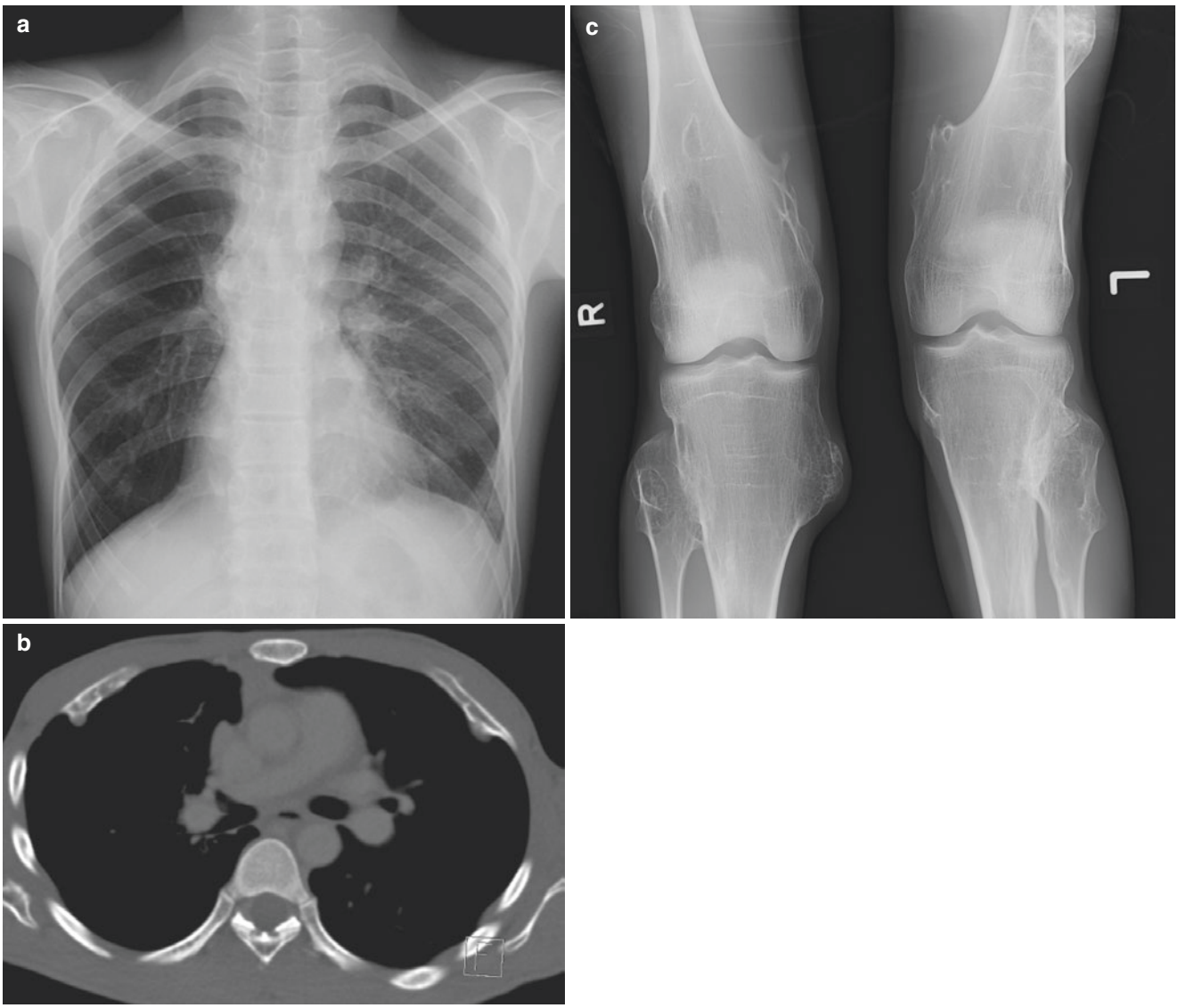

Fig. 12.9 A 28-year-old man with diaphyseal aclasis. (**a**) Frontal chest radiograph of the chest, (**b**) axial CT image, and (**c**) bilateral knee AP radiographs show multiple bony protuberances representing multiple exostoses

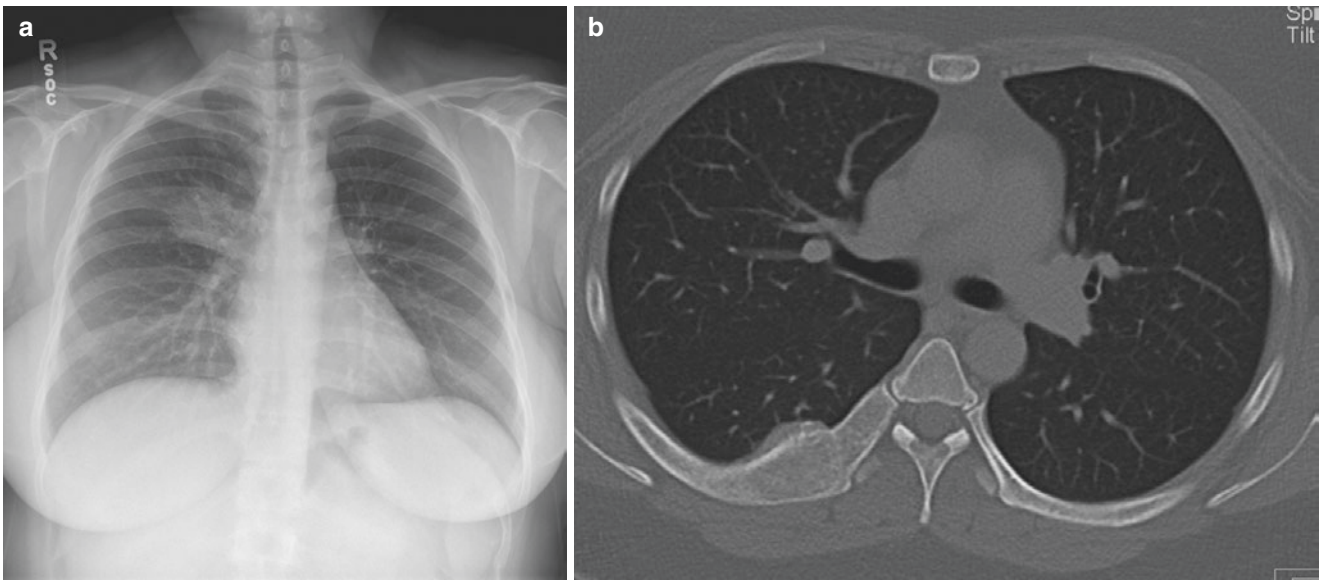

Fig. 12.10 A 36-year-old woman with fibrous dysplasia. (**a**) Frontal chest radiograph shows an expansile sclerotic right sixth rib lesion mimicking a pulmonary or hilar mass. (**b**) Axial CT image reveals ground-glass density in the expansile rib lesion

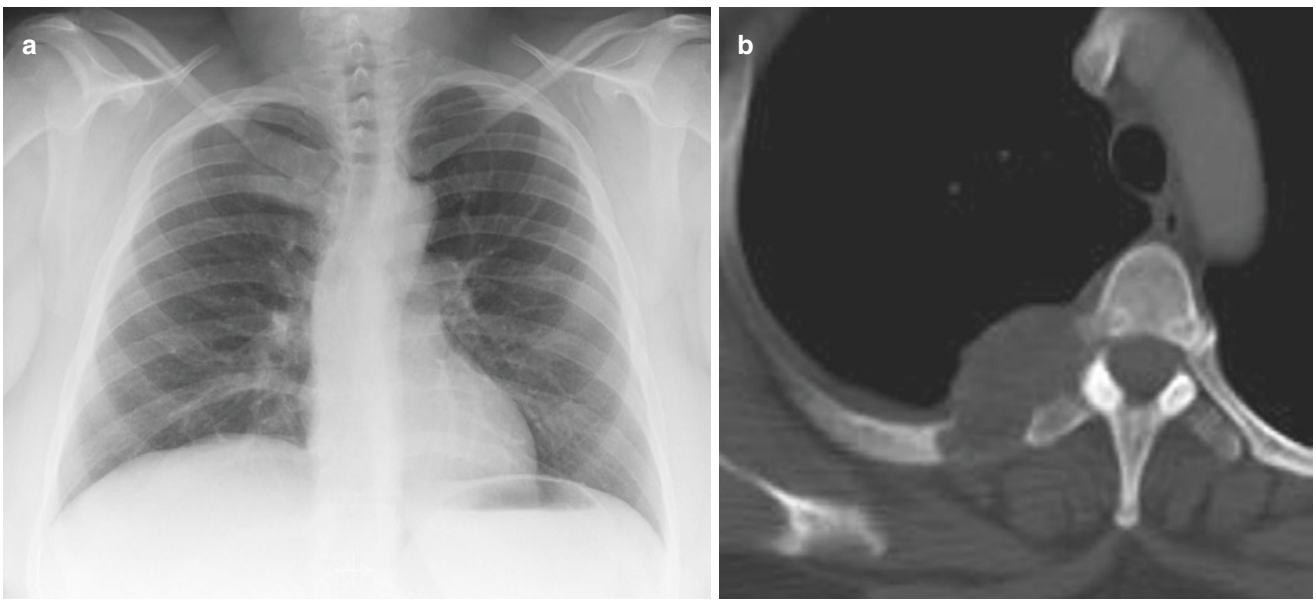

Fig. 12.11 A 31-year-old woman with giant cell tumor of the rib. (**a**) Frontal chest radiograph shows an area of sclerosis in posterior right fifth rib. (**b**) Axial CT image shows a lytic expansile lesion with soft-tissue component accounting for increased density on the radiograph. (**c**) Axial MRI T2WI demonstrate fluid-fluid levels in the lesion

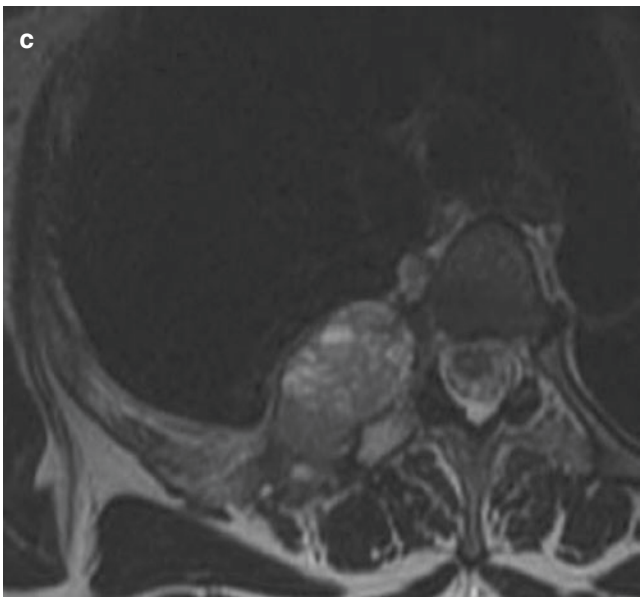

Fig. 12.11 (continued)

shows incomplete fat suppression and may show enhancement with a prominent feeding vessel (Fig. 12.13).

12.6.5 Fibroblastic-Myofibroblastic Tumors

Elastofibroma and fibromatosis are two examples of these lesions involving the chest wall. Elastofibroma dorsi is a benign soft-tissue tumor composed of fibrous tissue with internal fatty streaks, at a characteristic location. It is suggested that the elastofibroma results from hyperproliferation of fibroelastic tissue between the scapula and the thoracic wall due to repetitive microtrauma caused by friction. Imaging features of fibroblastic-myofibroblastic tumors are described in Table 12.9 (Fig. 12.14). Fibromatosis is also known as desmoid tumor and can arise from connective tissue and even from post-trauma or postsurgical scar [14]. These lesions are benign but locally aggressive, often seen in young adults.

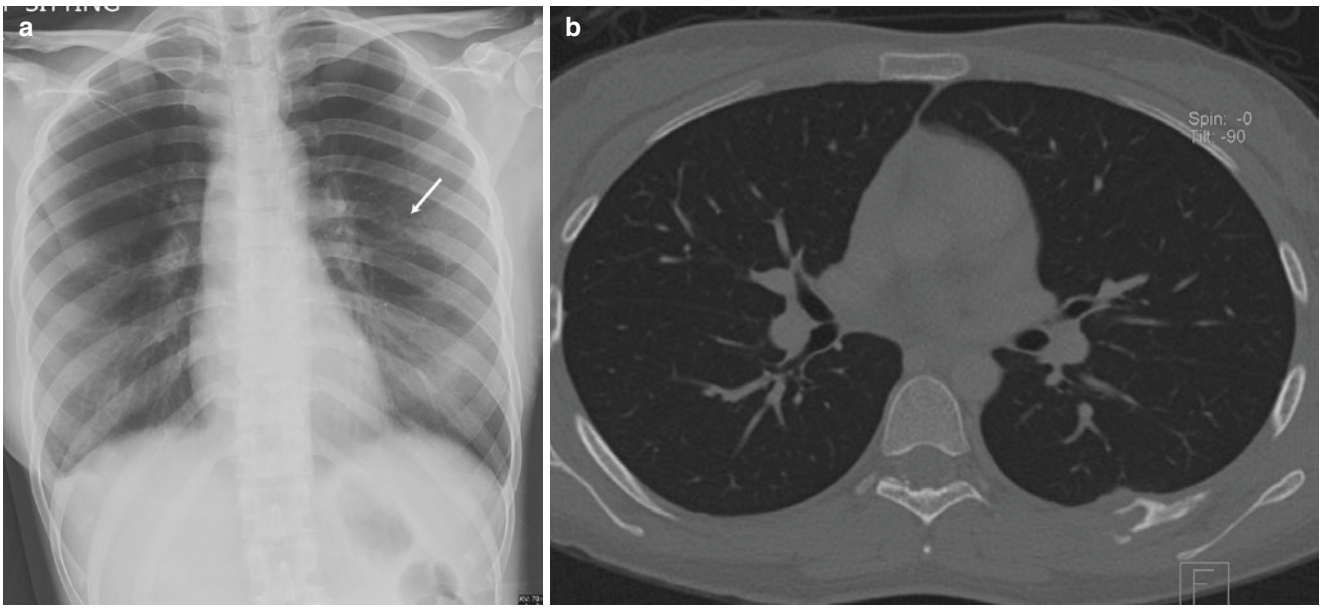

Fig. 12.12 Langerhans cell histiocytosis in a young man. (**a**) Frontal chest radiograph shows a lytic lesion in the left seventh rib (arrow). (**b**) Axial CT image and (**c**) whole body bone scan images demonstrate the solitary lytic rib lesion

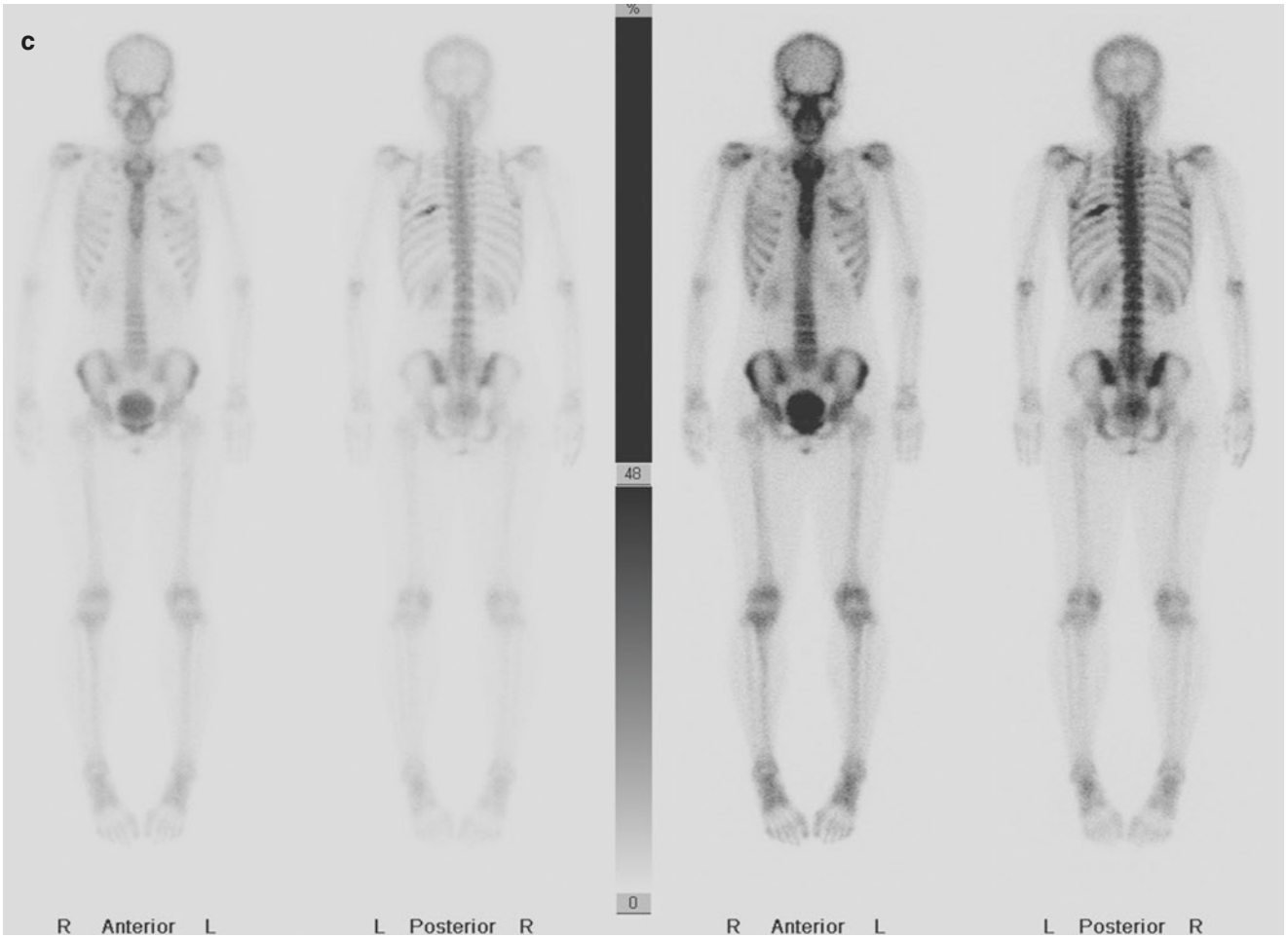

Fig. 12.12 (continued)

12.7 Malignant Tumors

Malignant chest wall neoplasms can arise from the bones or the soft-tissue structures and can be classified into osseous and soft-tissue malignancies [16].

12.7.1 Malignant Osseous Tumors

Malignant bony tumors demonstrate bone destruction and associated soft-tissue component. Identification of the matrix is important in distinguishing subtypes; hence CT plays an important role (Table 12.10).

Chondrosarcoma is the commonest primary malignancy of the chest wall, accounting for almost one-third of all cases of primary malignant lesions and about one-third cases of primary rib malignancies [17]. It can also arise due to malignant transformation of the benign chondroid lesion (enchondroma, osteochondroma) (Fig. 12.15) or following radiotherapy. These tumors are usually seen in the older population (fourth to seventh decade); patients usually present with the painful chest wall mass lesion. Osteosarcomas arise from the ribs, scapula, or clavicle (osseous form) or from soft tissues (extra osseous form). These tumors are usually seen in young adults and present as painful mass lesions. Chest wall osteosarcomas have higher rates of lung and

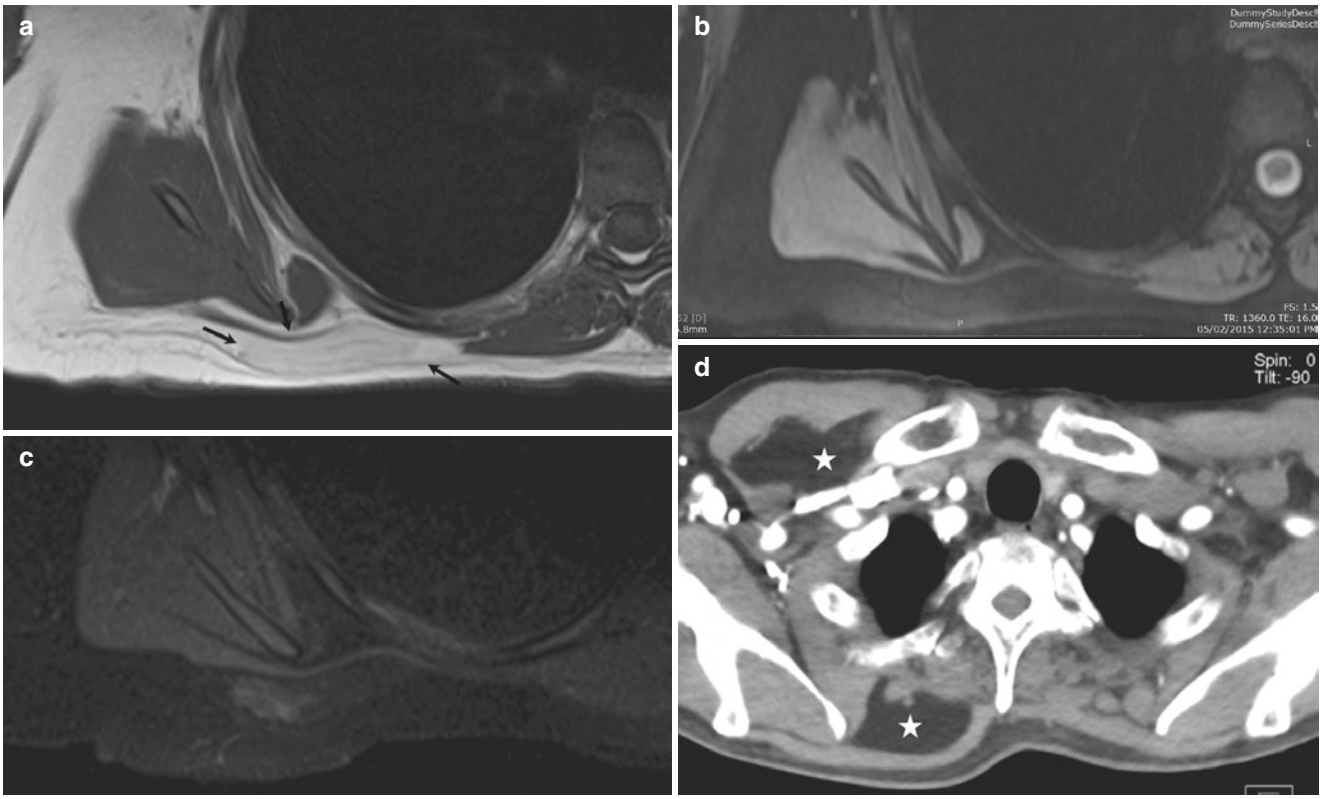

Fig. 12.13 A 55-year-old man with a vague lump over scapula since many years. (**a**) Axial T1W image shows a well-defined mass within subcutaneous fat but with slightly less bright as compared to the rest of the fat (arrows). Note linear band within the mass. (**b**) Fat-sat T2W image shows incomplete suppression of fat. (**c**) Postcontrast fat-sat image demonstrates the enhancement in the lesion with a prominent central feeding vessel. (**d**) Intermuscular lipomas (asterisks) in another patient

Table 12.9 Imaging findings in fibroblastic-myofibroblastic tumors

Elastofibroma	• Usually seen in elderly females with symptoms of dull pain and swelling present only in half of the cases • Classically found in the infrascapular regions, deep to the serratus anterior and latissimus dorsi muscles • 60% of elastofibromas are bilateral • Ultrasound (USG): soft-tissue mass with multilayered pattern (hypoechoic linear areas of fat with echogenic fibrous tissue) • CT: ill-defined mass similar in attenuation to the adjacent muscle with or without internal low-density foci • MRI: fascicular/layered pattern, as seen on USG. Signal intensity similar to muscle on T1WI and T2WI with fatty component seen as high signal intensity area. Heterogeneous mild enhancement
Fibromatosis	• CT: ill-defined mass with variable attenuation and enhancement • MRI: heterogeneous signal intensity mass with prominent enhancement, may show hypointense bands on T2WI

lymph nodal metastasis and local recurrence. Ewing sarcoma tumors include osseous Ewing sarcoma, extra-osseous Ewing sarcoma, and Askin tumor, also known as peripheral primitive neuroectodermal tumor of the chest wall [16]. These tumors are highly aggressive, typically seen in young patients, especially children. Lesions usually present with pain, sometimes as a palpable chest wall mass.

Solitary bone plasmacytoma, extramedullary plasmacytoma, and multiple myeloma are plasma cell tumors, typically seen in the older population (Fig. 12.16). The solitary disease can sometimes progress to multiple lesions over time. Patients can present with pain, anemia, and renal failure or with a pathological fracture. FDG PET-CT assessment is useful in assessing the number of lesions and in follow-up evaluation, as a response to treatment.

The osseous metastatic disease can involve the chest wall bones and can be seen as lytic, sclerotic, or mixed lesions (Fig. 12.17).

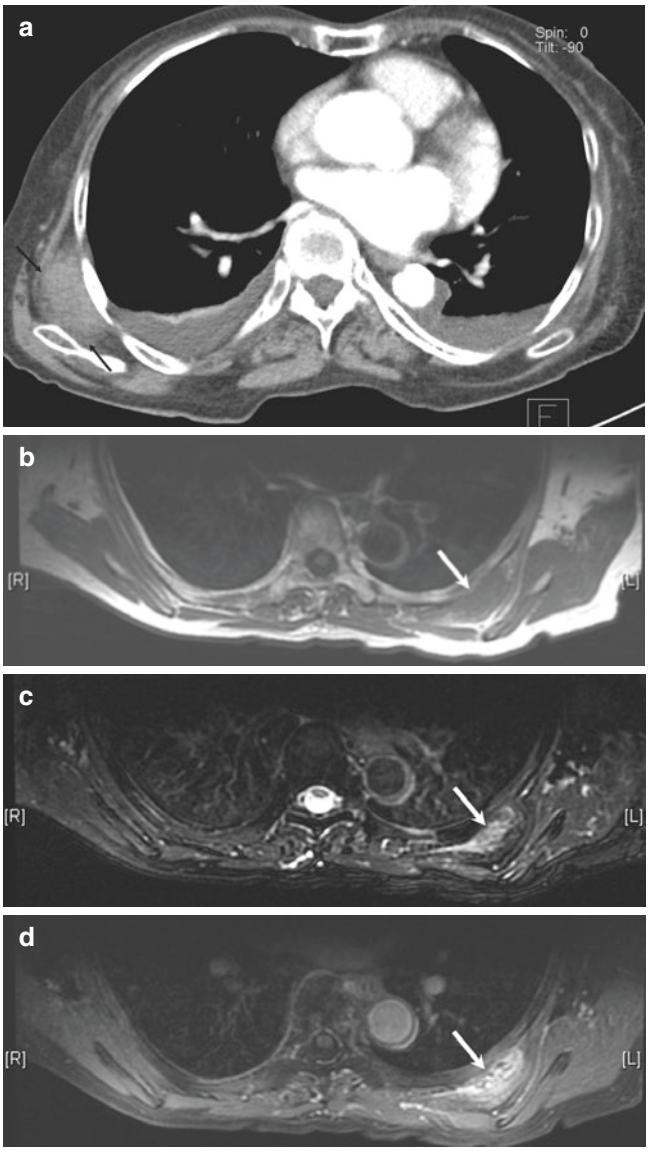

Fig. 12.14 Elastofibroma dorsi in two patients. Patient 1. (**a**) Axial CT shows an ill-defined soft tissue on the right side at characteristic location (arrows). Patient 2. (**b**–**d**) Axial T1W, T2W, and postcontrast T1W images show typical features of elastofibroma (arrow) on the left side

Table 12.10 Synopsis of imaging findings in malignant osseous chest wall tumors

Chondrosarcoma	• Most frequent involvement of upper ribs and anterior chest wall • Radiograph: lytic lesion, "rings and arcs" calcification, a wide zone of transition, endosteal scalloping, permeative pattern, cortical thickening, and periosteal reaction • CT: tumor matrix better identified with other radiographic features • MRI: variable signal on T1WI, the high signal on T2WI with areas of low signal (dense mineralization), inhomogeneous enhancement
Osteosarcoma	• Radiograph: features of the aggressive bone lesion with calcified/ossified matrix • CT: soft-tissue mass with calcified/ossified matrix (dense, cloud-like), areas of necrosis • MRI: soft-tissue component is hyperintense to muscle on T1WI, iso- to hyperintense to muscle on T2WI, heterogeneous postcontrast enhancement
Ewing sarcoma tumors	• Radiograph: features of the aggressive bone lesion • CT: heterogeneous mass lesion with necrosis, cystic areas, hemorrhage, onion skin periosteal reaction in osseous lesions • MRI: heterogeneous signal intensity on T1WI and T2WI (hyperintense), with areas of hemorrhage and intense postcontrast enhancement
Solitary and multiple myeloma	• Radiograph/CT: solitary or multiple bony expansile lytic lesion • MRI: – Non-treated: T1 hypointense, T2 hyperintense, postcontrast enhancement – Treated: heterogeneous signal on T1 and T2WI with heterogeneous enhancement – Inactive disease: T1 hyperintense, T2 hypointense, no enhancement

12.7.2 Malignant Soft-Tissue Tumors

Malignant soft-tissue tumors of the chest include leiomyosarcoma and rhabdomyosarcoma (arising from muscle), angiosarcoma and Kaposi sarcoma (from vascular structures), liposarcoma (arising from adipose tissue), and malignant peripheral nerve sheath tumors (Table 12.11) [18]. CT and MRI can be helpful in distinguishing the malignant lesion from benign by identifying the invasive features of the mass, associated bony destruction, lymphadenopathy, and metastases. CT/MRI can be diagnostic in liposarcoma by identifying the soft-tissue component in a fatty mass (Fig. 12.18). In contrast to benign masses, malignant chest wall masses are intensely PET avid. Leiomyosarcomas are usually seen in adult patients between 50 and 70 years of age and present as solitary masses (Fig. 12.19). Rhabdomyosarcomas are high-grade malignant tumors, seen in patients younger than 45 years of age. These tumors present as rapidly growing mass lesions with associated pain or compressive symptoms. Angiosarcomas present as rapidly growing, large, painful masses and may be associated with prior radiation treatment for breast cancer. MPNST should be suspected on

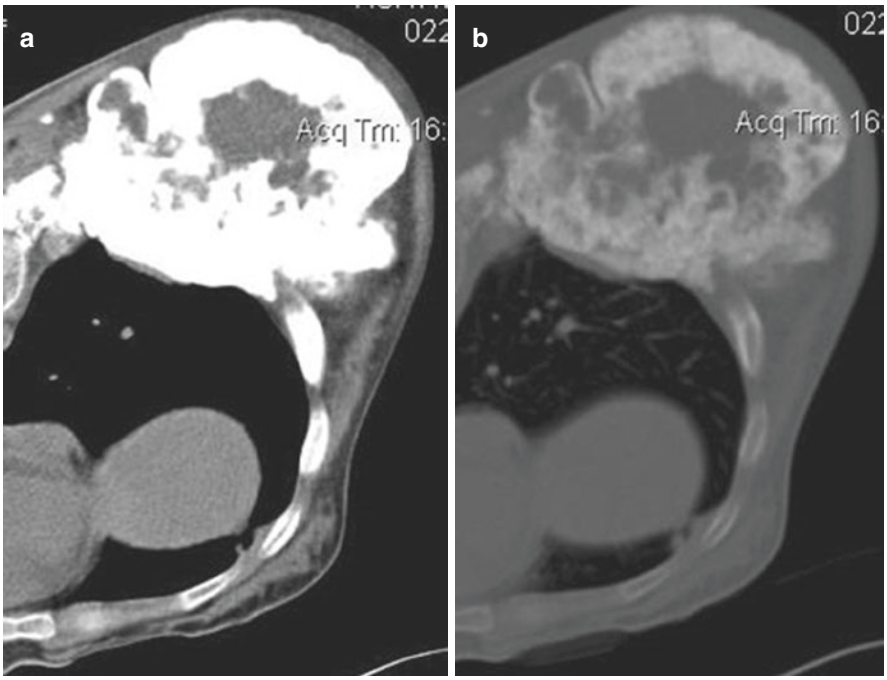

Fig. 12.15 Chondrosarcoma of the rib. (**a**, **b**) Axial CT images show a large cartilaginous tumor of the rib

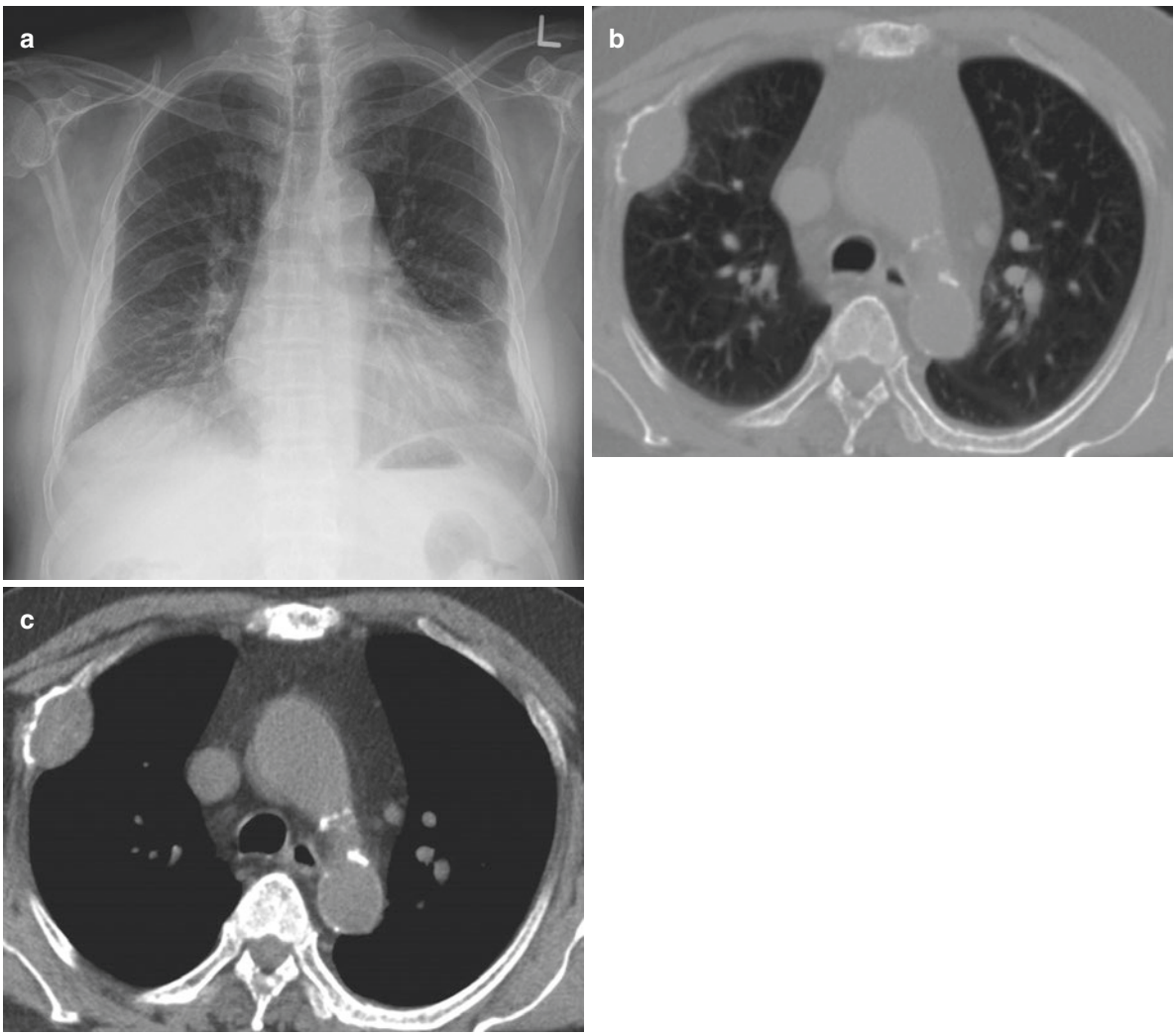

Fig. 12.16 Multiple myeloma in an elderly patient. (**a**) Frontal chest radiograph shows heterogeneous attenuation of ribs, clavicle, and scapulae and multiple rib fractures. (**b**, **c**) Axial CT images confirm all findings and in addition reveal an expansile right upper rib lesion

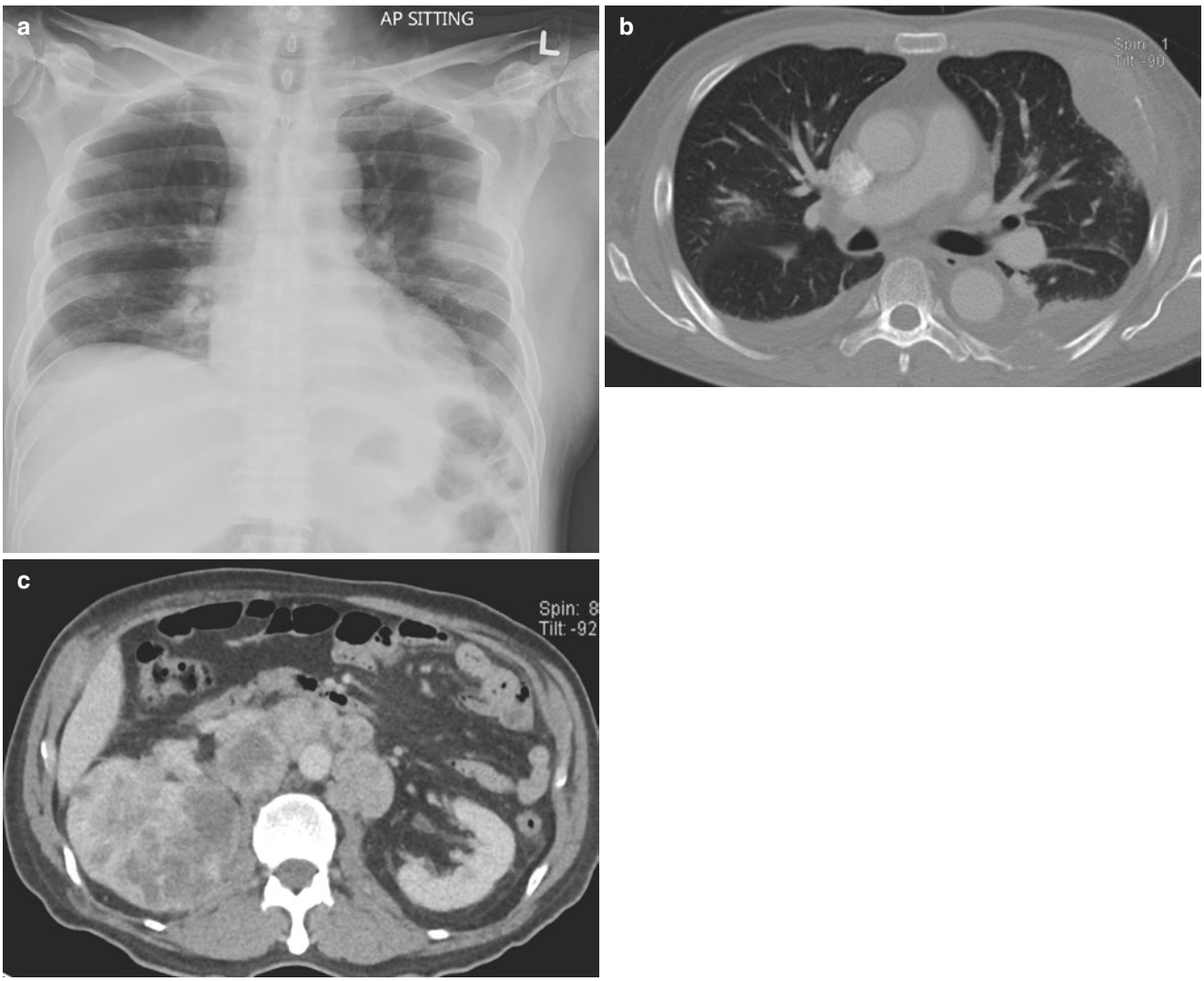

Fig. 12.17 Lytic expansile bony metastases. (**a**) Frontal chest radiograph shows lytic lesions associated with extrapulmonary soft tissue in the left fourth and sixth ribs. (**b**, **c**) Axial CT images show the lytic expansile rib lesions and advanced right renal cell carcinoma

Table 12.11 Synopsis of imaging findings in malignant soft-tissue chest wall tumors

Liposarcoma	• CT: large fatty tumors (>10 cm) with nodular soft tissue; density higher than normal fat, heterogeneous mass, may contain calcification/ossification • MRI (myxoid liposarcoma): high signal intensity on TWI1 and T2WI with enhancement of thick internal septa • MRI (round cell liposarcoma): low signal on T1WI, high signal intensity on T2WI • Dedifferentiated liposarcoma: new areas of T2 hyperintense signal or T1 hypointense signal in previous well-differentiated liposarcoma • Thick enhancing septa (>2 mm)
Leiomyosarcoma	• CT: large mass with areas of cystic change or necrosis • MRI: T1 hypointense and T2 hyperintense signal intensity, spindle shape, peripheral rim enhancement
Rhabdomyosarcoma	• CT: soft-tissue density mass, may show the associated bone destruction • MRI: T1WI: low-to-intermediate signal T2WI: hyperintense signal, may show flow voids Postcontrast: non-enhancing areas of necrosis alternating with ringlike areas of marked enhancement (alveolar and pleomorphic subtype)
Malignant peripheral nerve sheath tumor	• CT: large heterogeneous mass, may show bone destruction • MRI: large aggressive mass along peripheral nerve course Iso to hypointense on T1WI, hyperintense and heterogeneous appearance on T2WI, heterogeneous enhancement Target sign and fascicular sign are seldom seen
Angiosarcoma	• CT: heterogeneous appearance, marked enhancement, feeding vessels around the tumor • MRI: T2 hyperintense mass, may have flow voids, marked enhancement. Associated lymphedema is characteristic

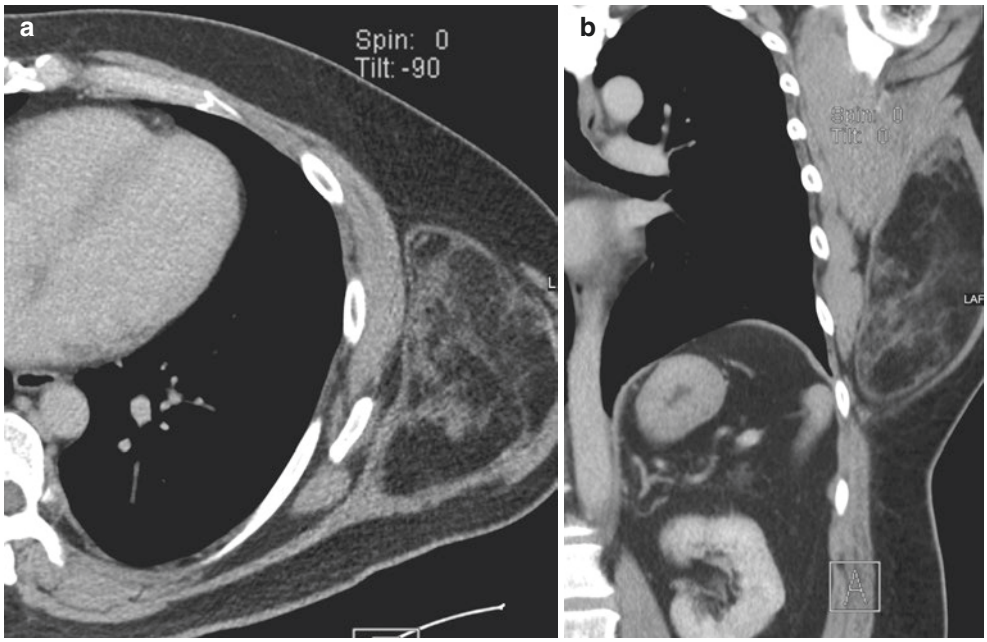

Fig. 12.18 A 44-year-old patient with left chest wall liposarcoma. (**a**, **b**) Axial and coronal contrast-enhanced CT images show a fat-density mass in the left lateral chest wall with internal soft-tissue component and septations

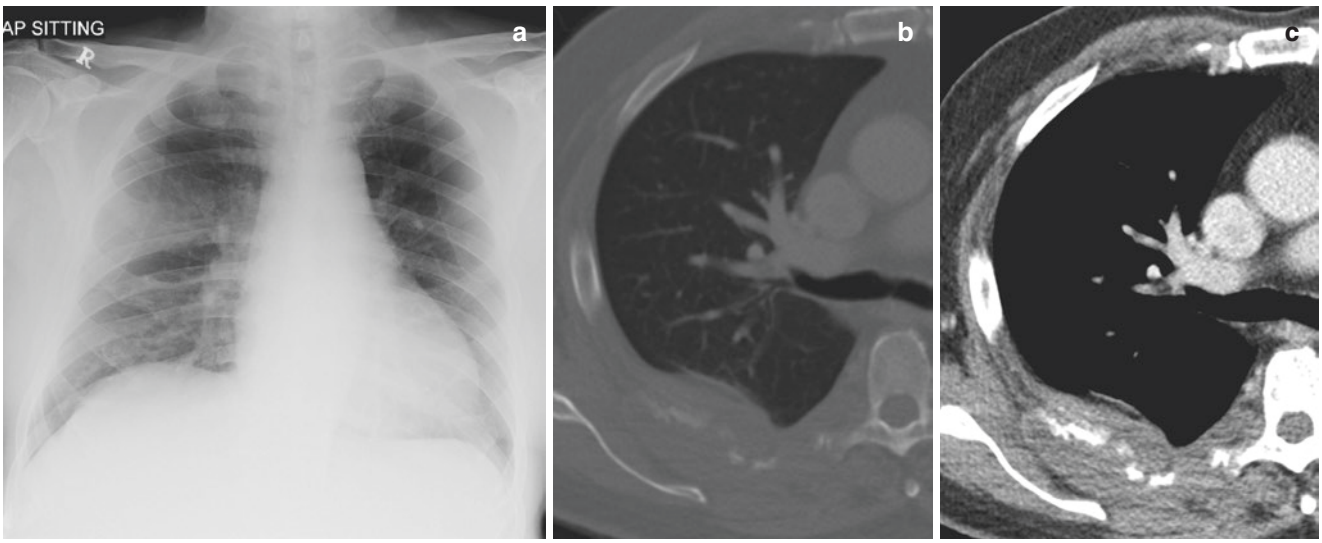

Fig. 12.19 A 59-year-old man with leiomyosarcoma. (**a**) Frontal chest radiograph shows a destruction of the right sixth rib. (**b**, **c**) Axial CT images show a destructive lesion of the rib with large associated soft tissue

MRI in a rapidly enlarging tumor with size more than 5 cm, the presence of peripheral enhanced pattern, presence of perilesional edema-like zone, and presence of intratumoral cystic change (Fig. 12.20). PET is useful in differentiating malignant from benign nerve sheath tumors as the malignant counterparts are intensely FDG-avid on PET.

Primary thoracic malignancies like breast cancer, lung cancer, pleural malignancies or even mediastinal malignancies can invade the chest wall directly [16] (Fig. 12.21).

12.8 Pearls and Pitfalls

Various normal variants and some benign conditions involving the chest wall can be misinterpreted as significant pathologies [2]. The common benign bone lesions like bone islands and old rib fractures can be misinterpreted as lung nodules on radiograph (Figs. 12.22 and 12.23). Other extrapulmonary masses like rib osteochondromas can grow both outward and inward (internal exostoses) and may pose a diagnostic challenge on radiograph (Fig. 12.24). Nipples and

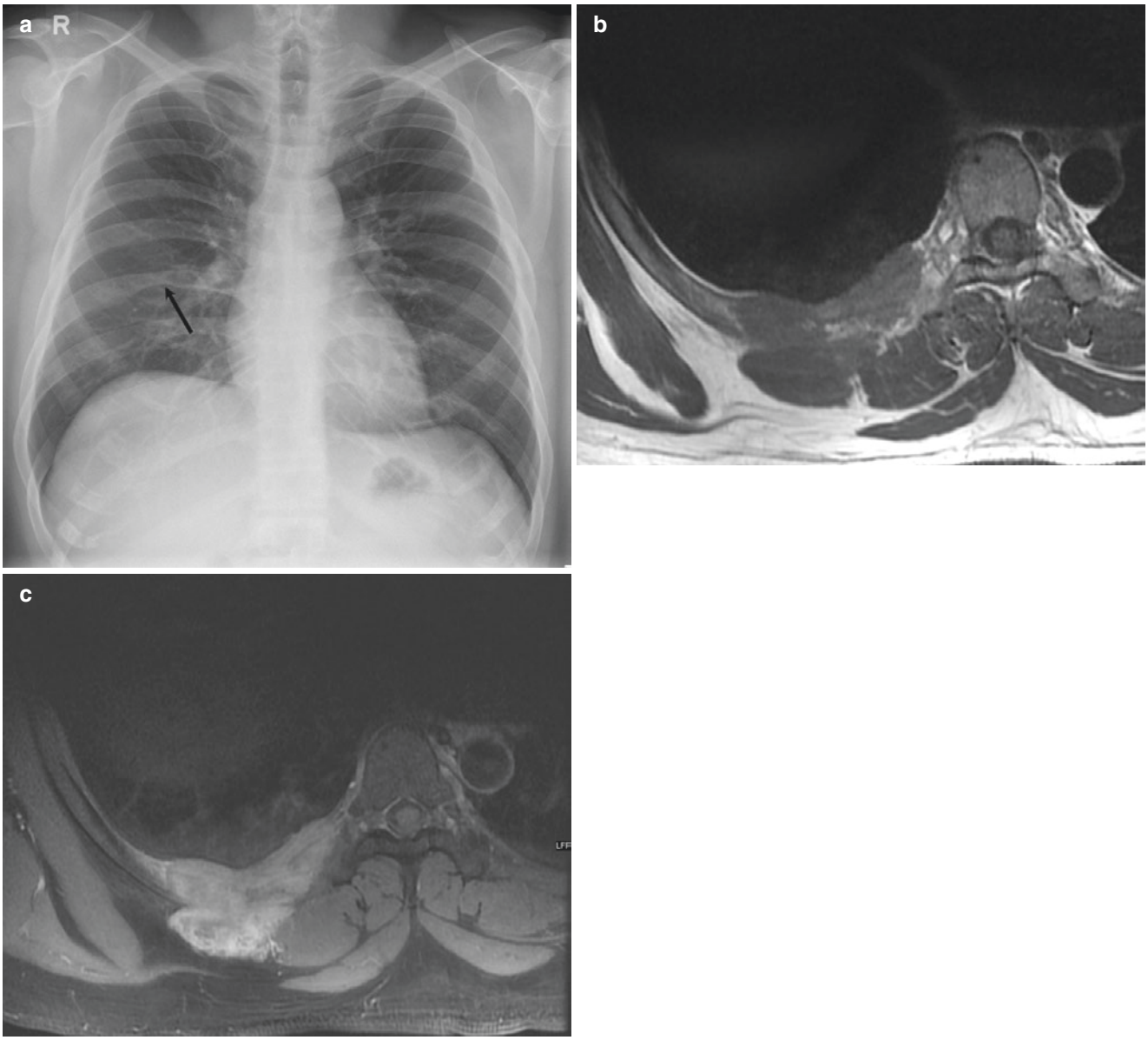

Fig. 12.20 A 45-year-old man with malignant peripheral nerve sheath tumor. (**a**) Frontal chest radiograph shows focal inferior notching of the right eighth rib posteriorly (arrow). (**b**, **c**) Pre- and postcontrast T1W images demonstrate the ill-defined mass along the inferior border of the rib with heterogeneous enhancement and advancing front invading the posterior chest wall muscles

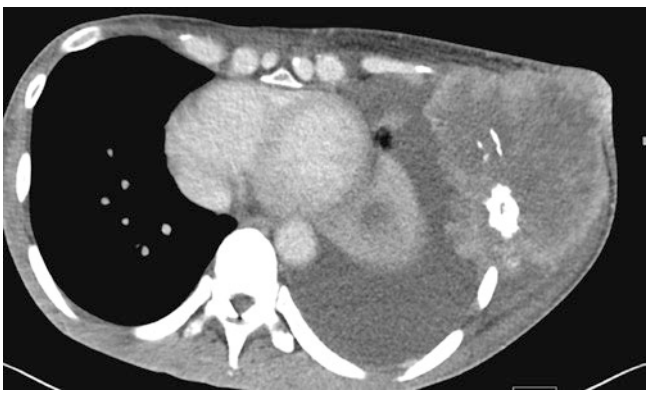

Fig. 12.21 Primary fungating breast cancer invading the chest wall, pleura, and causing the destruction of ribs

cutaneous nodules like neurofibromas can also be mistaken for lung nodules on a chest radiograph (Fig. 12.25). These pitfalls can be minimized by careful evaluation of the borders of the mass. Extrapulmonary masses form an obtuse angle and often show indistinct borders at least a portion of their margins at chest radiography termed "incomplete border sign." Incomplete border sign is seen in extraparenchymal lesions like loculated pleural effusions, rib lesions, skin nodules, and nipple shadows. The presence of abnormal lucencies in the supraclavicular region and chest wall on a chest radiograph is an important clue in diagnosing subcutaneous emphysema from pneumomediastinum (Fig. 12.26). One should remember that a large chest wall blister may mimic the radiographic appearance of subcutaneous emphy-

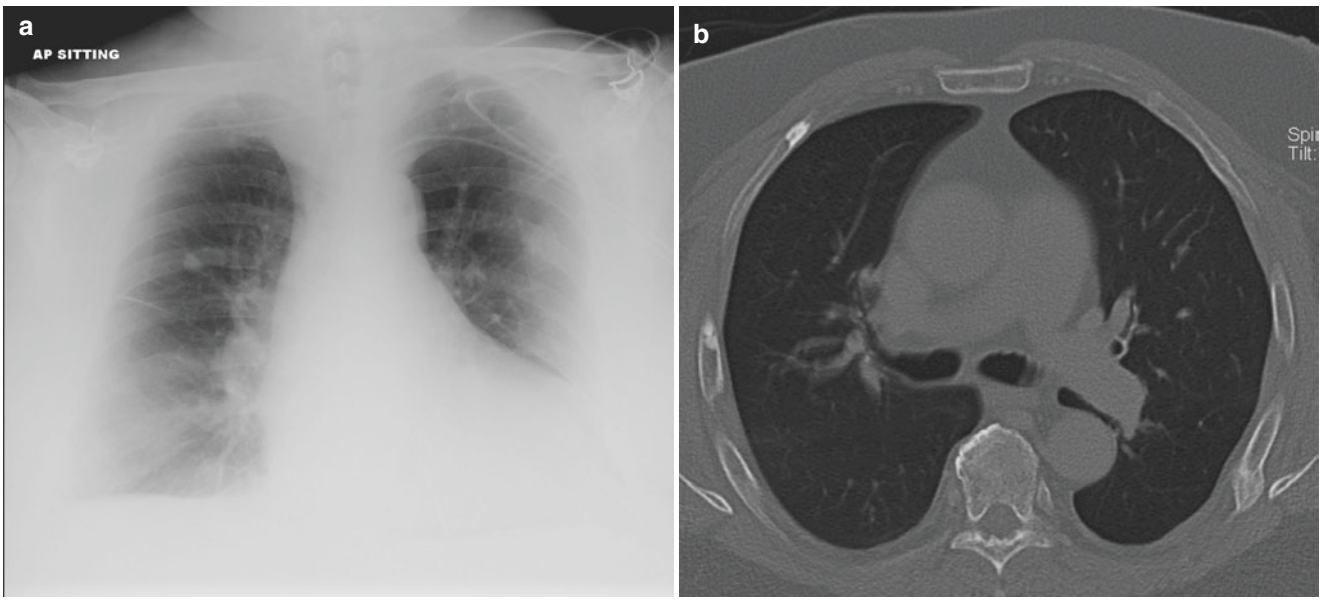

Fig. 12.22 Focal rib sclerosis mimicking nodule. (**a**) Frontal chest radiograph shows a nodule projecting over the right mid-zone. (**b**) Axial CT image reveals a vague sclerotic focus located in the rib accounting for the nodular shadow on the radiograph

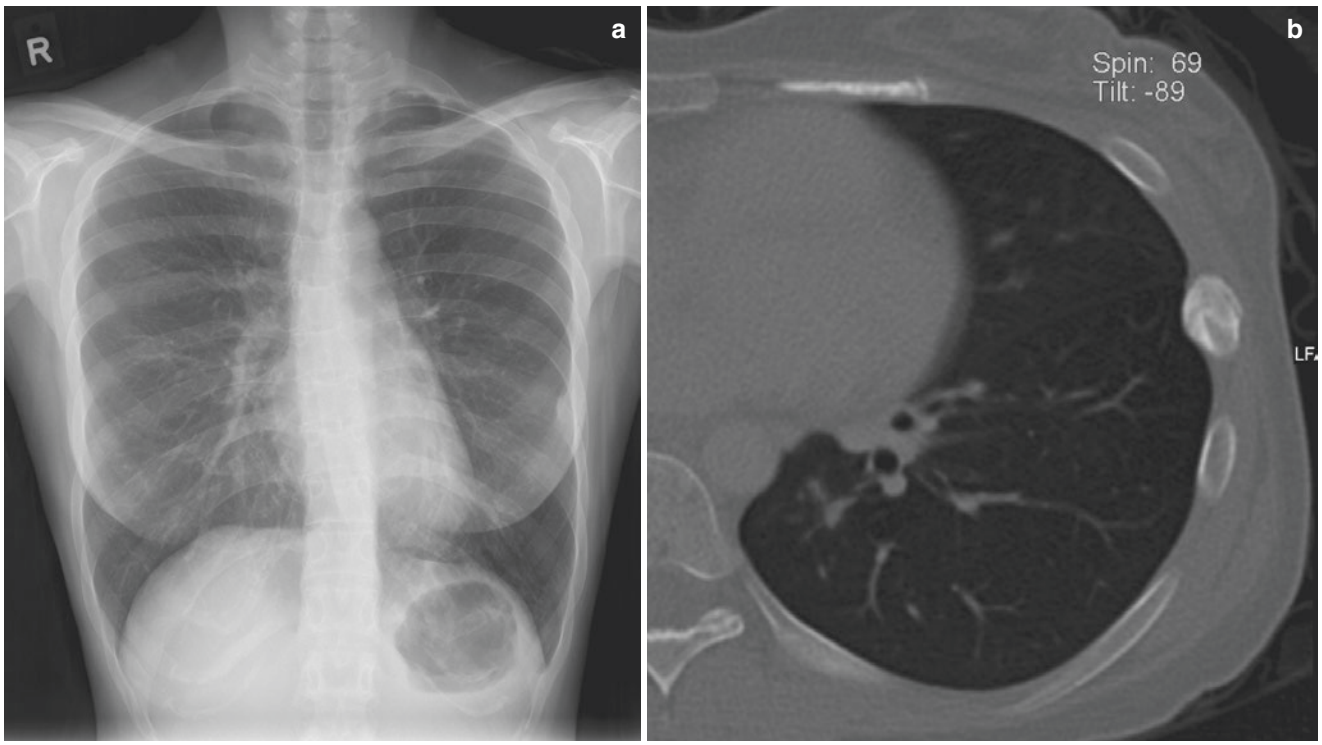

Fig. 12.23 Rib fracture mimicking a nodule. (**a**) Frontal chest radiograph shows a broad-based nodular opacity in the left mid-zone. Note the obtuse angle of the opacity with chest wall and incomplete border sign. (**b**) Axial CT image reveals a subacute rib fracture

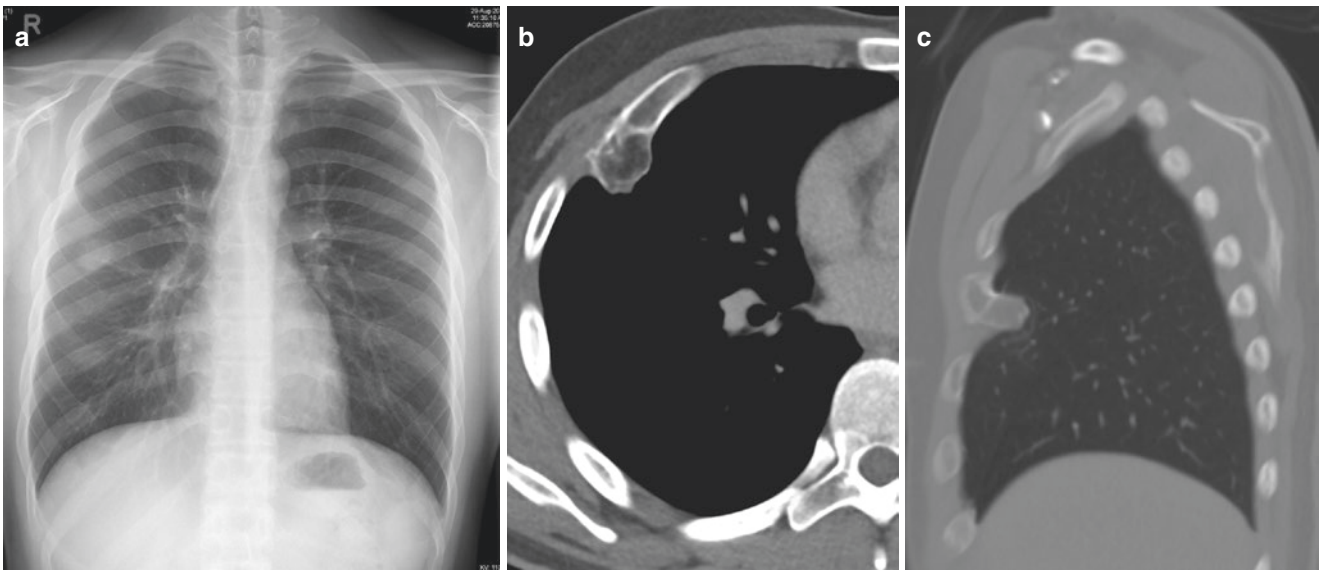

Fig. 12.24 Exostosis mimicking a lung nodule. (**a**) Frontal chest radiograph with a nodular opacity in the right mid-zone. Note the inner margins of nodule are sharp, while the lateral margin is blur (incomplete border sign). (**b**, **c**) Axial and sagittal CT images show exostoses growing inward

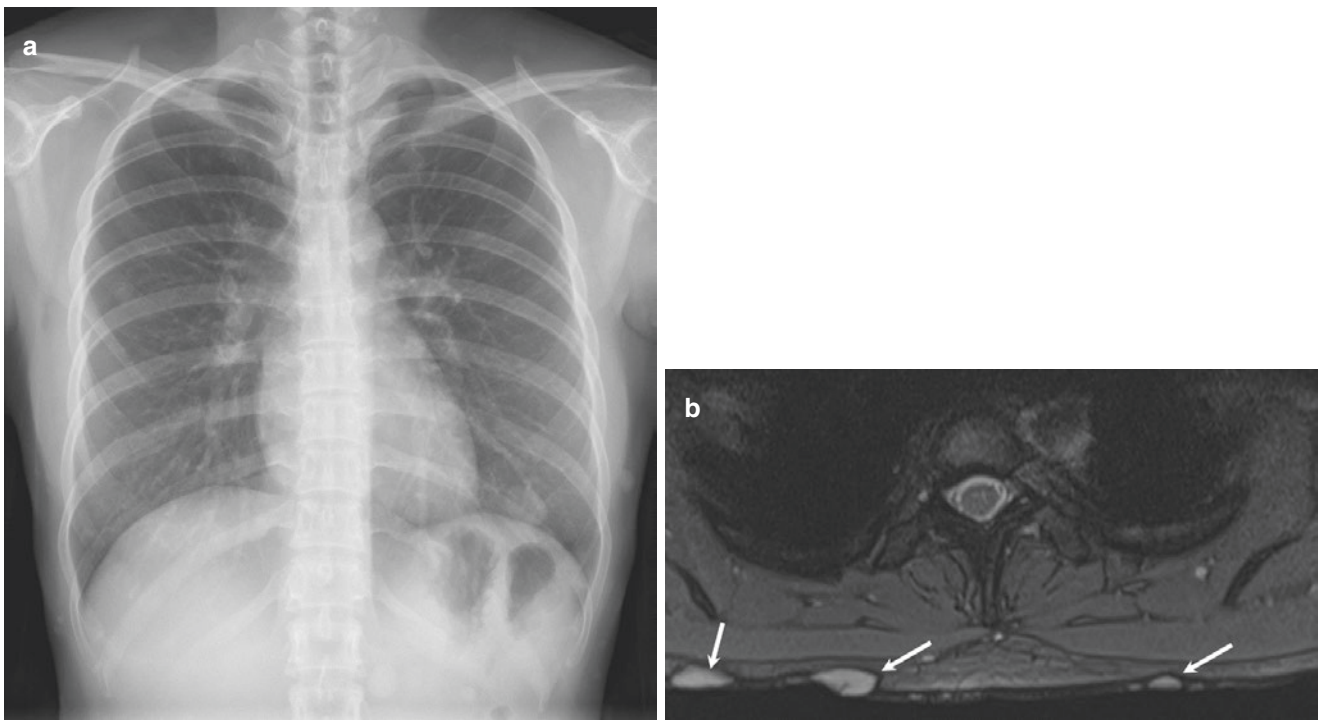

Fig. 12.25 Neurofibromas mimicking lung nodules in a patient with neurofibromatosis type 1. (**a**) Frontal chest radiograph shows small nodular opacities in bilateral lower zones. Note incomplete border sign. (**b**) Axial T2* MRI image reveals multiple cutaneous neurofibromas

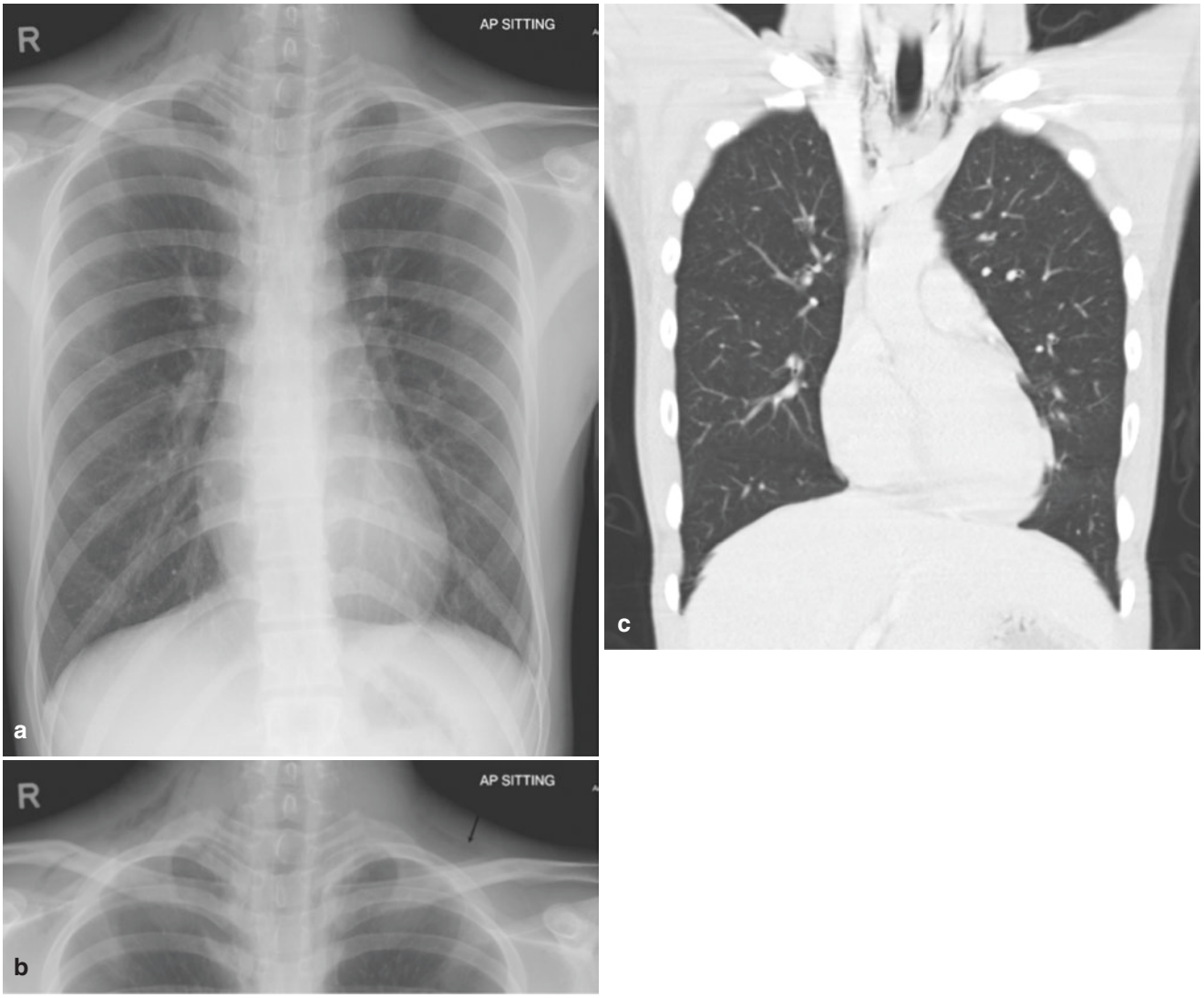

Fig. 12.26 Pneumomediastinum in a young male patient. (**a**, **b**) Frontal chest radiograph and a magnified view show multiple thick lucencies in the right supraclavicular fossa region and right paratracheal region. Note that there is always a thin horizontal lucent line in supraclavicular fossa from the intermuscular fat plane as on the left side (black arrow), but a thicker lucency or multiple lucent lines or mottled shadow is a red flag for subcutaneous emphysema. (**c**) Coronal CT image demonstrates changes of pneumomediastinum with tracking of gas in the deep neck spaces and right upper chest wall

sema (Fig. 12.27). One must also be aware of lung herniation through intercostal space in the chest wall that may present as a focal chest wall swelling. A lung hernia can be congenital, post-traumatic, or post-thoracotomy (Fig. 12.28).

12.9 Pleura

The pleura is a double-layered membrane around the lungs, composed of parietal and visceral layers, enclosing the pleural space. It is normally not visualized on the chest radiograph, save for interlobar fissures and junctional lines. Normal pleural layers can be seen as imperceptible thin lines on CT. The pleura can be involved in numerous infections, inflammatory processes, and benign and malignant neoplasms. Invasive lung carcinoma and asbestos-related disease account for the majority of the cases of pleural mass lesions [19]. The imaging manifestations of the pleural disease are focal or diffuse thickening, effusion, and calcification [20].

12.9.1 Pleural Effusion

Fluid in the pleural space can be secondary to a large number of causes. Pleural effusions can be transudative or exudative,

and the list of differentials for each type is quite extensive. Ultrasound has a higher sensitivity in detecting small pleural effusions, compared to radiographs. A chest radiograph can predict the approximate amount of pleural effusion (Table 12.12) [21, 22]. However, the prediction of the amount of pleural fluid on a supine or anterior-posterior radiograph is challenging due to the impact of positioning, and these radiographs frequently underestimate the pleural fluid. Large effusions without mediastinal shift suggest underlying lung collapse or mediastinal fixation [23]. Subpulmonic pleural effusion is an effusion localized to diaphragmatic pleural space mimicking diaphragmatic elevation, but the relatively flat appearance and lateral peaking of the apparent dome should suggest a subpulmonic effusion. This can be con-

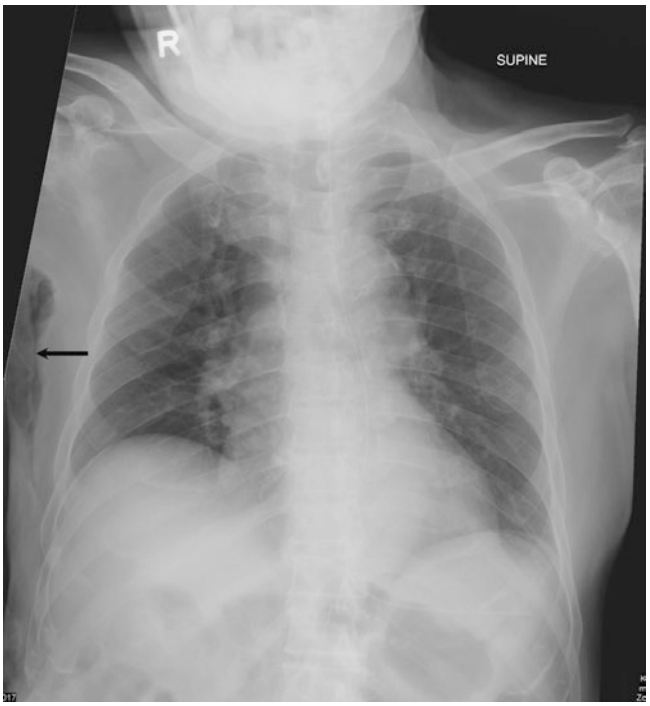

Fig. 12.27 Frontal chest radiograph in a patient with a right chest wall blister (arrow) mimicking subcutaneous emphysema

Table 12.12 Chest radiography of pleural effusion

Very small effusion (50 ml)	Only sign is blunting of posterior costophrenic angle on the lateral upright radiograph
Small effusion (200 ml)	Blunting of posterior as well as the lateral costophrenic angle on the erect posterior-anterior radiograph
Moderate pleural effusion (at least 500 ml)	Above signs and obliteration of hemidiaphragm
Massive pleural effusion	Opacification of hemithorax, mediastinal shift, inversion of the hemidiaphragm
Loculated effusion	Sharp medial margin, indistinct lateral margin, obtuse angle with the chest wall, may appear as a mass lesion
Subpulmonic effusion	Frontal radiograph: Elevation of hemidiaphragm, lateralization of the diaphragmatic peak Increased distance between the left lung base and gastric bubble (when on the left side) Lateral view: angular contour of lung base, peak at the oblique fissure

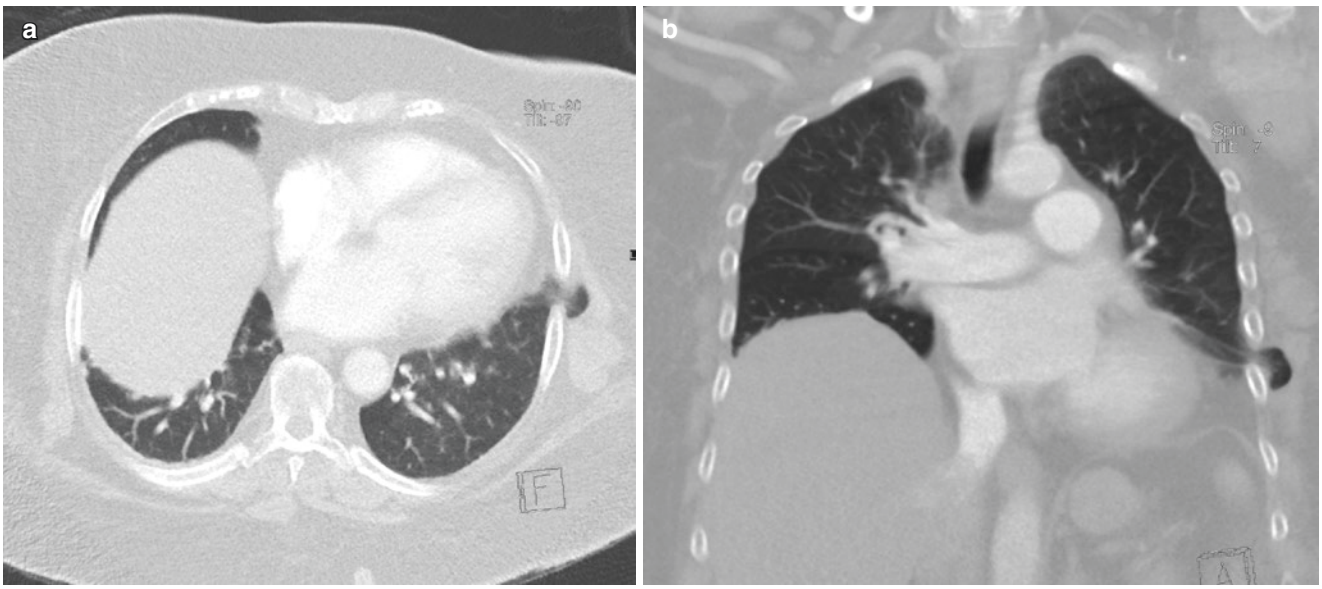

Fig. 12.28 Lung herniation in a middle-aged patient. (**a**, **b**) Axial and coronal CT images show intercostal herniation of the left lower lobe. This was presumed to be congenital as there was no history of trauma or surgery

firmed by a lateral decubitus radiograph or cross-sectional imaging (Fig. 12.29) [24]. Loculated pleural effusion can sometimes mimic a mass on radiograph termed as a vanishing tumor, pseudotumor, or phantom tumor. The mass-like loculated fluid within the fissures recurs with episodes of heart failure. Comparison with prior radiographs, close follow-up on radiograph, and frequently a lateral view help in localizing the pleural collection along the path of fissures (Fig. 12.29).

The clinical use of CT attenuation values to characterize pleural fluid (exudate versus transudate) is not accurate. However, acute hemothorax is seen as high attenuation pleu-

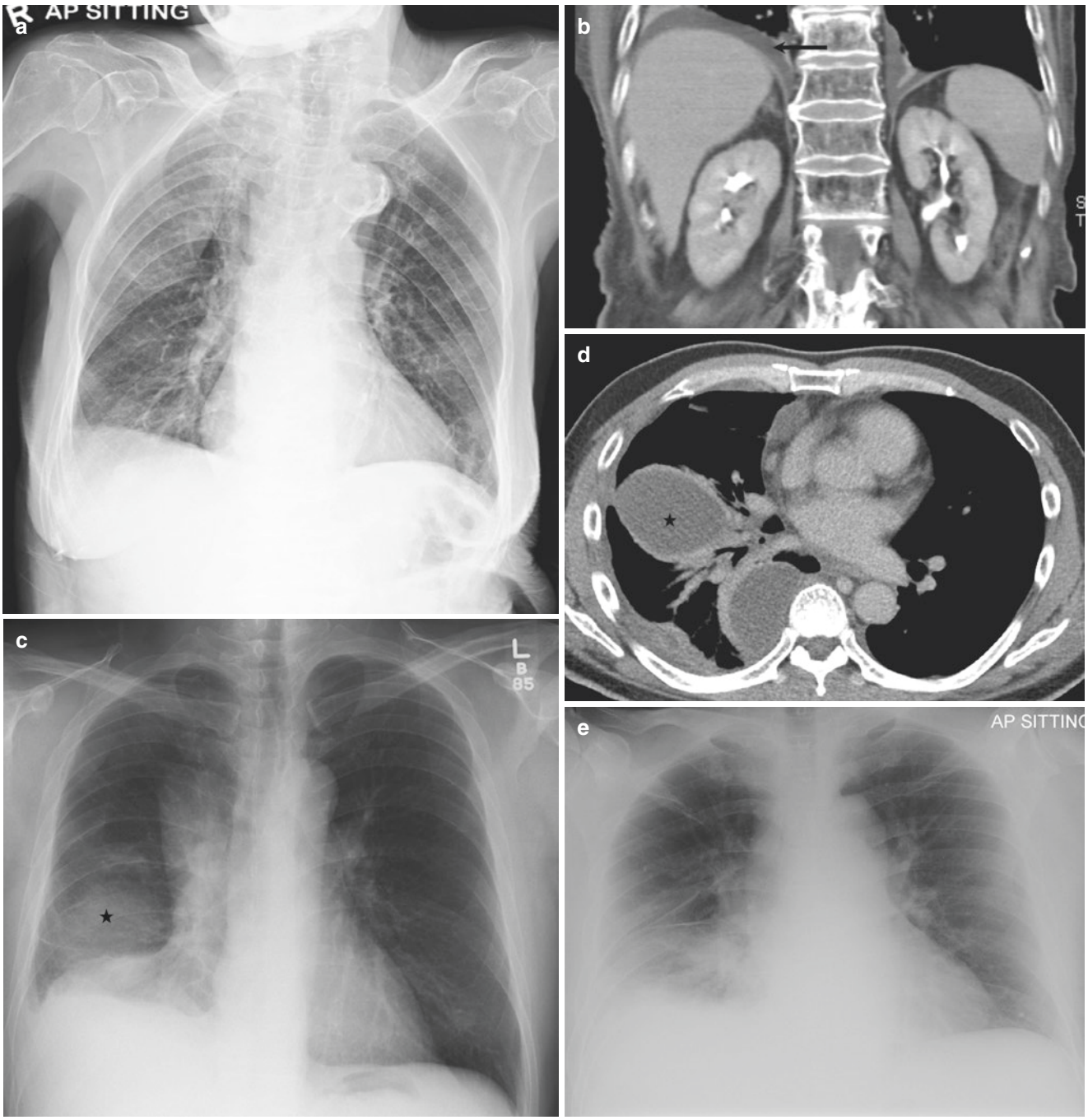

Fig. 12.29 Subpulmonic effusion. (**a**) Frontal chest radiograph shows a lateral peak of the right hemidiaphragm. (**b**) Coronal CT of the upper abdomen confirms a subpulmonic effusion (arrow). Vanishing tumor in another patient. (**c**) Frontal radiograph shows a mass-like opacity (asterisk) in the right lower zone. (**d**) Axial CT shows multiple loculated effusions and one in the right minor fissure (asterisk) accounting for the apparent mass on radiograph. (**e**) Follow-up radiograph after a week shows resolution of the vanishing tumor

ral fluid from 35 to 70 HU and may show fluid-fluid levels (Fig. 12.30). The density of hemothorax decreases with time. Infection and malignancy are the common cause for exudative pleural effusion and can be suspected by the presence of focal nodularity or diffuse thickening [25] (Fig. 12.31).

12.9.2 Empyema and Parapneumonic Effusions

Parapneumonic effusion is exudative pleural effusion associated with pneumonia that can proceed to complicated parapneumonic effusion, i.e., empyema, if left untreated. Uncomplicated parapneumonic effusion is treated by antibiotics and usually does not require drainage. Empyema or collection of pus in the pleural space requires prompt diagnosis and drainage (Fig. 12.32). On CT, the differentiation between uncomplicated pleural effusion and empyema is difficult. However, the presence of thickening enhancing pleura, pleural nodularity, and septations suggest the diagnosis of empyema in appropriate clinical settings. Tuberculous empyema may demonstrate calcification and can result in complications like bronchopleural fistula and empyema necessitans. "Trapped lung" is a clinical diagnosis when repeated pleural drainages fail to reexpand the chronically collapsed lung. It is due to fibrotic thickening of visceral pleural from a chronic inflammatory process. The visceral pleural along with noncompliant lung separates from the parietal pleura, and this space fills with fluid, with resultant hydropneumothorax (Fig. 12.33). Management of trapped lung is surgical, with the removal of the fibrosed visceral pleura.

12.9.3 Pneumothorax

Pneumothorax is the presence of gas in the pleural space. Tension pneumothorax is a potentially life-threatening condition and occurs due to progressive accumulation of gas,

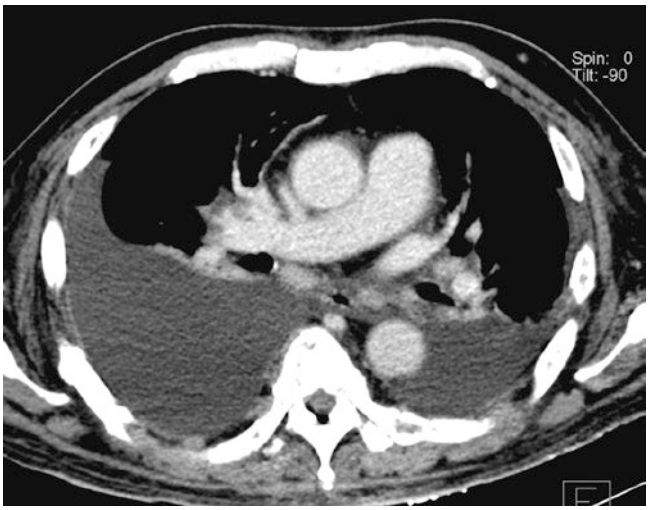

Fig. 12.31 Malignant pleural effusion. Axial CT images demonstrate bilateral pleural effusions with areas of nodular pleural thickening

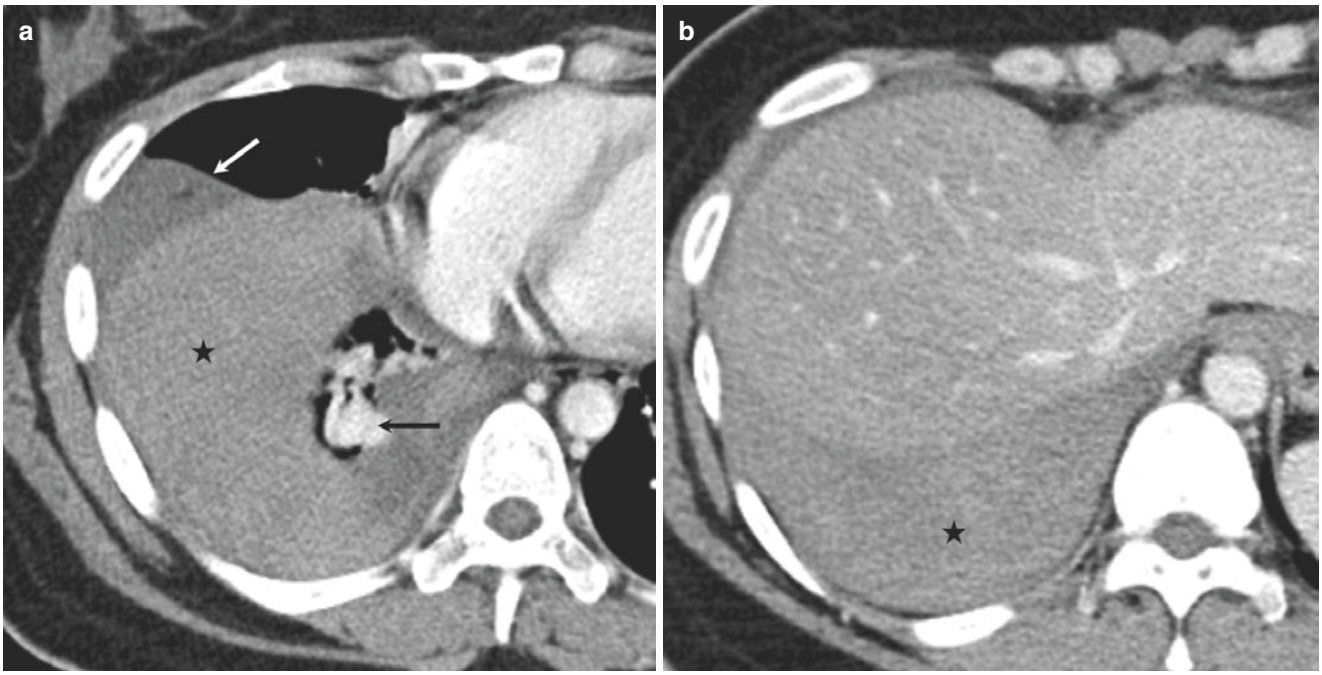

Fig. 12.30 Acute hemothorax from bleeding arteriovenous malformation (AVM). (**a**, **b**) Axial CT images show dependent high-density fluid with low-density fluid (white arrow) in the upper pleural compartment and an AVM (black arrow)

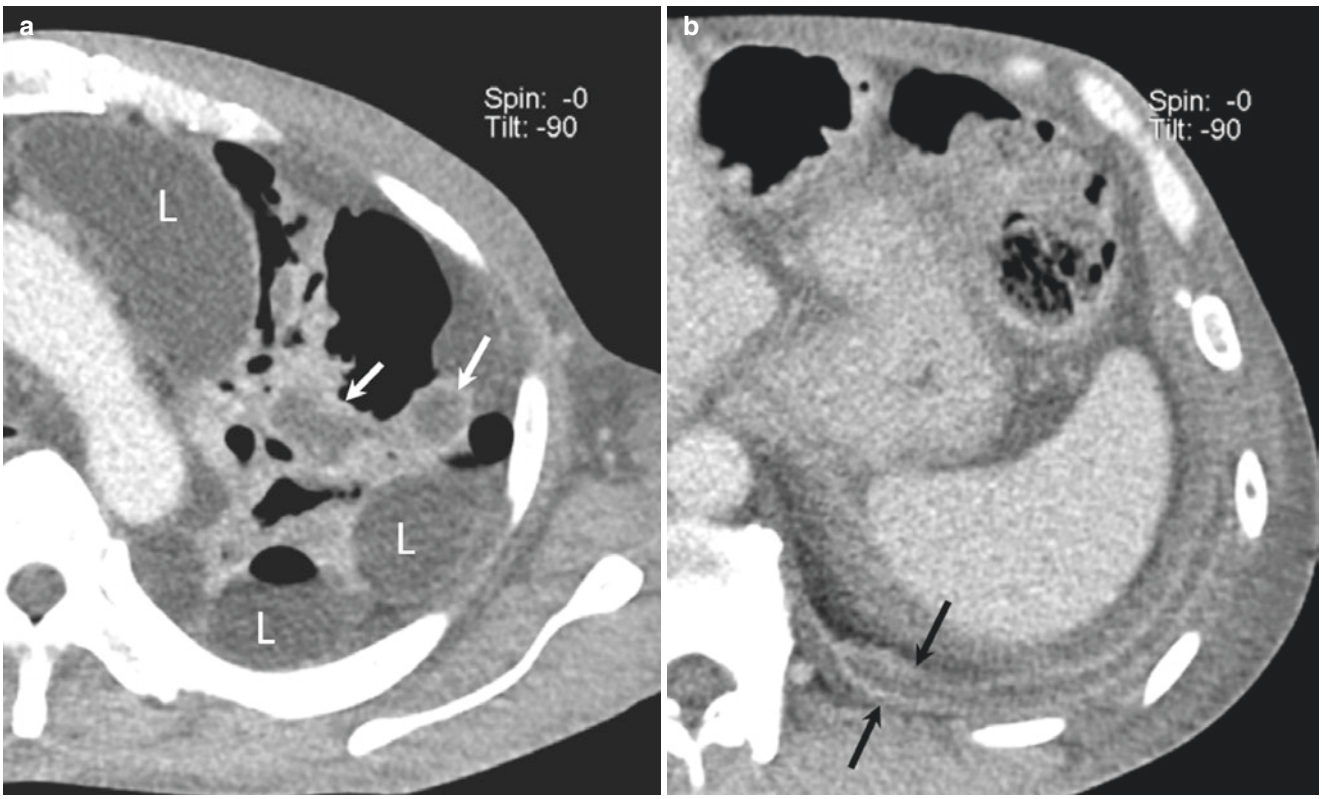

Fig. 12.32 Lung abscesses with empyema. (**a**) Axial CT image shows multiple abscesses (white arrows) in the left upper lobe with loculated empyema and (**b**) empyema in the left lower hemithorax (black arrows) (split-pleura sign). *L* loculated empyema

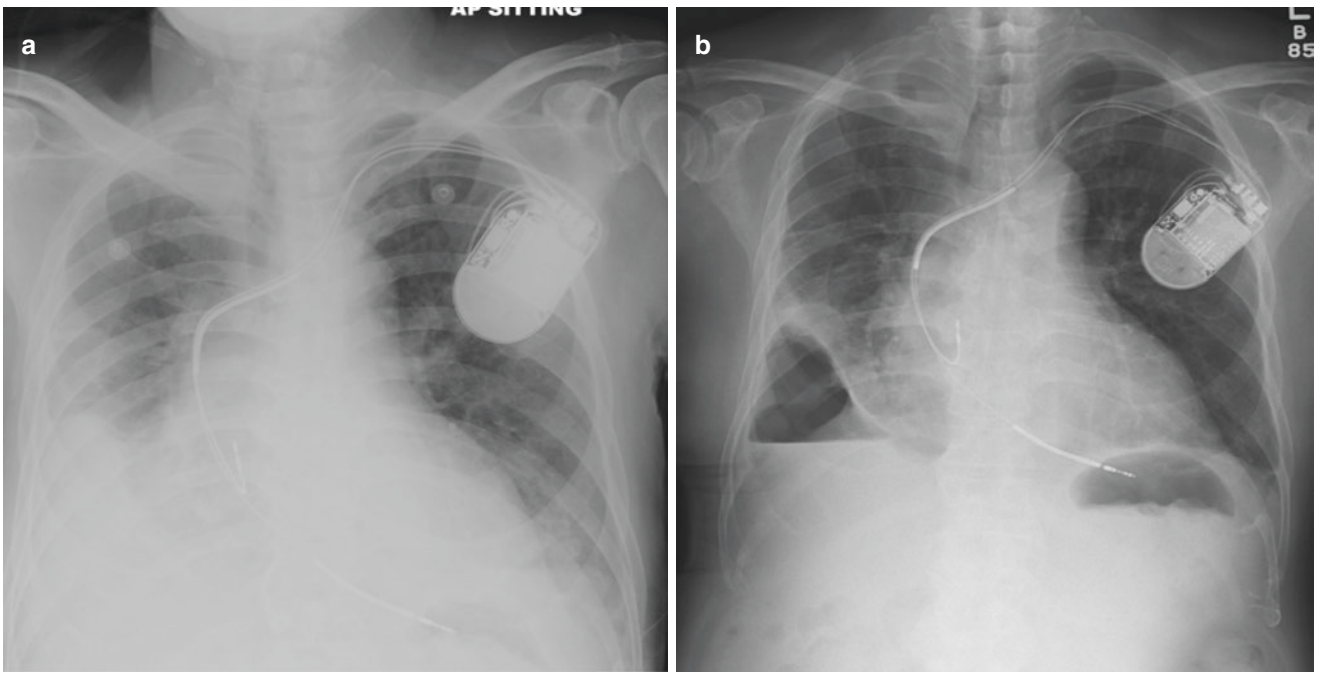

Fig. 12.33 A 78-year-old man with "trapped lung." (**a**) Frontal radiograph shows a right lower zone effusion. (**b**) Post-drainage, the lung remains collapsed with the development of the right hydropneumothorax. (**c**, **d**) Axial CT images reveal hydropneumothorax, thickened pleura, and round atelectasis (asterisk) of the right lower lobe

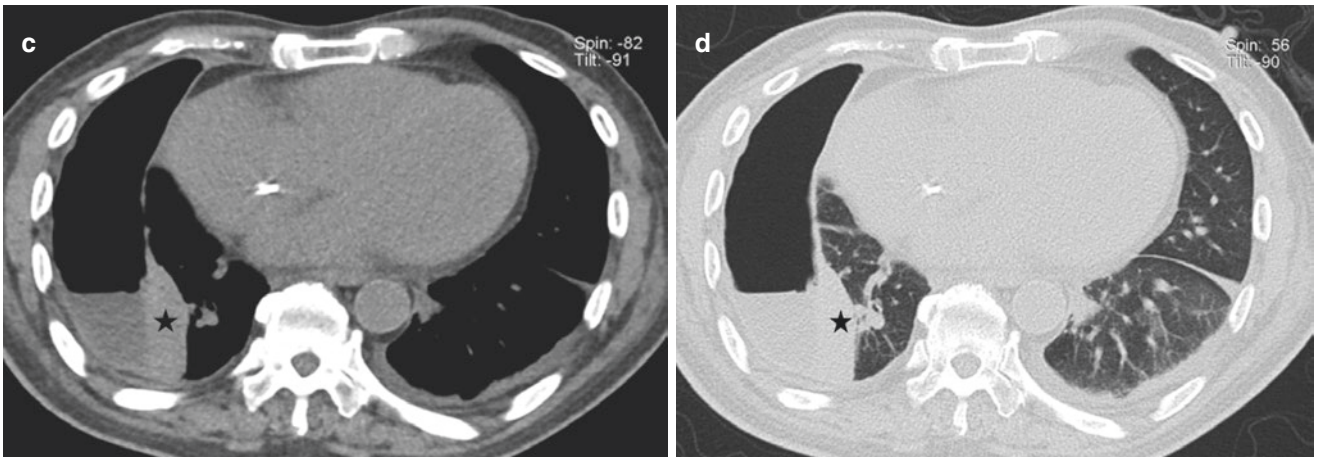

Fig. 12.33 (continued)

resulting in a significant mass effect on thoracic and mediastinal structures as well as the diaphragm (Fig. 12.34). Pneumothorax can be spontaneous (primary or secondary), iatrogenic, traumatic, or secondary to infections with gas-forming organisms. Catamenial pneumothorax is a condition with recurrent pneumothorax which occurs with the menstrual cycle and is resultant of implanted endometrial tissue in the pleural space [26].

12.9.4 Pleural Thickening and Calcification

A number of benign and malignant conditions can result in focal or diffuse thickening of the pleural layers (Table 12.13). Diffuse thickening is usually smooth, uninterrupted thickening and can be secondary to infection, inflammatory causes, or even due to neoplasms. Pleural plaques have been commonly described with an asbestos-related pleural disease and can undergo calcification (Fig. 12.35). Bilateral pleural plaques and pleural thickening are secondary to asbestos-related disease in most cases. The changes occur decades after the initial asbestos exposure and generally occur along the parietal pleura with a predilection for the dome of the diaphragm and lower costal pleura [27]. On chest radiography, large pleural plaques in asbestosis-related pleural disease show irregular thickened edges resembling holly leaf (holly leaf sign). Extrapleural fat can sometimes mimic pleural thickening, usually more common in obese patients and generally spares the costophrenic angles [28]. On a chest radiograph, extrapleural fat can mimic cardiomegaly or even pleural effusion in rare cases (Figs. 12.36 and 12.37). Pleural calcification can also be a sequel of post-infective empyema or post-traumatic hemothorax (Figs. 12.38 and 12.39). Talc pleurodesis appear as hyperdense focal pleural thickening and can be mistaken for plaques (Fig. 12.40).

12.9.5 Pleural Tumors

Pleural tumors can produce a spectrum of imaging findings, based on location, size, and associated features. A number of primary (both benign and malignant) and metastatic tumors can involve the pleura, the metastases being more frequent than primary tumors [29]. Pleural fibroma and lipoma are two common primary benign neoplasms with their imaging features described in Table 12.14 (Figs. 12.41 and 12.42). Pleural masses form an obtuse angle with the chest wall and displace the adjacent lung parenchyma [30, 31].

The solitary fibrous tumor (STF) arises from mesenchymal cells and accounts for approximately 10% of primary pleural tumors [10] (Figs. 12.43 and 12.44). Majority of these lesions are asymptomatic and are seen in older patients. Although they are considered to be benign tumors, the larger SFT can express malignant behavior and invasion. The solitary fibrous tumor can present with pain, cough, fever, features of pulmonary osteoarthropathy (Bamberg syndrome), and even with refractory hypoglycemia (Doege-Potter syndrome). Hypoglycemia as a paraneoplastic phenomenon is seen in larger SFT and is thought to be related to tumor secretion of the insulin-like growth factor II.

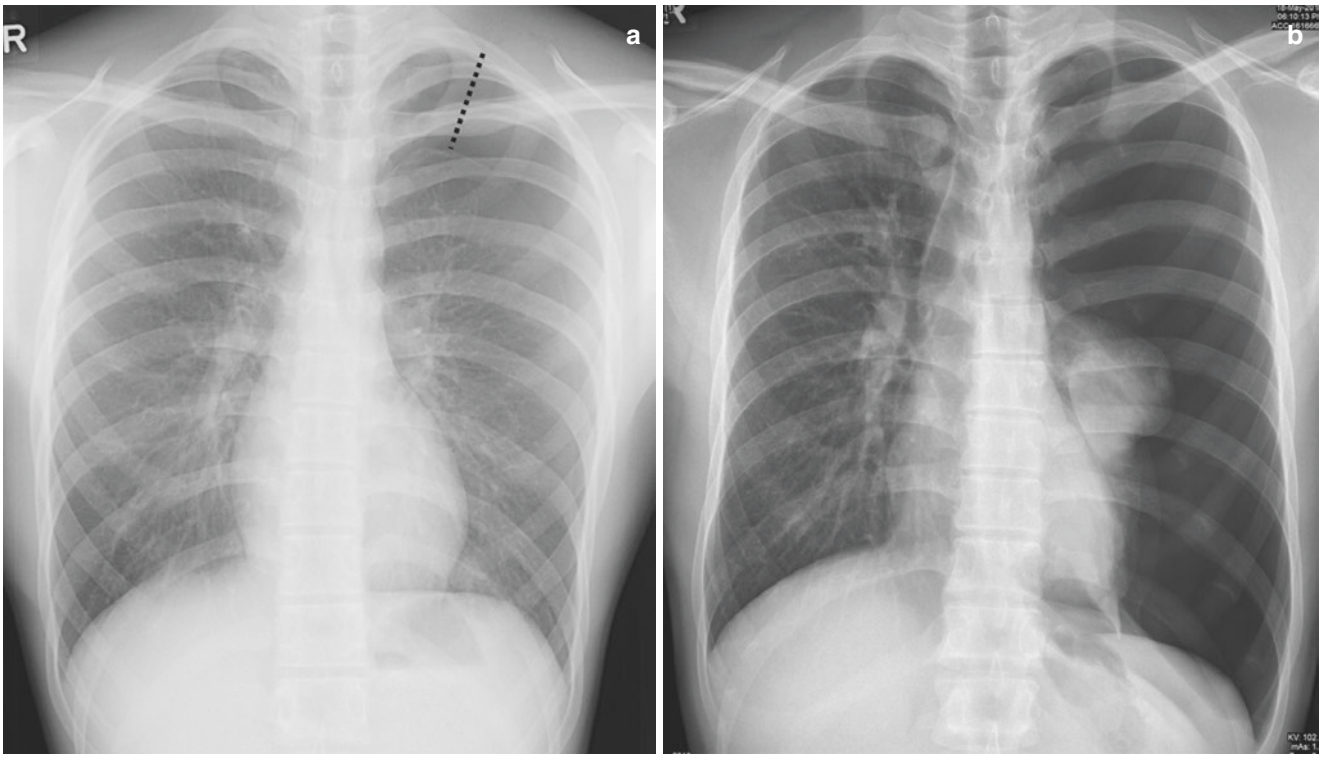

Fig. 12.34 Pneumothorax. (**a**) Frontal chest radiograph with small pneumothorax. (**b**) Tension pneumothorax in another patient

Table 12.13 Pleural thickening and calcification

Focal thickening	Calcification
• Prior effusion • Pleural plaque • Sarcoidosis (pseudo-plaques) • Benign/malignant/metastatic pleural tumor • Extension from lung carcinoma • Pleural lymphoma	• Chronic empyema • Asbestos-related pleural disease • Previous hemothorax • Silicosis • Talc exposure

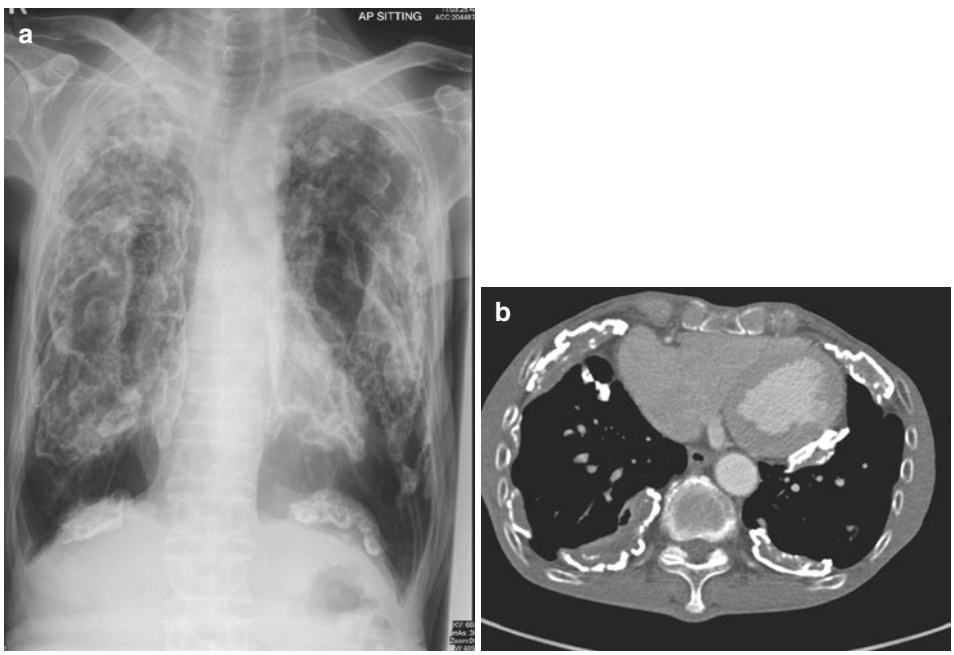

Fig. 12.35 Calcified pleural plaques in asbestos-related pleural disease. (**a**) Frontal chest radiograph shows large pleural plaques with irregular thickened edges resembling holly leaf (holly leaf sign). (**b**) Axial CT image shows bilateral calcified pleural plaques

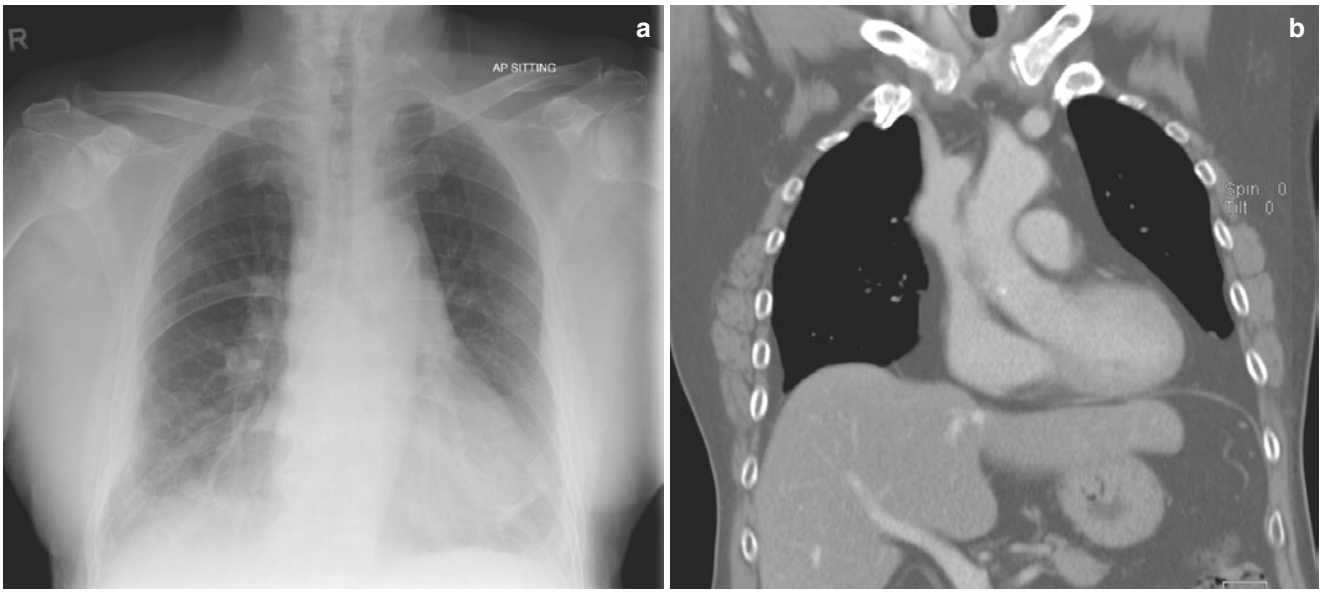

Fig. 12.36 Extrapleural fat mimicking cardiomegaly. (**a**) Frontal chest radiograph with the appearance of cardiomegaly. (**b**) Axial CT image shows excessive extrapleural fat mediastinal fat

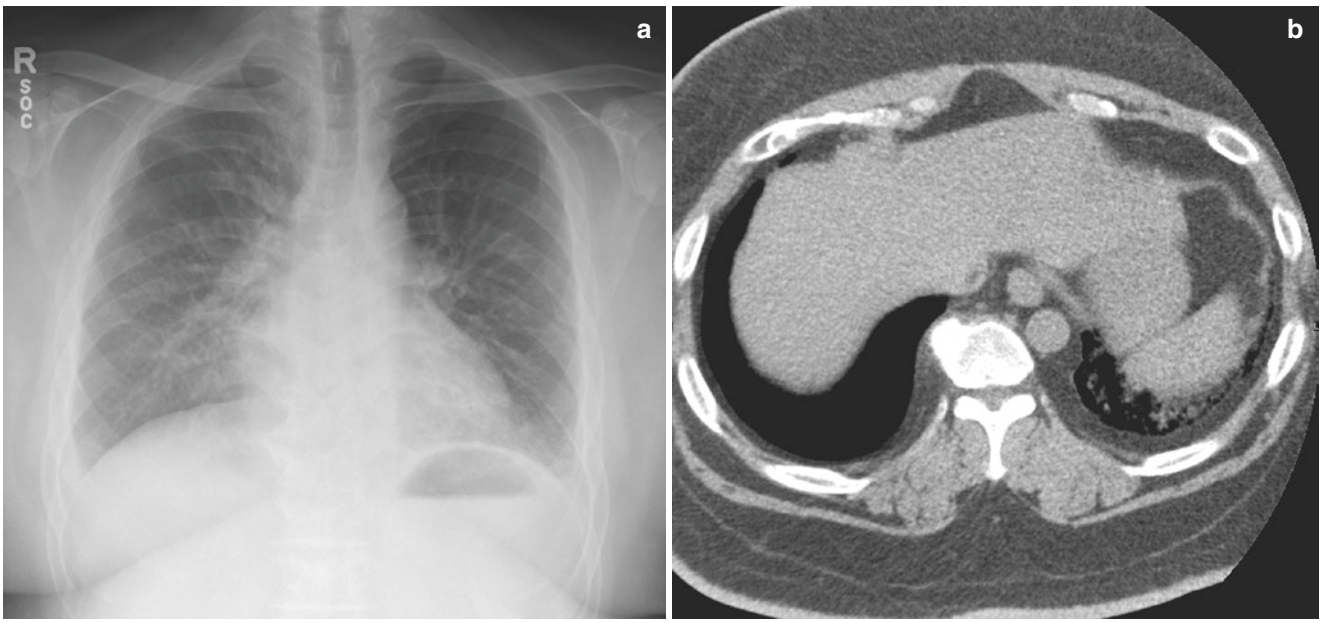

Fig. 12.37 Extrapleural fat mimicking pleural effusion. (**a**) Frontal chest radiograph shows blunting of the costophrenic angles. Note the opacity over the angles is of low attenuation (ground glass), the sharp interface of the diaphragm is preserved, and the density anterior and posterior to hemidiaphragm is not increased. (**b**) Axial CT image shows the extrapleural fat accounting for the blunting

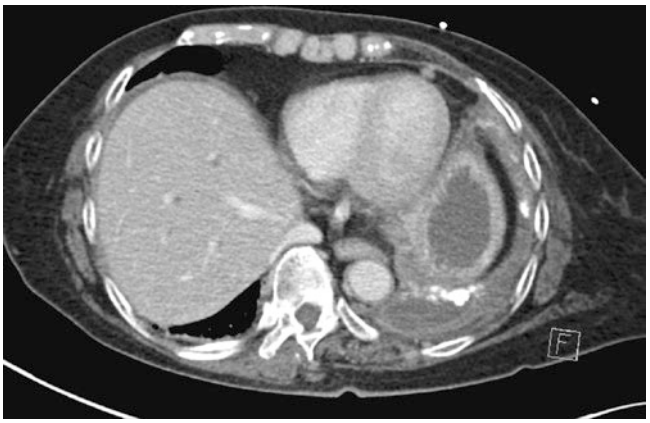

Fig. 12.38 Pleural calcification in a patient with the previous empyema was seen on axial CT image

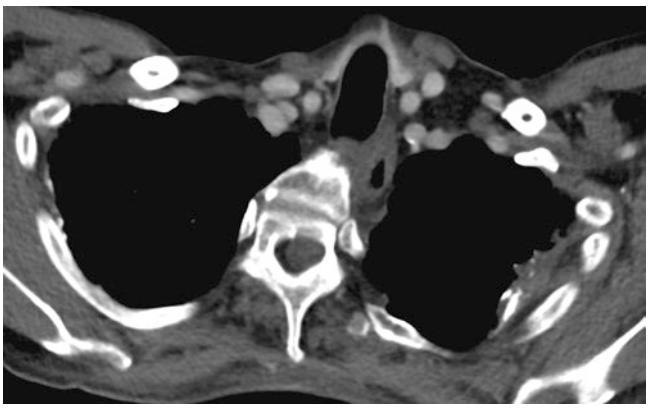

Fig. 12.39 Pleural calcification in a patient with previous hemothorax with old rib fractures (not shown) on axial CT image

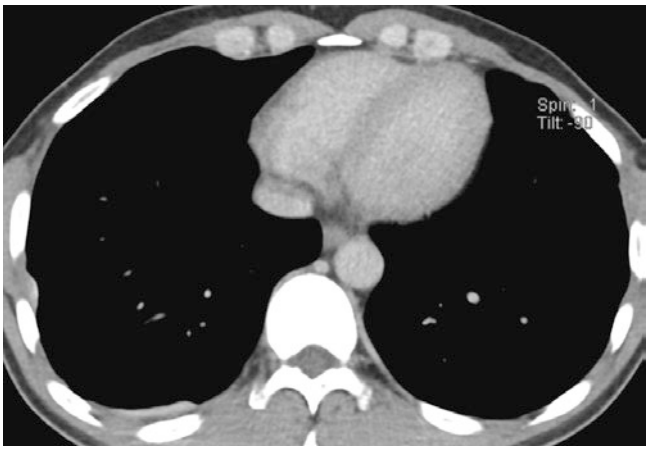

Fig. 12.40 Talc pleurodesis. Axial CT shows hyperdense thickened right posterior pleura in a patient with previous talc pleurodesis for recurrent pneumothorax

Table 12.14 Imaging features of primary pleural tumors

Pleural lipoma	• Radiograph: larger mass appears as a low-density extraparenchymal mass • CT: Fat-density lesion Heterogeneous appearance with HU value > −50 raises concern for malignant change
Solitary fibrous tumor	• Radiograph: rounded smooth mass with an obtuse angle to the pleural surface. Pedunculated tumor can change position, (more likely to be benign) • CT: Lobulated mass, larger mass may show invasive features Smooth tapering margin at junction with pleura Usually hypervascular masses with prominent collateral vessels May undergo malignant degeneration with central necrosis

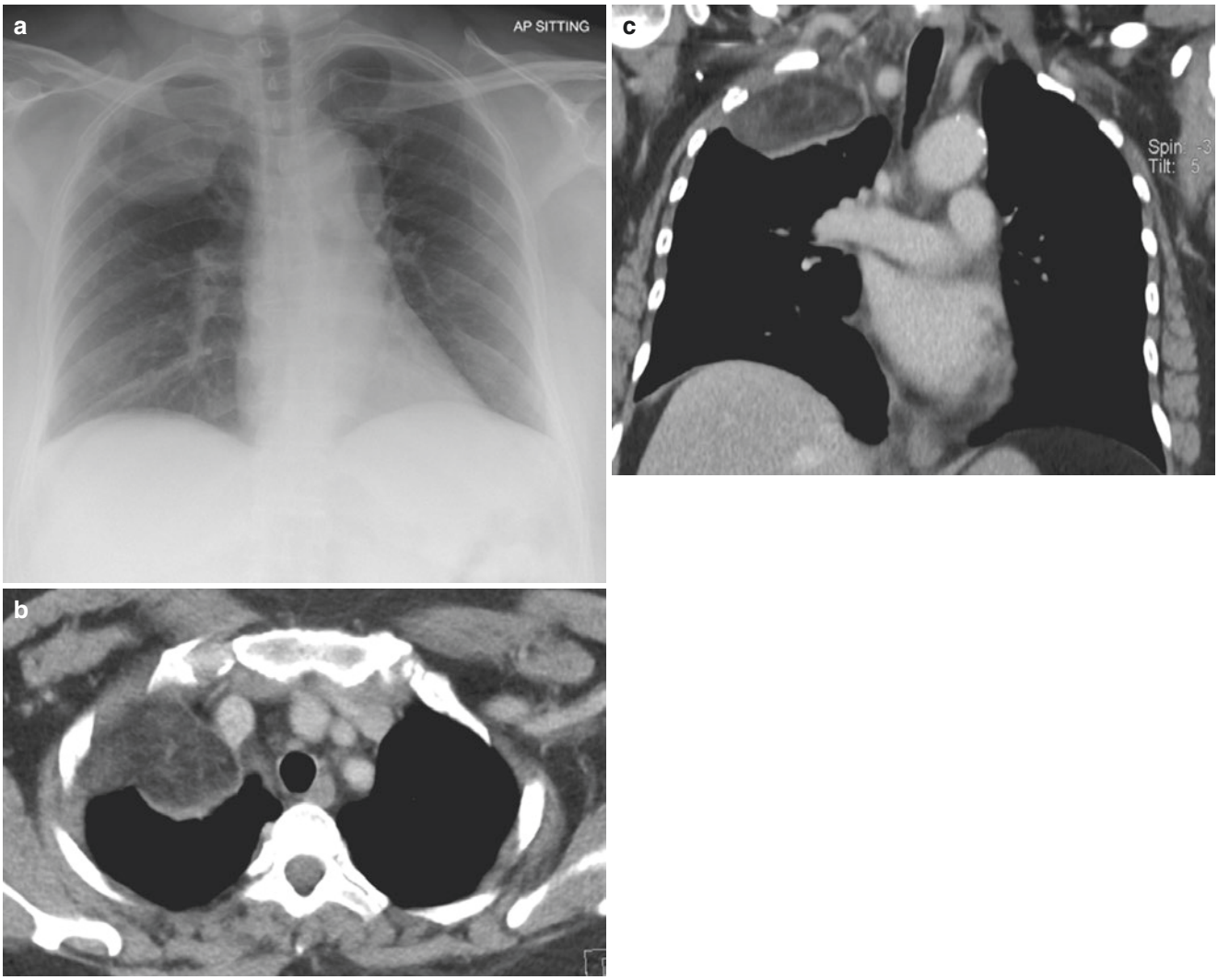

Fig. 12.41 A 49-year-old woman with an incidental pleural lipoma. (**a**) Frontal chest radiograph shows an extrapulmonary mass (incomplete border sign and an obtuse angle with chest wall) with low density over the right upper zone. (**b**, **c**) Axial and coronal CT images show a fat-density lesion broad-based to the pleura, with internal septations and soft-tissue density areas. The possibility of liposarcoma was raised on CT. However, histopathology of resected tumor revealed a benign pleural lipoma

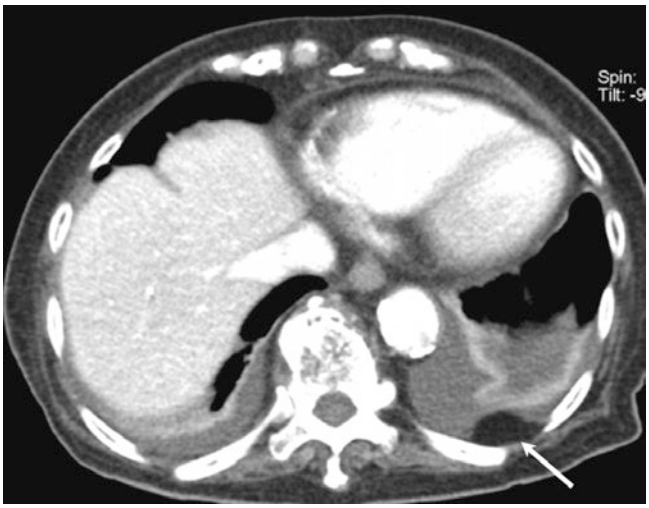

Fig. 12.42 Axial CT image shows an incidental pleural lipoma

Malignant pleural tumors are most commonly due to metastatic involvement, followed by other causes like a pleural extension of bronchogenic cancer and malignant mesothelioma. The commonest imaging presentation of metastatic pleural involvement is pleural effusion, followed by nodularity of the pleura (Fig. 12.45). Some common malignancies with pleural metastasis are bronchogenic carcinoma, breast cancer, lymphoma, ovarian cancer, and gastric carcinoma. Bronchogenic carcinoma from the lung apex (Pancoast tumor) can involve the superior pulmonary sulcus with the early invasion of vital structures and can present as Horner's syndrome. MRI evaluation is especially useful in these tumors.

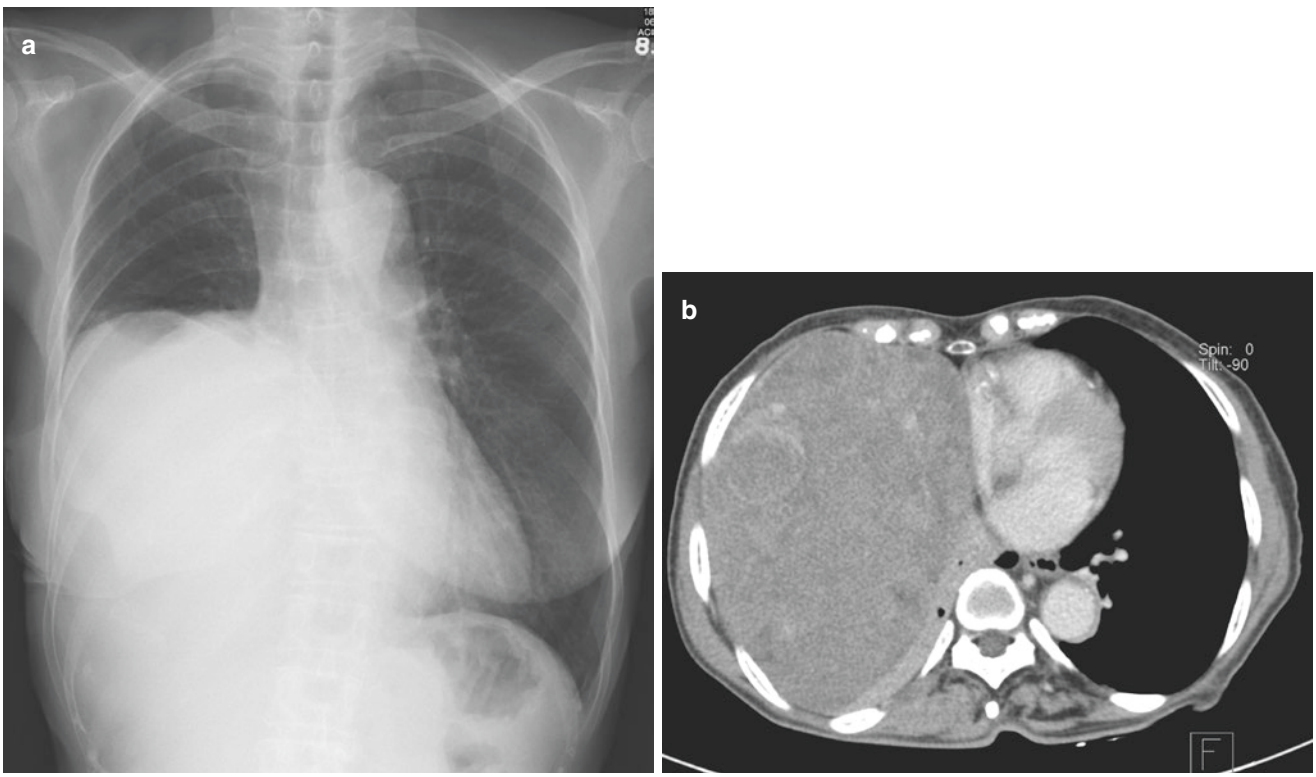

Fig. 12.43 A 58-year-old woman presenting with recurrent hypoglycemia. (**a**) Frontal chest radiograph shows a large opacity over the right lower zone. (**b**, **c**) Axial and coronal CT images show a large mass, confirmed to be a fibrous tumor on histopathology

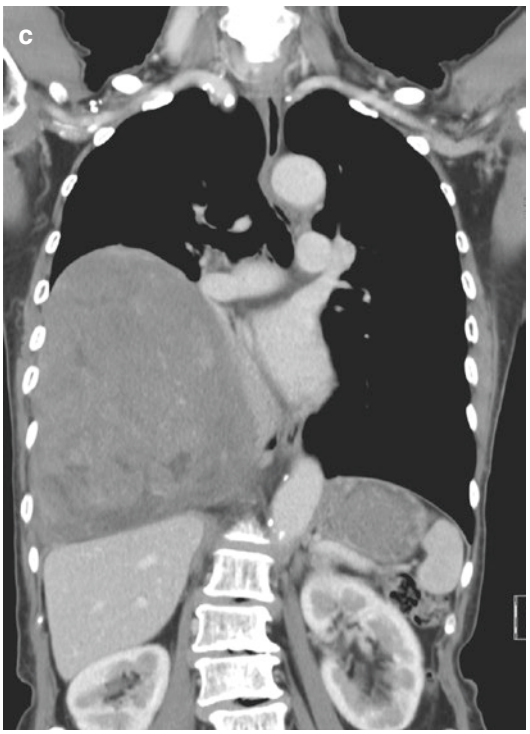

Fig. 12.43 (continued)

12.9.6 Malignant Pleural Mesothelioma

Malignant pleural mesothelioma is an uncommon tumor, usually presenting with chest pain, shortness of breath, cough, and loss of weight and is associated with poor survival rates [32] (Fig. 12.46). The majority of the cases of mesothelioma are associated with prior asbestos exposure. Treatment involves multiple modalities with a combination of surgery, chemotherapy, and radiotherapy. Imaging features of malignant mesothelioma are described in Table 12.15. CT plays an important role in staging and predicting survival by providing information about the involvement of regional lymph nodes and the extent of pleural involvement and metastatic disease [33]. CT-guided percutaneous biopsy is diagnostic in most of the cases, while some may need thoracoscopy or even thoracotomy for the tissue diagnosis [34].

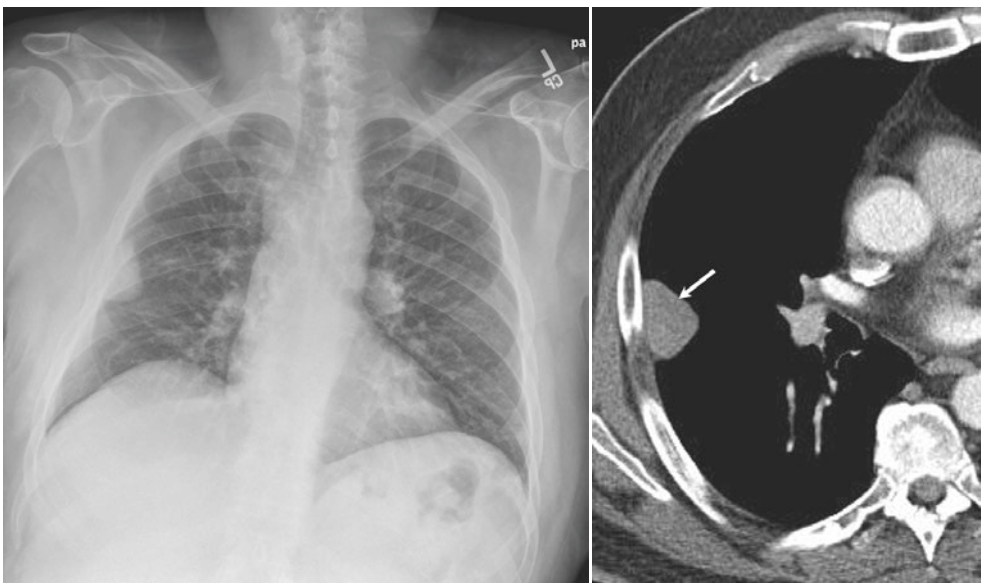

Fig. 12.44 Small solitary fibrous tumor in a middle-aged woman

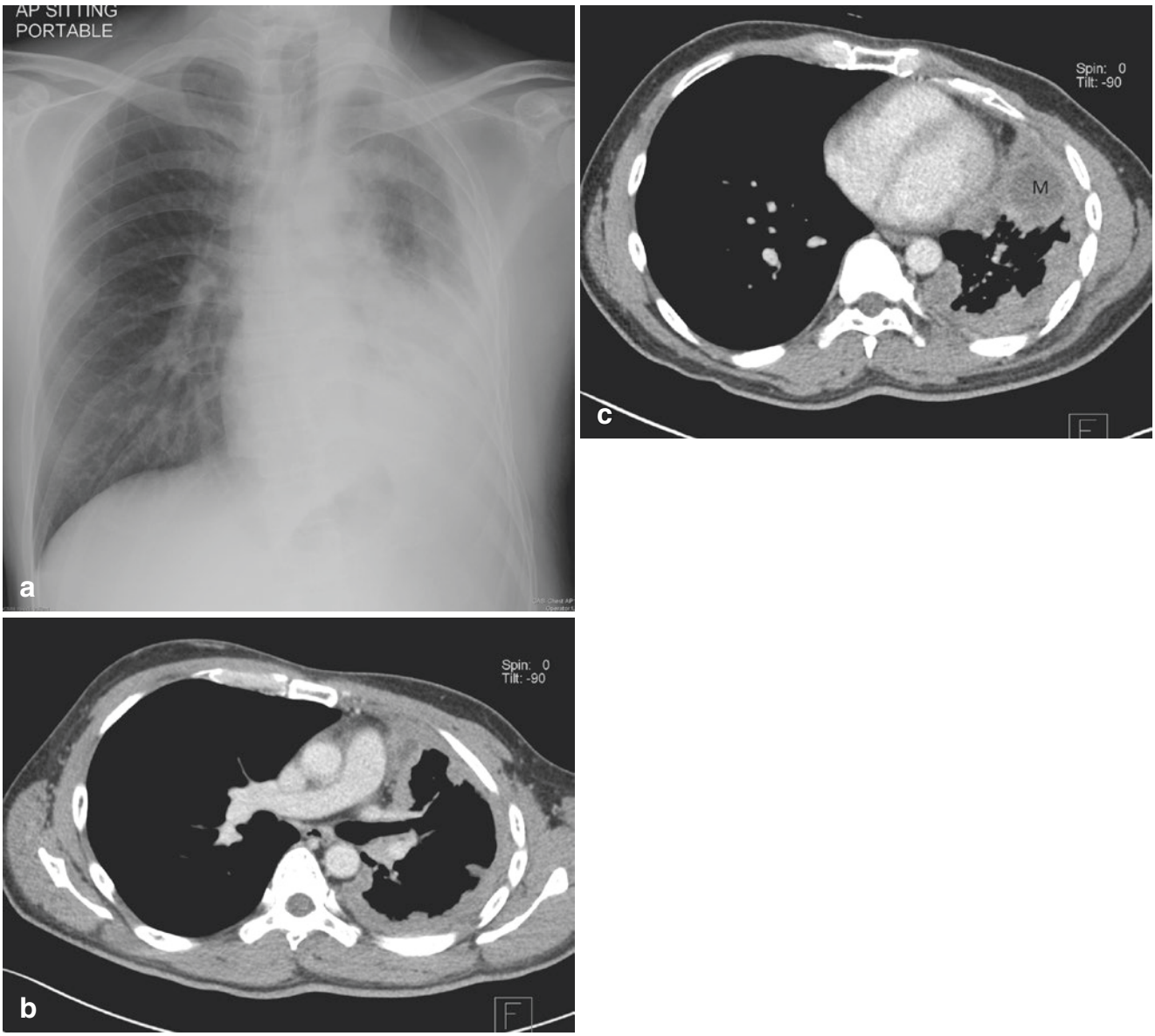

Fig. 12.45 Lung carcinoma with pleural metastases. (**a**) Frontal chest radiograph shows volume loss in the left hemithorax with left pleural effusion and patchy opacities. (**b**, **c**) Axial CT images show a lingular mass (M) with nodular pleural thickening

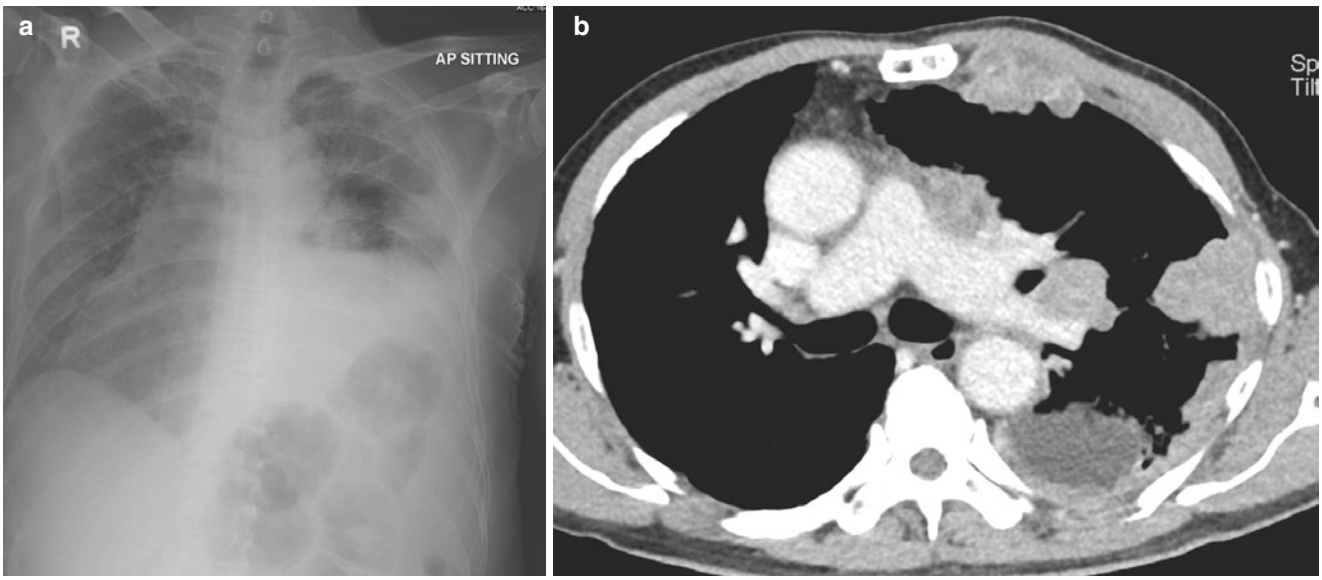

Fig. 12.46 Mesothelioma in a 55-year-old male patient. (**a**) Frontal chest radiograph shows volume loss in the left hemithorax, nodular peripheral left-sided opacities encasing the left lung. (**b**) Axial CT image shows multiple pleura-based contiguous nodules involving the costal and mediastinal pleura with left pleural effusion

Table 12.15 Imaging features of malignant mesothelioma

Radiograph	• Non-specific nodular pleural opacity, volume loss, rib destruction, pleural effusion • Few cases show only pleural effusion
CT	• Unilateral pleural effusion • Nodular pleural thickening • Interlobar fissural thickening • Can have background calcified plaques • Volume loss with ipsilateral mediastinal shift and elevation of the hemidiaphragm • Chest wall invasion, rib displacement, bone destruction • May invade mediastinal structures or extend across the diaphragm (peritoneal disease, hepatic involvement) • Pulmonary metastasis • Hilar, mediastinal lymph node involvement
MRI	• Useful in potentially resectable cases in identifying chest wall invasion, mediastinal and diaphragmatic involvement
FDG PET-CT	• Role in diagnosis, staging, and follow-up • Useful in identifying malignant focus in cases of diffuse pleural thickening

References

1. García-Peña P, Barber I. Pathology of the thoracic wall: congenital and acquired. Pediatr Radiol. 2010;40(6):859–68.
2. Donnelly LF, Frush DP, Foss JN, O'Hara SM, Bisset GS 3rd. Anterior chest wall: frequency of anatomic variations in children. Radiology. 1999;212(3):837–40.
3. Jeung MY, Gangi A, Gasser B, Vasilescu C, Massard G, Wihlm JM, et al. Imaging of chest wall disorders. Radiographics. 1999;19(3):617–37.
4. Mak SM, Bhaludin BN, Naaseri S, Di Chiara F, Jordan S, Padley S. Imaging of congenital chest wall deformities. Br J Radiol. 2016;89(1061):20150595.
5. Restrepo R, Lee EY. Updates on imaging of chest wall lesions in pediatric patients. Semin Roentgenol. 2012;47(1):79–89.
6. Raichura N, Entwisle J, Leverment J, Beardsmore CS. Breath-hold MRI in evaluating patients with pectus excavatum. Br J Radiol. 2001;74(884):701–8.
7. Han JY, Lee KN, Lee JK, Kim YH, Choi SJ, Jeong YJ, Roh MS, Choi PJ. An overview of thoracic actinomycosis: CT features. Insights Imaging. 2013;4(2):245–52.
8. Kawashima A, Kuhlman JE, Fishman EK, Tempany CM, Magid D, Lederman HM, et al. Pulmonary Aspergillus chest wall involvement in chronic granulomatous disease: CT and MRI findings. Skelet Radiol. 1991;20(7):487–93.

9. Incarbone M, Pastorino U. Surgical treatment of chest wall tumors. World J Surg. 2001;25(2):218–30.
10. Weyant MJ, Flores RM. Imaging of pleural and chest wall tumors. Thorac Surg Clin. 2004;14(1):15–23.
11. Mullan CP, Madan R, Trotman-Dickenson B, Qian X, Jacobson FL, Hunsaker A. Radiology of chest wall masses. AJR Am J Roentgenol. 2011;197(3):W460–70.
12. Tateishi U, Gladish GW, Kusumoto M, Hasegawa T, Yokoyama R, Tsuchiya R, et al. Chest wall tumors: radiologic findings and pathologic correlation: part 1. Benign tumors. Radiographics. 2003;23(6):1477–90.
13. Kuhlman JE, Bouchardy L, Fishman EK, Zerhouni EA. CT and MR imaging evaluation of chest wall disorders. Radiographics. 1994;14(3):571–95.
14. Nam SJ, Kim S, Lim BJ, Yoon CS, Kim TH, Suh JS, et al. Imaging of primary chest wall tumors with radiologic-pathologic correlation. Radiographics. 2011;31(3):749–70.
15. Kehoe NJ, Reid RP, Semple JC. Solitary benign peripheral-nerve tumours. Review of 32 years' experience. J Bone Joint Surg Br. 1995;77(3):497–500.
16. Carter BW, Benveniste MF, Betancourt SL, de Groot PM, Lichtenberger JP 3rd, Amini B, et al. Imaging evaluation of malignant chest wall neoplasms. Radiographics. 2016;36(5):1285–306.
17. Somers J, Faber LP. Chondroma and chondrosarcoma. Semin Thorac Cardiovasc Surg. 1999;11(3):270–7.
18. Tateishi U, Gladish GW, Kusumoto M, Hasegawa T, Yokoyama R, Tsuchiya R, et al. Chest wall tumors: radiologic findings and pathologic correlation: part 2. Malignant tumors. Radiographics. 2003;23(6):1491–508.
19. Bruns AS, Mastronarde JG. Imaging of pleural masses: which to choose? Respir Med. 2008;102(3):328–31.
20. Leung AN, Müller NL, Miller RR. CT in differential diagnosis of diffuse pleural disease. AJR Am J Roentgenol. 1990;154(3):487–92.
21. McLoud TC, Flower CD. Imaging the pleura: sonography, CT, and MR imaging. AJR Am J Roentgenol. 1991;156(6):1145–53.
22. Blackmore CC, Black WC, Dallas RV, Crow HC. Pleural fluid volume estimation: a chest radiograph prediction rule. Acad Radiol. 1996;3(2):103–9.
23. Na MJ. Diagnostic tools of pleural effusion. Tuberc Respir Dis. 2014;76(5):199–210.
24. Federle MP, Mark AS, Guillaumin ES. CT of subpulmonic pleural effusions and atelectasis: criteria for differentiation from subphrenic fluid. AJR Am J Roentgenol. 1986;146(4):685–9.
25. Feller-Kopman D, Light R. Pleural disease. N Engl J Med. 2018;378(18):1754.
26. Walker CM, Takasugi JE, Chung JH, Reddy GP, Done SL, Pipavath SN, et al. Tumorlike conditions of the pleura. Radiographics. 2012;32(4):971–85.
27. Helm EJ, Matin TN, Gleeson FV. Imaging of the pleura. J Magn Reson Imaging. 2010;32(6):1275–86.
28. Alfudhili KM, Lynch DA, Laurent F, Ferretti GR, Dunet V, Beigelman-Aubry C. Focal pleural thickening mimicking pleural plaques on chest computed tomography: tips and tricks. Br J Radiol. 2016;89(1057):20150792.
29. Dynes MC, White EM, Fry WA, Ghahremani GG. Imaging manifestations of pleural tumors. Radiographics. 1992;12(6):1191–201.
30. Müller NL. Imaging of the pleura. Radiology. 1993;186(2):297–309.
31. Wignall OJ, Moskovic EC, Thway K, Thomas JM. Solitary fibrous tumors of the soft tissues: review of the imaging and clinical features with histopathologic correlation. Am J Roentgenol. 2010;195(1):W55–62.
32. Wang ZJ, Reddy GP, Gotway MB, Higgins CB, Jablons DM, Ramaswamy M, et al. Malignant pleural mesothelioma: evaluation with CT, MR imaging, and PET. Radiographics. 2004;24(1):105–19.
33. Rusch VW. A proposed new international TNM staging system for malignant pleural mesothelioma. From the international mesothelioma interest group. Chest. 1995;108(4):1122–8.
34. Greillier L, Cavailles A, Fraticelli A, Scherpereel A, Barlesi F, Tassi G, et al. Accuracy of pleural biopsy using thoracoscopy for the diagnosis of histologic subtype in patients with malignant pleural mesothelioma. Cancer. 2007;110(10):2248–52.

Imaging of Interstitial Lung Diseases

13

Ashish Chawla, Tze Chwan Lim, Vijay Krishnan, and Chai Gin Tsen

13.1 Introduction

Acronyms Used in Interstitial Lung Diseases

AIP	Acute interstitial pneumonia
COP	Cryptogenic organizing pneumonia
CTD	Connective tissue disease
CTD-ILD	Connective tissue disease-related ILD
DIP	Desquamative interstitial pneumonia
GGO	Ground-glass opacity
HP	Hypersensitivity pneumonitis
IIP	Idiopathic interstitial pneumonia
ILD	Interstitial lung disease
IPF	Idiopathic pulmonary fibrosis
LIP	Lymphocytic interstitial pneumonia
NSIP	Nonspecific interstitial pneumonia
OP	Organizing pneumonia
PPFE	Pleuroparenchymal fibroelastosis
RB	Respiratory bronchiolitis
UIP	Usual interstitial pneumonia

A. Chawla (✉) · T. C. Lim · V. Krishnan
Department of Diagnostic Radiology, Khoo Teck Puat Hospital, Singapore, Singapore
e-mail: tze_chwan_lim@whc.sg

C. G. Tsen
Department of Respiratory and Critical Care Medicine, Tan Tock Seng Hospital, Singapore, Singapore
e-mail: gin_tsen_chai@ttsh.com.sg

13.2 Hallmarks of Interstitial Lung Diseases on CT

High-resolution computed tomography (HRCT) is an established technique of imaging ILDs. The strength of the HRCT lies in its ability to visualize the secondary pulmonary lobule—the small anatomic unit of the lung. The two essential requirements of HRCT technique are thin reconstruction (usually 1–2 mm), and the use of a high-spatial-frequency reconstruction algorithm. Thin sections reduce volume averaging artifact from the surrounding structures. High-spatial-frequency sharp algorithm reduces the image smoothing and increases spatial resolution, at the expense of increased image noise [1]. As multidetector CT scanners are more readily available, volumetric HRCT acquisition has replaced non-contiguous HRCT. The advantages of volumetric acquisition are the ability to perform multiplanar reconstructions at isotropic resolution, increased sensitivity for evaluation of pulmonary nodules and characterization of patchy ILD. Coronal reconstruction is important to define the craniocaudal extent of diffuse lung diseases, and in many centers, it is included in the standard imaging protocol and reconstructed in lung kernel. Volumetric HRCT allows for better differentiation between honeycombing and traction bronchiectasis, a crucial feature to diagnose or exclude UIP. The only concern of the volumetric technique is the relatively high radiation dose exposure [2]. HRCT, performed in supine end-inspiration, is the standard examination in all patients suspected of ILD. Prone images in end-inspiration are acquired as a baseline either in all patients or in those patients with posterior basal disease and/or significant dependent atelectasis. Dependent atelectasis occurs more often in admitted patients than in outpatients, smokers and with increasing age. Early ILDs usually involve posterior basal lungs, so it is recommended to acquire the prone images in order to detect and quantify early disease changes (Fig. 13.1). Further, prone images are useful to diagnose or exclude subcentimeter pulmonary nodules, often obscured in

A. Chawla (ed.), *Thoracic Imaging*, https://doi.org/10.1007/978-981-13-2544-1_13

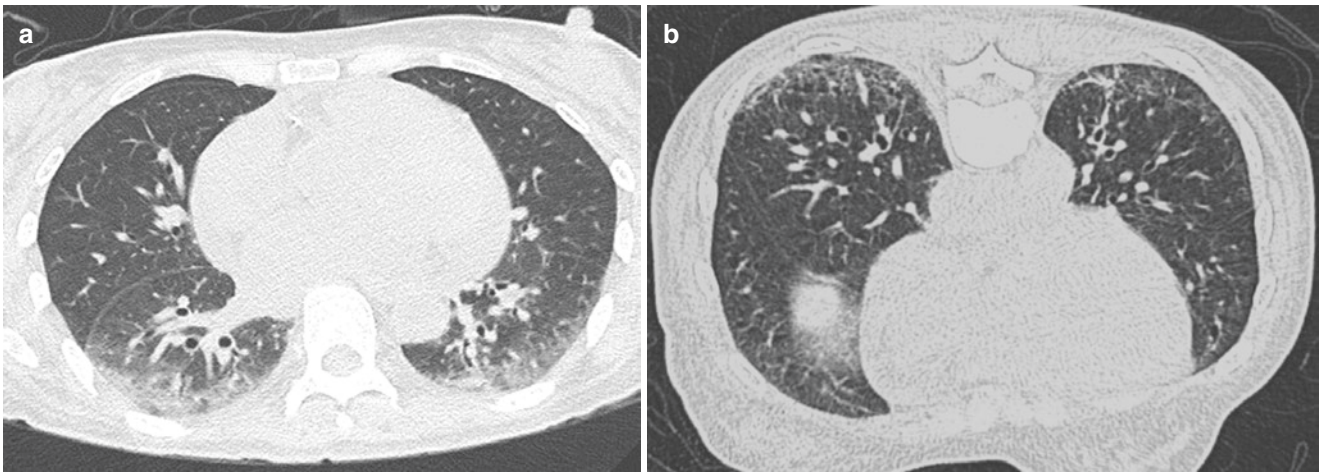

Fig. 13.1 Utility of prone images. (**a**) Supine axial CT image shows symmetrical GGOs in the posterior basal region. (**b**) Prone image reveals fine reticular opacities along with GGOs and early traction bronchiectasis confirming early ILD in this patient with SLE

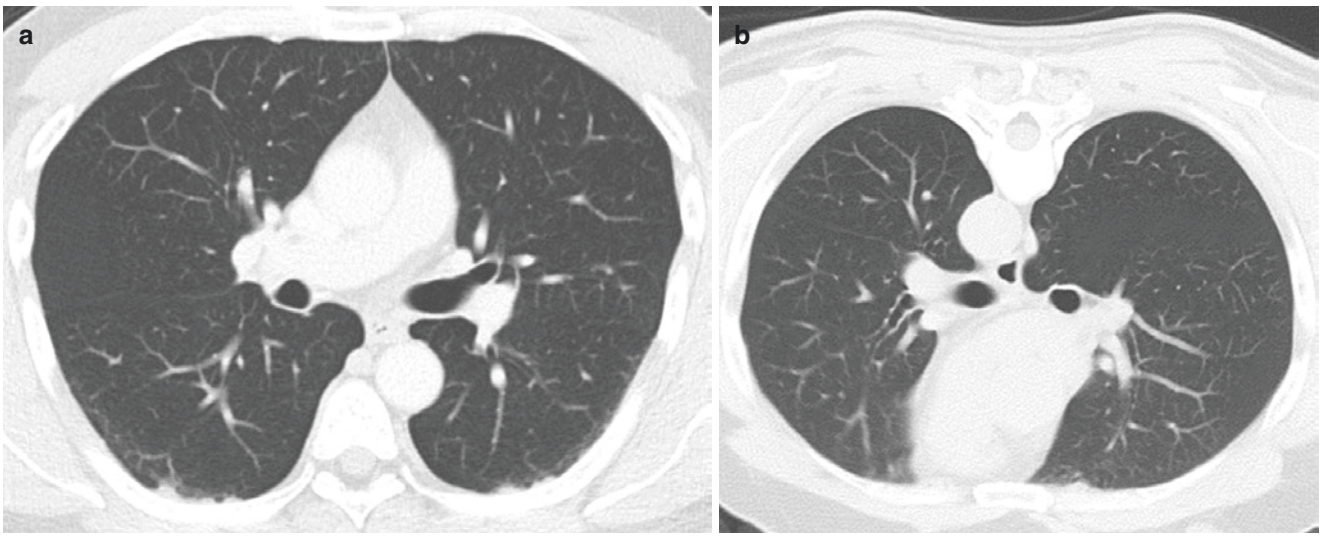

Fig. 13.2 Utility of prone images in cancer imaging. (**a**) Axial CT image shows subpleural opacities in both lungs posteriorly. (**b**) Prone image shows complete clearing of the opacities in this patient (scan performed for staging of breast cancer)

Table 13.1 HRCT protocol for the multidetector scanner (Siemens)

SN	Position	Phase	Plane	Thickness (mm)*	Gap (mm)	Algorithm	Window
1	Supine	Inspiration	Axial	1.2–1.5	10	B50f	Lung
2				3	-	B50f	Lung
3				3	-	B35f	Mediastinum
4[a]				6	3	B50f MIP	Lung
5			Coronal	2.5	-	B50f	Lung
6			Sagittal	2.5	-	B50f	Lung
7	Prone	Inspiration	Axial	1.5–2	15–20	B50f	Lung
8	Supine	Expiration	Axial	2	15–20	B50f	Lung

Protocol can be modified according to the indication, findings, and patient compliance. *Acquisition of 0.6 mm
[a]MIP images reconstruction, if there is a concern for lung nodules

dependent atelectasis (Fig. 13.2). End-expiratory CT scan is essential to differentiate between perfusion-related mosaic attenuation and small airway disease-related air-trapping. The HRCT protocol varies in different centers. A standard protocol for comprehensive evaluation is described in Table 13.1. This can be modified to reduce radiation dose and data volume (thereby reducing the burden on the departmental image storage facility). Reducing the scan range for prone and supine expiratory phase scans, i.e., covering from carina to lung base, helps in reducing the radiation dose.

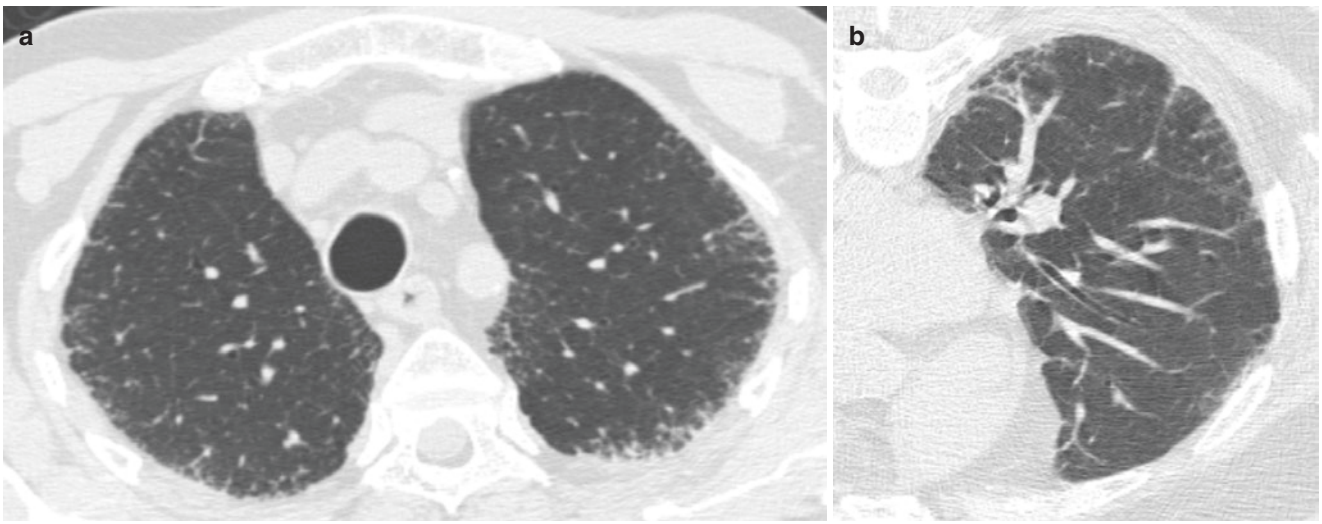

Fig. 13.3 (**a**, **b**) Linear opacities in two different patients

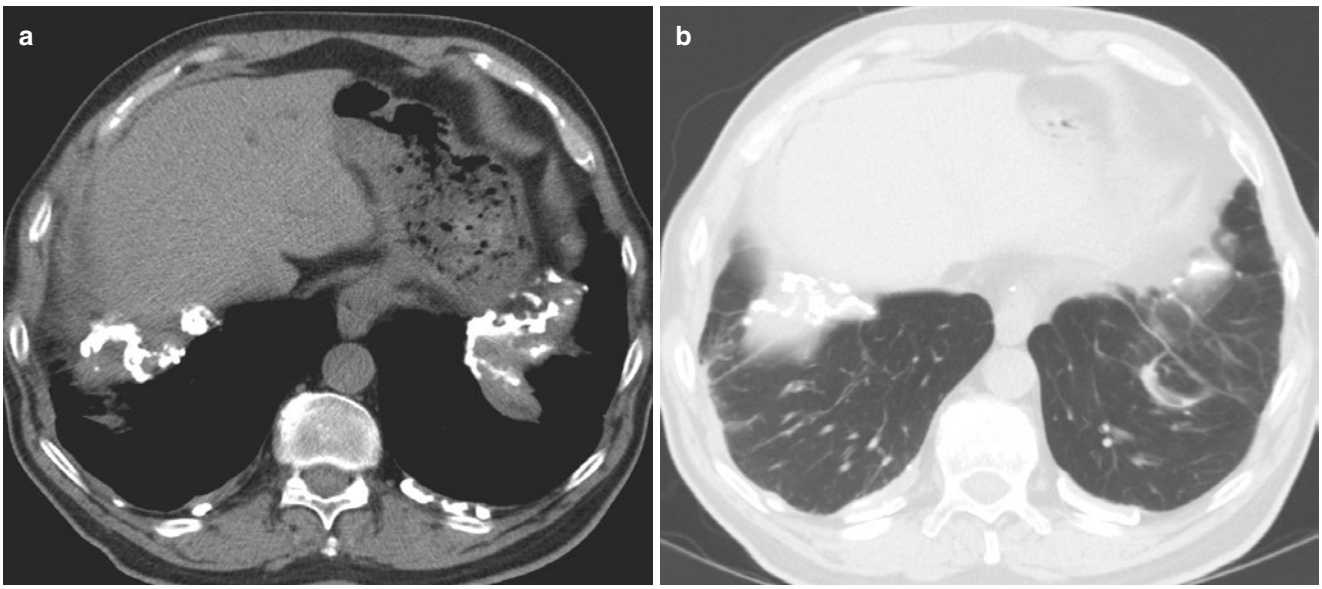

Fig. 13.4 Linear opacities in asbestosis. (**a**) Axial CT image in the soft-tissue window shows calcified pleural plaques. (**b**) CT image in lung windows shows subpleural linear opacities suggesting early parenchymal involvement

13.3 Pulmonary Findings

13.3.1 Linear Abnormalities

Linear abnormalities or linear opacities are subpleural short wavy lines representing thickening of septa at the earliest stage (Fig. 13.3). These must be differentiated from linear scarring, usually resulting from prior infection or infarction. Linear opacities are better seen as perpendicular lines to pleural surface in multiplanar reconstructions. Isolated presence of linear abnormalities is not a specific feature of any particular type of ILD. However, in the presence of relevant history (e.g., occupational exposure, smoking, clinical-laboratory feature for connective tissue diseases) or identification of other CT features (e.g., pleural plaques of asbestos-related pleural disease), these abnormalities serve as indicators of early ILD (Fig. 13.4). It is recommended to acquire images in the prone position to better visualize such early linear abnormalities.

13.3.2 Reticular Abnormalities

Linear abnormalities progress to reticular abnormalities or reticular opacities with time, and these changes represent fibrosis along the septa (Fig. 13.5). The reticular opacities result from thickening of interlobular septa associated with distortion of the lobular architecture. The thickening of septa

can be seen in various conditions (Table 13.2). It is essential to differentiate the reticular abnormalities of ILDs from thickening of interlobular septa associated with other conditions, such as interstitial edema, crazy-paving pattern, and tumor infiltration (Fig. 13.6). In these conditions, the lobular architecture is maintained, and outlines of the secondary pul-

Table 13.2 Causes of interlobular septa thickening

• Fibrotic lung diseases
• Lymphangitis carcinomatosis
• Lymphomatous diseases
• Crazy-paving pattern
• Pulmonary edema

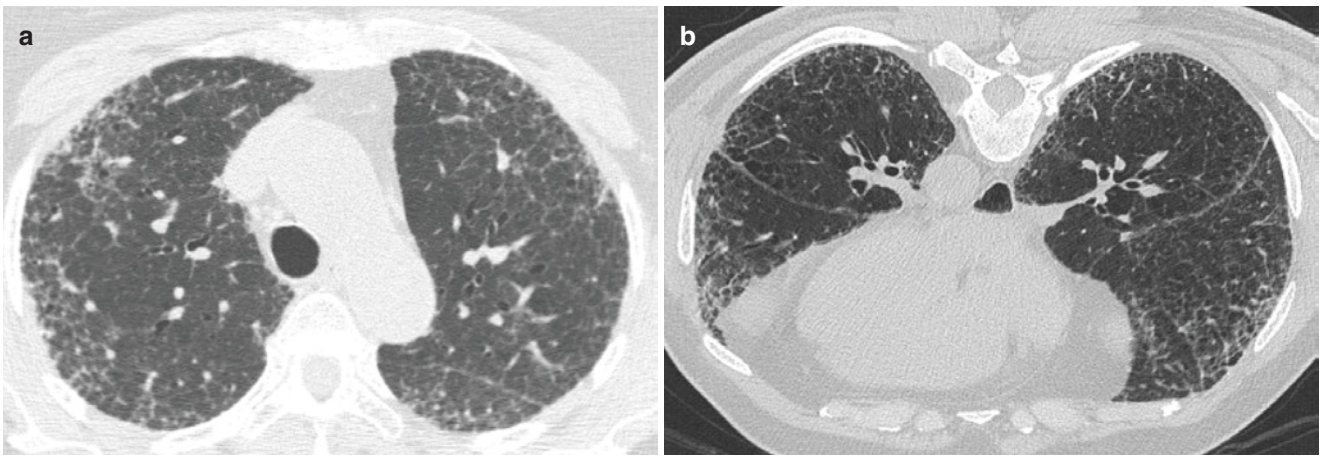

Fig. 13.5 (**a**, **b**) Reticular opacities in the peripheral lungs in two different patients

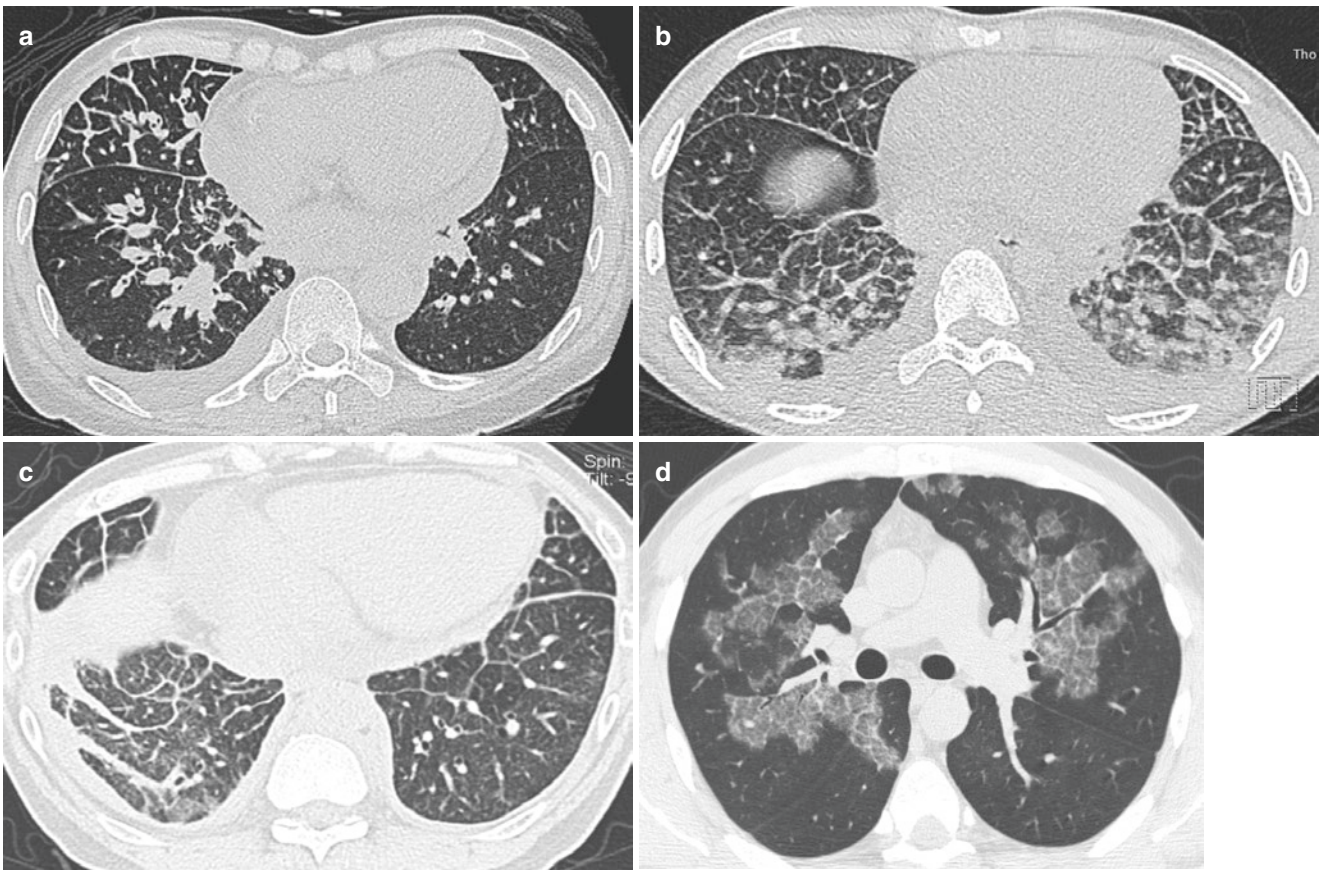

Fig. 13.6 Septal thickening with preserved lobular architecture in four different conditions. (**a**) Kaposi sarcoma with tumor infiltration along septa. (**b**) Interstitial pulmonary edema with fluid along septa. (**c**) Erdheim-Chester disease with infiltration of histiocytes along septa. (**d**) Pulmonary alveolar proteinosis with "crazy-paving" pattern

monary lobules are better defined. Reticular opacities are irreversible and are indicative of fibrotic lung disease.

13.3.3 Honeycombing

Historically, the term "honeycomb lung" was used to describe the appearance of multiple cysts seen on the cut surface of various diseases including chronic interstitial pneumonia, Langerhans cell histiocytosis, and lymphangioleiomyomatosis [3]. Subsequently, it was used to describe the appearance of end-stage chronic interstitial pneumonia regardless of etiology [4]. Honeycombing on HRCT is the hallmark of UIP. It was considered as a discriminator between probable and possible UIP [5]. In the new diagnostic criteria for idiopathic pulmonary fibrosis (IPF), honeycombing is the only discriminator between "typical" and "probable" UIP. Honeycombing on CT indicates poor prognosis not only in patients with UIP but also in NSIP [6, 7]. Hence, identification of honeycombing is considered as one of the most crucial aspects of imaging of ILD.

The Fleischner Society has defined honeycombing on CT as clustered cystic airspaces, typically of comparable diameters of the order of 3–10 mm but occasionally as large as 25 mm [8]. Honeycombing is usually subpleural and is characterized by well-defined walls [8] (Fig. 13.7). The

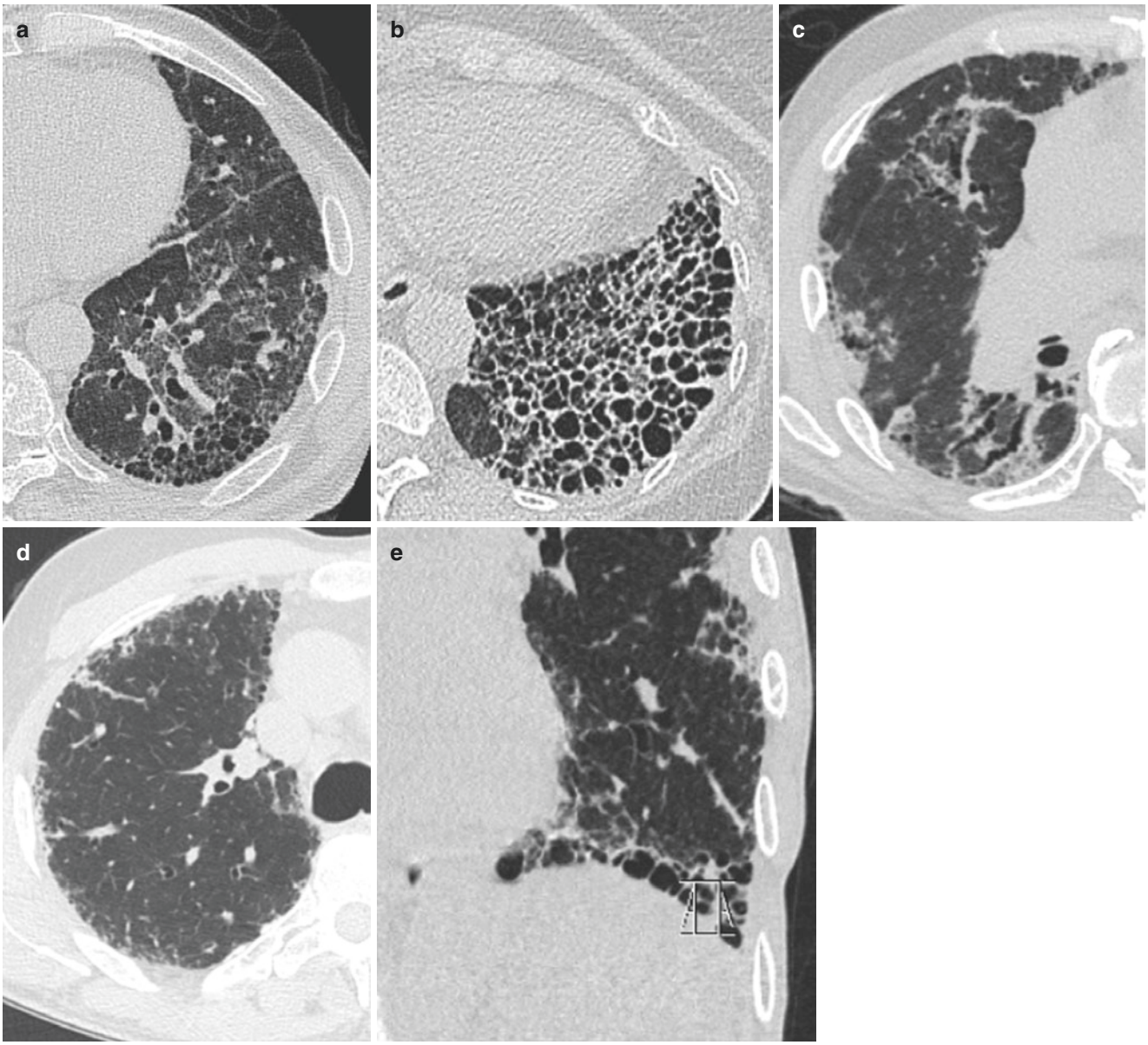

Fig. 13.7 Honeycombing in five different patients. (**a**) Subpleural multiple layers of cysts. (**b**) Exuberant honeycombing. (**c**) Single layer of cysts along chest wall. (**d**) Single layer of cysts along the mediastinal surface. (**e**) Honeycombing cysts in the basal lung

common mimics of honeycombing are traction bronchiectasis, cystic lung diseases, and paraseptal emphysema (Figs. 13.8, 13.9, and 13.10). Pitfalls in the diagnosis of honeycombing can be minimized by considering even the single layer of cysts as honeycombing [9]. If there are basal predominant reticular abnormalities in peripheral distribution with little ground-glass opacities (GGOs) and lung heterogeneity and a clinical diagnosis of UIP is suspected, honeycombing must be considered. Traction bronchiectasis can be identified by scrolling through contiguous thin-section images to identify a dilated airway or through careful reading of coronal reformats. Emphysema usually has no walls, but advanced confluent emphysema may show thinner walls formed by fibrosis at the interface between emphysematous and normal lung. In contrast, honeycombing is more thick-walled, subpleural without any intervening lung. Honeycombing is a CT feature of established pulmonary fibrosis. As the term "honeycombing" is often considered specific for pulmonary fibrosis and is an important criterion in the diagnosis of UIP, it should be applied with care, as the diagnosis and prognosis of ILD may be significantly affected.

Radiologically, honeycombing represents the extreme end of the spectrum of fibrosis, beginning as linear opacities and followed by reticular opacities. Over time, fibrosis progresses resulting in an increase in intralobular reticulations with gradual appearance of traction bronchiolectasis, eventually leading to honeycombing. As dilatation of the airways and collapse of fibrotic alveoli continues, honeycombing becomes more conspicuous in HRCT. Pathologically, honeycombing consists of multiple collapsed fibrotic alveoli and dilation of the alveolar ducts. There are two pathological findings corresponding to honeycomb cysts on CT: the first one is the tangential view of traction bronchiolectasis, and the second one is dilatation of peripheral airspace due to surrounded fibrosis. In patients with UIP, the extent of the latter is more than that of the former [9, 10]. Essentially, honeycombing of end-stage fibrosis represents a combination of dilated airspaces and associated airways.

Recent data demonstrates that due to lung remodeling in fibrotic lung diseases, cysts in areas of honeycombing are covered by epithelium expressing bronchiolar markers. In IPF, bronchiolization is the consequence of a variety of pathogenic events starting from alveolar stem cell exhaustion and ending in an abnormal or dysplastic proliferation of bronchiolar epithelium [11]. The size of honeycomb cysts usually increases during follow-up [12]. The large honeycomb cysts tend to have thinner walls and do not communicate with the airways and thus do not change in size during forced exhalation, whereas the small cysts may retain microscopic communication with the air-

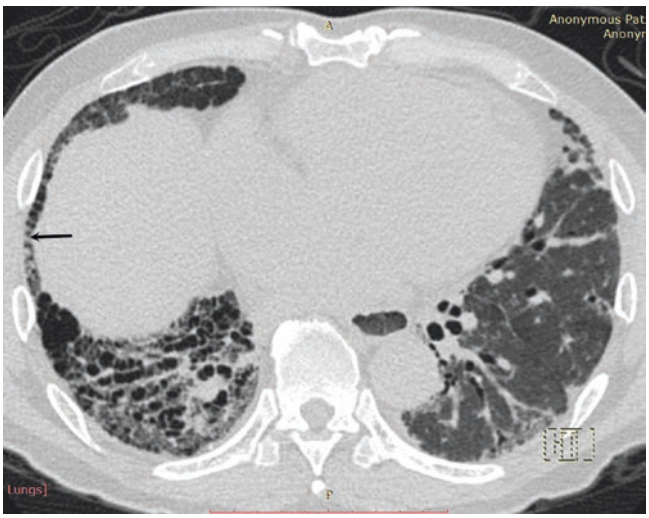

Fig. 13.9 Honeycombing versus traction bronchiectasis. Axial CT image shows varicoid bronchiectasis and subpleural honeycombing laterally (arrow)

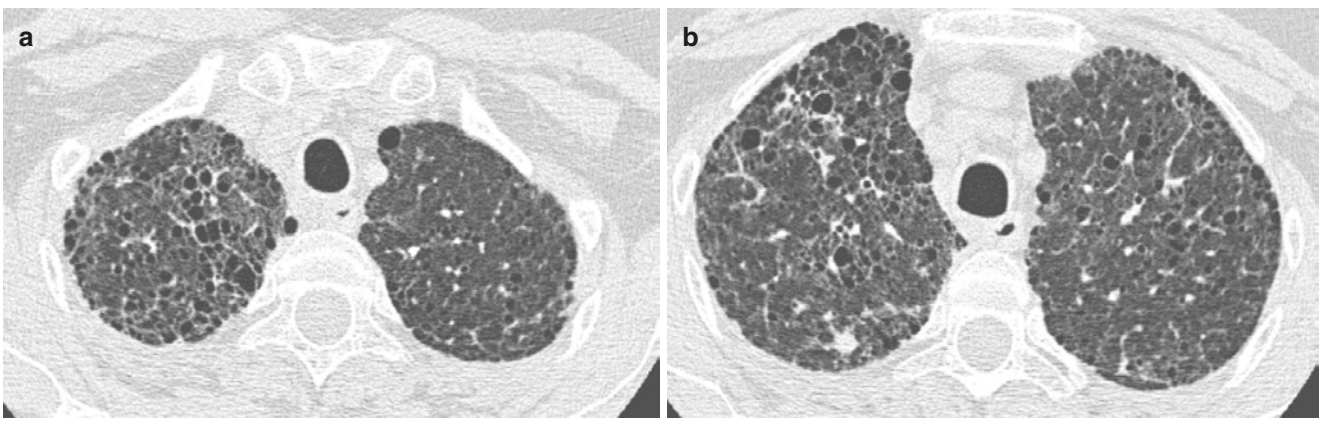

Fig. 13.8 Honeycombing versus cystic lung disease. (**a**, **b**) Axial CT images show subpleural honeycombing and centrally located small cysts in the same patient

ways that can explain their size decrease on expiration. The progressive enlargement of honeycomb cysts is partly due to air-trapping via the check-valve mechanism. It is presumed that a long asymptomatic period exists before honeycomb lung develops and the patient becomes symptomatic.

The extent of honeycombing is another important consideration when diagnosing UIP. It has been reported that the extent of honeycombing ranged from 3 to 21% of the lung parenchyma in UIP [10]. On the other hand, the extent of honeycombing in NSIP is reported as 0.3–3.7% of the lung parenchyma. The frequency and extent of honeycombing are significantly higher in UIP than in NSIP, although there is no defined threshold to differentiate UIP from NSIP.

13.3.4 Traction Bronchiectasis

"Traction bronchiectasis" is the term used to describe airway dilatation, usually peripheral, in the context of ILD. It is caused by surrounding retractile pulmonary fibrosis without any specific features and can be cylindrical or cystic. In UIP, traction bronchiectasis is seen in the peripheral lungs and has "beaded" or "varicoid" appearance, while in NSIP, the bronchial dilatation is central and cystic or cylindrical (Fig. 13.11). Exuberant traction bronchiectasis is one of the hallmarks of end-stage fibrotic NSIP. Along with fibrosis, traction bronchiectasis is a prognostic marker in patients with UIP [13]. One should remember that unlike other forms of bronchiectasis, "traction bronchiectasis" can be reversible to some extent. The peripheral confluence of traction bronchiectasis

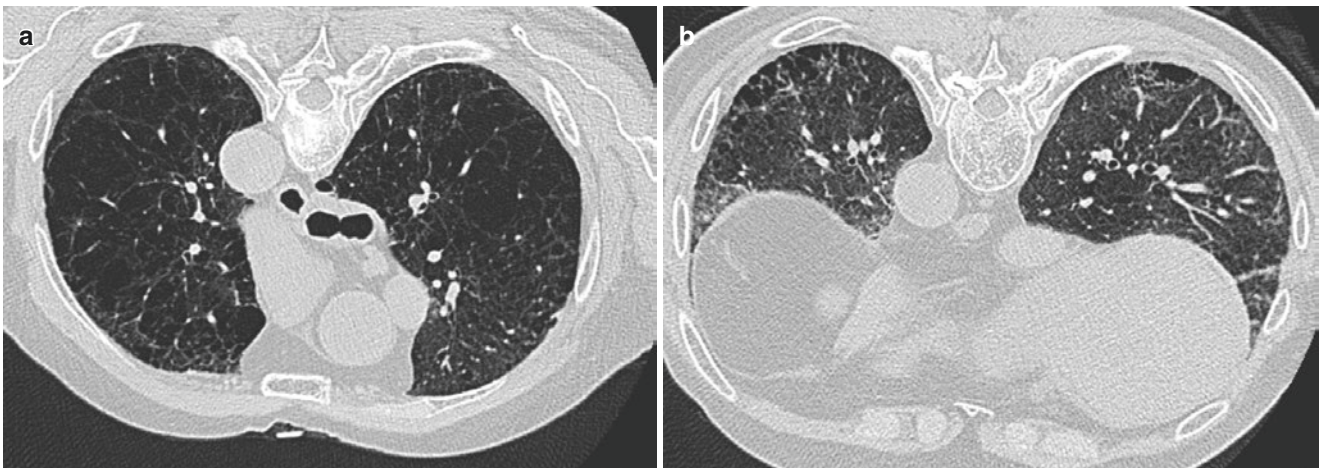

Fig. 13.10 Paraseptal emphysema versus honeycombing. (**a**, **b**) Axial prone CT images show confluent emphysema in upper lungs and paraseptal emphysema in posterior lung bases. Note irregular cystic spaces with irregular walls not satisfying the definition of honeycombing

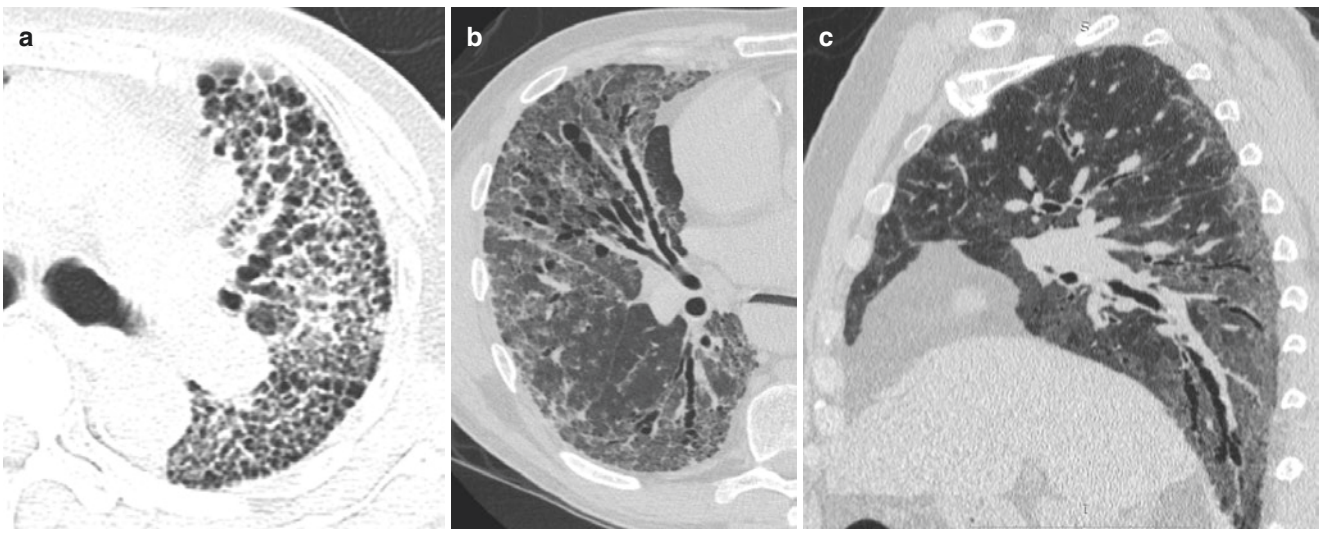

Fig. 13.11 Traction bronchiectasis in three patients. (**a**) UIP, (**b**) NSIP, (**c**) HP

is commonly mistaken for honeycombing on axial CT images. However, multiplanar reconstruction images are useful to diagnose traction bronchiectasis, through demonstrating interconnected spaces of bronchiectasis that eventually are continuous with more central airways. The cystic air spaces of a honeycomb lung tend to share walls, unlike traction bronchiectasis that has intervening lung between dilated airways. In addition, the use of post-processing tools such as minimum intensity projection (MinIP) may aid in differentiating traction bronchiectasis or discrete honeycombing. The differentiation of traction bronchiectasis from honeycombing on CT is critical for diagnosis of fibrotic NSIP (versus UIP).

13.3.5 Ground-Glass Opacities

GGOs reflect partial filling of the airspaces (e.g., fluid, blood, or inflammatory infiltrates), thickened septa, or a combination of the two (Fig. 13.12). In ILDs, the GGOs may be reversible on follow-up scans. GGOs alone may be due to inflammation, but when GGOs are accompanied with traction bronchiectasis and/or reticular abnormalities, they are predominantly due to fibrosis. If there is a component of inflammation, the GGOs may show improvement on follow-up imaging, after appropriate treatment.

13.3.6 Volume Loss

A frequent observation on HRCT of ILDs is volume loss in the lower lungs. There is striking volume loss in the lower lungs in patients with the antisynthetase syndrome. However, in certain conditions like combined pulmonary fibrosis and emphysema syndrome, the overall lung volumes may remain normal or increased due to the emphysema component. Volume assessment is helpful in follow-up radiographs and HRCT (Fig. 13.13).

13.3.7 Mosaic Attenuation and Air-Trapping

Mosaic attenuation refers to heterogeneous attenuation of lung parenchyma on CT, with alternating shades of gray

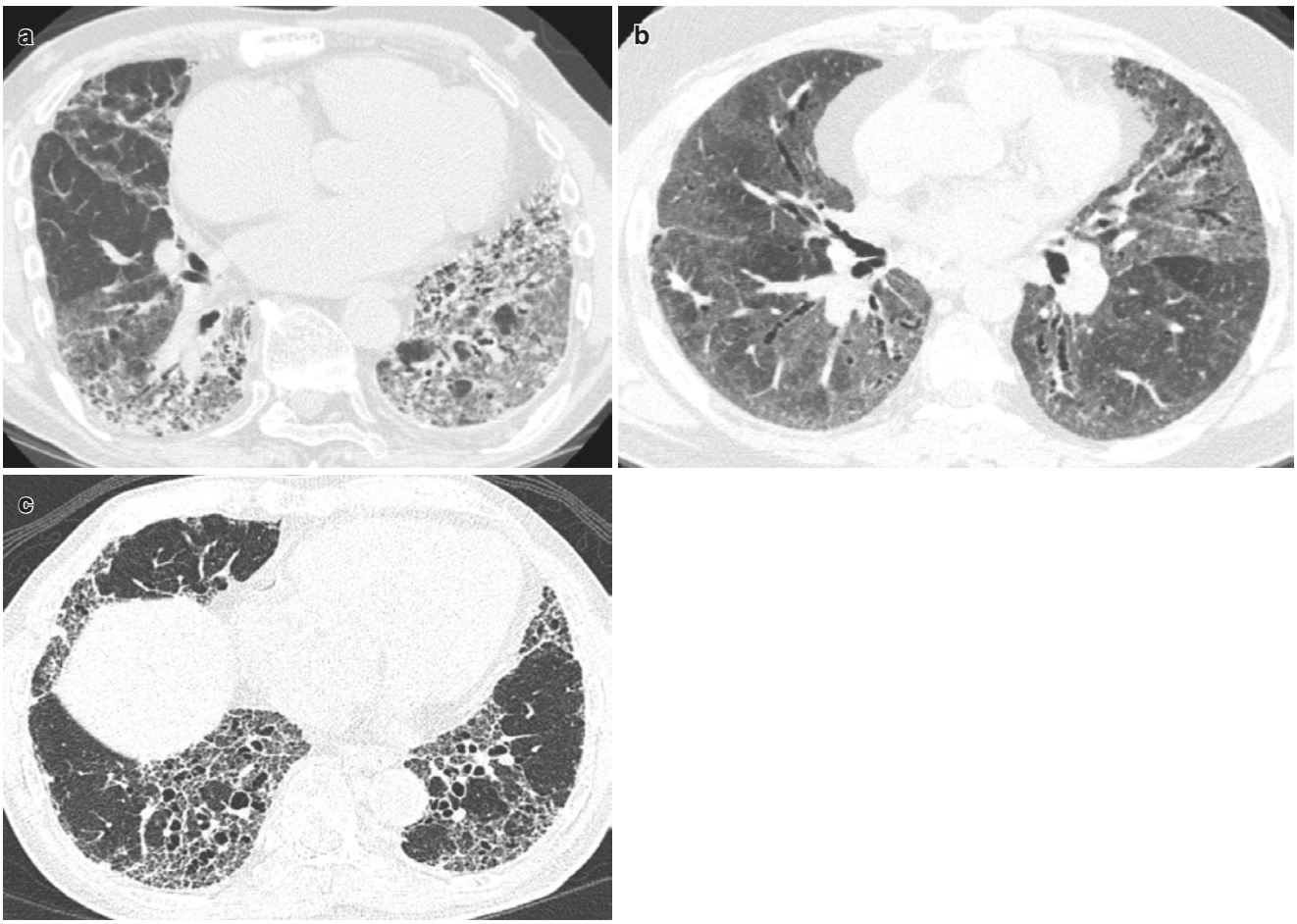

Fig. 13.12 (**a**, **b**, **c**) GGOs in three different patients

(Fig. 13.14). Mosaic attenuation of the lung can be due to air-trapping, vascular lung diseases, and parenchymal lung diseases. Table 13.3 describes the mosaic attenuation in detail with tips helpful in identifying the cause (Figs. 13.15, 13.16, and 13.17) [14, 15].

Mosaic attenuation is assessed on inspiratory scan while air-trapping assessment requires both inspiratory and expiratory phases.

Air-trapping is assessed by visual inspection of CT images (Fig. 13.18). When the expiratory images demonstrate areas of differential attenuation (lucent areas alternating with gray areas), one should correlate if such similar pattern is also present in the inspiratory images. In the case of air-trapping, there will be an accentuation of mosaicism with vessels in the lucent area being of smaller caliber than the vessels coursing the gray areas. Currently, there are three quantitative methods to assess air-trapping [16]. These are used in research studies and sometimes in clinical practice to quantify the extent air-trapping, so as to monitor the response to treatment. The expiratory to the inspiratory ratio of mean lung density (E/I-ratio MLD) is most appropriate for detecting air-trapping on low-dose screening CT and performs significantly better than other quantitative measures [16]. The expiratory mean lung density in HU is divided by the inspiratory mean lung density and presented as a percentage. Increase in air-trapping results in a higher E/I-ratio MLD.

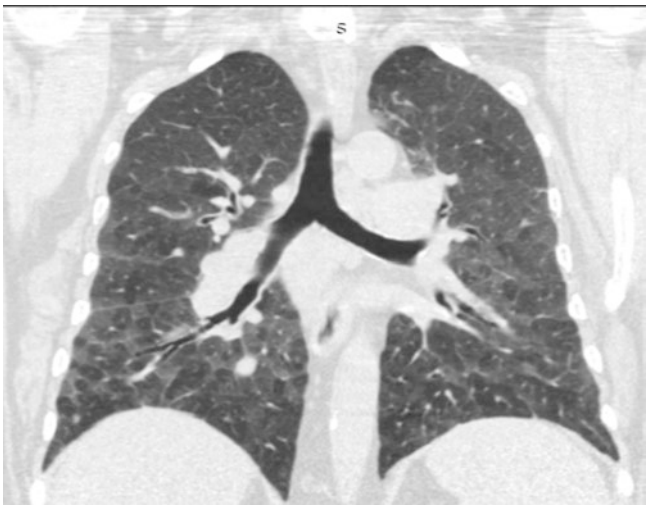

Fig. 13.14 Mosaic attenuation in a patient with HP

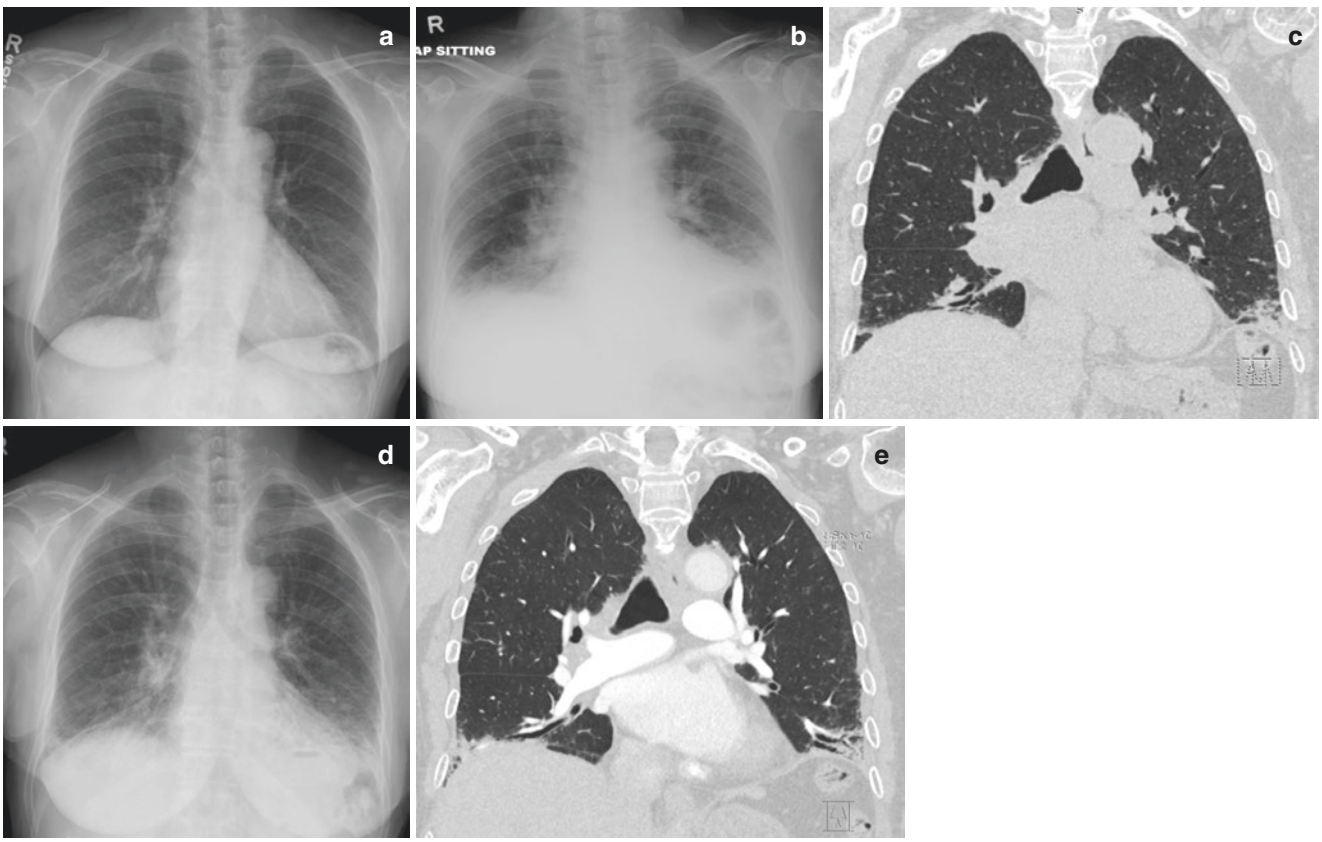

Fig. 13.13 Volume loss in lower lungs in a middle-aged woman with the antisynthetase syndrome. (**a**) Normal baseline radiograph. (**b**) Radiograph at presentation shows striking volume loss in lower lungs. (**c**) Coronal CT image confirms volume loss and bibasilar peribronchial organizing pneumonia. (**d**) Follow-up radiograph after 6 months of treatment show improvement in volume loss. But progression in scarring (**e**) coronal CT confirms the radiographic findings. Note inferior displacement of major fissures on CT due to volume loss in lower lobes

Table 13.3 Causes of mosaic attenuation

	Airway diseases/air-trapping	Vascular diseases	Parenchymal lung diseases
Causes	Bronchitis Bronchiolitis Asthma (reversible) Chronic HP Sarcoidosis Organizing pneumonia Chronic PE[b] DIPNECH[c] Relapsing polychondritis Tracheobronchomalacia	Chronic PE PAH[a] Cardiac shunts Pulmonary veno-occlusive disease Pulmonary capillary hemangiomatosis	Hemorrhage Infection Inflammation
Mechanism	Air-trapping due to small airway obstruction causing ball-valve obstruction	Reduced perfusion in lucent areas Increased perfusion in gray areas	Normal lung parenchyma intervening between abnormal lung
HRCT features	*Lucent area* – Small caliber vessels – Expiration: lucent areas show no or minimal increase in attenuation and no or minimal decrease in volume *Gray area* – Normal caliber vessels Expiration: increase in attenuation and decrease in volume *Other features* – Large airway disease – Centrilobular nodularity – Clinical history	*Lucent area* – Small caliber vessels – Expiration: lucent areas show increased attenuation and decrease the volume *Gray area* – Normal caliber vessels Expiration: increase in attenuation and decrease in volume *Other features* – Dilated pulmonary artery – Pulmonary artery: Bronchi >1 – Shunts – History	*Lucent area* – Normal caliber vessels – Expiration: lucent areas show increased attenuation and decrease the volume *Gray area* – Normal caliber vessels Expiration: increase in attenuation and decrease in volume *Other features* – Septal thickening – Clinical history

[a]Pulmonary artery hypertension
[b]Pulmonary embolism
[c]Diffuse idiopathic pulmonary neuroendocrine cell hyperplasia

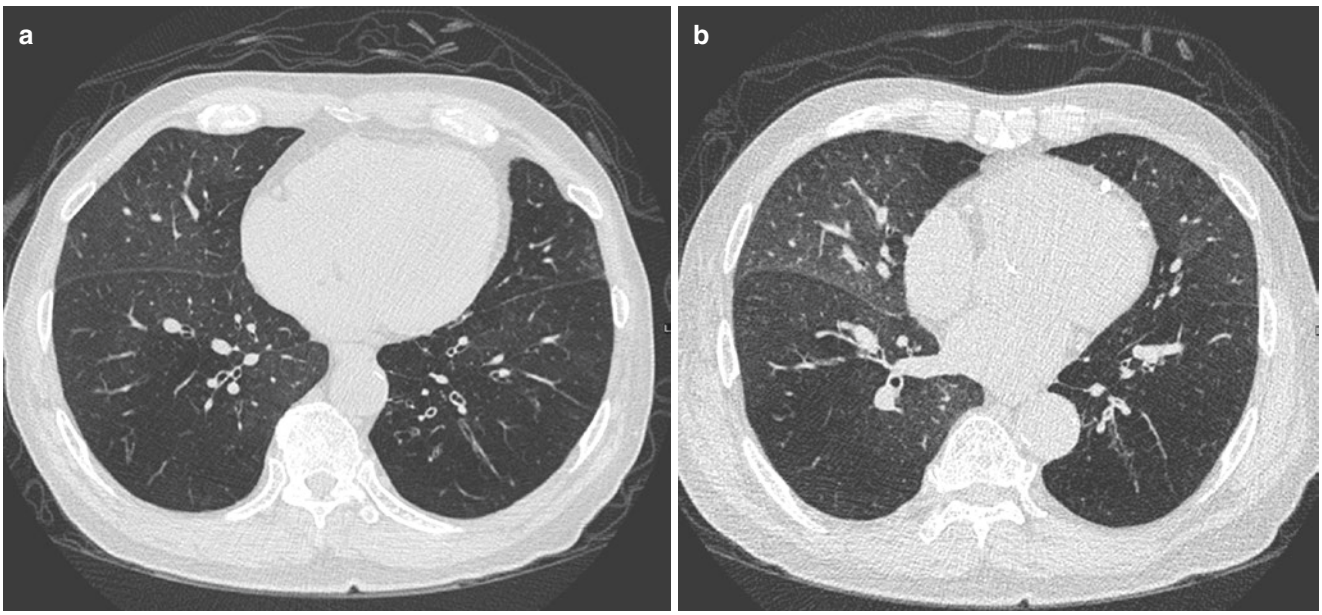

Fig. 13.15 Small airways disease. (**a**) Inspiratory image shows mosaic attenuation with small caliber vessels in lucent zones and large airways disease (bronchial wall thickening). (**b**) Expiratory CT image shows no change in attenuation and volume of lucent zones (air-trapping) but increased density of gray areas (normal lung)

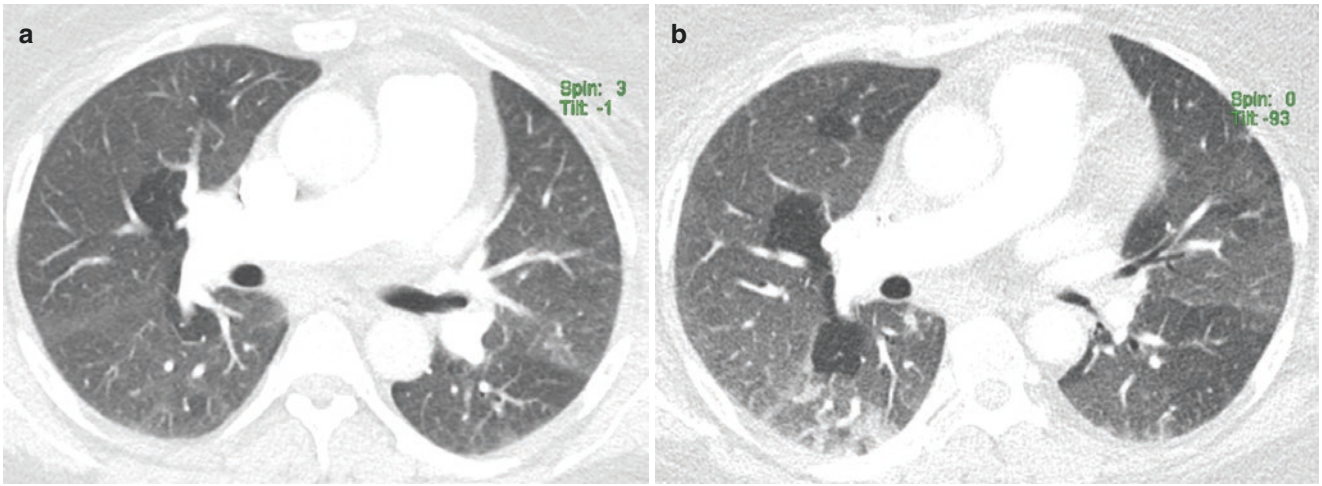

Fig. 13.16 Pulmonary artery hypertension. (**a**) Inspiratory and (**b**) expiratory CT images show dilated central pulmonary arteries and low caliber vessels in lucent zones (under perfused). Note the lack of signs of large airway disease

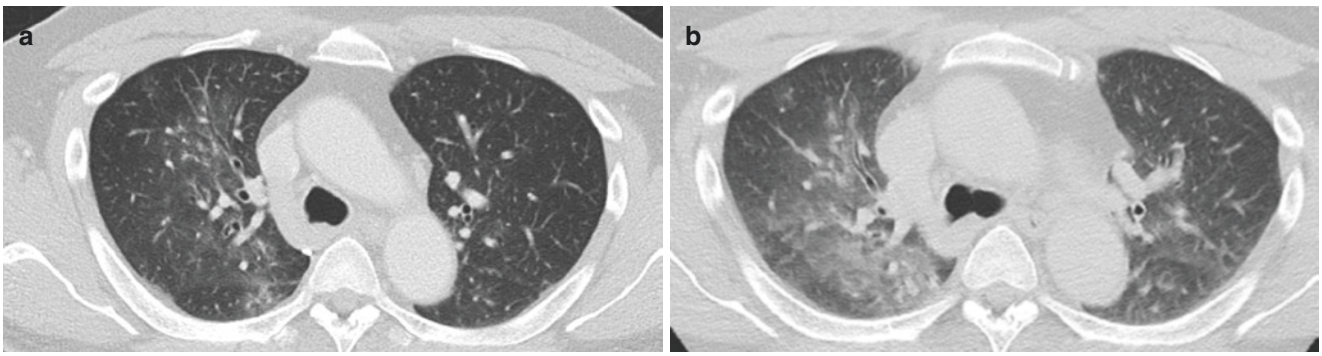

Fig. 13.17 Parenchymal lung disease (hemorrhage). (**a**) Inspiratory CT image shows the similar caliber of vessels in lucent as well as gray areas. (**b**) Expiratory CT image shows increased density and decreased volumes in both lucent and gray areas

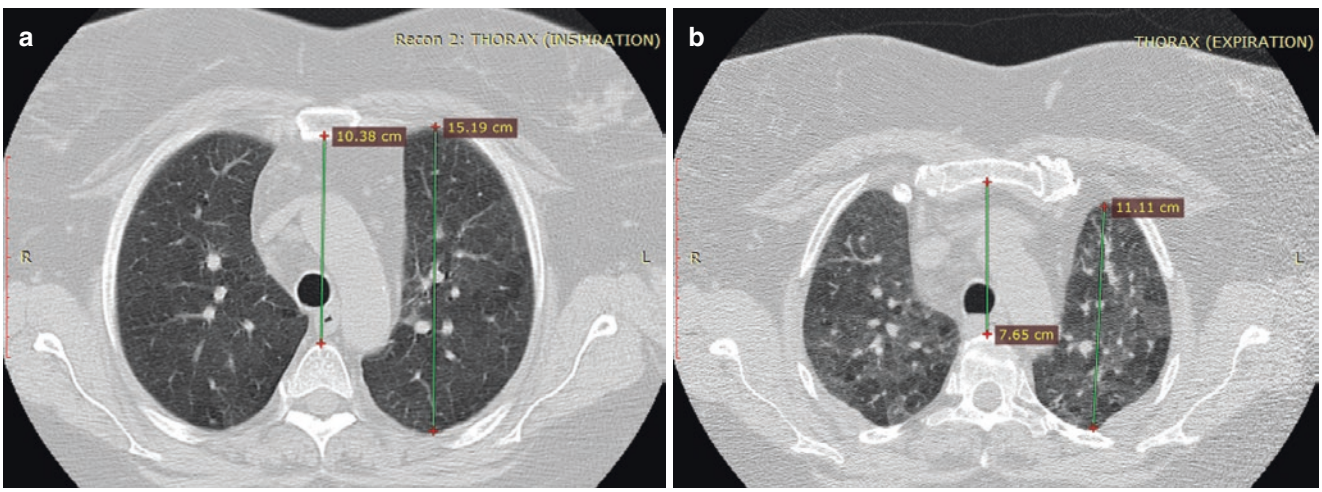

Fig. 13.18 Visual assessment of air-trapping on (**a**) inspiratory and (**b**) expiratory CT. Note that the tracheal shape has changed from "O" shape to "D" shape

Air-trapping is a marker of the small airway disease. Frequently, the air-trapping may be the only finding of a pulmonary disease in patients with a normal-appearing inspiratory CT scan. Air-trapping, usually limited to fewer than three adjacent secondary pulmonary lobules ("lobular air-trapping"), is frequently detected in asymptomatic healthy subjects with normal pulmonary function [17]. The high prevalence of air-trapping in patients with the normal pulmonary function may be due to the presence of a small airway disorder that is too mild to be detected by pulmonary function tests [17]. It is claimed that expiratory CT may be more sensitive in detecting local air-trapping than pulmonary function tests.

The severity of air-trapping increases with age and smoking. Air-trapping, seen along with ILD, is most often secondary to HP and rarely due to CTD-ILDs or sarcoidosis. Some degree of mosaic attenuation and air-trapping can be seen in patient with UIP, usually limited to the areas of advanced fibrosis in lower lobes. Other causes of air-trapping are discussed in Table 13.4 (Figs. 13.15, 13.19, and 13.20) [17–20].

Air-trapping is "patchy" in the majority of the cases but can also be "diffuse" in obliterative bronchiolitis as seen in lung transplant recipients. The identification of "diffuse" pattern of air-trapping is challenging on imaging as the inspiratory and expiratory images may appear similar. Before diagnosing "diffuse" air-trapping, it is essential to confirm that the expiratory phase is truly an expiratory scan by looking out for the collapse of the posterior tracheal wall. In patients with emphysema, the air-trapping in non-emphysematous lung must be reported.

13.3.8 Cysts

Cysts are not commonly seen in ILDs. However, these may be seen in DIP and LIP (Fig. 13.21). These may be difficult to differentiate from the other cystic lung diseases and emphysema, if other hallmarks like GGOs are absent.

13.4 Non-pulmonary Findings

Evaluation of mediastinum using HRCT contributes additional information for assessment of the lungs. Hence, it is recommended to reconstruct the axial images in 3 mm slices with soft-tissue kernel. Non-pulmonary findings may provide clues toward the etiology of interstitial lung diseases. The following non-pulmonary organs must be assessed on HRCT.

Table 13.4 Conditions associated with air-trapping

Bronchiolitis	In patients with obliterative bronchiolitis, since the amount of abnormal soft tissue in and around the bronchioles is relatively small, direct CT signs of bronchiolitis (i.e., tree-in-bud opacities) are usually absent in the inspiratory scan. Air-trapping can be the only HRCT sign of obliterative bronchiolitis
Asthma and bronchitis	HRCT almost always demonstrate air-trapping in patients with asthma and bronchitis. The medium and small bronchi in these conditions are thickened by the combination of inflammatory edema and an increase in the amount of smooth muscle bulk associated with an increase in the size of the mucous glands. HRCT demonstrates thickening of the bronchial wall or "peribronchial cuffing." However, in early stages of the disease, the obstruction of the pulmonary airways is reversible, and no abnormality is seen in the inspiratory CT. Air-trapping may be the only indicator of obstructive disease in an otherwise normal lung. In chronic asthmatic patients marked expiratory narrowing of the peripheral bronchi is due to bronchial hyper-responsiveness
Hypersensitivity pneumonitis (HP)	Early stage of the disease is characterized by cellular bronchiolitis with the presence of peribronchial inflammatory infiltrates (consisting of lymphocytes and plasma cells) causing bronchiolar obstruction. The small amount of cellular infiltration, which characterizes this stage of disease, cannot be detected on inspiratory CT scan. The presence of air-trapping with a lobular pattern helps in the diagnosis
Sarcoidosis	Granulomata developing in centrilobular and peribronchiolar lymphatics compromise the small airways, leading to air-trapping. The other causes of airway obstruction in sarcoidosis are compression of airways by lymph nodes, fibrotic scarring of endobronchial lesions, and bronchial distortion by peribronchial fibrosis
Tracheobronchomalacia	The cause of air-trapping in patients with tracheobronchomalacia is uncertain, but it may reflect chronic small airway disease due to abnormal respiratory mechanics related to excessive central airway collapse. The diagnosis of tracheobronchomalacia is made in the expiratory scan which demonstrates collapse of the trachea and/or large bronchi (reduction of anterior-posterior diameter more than 50%) and air-trapping. A cutoff of 70% reduction of anterior-posterior diameter may be a more specific finding. Dynamic expiratory CT is a highly sensitive method for detecting tracheobronchomalacia and has been shown to be concordant with dynamic flexible bronchoscopy
Pulmonary embolism	Air-trapping is seen in both acute and chronic pulmonary embolism. Air-trapping associated with areas of mosaic perfusion is reported in 75% of the patients with pulmonary embolism. Air-trapping in expiratory CT is seen not only in areas with pulmonary embolism but also in areas without embolism. Asthma-like wheezing is reported to occur in patients with acute pulmonary embolism and is attributed to bronchoconstriction in these patients. The proposed mechanism of bronchoconstriction in acute pulmonary embolism includes the release of serotonin and prostaglandins from platelets in the thrombus or a change in parasympathetic nervous system tension, which controls the bronchial smooth muscle tension

13.4.1 Esophagus

Gastroesophageal reflux disease (GERD) is common in patients with ILD [21–23]. Research studies have suggested a link between pulmonary fibrosis and esophageal reflux. Esophageal peristalsis is abnormal in up to 64% of the patients with ILD on manometric studies [23]. Ambulatory 24-hour pH monitoring is also abnormal in 66–94% of these patients [22, 23]. GERD is also common (more than 80%) in patients with connective tissue disease (CTD) [22, 24]. A study conducted by Vonk et al. revealed that the presence of esophageal dilatation on HRCT of the chest in ILD patients is suggestive of a diagnosis of scleroderma with a sensitivity of 63% and specificity of 88% [25]. The fact that ILD and GERD frequently coexist in patients with CTDs and that CTD patients with lung involvement may have a higher incidence of pathologic reflux reinforce the hypothesis that GERD may play a role in the pathogenesis of the interstitial lung fibrosis in patients with CTDs.

Esophageal dysmotility is assessed by barium swallow, manometry, pH monitoring, and scintigraphy. CT is a static study and dysmotility cannot be directly visualized in HRCT. However, CT can demonstrate indirect signs of dysmotility (Table 13.5) that may be overlooked (Fig. 13.22). The presence of these signs along with pulmonary changes may help with diagnosing CTDs, particularly scleroderma.

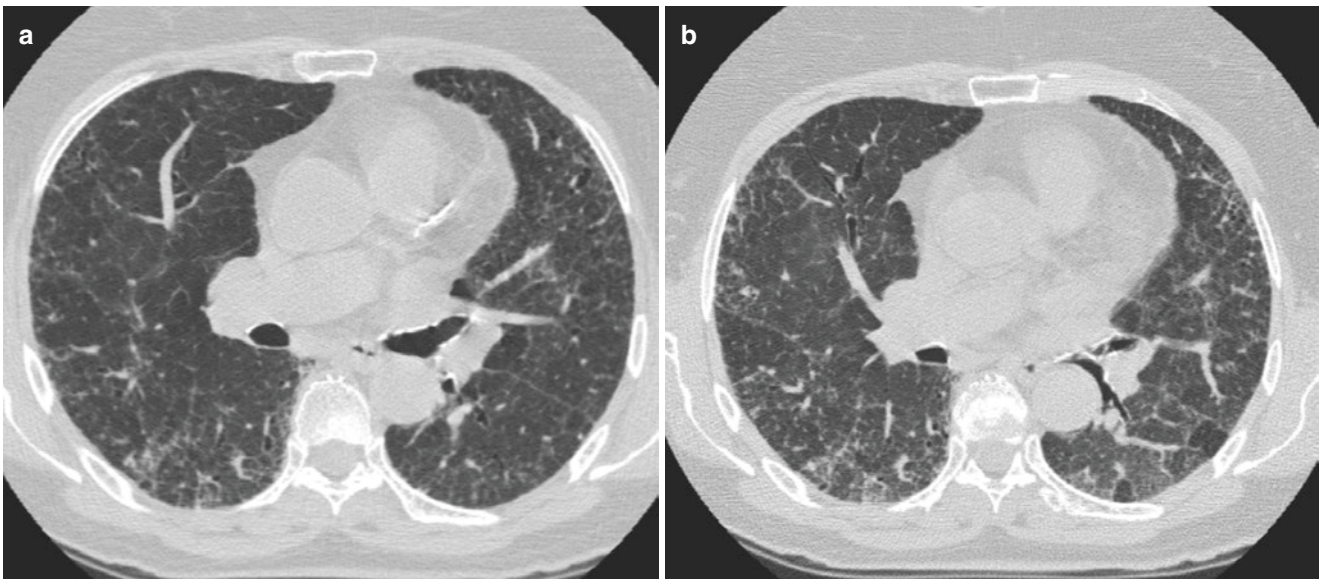

Fig. 13.19 Hypersensitivity pneumonitis. (**a**) Inspiratory and (**b**) expiratory CT images show fibrosis and air-trapping

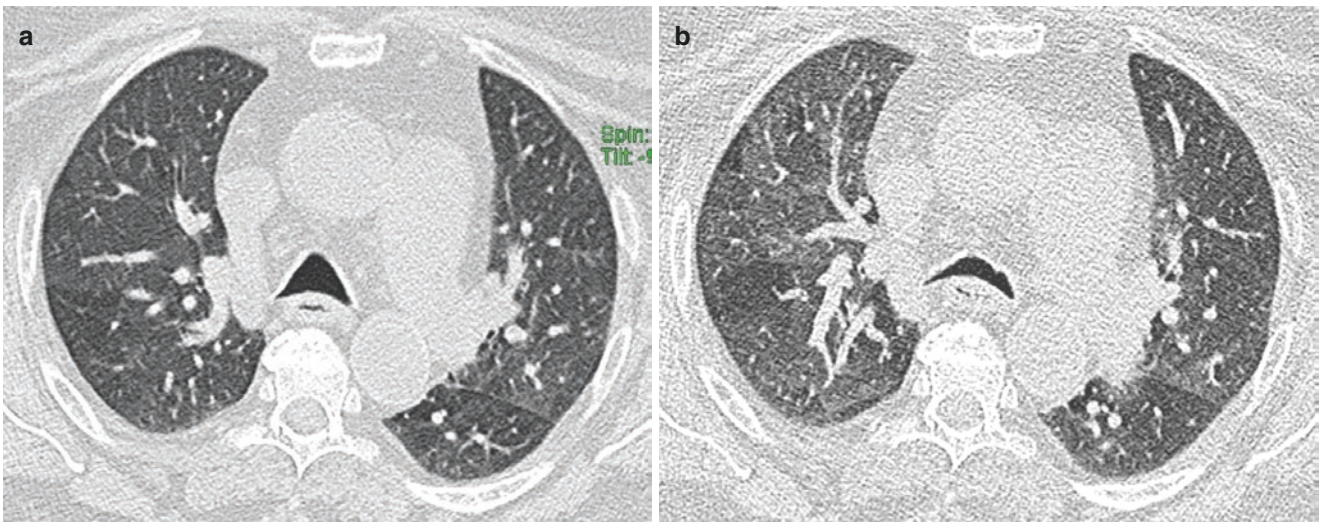

Fig. 13.20 Tracheobronchomalacia with air-trapping. (**a**) Inspiratory and (**b**) expiratory CT images show air-trapping. Note "Frown" sign

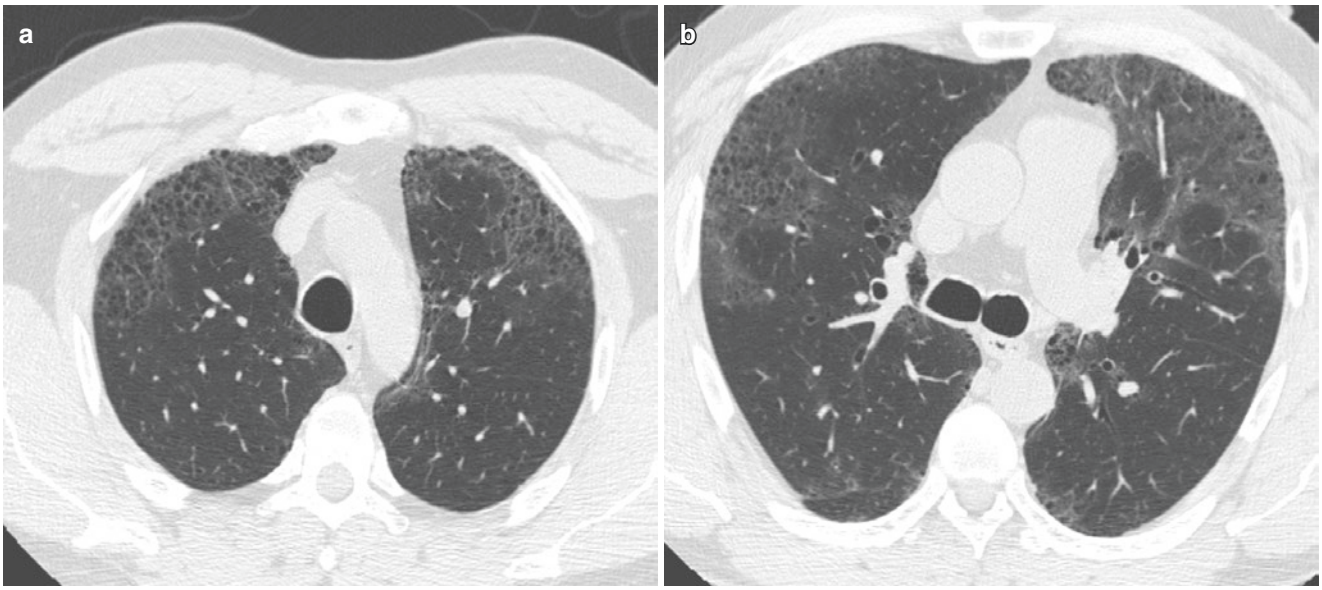

Fig. 13.21 50-year-old heavy smoker with desquamative interstitial pneumonia (DIP) on histopathology. (**a**, **b**) Axial CT images show ground-glass opacities in both lungs with small cysts formation. Surgical lung biopsy was performed due to upper lung distribution of the lung abnormalities

Table 13.5 Signs of esophageal dysmotility

• Segmental dilatation or diffuse dilatation – Transverse diameter more than 9 mm for infra-aortic esophagus – Focal dilatation of the upper thoracic esophagus
• Air throughout the course of the esophagus
• Air-fluid levels in the esophagus
• Patulous lower esophagus
• Large hiatal hernia

There is a good correlation between the HRCT-detected dilated esophagus and esophageal dysmotility confirmed either with esophageal transit scintigraphy [26] or with barium radiography [25].

A hiatal hernia is more common in IPF than in chronic obstructive pulmonary disease or asthma. One retrospective study found that 53% of the patients had hiatal hernia on CT scan at IPF diagnosis. The prevalence is similar to scleroderma-associated ILD but much higher than chronic hypersensitivity pneumonitis or other connective tissue disease-related ILDs [27]. This is either due to a hiatal hernia contributing to the development of IPF or a hiatal hernia being formed as a result of lung restriction, leading to the displacement of the diaphragm. Antacids are regularly prescribed to patients with IPF. So far, there are no prospective randomized clinical trials that address whether clinical outcomes in IPF are improved with GERD treatment. Although there is a conditional recommendation of using antacid therapy for patients with IPF [5], many questions remain with regard to the pathogenic role of gastroesophageal reflux in IPF and whether all patients should be treated regardless of symptoms [28].

13.4.2 Pulmonary Artery

The main pulmonary artery (PA) and the aorta are routinely imaged, and the respective diameters should be measured in every patient undergoing HRCT. Dilated PA is commonly seen in patients with CTD and may serve as a clue to the underlying etiology of pulmonary changes. Enlarged main PA diameter is a sign of pulmonary arterial hypertension (PAH) as the PA adapts to increased pulmonary arterial pressure—often a result of increasing pulmonary vascular resistance. The cutoff diameter of PA is reported as 29 mm in males and 27 mm in females in a large study [29]. Normal cutoff for the PA to aorta ratio is reported as 0.91 [29]. In patients with parenchymal lung diseases, PA diameter greater or equal to 29 mm has a sensitivity of 84%, specificity of 75%, the positive predictive value of 0.95, and positive likelihood ratio of 3.36, of predicting PAH [30]. Edwards et al. reported that the PA diameter of 33.2 mm has a sensitivity of 58% and specificity of 95% for the presence of PAH [31]. Selecting a higher cutoff value for PA diameter will increase the specificity at the cost of sensitivity. The ratio of the diameters of the main PA and of the ascending aorta in CT is also utilized to predict PAH [32]. If the ratio of PA diameter to ascending aorta diameter is greater than 1, there is a very high probability of PAH (Fig. 13.23). The ratio measurement is more valuable in elderly patients who have ectatic vessels. This method of ratio calculation has sensitivity, specificity, and positive and negative predictive values of 70%, 92%, 96%, and 52%, respectively, for determining PAH. However, a few studies have suggested that in the presence of signifi-

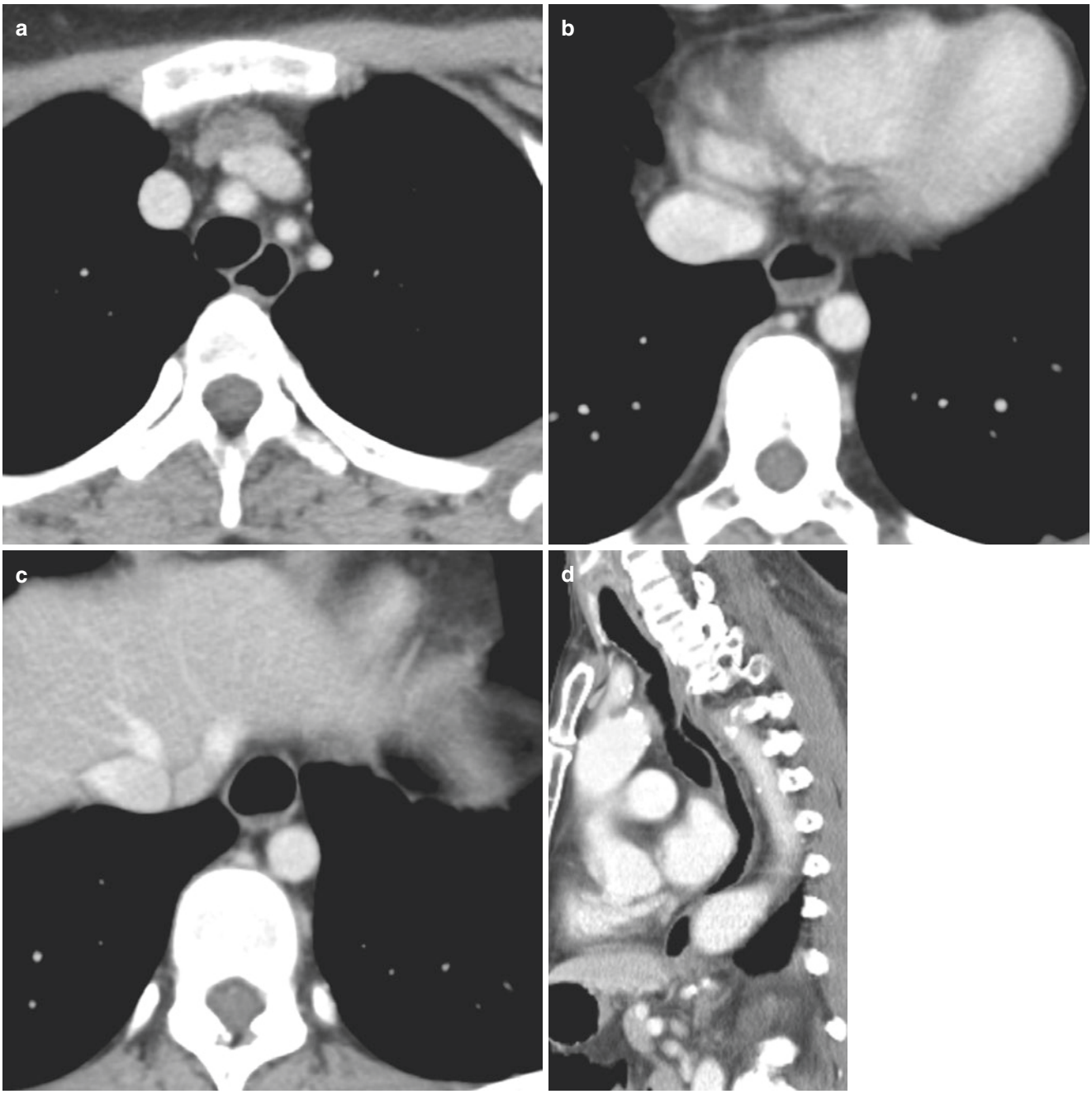

Fig. 13.22 Axial CT images (**a**–**c**) showing signs of esophageal dysmotility (dilated esophagus and air-fluid level). (**d**) Sagittal CT image in another patient shows air in the almost entire course of the esophagus

cant lung fibrosis, the main PA diameter does not correlate well with pulmonary arterial pressure [33, 34]. These studies concluded that the main PA dilatation occurs in the absence of PAH in patients with pulmonary fibrosis, and therefore HRCT cannot be used to screen for PAH in patients with advanced IPF. One also needs to be aware of "idiopathic dilatation of the pulmonary artery," which is a rare cause of main PA dilatation with normal pressure. Despite these pitfalls, it is good practice to mention the diameters of the aorta and main PA in the HRCT report.

13.4.3 Pericardium

Small amount of pericardial fluid can be a normal finding in HRCT of the thorax. It is essential to document if there is a

large pocket or recess. Normal pericardium can be up to 2 mm in thickness. Pericardial effusion can be due to serositis in the patients with CTD (Fig. 13.24). Fischer et al. reported an abnormal pericardium in 59% of patients with scleroderma [35]. The pericardial abnormalities include pericardial effusion, thickened pericardium, and thickened anterior pericardial recess. The sagittal dimension of the anterior pericardial recess is measured anteriorly between the ascending aorta and main pulmonary artery—a measurement of more than 10 mm is considered abnormal. In PAH, pericardial effusion is frequently present and may be considered an indirect sign. Pericardial fluid is known to flow back into the right atrium through lymph and venous drainage. In PAH, increased right atrial pressure limits this backflow and may lead to pericardial effusion. Pericardial effusion also serves as an independent predictor of mortality in PAH [36, 37].

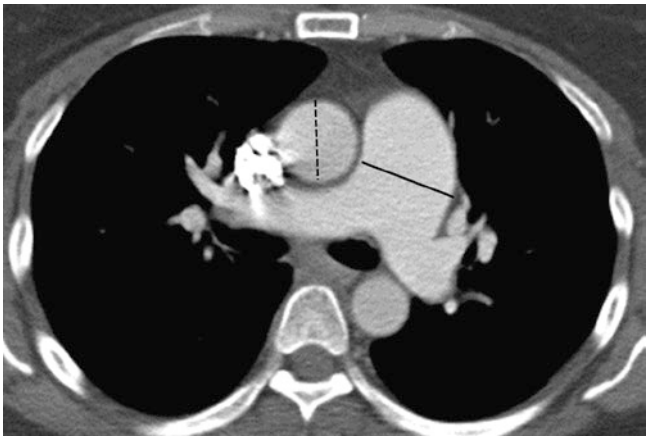

Fig. 13.23 PAH. Ratio of the diameter of the pulmonary artery to ascending aorta is more than 1

13.4.4 Mediastinal Lymph Nodes

Mild mediastinal lymphadenopathy is commonly seen in patients with ILDs and is not a cause for concern in the absence of sepsis or malignancy [38]. Bilateral enlarged hilar nodes, with or without calcification, may suggest sarcoidosis. Eggshell pattern of calcification suggests silicosis or sarcoidosis.

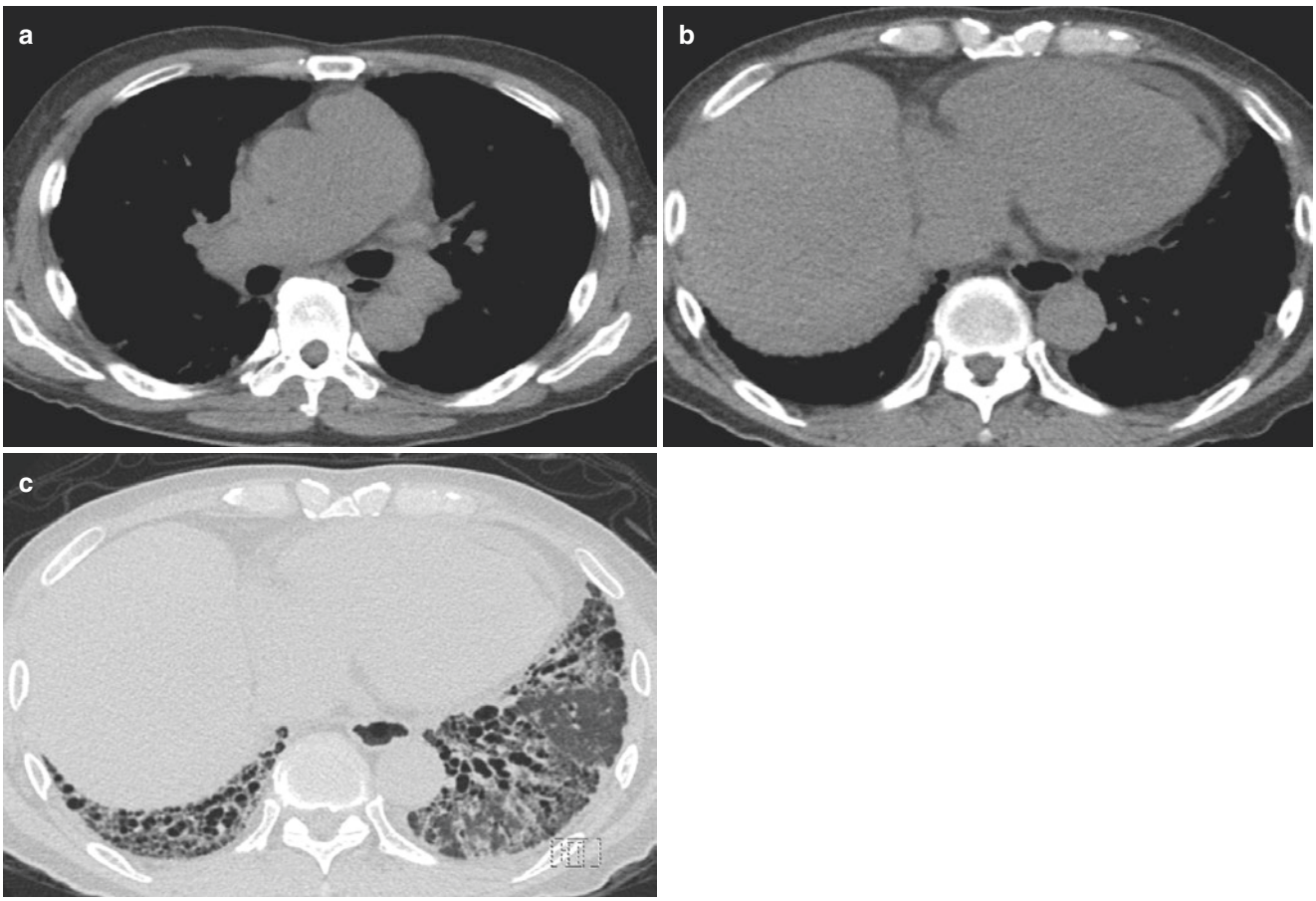

Fig. 13.24 Scleroderma-related ILD. (**a**–**c**) Axial CT images show small pericardial effusion, dilated pulmonary artery, air-fluid level in mid-esophagus, patulous lower esophagus, and fibrotic lung disease

13.4.5 Fat and Bones

Patients with known ILDs often receive high doses of steroids during the course of their management. Hence, it is common to observe the excessive amount of fat deposition in the chest wall and mediastinum. These patients are frequently osteopenic with resultant fractures in the ribs and vertebrae—findings always to be mentioned in the report. CT in patients with rheumatoid arthritis and other connective tissue disorders may demonstrate typical changes in the imaged bones and joints.

13.5 International Classification of the Idiopathic Interstitial Pneumonias

Idiopathic interstitial pneumonias (IIPs) are a subset of diffuse ILDs of unknown etiology. These IIPs demonstrate different radiological and histological characteristics but also share some common features [39]. The American Thoracic Society (ATS) and the European Respiratory Society (ERS) in 2013 came out with a statement reviewing the classification of IIPs [40] (Table 13.6). The most important impact of this classification has been in the development of novel drugs and the regimen for management. It is accepted that these IIPs are the outcome of an unknown injury that results in a different pattern of fibrotic response. Differentiation of the IIPs is important mainly because of the differences in prognosis. Each morphologic pattern of IIP has been defined radiologically on HRCT as well as histologically. By definition, these entities are idiopathic (including smoking-related IIPs), but the radiological and histological patterns of IIP included in the classification can be seen in known disorders, such as (1) CTDs, (2) drug toxicity, (3) chronic HP, and (4) asbestosis. Hence, the diagnosis is considered as unknown or idiopathic only after the exclusion of the known secondary association of the particular IIP pattern. This requires a multidisciplinary approach involving the radiologist, the pulmonologist, and the pathologist. In other words, the aforementioned four known conditions are always included in the list of differential diagnoses in the HRCT report, regardless of the morphologic pattern of disease. The radiologist's role is to comment on the morphologic pattern on HRCT, while the pulmonologist's role is to provide relevant clinical history with results of pulmonary function tests and related laboratory investigations. The pathologist helps in the interpretation of the relevant cytology and histology if a biopsy is available. Important information that is essential for meaningful multidisciplinary discussion includes serology (for CTD), history of exposure (for chronic HP), history of drug that has potential pulmonary toxicity (for drug toxicity), smoking history (for smoking-related ILDs), and occupational history (for asbestosis). The multidisciplinary discussion helps decide when a lung biopsy is needed in the diagnosis of IIPs or avoided in view of consensus on diagnosis and potential complications [40]. Most patients with a chronic IIP can be given a single clinical–radiologic–pathologic diagnosis. However, multiple pathologic and/or HRCT patterns may be found in the same patient. Different patterns may be seen in a single biopsy or in biopsies from multiple sites (e.g., UIP in one lobe and NSIP in another lobe) [41]. One should be aware that RB-ILD and DIP are strongly associated with smoking but are still included in the current classification of IIPs. Some patients with IIPs are difficult to classify, often because of mixed patterns of lung injury, and hence are grouped as "unclassifiable IIP."

Table 13.6 ATS/ETS classification of IIPs

• Major idiopathic interstitial pneumonias – Idiopathic pulmonary fibrosis – Idiopathic nonspecific interstitial pneumonia – Respiratory bronchiolitis-interstitial lung disease – Desquamative interstitial pneumonia – Cryptogenic organizing pneumonia – Acute interstitial pneumonia
• Rare idiopathic interstitial pneumonias – Idiopathic lymphoid interstitial pneumonia – Idiopathic pleuroparenchymal fibroelastosis
• Unclassifiable idiopathic interstitial pneumonia

13.5.1 UIP and IPF

UIP is a morphologic pattern of interstitial fibrosis that has gained most attention due to reasons listed in Table 13.7. IPF is the clinical syndrome associated with UIP pattern without any cause. As aforementioned, UIP pattern can also be seen in CTD, chronic HP, drug toxicity, and asbestosis. Chest radiographs are usually normal in the early phase but show reticular opacities in the lower lungs with volume loss and reticular pattern in the later stage. HRCT is an essential component of the diagnostic pathway in UIP and IPF. HRCT features of UIP are described in Table 13.8 [42–44]. UIP is a fibrotic lung disease and shows reticular opacities disproportionately higher compared to GGOs. Reticular opacities,

Table 13.7 Importance of UIP/IPF

• UIP is the most common morphologic pattern
• HRCT can be diagnostic of UIP—avoiding a lung biopsy
• IPF/UIP carries the worst prognosis among all patterns
• Unlike other IIPs, steroids in IPF/UIP are associated with increased risk of hospitalizations and death
• New anti-fibrotics such as pirfenidone and nintedanib are available for IPF/UIP which can slow the disease progression

Table 13.8 HRCT features of UIP

• Reticular opacities much more than GGOs
• Basal predominant disease
• Peripheral involvement
• Traction bronchiectasis is present
• Honeycombing almost always present
• Others – Architectural distortion – Asymmetrical involvement – Heterogeneity of findings – Dendriform pulmonary ossification

Table 13.9 Diagnostic criteria for IPF

• Presence of a UIP pattern on HRCT
• Specific combination of HRCT and histological pattern in patients subjected to surgical lung biopsy
• Exclusion of other known causes of ILD (e.g., domestic and occupational environmental exposures, CTD, and drug toxicity)

honeycombing, and traction bronchiectasis are salient features of UIP on HRCT. The histological hallmark of UIP is scattered fibroblastic foci composed of fibroblasts and myofibroblasts with temporal heterogeneity—different stages of inflammation and fibrosis interspersed with the relatively normal lung [45]. There should not be any histological features suggestive of an alternative diagnosis such as granulomas, hyaline membranes, marked inflammation, and organizing pneumonia. Similar to histology, HRCT frequently shows the involvement of the lungs as markedly asymmetrical and heterogeneous. Volume loss in the lower lungs is seen in advanced disease. Disseminated pulmonary dendriform ossification is seen in up to 7% of UIP on HRCT [46]. This pattern of ossification is also seen in chronic aspiration in the absence of UIP [47].

IPF is defined by the ATS/ERS as "a specific form of chronic, progressive fibrosing interstitial pneumonia of unknown cause, occurring primarily in older adults, limited to the lungs, and associated with the histopathologic and/or radiologic pattern of UIP" [5]. The diagnostic criteria of IPF are listed in Table 13.9 [5]. IPF affects people over 50 years of age and the incidence of disease increases with age, with presentation typically occurring in the sixth and seventh decades. The pulmonary fibrosis in a patient older than 70 years old is most of the time due to IPF [48]. Prevalence among men is more than women. Patients usually present with progressive dyspnea and nonproductive cough. Pulmonary function tests typically show a restrictive physiology with low diffusion capacity for carbon monoxide (DLCO). The etiology of IPF is unknown but studies have suggested an association with cigarette smoking, environmental exposures, viral infections, GERD, and genetic factors. Familial interstitial pneumonia occurs in a relatively younger population and presents with UIP pattern indistinguishable from IPF. Hence, family history must always be sought.

HRCT is considered as the backbone of IPF imaging. There is excellent correlation between UIP pattern on HRCT and biopsy findings, with more than 90% positive predictive value of HRCT [49–51]. The previous guidelines from the ATS and ERS included three levels of certainty for HRCT findings in IPF: (1) UIP, (2) possible UIP, and (3) inconsistent with UIP [5]. Honeycombing was considered a discriminator between "UIP" and "possible UIP" groups. Patients with UIP pattern on HRCT did not require lung biopsy. The possible UIP group included patients with HRCT showing all features of UIP but without honeycombing. These patients required further review in multidisciplinary discussions, and dependent on the available clinical information, decisions on further lung biopsy were made. The "inconsistent with UIP pattern" group required biopsy unless there was a definite alternative diagnosis like HP or there was a contraindication to biopsy. A study by Raghu et al. reported that more than 90% of patients with "possible UIP" had a histological diagnosis of UIP [49]. Another study revealed CT patterns of "UIP," "possible UIP," and "inconsistent with UIP" were associated with pathologic UIP in 89.6, 81.6, and 60.0% of the patients in the respective groups [52]. These and various other studies suggest that although honeycombing increases the confidence of detecting UIP, a large proportion of patient with UIP can be diagnosed even in the absence of honeycombing, in the appropriate clinical context. One should be reminded that the diagnosis of IPF cannot be made despite UIP disease pattern on HRCT, if there is evidence of CTD, chronic HP, drug toxicity, or asbestosis.

The Fleischner Society [53] has recently revised the diagnostic categories of UIP, based on CT patterns, into four subtypes: (a) typical UIP, (b) probable UIP, (c) indeterminate for UIP, and (d) most consistent with non-IPF (Table 13.10 published with permission from 54) (Figs. 13.25, 13.26, 13.27, 13.28, 13.29, 13.30, 13.31, 13.32, and 13.33). The aforementioned ATS and ERS guidelines have been superseded by this new classification in most of the centers. A diagnosis of IPF can be made confidently in patients with "typical UIP" pattern on CT without a need for lung biopsy, in the appropriate clinical setting, i.e., age older than 60 years, the absence of clinically significant medication or environmental exposure, and no evidence of CTD. In patients with "probable UIP" pattern, there is still an 82.4% likelihood of definite or probable histological UIP. In this group of patients, the clinical probability of IPF is much higher if the patients are older than 60 years old, current or former smoker without other causes of fibrotic disease. In the correct clinical context, a diagnosis of IPF can be made without biopsy, if there is the

Table 13.10 Diagnostic categories of UIP based on CT patterns

	Typical UIP CT pattern	Probable UIP CT pattern	CT pattern indeterminate for UIP	CT features most consistent with non-IPF diagnosis
Distribution	Basal predominant (occasionally diffuse) and subpleural predominant; distribution is often heterogeneous	Basal and subpleural predominant; distribution is often heterogeneous	Variable or diffuse	Upper lung or mid-lung predominant fibrosis; peribronchovascular predominance with subpleural sparing
Features	Honeycombing; reticular pattern with peripheral traction bronchiectasis or bronchiolectasis[a]; absence of features to suggest an alternative diagnosis	Reticular pattern with peripheral traction bronchiectasis or bronchiolectasis[a]; honeycombing is absent; absence of features to suggest an alternative diagnosis	Evidence of fibrosis with some inconspicuous features suggestive of non-UIP pattern	Any of the following: predominant consolidation, extensive pure ground-glass opacity (without acute exacerbation), extensive mosaic attenuation with extensive sharply defined lobular air-trapping on expiration, diffuse nodules or cysts

UIP usual interstitial pneumonia, *IPF* idiopathic pulmonary fibrosis
Pure ground-glass opacity, however, would be against the diagnosis of UIP or IPF and would suggest acute exacerbation, hypersensitivity pneumonitis, or other conditions
[a]Reticular pattern is superimposed on ground-glass opacity, and in these cases it is usually fibrotic

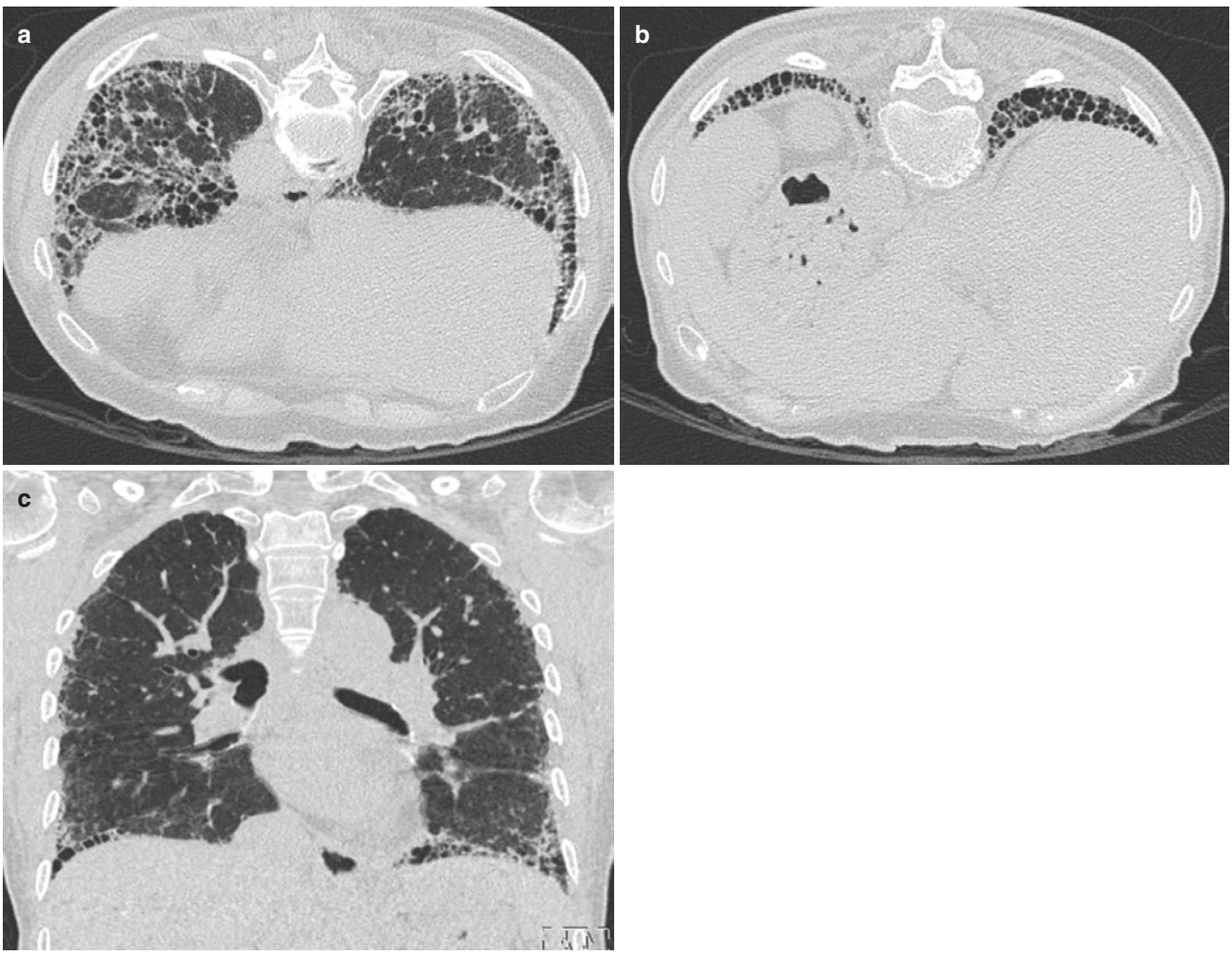

Fig. 13.25 Typical UIP. (**a**, **b**) Axial prone CT images show peripheral predominant reticular opacities, honeycombing with traction bronchiectasis. (**c**) Coronal CT image shows lower lung predominance

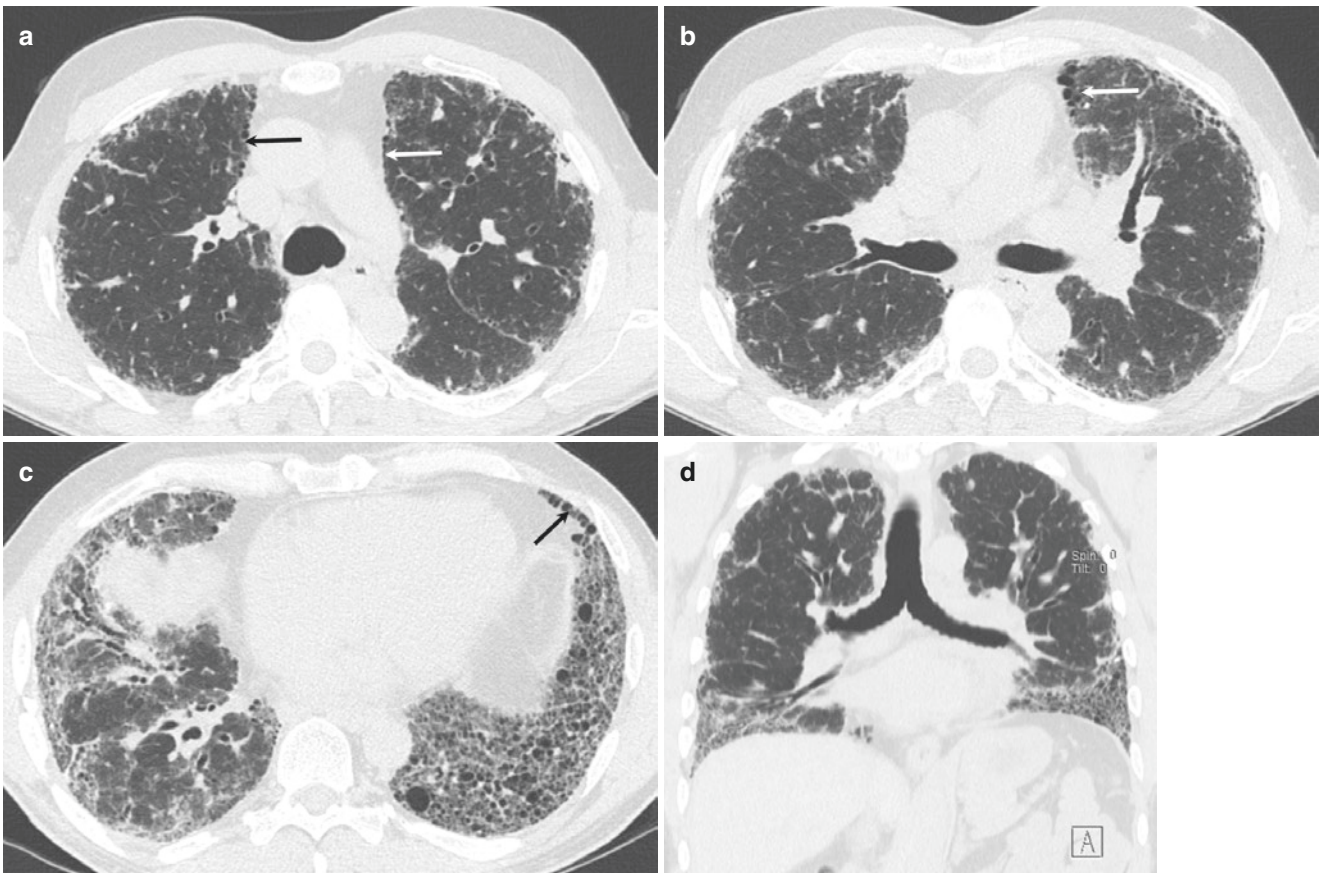

Fig. 13.26 Typical UIP. (**a**–**c**) Axial CT images show peripheral predominant reticular opacities, honeycombing (arrows) with traction bronchiectasis and GGOs. (**d**) Coronal CT image is useful to confirm lower lung predominance. Note the asymmetric involvement of lungs (left more than right)

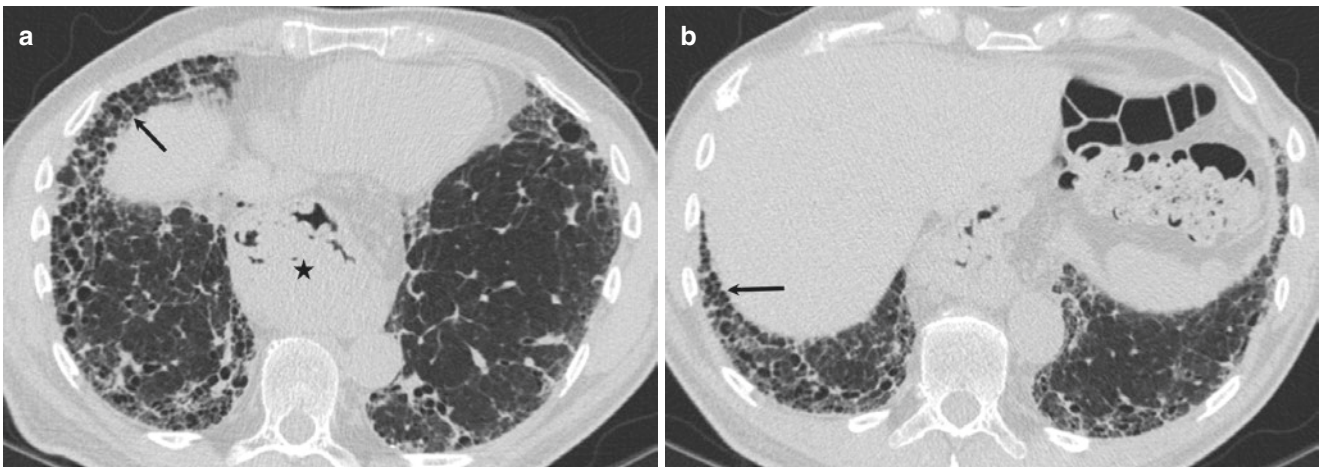

Fig. 13.27 Typical UIP with diffuse involvement. (**a**, **b**) Axial CT images reveal peripheral predominant reticular opacities with honeycombing (arrow). (**c**) Coronal CT image shows diffuse involvement in craniocaudal plane and asymmetric involvement of lungs (right more than left) included in "typical" UIP pattern. Mild mosaic attenuation is acceptable for this pattern. Note a large hiatal hernia (asterisk)

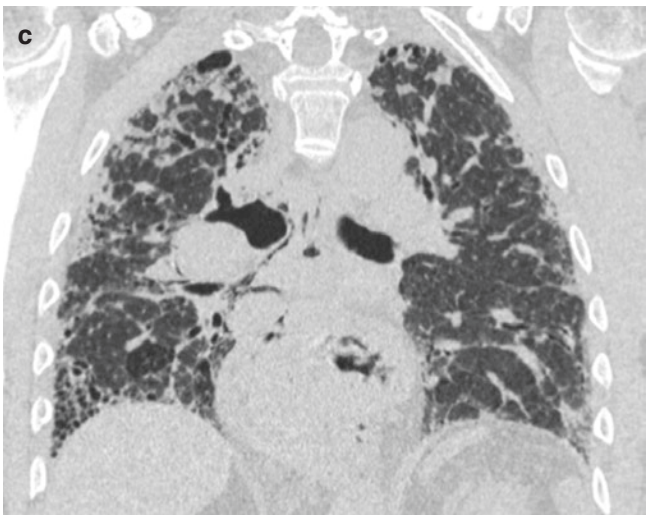

Fig. 13.27 (continued)

presence of "typical UIP" or "probable UIP" patterns on HRCT. Honeycombing is now a discriminator between "typical" and "probable" UIP. However, in patients with "indeterminate UIP" pattern, a lung biopsy should be considered as this pattern is associated with a lower likelihood of pathological UIP. Diagnosis of IPF in this group of patients will need a multidisciplinary assessment with integration of clinical, radiological, and pathological data. Finally, HRCTs showing predominant consolidation, upper lobe predominant fibrosis, extensive ground-glass opacity (without clinical features of acute exacerbation), extensive mosaic attenuation with air-trapping on expiration, diffuse nodules, or cysts are rarely observed in IPF, and alternative diagnoses need to be considered. However, there is still a small subgroup of IPF patients with these "atypical" CT findings, and imaging features may resemble NSIP, chronic HP, or sarcoidosis [6].

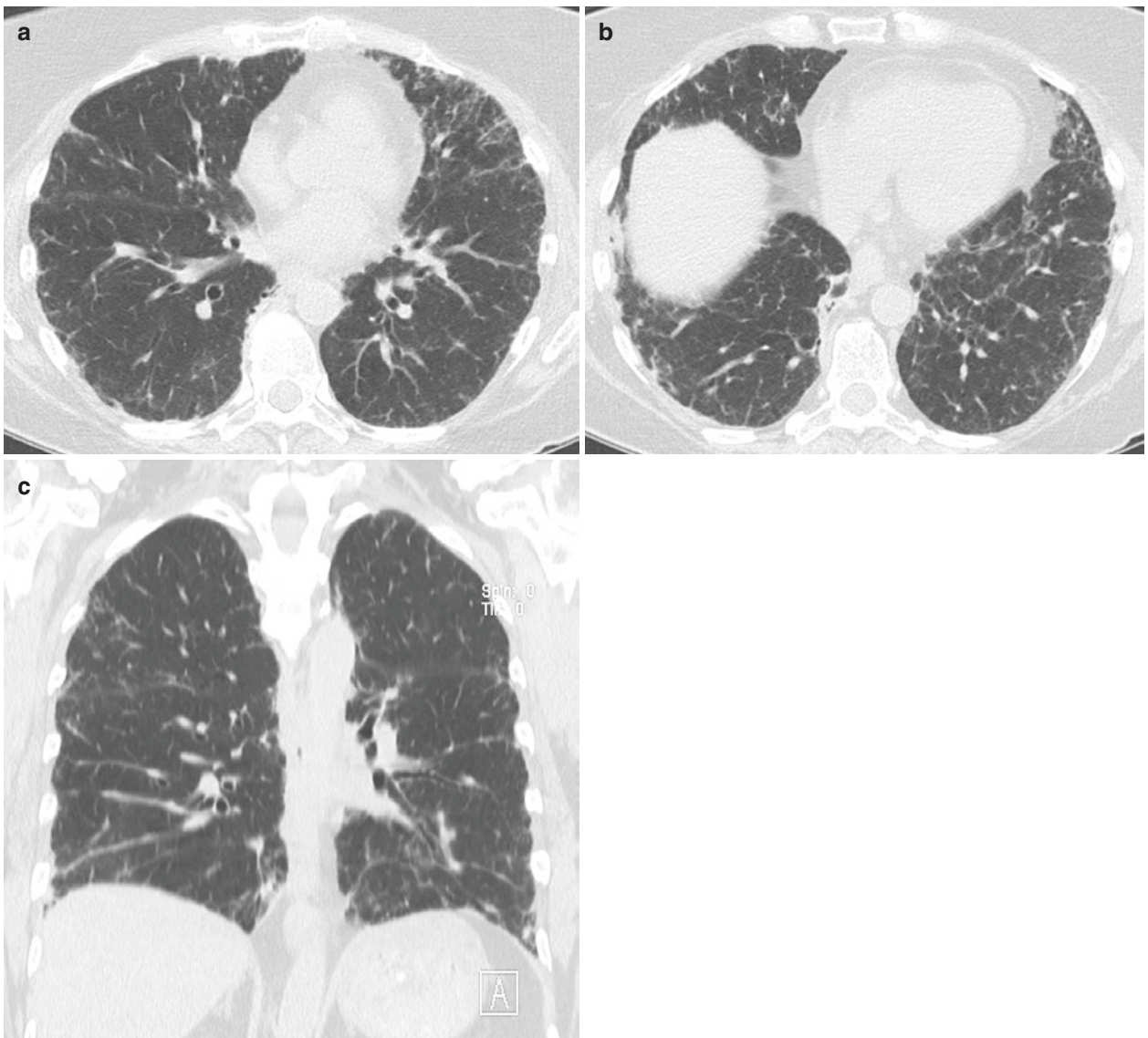

Fig. 13.28 Probable UIP. (**a**–**c**) Axial and coronal CT images show lower lung predominance, peripheral reticular opacities, and GGOs without honeycombing. There are no consolidation, nodules, mosaic attenuation, and cysts. Histopathology revealed UIP

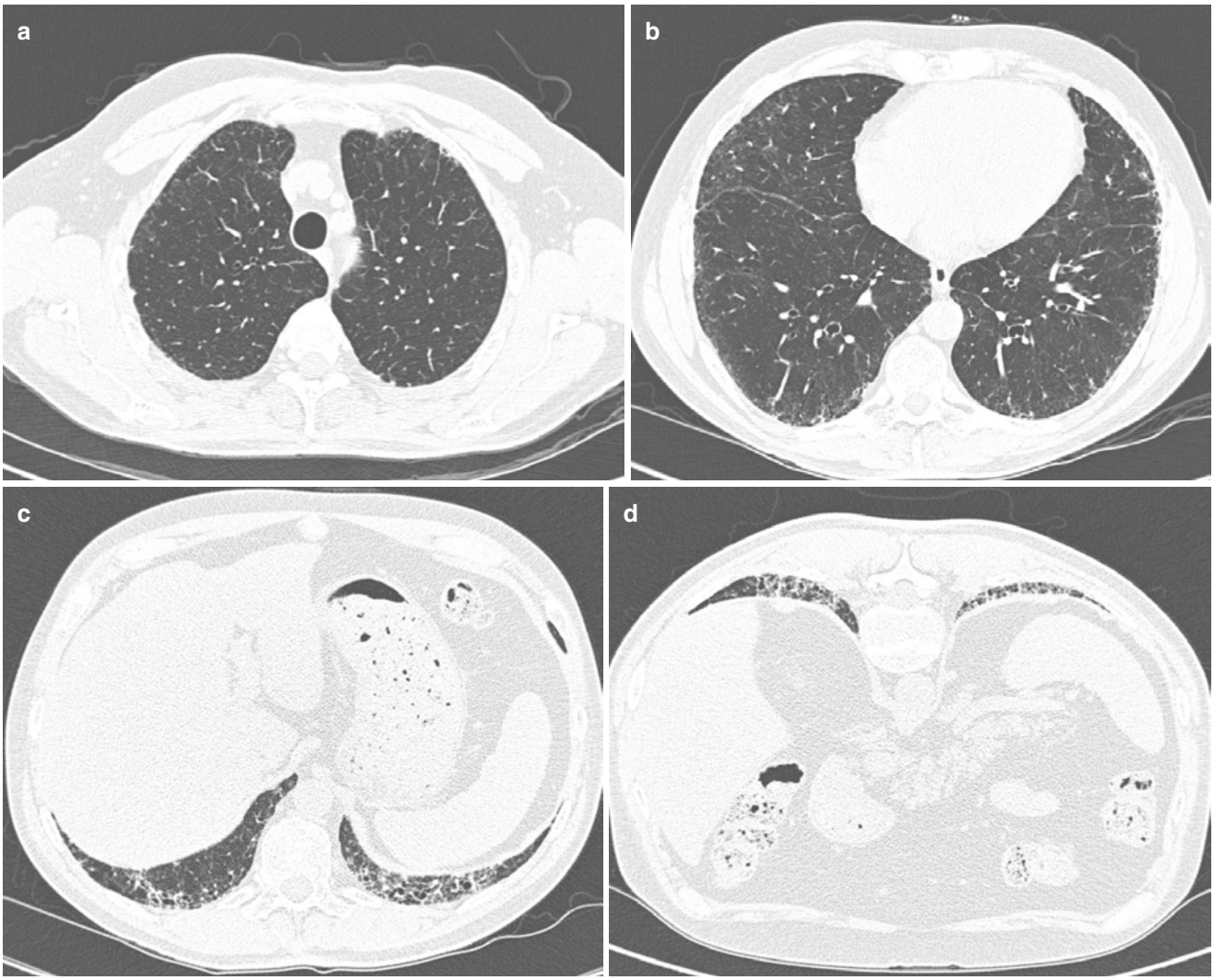

Fig. 13.29 Probable UIP. (**a**–**c**) Axial and coronal CT images show lower lung predominant, peripheral reticular opacities. (**d**) Axial prone image reveals peripheral traction bronchiectasis rather than honeycombing. There are no extensive consolidation, nodules, mosaic attenuation, and cysts. Histopathology revealed UIP

13.5.1.1 Complications of UIP/IPF

IPF has a heterogeneous but usually downhill course after diagnosis. While a few patients show an abrupt decline, the majority shows gradual deterioration. The disease course is further affected by life-threatening complications (Table 13.11) [54]. Many of these complications can also be seen in other IIPs.

Patients with fibrotic lung disease are predisposed to developing spontaneous pneumothorax and pneumomediastinum [55]. Pneumomediastinum may be asymptomatic or minimally symptomatic, whereas pneumothorax (usually spontaneous in IPF) can be poorly tolerated in patients with IPF. Chest radiographs have low sensitivity for diagnosing and quantifying these complications compared to HRCT, as the latter can evaluate the exact extent of extra-alveolar air [53].

Patients with IPF are also susceptible to infections, particularly those on immunosuppressive drugs. They can get infected with *Pneumocystis jirovecii*, *Mycobacterium*, and *Aspergillus* (Fig. 13.34) [54, 56, 57]. Although HRCT may provide useful information in suspected infections, in practice, it may be difficult to distinguish new infective opacities from acute deterioration of IPF and clinical as well as laboratory correlation is required.

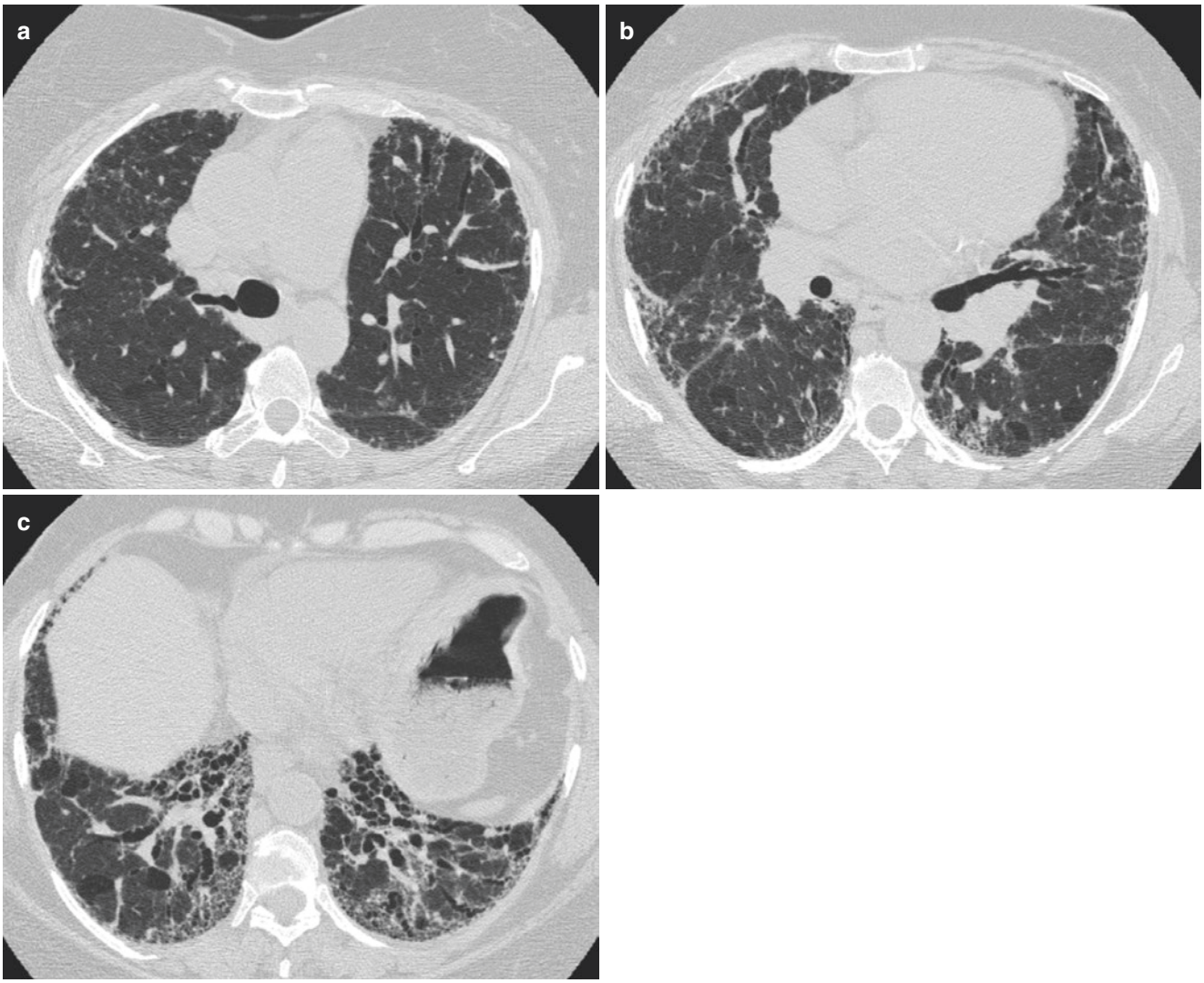

Fig. 13.30 CT pattern indeterminate for UIP. (**a–c**) Axial CT images show lower lung predominant fibrotic lung disease with reticular opacities and traction bronchiectasis but no honeycombing. However, due to peribronchovascular predominance and extensive sharply defined lobular mosaic attenuation, this pattern was called as indeterminate for UIP. UIP was proven at biopsy. Note right "tracheal bronchus"

Acute exacerbation or accelerated phase of IPF is perhaps the most feared complication of IPF. It is defined as "an acute, clinically significant respiratory deterioration characterized by evidence of new widespread alveolar abnormality" (Fig. 13.35) [58]. Acute deterioration can also be seen in chronic HP and idiopathic NSIP. An international working group has recently revised the diagnostic criteria for acute exacerbation of IPF. Previously, diagnosis of acute exacerbation required exhaustive exclusion of causes such as infections, drugs, and aspiration, but there seems to be little biological and clinical support this distinction of idiopathic and non-idiopathic events. Hence the word "idiopathic" was removed from the definition of acute exacerbation. Four diagnostic criteria need to be fulfilled for an acute exacerbation of IPF: (a) previous or concurrent diagnosis of IPF, (b) acute worsening or development of dyspnea typically less than 1-month duration, (c) CT with new bilateral ground-glass opacity and/or consolidation superimposed on a background pattern consistent with UIP pattern, and (d) deterioration not fully explained by cardiac failure or fluid overload [58].

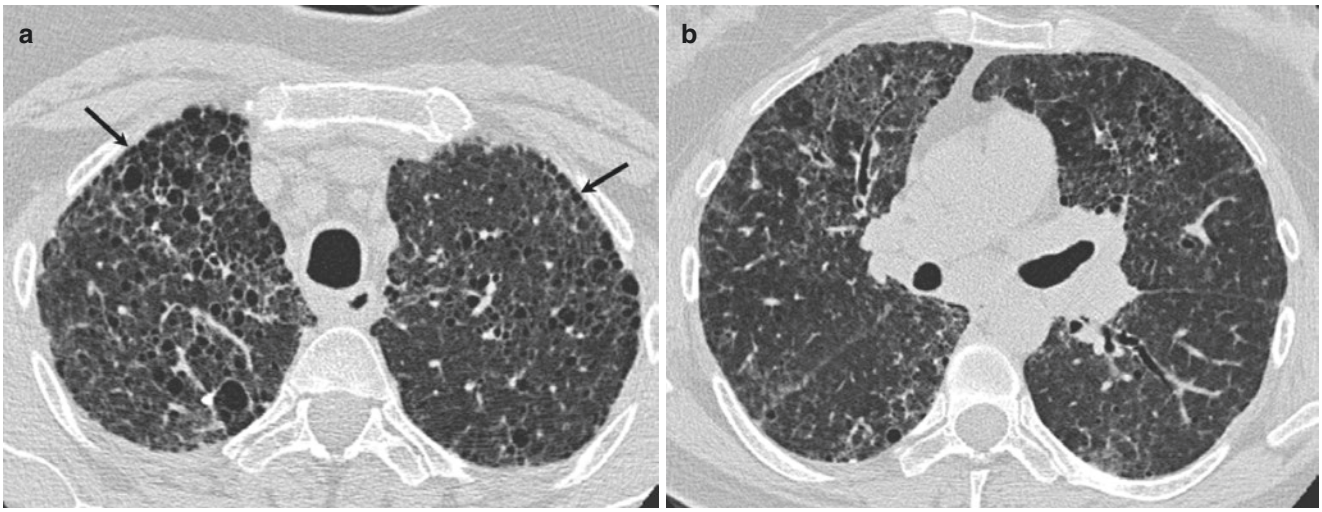

Fig. 13.31 CT pattern indeterminate for UIP despite honeycombing. (**a**, **b**) Axial CT images show honeycombing (arrows), but there is extensive cyst formation in the central lung associated with GGOs; hence the pattern was called as indeterminate for UIP. UIP was proven at biopsy

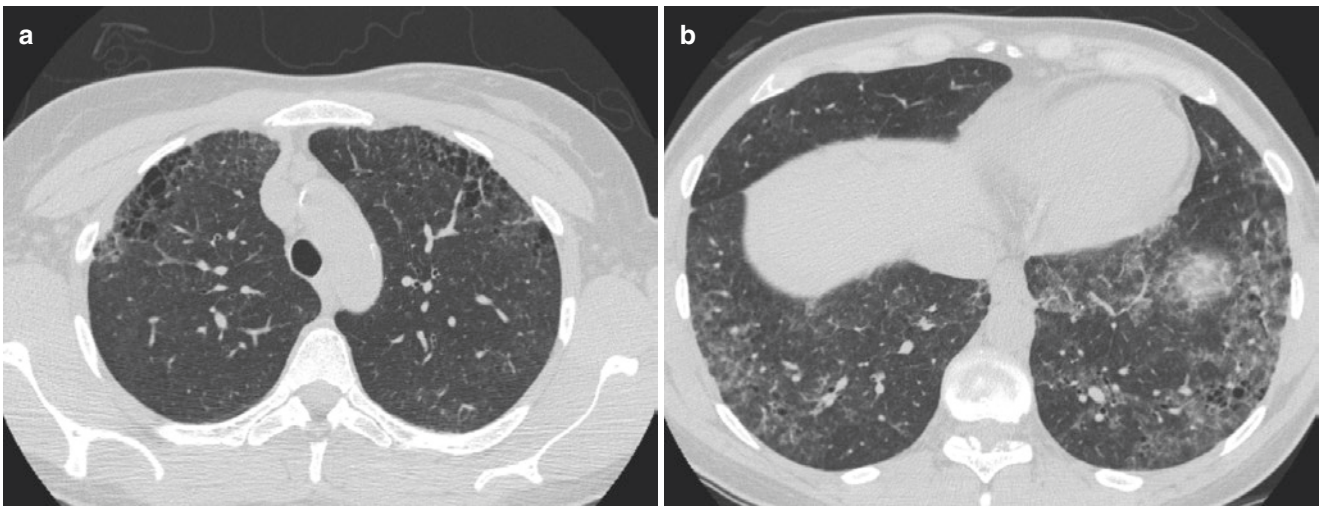

Fig. 13.32 CT pattern indeterminate for UIP. (**a**, **b**) Axial CT images show lower lung predominant GGOs without honeycombing, bronchiectasis, and reticular opacities. The upper lung shows emphysema associated with centrilobular nodularity, and the lower lungs show small cyst formation prompting for a radiological diagnosis of RB and DIP. UIP was proven at biopsy along with foci of RB, emphysema, and DIP

HRCT usually demonstrates new GGOs or consolidations that may be multifocal [59–61]. The diagnosis of an acute exacerbation is important as the prognosis is very poor with mortality exceeding 70%. Histological examination usually reveals patterns of OP, diffuse alveolar damage, and/or extensive fibroblastic foci [60, 62]. New GGOs in IPF can also be due to left heart failure that can be difficult to differentiate from an acute exacerbation. HRCT features of pulmonary edema including perihilar GGOs, septal thickening, and pleural effusions are helpful (Fig. 13.36). PAH is prevalent in a third of the patients with IPF, predisposing to right heart decompensation, which further hinders diagnosis.

The incidence of lung cancer is increased in patients with IPF, and this appears to be independent of the effect of cigarette smoking [63]. Identifying early lung cancer on HRCT of a fibrotic lung is challenging as the lung nodule may be mistaken for pulmonary scarring. Early nodules are often peripheral rather than central, with histology of either squamous cell carcinoma or adenocarcinoma (Fig. 13.37). Mild reactive mediastinal lymph node enlargement is common in patients with UIP, and these nodes increase in size with progressive disease, presumably due to chronic pulmonary inflammation [64]. Hence, detection of nodal metastasis in these patients can be a challenge.

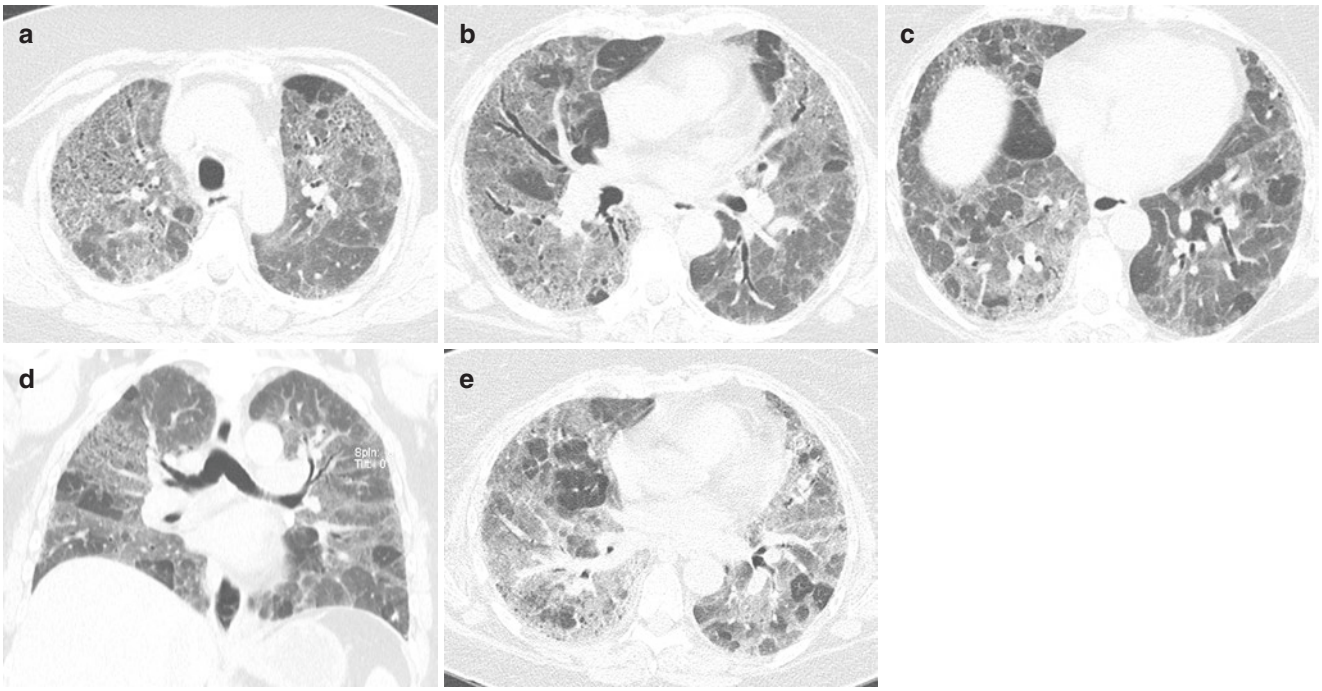

Fig. 13.33 CT features most consistent with non-IPF diagnosis. (**a**–**d**) Axial and coronal inspiratory CT images show GGOs and marked mosaic attenuation with upper lung fibrosis. (**e**) Expiratory CT image air-trapping and "head cheese" sign. Biopsy revealed mixed cellular and fibrotic NSIP with multinucleated giant cells and bronchiolocentric injury suggesting HP. Further history revealed mold exposure in this elderly woman

Table 13.11 Complications of IPF/UIP

• Pneumothorax
• Pneumomediastinum
• Infection
• Acute exacerbation
• Left heart failure
• Right heart failure
• Malignancy

13.5.1.2 Accuracy and Prognostication

HRCT plays a key role in the diagnosis of IPF. The accuracy of HRCT in the diagnosis of UIP/IPF is well established with a positive predictive value of over 90% in diagnosing UIP [51, 65, 66]. HRCT has reduced the number of lung biopsies required for the diagnosis of UIP/IPF due to its high specificity (90%) in diagnosing UIP [67]. A biopsy is still required in substantial number of cases due to low sensitivity in the diagnosis of new/early onset IPF [67]. There is moderate agreement among observers for the radiological diagnosis of UIP [68]. The disagreement among radiologists is probably related to interobserver variation in identifying honeycombing [69].

IPF is generally a fatal disorder with a reported median survival of 2.5–3.5 years. Among the IIPs, UIP/IPF carries the worst prognosis, compared to the other disease patterns. A histological diagnosis of UIP is associated with a nearly 30-fold greater risk of mortality than an alternative histological diagnosis in patients evaluated for suspected IIP [70]. HRCT findings predict mortality with greater sensitivity and specificity than histopathological features obtained from open lung biopsy, further strengthening the prognostic role of HRCT [71]. The extent of honeycombing has an adverse impact on prognosis [51, 70, 71]. Flaherty et al. reported that patients with typical HRCT pattern of UIP have a worse prognosis than those with an atypical or inconclusive HRCT pattern. Patients with a concordant diagnosis of UIP on HRCT and histology have less survival than those with a histological diagnosis of UIP in the absence of HRCT features of UIP [51]. Prognosis can also be affected by the associated clinical findings as a study had shown that prognosis of UIP in patients with CTD is better than the "idiopathic" group, i.e., IPF [72].

13.5.2 Idiopathic NSIP

NSIP is the second most common reported pattern of IIPs. NSIP varies in histology from cellular (rare) to fibrotic (more common), depending on the proportion of inflammatory cells and collagen deposition in the alveolar walls. In contrast to UIP, the histological hallmark of NSIP is the temporal homogeneity of pulmonary changes. Majority of the

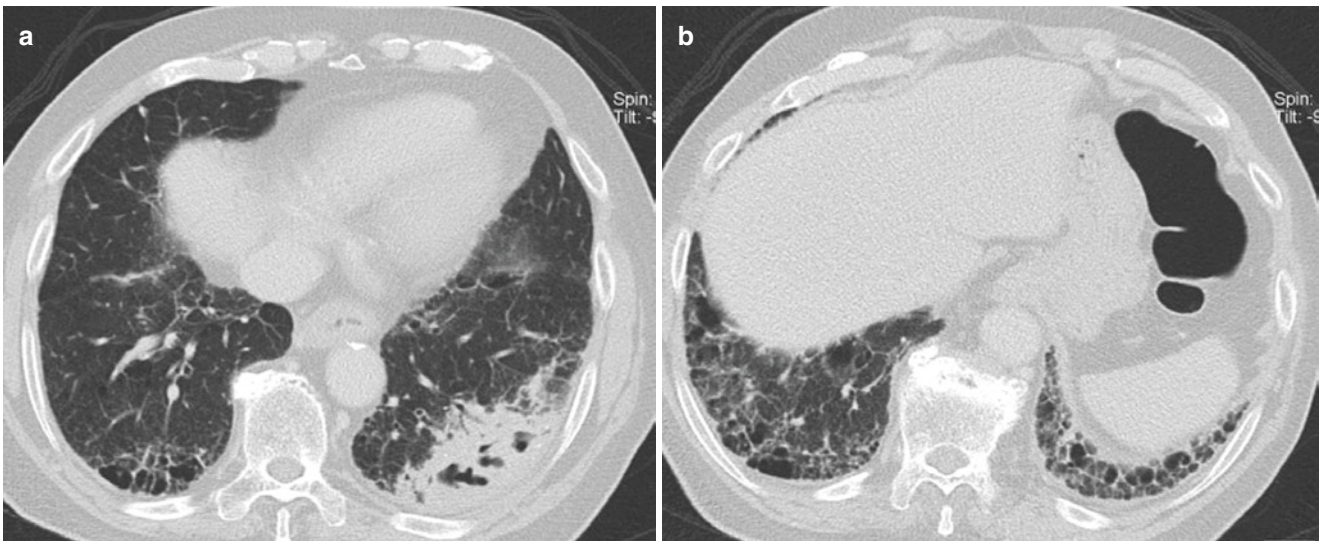

Fig. 13.34 UIP with cavitary tuberculosis. (**a**, **b**) Axial CT images show "typical" UIP pattern with cavitary consolidation in a patient from tuberculosis-endemic zone

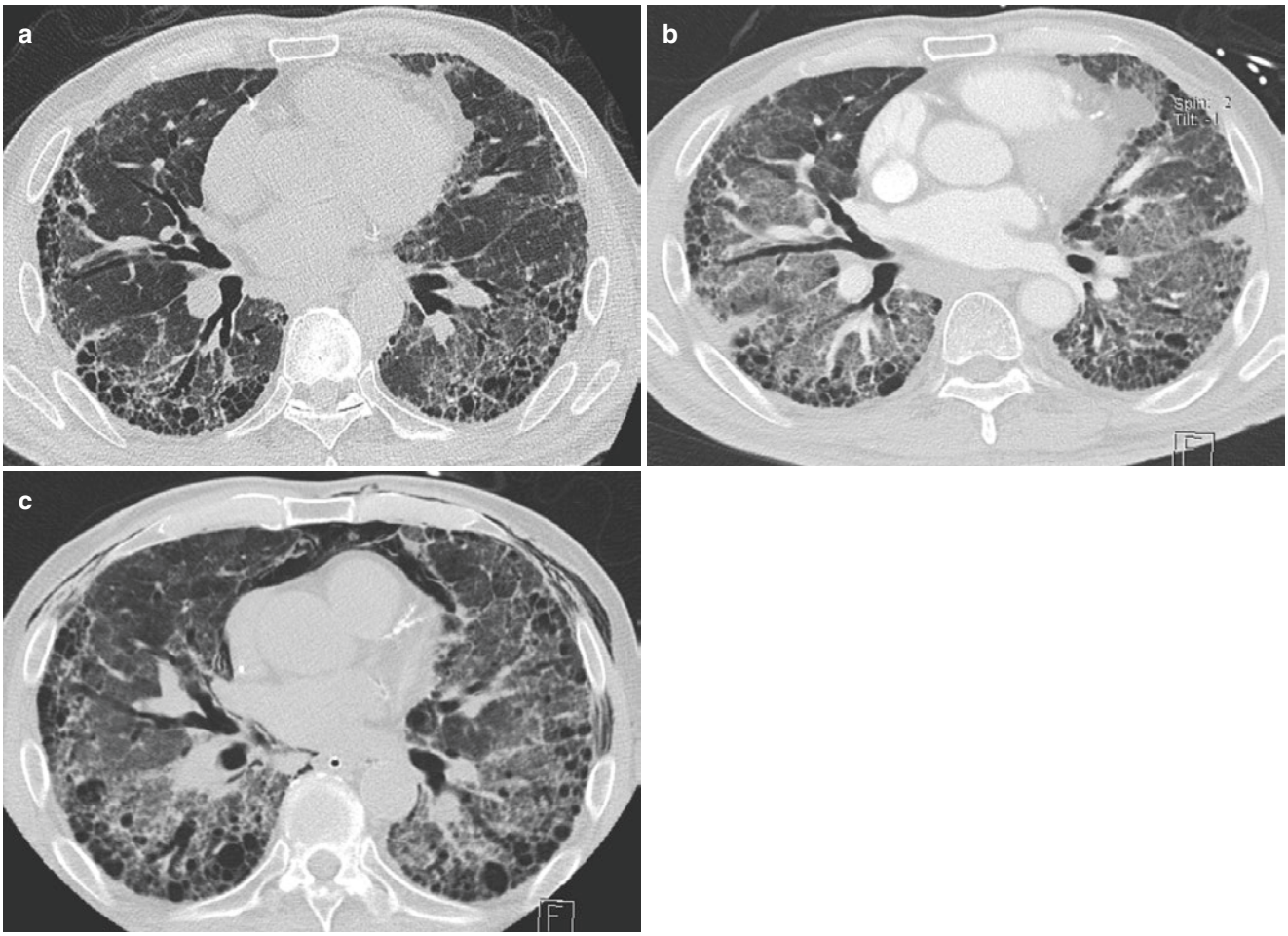

Fig. 13.35 Acute exacerbation of IPF. (**a**) "Typical" UIP pattern on baseline HRCT. (**b**) CT image during presentation with worsening dyspnea. (**c**) Further worsening of the lung with barotrauma resulting in pneumomediastinum and chest wall emphysema

patients are younger than those with UIP, usually 40–50 years of age at the time of presentation, with higher prevalence in women. The clinical presentation of UIP and NSIP is similar to other IIPs: a nonproductive cough and progressive dyspnea. Unlike UIP, only a small proportion of patients with NSIP are idiopathic, while the majority are associated with CTDs, HP, and drug toxicity. CTDs must be actively excluded, in patients showing HRCT pattern of NSIP. NSIP may precede the diagnosis of CTD or NSIP in some patients may be a manifestation of "lung-limited" or "lung-dominant" CTD [39]. In other words, NSIP may be the only manifestation of a CTD. Few patients with familial fibrosis show

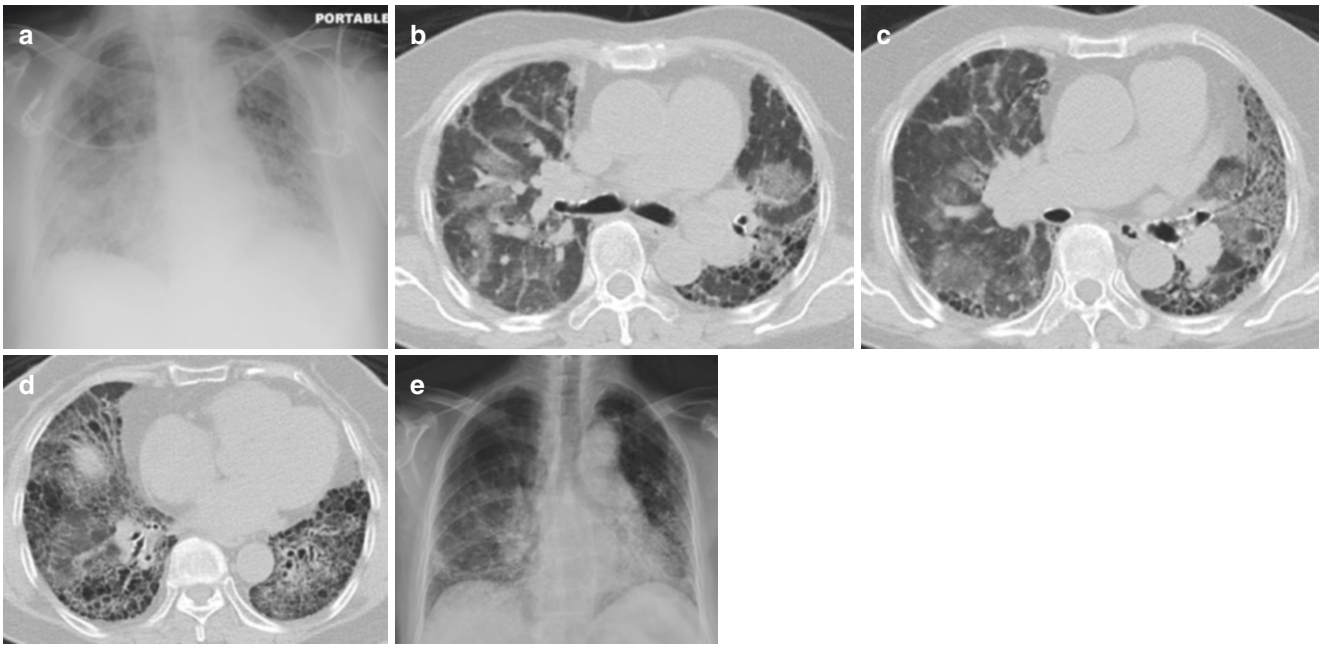

Fig. 13.36 UIP with pulmonary edema. (**a**) Chest radiograph at presentation shows diffuse GGOs and an enlarged heart with clinical features of heart failure. (**b–d**) HRCT images from next day show dilated central pulmonary arteries and bilateral ill-defined perihilar GGOs in a patient with "typical" UIP. (**e**) Chest radiograph on the third day shows resolution of GGOs further favoring the diagnosis of congestive heart failure

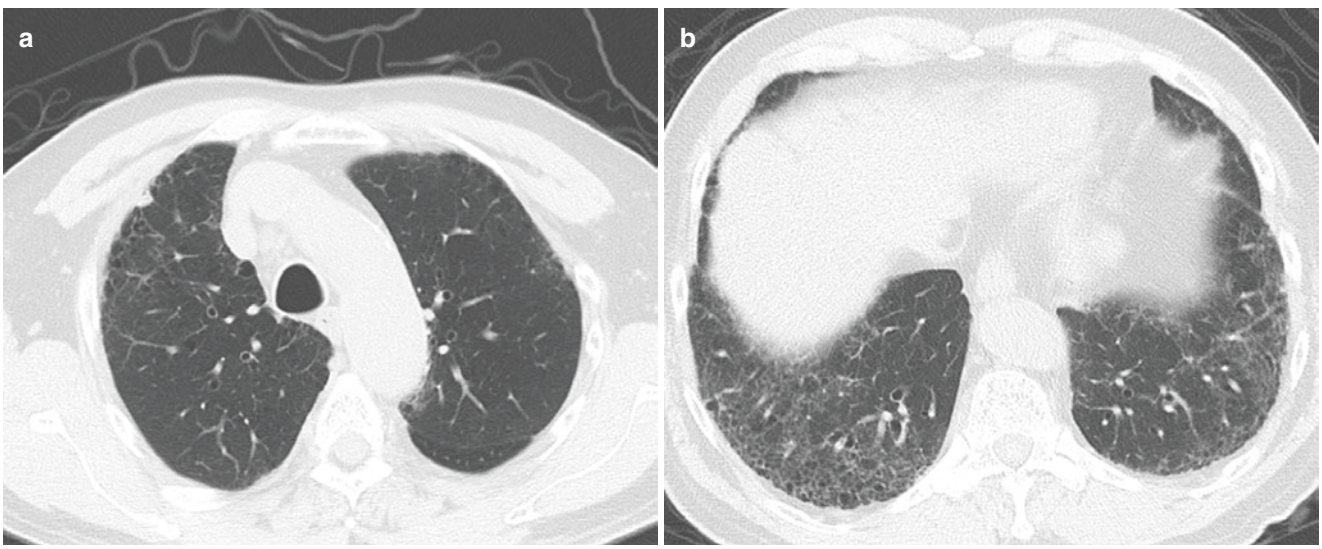

Fig. 13.37 UIP with squamous cell carcinoma. (**a–c**) Axial and coronal CT images show a 5 mm subpleural nodule in the right upper lobe in a smoker with "probable" UIP pattern. (**d**) CT scan 2 years later shows a marked increase in the size of the nodule with new cavitation

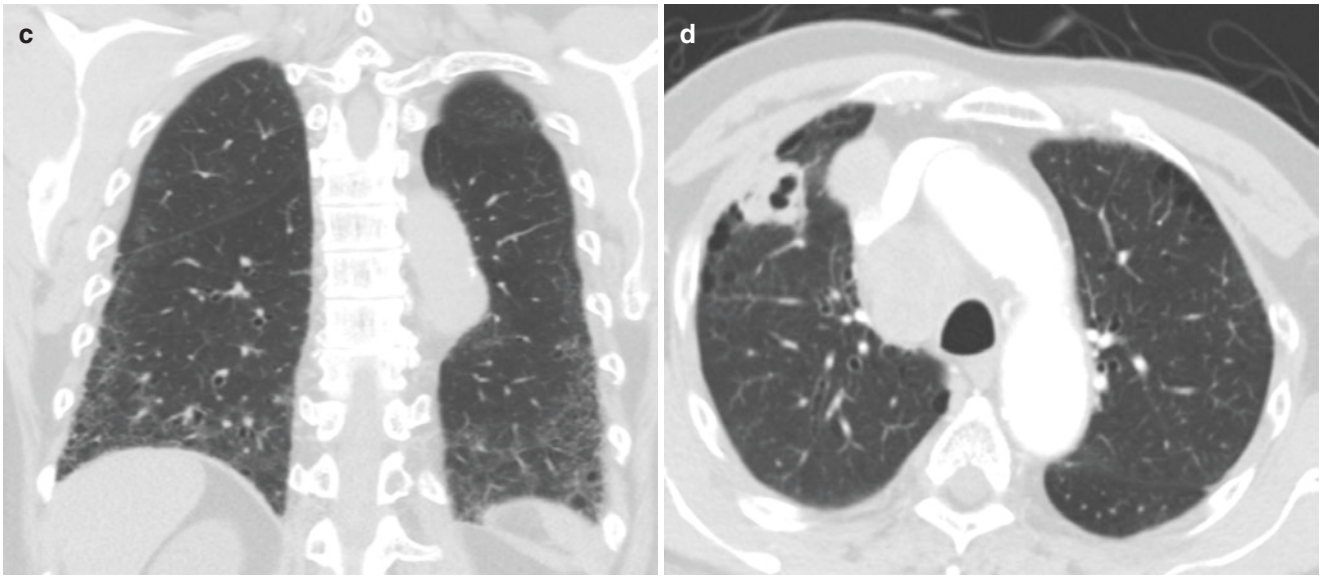

Fig. 13.37 (continued)

Table 13.12 HRCT features of NSIP

• GGOs more than reticular opacities
• Basal predominant disease
• Peribronchial or peripheral involvement
• Traction bronchiectasis may be present
• Honeycombing scant or absent
• Others – Subpleural sparing – Lobar volume loss – Symmetrical involvement – Scattered consolidations – Non-pulmonary findings in secondary NSIP

HRCT features of NSIP. HRCT features of NSIP and its differential diagnoses are described in Table 13.12 and 13.13 (Figs. 13.38, 13.39, and 13.40) [42–44]. GGOs are the hallmark of NSIP and may or may not be associated with traction bronchiectasis. The distribution of abnormalities in the axial plane can be either peripheral (outer one-third of the lung) or peribronchial (central) but usually symmetrical or near symmetrical. A characteristic imaging feature of NSIP is relative sharp subpleural sparing (peripheral distribution but not involving the region close to the visceral pleura) of the posterior lower lobes, seen in about 65% of patients [73]. Consolidative opacities are rare in NSIP, and when present indicates OP component, raising suspicion for underlying CTD (Fig. 13.41). Reticulations are present to some extent and are characteristically fine rather than the coarse reticulations seen in UIP. Honeycombing is inconspicuous or absent in NSIP and, when present, is exclusively in fibrotic NSIP. There is remarkable heterogeneity in the HRCT features of NSIP, and one should remember that the HRCT features of NSIP are characteristic but not as specific as UIP. Moreover, there is considerable overlap in HRCT and histological features of NSIP, with UIP, LIP, DIP, OP, and HP [73]. Recurrent or chronic aspiration can also mimic NSIP pattern on HRCT. Frequently, a combination of UIP and NSIP histology is present in different biopsy sites in the same patient, and the HRCT of such patient does not show UIP pattern [74, 75]. It is recommended to obtain a lung biopsy for accurate diagnosis of NSIP unless there is associative cause for this pattern, such as positive serology for CTD or clinical-bronchoscopic evidence of HP. Acute exacerbation occurs in NSIP but much less frequently in UIP.

13.5.2.1 Accuracy and Prognostication

There is no HRCT feature that is specific for NSIP. Overall, the specificity of diagnosing NSIP with HRCT is low, ranging from 40 to 65% [70, 74]. Flaherty et al. reported that only 18 of 44 patients (41%) thought to have NSIP pattern in HRCT had histological NSIP [70]. They also found that 26 of 44 (59%) of the patients with typical HRCT findings of NSIP had a histological diagnosis of UIP, highlighting the limitations of HRCT in the evaluation of NSIP. There is high interobserver variation even among pathologists in making a

Table 13.13 Differential diagnoses of NSIP pattern on HRCT

Idiopathic	CTD	HP	Drug toxicity	Familial fibrosis
Diagnosis of exclusion	NSIP pattern	NSIP pattern	NSIP pattern	NSIP pattern
	Consolidations may be present (mixed pattern)	Air-trapping may be dramatic	High-density fibrosis	Family history, i.e., presence of two or more cases of probable or definite IIP in individuals related within three degrees
	Air-trapping may be due to coexistent airway disease	Mid- or upper lung predominance	Temporal relationship between symptom onset and use of known pulmonary toxic drugs	
		GG density centrilobular nodules		
		History of exposure		
	Clues: dilated esophagus, PAH, bony changes, pericardial abnormalities, pleural effusion	BAL: lymphocytosis		
		Serum precipitins may be present		
	Positive autoimmune Serology			

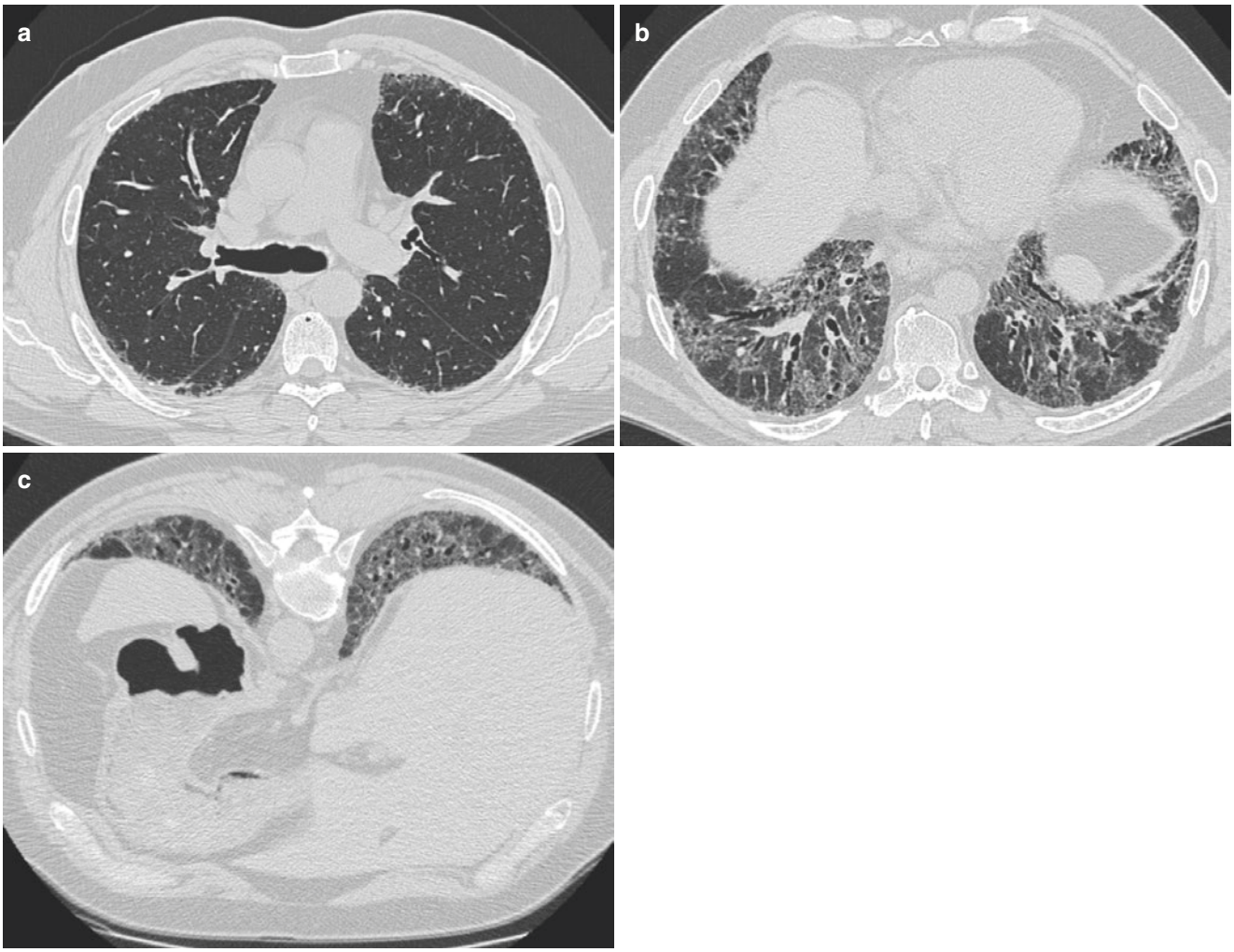

Fig. 13.38 NSIP. (**a**, **b**) Axial CT images show lower lung predominant GGOs and traction bronchiectasis with peribronchial distribution. (**c**) Prone image reveals subpleural sparing. Note the reticular opacities are much less than GGOs

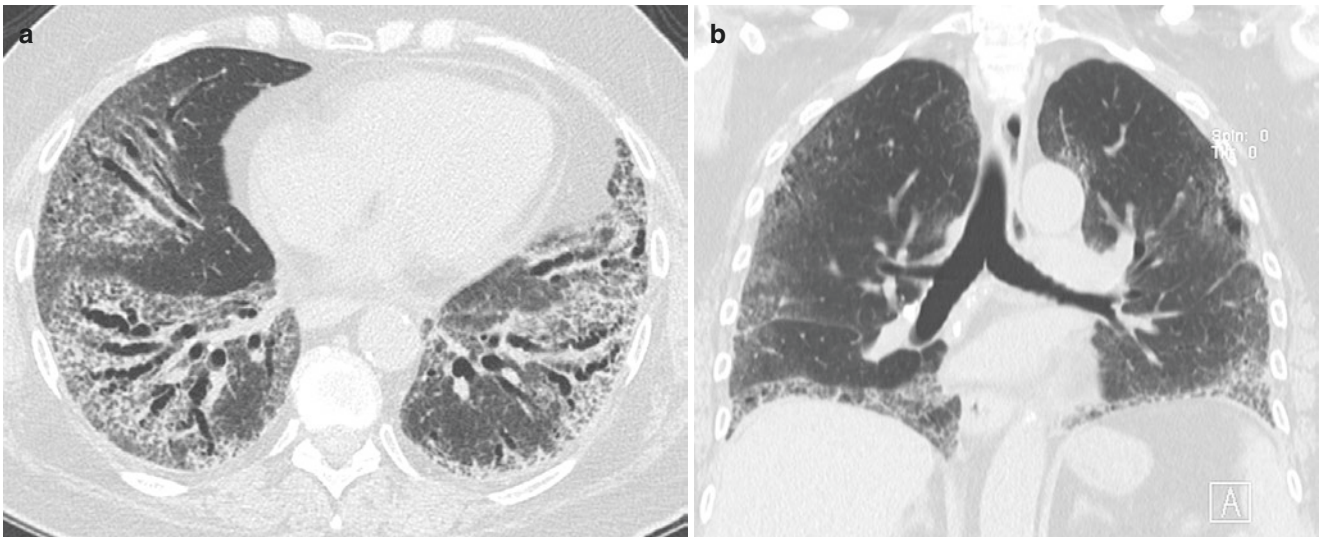

Fig. 13.39 Taxol-/carboplatin-induced NSIP. (**a**, **b**) Axial and coronal CT images show lower lung predominant GGOs and traction bronchiectasis with peribronchial distribution. Note subpleural sparing in right posterior lung and striking volume loss in lower lobes

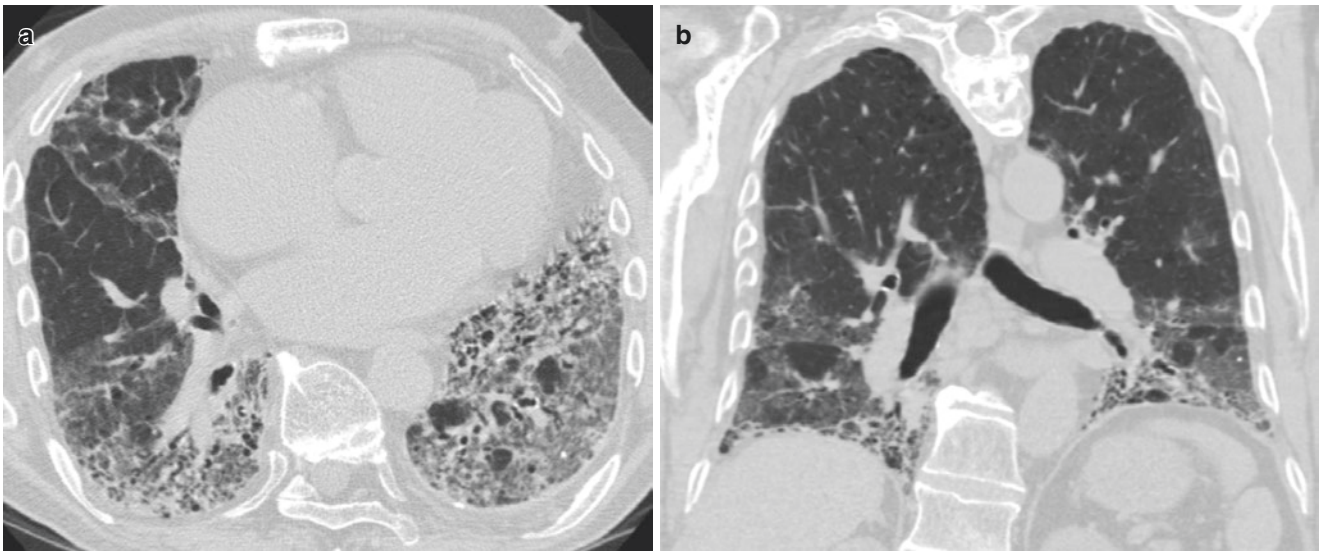

Fig. 13.40 NSIP. (**a**, **b**) Axial and coronal CT images with lower lung predominant GGOs with traction bronchiectasis. Note there is no subpleural sparing

histological diagnosis of NSIP, and this further affects the sensitivity and specificity of HRCT. One major reason to distinguish UIP/IPF and NSIP is the marked difference in prognosis—much better prognosis in NSIP. Survival of patients with idiopathic UIP or IPF is worse than that of patients with idiopathic fibrotic NSIP pattern [70, 76]. The 5-year survival rate of UIP is 43%, whereas 5-year survival rate of fibrotic NSIP is 90%, while 10-year survival rate of UIP is 15%, compared to the 10-year survival rate of fibrotic NSIP of 35% [76]. The histological type of NSIP also has an impact on survival. Patients with a cellular pattern of NSIP have a 5-year and 10-year survival rates of 100%. The survival rates for the fibrotic pattern of NSIP are different, with a 5-year survival of 90% and 10-year survival of 35% [76]. The clinical course of NSIP is more predictable than UIP and a small proportion of patients show gradual worsening. Follow-up HRCTs of patients with NSIP on treatment regimen show no change or decrease in the overall extent of disease. In most NSIP patients, GGOs and consolidation decrease, while coarseness of fibrosis increases despite treatment. A third of the patients may demonstrate honeycombing with an overall resemblance to UIP/IPF, on follow-up HRCT [73, 77]. There

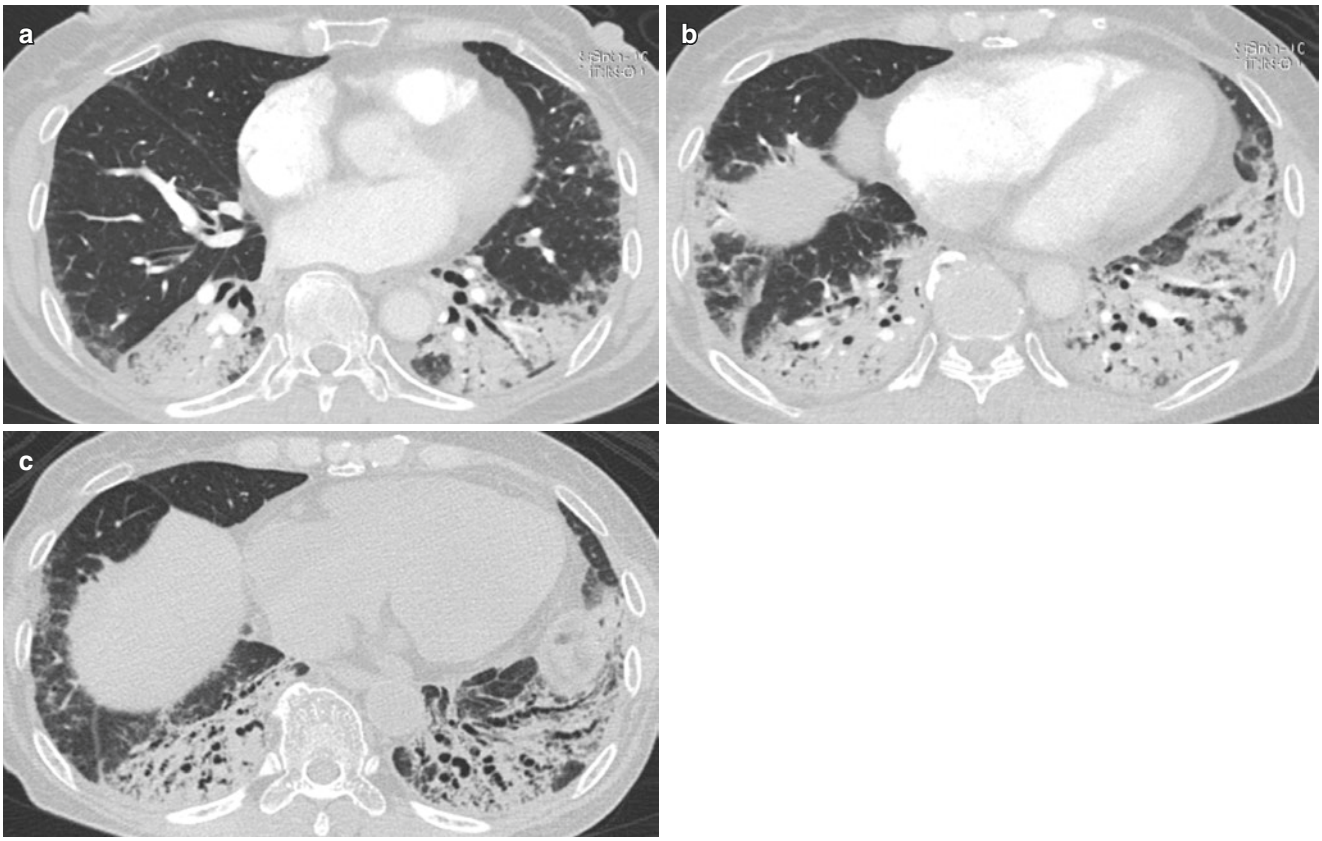

Fig. 13.41 NSIP with OP pattern in antisynthetase syndrome. (**a**, **b**) Axial CT images of CTPA at presentation show extensive peribronchial consolidative opacities with volume loss in lower lobes and bronchiectasis. Note posterior displacement of major fissures (**c**) Follow-up CT image shows improvement in consolidative opacities with progression in traction bronchiectasis signifying scarring

Table 13.14 UIP versus NSIP

	UIP	NSIP
HRCT	• Basal predominant • Peripheral distribution • GGOs are minimal • Coarse reticulations • Honeycombing is hallmark • Traction bronchiectasis present • Asymmetrical involvement	• Basal predominant • Peripheral or central • GGOs are hallmark • Fine reticulations • Honeycombing scanty or absent • Traction bronchiectasis is mild • Symmetrical involvement
Age	40–50 years	Above 50 years
Gender	More prevalent in men	Higher prevalence in women
Prognosis	Poor	Stable disease in majority
Association	Majority "idiopathic"	Majority "secondary"
Complications	Common	Less common
Treatment	For IPF/UIP: Anti-fibrotics like pirfenidone and nintedanib can reduce the rate of disease progression Steroids increase risk of hospitalization and death in IPF/UIP	Steroid-responsive

may be two separate NSIP subgroups, with one subgroup representing NSIP progressing to a pattern that resembles IPF and another subgroup that maintains the overall features of NSIP, even with the progression of fibrosis [73] (Table 13.14).

13.5.3 COP and OP

COP or OP is a group of IIP that used to be termed as "bronchiolitis obliterans organizing pneumonia" in the past. This term has been discontinued to avoid confusion with primary

airway disease. COP is included in the international classification of IIP as similar to the other IIPs. It is an idiopathic condition, considered as a response to lung injury, and its morphological features overlap with other IIPs. The term "organizing pneumonia (OP)" is commonly used in radiology as the pattern is more commonly associated with other conditions including CTDs, drug toxicity, infections, inflammatory bowel disease, aspiration, radiation therapy, and graft versus host disease [78, 79]. Hence, COP is a diagnosis of exclusion. OP affects both men and women equally, with a mean age of onset of 55 years. Patients typically present with a cough, mild dyspnea with a history of low-grade fever, and often myalgia over a few days to weeks. The histological hallmark is intraluminal plugs of granulation tissue and polyps within the alveolar ducts and alveoli, associated with interstitial and alveolar infiltrates of mononuclear cells and foamy macrophages [44].

The HRCT features of OP are diverse and described in Table 13.15 [42–44, 79, 80]. The HRCT appearance of OP overlaps with IIPs like NSIP, DIP, and HP as well as other diseases like eosinophilic pneumonia, vasculitis, angioinvasive aspergillosis, malignancy, and lymphomas. OP is characterized by patchy opacities usually an admixture of consolidations and GGOs [79–81]. On HRCT, the GGOs show random distribution, and the consolidations show subpleural or peribronchovascular distribution [80]. A combination of fibrosis and OP is almost always due to underlying CTDs, in particular, polymyositis and antisynthetase syndrome. There are a few HRCT signs in patients with OP that are helpful in diagnosis (Figs. 13.42 and 13.43) (Table 13.16). However, the final diagnosis requires a surgical lung biopsy.

Table 13.15 HRCT features of OP

Typical OP
• Bilateral patchy opacities
• Consolidations or GGOs or both
• Usually mid- and lower lung, rarely upper lung predominance
• Peripheral or peribronchovascular distribution
• Bronchial dilatation and air bronchograms may be present
• Reticular opacities
• Honeycombing is absent
• Others
Non-pulmonary findings in secondary OP
Atypical OP
• Solitary consolidation
• Crazy-paving pattern
• Multifocal GGOs
• Irregular linear opacities
• Pulmonary nodules
• Small pleural effusions

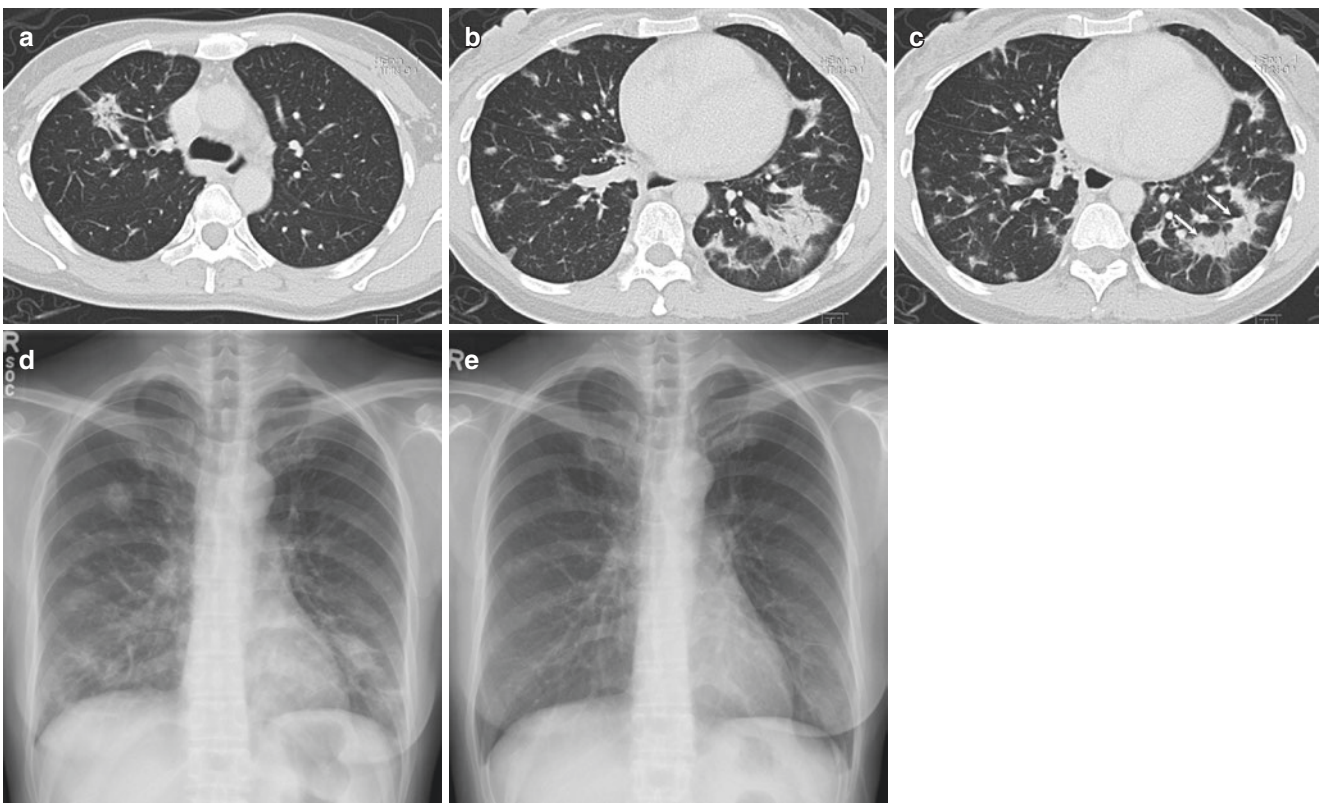

Fig. 13.42 "Perilobular" sign of OP in an elderly woman with SLE. (**a**–**c**). Axial CT images show patchy consolidative opacities with arcade-like bands of parenchymal consolidation (arrows). (**d**) Frontal radiograph also shows the consolidations. (**e**) Follow-up radiograph after a week of steroid treatment shows marked improvement in consolidations

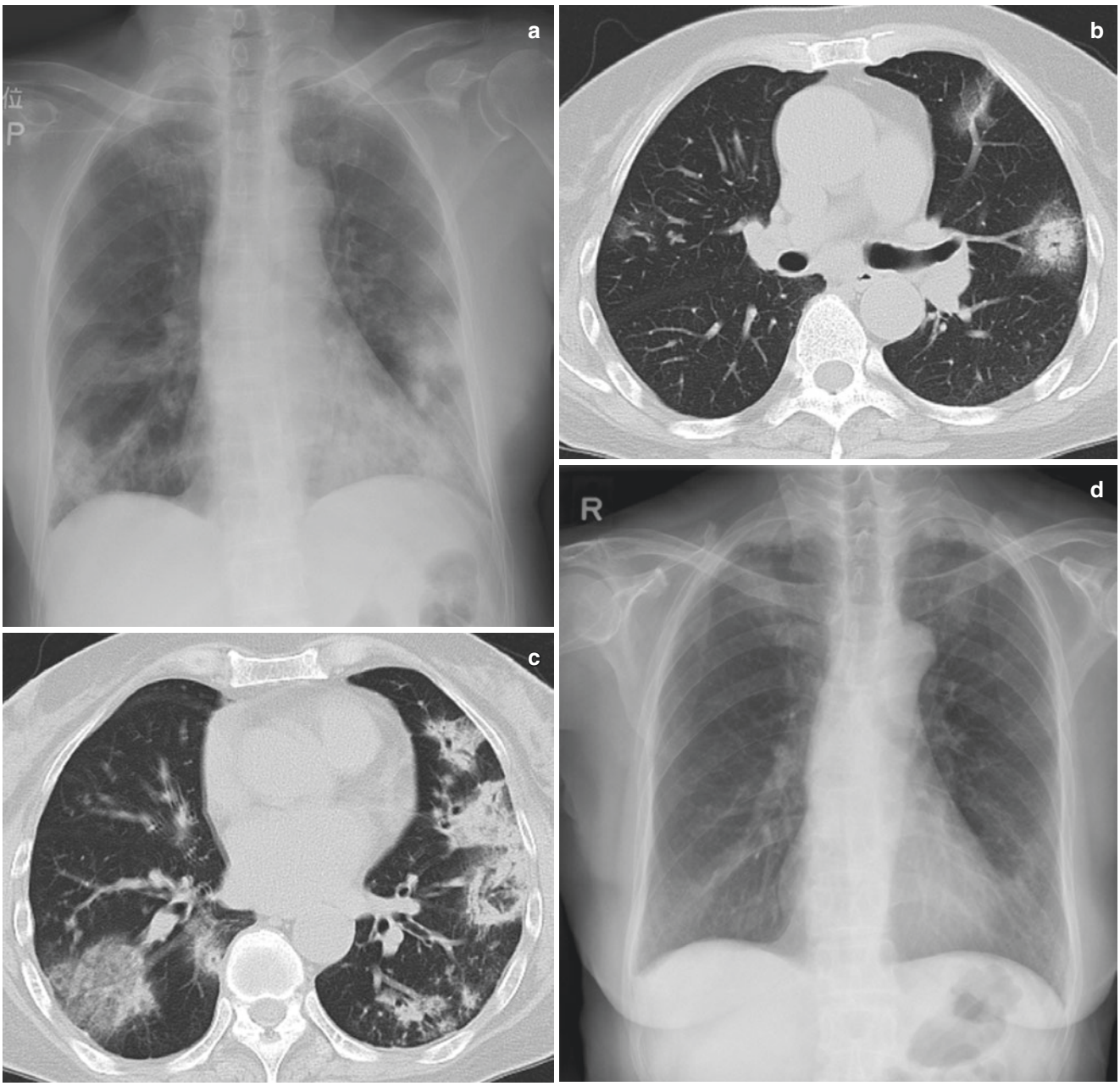

Fig. 13.43 "Halo" and "reverse halo" sign in OP in an elderly woman from interstitial pneumonia with autoimmune features (IPAF). (**a**) Frontal chest radiograph at presentation shows multiple peripheral lower lung consolidations. (**b**, **c**) Axial CT images show multiple peripheral opacities demonstrating "halo" and "reverse halo" sign. Transbronchial biopsy showed organizing pneumonia (not shown). (**d**) Chest radiograph after 6 weeks of steroid therapy shows resolution of opacities

Table 13.16 Useful signs of OP

• Migratory opacities on follow-up
• Perilobular pattern
• Halo sign
• Reverse halo sign or atoll sign

The parenchymal opacities may migrate on serial imaging, and OP must be included in the differential diagnoses of migratory opacities (together with recurrent aspiration, vasculitis, eosinophilic pneumonia, and hemorrhage). The reversed halo sign is seen in a fifth of the patients with OP, while a perilobular pattern is seen in more than half of the

patients [80, 81]. The perilobular pattern is considered specific for OP and is described as curved or arcade-like bands of parenchymal consolidation with blurred borders and may extend across the fissures. In practice, this is best appreciated on scrolling through the images on a PACS viewer.

Regardless of etiology, patients with OP generally show excellent response to steroid treatment although some patients are refractory to steroids or show worsening after a transient positive response. Post-treatment HRCT shows resolution of consolidations with residual GGOs. The reticular opacities, if present in initial CT, persist on follow-up scans despite treatment, with an overall resemblance to fibrotic NSIP [78, 79]. The patients with reticular opacities are the ones with poor response to steroids.

13.5.4 AIP

AIP is an acute onset, idiopathic, rapidly progressive form of IIP, with histology of diffuse alveolar damage that is similar to adult respiratory distress syndrome. However, unlike adult respiratory distress syndrome, there is no identifiable precipitating event [40]. The mean age at presentation is 50 years, and most patients present within 3 weeks of the first symptom [44]. The diffuse alveolar damage in AIP is characterized by three overlapping phases: an acute exudative phase, followed by a subacute proliferative phase, and lastly a chronic fibrotic phase. The CT findings in patients with AIP vary, depending on the histological phase of the disease (Table 13.17) (Fig. 13.44) [44, 82, 83]. The mid- and lower lungs are more commonly involved than the upper lungs. Opacities (GGOs and consolidations) without traction bronchiectasis represent the exudative phase or early proliferative phase, while opacities with traction bronchiectasis represent proliferative phase or fibrotic phase. The presence of honeycombing in the first week should lead to the suspicion of an underlying undiagnosed fibrosing lung disease. Pleural effusion, if present, is small. AIP must be differentiated from acute exacerbation of preexisting ILD, acute eosinophilic pneumonia, multifocal pneumonia, hemorrhage, and cardiogenic pulmonary edema. Although histologically ARDS and AIP are similar, CT imaging of AIP in later stage is more likely to be symmetrical and has a lower lung predominance, with higher prevalence of honeycombing and lower prevalence of septal thickening than ARDS. The mortality is more than 50%, with stable or progression of residual disease in survivors.

Table 13.17 HCRT features of AIP in different phases

Exudative phase	Proliferative phase	Fibrotic phase
• Bilateral patchy GGOs • Mild consolidation	• Progression of opacities • Bronchial dilatation • Architectural distortion	• Areas of low density and cysts • Honeycombing • Reticular opacities • Architectural distortion

Note: These phases are overlapping and different areas of the lung may be in different phases

13.5.5 PPFE

PPFE is a rare IIP included in ATS/ERS classification. The name itself is descriptive of the underlying disease process: bilateral intense visceral pleura fibrosis, upper lung fibrosis, and subpleural fibroelastosis. PPFE is seen in a wide age range from 24 to 85 years of age, with a median age of 57 years. There is no gender predilection [84, 85]. The presentation is similar to other IIPs: a mild cough and dyspnea. Pneumothorax is a common complication. The HRCT features of PPFE are listed in Table 13.18 [84, 85]. The striking HRCT feature is the apical predominance of disease with a downward gradient of normalcy toward the lung bases, except in cases with concomitant ILD. In our experience, there is intense irregular apical pleural thickening, extending along the posterior major fissures with perpendicular coarse bands encroaching into the upper lobe parenchyma, probably along interlobular septa. In more severe cases, the peripheral fibrosis extends to involve the mid-lung. 33–50% of the patients show changes of possible UIP, NSIP, or indeterminate fibrosis in HRCT. Histology of some patients also shows concomitant UIP and NSIP (Fig. 13.45). In practice, it may be difficult to differentiate extreme cases of "apical cap" from PPFE.

13.6 Smoking-Related Lung Diseases

Smoking-related lung diseases are covered in Chaps. 3 and 14.

13.7 Connective Tissue Disease-Related ILDs

Lung disease is common in CTDs, and it can affect various lung compartments such as the lung parenchyma, airways, pleura, and pulmonary vasculature. Interstitial lung disease is an important cause of morbidity and mortality in patients with CTD. The common CTDs include rheu-

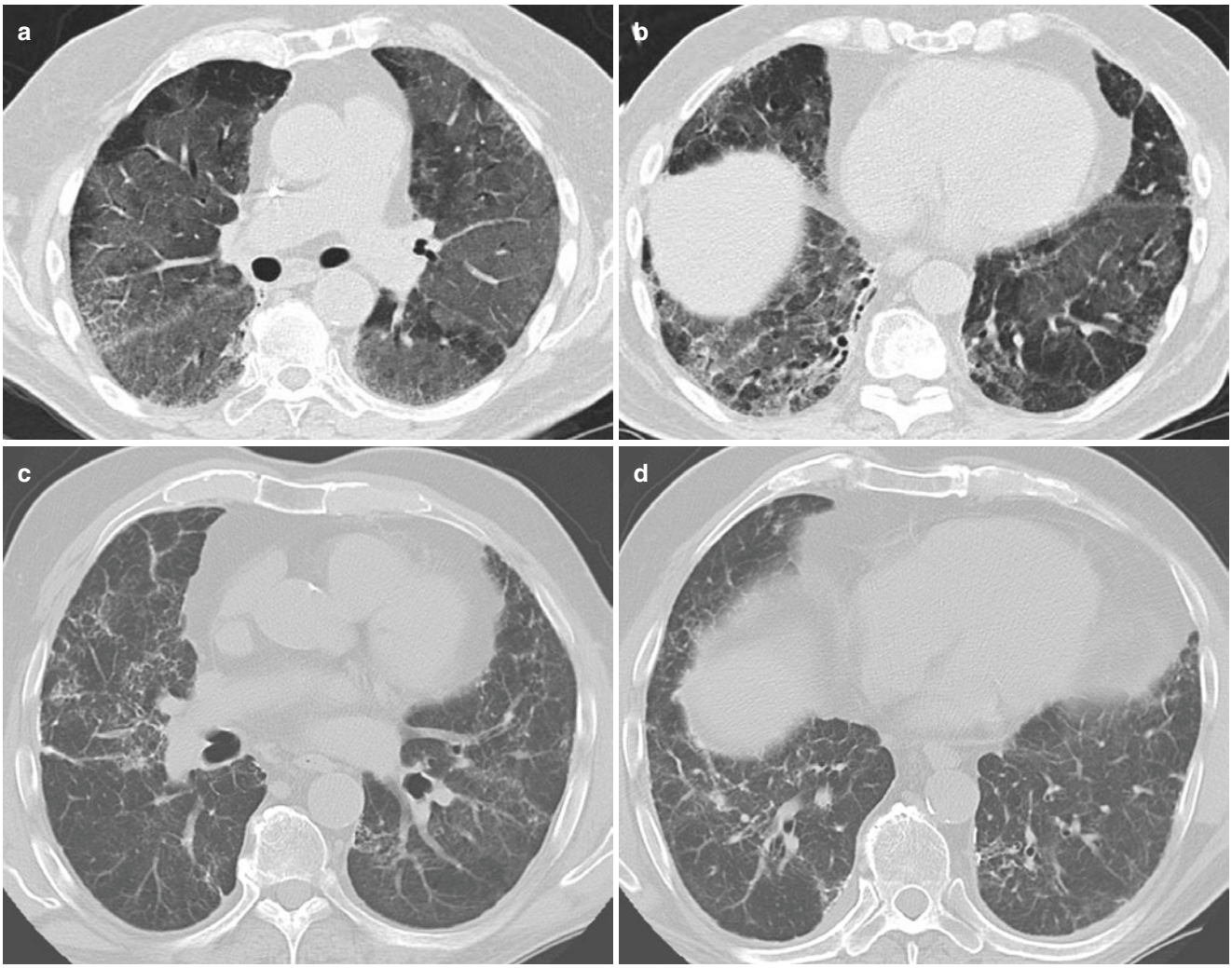

Fig. 13.44 AIP. (**a**, **b**) Exudative phase showing confluent GGOs with mild bronchial dilatation. (**c**, **d**) Proliferative phase in another patient showing multifocal bizarre scarring

Table 13.18 HRCT features of PPFE

• Bilateral irregular pleuroparenchymal thickening
• Subpleural reticular pattern/pleural tags
• Volume loss in upper lungs – Traction bronchiectasis – Architectural distortion – Pulled-up hilum – Extrapleural fat retraction
• Honeycombing in the upper lungs
• Concomitant ILD in the distant lung

matoid arthritis (RA), systemic sclerosis (SSc), Sjögren syndrome (SS), idiopathic inflammatory myopathies (IIM), systemic lupus erythematosus (SLE), and mixed CTD (MCTD). Other autoimmune conditions such as vasculitides, Behçet disease, and spondyloarthropathies have imaging features different from the above CTDs and are not discussed in this chapter.

There are two common scenarios faced by radiologists in the context of CTD-ILDs: (a) What is the pattern of ILD in a patient with clinically diagnosed CTD? (b) Are the HRCT changes in the lungs the first or the only manifestation of a CTD? The third less common scenario is when a patient is on treatment for CTD: whether the pulmonary changes are related to CTD, secondary to drug toxicity from the treatment given, or an infection (as these patients are commonly on immunocompromised). The spectrum of pulmonary involvement by CTDs ranges from mild linear abnormalities to full-blown UIP pattern. Accurate detection of CTD-ILDs is important due to reasons listed in Table 13.19. The morphologic patterns in CTD-ILDs, in general, are indistinguishable from those seen in IIPs. However, there

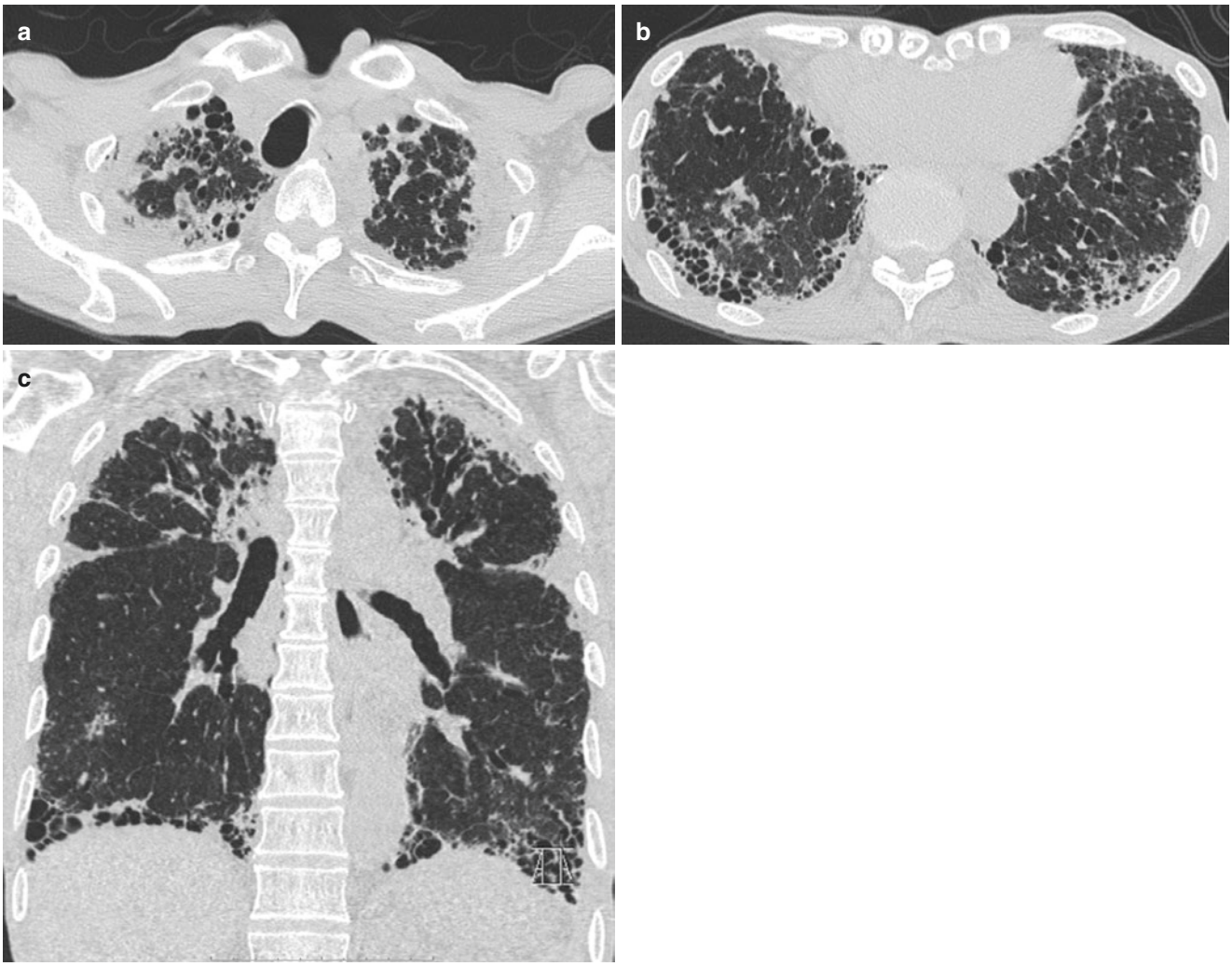

Fig. 13.45 Typical UIP with PPFE. (**a**, **b**) Axial CT images show peripheral predominant reticular opacities, honeycombing with traction bronchiectasis. (**c**) Coronal CT image shows lower lung predominance. Upper lung fibrotic changes were presumed to be due to PPFE

Table 13.19 Importance of accurate diagnosis of CTD-ILDs

• Pulmonary involvement may precede the diagnosis of CTD
• ILD may be the only manifestation of "lung-dominant" CTD
• Many ILDs are mixed or unclassifiable patterns
• Prognosis of CTD-ILDs is different, usually better than IIP for the same pattern
• Management of CTDs may change in the presence of pulmonary involvement

Table 13.20 Clues of CTD-ILDs on HRCT

• Esophageal abnormalities
• Pericardial abnormalities
• Features of PAH
• Features of airway disease
• Bones and joint changes
• Soft-tissue calcifications
• CTD-UIP signs – Anterior upper lobe sign – Exuberant honeycombing sign – Straight-edge sign

are certain radiological clues that may alert the radiologist to the presence of underlying CTDs (Table 13.20) (Fig. 13.24). Recently, three HRCT signs have been described to differentiate CTD-UIP from idiopathic UIP [86]: (a) the UIP pattern in CTD showing preferential involvement of the anterior aspect of the upper lobes with concomitant lower lobe involvement ("anterior upper lobe" sign), (b) exuberant honeycomb-like cyst formation within the lungs constituting greater than 70% of fibrotic portions of the lung ("exuberant honeycombing" sign), and (c) sharp demarcation between the non-fibrotic upper lungs from fibrotic lower lungs on coronal images ("straight-edge" sign) (Fig. 13.46). The presence of these signs should raise the possibility of underlying CTD which may prompt further workup. The pulmonary involvement in major CTDs is described below.

13.7.1 Rheumatoid Arthritis

Rheumatoid arthritis (RA) is the most common CTD. This is more common in women, but the pulmonary involvement may be equal or more common in men. The risk factors for developing RA-ILD include advanced age, smoking history, high titer of rheumatoid factor, high titer of anti-cyclic citrullinated peptide antibodies, family history of RA, and male gender. The thoracic manifestations of rheumatoid arthritis are described in Table 13.21 (Figs. 13.46 and 13.47) [87–91]. UIP pattern is the most common ILD morphology in patients with rheumatoid arthritis [91]. Combined pulmonary fibrosis and emphysema (CPFE) has also been described in patients with RA.

Table 13.21 Thoracic manifestations of rheumatoid arthritis

Pleural disease	Pleural thickening, pleural effusion Most common thoracic abnormality May be asymptomatic
Airway disease	Bronchiectasis; cylindrical or cystic Obliterative bronchiolitis Proliferative bronchiolitis termed "follicular bronchiolitis"
PAH	Mild PAH is common
ILDs	UIP: most common ILD pattern NSIP OP
Osteoarticular	Arthritis in the shoulder, costovertebral, and facet joints

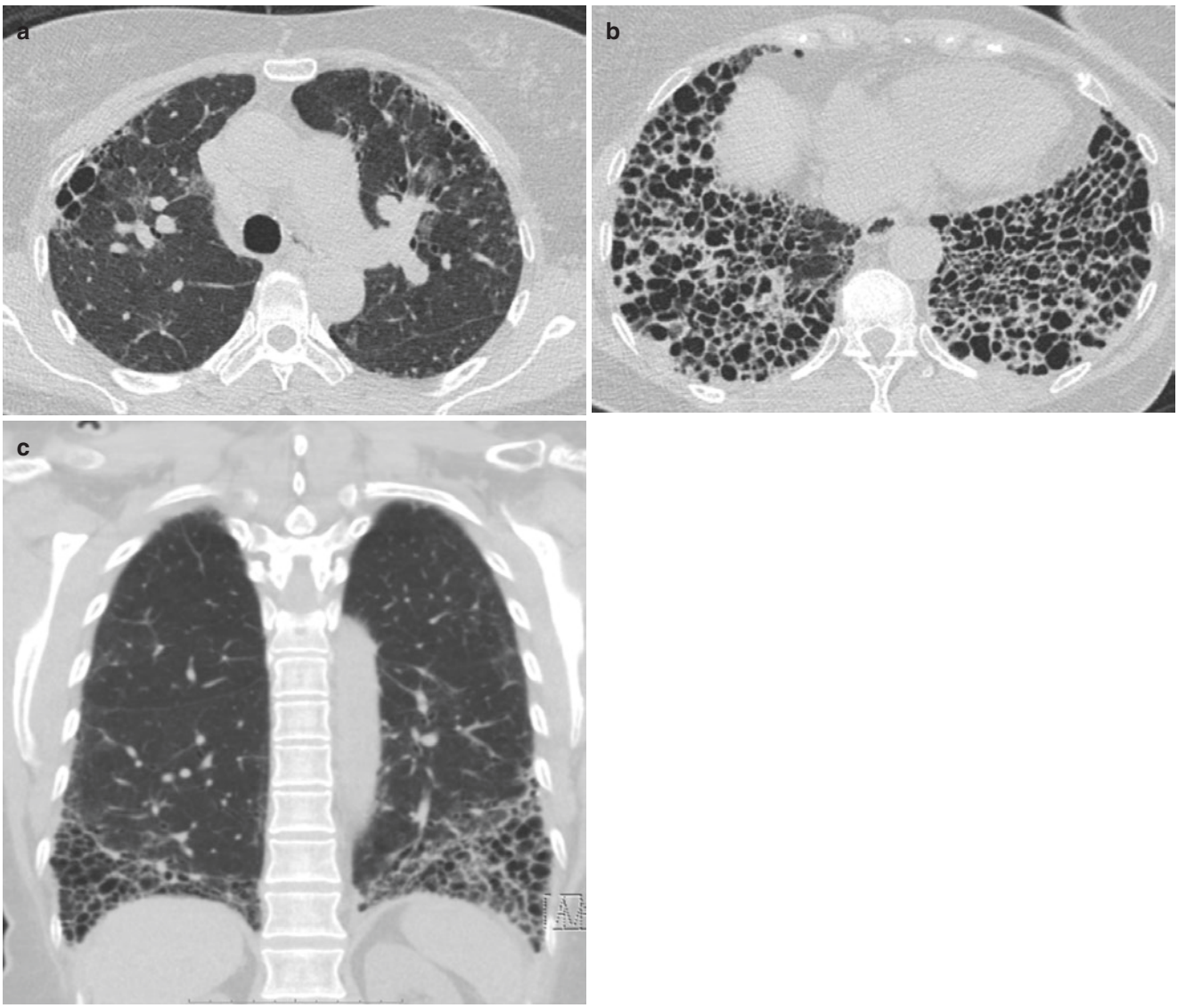

Fig. 13.46 HRCT signs of CTD-UIP. (**a**) "Anterior upper lobe" sign, (**b**) "exuberant honeycomb," (**c**) "straight-edge" sign in a patient with UIP from RA

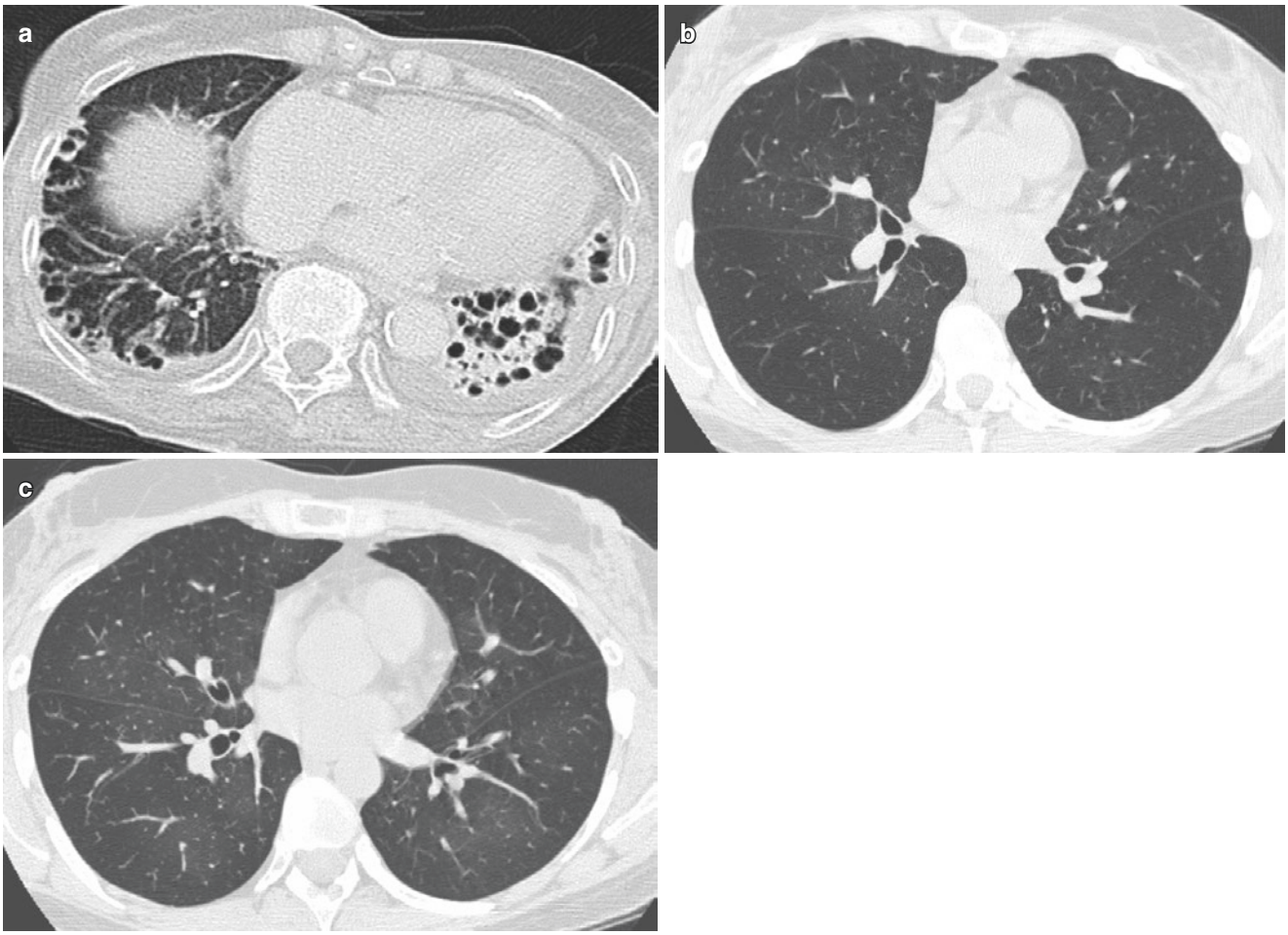

Fig. 13.47 RA with thoracic manifestations. (**a**) Cystic bronchiectasis with left pleural effusion. Obliterative bronchiectasis in another patient with RA. (**b**) Inspiratory and (**c**) expiratory CT image show air-trapping

13.7.2 Systemic Sclerosis/Scleroderma

There is a high prevalence of pulmonary abnormalities in patients with scleroderma, with ILDs being more common than the other manifestations (Table 13.22) (Figs. 13.24, 13.48, and 13.49) [88–90].

Table 13.22 Thoracic manifestations of scleroderma

ILDs	NSIP: most common ILD pattern UIP: less common
PAH	PAH in isolation or with ILD PAH is the leading cause of death
Lung cancer	Higher risk of malignancy in patients with fibrosis
Esophageal involvement	Seen in nearly all patients of scleroderma HRCT detects asymptomatic esophageal dilatation in high proportion of patients Aspiration and its complication are common
Heart and pericardium	High prevalence of pericardial and myocardial diseases

13.7.3 Sjögren Syndrome

Sjögren syndrome has a strong predilection for women with female-to-male ratio of 9:1. It can be a primary disease, termed primary Sjögren syndrome, or associated with another CTD, called secondary Sjögren syndrome. Pulmonary involvement is quite common in these patients (Figs. 13.50 and 13.51) (Table 13.23) [88–91]. Many patients demonstrate patchy GGOs, consolidations, cysts, and even honeycombing [92].

Nodules in the setting of Sjögren syndrome are common, but when they are more than 10 mm, lymphoma should be considered [89]. Multiple nodules with or without LIP in these patients can also be due to amyloidosis [93].

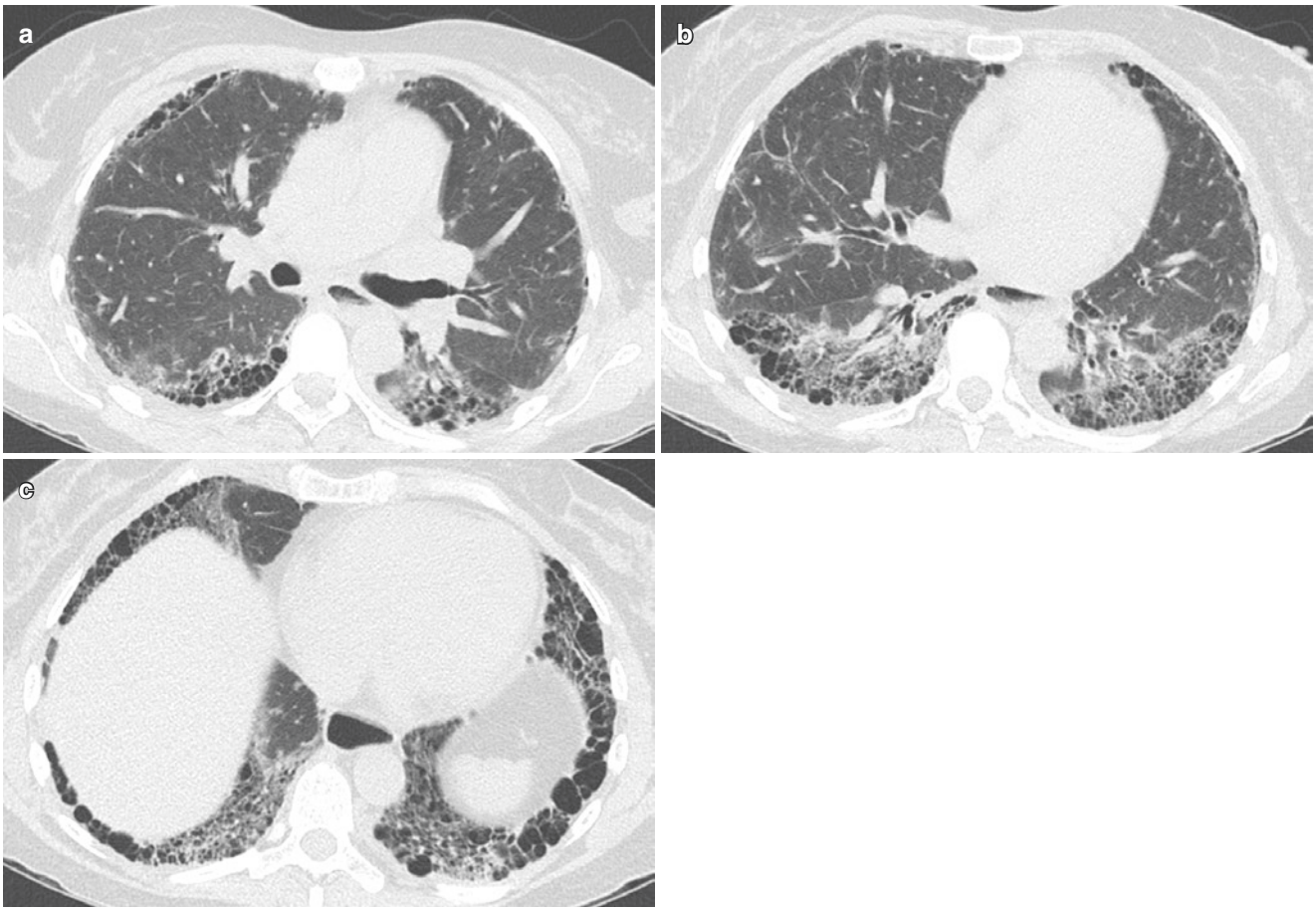

Fig. 13.48 Scleroderma with UIP. (**a**–**c**) Axial CT images show UIP pattern with an air-fluid level in the dilated esophagus

13.7.4 Systemic Lupus Erythematosus

Systemic lupus erythematosus (SLE) is more prevalent among women (female-to-male ratio of 6–9:1). Thoracic manifestations are summarized in Table 13.24 (Figs. 13.1, 13.42, and 13.52) [88–90]. Pleural disease is the most frequent pulmonary manifestation, often presenting with pleuritic chest pain, cough, and fever, associated with a relatively small pleural effusion. Pleuritis may occur with pericarditis as manifestation of serositis, which is one of the diagnostic criteria for SLE. Pneumonia is a common complication in these patients, both community-acquired and from atypical organisms, such as fungi and mycobacteria. Acute lupus pneumonitis is considered as a focal acute interstitial pneumonia characterized by focal consolidation and must be differentiated from acute infectious pneumonia before the commencement of steroids. Shrinking lung syndrome is an uncommon complication of SLE. It is characterized by progressive loss of lung volume in the absence of pleuroparenchymal abnormality, probably related to diaphragmatic fibrosis. Serial chest radiographs show the progressive elevation of the diaphragm, fluoroscopy may show decrease excursion of the diaphragm, and CT may show thinning of crura [88]. Diffuse alveolar hemorrhage is a rare complication of SLE with mortality approaching 50%. ILDs are uncommon in SLE, with NSIP pattern being the predominant type. The pathogenesis of PAH in the absence of pulmonary involvement is considered as multifactorial; genetic predisposition, environmental stimuli, and immune system dysfunction contributing to imbalance between vasoconstrictive and vasodilating mediators.

13.7.5 Idiopathic Inflammatory Myopathy (IIM)

Idiopathic inflammatory myopathy (IIM) encompasses a group of connective tissue diseases with muscle inflammation and extra-muscular involvement which includes der-

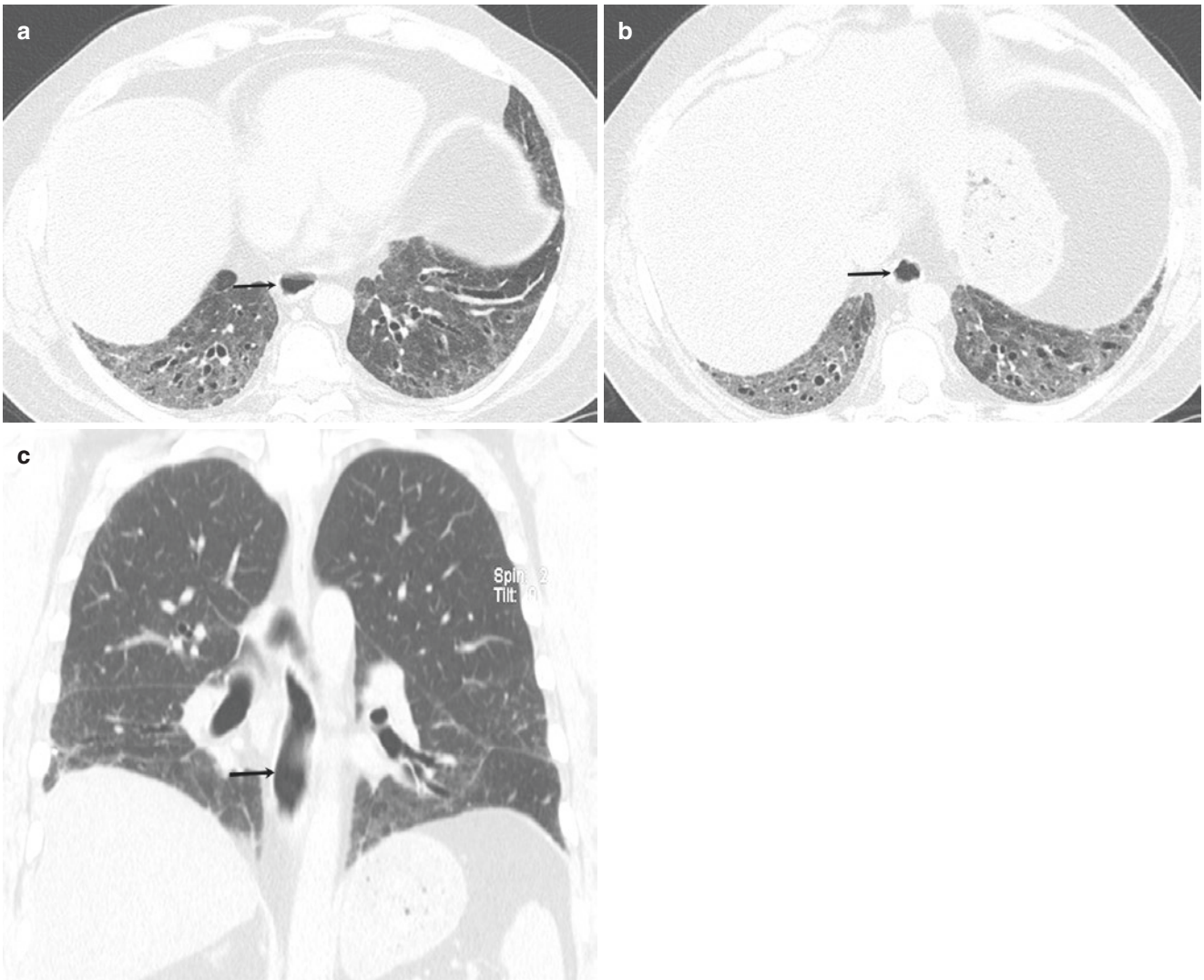

Fig. 13.49 Scleroderma-related NSIP. (**a**–**c**) Axial and coronal CT images show NSIP pattern with mildly dilated esophagus (arrow)

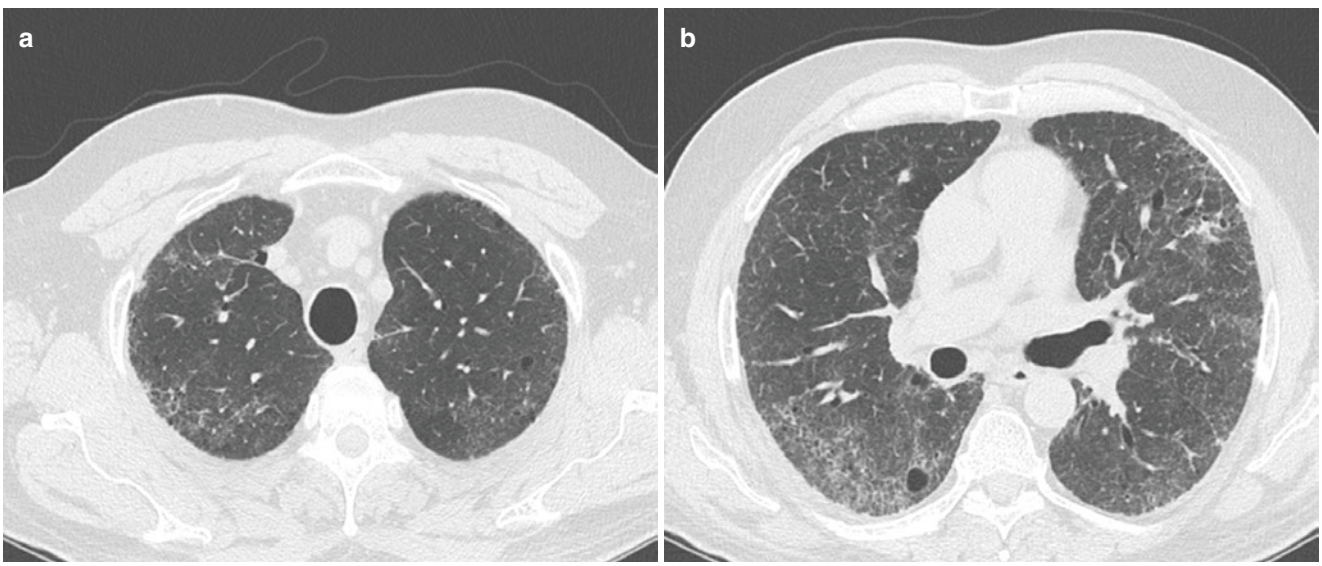

Fig. 13.50 65-year-old woman with Sjögren syndrome, fibrotic lung disease with cysts. (**a**–**d**) Axial images show multiple cysts scattered in both lungs with lower lung predominant reticular and ground-glass opacities and traction bronchiectasis

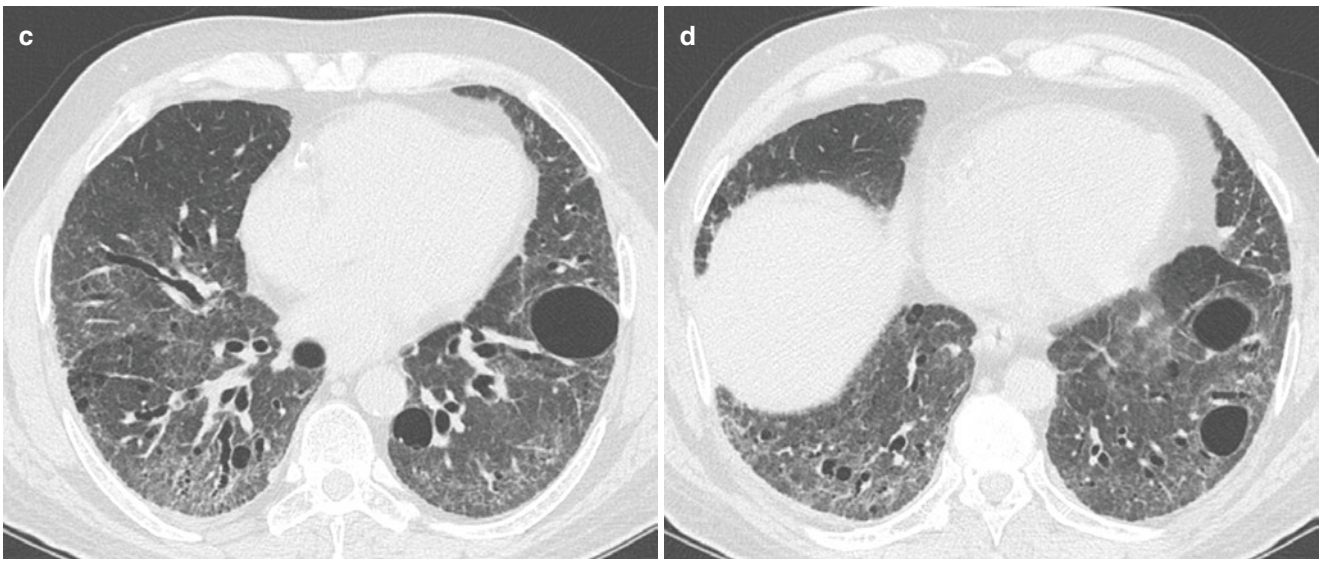

Fig. 13.50 (continued)

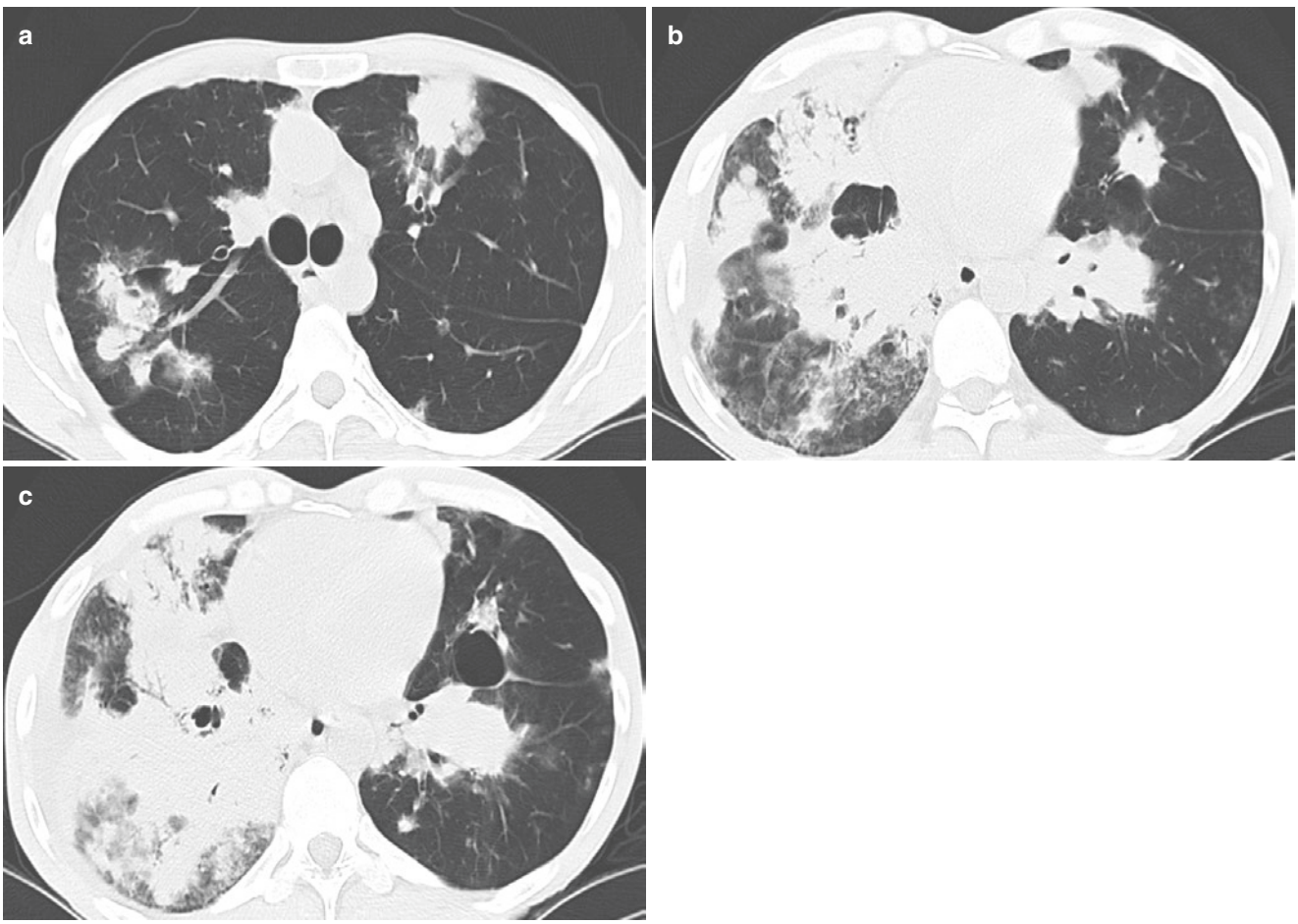

Fig. 13.51 Malignant lymphoma in a patient with LIP and Sjögren syndrome. (**a**–**c**) Axial CT images show multiple pulmonary masses with halo sign. Note cysts probably from LIP

matomyositis (DM), polymyositis (PM), and inclusion body myositis (IBM). As pulmonary manifestations almost do not occur in IBM, we will discuss DM and PM in this chapter. Not all patients with IIM have significant muscle inflammation, but they can present with ILD and classical skin findings of DM, an entity called amyopathic dermatomyositis. In addition, 20–30% of the patients can also present with ILD preceding the diagnosis of IIM. PM and DM are twice more prevalent in women than in men. The most characteristic pattern is mixed pattern, i.e., OP superimposed on NSIP [88, 89]. Patients with myositis can be subclassified according to various myositis-related antibodies, including anti-aminoacyl-tRNA (anti-ARS) antibody, anti-MDA5 antibody, and anti-TIF1 antibody. Patients from these sub-categories have a different clinical profile and show different imaging features. Antisynthetase syndrome is a subset of myopathy, but myositis may be absent or delayed after lung involvement, in more than a third of the patients. In these patients, anti-ARS antibodies, directed against a family of cytoplasmic enzymes, (anti-aminoacyl-tRNA synthetase) are present (Figs. 13.13, 13.41, and 13.53). The most commonly detected anti-ARS antibody is anti-Jo-1, and it is associated with NSIP, OP, or mixed pattern of ILD often associated with lower lobe predilection and volume loss [94–96]. Anti-CADM-140 antibody (anti-CADM-140), also referred to as anti-melanoma differentiation-associated gene 5 (MDA5) antibody, is a myositis-specific antibody identified in patients with clinically amyopathic dermatomyositis and is associated with a rapidly progressive ILD. HRCT findings of lower lobe consolidations or GGOs and random GGOs are the predominant patterns in anti-CADM-140-positive/MDA5-positive DM [94].

Table 13.23 Thoracic manifestations of Sjögren syndrome

ILDs	NSIP: most common ILD pattern UIP, OP, and LIP is also seen
Airway disease	Bronchiolitis, usually follicular Bronchiectasis
Others	Pulmonary amyloidosis
Malignancy	Higher risk of non-Hodgkin lymphoma

Table 13.24 Thoracic manifestations of systemic lupus erythematosus

Pleural disease	Pleural thickening, pleural effusion
Others	Shrinking lung syndrome Lupus pneumonitis Diffuse alveolar hemorrhage Typical and atypical pneumonia Pulmonary arterial hypertension
ILDs	Uncommon; NSIP, OP more than UIP

13.7.6 Mixed Connective Tissue Disease

Mixed connective tissue disease was first described in 1972 and is characterized by mixed features of four diseases: RA, SLE, SSc, and PM/DM together with high titers of anti-U1-RNP antibodies. The disease occurs predominantly in women (female-to-male ratio, 9:1). The pulmonary manifestations resemble those seen in SLE, SSc, and PM/DM (Table 13.25) [88–90].

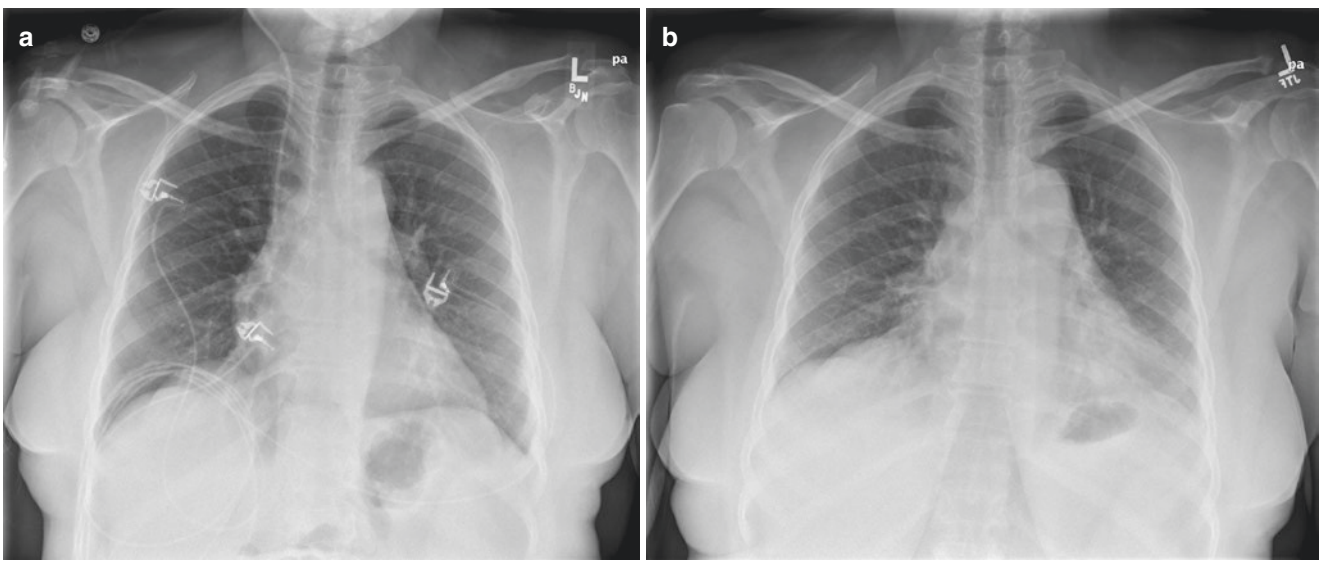

Fig. 13.52 Shrinking lung in a patient with SLE due to diaphragmatic myopathy. (**a**, **b**) Serial radiographs 6 months apart with worsening symptoms showing poorer diaphragmatic excursion

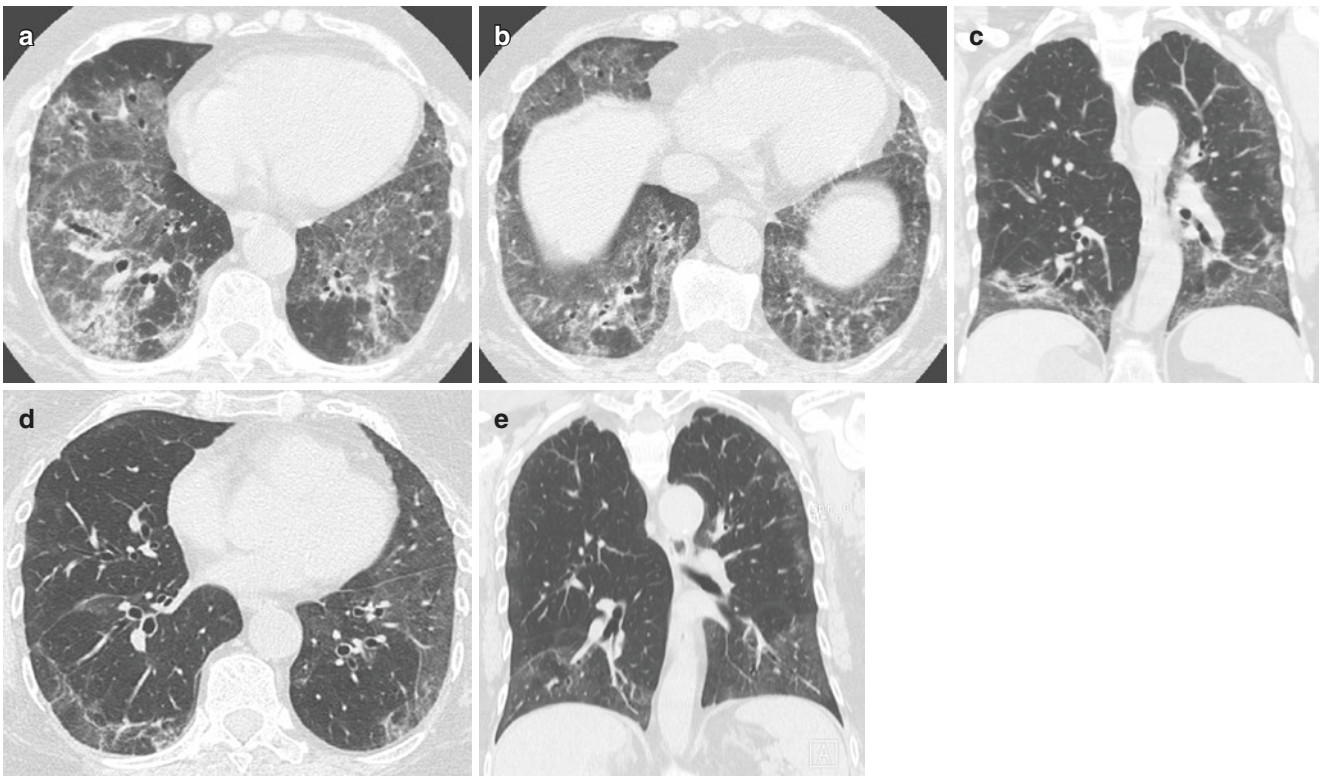

Fig. 13.53 Antisynthetase syndrome. (**a**–**c**) Axial and coronal CT images show GGOs and traction bronchiectasis with NSIP pattern with mild OP. (**d**, **e**) Follow-up CT images after 6 months of steroid treatment show improvement in GGOs and scarring

Table 13.25 Thoracic manifestations of mixed connective tissue disease

ILDs	NSIP: most common ILD pattern UIP and LIP less common
PAH	PAH in isolation or with ILD PAH is the major cause of morbidity and mortality
Esophageal involvement	Esophageal dilatation and dysmotility common Aspiration and its complication are common
Pleural disease	Pleural effusion seen in small number of patients

13.7.7 Interstitial Pneumonia with Autoimmune Features (IPAF)

Various names have been used to describe patients with interstitial pneumonia and autoimmune manifestations that do not fit into a defined CTD diagnostic criteria. They include undifferentiated connective tissue disease, autoimmune-featured ILD, and lung-dominant CTD. An international task force was convened in 2012 to standardize the nomenclature, and it proposed the term interstitial pneumonia with autoimmune features (IPAF) to describe this group of patients [97]. The interstitial pneumonia can be of UIP, NSIP, or OP pattern (Fig. 13.43). It is hoped that a standardized diagnostic criteria would facilitate future research, and it is likely that the criteria may be revised as we gain more understanding of this disease entity.

13.8 HP

HP is an ILD resulting from repeated inhalation of antigenic particles that include microbial agents, low-molecular-weight chemicals, and animal proteins. Based on the duration of symptoms, HP is divided into three rather unclear and overlapping categories: acute HP, subacute HP, and chronic HP. Acute HP has abrupt onset of fever, dyspnea, and malaise (hours or days), after exposure to the offending antigen, and is difficult to differentiate from the other causes of acute respiratory insufficiency. Subacute and chronic HP have more insidious onset and are due to continuous or intermittent exposure to HP antigens. Acute and subacute HP are considered as a non-fibrotic disease process, while chronic HP is considered as a fibrotic disease that can progress to end-stage fibrosis. More than 200 antigens have been identified as causes for HP, leading to various subsets of HP (Table 13.26). Serum precipitins against the specific antigen, when present, support the diagnosis of HP in the appropriate clinical settings. HRCT plays an important role in the diagnosis of HP and often shows characteristic findings (Table 13.27) (Figs. 13.14, 13.33, 13.54, 13.55, and 13.56) [98, 99]. Histology of HP is characterized by chronic bronchiolocentric inflammation and poorly formed epithelioid granulomas, with or without giant cells. The diagnostic pathway involves detail history taking for exposure, in particu-

Table 13.26 Common HPs

Disease	Agent	Source
Farmer's lung	Thermophilic actinomycetes	Moldy plant materials
Bird fancier's disease	Avian proteins	Bird excreta, blood, or feather
Hot tub lung	*Mycobacterium avium complex*	Warm contaminated water
Humidifier lung	Thermophilic actinomycetes	Warm contaminated water
Bagassosis	Thermoactinomyces sacchari	Sugar cane residue
Suberosis	*Aspergillus* species, cork dust	Cork

Table 13.27 HRCT features of HP

Acute/subacute	Chronic
• Mid- to upper lung predominance • Numerous ill-defined ground-glass density centrilobular nodules • or • Patchy symmetrical ill-defined GGOs • Air-trapping is characteristic	• Mid- to upper lung predominance in two-thirds of patients • One-third show lower lung predominance • Reticular opacities, GGOs, traction bronchiectasis, honeycombing, centrilobular GGOs • Air-trapping is characteristic • Head-cheese sign may be present

larly, the occupational history, a bronchoalveolar lavage, and HRCT. A third of the patients do not have any identifiable exposure. Bronchoalveolar lavage in HP is characterized by lymphocyte counts of more than 40% in bronchoalveolar lavage. This increase is unusual in other diseases generally considered as differential diagnoses, such as IPF [100]. However, the lack of lymphocytosis does not exclude HP, especially in the presence of fibrotic lung disease. The final diagnosis often requires a lung biopsy.

13.9 Sarcoidosis

Sarcoidosis is a multisystem granulomatous disease characterized by non-caseating epithelioid granulomata affecting almost every organ in the body. The most common presentation is in the third decade of life, with slightly higher prevalence among women. Thoracic involvement is seen in up to 90% of the patients with sarcoidosis, and bilateral, symmetrical hilar lymphadenopathy is the most characteristic finding [101, 102]. A chest radiograph is often the initial imaging study for patients with sarcoidosis and typically reveals symmetrical bilateral hilar opacities. The lymphadenopathy appears discrete and homogeneous in CT images (Figs. 13.57, 13.58, 13.59, 13.60, and 13.61). There may be associated

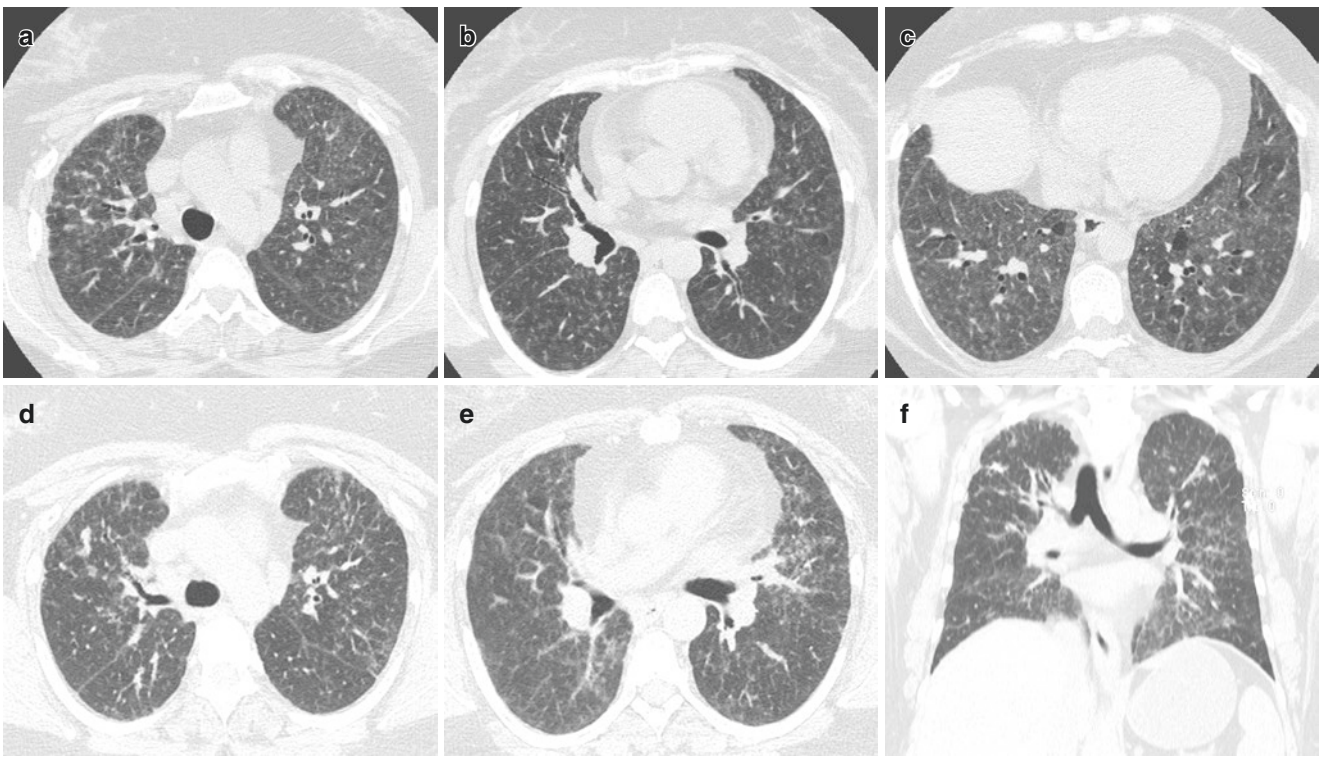

Fig. 13.54 45-year-old woman, a bird owner who presented with dyspnea. (**a**–**c**) Initial axial CT images show diffuse ground-glass density centrilobular nodules, GGOs, mild bronchial dilatation, and mild mosaic attenuation. (**d**–**f**) Follow-up after 1 year, CT images show upper lung fibrosis. "Bird fancier" disease

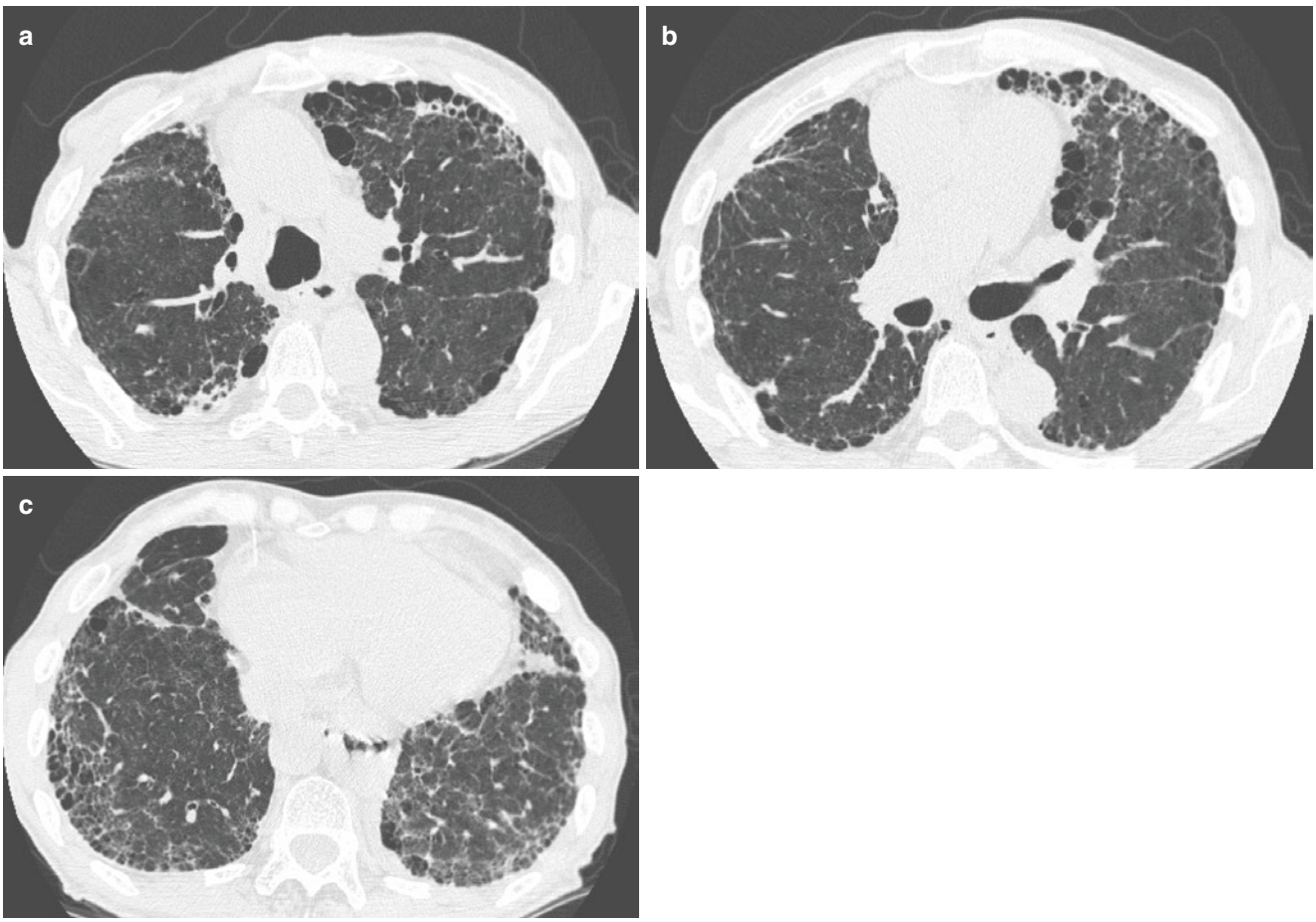

Fig. 13.55 HP mimicking UIP in a nonsmoker with exposure to pigeon's droppings. (**a**–**c**) Axial CT images show honeycombing with mild centrilobular nodularity. The honeycombing is more severe in the upper and mid-lung

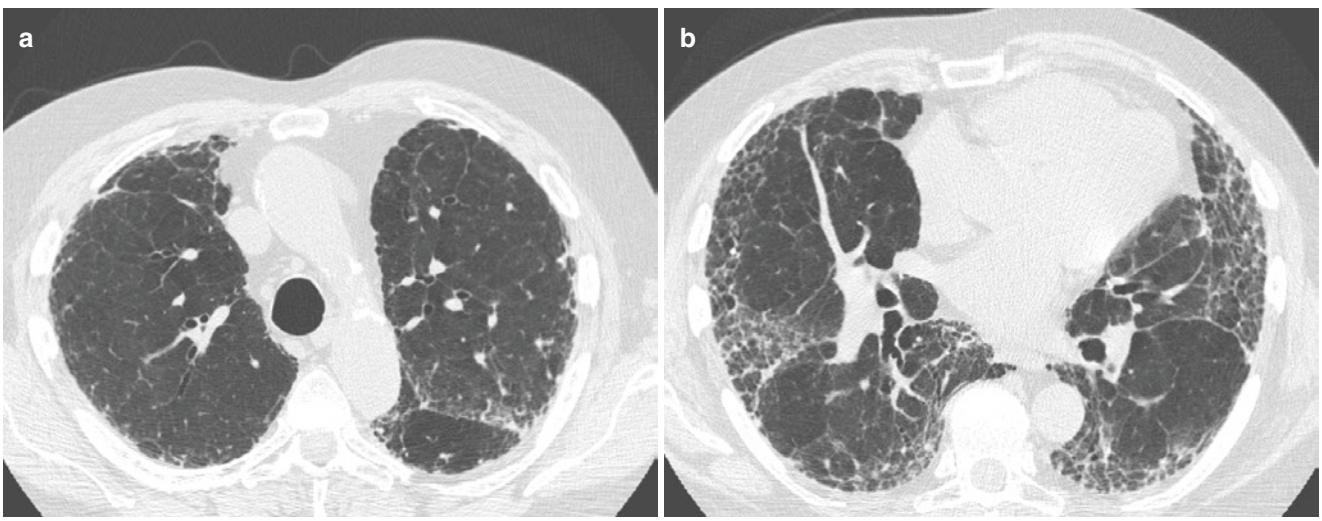

Fig. 13.56 HP from chronic exposure to hot tub and isolation of mycobacterial pathogens from the pool water. (**a**–**d**) Axial and coronal CT images reveal lower lung predominant fibrotic lung disease with mosaic attenuation and subtle centrilobular nodularity. Remember HP show lower lung predominance in one-third of the patients

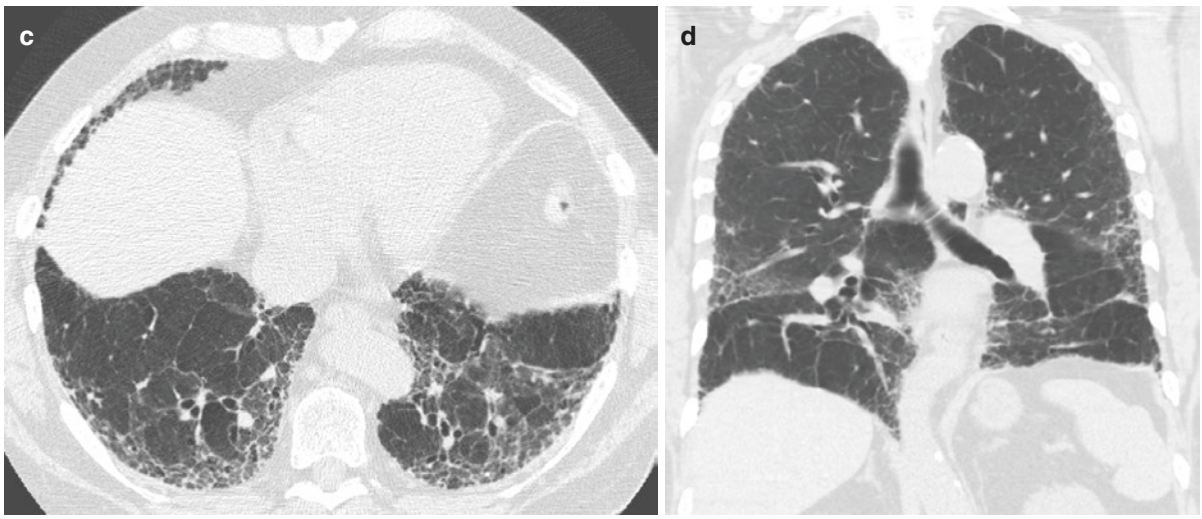

Fig. 13.56 (continued)

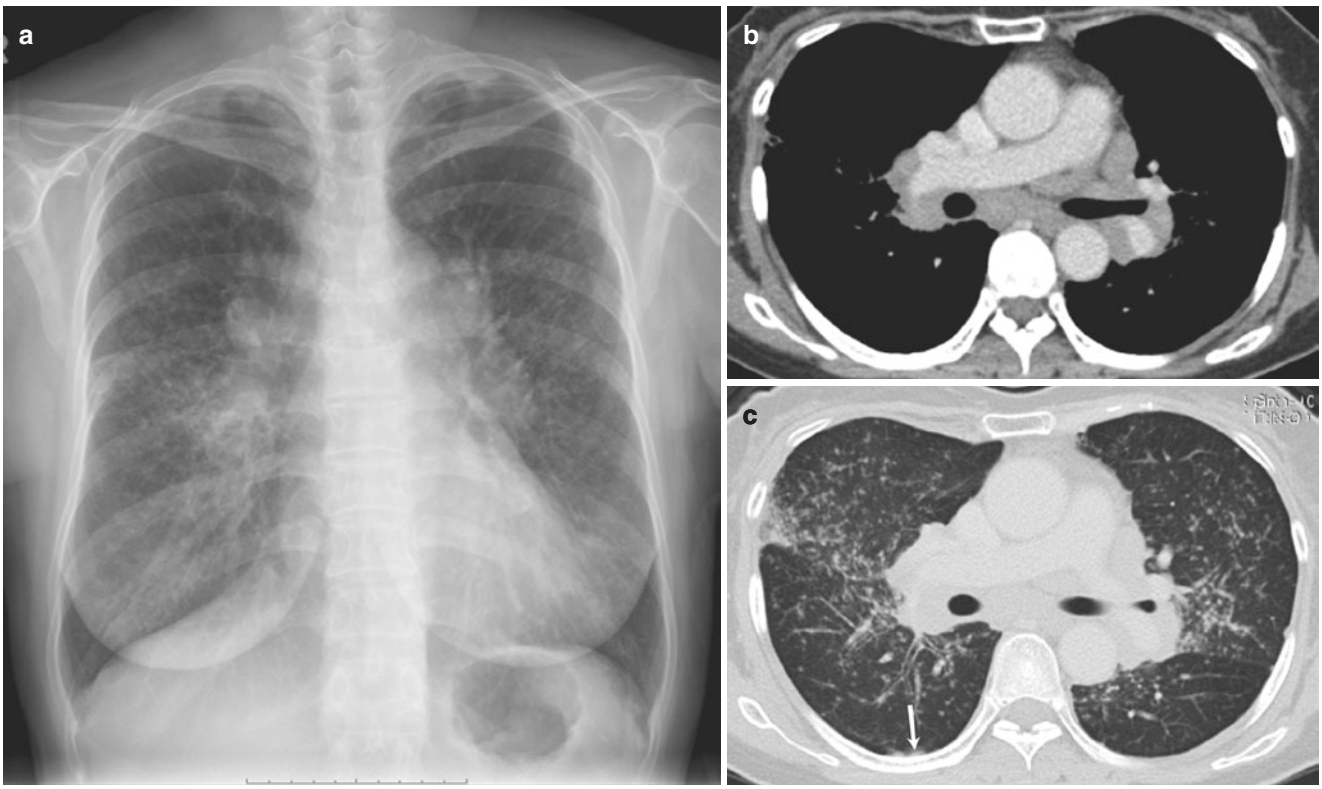

Fig. 13.57 (**a**, **b**, **c**) Stage 2 sarcoidosis. Bilateral hilar lymphadenopathy with fine nodularity in perihilar region. Note pseudo-plaque (arrow)

mediastinal lymph node enlargement, particularly nodes in paratracheal, aortopulmonary window and subcarinal location. Symmetrical lymphadenopathy is unusual in other radiological differential diagnoses such as tuberculosis, lymphoma, and metastatic malignancies. Isolated mediastinal lymph node involvement without hilar lymphadenopathy is rare.

Lung parenchymal involvement of thoracic sarcoidosis, when present, adds to the diagnostic confidence of HRCT. Sarcoidosis is an upper lung predominant disease. The commonest pattern of lung involvement is nodular thickening with perilymphatic distribution. HRCT reveals small rounded micro-nodules (2–4 mm) along the peribronchovascular interstitium, predominantly in the subpleural location and less often along interlobular septa. These nodules may coalesce and form macro-nodules of more than 5 mm in size resulting in "beaded" appearance of fissure. Nodules in the subpleural perilymphatic location may coalesce to form "pseudo-plaques." Most of the micro-nodules disappear over time. However, approximately 20% of

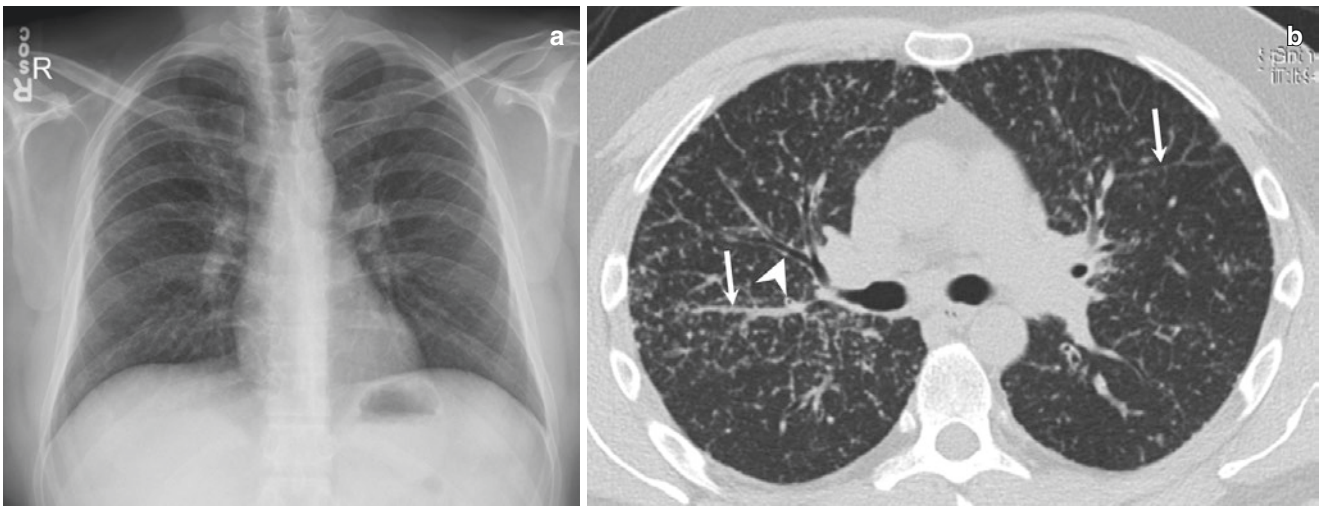

Fig. 13.58 Stage 3 sarcoidosis. (**a**) Frontal radiograph shows fine nodularity in both lungs without any hilar node enlargement. (**b**) Axial CT image shows perilymphatic nodules in the subpleural region, along the fissure (beaded right major fissure), along the pulmonary veins (arrows), and along the bronchiole wall (arrowhead)

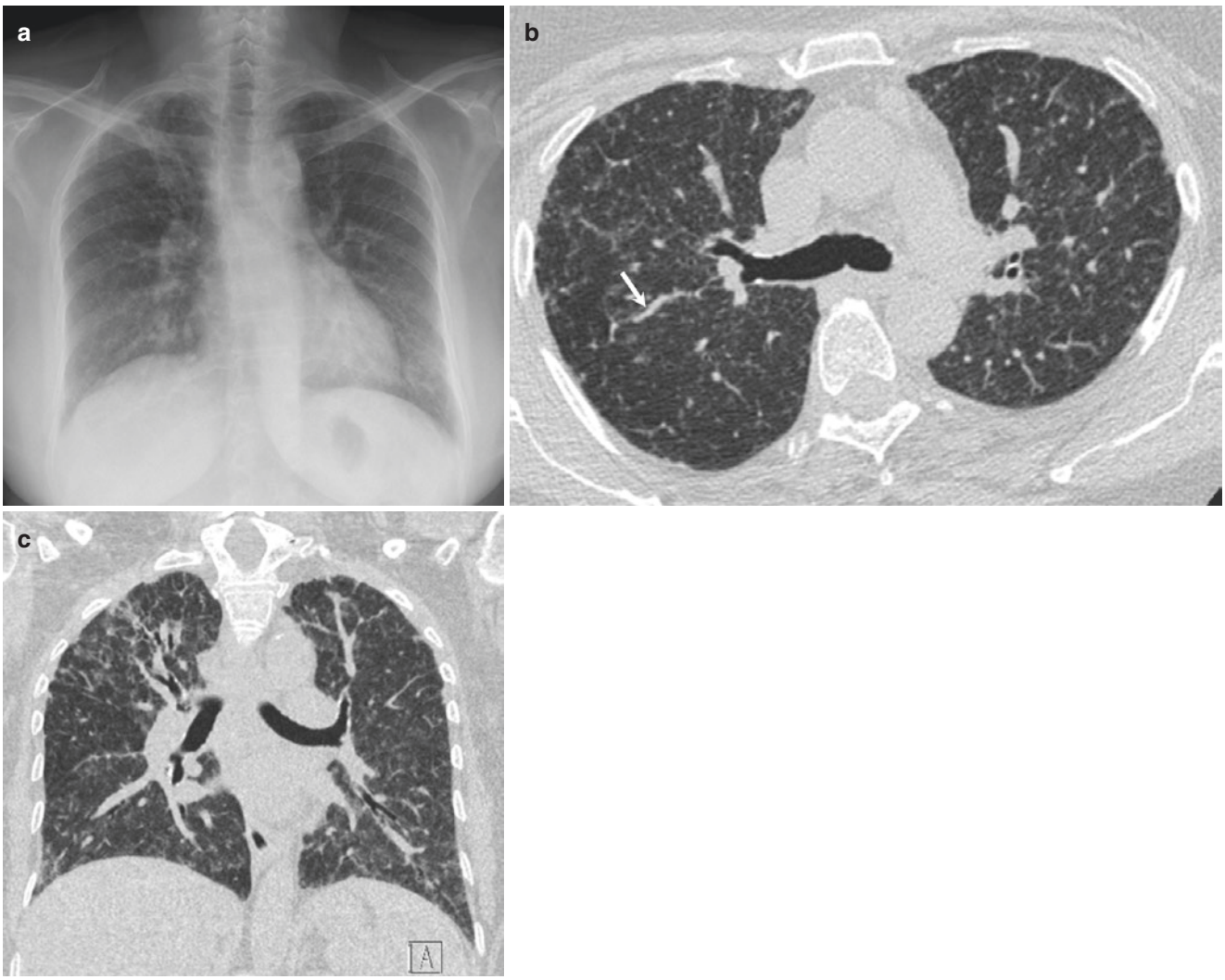

Fig. 13.59 Stage 4 sarcoidosis. (**a**) Frontal chest radiograph shows diffuse reticular opacities in both lungs. (**b**, **c**) Axial and coronal CT images show fibrosis and fine nodularity with mild upper lung predominance. The nodularity has perilymphatic distribution (subpleural and along pulmonary veins) with the pseudo-plaque formation in right major fissure (arrow)

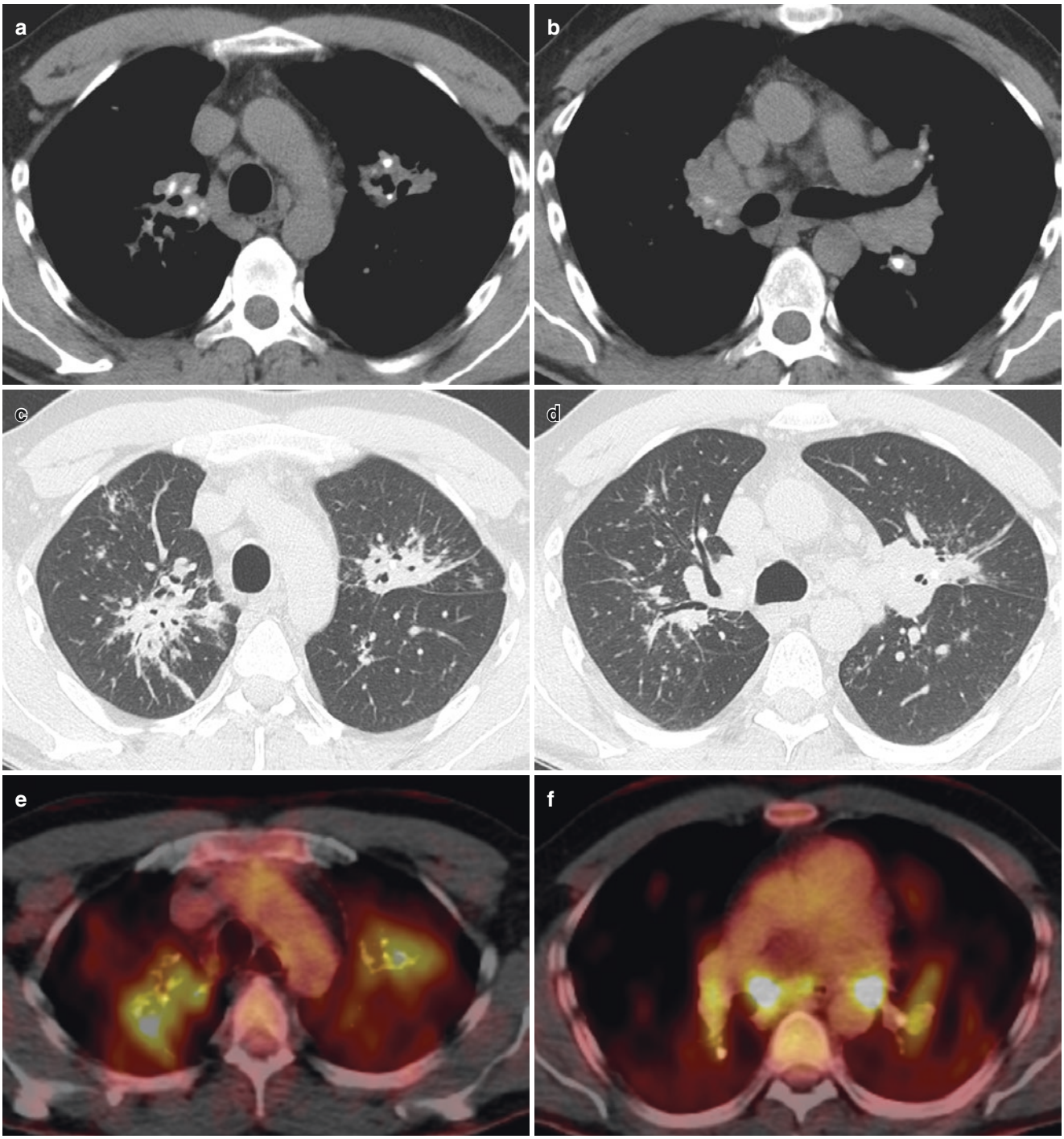

Fig. 13.60 43-year-old man with biopsy-proven sarcoidosis mimicking progressive massive fibrosis (PMF). (**a**, **b**) Axial CT images show bilateral hilar and mediastinal lymphadenopathy with punctate and amorphous calcifications. (**c**, **d**) There is volume loss in the upper lung with perihilar masses with surrounding nodularity. (**e**, **f**) PET-CT images show the nodes and masses as metabolically active. Unlike PMF in pneumoconiosis, the perihilar masses in sarcoidosis are more perihilar and move outward

the patients progress to fibrosis with resultant traction bronchiectasis and parenchymal architectural distortion.

There is a myriad of known atypical and less common imaging manifestations of pulmonary sarcoidosis involving the lymph nodes, pulmonary parenchyma, airways, and pleura. This presents a diagnostic challenge to the radiologists. Such atypical imaging manifestations, in approximately 25–30% of patients (especially in patients more than 50 years of age), may cause diagnostic confusion [103]. Unilateral hilar lymphadenopathy is seen in less than 5% of patients. The lymph nodes may show calcifications depending on the chronicity of disease, with up to 20% of the patients showing calcified lymph nodes after 10 years of disease. These calcifications may be amorphous, punctate, or

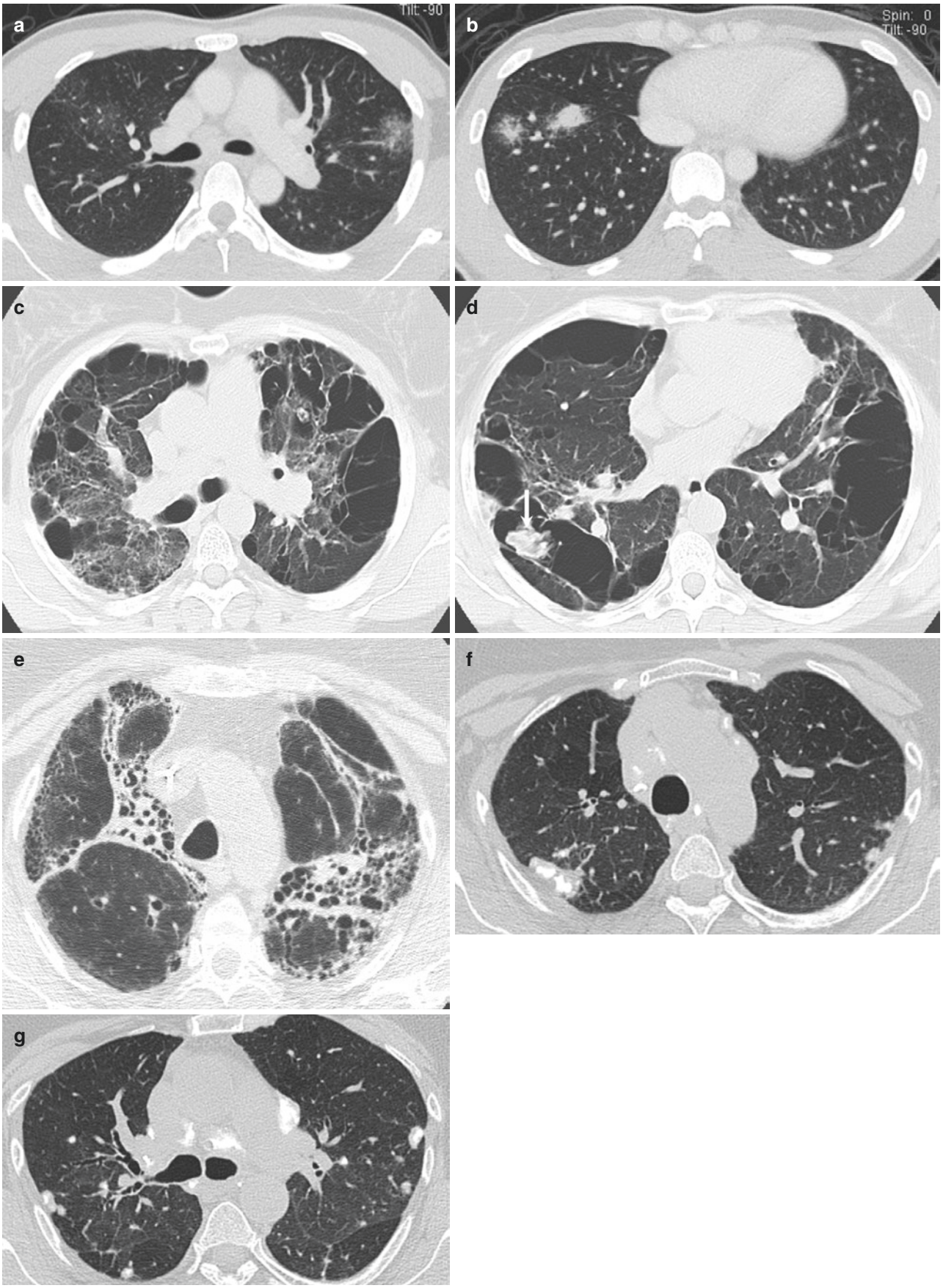

Fig. 13.61 Atypical findings in four different patients of sarcoidosis. (**a**, **b**) A cluster of nodules with the formation of masses ("galaxy" sign). (**c**, **d**) Fibrocystic changes with an aspergilloma (arrow). (**e**) Upper lung fibrosis with honeycombing. (**f**, **g**) Calcified pseudo-plaques and lymph nodes with mosaic attenuation due to airways involvement

eggshell-like [102]. The sarcoid nodules may coalesce over time forming a large conglomerate nodule which appears as a mass-like consolidation extending from the hilum to the peripheral lung. Such lesions are seen in approximately 15–25% of the cases. These confluent large opacities have irregular edges and blurred margins and are often accompanied by small satellite nodules (galaxy sign) [103, 104]. About 40% of the patients may have associated patchy GGOs, and these opacities typically occur in patients with other background parenchymal changes. Reticular opacities, produced by interlobular and intralobular septal thickening, are a predominant radiological feature in 15–20% of the patients with sarcoidosis [102]. The irregular interlobular thickening may mimic lymphangitis carcinomatosis, though the severity of interlobular septal involvement is often more severe in the latter [105]. Despite its characteristic feature of non-caseating granulomata, cavitation or necrosis may be seen in less than 1% of cases. This finding resembles other diseases like tuberculosis and fungal infection and hinders the diagnosis of sarcoidosis [103]. Advanced stage of sarcoidosis is characterized by fibrocystic changes including honeycomb appearance and paracicatricial emphysema. These changes are predominantly noted in upper and mid-zones of the lung. The cysts in the sarcoidosis may be complicated by mycetoma formation. Involvement of small airways by sarcoid granulomata and fibrosis may cause obstruction, leading to mosaic attenuation in HRCT images. Other features of airway involvement include air-trapping and bronchial stenosis. Bronchial stenosis is due to large airway involvement by endobronchial granulomata or compression by lymphadenopathy. Pleural involvement is seen in 1–4% of patients with sarcoidosis and manifests as pleural effusion, pleural plaques, or, rarely, calcifications. Pneumothorax may occur due to rupture of bullae [102, 103]. Sarcoid associated pulmonary hypertension occurs in a substantial proportion of the patients.

13.9.1 Staging

A staging system developed by Siltzbach, based on radiographic findings, has been widely used because of its prognostic importance (Table 13.28). This staging is not validated on chest CT, and it does not mean that radiology of sarcoidosis starts from stage 0 and progresses to the higher stages in an orderly manner. It also does not describe disease activity and response to treatment.

Table 13.28 Radiographic staging of sarcoidosis

Stage 0	Normal
Stage 1	Hilar lymphadenopathy
Stage 2	Lymphadenopathy and parenchymal abnormalities
Stage 3	Parenchymal abnormalities without nodes
Stage 4	Pulmonary fibrosis

Most of the patients (up to 50%) have stage 1 disease at initial presentation with decreasing order of frequency of initial presentation as the stage advances. Though only 5% of patients have pulmonary fibrosis at the initial presentation, up to 25% of the patients eventually develop fibrosis over the course of the disease. Patients have decreasing possibility of spontaneous remission as the disease advances. Patients presenting with stage 1 disease have approximately 60–90% chance of remission, whereas those with stage 4 disease do not have any possibility of spontaneous remission and the parenchymal changes are irreversible. Hence, the radiographic staging at initial presentation helps to predict the prognosis and possibility of disease remission [102].

13.10 Drug-Induced ILDs

A large number of drugs can cause drug-induced ILD. The diagnosis of drug-induced ILD is challenging and requires close collaboration between physicians, radiologists, and pathologists. A history of exposure to the offending drug that is a known pneumotoxic and associated with new-onset respiratory symptoms is imperative for suspecting drug-induced ILD. The symptoms usually improve after withdrawal of the offending drug but in certain cases, the toxicity may be irreversible and may progress even after discontinuation of the drug. There are two mechanisms involved in drug-induced ILD: one is direct (dose-dependent) toxicity, and the other is immune-mediated (duration-/dose-independent). HRCT demonstrates various patterns of ILDs (Table 13.29) (Fig. 13.39). In many of the cases, the HRCT findings do not fit into any established pattern, and these cases remain as unclassified ILD. Lung biopsy is required for the final diagnosis.

13.11 Occupational Lung Diseases

Occupational lung diseases (OLD) are the commonest work-related causes of mortality, responsible for up to 70% of deaths from occupational diseases [106]. They represent a group of pulmonary disorders resulting from inhalation of dust or chemicals. Pneumoconiosis is a subset of OLDs and is secondary to inhalation of inorganic mineral dusts with

Table 13.29 HRCT pattern of drug-induced ILD

- NSIP
- UIP
- HP
- OP
- Others
  - Diffuse alveolar damage
  - Eosinophilic pneumonia
  - Diffuse pulmonary hemorrhage

reactive fibrotic or non-fibrotic changes in the lung tissue (Table 13.30). Fibrotic type of pulmonary manifestations occur in silicosis, coal worker's pneumoconiosis, asbestosis, talcosis, and berylliosis, whereas inhalation of inert dust particles like iron, tin, and barium produces non-fibrotic type of pulmonary changes. In addition, hypersensitivity pneumonitis (HP), chemical pneumonitis, hard metal lung diseases, and organic dust toxic syndrome (ODTS) comprise the other diseases in the spectrum of OLDs [106–108]. Features of HP have been elaborated in the previous section of this chapter. Silicosis, coal worker's pneumoconiosis and asbestosis are the three most common types of pneumoconiosis (Table 13.30).

Table 13.30 Spectrum of occupational lung diseases

• Pneumoconiosis Fibrotic: – Silicosis – Coal workers pneumoconiosis – Asbestosis – Talcosis – Berylliosis Non-fibrotic – Siderosis (iron oxide) – Stannosis (tin oxide) – Baritosis (barium sulfate)
• Mixed dust pneumoconiosis
• Asbestos-related thoracic diseases
• Hypersensitivity pneumonitis
• Chemical pneumonitis
• Organic dust toxic syndrome
• Hard metal disease

13.11.1 Silicosis

Silicosis occurs due to inhalation of crystalline silicon dioxide. There are two clinical forms of silicosis: classic silicosis and acute silicosis. There are two further subtypes of classic silicosis—simple and complicated silicosis [106, 107, 109].

Simple silicosis occurs due to prolonged exposure to silicon dioxide, with the time interval between exposure and occurrence of pulmonary manifestations ranging from 10 to 20 years. Typical chest radiograph shows multiple small circumscribed nodules with predominant upper and posterior zone distribution. These nodules are usually about 2–5 mm in size and may measure up to 10 mm. Calcifications in these nodules can be seen in approximately 10–20% of these cases [107]. Other findings include mediastinal lymphadenopathy, pleural effusion, and pleural thickening. HRCT demonstrates small centrilobular nodules and nodules along perilymphatic distribution (Figs. 13.62 and 13.63). Confluence of nodules in the subpleural region may mimic plaques (pseudoplaques). Mediastinal lymphadenopathy may be seen with or without calcification. Such calcifications, if present, are typically seen at the periphery of these nodes (eggshell calcifications).

Complicated silicosis, also known as progressive massive fibrosis (PMF), occurs due to conglomeration of pulmonary nodules. Radiographically, they appear as mass-like opacities predominantly involving the midzones. On HRCT, they are initially situated at the periphery of lung and gradually migrate toward the center, appearing as soft-tissue masses with irregular margins and calcifications. Emphysematous lung is seen between these masses and pleura (Fig. 13.64).

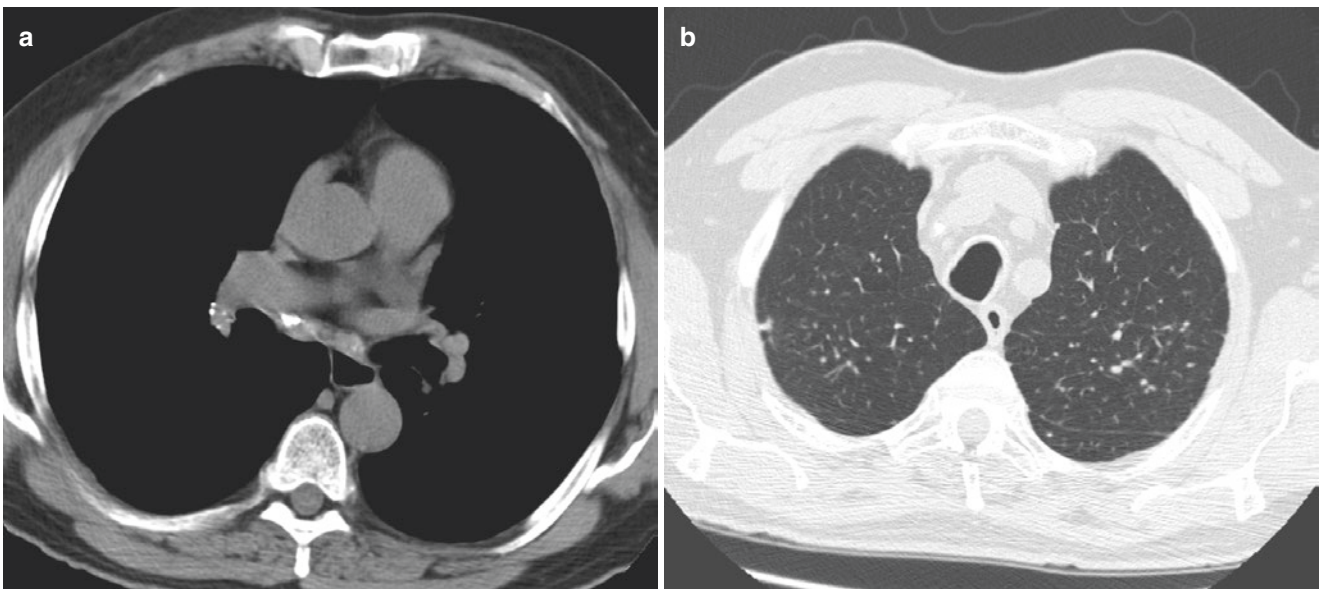

Fig. 13.62 Early simple silicosis. (**a**, **b**) Axial CT images show upper lung predominant tiny nodules in upper lungs with fine septal thickening and punctate and amorphous calcification in mediastinal and hilar lymph nodes

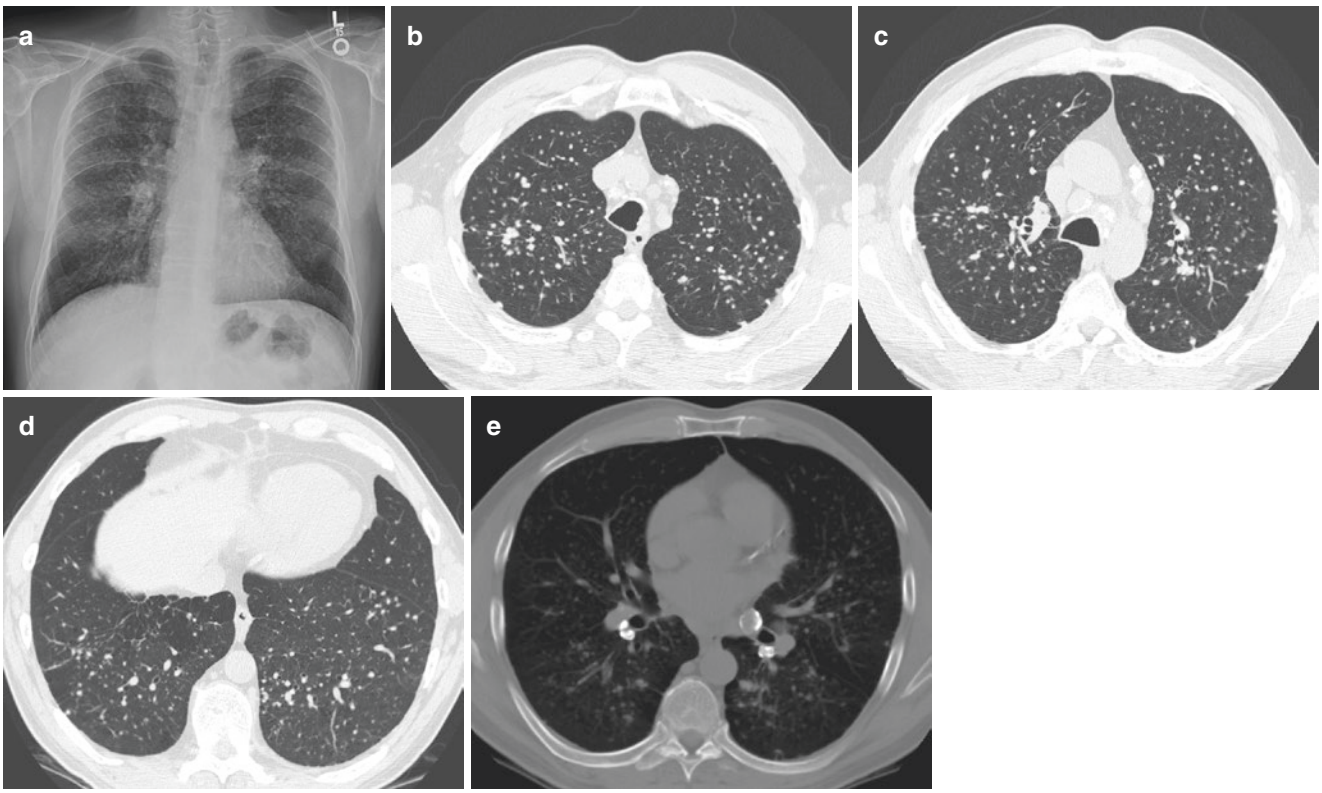

Fig. 13.63 Simple silicosis. (**a**) Frontal radiograph shows diffuse nodularity in both lungs. (**b–e**) Axial CT images show upper lung predominant perilymphatic nodules (subpleural and along centrilobular lymphatics) in both lungs with eggshell calcification in mediastinal and hilar lymph nodes

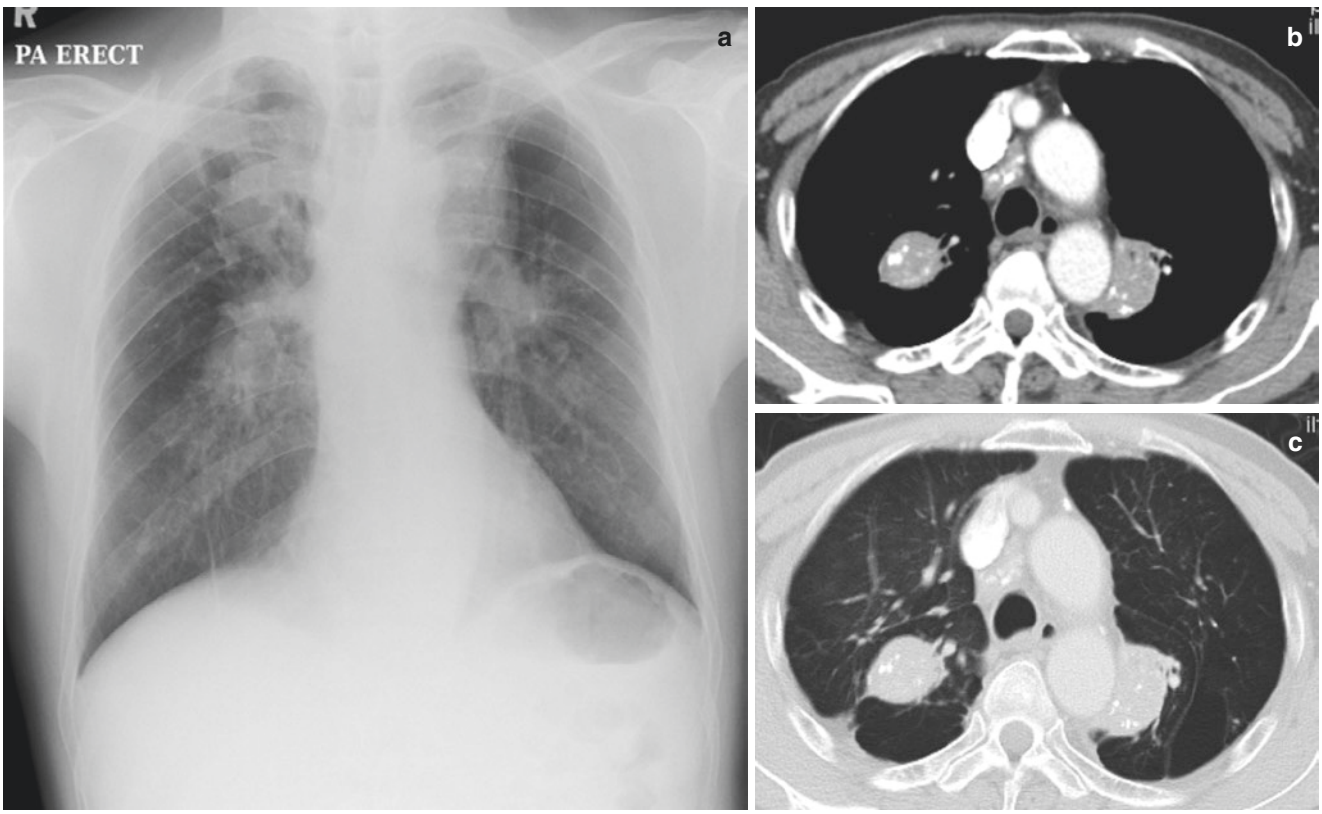

Fig. 13.64 Complicated silicosis with PMF. (**a**) Frontal radiograph shows bilateral upper lung masses with upper lung volume loss (upward displacement of hila with increased distance between mediastinal borders and pulmonary arteries—flying bird appearance of hila). (**b**, **c**) Axial CT images show calcified masses in posterior upper lungs with surrounding emphysema changes. Note calcified lymph nodes

The outer margin of these lesions is typically seen parallel to the lateral chest wall. Cavitation of these lesions may occur secondary to ischemic necrosis. The patients may also develop fibrosis in NSIP or UIP pattern.

Acute silicosis, also known as silicoproteinosis, follows heavy exposure to silica without proper protection and usually presents with clinical symptoms within 3 years of initial exposure [110]. There is proliferation of type II pneumocytes producing excessive surfactants. Filling of proteinaceous material in the alveoli produces an appearance resembling alveolar proteinosis. Typical chest radiograph shows ground-glass opacities in a perihilar distribution. HRCT reveals centrilobular ground-glass nodules, patchy ground-glass opacities, and interlobular septal thickening with crazy-paving pattern. Despite treatment, it usually leads to death as a result of cor pulmonale and respiratory failure [107, 110].

The incidence of tuberculosis in men with silicosis is 2.8 times more than men without silicosis. Twenty-five percent of patients with classic or acute silicosis have pulmonary tuberculosis. Features of silicotuberculosis include asymmetric consolidation, cavitation, and rapid disease progression [107]. Silicosis also increases the risk of lung carcinoma. In patients with silicosis, occurrence of tuberculosis or malignancy is independent predictors of mortality [111, 112] (Table 13.31).

Table 13.31 Imaging features of silicosis

Simple silicosis	Radiograph: • Small circumscribed nodules of 2–5 mm • Predominant upper and posterior zone distribution • Calcification of nodules (10–20%) • Pleural effusion and pleural thickening HRCT: • Small nodules with perilymphatic distribution • Confluence of nodules in subpleural region (pseudo-plaques) • Mediastinal lymphadenopathy with eggshell calcifications
Complicated silicosis (PMF)	Radiograph: • Mass-like opacities at midzones HRCT: • Soft-tissue masses with irregular margins and calcifications • Initially situated at the periphery of lung; gradually migrates toward the center • Emphysematous lung between the masses and pleura • Outer margin of lesions parallel to the lateral chest wall • Cavitation of masses secondary to ischemic necrosis • Fibrosis with NSIP or UIP pattern
Acute silicosis	Radiograph: • GGO in perihilar distribution HRCT: • Centrilobular ground-glass nodules • Patchy GGO • Interlobular septal thickening • Crazy-paving pattern

13.11.2 Coal Worker's Pneumoconiosis (CWP)

Inhalation of inorganic coal dust in the work environment (usually by miners) results in CWP. Development of CWP in exposed people depends on various factors, such as duration of exposure, type of coal, mining methods, and usage of personal protective devices/measures. Imaging characteristics of CWP is similar to silicosis, making differentiation of these two entities difficult with imaging alone—histologic differentiation is required.

In simple CWP, the chest radiograph shows small nodular or reticulonodular opacities predominantly in the mid- and upper zones with the nodules measuring from 1 to 4 mm. These nodules have relatively indistinct margins compared to that of silicosis. Calcifications are seen in 10–20% of these nodules, manifesting as a central dot. This is in contrast to silicosis where diffuse calcification of nodules is seen. Unlike silicosis, eggshell calcification pattern of lymph nodes is rare in CWP. The other findings of CWP, such as confluence of subpleural nodules mimicking plaques (pseudo-plaques), are similar to silicosis [107, 113].

The incidence of PMF is less common in CWP than compared to silicosis. PMF manifests as mass-like opacities that are initially seen at periphery. Migration of these opacities toward the hila results in emphysematous lung between them and chest wall. As in silicosis, CWP is associated with increased risk of tuberculosis and carcinoma (Fig. 13.65). In addition, coal dust inhalation is associated with increased risk of development of chronic obstructive pulmonary disease (COPD). COPD further increases the mortality in patients with CWP [106, 114] (Table 13.32).

13.11.3 Asbestos-Related Thoracic Diseases

Based on physical characteristics, there are two major groups of asbestos: serpentines and amphiboles. In the serpentines group, chrysotile is the only asbestiform mineral and the most commonly used asbestos. It is flexible, easily decomposable, and chemically stable. In contrast, amphibole fibers are stiff and straight with more fibrogenic and carcinogenic properties (Table 13.33).

Pleural Disease Pleural effusion is the earliest manifestation of asbestos exposure, whereas pleural plaque is the commonest manifestation [115]. Pleural effusions, though uncommon, manifest within 10 years of exposure in contrast to pleural plaques that occurs after 20–30 years. The pleural effusions may be unilateral or bilateral and are usually exudative in nature. Pleural plaques are seen in up to 80% of

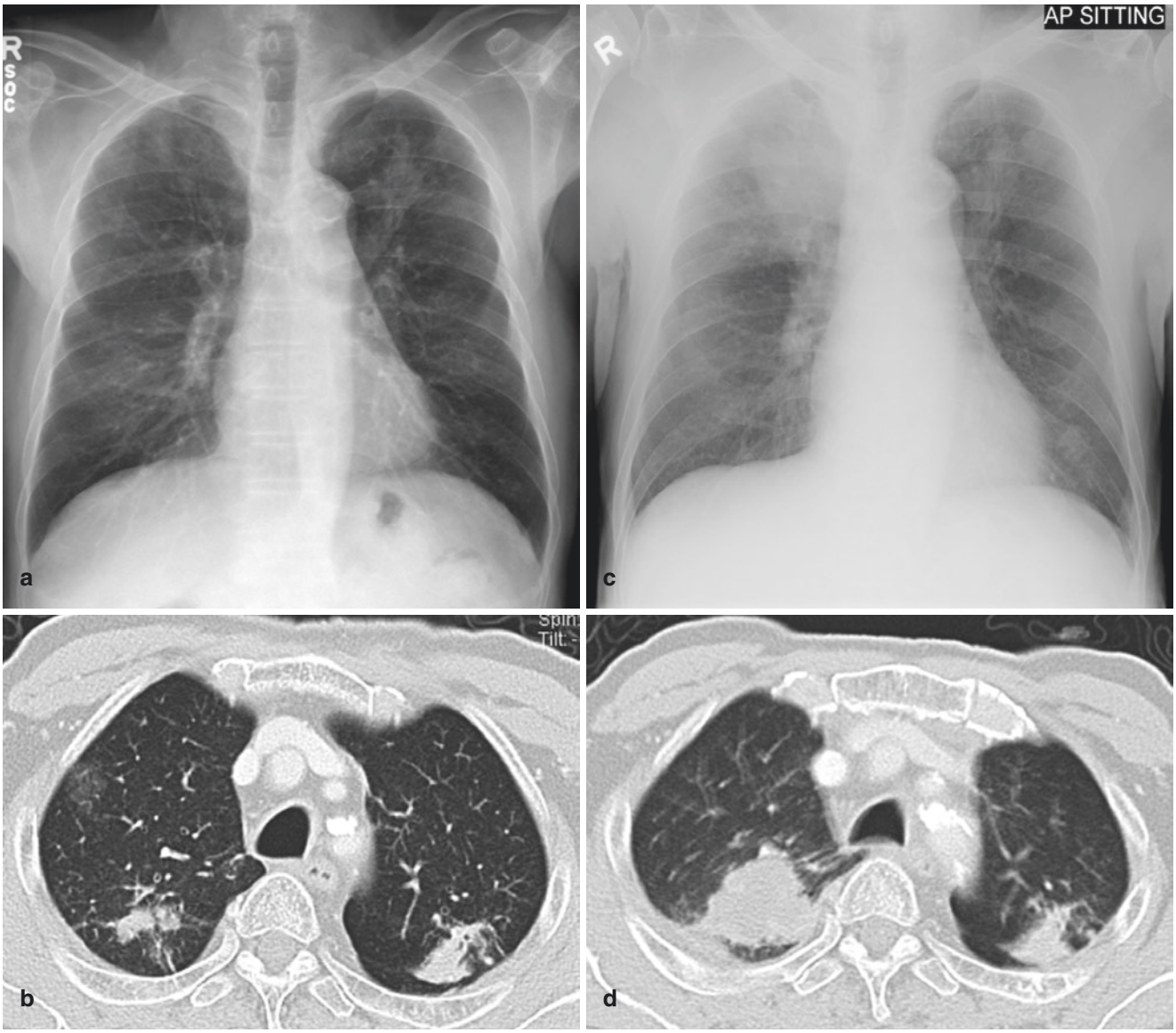

Fig. 13.65 Coal worker pneumoconiosis with PMF developing lung cancer. (**a**) Frontal chest radiograph shows bilateral upper lung opacities. (**b**) CT image shows opacities in bilateral posterior upper lungs. (**c**) One year follow-up radiograph shows an increase in the size of right upper lung opacity. (**d**) CT image confirms the finding. Biopsy revealed squamous cell carcinoma

Table 13.32 Imaging differentiation of silicosis and CWP

	Silicosis	CWP
Parenchymal nodules	Well-defined margin	Indistinct margin
Calcification pattern in nodules	Diffuse calcification	Central dot-like calcification
Lymph nodes with eggshell calcification	Common	Uncommon

Table 13.33 Asbestos-related thoracic diseases

- Benign pleural plaques
- Pleural effusion
- Diffuse pleural thickening
- Round atelectasis
- Asbestosis
- Mesothelioma
- Bronchogenic carcinoma

exposed persons. They are usually benign without causing any significant functional impairment (Figs. 13.66 and 13.67). Radiologically, they manifest as focal pleural thickening along the posterolateral chest wall, mediastinal pleura, and dome of diaphragm. Apices and costophrenic angles are relatively spared. These plaques may exhibit calcifications in 10–15% of patients [115, 116]. Occurrence of asbestosis is rare in the absence of pleural plaques.

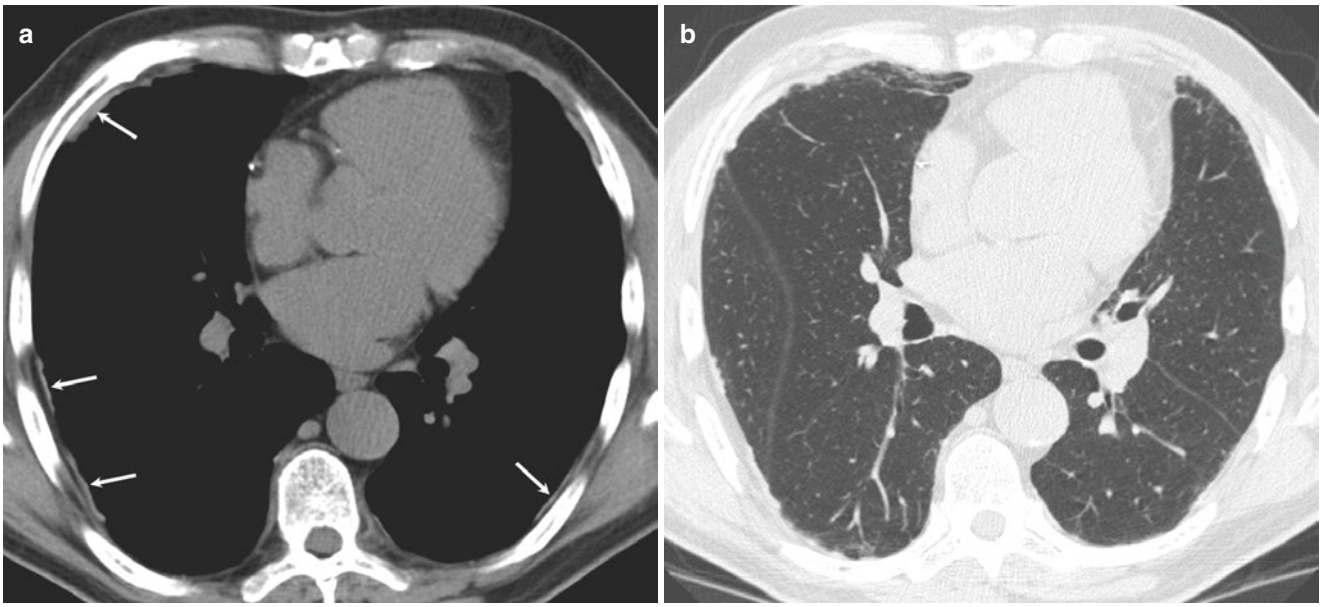

Fig. 13.66 (**a**, **b**) Noncalcified pleural plaques (arrows) with early subpleural parenchymal changes of asbestosis

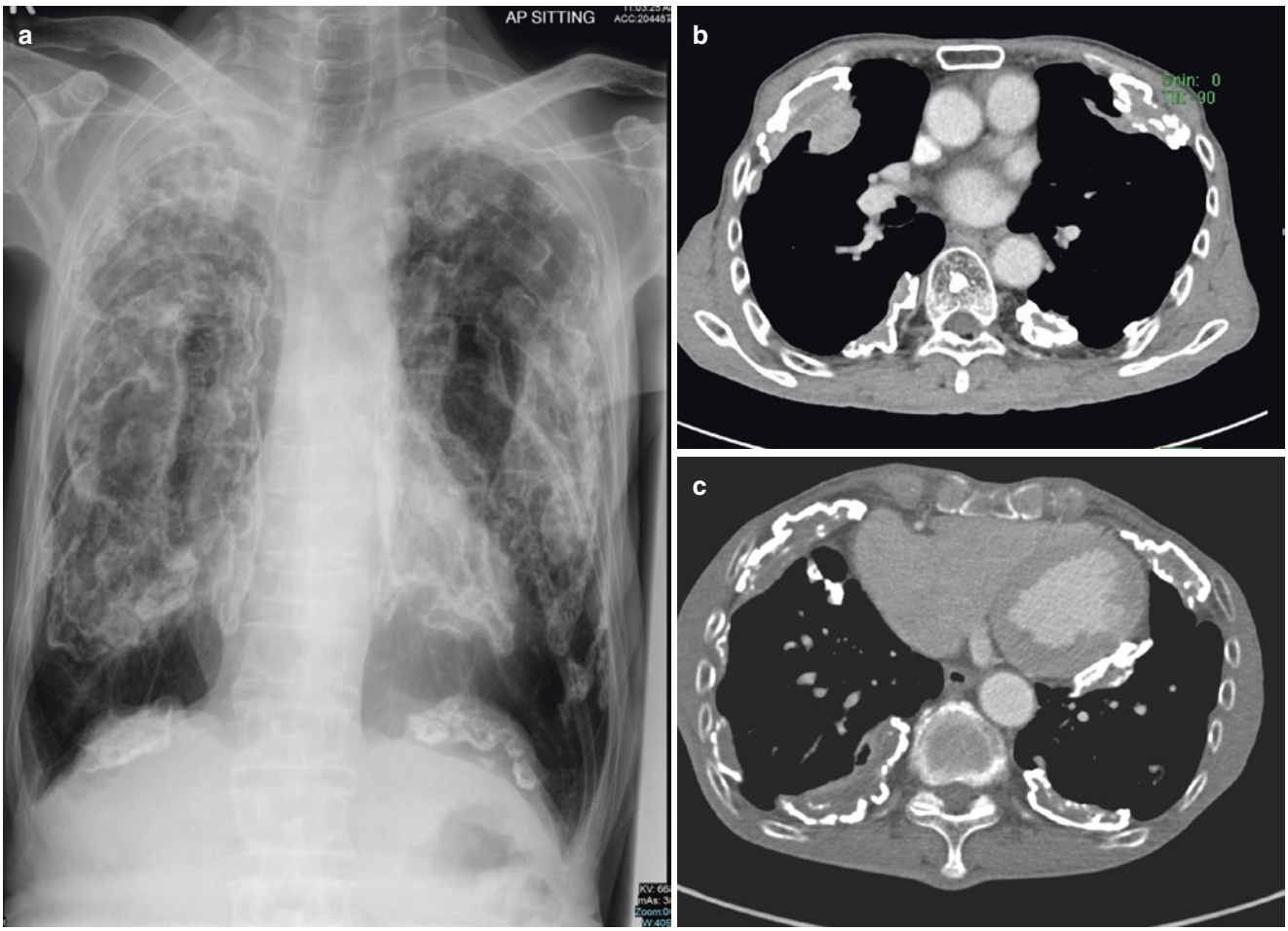

Fig. 13.67 Extensive changes of the asbestos-related pleural disease. (**a**) Frontal chest radiograph shows a bizarre pattern of calcification related to calcified plaques called "holy leaf" sign. (**b**, **c**) Axial CT images show extensive calcified pleural plaques with pleural thickening

Diffuse pleural thickening (DPT) is defined as continuous thickening of pleura involving at least 25% of the chest wall and is seen in up to 25% of people exposed to asbestos. Asbestos-related DPT is commonly due to prior pleural effusion which leaves diffuse visceral pleural thickening on regression. Another possible cause of DPT is confluence of pleural plaques [117]. DPT has ill-defined irregular margin and may involve the interlobar fissure. In contrast, pleural plaques do not extend beyond four intercostal spaces, usually have well-defined margins, and do not involve the visceral pleura (interlobar fissures) [106, 108, 115, 117]. Although DPT can occur as a result of various other diseases that are associated with pleural effusion or empyema, if seen together with pleural plaques, it is highly suggestive of asbestos-related DPT.

Rounded Atelectasis Also called as folded lung or Blesovsky syndrome, rounded atelectasis is usually seen in the posterior lower lobes, at the subpleural location (Fig. 13.68). The proposed pathogenesis is fibrosis along the pleura that subsequently contracts, which causes folding of the pleura into lung, with resultant atelectasis. CT shows a mass-like atelectasis with crowding of the bronchovascular structures extending from the margin of the mass (comet-tail sign) [108, 115]. The criteria for rounded atelectasis are "comet-tail" appearance, subpleural location, volume loss, and abnormal pleura. They can be calcified and can persist indefinitely.

Asbestosis Asbestosis is the occurrence of pulmonary fibrosis due to prior asbestos exposure. It usually manifests 20 years after the initial exposure. In contrast to pleural plaques, asbestosis results in functional impairment causing reduced vital capacity and diffusion capacity. Radiographs show reticular opacities preferentially involving the lower zones and posterior lobes. CT shows small subpleural nodules, curvilinear opacities, intralobular and interlobular lines, patchy ground-glass opacities, and, in the later stages, honeycombing (Figs. 13.69 and 13.70). These findings are similar to idiopathic pulmonary fibrosis (IPF). The presence of pleural thickening/plaques is highly suggestive of asbestosis than IPF.

Malignancy Related to Asbestos Exposure Asbestos exposure increases the risk of bronchogenic carcinoma, with approximately 20–25% of people with heavy exposure observed to develop malignancy. Asbestos exposure, when associated with smoking, results in further increased risk of carcinoma [108, 118]. Amphiboles are more carcinogenic than chrysotile [119]. The latent period varies from less than 10 years to more than 30 years from initial exposure [115]. Typical posterior and lower lobe locations further support the casual relationship.

Mesothelioma occurs approximately after 20–40 years of initial exposure with asbestos workers having a 10% estimated lifetime risk of developing mesothelioma. It starts as small nodule in the pleura which increases in size and eventually encasing the lung. Unilateral pleural effusion is the initial presentation in a chest radiograph. Mesothelioma should be suspected in a person with unilateral recurrent or non-resolving pleural effusion. CT findings may include nodular pleural thickening of more than 10 mm, mediastinal pleural involvement, circumferential pleural thickening, and invasion into chest wall, diaphragm, or mediastinum [106–108] (Table 13.34).

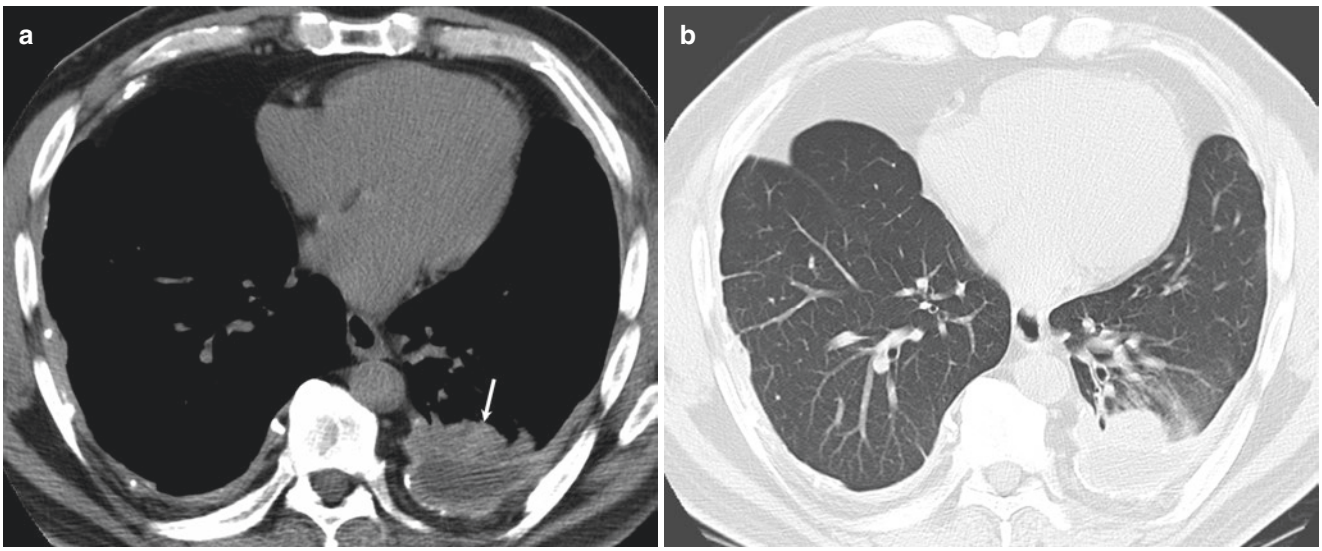

Fig. 13.68 Rounded atelectasis. (**a**, **b**) Axial CT images show subpleural opacity (arrow) under chronic pleural effusion with thickened and calcified pleura. Note all criteria for rounded atelectasis are present

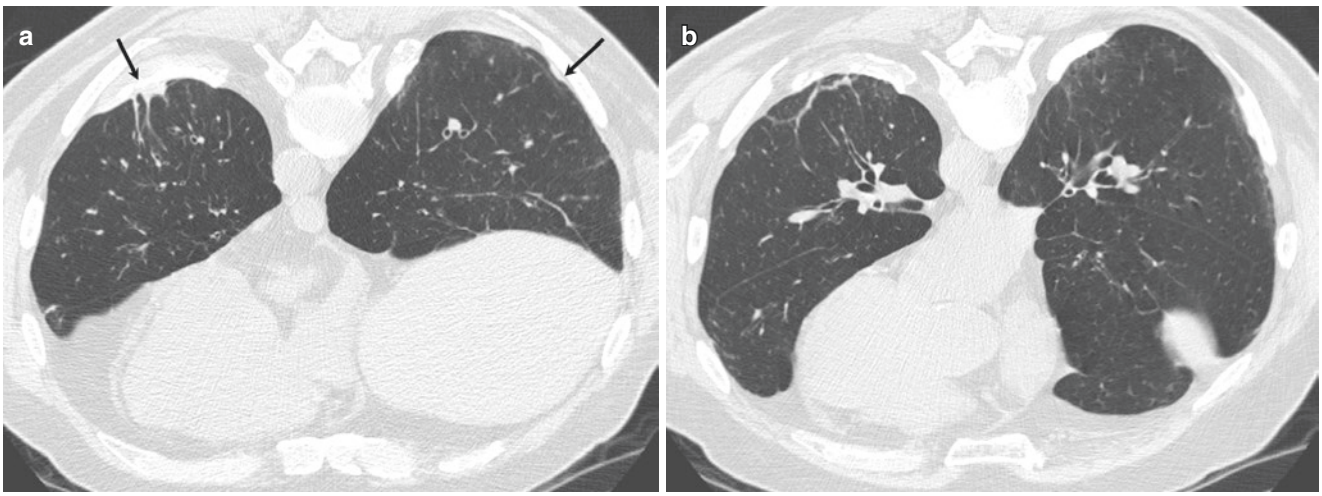

Fig. 13.69 Early asbestosis. (**a**, **b**) Axial CT images show calcified pleural plaques (arrows) with curvilinear and perpendicular subpleural linear opacities representing earliest changes of asbestosis

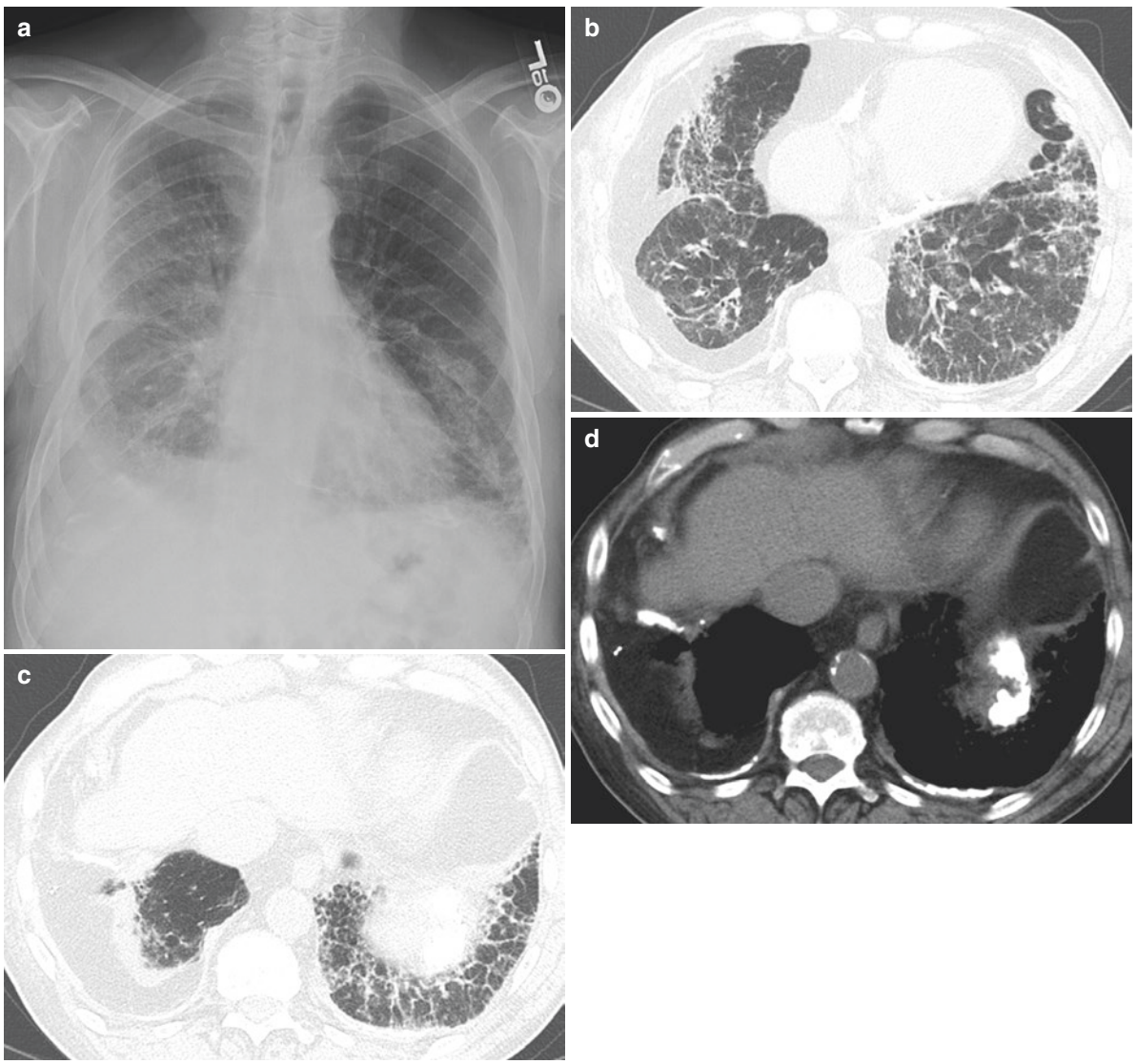

Fig. 13.70 Fibrosis from asbestosis. (**a**) Frontal chest radiograph shows fibrotic changes in lower lobes with pleural plaques. (**b**–**d**) Axial CT images show fibrotic lung disease, pleural plaques, and extraparenchymal fat retraction

Table 13.34 Imaging features of asbestos-related thoracic diseases

Benign pleural plaques	• Focal pleural thickening along posterolateral chest wall, mediastinal pleura, and dome of diaphragm • Apices and costophrenic angles are relatively spared
Diffuse pleural thickening	• Thickening of pleura of at least one-fourth of the chest wall • Ill-defined irregular margins
Round atelectasis	• Posterior aspect of lower lobes at subpleural location • CT: mass-like atelectasis with crowding of bronchovascular structures extending from the margin of the mass (comet-tail sign)
Asbestosis	Radiograph: • Reticular opacities • Preferentially in lower zone and posterior lobes CT: • Small subpleural nodules • Curvilinear opacities • Interlobular and intralobular lines • Patchy GGO • Honeycombing (in later stages)
Mesothelioma	Radiograph: • Unilateral recurrent or non-resolving pleural effusion CT: • Nodular pleural thickening of more than 10 mm • Mediastinal pleural involvement • Circumferential pleural thickening • Invasion into chest wall, diaphragm or mediastinum

13.11.4 Siderosis

Siderosis, also known as arc welder's pneumoconiosis occurs due to inhalation of inorganic iron dust. Siderosis does not cause functional impairment and may resolve following cessation of exposure. A typical radiograph will show diffuse nodular opacities, predominantly in the perihilar distribution, with the nodules having lower density than those seen in silicosis. CT findings include ill-defined centrilobular nodules, linear branching structures, GGOs, honeycombing similar to UIP pattern, and emphysematous changes in the lung. Silicosiderosis, which occurs due to combined inhalation of silica and iron oxide, may result in fibrosis and functional impairment [107, 108].

13.11.5 Talcosis

Pulmonary talcosis results from either inhalation (seen in the occupational setting) or intravenous infusion (in drug abusers) of hydrated magnesium silicate. Associated inhalation of silica (talco-silicosis) or asbestos (talco-asbestosis) results in mixed dust pneumoconiosis. Talc induces a non-necrotizing granulomatous inflammation with resultant fibrosis. Radiographic findings of talcosis include reticulonodular opacities with relative sparing of apices and costophrenic angles, together with mass-like opacities as seen in PMF. Hilar lymphadenopathy may be noted in some patients. CT shows small centrilobular nodules, conglomerating masses in perihilar region which may contain central high attenuation due to talc deposition. Other findings are GGOs, emphysema, and, rarely, honeycombing [107, 120, 121].

13.11.6 Berylliosis

Berylliosis occurs due to inhalation of beryllium dust or fumes in the occupational setting. Due to industrial regulations, acute form of berylliosis is no longer seen. Chronic berylliosis results from delayed hypersensitivity reaction that results in accumulation of CD4 lymphocytes and macrophages in the lung with non-caseating granuloma formation. Imaging features are similar to that of other granulomatous diseases like sarcoidosis. History and beryllium sensitization tests are helpful in making a distinction from sarcoidosis. Beryllium lymphocyte proliferation test (BeLPT) involves culturing lymphocytes with beryllium sulfate. Cells are then counted, and those with an elevated number of cells are considered abnormal, i.e., sensitized to beryllium. Reticulonodular opacities with mid- and upper zonal predominance are seen in chest radiographs. Mass-like opacities, fibrosis, and honeycombing are seen in the later stages. HRCT shows small nodules along peribronchovascular distribution and interlobular nodular septal thickening similar to sarcoidosis (Figs. 13.71 and 13.72). Other findings that may be seen are conglomerating mass, honeycombing, and lymphadenopathy. Berylliosis also increases the risk of lung carcinoma [107, 122].

13.11.7 Chemical Pneumonitis

Chemical pneumonitis is an uncommon OLD that occurs due to inhalation of noxious organic substances, inorganic chemicals (such as ammonia, sulfur dioxide, hydrogen sulfide, nitrogen oxide), and metals (such as mercury, cadmium, nickel, and vanadium). Soluble agents cause upper airway irritation, while less soluble agents reach lower airways producing pulmonary edema-like appearance. CT demonstrates patchy GGO in acute cases. Bronchiolitis obliterans, bronchiectasis, and mosaic perfusion with air-trapping are noted after weeks to months of exposure [108, 123].

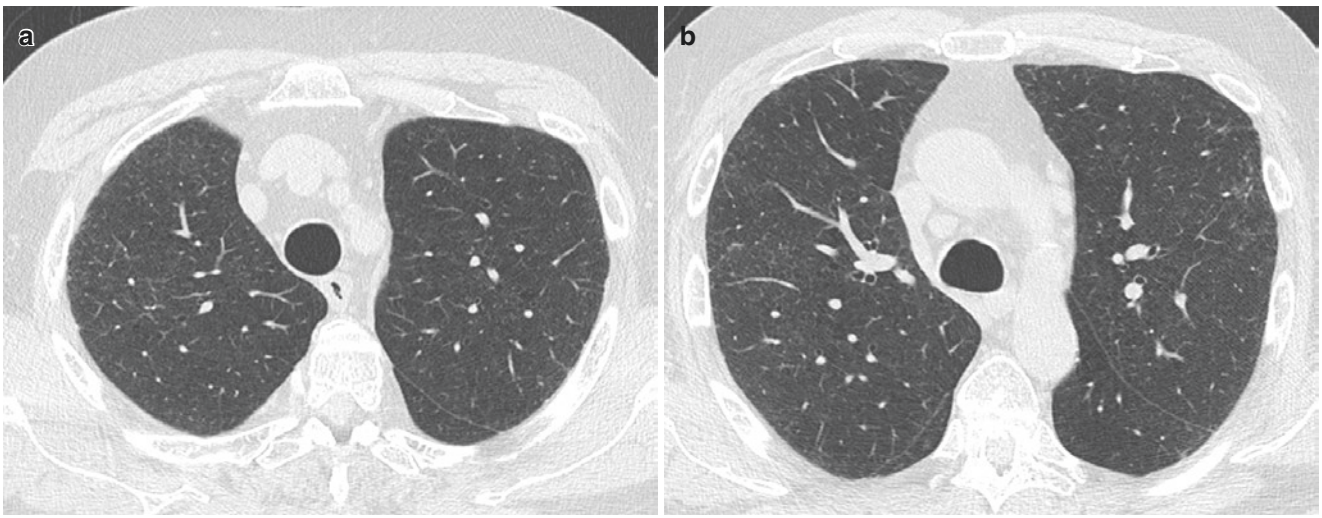

Fig. 13.71 Early berylliosis in a sensitized patient. (**a**, **b**) Axial CT images show fine nodularity with septal and subpleural thickening in upper lungs

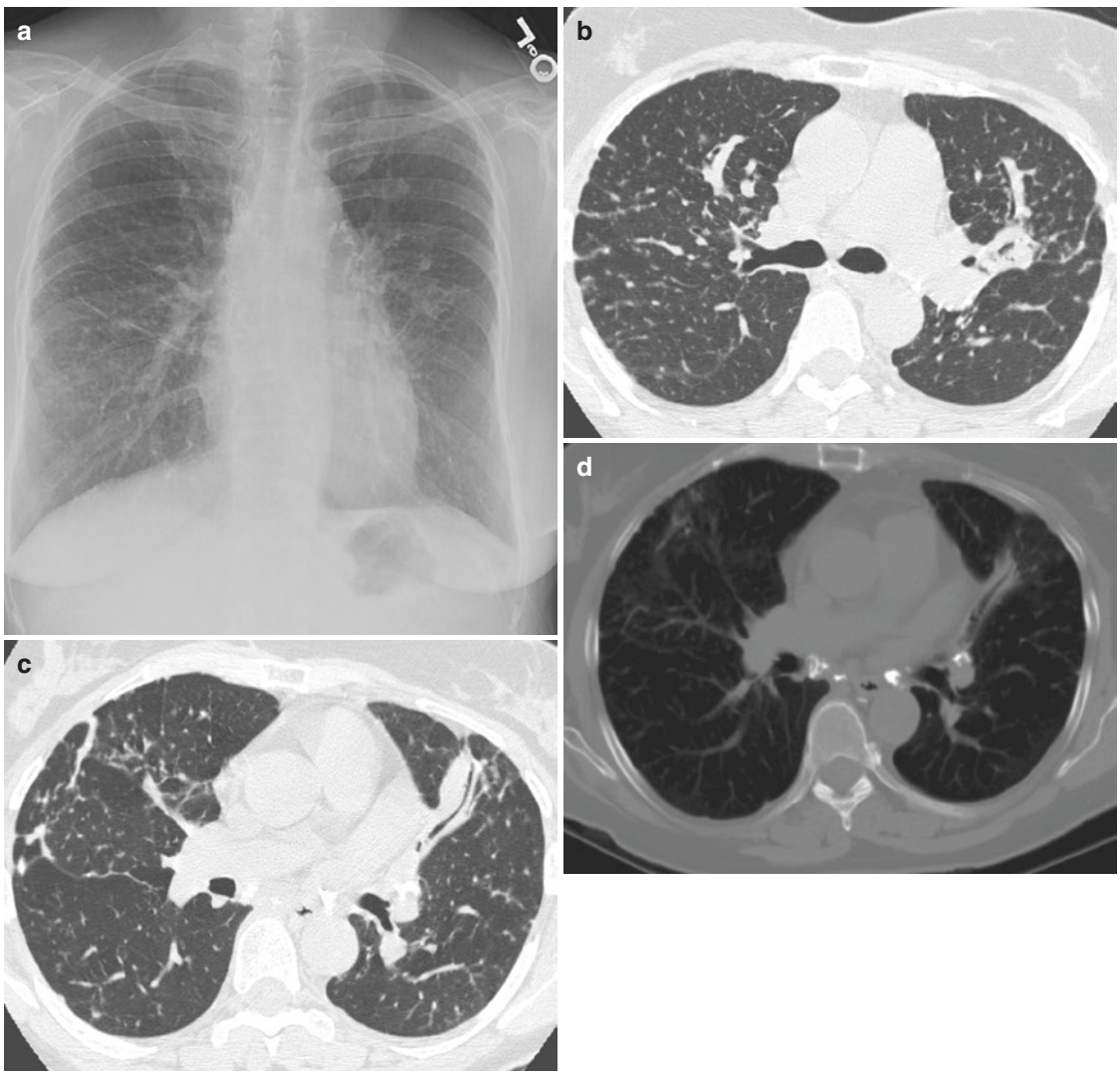

Fig. 13.72 Berylliosis. (**a**) Frontal chest radiograph shows a fine septal thickening in the perihilar region with calcific densities in both hila. (**b**–**d**) Axial CT images show irregular linear opacities, septal thickening, subpleural nodularity, focal atelectasis, and calcified lymph nodes. Note the calcification has "eggshell" pattern

13.11.8 Organic Dust Toxic Syndrome (ODTS)

Previously described with various terminologies including humidifier fever, cotton fever (byssinosis), grain fever, pig fever, and wood chip fever, ODTS encompasses febrile illness that occurs after exposure to inorganic dusts without features of HP. Even though ODTS and HP share some common clinical features, ODTS does not cause permanent functional impairment in the lungs. No distinct imaging features have been described in the current literature, although centrilobular nodules and basal predominant GGO have been reported [108, 123].

13.11.9 Hard Metal Lung Disease

Hard metal lung diseases are caused by exposure to dusts produced in hard metal industry (such as tungsten carbide and cobalt). The diagnostic criteria include a combination of various factors such as history of exposure, characteristic clinical findings (breathlessness, cough, dyspnea on exertion), radiologic features of ILD, histologic features (giant cell interstitial pattern), and pathological demonstration of metallic content in the lung tissue [107, 124, 125].

References

1. Kazerooni EA. High-resolution CT of the lungs. Am J Roentgenol. 2001;177(3):501–19.
2. Mayo JR. CT evaluation of diffuse infiltrative lung disease: dose considerations and optimal technique. J Thorac Imaging. 2009;24(4):252–9.
3. Oswald N, Parkinson T. Honeycomb lungs. QJM Int J Med. 1949;18(1):1–20.
4. Meyer EC, Liebow AA. Relationship of interstitial pneumonia honeycombing and atypical epithelial proliferation to cancer of the lung. Cancer. 1965;18(3):322–51.
5. Raghu G, Collard HR, Egan JJ, Martinez FJ, Behr J, Brown KK, Colby TV, Cordier JF, Flaherty KR, Lasky JA, Lynch DA. An official ATS/ERS/JRS/ALAT statement: idiopathic pulmonary fibrosis: evidence-based guidelines for diagnosis and management. Am J Respir Crit Care Med. 2011;183(6):788–824.
6. Flaherty KR, Thwaite EL, Kazerooni EA, Gross BH, Toews GB, Colby TV, Travis WD, Mumford JA, Murray S, Flint A, Lynch JP. Radiological versus histological diagnosis in UIP and NSIP: survival implications. Thorax. 2003;58(2):143–8.
7. Shin KM, Lee KS, Chung MP, Han J, Bae YA, Kim TS, Chung MJ. Prognostic determinants among clinical, thin-section CT, and histopathologic findings for fibrotic idiopathic interstitial pneumonias: tertiary hospital study. Radiology. 2008;249(1):328–37.
8. Hansell DM, Bankier AA, MacMahon H, McLoud TC, Muller NL, Remy J. Fleischner Society: glossary of terms for thoracic imaging. Radiology. 2008;246(3):697–722.
9. Johkoh T, Sakai F, Noma S, Akira M, Fujimoto K, Watadani T, Sugiyama Y. Honeycombing on CT; its definition, pathologic correlation, and future direction of its diagnosis. Eur J Radiol. 2014;83(1):27–31.
10. Arakawa H, Honma K. Honeycomb lung: history and current concepts. Am J Roentgenol. 2011;196(4):773–82.
11. Piciucchi S, Tomassetti S, Ravaglia C, Gurioli C, Gurioli C, Dubini A, Carloni A, Chilosi M, Colby TV, Poletti V. From "traction bronchiectasis" to honeycombing in idiopathic pulmonary fibrosis: a spectrum of bronchiolar remodeling also in radiology. BMC Pulm Med. 2016;16(1):87.
12. Mino M, Noma S, Kobashi Y, Iwata T. Serial changes of cystic air spaces in fibrosing alveolitis: a CT-pathological study. Clin Radiol. 1995;50(6):357–63.
13. Sumikawa H, Johkoh T, Colby TV, Ichikado K, Suga M, Taniguchi H, Kondoh Y, Ogura T, Arakawa H, Fujimoto K, Inoue A. Computed tomography findings in pathological usual interstitial pneumonia: relationship to survival. Am J Respir Crit Care Med. 2008;177(4):433–9.
14. Kligerman SJ, Henry T, Lin CT, Franks TJ, Galvin JR. Mosaic attenuation: etiology, methods of differentiation, and pitfalls. Radiographics. 2015;35(5):1360–80.
15. Stern EJ, Swensen SJ, Hartman TE, Frank MS. CT mosaic pattern of lung attenuation: distinguishing different causes. AJR Am J Roentgenol. 1995;165(4):813–6.
16. Mets OM, Zanen P, Lammers JW, Isgum I, Gietema HA, van Ginneken B, Prokop M, de Jong PA. Early identification of small airways disease on lung cancer screening CT: comparison of current air trapping measures. Lung. 2012;190(6):629–33.
17. Arakawa H, Webb WR. Air trapping on expiratory high-resolution CT scans in the absence of inspiratory scan abnormalities: correlation with pulmonary function tests and differential diagnosis. AJR Am J Roentgenol. 1998;170(5):1349–53.
18. Gaeta M, Minutoli F, Girbino G, Murabito A, Benedetto C, Contiguglia R, Ruggeri P, Privitera S. Expiratory CT scan in patients with normal inspiratory CT scan: a finding of obliterative bronchiolitis and other causes of bronchiolar obstruction. Multidiscip Respir Med. 2013;8(1):44.
19. Arakawa H, Kurihara Y, Sasaka K, Nakajima Y, Webb WR. Air trapping on CT of patients with pulmonary embolism. AJR Am J Roentgenol. 2002;178(5):1201–7.
20. Baroni RH, Feller-Kopman D, Nishino M, Hatabu H, Loring SH, Ernst A, Boiselle PM. Tracheobronchomalacia: comparison between end-expiratory and dynamic expiratory CT for evaluation of central airway collapse. Radiology. 2005;235(2):635–41.
21. Mays EE, Dubois JJ, Hamilton GB. Pulmonary fibrosis associated with tracheobronchial aspiration: a study of the frequency of hiatal hernia and gastroesophageal reflux in interstitial pulmonary fibrosis of obscure etiology. Chest. 1976;69(4):512–5.
22. Soares RV, Forsythe A, Hogarth K, Sweiss NJ, Noth I, Patti MG. Interstitial lung disease and gastroesophageal reflux disease: key role of esophageal function tests in the diagnosis and treatment. Arq Gastroenterol. 2011;48(2):91–7.
23. Tobin RW, Pope CE 2nd, Pellegrini CA, Emond MJ, Sillery J, Raghu G. Increased prevalence of gastroesophageal reflux in patients with idiopathic pulmonary fibrosis. Am J Respir Crit Care Med. 1998;158:1804–8.
24. Fagundes MN, Caleiro MT, Navarro-Rodriguez T, Baldi BG, Kavakama J, Salge JM, Kairalla R, Carvalho CR. Esophageal involvement and interstitial lung disease in mixed connective tissue disease. Respir Med. 2009;103(6):854–60.
25. Vonk MC, Van Die CE, Snoeren MM, Bhansing KJ, van Riel PL, Fransen J, van den Hoogen FH. Oesophageal dilatation on high-resolution computed tomography scan of the lungs as a sign of scleroderma. Ann Rheum Dis. 2008;67(9):1317–21.
26. Pitrez EH, Bredemeier M, Xavier RM, Capobianco KG, Restelli VG, Vieira MV, Ludwig DH, Brenol JC, Furtado AP, Fonseca LM, Gutfilen B. Oesophageal dysmotility in systemic sclerosis: comparison of HRCT and scintigraphy. Br J Radiol. 2006;79(945):719–24.
27. Noth I, Zangan SM, Soares RV, Forsythe A, Demchuk C, Takahashi SM, Patel SB, Strek ME, Krishnan JA, Patti MG, MacMahon

H. Prevalence of hiatal hernia by blinded multidetector CT in patients with idiopathic pulmonary fibrosis. Eur Respir J. 2012;39(2):344–51.
28. Johannson KA, Strâmbu I, Ravaglia C, Grutters JC, Valenzuela C, Mogulkoc N, Luppi F, Richeldi L, Wells AU, Vancheri C, Kreuter M. Antacid therapy in idiopathic pulmonary fibrosis: more questions than answers? Lancet Respir Med. 2017;5(7):591–8.
29. Truong QA, Massaro JM, Rogers IS, Mahabadi AA, Kriegel MF, Fox CS, O'donnell CJ, Hoffmann U. Reference values for normal pulmonary artery dimensions by noncontrast cardiac computed tomographyclinical perspective: the Framingham Heart Study. Circ Cardiovasc Imaging. 2012;5(1):147–54.
30. Tan RT, Kuzo R, Goodman LR, Siegel R, Haasler GR, Presberg KW. Utility of CT scan evaluation for predicting pulmonary hypertension in patients with parenchymal lung disease. Chest. 1998;113(5):1250–6.
31. Edwards PD, Bull RK, Coulden R. CT measurement of main pulmonary artery diameter. Br J Radiol. 1998;71(850):1018–20.
32. Ng CS, Wells AU, Padley SP. A CT sign of chronic pulmonary arterial hypertension: the ratio of main pulmonary artery to aortic diameter. J Thorac Imaging. 1999;14(4):270–8.
33. Montanil D, Zisman DA, Karlamangla AS, Ross DJ, Keane MP, Belperio JA, Saggar R. High-resolution chest CT findings do not predict the presence of pulmonary hypertension in advanced idiopathic pulmonary fibrosis. Chest. 2007;132:773.
34. Devaraj A, Wells AU, Meister MG, Corte TJ, Hansell DM. The effect of diffuse pulmonary fibrosis on the reliability of CT signs of pulmonary hypertension. Radiology. 2008;249(3):1042–9.
35. Fischer A, Misumi S, Curran-Everett D, Meehan RT, Ulrich SK, Swigris JJ, Frankel SK, Cosgrove GP, Lynch DA, Brown KK. Pericardial abnormalities predict the presence of echocardiographically defined pulmonary arterial hypertension in systemic sclerosis-related interstitial lung disease. Chest. 2007;131(4):988–92.
36. Baque-Juston MC, Wells AU, Hansell DM. Pericardial thickening or effusion in patients with pulmonary artery hypertension: a CT study. AJR Am J Roentgenol. 1999;172(2):361–4.
37. Akdeniz B, Ozpelit E. Which prognostic factors should be used in pulmonary arterial hypertension in elderly patients? J Geriatr Cardiol JGC. 2017;14(1):28.
38. Bhalla ME, Silver RM, Shepard JA, McLoud TC. Chest CT in patients with scleroderma: prevalence of asymptomatic esophageal dilatation and mediastinal lymphadenopathy. AJR Am J Roentgenol. 1993;161(2):269–72.
39. Hobbs S, Lynch D. The idiopathic interstitial pneumonias: an update and review. Radiol Clin. 2014;52(1):105–20.
40. Travis WD, Costabel U, Hansell DM, King TE Jr, Lynch DA, Nicholson AG, Ryerson CJ, Ryu JH, Selman M, Wells AU, Behr J. An official American Thoracic Society/European Respiratory Society statement: update of the international multidisciplinary classification of the idiopathic interstitial pneumonias. Am J Respir Crit Care Med. 2013;188(6):733–48.
41. Monaghan H, Wells AU, Colby TV, Du Bois RM, Hansell DM, Nicholson AG. Prognostic implications of histologic patterns in multiple surgical lung biopsies from patients with idiopathic interstitial pneumonias. Chest. 2004;125(2):522–6.
42. Lynch DA, Travis WD, Muller NL, Galvin JR, Hansell DM, Grenier PA, King TE Jr. Idiopathic interstitial pneumonias: CT features. Radiology. 2005;236(1):10–21.
43. Ferguson EC, Berkowitz EA. Lung CT: Part 2, The interstitial pneumonias—clinical, histologic, and CT manifestations. Am J Roentgenol. 2012;199(4):W464–76.
44. Mueller-Mang C, Grosse C, Schmid K, Stiebellehner L, Bankier AA. What every radiologist should know about idiopathic interstitial pneumonias. Radiographics. 2007;27(3):595–615.
45. Hashisako M, Fukuoka J. Pathology of idiopathic interstitial pneumonias. Clin Med Insights Circ Respir Pulm Med. 2015;9:123–33.
46. Kim TS, Han J, Chung MP, Chung MJ, Choi YS. Disseminated dendriform pulmonary ossification associated with usual interstitial pneumonia: incidence and thin-section CT–pathologic correlation. Eur Radiol. 2005;15(8):1581–5.
47. Gruden JF, Green DB, Legasto AC, Jensen EA, Panse PM. Dendriform pulmonary ossification in the absence of usual interstitial pneumonia: CT features and possible association with recurrent acid aspiration. Am J Roentgenol. 2017;209(6):1209–15.
48. Fell CD, Martinez FJ, Liu LX, Murray S, Han MK, Kazerooni EA, Gross BH, Myers J, Travis WD, Colby TV, Toews GB. Clinical predictors of a diagnosis of idiopathic pulmonary fibrosis. Am J Respir Crit Care Med. 2010;181(8):832–7.
49. Raghu G, Lynch D, Godwin JD, Webb R, Colby TV, Leslie KO, Behr J, Brown KK, Egan JJ, Flaherty KR, Martinez FJ. Diagnosis of idiopathic pulmonary fibrosis with high-resolution CT in patients with little or no radiological evidence of honeycombing: secondary analysis of a randomised, controlled trial. Lancet Respir Med. 2014;2(4):277–84.
50. Chung JH, Oldham JM, Montner SM, Vij R, Adegunsoye A, Husain AN, Noth I, Lynch DA, Strek ME. CT-pathologic correlation of major types of pulmonary fibrosis: insights for revisions to current guidelines. Am J Roentgenol. 2018;210(5):1034–41.
51. Lynch DA, Sverzellati N, Travis WD, Brown KK, Colby TV, Galvin JR, Goldin JG, Hansell DM, Inoue Y, Johkoh T, Nicholson AG. Diagnostic criteria for idiopathic pulmonary fibrosis: a Fleischner Society White Paper. Lancet Respir Med. 2017. https://doi.org/10.1016/S2213-2600(17)30433-2.
52. Sverzellati N, Wells AU, Tomassetti S, Desai SR, Copley SJ, Aziz ZA, Zompatori M, Chilosi M, Nicholson AG, Poletti V, Hansell DM. Biopsy-proved idiopathic pulmonary fibrosis: spectrum of nondiagnostic thin-section CT diagnoses. Radiology. 2010;254(3):957–64.
53. Chung JH, Chawla A, Peljto AL, Cool CD, Groshong SD, Talbert JL, McKean DF, Brown KK, Fingerlin TE, Schwarz MI, Schwartz DA. CT scan findings of probable usual interstitial pneumonitis have a high predictive value for histologic usual interstitial pneumonitis. Chest. 2015;147(2):450–9.
54. Lloyd CR, Walsh SL, Hansell DM. High-resolution CT of complications of idiopathic fibrotic lung disease. Br J Radiol. 2011;84(1003):581–92.
55. Franquet T, Gimenez A, Torrubia S, Sabate JM, Rodriguez-Arias JM. Spontaneous pneumothorax and pneumomediastinum in IPF. Eur Radiol. 2000;10(1):108–13.
56. Chung MJ, Goo JM, Im JG. Pulmonary tuberculosis in patients with idiopathic pulmonary fibrosis. Eur J Radiol. 2004;52(2):175–9.
57. Vidal S, De la Horra C, Martin J, Montes-Cano MA, Rodríguez E, Respaldiza N, Rodriguez F, Varela JM, Medrano FJ, Calderón EJ. Pneumocystis jirovecii colonisation in patients with interstitial lung disease. Clin Microbiol Infect. 2006;12(3):231–5.
58. Collard HR, Ryerson CJ, Corte TJ, Jenkins G, Kondoh Y, Lederer DJ, Lee JS, Maher TM, Wells AU, Antoniou KM, Behr J. Acute exacerbation of idiopathic pulmonary fibrosis. An international working group report. Am J Respir Crit Care Med. 2016;194(3):265–75.
59. Kim DS, Park JH, Park BK, Lee JS, Nicholson AG, Colby T. Acute exacerbation of idiopathic pulmonary fibrosis: frequency and clinical features. Eur Respir J. 2006;27(1):143–50.
60. Silva CI, Müller NL, Fujimoto K, Kato S, Ichikado K, Taniguchi H, Kondoh Y, Johkoh T, Churg A. Acute exacerbation of chronic interstitial pneumonia: high-resolution computed tomography and pathologic findings. J Thorac Imaging. 2007;22(3):221–9.
61. Akira M, Hamada H, Sakatani M, Kobayashi C, Nishioka M, Yamamoto S. CT findings during phase of accelerated deterioration in patients with idiopathic pulmonary fibrosis. AJR Am J Roentgenol. 1997;168(1):79–83.
62. Churg A, Müller NL, Silva CI, Wright JL. Acute exacerbation (acute lung injury of unknown cause) in UIP and other forms of fibrotic interstitial pneumonias. Am J Surg Pathol. 2007;31(2):277–84.

63. Hubbard R, Venn A, Lewis S, Britton J. Lung cancer and cryptogenic fibrosing alveolitis: a population-based cohort study. Am J Respir Crit Care Med. 2000;161(1):5–8.
64. Souza CA, Müller NL, Lee KS, Johkoh T, Mitsuhiro H, Chong S. Idiopathic interstitial pneumonias: prevalence of mediastinal lymph node enlargement in 206 patients. Am J Roentgenol. 2006;186(4):995–9.
65. Swensen SJ, Aughenbaugh GL, Myers JL. Diffuse lung disease: diagnostic accuracy of CT in patients undergoing surgical biopsy of the lung. Radiology. 1997;205(1):229–34.
66. Lee KS, Primack SL, Staples CA, Mayo JR, Aldrich JE, Müller NL. Chronic infiltrative lung disease: comparison of diagnostic accuracies of radiography and low-and conventional-dose thin-section CT. Radiology. 1994;191(3):669–73.
67. Raghu G, Mageto YN, Lockhart D, Schmidt RA, Wood DE, Godwin JD. The accuracy of the clinical diagnosis of new-onset idiopathic pulmonary fibrosis and other interstitial lung disease: a prospective study. Chest. 1999;116(5):1168–74.
68. Walsh SL, Calandriello L, Sverzellati N, Wells AU, Hansell DM. Interobserver agreement for the ATS/ERS/JRS/ALAT criteria for a UIP pattern on CT. Thorax. 2016;71:45–51.
69. Watadani T, Sakai F, Johkoh T, Noma S, Akira M, Fujimoto K, Bankier AA, Lee KS, Müller NL, Song JW, Park JS. Interobserver variability in the CT assessment of honeycombing in the lungs. Radiology. 2013;266(3):936–44.
70. Flaherty KR, Toews GB, Travis WD, Colby TV, Kazerooni EA, Gross BH, Jain A, Strawderman RL, Paine R, Flint A, Lynch JP. Clinical significance of histological classification of idiopathic interstitial pneumonia. Eur Respir J. 2002;19(2):275–83.
71. Gay SE, Kazerooni EA, Toews GB, Lynch III JP, Gross BH, Cascade PN, Spizarny DL, Flint A, Anthony Schork M, Whyte RI, Popovich J. Idiopathic pulmonary fibrosis: predicting response to therapy and survival. Am J Respir Crit Care Med. 1998;157(4):1063–72.
72. Park JH, Kim DS, Park IN, Jang SJ, Kitaichi M, Nicholson AG, Colby TV. Prognosis of fibrotic interstitial pneumonia: idiopathic versus collagen vascular disease–related subtypes. Am J Respir Crit Care Med. 2007;175(7):705–11.
73. Silva CI, Muller NL, Hansell DM, Lee KS, Nicholson AG, Wells AU. Nonspecific interstitial pneumonia and idiopathic pulmonary fibrosis: changes in pattern and distribution of disease over time. Radiology. 2008;247(1):251–9.
74. Tsubamoto M, Müller NL, Johkoh T, Ichikado K, Taniguchi H, Kondoh Y, Fujimoto K, Arakawa H, Koyama M, Kozuka T, Inoue A. Pathologic subgroups of nonspecific interstitial pneumonia: differential diagnosis from other idiopathic interstitial pneumonias on high-resolution computed tomography. J Comput Assist Tomogr. 2005;29(6):793–800.
75. Flaherty KR, Travis WD, Colby TV, Toews GB, Kazerooni EA, Gross BH, Jain A, Strawderman III RL, Flint A, Lynch III JP, Martinez FJ. Histopathologic variability in usual and nonspecific interstitial pneumonias. Am J Respir Crit Care Med. 2001;164(9):1722–7.
76. Travis WD, Matsui K, Moss J, Ferrans VJ. Idiopathic nonspecific interstitial pneumonia: prognostic significance of cellular and fibrosing patterns: survival comparison with usual interstitial pneumonia and desquamative interstitial pneumonia. Am J Surg Pathol. 2000;24(1):19.
77. Akira M, Inoue Y, Arai T, Okuma T, Kawata Y. Long-term follow-up high-resolution CT findings in non-specific interstitial pneumonia. Thorax. 2011;66(1):61–5.
78. Lee JS, Lynch DA, Sharma S, Brown KK, Müller NL. Organizing pneumonia: prognostic implication of high-resolution computed tomography features. J Comput Assist Tomogr. 2003;27(2):260–5.
79. Lee JW, Lee KS, Lee HY, Chung MP, Yi CA, Kim TS, Chung MJ. Cryptogenic organizing pneumonia: serial high-resolution CT findings in 22 patients. Am J Roentgenol. 2010;195(4):916–22.
80. Kim SJ, Lee KS, Ryu YH, Yoon YC, Choe KO, Kim TS, Sung KJ. Reversed halo sign on high-resolution CT of cryptogenic organizing pneumonia: diagnostic implications. Am J Roentgenol. 2003;180(5):1251–4.
81. Ujita M, Renzoni EA, Veeraraghavan S, Wells AU, Hansell DM. Organizing pneumonia: perilobular pattern at thin-section CT. Radiology. 2004;232(3):757–61.
82. Primack SL, Hartman TE, Ikezoe J, Akira M, Sakatani M, Müller NL. Acute interstitial pneumonia: radiographic and CT findings in nine patients. Radiology. 1993;188(3):817–20.
83. Ichikado K, Johkoh T, Ikezoe J, Takeuchi N, Kohno N, Arisawa J, Nakamura H, Nagareda T, Itoh H, Ando M. Acute interstitial pneumonia: high-resolution CT findings correlated with pathology. AJR Am J Roentgenol. 1997;168(2):333–8.
84. Reddy TL, Tominaga M, Hansell DM, von der Thusen J, Rassl D, Parfrey H, Guy S, Twentyman O, Rice A, Maher TM, Renzoni EA. Pleuroparenchymal fibroelastosis: a spectrum of histopathological and imaging phenotypes. Eur Respir J. 2012;40(2):377–85.
85. Frankel SK, Cool CD, Lynch DA, Brown KK. Idiopathic pleuroparenchymal fibroelastosis: description of a novel clinicopathologic entity. Chest. 2004;126(6):2007–13.
86. Chung JH, Cox CW, Montner SM, Adegunsoye A, Oldham JM, Husain AN, Vij R, Noth I, Lynch DA, Strek ME. CT features of the usual interstitial pneumonia pattern: differentiating connective tissue disease–associated interstitial lung disease from idiopathic pulmonary fibrosis. Am J Roentgenol. 2018;210(2):307–13.
87. Massey H, Darby M, Edey A. Thoracic complications of rheumatoid disease. Clin Radiol. 2013;68(3):293–301.
88. Ahuja J, Arora D, Kanne JP, Henry TS, Godwin JD. Imaging of pulmonary manifestations of connective tissue diseases. Radiol Clin. 2016;54(6):1015–31.
89. Lynch DA. Lung disease related to collagen vascular disease. J Thorac Imaging. 2009;24(4):299–309.
90. Henry TS, Little BP, Veeraraghavan S, Bhalla S, Elicker BM. The spectrum of interstitial lung disease in connective tissue disease. J Thorac Imaging. 2016;31(2):65–77.
91. Tanaka N, Kim JS, Newell JD, Brown KK, Cool CD, Meehan R, Emoto T, Matsumoto T, Lynch DA. Rheumatoid arthritis–related lung diseases: CT findings. Radiology. 2004;232(1):81–91.
92. Franquet T, Gimenez A, Monill JM, Diaz C, Geli C. Primary Sjögren's syndrome and associated lung disease: CT findings in 50 patients. AJR Am J Roentgenol. 1997;169(3):655–8.
93. Rajagopala S, Singh N, Gupta K, Gupta D. Pulmonary amyloidosis in Sjogren's syndrome: a case report and systematic review of the literature. Respirology. 2010;15(5):860–6.
94. Tanizawa K, Handa T, Nakashima R, Kubo T, Hosono Y, Watanabe K, Aihara K, Oga T, Chin K, Nagai S, Mimori T. HRCT features of interstitial lung disease in dermatomyositis with anti-CADM-140 antibody. Respir Med. 2011;105(9):1380–7.
95. Waseda Y, Johkoh T, Egashira R, Sumikawa H, Saeki K, Watanabe S, Matsunuma R, Takato H, Ichikawa Y, Hamaguchi Y, Shiraki A. Antisynthetase syndrome: pulmonary computed tomography findings of adult patients with antibodies to aminoacyl-tRNA synthetases. Eur J Radiol. 2016;85(8):1421–6.
96. Debray MP, Borie R, Revel MP, Naccache JM, Khalil A, Toper C, Israel-Biet D, Estellat C, Brillet PY. Interstitial lung disease in anti-synthetase syndrome: initial and follow-up CT findings. Eur J Radiol. 2015;84(3):516–23.
97. Fischer A, Antoniou KM, Brown KK, Cadranel J, Corte TJ, Du Bois RM, Lee JS, Leslie KO, Lynch DA, Matteson EL, Mosca M. An official European Respiratory Society/American Thoracic Society research statement: interstitial pneumonia with autoimmune features. Eur Respir J. 2015;46:976–87.
98. Silva CI, Churg A, Müller NL. Hypersensitivity pneumonitis: spectrum of high-resolution CT and pathologic findings. Am J Roentgenol. 2007;188(2):334–44.

99. Hirschmann JV, Pipavath SN, Godwin JD. Hypersensitivity pneumonitis: a historical, clinical, and radiologic review. Radiographics. 2009;29(7):1921–38.
100. Selman M, Pardo A, King TE Jr. Hypersensitivity pneumonitis: insights in diagnosis and pathobiology. Am J Respir Crit Care Med. 2012;186(4):314–24.
101. Lynch JP, Kazerooni EA, Gay SE. Pulmonary sarcoidosis. Clin Chest Med. 1997;18(4):755–85.
102. Criado E, Sánchez M, Ramírez J, Arguis P, de Caralt TM, Perea RJ, Xaubet A. Pulmonary sarcoidosis: typical and atypical manifestations at high-resolution CT with pathologic correlation. Radiographics. 2010;30(6):1567–86.
103. Park HJ, Jung JI, Chung MH, Song SW, Kim HL, Baik JH, Han DH, Kim KJ, Lee KY. Typical and atypical manifestations of intrathoracic sarcoidosis. Korean J Radiol. 2009;10(6):623–31.
104. Nakatsu M, Hatabu H, Morikawa K, et al. Large coalescent parenchymal nodules in pulmonary sarcoidosis: "sarcoid galaxy" sign. AJR Am J Roentgenol. 2002;178(6):1389–93.
105. Honda O, Johkoh T, Ichikado K, et al. Comparison of high resolution CT findings of sarcoidosis, lymphoma, and lymphangitic carcinoma: is there any difference of involved interstitium? J Comput Assist Tomogr. 1999;23(3):374–9.
106. Champlin J, Edwards R, Pipavath S. Imaging of occupational lung disease. Radiol Clin N Am. 2016;54(6):1077–96.
107. Chong S, Lee KS, Chung MJ, Han J, Kwon OJ, Kim TS. Pneumoconiosis: comparison of imaging and pathologic findings. Radiographics. 2006;26(1):59–77.
108. Kim KI, Kim CW, Lee MK, Lee KS, Park CK, Choi SJ, et al. Imaging of occupational lung disease. Radiographics. 2001;21(6):1371–91.
109. Pipavath SNJ, Godwin JD, Kanne JP. Occupational lung disease: a radiologic review. Semin Roentgenol. 2010;45(1):43–52.
110. Marchiori E, Souza CA, Barbassa TG, Escuissato DL, Gasparetto EL, Souza AS. Silicoproteinosis: high-resolution CT findings in 13 patients. AJR Am J Roentgenol. 2007;189(6):1402–6.
111. Steenland K, Ward E. Silica: a lung carcinogen. CA Cancer J Clin. 2014;64(1):63–9.
112. Ng TP, Chan SL, Lee J. Predictors of mortality in silicosis. Respir Med. 1992;86(2):115–9.
113. Williams JL, Moller GA. Solitary mass in the lungs of coal miners. Am J Roentgenol. 1973;117(4):765–70.
114. Tomášková H, Šplíchalová A, Šlachtová H, Urban P, Hajduková Z, Landecká I, et al. Mortality in miners with coal-workers' pneumoconiosis in the Czech Republic in the period 1992–2013. Int J Environ Res Public Health. 2017;14(3):269.
115. Roach HD, Davies GJ, Attanoos R, Crane M, Adams H, Phillips S. Asbestos: when the dust settles an imaging review of asbestos-related disease. Radiographics. 2002;22:S167–84.
116. Peacock C, Copley SJ, Hansell DM. Asbestos-related benign pleural disease. Clin Radiol. 2000;55(6):422–32.
117. McLoud TC, Woods BO, Carrington CB, Epler GR, Gaensler EA. Diffuse pleural thickening in an asbestos-exposed population: prevalence and causes. AJR Am J Roentgenol. 1985;144(1):9–18.
118. Staples CA. Computed tomography in the evaluation of benign asbestos-related disorders. Radiol Clin N Am. 1992;30(6):1191–207.
119. Hodgson JT, Darnton A. The quantitative risks of mesothelioma and lung cancer in relation to asbestos exposure. Ann Occup Hyg. 2000;44(8):565–601.
120. Padley SP, Adler BD, Staples CA, Miller RR, Müller NL. Pulmonary talcosis: CT findings in three cases. Radiology. 1993;186(1):125–7.
121. Marchiori E, Souza Júnior AS, Müller NL. Inhalational pulmonary talcosis: high-resolution CT findings in 3 patients. J Thorac Imaging. 2004;19(1):41–4.
122. Harris KM, McConnochie K, Adams H. The computed tomographic appearances in chronic berylliosis. Clin Radiol. 1993;47(1):26–31.
123. Satija B, Kumar S, Ojha UC, Gothi D. Spectrum of high-resolution computed tomography imaging in occupational lung disease. Indian J Radiol Imaging. 2013;23(4):287–96.
124. Fischbein A, Luo JC, Solomon SJ, Horowitz S, Hailoo W, Miller A. Clinical findings among hard metal workers. Br J Ind Med. 1992;49(1):17–24.
125. Choi JW, Lee KS, Chung MP, Han J, Chung MJ, Park JS. Giant cell interstitial pneumonia: high-resolution CT and pathologic findings in four adult patients. AJR Am J Roentgenol. 2005;184(1):268–72.

Imaging of Miscellaneous Diseases

14

Ashish Chawla

14.1 Introduction

There are many other diseases affecting the lungs that are described briefly in this chapter. These can be encountered in the emergency department or can be discovered incidentally.

14.2 Asthma and Its Complications

Patients with asthma present to the emergency department with acute exacerbation and/or many other complications (Table 14.1). Chest radiography must be avoided in a patient with known asthma who is responding to treatment. The chest radiograph is indicated if the patient does not respond to treatment or if any serious complication like pneumothorax is suspected. Most of the time, the chest radiograph is normal or may show signs of hyperinflation (increased lung volumes and flattening of diaphragms) [1] (Fig. 14.1). CT of the thorax is performed to evaluate complications of asthma and to rule out other conditions mimicking asthma. The most common CT findings in asthmatic patients are increased lung volumes and features of small and large airway disease (bronchial dilatation, bronchial wall thickening, air trapping, centrilobular nodularity, and mild tree-in-bud opacities) (Fig. 14.2). The extent of airway wall thickening and expiratory air trapping correlates directly with the severity of the disease and can be measured quantitatively on CT [2, 3]. There is a growing focus on these quantitative methods that may serve as prognostic markers.

Radiological features of spontaneous pneumomediastinum have been discussed in detail in Chap. 8. High level of suspicion is required in a young asthmatic patient who typically presents to the emergency department with chest pain. The findings can be subtle on a frontal chest radiograph and can be overlooked (Fig. 14.3).

Idiopathic chronic eosinophilic pneumonia (ICEP) and asthma are frequently associated with each other. Approximately, half of the ICEP patients have a history of asthma [4, 5]. Asthma commonly precedes the diagnosis of ICEP and less often develops after ICEP. The occurrence of idiopathic chronic eosinophilic pneumonia in asthmatics is often associated with the development of severe asthma. Chest radiograph shows peripheral pulmonary infiltrates, usually bilateral but may be unilateral in few cases. Always apical predominant, when these opacities surround the lung, the appearance is that of a photographic negative or reversal of the shadows, which is frequently seen in pulmonary edema [6] (Fig. 14.4). The "photographic negative" sign is seen in more than half of the cases of ICEP and is more obvious on CT [7]. CT usually shows upper lung predominant peripheral consolidation and/or ground-glass opacities (Fig. 14.4). Pleural effusion is usually absent, while mediastinal lymph node enlargement can be seen in half of the patients [7]. These CT features are not specific and can also be seen in infection or vasculitis. Blood eosinophilia is present in the majority of the ICEP and is useful to differentiate it from infective pneumonia. In those without eosinophilia, bronchoalveolar lavage (BAL) eosinophilia is supportive of the diagnosis of ICEP. ICEP responds dramatically to steroid therapy with noticeable changes on imaging in 3 days to

Table 14.1 Asthma and associated complications

• Small and large airway disease
• Esophageal wall thickening
• Pneumothorax
• Pneumomediastinum
• Bronchial tear
• Eosinophilic pneumonia
• Infectious pneumonia
• ABPM[a]
• Churg-Strauss vasculitis

[a]Allergic bronchopulmonary aspergillosis

A. Chawla (✉)
Department of Diagnostic Radiology, Khoo Teck Puat Hospital, Singapore, Singapore

A. Chawla (ed.), *Thoracic Imaging*, https://doi.org/10.1007/978-981-13-2544-1_14

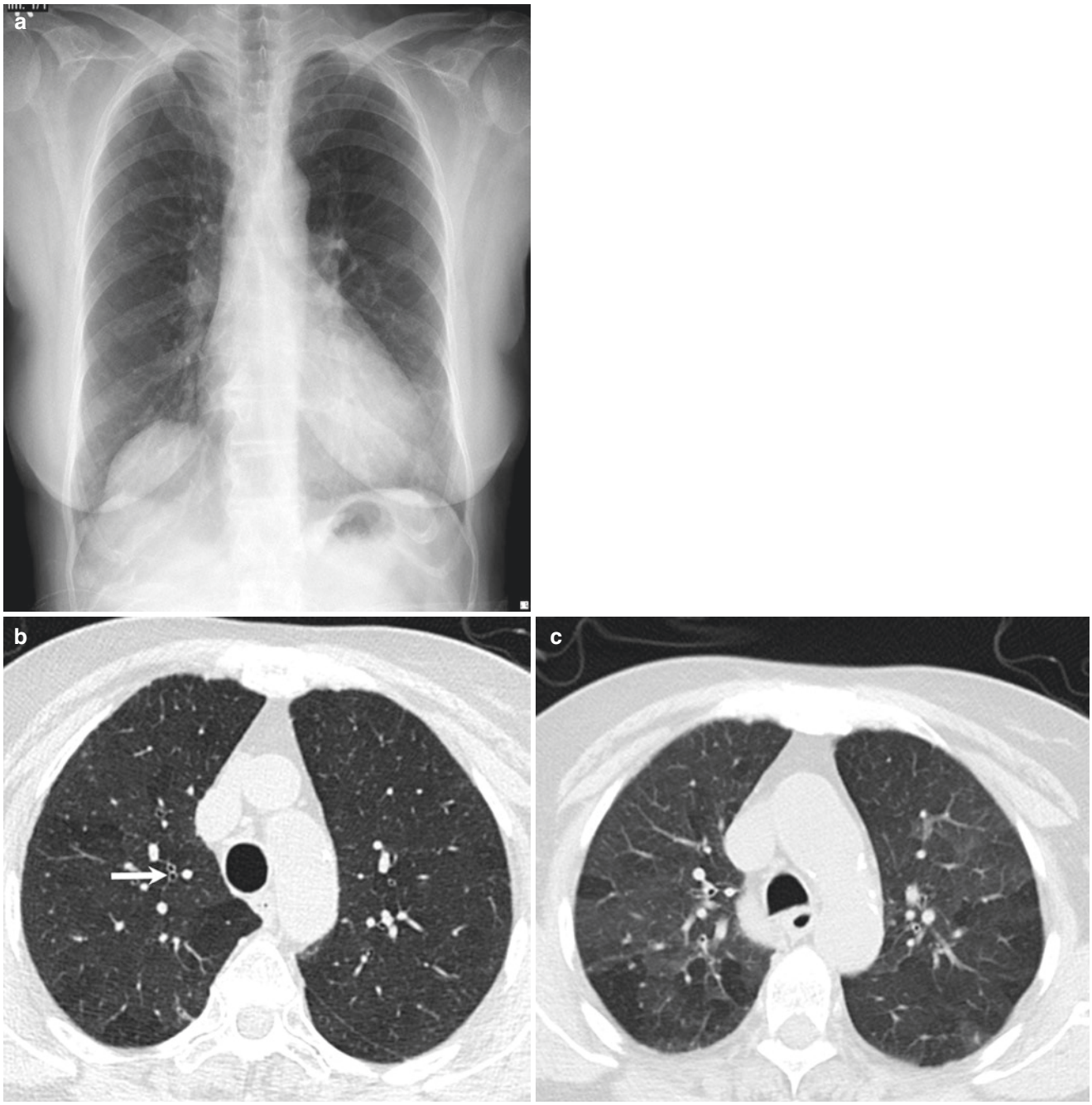

Fig. 14.1 A 39-year-old woman with acute exacerbation of asthma. (**a**) Frontal chest radiograph shows overinflated lungs with increased lung volumes and flattening of the diaphragm. Note the focal eventration of the right hemidiaphragm. (**b**) Inspiratory image shows mosaic attenuation, bronchiole wall thickening (white arrow), and diffuse centrilobular nodularity. (**c**) Expiratory image shows air trapping

complete the resolution in 3 weeks [6]. Relapse of ICEP is not uncommon, and recurrence of peripheral lesions in exactly the same location and of the same size and shape has been well known and is considered further supportive of a diagnosis of ICEP [6].

Allergic bronchopulmonary aspergillosis (ABPA) is a chronic complication of asthma, usually seen in long-term asthma and rarely in cystic fibrosis. ABPA is an immune-mediated inflammatory syndrome caused by hypersensitivity to a ubiquitous fungus, *Aspergillus fumigatus*,

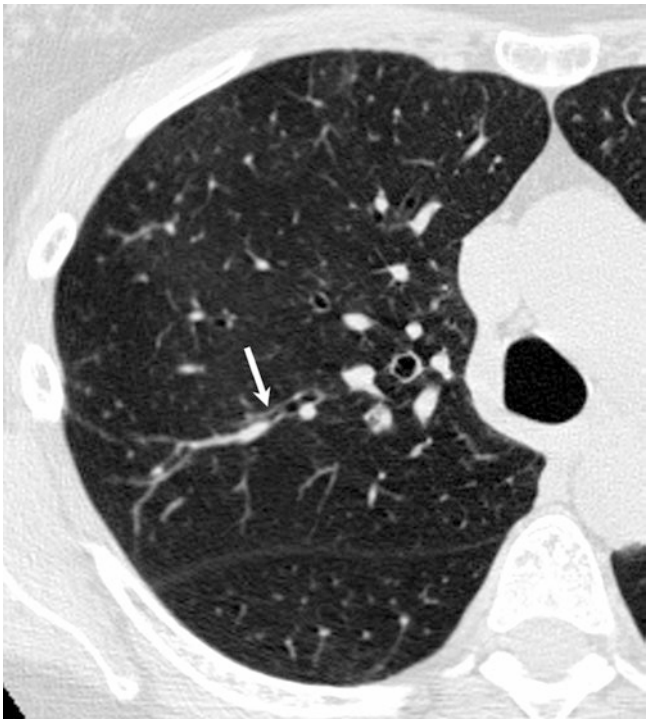

Fig. 14.2 A 56-year-old woman with acute exacerbation of asthma. HRCT shows subtle mosaic attenuation, diffuse centrilobular nodularity, mild bronchial dilatation, and bronchial wall thickening (white arrow)

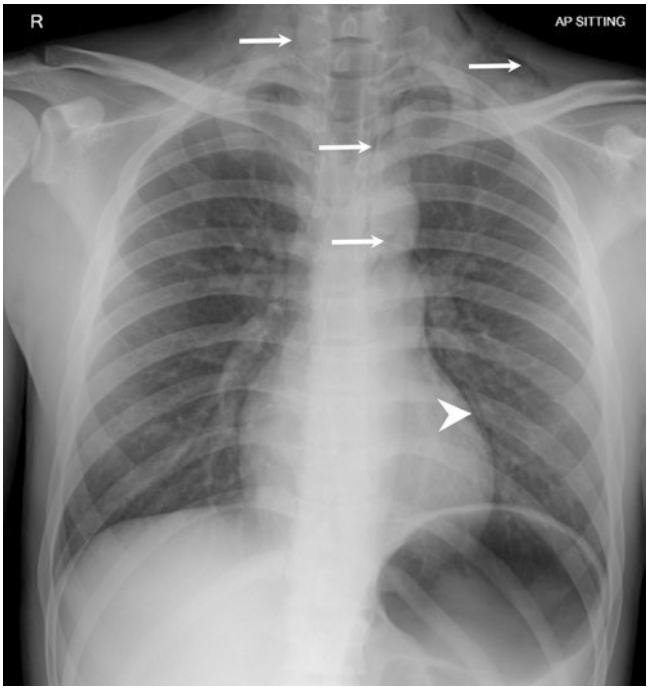

Fig. 14.3 A 29-year-old asthmatic presenting to emergency department with acute onset chest pain. Frontal chest radiograph shows paracardiac lucency (arrowhead) and streaky lucencies over the mediastinum extending in the neck and supraclavicular fossa (white arrows)

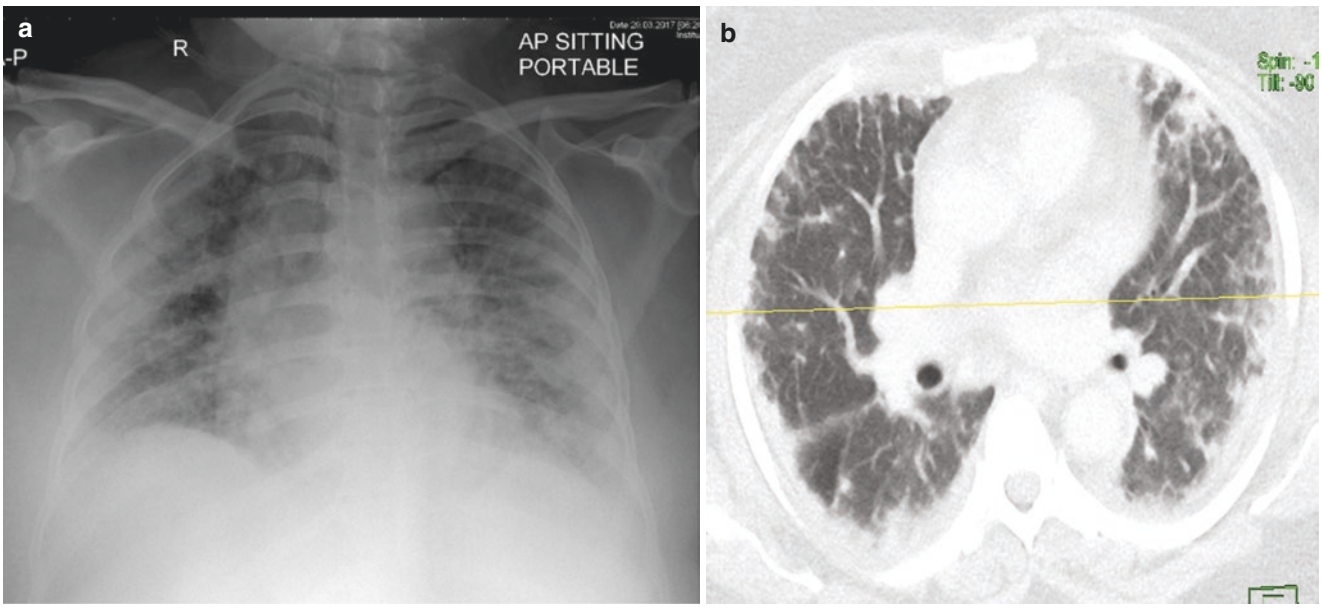

Fig. 14.4 Idiopathic chronic eosinophilic pneumonia (ICEP) in a 54-year-old woman with childhood asthma presenting to emergency department with acute onset dyspnea. (**a**) A-P chest radiograph shows peripheral opacities in both lungs creating "photographic negative of pulmonary edema." (**b**, **c**) Axial and coronal CT images show peripheral symmetrical opacities in both lungs

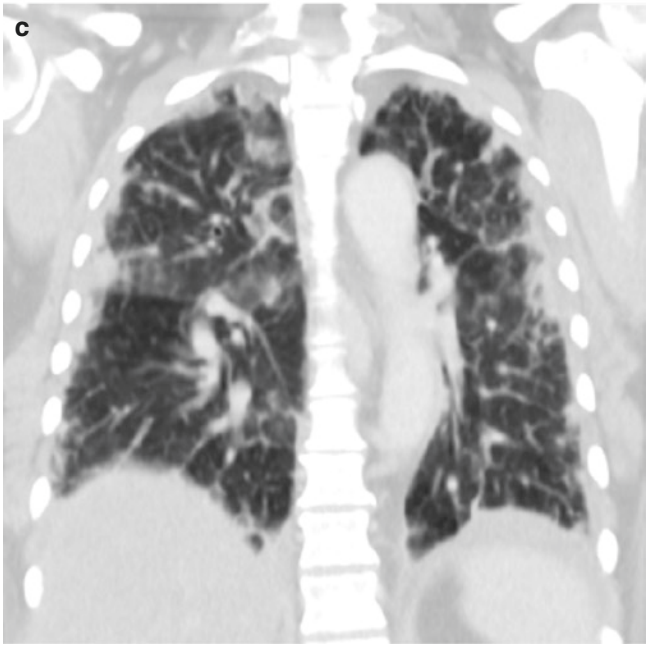

Table 14.2 Clinical, lab, and imaging features of ABPA

Clinical	• Poorly controlled asthma
	• Cough with thick mucoid expectoration, commonly containing brownish-black mucus plugs
	• Hemoptysis
Lab. findings	• Elevated total serum IgE levels
	• Elevated *A. fumigatus*-specific IgE levels
	• High *Aspergillus*-specific IgG antibodies
	• Elevated precipitins
	• Serum eosinophilia
Imaging	*Radiograph*
	• Fleeting parenchymal opacities
	• Bronchiectasis
	• "Finger-in-glove" sign (mucoid impaction in dilated bronchi)
	HRCT
	• Central bronchiectasis
	• High-attenuation mucus plugs in dilated bronchi
	• Tree-in-bud opacities
	• Atelectasis
	• Fibrosis and cavitation in late stage

Fig. 14.4 (continued)

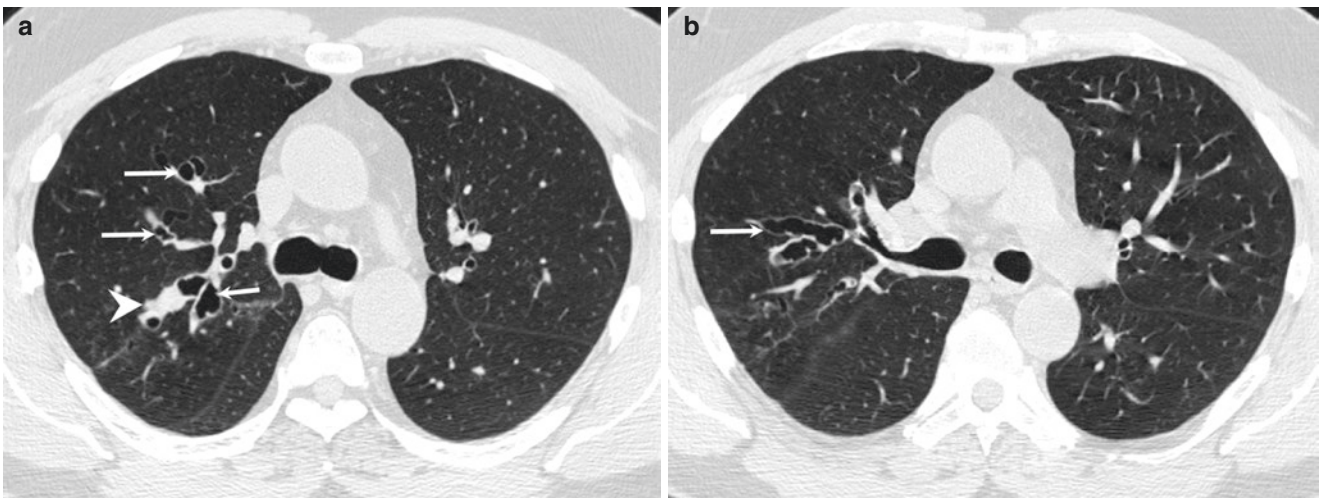

Fig. 14.5 ABPA in a 50-year-old man with asthma. (**a**, **b**) CT images show focal central "varicose" bronchiectasis (white arrows) with some mucus plugging in the right upper lobe (arrowhead). Note diffuse centrilobular nodularity in both lungs that is probably due to underlying asthma

complicating approximately 2% of patients with asthma [8]. The diagnosis is made on the basis of a combination of clinical, immunological, and radiological findings (Table. 14.2) [8, 9]. Lab investigations play an important role in diagnosis [8, 9]. The hallmark of ABPA is elevated total serum IgE levels of at least 1000 IU/ml [8, 9]. Blood eosinophilia when present supports the diagnosis of ABPA, but it may be absent particularly in those who are on systemic steroids. On CT, central bronchiectasis in the upper lobes is the hallmark of ABPA (Figs. 14.5 and 14.6). Bronchiectasis can be seen in peripheral lungs and can involve lower lobes in few cases. The impacted mucoid plugs are of variable attenuation but usually of high attenuation due to deposition of calcium, iron, and manganese [9] (Fig. 14.7). HRCT in asthmatic patients without ABPA commonly shows mild cylindrical bronchiectasis; hence the presence of bronchiectasis alone is not specific for ABPA. Presence of varicose or cystic bronchiectasis in three or more lobes, along with centrilobular nodules and mucoid impaction, is highly suggestive of ABPA [10].

Eosinophilic granulomatosis with polyangiitis (EGPA), formerly known as Churg-Strauss vasculitis, is a systemic necrotizing granulomatous vasculitis seen in asthmatic patients and is always associated with blood eosinophilia. It

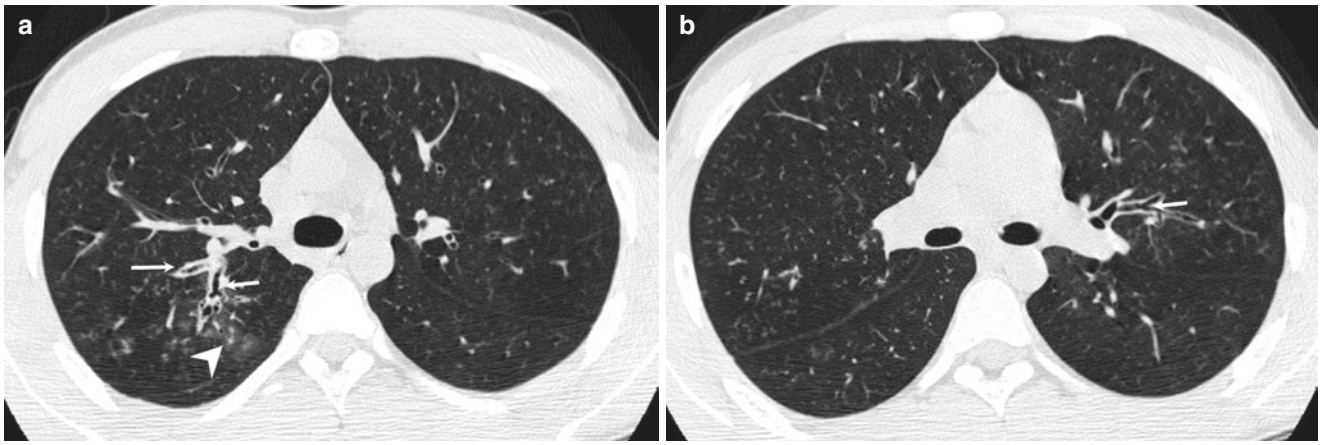

Fig. 14.6 An 18-year-old boy with steroid-resistant asthma and ABPA. (**a**, **b**) Axial CT images show bronchiectasis (white arrows) with marked bronchial wall thickening. There are "tree-in-bud" opacities and diffuse centrilobular nodularity with areas of ground-glass opacities (arrowhead) in the right upper lobe representing areas of eosinophilic pneumonia

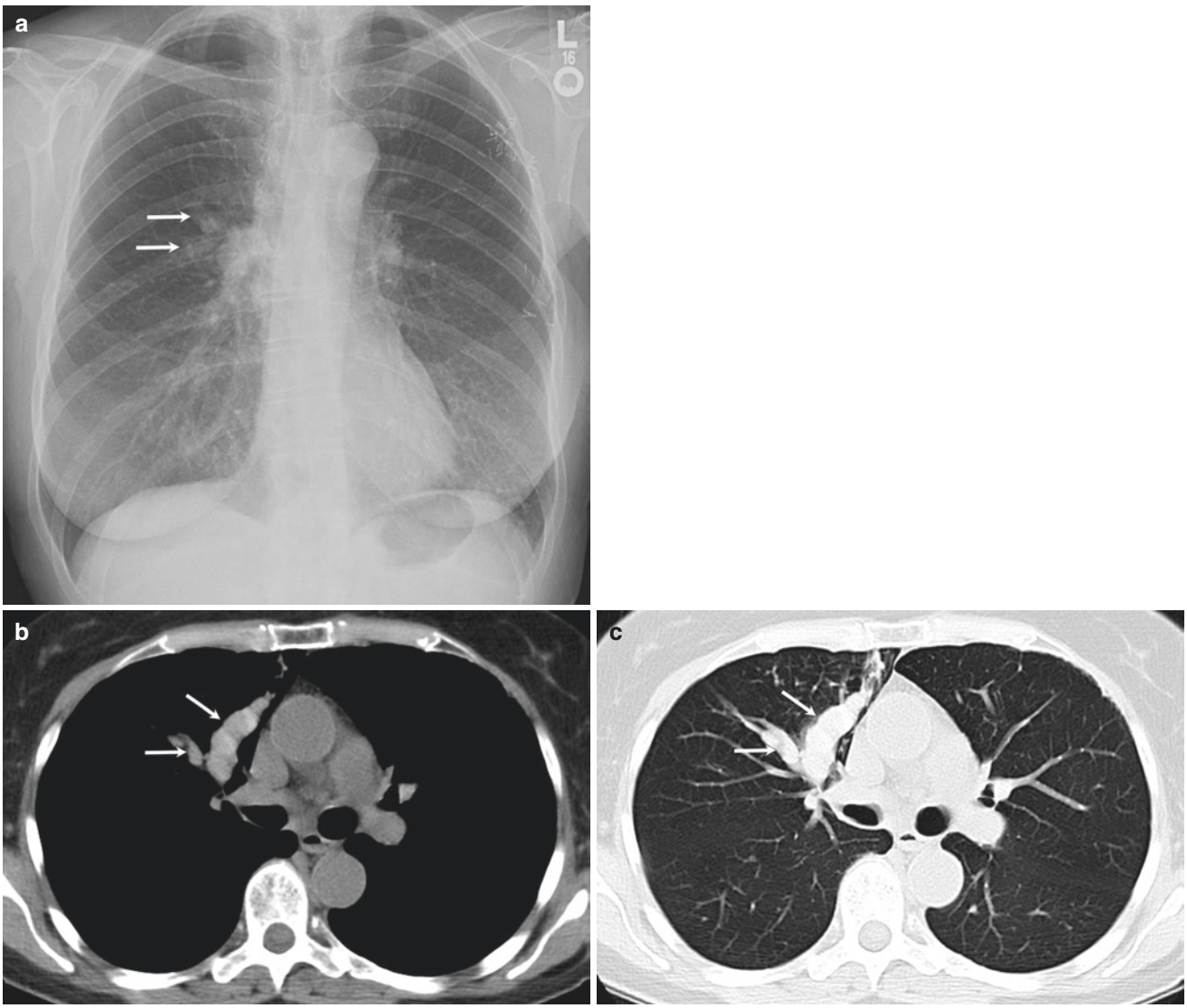

Fig. 14.7 ABPA in a 68-year-old woman with asthma and eosinophilia. (**a**) Frontal radiograph shows branching opacities (finger-in-glove sign) in the right perihilar region. (**b**, **c**) Axial CT images in soft-tissue and lung window show dilated bronchioles containing hyperdense tubular impacted mucus (white arrows)

is encountered in late third decade with onset from 3 to 13 years after the diagnosis of asthma. The diagnosis of EGPA requires the presence of four or more of six criteria as defined by the American College of Rheumatology in 1990 [11]. These criteria include asthma, eosinophilia >l0% on the white blood cell differential count, mononeuropathy or polyneuropathy, non-fixed pulmonary infiltrates on imaging, paranasal sinus abnormality, and extravascular eosinophils on biopsy. Antineutrophil cytoplasmic antibodies (ANCAs) are detected in 40% of the patients. Cardiac involvement is seen in half of the cases and is the cause of mortality in these patients. Peripheral scattered lung opacities resulting in "photographic negative of pulmonary edema" appearance on radiograph have been described in EGPA. CT features of EGPA are not specific, and diagnosis requires correlation with clinical and lab work-up; otherwise a surgical lung biopsy is confirmatory. On CT, there are peripheral consolidation or ground-glass opacities. These are patchy and distributed in upper lobes and lower lobes [12, 13] (Fig. 14.8). The other pattern is of multiple nodules that can show cavitation or air bronchograms, ranging in size from 1 to 3 cm [12]. "Halo" or "reverse halo" sign can be seen in these patients [13]. Bronchial wall thickening, tree-in-bud opacities, and centrilobular nodules identified in these patients may be due to underlying asthma. However, if these changes are extensive with or without subtle ill-defined ground-glass opacities and positive relevant clinical information, they represent necrotizing vasculitis changes [13] (Fig. 14.9). Similarly, the

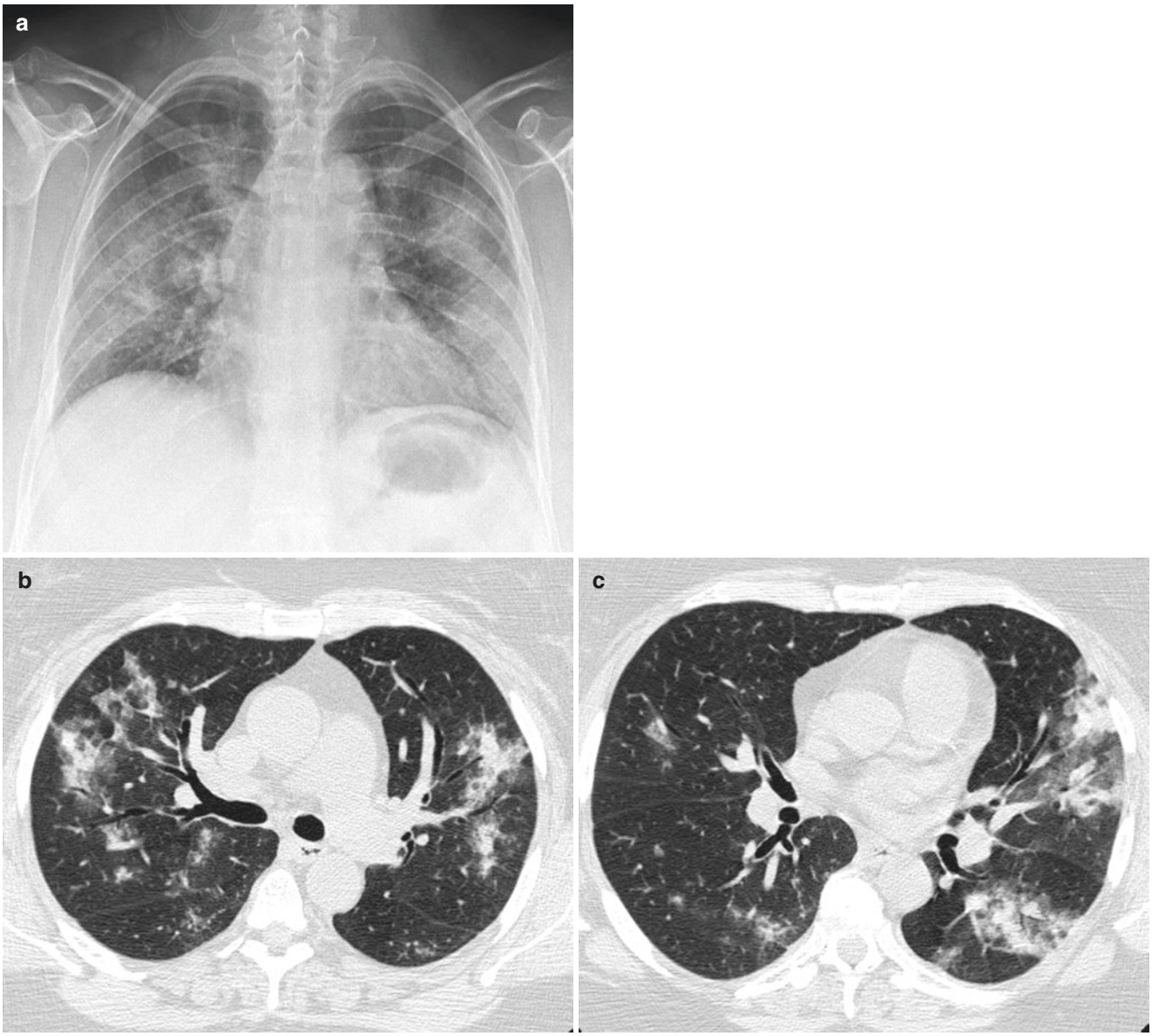

Fig. 14.8 A 54-year-old woman with sinusitis and asthma complicated by Churg-Strauss vasculitis. (**a**) Frontal chest radiograph shows peripheral opacities in both lungs "photographic negative of pulmonary edema." (**b**, **c**) Axial CT images show peripherally scattered consolidative opacities with surrounding ground-glass opacities "halo sign"

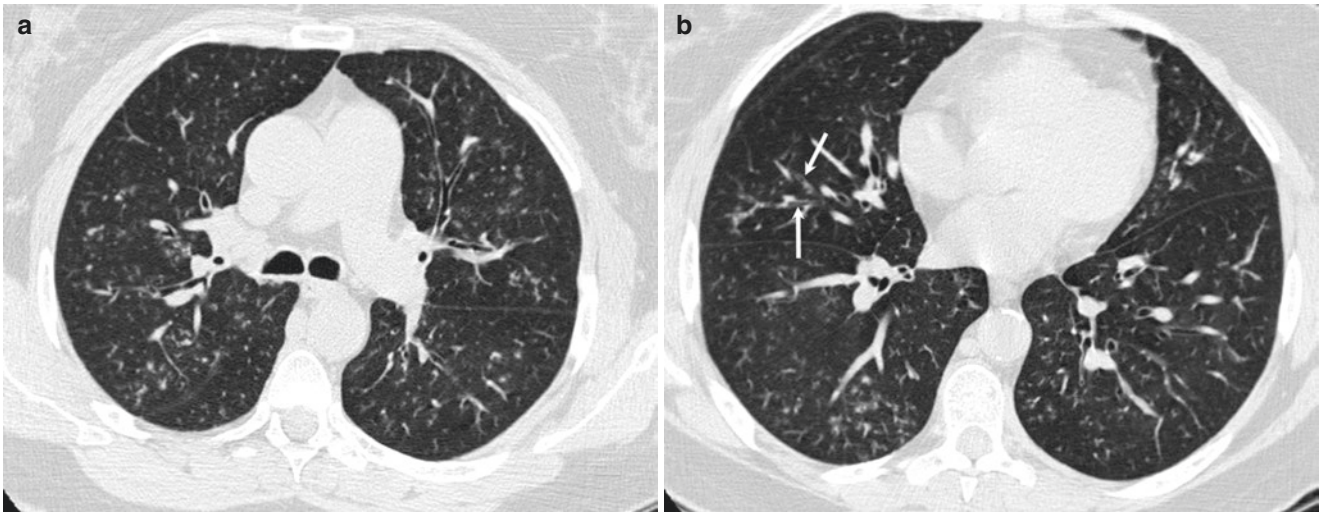

Fig. 14.9 Churg-Strauss vasculitis in a 56-year-old woman with asthma, mononeuritic multiplex, sinusitis, eosinophilia, and positive antineutrophil cytoplasmic antibodies. (**a**, **b**) Axial CT images show extensive centrilobular nodularity and tree-in-bud opacities in both lungs that cannot be explained by asthma alone. Note bronchiectasis in the left upper anterior lobe and right middle lobe with mucus plugging (white arrows)

presence of interlobular septal thickening and pleural effusion signifies interstitial edema secondary to cardiac involvement. Despite high prevalence, cardiac involvement is not yet included in diagnostic criteria. Cardiac MRI shows diffuse late gadolinium enhancement characteristically involving the subendocardial region without any territorial distribution. Cardiac MRI can show pericardial effusion, thrombus, and valvular regurgitation in these asthmatic patients with cardiac involvement.

14.3 Eosinophilic Lung Diseases

Eosinophilic lung diseases are a diverse group of disorders that include a large variety of diseases characterized by pulmonary opacities on imaging and any or combination of these features: serum eosinophilia, eosinophilia in BAL, and tissue eosinophilia on biopsy. More than 10% eosinophils in BAL is more sensitive and accurate criteria for the diagnosis of eosinophilic lung diseases as in certain diseases like acute eosinophilic pneumonia; the blood eosinophil count may be within normal range in the early phase [14]. Mild eosinophilia may be present in few other diseases like asthma, tuberculosis, fungal infection, non-small cell lung cancer, lymphoma, and leukemia as well as vasculitis, but these are not included in eosinophilic lung diseases [15]. Eosinophilic lung diseases can be divided into primary (idiopathic) or secondary (known cause like drugs, ABPA, EGPA) diseases. The primary pulmonary eosinophilic diseases are described in Table 14.3 [14, 15]. The imaging features of these diseases are not diagnostic. Except for hypereosinophilic syndrome, all other diseases are characterized by peripheral patchy consolidative or ground-glass opacities with septal thickening and centrilobular nodularity [14, 15]. The peripheral distribution of simple pulmonary eosinophilia and chronic eosinophilic pneumonia can result in "photographic negative of pulmonary edema" appearance on chest radiograph and CT (Figs. 14.10 and 14.11). The other pattern is of peripherally distributed nodules with surrounding ground-glass opacities (Fig. 14.12). These opacities may be migratory on follow-up imaging. Mediastinal lymphadenopathy and effusion are not seen in the absence of cardiac involvement. Hypereosinophilic syndrome is characterized by interstitial edema and pleural effusions probably secondary to cardiac failure [14, 15].

Table 14.3 Primary pulmonary eosinophilic diseases

Simple pulmonary eosinophilia	• Usually unknown cause
	• Can be drug-induced or seen in ABPA
	• Loeffler syndrome is a self-limiting disease
	• Resolution in 1 month
Acute eosinophilic pneumonia	• Acute onset of fever, cough, and dyspnea of fewer than 5 days duration
	• Difficult to differentiate from infective pneumonia in the absence of blood eosinophilia in early stages
	• Complete resolution on steroids with no recurrence
Chronic eosinophilic pneumonia	• Usually seen in patients with atopic diseases (asthma, rhinitis)
	• Insidious onset with symptoms present for 1 month
	• Rapid response to steroid and recurrence in more than half at same site
Idiopathic hypereosinophilic syndrome	• Multisystem rare disorder
	• Prolonged and marked eosinophilia exceeding 1500 cells/mL of 6 months duration
	• Cardiac involvement accounts for poor prognosis
	• Cardiac MRI shows diffuse late gadolinium enhancement in subendocardium, thrombus, and valvular abnormalities
	• Respond to steroid is not as dramatic as in other syndromes

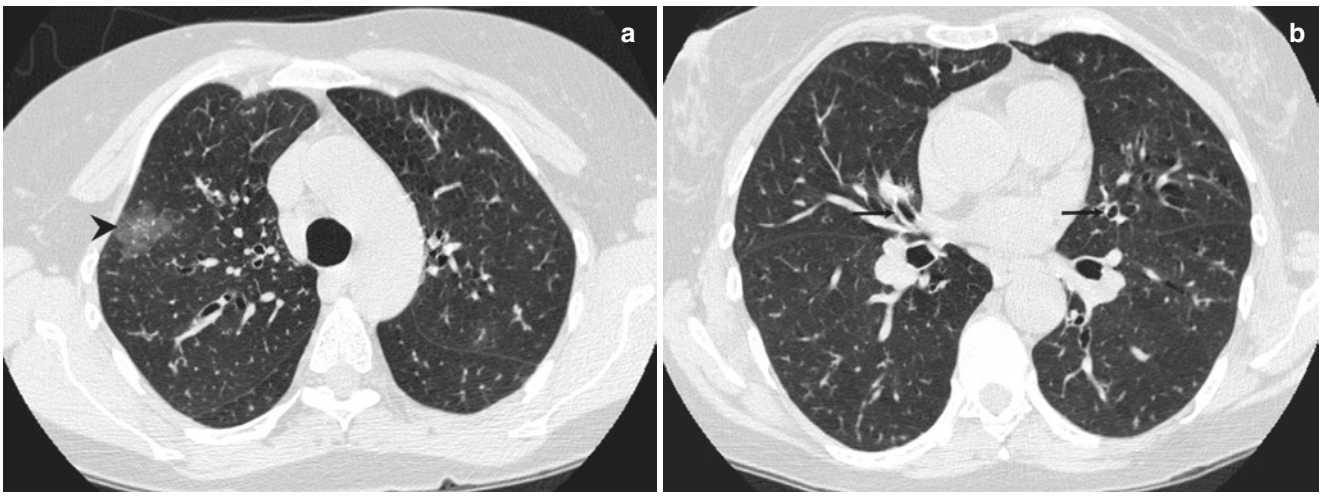

Fig. 14.10 A 59-year-old woman with ABPA and presumed Loffler pneumonia. (**a**, **b**) Focal ground-glass opacity (arrowhead) in an asthmatic patient associated with central bronchiectasis (black arrows)

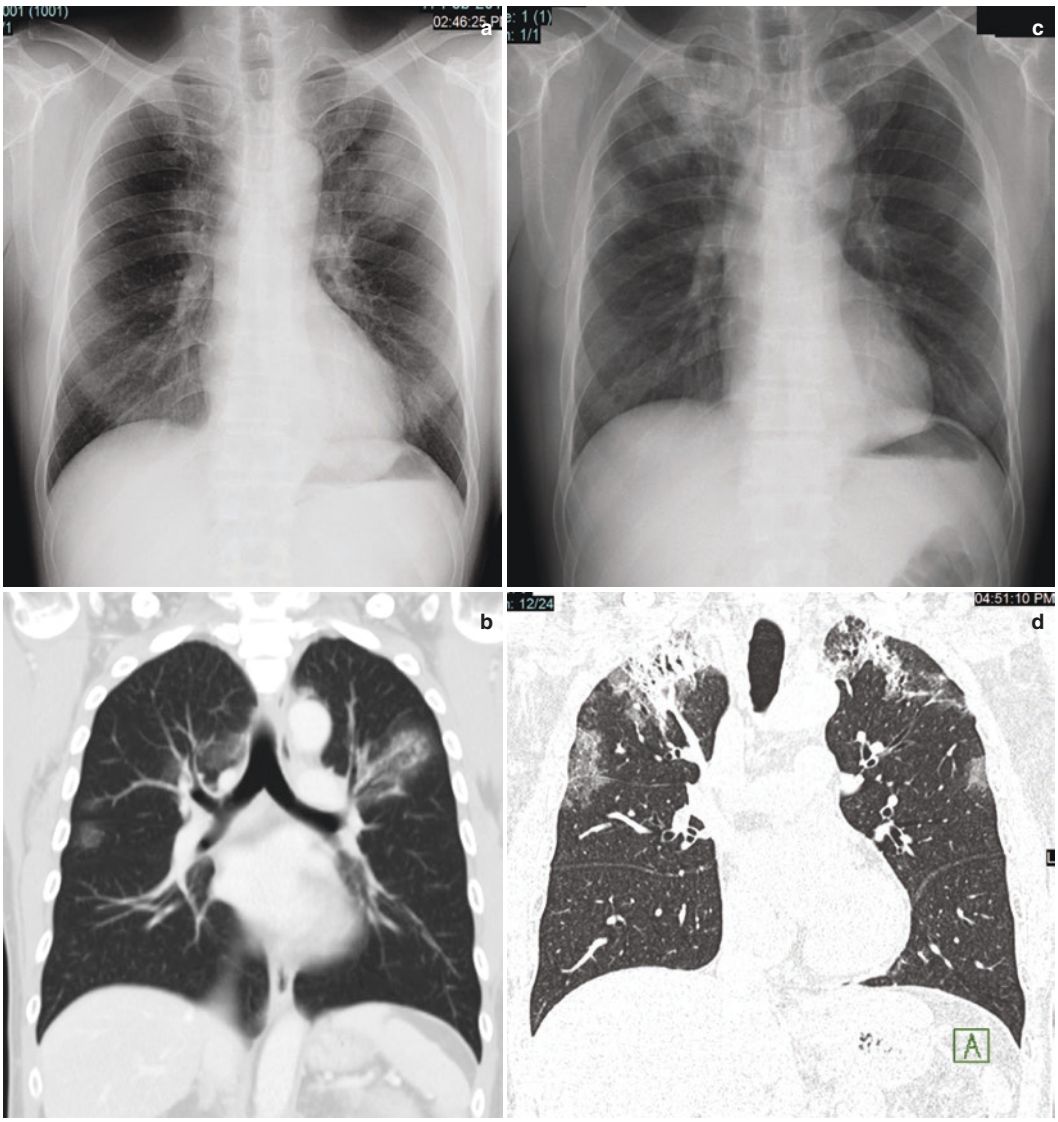

Fig. 14.11 A 69-year-old man with asthma and chronic eosinophilic pneumonia. (**a**) Initial chest radiograph shows a peripheral opacity in the left upper zone. (**b**) Coronal CT image reveals bilateral upper lung peripheral ground-glass opacities. (**c**) Follow-up radiograph after 1 month of steroid therapy shows improvement in opacities in the left upper zone and progression in opacities in the right upper zone. (**d**) Follow-up coronal CT image also demonstrates the same changes

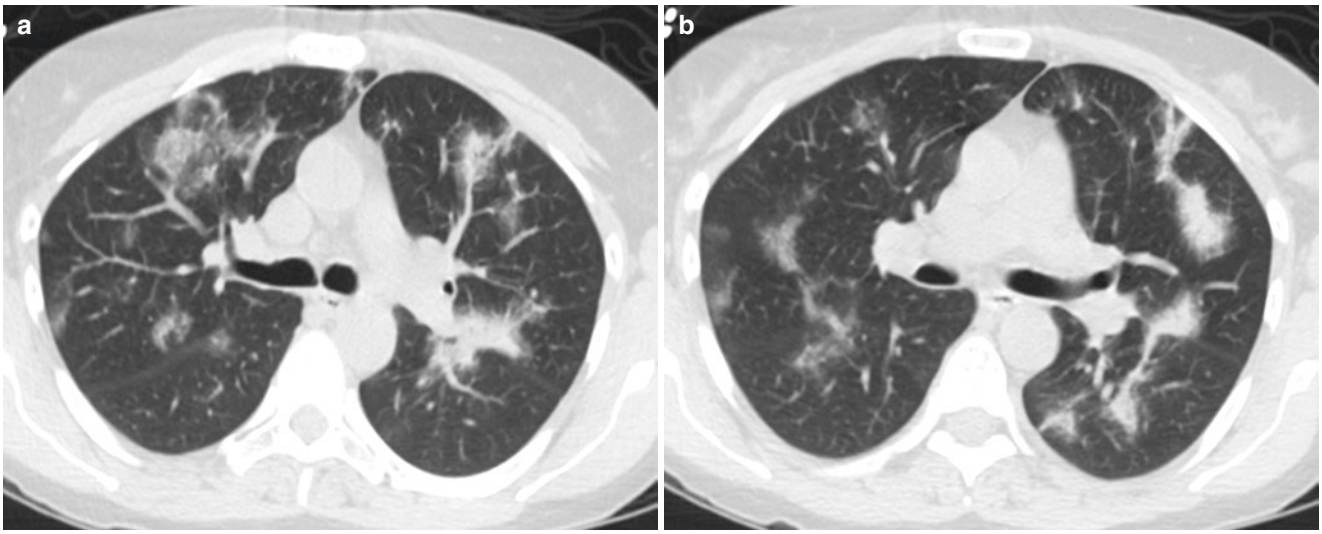

Fig. 14.12 A 55-year-old woman with asthma and chronic eosinophilic pneumonia. (**a**, **b**) Axial CT images show bilateral peripheral consolidative opacities with surrounding ground-glass "halo," particularly on the left side

14.4 Smoking-Related Lung Diseases

Smoking is associated with variety of airway, parenchymal, and interstitial lung diseases (Table 14.4). Desquamative interstitial pneumonitis (DIP) and pulmonary Langerhans cell histiocytosis (LCH) are discussed in cystic lung disease. Pleural-parenchymal malignancies are discussed in the Chap. 5.

Table 14.4 Smoking-related lung diseases

• Emphysema and bronchitis
• Respiratory bronchiolitis (RB)
• Respiratory bronchiolitis ILD (RB-ILD)
• Desquamative interstitial pneumonitis (DIP)
• Pulmonary Langerhans cell histiocytosis (LCH)
• Combined pulmonary fibrosis and emphysema (CPFE)
• Pleural-pulmonary malignancies

Emphysema is defined as irreversible destruction of alveolar walls with resultant permanent enlargement of air spaces distal to terminal bronchioles. Chest radiograph has limited accuracy in diagnosis of emphysema, particularly in detecting mild to moderate emphysema. In moderate to severe emphysema, chest radiograph shows a paucity of vessels in the outer half of the lung and signs of hyperinflation (flattening of the diaphragm and increase retrosternal space >2.5 cm) [16–18] (Fig. 14.13). CT is a sensitive modality for detecting emphysematous spaces more than 5 mm in size. The etiology of emphysema is attributed to an imbalance between protease and antiprotease enzymes in the lung. Proteases are produced by polymorphonuclear leukocytes that are neutralized by alpha-1 antiproteases. Cigarette smoke inactivates alpha-1 antitrypsin by oxidizing it. Morphologically, three different types of emphysema patterns are recognized based on their location in the secondary pulmonary nodule (SPL): (a) centrilobular emphysema, (b) paraseptal emphysema, and (c) panlobular emphysema.

Centrilobular emphysema (CLE) or more correctly termed "centriacinar emphysema" results from destruction of alveoli around the proximal respiratory bronchiole. CLE is the most common form of emphysema and results from smoking and dust inhalation. CLE is usually seen in the upper lungs probably due to increased negative pleural pressure and reduced antiprotease activity in the upper lungs. On CT, early CLE appears as wall-less punch holes of 5–10 mm termed "moth-eaten" pattern (Fig. 14.14a). There is striking density difference between emphysematous lungs and normal parenchyma. Progression of emphysema results in more conspicuous low attenuation area with an eccentric dot representing a displaced centrilobular artery of the SPL (Fig. 14.14b). Coalescence of emphysema results in polygonal areas of low attenuation that develops false walls from compressed normal lung parenchyma and fibrosis (Fig. 14.14c). Further progression leads to bullae formation. Paraseptal emphysema or distal lobular emphysema is the outcome of the predominant destruction of peripheral areas of SPL. This pattern is also associated with smoking and is characterized by low attenuated areas in the subpleural location, with preferential upper lung involvement (Fig. 14.14d). Progression of this pattern also results in the formation of bullae predisposing for pneumothorax. "Confluent emphysema" is an acceptable radiology term to explain severe coalescent CLE and paraseptal emphysema in the upper lungs. Panlobular emphysema (PLE) is characterized by diffuse destruction of all air spaces within the SPL. In contrast to CLE and paraseptal emphysema, PLE predominantly involves the lower lungs and presents in the younger population. On CT, instead of holes, PLE appears as diffuse low attenuation areas with small caliber vessels that may be overlooked or mistaken for bronchiolitis [17, 18] (Fig. 14.15). As there is diffuse involvement of the entire SPL, the contrast between emphysema and nonemphysematous lung is subtle. PLE pattern is seen in alpha-1 antitrypsin deficiency and

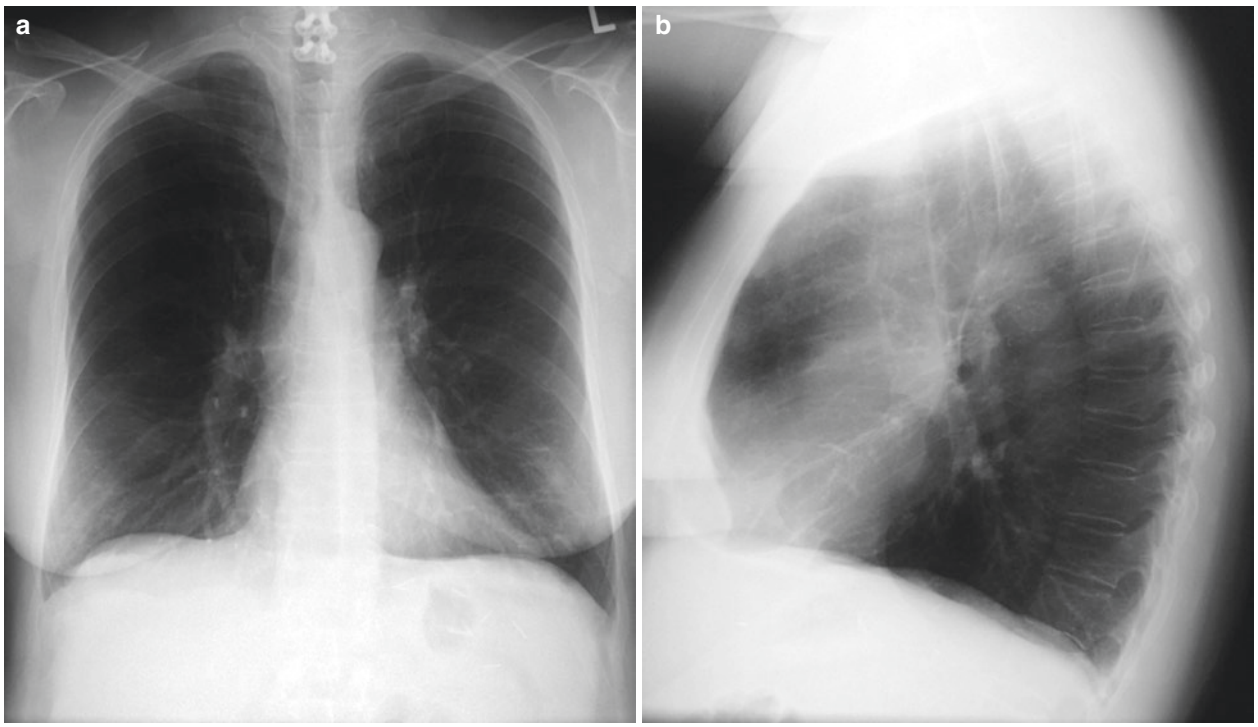

Fig. 14.13 Advanced emphysema. (**a**, **b**) Frontal and lateral chest radiographs show classic findings of severe emphysema of overinflation and paucity of vascular markings

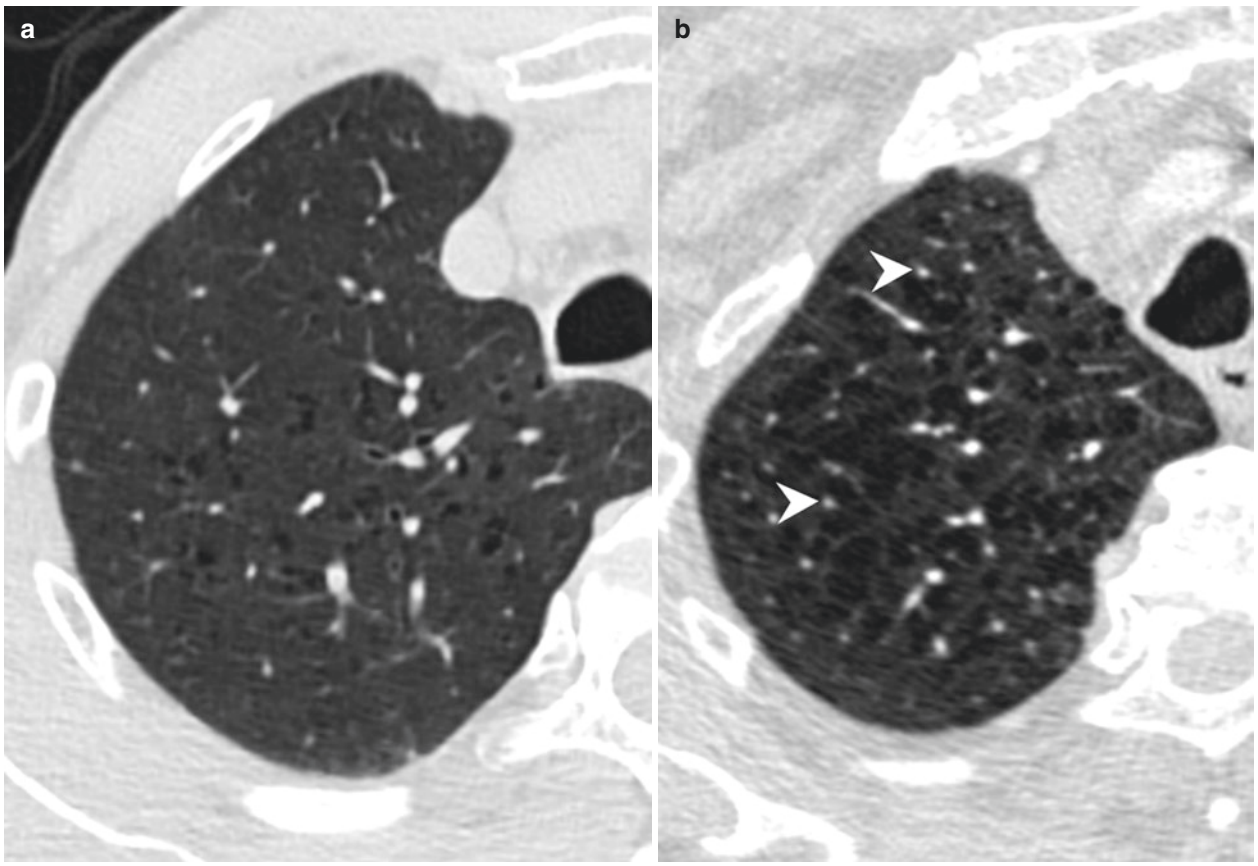

Fig. 14.14 Types of emphysema. (**a**) Early centriacinar emphysema involving acini with "moth-eaten" wall-less punch holes. (**b**) Moderate emphysema involving the lobules with eccentric dots (arrowheads). (**c**) Severe confluent emphysema with false walls. (**d**) Paraseptal emphysema involving the subpleural lung

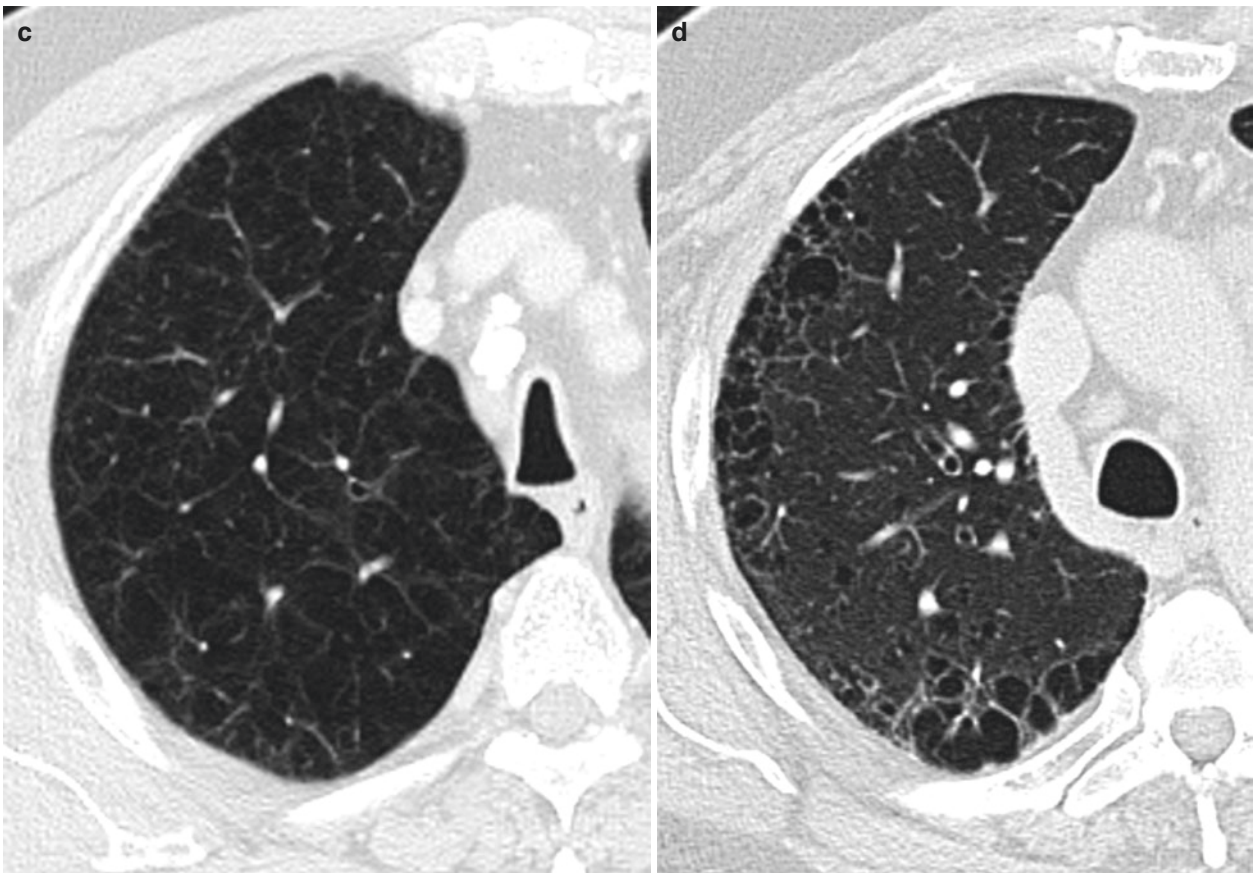

Fig. 14.14 (continued)

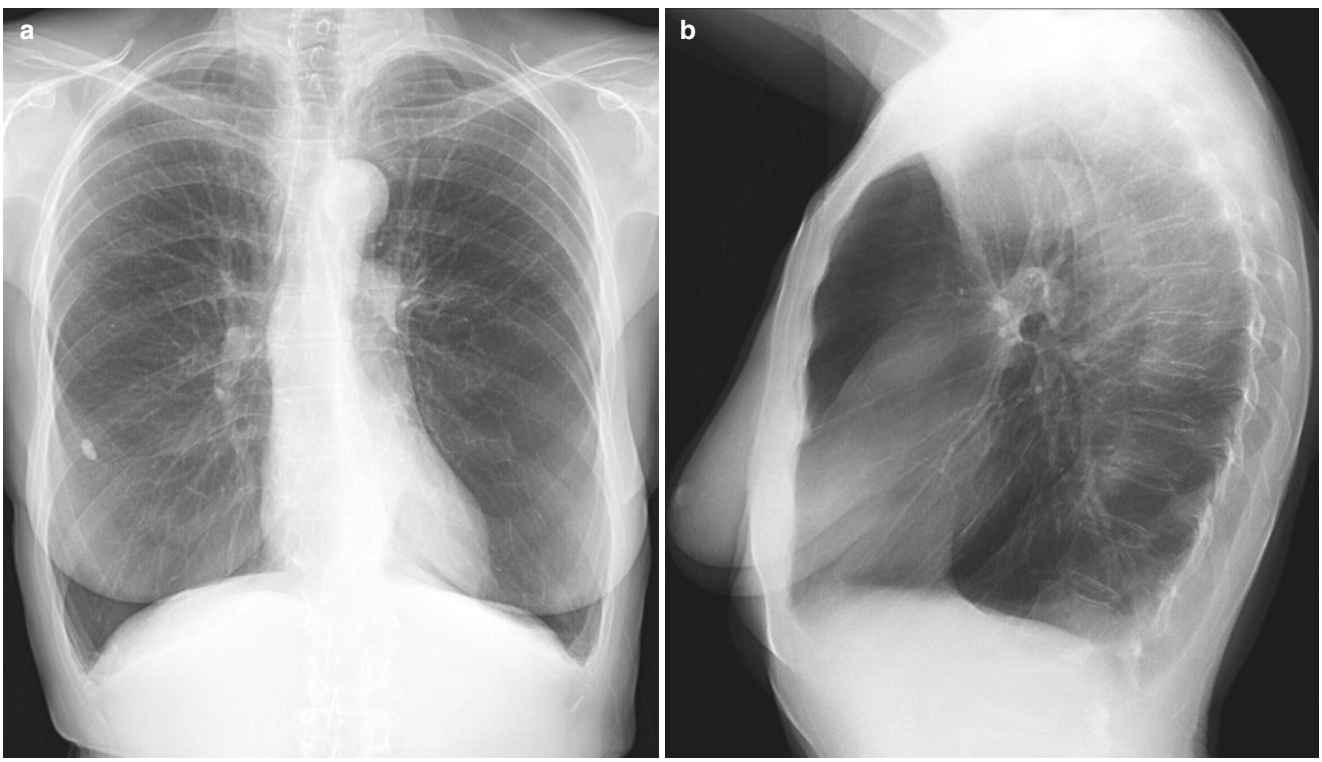

Fig. 14.15 Panlobular emphysema in an elderly lady with alpha-1 antitrypsin deficiency. (**a**, **b**) Frontal and lateral chest radiographs show overinflated lungs and the paucity of vascular markings in lower lungs. (**c**–**e**) Axial CT images show emphysema more severe in lower lungs with a gradual transition to relatively preserved upper lungs. Note the bronchiectasis (white arrows), commonly seen along with panlobular emphysema

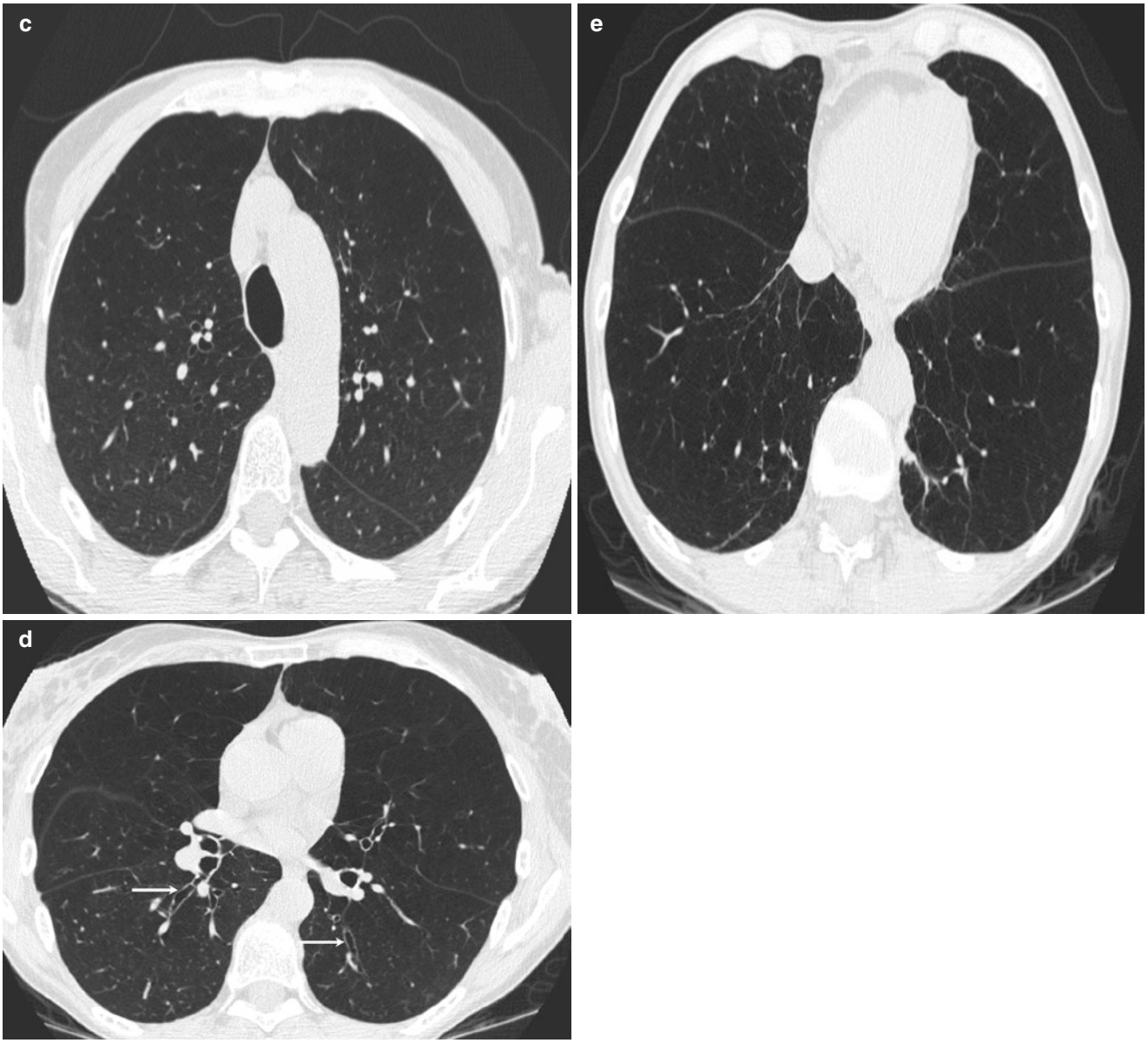

Fig. 14.15 (continued)

Swyer-James syndrome. A similar radiological and pathological pattern of emphysema is seen in IV methylphenidate (Ritalin) abusers.

Respiratory bronchiolitis (RB), respiratory bronchiolitis ILD (RB-ILD), and desquamative interstitial pneumonitis (DIP) are considered as a continuum of smoking-induced disease. RB was initially described in young asymptomatic cigarette smokers, characterized pathologically by the accumulation of pigmented macrophages within respiratory bronchioles and adjacent alveoli [19]. In fact, RB is seen in histopathology specimen of virtually all smokers regardless of the duration of smoking who may be symptomatic due to the presence of other smoking-related diseases like emphysema.

RB-ILD is exaggerated RB with more extensive infiltration by pigmented macrophages, peribronchial inflammation, and fibrosis [20]. RB-ILD presents in patients aged 30–60 years with cough and shortness of breath and restrictive pattern on pulmonary function tests. Smoking history in these patients has a wide range with a mean between 30 and 40 pack-years; younger patients usually have a history of heavy smoking [20]. Radiologically, RB and RB-ILD have similar features (Fig. 14.16), but patients with RB-ILD are symptomatic. RB-ILD may regress with discontinuation of smoking but often persists with no functional improvement despite smoking cessation and treatment.

DIP is another end of the spectrum of smoking-related disease with considerable overlap with RB-ILD on histopathology and imaging (Figs. 14.17 and 14.18). However, DIP can also be seen in nonsmokers with occupational disorders, autoimmune diseases, and drug toxicity. DIP is characterized histopathologically by the presence of large numbers of mac-

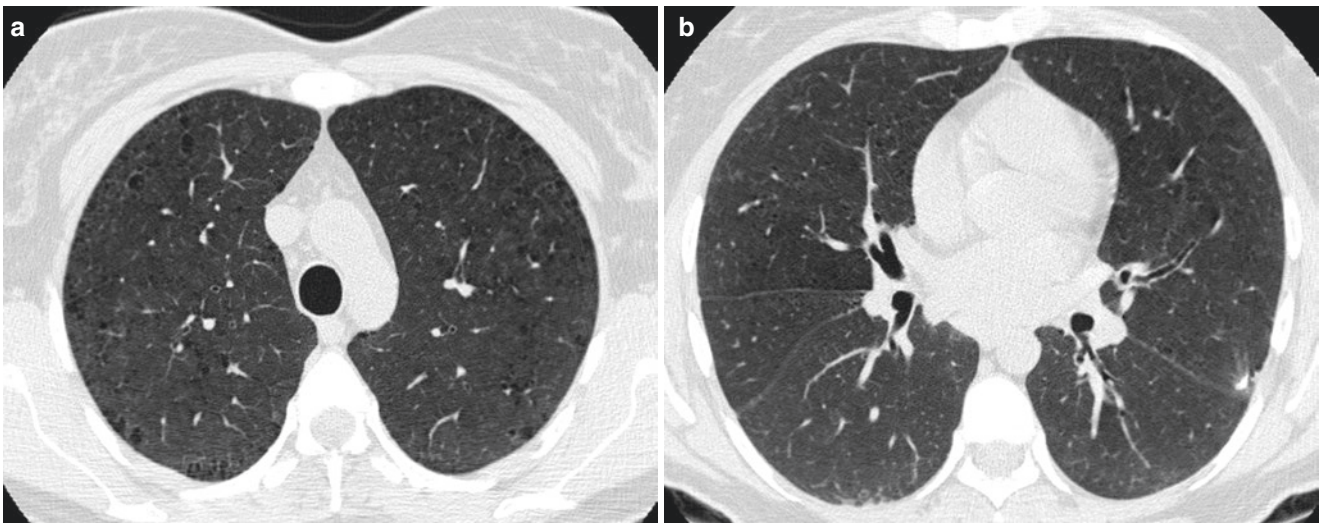

Fig. 14.16 Respiratory bronchiolitis-interstitial lung disease in a young smoker who presented with progressive dyspnea. (**a**, **b**) Axial CT images show emphysema and subtle scattered ground-glass density centrilobular nodules resulting in a diffuse haze in upper lungs. There is bronchiectasis and bronchial wall thickening

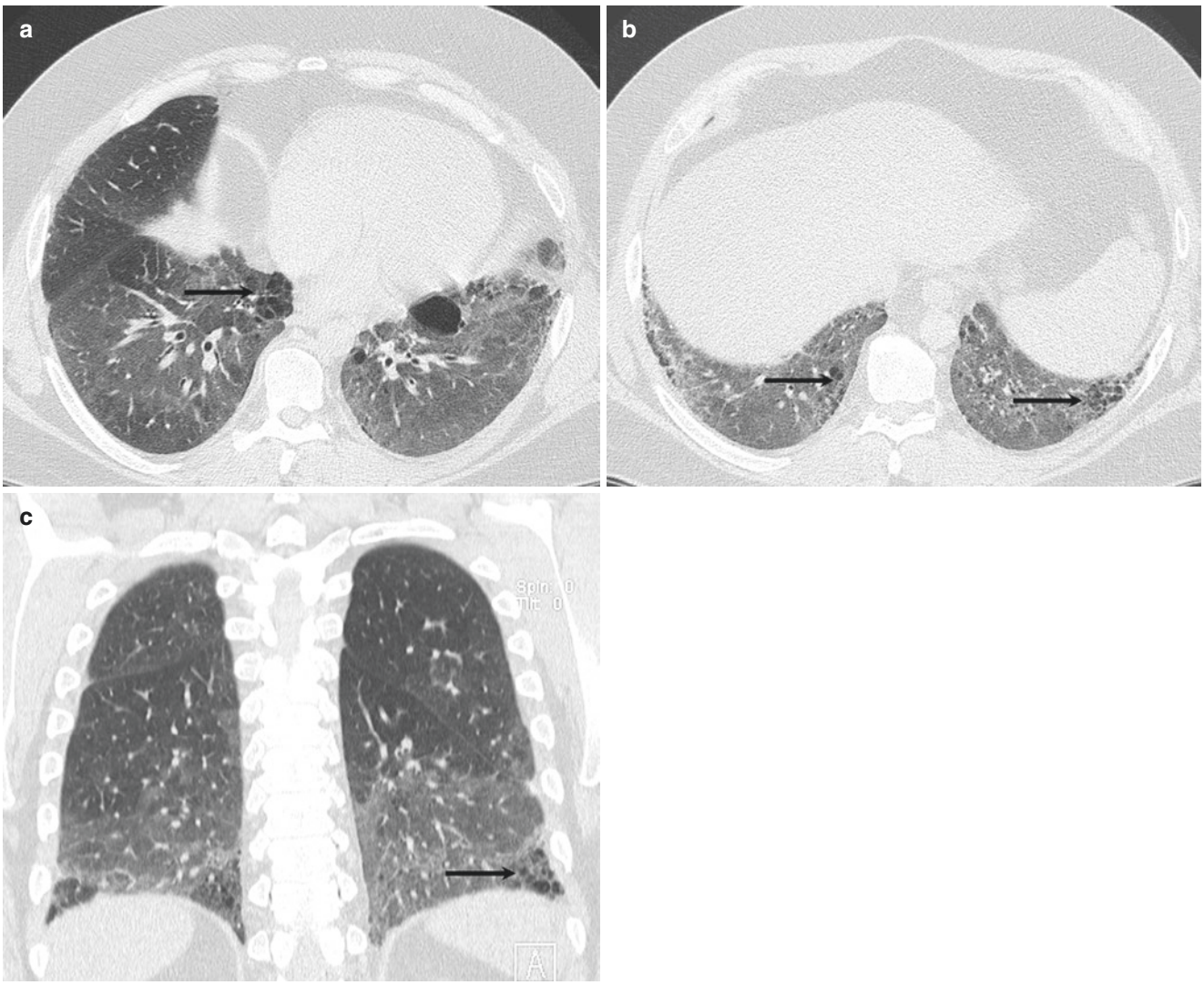

Fig. 14.17 A 34-year-old man with desquamative interstitial pneumonia on surgical lung biopsy. (**a**, **b**) Axial CT and (**c**) coronal images show confluent ground-glass opacities in the lower lungs with small cysts formation (black arrows) within abnormal regions

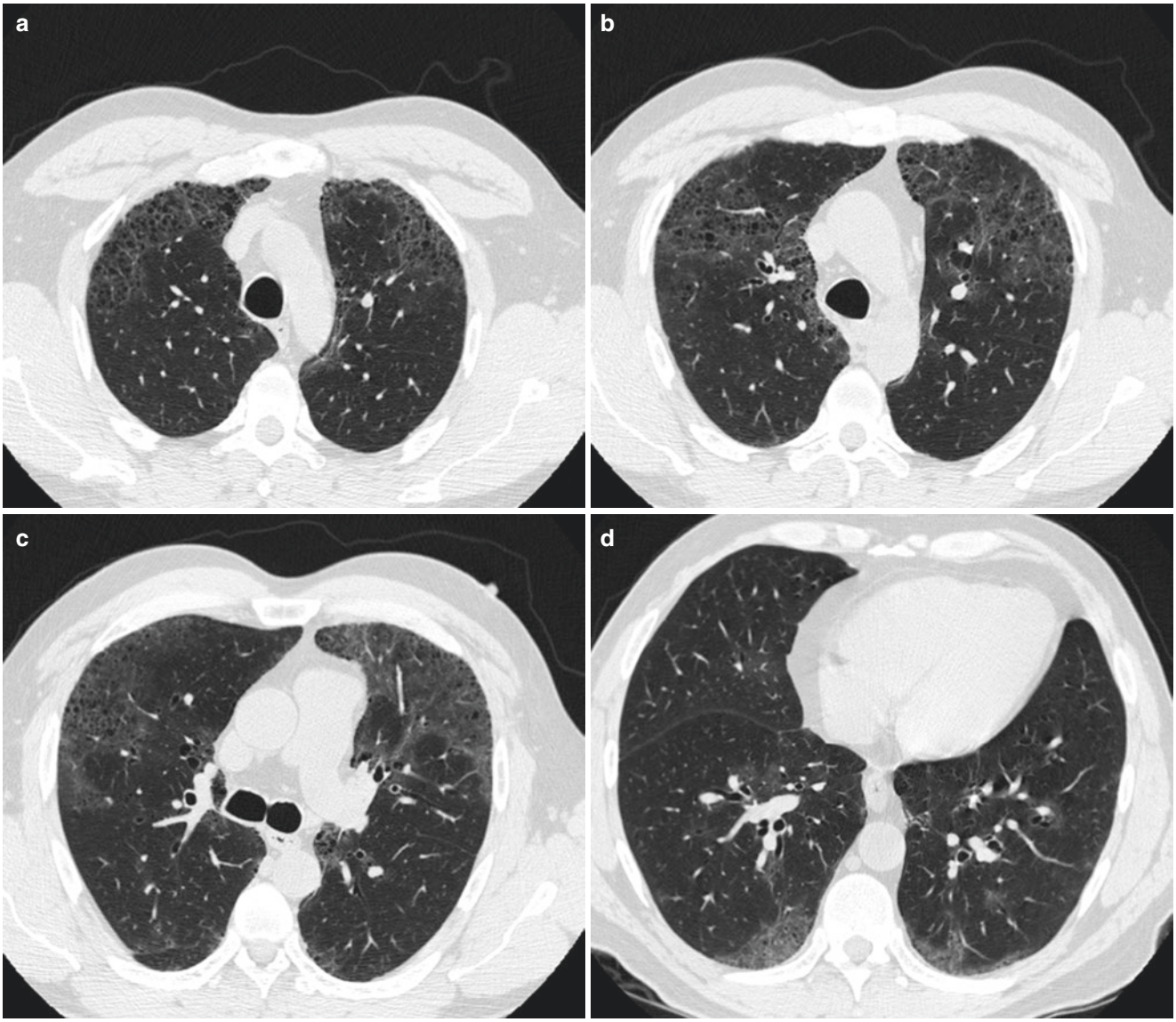

Fig. 14.18 A 50-year-old heavy smoker with desquamative interstitial pneumonia on histopathology. (**a**–**d**) Axial CT images show ground-glass opacities in both lungs with small cyst formation. Surgical lung biopsy was performed due to upper lung distribution of the lung abnormalities

rophages within the alveoli, diffusely distributed throughout the pulmonary acini, and associated with alveolar septal thickening and hyperplasia of type II pneumocytes [21]. Practically, the histopathological distinction between RB-ILD and DIP is arbitrary. DIP is insidious in onset in the age group of 40–60 years with cough and shortness of breath. DIP in contrast to RB-ILD often responds to steroids that can be tapered to avoid potential side effects.

The presence of clinical symptoms is the best way to differentiate between RB-ILD and RB. Bronchoalveolar lavage, pulmonary function tests, and HRCT features (Table 14.5) are helpful in noninvasive diagnosis [22–24] (Fig. 14.16). Lack of lymphocytosis in BAL also helps in excluding radiological differential diagnoses of hypersensitivity pneumonitis and lymphocytic interstitial pneumonia. It has been proposed to use the term "smoking-related interstitial lung diseases" to describe the HRCT features instead as there is considerable overlap in the imaging and histopathological features. Moreover, all the three entities can be present in the different locations of the same lung. However, the distinction may be essential due to the difference in management and prognosis between RB-ILD and DIP [22]. The diagnosis must be made in a multidisciplinary discussion considering clinical severity, PFTs, BAL, and imaging findings. A surgical lung biopsy is required for confirmatory diagnosis and is indicated, if the symptoms cannot be explained by the amount of fibrosis on HRCT or if there is a dilemma in diagnosing idiopathic pulmonary fibrosis.

Table 14.5 Features of RB, RB-ILD, and DIP

RB	• RB is asymptomatic by itself, but symptoms may be due to another respiratory manifestation related to smoking
	• PFTs are usually within normal limits
	• BAL shows brown-pigmented macrophages
	• HRCT is normal in most cases
	• Few cases show ill-defined centrilobular nodules in the upper lung with or without small patchy ground-glass densities
RB-ILD	• Usually presents with cough and shortness of breath
	• PFTs show mixed, predominately restrictive pattern that may be complicated by concurrent emphysema. DLCO is reduced
	• BAL shows brown-pigmented macrophages
	• Absence of lymphocytosis in BAL (excludes radiological differential diagnoses of hypersensitivity pneumonitis and lymphocytic interstitial pneumonia)
	• HRCT may be normal
	• Most of the cases show ill-defined centrilobular nodules in the upper lung with or without small patchy ground-glass densities
	• Inspiratory mosaic and expiratory air trapping may be present
DIP	• Most common presentation is cough and shortness of breath
	• PFTs show restrictive pattern with reduced DLCO
	• BAL may show increase neutrophils or eosinophils (can be misdiagnosed as eosinophilic pneumonia)
	• HRCT shows areas of ground-glass opacities associated with reticulation
	• Opacities are subpleural, predominantly in mid and lower lungs but can be in upper lungs in certain cases (Fig. 14.18)
	• Small cysts may develop within the ground-glass opacities

Please refer to text for the acronyms

14.5 Combined Pulmonary Fibrosis and Emphysema (CPFE)

Combined pulmonary fibrosis and emphysema (CPFE) syndrome is a recently added smoking-related lung disease that is characterized by emphysema in the upper lungs and fibrosis in the lower lungs. It's debatable whether the combination of emphysema and pulmonary fibrosis is a distinct clinical entity from idiopathic pulmonary fibrosis (IPF) or not. Some degree of fibrosis is usually present in a patient with emphysema on histopathology, while smokers with IPF have emphysema on histopathology that may not be seen on imaging [25]. Due to higher prevalence and mortality from pulmonary hypertension and lung cancer among CPFE patients, there is increasing stress on recognizing this entity as a separate condition. The typical patient is a heavy smoker or former smoker and presents with dyspnea. Pulmonary function tests show mixed pattern due to the obstructive pattern from emphysema and restrictive pattern from fibrosis. There is marked impairment in diffusion capacity as reflected by marked reduction in DLCO. HRCT shows centrilobular or paraseptal emphysema in upper lobes and fibrosis in the lower lobes. The prevalence of paraseptal emphysema in CPFE is much more than in patients without CPFE. The fibrotic changes are in the form of reticular opacities and honeycombing. Many times areas of ground-glass opacities are present. HRCT pattern in most cases of CPFE is usual interstitial pneumonia (UIP) but can be nonspecific interstitial pneumonia or even unclassifiable fibrotic lung disease [26]. A unique feature on pathology and HRCT is the presence of thick-walled cystic lesions (TWCLs) that are seen in up to three-quarters of the patients (Figs. 14.19 and 14.20). TWCLs are described as cysts more than 1 cm in size delineated by a 1-mm-thick wall distributed in the area of fibrosis [27]. TWCLs can be seen along with honeycombing, but unlike honeycombing, they are centrilobular in distribution and usually larger than honeycombing cysts. Nevertheless, the distinction may not be easy, but attempts must be made to not to confuse TWCLs with honeycombing and overdiagnose UIP by following the definition of honeycombing.

14.6 Pulmonary Alveolar Proteinosis

Pulmonary alveolar proteinosis is an unusual pulmonary disease characterized by the alveolar accumulation of surfactant that results in gas exchange impairment leading to symptoms like dyspnea and alveolar opacities on imaging. The etiology appears to be a mutation, critically impairing the process of surfactant clearance in the lung. Two types of PAP have been recognized, idiopathic and acquired, with former being more common. The acquired form can be due to exposure to industrial dust, infection, hematological malignancy (myelodysplastic syndrome and acute myeloid leukemia), and collagen vascular diseases (rheumatoid arthritis, dermatomyositis, and Behcet's disease) [28–30]. A rare congenital form of PAP has also been recognized. The idiopathic type presents in third and fourth decades with reported male preponderance. The prevalence among smokers is higher compared to

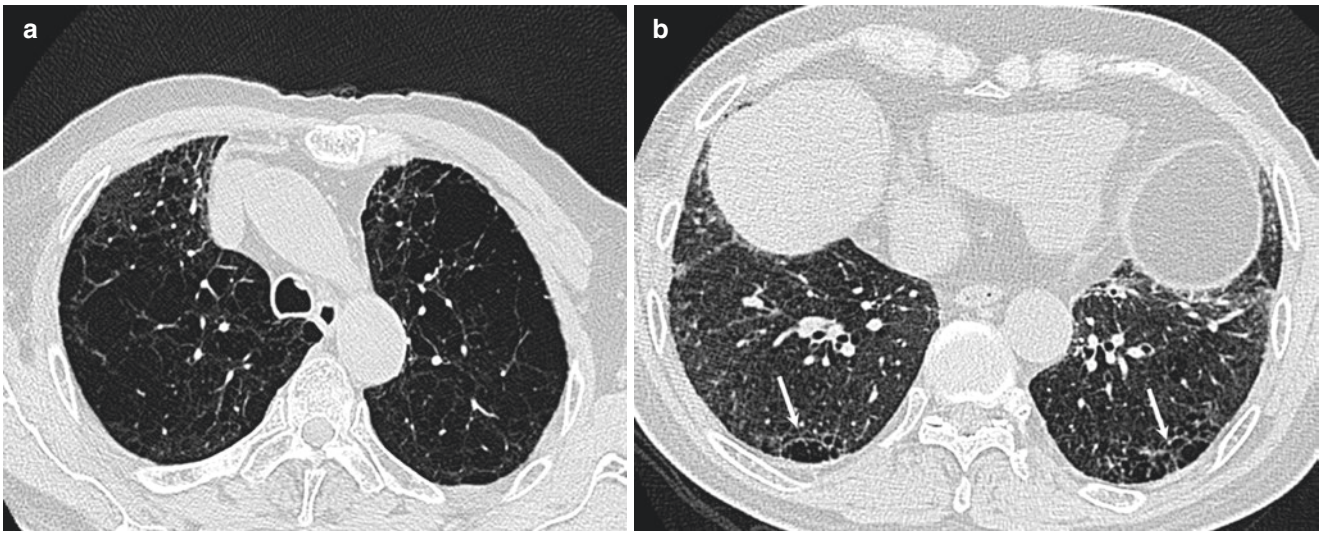

Fig. 14.19 Presumed CPFE syndrome in a heavy smoker with severe pulmonary artery hypertension. (**a**) Axial CT image of the upper lung shows predominantly paraseptal emphysema. (**b**) Axial image of lower lungs shows mild fibrosis with TWLCs (white arrows)

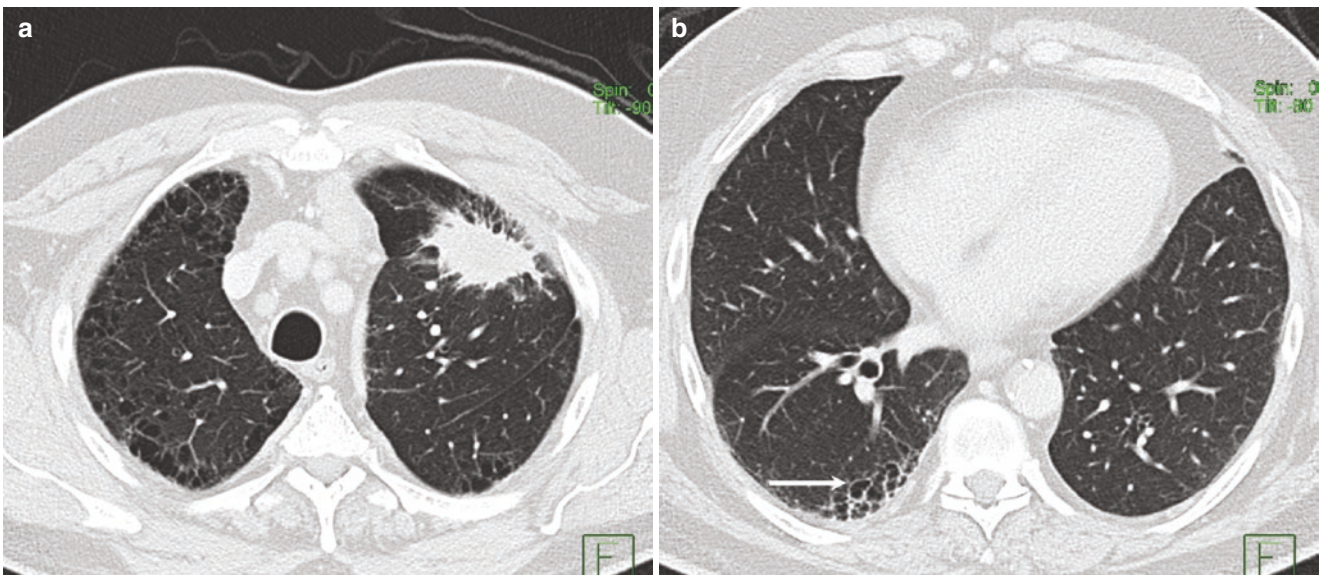

Fig. 14.20 Presumed CPFE with lung cancer. (**a**) Axial CT image of the upper lungs shows paraseptal emphysema and a spiculated nodule. (**b**) Axial image of the lower lung shows a cluster of TWLCs (white arrow) in the right lower lobe. There was fibrosis in the lung bases (not shown)

nonsmokers. The patient may be asymptomatic with abnormal radiograph but usually presents with progressive dyspnea on exertion and cough. Few patients also present with fever due to superadded infection. Chest radiograph shows symmetrical perihilar opacities (consolidation and/or ground-glass) resembling pulmonary edema. In many cases, the distribution of opacities is peripheral and may be basal and asymmetrical [30]. However, the radiological appearance is much severe than the clinical findings that serve as a clue for suspicion for this entity. The opacities persist for a long period of time despite antibiotics with no change in symptomatology. CT shows typical "crazy-paving" pattern that is defined as thickened septa within ground-glass opacities but without any volume loss. The areas of crazy paving are extensive and sharply marginated with a variable pattern of distribution [28–30] (Figs. 14.21 and 14.22). There are no

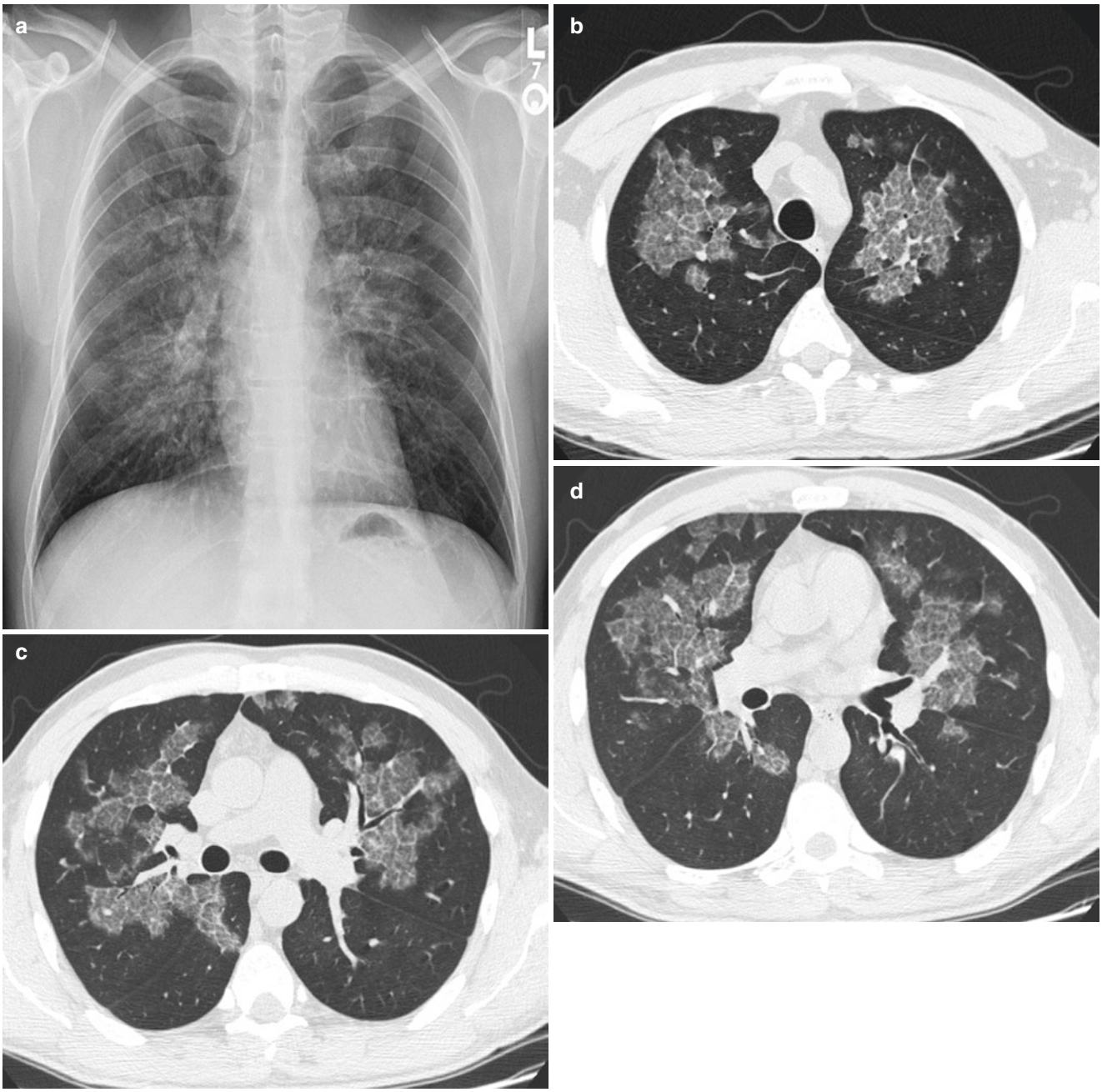

Fig. 14.21 Primary alveolar proteinosis in a 40-year-old man from GM-CSF antibodies. (**a**) Frontal chest radiograph shows parahilar ground-glass opacities without cardiomegaly. (**b–d**) Axial CT images show "sharply marginated" areas of "crazy-paving" pattern

bronchograms, and usually, there are no pleural effusions or mediastinal lymphadenopathy in the absence of infection. The crazy-paving pattern is not specific for PAP, and it can be seen in other conditions like pulmonary edema, sarcoidosis, nonspecific interstitial pneumonia, pneumocystis carinii pneumonia, cryptogenic organizing pneumonia, mucinous bronchioloalveolar carcinoma, pulmonary hemorrhage syndromes, and even simple bacterial pneumonia [30]. Crazy-paving pattern in a relatively less sick patient is a clue to the diagnosis of PAP. BAL fluid analysis and staining along with CT features are diagnostic, and open lung biopsy is rarely required.

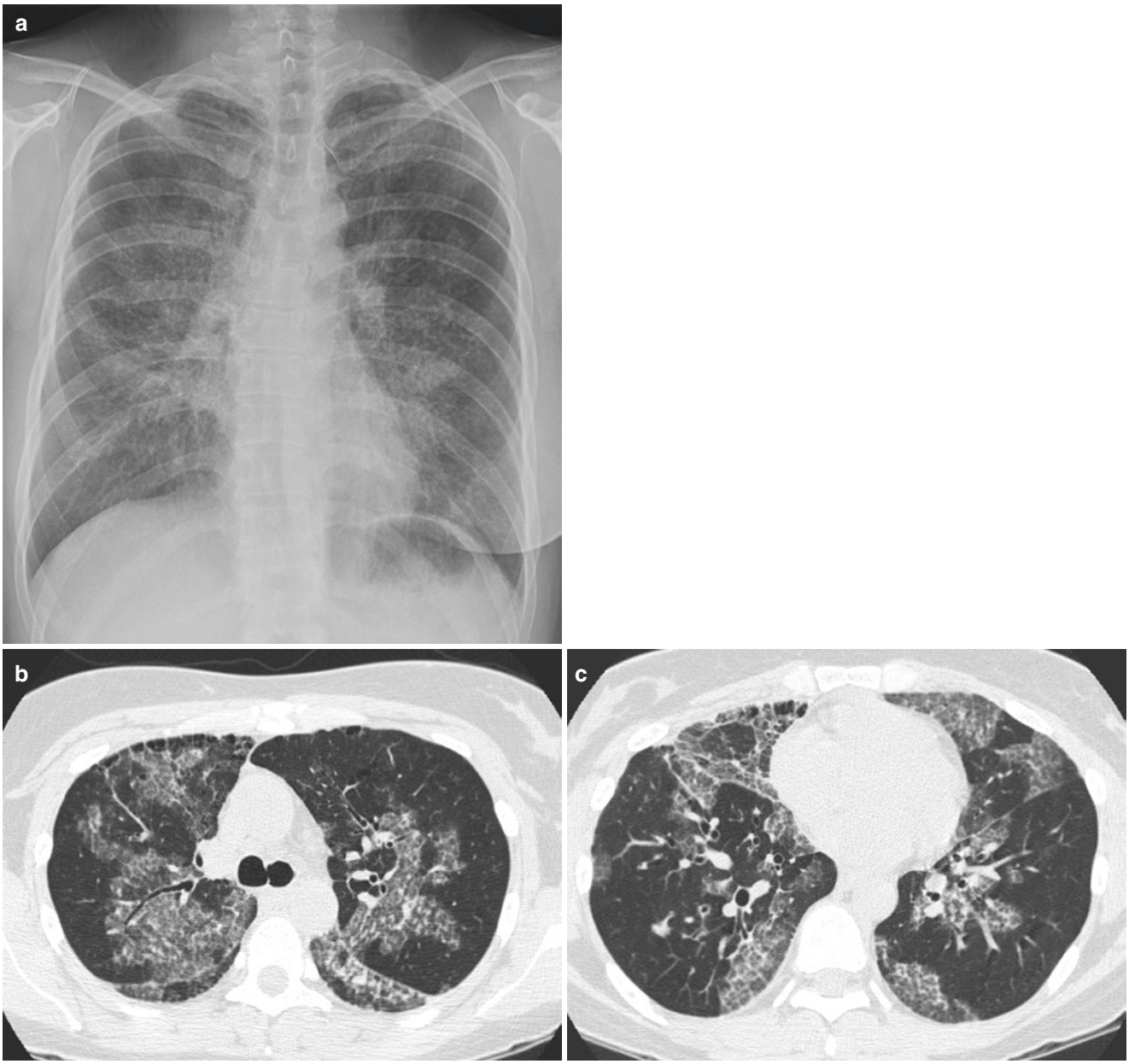

Fig. 14.22 Primary alveolar proteinosis in a 44-year-old woman. (**a**) Frontal chest radiograph shows parahilar fine reticulonodular opacities without cardiomegaly. (**b**, **c**) Axial CT images show "sharply marginated" areas of "crazy-paving" pattern. Note the paraseptal emphysema anteriorly in upper lungs, from smoking

14.7 Congenital Pulmonary Diseases Presenting in Adult

Congenital developmental anomalies of the lungs can present in the adulthood. These anomalies may be overlooked or misdiagnosed resulting in mismanagement of the patient. The common congenital anomalies are listed in Table 14.6. Congenital bronchial atresia and bronchogenic cyst have been discussed elsewhere in this book.

Table 14.6 Congenital anomalies presenting in adults

• Congenital lobar emphysema
• Pulmonary sequestration
• Congenital cystic adenomatoid malformation
• Congenital bronchial atresia
• Partial anomalous pulmonary venous return
• Interruption of a main pulmonary artery
• Bronchogenic cyst

14.7.1 Congenital Lobar Emphysema

Congenital lobar emphysema is rarely seen in adults. It results from a congenital defect of bronchial cartilage resulting in bronchial obliteration. The affected lobe is hyperexpanded and appears hyperlucent with mass effect on the rest of the lung. There is a paucity of vascular markings in that lobe, better appreciated on CT. The left upper lobe is classically involved followed by the right middle lobe. In an adult patient, it may be difficult to differentiate this condition from Swyer-James syndrome that is a post-infectious bronchiolitis affecting segments, lobe, or the entire lung. Congenital bronchial atresia (CBA) is another differential diagnosis. However, atretic bronchus containing high density or calcified mucus plug (mucocele) is almost always seen near the hilum in CBA.

14.7.2 Pulmonary Sequestrations

Pulmonary sequestration is defined as a segment of lung parenchyma that is not communicating with normal tracheobronchial tree and derives its blood supply from system arteries, above or below the diaphragm. The most common source of arterial supply is the aorta, but there are cases where arterial supply comes from splenic artery, intercostal artery, phrenic artery, and rarely coronary arteries, or there can be multiple feeders. There are two forms of sequestrations: (a) intralobar and (b) extralobar (Table 14.7). Intralobar form accounts for three-quarters of sequestration cases and may remain undiagnosed till adulthood. Venous drainage in intralobar sequestration is in pulmonary veins with a left-to-left shunt, unique for only this condition [31]. When the aberrant artery arises below or above the diaphragm, the vein also drains below or above the diaphragm. The extralobar form usually presents in neonates and infants and is commonly found between the lower lobe and diaphragm but in some cases may be located in or below the diaphragm, lungs, pericardium, or even mediastinum. The commonest site of sequestration for both forms is the left lower lobe. Intralobar sequestration is usually suspected in a patient with recurrent left lower lobe pneumonia or sometimes detected incidentally (intralobar form) on imaging. Multiphasic CT angiogram and MR angiogram are helpful in diagnosis and surgical planning (Fig. 14.23). Comprehensive imaging evaluation must be performed to assess the sequestrated segment, its arterial supply, venous drainage, any communication with gastrointestinal tract (in extralobar form), associated lung anomalies (horseshoe lung, hypoplasia of the lung), and defect in the diaphragm

Table 14.7 Features of sequestrations

	Intralobar	Extralobar
Arterial supply	Systemic arteries	Systemic arteries
Pleura	Sequestrated segment lies within normal visceral pleura	Sequestrated segment has its own pleural investment
Venous drainage	Pulmonary veins or rarely systemic veins into the right atrium	Systemic veins into the right atrium (azygos, hemiazygos, and inferior vena cava)
Associations	None	Congenital heart diseases, diaphragmatic hernia
Imaging	Soft-tissue mass, solid-cystic mass, fibrotic mass, or hypervascular mass	Homogeneous soft-tissue mass

[31]. There can be cases where there is systemic supply to a segment of the normal lung that is communicating with tracheobronchial tree. Such abnormalities are categorized in "pulmonary malinosculation spectrum" [32].

14.7.3 Congenital Cystic Adenomatoid Malformation

Congenital cystic adenomatoid malformation (CCAM) or congenital pulmonary airway malformation as they are termed now is a diverse group of disorders of cystic and noncystic lung lesions resulting from early airway maldevelopment that usually present in childhood. In fact, 90% are diagnosed within 2 months of age. In this era of imaging, more and more cases of CCAM are being recognized in adulthood in age from 20 to 60 years [33]. Most of the cases fall in CCAM type 2, while there are rare cases of type 1 category [33, 34]. Most of the cases in adults present with recurrent pneumonia, and CCAM in such patients is usually located in the lower lobes with few cases of upper lobe involvement. Chest radiograph usually shows a complex mass or a cystic mass with air-fluid levels. On CT, CCAM is usually lobar or segmental, with multiple cysts that may or may not contain air-fluid levels associated with an eccentric soft-tissue component within the complex mass [33, 34] (Fig. 14.24). The cysts can be larger than 2 cm. The differential diagnosis of CCAM includes pulmonary sequestration (systemic vascular supply) (Fig. 14.25), cystic bronchiectasis (continuity with the bronchial tree), and recurrent infection with pneumatoceles [33]. Nevertheless, adult CCAM must be suspected in a patient with recurrent pneumonia in the same location that shows multiple cysts with air-fluid levels and soft-tissue component [34].

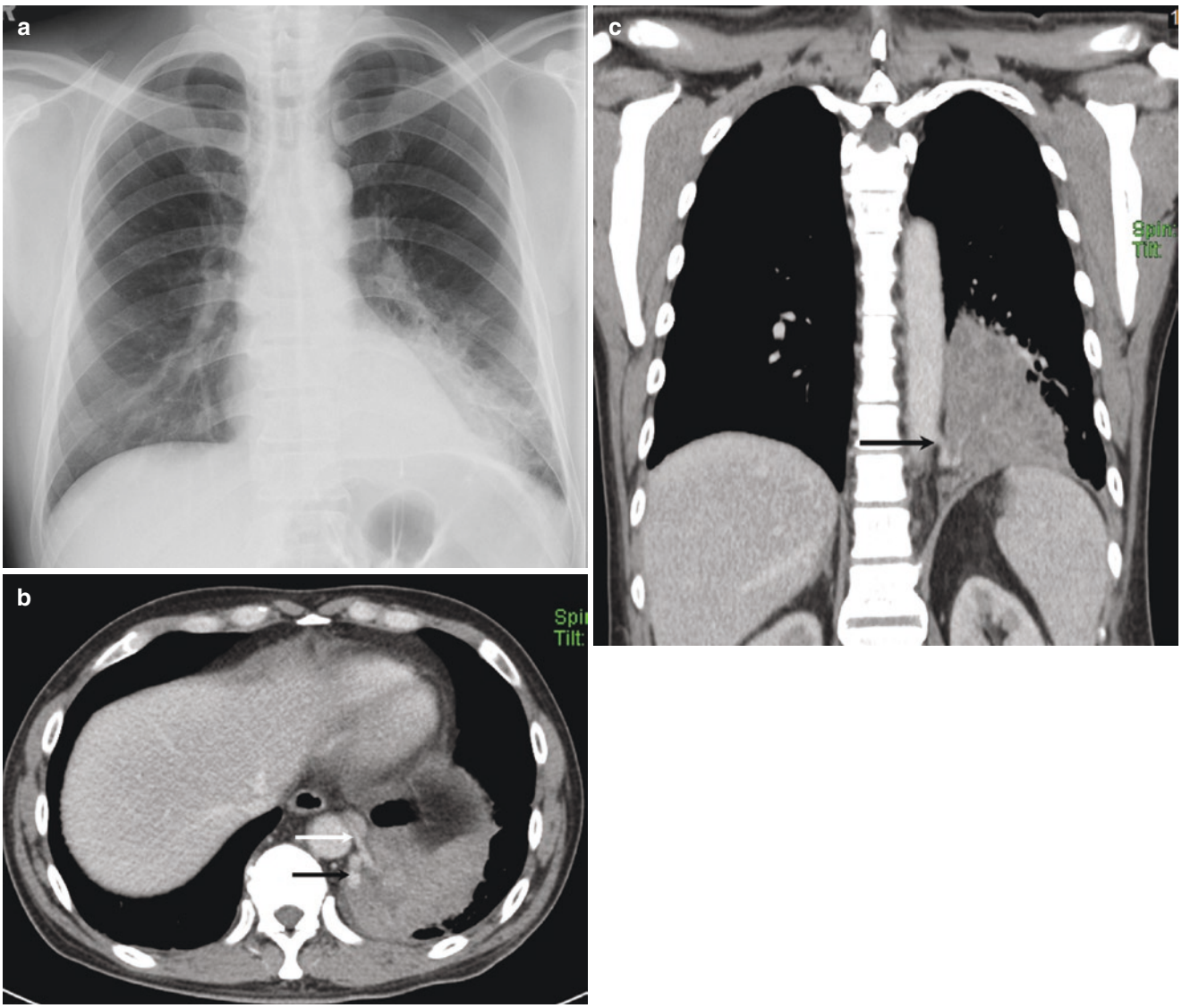

Fig. 14.23 Intralobar sequestration in a 49-year-old man presenting with recurrent left lower zone pneumonia. (**a**) Frontal radiograph shows a left retrocardiac area of consolidation without any effusion. (**b**, **c**) Axial and coronal contrast-enhanced CT images show dense consolidation in left lower hemithorax with supply arterial from the aorta (black arrow) and venous drainage (white arrow) in IVC (not shown)

14.7.4 Partial Anomalous Pulmonary Venous Return

Partial anomalous pulmonary venous drainage (PAPVD) is defined as the connection of at least one pulmonary vein, but not all, to the systemic venous system or right atrium (RA), resulting in the formation of an extracardiac left-to-right shunt [35]. Most patients are either mildly symptomatic or asymptomatic. Drainage of all the pulmonary veins outside the left atrium is termed as total anomalous pulmonary venous drainage (TAPVD). TAPVD is associated with septal defects or patent ductus arteriosus, i.e., right-to-left shunt, for compatibility. PAPVD cases are increasingly diagnosed in adults due to the availability of multidetector CT. The commonest form of PAPVD is on the right side with drainage of the right superior pulmonary vein (RSPV) in the superior vena cava (SVC) at the junction of the SVC and right atrium [36]. This condition is commonly associated with sinus venosus type of atrial septal defect. Rare PAPVD on the right side include the connection between pulmonary veins and coronary sinus or IVC or azygos vein. The most

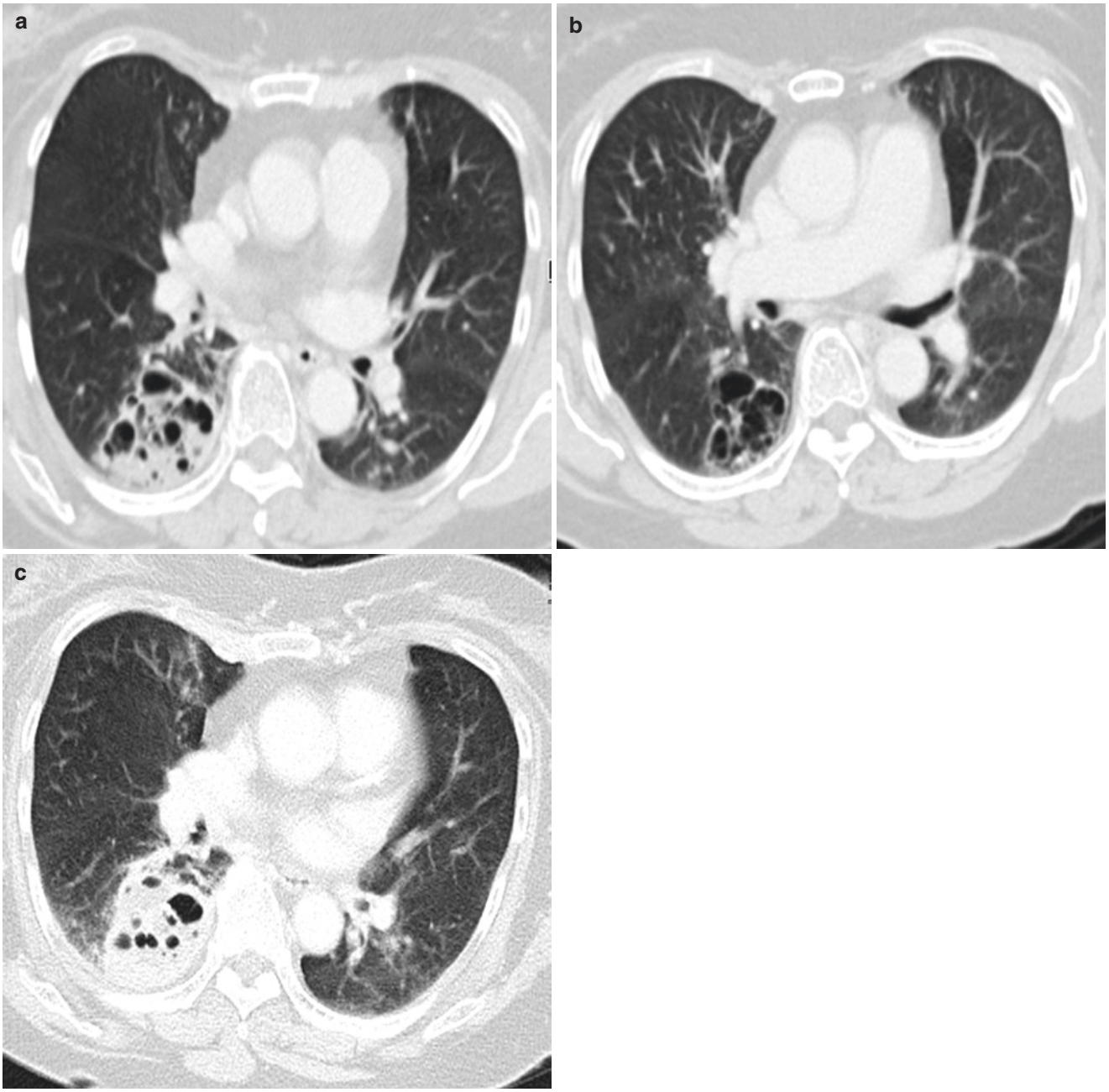

Fig. 14.24 A 41-year-old woman with CCAM presenting with recurrent pulmonary infection. (**a**) Axial CT image on initial presentation shows a multicystic mass with the eccentric solid component. (**b**) Follow-up CT scan after 6 months shows resolution of the solid component. (**c**) Two years later the patient presented again with infection, and the CT reveals reappearance of the soft-tissue component with air-fluid levels. The CCAM was resected

common PAPVD on the left side is drainage of the left superior pulmonary vein (LSPV) in the left brachiocephalic vein [36] (Fig. 14.26). Contrast-enhanced CT or MR is helpful in the diagnosis of this condition. On axial CT images, the left PAPVD may be mistaken for a persistent left SVC [36] (Fig. 14.27). However, following the vessel in the sequential images or using coronal reconstruction is useful in differentiation.

Scimitar syndrome or hypogenetic lung syndrome or pulmonary venolobar syndrome is a rare category of PAPVD characterized by anomalous pulmonary vein draining a part or the entire right lung into the IVC [35]. The anomalous vein or "scimitar vein" has a scimitar-like configuration (a Turkish sword) and drains classically in subdiaphragmatic or supradiaphragmatic IVC but can drain in another vein like portal vein or even directly in the right atrium. Other features that may or may not be present include hypoplasia of the right lung with dextroposition of the heart, anomalies of the right lung lobation (two lobes as in left lung), hypoplasia of the right pulmonary artery, and anomalous systemic supply to the lung from the abdominal aorta or its branches [31]. Since scimitar syndrome can be associated with congenital

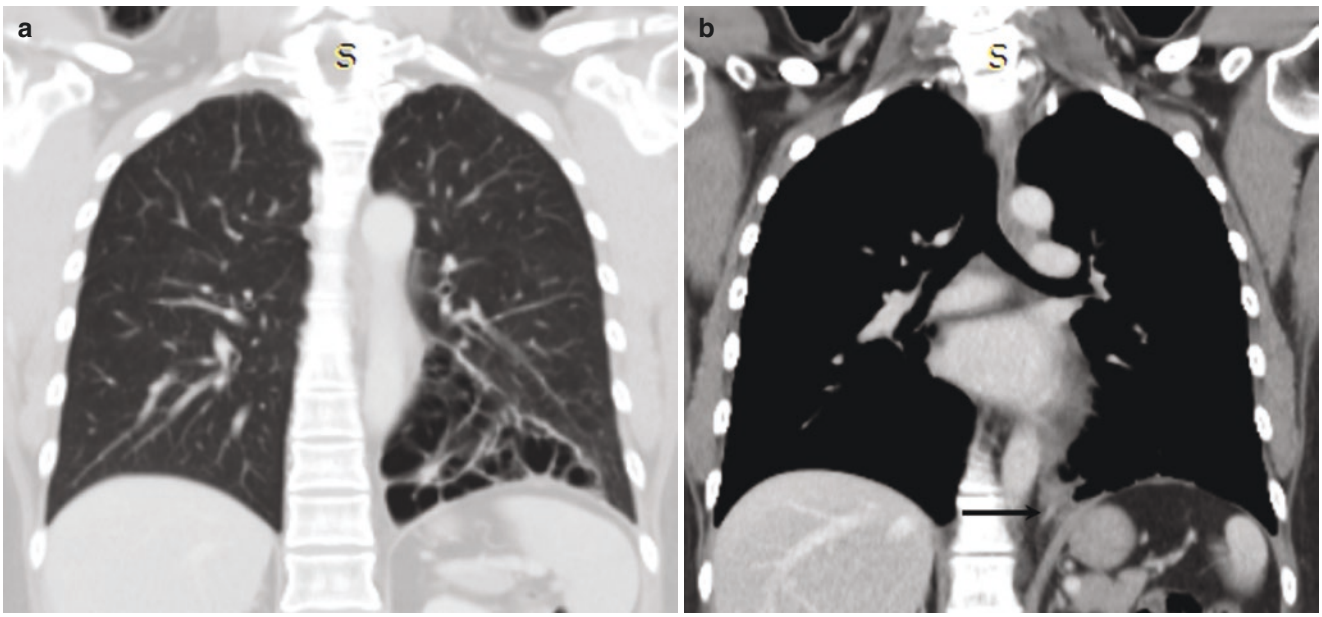

Fig. 14.25 Incidental sequestration in a 69-year-old woman. (**a**) Coronal CT image shows multicystic changes in the left lower lobe mimicking CCAM. (**b**) Coronal image in the mediastinal window shows a tiny vessel (arrow) coursing toward the cystic abnormality. This artery was traced back to the celiac artery (not shown) and was supplying the sequestrated segment

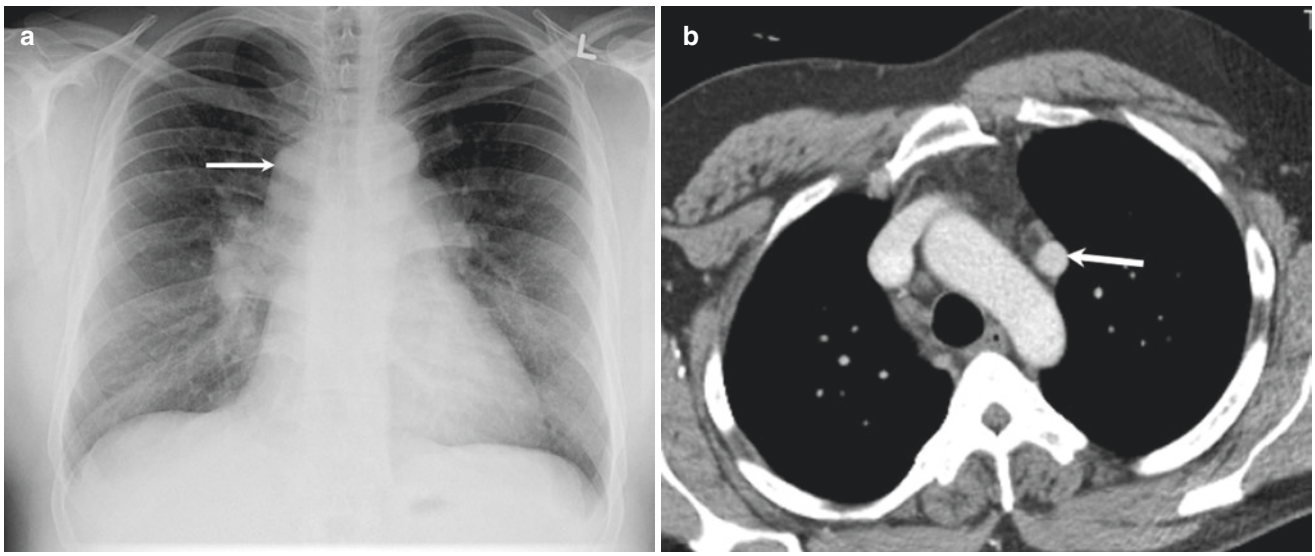

Fig. 14.26 PAPVD in a 56-year-old woman with abnormal chest radiograph. (**a**) Frontal chest radiograph shows an opacity in the right trachea-bronchial angle (white arrow). (**b–d**) Axial CT images show that the right paratracheal opacity is due to dilated azygos vein (AV) with a left upper lobe pulmonary vein draining in left brachiocephalic vein (white arrows). (**e**) Coronal CT image shows the PAPVD (white arrow) draining into the brachiocephalic vein (asterisk)

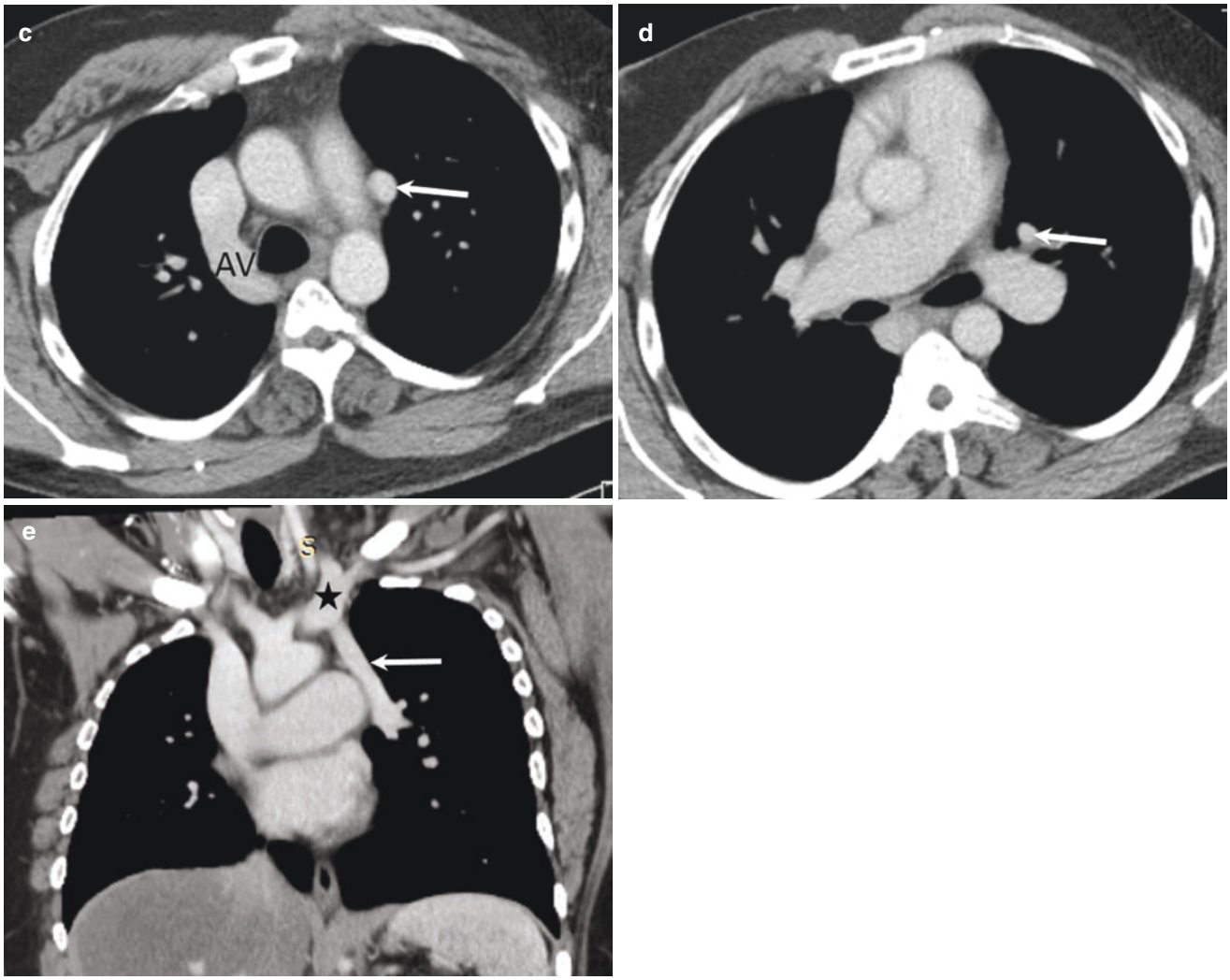

Fig. 14.26 (continued)

cardiac anomalies that include a ventricular septal defect, a careful assessment of the heart must be done. A rare "horseshoe lung" can be associated with scimitar syndrome where the posterior-basal segments of the lower lobes of two lungs join behind the posterior pericardium (Fig. 14.28). "Peudoscimitar syndrome" is a rare mimicker where a tortuous anomalous pulmonary vein drains into the left atrium [36]. Chest radiograph shows classic "scimitar sign" in the right lower zone. CT helps to accurately map the anomalous vein and associated anomalies.

14.7.5 Interruption of a Main Pulmonary Artery

Unilateral absence of the main pulmonary artery is a rare anomaly that is more common on the right side than on the left side. This condition is usually associated with congenital cardiac anomalies including tetralogy of Fallot, ventricular septal defect, right-sided aortic arch, truncus arteriosus, and transposition of great vessels [37]. This condition may remain asymptomatic until adulthood if there are minor or no associated congenital cardiac anomalies. Chest radiograph shows a small hemithorax with volume loss and asymmetrically smaller hilum. CT shows absent pulmonary artery on the smaller hemithorax (Fig. 14.29) with multiple small arteries supplying the affected lungs. These are the branches of systemic arteries and transpleural collaterals, compensating, to some extent, the absent flow of pulmonary artery. Ventilation-perfusion scan shows absent perfusion with normal ventilation and is a useful study to separate absent pulmonary artery from post-infectious bronchiolitis that also can present with small pulmonary artery [38] (Fig. 14.30).

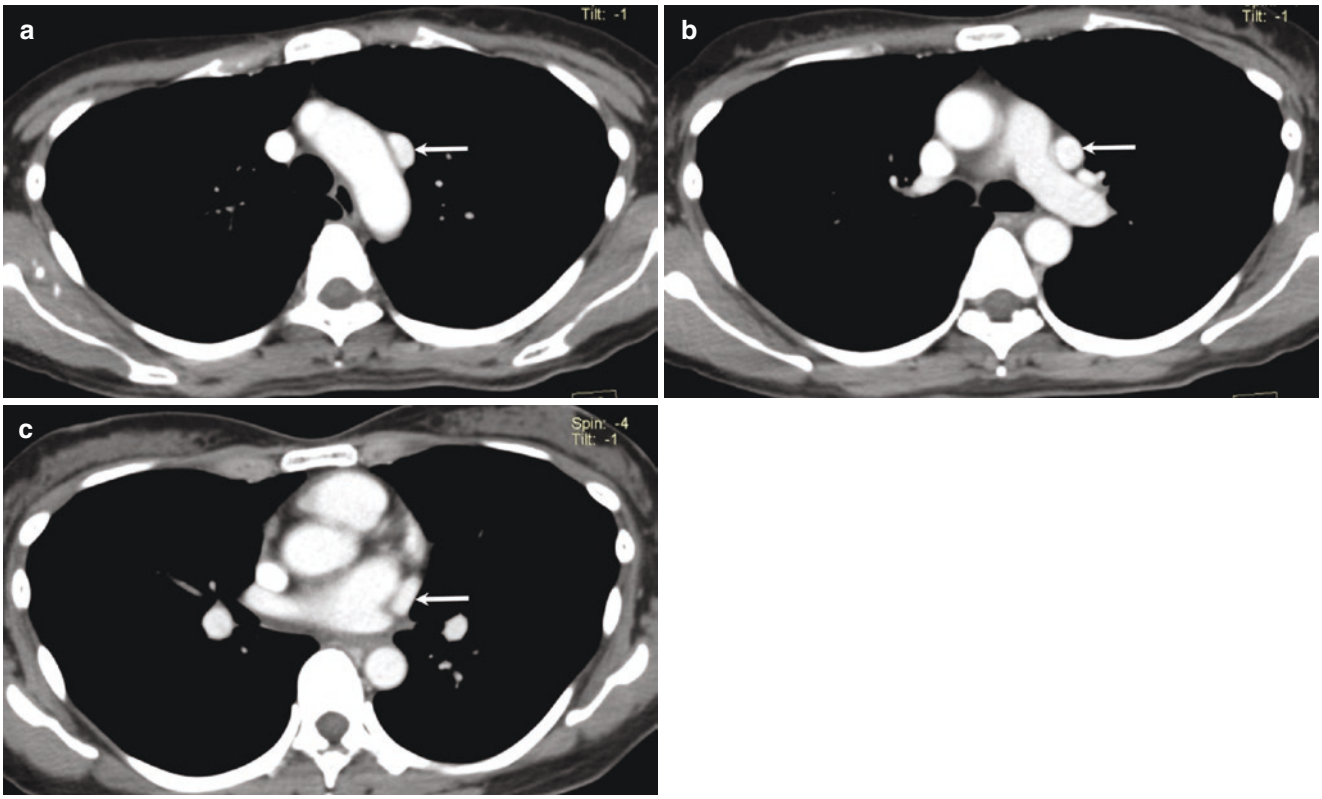

Fig. 14.27 Left SVC may be mistaken for PAPVD. (**a**–**c**) Axial CT images show left SVC (white arrow) with more medial downward course toward coronary sinus

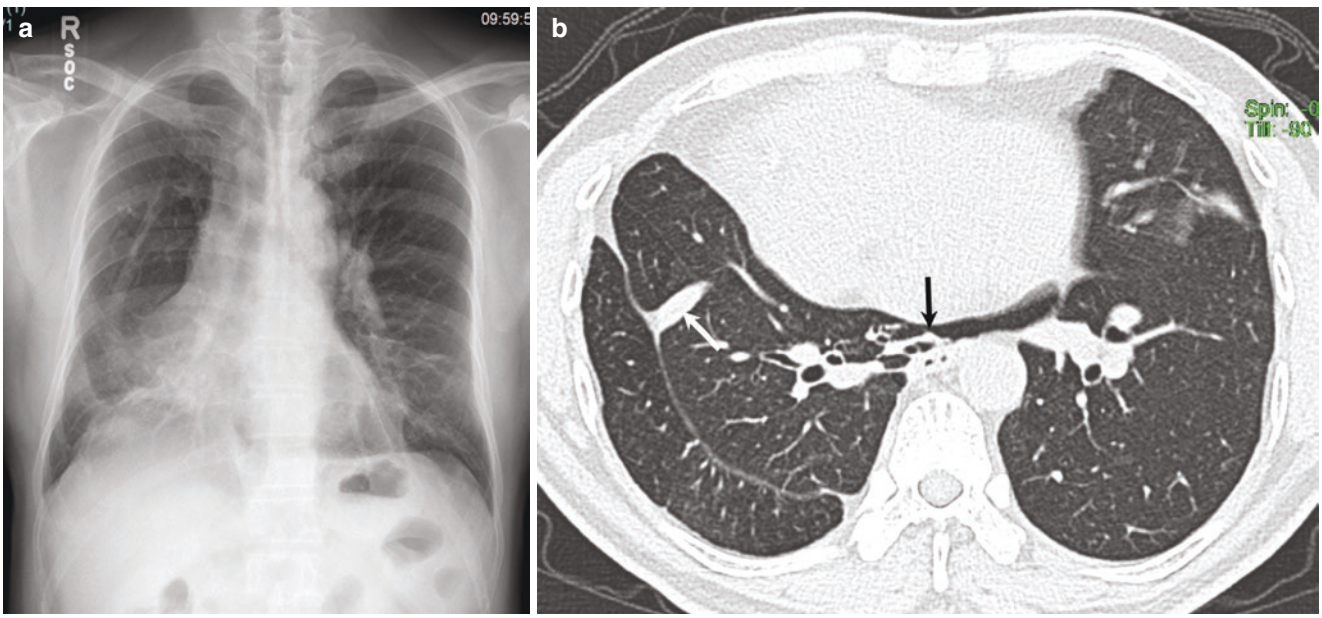

Fig. 14.28 A 64-year-old man with Scimitar syndrome on health screening. (**a**) Frontal chest radiograph shows a sword-shaped vertically oriented opacity in right lower lung associated with right lower lung hypoplasia and shift of the heart toward the right. (**b**) Axial CT image shows the anomalous vein (white arrow) coursing toward the inferior vena cava with fusion of lungs behind the posterior pericardium (black arrow)

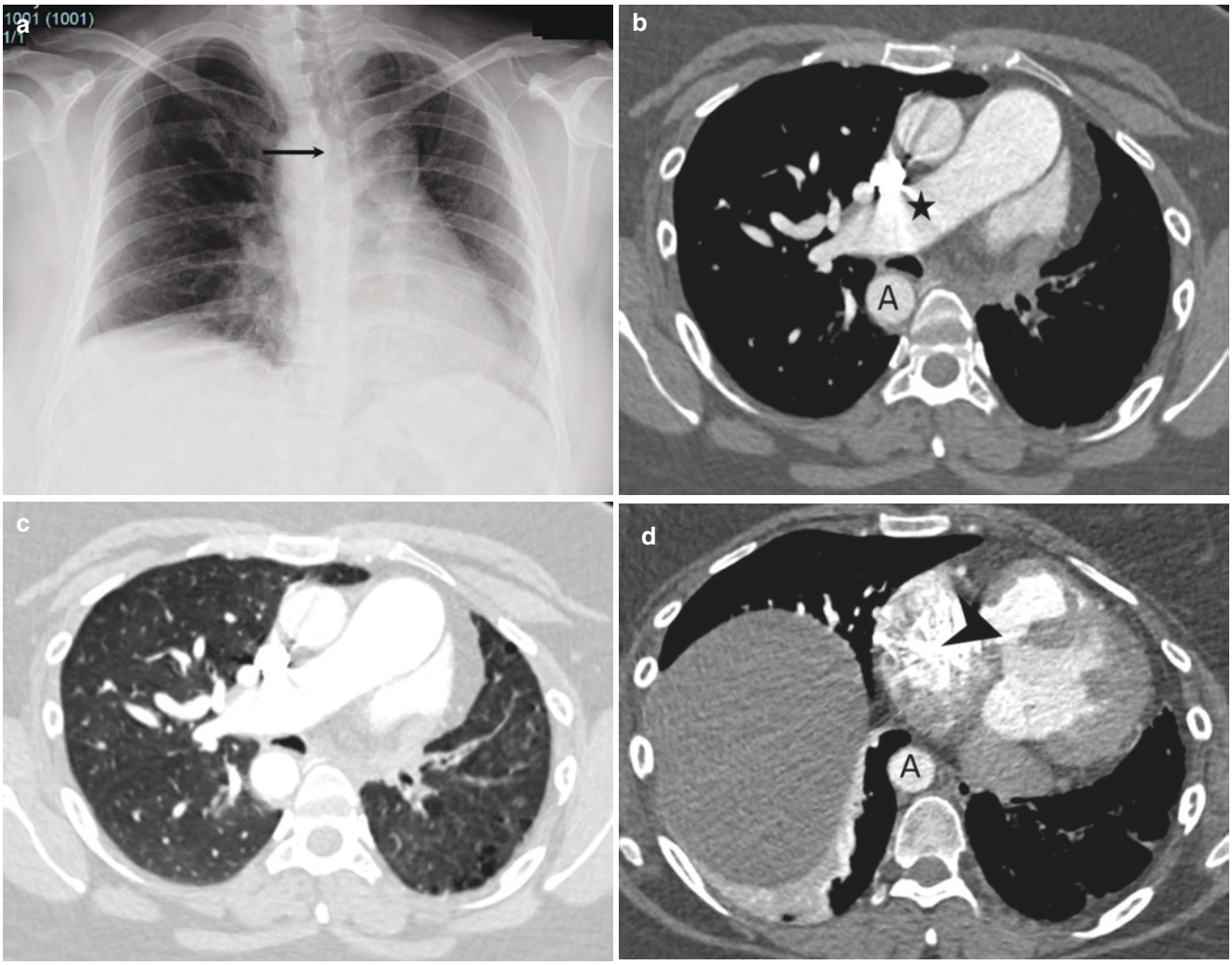

Fig. 14.29 Absent left pulmonary artery in a 27-year-old woman. (**a**) Frontal chest radiograph shows volume loss in left hemithorax with a leftward shift of mediastinum. Note the right aortic arch indenting the right lateral wall (black arrow) of the trachea. (**b**) Axial CT image shows a continuation of main pulmonary as a right pulmonary artery (asterisk) with absent left pulmonary artery. (**c**) Axial image in lung window settings shows smaller left lung with smoking-induced paraseptal emphysema but no difference in attenuation of lungs. (**d**) More caudal axial CT image shows a membranous ventricular septal defect (arrowhead). Note the right aortic arch (A)

14.8 Pulmonary Complications of Cirrhosis

Chronic liver diseases, most commonly cirrhosis, can lead to major changes in the pulmonary circulation. These secondary changes in pulmonary microcirculation may override the liver disease in clinical presentation. The two most important pulmonary complications in cirrhotic patients are hepatopulmonary syndrome (HPS) and portopulmonary hypertension (PPH). The presence of portal hypertension is the trigger in the pathogenesis of each of these disorders.

Hepatopulmonary syndrome (HPS) is the most common condition, found in 5–30% of cirrhosis patients. HPS consists of a triad of chronic liver disease, PaO2 < 70 mm Hg or alveolar-arterial oxygen gradient >20 mm Hg, evidence of intrapulmonary vascular dilatation [39]. Majority of the patients present with symptoms and signs of liver disease. Dyspnea is presenting symptom in up to 18% of patients. Platypnea and orthodeoxia (dyspnea and hypoxemia induced or worsened by upright posture and improved by recumbency) are the two most important clinical signs, highly suggestive of HPS in cirrhosis patients. Since the first description in the literature, the underlying pathophysiology of HPS still remains unclear. Dilatation of small peripheral pulmonary vessels is the hallmark of HPS. Nitrous oxide (NO) has been

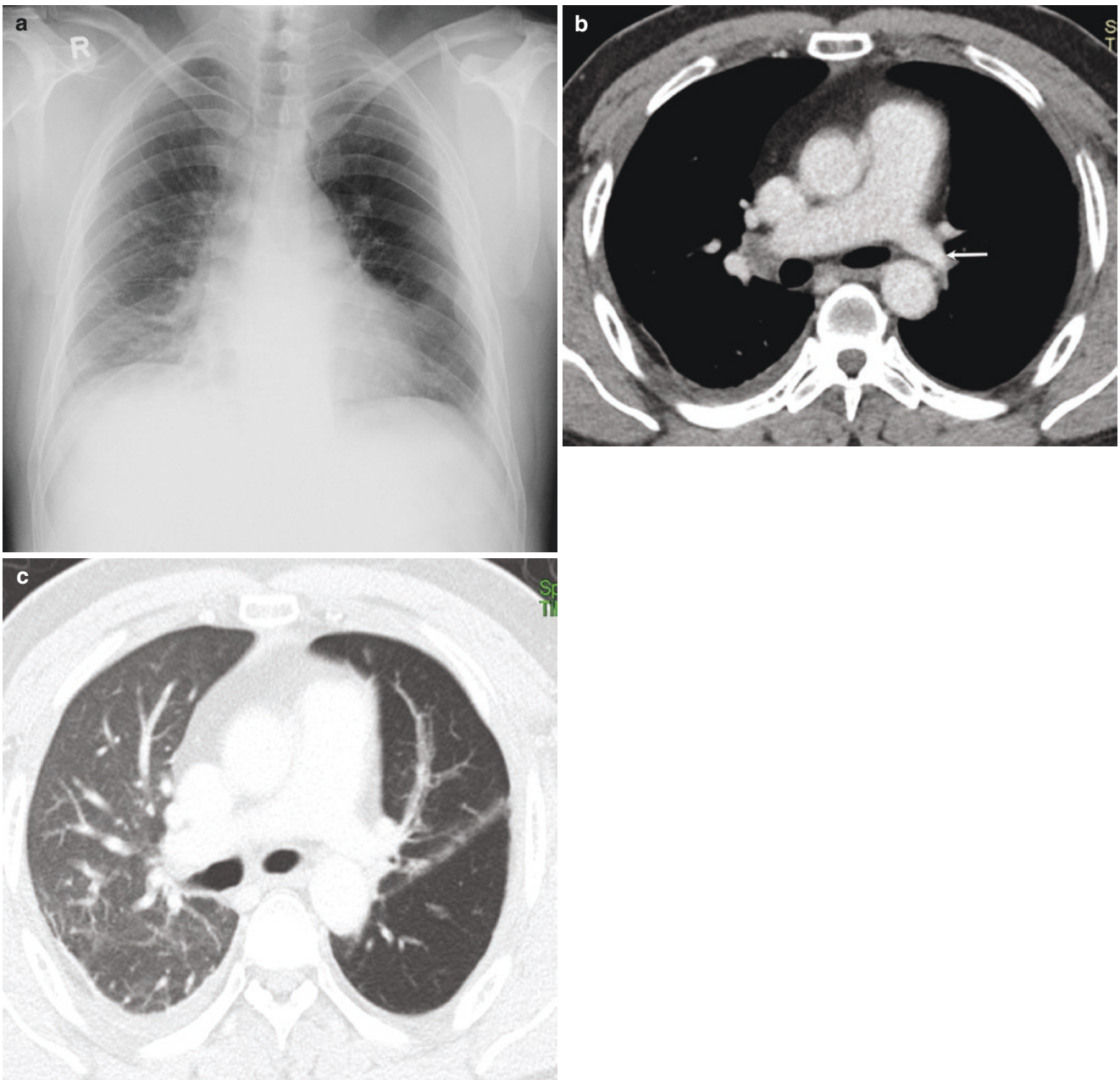

Fig. 14.30 Post-infectious bronchiolitis in a 21-year-old woman. (**a**) Frontal chest radiograph shows a translucent left hemithorax with a paucity of vascular markings in the left lung. (**b**, **c**) Axial CT images show small left pulmonary artery (white arrow) associated with small hyperlucent left lung due to post-infectious obliterative bronchiolitis

implicated for dilatation of pulmonary vessels as NO has been demonstrated to be present at a higher level in cirrhotic patients. Vasodilatation leads to severe hypoxemia, the essential component of HPS. Three mechanisms have been suggested to explain the hypoxemia due to vasodilatation: ventilation-perfusion mismatch, diffusion-perfusion limitation, and intrapulmonary shunting [40]. Ventilation-perfusion mismatch results from increased local perfusion due to dilated capillaries, while the ventilation remains relatively unchanged or low. Limitation of perfusion results from increased diameter of capillaries that require the oxygen molecule to travel a longer distance to bind to erythrocytes, further compromised by the faster motion of blood due to hyperdynamic circulation, seen in cirrhosis. The pulmonary arteriovenous shunting due to fistula formation can lead to insufficient oxygenation due to the mixing of arterial and venous blood. The usefulness of chest radiograph lies in the fact that it can help in excluding more common cause of dys-

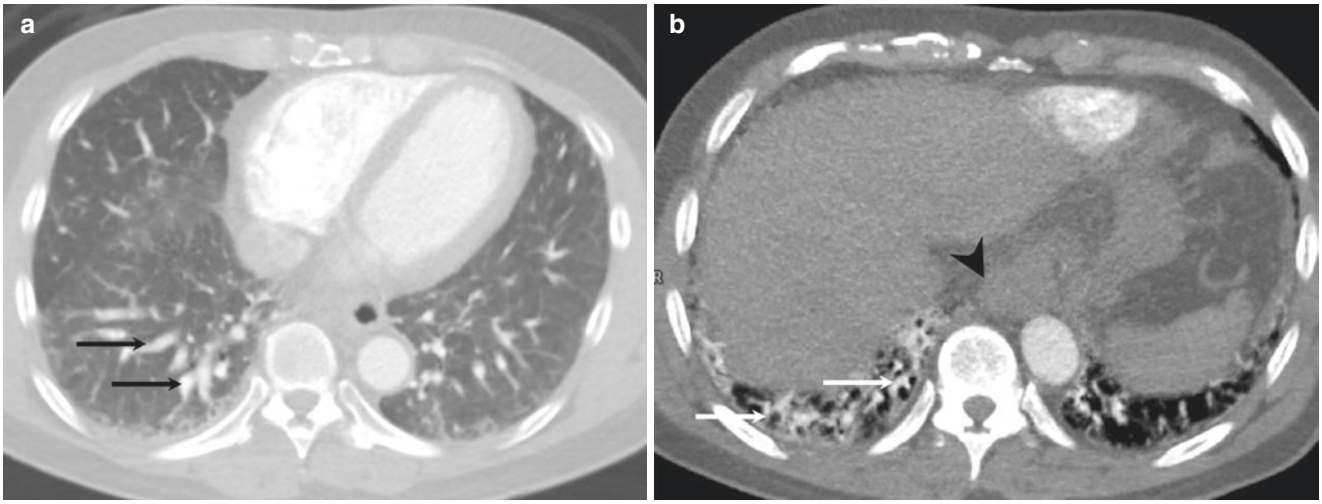

Fig. 14.31 A 57-year-old man with hepatopulmonary syndrome. (**a**, **b**) Axial CT images show dilatation of branches of right lower lobe pulmonary artery (black arrows) as compared to adjacent bronchioles. (**b**) Caudal CT image shows aneurysmal dilatation (white arrows) of peripheral branches of the pulmonary artery. Note the non-enhancing varices (arrowhead) and surface nodularity of liver suggesting cirrhosis

pnea in patients with a chronic liver disease like hydrothorax. CT thorax in HPS shows multiple dilated vessels extending till pleural surface (Fig. 14.31). The ratio of the diameter of lower lobe segmental pulmonary artery branches to adjacent bronchiole is increased and may approach 2:1 [41]. There is an inverse relation between the diameter of peripheral vessels and partial pressure of arterial oxygen [41]. CT pulmonary angiogram may show frank aneurysms in the lower lobe peripheral branches of the pulmonary artery [42].

Portopulmonary hypertension (PPH) is defined as pulmonary artery hypertension (PAH) that develops in the setting of portal hypertension. Radiological features of PPH are the same as idiopathic pulmonary hypertension. The etiology of the PPH is unclear with three presumed mechanisms by which portal hypertension causes pulmonary hypertension [43]. The vasoconstrictive chemicals like serotonin and thromboxane are bypassed due to port-systemic shunts and not cleared adequately from the circulation by cirrhotic liver, or microemboli from the portal circulation reach the pulmonary circulation through portosystemic shunts, or the high cardiac output in cirrhosis leads to PAH.

14.9 Erdheim-Chester Disease

Erdheim-Chester disease is a systemic disorder similar to Langerhans cell histiocytosis and characterized by with infiltration lipid-containing foamy histiocytes in the skeleton, usually long bones. The two conditions are probably closely interrelated, and histiocytes may actually undergo transformation between the two cell lines. A substantial proportion of cases show thoracic involvement. Diffuse or patchy sclerosis in the long bones, a coarsened trabecular pattern, and cortical thickening associated with persistent interstitial septal thickening helps in radiological diagnosis. A biopsy is required for confirmatory diagnosis. The thoracic manifestations are described in Table 14.8 (Fig. 14.32) [44].

Table 14.8 Thoracic manifestations of Erdheim-Chester disease

• Pleural-pulmonary changes
– Smooth interlobular septa
– Centrilobular nodular opacities
– Ground-glass opacities
– Pleural thickening
– Pleural effusion
• Cardiomediastinal involvement
– Periaortic infiltration extending around the aortic branches
– Infiltration in the right atrium wall
– Narrowing of the right atrium
– Perivascular infiltration extending into the cardiac sulci
– Pericardial effusion and/or thickening

14.10 Granulomatosis with Polyangiitis (GPA)

Granulomatosis with polyangiitis (GPA), previously known as Wegener granulomatosis, is a multisystem necrotizing vasculitis commonly affecting the airways, lungs, and kidneys and less commonly the central nervous system. The mean age at diagnosis is 40 years without any gender predilection. The clinical presentation ranges from sinusitis to dyspnea and chest pain. Churg-Strauss vasculitis and GPA

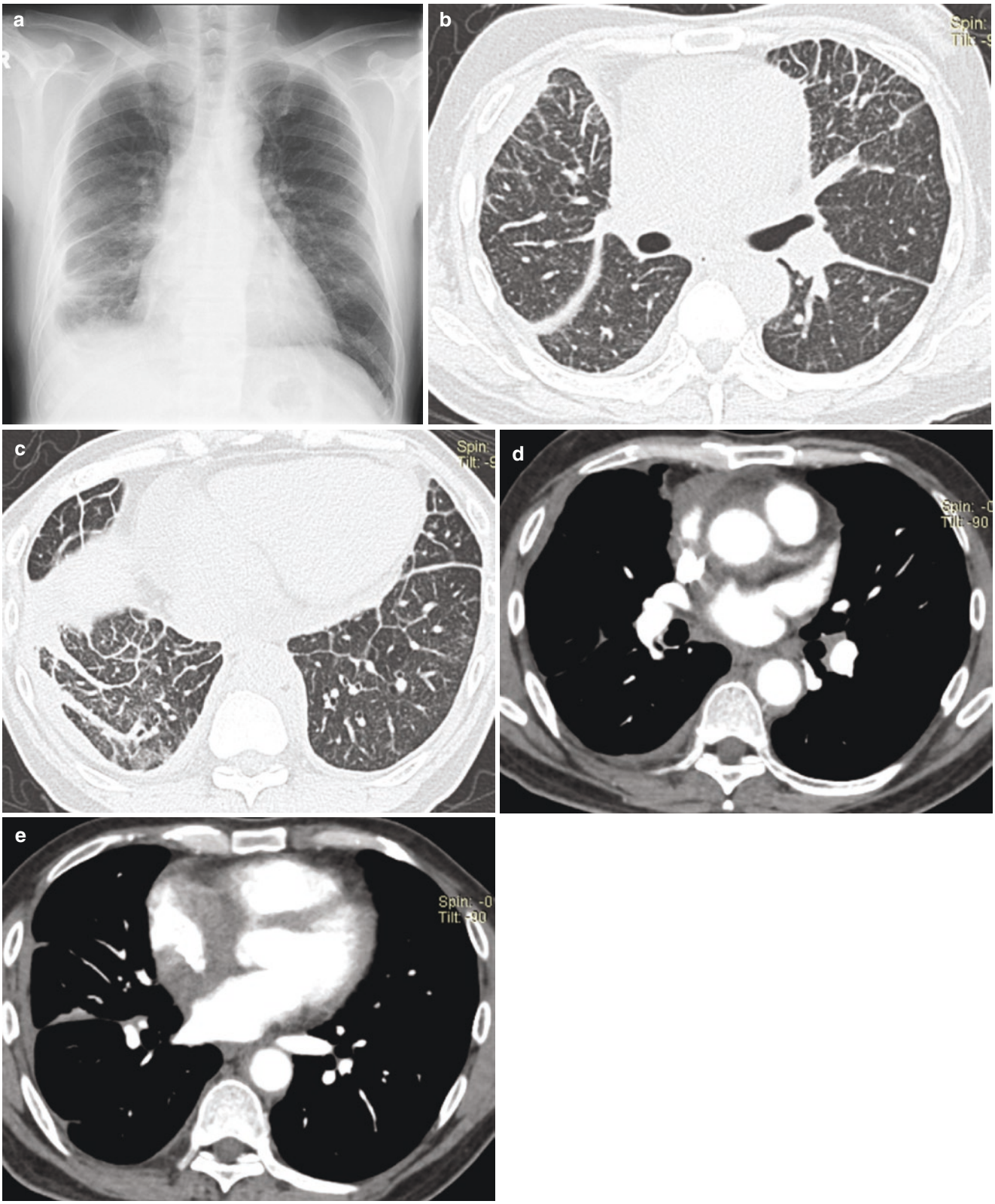

Fig. 14.32 A 58-year-old man with Erdheim-Chester disease. (**a**) Frontal chest radiograph shows cardiomegaly with right pleural effusion, round atelectasis, and septal thickening in lower lungs. (**b**, **c**) Axial CT images show septal thickening, pleural effusion, and an area of round atelectasis in the right lower lobe. (**d**, **e**) Axial contrast-enhanced CT aortogram images show pericardial thickening; infiltration along the cardiac sulci, particularly the right atrial walls with narrowing of the right atrium; and infiltration around the aorta and left main coronary artery

are included in ANCA-associated vasculitides. Elevation of serum c-antineutrophil antibodies against protease 3 in cytoplasmic granules (c-ANCA) titer is useful for diagnosis and monitoring disease activity. Since there is no eosinophilia, GPA is excluded from eosinophilic lung diseases. Renal functions may be elevated with concomitant renal involvement, and renal biopsy is commonly used for confirmation. The imaging features overlap with septic pulmonary emboli, abscess, invasive aspergillosis, and metastases (Figs. 14.33 and 14.34) (Table 14.9) [45, 46]. The vasculitis may lead to pulmonary infarctions, or the parenchymal lesions may get secondarily infected.

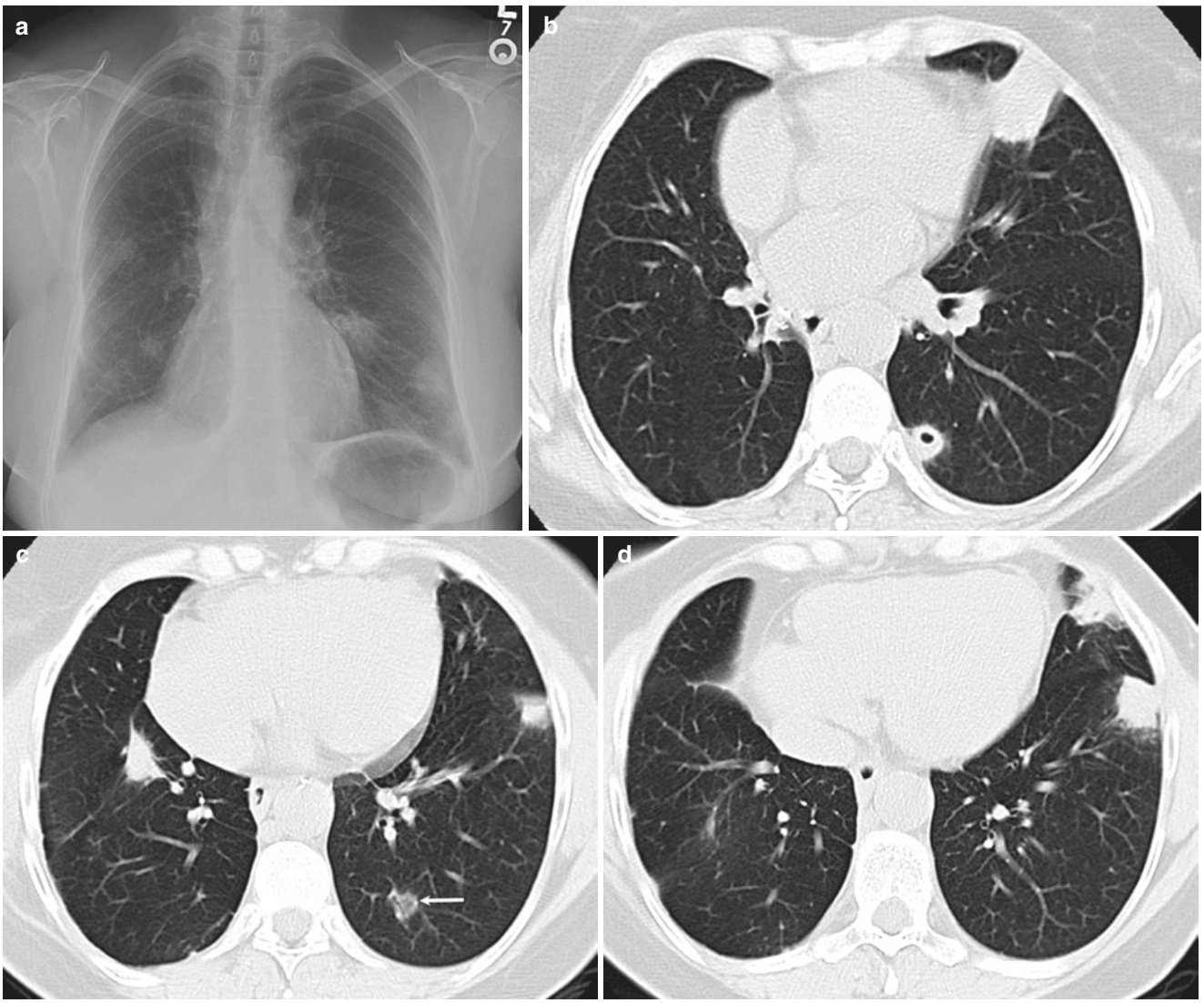

Fig. 14.33 A 5 3-year-old woman with granulomatosis with polyangiitis. (**a**) Frontal radiograph shows multiple ill-defined peripheral nodules. (**b–d**) Axial CT images show multiple cavitary nodules and nodules with reverse halo sign and halo sign

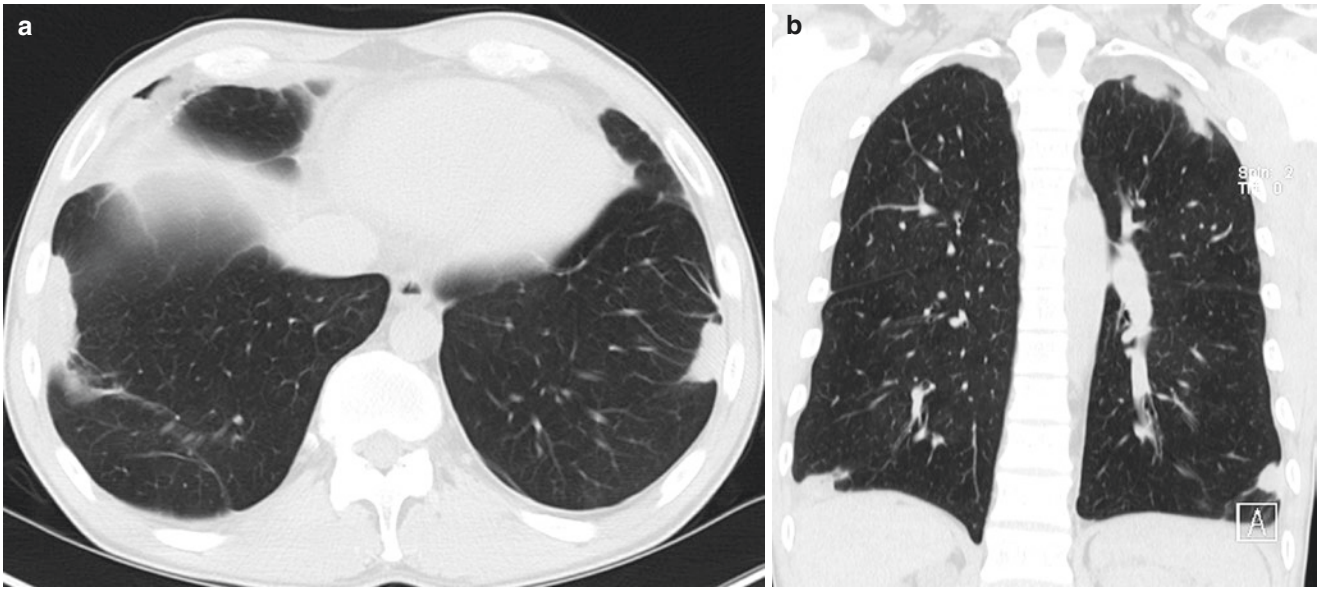

Fig. 14.34 A 39-year-old man with granulomatosis with polyangiitis. (**a**, **b**) Axial and coronal CT images show subpleural opacities in bilateral upper and lower lungs. Pathologically, biopsy of the right upper, middle, and lower lobes demonstrated medium vessel vasculitis with associated pulmonary infarctions

Table 14.9 Imaging features of GPA

Tracheobronchial tree
• Subglottic tracheal stenosis (eccentric)
• Bronchostenosis
Pulmonary
• Nodules and masses
– Cavitary nodules
– Halo sign
– Reverse halo sign
• Consolidation and ground-glass opacities

References

1. Lynch DA. Imaging of asthma and allergic bronchopulmonary mycosis. Radiol Clin N Am. 1998;36(1):129–42.
2. Niimi A, Matsumoto H, Amitani R, Nakano Y, Mishima M, Minakuchi M, Nishimura K, Itoh H, Izumi T. Airway wall thickness in asthma assessed by computed tomography: relation to clinical indices. Am J Respir Crit Care Med. 2000;162(4):1518–23.
3. Busacker A, Newell JD, Keefe T, Hoffman EA, Granroth JC, Castro M, Fain S, Wenzel S. A multivariate analysis of risk factors for the air-trapping asthmatic phenotype as measured by quantitative CT analysis. Chest J. 2009;135(1):48–56.
4. Naughton M, Fahy J, FitzGerald MX. Chronic eosinophilic pneumonia: a long-term follow-up of 12 patients. Chest. 1993;103(1):162–5.
5. Marchand E, Etienne-Mastroianni B, Chanez P, Lauque D, Leclerc P, Cordier JF. Groupe d'Etudes et de Recherche sur les Maladies Orphelines Pulmonaires. Idiopathic chronic eosinophilic pneumonia and asthma: how do they influence each other? Eur Respir J. 2003;22(1):8–13.
6. Gaensler EA, Carrington CB. Peripheral opacities in chronic eosinophilic pneumonia: the photographic negative of pulmonary edema. Am J Roentgenol. 1977;128(1):1–3.
7. Mayo JR, MUller NL, Road J, Sisler J, Lillington G. Chronic eosinophilic pneumonia: CT findings in six cases. Am J Roentgenol. 1989;153(4):727–30.
8. Agarwal R. Allergic bronchopulmonary aspergillosis. Chest J. 2009;135(3):805–26.
9. Krenke R, Grabczak EM. Tracheobronchial manifestations of Aspergillus infections. Sci World J. 2011;11:2310–29.
10. Ward S, Heyneman L, Lee MJ, Leung AN, Hansell DM, Müller NL. Accuracy of CT in the diagnosis of allergic bronchopulmonary aspergillosis in asthmatic patients. Am J Roentgenol. 1999;173(4):937–42.
11. Masi AT, Hunder GG, Lie JT, Michel BA, Bloch DA, Arend WP, Calabrese LH, Edworthy SM, Fauci AS, Leavitt RY, Lightfoot RW. The American College of Rheumatology 1990 criteria for the classification of Churg-Strauss syndrome (allergic granulomatosis and angiitis). Arthritis Rheum. 1990;33(8):1094–100.
12. Worthy SA, Müller NL, Hansell DM, Flower CD. Churg-Strauss syndrome: the spectrum of pulmonary CT findings in 17 patients. Am J Roentgenol. 1998;170(2):297–300.
13. Kim YK, Lee KS, Chung MP, Han J, Chong S, Chung MJ, Chin AY, Kim HY. Pulmonary involvement in Churg-Strauss syndrome: an analysis of CT, clinical, and pathologic findings. Eur Radiol. 2007;17(12):3157–65.
14. Bernheim A, McLoud T. A review of clinical and imaging findings in eosinophilic lung diseases. Am J Roentgenol. 2017;208(5):1002–10.
15. Jeong YJ, Kim KI, Seo IJ, Lee CH, Lee KN, Kim KN, Kim JS, Kwon WJ. Eosinophilic lung diseases: a clinical, radiologic, and pathologic overview. Radiographics. 2007;27(3):617–37.
16. Friedman PJ. Imaging studies in emphysema. Proc Am Thorac Soc. 2008;5(4):494–500.
17. Stern EJ, Frank MS. CT of the lung in patients with pulmonary emphysema: diagnosis, quantification, and correlation with pathologic and physiologic findings. Am J Roentgenol. 1994;162(4):791–8.
18. Foster WL Jr, Gimenez EI, Roubidoux MA, Sherrier RH, Shannon RH, Roggli VL, Pratt PC. The emphysemas: radiologic-pathologic correlations. Radiographics. 1993;13(2):311–28.

19. Niewoehner DE, Kleinerman J, Rice DB. Pathologic changes in the peripheral airways of young cigarette smokers. N Engl J Med. 1974;291(15):755–8.
20. Moon J, Du Bois RM, Colby TV, Hansell DM, Nicholson AG. Clinical significance of respiratory bronchiolitis on open lung biopsy and its relationship to smoking related interstitial lung disease. Thorax. 1999;54(11):1009–14.
21. Liebow AA, Steer A, Billingsley JG. Desquamative interstitial pneumonia. Am J Med. 1965;39(3):369–404.
22. Davies G, Wells AU, du Bois RM. Respiratory bronchiolitis associated with interstitial lung disease and desquamative interstitial pneumonia. Clin Chest Med. 2004;25(4):717–26.
23. Heyneman LE, Ward S, Lynch DA, Remy-Jardin M, Johkoh T, Müller NL. Respiratory bronchiolitis, respiratory bronchiolitis-associated interstitial lung disease, and desquamative interstitial pneumonia: different entities or part of the spectrum of the same disease process? Am J Roentgenol. 1999;173(6):1617–22.
24. Sieminska A, Kuziemski K. Respiratory bronchiolitis-interstitial lung disease. Orphanet J Rare Dis. 2014;9(1):106.
25. Lin H, Jiang S. Combined pulmonary fibrosis and emphysema (CPFE): an entity different from emphysema or pulmonary fibrosis alone. J Thorac Dis. 2015;7(4):767.
26. Jankowich MD, Rounds S. Combined pulmonary fibrosis and emphysema alters physiology but has similar mortality to pulmonary fibrosis without emphysema. Lung. 2010;188(5):365–73.
27. Inomata M, Ikushima S, Awano N, Kondoh K, Satake K, Masuo M, Kusunoki Y, Moriya A, Kamiya H, Ando T, Yanagawa N. An autopsy study of combined pulmonary fibrosis and emphysema: correlations among clinical, radiological, and pathological features. BMC Pulm Med. 2014;14(1):104.
28. Shah PL, Hansell D, Lawson PR, Reid KB, Morgan C. Pulmonary alveolar proteinosis: clinical aspects and current concepts on pathogenesis. Thorax. 2000;55(1):67–77.
29. Borie R, Danel C, Debray MP, Taille C, Dombret MC, Aubier M, Epaud R, Crestani B. Pulmonary alveolar proteinosis. Eur Respir Rev. 2011;20(120):98–107.
30. Frazier AA, Franks TJ, Cooke EO, Mohammed TL, Pugatch RD, Galvin JR. Pulmonary alveolar proteinosis. Radiographics. 2008;28(3):883–99.
31. Felker RE, Tonkin IL. Imaging of pulmonary sequestration. Am J Roentgenol. 1990;154(2):241–9.
32. Clements BS, Warner JO. Pulmonary sequestration and related congenital bronchopulmonary-vascular malformations: nomenclature and classification based on anatomical and embryological considerations. Thorax. 1987;42(6):401–8.
33. Patz EF Jr, Müller NL, Swensen SJ, Dodd LG. Congenital cystic adenomatoid malformation in adults: CT findings. J Comput Assist Tomogr. 1995;19(3):361–4.
34. Oh BJ, Lee JS, KIM JS, LIM CM, Koh Y. Congenital cystic adenomatoid malformation of the lung in adults: clinical and CT evaluation of seven patients. Respirology. 2006;11(4):496–501.
35. Lyen S, Wijesuriya S, Ngan-Soo E, Mathias H, Yeong M, Hamilton M, Manghat N. Anomalous pulmonary venous drainage: a pictorial essay with a CT focus. J Congen Cardiol. 2017;1(1):7.
36. Demos TC, Posniak HV, Pierce KL, Olson MC, Muscato M. Venous anomalies of the thorax. Am J Roentgenol. 2004;182(5):1139–50.
37. Ellis K. Fleischner lecture developmental abnormalities in the systemic blood supply to the lungs. Am J Roentgenol. 1991;156(4):669–79.
38. Zylak CJ, Eyler WR, Spizarny DL, Stone CH. Developmental lung anomalies in the adult: radiologic-pathologic correlation. Radiographics. 2002;22(suppl_1):S25–43.
39. Rodriguez-Roisin R, Krowka MJ, Herve PH, Fallon MB. Pulmonary–hepatic vascular disorders (PHD). Eur Respir J. 2004;24(5):861–80.
40. Fritz JS, Fallon MB, Kawut SM. Pulmonary vascular complications of liver disease. Am J Respir Crit Care Med. 2013;187(2):133–43.
41. Lee KN, Lee HJ, Shin WW, Webb WR. Hypoxemia and liver cirrhosis (hepatopulmonary syndrome) in eight patients: comparison of the central and peripheral pulmonary vasculature. Radiology. 1999;211(2):549–53.
42. Chawla A, Gaikwad V, Dubey N, Bosco J. CT pulmonary angiography features of a hepatopulmonary syndrome. Korean J Radiol. 2015;16(4):951.
43. Kim YK, Kim Y, Shim SS. Thoracic complications of liver cirrhosis: radiologic findings. Radiographics. 2009;29(3):825–37.
44. Brun AL, Touitou-Gottenberg D, Haroche J, Toledano D, Cluzel P, Beigelman-Aubry C, Piette JC, Amoura Z, Grenier PA. Erdheim-Chester disease: CT findings of thoracic involvement. Eur Radiol. 2010;20(11):2579–87.9999.
45. Ananthakrishnan L, Sharma N, Kanne JP. Wegener's granulomatosis in the chest: high-resolution CT findings. Am J Roentgenol. 2009;192(3):676–82.
46. Martinez F, Chung JH, Digumarthy SR, Kanne JP, Abbott GF, Shepard JA, Mark EJ, Sharma A. Common and uncommon manifestations of Wegener granulomatosis at chest CT: radiologic-pathologic correlation. Radiographics. 2011;32(1):51–69.